NUKLEAR MALAYSIA

Individual R&D Contribution Review IRCR



# Individual Research Contribution Review 2024
# Malaysian Nuclear Agency
# Research and Development Programme

(The front cover is a slice of 3D neutron tomographic image of a fake fossilized spider)

eISSN 3083-922X

**EDITORIAL BOARDS**

**Patron**
Rosli Darmawan, Ph.D

**Chief Editor**
Muhammad Rawi Mohamed Zin, Ph.D

**Overleaf LaTeX Editors**
Nik Arlina Nik Ali
Fairuz Faisal
Nor Dalila binti Desa
Mark Dennis Anak Usang, Ph.D
Wan Dalila binti Wan Chik, Ph.D

Publishing Office
Research Management Centre
Malaysian Nuclear Agency, Bangi,
43000 Kajang, Selangor Darul Ehsan,
MALAYSIA
Tel : +6 03 8911 2000
Fax : +6 03 8911 2154

Website
http://www.nuclearmalaysia.gov.my

**FOREWARD**

Thank you to all Research Officers who contributed articles for this IRCR 2024 issue. IRCR 2024 is an extended abstract that is printed electronically online for the 2nd time. Each article is a summary of research activities conducted by each researcher in 2024. The data and research results reported are divided into eight sectors, namely Agrotechnology and Biosciences, Medical Technology, Radiation Processing Technology, Radiation Health and Safety, Technical Support, Waste Technology and Environmental, Industrial Technology and Strategic Management.

These sectors are in line with the main sectors in the National Nuclear Technology Policy 2030. The objective of IRCR is as a space for researchers to disseminate research information and results to readers consisting of academics, researchers, industry and so on. Thus, it can attract the interest of stakeholders to establish Collaboration with researchers at the Malaysian Nuclear Agency.

The collaboration that can be established depends on the status of the research results, namely whether at the basic research or applied research level or at the product level that can be commercialized and fully used. Thank you to all readers and contributors to the articles in this issue of IRCR 2024. Thank you again for your cooperation and support. Happy reading!

Rosli Bin Darmawan, PhD
Director General,
Malaysian Nuclear Agency,
Ministry of Science, Technology and Innovation

Printed in Malaysia
All rights reserved by Nuclear Malaysia
Copyright ©2024 Nuclear Malaysia
Reproduction without permission is prohibited

This publication is issued by Nuclear Malaysia on a yearly basis. Inquiries about availability and/or copyright of the contents in this publication should be address to Research Management Center, Malaysian Nuclear Agency.

# Contents

**Research Articles**

**Agrotechnology and Biosciences**

Distinctiveness, Uniformity and Stability (DUS) Assesstment of Kenaf Mutant Lines Generated Through Mutation Breeding . . . . . 1
*Affrida Abu Hassan*

Greenhouse Gases Emission and Mitigation Under Climate Smart Agricultural Practices in Rice Ecosystem Using Direct Analytical and Stable Isotope Techniques (NM-R&D-22-115) . . . . . 3
*Ahmad Nazrul Abd Wahid*

Investigation of 3 MeV Electron Beam Dose Depth Penetration in Food Paste using Radiochromic Film . . . . . 5
*Ahmad Zainuri Mohd Dzomir*

Minimum Inhibitory Concentration (MIC) of $\gamma$-Synthesised Silver Nanoparticles Against Dickeya zeae . . . . . 7
*Anis Nadia Mohd Faisol Mahadeven*

Morphological and Molecular Identifications of Fungi Isolated From Rice Advanced Mutant lines . . . . . 9
*Asma Aris*

Preliminary Study on the Enhancement of Lignocellulose-Degrading Fungi for Cellulolytic Agrowaste Recycling via Gamma Radiation . . . . . 11
*Azhar Mohamad*

Improving the Acid Sulphate Soil Attributes with Application of Biochar and Urea Deep Placement Technique for Extended Abstracts . . . . . 13
*Azilah Binti Abdul Malek*

Rapid Generation Cycling In Tomato . . . . . 15
*Chong Saw Peng*

Radiosensitivity Study of Early Maturity Malaysian Mega Rice Cultivar MR220CL2 Using Ion Beam Irradiation . . . . . 17
*Faiz Ahmad*

Generation of PHA by Azotobacter vinelandi from Raw (Untreated) Palm Oil Mill Effluent . . . . . 19
*Liew Woan Ying Pauline*

Aerial Multispectral Imaging: NDT Technique for Precision Agriculture . . . . . 21

*Mohamad Syafiq bin Mohd Amin*

Soil Water Content using Nuclear Technique . . . . . 23
*Mohamad Syafiq bin Mohd Amin*

Detection of Pantoea ananatis causing Bacterial Leaf Blight (BLB) of Rice in Kedah and Selangor using Species-Specific PCR Assays . . . . . 25
*Mohammad Malek Faizal Azizi*

Detecting Food Fraud in Malaysian Tiger Prawn Using Nuclear Technology and Related Techniques . . . . . 27
*Mohd Noor Hidayat Adenan*

Effects of Chronic Gamma Irradiation on Cassava Var. Ubi Kuning . . . . . 29
*Muniroh Md Saad*

Gamma-Irradiation Response of Cassava (Var. Ubi Kuning) . . . . . 31
*Mustapha Akil*

RISE Project: Development of Protocol for Large-Scale Micropropagation of Banana var. Pisang Tanduk . . . . . 33
*Norazlina Noordin*

Harnessing Stable Isotope Technology for Halal Meat Authentication and Traceability: Ensuring Integrity from Farm to Fork . . . . . 35
*Nur Hafizati Abdul Halim*

Evaluation of Methods for Homogenization of Freeze-dried Broiler Chicken Meat (pectoralis major muscle) Sample for Stable Isotope Ratio Analysis . . . . . 37
*Nur Humaira' Lau Abdullah*

Developing Laboratory Scale Rearing of Cocoa Pod Borer Conopomorpha cramerella (Snellen) (Lepidoptera: Gracillariidae) . . . . . 39
*Nur Siti Aisyah Zarimin*

Preliminary Evaluation of the Application of Fourier Transform InfraRed (FTIR) Spectroscopy for the Analysis of Halal Food . . . . . 41
*Nurul Elma binti Sabri*

Development of Gamma Radiation-Induced Silica-Solubilizing Bacteria (SSB) for Sustainable Agriculture . . . . . 43
*Phua Choo Kwai Hoe*

Photostimulated Luminescence (PSL) Technique For Detecting Selected Irradiated Dried Foods . . . . . 45
*Ros Anita Ahmad Ramli*

Application Of Nuclear Technology In Extending Storage Time Of Selected Perishable Food Products . . . . . 47
*Seri Chempaka Bt. Mohd. Yusof*

Radiosensitivity and Morphology of Chili Plants After Acute Gamma Irradiation . . . . 49
*Shakinah Salleh*

Study of Soil Management and Nutrient Requirement For Harumanis Mango Using Remote Sensing and Nuclear Technology . . . . . 51

*Shyful Azizi bin Abdul Rahman*

Biochemical and Transcriptomic Analysis of Disease Resistance and Early- Maturity Related Genes in NMR-191 and NMR-192 Rice Mutant Lines . . . . . 53
*Sobri Hussein*

Whole Genome Sequencing and Genetic Analysis of An Advanced Rice Mutant Line (NMR191) with Blast Resistance and Early Maturity Traits . . . . . 55
*Wan Dalila Wan Chik*

Assessing Nutritive Values of M1V5 Napier Grass Mutant Lines Generated from Gamma Irradiation . . . . . 57
*Zaiton Ahmad*

**Medical Technology**

Pre-Clinical Assessment Of $^{99m}$Tc-DTPA Kit For Renal Scintigraphy . . . . . 59
*Anee Suryani Sued*

Development and Physicochemical Characterization Of A Biodegradable Microspheres Formulation Loaded With Samarium-153 And Doxorubicin For Chemoradioembolization Of Liver Tumours . . . . . 61
*Azahari Kasbollah*

QPCR-Based Validation of Coxiella Burnetii Culturing in Vero Cells: Detection of IS1111 and ICD Genes . . . . . 63
*Daryl Jesus Arapoc*

Potential Radioprotective Effects of Polygonum Minus Methanol Extract through Antioxidant and Free Radical Scavenging Activities . . . . . 65
*Fazliana Mohd Saaya*

Pre-Treatment With Rnase A In Cytokinesis Block Micronucleus Assay For Analysis Using Automated System . . . . . 67
*Juliana Mahamad Napiah*

Ensuring Safety And Efficiency In The R&D Of Chromium-51 EDTA: Addressing Vapour Concerns And Handling Improvements . . . . . 69
*Muhammad Hanaffi Bin Mohamad Mokhtar*

Dosimetry Analysis: Analyzing Astatine-211 (At-211) Dose Distribution with PHITS Data and Convolution Kernel Implementation in Python . . . . . 71
*Nadhirah Razanah Shahrol*

Instant Kit For Rapid Production Of 68GA-DOTANOC Radiopharmaceutical . . . . . 73
*Ng Yen*

Preliminary Quality Evaluation of Radiopharmaceutical-Grade Zoledronic Acid Kits . 75
*Ng Yen*

Impact of Fetal Bovine Serum (FBS) on Dicentric Chromosome Assay in Increasing the Number of Cells and Improving the Size of Chromosome from the Cells Harvest . . . . . 77
*Nurul Nazeerah Juarimi*

Quality Control On Sodium Iodide (I-131) Capsule Produced By Agensi Nuklear Malaysia . . . . . 79

*Rahimah Abdul Rahim*

NMR Spectroscopic Characterization of 3-(4-methylphenyl)-1-(3-methylphenyl) prop-2-en-1-one Synthesized via Claisen-Schmidt Condensation . . . . . 81
*Rosniza Razali*

Stability Study and the Effect of Different Raw Material Handling Conditions on Stannous (II) Chloride Content of Sterile and Pyrogen Free Lyophilised DMSA Cold Kit . . . . . 83
*Saifullizan Mohamad*

Conjugation, Radiolabeling, and Purification of $^{68}$Ga-NOTA-Rituximab: A Step Toward Radioimmunotherapy (RIT) . . . . . 85
*Siti Aminah Muhamad*

Schiff Based Manganese Nanoparticles (MN-L2) As Radiosensitizer On Neutron Therapy Against Breast Cancer Cell . . . . . 87
*Siti Selina Abdul Hamid*

Functionalization Of Gold Nanoparticles with Irradiated Chitosan ($^{68}$Ga-DOTA-CHITOSAN-AuNPs) For Tumor Imaging . . . . . 89
*Wan Hamirul Bahrin Wan Kamal*

Exploring the Potential of Gamma Irradiation for Effective Newcastle Disease Virus (NDV) Inactivation . . . . . 91
*Zainah Adam*

**Radiation Processing Technology**

Physicochemistry Studies on Irradiation-Induced Biochar Recovery from Empty Fruit Bunch via Microwave Pyrolysis . . . . . 93
*Ahmad Zuhdi Mohd On*

Innovative UV-Blocking Packaging Materials Derived from Banana Peel Waste Using Radiation Crosslinkings . . . . . 95
*Farah Fadzehah Hilmi*

FLOODCOM: Floating Flood Disaster Command Center . . . . . 97
*Khairil Nor Kamal Umar*

Synthesis and Properties of Waterborne Polyurethane Acrylate (WPUA) Dispersions: A Comparative Study of PPG and Palm Oil-Based Polyol . . . . . 99
*Khairul Azhar Abdul Halim*

Electron Beam Irradiation Induced Degradation Mixture of Diclofenac, Gliclazide, Metformin and Amlodipine in STP Effluent . . . . . 101
*Khomsaton Abu Bakar*

Chemical composition and morphology observation of cellulose from sago pith waste 103
*Mahathir Mohamed*

Polyethylene Glycol Diacrylate/ Epoxidized Palm Oil Acrylate by Stereolithography 3D Printing for Tissue Scaffold Application . . . . . 105
*Marina Talib*

Molecular Weight Effects of Gamma-Irradiated $\kappa$-Carrageenan on Plant Growth Enhancement . . . . . 107

*Maznah Binti Mahmud*

Analysis of PE Irradiation Tubes for High-Performance PTS and RR Systems in PUSPATI TRIGA Research Reactor . . . . . 109
*Mohammed Iqbal bin Shueb*

Characterization of Recycled Electron Beam Irradiated Polyethylene terephthalate (PET) flakes for Potential Synthesis of Carbon Nanomaterials as Functional Fillers for Radiation Curable Radon Mitigation Coating and Antiviral Coating . . 111
*Mohd Hamzah Harun*

The Effects of Gel Content and Swelling Ratio of Irradiation and Chemically Crosslinked Optimized Plasticized Gelatin Biopolymer Films . . . . . 113
*Mohd Shahrulnizam Ahmad*

X-ray diffraction (XRD) analysis for Graphene Oxide as Corrosion Agent Preventive In POBUA . . . . . 115
*Mohd Sofian Alias*

Gamma-Induced Synthesis of Silver Nanoparticles . . . . . 117
*Mohd Yusof Hamzah*

Gamma Radiation-Induced Synthesis of Tin Oxide (SnO2) Nanoparticles: Investigating Concentration and Dose-Dependent Yield for Scalable Production . . . . 119
*Muhammad Aidell Amir*

Determination of Factor Influence on Irradiated Waste Polyethylene Terephthalate (PET) as a Filler for Construction Material . . . . . 121
*Muhammad Hazim Muhammad Sayuti*

The Effectiveness of Ultraviolet Germicidal Irradiation (UVGI) in Eradicating the Fomite Transmission ESKAPE Pathogen . . . . . 123
*Naurah Mat Isa*

Thermogravimetric Analysis of Electron Beam-Irradiated Polypropylene waste . . . . 125
*Noora'tiqah Mohamad Fauzi*

Case study assessment of microplastic pollution on agricultural soil in Malaysia . . . 127
*Nor Azwin Shukri*

A Dual Approach: Super Water Absorbents and Plant Growth Promoters on Vegetable Crop Performance . . . . . 129
*Norhashidah Talip*

Performance of Radiation-Induced Grafted Polyethylene (PE) Filter Cartridges as Adsorbent for Heavy Metal Removal . . . . . 131
*Norliza Ishak*

Thermal Properties of Repetitive Hot Compression Cycle in Plasticized PVC . . . . . 133
*Norshafarina Ismail*

Chemical composition and morphology observation of cellulose from sago pith waste 135
*Norzita Yacob*

Investigation of mechanical properties of self-healing coating based on jatropha oil resin . . . . . 137

*Nurul Huda Mudri*

Study on The Stability of TPE With Silica Using Various Mixing Method . . . . . 139
*Pairu bin Ibrahim*

Performance Evaluation of Palm Oil-Based UV Curable Coatings for Diverse Environmental Applications . . . . . 141
*Rida Tajau*

Characteristics of treated shrimp shells for agricultural component . . . . . 143
*Sarada Idris*

Preliminary study on gamma irradiation-aided treated shrimp shell as soil conditioner 145
*Sarada Idris*

Preparation of an adsorptive membrane of polyvinylidene fluoride incorporated functionalized boron nitride nanosheets for arsenic removal . . . . . 147
*Sarala Selambakkannu*

Effect of Radiation Sensitizer on the Friction Behaviour of Electron Beam cured FKM-PTFE Composite . . . . . 149
*Sivanesan Appadu*

**Radiation Health and Safety**

PGEC-18 Participant Dosimetry Report: Monthly Analysis for August 2024 . . . . . 151
*Ahmad Bazlie Bin Abdul Kadir*

Enhancing Safety Culture Practice through Conducting Safety Culture Self-Assessment Based on IAEA Guidelines . . . . . 153
*Andy Kong Shin Shyen*

Comparison of air kerma measurements between Medical Physics Laboratory (MPL) and the IAEA Dosimetry Laboratory for X-radiation qualities used in general diagnostic radiology . . . . . 155
*Asmaliza Hashim*

Radiological and Nuclear Emergencies Exercise at Malaysia Nuclear Agency . . . . . 157
*Azimawati binti Ahmad*

Flexi Rad Joint Compound as Architectural Radiation Shielding Materials . . . . . 159
*Azuhar bin Ripin*

Radon Concentration in Hot Springs of Peninsular Malaysia . . . . . 161
*Faizal Azrin Bin Abdul Razalim*

Dose Mapping of OB-Servo Ignis Gamma Irradiator . . . . . 163
*Hasan bin Sham*

Monitoring Radiation in Working Area: Annual Dose Trend in Selected Facility Within Malaysia Nuclear Agency from 2020 to 2023 . . . . . 165
*Hasbi Husein Bin Sulkifli*

Self-Assessment of Nuclear Security Culture in Malaysian Nuclear Agency . . . . . 167
*Hasfazilah binti Hassan*

Remediation of Contaminated Norm Site . . . . . 169

*Khairuddin Mohamad Kontol*

Strengthening Emergency Preparedness And Response In Malaysian Nuclear Agency 171
*Mohd Fazlie bin Abdul Rashid*

Development of Comprehensive Safety Analysis Report for the JS10000 Gamma Irradiator: Design, Risk Assessment and Regulatory Compliance Based on IAEA Guidelines (Technical Cooperation IAEA MAL 9019) . . . . . 173
*Mohd Khairul Azfar Bin Ramli*

Quality Control in Mammography System: HVL and Image Quality Test . . . . . 175
*Mohd Khalid Matori*

Radiation Metrology Group (KMS); Technical Service Achievements Throughout Its Establishment . . . . . 177
*Mohd Khalid Matori*

Validation of The Current Measurement for FAC-LO2 Free Air Chamber in Low-Energy X-Ray . . . . . 179
*Mohd Taufik Bin Dolah*

Evaluation of Nuclear Security Architecture Design Training Workshop . . . . . 181
*Muhamad Zahidee Taat*

Online Permit to Work Process: Transition from Manual to Digital . . . . . 183
*Muhamad Zahidee Taat*

Radiation Safety Assessment for Consumer Products . . . . . 185
*Noor Ezati Shuib*

Assessing Wholebody Counting Accuracy for Internal Dosimetry . . . . . 187
*Noor Fadilla binti Ismail*

Comparison of Dose-Response and Performance Between OSL Reader in Secondary Standard Dosimetry Laboratories (SSDL), Malaysia Nuclear Agency (MNA) & Nuclear Medicine Department, National Cancer Institute (NCI) . . . . . 189
*Noor Fatin Shuhada Binti Ab Hamid*

Preliminary study on lens of eye dose measurement using head phantom and nanodots 191
*Norriza Mohd Isa*

Determination of the Need for Internal Exposure Monitoring of Radiation Workers . . 193
*Nur Khairunisa Zahidi*

Estimates of Collective Dose due to the Discharging of Radioactive Substances to the Environment using IAEA Generic Model . . . . . 195
*Raymond Yapp Tze Loong*

Radiofrequency Electromagnetic Field (RF- EMF) Exposure Assessment For Occupational Workers of Telco Industry in Malaysia . . . . . 197
*Roha Binti Tukimin*

Performance Characteristics of Nanodot Optically Stimulated Luminescence Dosimeter (OSLD) . . . . . 199
*Rozaimah Binti Abdul Rahim*

Navigating Laser Safety in Industrial and Medical Setting . . . . . 201

*Shamesh Raj Parthasarathy*

Occupational UVR Exposure: Case Study from A UV Disinfection System . . . . . 203
*Shamesh Raj Parthasarathy*

Roles of Radiation Protection Officer Malaysian Nuclear Agency in Supporting Global Radium-226 Management Initiative . . . . . 205
*Suzilawati Muhd Sarowi*

Occupational and Environmental Monitoring for Reactor TRIGA PUSPATI 2023 . . . 207
*Syed Asraf Fahlawi Wafa bin Syed Mohd Ghazi*

Radiation-Induced Bystander Effect: Molecular Mechanisms and Its Clinical Implications . . . . . 209
*Tengku Ahbrizal Tengku Ahmad*

Study on the accuracy of optically stimulated luminescence dosimeter (OSLDs) dose measurement using MicroStar reader calibrated for low dose diagnostic range at Nuklear Malaysia . . . . . 211
*Wan Hazlinda Binti Ismail*

Study on the Irradiance Level of Ultraviolet (UV) Radiation from Environment . . . . . 213
*Wan Syazlin Wan Yunoh*

**Technical Support**

Development of IoT Platform using Thingsboard for Nuklear Malaysia . . . . . 215
*Ahmad Adib bin Abdul Rahman*

Sustaining Cyber and ICT Security Preparedness Through Disaster Recovery Testing and Simulations . . . . . 217
*Amy Hamijah Ab. Hamid*

UV Irradiation on Coagulated Latex Film . . . . . 219
*Chai Chee Keong*

Assessment of Structural Integrity of Biological Shielding Structure at RTP . . . . . 221
*Hasniyati Md binti Md Razi*

Development of Neutron Radiography and CT(NuRCT) facility at RTP . . . . . 223
*Khairiah Yazid*

High voltage and battery charging circuits for the G2TAG RADIGMETER V2 . . . . . 225
*Lojius Lombigit*

Predicting Insider Threats for Nuclear Security: A New Method for Quantifying Personnel Trustworthiness Using a Combination of Organizational and Social Media Data . . . . . 227
*Maizura Ibrahim*

Lesson Learnt In Operating RN42 Station Located In Equatorial Doldrum Area For Stable Electrical Power Supply . . . . . 229
*Mohamad Suhaimi Yahaya*

Studying on Cost Saving After Installation of Solar PV in Complex Bangi Malaysian Nuclear Agency . . . . . 231
*Mohamad Suhaimi Yahaya*

Monte Carlo Studies on Depth Penetration of the Low Energy Electron Accelerator using PHITS in Difference Distance of PTFE Material . . . . . 233
*Mohd Azhar Ahmad*

Development of Rogowski Coil Diagnostics for the MNA Plasma Focus and Characterization of Its Focus Mode . . . . . 235
*Mohd Faiz Bin Mohd Zin*

Preliminary Study on the Relationship Between Be-7 Concentration and Northeast Monsoon Dynamics: Insights from Indices of Monsoon Activity . . . . . 237
*Mohd Fauzi Haris*

Dust Collector System Design Consideration for Analytical Chemistry Application Group (ACA) . . . . . 239
*Mohd Rizal Mamat bin Ibrahim*

Review on Slam Methods for Unmanned Ground Vehicle Autonomous Mapping . . . 241
*Mohd Shafiq Bin Sazali*

Comparative Analysis of Commercial Robots for Radiation Mapping . . . . . 243
*Muhammad Izzuan bin Mohd Ghazali*

Wireless Transmission of Radiation Pulse Data Using NRF24L01 Modules . . . . . 245
*Nabilah Ramli*

Probabilistic Framework for Radiation Source Localization and Anomaly Detection Using Gaussian Mixture Models . . . . . 247
*Nolida Yussup*

Real-Time IoT-Based Temperature Monitoring System for High Purity Germanium (HPGe) Detectors . . . . . 249
*Noor Farhana Husna A. Aziz*

Energy Dependence Evaluation from Model 001 of G2Tag Radig Meter . . . . . 251
*Nor Arymaswati Abdullah*

Computational Modeling of Neutron Flux for Boron Neutron Capture Therapy Applications . . . . . 253
*Norfarizan Mohd Said*

Migration of the AMoRA Algorithm Implementation from ROS1 to ROS2 . . . . . 255
*Nur Aira binti Abd Rahman*

Study of Existing Shielding for Malaysian Nuclear Agency - Dense Plasma Focus (MNA-PF) using Monte Carlo PHITS . . . . . 257
*Puteri Nuraliah Husna binti Mohd Tajuddin*

Gel Content and Hot Set Test as Main Requirements for Heat Shrink Tube Irradiation at ALURTRON . . . . . 259
*Ruzalina Baharin*

Ageing Management of EPS-3000 . . . . . 261
*Shalina Sheik Muhamad*

Effect of Hydroxyacetone On Mechanical Properties of Hybrid Ultraviolet-Peroxide Prevulcanized Natural Rubber Latex . . . . . 263

*Sofian Ibrahim*

Ludlum 44-7 HV Plateau Analysis Through Responding with SR-90 . . . . . 265
*Syirrazie Shaari*

Dose Mapping Process of Old Books for Cultural Heritage Preservation at Sinagama 267
*Syuhada Ramli*

Surface Analysis of Silicon Dioxide Thermally Grown on Atomically Flat Silicon Surface at Different Oxidation Time . . . . . 269
*Umi Zulaikha Mohd Azmi*

**Waste Technology and Environmental**

Comparison of Uranium $^{238}$U and Thorium $^{232}$Th Isotopes in Minerals from Two Industrial Sources . . . . . 271
*Azian Hashim*

Radiological Impact of Natural Radioactivity in Malaysian Building Bricks . . . . . 273
*Engku Mohd Fahmi Engku Chik*

Post-closure Safety Assessment Calculation Using AFRY Intelligent Scenario Modeling (AISM) for Borehole Disposal in Malaysia . . . . . 275
*Esther Phillip*

Development of a Predictive Model for Terrestrial Gamma Radiation Based on Weathered Soil and Rock Characteristics in Sarawak, Malaysia . . . . . 277
*Hairul Nizam Idris*

The depth distribution of Beryllium-7 in different land uses study . . . . . 279
*Jalal Bin SharibSarip*

Seepage Water Study in Pedu Dam, Kedah . . . . . 281
*Jeremy Andy Anak Dominic Daung*

Groundwater potential investigation using resistivity imaging and isotope hydrology at Universiti Malaysia Sabah Campus, Sabah . . . . . 283
*Lakam Anak Mejus*

Distribution of Rare Earth Elements (REEs) Concentration in Soil Samples from Kapar Industrial Area . . . . . 285
*Md Suhaimi Elias*

Radon in Water as a Tracer to Identify Connection Between Surface Water and Groundwater in Melaka River Basin . . . . . 287
*Mohamad Syahiran Bin Mustaffa*

Distribution of Natural Radionuclide Radioactivity in soil near Kuala Selangor Nature Park (KSNP), Selangor . . . . . 289
*Mohd Izwan Bin Abdul Adziz*

Application of 2-D geoelectrical resistivity tomography for subsurface geological investigation at Blok 33, Malaysian Nuclear Agency . . . . . 291
*Mohd Muzamil Bin Mohd Hashim*

Global Radium-226 Management Initiative . . . . . 293
*Mohd Zaidi Ibrahim*

LEXSYG SMART- Thermoluminescence Optically Stimulated Luminescence (TL OSL) Reader At Nuclear Dating Laboratory, Malaysia Nuclear Agency . . . . . 295
*Mohd Zuhair bin Mohd Sanusi*

Assessment of Heavy Metal and Toxic Elements in Industrial Zones in Nilai 3 . . . . . 297
*Muhammad Azfar Azman*

Level of Cadmium (Cd) in Clam Tissues from Selected Coastal Areas in Peninsular Malaysia . . . . . 299
*Munirah binti Abdul Zali*

Total and Isotope Carbon in Indigenous Rice from Kota Belud, Sabah . . . . . 301
*Nazaratul Ashifa Abdullah Salim*

Spatial Distribution of Heavy Metal and Land Use Assessment Using Fallout Radionuclides (FRNs) Technique . . . . . 303
*Nurrul Assyikeen binti Md. Jaffary*

Seasonal Variations in Elemental Concentrations in Putrajaya Constructed Wetland System: Implications for Sedimentation and Water Quality Standards . . . . . 305
*Nurul Fairuz Diyana Bahrudin*

Studies on Optimum Mix Design for Immobilization of Spent Resin from Low Level Effluent Treatment Plant (LLETP), Malaysian Nuclear Agency Using Fly Ash Based Geopolymer . . . . . 307
*Nurul Wahida Ahmad Khairuddin*

2024 Annual Report on Radioactive Waste Disposal and Inventory Management in Malaysia . . . . . 309
*Nurul Wahida Ahmad Khairuddin*

Study on Agro-contaminants Distribution in Selangor North-West Integrated Agriculture Development Area (IADA) Using Stable Isotope Approach . . . . . 311
*Roslanzairi Mostapa*

Method for quick screening $^{226}$Ra level in water samples . . . . . 313
*Yii Mei-Wo*

Comprehensive Characterization of Radioactive Source Casings Using Multi-Technique Methods for Nuclear Forensics . . . . . 315
*Zalina Laili*

**Industrial Technology**

Pioneer On Phosphate Leaching From Monazite Mineral Using Alkaline Treatment . 317
*Abdul Rahman Norazumin*

Review: Advances in PLLA/CMS/$\beta$-TCP Nanofiber Scaffolds for Biomedical Applications . . . . . 319
*Abul Adli bin Anuar*

Characterization and Silica Aerogel Performance in Solvent-based Paint . . . . . 321
*Ahmad Hambali Ismail*

Impact of Focal Spot Size on Film Image Quality by using YXLON Y.XMB 225 X-ray system: A Comparative Study . . . . . 323

*Amer Hazreq Bin Haron*

Simulating Qualitative Phased Array Ultrasonic Testing Defect Indication on Flange Face Using CIVA . . . . . 325
*Amry Amin Abas*

Emissivity Evaluation Using Thermography for Different Composites . . . . . 327
*Asyraf Arif Bin Abu Bakar*

A Preliminary Characterization of Graphene-Enhanced Aluminium: Effects on Hardness and Electrical Resistance . . . . . 329
*Azlan Shah Nerwan Shah Nintin*

In Situ Synthesis and Deposition of Palladium Nanoparticles on Gas Diffusion Layers via Gamma Radiolysis for Cathode Electrodes in Proton Exchange Membrane Fuel Cells . . . . . 331
*Choo Thye Foo*

Characterization of physico-chemical properties of gold nanoparticles . . . . . 333
*Cik Rohaida Che Hak*

Room Temperature Synthesis and Characterization of HKUST-1, Metal-Organic Frameworks (MOFs) . . . . . 335
*E. M. Mahdi*

Bibliometric Analysis of Research on Hydrometallurgy Process on Rare Earth Extraction Based on SCOPUS Database . . . . . 337
*Fazila binti Said*

Bibliometric Analysis on the Research Trends of Dust Explosions from the Year 2001 to 2023 . . . . . 339
*Fazila binti Said*

Small Angle X-ray Scattering Technique (SAXS) Analysis of BAM (Cat. Number 2005) Standard Sample . . . . . 341
*Hafizal Yazid*

Development of Gamma Densitometry Scanning System for Multiphase Column Analysis . . . . . 343
*Hanafi Ithnin*

The IAEA Technical Cooperation Project RAS1027 - Improving the Utilization of Nuclear Techniques for Cultural Heritage Characterization, Consolidation, and Preservation . . . . . 345
*Hishamuddin Husain*

Acoustic Emission Analysis of Gate Valve Performance Using Machine Learning Clustering Techniques . . . . . 347
*Ismail Bin Mustapha*

Elemental Analysia Using XRF on Rare Books . . . . . 349
*Izura Izzuddin*

Recovery of Cerium, Neodymium, Lanthanum and Thorium from Monazite . . . . . 351
*Jacqueline Kones*

Study on Neutron Flux of Different Shielding Materials at reactor TRIGA PUSPATI (RTP) . . . . . 353
*Julie Andrianny Murshidi*

Selective Precipitation and Recovery of Rare Earth Elements from Monazite Concentrate . . . . . 355
*Khaironie Mohamed Takip*

Evaluation of Radiographic Testing - Digital (RT-D) in NDT: A Comparative Analysis of Modulation Transfer Function (MTF) and Basic Spatial Resolution ($SR_b$ . . . . 357
*Khairul Anuar Mohd Salleh*

Study of Multiphase Hold-Up of Packed Bed Reactor Using Gamma Densitometry with Varying Flow Rates . . . . . 359
*Lahasen Dahing*

Collaboration Program: Capacity Development of RSA Academy Sdn. Bhd. to Implement Electromagnetism Testing Courses to Industry . . . . . 361
*Mahmood Dollah*

Burstein-Moss Effect on the Optical Properties of Zr Doped $TiO_2$ Nanorods Thin Films 363
*Masliana Muslimin*

A Study on Detection of Water Detection in Process Pipeline in Oil & Gas Plant using Neutron Backscattered Technique . . . . . 365
*Md Fakarudin Ab Rahman*

Research and Commercial Opportunities in Developing Artificial Intelligence Assisted NDT Micro-SaaS System . . . . . 367
*Megat Harun Al Rashid Megat Ahmad*

Acoustic Emission Testing on Cargo Oil Tank . . . . . 369
*Mohamad Ridzuan Ahmad*

Development of International Standard (ISO) for Residence Time Distribution (RTD) Formulation and Applications Using Industrial Radioactive Tracer . . . . . 371
*Mohd Amirul Syafiq Mohd Yunos*

Concrete Slab Detection Using Ground Penetrating Radar . . . . . 373
*Mohd Fajri Bin Osman*

Effect of Internal Gas Hold-up on Packed Bed Reactor Using Gamma Densitometry 375
*Mohd Fitri Abdul Rahman*

Development of Hybrid Nanofibers . . . . . 377
*Mohd Reusmaazran bin Yusof*

Potential Application of Laser Shearography for Analysis of Corrosion in Petroleum Pipeline . . . . . 379
*Mohd Yusnisyam Bin Yusof*

Development of Image Reconstruction and Analysis for Gamma Process Computed Tomography . . . . . 381
*Muhamad Noor Izwan Bin Ishak*

Evaluation of Impact Damage in Carbon/Carbon Composites Using Piezoelectric transducer-based Vibrothermography . . . . . 383

*M.Z. Umar*

Evaluation of Gamma Radiation Disinfection of Rare Books . . . . . 385
*Nadira Kamarudin*

Enhancing Neutron Shielding: Investigating The Absorption Properties Of Mortar With Colemanite Mineral . . . . . 387
*N.M.Azreen*

Impact of Scanning Time Delay on Radiographic Image Quality in Computed Radiography for Non-Destructive Testing . . . . . 389
*Noorhazleena Azaman*

Investigation of Process Flow inside Demineralizer Using Radiotracer Technique: A Qualitative Analysis . . . . . 391
*Noraishah Othman*

Relative Difference in Mass Attenuation Coefficient of Synthesized Glasses: XCOM Software Analysis and Experimental Lead Equivalent Testing at Makmal Fizik Perubatan Nuklear Malaysia . . . . . 393
*Nor Hayati Alias*

Fuel Cell Electrode Preparation: Transfer Efficiency and Morphology at Different Catalyst's Ink Concentrations . . . . . 395
*Norhazirah Azhar*

Removal of Inorganic Element of Rare Earth Oxalates by Preliminary Scrubbing . . . 397
*Nur Aqilah binti Sapiee*

Characterization of Cobalt Oxide Nanoparticles Prepared by Co-precipitation Method 399
*Nurazila Mat Zali*

Solvent Extraction of Cerium from Acidic Chloride Medium using Synergist Extractant 401
*Nurliana Roslan*

Tannic Acid-based Rust Inhibitor with Metal Fillers for Corrosion Protection of Mild and Low Carbon Steel . . . . . 403
*Nur Ubaidah Saidin*

Experimental Investigation of Time Domain Pulsed Eddy Current Technique on Non-Ferromagnetic Conductivity Plates . . . . . 405
*Nurul A'in Binti Ahmad Latif*

Morphology Changes of Single Crystal Silicon Electrode (100 and 111) By an Ex-Situ Operando Synchrotron Tomography Imaging . . . . . 408
*Rafhayudi Jamro*

The Utilisation of Alkaline Fusion for the Removal of Phosphates from Xenotime Minerals . . . . . 410
*Roshasnorlyza Hazan*

Image Optimization Using Predetermined Voltage and Filter on the 1172 Micro Computed Tomography (MicroCT) System . . . . . 412
*Roslan Yahya*

Development of an Electrolysis System for Rust Removal . . . . . 414

*Siti Aishah Ahmad Fuzi*

PreliminaryWork on Automated Defect Recognition for Thermography Impact Damage Defects . . . . . 416
*Siti Madiha Muhammad Amir*

Effect of the Elevated Temperatures on the Corrosion Behaviour of the Nurust-Coated Samples . . . . . 418
*Siti Radiah Mohd Kamarudin*

Effect of Heating Temperature on Properties of Titanium Dioxide Nanoparticles . . . 420
*Siti Salwa Zainal Abidin*

Development of data collection system from scaler ratemeter using open source software . . . . . 422
*Soleha Binti Mohamat Yusuff*

Preliminary Study on the Properties of Diverse TropicalWoods . . . . . 424
*Suhaila Hani Ilias*

Ultrasonic Signals Fusion Datasets for Enhanced Weld Defect Classification Using Convolutional Neural Networks Models . . . . . 426
*Suhairy bin Sani*

Ensuring Safety in Industrial Inspection: A Focus on Gamma Ray Tomography . . . . 428
*Susan Maria Sipaun*

Comparative Analysis of Yxlon Imaging Systems with Different Focal to Film Distance (FFD): 700mm vs 1010mm . . . . . 430
*Tengku Sarah Tengku Amran*

Characterization of Cerium Phosphate from Malaysian Monazite . . . . . 432
*Wilfred Paulus*

Fabrication and Characterization of Aluminium Matrix Composite Reinforced with Micro Particle Boron Carbide using Stir Casting . . . . . 434
*Zaifol Bin Samsus*

**Strategic Management**

Intellectual Property Rights : Trend and Performance . . . . . 436
*Abdul Quddoos Abu Bakar*

Management of the Quality Program at the Malaysian Nuclear Agency (Nuklear Malaysia) . . . . . 438
*Aisya Raihan bt Abdul Kadir*

Analysis of Potential Bilateral Cooperation in the Field of Nuclear Science and Technology Between Malaysian Nuclear Agency (Nuklear Malaysia) and Foreign Countries for the Year 2022-2024 . . . . . 440
*Azlinda Binti Aziz*

Nuclear Energy to Support Net-Zero Transition in Malaysia by 2050: Strategies for Success . . . . . 442
*Fairuz Suzana binti Mohd Chachuli*

Potential and Optimization of Distributed Small Modular Nuclear Reactor-Solar Photovoltaics (DSMPV) Hybrid Energy Systems in Malaysia (IAEA CRP Project Code 25174) . . . . . 444
*Fairuz Suzana binti Mohd Chachuli*

Malaysia: Advancing Research and Development on Nuclear Science and Technology through IAEA Technical Cooperation Program . . . . . 446
*Hazmimi Kasim*

Outcome Based Analysis: Budget Process vs Performance . . . . . 448
*Mohd Azmi*

CTBT National Data Centre: Roles and Function . . . . . 450
*Rozilawati Mohd Japar*

Glabellan: Advancing from Process Development and IP Protection to Product Formulation and Validation . . . . . 452
*Shaiful Azuar Mohamad*

Research Distribution and Impact: A Strategic Assessment of Malaysian Nuclear Agency's R&D Portfolio (2024) . . . . . 454
*Siti Najila Mohd Janib*

Quarter Century of Progress: Malaysia's Nuclear Technology Journey Through FNCA Collaboration . . . . . 456
*Siti Syarina Mat Salo*

Individual Research Contribution Review, 2024: 1–2
*ISSN: 3083-922X*

IRCR

# Distinctiveness, Uniformity and Stability (DUS) Assesstment of Kenaf Mutant Lines Generated Through Mutation Breeding

**Affrida Abu Hassan**
Agrotechnology and Biosciences Division, Malaysian Nuclear Agency
43000 Kajang, Selangor
affrida@nm.gov.my

## Abstract

Kenaf *Hibiscus cannabinus L.* is a fibre plant commonly used as a raw material for various industries such as paper, furniture, construction and automotive. In early 2000, it was introduced in Malaysia as part of government effort to replace tobacco nationwide. Due to its emerging use, there is a need to develop new kenaf variety with improved agronomic traits. In collaboration with the National Kenaf and Tobacco Board (NKTB), development of new variety was carried out using gamma irradiation to induce genetic mutation in Kenaf V36 variety. 30 potential lines have been selected and evaluation of agronomic traits of these promising lines was carried out in 2022. From this, a total of 13 potential mutant lines and 2 mutant hybrids were further tested in the field for distinctiveness, uniformity and stability (DUS) test. This paper discusses the morphological traits distinctiveness, uniformity and stability of these potential mutant lines. Based on the observation and findings, these mutant lines have the potential to be registered as new varieties and introduced as new planting materials for kenaf in Malaysia.

**Keywords:** Kenaf, *Hibiscus cannabinus L.*, mutation breeding, DUS

## 1 Introduction

Kenaf *Hibiscus cannabinus L.* is originated from Africa and belongs to Malvaceae family. It is an herbaceous annual plant and usually planted for fiber (LeMahieu, 2003). The fibre is one of the important sources of raw materials for the traditional production of rope, canvas and carpet. In 2000, the Malaysian government has decided to replace domestic tobacco cultivation with kenaf, introducing a new agricultural commodity to the nation (Basri et al., 2014). As a result of this shift and the emerging interest, many researches on kenaf have been actively carried out in Malaysia, mainly in the aspects of screening of suitable varieties adaptable to local weather, development of good agronomic practices, mechanization of planting and harvesting processes. In collaboration with the National Kenaf and Tobacco Board (NKTB), Nuclear Malaysia has carried out research on development of new Kenaf variety with improved characteristics using gamma irradiation to induce genetic mutation in Kenaf V36 variety. 30 potential lines have been selected and evaluation of agronomic traits of these promising lines was carried out in 2022. From this, a total of 13 mutant lines and 2 mutant hybrids has the potential with improved traits and further tested in the field for distinctiveness, uniformity and stability (DUS) test. The DUS test will be discussed in this paper. It is hope that some of these potential mutant lines will pass the DUS test and consequently registered for the Registration of New Plant Varieties and the Granting of Breeder's Rights under the Protection of New Plant Varieties Act 2004, used commercially.

## 2 Methods

### 2.1 Plant Materials

13 mutant lines and 2 hybrids including the control (Variety: V36) were used and obtained from Nuclear Malaysia's seed collection. The details of the samples with its traits is as listed in Table 1.

### 2.2 Field Planting of Mutant Lines

The field planting was carried out at the NKTB's field plot at Chuping, Perlis. The soil type of the plot was sandy loam and the climatic condition during this period was hot and humid. Seed sowing was done by NKTB Perlis. The plants were allowed to grow on the nursery trays for about 10 days before being transferred to the plot. Irrigation was done manually twice a day. Fertilizer, herbicide and pesticide treatments were carried out according to NKTB's standard practice (Lembaga Kenaf Dan Tembakau Negara, 2013).

| No. | Mutant | Dose (Gy) | Irradiation | Character |
|---|---|---|---|---|
| 1 | ML5 | 300 | Acute | High fiber, palmate leaves |
| 2 | ML9 | 300 | Acute | High fiber |
| 3 | ML10 | 300 | Acute | High fiber |
| 4 | 36-3 | 300 | Acute | High fiber |
| 5 | 36-8 | 300 | Acute | High fiber |
| 6 | 36-11 | 300 | Acute | High fiber |
| 7 | 36-20 | 800 | Acute | High fiber |
| 8 | 36-10 | 300 | Acute | High fiber, fast grow |
| 9 | 36-21 | 800 | Acute | High fiber, high seed pods |
| 10 | 36-24 | 1300 | Acute | High fiber |
| 11 | 36-25 | 1300 | Acute | High fiber |
| 12 | 36-27 | 1300 | Acute | High fiber, fast grow |
| 13 | ML Ring 4 | 230 | Chronic | High fiber, fast grow |
| 14 | ML36-25 × LR4P2 | - | - | Tall plant |
| 15 | ML36-24 × BJR1 | - | - | Tall plant |
| 16 | V36 | 0 | NA | Control |

Table 1: List of 13 mutant lines, 2 hybrids, and 1 control variety (V36).

### 2.3 Agronomic Characterization of Mutant Lines

The agronomic data collected during the harvesting period; (i) plant height (cm), (ii) bast fibre weight (g), (iii) basal and middle stem diameter (mm), (iv) number of pods per plant, (v) leaf morphology, (vi) flower morphology and (vii) percentage of seed maturity. The characters for the mutant lines were analyzed and compared with the control.

## 3 Results and discussion

Unexpected weather change in Perlis, particularly the prolonged dry spells and extreme heat, have had a significant impact on the growth of the plants at the test plot. Kenaf, a fast-growing fiber crop, thrives in warm and humid conditions. The unforseen climate conditions have created a challenging environment and a complete data was not able to be collected. However, only the morphological data for leaf shape ware collected as shown in Figure 1. All of the mutant lines and hybrids sustained its leaf shape. ML5 has produced and maintained its palmate characteristic of the leaf shape. The test will be repeated in order to obtain a comprehensive data.

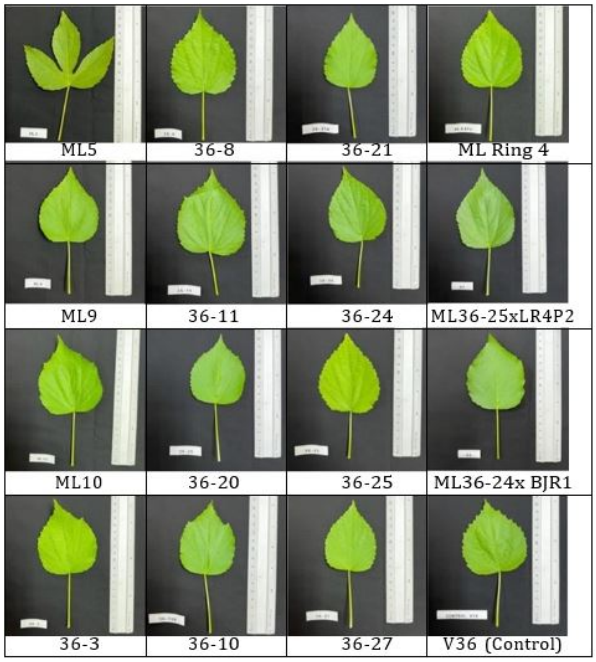



Figure 1: The morphological data of leaf shape in all potential lines.

## 4 Conclusions

A complete morphological and agronomic data on kenaf mutant lines was not obtained due to unexpected weather change that affected growth of the plants However, planting trial for another two seasons will be carried out simultaneously at Chuping and Baseri Plot. Five best lines will be setected and the data will be used to register these mutant lines.

## References

M.H.A. Basri, A. Abdu, N. Junejo, H.A. Hamid, and K. Ahmed. 2014. Journey of kenaf in malaysia: A review. *Scientific Research and Essays*, 9(11):458–470.

E.S. Putnam D.H. LeMahieu, P.J. Oplinger. 2003. Kenaf. alternative field crops manual. *http://www.corn.agronomy.wisc.edu/FISC/Alternatives/Kenaf*.

Individual Research Contribution Review, 2024: 3–4
*ISSN: 3083-922X*

# Greenhouse Gases Emission and Mitigation Under Climate Smart Agricultural Practices in Rice Ecosystem Using Direct Analytical and Stable Isotope Techniques (NM-R&D-22-115)

**Ahmad Nazrul Abd Wahid**
Agrotechnology and Biosciences Division, Malaysian Nuclear Agency
43000 Kajang, Selangor
a_nazrul@nm.gov.my

## Abstract

This project was initiated in 2023 with the aim to evaluate greenhouse gas (GHGs) emissions and find mitigation measures for GHGs emission reduction through climate-smart agricultural practices in the rice crop ecosystem. In this project, several practices such as alternate wetting and drying irrigation (AWD), biochar application, and optimal nitrogen fertilizer application will be implemented to reduce the emissions of methane ($CH_4$), carbon dioxide ($CO_2$), and nitrous oxide ($N_2O$). This project also aims to develop several related SOPs and establish a new and efficient method for GHGs sampling and measurement in the field using direct analytical techniques.

**Keywords:** Greenhouse Gases, Alternate Wetting and Drying, Biochar, Nitrogen Optimization

## 1 Introduction

In the agricultural sector, rice covers 11% of the world's arable land and is responsible for 10.1% of total agricultural emissions and approximately 1.3%–1.8% of global anthropogenic GHG emissions (Meijide et al., 2017). Rice cultivation contributes to global climate change through the release of $CH_4$, $CO_2$, and $N_2O$ gases into the atmosphere. Rice fields act as sources of $CH_4$ and $N_2O$ emissions depending on soil organic matter status, land management, cropping intensity, irrigation and drainage, fertilizer management, soil microbial population and activity, and soil properties (Wang et al., 2017). In Malaysia, GHG emissions have been increasing yearly over the past decade, likely due to excessive fertilizer use and inefficient water and soil management.

Malaysia aims to reduce the intensity of GHG emissions across the economy by 40% based on Gross Domestic Product (GDP) by 2030. The former Prime Minister, Dato' Seri Ismail Sabri Yaakob, stated that the reduction in intensity was unconditional and 10% higher than the previous target. The current Prime Minister, Dato' Seri Anwar Ibrahim, also stated that Malaysia needs to reduce $CH_4$ production by 40% by 2023. Climate change has negatively impacted the country and the national economy, highlighting the need for high-performing varieties suitable for local conditions, especially in terms of biomass yield.

Nuclear Malaysia is taking the initiative to support the National Climate Change Policy, the National Agrofood Policy 2021–2030 (NAP 2.0), and the Sustainable Development Goals (SDGs). A study on climate-smart agricultural practices, focusing on soil, water, and nutrition management in rice ecosystems, will be conducted. Greenhouse gas measurements will be performed using modern methods, including direct measurement equipment such as the Laser Spectrometer and LSE $N_2O$-4405 Analyzer. Stable isotope techniques at enriched and natural abundance levels will be used to quantify fertilizer use efficiency, biological nitrogen fixation, and GHG source identification.

This project also includes collaboration with the Malaysian Department of Agriculture under project NM-DOA-24-5, with field sites at Sungai Burong, Selangor, and Sungai Balang, Johor.

## 2 Materials and Methods

### 2.1 Field Preparation

Studies were conducted at the Nuclear Malaysia Rice Research and Breeding Site, established in 2021. Collaborative research sites are located at the BPIT paddy plot in Sungai Burong, Selangor, and Sungai Balang, Johor.

### 2.2 GHGs Sampling and Measurement

#### 2.2.1 GHGs Sampling

At Nuclear Malaysia Rice Plot, a stainless steel closed chamber is used to trap GHGs. The chamber septum connects via a 3-way stopcock to the Laser Spectrometer and LSE Analyzer using Teflon tubing. A distributor system with a sampling control panel enables simultaneous readings of $CH_4$, $CO_2$, and $N_2O$.

#### 2.2.2 GHGs Measurement

At field locations (e.g., Sungai Burong and Sungai Balang), stainless steel chambers are used to trap GHGs. The chambers connect via a 3-way stopcock to a mobile $CH_4$ and $CO_2$ Analyzer (LICOR 7810) through Teflon tubing for direct field measurement.

### 2.3 Climate-Smart Agricultural Practices

#### 2.3.1 Alternate Wetting and Drying (AWD)

A PVC tube is used to monitor water depth. After irrigation, the water level drops due to evapotranspiration and percolation. When the level reaches 15 cm below the soil surface, irrigation is reapplied to a depth of 5 cm. Fields remain flooded during flowering. Post-flowering, the water level is allowed to drop again to 15 cm below the surface before re-irrigation.

#### 2.3.2 Biochar Application

Crushed charcoal wood is used as a soil amendment. Biochar is applied using top dressing one week before watering and planting.

#### 2.3.3 Optimum Nitrogen Fertilizer Application

Optimal nitrogen use is evaluated using isotope tracer techniques. Urea with 5% atom excess is used, and microplots differentiate normal vs. isotope-labeled applications. NUE data are fitted to the Mitscherlich crop response model to determine optimal fertilizer rates.

## 3 Results and Discussion

| **Treatments** | **Cumulative $CH_4$ (kg/ha)** | **Cumulative $CO_2$ (kg/ha)** | **GWP (kg $CO_2$ eq/ha)** |
|---|---|---|---|
| Continuous Flooding | 27.53 | 767.95 | 1533.63 |
| AWD | 16.36 | 757.19 | 1215.77 |
| Biochar | 20.56 | 820.42 | 1392.42 |
| N rates (60N) | 20.34 | 600.92 | 1166.57 |

Table 1: Impact of different treatments on GHG emissions in rice cultivation.

For CF treatment, cumulative $CH_4$ emissions are 27.53 kg/ha, the highest among all treatments. Cumulative $CO_2$ emissions in this treatment are 767.95 kg/ha. Global Warming Potential (GWP) is 1533.63 kg $CO_2$ eq/ha, indicating the highest overall GHG impact. CF significantly increases $CH_4$ emissions due to anaerobic soil conditions, which promote the activity of methane-producing microorganisms. For AWD, cumulative $CH_4$ emissions are 16.36 kg/ha, the lowest among treatments. Cumulative $CO_2$ emissions are 757.19 kg/ha. GWP for AWD is 1215.77 kg $CO_2$ eq/ha, lower than CF. For Biochar application, cumulative $CH_4$ emissions is 20.56 kg/ha. Cumulative $CO_2$ emissions is 820.42 kg/ha, where is the highest among treatments. While, the GWP for biochar application is 1392.42 kg $CO_2$ eq/ha. For N rates, cumulative $CH_4$ emissions are 20.34 kg/ha. Cumulative $CO_2$ emissions are 600.92 kg/ha, the lowest among treatments. GWP for this treatment is 1166.57 kg $CO_2$ eq/ha, the lowest overall.

## 4 Acknowledgments

The authors wish to thank Malaysian Nuclear Agency, and everyone who has directly and indirectly support this project.

## References

A. Meijide, C. Gruening, I. Goded, G. Seufert, and A. Cescatti. 2017. Water management reduces greenhouse gas emissions in a mediterranean rice paddy field. *Agriculture, Ecosystems Environment*, 238:168–178.

C. Wang, D.Y.F. Lai, J. Sardans, W. Wang, C. Zeng, and J. Peñuelas. 2017. Factors related with ch4 and n2o emissions from a paddy field: Clues for management implications. *PLoS ONE*, 12(1):e0169254.

Individual Research Contribution Review, 2024: 5–6
*ISSN: 3083-922X*

# Investigation of 3 MeV Electron Beam Dose Depth Penetration in Food Paste using Radiochromic Film

**Ahmad Zainuri Mohd Dzomir**
Agrotechnology and Biosciences Division, Malaysian Nuclear Agency
43000 Kajang, Selangor
zainuri@nm.gov.my

## Abstract

In this study, we investigated the depth dose penetration in food paste of varying numbers and thicknesses using single and double side irradiation. FWT-60 radiochromic film dosimeter was used to measure the dose. A stack of 1 to 5 sachets of food paste, each with a thickness of 0.75 cm, was used as phantom, interleaved with 2 to 6 pieces of radiochromic film in duplicates. The phantom was exposed to a 3 MeV electron beam at 5 kGy to obtain the depth dose profile. The results showed that single-side treatment could deliver an even dose if not more than one food paste was stacked together. The optimal thickness for double-side treatment was 2.25 cm when three food pastes stacked together. This investigation of the depth dose profiling using radiochromic film is very helpful for monitoring DUR of foodstuff processing with electron beam.

**Keywords:** electron beam, dose depth penetration, FWT-60, food irradiation, dose uniformity ratio

## 1 Introduction

Gamma rays, emitted from isotopes like Cobalt-60 or Cesium-137, have high penetration capabilities due to their high energy and lack of mass. This allows them to penetrate deeply into food products, making gamma radiation suitable for treating bulk or densely packed items. The deep penetration ensures that even the innermost parts of the food receive the necessary dose for effective microbial decontamination and/or pest control. Electron beams (EB), in contrast, consist of high-energy electrons generated by an electron accelerator. Unlike gamma rays, EB has relatively shallow penetration because electrons have mass and charge, which causes them to interact more readily with the food's surface and near-surface layers. The penetration depth of EB typically ranges from a few millimeters to a few centimeters, depending on the energy level of the electrons. This makes EB ideal for treating thin or surface-contaminated food products.

Dosimetry is crucial for ensuring the correct dose of radiation is delivered and distributed to food products. For EB radiation, dosimetry films are often used owing to advantages such as being thin, uniform and flexible easily adapted to complicated geometry of agricultural products. The most common types include radiochromic B3 (5-80 kGy) and FWT-60 (0.5-200 kGy), CTA (5-300 kGy) and Gafchromic HD-V2 (10-1000 Gy). The Dose Uniformity Ratio (DUR) is a critical parameter in food irradiation, representing the ratio of the maximum dose to the minimum dose within the product. The goal is to achieve a DUR as close to 1 as possible, indicating uniform dose distribution. Gamma radiation typically achieves a DUR around 1.5 to 3.0, depending on the product's density and geometry ((IAEA)., 2017). Electron beam generally difficult to achieve DUR below 2.0 due to its poor penetration and more surface-focused nature (FAO/IAEA, 2021). In addition, this can vary significantly with product thickness, density and treatment configuration. Achieving a low DUR is crucial for ensuring the food is effectively treated without overexposing any part to excessive radiation, which could affect quality. Uniform dose distribution ensures that microbial decontamination and/or pest control is consistently effective throughout the product.

Thus, the aim of this study is to investigate 3 MeV electron beam dose depth penetration in food paste using radiochromic film, FWT-60 during single and double-side irradiation with known penetration depth value, Rp at 1.45 g/cm$^2$ (IAEA, 2023).

## 2 Methods

Commercial food paste samples used as phantoms were purchased from grocery store with following specifications; 40g weight, 0.75 cm height, 10.7 cm length and 7.8 cm width. Film dosimeter pouch of FWT-60 (Far West Technology, US) (0.5-200 kGy) which contained duplicates were carefully inserted one by one between every sample layers. Consequently, the phantoms were constituted by a stack of 1 to 5 samples interleaved with 2 to 6 pieces of aluminum pouches contained radiochromic film. The samples were irradiated in single or double side treatment at 5 kGy by electron beam irradiator EPS3000 (Nissin High Voltage, Japan) which generates continuous electron beam with the maximum energy 3 MeV, current 5 mA and trolley speed 11.20 m/min. After irradiation, the dosimetry films were withdrawn and rested about an hour due to post-irradiation polymerization. Dosimetry films were analyzed using Genesys 20 visible spectrophotometer (Thermo Scientific, US) and converted to dose readings using AerODE software (Aerial, France). To avoid any false color development, films are covered from being exposed to pendaflour lamp light as soon as they were taken out from pouches for the purposes of reading.

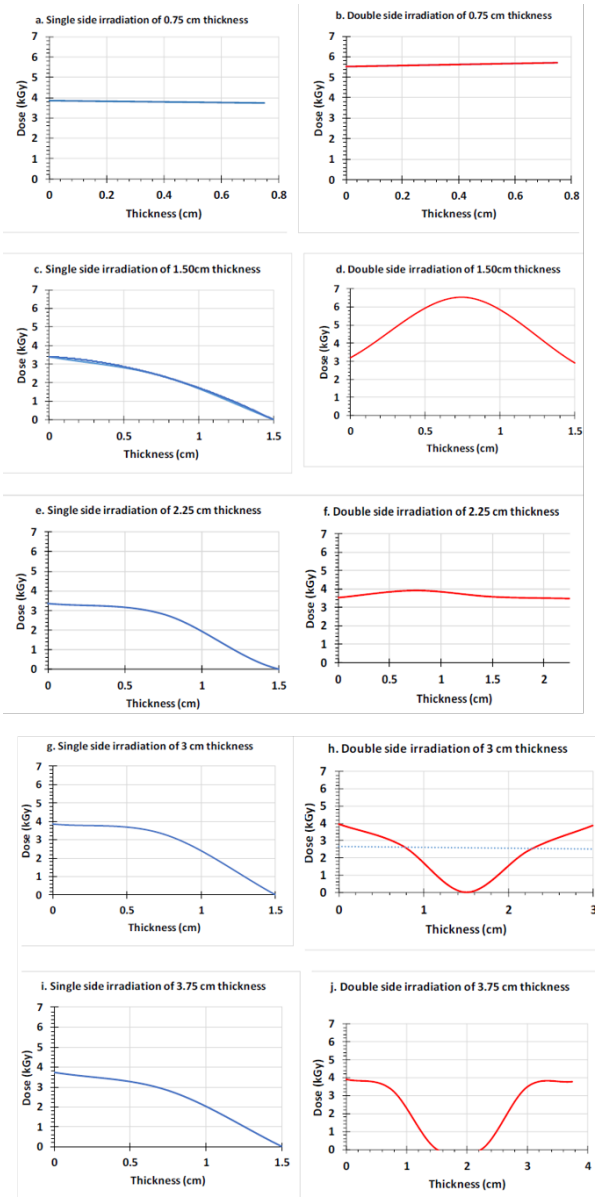



Figure 1: Depth dose penetration of electron beam within different thickness of food samples (a & b, 0.75 cm; c & d, 1.5 cm; e & f, 2.25 cm; g & h, 3 cm and, i & j, 3.75 cm) towards single side (blue lines) and double sides irradiation (red lines) with dose uniformity ratio (DUR) of 1, 2.2, 1.1, ∞ and ∞,respectively.

## 3 Data/Results

The results showed that both single and double side treatment could deliver an even dose with low DUR of 1.0 if not more than one food paste (0.75 cm thickness) was stacked (Figure 1, a and b). From Figure 1d, when the total thickness of food paste was comparable to Rp value, the center portion received dose from both sides of irradiation session, resulting in DUR of 2.2. Stack of four and more food pastes prevented the center portion from being irradiated (Figure 1, g, h, i and j). The optimal thickness for double-side treatment was achieved with three stacked food pastes at total thickness of 2.25cm (Figure 1, e and f) with low DUR of 1.1.

## 4 Discussion/Conclusions

This investigation of the depth dose profile using radiochromic film is very helpful for monitoring DUR of foodstuff processing with electron beam. The optimal thickness for double-sided irradiation was achieved when three food pastes were stacked together at a total thickness of 2.25 cm.

## References

FAO/IAEA. 2021. A comparison of gamma, electron beam and x-ray sources of radiation for food irradiation. vienna, austria (draft). *FAO/IAEAl*.

International Atomic Energy Agency (IAEA). 2017. Nuclear techniques for sustainable agriculture and water resources management. vienna. *IAEA*, 48.

IAEA. 2023. Expert end of mission report ras5087- rer1021-evt2101729 validation and verification of dosimetry system at 3 mev electron beam (eb) machine for sanitary (1-10 kgy) and phytosanitary (¡ 1 kgy) purpose. *IAEA*.

Individual Research Contribution Review, 2024: 7–8
*ISSN: 3083-922X*

# Minimum Inhibitory Concentration (MIC) of $\gamma$-Synthesised Silver Nanoparticles Against *Dickeya zeae*

**Anis Nadia Mohd Faisol Mahadeven**
Agrotechnology and Biosciences Division, Malaysian Nuclear Agency
43000 Kajang, Selangor
anisnadia@nm.gov.my

## Abstract

The increasing prevalence of bacterial plant pathogens poses significant challenges to global agriculture, making it crucial to develop novel antimicrobial strategies. This study investigates the minimum inhibitory concentration (MIC) of gamma-irradiated silver nanoparticles (AgNPs) against *Dickeya zeae*, a pathogen associated with fruit collapse and bacterial heart rot. Gamma irradiation was used to synthesize AgNP from silver nitrate solution, followed by determination of MIC against *D. zeae* using the variant agar diffusion method. Different concentrations of silver nanoparticles were compared to Gentamicin disk as control. The results demonstrated that gamma-irradiated AgNPs exhibit a significant inhibitory effect on *D. zeae*, with the MIC determined to be at a concentration of 25 ppm. This study highlights the potential of gamma-irradiated silver nanoparticles as an effective alternative for controlling *D. zeae* and suggests further research into their application in agricultural practices. The findings contribute to the understanding of nanotechnology in plant protection and may pave the way for innovative solutions in managing bacterial diseases in crops.

**Keywords:** Minimum inhibitory concentration, pineapple,*Dickeya zeae*

## 1 Introduction

Pineapple *(Ananas comosus)* is a tropical fruit celebrated for its sweet and tangy flavour, as well as its nutrients. It is a versatile ingredient found in many culinary dishes, beverages, and desserts. Major pineapple-producing countries like Thailand, the Philippines, and Costa Rica benefit significantly from this fruit's popularity, both for local consumption and international export. As global demand continues to grow, the economic significance of pineapple is increasingly recognized, highlighting its critical role in supporting the livelihoods of farmers and the economies of tropical nations (Kumar et al., 2021). However, pineapple cultivation comes with its challenges, particularly from plant pathogens that threaten crop yields. One of the most concerning threats is *D. zeae*, a bacterial pathogen that leads to wilting and fruit collapse, which not only diminishes the quantity but also the quality of the harvest. The impact of *D. zeae* is profound, posing substantial risks to farmers and exporters alike as they strive to meet the increasing global demand for pineapples (Wang et al., 2020). Effectively managing this pathogen is vital for the sustainability of pineapple farming and the protection of farmers' livelihoods.

In light of these challenges, researchers have begun exploring innovative solutions, such as silver nanoparticles (AgNPs), to combat bacterial pathogens like *D. zeae*. Known for their potent antimicrobial properties, silver nanoparticles release silver ions that disrupt bacterial cell membranes, effectively inhibiting growth. Studies have demonstrated that AgNPs can lessen the impact of *D. zeae* infections in various plants, suggesting their potential as a tool for sustainable agriculture (Sadeghi et al., 2022). Additionally, the use of gamma-irradiated silver nanoparticles has been investigated to enhance their effectiveness while ensuring safety for both crops and consumers. This cutting-edge approach not only addresses the threats posed by *D. zeae* but also aligns with the growing trend of utilising nanotechnology in agriculture to promote healthier crop production and reduce dependence on chemical pesticides (Khan et al., 2023; Dutta et al., 2021; Duran et al., 2019).

## 2 Methods

### 2.1 Synthesis of silver nanoparticles

For the synthesis of Ag/Kln NPs, six different doses of irradiation is used. The $AgNO_3$ solution was prepared at five concentrations (5, 10, 25, 50 and 100 ppm) the samples are irradiated at 10, 20, 30, 40 and 50 kGy. The suspensions were centrifuged, filtered and washed twice using distilled water to remove the silver ion residue, and dried in an oven. All the experiments were conducted at ambient temperature similar to the above. Gamma irradiations were carried out in a Co-60 gamma chamber having a radiation dose rate of 4 kGy hr-1 determined by Fricke dosimetry.

### 2.2 Preparation of microbial suspension

Prepare 5 ml overnight culture of *D. zeae* in Mueller-Hinton broth (MBH) from Mueller-Hinton agar (MHA) plate using aseptic technique and incubate at 28°C for 24 hours. The number of cells is determined following the protocol by Rutten et al. (Rutten et al., 2019) with some modifications. After incubation for 24 hours, prepare 1 ml of 1:8 dilution of the overnight culture using MHB and determine OD600 value using sterile broth as blank. Then dilute the culture to OD600 = 0.1 in 1 mL MHB (starting culture), in triplicates. Prepare three 2.0 ml tubes with 1900 $\mu$L of MHB for dilutions

1 ($2 \times 10^{-1}$), 2 ($4 \times 10^{-2}$), and 3 ($8 \times 10^{-3}$). Then prepare two 1.5 mL tubes for dilutions 4 ($8 \times 10^{-4}$) and 5 ($8 \times 10^{-6}$). Pipette 100 $\mu$L of starting culture into dilution 1, vortex then repeat with for each dilution through dilution 5. Finally aspetically spread 100 $\mu$L of cultures in dilutions 3, 4, and 5 onto MHA plates. The agar plates are incubated at 28°C for 24 hours. After 24 hours, the number of colonies are counted and the concentration (cfu/ml) of *D. zeae* at OD600 = 0.1 is determined. The correlation between OD600 readings and the cfu/ml is determined and is used throughout the experiment. Suspension is diluted accordingly to prepare an inoculum containing 5.9 ml of $1 \times 10^{-6}$ cells.

### 2.3 Antimicrobial susceptibility testing

Mueller-Hinton agar plates are dried and labelled accordingly. Next 100 $\mu$L of *D. zeae* inoculum is pipetted onto the agar and spread using an L-shape cell spreader aseptically. Holes are then punched on the agar with a 6-mm cork borer using aseptic technique then remove agar plugs using a scalpel to make wells. Silver nanoparticle (AgNP) solutions are mixed thoroughly then 50 $\mu$L of the solution at different concentrations and irradiation doses are dropped into respective wells. Sterile Gentamicin discs (10 $\mu$g) and sterile distilled water (SDW) were used as control. The test was done in triplicates. Solutions in each well was left to dry before incubating the plates at 28°C for 24 hours. After overnight incubation, the diameter of the inhibition zone was measured and the data was recorded.

## 3 Results and Discussion

The minimum inhibitory concentration (MIC) of *D. zeae* to the gamma-irradiated silver nanoparticles was evaluated by measuring the zone of inhibition and the results are as shown in Table 1.

| Concentration | Irradiation Dose kGy) | | | | |
|---|---|---|---|---|---|
| (ppm) | 10 | 20 | 30 | 40 | 50 |
| 5 | 0 | 0 | 0 | 0 | 0 |
| 10 | 0 | 0 | 0 | 0 | 0 |
| 25 | 10.1 | 9.8 | 11.2 | 11.1 | 11.1 |
| 50 | 10.5 | 10.0 | 9.6 | 10.1 | 10.0 |
| 100 | 11.6 | 10.9 | 11.0 | 12.1 | 11.3 |
| Control (Gm, 10 $\mu$g) | | | 10.6 | | |

Table 1: Diameter of inhibition zone (in mm) of *D. zeae* with different concentration of Ag-NP and irradiation doses.

The minimum inhibitory concentration (MIC) is determined by identifying the lowest concentration that exhibits an inhibitory effect compared to the control value. For concentrations of 5 ppm and 10 ppm, there are no inhibition at any irradiation dose suggesting these concentrations did not yield measurable effects. At 25 ppm, the values are relatively consistent, ranging from 9.6 to 11.2. The highest value, 11.2, at dose of 30 kGy, indicates that this as an optimal dose for this concentration. The results show dependency to irradiation, though the variation across doses is minimal. At 50 ppm, the values remain below the control across all doses, that higher concentrations might not yield significantly better antibacterial effects with irradiation. On the other hand, 100 ppm demonstrates inhibition at all doses, with values consistently above 10.6, indicating stronger and more reliable inhibitory effects independent of the dose. The maximum value 12.1 at 40 kGy indicates that this combination might produce a pronounced effect. Under standard conditions, the MIC is 25 ppm under specific conditions (doses of 30 kGy or higher). However consistent inhibition across all irradiation doses requires a higher concentration, such as 100 ppm. This highlights the need to account for both the concentration and the irradiation dose when optimizing conditions for effective inhibition. While lower concentrations might work in certain scenarios, higher concentrations are generally more reliable for consistent and broader applications.

## 4 Conclusion

The results show that both concentration and irradiation dose affect inhibitory effects. At lower concentrations (5 and 10 ppm), no inhibition is observed, making them ineffective. At 25 ppm, inhibition appears at higher doses (30 kGy and above) making it the MIC but it's not consistent across all doses. Surprisingly, 50 ppm doesn't reach the control value at any dose, showing it's less effective. In contrast, 100 ppm provides strong and consistent inhibition across all doses, making it the most reliable choice. This highlights the importance of selecting the right combination of concentration and dose, with higher concentrations being more dependable for consistent results.

## References

N. Duran, P. D. Marcato, and O. L. Alves. 2019. Potential applications of silver nanoparticles in agriculture. *Nature Sustainability*, 2(5):416–429.

S. Dutta, A. Mukherjee, and S. Ghosh. 2021. Gamma-irradiated silver nanoparticles: A novel antimicrobial agent. *Advanced Materials Letters*, 12(5):246–254.

Y. Khan, S. Ghafoor, and M. Asghar. 2023. Silver nanoparticles: A sustainable approach in agriculture. *Nanotechnology in Agriculture*, 8(1):12–25.

S. Kumar, R. Singh, and P. Kumar. 2021. Economic importance and cultivation of pineapple. *Journal of Tropical Agriculture*, 59(2):45–55.

P. Rutten, R. Tennant, J. Beal, C. Workman, T. Haddock-Angelli, N. Farny, and V. Selvarajah. 2019. Calibration protocol – conversion of od600 to colony forming units (cfus). *protocols.io*.

A. Sadeghi, S. Zare, and R. Miri. 2022. Antimicrobial activity of silver nanoparticles against bacterial pathogens in crops. *International Journal of Biological Macromolecules*, (195):687–693.

Y. Wang, J. Ding, and J. Xu. 2020. Pathogenicity of dickeya zeae on pineapple and its control. *Plant Pathology Journal*, 36(3):169–178.

Individual Research Contribution Review, 2024: 9–10
*ISSN: 3083-922X*

# Morphological and Molecular Identifications of Fungi Isolated From Rice Advanced Mutant lines

**Asma Aris**
Agrotechnology and Biosciences Division, Malaysian Nuclear Agency
43000 Kajang, Selangor
asmaaris@nm.gov.my

## Abstract

The identification of fungi associated with advanced rice mutant lines is crucial to understand their potential impacts on rice health and productivity. This study aimed to characterize fungi isolated from advanced rice mutant lines using both morphological and molecular approaches. Based on the results there is a diverse array of fungal species with a predominant genus of *Nigrospora*, *Talaromyces*, **Fusarium** and *Culvularia*.

**Keywords:** Rice advanced mutant lines, fungi, morphology, phylogenetic analysis

## 1 Introduction

Fungi are diverse organisms that play significant roles in both ecological systems and agricultural production. Recent advancements in plant breeding, particularly the development of rice advanced mutant lines, offer new opportunities to explore fungal resistance mechanisms and improve crop resilience. This research will enhance our understanding of rice-fungal interactions and could serve as a foundation for future studies in fungal pathogenesis, resistance breeding, and sustainable rice production.

## 2 Materials and Methods

### 2.1 Fungal isolation

Symptomatic plant samples from advanced rice mutant lines 182-2, 57-106 and 5-2 were collected at Kg. Sanglang, Kedah plot. The diseased tissues were surface sterilized using 70% ethyl alcohol (EtOH) and sterile distilled water (dH2O), in a ratio of 1:2. The samples were then grown in a potato dextrose agar (PDA) medium. The mixed cultures obtained were further purified by subculturing each colony into new PDA medium using hyphal tip technique, till pure cultures were obtained.

### 2.2 Morphological identification of fungi

Both microscopic and macroscopic characteristics observations were made on each isolate. Cultures were grown on PDA for 5 days at 30°C. Pigmentation, colony features and growth rate of the pure isolates were recorded at 72 hours. For microscopic examination, cultures were grown on water agar using slide culture technique and incubated for 72 hours at 30°C. Matured culture was observed under light microscope.

### 2.3 DNA extraction

DNA extraction was performed for 18 isolates following the protocol in PrimeWay Genomic II DNA Extraction Kit, with some modifications.

### 2.4 PCR amplification

The DNA fragments were amplified by T100TM Thermal Cycler Bio-Rad. The 25 $\mu$L reaction mastermix consists of 12.5 $\mu$L of mastermix, 0.5 $\mu$L of ITS1 (forward primer), 0.5 $\mu$L of ITS4 (reverse primer), 8.5 $\mu$L nuclease free water and 3 $\mu$L of DNA sample. The DNA was amplified under following program initial denaturation at 94°C for 2 min, denaturation at 94°C for 30 sec, annealing at 55°C for 30 sec, extension at 72°C for 5 min and final extension at 72°C for 5 min. The cycles run for 40 cycles. The PCR products then stored at 4°C.

### 2.5 Sequencing analysis

To identify the genus and species of the isolates, the sequences were analyzed using the BLAST program (http://blast.ncbi.nlm.nih.gov) of the National Center for Biotechnology Information (NCBI, Bethesda, MD, USA).

### 2.6 Phylogenetic analysis

Phylogenetic tree was constructed using the MEGA 7.0.

## 3 Results and Discussion

A total of 18 fungi isolates labeled A to R were obtained from the infected rice advanced mutant line samples and observed for their macroscopic and microscopic characterizations. The isolates with the most traits and morphological visuals were chosen as shown in Figure 1 and Figure 2. The morphological characterization of isolated fungi revealed diverse characteristics at macroscopic and microscopic levels.

Identification of some fungal species such as Talaromyces and Fusarium based on the morphological features, were difficult to perform. Therefore, molecular characterization of the fungal species was conducted for proper identification using sequence analysis of ITS region.The results obtained from the BLAST database showed 100% nucleotide identities with *Nigrospora sphaerica*, *Fusarium proliferatum*, *Curvularia geniculata*, and *Fusarium oxysporum*. 99% nucleotide identities with *Talaromyces pinophilus*, *Nigrospora oryzae* and *Fusarium verticillioides*.

Phylogenetic tree analysis reveals the evolutionary relationships among the fungal isolates from the advanced rice mutant

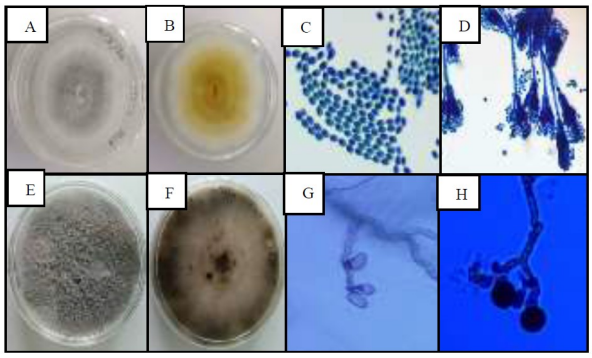



Figure 1: Morphology of isolate B (A-D) and F (E-H): Colony on PDA from the top (A, E) and bottom view (B, F); diverse shape of conidia (C, G) and cellular features like phialide and chlamydospore structure (D, H).

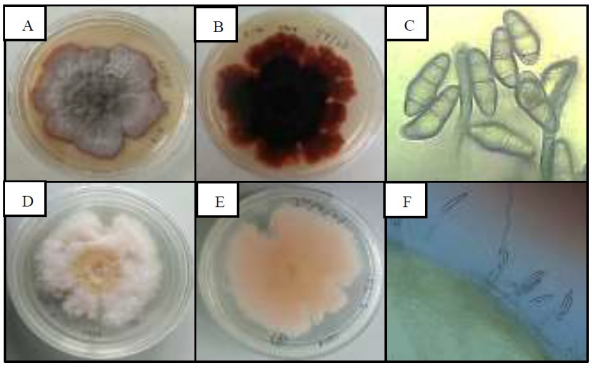



Figure 2: Morphology of isolate P (A-C) and R (D-F): Colony on PDA from the top (A, D) and bottom view (B, E) and diverse shape of conidia (C, F).

line 182-2, 57-106, and 5-2 (Figure 3). *Nigrospora sphaerica* identified from isolate A and H of the samples 182-2 seed and 57-106 leaf are reported to cause black leaf spot disease in rice plants (Liu et al., 2024). The fusarium species isolated from 182-2 leaf, 182-2 seed and 57-106 leaf are commonly known to cause bakanae disease in rice plants. *Fusarium oxysporum* is reported to cause fusarium wilt (Liu et al., 2024). *Fusarium proliferatum* is reported to cause spikelet rot disease (RSRD), which is a panicle disease that occurs during the late growth stage in rice. *Fusarium verticillioides* are known to cause fusarium ear rot and fusarium stalk rot which has been reported to cause yield reductions up to 30%–50% in maize (Xu et al., 2023). Another fungus isolated from sample 182-2 leaf, identified as *N. oryzae* is reported to cause rice leaf brown stripe disease in rice plants. Meanwhile, fungus *Curvularia geniculata* isolated from sample 5-2 seed is reported to cause leaf spot disease in rice plants (Kusai et al., 2015). Lastly, *Talaromyces pinophilus* isolated from sample 182-2 seed is reported to act as bioactive control agents in various crops.

## 4 Conclusions

The results indicate that the advanced rice mutant lines in Malaysia harbor a diverse fungal community, including

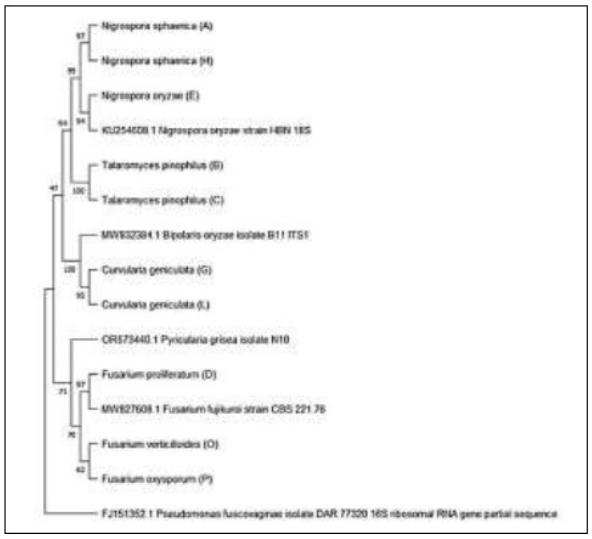



Figure 3: Phylogenetic tree analysis of the ten samples constructed using the maximum likelihood method

pathogenic species such as *Curvularia geniculata*, *Nigrospora sphaerica*, *Fusarium verticillioides*, and *Fusarium oxysporum*. These fungi can infect rice plants through various modes, including direct penetration of leaf surfaces, wounds, and seeds. To mitigate the impact of these fungal pathogens, it is crucial to develop effective disease management strategies. Further research on the hostpathogen interactions and the development of sustainable control measures would be beneficial for ensuring the success of advanced rice mutant lines in agricultural production.

## 5 Acknowledgments

This project is supported by Malaysian Nuclear Agency, under the Ministry of Science, Technology and Innovation (MOSTI). The authors send their gratitude to the undergraduates of University Putra Malaysia (UPM) and Mara University of Technology (UITM) for their cooperation. This work is also supported by a project grant SRF-APP by MOSTI

## References

N. A. Kusai, M. M. Z. Azmi, S. Zulkifly, M. T. Yusof, and N. a. I. M. Zainudin. 2015. Morphological and molecular characterization of curvularia and related species associated with leaf spot disease of rice in peninsular malaysia. *Rendiconti Lincei. Scienze Fisiche E Naturali*, 27(2):205–214.

Y. Liu, J. An, A. Safdar, Y. Shen, Y. Sun, W. Shu, X. Tan, B. Zhu, J. Xiao, J. Schirawski, F. He, and G. Zhu. 2024. Identification and characterization of nigrospora species and a novel species, nigrospora anhuiensis, causing black leaf spot on rice and wild rice in the anhui province of china. *Journal of Fungi*, 10(2):156.

Y. Xu, Z. Zhang, P. Lu, R. Li, P. Ma, J. Wu, T. Li, and H. Zhang. 2023. Increasing fusarium verticillioides resistance in maize by genomics-assisted breeding: Methods, progress, and prospects. *The Crop Journal*, 11(6):1626–1641.

Individual Research Contribution Review, 2024: 11–12
*ISSN: 3083-922X*

# Preliminary Study on the Enhancement of Lignocellulose-Degrading Fungi for Cellulolytic Agrowaste Recycling via Gamma Radiation

**Azhar Mohamad**
Agrotechnology and Biosciences Division, Malaysian Nuclear Agency
43000 Kajang, Selangor
azhar_m@nm.gov.my

## Abstract

Enhancing lignocellulose-degrading fungi for cellulolytic agrowaste recycling is essential to improving the efficiency and speed of biomass conversion into valuable bioproducts. The natural degradation of lignocellulosic materials is often slow and inefficient. However, exposure to gamma radiation at 750Gy significantly enhanced the cellulolytic capacity and activity of the selected fungi. Gripping tests revealed that the lignocellulose degradation process involving the three selected fungi was completed within 3 to 5 days. These findings highlight the potential of these fungi for efficient lignocellulose degradation, particularly in the context of agrowaste composting.

**Keywords:** Lignocellulose-degrading, fungi, gamma radiation, compost

## 1 Introduction

This study investigates the enhancement of lignocellulose-degrading fungi to facilitate efficient recycling of agricultural waste (agrowaste) in composting. Lignocellulose, composed of cellulose, hemicellulose, and lignin, is resistant to natural decomposition due to its structural complexity. Gamma radiation is employed as an innovative method to modify fungal traits, enhancing their enzymatic capacity for breaking down lignocellulose into simpler compounds such as sugars and phenols, which are metabolized further by bacteria and other microbes (Yamamoto et al., 2024).

Fungi secrete key extracellular enzymes, including cellulases, hemicellulases, and ligninases, essential for degrading plant cell walls. Their hyphal growth, exhibiting chemotropic behaviour toward nutrient-rich substrates, improves the targeted breakdown of biomass, optimizing the degradation of agrowaste for bioenergy and bioproduct applications.

Gamma irradiation has demonstrated potential in improving fungal cellulolytic activity by inducing genetic and physiological modifications, thereby accelerating lignocellulose degradation (Zheng et al., 2022). Enhanced fungal strains can adapt to diverse environmental conditions, making them valuable for sustainable biotechnology and waste management.

These findings contribute to the development of bio-based products from agricultural residues, particularly mushroom waste, supporting eco-friendly recycling and bioeconomy advancements (Fricker et al., 2017).

## 2 Materials and Methods

Fungal spores were collected from agrowaste, isolated, and suspended in sterile distilled water to select vigorous, clean, and healthy single spores for subsequent irradiation. The mycelial growth performance was evaluated based on the rate of mycelial expansion from the germinated spores. A gripping test was conducted to assess the growth characteristics of the mycelium, which is indicative of the fungus's lignocellulose-degrading potential. This method provides insights into the efficiency of the fungal strains in breaking down complex biomass, crucial for applications in agrowaste recycling and biomass conversion.

## 3 Results and Discussion

Variability of the hyphal network showing reflected the capabilities of the fungi for degradation of the substrate especiallah lignocellulose. By modifying the growth dynamics of hyphal networks via gamma radiation, the fungi is expected to show more effective activities in breaking down complex plant materials, addressing the challenge of slow and inefficient natural degradation processes.

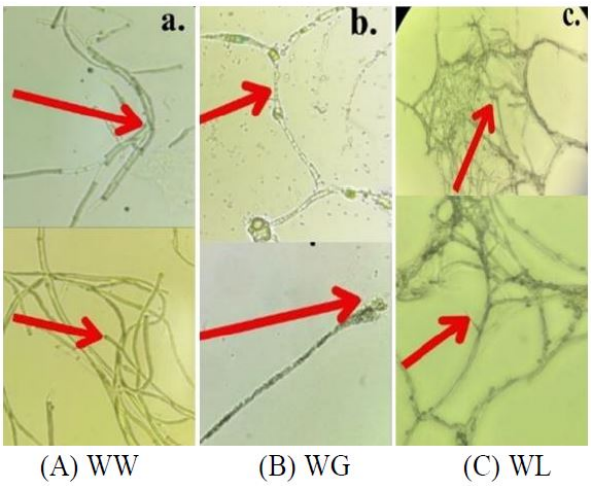



Figure 1: Hyphae network of selected fungi. This hyphal network is essential for the degradation of lignocellulose, enabling the fungus to break down complex biomass into simpler compounds.

By modifying the growth dynamics of hyphal networks, the aim is to make fungi more effective in breaking down

complex plant materials, addressing the challenge of slow and inefficient natural degradation processes (Fricker et al., 2017).

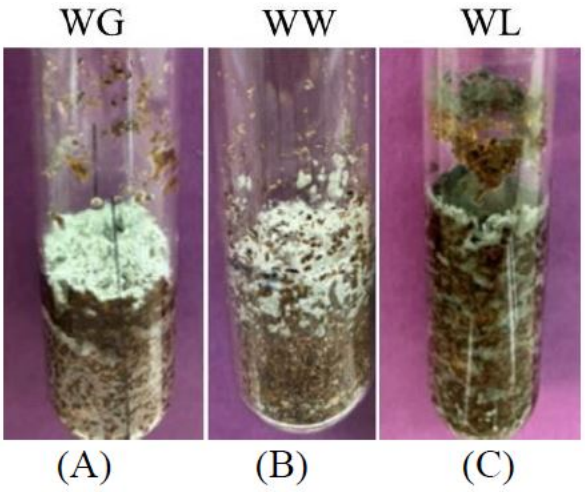



Figure 2: Gripping-test of the selected fungi strains lignocellulose-degrading performance (A) 4 days, (B) 3 days and (C) 5 days

Exposure to gamma radiation can enhance the fungi's tolerance to environmental stresses, such as inhibitors found in lignocellulose. This enables them to sustain high performance even in challenging substrates (Zheng et al., 2022). The composting process relies on microbial communities, including fungi, for efficient organic matter breakdown. Fungi contribute to the degradation of recalcitrant materials, aiding in faster compost stabilization and nutrient cycling (Hanc et al., 2022).

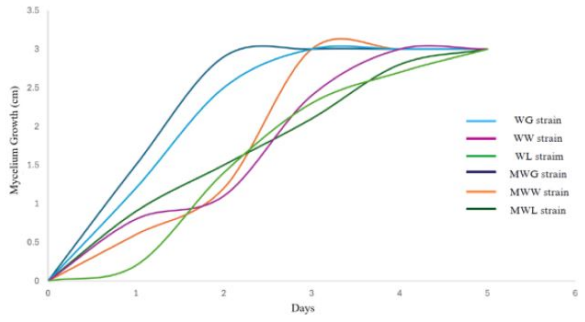



Figure 3: The graph shows the comparison of the control and potential mutated strains (750 Gy) patterns of the degradation activity in the agrowaste substrate.

Gamma radiation impacts the cellular membranes and intracellular structures of fungi, enhancing permeability and nutrient uptake, which subsequently accelerates growth and enzymatic productivity (Zheng et al., 2022). However, the degree of tolerance to gamma radiation varies among fungal strains, reflecting their genetic and physiological diversity.Gamma rays induce mutations in fungal DNA, potentially enhancing enzymatic activity. These mutations can lead to the overexpression or structural modification of cellulase and ligninase enzymes, improving their efficiency in degrading lignocellulosic components (Zheng et al., 2022). Such modifications hold significant potential for optimizing fungal strains in industrial and biotechnological applications, particularly in recycling lignocellulosic biomass.

Besides, the radiation may also altered metabolic pathways: Some mutations optimize metabolic pathways, enabling fungi to process lignocellulose more effectively. Preliminary findings highlight the need for further research into the genetic traits, physical properties, enzymatic production, and stress tolerance of fungi. Fungal strains with enhanced resilience to environmental stresses are particularly valuable for industrial-scale applications. Advanced techniques, such as gamma irradiation, offer promising avenues to improve fungal tolerance, enabling them to maintain high efficiency under challenging conditions. These advancements could significantly expand the applicability of fungi in waste recycling, bioenergy production, and other biotechnological processes.

## 4 Conclusions

Gamma rays introduce structural and functional changes in both the fungi and the lignocellulosic substrate, creating a synergistic effect that enhances the biodegradation process. This makes gamma irradiation a powerful tool in biotechnology for recycling agricultural waste and producing bio-based products efficiently.

## 5 Acknowledgments

The author would like to thank Ministry of Science, Technology and Innovation (MOSTI) and Malaysian Nuclear Agency for providing the fund to carry this project.

## References

M.D. Fricker, L.M. Heaton, N.S. Jones, and L. Boddy. 2017. The mycelium as a network. *Microbiol Spectr*, (5).

A. Hanc, B. Dume, and T. Hrebeckova. 2022. Differences of enzymatic activity during composting and vermicomposting of sewage sludge mixed with straw pellets. *Front. Microbiol.*, (12)::801107.

R. Yamamoto, H. Miki, A. Itani, and N. Takeshita. 2024. Hyphae of the fungus aspergillus nidulans demonstrate chemotropism to nutrients and ph. *PLOS Biology*, 22(7):e3002726.

B. Zheng, S. Yu, Z. Chen, and Y.X. Huo. 2022. A consolidated review of commercial-scale high-value products from lignocellulosic biomass. *Front. Microbiol.*, (13):933882.

Individual Research Contribution Review, 2024: 13–14
*ISSN: 3083-922X*

# Improving the Acid Sulphate Soil Attributes with Application of Biochar and Urea Deep Placement Technique for Extended Abstracts

**Azilah Binti Abdul Malek**
Agrotechnology and Biosciences Division, Malaysian Nuclear Agency
43000 Kajang, Selangor
azilah@nm.gov.my

## Abstract

Acid sulfate (AS) soil is considered infertile and would result in producing low-quality plants and poor yield. This is because the soil has a low pH value thus limiting the nutrients available for plant growth such as nitrogen. To combat these problems, biochar was applied to improve the soil attributes. Besides, a unique fertilization technique, Urea Deep Placement (UDP) also was applied to optimize the nitrogen uptake by plant while minimizing the risks on the environment. Following these treatments, the greenhouse gas (GHG) emission also was monitored between the biochar-treated plots to the no-biochar-treated plots as the emission of GHG is influenced by the nitrogen fertilizer.

**Keywords:** Acid Sulfate Soil, Greenhouse Gas, Urea Deep Placement, Biochar

## 1 Introduction

Acid sulphate soil (AS soil) has a light texture, poor water-holding and cation exchange capacities, and poor organic matter content making it unsuitable for plant cultivation. Naturally safe, but when disturbed, this natural sediment would react with oxygen to produce acid and toxic aluminum which would impose dreadful effects on the environment and living creatures in the surroundings. The AS soil covers about 110,000 hectares of Peninsular Malaysia and is recognized as one of the problematic soils but is often used in the agricultural sector since we have limited arable land for cultivation (Shamshuddin et al., 2016). In this project, a paddy field planted on the AS soil was used for evaluation. Located in a coastal region, the paddy soil is constantly oxidized and remained low in pH value.

One of the managements to improve the AS soil attributes is by applying a different fertilization technique to optimize the nitrogen uptake by plant. Nitrogen is one of the vital nutrients for plant development apart from encourages the uptake and employment of other nutrients including phosphorous and potassium. Thus, farmers often to over abuse the usage of this fertilizer to meet the market demand. According to the FAO, the global demand for nitrogen was high in 2022 with 111 591 metric tonnes (mt) when compared to the year 2021 with 110 193 mt and it is expected to increase in the following years. The increased demand shows the dependency of farmers on synthetic nitrogen fertilizers especially in problematic soils such as AS soil.

Therefore, to ensure the maximum uptake of nitrogen fertilizer, an improved fertilizer technique should be performed. Conventionally, farmers would spread the fertilizer uniformly over the paddy plot which is known as the broadcast method. However, it is hard to ensure the uniformity as the application would depend on several technical and environmental factors such as uneven planting depths, poor plant distribution, suitable equipment used, wind movement, and others. Besides, this technique is considered inefficient as 60% to 70% of the nitrogen applied would be lost, and contributes to greenhouse gas (GHG) emissions and water pollution. These would lead to fertilizer wastage thus doubling the fertilizer cost. To encounter these problems, the UDP technique is an alternative using an isotopic approach by evaluating the nitrogen use efficiency (NUE) of the paddy.

The research on this technique has been widely investigated and proven to reduce the environmental issues. In a study conducted in China on paddy, the UDP technique was proven to reduce ammonia volatilization by 20-45% in comparison to the broadcast technique (Liu et al., 2015). Besides, it also improved the nitrogen uptake by 28% by supplying higher ammonium concentration in the soil during the early growth stage and stays longer in the soil. Moreover, this slow-release technique also was noted to significantly enhance the yield by 10% under favorable conditions.

In a different study, the UDP technique showed a remarkably increased in the yield, NUE, and total nitrogen uptake on corn by 6.3%–13.4%, 82.9%–140.1%, and 27.9%–39.5%, respectively (Liu et al., 2019). Not only that, but this technique also improved the gas exchange attributes, soil nitrate and ammonium concentrations at 0-40 cm of soil depth, especially during later crop growth stages, and the root morphology traits. However, in most research, the UDP technique was adopted on arable soil, but none on acid sulphate soil. Therefore, it is important to study the capability of the UDP technique to improve the crops' NUE especially in the field since this soil often lost its acidity when evaluated in the glasshouse.

Apart from the fertilization technique, biochar application is also a good practice when handling the crop planted in the AS soil. Biochar is characterized as a porous and lightweight compound with a charcoal-like appearance. It is obtained from a process called pyrolysis (thermal decomposition with limited oxygen) by the burning of dried plant materials. Biochar helps in reducing soil acidity by altering

the pH value from 3.5 – 5.5 to 5.5 – 7. At this pH value, the microbe works at its best by changing the nitrogen from biochar and fertilizers for plant uptake while boosting the soil structure. Besides, the spongy and porous traits would attract the nutrients, stores them, and readily available for plants, thus increasing the crops yield. The large surface area of biochar also would help in reducing the soil pollutants such as aluminum and improves plant resistance to diseases while enriching the soil carbon by capturing and storing them, thus fixing the soil. Greenhouse gas (GHG) emission from the biochar-treated and no-biochar-treated paddy plot also was monitored in this experiment as the emission of the gases are nitrogen-derived.

Therefore, the objective of this project is to, 1) To evaluate the nitrogen used efficiency (NUE) between UDP and conventional fertilization techniques in biochar-treated and non-treated AS soil, 2) To evaluate the yield performance by UDP and conventional techniques in biochar-treated and non-treated AS soil, and 3) To evaluate the emission of greenhouse gas (GHG) in biochar-treated and non-treated AS soil.

## 2 Materials and Methods

### 2.1 Acid Sulphate Soil Evaluation

1kg of soil sample was taken during land preparation phase for soil profiling analysis.

### 2.2 Biochar Application

The rice husks biochar product was used and applied at rate of 10 t/ha 2 weeks before transplanting.

### 2.3 Nitrogen Use Efficiency

The plots were irrigated and fertilized following the normal farmer's practice. The square-shaped microplot (1m x 1m x 0.4m) was used and placed 10 cm deep in the paddy plot (3 replications for each treatment). Four treatments were adopted in a completely randomized design with three replications for each treatment as follows:

| Treatment | Experiment |
|---|---|
| T1 | With biochar, UDP practice (BUDP) |
| T2 | With biochar, broadcast practice (BB) |
| T3 | Without biochar, UDP practice (UDP) |
| T4 | Without biochar, broadcast practice (B) |

Table 1: Treatments adopted in a randomized design with three replications

Labelled 15N urea was broadcasted in the microplot for BB and B treatments, while labelled 15N urea will be inserted at 15 cm deep in the soil between rows for BUDP and UDP treatments (4 points per microplot). Plant and soil samples will be collected at maturity stage. The total nitrogen and 15N isotope values from samples will be determined using an analytical instrument (EA-IRMS) using the following parameters:

**a.** Plant height

**b.** Tiller number

**c.** Yield weight

**d.** 1000 grain weight

**e.** Harvest Index

**f.** Total Nitrogen

**g.** Nitrogen Derived from Fertilizer (NDFF)

**h.** Nitrogen Yield

**i.** NUE

### 2.4 Greenhouse Gas (GHG) Emission

The emission of carbon dioxide and methane were monitored weekly using the laser spectrometer.

## 3 Discussion/Conclusions

The experiment is still on-going. Currently, the paddy has grown normally and fertilized according to the schedule. The NUE and yield will be evaluated once the cycle is over. However, from the current GHG data collected, the methane and carbon dioxide emission showed a significant reduction in biochar-treated plot compared to the no-biochar-treated plot.

## References

T. Q. Liu, Zhang X. X. Fan, D. J., J. Chen, C. F. Li, and C. G. Cao. 2015. Ammonia volatilization and increases nitrogen utilization efficiency in no-tillage paddy fields in central china. *Field Crops Research*, (184):80–90.

W. Liu, Y. Xiong, X. Xu, F. Xu, S. Hussain, H. Xiong, and J. Yuan. 2019. Deep placement of controlled-release urea effectively enhanced nitrogen use efficiency and fresh ear yield of sweet corn in fluvo-aquic soil. *Scientific Reports*, 9(1):20307.

J. Shamshuddin, Q. A. Panhwar, M. A. R. S. Shazana, A. A. Elisa, C. I. Fauziah, and U. A. Naher. 2016. Improving the productivity of acid sulfate soils for rice cultivation using limestone, basalt, organic fertilizer and/or their combinations. *Sains Malaysiana*, 45(3):383–392.

Individual Research Contribution Review, 2024: 15–16
*ISSN: 3083-922X*

# Rapid Generation Cycling In Tomato

**Chong Saw Peng**
Agrotechnology and Biosciences Division, Malaysian Nuclear Agency
43000 Kajang, Selangor
sawpeng@nm.gov.my

## Abstract

Speed breeding is an innovative method to accelerate plant breeding by manipulating environmental factors such as light, temperature, and photoperiod. This study investigates using LED lighting systems to optimize tomato growth and accelerate breeding cycles. Specifically, we explored the effects of different photoperiods (16/8, 12/12, and 8/16 hours light/dark cycles) on the Tomato Malaysia 552 variety, using LED lights with tailored spectrums of deep red, far red, and white light. The results show that longer photoperiods (16/8 hours) enhanced tomato growth, increased plant height and weight, and shortened the flowering period from 98 to 63 days, thereby reducing the time to flowering by 35 days. Additionally, the study found that extending light exposure to 20/4 hours in tissue culture plantlets triggered fruiting without flowering. These findings demonstrate the potential of LED-based photoperiod manipulation to accelerate generation cycling, improve crop yield, and contribute to more sustainable, resilient agriculture.

**Keywords:** Rapid cycling, tomato, artificial lighting

## 1 Introduction

Speed breeding refers to methods used to accelerate the breeding process of plants, and one technique involves manipulating environmental factors like light, temperature, and photoperiod (Potts et al., 2023). In Malaysia, research focused on optimizing light conditions for tomato growth, using specialized LED lighting systems. These systems, developed by Philips, use a tailored light spectrum (white, far-red, and deep-red wavelengths) to support optimal photosynthesis, growth, and flowering (Koninklijke Philips Electronics, 2012). This approach produces more energy-efficient and effective plant growth than traditional fluorescent lighting. Tomatoes, a popular warm-season fruit under the Solanaceae family, require at least 6-8 hours of sunlight per day for optimal growth (Song et al., 2022). They are considered day-neutral plants, meaning their flowering is not heavily influenced by the length of day or night (Mizoguchi et al., 2007). The manipulation of photoperiods and light intensity can still enhance growth cycles, which is a key focus of speed breeding.

## 2 Materials and Methods

In the rapid cycling study on tomato breeding, photoperiod manipulation using artificial lighting, specifically LED lights, was explored to enhance crop yield. While tomatoes are day-neutral plants and do not rely on specific day lengths to flower, this study demonstrated that increased light intensity and longer light durations can positively influence their growth and flowering (Mizoguchi et al., 2007). Sufficient light exposure is essential for photosynthesis, which boosts energy production for flower and fruit development. A study focused on the Tomato Malaysia 552 variety, using gamma radiation (36.3 Gy LD50 dose) from a Gamma Cell Biobeam GM8000 as part of the mutation breeding process. The goal was to accelerate generation cycling through LED lighting and obtain tomatoes with improved yield and nutritional content. For the rapid generation cycling experiment, the researchers tested three different photoperiods (16/8, 12/12, and 8/16 hours light/dark cycles) using LED lamps with a 1:2:1 ratio of deep red (660 nm), far red (735 nm), and white light (Koninklijke Philips Electronics, 2012). The experiment was conducted under controlled conditions with a temperature of 23±2°C and 61±2% humidity. The LED lighting intensity was 163±2 $\mu$mol/$m^2$/s (Chong et al., 2023). This research aimed to optimize the light conditions that trigger flowering and improve overall growth for enhanced breeding outcomes.

## 3 Results and Discussion

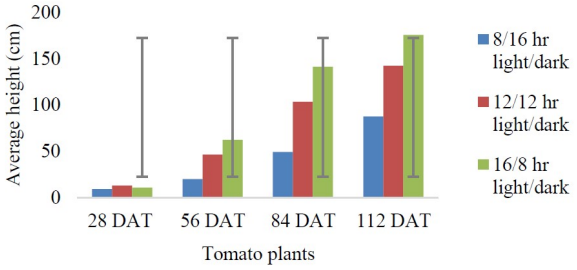



Figure 1: The tomato plants heights at different photoperiods after growing for 28, 56, 84, and 112 days after transplant (DAT). Analysis One-way ANOVA showed that the total standard deviation at 112 DAT was 77.57 and the p-value was 0.000031. The result was significant at $p < 0.05$.

In our study on tomato growth, we observed that longer photoperiods promoted faster growth, as evidenced by in-

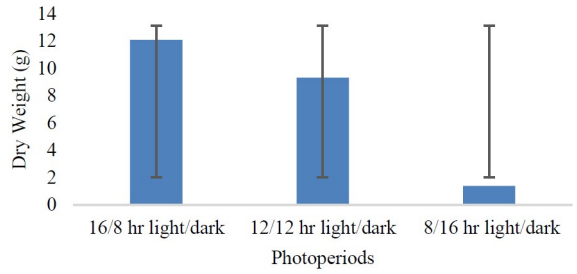



Figure 2: The tomato plants dry weights at different photoperiods after growing for 20 weeks. Analysis One-way ANOVA showed that the total standard deviation was 6.40 and the p-value was 0.000944. The result was significant at $p < 0.05$.



Figure 3: Flowering and fruiting in tomato plants under LED lighting treatment for 16/8 hr light/dark photoperiod.

creased plant height and weight (Fig. 1 & 2). Specifically, the long-day photoperiod (16/8 hours light/dark) accelerated plant development compared to day-neutral and short-day photoperiods (Chong et al., 2023). This finding aligns with previous research showing that light quality and duration significantly impact plant growth and photosynthetic rates (Gilbert, 2000). By optimizing light exposure, we successfully induced earlier flowering and fruiting in tomatoes, shortening the flowering period from 98 days to 63 days, and reducing the time to flowering by 35 days (Fig. 3). Tomato plants grown under 16/8 hour light/dark cycles began flowering while plants under 8/16 hour and 12/12 hour cycles were still in the stem elongation phase.

## 4 Conclusions

Rapid cycling through artificial lighting offers an effective tool for accelerating the speed breeding process in plants to address challenges such as food security and climate change. By speeding up the processes required to develop new crop varieties, speed breeding can improve sustainability, resilience, and productivity in agriculture globally.

## References

S.P. Chong, Z. Ahmad, and N Bahari. 2023. Influence of light intensity and photoperiod on growth and flower initiation in tomato plant. *15th Malaysia International Genetics Congress 2023 (MiGC15)*, 7-9 March 2023(Bangi Resort Hotel, Bandar Baru Bangi, Selangor, Malaysia).

S.F. Gilbert. 2000. Developmental biology. 6th edition. sunderland (ma): Sinauer associates. *The Vegetative-to-Reproductive Transition*.

N.V. Koninklijke Philips Electronics. 2012. *Philips LED Lighting in horticulture*. Philips LED Lighting in horticulture.

T. Mizoguchi, K. Niinuma, and R. Yoshida. 2007. Day-neutral response of photoperiodic flowering in tomatoes: possible implications based on recent molecular genetics of arabidopsis and rice. *Plant Biotechnology*, (24):83–86.

J. Potts, S. Jangra, V.N. Michael, and X. Wu. 2023. Speed breeding for crop improvement and food security. *Crops*, 3(4):276–291.

J. Song, Z. Chen, A. Zhang, M. Wang, M.S. Jahan, Y. Wen, and X. Liu. 2022. The positive effects of increased light intensity on growth and photosynthetic performance of tomato seedlings in relation to night temperature level. *Agronomy*, 12(2):343.

Individual Research Contribution Review, 2024: 17–18
*ISSN: 3083-922X*

# Radiosensitivity Study of Early Maturity Malaysian Mega Rice Cultivar MR220CL2 Using Ion Beam Irradiation

**Faiz Ahmad**
Agrotechnology and Biosciences Division, Malaysian Nuclear Agency
43000 Kajang, Selangor
faiz@nm.gov.my

## Abstract

Rice (*Oryza sativa*) is a cereal crop classified under the Graminae family and is indigenous to Asia. The self- sufficiency ratio of rice in Malaysia around 56.2%. Early maturity and resilient to climate change is the preferable traits among the rice farmers. One mega-variety, MR220CL2 has been developed in 2012, however this variety is susceptible towards abiotic and biotic stress. Improvement of this early maturity variety is needed. Ion beam irradiation is a quick method for developing the climate resilient traits. The hulled seeds of MR220CL2 were irradiated to carbon ion beam irradiation at 0, 10, 20, 40, 60, 80, 100 and 120 Gy respectively. The growth reduction ($GR_{30}$ and $GR_{50}$) of MR220 CL2 cultivar is 19 Gy and 38 Gy respectively. The screening and selection process for subsequent population will be continued for selection the desirable mutant individuals.

**Keywords:** *Oryza sativa*, Ion beam irradiation, Mutant rice, Climate resilient rice, Early maturity rice

## 1 Introduction

Rice (*Oryza sativa*) is a cereal crop classified under the Graminae family and indigenous to Asia (Rijal and Devkota, 2020). Malaysia is between 60% and 70% self-sufficient in rice. This heavy reliance on rice imports poses economic risks. To address this, Malaysia MARDI, the Malaysian Research and Agriculture Development Institute, has introduced one mega rice variety, MR220 CL2. This variety categorizes as an early maturation at around 97-100 days, respectively.

However, climate change, which affects precipitation, farm seasons, severe drought, flooding, and economic stagnation, is increasing hunger. This means climate change would affect the rice industry in Malaysia based on the current climate change issue. In addition to abiotic factors, biotic factors significantly reduce rice yields in the main granary area (Simoli et al., 2021). The biotic factors limiting rice production in Malaysia include diseases caused by fungi, bacteria, and viruses.

Ion beams, especially those with high linear energy transfer (LET) like carbon ions, tend to induce a broader spectrum of mutations, including smaller deletions and large rearrangements compared to gamma rays.The radiosensitivity test is a relative measure that indicates the number of recognizable effects of radiation on irradiated objects (Hasan et al., 2020). Its purpose is to determine the ideal dose for irradiation by calculating the lethal dose (LD50) and shoulder dose, which create maximum variability with the minimum number of undesirable mutants. Understanding the general radiation sensitivities of plants is very useful for determining the optimum irradiation doses (Fifika et al., 2023).

## 2 Materials and Methods

### 2.1 Plant materials

Malaysian rice cultivar MR220CL2 was used in this study. The seeds were supplied by MARDI Rice Genebank, Seberang Perai, Pulau Pinang.

### 2.2 Irradiation process

The MR220 CL2 rice variety's hulled seeds were irradiated with carbon-ion beams (0,10,20,40,60,80,100,120Gy) at the Quantum and Radiological Science and Technology (QST) facility in Takasaki, Japan. The Takasaki Ion Accelerators for Advanced Radiation Application (TIARA) utilized an electron cyclotron resonance heavy-ion source to generate a vertical ion beam of carbon ion (12C+6; 320 MeV), which was then accelerated by an Azimuthally Varying Field (AVF) cyclotron (Hidema et al., 2003). To ensure homogeneous irradiation, the resulting beam underwent scanning in an irradiation field larger than 60 x 60 $mm_2$.

This entire process occurred under vacuum conditions. After production, the beam exited to atmospheric conditions through a 30 $\mu$L thick titanium foil used as a filter in the beam window. The carbon ion-beam's physical properties included an incident energy of 311 MeV (25.9MeV/u) at the target surface. The irradiated seeds were then cultivated to obtain survival curves and offspring, while non-irradiated seeds (0Gy) served as the control.

### 2.3 Experimental design

The experimental design consists of 8 treatments of 0, 10, 20, 40, 60, 80, 100 and 120 Gy, with 3 replications. The experiment was arranged in a randomized complete block design (RCBD) where each replication consisted of 10 seedlings.

### 2.4 Data Collection

The effects of irradiation measured 20 days after sowing in terms of shoot length.

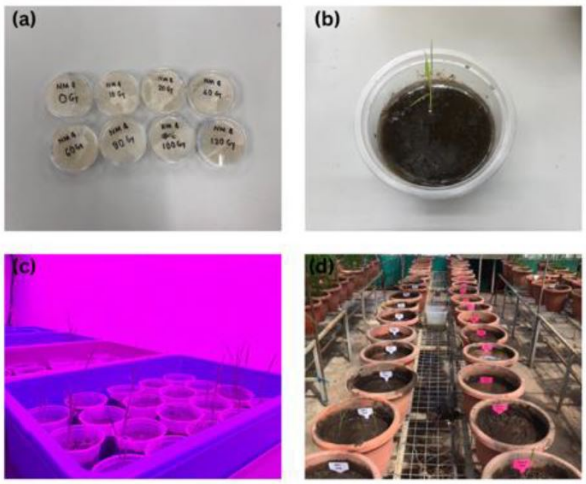



Figure 1: (a) Seed germination. (b) Seedling at 10th day of planting before transplant. (c) RCBD design arrangement of pot in speed breeding room. (d) Seedling at 20th day of planting.

### 2.5 Data Analysis

An analysis of variance (ANOVA) of all traits was calculated using STAR program version 9.3 to determine the variation among the Ion Beam doses. Mean comparisons were performed using the Least Significant Difference (LSD).

## 3 Results and Discussion

### 3.1 Determination of the Effect of Irradiation on Rice Seedling Traits

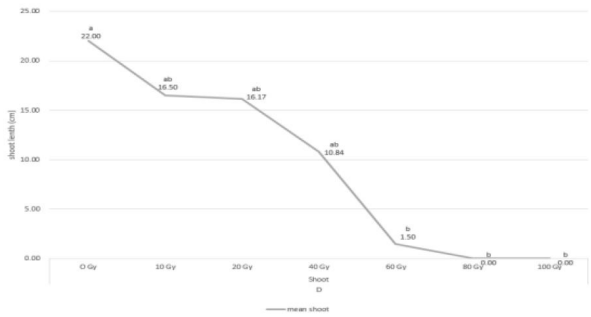



Figure 2: Shoot length at $20_{th}$ days after germination

### 3.2 Determination of $GR_{30}$ and $GR_{50}$

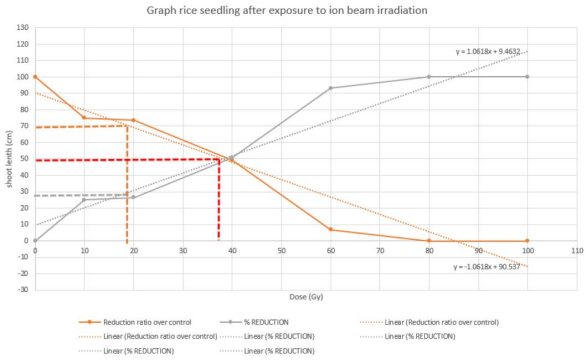



Figure 3: Determination of $GR_{30}$ and $GR_{50}$ of MR220 CL2 based on shoot length at $20_{th}$ days after germination.

## 4 Conclusions

- From the radiosensitivity study for the MR220 CL2 rice variety, the $GR_{30}$ for shoot length under ion beam irradiation was 19 Gy, and $GR_{50}$ was 38 Gy.
- The optimum dose for ion beam irradiation of MR220 CL2 is approximately 20–40 Gy.

## 5 Acknowledgement

This research is subproject under FNCA Mutation Breeding Project (Mutation Breeding of Major Crops and Application of New Technologies Towards a Sustainable Agriculture).

## References

A. W. Fifika, A. M. Ikmal, A. A. S. Noraziyah, A. Faiz, H. A. Rahim, H. Sobri, and H. Nor'aishah. 2023. Carbon-ion beam radiosensitivity study and biological responses of high-yielding rice line, mr219-pl-5. *Sains Malaysiana*, 50(12):3481–3491.

N. A. Hasan, M. Y. Rafii, A. R. Harun, F. Ahmad, N. N. Jaafar, K. Ramachandran, and S. Hussein. 2020. Radiosensitivity response to acute gamma irradiation in a malaysian rice variety, mr284. *Jurnal Sains Nuklear Malaysia*, 32(2):1–7.

J. Hidema, M. Yamoto, T. Kumagai, Y. Hase, A. Sakamoto, and A. Tanaka. 2003. Biological effects of carbon ion on rice (oryza sativa l.). *JAERI review*, (33):85–87.

S. Rijal and Y. Devkota. 2020. A review on various management method of rice blast disease. *Malaysian Journal of Sustainable Agriculture*, 4(1):29–33.

J. M. Simoli, F. Ahmad, S. Salleh, Y. Hase, M. R. Yusop, and A. R. Harun. 2021. Effect of ion beam irradiation on agro- morphophysiological traits of ma03 rice genotype. *Malaysian Journal of Genetics*, (1):7–15.

Individual Research Contribution Review, 2024: 19–20
*ISSN: 3083-922X*

# Generation of PHA by *Azotobacter vinelandii* from Raw (Untreated) Palm Oil Mill Effluent

**Liew Woan Ying Pauline**
Agrotechnology and Biosciences Division, Malaysian Nuclear Agency
43000 Kajang, Selangor
paulineliew@nm.gov.my

## Abstract

*Azotobacter vinelandii* was studied for its generation of polyhydroxyalkanoate (PHA) from raw (untreated) palm oil mill effluent (POME). When appropriate, minor concentrations of sucrose and glycerol were added to POME medium to boost PHA generation. A compilation of the bacterial performance showed 0.5-6.0 g/L of PHA/B were generated from batch fermentation of POME/sucrose/glycerol based on one-factor-at-a-time (OFAT) analysis, and 2.0-13.0 g/L of PHA/B were generated from batch fermentation of POME/sucrose/ glycerol based on RSM analysis.

**Keywords:** PHA,*Azotobacter vinelandii*, POME

## 1 Introduction

*Azotobacter vinelandii* is a soil-dwelling nitrogen-fixing bacteria which was known to also synthesize polyhydroxyalkanoate (PHA). PHA is an accumulative terminology used to refer to the bioplastics, or the plastic/polymer/polyester generated by bacteria via conversion of carbon substrates. There are more than 150 different monomers which can be combined to generate PHAs with different physicochemical properties (Doi and Steinbuchel, 2002). Post synthesis, PHA(s) was accumulated in the bacterial cells. In general, *A. vinelandii* is able to synthesize PHA(s) from various carbon sources which include laboratory sugars and organic wastes from various industries. The PHAs generated by bacteria are biodegradable and biocompatible. In view of the increasing concern over global plastic pollution, the production of bacterial plastic/polymer/polyester offers a biological solution towards enhancing the sustainability of natural environment as well as human well-being. In our study, we aimed to characterize the generation of *A. vinelandii's* PHA from organic wastewater, palm oil mill effluent (POME). The utilization of POME promotes a waste-to-wealth approach via waste reduction and sustainable bioplastics production.

## 2 Materials and Methods

*A. vinelandii* Δ*Avin_16040* strain (Liew et al., 2015) was cultured in a modified Azotobacter medium using raw (untreated) POME as the carbon source (Liew et al., 2023). The composition of POME was analyzed to determine the suitable concentration for bacterial growth and PHA/B production. When appropriate, minor concentrations of sucrose and glycerol were added to the POME medium as complementary carbon sources. Fermentation was initially conducted in shake flasks, and later scaled up to a 3-L volume in a fermenter (Infors HT, Switzerland). Samples were collected after designated fermentation periods. Bacterial density was estimated using a UV/Vis spectrophotometer (Biomate 3, Thermo Fisher Scientific, USA). PHA/B {P(3HB)} was quantitated by the crotonic acid methodology with modifications (Law and Slepecky, 1961; Wang et al., 2020; Liew et al., 2023).

## 3 Data/Results

The generation of PHA/B by *A. vinelandii* was performed by quantitating P(3HB). A compilation of the bacterial PHA/B generations showed 0.5-6.0 g/L of PHA/B were generated from batch fermentation of POME/sucrose/glycerol based on one-factor-at-a-time (OFAT) analysis, and 2.0-13.0 g/L of PHA/B were generated from batch fermentation of POME/sucrose/glycerol based on RSM analysis. In comparison, the bacterial strain generated 1-3 g/L of PHA/B from batch fermentation of sucrose based on OFAT, 1.7-3.5 g/L of PHB from batch fermentation of sucrose based on RSM, and 10-20 g/L of PHB from fed batch fermentation of sucrose. A demonstration of PHA/B generated by *A. vinelandii* was shown in Figure 1.

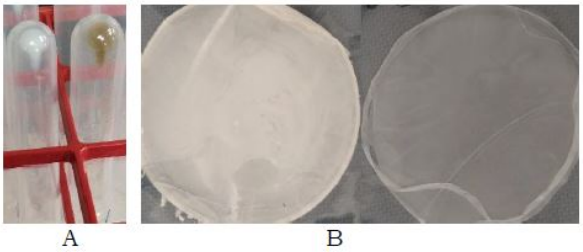



Figure 1: PHA/B generated by *A. vinelandii* Δ*Avin_16040*. A, Extracts of PHA/B from sucrose (left) and POME (right) media. B, Thin films of PHA/B generated from POME (left) and sucrose (right) substrates.

## 4 Discussion/Conclusions

The results showed that *A. vinelandii* successfully generated PHA/B by utilizing POME as carbon substrate. The amount of PHA/B generated from POME medium was comparable with the amount of PHA/B generated when sucrose was utilized as the single carbon source. RSM has significantly improved

*A. vinelandii's* PHA/B generation in both POME medium and sucrose medium.

## References

Y. Doi and A. Steinbuchel. 2002. *Biopolymers*, volume ISBN 978-3-527-30225-3. Weinheim, Germany: Wiley-VCH.

J. H. Law and R. A Slepecky. 1961. Assay of poly-beta-hydroxybutyric acid. *Journal of Bacteriology*, 82(1):33–36.

P. W. Y. Liew, B. C. Jong, and N. Najimudin. 2015. Hypothetical protein avin_16040 as the s-layer protein of azotobacter vinelandii and its involvement in plant root surface attachment. *Applied and Environmental Microbiology*, 81(21):7484–7495.

P. W. Y. Liew, B. C. Jong, K. Sudesh, N. Najimudin, and P.S. Mok. 2023. Characterization of p(3hb) from untreated raw palm oil mill effluent using azotobacter vinelandii avin_16040 lacking s-layer protein. *World Journal of Microbiology and Biotechnology*, 39(68).

Y. Wang, J. Ding, and J. Xu. 2020. Pathogenicity of dickeya zeae on pineapple and its control. *Plant Pathology Journal*, 36(3):169–178.

Individual Research Contribution Review, 2024: 21–22
*ISSN: 3083-922X*

# Aerial Multispectral Imaging: NDT Technique for Precision Agriculture

**Mohamad Syafiq bin Mohd Amin**
Agrotechnology and Biosciences Division, Malaysian Nuclear Agency
43000 Kajang, Selangor
syafiqamin@nm.gov.my

## Abstract

The purposes of this extended abstract in to present the current progress of the work associated with aerial multispectral imaging technique for various agriculture study. Remote Sensing Lab in Agrotechnology and Bioscience Division currently carries out research using Unmanned Aerial Vehicle (UAV) with multispectral sensor to evaluate plant health of Harumanis Mango in Perlis. In this study, aerial multispectral images that have been acquired once every month for the last 13 months from altitude of 30 meter is presented. All the data presented have been computed by subscribed software and corelated with actual field data.

## 1 Introduction

Traditionally, manual plant health monitor is a very time consuming task that will make early disease detection impossible. Non destructive testing, NDT via remote sensing data permits measurement of biophysical and biochemical parameters of plants for nondestructive monitoring of plant growth and health (Lu et al., 2015; Sankaran et al., 2012). Precision agriculture, PA then continue this process by collecting and evaluating field and real-time environmental data in order to develop a predictive management (Lum et al., 2016). Combining Unmanned Aerial Vehicle UAV) and remote sensing data like multispectral imaging is becoming one of the technique that enable fast and accurate plant health monitoring for large scale agriculture farm. The primary goal of this study is to develop a database of indices map that can be use for plant health monitoring, phenological stages study, development yield model, and others.

## 2 Aerial Multispectral UAV

In this study, we employ an DJI Phantom 4 Multispectral UAV (Figure 1) that carry a multispectral sensor which include 6 spectrum such as Blue (B): 450 nm ± 16 nm; Green (G): 560 nm ± 16 nm; Red (R): 650 nm ± 16 nm; Red edge (RE): 730 nm ± 16 nm; Near-infrared (NIR): 840 nm ± 26 nm and visible light spectrum.Autonomous Radiation Mapping Autonomous Radiation Mapping.

## 3 Result and Discussion

The study was carried out at Malaysian Department of Agriculture facility in Bukit Temiang, Perlis. Aerial Multispectral



Figure 1: DJI Phantom 4 Multispectral UAV

Mapping at Bukit Temiang Harumanis Plot covered 4 research plot sizing 5.99 hectare or 59,891 $m^2$ (Figure 2).



Figure 2: Orthomosaic Map of Harumanis Research Plot

For every fly mission, 6 indices maps (one for each spectrum) was created using photogrammetry software and then been analyze into required index map such as Normalize Differential Vegetative Index (NDVI), Landsat Enhanced Vegetation Index (EVI), Normalized Difference Red Edge Index (NDRE) using geographic information system,GIS application (Figure 3).

All index map will then be crop using each plant/area boundary which will produce specific index value for each plant or area (Figure 4). The index value of each plant/area then will be collected and compile into database system which can be use to various study. Chart 1 show individual value of NDVI for selected Harumanis plant.

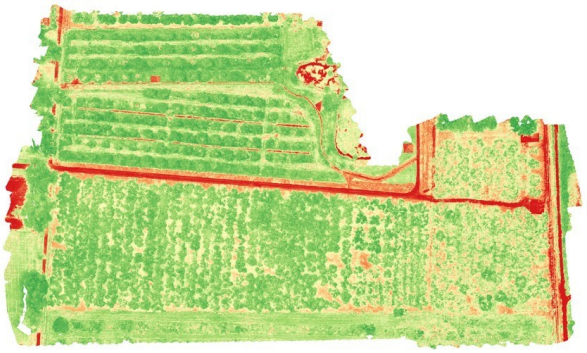


Figure 3: NDVI Map

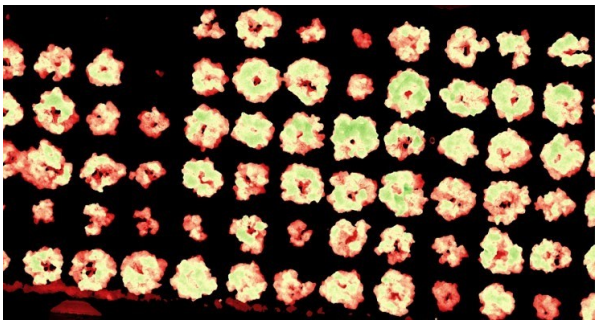


Figure 4: NDVI Map after soil removal and plant isolation process

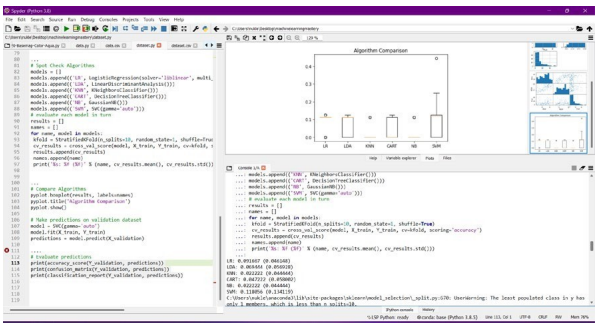


Figure 5: Correlation between multispectral data and manual data using Phyton programming

This individual plant multispectral index data will then be correlated with manual measurement data that provided by Malaysian Department of Agriculture personnel. Based on our current finding, although there is a pattern regarding the correlation of NDVI value with actual yield data and NDVI value with plant growth, we still need to collect more data to further proof our correlation in order to develop any prediction or estimation model (Figure 5).

## 4 Conclusion

As a conclusion, the results presented in this extended abstract have shown the capability of aerial multispectral imaging to monitor plant health, predict yield and assist on phenological stages study in the long run.

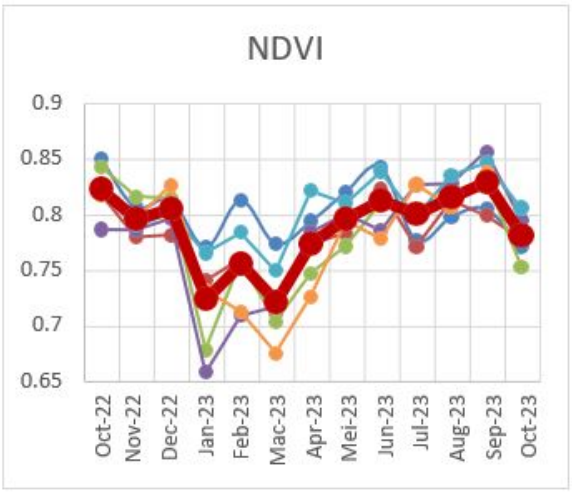



Figure 6: Individual plant NDVI value.

## References

S. Lu, X. Lu, W. Zhao, Y. Liu, Z. Wang, and K. Omasa. 2015. Comparing vegetation indices for remote chlorophyll measurement of white poplar and chinese elm leaves with different adaxial and abaxial surfaces. *Journal of Experimental Botany*, 66(18):5625–5637, 06.

C. Lum, M. Mackenzie, C. Shaw-Feather, E. Luker, and M. Dunbabin. 2016. Multispectral imaging and elevation mapping from an unmanned aerial system for precision agriculture applications. *Proceedings of the 13th International Conference on Precision Agriculture*.

S. Sankaran, R. Ehsani, S.A. Inch, and R.C. Ploetz. 2012. Evaluation of visible-near infrared reflectance spectra of avocado leaves as a non-destructive sensing tool for detection of laurel wilt. *Deleted Journal*, 96(11):1683–1689.

Individual Research Contribution Review, 2024: 23–24
*ISSN: 3083-922X*

# Soil Water Content using Nuclear Technique

**Mohamad Syafiq bin Mohd Amin**
Agrotechnology and Biosciences Division, Malaysian Nuclear Agency
43000 Kajang, Selangor
syafiqamin@nm.gov.my

## Abstract

This extended abstract explores soil water content measurement using advanced nuclear techniques, Cosmic Ray Neutron Sensor (CRNS) and Nuclear Density and Moisture Gauge (NDMG). CRNS offers non-invasive, landscape-scale monitoring, while NDMG provides high-resolution in situ measurements of soil density and moisture. Combined with complementary methods such as remote sensing and ground-truthing using Watermark soil sensors, the research enhances the precision of soil water assessments. These techniques are critical for understanding hydrological processes, improving agricultural water management, and mitigating climate change impacts. The study contributes to developing robust methodologies for sustainable water resource management and environmental conservation.

## 1 Introduction

Soil water content is a fundamental parameter influencing crop growth, hydrological processes, and ecosystem dynamics. Precise and scalable measurement is critical for effective water resource management, agricultural planning, and climate change mitigation. Traditional in-situ methods, while reliable, are limited in spatial coverage. Remote sensing provides large-scale data but lacks ground-level precision. Bridging this gap, nuclear- based techniques, such as the CRNS and NDMG offer innovative solutions.

CRNS uses interactions between cosmic rays and hydrogen atoms in soil to estimate field-scale soil moisture within a 240-meter radius, enabling non- invasive, real-time monitoring (Flynn et al., 2021). Its ability to provide comprehensive spatial data has been validated in diverse landscapes, enhancing the accuracy of soil-water balance studies and hydrological modeling (Heidbüchel et al., 2016). Complementing CRNS, NDMG provides precise in- situ measurements by using neutron scattering and gamma-ray attenuation, which are highly effective for localized soil density and moisture assessments ((IAEA)., 2017).

These nuclear approaches, combined with calibration from soil sampling and remote sensing observations, address spatial variability and scalability challenges. Their adoption aligns with global efforts to improve water conservation, support sustainable agriculture, and build resilience against climate variability. This integration advances modern soil water content research significantly.

## 2 Methodology

CRNS (Figure 1) is a cutting-edge tool for measuring soil water content at the field scale. It works by detecting high-energy neutrons from cosmic rays that interact with hydrogen in soil, which is mainly present in water molecules. This non-invasive technology provides real-time data over large areas (up to 240 meters radius) and varying depths, bridging the gap between point-scale in-situ sensors and large-scale satellite measurements.



Figure 1: Cosmic Ray Neutron Sensor (CRS 100-B).

NDMG (Figure 2) is a field instrument that uses gamma and neutron sources to measure soil density and moisture. It operates by emitting gamma rays to determine soil density and neutrons to measure hydrogen content, which correlates with soil moisture. NDMG provides precise, localized data, making it invaluable for construction, agriculture, and hydrology. Its portability and accuracy support site-specific soil analyses for optimal resource management.



Figure 2: Cosmic Ray Neutron Sensor (CRS 100-B).

## 3 Result and Discussion

CRNS provides real-time monitoring capabilities, offering hourly updates on soil volumetric water content for the area it covers (Figure 3). This allows for near-instantaneous tracking of changes in soil moisture dynamics, crucial for water management and agricultural decision-making. In addition to soil moisture, the CRNS system integrates sensors that measure environmental parameters, including temperature, atmospheric pressure, relative humidity, and precipitation. These additional data streams enhance the understanding of factors influencing soil water content. CRNS data can be accessed remotely via online platforms, enabling seamless monitoring across various scales and promoting efficient resource management.

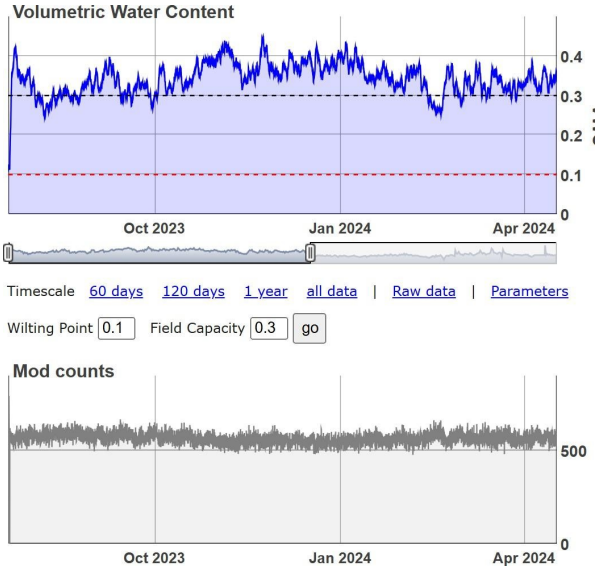



Figure 3: Real-time CRNS online data

NDMG is a portable device for precise soil analysis. Data collection involves traveling to specific locations, measuring soil properties, and recording GPS coordinates. The gauge emits gamma rays to determine soil bulk density and uses neutron scattering to measure moisture content. The collected data is then mapped based on GPS coordinates to visualize spatial distribution of soil bulk density or moisture across the area. This process is invaluable for site-specific management in agriculture.

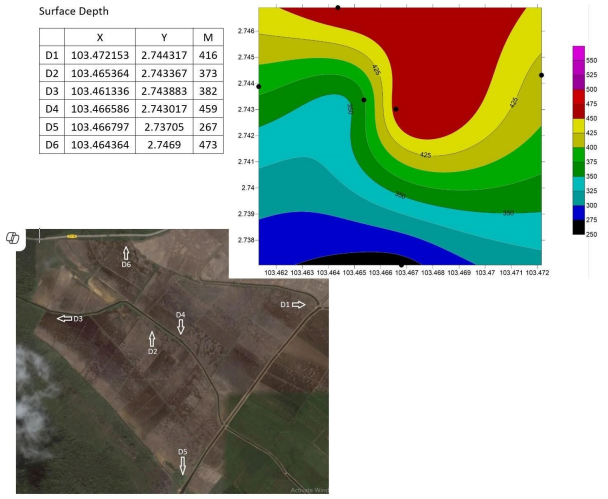



Figure 4: NDMG data visualization

## 4 Conclusion

Nuclear techniques, including the CRNS and NDMG, revolutionize soil water content monitoring by offering precise, scalable, and real-time data. These technologies enhance resource management by bridging spatial and temporal measurement gaps, supporting sustainable agriculture, hydrological studies, and climate resilience strategies.

## References

K. D. Flynn, B. M. Wyatt, and K. J. McInnes. 2021. Novel cosmic ray neutron sensor accurately captures field-scale soil moisture trends under heterogeneous soil textures. *Water*, 13(21):3038.

I. Heidbüchel, A. Güntner, and T. Blume. 2016. Use of cosmic-ray neutron sensors for soil moisture monitoring in forests. *Hydrology and Earth System Sciences*, 20(3):1269–1288.

International Atomic Energy Agency (IAEA). 2017. Nuclear techniques for sustainable agriculture and water resources management. vienna. *IAEA*, 48.

Individual Research Contribution Review, 2024: 25–26
*ISSN: 3083-922X*

# Detection of *Pantoea ananatis* causing Bacterial Leaf Blight (BLB) of Rice in Kedah and Selangor using Species-Specific PCR Assays

**Mohammad Malek Faizal Azizi**
Agrotechnology and Biosciences Division, Malaysian Nuclear Agency
43000 Kajang, Selangor
malek@nm.gov.my

## Abstract

*Pantoea ananatis* is a Gram-negative bacterium in the Enterobacteriaceae family. This bacterium is known to cause bacterial leaf blight (BLB) disease in rice plants, resulting in significant economic losses in rice production worldwide. To facilitate rapid and precise detection of 20 *P.ananatis* strains in PCR assays, attempts have been made to develop species-specific primers (PANAN_gyrb_F and PANAN_gyrb_R). Subsequently, PCR assays were performed using these species-specific primers. The results obtained demonstrated the specificity of the *P.ananatis*- specific primer pair towards its *Pantoea* target species. The primers successfully distinguished these strains specifically as *P.ananatis*.

**Keywords:** *Pantoea ananatis*, bacterial leaf blight, species-specific primers

## 1 Introduction

Bacterial leaf blight (BLB) disease is one of the most damaging diseases of rice crops, causing widespread devastation in rice agroecosystems (Doni et al., 2022). Blight disease refers to a variety of plant diseases that cause abrupt and severe drooping, withering, and death of plant components such as leaves, stems, and fruits (Zakaria, 2022). Blight can be caused by various pathogens, including bacteria, fungus, and oomycetess. *Xanthomonas oryzae pv. oryzae (Xoo)* is a bacterial pathovar that causes a serious bacterial leaf blight (BLB) disease of rice. This disease poses a significant constraint on food security in Asia, as it causes yield loss in rice. However, from 2008 to 2019, *Pantoea* species was identified as the primary agent of leaf blight disease in several rice-growing nations, including Malaysia, Thailand, India, and others (Doni et al., 2022). *Pantoea* spp. was recently identified as the cause of a novel rice bacterial disease with up to ≥ 70% occurrence in susceptible rice varieties, resulting in BLB-like symptoms (Doni et al., 2019). *Pantoea* species have been identified as the cause of a leaf blight outbreak in Malaysia between 2016 and 2018 (Azizi et al., 2019). The need for rapid and precise diagnosis of BLB is crucial due to its potential threat to rice production and its capacity to disrupt rice sustainability in the future. Therefore, utilising a particular primer as a detection marker for *Pantoea ananatis* is of extreme relevance. This method assures accurate and timely diagnosis, improves plant management, and plays a vital role in the development of BLB-resistant rice cultivars.

## 2 Methods

### 2.1 Sampling Rice Leaves with BLB Symptoms

Symptomatic rice leaves were collected from Sekinchan, Selangor and Sanglang, Kedah. The samples were placed in labeled plastic bags and stored in an icebox with ice to keep them fresh.

### 2.2 Bacterial Isolation from Rice Leaves Samples

Surface sterilization was performed on samples using ≥ 70% ethanol and sterile distilled. 200 µL of the sample solution is pipetted onto labeled Nutrient Agar and incubated at a temperature of 30-35 °C for two days. After the incubation period, the bacterial colony was isolated into Nutrient Broth and incubated overnight in a shaking incubator at 180 Revolutions Per Minute (RPM).

### 2.3 DNA Extraction from Bacterial Isolation

A 1st BASE PrimeWay Plant DNA Extraction kit was utilized in this step. Methods are as provided in the manual of the kit.

### 2.4 Polymerase Chain Reaction (PCR) Amplification

PCR amplification using the species-specific primer (PANAN_gyrb_F and PANAN_gyrb_R). The PCR reaction was performed in a total volume of 25 µL, containing 2 µL of DNA template, 0.5 µL each of forward and reverse primers, and 1.5 Taq polymerase. The thermal cycling conditions included an initial denaturation at 95 °C for 2 minutes, followed by 30 cycles of denaturation at 95 °C for 1 minute, annealing at 58 °C for 1 minute, and extension at 72 °C for 30 seconds. A final extension was carried out at 72 °C for 5 minutes, and the reaction was held at 4 °C until further analysis.

### 2.5 Gel Electrophoresis and Visualization

Gel electrophoresis was carried out using a ≥ 1.5% agarose gel. The power supply was connected and electrophoresis ran at 75V for 1 hour. Finally, DNA bands were visualized through a bio-imaging system.

### 2.6 Sequencing and BLASTn Analysis

The PCR products were sent for sequencing, and the raw sequences were analyzed using NCBI BLAST. The tool identified the closest relatives along with their descriptions and similarity percentages.

## 3 Data/Results

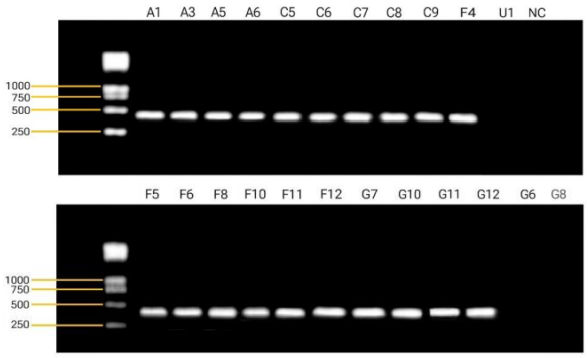



Figure 1: Figure 1: Gel electrophoresis of twenty strains of *Pantoea ananatis* using specific-species primer (PANAN_gyrb_F and PANAN_gyrb_R) and 4 samples as negative control. A1-G12: *P. ananatis*; G6: *M. testaceum*; U1: *P. stewartii*; G8: *P. walisii* and NC: negative control. Amplicon size (bp) for *P. ananatis* gene in 423 base pair.

Table 1: Blastn identification of 20 strains of *Pantoea ananatis* isolates.

| Line | Isolate Code | Closest Relative | Percentage Identity | Source[a] |
|---|---|---|---|---|
| 82-2 | A1 | *Pantoea ananatis* | 98.67 | OL742772 |
| 82-2 | A3 | *Pantoea ananatis* | 98.45 | OL742772 |
| 82-2 | A5 | *Pantoea ananatis* | 97.78 | OL742735 |
| 82-2 | A6 | *Pantoea ananatis* | 98.34 | MZ007856 |
| 82-2 | C5 | *Pantoea ananatis* | 98.84 | OL742772 |
| 82-2 | C6 | *Pantoea ananatis* | 98.59 | OL742772 |
| 82-2 | C7 | *Pantoea ananatis* | 97.69 | OL742772 |
| 82-2 | C8 | *Pantoea ananatis* | 98.09 | OL742772 |
| 82-2 | C9 | *Pantoea ananatis* | 97.96 | OL742786 |
| ML 10 | F4 | *Pantoea ananatis* | 94.32 | MZ501308 |
| ML 10 | F5 | *Pantoea ananatis* | 98.78 | OL742735 |
| ML 10 | F6 | *Pantoea ananatis* | 95.56 | MZ007857 |
| NMR151 | F8 | *Pantoea ananatis* | 94.51 | OR781534 |
| CL 2 | F10 | *Pantoea ananatis* | 98.87 | OL742735 |
| CL 2 | F11 | *Pantoea ananatis* | 99.66 | OL742735 |
| CL 2 | F12 | *Pantoea ananatis* | 99.49 | OL742735 |
| NMR192 | G7 | *Pantoea ananatis* | 98.53 | OL742735 |
| MR297 | G10 | *Pantoea ananatis* | 94.74 | MZ007857 |
| MR297 | G11 | *Pantoea ananatis* | 99.27 | OL742735 |
| MR297 | G12 | *Pantoea ananatis* | 95.36 | MZ007857 |

[a] Accession number of the closest relative sequence found by Blast search.

## 4 Discussion

### 4.1 Bacteria DNA Amplification

In the present study, we conducted a thorough assessment of the primers that were specifically designed to accurately target identified *P. ananatis* species through the sequencing of housekeeping genes. Subsequently, PCR assays were performed using the species-specific primers which are (PANAN_gyrb_F and PANAN_gyrb_R). The gel electrophoresis result shows the successful amplification of 20 strains (A1 until G12) of *P. ananatis* using species-specific primers mentioned (Figure 1). These primers demonstrated high specificity to target specific genetic markers without cross-reactivity with other bacterial species. Those DNA strains were amplified at 423 base pairs which confirm the precise identification of *P. ananatis* strains. On the other hand, four samples were used as the negative control; G6 (*M. testaceum*), U1 (*P. stewartii*), G8 (*P. walisii*), and NC (negative control), respectively.

### 4.2 Bacteria DNA Amplification

Each 20 isolates were matched to its closest relative in the database which was confirmed as Pantoea ananatis with percentage identity ranging from ≥ 94.32% to ≥ 99.66% (Table 1). This precise identification exhibits the reliability of the PCR-based detection method in ensuring no misidentification with non-target species. Blastn analysis showed that all twenty strains were accurately identified as *P. ananatis* and the species-specific primers developed were effective and accurate. Therefore, these primers can be used in various diagnostic applications specifically in *P. ananatis* detection, thus aiding in effective disease management and improving agricultural productivity.

## 5 Conclusion

In summary, the study successfully detected 20 strains of *Pantoea ananatis*, responsible for BLB disease in Selangor and Kedah, utilizing a species-specific PCR assay. The primers (PANAN_gyrb_F and PANAN_gyrb_R) proved effective in identifying these strains, highlighting the assay's accuracy and specificity for this pathogen.

## References

M. M. F. Azizi, D. Zulperi, M. a. A. Rahman, B. Abdul-Basir, N. A. Othman, S. I. Ismail, E. M. Hata, M. Y. Ina-Salwany, and M. a. F. Abdullah. 2019. First report of pantoea ananatis causing leaf blight disease of rice in peninsular malaysia. *Plant Disease*, 103(8):2122, 06.

F. Doni, Ishak M. N., S. Mohd, Syaputri Y., L. Han, M. Zeriouh, and Mispan M. S. 2022. Leaf blight disease of rice caused by pantoea: profile of an increasingly damaging disease in rice. *Tropical Plant Pathology*, 48(1):1–10.

L. Zakaria. 2022. Fungal and oomycete diseases of minor tropical fruit crops. *Horticulturae*, 8(4).

Individual Research Contribution Review, 2024: 27–28
*ISSN: 3083-922X*

# Detecting Food Fraud in Malaysian Tiger Prawn Using Nuclear Technology and Related Techniques

**Mohd Noor Hidayat Adenan**
Agrotechnology and Biosciences Division, Malaysian Nuclear Agency
43000 Kajang, Selangor
hidayat@nm.gov.my

## Abstract

This study utilizes stable isotope analysis to distinguish wild and farmed tiger prawns (Penaeus monodon), addressing food fraud concerns in Malaysia. Carbon-13 ($\delta^{13}$C), nitrogen-15 ($\delta^{15}$N), and sulfur-34 ($\delta^{34}$S) isotopes, indicative of diet, environmental influences, and protein sources, were analyzed to differentiate prawns from various regions. Samples from farms and wild habitats across Malaysia exhibited clear isotopic distinctions, verified by multivariate statistical models. These findings demonstrate the potential of stable isotopes for enhancing traceability, authenticity, and combating food fraud in aquaculture.

**Keywords:** : Stable isotope analysis, Food fraud, Tiger prawn, Aquaculture traceability, $\delta^{13}$C, $\delta^{15}$N, $\delta^{34}$S

## 1 Introduction

The increasing demand for tiger prawns (*Penaeus monodon*) as a high-value seafood product has led to fraudulent practices, including mislabeling of farmed prawns as wild- caught to command higher prices. Addressing this issue is crucial for protecting consumer trust and ensuring fair trade practices. This study employs stable isotope analysis to differentiate wild and farmed tiger prawns based on their isotopic signatures, providing a scientific basis for verifying product authenticity.

## 2 Materials and Methods

The project involves sampling of wild and farm tiger prawn, analysis, and compilation of chemical properties of samples. Multivariate statistical tool (SIMCA) is used to analyze and interpret the data.

### 2.1 Sampling of Wild and Farm Tiger Prawn

A total of 50 tiger prawn samples were collected from three locations namely Setiu (Farm, East Coast), Mersing (Farm, South) and Mersing (Wild, South).

### 2.2 Stable Isotope Analysis

$\delta^{13}$C, $\delta^{15}$N and $\delta^{34}$S isotopes respectively reflect the prawn's carbon sources, nitrogen sources and trophic levels, and protein sources with marine influences, enabling differentiation between consistent farm feeds and diverse natural diets in wild habitats.

## 3 Data/Results

Distinct isotopic patterns were observed between farmed and wild tiger prawns (Figure 1). Farmed prawns displayed consistent $\delta^{13}$C, $\delta^{15}$N and $\delta^{34}$S values, which can be attributed to their uniform feed and the controlled conditions of aquaculture environments (Nguyen et al., 2022). In contrast, wild prawns exhibited greater variability in these isotopic ratios, reflecting the influence of diverse environmental conditions and natural dietary inputs (Sanchez et al., 2020).

The isotopic data clustered farmed and wild prawns accurately, confirming the PCA model's efficacy in detecting food fraud. Variability in $\delta^{34}$S signatures highlighted differences in protein sources and marine influences.

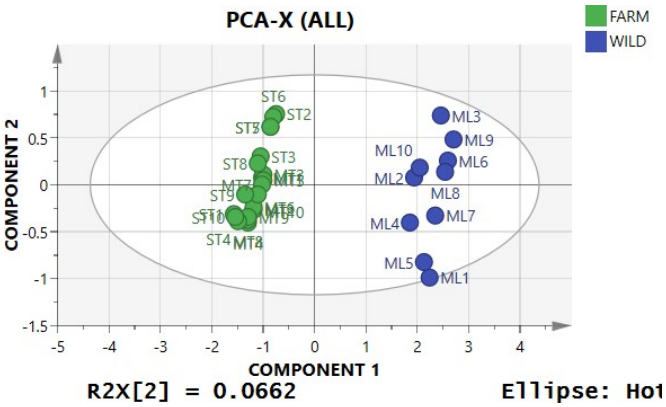



Figure 1: PCA-X Plot of Isotopic Signatures Differentiating Farmed and Wild Tiger Prawns.

## 4 Discussion/Conclusions

Stable isotope analysis, including$\delta^{13}$C, $\delta^{15}$N and $\delta^{34}$S, proves effective in distinguishing wild and farmed tiger prawns, addressing critical gaps in aquaculture traceability and fraud detection. The method provides a robust scientific framework for ensuring product authenticity and protecting consumer trust. Future work will expand sampling to other regions and explore additional isotopic markers to enhance the model's robustness.

## References

T. M. Nguyen, H. T. Le, and Q. A. Pham. 2022. Application of stable isotope technique to authenticate the geographical origin of apples imported into vietnam. *Journal of Radioanalytical and Nuclear Chemistry*, 331(2):459–470.

M. P. Sanchez, M. Díaz, and R. Gutiérrez. 2020. Tracing the geographical origin of spanish mango (mangifera indica l.) using stable isotopes and elemental composition. *Scilit*, 8(2):58–68.

Individual Research Contribution Review, 2024: 29–30
*ISSN: 3083-922X*

# Effects of Chronic Gamma Irradiation on Cassava Var. *Ubi Kuning*

**Muniroh Md Saad**
Agrotechnology and Biosciences Division, Malaysian Nuclear Agency
43000 Kajang, Selangor
muniroh@nm.gov.my

## Abstract

In Malaysia, Cassava produces various food items, including tapioca pearls, and cassava chips. During the past two decades advances mutation breeding techniques have contributed significantly of the genetic improvement of cassava, addressing challenges such as low yield, disease susceptibility, and poor nutritional content. Additionally, mutation breeding has facilitated the enhancement of root quality, including higher starch content and improved cooking properties. Cassava stem cuttings were exposed to various gamma irradiation dose rates (0.07 to 2.67 Gy/hour) over eight weeks. The results showed that survival rates remained high across most treatments, indicating cassava's resilience to radiation. However, plant height and bud formation were adversely affected by higher doses, with the highest cumulative dose (1709.49 Gy) resulting in the lowest plant height (30.4 cm) and reduced bud counts. Morphological changes, such as chlorophyll degradation and leaf abnormalities, were prevalent at higher doses. This suggests that while cassava can tolerate significant gamma irradiation, substantial doses impede growth and induce notable morphological mutations.

**Keywords:** Cassava, Chronic gamma irradiation, mutation breeding

## 1 Introduction

Cassava (Manihot esculenta), or ubi kayu, is a vital tropical crop with significant adaptability to various agroecological conditions. It provides essential calories and supports food security, especially in regions with poor soils where other crops fail. Cassava thrives in tropical and subtropical climates, offering year-round harvests for smallholder farmers and raw materials for industries. In Malaysia, cassava is mainly cultivated for producing starch-based foods such as tapioca pearls and chips. Despite its importance, cassava farming faces challenges such as low yields, pests, and diseases. Recent efforts focus on improving varieties like Ubi Kuning to enhance yield, quality, and resistance to environmental stresses.

Mutation breeding using gamma irradiation is a promising approach to improving cassava traits. This study examines the effects of chronic gamma irradiation on Ubi Kuning, with stem cuttings exposed to varying doses (0.07–2.67 Gy/hour) over eight weeks. The findings explore survival, growth, and morphological changes, shedding light on potential genetic improvements and the trade-offs between enhanced traits and growth limitations.

## 2 Methods

### 2.1 Plant Materials and preparation

Ubi Kuning stem cutting was obtained from Taman Kekal Pengeluaran Makanan (TKPM) Ulu Chuchoh, Sepang, Selangor. A total of 70 stem cuttings were used in this study. The stem cutting was chosen based on their diameter approximately five cm in diameter and was cut into 15 cm lengths each. The experiment was conducted with seven treatments which are control, isodose ring 1,2,3,4,5, and isodose ring 6 with 10 replicates for each treatment.

### 2.2 Chronic gamma irradiation exposure

A total of 60 Ubi Kuning stem cuttings were exposed to chronic gamma irradiation in the Gamma Green House (GGH) facility in the Malaysian Nuclear Agency. The stem cuttings were placed in pots at 6 different dose rates ranging from 0.07 Gy/hour, 0.11 Gy/hour, 0.17 Gy/hour, 0.3 Gy/hour, 0.66 Gy/hour, and 2.67 Gy/hour. As for control treatment, a total of 10 stem cuttings were grown outside the gamma house under conditions very similar to those irradiated plants. Data on Plant Survival, plant height, number of buds, morphological changes of the plants were observed during the experiment. Plants were taken out from GGH at Week 8 after planting and an accumulated dose of gamma irradiation for each treatment was collected at the end of the experiment.

### 2.3 Statistical Analysis

Analysis of variance was performed using Statistical Analysis System (SAS) version 9.2 to measure significant differences ($p \leq 0.05$) or ($p \leq 0.01$) among characteristics data. The mean difference between doses was further tested using the least significant difference (LSD) method at 5%.

## 3 Results and Discussion

Stem cuttings of Ubi Kuning were subjected to chronic gamma irradiation for 8 weeks (32 days) to study the plant's response to varying doses of gamma rays. A previous study has reported that mutagenic treatment significantly affects plant survival rates and morphological traits. The data, including survival percentages, plant height, and number of buds are presented in Table 1.

| Isodose Ring | Dose Rate (Gy/hr) | Accumulative Dose (Gy) | Survival Rate (%) | | Plant Height (cm) | | Number of Buds | |
|---|---|---|---|---|---|---|---|---|
| | | | Week 2 | Week 8 | Week 2 | Week 8 | Week 2 | Week 8 |
| Control | 0.00 | 0.00 | 100 | 100 | 4.83 | 50.4 | 3.4 | 3.4 |
| 1 | 2.67 | 1709.49 | 100 | 100 | 5.67 | 30.4 | 3.4 | 2.5 |
| 2 | 0.66 | 450.58 | 100 | 100 | 6.10 | 58.1 | 3.1 | 2.5 |
| 3 | 0.30 | 192.80 | 100 | 8.9 | 48.1 | 3.3 | 2.5 | – |
| 4 | 0.17 | 109.25 | 100 | 10 | 12.25 | 52.6 | 3.3 | 2.7 |
| 5 | 0.11 | 70.69 | 100 | 100 | 10.8 | 48.4 | 3.6 | 2.7 |
| 6 | 0.07 | 44.99 | 100 | 90 | 12.1 | 56.6 | 3.0 | 2.7 |

Table 1: Survival percentages, plant height, and number of buds at Week 2 and Week 8 for each isodose ring treatment.

The survival rate of cassava remained consistently high (around 100%) across most treatment conditions at week 8, with a minor decrease to 90% observed at an accumulated dose of 44.99 Gy. This suggests that the accumulated dose had minimal impact on survival, indicating a potential threshold effect or inherent resistance to radiation. The height of Ubi Kuning plants was significantly affected by the cumulative doses of radiation. At week 2, plant height increased with lower doses, peaking at 12.25 cm for moderate doses. By week 8, the plants exposed to the highest dose showed the lowest height at 30.4 cm. These results indicate that excessive radiation negatively affects plant growth (Tiwari and Kumar, 2011). The effect of cumulative gamma irradiation doses on the number of buds in Ubi Kuning was observed at two time points: week 2 and week 8. The results suggest radiation does not significantly affect bud count in the short term, it causes a gradual reduction in bud formation over time (Hartati et al., 2021).

The study observed notable morphological changes in cassava plants exposed to chronic gamma radiation, with variation depending on the radiation dose (Figure 1). The results suggest the chronic gamma radiation disrupts normal plant growth and development, leading to visible morphological changes (Riviello-Flores et al., 2022).

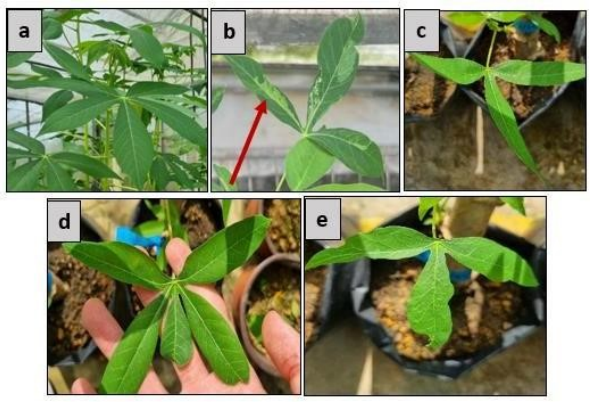



Figure 1: Leaves show (a) Normal color with 5 lobes (Control); (b) chlorophyll degradation; (c) Different numbers of lobes; (d) Different shapes of leaves; and (e) crinkled leaves

## 4 Conclusion

The study investigated the impact of chronic gamma irradiation on Ubi Kuning stem cuttings over 8 weeks, revealing that high doses of gamma rays can significantly alter plant morphology and growth. These findings suggest that while Ubi Kuning can withstand substantial gamma radiation exposure, significant doses impede its growth and induce notable morphological mutations. This study can later be improved by observing the growth of the next mutant generation.

## References

T. M. Hartati, C. Roini, and I. Rodianawati. 2021. Growth response of local cassava to cutting models and the number of buds. *Caraka Tani: Journal of Sustainable Agriculture*, 36(2):379–391.

M. D. L. L. Riviello-Flores, J. Cadena-Iñiguez, L. D. M. Ruiz-Posadas, M. D. L. Arévalo-Galarza, I. Castillo-Juárez, M. Soto Hernández, and C. R. Castillo-Martínez. 2022. Use of gamma radiation for the genetic improvement of underutilized plant varieties. *Plants*, 11(9):1161.

A. K. Tiwari and V. Kumar. 2011. Gamma-rays induced morphological changes in pot marigold (calendula officinalis). *Progressive Agriculture*, 11(1):99–102.

Individual Research Contribution Review, 2024: 31–32
*ISSN: 3083-922X*

# Gamma-Irradiation Response of Cassava (Var. Ubi Kuning)

**Mustapha Akil**
Agrotechnology and Biosciences Division, Malaysian Nuclear Agency
43000 Kajang, Selangor
mustapha@nm.gov.my

## Abstract

Cassava *(Manihot esculenta)* is a key staple crop in tropical and subtropical regions, renowned for its ability to thrive in poor soils and withstand drought conditions. Despite its economic importance, traditional breeding methods in cassava are challenged by complex polyploid genome and predominantly vegetative propagation. In this study, evaluation of the acute radiosensitivity of cassava cuttings (Cassava var. Ubi Kuning) to gamma irradiation, using doses of 0 (control), 5, 10, 15, 20, 25, 30, 40, 50, and 60Gy was conducted. The cuttings were irradiated with a Biobeam GM8000 using Ceasium-137 as the source, and subsequently planted in polybags in a glasshouse. The survival data indicated an LD50 of approximately 33 Gy. The results show that as the gamma radiation dose increases, both data of the survival and growth of cassava decrease, demonstrating the plant's sensitivity to gamma irradiation. The findings suggest that doses around 33 Gy induce significant genetic variability while maintaining sufficient viability for mutation breeding programs. Gamma irradiation was also found to have impacts of the leaves morphology. This study emphasizes the importance of optimizing irradiation doses as a foundation for developing improved cassava cultivars through mutation breeding.

**Keywords:** Acute gamma irradiation; mutation breeding; radiosensitivity test; cassava

## 1 Introduction

Cassava provides crucial calories to over 800 million people worldwide and is particularly resilient to poor soils and drought (Burns et al., 2010). In Malaysia, cassava is essential for agriculture and industry, including food and bioethanol production. Ubi Kuning, a yellow- fleshed variety, supports economic stability in rural Malaysia due to its versatility and nutritional benefits. However, breeding improvements are hampered by cassava's limited genetic diversity and susceptibility to pests and diseases. Mutation breeding offers a promising approach to enhance cassava by creating novel genetic variability (Ahloowalia et al., 2004). This method, particularly through gamma irradiation, has successfully improved various crops by enhancing desirable traits like disease resistance and yield. To initiate mutation breeding, radiosensitivity tests are critical for determining optimal radiation doses that maximize genetic variation while preserving plant viability (Spencer-Lopes et al., 2018). This study assesses the radiosensitivity of cassava cuttings to gamma irradiation, setting a foundation for cassava improvement programs.

## 2 Materials and Methods

### 2.1 Plant Material and Irradiation

Cassava cuttings (15 cm long, 5 cm diameter) were collected from TKPM Ulu Chuchoh, Selangor. Using a BioBeam GM 8000 irradiator with Cesium-137, cuttings were exposed to 0, 5, 10, 15, 20, 25, 30, 40, 50, and 60Gy doses. Each dose had three biological replicates and ten technical replicates.

### 2.2 Data Collection and Analysis

Eight weeks post-planting, survival rate was assessed. Statistical analyses were conducted using ANOVA with SAS 9.2, and LD50 value was estimated using Curve Expert 1.3.

## 3 Results and Discussion

### 3.1 Lethal Dose 50 (LD50)

The survival rate of cassava under gamma irradiation is illustrated in Table 1 from 0Gy to 60Gy revealed a notable LD50 dose of approximately 32Gy. Different letter in t grouping shows significant differences among treatments. Lower doses like 10Gy and 20Gy showed survival rates of ≥ 90%, comparable to the control (0Gy), while the highest survival (≥ 100%) was at 15Gy. Doses above 30Gy led to decreased survival, with no survival at 50Gy and 60Gy. These results align with previous study that highlight moderate gamma doses as tolerable and high doses as detrimental to plant health, causing significant cellular damage (Kodym and Afza, 2003).

The fitted curve extracted from Curve Expert 1.3 as shown in Fig. 1, with a high correlation coefficient (r = 0.977), indicates a strong fit to the observed data, suggesting the model accurately represents the relationship between gamma irradiation doses and cassava survival rate. The LD50 which is the dose at ≥ 50% of the cassava plants survive in comparison with control population, was estimated to be around 32Gy.

### 3.2 Leaf Morphology

Gamma irradiation impacts leaf morphology differently across plant species and doses. Leaves are essential for photosynthesis and gas exchange, so changes to their structure can significantly affect plant health. Generally, gamma irradiation

| No. | Dose | Means | t Grouping | | |
|---|---|---|---|---|---|
| 1 | 0Gy | 0.9 | b | a | |
| 2 | 5Gy | 0.8 | b | a | c |
| 3 | 10Gy | 0.9 | b | a | |
| 4 | 15Gy | 1.0 | | a | |
| 5 | 20Gy | 0.9 | b | a | |
| 6 | 25Gy | 0.7 | b | | c |
| 7 | 30Gy | 0.6 | | | c |
| 8 | 40Gy | 0.1 | | d | |
| 9 | 50Gy | 0 | | d | |
| 10 | 60Gy | 0 | | d | |

Table 1: Cassava var. Ubi Kuning survival rate at 8th week after planting

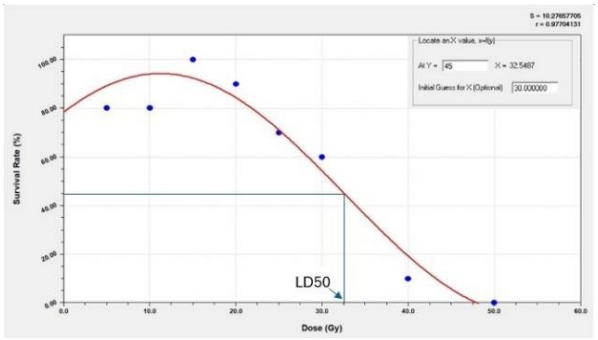



Figure 1: Survival rate (%) of irradiated cassava and control against dose (Gy) at 8th week after planting

alters leaf size, shape, color, and structure. In this study, cassava var. Ubi Kuning showed notable morphological changes at 5Gy, with an increased leaf count and healthy development, indicating low-dose irradiation can boost leaf production as shown in Fig. 2.

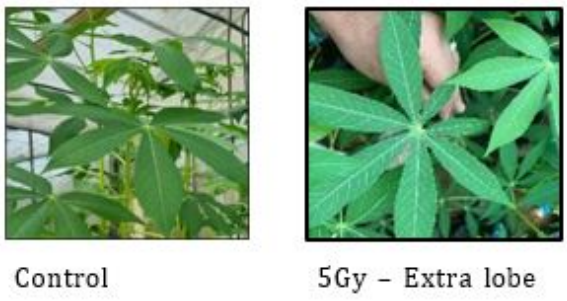



Figure 2: Comparison of cassava var. Ubi Kuning between control and 5Gy treatment

This effect may result from growth-promoting genes and hormonal changes triggered by irradiation (Kovács and Keresztes, 2002). However, some irradiated leaves displayed irregular shapes, hinting at potential unintended effects. Higher doses, as seen in Fig. 3, led to reduced leaf size, chlorophyll loss, and tissue necrosis, reflecting severe cellular damage and impaired chloroplast function essential for photosynthesis (Wi et al., 2007). These findings highlight the dose-dependent nature of gamma irradiation: low doses may enhance growth, while higher doses disrupt physiological processes. Understanding this dose-response relationship is crucial for optimizing gamma irradiation in plant mutation breeding to balance beneficial and harmful effects.




Figure 3: Comparison of cassava var. Ubi Kuning between control with 15Gy and 30 Gy treatment

## 4 Conclusions

In summary from the experimental results, gamma ray at different doses has adverse effect to significantly alter the morpho-physiological characteristic of grain corn. From the early observation, LD50 is calculated approximately 527Gy for grain corn and can be used in the next subsequent mutation induction. The development of a new variety of grain corn using mutation breeding is essential to reduce the country's dependency on grain corn importation and strengthen our national food security.

## 5 Acknowledgments

The authors would like to thank the officers and staff from the Division of Agrotechnology and Biosciences, Malaysian Nuclear Agency for the support. This acknowledgment also goes to all project members.

## References

B. S. Ahloowalia, M. Maluszynski, and K. Nichterlein. 2004. Global impact of mutation-derived varieties. *Euphytica*, 135(2):187–204.

A. Kodym and R. Afza. 2003. Physical and chemical mutagenesis. *Methods in molecular biology (Clifton, N.J.*, 236:189–204.

E. Kovács and Á. Keresztes. 2002. Effect of gamma and uv-b/c radiation on plant cells. *Micron*, 33(2):199– 210.

M. M. Spencer-Lopes, B. P. Forster, and L. Jankuloski. 2018. Manual on mutation breeding. *Methods in molecular biology (Clifton, N.J.*, 3rd Edition:189–204.

S. G. Wi, B. Y. Chung, J. S. Kim, J. H. Kim, J. W. Lee, ... Kim, Y. S. and, and S. H. Kim. 2007. Effects of gamma irradiation on morphological changes and biological responses in plants. *Micron*, 38(6):553–564.

Individual Research Contribution Review, 2024: 33–34
*ISSN: 3083-922X*

# RISE Project: Development of Protocol for Large-Scale Micropropagation of Banana *var.* Pisang Tanduk

**Norazlina Noordin**
Agrotechnology and Biosciences Division, Malaysian Nuclear Agency
43000 Kajang, Selangor
azlina@nm.gov.my

## Abstract

Malaysia is one of the major banana-producing countries in Southeast Asia. It holds economic significance in Malaysia as it is widely cultivated for both domestic consumption and export. Pisang Tanduk can fetch higher price in market in comparison to other banana varieties due to its limited supply and large fruit bunch size. Propagation of pisang Tanduk through tissue culture method is difficult due to its high phenolic compound and only small number of commercial tissue culture laboratories have successfully propagated Pisang Tanduk. Mie Agrofarm Sdn. Bhd. is a commercial company that is involved in supplying planting materials such as Pisang Berangan, Pisang Nangka. Currently, the company is having difficulties to develop an efficient protocol for commercial micropropagation of Pisang Tanduk. With this RISE collaboration, a protocol has been successfully established and optimized for producing Pisang Tanduk via tissue culture. This procedure will enable continuous and sustainable production and supply Pisang Tanduk banana seedlings.

**Keywords:** Banana, Micropropagation, Pisang Tanduk,

## 1 Introduction

Malaysia is one of the major banana-producing countries in Southeast Asia. It holds economic significance in Malaysia as it is widely cultivated for both domestic consumption and export. Malaysia cultivates various banana varieties, including the popular Cavendish, Pisang Tanduk, Pisang Berangan, Pisang Nangka, and Pisang Mas. Amongst these varieties, Pisang Tanduk can fetch higher price in market due to its limited supply and large fruit bunch size. The versatile nature of this banana variety, which is primarily used for cooking, makes it a valuable ingredient in various traditional dishes, snacks, and desserts makes it popular amongst consumers.

Currently, the planting materials for Pisang Tanduk is limited as every banana tree can only produce limited number of suckers per crop cycle. Propagation of pisang Tanduk through tissue culture method is difficult due to its high phenolic compound and only small number of commercial tissue culture laboratories have successfully propagated Pisang Tanduk. Therefore, MIE Agrofarm Sdn. Bhd. is trying to develop an efficient protocol for commercial micropropagation of Pisang Tanduk.

With the establishment of Researcher-Industry Scientific Exchange (RISE) program initiated by the Ministry of Science, Technology and Innovation of Malaysia (MOSTI), collaboration is forged between MIE Agrofarm Sdn. Bhd. and Malaysian Nuclear Agency. Malaysian Nuclear Agency has successfully established and developed Standard Operating Procedure (SOP) on the Micropropagation of Banana Tissue Culture Seedlings (Norazlina et al., 2019). With this RISE project, team of researchers from Nuklear Malaysia managed to assist MIE Agrofarm in developing a micropropagation protocol for Pisang Tanduk. With this collaboration, the protocol, hands-on training and consultation on production of Pisang Tanduk seedlings via tissue culture was successfully developed and delivered. With this protocol, it offers attractive and reliable solution for rapid and continuous production of Pisang Tanduk seedlings.

## 2 Materials and Methods

**Hands-on training and initiation of Pisang Tanduk micropropagation process using SOP: NUKLEAR-MALAYSIA/M/2019/7 developed by Malaysian Nuclear Agency:** The technical team of MIE Agrofarm was given consultation and hands-on training for the establishment of Pisang Tanduk micropropagation protocol.

### 2.1 Collection of healthy and disease-free suckers of Pisang Tanduk

Disease-free sword-like suckers were collected farmer's plot in Sungai Besar, Selangor. The suckers were obtained by MIE Agrofam Sdn. Bhd and brought back to the lab as the starting materials/explants for surface sterilization process.

### 2.2 Preparation of banana micropropagation media

Two types of media were used. Initiation Media, modified Murashige and Skoog medium (MS medium, 1962) (Murashige and Skoog, 1962) supplemented with 5.0 mg/L 6-Benzylamino purine (BAP) and 0.1 mg/l Naphthaleneacetic acid (NAA) and Multiplication Media, MS medium supplemented with 2.5 mg/l BAP + 0.1 mg/l NAA

### 2.3 Surface sterilization of meristem tissue and initiation of shoot buds

The cleaned explants were surface sterilized using 50% and 30% (v/v) commercial sodium hypochlorite with a few drops of Tween 20 for 20 minutes each. Rinsed with sterile Reverse Osmosis (RO) water, excess water adhering to the explants

must be air-dried then the explants are ready to be cultured. The explants that are successfully sterilized and considered as 'clean cultures' were used as the starting materials for the initiation of in vitro shoot buds in Initiation Media. The blackening parts of meristem explants need to be removed, this is crucial step to ensure successful shoot buds initiation.

### 2.4 Multiplication of banana shoots

Multiple shoot buds (2-5) emerged and initiated from the meristem tissues after 8-12 weeks in Initiation Medium, modified Murashige and Skoog medium supplemented with 5.0 mg/L 6-Benzylamino purine (BAP) and 0.1 mg/l Naphthaleneacetic acid (NAA). The newly formed shoots or bud clusters were transferred onto multiplication medium for proliferation and multiplication of in vitro shoots. Monthly subculture in multiplication media (2.5 mg/l BAP + 0.1 mg/l NAA) is being carried out by the MIE Agrofarm technical team.

### 2.5 Rooting of in vitro rooted plantlets

For root induction, plantlets with pseudo-stem height of 5-6 cm were cultured in MS medium supplemented with Indolebutyric acid (IBA) + activated charcoal. Cultures were incubated in the incubation room at 24 ºC with 16 hours photoperiod (3500 lux). Roots start to form after 10 days in culture. After 3 weeks, the in vitro plantlets with the pseudo-stem height of 7-10 cm showed strong and sturdy rooting system and advanced for acclimatization phase.

### 2.6 Hardening and transplanting of in vitro rooted plantlets

The *in vitro* rooted plantlets (pseudo-stem height ¿7 cm) were removed gently from medium, washed in running tap water to remove any traces of adhering agar/media and. These rooted plantlets/ramets were advanced into acclimatization phase for further growth and development. The seedlings are planted at MIE Agrofarm plot in Rawang, Selangor.

## 3 Results and Discussion

A protocol on production of Pisang Tanduk via tissue culture from surface sterilization, initiation of shoot cultures, multiplication of shoots, rooting of plantlets and acclimatization of rooted plantlets has been developed and optimized. Hands-on training on the micropropagation procedure and consultation to MIE Agrofarm Sd. Bhd. has been successfully conducted.



Figure 1: Hands-on training on the micropropagation procedure and consultation to MIE Agrofarm Sd. Bhd.

## 4 Conclusions

From this RISE collaboration, MIE Agrofarm Sdn. Bhd managed to gain the know-how, experience and skills on the banana micropropagation procedure. Agensi Nuklear Malaysia technical team managed to successfully trained the collaborator in plant tissue culture technology. With the established protocol, continuous and sustainable supply of Pisang Tanduk tissue culture seedlings could be obtained. This established micropropagation offers attractive, reliable, rapid and ensure continuous and sustainable production of this popular and high demand banana seedlings.

## 5 Acknowledgments

The authors would like to thank the management of Malaysian Nuclear Agency and MIE Agrofarm Sdn. Bhd for their continuous support and assistance provided in this project.

## References

T. Murashige and F. Skoog. 1962. Revised medium for rapid growth and bioassay with tobacco tissue culture. *Physiol. Plant*, (15):473–497.

N. Norazlina, A.H. Affrida, A. Zaiton, A. Sakinah, I. Nurhayati, H. Nashimatul Adadiah, and T. Norhafiz. 2019. Production of banana seedlings via tissue culture technology and in vitro mutagenesis of banana (cv. berangan). *A Manual: NUKLEARMALAYSIA/M/2019/7*.

Individual Research Contribution Review, 2024: 35–36
*ISSN: 3083-922X*

# Harnessing Stable Isotope Technology for Halal Meat Authentication and Traceability: Ensuring Integrity from Farm to Fork

**Nur Hafizati Abdul Halim**
Agrotechnology and Biosciences Division, Malaysian Nuclear Agency
43000 Kajang, Selangor
hafizati@nm.gov.my

## Abstract

Food fraud has become a significant concern in this country, with traders employing various deceptive practices to maximize profit. Among these, the issue of illegal meat cartels stands out as a critical form of food fraud. This includes concerns over the safety of imported meat, operations of unregulated slaughterhouses, processing of non-halal meat, and broader supply chain vulnerabilities. Recent studies highlight the potential of stable isotope analysis to address these challenges. The natural isotopic fractionation of bioelements such as hydrogen, carbon, nitrogen, and oxygen can be leveraged to determine the geographical origin of beef and associated dietary patterns. These isotopic markers serve as reliable proxies for provenance identification, offering a robust scientific approach to ensure meat authenticity and traceability.

**Keywords:** stable isotope, meat authenticity, meat traceability

## 1 Introduction

Meat is a primary target for food fraud due to its popularity worldwide, including in Malaysia, where demand continues to grow annually (Ritchie and Roser, 2017). A significant portion of Malaysia's meat supply is imported, driven by limited local resources and lower costs. In 2020, Malaysian authorities seized 1,500 tons of non-halal meat smuggled from China, Ukraine, Brazil, and Argentina, exposing vulnerabilities in the supply chain (Halim et al., 2023). This highlights the need for robust analytical methods to verify origin labels and ensure authenticity. Multi-isotopic and multi-element analyses, such as combined isotope ($^{2}$H, $^{13}$C, $^{15}$N, $^{18}$O) and trace element analysis of beef defatted dry mass and lipids, have proven effective in determining geographical origin (Heaton et al., 2008), offering a scientific approach to safeguard meat traceability and consumer trust.

## 2 Materials and Methods

### 2.1 Beef muscle samples

Several beef muscles were obtained from three different countries; Australia, New Zealand and Malaysia. These samples were bought from the trusted meat supplier. Beef samples were frozen at -18 °C directly after collection. Once at the laboratory, all beef samples were stored frozen until partially thawed before sample preparation. Samples were re-frozen after sub-sampling.

### 2.2 Sample preparation

About 100 g of ground beef samples were freeze-dried and homogenized using ceramic scissors and/or an agate pestle and mortar. The lipid component from approximately 20 g of the homogenized material was extracted with a petroleum ether mixture according to the method of Kelly (2011). The round-bottomed flask with the extracted fat is stored. Meanwhile, the extraction thimble containing the fat free dry mass (FFDM) was removed from the Soxhlet apparatus, remove the quartz wool and filter paper, and leave the thimble containing the FFDM to stand for several hours in a fume cupboard to allow any remaining solvent to evaporate. Drying is also facilitated by breaking-up the compacted mass of FFDM before leaving it to air dry. The solvent-free FFDM is homogenized using an agate pestle and mortar. The samples are stored in airtight container until measurement. The fat containing petroleum ether solution in the 250mL round-bottomed flask is reduced to about 5 - 10 ml with a rotary evaporator. The liquid is transferred with a wash of fresh petroleum ether into a roll glass vial and the solvent is removed in a gentle stream of nitrogen with warming (40ºC). The vial is sealed and stored under nitrogen until IRMS-measurement.

### 2.3 Stable isotope analysis

For stable isotope ratio measurement the solid sample is weighted into a tin capsule. The capsule has to be closed and folded to a bullet with tweezers. The stable isotope ratio of ($^{2}$H, $^{13}$C, $^{15}$N, $^{18}$O) will be analyze using elemental analyzer isotope ratio mass spectrometer (EA-IRMS).

## 3 Result and Discussion

Figure 1 and 2 below shows the fat free dry mass (FFDM) and lipid extracted from the meat's muscles. The analysis of stable isotope ratio will be carry out when all the samples are ready to be analyze.



Figure 1: Fat free dry mass (FFDM)

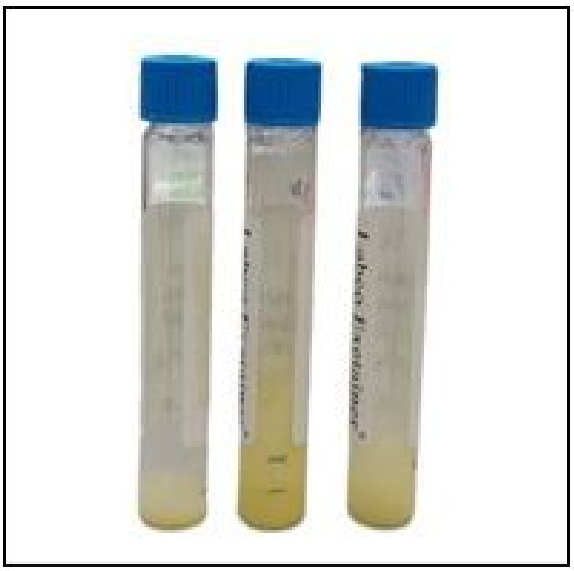


Figure 2: Extracted lipid

## 4 Conclusions

This study has laid the groundwork for stable isotope ratio analysis, which will determine the geographical origin and authenticity of beef samples. The findings aim to address meat fraud and strengthen halal certification processes. The final conclusions will be made after the analysis has been completed.

## References

M. A. A. Halim, M. S. Hassan, H. M. Ali, M. Z. M. Zahir, and R. Murjiyanto. 2023. Meat cartels and their manipulation of halal certification in malaysia. *IIUM Law Journal*, (31):167–186.

K. Heaton, S. D. Kelly, Hoogewerff. J., and M. Woolfe. 2008. Verifying the geographical origin of beef: The application of multi-element isotope and trace element analysis. *Food Chemistry*, (107):506–515.

H. Ritchie and M. Roser. 2017. Meat and dairy production. *OurWorldInData.org*.

Individual Research Contribution Review, 2024: 37–38
*ISSN: 3083-922X*

# Evaluation of Methods for Homogenization of Freeze-dried Broiler Chicken Meat (pectoralis major muscle) Sample for Stable Isotope Ratio Analysis

**Nur Humaira' Lau Abdullah**
Agrotechnology and Biosciences Division, Malaysian Nuclear Agency
43000 Kajang, Selangor
humaira@nm.gov.my

## Abstract

Studies on authentification of different types of organic animal products including chicken meat have been carried out using stable isotope. Stable isotope ratio analysis also has been studied for the authentification of geographical origin of animal products including chicken. The objective of this study was to evaluate the most appropriate method and apparatus for homogenization of freeze-dried broiler chicken meat sample for stable isotope ratio analysis. Three homogenization methods were evaluated i.e. using ultracentrifugal milling at 16,000 and 6,000 rpm, Waring blender and cryogenic grinding. Homogenization of sample using ultracentrifugal mill at 16,000 rpm was observed to generate heat and changed the sample form and colour. Waring blender was not effective to homogenize the sample. Both ultracentrifugal milling at 6,000 rpm and cryogenic grinding were able to homogenize the sample to desired fineness without changing the sample's form and colour. This study demonstrated that cryogenic grinding was the most appropriate homogenization method of freeze-dried broiler chicken meat sample for stable isotope ratio analysis in our laboratory.

**Keywords:** stable isotope ratio analysis, authenticity, geographical origin, broiler chicken, homogenization

## 1 Introduction

Stable isotope ratio analysis can be used to establish sample's isotope fingerprint, which gives it applications in evaluating the authenticity and geographical origin of products and materials. Studies on authentification of different types of organic animal products including chicken meat (Jun and Zhao, 2016) have been carried out using stable isotope. Stable isotope ratio analysis also has been studied for the authentification of geographical origin of animal products including chicken (Dehelean et al., 2022; Rees et al., 2016). Measuring isotopic variation in premium regional products is arguably the best analytical strategy for accurately verifying geographical origin (Rees et al., 2016). Currently we are studying on the differentiation of organic and conventional chicken meat in Malaysia using stable isotope ratio analysis. In this study, proper sample preparation is essential for accurate analysis. Typical sample preparation steps include drying, homogenization and after which a suitable amount of sample is weighed for analysis. The objective of this study was to determine the most appropriate method and apparatus for homogenization of freeze-dried broiler chicken meat samples for stable isotope ratios analysis in our laboratory.

## 2 Materials and Methods

Freeze-dried broiler chicken meat (pectoralis major muscle) samples were homogenized using different methods and apparatus available in our laboratory.

### 2.1 Homogenization using ultracentrifugal mill

Freeze-dried samples were homogenized using ultracentrifugal mill (ZM 200; Retsch GmbH, Haan, Germany). Two speeds were tested i.e. 16,000 rpm and 6,000 rpm. A 0.08 mm aperture size ring sieve was used. Samples were fed slowly into the grinding chamber. from an inlet. Homogenized samples were transferred from the collecting vessel into laboratory vial.

### 2.2 Homogenization using Waring blender

Freeze-dried samples were homogenized using Waring blender (New Hartford, Connecticut) with a 250 mL stainless steel container. The blender was on and off alternately during sample homogenization.

### 2.3 Homogenization by cryogenic grinding

Freeze-dried samples were transferred into an agate mortar using a clean spatula. Liquid nitrogen was added to the mortar enough to cover the sample. The liquid nitrogen was allowed to evaporate until there was just enough remaining to be visible. The sample was ground and pounded quickly and carefully with the pestle.

## 3 Results

### 3.1 Homogenization using ultracentrifugal mill

The freeze-dried chicken meat sample appeared as mustard yellow-coloured cake adhering to the rotor after being ground at 16,000 rpm (Figure 4a). On the other hand, when ground at 6,000 rpm, the sample appeared as cream-coloured fine fibrous powder that mostly did not passed through the ring sieve (Figure 4b). Heat generation was observed during both the grinding speed.




Figure 1: The freeze-dried broiler chicken meat sample after homogenization using ultracentrifugal mill at a) 16, 000 rpm and b) 6,000 rpm.

### 3.2 Homogenization using Waring blender

The use of Waring blender with the blender container of 250 mL was unable to homogenize the freeze-dried chicken meat sample. The sample still maintained its chunky form (Figure 5b). Heat was not generated during the blending process.

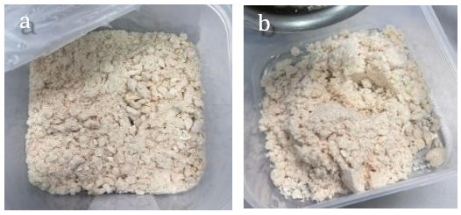



Figure 2: The freeze-dried broiler chicken meat sample a) before and b) after homogenization using Waring blender.

### 3.3 Homogenization using cryogenic grinding

The chuncky freeze-dried broiler chicken sample appeared as quite fine fibrous powder after repeated pounding and grinding using agate mortar and pestle in the presence of liquid nitrogen (Figure 6b).




Figure 3: The freeze-dried broiler chicken meat sample a) before and b) after grinding with agate mortar and pestle in the presence of liquid nitrogen

## 4 Discussion

In this study, three different methods and apparatus were used to homogenize freeze-dried broiler chicken meat (pectoralis major muscle) sample. Among the three methods, two methods were found did not generate heat during sample homogenization i.e. the Waring blender and cryogenic grinding. Although Waring blender did not generate heat, it was not effective to homogenize freeze-dried sample as the sample remained chuncky as before blending. Homogenization of sample using ultracentrifugal mill at 16,000 rpm was observed to generate heat and changed the sample form and colour. Both ultracentrifugal milling at 6,000 rpm and cryogenic grinding was found to produce cream-coloured fine fibrous powder, which was the acceptable form and fineness of sample for stable isotope ratio analysis. In this study, as we found heat was generated during ultracentrifugal milling at 6,000 rpm, we favored homogenization of freeze-dried broiler chicken meat sample using cryogenic grinding which did not generate heat. This method will ensure the sample being maintained in its original form and thus data from stable isotope analysis was reliable. Denadai et al. (2019) and Cruz et al. (2004) also cryogenically ground their dried chicken meat sample for isotopic analysis (Cruz et al., 2004).

This study demonstrated that cryogenic grinding was the most appropriate homogenization method of freeze-dried broiler chicken meat sample for stable isotope ratio analysis in our laboratory as it ensure sample integrity while reducing sample to desired fineness.

## References

V.C. Cruz, A.C. Pezzato, C. Ducatti, D. F. Pinheiro, J.R. Sartori, and J.C. Goncalves. 2004. Tracing metabolic toutes of feed ingredients in tissues of broiler chickens using stable isotopes. *Poultry Science*, (83):1376–1381.

A. Dehelean, G. Cristea, R. Puscas, A.R. Hategan, and D.A. Magdas. 2022. Tracing metabolic toutes of feed ingredients in tissues of broiler chickens using stable isotopes. *Appl. Sci.*, (12):12391.

Lv. Jun and Y. Zhao. 2016. Combined stable isotopes and multi-elements analysis to research the difference between organic and conventional chicken. *Food Anal. Methods*.

G. Rees, S. D. Kelly, P. Cairns, H. Ueckermann, S. Hoelzl, A. Rossmann, and M. J. Scotter. 2016. Verifying the geographical origin of poultry: The application of stable isotope and trace element (site) analysis. *Food Control*, (67):144–154.

Individual Research Contribution Review, 2024: 39–40
*ISSN: 3083-922X*

# Developing Laboratory Scale Rearing of Cocoa Pod Borer *Conopomorpha cramerella* (Snellen) (Lepidoptera: Gracillariidae)

**Nur Siti Aisyah Zarimin**
Agrotechnology and Biosciences Division, Malaysian Nuclear Agency
43000 Kajang, Selangor
nursiti@nm.gov.my

## Abstract

Cocoa pod borer (CPB), *Conopomorpha cramerella* (Snellen) (Lepidoptera: Gracillariidae), is a major insect pest affecting cocoa production, particularly in Southeast Asia. The larval stage of *C.cramerella* is particularly destructive, inhibiting cocoa bean development. To address this issue, the sterile insect technique (SIT) has been proposed as an environmentally friendly and alternative method to reduce *C.cramerella* populations. A critical aspect of SIT involves mass rearing, which requires understanding the pest's life cycle and morphology. This study aimed to determine the rearing duration of each life stage and examine the morphology of *C.cramerella* under laboratory conditions. The larvae were reared at room temperature with a 10% honey solution provided as sustenance, and their morphology was observed using a microscope. The study successfully documented the duration and morphological characteristics of each developmental stage. In conclusion, this *C.cramerella* rearing procedure can help maintain the population in the laboratory, supporting the development of SIT.

**Keywords:** *C.cramerella*, laboratory rearing, life cycle, sterile insect technique

## 1 Introduction

Since 1986, *C.cramerella* has become the most serious insect pest of cocoa in Southeast Asia (Bradley, 1986). In Malaysia, cocoa bean production once at 225,000 tonnes. In contrast, current output has significantly declined to approximately 500 tonnes (Birruntha, 2024). One of the reasons for this decline is the infestation *C.cramerella*. Sterile Insect Techniques (SIT) are recognized as environmentally friendly and species-specific methods for pest management (Zhao et al., 2022). The integration of SIT with other control measures offers potential for effectively reducing *C.cramerella* infestations. However, there is a notable research gap in applying SIT to *C.cramerella*, particularly at the laboratory stage. To bridge this gap, it is essential to establish reliable rearing methods for *C.cramerella* before advancing to the radiation procedures required for SIT implementation.

## 2 Materials and Methods

### 2.1 Collection of larvae

The infested cocoa pod utilized in this study was collected from a cocoa orchard at Lembaga Koko Perak, Malaysia. It was manually harvested based on visible signs of infestation on its surface. The number of larvae inside the pod was not recorded, as they were already harvested within it.

### 2.2 Insecterium

The experiment was conducted in the insectary of the Entomology Laboratory at the Malaysia Nuclear Agency. The rearing conditions were maintained at temperatures of 31 ± 3 °C and 71 ± 7% humidity, with a natural light phase of 14 hours of light and 10 hours of dark condition in a cycle.

### 2.3 Supplements

A 10% sugar solution was provided in the rearing cage.

### 2.4 Oviposition Device

An oviposition device is a tool designed to facilitate egg-laying by female insects. In this experiment, an immature cocoa pod served as the oviposition device. The pods were lightly sprayed with sterile distilled water and covered with Kimwipe sheets. Each pod was placed upright in a plastic cup, prepared for placement inside the rearing cage.

### 2.5 Oviposition Device

The rearing method was adapted from Lembaga Koko Perak and Niogret et al. (2023) (Niogret et al., 2023). The infested cocoa pod was placed in a heap inside a container and covered with dry leaves. Upon exiting the pod, the larvae roam, spin cocoons, and undergo pupation underneath the dry leaf. After 24 hours, the undersides of the dry leaves are inspected for the presence of cocoons. When cocoons are detected, the sections of leaves containing them are carefully cut out and positioned cocoon-side up in a petri dish for further observation. Number of pupae were recorded. After six days, the petri dishes were examined for adult emergence. Upon emergence, the adults were counted, and their sexes were determined. The number of adults and their respective sexes were recorded. Subsequently, five pairs of adults were introduced into a cage, which was labeled with a cage number and the setup date. The adults were provided with a 10% honey solution, applied to the cage using cotton wool. An oviposition device was also placed in the cage to facilitate mating and oviposition. The females laid eggs individually on the surface of the Kim

Wipes overnight, 24 hours after introduction. After this period, the oviposition device was removed from the cage. The Kim Wipes covering the cocoa pod were also removed and labeled with the corresponding cage number. The presence of eggs was observed, with the small, orange, oval-shaped eggs being easily identifiable. The duration to complete the life cycle was also recorded.

## 3 Results and Discussion

Figure 1 illustrates the complete life cycle of *C.cramerella* observed during the study. The rearing process began at the larval stage, with pupation occurring up to 16 days after the infested cocoa pods were harvested. This aligns with findings by Saripah et al. (2022), who reported that the larvae burrow into the pre-sclerotic layer and feed on the placenta and mucilage for 14–17 days. Similarly, Reynolds (2019) described the larval stage as spanning 14–18 days, during which the insect completes 4–6 instars. The pupal stage of *C.cramerella* was observed to last an average of 7 days, with adult emergence occurring between days 6 and 8. During this stage, the pupa underwent noticeable changes in coloration, starting as greenish and transitioning to pale brown as development progressed. Additionally, the length of the pupa decreased throughout the pupation process. These findings are consistent with (Saripah et al., 2022), who reported adult emergence occurring between days 7 and 9. Similarly, Reynolds (Reynolds, 2019) documented a pupation period of 6–8 days before adult emergence. The average longevity of adult *C.cramerella* observed in this study was 10 days. This finding aligns with Saripah et al. (2022), who reported adult lifespans of up to 14 days. However, Reynolds (2019) documented a shorter average adult longevity of approximately one week.

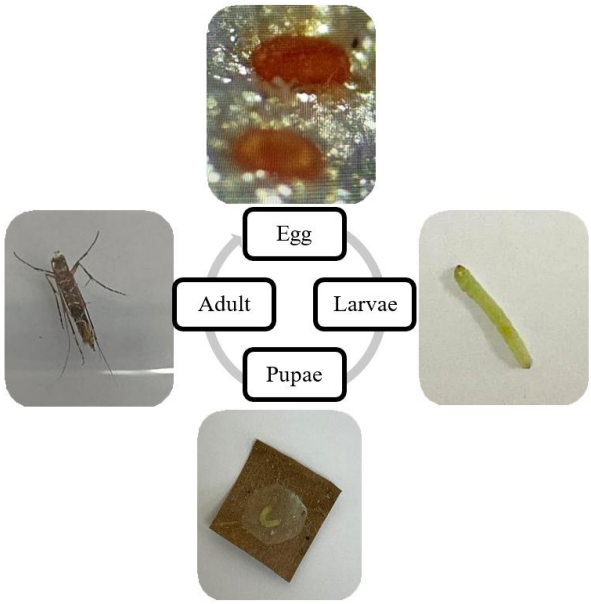



Figure 1: Life cycle of *C.cramerella* from rearing in laboratory scale.

The sex ratio of emerged adults was observed to be 1:1 (male:female), consistent with findings by Saripah et al. (2022). Furthermore, 100% of the adults demonstrated strong flight ability, successfully flying more than 10 cm upon release. The observed consistency with these studies suggests that the duration and morphological changes are stable characteristics of *C.cramerella*, although slight variations may arise due to environmental conditions or genetic factors.

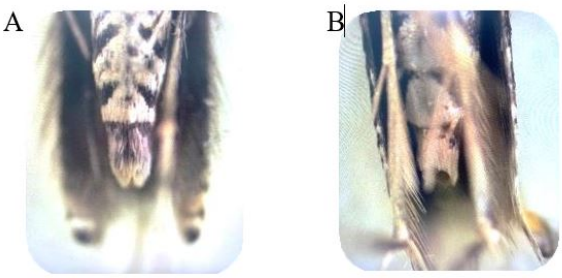



Figure 2: Ventral views of the end of the abdomen of male (A) and female (B) adult of *C.cramerella*

## 4 Conclusions

This study successfully established a laboratory-scale rearing method for *Conopomorpha cramerella*, achieving healthy adult development and documenting key biological characteristics of the species. While conducted on a small scale, the findings provide valuable baseline data for further research and serve as foundational reference information for the potential development of Sterile Insect Technique (SIT) programs in the future.

## References

S. Birruntha. 2024. Malaysia cocoa sector not yet sustainable. *New Straits Times.*

J. D. Bradley. 1986. Identity of the south east asian cocoa moth, conopomorpha cramerella (snellen) (lepidoptera: Gracillariidae), with descriptions of three allied new species. *Bulletin of Entomological Research*.

J. Niogret, A. Savantil, A. B.and Ekayanti, M. P. Jaus, W. Wulan, E. Mitzo, J.P. Marelli, and D. Conlong. 2023. Development of a diet production system for conopomorpha cramerella (lepidoptera: Gracillariidae), a major cocoa production pest in southeast asia and the pacific islands. *Insects*.

O. L. Reynolds. 2019. Basic research on the cocoa pod borer in papua new guinea to permit effective pest management (project no. hort/2018/114). *Australian Centre for International Agricultural Research.*

B. Saripah, M. Navies, and R. Haya. 2022. Kenali serangga perosak koko di malaysia. *Lembaga Koko Malaysia*.

J. Zhao, S. Li, X. Li, C. Liu, Q. Li, Y. Dewer, and K. Wu. 2022. Effects of x-ray irradiation on biological parameters and induced sterility of ephestia elutella: Establishing the optimum irradiation dose and stage. *Frontiers in Physiology*, (13).

Individual Research Contribution Review, 2024: 41–42
*ISSN: 3083-922X*

# Preliminary Evaluation of the Application of Fourier Transform InfraRed (FTIR) Spectroscopy for the Analysis of Halal Food

**Nurul Elma binti Sabri**
Agrotechnology and Biosciences Division, Malaysian Nuclear Agency
43000 Kajang, Selangor
nurulelma@nm.gov.my

## Abstract

Consumption of meat from halal sources is mandatory for Muslims. The identification of non-halal meat is constantly the main issues that face Muslim consumers in meat markets. Pig is one of the non-halal sources of meat, and hence pig meat and its derivatives are prohibited for Muslims to consume. The purpose of this study is to use Fourier Transform Infrared Spectroscopy (FTIR) for rapid discrimination of Halal and non-Halal of raw food products.

**Keywords:** Halal, FTIR, Brush, Lard, Gelatin

## 1 Introduction

Islam is the primary religion in Malaysia and is acknowledged as the national's official religion, thus it is significant to certify the halalness of food products. The identity of the ingredients in processed or composite mixtures is not always readily apparent. Therefore, verification that the components are from sources acceptable to special consumers may be required (Xu et al., 2012). This study was designed to determine the ability of Fourier Transform (FTIR) Spectroscopy on the rapid discrimination of Halal and non-Halal of raw food products.

## 2 Materials and Methods

supermarket. Raw samples used in this study are wild boar, which is labeled as BH, pink pig labeled as BP, chicken, minched chicken, minched meat, sausage samples (NH White, NH Red, Raffie Honey, Fiesta Jimat, CP Bfast, CP Smoked and Lotus Smoked). All raw samples were washed using tap water to remove dirt and rinsed using distilled water, except for minched chicken and minched meat. The BP, BH and chicken meat were cut small and thin and labeled as Daging BP, Daging BH and Daging Ayam, respectively. For lard sample, we did not heat the samples, but we just take the fat attached under the skin and attached to the meat. Thus, BP, BH and chicken fat under the skin was labeled as Lemak BP (Kulit), Lemak BH (Kulit) and Lemak Ayam (Kulit), meanwhile BP, BH and chicken fat attached with the meat labeled as Lemak BP (Daging), Lemak BH (Daging) and Lemak Ayam (Daging), respectively. For BP, BH and human hair and makeup brush, all samples were washed using tap water and rinsed using distilled water and then store in microcentrifuged tube, individually prior to analysis.

## 3 Discussion/Conclusions

FTIR spectrum can be divided into two regions which are functional group region and fingerprint region (Jiang et al., 2023). The wavelengths for infrared spectra are ranging from 4000 $cm^{-1}$ to 450 $cm^{-1}$ the functional group region lies from 4000 $cm^{-1}$ to 1450 $cm^{-1}$ (Alex et al., 2018) while the other study stated that vibrational fingerprint region lies from 1000 $cm^{-1}$ to 2000 $cm^{-1}$ (Rehault et al., 2017). In this study, all type of samples was analyzed using Agilent Cary 630 FTIR Spectrometer from 4000 $cm^{-1}$ to 500 $cm^{-1}$ with 32 scans per pixel at a spectral resolution of 4 $cm^{-1}$ in term of the value of Transmittance (%T). Figure 1 shows the overlaid spectrum of Halal and non-Halal meat.

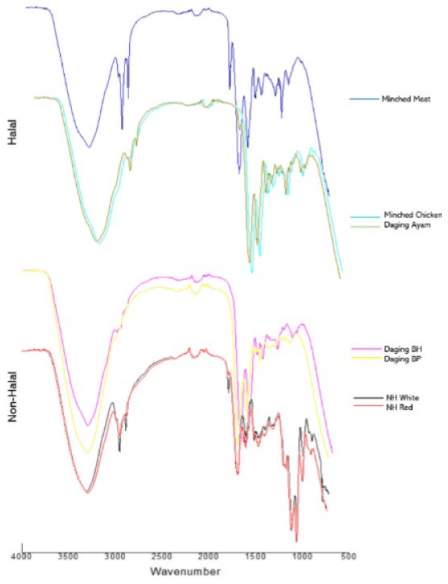



Figure 1: FTIR Spectrum of Halal (Minched Meat, Minched Chicken and Daging Ayam) and non-Halal (Daging BH, Daging BP, NH White and NH Red).

Peak ranging from 2800.00 $cm^{-1}$ cm-1 to 3100.00 $cm^{-1}$ a strong intensity band were observed in Minched Meat, medium intensity in both Halal (Minched Chicken and Daging Ayam) and non-Halal (NH White and NH Red). Furthermore, a weak intensity was observed in Daging BH and Daging BP. A strong intensity band at 1800 $cm^{-1}$ to 1900 $cm^{-1}$ were observed in Minched Meat, medium intensity band were observed NH White and Daging Ayam and no peaks observed in Minched Chicken, Daging BH, Daging BP and NH Red. In

fingerprint region from 1750.00 $cm^{-1}$ to 500 $cm^{-1}$, a strong intensity band were observed in all Halal and non-Halal (Daging BH and Daging BP) spectra and the pattern of the spectra is almost the same. The different between meat, chicken and pig is the band intensity. On the other hand, in non-Halal samples (NH White and NH Red), a different pattern of the spectra was observed. We assumed that this samples are from another non-Halal source. From the pig hair spectrum, Bulu BH and Bulu BP has slightly different which can be observed from 3700 $cm^{-1}$ to 3800 $cm^{-1}$ and from 700 $cm^{-1}$ to 1200 $cm^{-1}$. Besides that, the human hair and makeup brushes spectrum can be considered as identical because the lines of the spectra are aligned, except for MK_Cheek sample. However, lard samples labeled as Lemak BH (Kulit), Lemak BH (Daging), Lemak BP (Kulit) and Lemak BP (Daging) were compared to chicken fat labeled as Lemak Ayam (Kulit) and Lemak Ayam (Daging), and food products such as Gelatin, Gelatin 2, Shortening and Krimwell.

A strong and broad band in lard and chicken fat spectrum and medium band in food products with peak ranging from 3200.00 $cm^{-1}$ to 3500.00 $cm^{-1}$ were observed. However, no peak was observed in Shortening sample. Meanwhile, from 2800.00 $cm^{-1}$ to 3100.00 $cm^{-1}$ a strong intensity band were observed in Shortening and Krimwell, followed by Lemak BP (Kulit) and Lemak BP (Daging) and medium intensity in Lemak BH (Kulit), Lemak BH (Daging), Lemak Ayam (Kulit) and Lemak Ayam (Daging). No peak was observed in other samples. In fingerprint region from 1800.00 $cm^{-1}$ to 500.00 $cm^{-1}$, the pattern is almost the same for all spectra, except for Shortening and Krimwell. We assumed that this samples might be from other source such as vegetable oil, whereas both samples Gelatin and Gelatin 2 might be from animal fat. Raffie Honey, Fiesta Jimat, CP Bfast, CP Smoked and Lotus Smoked are classified as Halal sausages while NH White and NH Red are classified as non-Halal sausages.

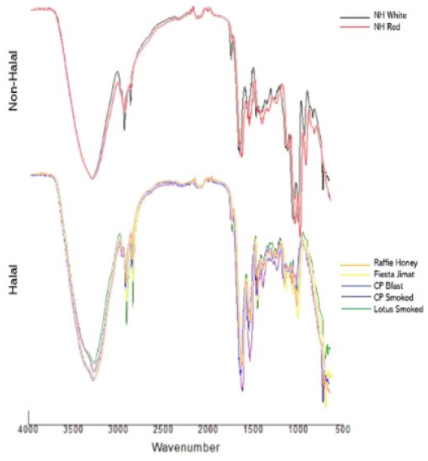



Figure 2: FTIR Spectrum of Halal and non-Halal sausages.

In fingerprint region from1800.00 $cm^{-1}$ to 500.00 $cm^{-1}$, the pattern is different between Halal and non-Halal sausages (Figure 2). Strong intensity band was observed in Halal sausages from 1450.00 $cm^{-1}$ to 1750.00 $cm^{-1}$, but strong intensity band was observed in non-Halal sausages spectra from 800.00 $cm^{-1}$ to 1150.00 $cm^{-1}$. Principal Component Analysis (PCA) was performed using Unscrambler 10.3 (CAMO Software, Norway) on FTIR spectra for sausage samples. PCA scores plot were used to assist in comprehending the clustering patterns of observation. The pattern of PCA scores plot could be seen clearly as the halal and non-halal sausages were distributed far from each other as illustrated in Figure 3. Non-halal sausages (red circle) lies in negative values of PC-1 while halal sausages (blue circle) lies in positive values of PC-1.

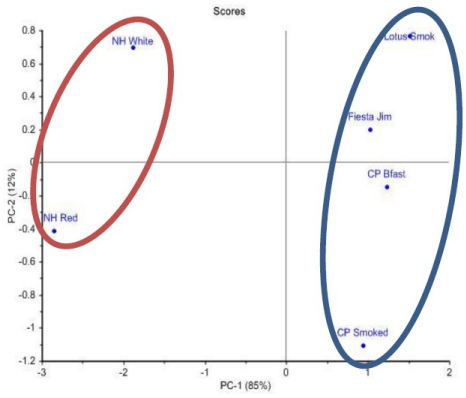



Figure 3: Data distribution of Halal and non-Halal sausages.

## 4 Conclusion

These preliminary results clearly indicate that there is a possibility to find biomarkers for non-halal identification. To develop a good model, bigger sample size which varies type of halal and non-halal samples are necessary. To identify the biomarkers for halal and non-halal food products, other chromatography techniques are compulsory. Multivariate data analysis such as PCA is very helpful to visualize the large data and reduce the complexity of the data sets.

## References

B. K. Alex, E. P. Koshy, and G. Thomas. 2018. Comprehensive metabolite profiling of haematocarpus validus (miers) bakh.f. ex forman leaf and fruit samples using ftir spectroscopic analysis. *Plant Archives*, 18(1):897–900.

B. Jiang, C. F. Yu, L. Yuan, K. Lu, W. Tao, H. Lin, and Y. Zhou. 2023. Investigation on oxidative pyrolysis characteristics of bituminous coal through thermal analysis and density functional theory. *Applied Energy*, (349):121680.

J. Rehault, R. Borrego-Varillas, A. Oriana, C. Manzoni, C. P. Hauri, J. Helbing, and G. Cerullo. 2017. Fourier transform spectroscopy in the vibrational fingerprint region with a birefringent interferometer. *Optics Express*, 25(4):4403–4413.

L. Xu, C.-B. Cai, H.-F. Cui, Z.-H. Ye, and X.P. Yu. 2012. Rapid discrimination of pork in halal and non-halal chinese ham sausages by fourier transform infrared (ftir) spectroscopy and chemometrics. *Meat science*, 92(4):506–510.

Individual Research Contribution Review, 2024: 43–44
*ISSN: 3083-922X*

# Development of Gamma Radiation-Induced Silica-Solubilizing Bacteria (SSB) for Sustainable Agriculture

**Phua Choo Kwai Hoe**
Agrotechnology and Biosciences Division, Malaysian Nuclear Agency
43000 Kajang, Selangor
phua@nm.gov.my

## Abstract

The use of silicate solubilizing bacteria was reported to be one of the important mechanisms for the biological suppression of rice phytopathogens through the polymerization of silicates in the soil for plant uptake. It has been previously reported that the solubilized Si improves the availability of phosphorus to plants by competing with P fixation sites in the soil. Thus, Si acts as a substitute for P in the plant system. Several potential SSB strains will be obtained, and it is expected that the inoculation of SSB will render beneficial impacts on the plant, reduce lodging and disease incidences, and improve the growth and yield. Gamma irradiation is used to obtain potential enhancement silica solubilizing bacteria.

**Keywords:** Mutagenesis, Gamma irradiation, Silicate solubilizing bacteria

## 1 Introduction

Microorganisms, as the major biota in soil, play a critical role in the restoration of the land ecosystem. Rhizosphere microecology directly or indirectly affects the growth and development, metabolic regulation and active ingredient accumulation of plants (Su and Han, 2022). Microbial resources, with the advantages of economic efficiency, harmless to environment and non-toxic to organisms, have been recommended as a promising alternative to conventional fertilizers and pesticides. Silica-Solubilizing Bacteria (SSB) play a vital role in enhancing crop productivity and resilience through biological mechanisms such as improved nutrient uptake and disease suppression (Figure 1). SSB has been identified as a key component in sustainable rice cultivation, promoting phosphate binding, accelerating plant growth, and enhancing crop resistance to diseases (Etesami and Schaller, 2023). However, challenges such as environmental stressors often limit the effectiveness of native SSB strains. This necessitates the development of improved strains that can function efficiently under varied conditions.

## 2 Materials and Methods

This study aims to enhance the functionality of SSB through gamma radiation-induced mutagenesis. Gamma radiation has been extensively used for inducing mutations to improve crop traits such as disease resistance, stress tolerance, and yield.

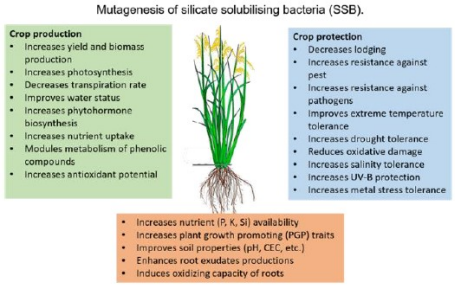



Figure 1: Beneficial effects of silicate solubilizing microbes (SSMs) in crop production and protection (Das and Kim, 2024)

It enhances genetic variability, enabling the development of high-yielding and stress-tolerant crop varieties (Riviello-Flores et al., 2022). Gamma radiation, a proven tool for inducing beneficial mutations in microorganisms (Phua et al., 2019; Hing et al., 2023), is utilized to improve SSB's silica solubilization capability and its resilience to environmental stresses. To achieve this, key steps include:

(I) **Isolation of SSB:** Strains were isolated from silica-rich environments to identify candidates with high silica solubilization potential.

(II) **Determination of $LD_{50}$ for SSB:** The lethal dose ($LD_{50}$) of gamma radiation for SSB was identified to ensure effective mutagenesis without excessive lethality.

(III) **Development of Mutagenesis Protocols:** A standardized protocol for gamma radiation-induced mutagenesis was established, ensuring reproducibility and effectiveness.

(IV) **Improvement of SSB Strains:** Enhanced SSB strains were developed and evaluated for their silica solubilization efficiency and environmental stress tolerance.

## 3 Data/Results

The project, undertaken as part of the Forum for Nuclear Cooperation in Asia (FNCA) regional collaboration, is the first reported effort to apply gamma radiation-induced mutagenesis to SSB. This study underscores the potential of nuclear technology in advancing agricultural productivity and food security. By leveraging SSB's enhanced capabilities, this

research aligns with Malaysia's National Food Security Action Plan (2021–2025), National Nuclear Technology Policy (2030).

The findings are anticipated to contribute significantly to sustainable agriculture by providing:

(I) **Improved SSB Strains:** Improved SSB strains capable of functioning under diverse environmental conditions.

(II) **Mutagenesis Protocol Development:** A robust mutagenesis protocol for future research and development efforts.

## 4 Discussion/Conclusions

Impact and benefits of the project is the use of improved SSB strains is expected to increase crop yields and boost farmers' incomes while reducing dependency on chemical fertilizers and pesticides. This will not only minimize the negative environmental impacts associated with agrochemical use but also reduce reliance on imported fertilizers and pesticides. These benefits align with Malaysia's commitment to promoting sustainable agricultural practices while strengthening food security and economic resilience.

## References

S. Das and P. J. Kim. 2024. Biofertilizers based on silicate-solubilizing microbes for crop production and protection. asi-pacific biofertilizers and biopesticides information platform. *FTTC Agricultural*.

H. Etesami and J. Schaller. 2023. Improving phosphorus availability to rice through silicon management in paddy soils: A review of the role of silicate-solubilizing bacteria. *Rhizosphere*, (27):100749.

J. N. Hing, B. C. Jong, P. W. Y. Liew, E. E. Rashid, and S. Shamsudin. 2023. Gamma radiation dose-response of gram-positive and gram-negative bacteria. *Malaysian Applied Biology*, 51(5):107–112.

C. K. H. Phua, H. M. Saud, K. Abdul Rahim, C. F. Ishak, and P. E. M. Wahab. 2019. *Radiation mutagenesis of microbial biofertiliser for functionalities improvement in cucumber and green mustard.* Ph.D. thesis, Universiti Putra Malaysia, Selangor, Malaysia.

M. D. L. L. Riviello-Flores, J. Cadena-Iñiguez, L. D. M. Ruiz-Posadas, M. D. L. Arévalo-Galarza, I. Castillo-Juárez, M. Soto Hernández, and C. R. Castillo-Martínez. 2022. Use of gamma radiation for the genetic improvement of underutilized plant varieties. *Plants*, 11(9):1161.

Y. Su and J. Han. 2022. Contributions of beneficial microorganisms in soil remediation and quality improvement of medicinal plants. *Malaysian Applied Biology*, (11):3200.

Individual Research Contribution Review, 2024: 45–46
*ISSN: 3083-922X*

# Photostimulated Luminescence (PSL) Technique For Detecting Selected Irradiated Dried Foods)

**Ros Anita Ahmad Ramli**
Agrotechnology and Biosciences Division, Malaysian Nuclear Agency
43000 Kajang, Selangor
anita@nm.gov.my

## Abstract

Photostimulated luminescence (PSL) is one of the physical methods for the identification of Irradiated dried foods. Four types of samples were analyzed: dried mushrooms, dried dates, dried threadfin and dried shrimp. The samples were irradiated with a gamma source at dose levels of 1, 3, and 5 kGy. The PSL intensity of both non-irradiated and irradiated samples dried food was measured. The results show that PSL intensities of non-irradiated and irradiated samples from each type of dried food are relatively well-distributed. The result showed that, irradiated dried food can be distinguished after storage periods of 12 months. The findings of this study provide a useful database for the applicability of the PSL technique in detecting irradiated dried food. The availability of a method to detect irradiated food will be useful to the regulatory authority for enforcing labelling control in Malaysia.

**Keywords:** Photo-stimulated luminescence (PSL), irradiation, dried food.

## 1 Introduction

Food irradiation has been proven as one of the alternative techniques to the existing methods for improving the hygienic quality, increasing the shelf-life, and enhancing the functional properties of different food items. Over 60 countries worldwide have sanctioned specific uses of food irradiation in their national regulations. Research on detection methods for irradiated food has focused on physical, biological, and chemical aspects of foods exposed to ionizing radiation over the past few decades (Delincée, 2002). The PSL detection method is particularly useful for the rapid screening of various irradiated foods, including herbs and seasonings (Sanderson et al., 1996). The development of analytical methods for correct identification of irradiated samples from non-irradiated samples has thus become important for upholding regulatory controls, checking compliance against labelling requirements, facilitating international trade, and reinforcing consumer confidence. The objective of this study was to further investigate the applicability of this PSL technique can be to identify four different types of dried food. The aim was to establish baseline data on PSL measurement for dried food and to examine key characteristics such as dose response and signal stability during storage 12 months.

## 2 Materials and Methods

### 2.1 Preparation of Samples

Four types of dried food (dried mushrooms, dried dates, dried threadfin and dried shrimp) were purchased from a local market near Bangi. The samples were exposed to -radiation at doses of 1, 3, and 5 kGy using a cobalt-60 gamma source. All samples (both non-irradiated and irradiated) were stored in the dark for 1 day - 12 months to assess the stability of detection parameters.

### 2.2 Measurement of Photostimulated Luminescence (PSL)

The PSL of the control and irradiated samples were measured using a PSL Irradiated Food Screening System at Malaysian Nuclear Agency. The PSL measurements were performed according to EN 13751 (13751, 2009). Sample was placed in 50 mm diameter disposable petri dish. All measurements were done in duplicates. Table 1, samples producing signals below the lower threshold value of 700 counts/60s (T1) are categorized as non-irradiated (negative) while above the upper threshold of 5000 counts/60s (T2) suggests irradiated samples (positive). Samples with signal levels between the two thresholds (700-5000 counts/60s) were classified as intermediate (M).

| Total Count | Response | Classification |
|---|---|---|
| Total counts $< T_1$ | Negative | Not irradiated |
| $T_1 <$ Total counts $< T_2$ | Intermediate | Intermediate (M) |
| Total counts $> T_2$ | Positive | Irradiated |

Table 1: Classification of the sample with the EN 13751 method.

## 3 Results and Discussion

Figure 1 shows the Effect of irradiation dose on the signal intensity of dried mushroom, dried dates, dried threadfin and dried shrimps after fading one year. All samples analysed were identified correctly, both for non-irradiated and irradiated at different dose levels. The results indicated that PSL signals for all samples slightly decreased after 12 months of storage. PSL signals remained higher than the initial counts after one year of storage in dark condition, indicating their stability as reported by Jae-Jun et al. (Jae-Jun et al., 2011). The photon counts during the storage in the dark after irradiation treatment

were consistent with those reported earlier by Goulas, et al., 2008 (Goulas et al., 2008).

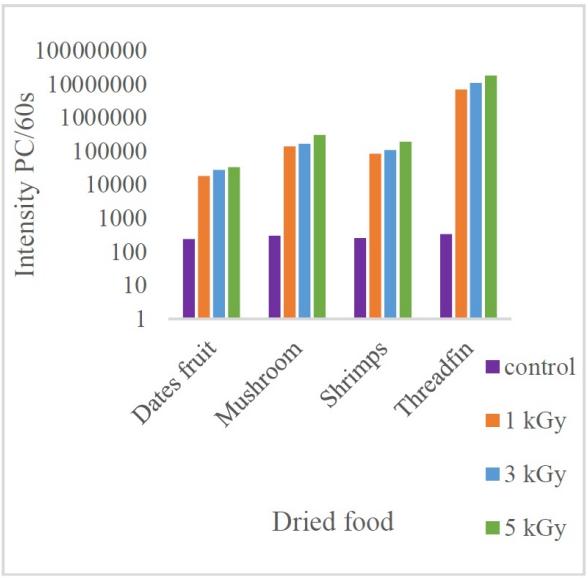



Figure 1: Effect of irradiation dose on the signal intensity of selected dried food.

The other hand, the PCs of store in dried food at dose 1, 3 and 5 kGy, for 12 months storage were respectively, which were upper threshold values 5000 counts/60s indicated the samples irradiated (EN 13751: 2009). According to Yi (Yi and Yang, 2000), if the PSL responses of the irradiated food are significantly greater than those of unirradiated ones or if the fading of the PSL response is low during the long-term storage, the PSL measurement suitable for the detection of food irradiation.

## 4 Conclusions

The photostimulated luminescence (PSL) detection methods has proven effective for identifying irradiation treatment in dried food. The PSL signal intensity remained high even after 12 months of storage for irradiated dried mushrooms, dried dates, dried threadfin and dried shrimp, indicating the method suitability for detecting dried food ingredients with long shelf life. All irradiated samples were successfully distinguished from the non-irradiated control samples analyzed in this study. These results provide a valuable database on the applicability of the PSL technique for detecting irradiated dried food. The availability of this method for detecting irradiated food in Malaysia will be beneficial to the Ministry of Health for enforcing labelling (RADURA) regulations.

## 5 Acknowledgments

The authors wish to express their gratitude to the Malaysian Nuclear Agency (MOSTI) for their support in this project.

## References

European Standard EN 13751. 2009. Foodstuff-detection of irradiated food using photostimulated luminescence. brussels, belgium: European committee for standardization. *European Standard EN 13751*.

H. Delincée. 2002. Analytical methods to identify irradiated food - a review. *Radiat. Phys. Chem.*, (63):455–458.

A.E. Goulas, M. Stahl, and K.A. Riganakos. 2008. Effect of various parameters on detection of irradiated fish and oregano using the esr and psl methods. *Food Control*, 19(11):1076–1085.

A. Jae-Jun, K. Kashif A. Gui-Ran, K. Kyong-Su, and K. Joong-Ho. 2011. Effect of storage conditions on photostimulated luminescence of irradiated garlic and potatoes. *Food Research International*, pages 1–6.

D. C. W. Sanderson, L. A. Carmichael, J. Q. Spencer, and J. D Naylor. 1996. Luminescence detection of shell fish. in c. h. mcmurray, e. m. stewart, r. gray, and j. pearce (eds.), detection methods of irradiated foods. *Cambridge: The Royal*, page 139–148.

S. D Yi and J.S. Yang. 2000. The application of pulsed photostimulated luminescence (ppsl) methods for the detection of irradiated foodstuffs. *J. Food Sci. Nutri*, (5):136–141.

Individual Research Contribution Review, 2024: 47–48
*ISSN: 3083-922X*

# Application Of Nuclear Technology In Extending Storage Time Of Selected Perishable Food Products)

**Seri Chempaka Bt. Mohd. Yusof**
Agrotechnology and Biosciences Division, Malaysian Nuclear Agency
43000 Kajang, Selangor
seri@nm.gov.my

## Abstract

Food products such as bread, cakes and other delicacies are highly perishable products which are mainly deteriorate due to staling, moisture loss and microbial spoilage. More than 90% of mould contamination occurs during cooling, slicing, or wrapping operations. Studies were carried out to overcome arisen of the safe shelf-stable food and to evaluate the suitability of irradiation in preserving local sliced breads and bahulu cakes. Generally, these food products can be kept in room temperature only for one or two weeks respectively. Fresh packed products were obtained from local producers and irradiated at doses of 2.0 kGy, 5.0 kGy and 10 kGy, using 60Co gamma irradiation source at MINTec-Sinagama. The irradiated and non-irradiated samples were displayed at room temperature storage periods for 1 month. Microbiological analysis was carried out to determine status of bacteria (Total Plate Count) and fungi counts (cfu/g). The color changes of the products were recorded using the Colorimeter (Minolta) instrument for the (L) lightness, (a) redness, and (b) yellowness values. Acceptability of the irradiated products were determined through sensory evaluation by using 30 members (male and female) of untrained panellists. Results showed that irradiation at 2 kGy reduced the microbial loads (bacterial and fungal colonies) in the irradiated samples and no presence of microbes after irradiated at 5 and 10kGy. Nevertheless, after 1 month of storage, the microbial load increased in the control samples but remained low in the irradiated samples. lightness of the sample after irradiation. The samples become darker after irradiation at 10 kGy. These results demonstrated the ability of gamma irradiation for the decontamination of selected perishable food products and reliable process for food storage in commercial industry.

**Keywords:** Gamma, Irradiation, Perishable food, Microbial, Storage

## 1 Introduction

Food irradiation is closely related with nuclear technology, hence application of it must follow food regulation act 1985 where the related industry must gain permission from Ministry of Health Malaysia. In 2011, Malaysia have achieved one of the biggest achievements in this industry when Ministry Health of Malaysia have approved food irradiation process up to 10kGy through food irradiation regulation 2011. Food irradiation technology involve exposing food product with ionizing radiation under controlled environment. This technology has been used widely as an alternative method to preserve food product by increasing food shelf-life without changing food original taste, color, texture and food's nutritional content. Scientifically findings, show that food irradiation has the ability to increase food safety, reduce post-harvest lost and overcome the trade barriers.

Bread and cakes are highly perishable products that mainly deteriorates due to staling, moisture loss and microbial spoilage. More than 90% of mould contamination occurs during cooling, slicing or wrapping operations (Magan et al., 2003). There is increasing public concern about food preservatives and an urge to reduce their amounts exist in the food industry, which affects bread production and also associated mould spoilage. The benefits of irradiation as a sanitary treatment of many types of food are well known, some of which are applied commercially in several countries. Gamma irradiation technology has positive effects for destroying the pathogen microorganisms and by improving the safety and shelf stability of food products without compromising the nutritional or sensory quality and its use is gradually increasing worldwide (Ahn and Nam, 2004). Thus, this preliminary study was conducted to gain early information about the suitability of bread and bahulu cakes to be irradiated and stored at room temperature.

## 2 Materials and Methods

Fresh samples sliced breads and bahulu cakes were obtained from local producers, packed, sealed and irradiated at irradiation doses of 2 kGy, 5 kGy and 10 kGy, using 60Co gamma irradiation at MINTec-Sinagama. The irradiated and non-irradiated samples were displayed at room temperature storage period of one month. Total plate count by pour plate method, was determined using Plate Count Agar incubated at 30oC for 48 hours and Potato Dextrose Agar for molds (incubated at 30oC for 5 days). The results were expressed as colony forming units per gram (cfu/g). Colour changes of the products were recorded using Colorimeter (Minolta) with L, a, b values i.e. Lightness (L), redness (a) and yellowness (b). Acceptability of the irradiated products were determined through sensory evaluation using 30 members (male and female) of untrained panellists. A 5-point hedonic rating scale

was used with 5 points as the most acceptable and 1 point as the most unacceptable. Statistical analysis using ANOVA test and comparisons were made by Duncan's multiple range tests.

## 3 Results and Discussion

Irradiation at 2 kGy reduced the fungal and microbial loads in irradiated sliced breads and bahulu caked compared to the control samples (not irradiated). The fungal and microbial loads in samples irradiated at 5 and 10 kGy were more lowered than samples irradiated at 2kGy. After storage at one month, the fungal and microbial loads were increased in the control samples but maintained low in samples irradiated at 2, 5 and 10 kGy (Table 1). There were significant changes in the morphology of in samples that irradiated at 2, 5 and 10 kGy. Samples irradiated at 2 kGy were more accepted in sensory evaluation especially the texture and taste. Samples irradiated at 5 kGy and 10 kGy were totally changed in the texture and taste acceptance (Figure 1). This can be concluded by increasing doses, the dryness and the sweetness of the samples were also increased proportionally. Bread irradiated with higher dose experience bitter taste compared to bread exposed to lower radiation.

| BAHULU | | |
|---|---|---|
| **Irradiation dose (kGy)** | **Fungal Counts (cfu/g) - 0 Day** | **Fungal Counts (cfu/g) - 1 Month** |
| 0 (control) | $2.96 \times 10^6$ | $9.00 \times 10^6$ |
| 2 | $2.00 \times 10^6$ | $1.33 \times 10^6$ |
| 5 | 0 | 0 |
| 10 | 0 | 0 |
| BREAD | | |
| **Irradiation dose (kGy)** | **Fungal Counts (cfu/g) - 0 Day** | **Fungal Counts (cfu/g) - 1 Month** |
| 0 (control) | $1.30 \times 10^6$ | $2.30 \times 10^6$ |
| 2 | $1.00 \times 10^6$ | $1.40 \times 10^6$ |
| 5 | 0 | 0 |
| 10 | 0 | 0 |

Table 1: The number of fungal colonies in breads and bahulu cakes irradiated with different doses and storage time

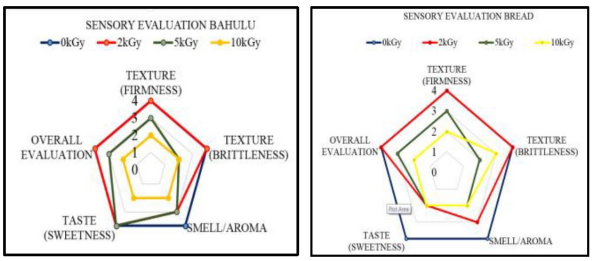



Figure 1: Sensory evaluation of irradiated bahulu cakes and breads samples after 1 month storage.

There is no significant different for the L (lightness) of bahulu and bread irradiated with 2kGy of gamma with control in 0 day of storage. However, the L value decrease significantly when radiated with 5kGy and 10kGy in 0 day of storage for both bahulu and bread (Figure 3, 4, 5 and 6). This showed that high dose of radiation more than 5kGy have effect on the lightness of the food. For a value, the redness (a) and yellowness (b) of the irradiated bahulu cakes increased when the radiation dose increases during the 0 day of storage. The yellowness (b value) of the bahulu cakes increased after one month storage meanwhile there was no significant changes of yellowness of irradiated bread samples after 1 month storage.

From the result it can be concluded that increased radiation doses will decrease the overall sensory acceptance. This show that, radiation dose has effect on the sensory aspect of these samples. This result supported by Bandyopadhyay, et al. (Bandyopadhyay et al., 2020) from his experiment when food irradiated with 5 kGy of gamma radiation reduced the firmness of the food. Other than that, it can be concluded that increased irradiation dose increased the dryness and sweetness of these bahulu cake samples. Bread irradiated with higher dose experience bitter taste compared to bread exposed to lower radiation. Ionizing irradiation is one of the food preservation techniques with minimum interruption of to the functional, nutritional, and sensory properties of food products at lower doses. However, higher dose of irradiation, especially higher than 10 kGy, can lead to physicochemical changes and significantly deteriorate sensory properties of foods (Miller, 2005; **?**). Food irradiation offers a potential to enhance microbiological safety and quality of food through shelf-life extension. It is considered a more effective and appropriate method to enhance food stability and safety, when compared to other processing methods like heat and chemical methods (Arapcheska et al., 2020).

## 4 Conclusions

Irradiation at dose 2 kGy was suitable in preserving local perishable food products such as bread and bahulu cakes. Therefore, any food industry that interested to use this technology need to improvise their formulation in order to maintain the originality acceptance of the product. The results showed the ability of gamma irradiation for the decontamination of selected food and reliable process for food storage in commercial industry. Irradiation can offer a great potential effort to enhance microbiological safety and quality of food through shelf-life extension.

## References

D.U. Ahn and K.C. Nam. 2004. Effects of ascorbic acid and antioxidants on color, lipid oxidation and volatiles of irradiated ground beef. *Radiation Physics and Chemistry*, (71):149–154.

M. Arapcheska, H. Spasevska, and M. Ginovska. 2020. Effect of irradiation on food safety and quality. *Current Trends in Natural Sciences*, 9(18):100–106.

N. C. Bandyopadhyay, V. More, J. Tripathi, and S. Gautam. 2020. Gamma radiation treatment to ensure microbial safety of ready to bake (rtb) vegetable toppings/ fillers and retain their nutritional qualities during cold storage. *Radiation Physics and Chemistry*, 176:108939.

N. Magan, M. Arroyo, and D. Aldred. 2003. Mould prevention in bread. in s. p. cauvain (ed.), bread making: Improving quality (1st. ed., pp. 500-514). *Raton: Woodhead Publishing Limited and CRC Press.*, 1st Edition:500–514.

R.B. Miller. 2005. Electronic irradiation of foods: An introduction to the technology. *Springer, New York*.

Individual Research Contribution Review, 2024: 49–50
*ISSN: 3083-922X*

# Radiosensitivity and Morphology of Chili Plants After Acute Gamma Irradiation

**Shakinah Salleh**
Agrotechnology and Biosciences Division, Malaysian Nuclear Agency
43000 Kajang, Selangor
shakinah@nm.gov.my

## Abstract

Chili (*Capsicum annum*) is a flowering herbaceous vegetable plant in the Solanaceae family. Chili is used in dishes and snacks to provide flavor and pungency. The self-sufficiency level (SSL) of vegetables in Malaysia is only 44.7%, where chili is one of the main vegetables that need to be imported. This project was developed with the objective to improve chili varieties with enhanced adaptability to Malaysian conditions, high yield as well as tolerance to diseases and pests. The variety 'Cilibangi-3' was used in this project and the seeds were irradiated using acute gamma irradiation (Gamma Cell Biobeam GM8000) at dose 0, 20, 40, 60, 80, 100, 200, 300, 400, 500 and 600 Gy to perform radiosensitivity test. The 50% Lethal Dose (LD50) for chili cv. 'Cilibangi-3' was around 400 Gy. The germination percentage was generally decreasing with increasing dose of acute gamma radiation. Higher morphological mutation rate (85%) was observed at dose 300 Gy, whilst doses above 400 Gy showed negative effects of acute gamma irradiation particularly on the morphological characteristics such as reduced plant height, leaf size and number. Based on this radiosensitivity result, 300 Gy was chosen for inducing mutation in chili cv. 'Cilibangi-3'. The irradiated plants will be screened for multiple generations until stable mutants with targeted traits of interest were obtained.

**Keywords:** Rapid cycling, tomato, artificial lighting

## 1 Introduction

material. The main constraint to large-scale chili production in Malaysia is pest and disease attacks due to hot summers and year-round rains. Therefore, there is a need to improve chili varieties with enhanced adaptability to Malaysian conditions, high yields, and tolerance to diseases and pests. Gamma irradiation is a promising method to induce genetic variations in a large number of crops (Harten, 1998; Shu, 2012). The objective of this study is to improve chili through mutation breeding with enhanced adaptability to Malaysian conditions, high yield as well as tolerance to diseases and pests.

## 2 Materials and Methods

### 2.1 Plant Material

Packaged chili cv. 'Cilibangi-3' seeds are purchased from authorized seed producers. Each package contains 30 seeds.

### 2.2 Acute Gamma Irradiation

In this study, acute irradiation was carried out using Gamma Cell (Biobeam GM8000, Germany). The total of 30 seeds were packed in the petri dish and labeled for each dose which were 0 (Control), 20, 40, 60, 80, 100, 200, 300, 400, 500 and 600 Gray. Then the petri dish was loaded into BB13-5 container of 29.2 cm height and 10 cm diameter for irradiation. The dose rate for this acute gamma irradiation is 15.7 Gy/minute.

### 2.3 Determination of optimal dose

Irradiated seeds were then soaked for overnight and planted into seedling tray for germination. After three weeks, all the germinated seeds were counted and the percentage of survival seedling was plotted using CurveExpert 1.3 software (CurveExpert, 2024) for determination of the optimal dose.

### 2.4 Bulked irradiation

The optimal dose is used for bulked mutation induction of Chili cv. 'Cilibangi-3' to get first mutant generation (M1). At M1 generation, the observation only focuses on resistance to pest and diseases and fruit variations. Then, all M1 seeds are collected for M2 planting materials and further screening.

## 3 Results and Discussion

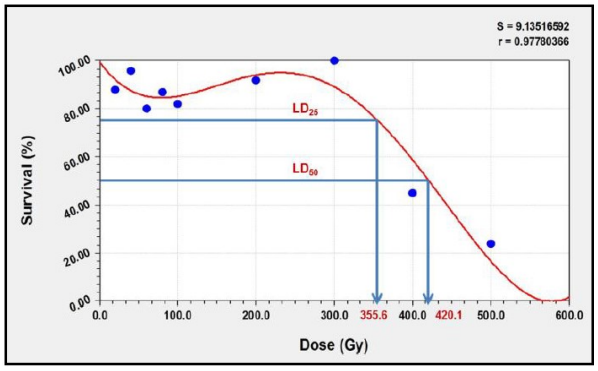



Figure 1: The percentage of survival seedlings with different doses of acute gamma.




Figure 3: Variations of fruits from (1) Tolerance to pest and diseases (2) Control (3) 300Gy.

From this study, the 50% Lethal Dose (LD50) for chili cv. 'Cilibangi-3' was 420 Gy (Figure 1) and higher morphological mutation rate (85%) was observed at dose 300 Gy. The doses above 400 Gy showed negative effects of acute gamma irradiation particularly on the morphological characteristics such as reduced plant height, leaf size and number. Based on this radiosensitivity result, 300 Gy was chosen for inducing mutation in chili cv. 'Cilibangi-3'.

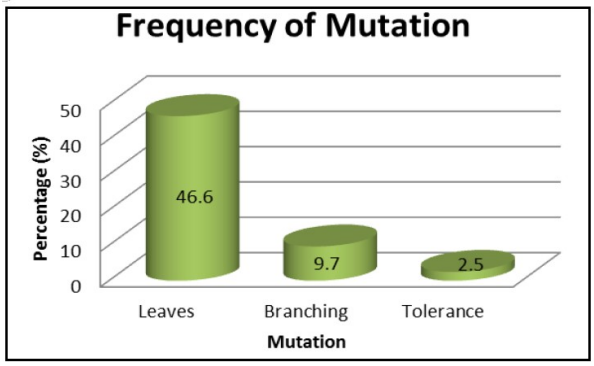



Figure 2: Frequency of mutation after acute gamma irradiation at dose 300 Gy.

Observation at M1 mutant generation (Figure 2) showed percentage of leaf morphological mutations (46.6%) were the most frequent type, followed by branching mutations (9.7%), and tolerance to pest and diseases (2.3%). All the M1 seeds are collected for planting M2 mutant generation and further screening (Figure 3).

## 4 Conclusions

Based on this study, the optimum dose for mutation induction of Chili cv. 'CiliBangi-3' using acute gamma was 300 Gy. Observation at M1 generation showed the potential to develop mutants that tolerance to pest and diseases by using acute gamma irradiation. However, further observation and research are needed in order to conclude these finding.

## 5 Acknowledgments

The authors would like to thank Nuclear Malaysia and Department of Agriculture Malaysia (DOA). This study was a sub topic for the Strategic Cooperation Projects between Nuclear Malaysia and DOA. Also special thanks to those who helped in completing this study.

## References

CurveExpert. 2024. Curveexpert 1.3 software. *Hyams Development*.

V. A. M. Harten. 1998. Mutation breeding.theory and practical applications. *UK: Cambridge University Press*.

Q. Shu. 2012. Plant mutation breeding and biotechnology. *CAB International and FAO*.

Individual Research Contribution Review, 2024: 51–52
*ISSN: 3083-922X*

# Study of Soil Management and Nutrient Requirement For Harumanis Mango Using Remote Sensing and Nuclear Technology

**Shyful Azizi bin Abdul Rahman**
Agrotechnology and Biosciences Division, Malaysian Nuclear Agency
43000 Kajang, Selangor
shyful@nm.gov.my

## Abstract

The Harumanis mango is an important fruit crop for Perlis, contributing significantly to the state's economy. However, its yield has declined in recent years due to various challenges. A two-year study conducted at the Harumanis Model Plot under the Department of Agriculture in Perlis investigated key agronomic factors, including soil and plant nutrient levels, weather conditions, and soil water status. The study identified imbalances in essential macronutrients, as a major contributing factor to reduced flower and fruit retention. Excessive nitrogen was found to cause vegetative flushing during the flowering phase, disrupting the plant's reproductive cycle. The study emphasized the importance of maintaining specific nitrogen levels in leaves and soil to prevent unwanted flushing, along with ensuring proper water management for each growth stage. Hyperspectral UAS remote sensing data, using the Normalized Difference Vegetative Index (NDVI), supported these observations. Accurate and modern methods for soil and leaf chemical analysis and water content measurement are critical for effective crop management. The development of updated guidelines on soil, water, and nutrient management is essential to sustain the production of Harumanis, ensuring its role as a valuable strategic crop in Malaysia.

**Keywords:** nutrient imbalance, plant phenology, remote sensing

## 1 Introduction

Economic importance, especially for the state of Perlis. Its production is comparable to other major mango-producing countries. However, in recent years, Harumanis production has seen a noticeable decline due to various factors, including pest and diseases such as Insidious Fruit Rot (IFR), issues with flower production, and low fruit retention. In addition to the effects of climate change, other contributing factors need to be studied, and recovery strategies must be developed.

A condition known as "unwanted flushing" occurs during the flowering phase due to high nitrogen availability in the soil (Ramirez and Davenport, 2010). Soil moisture also increases nitrogen availability to plants. To prevent this, nitrogen content in leaves must remain below 1.5% at every growth stage, while the optimal total nitrogen content in soil should be less than 10 mg/kg.

Multispectral UAS (Unmanned Aerial System) drones are increasingly used for nutrient monitoring in orchard trees like mango. Vegetation indices, such as the Normalized Difference Vegetation Index (NDVI), are calculated from the images data to assess the chlorophyll content and overall photosynthetic activity of the trees. NDVI values help identify nutrient deficiencies or imbalances, as stressed or undernourished trees exhibit lower index values compared to healthy ones. This method provides a non-invasive, rapid, and precise way to monitor the nutritional status of large orchards, guiding targeted fertilization and management practices (Torgbor et al., 2022).

A two-year study was conducted at the Harumanis Model Plot of the Department of Agriculture in Bukit Temiang, Perlis from August 2022 to August 2024. Various agronomic aspects, including soil and plant nutrient levels, weather impacts on plant phenology, and soil water status, were examined using remote sensing and nuclear technologies combined with conventional techniques.

## 2 Methodology

### 2.1 Drone mission and NDVI analysis

Aerial images were collected using multispectral drone DJI Phantom P4 with RTK in monthly interval for two years. The collected data were processed and NDVI values were individually generated for each tree.



Figure 1: Multispectral DJI Phantom P4

### 2.2 Soil and foliar analysis

Soil samples were collected at the beginning of the season, and leaf samples were taken during the dormancy stage. These samples were submitted to both the Department of Agriculture laboratory and a private laboratory for physico-chemical analysis (IAEA, 2023).

### 2.3 15N Experiment

A nitrogen uptake study was conducted using the current and standard farmer practices. The experiment utilized isotope-labeled 15N Ammonium Nitrate fertilizer and plant sam-

| Location | 1:2.5 pH | microS/cm EC | cmol/kg CEC | mg/kg Avail P | % Total N | % C/N ratio | % Organic Carbon | % Total Carbon | % Organic Matter |
|---|---|---|---|---|---|---|---|---|---|
| SN1-MF | 5.90 | 20.15 | 7.46 | 25.55 | 0.20 | 5.07 | 0.99 | 1.31 | 1.71 |
| Simplify-MF | 5.86 | 16.53 | 8.61 | 27.77 | 0.19 | 5.29 | 1.01 | 1.33 | 1.74 |
| SN2-MF | 6.34 | 64.05 | 11.93 | 290.66 | 0.58 | 2.90 | 1.70 | 2.26 | 2.94 |
| Blok A | 5.43 | 29.05 | 5.75 | 21.29 | 0.36 | 2.23 | 0.81 | 1.07 | 1.39 |
| BC | 6.69 | 116.90 | 19.69 | 13.69 | 0.17 | 11.26 | 1.84 | 2.44 | 3.18 |
| Simplify-BB1 | 6.19 | 69.61 | 13.18 | 70.88 | 0.13 | 13.69 | 1.74 | 2.22 | 3.00 |

Table 1: Physico-chemical data of soil in early 2022 seasons

ples were analyzed using Isotope Ratio Mass Spectrometry (IRMS).

## 3 Data/Result

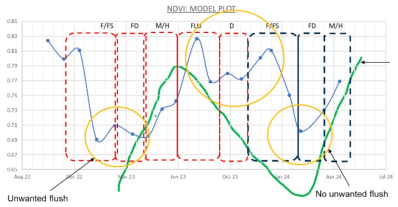



Figure 2: Average Normalized Difference Vegetative Index (NDVI) pattern of Harumanis trees aerial images in experimental plot for 2 seasons

### 3.1 Soil and foliar nutrient status

| Parameter | Unit | SN1. MF | SN2. MF | Simplify. BB1 | BC |
|---|---|---|---|---|---|
| N | % | 1.527 | 1.581 | 2.081 | 1.735 |
| P | % | 0.150 | 0.140 | 0.161 | 0.192 |
| K | % | 1.000 | 1.025 | 0.850 | 1.050 |
| Ca | % | 1.803 | 1.916 | 1.413 | 1.182 |
| Mg | % | 0.216 | 0.248 | 0.241 | 0.260 |
| B | ppm | 18 | 19 | 19 | 16 |
| Cu | ppm | 10 | 10 | 10 | 8 |
| Zn | ppm | 18 | 16 | 18 | 15 |
| Fe | ppm | 60 | 73 | 96 | 46 |
| Mn | ppm | 220 | 166 | 548 | 84 |

Table 2: Sample Type/Project/Supplier Data

### 3.2 Gel Electrophoresis and Visualization

Gel electrophoresis was carried out using a ≥ 1.5% agarose gel. The power supply was connected and electrophoresis ran at 75V for 1 hour. Finally, DNA bands were visualized through a bio-imaging system.

### 3.3 15N uptake

The PCR products were sent for sequencing, and the raw sequences were analyzed using NCBI BLAST. The tool identified the closest relatives along with their descriptions and similarity percentages.

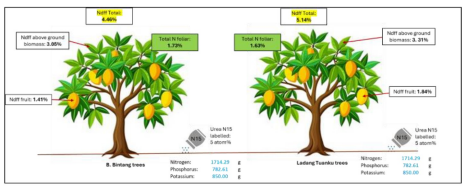


Figure 3: Nitrogen uptake derive from fertilizer and total nitrogen uptake.

## 4 Discussion

### 4.1 NDVI pattern and yield

The NDVI pattern shows that during the 2022 season, unwanted flushing occurred during the flowering and fruit set stages. This condition led to flower drop and low fruit retention. In contrast, during the 2023 season, no unwanted flushing occurred during the flowering and fruit development stages, although it was observed during dormancy. The stable conditions during the flowering and fruit set stages resulted in a significantly higher fruit yield in the 2023 season, which was seven times greater than that of the 2022 season.

### 4.2 Effect of nitrogen to fruit production

Laboratory analysis data showed that nitrogen content in both soil and leaves was significantly high, exceeding the recommended levels of below 10 mg/kg in soil and below 1.5% in leaves at all growth stages. This elevated nitrogen content likely disrupted the flowering and fruit set stages of Harumanis mango during the 2022 season.

### 4.3 Nitrogen use efficiency

Results from nitrogen uptake experiments using the isotope 15N revealed that nitrogen uptake from fertilizer applied at the recommended rate was low, at only 4-5%. However, the total nitrogen content in the plants was high. This is likely due to the high levels of existing nitrogen availability in the soil. Therefore, improvements to fertilizer recommendations, particularly for nitrogen, are necessary to enhance efficiency, reduce costs, and minimize environmental impact (Hamilton et al., 2017).

## References

D. Hamilton, C. Martin, M. Hearden, and C.A. Asis. 2017. Effect of tree leaf n status and n application time on yield and fruit n partitioning of mango. *Acta Horticulturae*, (1183).

IAEA. 2023. Expert end of mission report ras5087- rer1021-evt2101729 validation and verification of dosimetry system at 3 mev electron beam (eb) machine for sanitary (1-10 kgy) and phytosanitary (¡ 1 kgy) purpose. *IAEA*.

F. Ramirez and T. L. Davenport. 2010. Mango (mangifera indica l.) flowering physiology. *Scientia Horticulturae, v*, (2):65–72.

B.A. Torgbor, M.M. Rahman, A. Robson, J. Brinkhoff, and A. Khan. 2022. Assessing the potential of sentinel-2 derived vegetation indices to retrieve phenological stages of mango in ghana. *Horticulturae*, (8):11.

Individual Research Contribution Review, 2024: 53–54
*ISSN: 3083-922X*

IRCR

# Biochemical and Transcriptomic Analysis of Disease Resistance and Early-Maturity Related Genes in NMR-191 and NMR-192 Rice Mutant Lines

**Sobri Hussein**
Agrotechnology and Biosciences Division, Malaysian Nuclear Agency
43000 Kajang, Selangor
sobri@nm.gov.my

## Abstract

The transcriptomic profiling analysis revealed that *Os07g0129300*, *Os12g0270300*, and *Os03g0235000* were the disease-resistance genes whereas *Os03g0195300*, *Os01g0704100*, *Os11g0143200*, *Os06g0569900*, and *Os06g0568600* were the early maturity genes found in NMR191 and NMR192. This study validates that NMR191 and NMR192 could be better varieties than the parent line due to the presence of their early maturity and disease resistance traits.

**Keywords:** Chlorophyll content, Mutation breeding, *Oryza Sativa*, Proline content, Total soluble protein content

## 1 Introduction

In this study, the mutation breeding method, which is ion beam radiation was applied on the parent line, Pongsu Seribu 2 (PS2) in developing two new rice mutant lines, Nuclear Malaysia Rice Line 1 (NMR191) and Nuclear Malaysia Rice Line 2 (NMR192). The PS2 was chosen as the parent line due to its natural resistance against Magnaporthe oryzae blast disease (Aluko et al., 2023; Andrew-Peter-Leon et al., 2021).

## 2 Materials and Methods

### 2.1 Plant materials

The parent line, Pongsu Seribu 2 (PS2) as well as NMR191 and NMR192 rice mutant lines were generated using ion beam radiation at QST-Takasaki, Japan and were provided by Malaysia Nuclear Agency.

### 2.2 Germination of Seeds

A total of 24 seeds were chosen from each of the NMR191 and NMR192 rice mutant lines and their corresponding parent line, Pongsu Seribu 2. The seeds were soaked in fungicide for 24 hours followed by rinsing with sterile ultrapure water.

### 2.3 Determination of total soluble protein content

The total soluble protein content of NMR191, NMR192, and Pongsu Seribu 2 were extracted using Tris protein extraction buffer with a total volume of 1.5 mL using mortar and pestle in cold condition. Following that, the crude extract was subjected to centrifugation using Centrifuge 5427 R (Eppendorf, Germany) at 12,000 rpm for 20 minutes at 4 °C.

### 2.4 Determination of chlorophyll content

The determination of chlorophyll content was performed using the Lichtenthaler method. Calcium carbonate ($CaCO^3$) (R & M Chemicals, UK) was added to the sample in a 2:1 ratio.

### 2.5 Determination of proline content

The determination of proline content was performed using Bates et al. method (Ghanem et al., 2021). To begin with, the plant sample was ground with ≥ 3% sulfosalicyclic acid (Boer, China) with mortar and pestle in ice-cold condition.

### 2.6 RNA extraction and RNA-Sequencing analysist

The plant samples were sent to the Apical Scientific Sdn. Bhd. for RNA extraction and RNA-Sequencing analysis. The total RNA content of the plant samples was extracted using PrimeWay Total RNA Extraction Kit (1st BASE Kits, KIT-9021-50). The microvolume UV/Vis spectrometer and RNA labchip, RNA 6000 Nano Kit (Agilent, 5067-1511) were utilized to measure the quality and quantity of purified RNA.

### 2.7 Transcriptomic analysis

The transcriptomic analysis for all of the mutant lines was sent to the Apical Scientific Sdn. Bhd. for results reading. STRING database was utilized to analyze the protein-protein interaction of the DEGs. This analysis was used to identify functionally related genes, particularly those associated with disease resistance and early maturity traits.

### 2.8 Statistical analysis

The experimental procedures in this study were conducted with 3 replicates for biochemical analyses. The data obtained was subjected to one-way analysis of variance (ANOVA) followed by Tukey's honestly significant difference (HSD) test at a significance level of P ≥0.05.

## 3 Results and Discussion

### 3.1 Total Soluble Protein Content

In general, the study revealed that the total soluble protein content found in the mutant line NMR191 and NMR192 was significantly higher than the parent line PS2. It demonstrated that the protein content found in NMR191 and NMR192 was ≥ 236.2% and ≥ 277.34% higher than the parent line PS2. These results indicate that the mutant line could possibly have better disease resistance and early maturity characteristics compared to the parent line (Bado et al., 2015).

### 3.2 Chlorophyll content

Based on current findings as shown in Figure 2, the NMR192 has demonstrated a significantly higher Ca and Cb content compared to the parent line PS2. There was also ≥ 377.78% and ≥ 370% higher of Ca and Cb in NMR191 in respect to PS2. Nevertheless, the increase was not significant. The results in this study indicate that the mutant lines have better disease resistance and early maturity traits compared to the parent line.

### 3.3 Proline content

Based on the current findings, both of the mutant lines demonstrated a significantly higher proline content in the plant samples compared to the parent line as shown in Figure 3. The proline content in NMR191 and NMR192 was shown to be ≥ 181.8% and ≥ 245.45% higher than the PS2.

### 3.4 Transcriptomic Profiling Analysis

#### 3.4.1 Coexpression Venn diagram of differentially expressed genes (DEGs) at different rice mutant lines

A total of 832 genes were found to be unique in the mutant line NMR191 where these genes were not found to be expressed in the parent line PS2 and mutant line NMR192. A total of 1106 genes were found to be unique in the mutant line NMR192 where these genes were not found to be expressed in the parent line PS2 and mutant line NMR191.

#### 3.4.2 Gene Ontology Enrichment Analysis

In this study, the gene ontology (GO) bar was utilized to demonstrate the top 5 representative genes found in both the mutant line NMR191 and NMR192, when they were compared with their parent line. This signifies that the cellular components and molecular functions of the plant cells in mutant lines NMR191 and NMR192 contribute the major role in disease resistance and early maturity traits, where the biological process of the plant only contribute minor role in these traits (Banerjee et al., 2019).

## 4 Conclusion

Based on the findings from the current studies, the rice mutant lines NMR191 and NMR 192 have been validated with disease resistance and early maturity traits with a significant increase in the plant biochemical parameters. This includes a significantly higher content of total soluble protein, chlorophyll content, and proline content. Additionally, it was further supported by the presence of highly expressed disease resistance and early maturity genes. The disease resistance genes that were highly expressed in both the mutant lines NMR191 and NMR192 include *Os07g0129300*, *Os12g0270300* and *Os03g0235000*. Meanwhile, the early maturity genes that were highly expressed in both the mutant lines NMR191 and NMR192 include *Os03g0195300*, *Os01g0704100*, *Os11g0143200*, *Os06g0569900*, and *Os06g0568600*.

## 5 Acknowledgements

This project was supported by IMU University under the project number [MBT I-2023(01)]. The authors extend their gratitude to the Malaysian Government under the Ministry of Science, Technology, and Innovation (MOSTI), and the Malaysia Nuclear Agency for generously providing the research materials as part of MOSTI Strategic Research Fund (project code SRF-APP).

## References

O.O. Aluko, S. Kant, C. Adedire, O.M.and Li, H. Yuan, G.and Liu, and Q. Wang. 2023. Unlocking the potentials of nitrate transporters at improving plant nitrogen use efficiency. *Frontiers in Plant Science*, 14(1074839).

M.T. Andrew-Peter-Leon, R. Selvaraj, K.K. Kumar, M. Muthamilarasan, J.K. Yasin, and M.A. Pillai. 2021. Loss of function of osfbx267 and osga20ox2 in rice promotes early maturing and semi- dwarfism in -irradiated iwp and genome-edited pusa basmati-1. *Frontiers in Plant Science*, 12(714066).

S. Bado, B.P. Forster, A.M.and Lagoda P.J. Nielen, S.and Ali, B.J. Till, and M Laimer. 2015. Loss of function of osfbx267 and osga20ox2 in rice promotes early maturing and semi- dwarfism in -irradiated iwp and genome-edited pusa basmati-1. *Plant Breeding Reviews*, 39.

P. Banerjee, V. Visha Kumari, and P. Nath, R.and Bandyopadhyay. 2019. Seed priming and foliar nutrition studies on relay grass pea after winter rice in lower gangetic plain. *Journal of Crop and Weed*, 15.

Individual Research Contribution Review, 2024: 55–56
*ISSN: 3083-922X*

# Whole Genome Sequencing and Genetic Analysis of An Advanced Rice Mutant Line (NMR191) with Blast Resistance and Early Maturity Traits

**Wan Dalila Wan Chik**
Agrotechnology and Biosciences Division, Malaysian Nuclear Agency
43000 Kajang, Selangor
wandalila@nm.gov.my

## Abstract

Malaysian Nuclear Agency has successfully developed a blast resistance, early maturity and high-yielding advanced mutant line, NMR191, through a series of stringent phenotypic and genotypic selections. These selections were based on its parental line Pongsu Seribu (PS2) using ion beam irradiation at 120 Gy. Whole genome sequencing (WGS) and genetic analysis were conducted on NMR191 and PS2; and its genomic landscape was characterized to identify key genetic variations contributing to these agronomically important traits. WGS analysis revealed a range of single nucleotide polymorphisms (SNPs), insertions, and deletions (INDELs), which were systematically compared to the reference rice genome to pinpoint candidate genes associated with blast resistance and early maturity. The results from this study provide a comprehensive genetic profile of NMR191, which can inform future breeding programs aimed at developing rice varieties with enhanced disease resistance and accelerated growth cycles, contributing to improved yield stability and food security in regions impacted by rice blast disease.

**Keywords:** NMR191, PS2, WGS, Genomics

## 1 Introduction

Malaysia has focused its self-sufficiency policy on rice and paddy production, which are the country's primary staple food and food crops. To meet future rice demand, the National Agro-food Policy 2021-2030 (NAP 2.0) (of Agriculture and Industries, 2021) advocates for the expansion of local rice production. Nuclear Malaysia has successfully developed a blast resistance, early maturity and high-yielding advanced mutant line, NMR191, through a series of stringent phenotypic and genotypic selections. These selections were based on its parental line, Pongsu Seribu (PS2) using ion beam irradiation at 120 Gy. Identifying the genes and their superior variants would be beneficial for a comprehensive understanding of blast resistance and early maturity mechanisms. It would also aid in rice breeding activities through marker-assisted selection. With the increased speed and reduced cost of sequencing, next generation sequencing technologies (NGS) have played a significant role in accelerating the development and adoption of novel strategies for crop improvement. The availability of a high-quality reference genome allows for rapid and precise alignment and mapping of sequences generated by NGS technologies, resulting in the identification of genome-wide variants.

## 2 Methods

### 2.1 Plant material, sample collection and DNA extraction

About 2 mg of leaves was collected from each NMR191 and PS2 during the two-weeks old seedlings (vegetative states) prior DNA extraction process. The extraction was performed in three replicates. Total DNA was extracted using the cetyl trimethyl ammonium bromide (CTAB) method (Murray and Thompson, 1980). Quantity and quality of the genomic DNA were assessed using a spectrophotometer, fluorometer, and agarose gel electrophoresis.

### 2.2 Whole Genome Sequencing of NMR191 and PS2

llumina sequencing was performed by sequencing service provider at the Novogene Bioinformatics Technology Co., Ltd. (Beijing, China) using Illumina HiSeq 4000 according to the manufacturer's instructions (Illumina, San Diego, CA, USA). Briefly, DNA libraries were made using Illumina TruSeq DNA sample preparation kit (Illumina, USA) and paired-end sequencing was performed with Illumina HiSeq 4000.

### 2.3 Mapping of whole genome sequences to the reference genome

The primer/adopter sequences and low-quality reads with Phred quality score < 30 were removed using the NGS QC Toolkit (v2.3.3; http://www.nipgr.res.in/ngsqctoolkit.html). Only high- quality filtered reads were used for mapping on the rice reference genome (Genome assembly IRGSP-1.0 *Oryza sativa indica*; using Burrows Wheeler Alignment (BWA) software (v0.7.12). The SAMtools (v1.21) (Danecek et al., 2021) was used to determine the reference genome coverage.

### 2.4 Identification and annotation of variants

GATK analysis tools (Version 4.6.1.0) were employed to identify the SNPs and InDels using the following criteria: (a) the minimum variant frequency of ≥ 90‰, (b) average quality of the SNP base ≥ 30, and (c) minimum read depth of 10. The distribution of DNA polymorphisms in different genomic regions were assessed by combining genome annotation information and positions of DNA polymorphisms. Identification of synonymous/nonsynonymous SNPs, and large-effect

| Genotype | Characteristic | Total raw nucleotides (bp) | Total clean nucleotides (bp) |
|---|---|---|---|
| NMR191 | Early maturity, high yield, blast resistant, semi-dwarf | 25,268,466,900 | 24,820,597,800 |
| PS2 | Blast resistant, High-yield | 29,115,420,300 | 28,550,580,300 |
| Total | | 54,383,887,200 | 53,371,178,100 |

Table 1: Summary of raw data for rice mutant lines, NMR191, and their parental line, PS2.

SNPs/InDel were accomplished using single-nucleotide polymorphism effect predictor (SnpEff, v4.1 k) with default parameters.

## 3 Results/Discussion/Conclusions

The whole genome sequencing (WGS) of the NMR191 rice mutant line produced a comprehensive data set that provided significant information on the genetic variations associated with blast resistance and early maturity traits. After sequencing, we identified approximately 121,8598 SNPs and 188, 038 InDels compared to the reference rice genome. The analysis revealed several important genetic variations located in genes previously associated with resistance to disease and traits of early maturity. In particular, genes involved in the pathogen recognition pathway, such as *OsPR1aL* and *POXN*, were found to be expressed in NMR191, potentially contributing to its increased resistance to rice blast caused by *Magnaporthe oryzae* (Yip et al., 2024). Furthermore, mutations in genes related to flowering time regulation, such as *OsSultr2* and *OsNRT2.3*, were identified, which may explain the early maturity observed in NMR191 (Yip et al., 2024). The genetic diversity within NMR191 was also examined by comparing it with other known rice varieties, PS2. Table 1 shows the summary of the raw data for the rice mutant lines, NMR191 and their parental line, PS2.

While NMR191 shared some common genetic features with well- established blast-resistant cultivars, it also exhibited unique variations, which may provide novel sources of resistance that could be exploited in future breeding programs. The identified mutations in flowering time pathways also highlight the potential of NMR191 as a candidate for accelerated rice breeding, particularly in regions where early harvests are critical to mitigate the impact of biotic stresses such as rice blast. This study underscores the importance of integrating the whole genome sequencing and phenotyping study in understanding the genetic basis of complex agronomic traits. Identification of key loci associated with blast resistance and early maturity in NMR191 offers a valuable resource for marker-assisted selection in rice breeding programs. Furthermore, the findings suggest that NMR191 could serve as an ideal parent line for developing rice varieties with enhanced resistance to disease and improved adaptability to varying climatic conditions. However, more research is needed to validate the functional role of the identified candidate genes and explore their interactions with other genetic factors that influence these traits. This would enable more targeted and efficient breeding strategies to enhance rice productivity and resilience against biotic stresses.

## 4 Conclusion

In conclusion, the whole genome sequencing and genetic analysis of the advanced rice mutant line NMR191 have provided valuable insights into the genetic underpinnings of its blast resistance and early maturity traits. The identification of key SNPs, InDels, and candidate genes linked to these traits enhances our understanding of the genetic mechanisms governing disease resistance and growth cycles in rice. The findings not only contribute to the ongoing efforts to combat rice blast diseases but also offer an avenue for improving rice productivity and supporting food security. Future studies should focus on validating the identified genetic markers and incorporating them into breeding strategies to develop new rice cultivars.

## References

P. Danecek, J.K. Bonfield, J. Liddle, J. Marshall, V. Ohan, M.O. Pollard, A. Whitwham, T. Keane, S.A. McCarthy, R.M. Davies, and H. Li. 2021. Twelve years of samtools and bcftools. *GigaScience*, 10(2):giab008, 02.

M.G. Murray and W.F. Thompson. 1980. Rapid isolation of high molecular weight plant dna. *Nucleic Acids Research*, 8(19):4321–4326, 10.

Ministry of Agriculture and Food Industries. 2021. National agrofood policy 2021-2030 (nap 2.0).

T.M. Yip, S. Hussein, F. Ahmad, Y. Hase, Y.P. Wong, R. Y. Koh, and P. K.L., Anna. 2024. Biochemical and transcriptomic analysis of disease resistance and early-maturity related genes in nmr-191 and nmr-192 rice mutant lines. *International Journal of Science and Technology*, 10(2):01–24, Sep.

Individual Research Contribution Review, 2024: 57–58
*ISSN: 3083-922X*

# Assessing Nutritive Values of M1V5 Napier Grass Mutant Lines Generated from Gamma Irradiation

**Zaiton Ahmad**
Agrotechnology and Biosciences Division, Malaysian Nuclear Agency
43000 Kajang, Selangor
zaitonahmad@nm.gov.my

## Abstract

In this project, improvement of Napier grass was done through mutation induction using gamma irradiation to improve several traits especially biomass yield and protein content. Irradiation was carried out using acute gamma ray (BioBeam GM8000) at doses between 10 to 100 Gy and chronic gamma (Gamma Greenhouse) at cumulative doses up to 1090 Gy involving two cultivars (Dwarf and Taiwan). The mutagenesis project which was started in December 2018, has generated 29 selected mutant lines at M1V5 stage (24 Dwarf and 5 Taiwan) based on biomass yield. Analysis of crude protein (CP) content on 42-day-old plants showed that 15 out of 24 mutant lines of Dwarf variety have higher CP content whilst for Taiwan, two mutant lines have higher CP content than their respective parents. Other nutritional compositions were also analysed and recorded.

**Keywords:** Napier Grass, mutant, Gamma Irradiation

## 1 Introduction

Malaysia has been facing the impact of climate change, post COVID19 pandemic and geopolitical issues that badly affected food crop, livestock productivity and the supply chain of food that threaten our food security. One of the industries that is particularly affected by this impact is livestock because Malaysia relies heavily on imported raw materials for livestock feed. Malaysian government realizes that there is an urgent need to empower this industry to achieve a level of self-sufficiency and manage the cost of livestock feed without any external factor.

Napier grass *(Pennisetum purpureum)* is an important perennial tropical forage crop for livestock feed in Malaysia. It was introduced to Malaysia almost a century ago and used as direct feeding to cattle or processed into silage or hay (Haryani et al., 2018). Even though it has been planted for many years, very little research was done to improve its traits that makes it valuable to the local livestock industry.

Mutagenesis using gamma irradiation has long been used to generate new variety of plants with good agronomic traits. At present, a total of 3,448 new mutants from all crop varieties have been officially registered at the IAEA Mutant Variety Database, including three grass mutants (one Grass Plavine and two Guinea Grass) (mut, ).

The mutagenesis work on Napier Grass in Malaysia was started in December 2018 and has generated 29 selected mutant lines at M1V5 stage (24 Dwarf and 5 Taiwan cultivars) based on biomass yield (Salleh et al., 2021). Further evaluation was carried out to determine nutritive values of these potential mutant lines. Good nutritional composition is a very important trait in Napier Grass as it will make the plant an ideal feed for livestock and subsequently improve animal productivity.

## 2 Methods

Sample preparation, radiosensitivity tests, mutation induction using gamma irradiation, M1V1 to M1V5 generation screening and selection of potential mutant lines have been discussed previously by Shakinah et al., 2021 and Shakinah et al. 2024 (Salleh et al., 2024).

### 2.1 Preparation of samples for nutritional composition analysis

Napier grass mutant lines were planted in a glasshouse at Malaysian Nuclear Agency, Bangi. The mutants were harvested according to their individual lines at 42 days old after planting. The samples were brought to Food Analysis Laboratory, Malaysian Nuclear Agency for processing and drying. The samples of Napier stem and leaves were cleaned from any debris and remaining soil. Then they were cut into small pieces and grounded using Waring Blender to produce fine samples. The fine samples were dried for 72 hours in an oven at 70°C until constant weight. The dried samples were later placed in the zip lock plastic bag to maintain their freshness before running the proximate analysis.

### 2.2 Assessment of nutritional composition

Dried Napier Grass samples were sent to Universiti Kebangsaan Malaysia's Unipeq Laboratory in Bangi, Selangor for nutritional composition analysis. Proximate analysis that was carried out including total ash, moisture, crude protein (CP), total fat- soxhlate, carbohydrate and energy.

## 3 Results/Discussion/Conclusions

### 3.1 Analysis of nutritional composition

Proximate analysis is a quantitative analysis used for macromolecules estimation in dry matter (DM) of grass which includes the percentage of moisture, ash, crude protein (CP), crude fibre (CF) and fat. Analysis of CP content on 42-day-old plants showed that 15 Dwarf mutant lines have higher

CP content whilst for Taiwan, two mutant lines have higher CP content than their respective parents. Detailed nutritional characteristics of all mutant lines are shown in Table 1. The example of mutant lines in the field is shown in Figure 1.

| No | Parent | Mutant | Ash (%) | Moisture (%) | Protein (%) | Fat (%) | Carbs (%) | Energy (kcal) |
|---|---|---|---|---|---|---|---|---|
| 1 | Dwarf | DO* | 11 | 10 | 6.3 | 1.9 | 70.8 | 326 |
| 2 | Dwarf | DA 20 A | 10.8 | 10.2 | 7.6 | 2 | 69.4 | 326 |
| 3 | Dwarf | DA 20 B | 9.5 | 9.9 | 6 | 2 | 72.6 | 332 |
| 4 | Dwarf | DA 20 C | 7.7 | 10.3 | 7.6 | 3.3 | 71.1 | 345 |
| 5 | Dwarf | DA 30.5 | 7.3 | 9.5 | 5.7 | 2.9 | 74.6 | 347 |
| 6 | Dwarf | DA 40A | 7.2 | 9.8 | 5.4 | 2 | 75.6 | 342 |
| 7 | Dwarf | DA 40B | 10.8 | 10.6 | 6.9 | 2.5 | 69.2 | 327 |
| 8 | Dwarf | DA 40C | 7.9 | 10.4 | 7.5 | 2.7 | 71.5 | 340 |
| 9 | Dwarf | DA 40D | 12.5 | 9.8 | 6.2 | 1.9 | 69.6 | 320 |
| 10 | Dwarf | DA 40E | 11.1 | 9.2 | 6.9 | 1.9 | 70.9 | 328 |
| 11 | Dwarf | DA 40.4 | 7.7 | 10.7 | 7.5 | 1.5 | 72.6 | 334 |
| 12 | Dwarf | DA 60A | 12.1 | 10.5 | 7.6 | 1.6 | 68.2 | 318 |
| 13 | Dwarf | DA 80A | 9 | 10.3 | 7 | 1.8 | 71.9 | 332 |
| 14 | Dwarf | DA 80B | 13.5 | 10.7 | 6.9 | 1.8 | 67.1 | 312 |
| 15 | Dwarf | DA 80C | 8.7 | 10 | 6.5 | 1.7 | 73.1 | 334 |
| 16 | Dwarf | DA 100A | 10.3 | 9 | 5.7 | 2.7 | 72.3 | 336 |
| 17 | Dwarf | DA 100.2 | 7.1 | 9.2 | 6.3 | 2.2 | 75.2 | 346 |
| 18 | Dwarf | DA 100.5 | 6.6 | 9 | 5.7 | 2 | 76.7 | 348 |
| 19 | Dwarf | DA 140A | 9.5 | 9.5 | 9.2 | 1.7 | 73.1 | 333 |
| 20 | Dwarf | DA 180A | 9.3 | 8.8 | 6.1 | 2.5 | 73.3 | 340 |
| 21 | Dwarf | DA 180B | 9 | 9.4 | 8.6 | 1.7 | 71.3 | 335 |
| 22 | Dwarf | DC 80.2 | 6.5 | 8.8 | 5.5 | 2.1 | 77.1 | 349 |
| 23 | Dwarf | DC95.3 | 8.3 | 9.1 | 6.6 | 2.1 | 73.9 | 341 |
| 24 | Dwarf | DC150.5 | 8.1 | 9.4 | 8.6 | 2 | 71.9 | 340 |
| 25 | Dwarf | DC 409.5 | 7.9 | 10.4 | 8.8 | 1.6 | 71.3 | 335 |
| 26 | Taiwan | T0* | 9.3 | 9.6 | 9.1 | 1.6 | 70.4 | 332 |
| 27 | Taiwan | TC 65.1 | 7.6 | 9.5 | 7.7 | 1.3 | 73.9 | 338 |
| 28 | Taiwan | TC 178.3 | 11.1 | 9.4 | 11.4 | 1.5 | 66.6 | 326 |
| 29 | Taiwan | TC178.4 | 8.1 | 10.1 | 8.7 | 1.3 | 71.8 | 334 |
| 30 | Taiwan | TA 20.5 | 10 | 10 | 8.5 | 1.3 | 70.2 | 327 |
| 31 | Taiwan | TA 30.3 | 7.8 | 9.7 | 10.7 | 1.9 | 69.9 | 340 |

Table 1: Nutrition composition of M1V5 Napier Grass mutant lines. (*DO = Dwarf Control; TO = Taiwan Control)



Figure 1: M1V5 mutant lines TC178.4 and DC150.5 in the field

## 4 Acknowledgement

The author would like to thank all team members for their hard work and dedication; Shakinah Salleh, Mustapha Akil, Affrida Abu Hassan, Ros Anita Ahmad Ramli, Muniroh Md Saad, Suhaimi Musa, Mohamed Najli, Norhafiz Talib, Mohamed Hasyraf and others. Acknowledgement to MARDI counterparts for providing breeding materials. This project was a part of IAEA TC MAL 5031 and MAL5032.

## References

H. Haryani, A.P. Norlindawati, F. Norfadzrin, A. Aswanimiyuni, and A. Azman. 2018. Yield and nutritive values of six napier (*Pennisetum purpureum*) cultivars at different cutting age. *Malaysian Journal of Veterinary Research*, 9:6–12.

Mutant variety database.

Shakinah Salleh, Zaiton Ahmad, Affrida Hassan, Faiz Ahmad, Mustapha Akil, Mohammad Fitri, Rimi Hamidan, and Nurulhayati Bakar. 2021. Assessment of major morphological and physiological characteristics of napier grass (pennisetum purpureum) from acute and chronic gamma irradiated m1v5 population, 03.

Shakinah Salleh, Zaiton Ahmad, and Affrida Abu Hassan. 2024. Standard operating procedure mutagenesis of napier grass using acute and chronic gamma irradiation, 02.

Individual Research Contribution Review, 2024: 59–60
*ISSN: 3083-922X*

IRCR

# Pre-Clinical Assessment Of $^{99m}$Tc-DTPA Kit For Renal Scintigraphy

**Anee Suryani Sued**
Medical Technology Division, Malaysian Nuclear Agency
43000 Kajang, Selangor
anee@nm.gov.my

## Abstract

Dynamic renal scintigraphy which was taken between certain time intervals can show renal parenchymal defect through imaging of the kidney. Radiopharmaceutical that usually being used for dynamic renal scintigraphy is Tc99m-DTPA (diethylentriamine pentaacetic acid). Biodistribution study using Sprague Dawley rats is one of the pre- clinical assessment of the DTPA kit produced in Medical Technology Division (BTP). The result shows excellent preparation of the DTPA kit as renal scintigraphy radiopharmaceutical and efficient radiolabelling of $^{99m}$Tc-DTPA.

## 1 Introduction

Renal scintigraphy is one of the nuclear medicine techniques that uses radionuclide to evaluate the renal function. Renal scintigraphy can be divided into two modes of imaging; static and dynamic. Static renal scintigraphy is to demonstrate renal parenchyma function which frequently used to determine the cortical damage caused by urinary tract infection and additionally can give relative and absolute kidney functions. Radiopharmaceutical that usually being used for static renal scintigraphy is Tc99m-DMSA (dimercaptosuccinic acid). Dynamic renal scintigraphy can show renal parenchymal defect through imaging of the kidney that I taken between certain time intervals. Radiopharmaceutical that usually being used for dynamic renal scintigraphy is Tc-99m-DTPA (diethylentriamine pentaacetic acid) and Tc-99m-MAG3 (mercaptoacethytriglycine). (Demirel et al., 2012). DTPA is the gold standard method to check on the glomerular filtration rate (GFR) because it is serum creatinine independent. Therefore, more accurate and reliable data can be obtained by using this short half-life radiopharmaceutical.

## 2 Materials/Method

### 2.1 Materials

#### 2.1.1 Equipment

Gamma counter (WIZARD2 2470 Perkin Elmer, USA), animal weighing balance (SB12001 Mettler Toledo, Switzerland), analytical balance (GF300 AND, Japan), anaesthesia system (Perkin Elmer, USA), dosimeter (CRC-25W Capintec Inc, USA)

#### 2.1.2 Chemicals

DTPA, isoflurane USP (Piramal, India), $^{99m}$Tc eluted from $^{99}$Mo/$^{99m}$Tc Generator (Curium, France).

#### 2.1.3 Animals

Animals used in this study were *Sprague Dawley* rats bred in Animal Facility, Malaysian Nuclear Agency.

### 2.2 Method

The pre-clinical assessment in this study involved invivo study using *Sprague Dawley* rats. It involved biodistribution study at four time-points. Total of 24 rats were utilized in biodistribution study. All animals were acclimatised to laboratory conditions for one week prior to experiment and food and drinks were given ad libitum. Food and water were withdrawn overnight prior to experiment.

#### 2.2.1 Biodistribution Study

Four time points (1h, 2h, 4h and 24 h) study was conducted in the quantitative biodistribution study where three animals were utilised per time point. One mCi of $^{99m}$Tc in the form of $^{99m}$Tc-DTPA complex was administered intravenously in the animal. At each time point designated animals were placed in anaesthesia chamber and anaesthetised using isoflurane. Blood was collected through cardiac puncture procedure. The animals were then culled through exsanguination/cervical dislocation and their organs were harvested, placed singly in preweighted test tube, weighed using analytical balance (AND, Japan) and kept overnight at 4 °C. The radioactivity of $^{99m}$Tc in each sample was counted using gamma counter (WIZARD2, Perkin Elmer, USA)

#### 2.2.2 $^{99m}$Tc activity determination in animals' samples

$^{99m}$Tc-DTPA complex with above 95% RCP was chosen for *invivo* biodistribution study in male *Sprague Dawley* rat. The complex was injected intravenously into the rat's tail and quarantined in the metabolic cage until reaching a specific time point. The rats were then euthanised before collecting their organs into the pre-weighed tube. Decay-corrected uptake of $^{99m}$Tc in each organ was determined as the percentage injected dose per gram of tissue (%ID). The percentage values of the injected dose per gram organ (%ID/g ± SD) in a population of 3 rats for each time point were then calculated using the formula below:

$$\%\text{ID} = \frac{\%\text{ Radioactivity of sample}}{\text{Weight of sample}}$$

## 3 Results and Discussion

### 3.1 Biodistribution Study

#### 3.1.1 $^{99m}$Tc activity determination in animals' samples

The slight uptake of $^{99m}$Tc-DTPA in the blood at 1h (0.45 ± 0.03 %ID/g) was due to the weak affinity of the complex towards the blood components, which affect the radiopharmaceutical distribution to the blood. $^{99m}$Tc-DTPA is a low protein-bound radiopharmaceutical. Therefore, it is likely to cross the capillary membrane into the tissue during the short residence time of blood in capillaries (Berridge, 2009). Thus, it explains why there was also a slight accumulation in the skin, lung, heart, and stomach at initial time points.

Figure 1 representing the comparison of $^{99m}$Tc activity in each organ at one and four h time-point. It clearly showed that $^{99m}$Tc-DTPA complex was successfully administered into the target organ; i.e kidney and no significant traces were found in main organs such as liver, lungs and heart. This result shows excellent preparation of the DTPA kit as renal scintigraphy radiopharmaceutical and efficient radiolabelling of $^{99m}$Tc-DTPA.

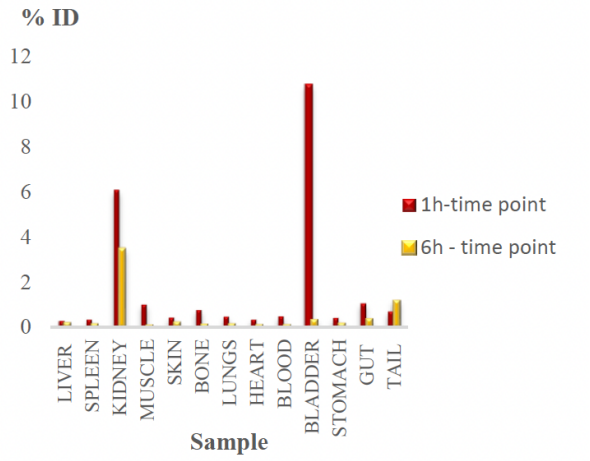



Figure 1: Biodistribution study of $^{99m}$Tc- DTPA in *Sprague Dawley* rats at 1 h and 6 h time point

## 4 Conclusion

$^{99m}$Tc-DTPA developed in this study can be used for renal imaging and diagnosis. Based on the biodistribution studies and imaging of $^{99m}$Tc-DTPA, this $^{99m}$Tc-DTPA radiopharmaceutical is most suited for renal scintigraphy in the kidney. The biodistribution study also revealed that kidneys quickly excrete $^{99m}$Tc -DTPA, and that practically the whole $^{99m}$Tc-DTPA complex is excreted out from the body within 24 h after intravenous administration. This $^{99m}$Tc-DTPA serve as the best radiopharmaceuticals for renal scintigraphy to determine the glomerular filtration rate (GFR) in kidney defective patients.

## References

H. Alsabea. 2017. Type of renal scintigraphy. *Journal of Nuclear Medicine & Radiation Therapy*, 8(6):2–9.

M. S. Berridge. 2009. The importance of kinetic enhancement. *Journal of Nuclear Medicine*, 50(8):1203–1204.

B. B. Demirel, T. A. Balci, B. Tasdemir, and Z. P. Koc. 2012. Comparison of dtpa and mag3 renal scintigraphies in terms of differential renal function based on dmsa renal scintigraphy. *Pakistan Journal of Medical Sciences*, 28(5):795–799.

P. R. Franken, J. Guglielmi, C. Vanhove, M. Koulibaly, M. Defrise, J. Darcourt, and T. Pourcher. 2010. Distribution and dynamics of $^{99m}$tc-pertechnetate uptake in the thyroid and other organs assessed by single-photon emission computed tomography in living mice. *Thyroid*, 20(5):519–526.

S. M. Rathmann, Z. Ahmad, S. Slikboer, H. A. Bilton, D. P. Snider, and J. F. Valliant. 2019. The radiopharmaceutical chemistry of technetium-99m.

Individual Research Contribution Review, 2024: 61–62
*ISSN: 3083-922X*

# Development and Physicochemical Characterization Of A Biodegradable Microspheres Formulation Loaded With Samarium-153 And Doxorubicin For Chemoradioembolization Of Liver Tumours

**Azahari Kasbollah**
Medical Technology Division, Malaysian Nuclear Agency
43000 Kajang, Selangor
azahari@nm.gov.my

## Abstract

Transarterial chemoembolization (TACE) and transarterial radioembolization (TARE) are promising treatments for unresectable liver tumours. Some recent studies suggested that combining TACE and TARE in one treatment course might improve treatment efficacy through synergistic cytotoxicity effects. Nonetheless, current formulations do not facilitate a combination of chemoand radio-embolic agents in one delivery system. Therefore, this study aimed to synthesise a hybrid biodegradable microsphere loaded with both radioactive agent, samarium-153 ($^{153}$Sm) and chemotherapeutic drug, doxorubicin (Dox) for potential radio-chemoembolization of advanced liver tumours. $^{152}$Sm and Dox-loaded polyhydroxybutyrate-co-3-hydroxyvalerate (PHBV) microspheres were prepared using water-in-oil-in-water solvent evaporation method. The microspheres were then sent for neutron activation in a neutron flux of 2 1012 n/cm$^2$/s. The physicochemical properties, radioactivity, radionuclide purity, $^{153}$Sm retention efficiency, and Dox release profile of the Dox-$^{153}$SmPHBV microspheres were analysed. In addition, in vitro cytotoxicity of the formulation was tested using MTT assay on HepG2 cell line at 24 and 72 h. The mean diameter of the Dox$^{153}$Sm-PHBV microspheres was 30.08 ± 2.79 $\mu$m. The specific radioactivity was 8.68 ± 0.17 GBq/g, or 177.69 Bq per microsphere. The $^{153}$Sm retention efficiency was more than 99%, tested in phosphate-buffered saline (PBS) and human blood plasma over 26 days. The cumulative release of Dox from the microspheres after 41 days was 65.21 ± 1.96% and 29.96 ± 0.03% in PBS solution of pH 7.4 and pH 5.5, respectively. The Dox1$^{153}$Sm-PHBV microspheres achieved a greater in vitro cytotoxicity effect on HepG2 cells (85.73 ± 3.63%) than $^{153}$Sm-PHBV (70.03 ± 5.61%) and Dox-PHBV (74.06 ± 0.78%) microspheres at 300 $\mu$g/mL at 72 h. In conclusion, a novel biodegradable microspheres formulation loaded with chemotherapeutic drug (Dox) and radioactive agent ($^{153}$Sm) was successfully developed in this study. The formulation fulfilled all the desired physicochemical properties of a chemo-radioembolic agent and achieved better in vitro cytotoxicity on HepG2 cells. Further investigations are needed to evaluate the biosafety, radiation dosimetry, and synergetic anticancer properties of the formulation

**Keywords:** biodegradable microspheres, chemo-radioembolization, doxorubicin, liver cancer, Sm-153.

## 1 Introduction

Liver cancer remains as the sixth most common cancer and the third leading cause of cancer death worldwide.1 The World Health Organization (WHO) predicted that the incidence rate of liver and intrahepatic bile duct cancers would increase by 58.6% and the number of deaths would increase by 60.9% in 2040. In unresectable liver cancer, transarterial chemoembolization (TACE) and transarterial radioembolization (TARE) are recommended to downstage the disease or improve the patient's quality of life. The treatment involves intra-arterial delivery of an embolic agent that contains either a chemotherapeutic drug or a radionuclide to block the blood supply as well as to kill the tumour(s) by the mean of targeted chemotherapy or radionuclide therapy.2 In TACE, drug-eluting beads such as polyvinyl alcohol microspheres loaded with doxorubicin (Dox) are commonly used, while in TARE, resin or glass microspheres labelled with radioactive yittrium-90 ($^{90}$Y) are currently practised. However, there are limitations with the use of $^{90}$Y as it is extremely costly to produce using a highenergy cyclotron and a complicated separation and purification process. Furthermore, $^{90}$Y is a pure beta emitter with no imaging characteristics for theranostics purposes. Therefore, this study investigated the use of Samarium-153 ($^{153}$Sm), a radionuclide that emits both beta and gamma radiations, as a potential alternative to Y. The therapeutic and imaging capabilities of $^{153}$Sm have been validated in multiple studies. Therefore, in this study, we expected to develop a hybrid- biodegradable microspheres formulation containing both radioactive agent ($^{153}$Sm) and chemotherapeutic drug (Dox) for synergistic chemo-radioembolization effects in unresectable liver cancer treatment. The synthesis method, physiochemical properties, $^{153}$Sm retention efficiency, Dox release profile, and in vitro cytotoxicity test using HepG2 cells are reported in this article.

## 2 Methods

The $^{152}$SmAcAc- and Dox-loaded PHBV (Dox- $^{152}$SmPHBV) microspheres were synthesized using water1-inoil-in-water2 (W1/O/W2) solvent evaporation method as 2 ALREGIB ET AL. described by Mosafer and Teymouri9 with slight modifi-

cation. To prepare the oil phase, 0.15 g of PHBV and 0.215 g of $^{152}$SmAcAc were added to 4.0 mL of chloroform and incubated at 80 °C for 1 min. The $^{152}$SmAcAcPHBV mixture was then stirred at 300 rpm overnight at room temperature. The W1 phase was prepared by mixing 10 mg of Dox, 300 $\mu$L of TEA, and 100 $\mu$L of distilled water under mechanical stirring of 300 rpm for 1 h. Before adding the W1 phase to the oil phase, the oil phase was sonicated using an ultrasonicate for 1 min. The W1/O solution mixture was then homogenized at 23, 600 rpm using a homogenizer (T25 digital UltraTurrax, IKA, Germany) for 3 cycles of 30 s with a 30-s stop interval. The W1/O solution mixture was then added to 150 mL of 3.5% (w/v) PVA (W2 phase) and stirred at 850 rpm for 4 h. The microspheres were formed after centrifugation at 8500 rpm for 10 min. The Dox-$^{153}$Sm-PHBV microspheres were sent for neutron activation using a nuclear research reactor (1-MW thermal TRIGA MARK II, General Atomics, USA) located at the Malaysian Nucelar Agency. The samples were placed in a polyethylene vial and heat sealed. Then, the samples were irradiated in a rotary specimen rack with a thermal neutron flux of 2 1012 n/cm$^2$/s for 5 h.

## 3 Results and Discussion

The specific activity of the Dox-$^{153}$Sm-PHBV microspheres was $8.68 \pm 0.17$ GBq/g measured at 24 h postneutron activation (to allow for the radioactive decay of short-lived radionuclides). The average activity per microsphere was 177.69 Bq. One of the factors to be considered in a drug delivery system is the body's reactions towards the carrier. Therefore, the microspheres must be able to dissolve safely in the body after delivering the active drugs without causing toxicity to the host.11 PHBV is a favourable polymer for biomedical applications due to its null toxicity, absorption capacity, high biocompatibility, low cytotoxicity, and thermoplastic properties. PHBV has been used in several applications, such as drug release, transportation, absorbable surgical sutures, and medical packaging.12 Therefore, it is an excellent choice of carrier for chemoradioembolization of liver tumours. The current FDA-approved radioembolic agents for liver tumours include SIR-Spheres ($^{90}$Y resin microspheres) and TheraSphere ($^{90}$Y glass-beads microspheres). $^{90}$Y is a pure beta emitter, with a physical halflife of 64.1 h.13 However, the absence of diagnostic properties in $^{90}$Y makes it a less suitable radionuclide for theragnostic purposes. Therefore, a substitute radionuclide (e.g., 99mTc) is required for pretreatment planning, and a special imaging technique (e.g., Bremsstrahlung X-ray imaging and quantitative positron emission tomography) is performed for post delivery assessment.

## 4 Conclusions

A novel biodegradable PHBV microsphere loaded with both radioactive $^{153}$Sm and chemotherapeutic Dox was successfully developed. The formulation fulfilled all the desired physicochemical properties of a chemoradioembolic agent potentially useful for intermediate to advanced-stage liver cancer treatment. The microspheres have the combined effects and benefits of biocompatibility, biodegradability, chemotherapeutic release, and emission of therapeutic radiations and diagnostic radiations (i.e., beta and gamma radiation). In addition, the neutron activation method is cheaper, easier, and more readily available than 90Y. However, the therapeutic efficacy of the formulation should be further evaluated and compared with the commercial TACE and TARE treatments. For future development, in-vivo animal studies are planned to study the synergistic effects of chemo-radioembolization using the developed formulation.

## References

Céline Bouvry, Xavier Palard, Julien Edeline, et al. 2018. Transarterial radioembolization (tare) agents beyond 90y-microspheres. *BioMed Research International*, 2018:1435302.

NAA Hashikin, CH Yeong, BJJ Abdullah, et al. 2015. Neutron activated samarium-153 microparticles for transarterial radioembolization of liver tumour with post-procedure imaging capabilities. *PLoS ONE*, 10(9):e0138106.

Rebecca L Siegel, Kimberly D Miller, Hannah E Fuchs, and Ahmedin Jemal. 2022. Cancer statistics, 2022. *CA: A Cancer Journal for Clinicians*, 72(1):7–33.

HY Tan, YH Wong, A Kasbollah, et al. 2022. Development of neutron-activated samarium-153-loaded polystyrene microspheres as a potential theranostic agent for hepatic radioembolization. *Nuclear Medicine Communications*, 43(4):410–422.

Chai Hong Yeong, BJJ Abdullah, KH Ng, et al. 2012. Production and first use of $^{153}$smcl$_3$-ion exchange resin capsule formulation for assessing gastrointestinal motility. *Applied Radiation and Isotopes*, 70(3):450–455.

Individual Research Contribution Review, 2024: 63–64
*ISSN: 3083-922X*

IRCR

# QPCR-Based Validation of Coxiella Burnetii Culturing in Vero Cells: Detection of IS1111 and ICD Genes

**Daryl Jesus Arapoc**
Medical Technology Division, Malaysian Nuclear Agency
43000 Kajang, Selangor
daryl@nm.gov.my

## Abstract

Coxiella burnetii (C. burnetii) is a Gram-negative bacterium that causes Q fever, a zoonotic disease. It interacts with host cells to establish infection and replicate within a specialised intracellular niche. African green monkey kidney (Vero) cells used in in vitro studies of C. burnetii provide an ideal environment for growth and replication, resembling intracellular conditions in vivo. More studies are performed culturing C. burnetii in Vero cells to evaluate host–pathogen interactions in a controlled system. It is imperative to validate C. burnetii culturing in Vero cells for accurate bacterial load quantification. This study presents a comprehensive overview of the validation method by detecting and quantifying C. burnetii-specific DNA using real-time polymerase chain reaction (qPCR). To validate presence using qPCR, DNA was extracted from Vero cells. Primers and probes targeted the IS1111 and icd genes. Separate qPCR reactions were set up for each gene, and a standard curve generated to quantify C. burnetii DNA. Based on qPCR, IS1111 and icd genes were substantially higher in cultured Vero cell samples compared to non-cultured cells. These results support successful C. burnetii culturing in Vero cells and provide insights into its molecular detection, advancing knowledge of host–pathogen interactions and facilitating future research.

**Keywords:** N Coxiella burnetii, Vero, qPCR

## 1 Introduction

Q fever is a notable zoonotic disease and occupational hazard for individuals working with animals. It was first identified in 1935 in Queensland, Australia, following an outbreak of an unexplained febrile illness (Query fever). Vero cells provide an ideal environment for the growth and replication of the bacterium, closely resembling intracellular conditions in vivo. Culturing C. burnetii in Vero cells allows researchers to investigate host–pathogen interactions in a controlled, reproducible system. Validating C. burnetii culturing in Vero cells is imperative to ensure precise quantification of bacterial load. This study aims to confirm successful cultivation of Coxiella burnetii in Vero cells using qPCR. Validation is based on measuring expression levels of two bacterial genes, IS1111 and icd (isocitrate dehydrogenase), which serve as key markers for detecting the pathogen.

## 2 Methods

### 2.1 Cell Preparation

The Vero cell line (ATCC, CCL-81), kidney epithelial cell line derived from a normal African green monkey were utilised to culture C. burnetii in this study. The cell lines were cultured with Dulbecco's Modified Eagle Medium (DMEM), supplemented with 10% fetal bovine serum (FBS; ThermoFisher, A4766801), 1% of GlutaMAX (ThermoFisher, 10566024) and 1% of Penicillin streptomycin (ThermoFisher, 15140163) in a T75 flask. When cells attained a confluent monolayer, they were passaged (1:3) and maintained in an incubator set to 37 °C and 5% carbon dioxide ($CO_2$). Prior to passage 20, cells were used in enrichment experiments (Anderson et al., 2023).

### 2.2 Inoculation of C. burnetii

All work to isolate and propagate C. burnetii from sample materials was carried out in a protection level BSL-level 3 laboratory. Vero cells were seeded at a sufficient density in a tissue culture flask with a confluence rate of 70-80 percent, then incubate them overnight to facilitate adhesion. Inoculum of C. burnetii from a well characterised strain of bacterium was prepared. These initial inoculam (P0) and supernatants (P1 P3) were placed immediately into ACCM-2 for one week to generate enough C. burnetii for LPS extraction and characterisation before being added to Vero cell cultures plated in T75 flasks. At an adequate multiplicity of infection (MOI), C. burnetii was introduced to T75 flasks containing a confluent layer of Vero cells. The incubation period of C. burnetii in Vero cell lines at 37°C in a humidified atmosphere supplemented with 5% $CO_2$ for 18- 72 hours. The cellular morphology of Vero cell infected with C. burnetii was observed through an inverted light microscope.

### 2.3 Harvest of C. burnetii

Following incubation, supernatants were discarded and washed thrice with sterile phosphate saline buffer (PBS). Vero cells were then scraped with a cell scrapper and scrapped cells in ice cooled PBS placed into centrifuge tube filter. The tubes were centrifuged at 10,000xg for 5 minutes. The pellet obtained prior to centrifugation weremdissolved in 10 mL PBS. The bacterial density was calculated using decitometer. This

procedure was performed repeatedly for a total of three Vero cell-C. burnetii passages.

### 2.4 Detection and Quantification of Coxiella burnetii Using icd and IS1111 Realtime PCR (qPCR)

#### 2.4.1 Materials

PCR plates, and filter tips, along with TE buffer (10mM Tris-HCl, 1mM EDTA) for dilution and preparation. Commercial mastermixes such as Quanti Nova (QIAGEN) and MaximaProbe (Thermo Fisher) are used for amplification. The primers and probes differ for each assay: for the icd assay, the forward primer icd-439F, reverse primer icd-514R, and probe Coxburicd-464TM (FAM-labeled) are used; for the IS1111 assay, the forward primer CoxbS, reverse primer CoxbAs, and probe CoxbMGB (FAM-labeled) are included. Additionally, standard DNA fragments for both icd and IS1111 genes are used for quantification.

#### 2.4.2 Preparation primer and probe

The PCR master mix must be prepared separately from the samples in different rooms, using UV-C workstations to prevent cross-contamination. Every qPCR run should include essential controls: a negative control (NTC) to check for contamination, a positive control (PC) to confirm assay functionality, and a negative extraction control (NEC) to verify the DNA extraction process. For primer and probe preparation, lyophilized primers and probes should be dissolved in TE buffer to a final concentration of 100 µM, vortexed, and centrifuged. A 10 µM working solution should be prepared and stored at -20°C. The IS1111 and icd standards are initially dissolved in TE buffer to a concentration of $1\times10^9$ copies/µl, followed by vortexing, incubation at room temperature for one hour, and centrifugation. A dilution series should then be prepared, ranging from $10^6$ to $10^1$ copies/2µl, and stored at -20°C, separately from the primers, probes, and master mix.

#### 2.4.3 PCR setup

Reaction Mix (20 µl per sample, separate for each target gene) and thermal profile.

| Component | Working Solution | icd Final Conc. | icd Volume (µl) | IS1111 Final Conc. | IS1111 Volume (µl) |
|---|---|---|---|---|---|
| Mastermix | 2x | 1x | 10 | 1x | 10 |
| Forward Primer | 10 µM | 300 nM | 0.6 | 800 nM | 1.6 |
| Reverse Primer | 10 µM | 300 nM | 0.6 | 800 nM | 1.6 |
| Probe | 10 µM | 100 nM | 0.2 | 300 nM | 0.6 |
| Water | — | — | 6.6 | — | 4.2 |
| Template DNA | — | — | 2 | — | 2 |

Figure 1: Primer and probe preparation

| Step | Temperature (°C) | Time | Cycles |
|---|---|---|---|
| Decontamination | 50 | 2 min | 1 |
| Initial Denaturation | 95 | 10 min | 1 |
| Denaturation | 95 | 15 sec | 45 |
| Annealing/Extension | 60 | 30 sec | 45 |

Figure 2: Thermal profile

## 3 Results and Discussion

Over the years, real-time polymerase chain reaction (qPCR) has become the gold standard for detecting Coxiella burnetii due to its high specificity, rapid turnaround, and sensitivity in detecting low bacterial loads. The icd gene is a single-copy gene encoding an enzyme essential for bacterial metabolism,

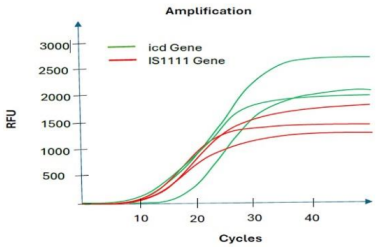



Figure 3: Amplification of icd gene and IS1111 gene

conserved across all C. burnetii strains (Kersh et al., 2010). Its presence in qPCR results is a reliable marker confirming C. burnetii DNA, ensuring it originates from this pathogen rather than environmental contaminants or non-pathogenic bacteria. The IS1111 gene is a multi-copy transposon, with 7–110 copies in the bacterial genome, making it a highly sensitive target for detecting minimal bacterial DNA. IS1111 increases the likelihood of detecting low bacterial loads, such as in early-stage or asymptomatic cases (Eldin et al., 2017).

Interpretation of qPCR depends on these genes. Detection of both icd and IS1111 strongly indicates C. burnetii and a high bacterial load. Detection of IS1111 without icd suggests a low bacterial load or an IS1111-positive but icd-negative variant. Detection of icd without IS1111 could indicate a rare strain with few IS1111 copies, as reported in epidemiological studies. Negative results for both genes suggest absence of the pathogen or PCR inhibition. To reduce false negatives, internal amplification controls should be included in each qPCR run.

In conclusion, combining icd and IS1111 in qPCR assays enhances diagnostic accuracy for C. burnetii, offering both sensitivity and specificity. The icd gene reliably quantifies bacterial DNA, while IS1111 improves detection of low loads due to its multiple copies. However, variability in IS1111 copy number poses challenges, requiring confirmatory tests, such as alternative molecular markers or serology, for accurate diagnosis. Given the risk of undetected transmission, especially in asymptomatic carriers or low-load environments, a multi-target approach remains critical for effective surveillance and control.

## References

M. W. Anderson, P. Binette, C. Richards, P. A. Beare, R. A. Heinzen, and C. M Long. 2023. simple method for enrichment of phase i coxiella burnetii. *Journal of Microbiological Methods*, 211(106787).

C. Eldin, C. Mélenotte, O. Mediannikov, E. Ghigo, M. Million, S. Edouard, and D. Raoult. 2017. From q fever to coxiella burnetii infection: A journey through history, clinical aspects, and ongoing challenges. *Clinical Microbiology Reviews*, 30(1):115–190.

G. J. Kersh, K. A. Fitzpatrick, J. S. Self, R. A. Priestley, H. T. Trinh, A. D. Loftis, and C. D. Paddock. 2010. Presence of coxiella burnetii dna in the environment of the united states, 2006 to 2008. *Applied and Environmental Microbiology*, 76(13):4469–4475.

Individual Research Contribution Review, 2024: 65–66
*ISSN: 3083-922X*

# Potential Radioprotective Effects of Polygonum Minus Methanol Extract through Antioxidant and Free Radical Scavenging Activities

**Fazliana Mohd Saaya**
Medical Technology Division, Malaysian Nuclear Agency
43000 Kajang, Selangor
fazliana@nm.gov.my

## Abstract

Products of plant origin has become an exciting area of research in drug discovery and development based on its therapeutic application and low in toxicity. Most of the herbs and medicinal plants rich with various phytochemicals with antioxidant properties that scavenge free radicals produced due to radiation exposure, thus imparting radioprotective efficacy.

**Keywords:** phytochemicals, antioxidant, Free radicals

## 1 Introduction

Active plant constituents seem to exert the radioprotection through antioxidant and free radical-scavenging activities (Kuntić et al., 2013). Additionally, many herbal formulations also exhibit highly promising effects when delivered in case of free radicals-mediated diseases like Parkison's disease, Alzheimer's diseases, Rheumatoid Arthritis, cancer, and many other inflammatory diseases (Jena et al., 2010). The most practical methodology to choose the promising candidate for assessing its radioprotective effect is to investigate the available properties of the substance. A substance with anti- inflammatory, antioxidant, antimicrobial, immunomodulatory, free radical scavenging, or anti- stress properties may act as a potential radioprotector. Pre-clinical studies in the past two decades have shown that some commonly used medicinal plants and their phytochemicals possess radioprotective effects (Bhandari, 2013).

## 2 Methods

### 2.1 Phytochemical screening

The qualitative phytochemical screening was conducted on 100 mg of methanolic Polygonum minus (P. minus) extract to identify the presence of alkaloids, saponins, flavonoids, tannins, triterpenes, and steroids. The determination of phytochemical constituents was performed in accordance to (Veshalini et al., 2022).

### 2.2 Analysis & Identification of Compound (HPLC)

The Knauer HPLC (Germany) system, that comprises a pump (Maxi-Star K-1000, Knauer, Germany), a degasser, an automated injector, a column oven, and a UV detector, was used to analyse each sample. In a Eurospher-100 C18 column (5 M, 4.6 250 mm), chromatographic conditions were assessed and adjusted for the measurement of the phenolic compounds in samples. At 254 nm, the chromatographic detection was observed

### 2.3 Total phenolic content (TPC)

The total phenolic content (TPC) of P. minus methanolic extract was determined by utilising the Folin-Ciocalteu reagent [10]. Following the steps outlined for standard gallic acid, the absorbance for each concentration of the extracts was recorded. To determine the amount of phenolics in the extracts, the samples were prepared in triplicate for each analysis, and the calibration curve was plotted using the average value of absorbance. The results were expressed on a fresh weight basis as mg gallic acid equivalents/100 g of sample.

### 2.4 Antioxidant assay DPPH free radical scavenging assay

The ability of the antioxidant in methanolic extract of P. minus to scavenge free radicals on the 1,1-diphenyl-2- picrylhydrazyl (DPPH) radical was assessed based on the approach suggested by (Yang et al., 2011).

### 2.5 Superoxide free radical scavenging assay

The stated approach was used by (Sharma and Singh, 2012) to test the superoxide anion scavenging activity. The formula below was used to compute the percentage of superoxide radical scavenging: $\%\ \text{scavenging activity} = \left(\frac{A_{\text{control}} - A_{\text{sample}}}{A_{\text{control}}}\right) \times 100\%$. The $A_{\text{control}}$ indicates the absorbance of the control, while $A_{\text{sample}}$ indicates the absorbance of the extracts/standard.

### 2.6 Oxygen radical absorbance capacity (ORAC) assay

A fluorescence plate reader (Thermo Fisher Scientific, Waltham, Mass., USA) was used to perform the ORAC test on a 96-well microplate. Each assessment was conducted in triplicates.

## 3 Data/Results

Phytochemical results were stated as + to refer as present and - to refer as absent (see Figure 1)

| Secondary Metabolites | Methanolic extract *P. minus* |
|---|---|
| Terpenoids | + |
| Flavonoids | + |
| Saponins | - |
| Tannins | + |
| Alkaloids | - |
| Steroids | + |
| Triterpenes | + |

Figure 1: The phytochemical constituents in methanolic extract of P. minus.

| Sample | Compound | Average conc. ± RSD (ppm) | Average % in sample ± RSD (w/w) |
|---|---|---|---|
| Methanol extract *P. Minus* | Gallic Acid | 99.67 ± 0.42 | 0.50 ± 0.43 |
| | Quercetin | 20.37 ± 2.12 | 0.10 ± 2.12 |

Figure 2: The total phenolic compound (TPC) in methanolic P. minus extract.

| Sample | TPC (mg GAE/100g) | Positive control (mg GAE/100g) |
|---|---|---|
| Methanolic extract of *P. minus* | 8876 ± 65.8 | Green tea 15351 ± 61.6 |

Figure 3: Determination of phenolic compound in methanolic extract of P. minus

| No | Sample | DPPH free radical scavenging activity | Superoxide free radical scavenging activity | Remark |
|---|---|---|---|---|
| 1 | Methanolic extract of P. minus | 90.09 ± 0.06 (H) | 72.07 ± 1.55 (H) | High (H)- 70- 100% Moderate (M) -50- 69% Low (L) – 0-49% |
| 2 | Green tea | 94.01 ± 0.09 (H) | 81.40 ± 0.52 (H) | |
| 3 | Reference | Trolox: 96.61 ± 0.03 | SOD: 72.72 ± 2.07 | |

Figure 4: The DPPH and superoxide free radical scavenging activity of methanolic P. minus extract.

## 4 Discussion/Conclusions

Based on the study performed, multiple phytochemical constituents were in the methanolic extract of P. minus. These findings is in accordance to literature by (Hamid et al., 2020), stating flavonoids, phenolic acids, ascorbic acid, aliphatic compounds, organic acids, essential oils, and alkaloids were among the phytoconstituents found in P. minus. The flavonoids apigetrin, hyperoside, isoquercetin, astragalin, miquelianin, quercetin, and quercitrin, as well as the phenolic acids gallic acid and coumaric acid, were also available in P. minus (Hamid et al., 2020). In addition, P. Minus methanolic extract contain high antioxidant and have free radical scavenging activities. ORAC value of the extract was considered higher based on the value of ≥ 10,000 umol TE per day, enough for the maintenance of good health (Ronald et al., 2015). Previously, it was postulated that P. minus's high polyphenol content, vitamin C, and beta-carotene were

| NO | Sample | ORAC Value TE/100g |
|---|---|---|
| 1 | Methanolic extract of P. minus | 89,000 |

Figure 5: The ORAC activity of methanolic P. minus extrac

to account for its antioxidant action. According to reports, the aqueous, methanol, and ethanol extracts exhibit significant antioxidant capacity that is equivalent to that of synthetic antioxidants such butylhydroxytoluene (BHT) and gallic acid (Christapher et al., 2015). Methanolic extract of P. minus is a promising candidate for radioprotector development with the highlight in antioxidant and radical scavenging mechanism of the radioprotective strategies.

## References

P. R. Bhandari. 2013. Plant products for radioprotection: Boon or bane? *Journal of Cancer Research and Therapeutics*, 9:545–546.

P. V. Christapher, S. Parasuraman, J. M. Christina, M. Asmawi, and M. Vikneswaran. 2015. Review on polygonum minus. huds, a commonly used food additive in southeast asia. *Pharmacognosy Research*, 7:1–6.

A. A. Hamid, A. Aminuddin, M. H. M. Yunus, J. K. Murthy, C. K. Hui, and A. Ugusman. 2020. Antioxidative and anti-inflammatory activities of polygonum minus: a review of literature. *Reviews in Cardiovascular Medicine*, 21(2):275–288.

G. Jena, A. Vikram, D. N. Tripathi, and P. Ramarao. 2010. Use of chemoprotectants in chemotherapy and radiation therapy: the challenges of selecting an appropriate agent. *Integrative Cancer Therapies*, 9(3):253–258.

V. S. Kuntić, M. B. Stanković, Z. B. Vujić, J. S. Brborić, and S. M. Uskoković-Marković. 2013. Radioprotectors - the evergreen topic. *Chemistry & Biodiversity*, 10(10):1791–1803, Oct.

S. K. Sharma and A. P. Singh. 2012. In vitro antioxidant and free radical scavenging activity of nardostachys jatamansi dc. *Journal of Acupuncture and Meridian Studies*, 5(3):112–118.

K. Veshalini, D. J. Arapoc, Z. Adam, R. Razali, N. A. Suliman, and N. A. A. Bakar. 2022. Phytochemical screening, in vitro antioxidant activities and zebrafish embryotoxicity of abelmoschus esculentus extracts. *Pharmacognosy Journal*, 14(3):690–701.

H. Yang, Y. Dong, H. Du, H. Shi, Y. Peng, and X. Li. 2011. Antioxidant compounds from propolis collected in anhui, china. *Molecules*, 16(4):3444.

Individual Research Contribution Review, 2024: 67–68
*ISSN: 3083-922X*

# Pre-Treatment With Rnase A In Cytokinesis Block Micronucleus Assay For Analysis Using Automated System

**Juliana Mahamad Napiah**
Medical Technology Division, Malaysian Nuclear Agency
43000 Kajang, Selangor
juliana_m@nm.gov.my

## Abstract

Cytokinesis Block Micronucleus (CBMN) Assay is a simple and an alternative way for indicator of chromosome damage. In a large radiation accident, CBMN Assay can be early detect for chromosome damage before we do aberration chromosome assay. RNase as an agent to remove residual stainable cytoplasmic material. Clear background help to easier in analysis of micronuclei (MN). The clear image of background useful for slides assessed with automatic image analysis system.

**Keywords:** Micronuclei, Rnase A, Remove Residual

## 1 Introduction

The dicentric chromosome assay is the "gold standard" in biodosimetry for estimating radiation exposure, meanwhile the cytokinesis-block micronucleus (CBMN) assay is a comprehensive technique for measuring DNA damage, including lymphocytes. CBMN assay is a simple and an alternative way for indicator of chromosome damage. It is because researchers only need to measure visible micronuclei (MN) in binucleated cells, micronuclei analysis is much easier than metaphase chromosome aberration analysis. The micronucleus technique was proposed as a reliable method for measuring chromosomal damage caused by cytotoxic agents "in vivo" (Fenech and Morley, 1985) and very useful in a large radiation accident case because of its simplified technique and much easier to analysis. Treatment with RNase A is a pretreatment step in the protocol to remove any residual RNA present. Objective of this study to prove RNase A is a treatment that very useful for analyse binucleated cell using automated analysis system. Automated system is more sensitive to analyse image compared to manual microscope. Digital image analysis tools help automate and quantify findings, reducing or eliminating manual work and providing more objective and quicker input to the final diagnosis compared to traditional microscopy. It helps handle high sample volumes efficiently, improving productivity and reducing turnaround time.

## 2 Methods

### 2.1 Cytokinesis Block Micronucleus Assay (CBMN)

Peripheral blood sample were collect using heparinized vacutainer tube. Blood was cultured in 10ml complete media and incubate for 72 h in incubator at $37°C$ and 5% CO2. The complete media consisted of 87% of RPMI supplemented with 10% of heat-inactivated fetal bovine serum, 2% of streptomycin-penicillin and 1% of Glutamine. Each 10ml complete media will add with 1 ml blood and 300 $\mu l$ of phytohemagglutinin (PHA). At 44 h, 6 $\mu g/ml$ of cytochalasin B was added to all the culture flasks. The cell then was centrifuged for 10 minutes at 180 g and the supernatant culture medium is removed. 5 ml of 0.075 M cold ($4°C$) KCL re- suspended and centrifuge for 10 minutes. The cells then were wash with freshly made fixative consisting of methanol: acetic acid (10:1) with three or four further changes of the fixative until the cell pellet is clear.

### 2.2 RNase A Treatment and Slide Analysis

Cell pellet were dropped onto clean slides, the slides then treated with RNase A. 1250 $\mu l$ RNase A is heated in water bath for 10 minutes at $70°C$ and then allowed to cool slowly at room temperature. Slides are rinsed in distilled water and place in RNase A solution (stock solution: distilled water 1:39) for 10 minutes at $37°C$. The slides then washed in distilled water again and placed in 3:1 (methanol: acetic acid) fixative for 2 minutes, keep the slides overnight to dry it. Next, slides were stained in 2% of Giemsa stain for 10 minutes and dry it overnight. Each slide was scan and capture using Microscope Zeiss with Metafer 4 software.

## 3 Results and Discussions

Figure 1 show microscopic view of binucleated cells with and without treatment of RNase A. background for image (a) is darker than image (b). RNase A was reducing the background so that the image much easier to analyse.

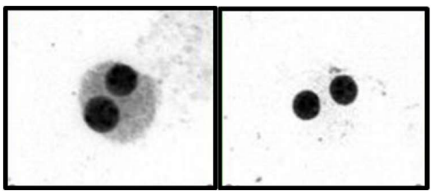


Figure 1: Microscopic view of binucleated cells without RNase A treatment (A) and with treatment RNase A (B).

Binucleated cells with micronuclei shown in Figure 2. Image clearly shows a micronuclei, micronuclei size is small than the binucleated cell and same colour with binucleated

cell. Without treatment, the background was darker, and micronuclei look-a-like image will be confusing to analyse.

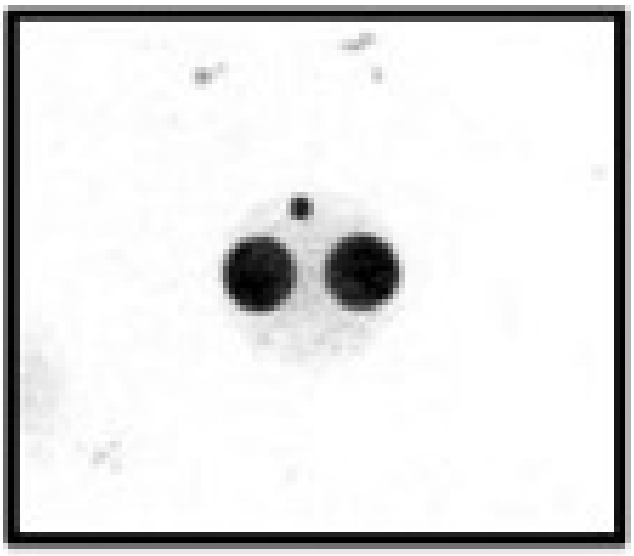


Figure 2: Microscopic view of binucleated cells with 1 MN (slide treated with RNase A).

## 4 Conclusion

This study improves the method for analysing Giemsa stained CBMN microscopic images quickly and automatically, with a high detection rate and processing speed. Automated system is more sensitive compared to manual microscope. Clear background of cell is more helpful to analyse the cell.

## References

International Atomic Energy Agency (IAEA). 2011. Cytogenetic dosimetry: Applications in preparedness for and response to radiation emergencies.

Lidiya Luzhna, Palak Kathiria, and Olga Kovalchuk. 2013. Micronuclei in genotoxicity assessment: From genetics to epigenetics and beyond. *Frontiers in Genetics*, 4:131.

Qing-Zeng Qian, Xiang-Ke Cao, Fu-Hai Shen, and Qian Wang. 2016. Effects of ionising radiation on micronucleus formation and chromosomal aberrations in chinese radiation workers. *Radiation Protection Dosimetry*, 168(2):197–203.

M. Syaifudin, V. P. Defiyandra, S. Nurhayati, S. Purnami, and E. Pudjadi. 2018. Micronucleus assay-based evaluation of radiosensitivity of lymphocytes among inhabitants living in high background radiation area of mamuju, west sulawesi, indonesia. *Genome Integr*, 9:2.

Individual Research Contribution Review, 2024: 69–70
*ISSN: 3083-922X*

# Ensuring Safety And Efficiency In The R&D Of Chromium-51 EDTA: Addressing Vapour Concerns And Handling Improvements

**Muhammad Hanaffi Bin Mohamad Mokhtar**
Medical Technology Division, Malaysian Nuclear Agency
43000 Kajang, Selangor
mhanaffi@nm.gov.my

## Abstract

The production of Chromium-51 EDTA, a radiopharmaceutical used to measure kidney function, is currently in the research and development (R&D) stage. A key concern is the potential release of vapour from radiated Chromium-51, posing health and environmental risks. Preliminary findings suggest these risks may not be as severe as initially anticipated. The study focuses on improving the handling and safety of radiated Chromium-51 through the use of larger glass ampoules and other measures to ensure both efficiency and safety in the development of Chromium-51 EDTA.

**Keywords:** Chromium-51 EDTA, Cr-51, Glomerular filtration rate

## 1 Introduction

Chromium-51 EDTA is a critical radiopharmaceutical in nuclear medicine, particularly for chronic kidney disease diagnostics. The Medical Technology Division (BTP) is currently undertaking research and development to ensure the safety and efficacy of chromium powder in the production process. The

potential release of vapour from radiated Chromium- 51 is a primary concern, necessitating careful handling

to prevent contamination and ensure personnel safety. This study addresses vapour concerns and implements handling practices to minimise contamination risks. The aim is to refine the production process by incorporating safety measures, ensuring both efficiency and safety in the development of Chromium-51 EDTA.

## 2 Methods

Production of Cr51 from chromium powder (metal). The study involved preparing chromium powder samples in the range of 380 to 752 mg. The powder was distributed into various containers: larger and smaller diameter quartz glass ampoules and NAA radiation tubes. Samples were marked and prepared with different properties, including dissolving chromium powder in 8M HCl and drying in an oven.

The samples were irradiated in the Triga Puspati reactor with specific parameters: location at the central thimble (CT), reactor power level at 500 kW, duration of 5 hours, and a cooling period of 1 day. After irradiation, samples were processed at the Samarium laboratory under a special laminar flow cabinet to prevent any unexpected release of vapour. The glass ampoules were cracked, and NAA radiation tubes were pricked to remove the Cr-51. Acetone was used to dissolve Cr-51 sticking to the containers. Radioactivity was measured using a dose calibrator, and radionuclide purity was determined using gamma spectroscopy.

## 3 Results

Out of five samples prepared, only three survived the irradiation process (Samples C, D, and E). The radioactivity of each sample was measured (Table 1), and their reaction to 8M HCl and acetone was observed. Radionuclide purity studies were conducted, with the main energy for Cr-51 detected. The method used to seal the quartz glass ampoule was also observed. Sample C (central thimble) showed 320.17 keV with 66679 counts. Sample D (rotary rack) showed 320.17 keV with 3226 counts. Sample E (rotary rack) showed 320.18 keV with 64818 counts. Radioactivity of each sample in corresponding container (excluding the aluminum can) can be seen in the table below.

| **Samples** | Radioactivity in container ($\mu$Ci) | Radioactivity in 1 $\mu$l ($\mu$Ci) |
|---|---|---|
| C | 760 | 3.53 |
| D | 320 | 3.29 |
| E | 304 | 3.41 |

Table 1: Radioactivity of samples

## 4 Discussion/Conclusions

The study observed the properties of Cr-51 after irradiation, noting that it is not volatile and tends to clump. The use of chromium powder in this study, as opposed to chips, was found to be more suitable due to solubility issues with chromium chips. The production process monitored the potential release of radioactive vapour by measuring radiation levels in the processing room. Chromium in the range of 380-752 mg produced radioactivity within the range specified by IAEA-TECDOC 1340 for Cr-51 EDTA radiopharmaceuticals. The yield from NAA radiation tubes was higher compared to quartz glass ampoules. The study also found that chromium powder reacts with 8M HCl, while it does not react with acetone.



Figure 1: Seals on quartz glass ampoules, machine- sealed (left) and manually sealed (right)

## 5 Conclusions

The study concludes that Cr-51 is not volatile and clumps after being irradiated. Acetone is a suitable solvent, and larger quartz ampoules are needed for easier processing. Placing samples at the central thimble ensures maximum exposure. The use of a double-layer NAA radiation vial and sealing quartz glass ampoules with a rotating machine are advisable.

## References

A. J. Anderson, R. A. Turner, and K. R. Smith. 2012. Analysis of chromium-51 in environmental samples. *Journal of Environmental Radioactivity*, 102(2):134–142.

M. S. Baxter and J. G. Farmer. 2011. Chromium-51 in marine sediments: Distribution and implications. *Marine Chemistry*, 117(1–4):95–104.

F. P. Castronovo. 2009. Chromium-51 labeled compounds in clinical diagnostics. *Nuclear Medicine and Biology*, 36(5):453–459.

K. L. Davis and T. P. Hansen. 2013. Chromium-51: A tool for studying red blood cell survival. *Journal of Hematology & Oncology*, 6(1):45–53.

R. L. Edwards and R. J. Mathur. 2008. Chromium-51 as a tracer in biochemical research. *Analytical Chemistry*, 80(22):8787–8794.

P. H. Fitzgerald and S. L. Martin. 2010. Radioisotopes in biomedical research: Chromium-51 applications. *Biochimica et Biophysica Acta (BBA) - General Subjects*, 1800(9):987–996.

S. J. Goldstein and S. B. Jacobsen. 2007. Chromium-51 in geological and environmental studies. *Earth and Planetary Science Letters*, 262(3–4):347–358.

W. R. Harris and C. M. Lytle. 2006. Chromium-51 as a radiotracer for studying metal ion uptake. *Journal of Inorganic Biochemistry*, 100(4):761–769.

S. A. Ibrahim and F. W. Whicker. 2005. Environmental behavior of chromium-51. *Health Physics*, 88(1):15–25.

M. L. Jackson and R. C. Knox. 2014. Applications of chromium-51 in hydrogeology. *Ground Water*, 52(4):545–555.

Individual Research Contribution Review, 2024: 71–72
*ISSN: 3083-922X*

# Dosimetry Analysis: Analyzing Astatine-211 (At-211) Dose Distribution with PHITS Data and Convolution Kernel Implementation in Python

**Nadhirah Razanah Shahrol**
Medical Technology Division, Malaysian Nuclear Agency
43000 Kajang, Selangor
nrazanah@nm.gov.my

## Abstract

Accurate dose distribution modeling is essential for optimizing targeted radionuclide therapy (TRT), particularly for alpha emitters like Astatine-211 (At-211). This study develops a computational framework for dosimetry analysis using Python to process and visualize energy deposition data from Particles and Heavy Ion Transport System (PHITS) simulations. A 2D (5×5) and 3D (5×5×5) voxel-based approach was employed, where convolution kernels simulate dose spread within the grid. The calculated dose values in Grays (Gy) confirm a steep dose gradient, characteristic of At-211's short-range alpha emissions. The findings validate the feasibility of voxel- based dosimetry using PHITS and Python for precise TRT dose calculations.

**Keywords:** Astatine-211, targeted alpha therapy, dosimetry, PHITS, Python, convolution kernel, voxel- based modeling

## 1 Introduction

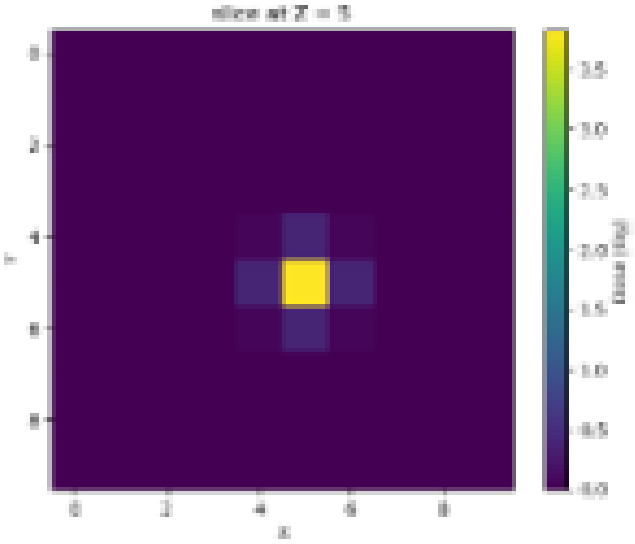
Dosimetry is crucial for determining optimal radiation dose delivery in TRT while minimizing damage to surrounding healthy tissues. At-211, an alpha emitter with high linear energy transfer (98.84 keV/µm) and short penetration range (50–90 µm), is highly effective for precise tumor targeting. However, its steep dose gradients necessitate high-resolution modeling for accurate dose assessment. Traditional dosimetry approaches struggle with microdosimetric effects, making voxel-based methods essential. Python, coupled with PHITS-generated energy deposition data, provides an efficient solution for modeling and visualizing At-211 dose distributions. This study focuses on developing a voxel-based dosimetry approach, leveraging Python for convolution kernel implementation to simulate energy spread.

## 2 Methods

A voxel grid system was developed to analyze At-211 dose distribution by processing energy deposition data from PHITS simulations. A 2D simulation was first conducted using a 5×5 kernel grid to model dose distribution in a pixel- based format. A 10×10 source map was created and convolved with the kernel to simulate radiation spread. The data was saved in CSV format and processed in Python using NumPy, pandas, and matplotlib for numerical computation and visualization. Following this, a 3D voxel-based simulation was performed using a 5×5×5 grid to enhance dose calculation precision. PHITS-generated kernel values were incorporated, and Python scripts were used to automate convolution operations, generating visual dose maps. To ensure accuracy, manual calculations were performed using Excel, and visual inspections of dose distributions were conducted.

## 3 Results

The 2D convolution model successfully replicated localized dose distribution patterns, demonstrating the sharp decline in dose outside the source voxel. The 3D voxel modeling further improved spatial resolution, reinforcing the dose fall-off effect expected from At-211's short-range alpha emissions. Cross-verification of dose values at selected voxel coordinates confirmed the accuracy of the convolution method. Python-generated dose maps illustrated a peak radiation concentration near the source, with a rapid decline in peripheral voxels, aligning with theoretical expectations for alpha particle behaviour.



## 4 Discussion

This study highlights the importance of voxel-based dosimetry for alpha-emitting radionuclides. The results align with es-

tablished microdosimetric principles, demonstrating that At-211 exhibits highly localized energy deposition. The Python-based convolution kernel method effectively models dose distribution, providing a computationally efficient alternative to Monte Carlo simulations. Future improvements may involve incorporating heterogeneous tissue compositions and dynamic activity distributions to enhance dosimetric precision.

## 5 Conclusion

Voxel-based dose modeling using PHITS and Python enables high-resolution dosimetry analysis for At-211. The computational framework developed in this study provides an accessible and efficient method for modeling dose deposition in TRT applications. Future work will focus on applying the techniques to different kind of radioisotopes and doing experimental validation using physical phantoms.

## References

H. Ma et al. 2022. In vitro and in vivo evaluation of $^{211}$at-labeled fibroblast activation protein inhibitor for glioma treatment. *Bioorganic & Medicinal Chemistry*, 55:116600.

2022. Mird primer: A complete guide to radiopharmaceutical dosimetry. Accessed: 2025-06-17.

T. Sato et al. 2021. Individual dosimetry system for targeted alpha therapy based on phits coupled with microdosimetric kinetic model. *EJNMMI Physics*, 8(4):1–18.

S. Tronchin et al. 2022. Dosimetry in targeted alpha therapy: A systematic review. *Physics in Medicine & Biology*, 67(9):09TR01.

Individual Research Contribution Review, 2024: 73–74
*ISSN: 3083-922X*

IRCR

# Instant Kit For Rapid Production Of 68GA-DOTANOC Radiopharmaceutical

**Ng Yen**
Medical Technology Division, Malaysian Nuclear Agency
43000 Kajang, Selangor
yen@nm.gov.my

## Abstract

Receptor targeted imaging using highly specific peptides labeled with radioisotopes are the gold standard for cancer diagnostic imaging with Positron Emission Tomography in Nuclear Medicine. Somatostatin peptide conjugates (SSTR) have emerged as the most important tracers in the diagnosis of neuroendocrine tumors. Currently, the radiolabeling of Gallium-68-DOTANOC are often carried out manually or employing a costly synthesis module, both methods require longer time of synthesis and much higher radiation exposure to the personnel. Here, we have developed and investigated a simpler and faster kit-based synthesis method for direct, time saving, robust and reliable labeling of Ga-68 for rapid production of small volume clinical grade Ga-68 tracers.

## 1 Introduction

Receptor targeted imaging using specific Ga-68-peptides are the best known gold standard for cancer diagnostic imaging with PET. Gallium-68 (Ga-68) labeled radiopharmaceuticals, are used in nuclear medicine departments for the PET/CT imaging to locate and stage several types of tumors (6). Ga-68, obtained from Germanium-68/Gallium-68 generator, well established labeling chemistry method, independent of reliance on in-house cyclotrons, as well as multiple dosages preparation using the same generator that can last for one year. The future development of Ga-68-radiopharmaceuticals must be put in the context of several aspects. Our aim is to develop kit formulation for direct and reliable labeling of Ga-68 for rapid production of clinical grade Ga-68 tracers akin to 99Mo/99mTc radiopharmacy. Through this attempt, the cost of production, time of synthesis as well as radiation exposrue to operator could be substantially reduced. The same kit product can also be used for radiolabeling with beta emmitter radioisotopes such as Luthetium-177 for cancer therapy.

## 2 Methods

Kit pre-formulation and optimization study: The preformulation study was carried to determine the optimum concentration of sodium acetate buffers used to optain desired pH (3.5-4.0) for optimum 68Ga complexation with peptide. The concentration and volume of sodium acetate were determined by using titration method, until the optimum Ga- 68 complexation and labeling were obtained. Kit formulation of DOTA-NOC peptide and freeze- drying cycle optimization: The final stock solution was prepared by adding peptide solution to the optimized volume of sodium acetate buffer to acheive a pH of 3-4 upon addition of 0.1N and/or 0.05M HCL. The final solution was filtered using 0.22um PVDF filter and then was dispensed into sterile 5 ml glass vials for a peptide concentration of 50ug per vial. Performance investigation of the lyophilized peptide kit: The quality of the lyophilized kits was investigated by studing the dissolution time, pH of the resultant solution by adding 1 ml of 68Ga eluate, radiolabeling yield, elapsed time from time of elution to time of injection, as well as in vitro stability of the 68Ga- labeled peptide

## 3 Results

Various concentration of sodium acetate buffer were prepared such as 0.1, 0.3, 0.5 ,0.8 and 1.0 M. Hydrochloric acid (0.1M) was prepared by using ultrapure water. Sodium acetate buffer was slowly added to HCL by titration to achieve pH of 3.5-4.0, which is the optimum pH for Ga-68 complexation with peptide after the addition of 68Ga from the 68Ge/68Ga generator. After optimization of the buffer conditions, the amount of the peptide to be used in formulation was also optimized. In order to obtain best radiolabbeling yield, temperature of labeling reaction at 900C for 10 min was choosen after adding Ga-68 eluate.

| Sodium acetate concentration (M) | Volume of Sodium acetate (mL) n=3 | Volume of HCL (0.1M) mL | Final pH |
|---|---|---|---|
| 0.1 | 20.4 ± 0.1 | 20 | 3.74 ± 0.01 |
| 0.3 | 7 ± 0.05 | 20 | 3.74 ± 0.01 |
| 0.5 | 4.1 ± 0.1 | 20 | 3.74 ± 0.01 |
| 0.8 | 2.6 ± 0.03 | 20 | 3.75 ± 0.03 |
| 1.0 | 2.1 ± 0.01 | 20 | 3.76 ± 0.2 |

Table 1: Preformulation studies of kits to determine the optimum concentration of sodium acetate to obtain the required pH (3.5-4.0)

## 4 Discussion

The quality of the kits was evaluated by studying the dissolution time, pH fo the solution after adding the Ga-68 eluate for generator, percentage of radiolabbeling yield, The cold kits

| Storage time (month) | pH of Ga-68 DOTANOC (n=3) | **Appearance** |
|---|---|---|
| 0 | 3.75 ± 0.02 | Clear and colourless |
| 2 | 3.69 ± 0.01 | Clear and colourless |
| 4 | 3.65 ± 0.03 | Clear and colourless |
| 6 | 3.65 ± 0.02 | Clear and colourless |
| 8 | 3.75 ± 0.01 | Clear and colourless |
| 10 | 3.65 ± 0.02 | Clear and colourless |

Table 2: Stability studies of cold kits over the period of 10 months

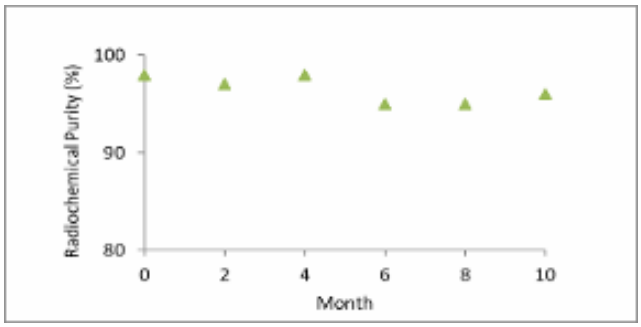



Figure 1: Radiochemical yields of 68Ga-DOTANOC studied over a period of 10 months. It was observed that all radiolabeled peptides shown > 95% radiochemical purity and does not show the presence of product degradation

dissolved instantly to provide clear solution upon the reconstitution of 1 mL of Ga-68 in HCl (0.1M) eluate, without any particulate observed, and the pH was also maintained in the range of 3.5-4.0 (Tab;e 1), the radiolabeling yield obtainedas consistently greated than 99labeled complex exhibited excellent stability both in saline and serum when studied up to 7 hours post-labeling. The stability study showed that the kits remaied intact and stable up to 10 months (period of the study). The radiolabeling percentage remained > 95%, as shown in Table 2.

## 5 Conclusion

This work has demonstrated that the innovative methods for the production of lyophilized single vial kits of peptide for reproducible, raliable and robust radiotracer radiolabeling can be achieved. The availability of freeze-dried kit formulation for the preparation of PET-based radiopharmaceutical certainly will expand the scope of their application in PET imaging.



Figure 2: DOTANOC peptide kits ready for instant radiolabeling with Ga-68 radioisotopes

## References

R. J. Boo et al. 2018. The use of therapeutic peptides to target and to kill cancer cells. *Current Medicinal Chemistry*, 19(22):3794–3804.

W. A. Breeman, E. de Blois, H. S. Chan, et al. 2011. $^{68}$Ga-labeled-dota-peptide and $^{68}$ga-labeled radiopharmaceuticals for positron emission tomography: current status of research, clinical application and future perspectives. *Seminars in Nuclear Medicine*, 41(4):314–321.

Clemens Decristoforo. 2012. Gallium-68—a new opportunity for pet available from a long shelf-life generator: automation and application. *Current Radiopharmaceuticals*, 5:212–220.

M. Hofmann, H. Maecke, A. Borner, et al. 2001. Biokinetics and imaging with the somatostatin receptor pet radioligand $^{68}$ga-dotatate: preliminary data. *European Journal of Nuclear Medicine*, 28:1751–1757.

L. Wang, K. Tang, Q. Zhang, et al. 2013. Somatostatin receptor-based molecular imaging and therapy of neuroendocrine tumors. *BioMed Research International*, page 102819.

Individual Research Contribution Review, 2024: 75–76
*ISSN: 3083-922X*

# Preliminary Quality Evaluation of Radiopharmaceutical-Grade Zoledronic Acid Kits

**Ng Yen**
Medical Technology Division, Malaysian Nuclear Agency
43000 Kajang, Selangor
yen@nm.gov.my

## Abstract

Cancer is a leading cause of death worldwide. In 2022, there were about 9.7 million cancer deaths globally. Approximately 70% of deaths from cancer occur in low and middle-income countries. The most common cancers are lung, breast, colorectal, prostate, stomach and liver cancer. Cancer mortality can be reduced significantly if detected and treated early. Some cancer may metastases to the bone at the late stages. Detection of cancer bone metastases using radiolabeled-bisphosphonate agents are known to be the most specific agent. Zoledronic acid (ZA), a bisphosphonate agent, is currently being widely used in clinical as osteoclast bone resorption inhibitor with high binding capacity to bone.

## 1 Introduction

Development of lyophilized ZA cold kit as a new radiopharmaceutical agent for bone imaging is being carried out in our laboratory. A radiopharmaceutical is a product which is usually used after labelling with radioisotopes for diagnostic or therapeutic, or both. Technetium-99m (Tc-99m) radioisotope is chosen in this study due to its excellent physical characteristics and easy availability from a generator. The performance of this newly formulated kit was throughly examined. The main objective of this study was to obtain the optimized formulation of ZA kit for the lyophilization process. Several other quality parameters of the cold kits were also evaluated, such as the radiolabelling yield, the pH, and the stannous content in the kit post-lyoplilized.

## 2 Methods

A stock solution was prepared by dissolving ZA acid, ascorbic acid, and stannous chloride dihydrate in 0.9% saline solution. The pH was adjusted to 4.5-5.5 using NaOH solution, the final solution was filtered using 0.22um PVDF filter and then was dispensed into sterile 5 ml glass vials and followed by lyophilization process using Labconco freeze dryer. The whole process required 2-3 days. The quality of the lyophilized kits was investigated by studying the pH of the resultant solution by adding 1 ml of Tc-99m eluate, the radiolabeling yield, and the stannous cloride concentrations assay using Polarography method.

## 3 Results

### 3.1 Radiolabelling performance of ZA kits with Tc-99m:

This study was performed using $Na^{99m}TcO_4^-$ by reduction with stannous. Final pH of the reconstituted solution obtained was 5.5-6. The radiochemical purity was determined using ITLC method using acetone and normal saline as mobile phases.

### 3.2 Determination of total stannous (II) in the ZA kit using Polarography method:

Stannous chloride (SnCl ) is crucial for the successful radiolabeling of ZA with Tc-99m radioisotope. According to USP guidelines, at least 50% of the initial SnCl concentration must remain at the end of the lyophilization process.

| $SnCl_2$ pre-freeze drying (mg)/vial | $SnCl_2$ post-freeze drying determined (mg/vial) ($n = 4$) |
|---|---|
| 0.45 | $0.27 \pm 0.02$<br>$60.7 + 4.5\%$<br>$> 50\%$ present |

Table 1: In this study, the results indicated that the percentage of Sn(II) present in the ZA kit at the end of the lyophilization process was $60.7 \pm 4.5\%$, which exceeds the 50% threshold, as determined by the polarography method.

## 4 Discussion

Currently, the development of ZA labeled with Tc-99m as potential bone imaging agent has gained extensive interest among researchers. According to (Asikoglu and Durak, 2009), the radiolabelling of ZA and Tc-99m is feasible and the stability of the complex is long enough to allow imaging study. The image shown similar uptake to the diagnostic dose of Tc-99m-MDP. Another group has successfully labeled the ZA with Lu-177 and the results showed excellent labelling yield and high uptake in skeleton for up to 7 days (Rasheed and others, 2015). In our study, the quality of the ZA kits was evaluated by studying the radiolabelling yield, pH fo the solution after adding the Tc-99m eluate from generator. The cold kits dissolved instantly to provide clear and colorless solution upon the reconstitution of 1 mL of Tc-99m eluate, without any particulate observed, and the pH was also maintained in the range of 5-6. The radiolabeling yield obtained was consistently greated than 99%, respectively. The percentage of

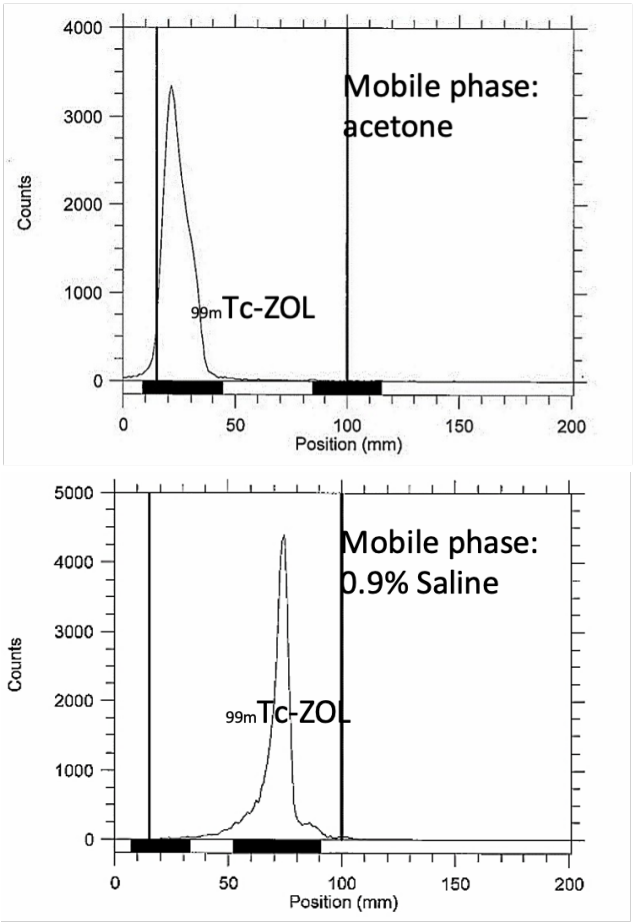



Figure 1: Radiochemical yields of $^{99m}$Tc-ZA studied. To determine the radiochemical purity, a two-solvent system must be used, one to separate the amount of free pertechnetate (Fig B: saline) and another to separate the hydrolyzed reduced technetium (Fig A: acetone) The percent of $^{99m}$Tc in these two forms cannot exceed 10%. Our study showed that the labelling yield of ZA obtained consistently exceeded 99%. The labelling reaction took less than 5 minutes, and the tracer remained stable for at least 5 hours.

SnCl2 present in the ZA kit at the end of lyophilizatoin process were more than 50% as determinded by polarography method. These preliminary results indicated that the preparation and formulation of the ZA kits are optimized and effective.

## 5 Conclusion

For the first time, we have successfully developed and formulated the ZA kit. Radiolabelling of 99mTc-ZOL was successful with radiochemical purity (> 99%). The complex also exhibited significant stability in room temperature for up to 5 hours in vitro. Our preliminary results showed that the kit-based radiosynthesis of Tc-99m-ZA is rapid, robust, and highly reliable for delivering Tc-99m-ZA for bone imaging. However, it is crucial to thoroughly study several additional parameters before using this in humans.

## References

M. Asikoglu and F. G. Durak. 2009. The rabbit biodistribution of a therapeutic dose of zoledronic acid labelled with tc-99m. *Applied Radiation and Isotopes*, 67(9):1616–1621.

J. J. Body. 1997. Clinical research update: Zoledronate. *Cancer*, 80(8):1699–1701.

M. Coronado et al. 2006. Clinical role of sm-153 edtmp in the treatment of painful bone metastatic disease. *Clinical Nuclear Medicine*, 31(10):605–610.

J. R. Green. 2005. Zoledronic acid: pharmacologic profile of a potent bisphosphonate. *Journal of Organometallic Chemistry*, 690(10):2439–2448.

J. Lin, L. Qiu, W. Cheng, S. Luo, L. Xue, et al. 2012. Development of superior bone scintigraphic agent from a series of $^{99m}$tc-labeled zoledronic acid derivatives. *Applied Radiation and Isotopes*, 70:848–855.

E. Pituskin, A. Fairchild, J. Dutka, L. Gagnon, A. Driga, P. Tachynski, et al. 2010. Multidisciplinary team contributions within a dedicated outpatient palliative radiotherapy clinic: a prospective descriptive study. *International Journal of Radiation Oncology Biology Physics*, 78(2):527–532.

R. Rasheed et al. 2015. Radio-synthesis, and in-vivo skeletal localization of 177lu-zoledronic acid as novel bone seeking therapeutic radiopharmaceutical. *Journal of Anesthesia & Clinical Research*, 6(3).

R. P. Warell. 1997. Metabolic emergencies. pages 2486–2493.

Individual Research Contribution Review, 2024: 77–78
*ISSN: 3083-922X*

IRCR

# Impact of Fetal Bovine Serum (FBS) on Dicentric Chromosome Assay in Increasing the Number of Cells and Improving the Size of Chromosome from the Cells Harvest

**Nurul Nazeerah Juarimi**
Medical Technology Division, Malaysian Nuclear Agency
43000 Kajang, Selangor
nazeerah@nm.gov.my

## Abstract

Chromosome aberration frequency is the most reliable biological marker for detecting acute accidental radiation exposure. In biological dosimetry, dicentric assay using blood lymphocytes is one of the techniques that frequently used. After taking blood sample, several replicate of cultures should be prepared which using Roswell Park Memorial Institute (RPMI) 1640 as the culture media used and supplemented with FBS serum, antibiotics and L-glutamine. Serum is used to act as nutrient source in lymphocyte culture media which support the growth of the lymphocyte cells. This study using 10% and 20% FBS serum in dicentric chromosome aberration assay. After 48 hours of incubation, followed by harvesting, the amount of cells in both serum content are being observed with naked eyes. Then, number of cells will be counted from the auto-capture image using automated Metaphase Finder System. Besides, the size of chromosomes from both serum content will be compared. In general, the amount of cells increases as the percentage of FBS serum used is higher.

## 1 Introduction

The frequency of chromosome aberrations provides the most reliable biological marker to detect acute accidental radiation exposure (Lloyd et al, 2011). Radiation can cause different types of chromosomal aberrations, which can be divided to stable aberrations like translocations and unstable aberrations like dicentric chromosomes (DC), micronuclei, acentric, and ring-form (Agarwal et al., 2023). Dicentric chromosome assay (DCA) using blood lymphocytes has become the "gold standard" of radiation biological dosimetry due to its reproducibility, relative specificity to radiation and its sensitivity to doses below acute medical significance (Manello and Tonti, 2007). Fetal bovine serum (FBS) and fetal calf serum (FCS) are widely used growth supplements for cell culture, principally due to their high concentrations of growth stimulatory hormones and low concentrations of growth inhibitory factors. FBS act as one of the factors which influence the cell progression rate in cell culture, hence may affect the chromosome aberration frequencies (Kanda, 2000). In this facility, FBS is used as the standard procedure following International Atomic Energy Association (IAEA) technical document and the percentage used as a common practice is 10% FBS for the samples that being received. However, there are only a few journals reported on the effect of different percentage of FBS in the dicentric chromosome aberration assay for higher radiation dose exposure. Hence, the goal of this study is to compare the cells count in chromosome aberration assay using 10% and 20% FBS. In addition, the size of the chromosomes is being observed using automated Metaphase Finder System.

## 2 Methods

In this study, dicentric chromosome aberration assay using standard method from International Atomic Energy Association (IAEA) technical document is used. A coagulation tube containing lithium heparin is used to hold blood specimens. The blood specimen must be received within 24 hours of the blood sample time and should be transported at a temperature between 18°C and 24°C. Following the receipt of blood samples, the media for the cell culture should be ready, and every process needs to be carried out in a biosafety cabinet using aseptic technique.

The culture medium is using Roswell Park Memorial Institute 1640 (RPMI-1640) which then supplemented with Fetal Bovine Serum (FBS), antibiotics, L glutamine. In this investigation, two different FBS percentage which are 10% and 20% FBS being employed to compare the number of cells and the effects on the chromosomes size from the cells harvest. For media flask 10% FBS (10A), contains 0.1ml 1% Glutamine, 0.2ml 2% antibiotics, 1.0ml FBS and 8.7ml RPMI-1640 to made up 10.0ml media. In the media flask for 20% FBS (20A), contains 0.1ml 1% Glutamine, 0.2ml 2% antibiotics, 2.0ml FBS and 7.7ml RPMI-1640 to made up 10.0ml media. Then, 2.0ml of blood specimen are being added into each media flask respectively. At final stage of media preparation, add 0.3ml Phytohaemagglutinin (PHA) into each media flasks. After that, incubate the cells at 37°C with 5% $CO_2$ for 48 hours. At 45 hours of incubation period, add 50µl of colcemide into each flask.

After complete 48 hours incubation period, cells should be harvested by transferring the cell culture into two tubes, labelled with 10A and 20A. Centrifuging the cell cultures with speed of 1000rpm for 10 minutes, then discard the supernatant and replace with hypotonic solution which is 5.0ml of 0.075M Potassium Chloride (KCl). After that, repeat centrifuging with speed of 1000rpm for 10 minutes. Potassium Chloride (KCl) should be removed and replace with 5.0ml freshly prepared fixative (3:1, methanol:acetic acid). During the initial addition, introduce the fixative slowly and steadily at constant rate while stirring it using vortex mixer. Following that, centrifuge

the cells with speed of 1000rpm for 5 minutes, resuspended and repeat in four changes fixative. After removing the final wash of fixative, there should left with sufficient volume of suspension for dispensing onto slides. All the process should be done for both tube 10A and 20A.

In slides preparation, use clean and grease free slides. Dispensing the cells from both suspension 10A and 20A onto the slides respectively and pre-treated the slides with RNase. A 10mg/ml RNase solution is heated at 70°C for 10 minutes and then allowed to cool slowly. During pre-treatment of slides with RNase, distilled water, KCl and RNase are used following the sequences. During soaking the slides in the RNase solution, left it in water bath at 70°C for 30 minutes. Next, the slides need to be stained with 2% Giemsa and let to dry. Then, slides are mounted using Dibutylphthalate Polystyrene Xylene (DPX) mountant and a coverslip. Finally, auto-capturing image of chromosome by using Metaphase Finder System.

## 3 Results and Discussion

In this study, the amount of cells that being harvest, were observed with naked eyes before removing the final wash fixative. The result in Figure 1 shows that the amount of cells in Tube 10A and Tube 20A cannot be differentiated with naked eyes. This may happen when the amount of cells in both tubes are almost the same.

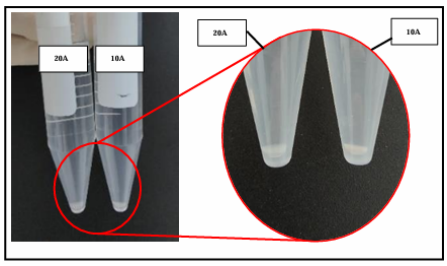



Figure 1: Comparison for amount of cells in Tube 10A (cells with 10% FBS) and Tube 20A (cells with 20% FBS) that were observed with naked eyes.

The slides with cells from both samples were being analysed using automated Metaphase Finder System. The system able to scan through and count the number of cells with chromosome as reported in Table 1. The number of cells when sample added with 20% FBS are slightly higher than sample added with 10% FBS. This may indicate there is effect when increasing the percentage of FBS in the sample. Thus, higher percentage of FBS, 20% can be used when receving sample for higher radiation dose exposure. The samples with high radiation dose exposure received may come in small volume and the cells that will be harvested may be less, hence using percentage of 20% FBS may help in increasing the number of cells during culture and more cells can be seen after harvesting. Kanda R. stated that the measurement of aberration frequencies may be affected by any factor influencing the cell progression rate in culture.

In addition, from the image auto-captured with Metaphase Finder System, it shows that when higher percentage of FBS, 20% used in the sample, it gave bigger size of chromosomes

Table 1: Comparison of number of cells in sample with 10% FBS and sample with 20% FBS

| FBS percentage | Number of cells |
|---|---|
| 10% (Tube 10A) | 1188 |
| 20% (Tube 20A) | 1236 |

in the cells that harvested (Figure 2). Hence, this demonstrate that using higher percentage of FBS may results in better size of the chromosomes from the cells harvest.

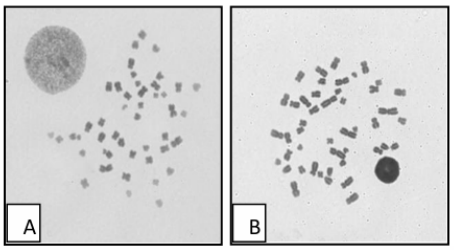



Figure 2: Image of chromosomes in cell with 10% FBS from Tube 10A (A) and cell with 20% FBS from Tube 20A (B) auto-captured with Metaphase Finder System.

## 4 Conclusions

In conclusion, this study shows that the usage of 20% of Fetal Bovine Serum increased the number of cells in the sample of chromosome aberration assay and better size of chromosome captured by the Metaphase Finder System from the cells cultured and harvested. This indicate that this concept can be considered and adapt for higher radiation dose exposure sample. Further study on the usage of percentage 20% of FBS need to be done in higher radiation dose exposure sample, in order to get better view of the results.

## References

N. Agarwal, A.K. Rathi, S. Kapoor, K. Singh, S. Arora, and A. Jindal et al. 2023. Biodosimetric analysis of head and neck cancer patients undergoing radiotherapy by dicentric chromosome aberration assay. *Journal of Cancer Research and Therapeutics*.

R. Kanda. 2000. Improvement of accuracy of chromosome aberration analysis for biological radiation dosimetry. *Journal of Radiation Research*, 41(1):1–8.

D.C Lloyd et al. 2011. Cytogenetic dosimetry: Applications in preparedness for and response to radiation emergencies. *International Atomic Energy Agency.*, pages pp. 53–61.

F. Manello and G.T. Tonti. 2007. Concise review: No breakthroughs for human mesenchymal and embryonic stem cell culture: Conditioned medium, feeder layer, of feeder-free; medium with fetal calf serum, human serum, or enriched plasma; serum-free, serum replacement nonconditioned medium, or ad hoc formula? all that glitters is not gold! *Journal of Stem Cells*, 25:1603–1609.

Individual Research Contribution Review, 2024: 79–80
*ISSN: 3083-922X*

# Quality Control On Sodium Iodide (I-131) Capsule Produced By Agensi Nuklear Malaysia

**Rahimah Abdul Rahim**
Medical Technology Division, Malaysian Nuclear Agency
43000 Kajang, Selangor
rahimah@nm.gov.my

## Abstract

Radioiodine (Iodine-131) hard gelatin capsules are widely used for the diagnosis and treatment of various thyroid disorders including toxic nodules, thyroid hypofunction, carcinoma of the thyroid gland and hyperthyroidism. Radioiodine with capsule has several advantages compared to radioiodine supplied in the form of a solution. At Bahagian Teknologi Perubatan (BTP), Agensi Nuklear Malaysia, Iodine-131 solution was dispensed into the capsule in the dedicated hot cell using calibrated pipettor. Aim of this study is to test the quality of sodium iodide (I-131) capsule produced by Agensi Nuklear Malaysia.

**Keywords:** Sodium iodide (I-131) capsule, quality control

## 1 Introduction

Iodine-131($^{131}$I) is an important radioisotope of iodine discovered by Glenn Seaborg and John Livingood in 1938 at the University of California, Berkeley (1). It is highly radioactive with a half-life of about 8.02 days. $^{131}$I is the most used iodine radioisotope, and it decays mostly by beta-emission (606 keV; 90%). It is well- known for causing the death of cells because it can penetrate other cells up to several millimeters away. For this reason, 131I is used for the treatment of thyrotoxicosis (hyperthyroidism) and some types of thyroid cancer that absorb iodine (2). Quality control and quality assurance are crucial prerequisite for all classes of pharmaceuticals production. A deficient quality of diagnostic radiopharmaceutical, will contribute to the unsafe product, give erroneous information about the patient's condition leading to inappropriate determination of therapy and could lead to excess radiation exposure to non-target tissues and reduced efficacy. Therefore, quality control testing is vital to ensure the radiopharmaceuticals are safe and effective.

## 2 Methods

The quality control procedures namely the appearance, disintegration, radionuclide identification, radiochemical purity, and microbiology test were carried out at the laboratory as required by standard pharmacopeia. Two batches of capsules were produced with the activity of each capsule was 10 mCi and 100 mCi. The capsule was homogenized with water and methanol and then used for radiochemical purity and radionuclide identification test. Six capsules were placed in each of the tubes of the basket with 800 ml of specified medium maintained at $37 \pm 20\,^{\circ}$C for the disintegration test. Meanwhile for the microbial test, the decayed capsule was dissolved aseptically in sterile phosphate buffer solution and test for bioburden dan E.coli.

## 3 Results

The $^{131}$I solution is dispense and adsorbed on a di- sodium hydrogen phosphate anhydrous in gelatin bovine capsule. BTP has produced two batches of sodium iodide (I-131) capsule with the activity of each capsule was 10 mCi and 100 mCi. Each batch contains 10 capsules. The quality control procedures were carried out at the laboratory as required by standard pharmacopeia procedure for days 1, 2, 7 and 14. The tests were done until day 14 is indirectly to find out the stability of the product. For the disintegration test procedure, a non-radioactive capsule with filler (di- sodium hydrogen phosphate anhydrous) was tested. This procedure is acceptable been tested without radioactive material. The specification and the result of sodium iodide (I-131) capsule test as in Table 1 and Table 2.

| | Type of test | Specifications |
|---|---|---|
| 1 | Physical appearance | White and grey powder in colorless capsule |
| 2 | Disintegration | Dissolve completely within 15 minutes |
| 3 | Radionuclide identification | Gamma ray at energy 0.364 MeV |
| 4 | Radiochemical purity | ≥ 95% |
| 5 | Microbial test; | |
| | Total viable microbial | Not more than 1000 cfu/ml |
| | Total fungal count | Not more than 100 cfu/ml |
| | *Escherichia coli* | Absent |

Table 1: Specification of sodium iodide (I-131) capsule.

## 4 Discussion

Both batches of sodium iodide (I-131) capsule with activity 10 mCi and 100 mCi respectively was tested and results met the specifications accordance in British Pharmacopeia and the United States Pharmacopeia. However, production of sodium

| **Sample/Test** | **10 mCi** | | | | **100 mCi** | | | |
|---|---|---|---|---|---|---|---|---|
| | **1** | **2** | **7** | **14** | **1** | **2** | **7** | **14** |
| Physical appearance | White and grey powder in colorless capsule | | | | White and grey powder in colorless capsule | | | |
| Disintegration (minute) | 3.2 | 3.2 | 2.6 | 3.3 | 2.6 | 2.1 | 2.8 | 2.6 |
| Radionuclide identification | Gamma ray at energy 0.364 MeV | | | | Gamma ray at energy 0.364 MeV | | | |
| Radiochemical purity (%) | 96.2 | 95.6 | 96.6 | 95.7 | 98.3 | 96.3 | 97.1 | 95.4 |
| **Microbial test** | | | | | | | | |
| Total viable microbial count | Nil | | | | Nil | | | |
| Total fungal count | Nil | | | | Nil | | | |
| *Escherichia coli* | Absent | | | | Absent | | | |

Table 2: Quality control test results of $^{131}$I gelatin capsules at different activity levels over time.

iodide (I-131) capsule needs some improvement to achieve more than 99% of radiochemical purity determination.

## References

Vicky V. Mody, Ajay N. Singh, Rahul Deshmukh, and Samit Shah. 2025. Thyroid hormones, iodine and iodides, and antithyroid drugs. *Advanced Drug Delivery Reviews*. Available at: `https://www.sciencedirect.com/science/journal/03786080`.

a.

b. British pharmacopeia.

c. Production of $^{131}$i iodide capsules in argentina.

d. Refer to operation manual for automated gamma counter.

e. United state pharmacopeia.

n.d. Production of $^{131}$i gelatin capsule.

Individual Research Contribution Review, 2024: 81–82
*ISSN: 3083-922X*

# NMR Spectroscopic Characterization of 3-(4-methylphenyl)-1-(3-methylphenyl) prop-2-en-1-one Synthesized via Claisen-Schmidt Condensation

**Rosniza Razali**
Medical Technology Department, Malaysian Nuclear Agency
43000 Kajang, Selangor
rosniza@nm.gov.my

## Abstract

The chalcone derivative, (3-(4-methylphenyl)-1-(3- methylphenyl) prop-2-en-1-one), was successfully synthesized via Claisen-Schmidt condensation, employing 3-methylacetophenone and 4-methylbenzaldehyde in a sodium hydroxide medium with ethanol as the solvent. The resulting compound underwent purification through preparative liquid chromatography and was subsequently characterized using $^{1}$H NMR and $^{13}$C NMR spectroscopy. This research highlights the synthesis of 3-(4- methylphenyl)-1-(3-methylphenyl) prop-2-en-1-one through Claisen-Schmidt condensation, alongside its structural elucidation via Nuclear Magnetic Resonance (NMR) techniques. The findings confirm the compound's successful synthesis and provide comprehensive insights into its molecular structure.

**Keywords:** Chalcone, $^{1}$H NMR, $^{13}$C NMR

## 1 Introduction

Chalcones, chemically designated as 1,3-diphenyl-2- propen-1-ones, hold significant importance in the fields of organic and medicinal chemistry owing to their structural simplicity and wide-ranging biological activities. These compounds are characterized by the presence of two aryl rings connected through an $\alpha,\beta$-unsaturated carbonyl system. Over recent decades, both naturally occurring and synthetically derived chalcones have gained attention as crucial entities in pharmacological studies, demonstrating antibacterial, anti-inflammatory, analgesic, anticholinergic, antiplatelet, antiulcer, antioxidant, antimalarial, anticancer, and antiviral properties (Elkanzi et al., 2022).

In this study, chalcone derivatives were synthesized via the Claisen-Schmidt Condensation, a reaction involving benzaldehyde derivatives and acetophenones under acidic or basic catalytic conditions in a polar solvent, typically at moderate temperatures (50– 100°C). The method is widely recognized for its efficiency and straightforward approach to the formation of carbon–carbon double bonds (Mona et al., 2023). The successful synthesis of these chalcone derivatives was verified using nuclear magnetic resonance (NMR) spectroscopy, including both $^{1}$H and $^{13}$C NMR, which provided detailed insights into the molecular structure of the synthesized chalcones (Hwang et al., 2011). This study aimed to assess the efficiency of the Claisen-Schmidt condensation in chalcone synthesis and to elucidate the structural integrity of the products through NMR spectral analysis.

## 2 Methods

Chalcone was synthesized using the Claisen- Schmidt condensation method using sodium hydroxide solution as catalyst in ethanol solvent. A mixture of 3-methylacetophenone (1.3418 g, 10 mmol) and 4-methylbenzaldehyde (1.2015 g, 10 mmol) in 40 ml ethanol was stirred in a conical flask placed in an ice bath. Then, 10$ml$ of 60% sodium hydroxide was added dropwise to the solution with continuous stirring for 30 min in an ice bath and continued to stir for another 3 h at room temperature. The conical flask was covered with para film and kept in the refrigerator overnight. Upon completion, the reaction mixture was diluted with 40 ml of ice-cold water until all the ice melted. Next, the reaction mixture was filtered and washed well with cold water. The resulting solid on the filter paper was air-dried and recrystallized from rectified methanol (Figure 1).

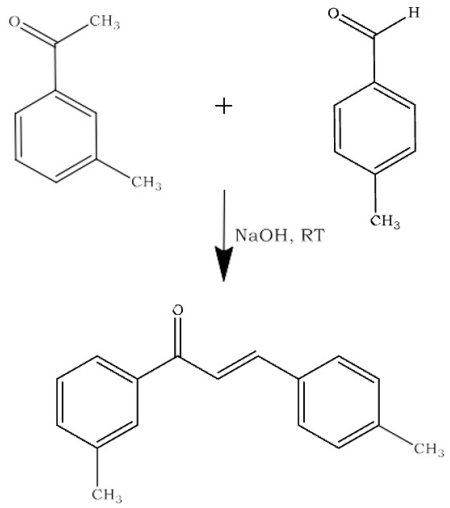



Figure 1: Synthetic scheme for 3-(4- methylphenyl)-1-(3-methylphenyl) prop-2-en-1- one.

The resulting compounds were then purified using preparative liquid chromatography and structural determination using NMR spectroscopy. 1HNMR and 13CNMR spectra were recorded using CDCl3 on a JEOL (500 MHz) and the chem-

ical shifts were recorded in $\delta$ units (parts per million) with respect to tetramethyl silane (TMS) as an internal standard.

## 3 Results and Discussion

Synthesize of chalcone derivative is a simple step method. The structure of the synthesized chalcone was confirmed by NMR. Figure 2 illustrates the $^{1}$H NMR spectrum of 3-(4-methylphenyl)-1-(3-methylphenyl) prop-2-en-1-one. Based on the resulting spectrum, it was found that the aromatic proton (Ar-H) from the benzene ring appeared between 7.0–8.0 ppm as a multiple due to the substitution on both rings. Meanwhile, the $\alpha$, $\beta$- unsaturated proton (C=C-H) showed a double feature: the $\alpha$-proton near the carbonyl appeared at 7.5–7.7 ppm, indicating a trans (E) configuration, while the $\beta$-proton closer to the phenyl ring was observed in the conjugated system at 7.3–7.5. In addition, the methyl proton ($-CH_3$) attached to the 3- and 4' positions of the benzene ring was detected as a singlet around 2.3–2.4 ppm, with the two groups not being equivalent but exhibiting similar chemical shifts

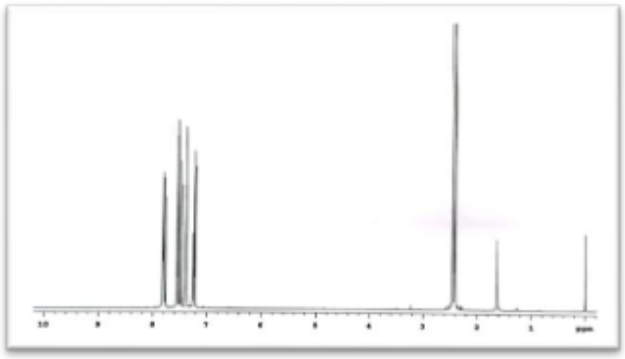


Figure 2: $^{1}$H NMR spectrum of 3-(4-methylphenyl)-1- (3-methylphenyl) prop-2-en-1-one.

Figure 3 illustrates the $^{13}$C NMR spectrum of 3-(4-methylphenyl)-1-(3-methylphenyl) prop-2-en-1-one, providing detailed insights into its carbon framework. The spectrum reveals that the carbonyl carbon (C=O, ketone) exhibits a highly shielded signal within the range of ~190–195 ppm. The $\alpha$, $\beta$-unsaturated carbons (C=C) produce signals in the 120–145 ppm range, where the $\alpha$-carbon (adjacent to the carbonyl group) appears between 120–140 ppm, and the $\beta$- carbon signals are observed around 130–145 ppm. Aromatic carbons from the benzene rings contribute to signals between 120–140 ppm, with subtle variations attributed to meta and para substitutions. Furthermore, the methyl carbons ($-CH_3$) located at the 3- and 4' positions are identified by singlets in the 21–25 ppm range, confirming the presence of these substituents.

## 4 Conclusions

In conclusion, this study successfully synthesized a chalcone derivative, specifically 3- (4-methylphenyl)-1-(3-methylphenyl) prop-2-en- 1-one, utilizing the Claisen-Schmidt condensation method. The structural confirmation

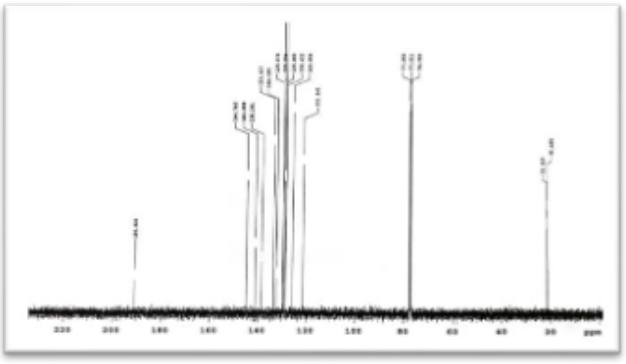


Figure 3: $^{13}$C NMR spectrum of 3-(4- methylphenyl)-1-(3-methylphenyl) prop-2-en- 1-one.

of the synthesized compound was achieved through nuclear magnetic resonance (NMR) spectroscopy, including both $^{1}$H NMR and $^{13}$C NMR analyses.

### 4.1 Acknowledgements

I would like to thank all the staff of the Phytopharmaceutical Technology Group, Medical Technology Division, for their commitment to making this study a success.

## References

Nadia A. A. Elkanzi, Hajer Hrichi, Ruba A. Alolayan, Wassila Derafa, Fatin M. Zahou, and Rania B. Bakr. 2022. Synthesis of chalcones derivatives and their biological activities: A review. *ACS Omega*, 7(32):27769–27786.

Doseok Hwang, Jiye Han, Geunhyeong Jang, Dongsoo Kim, and Yoongho Lee. 2011. Synthesis and complete assignment of nmr data of 20 chalcones. *Magnetic Resonance in Chemistry*, 49:41–45.

A. S. Mona, A. R. Sameh, and M. F. Asmaa. 2023. Synthesis, reaction and application of chalcone: A systematic review. *Organic & Biomolecular Chemistry*, 21:5317.

Individual Research Contribution Review, 2024: 83–84
*ISSN: 3083-922X*

# Stability Study and the Effect of Different Raw Material Handling Conditions on Stannous (II) Chloride Content of Sterile and Pyrogen Free Lyophilised DMSA Cold Kit

**Saifullizan Mohamad**
Medical Technology Division, Malaysian Nuclear Agency
43000 Kajang, Selangor
saifullizan@nm.gov.my

## Abstract

A sterile and pyrogen free dimercaptosuccinic acid (DMSA) lyophilized cold kit is formulated in nuclear medicine by radiolabelling with radioisotope $^{99m}$Tc (Technetium-99m) to form $^{99m}$Tc-DMSA complexes which acts as diagnostic agent to study the morphology of kidneys was formulated. However, radiochemical purity (RCP) and quality control testing should be conducted towards each product batches after its production up to one year at the recommended storage conditions for ensuring the products quality, efficacy and safety. Hence, stability study was conducted for the three batches of kit formulation to evaluate the stability of lyophilized DMSA cold kit. The lyophilized kit was reconstituted with 1 mL addition of $^{99m}$Tc solution (20 - 30 mCi) at the optimum pH. By using the Instant Thin Layer Chromatography (iTLC) method, 2-3 $\mu$L sample was spotted at the origin of the 1.5 cm pencil marked at the bottom, later the strip was developed with the mobile phase solution of acetone to reach the solvent front which 1.0 cm from the top. The dried duplicate strips were then evaluated by TLC scanner. A single important raw material that is called stannous (II) chloride. Stannous (II) chloride contents in every batch of lyophilized kit also be tested via a polarography technique by using polarography instrument. Each batch of kit represented different raw material handling conditions such as open lab, dry cabinet and glove box. In this study, stability and the effect of different raw material handling conditions on the stannous (II) chloride content of sterile and pyrogen free DMSA lyophilized cold kit will be determined.

**Keywords:** DMSA, Technetium-99m, Stannous (II) chloride, Polarography, Lyophilised kit

## 1 Introduction

Radiopharmaceuticals are generally formulated from kits prepared in authorized manufacturing facilities. A cold kit contains the ligand at which Tc-99m is to be complexed, an adequate quantity of reducing agent (stannous chloride), buffer to adjust the pH to suit the labelling conditions, stabilizing agents and excipients. The radiopharmaceutical kits are prepared in a lyophilized form and have a long shelf life of up to one year. A nuclear medicine renal scan uses radiopharmaceuticals such as $^{99m}$Tc-DTPA and $^{99m}$Tc-MAG3 injected into a vein, to provide clear images of the kidneys taken with a special camera called a gamma camera or SPECT/CT. A $^{99m}$Tc-DMSA is one of the technetium radiopharmaceuticals also used in renal imaging and primarily used to study the morphology of renal cortex. In this study, locally produced lyophilized sterile and pyrogen free DMSA kit (to be reconstituted with Tc-99m) were prepared.

## 2 Methods

Three batches of lyophilised sterile and pyrogen free DMSA cold kits were formulated at Malaysian Nuclear Agency. Then, the stability study of the $^{99m}$Tc-DMSA for one year of storage were carried out by reconstituting lyophilized kit with 1 mL addition of $^{99m}$Tc solution (20 - 30 mCi) at the optimum pH that is then analysed by the Instant Thin Layer Chromatography (iTLC) method. About 2-3 $\mu$L sample was spotted at the origin of the 1.5 cm pencil marked at the bottom, later the strip was developed with the mobile phase solution of acetone to reach the solvent front which 1.0 cm from the top. The dried duplicate strips were then evaluated by TLC scanner in order to obtain radiochemical purity (RCP) values. Stannous (II) chloride content were also conducted to all three batches of lyophilized cold kit. The percentage of stannous (II) chloride content for each batch of kit represented different raw material handling conditions such as open lab, dry cabinet and glove box were calculated by polarography instrument (884 Professional VA, Metrohm, Switzerland) as shown in Figure 1 using the following equation;

$$\text{Percentage of stannous (II) chloride (\%)} = \frac{\text{stannous (II) chloride } (\mu\text{g/vial})}{400\ (\mu\text{g/vial})} \times 100$$



Figure 1: Polarography instrument (884 Professional VA, Metrohm, Switzerland).

## 3 Results and Discussion

Three batches of lyophilised sterile and pyrogen free DMSA cold kits were formulated at Malaysian Nuclear Agency as shown in Figure 2.

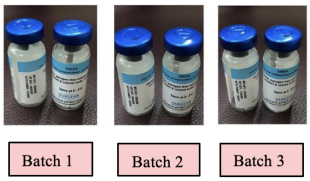



Figure 2: Batch 1(BN01), Batch 2(BN02) and Batch 3(BN03) of lyophilised DMSA cold kit.

Radiochemical purity (RCP) values for all three batches of lyophilised DMSA cold kit were an important parameter to determine the efficacy of radiolabelling DMSA kit with the $^{99m}$Tc radionuclide. In this test, $^{99m}$Tc-DMSA was subjected to the iTLC in the acetone solvent system to detect the separation between product that is $^{99m}$Tc-DMSA and the impurity which is free $^{99m}$Tc-pertechnetate. The RCP of radiolabelled complex was determined by subtracting the percentage of impurity from 100%. The higher the RCP, the better the radiolabelling efficiency of the DMSA kit. The equation of RCP was stated in the equation below.

$$\text{RCP values} = 100\% - {}^{99m}\text{Tc-pertechnetate}$$

Figure 3 and Table 1 show the iTLC of $^{99m}$Tc-DMSA in the acetone solvent system. $^{99m}$Tc-DMSA complex, which has Rf value of 0.0, was separated from $^{99m}$Tc-pertechnetate, which has Rf value of 0.9 to 1.0.

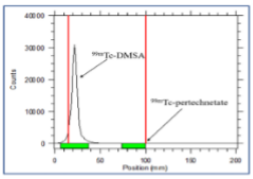



Figure 3: Separation graph of $^{99m}$Tc-DMSA and $^{99m}$Tc-pertechnetate in acetone solvent system.

| | Rf | Percentage |
|---|---|---|
| $^{99m}$Tc-DMSA | 0.0 | 99.47% ± 0.018 |
| $^{99m}$Tc-pertechnetate | 0.9 - 1.0 | 0.53% ± 0.018 |

Table 1: iTLC result in the acetone solvent system.

Figure 4 shows the percentage of RCP for all three batches for month 1, month 2, month 3 and month 12. After 1 month of storage, the RCP values for BN01, BN02 and BN03 were 99.15% ± 0.012, 99.19 ± 0.018 and 99.33 ± 0.013 respectively. The RCP values for BN01, BN02 and BN03 were 99.21 ± 0.017, 99.30 ± 0.032 and 99.25 ± 0.007 respectively during the second month of storage. During the third month, the RCP values for BN01, BN02 and BN03 were 99.32 ± 0.021, 99.27 ± 0.028, and 99.27 ± 0.022 respectively. The RCP values during month twelve were 99.34 ± 0.018, 99.38 ± 0.022 and 99.41 ± 0.021 for BN01, BN02 and BN03 respectively. $^{99m}$Tc-DMSA complexes showed the RCP values of more than 95% up to one year of storage at 2–8 °C.

Figure 5 shows that the percentage of stannous (II) chloride content in DMSA lyophilized cold kit were 38.48%, 48.50%

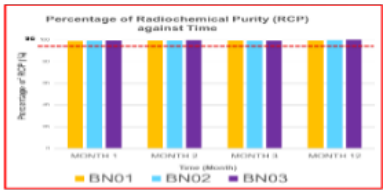



Figure 4: RCP values for all three batches, BN01, BN02 and BN03 of lyophilised DMSA cold kits.

and 53.70% at which the raw material handling condition in open lab, dry cabinet and laboratory glove box respectively. The raw material, stannous (II) chloride tends to be oxidized when is exposed to the atmospheric oxygen. The inert condition in the laboratory glove box contains less oxygen to oxidize the stannous (II) chloride when is compared to open laboratory and dry cabinet. Thus, the percentage of stannous(II) chloride content was higher when it is handled in laboratory glove box.

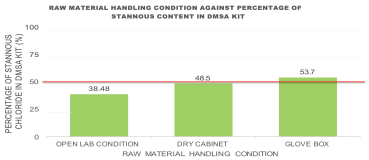



Figure 5: Different raw material handling condition against percentage of stannous (II) chloride in DMSA kit.

## 4 Conclusions

All three batches of DMSA lyophilized cold kit developed in this work is stable up to one year at the recommended storage conditions of 2–8 °C. According to European Pharmacopeia (2005), RCP value should pass above 95%. The $^{99m}$Tc-DMSA complexes showed the RCP values of more than 95% after a year of storage. In addition, the content of stannous (II) chloride in DMSA kit was affected by the way raw materials are handled. The stannous (II) chloride contents that were handled in a laboratory glove box was found to be higher compared to handling in a dry cabinet followed by an open laboratory environment.

## References

Zeki Dostbil, Necmettin Pembegül, Mehmet Küçüköner, Yaar Bozkurt, Ahmet Ali Sancaktutar, Smail Yildiz, and Güven Tekba. 2011. Comparison of split renal function measured by 99mtc-dtpa, 99mtc-mag3 and 99mtc-dmsa renal scintigraphies in paediatric age groups. *Clinical Reviews and Opinions*, 3(2):20–25.

European Directorate for the Quality of Medicines. 2005. Technetium (99mtc) succimer injection. page 865.

International Atomic Energy Agency. 2008. Technetium-99m radiopharmaceuticals: Manufacture of kits. (466):86–88.

Individual Research Contribution Review, 2024: 85–86
*ISSN: 3083-922X*

# Conjugation, Radiolabeling, and Purification of $^{68}$Ga-NOTA-Rituximab: A Step Toward Radioimmunotherapy (RIT)

**Siti Aminah Muhamad**
Medical Technology Division, Malaysian Nuclear Agency
43000 Kajang, Selangor
aminah_m@nm.gov.my

## Abstract

Radioimmunotherapy (RIT) represents a groundbreaking approach in the treatment of non-Hodgkin lymphoma (NHL), combining the specificity of monoclonal antibodies with radioactive isotopes. Rituximab is a chimeric monoclonal antibody directed against the B-lymphocyte-specific antigen CD20, widely used for treating B-cell malignancies. The aim of this study was to develop a radiolabeled form of rituximab to enhance its therapeutic activity. Rituximab was conjugated with p-SCN-Bn-NOTA at molar ratios of 1:10 and 1:50. The conjugated rituximab was collected using preparative high-performance liquid chromatography (HPLC). Subsequently, the conjugated antibody was radiolabeled with $^{68}$Ga and purified using a PD-10 desalting column. Quality control parameters, such as radiochemical purity (RCP) of $^{68}$Ga-NOTA-Rituximab, were determined, and the labeling conditions were optimized. For the 1:10 conjugation ratio, the RCP was 97.34 ± 0.16% prior to purification, which increased to 99.63 ± 0.16% post-purification. Similarly, the 1:50 conjugation ratio showed an RCP of 89.02 ± 2.24% before purification, improving to 99.06 ± 0.01% following purification. From these results, we conclude that rituximab was successfully conjugated with p-SCN-Bn-NOTA, purified via preparative HPLC, and effectively radiolabeled with $^{68}$Ga.

## 1 Introduction

Radioimmunotherapy (RIT) has emerged as a promising strategy in the treatment of non-Hodgkin lymphoma (NHL), integrating the specificity of monoclonal antibodies with the cytotoxic potential of radionuclides. Rituximab, a chimeric monoclonal antibody specific to the CD20 antigen, is widely used as an immunotherapeutic agent in B-cell NHL(Salles et al., 2017). However, repeated cycles of rituximab often lead to resistance, reducing tumour response and resulting in relapse in a significant proportion of patients(Stolz and Schuler, 2009). RIT, in particular, has shown maximum efficacy in the treatment of NHL, as evidenced by preclinical and clinical studies in patients(Steiner and Neri, 2011). Hence, this study aims to develop and optimize the radiolabelling of rituximab with gallium-68 ($^{68}$Ga) to enhance its therapeutic utility in RIT. The conjugation and radiolabelling process with radiochemical purity (RCP) characterization of $^{68}$Ga-NOTA-Rituximab were systematically evaluated to establish a foundation for further preclinical investigations.

## 2 Methods

The NOTA-Rituximab immunoconjugate was synthesized following a protocol similar to Suman et al., [2019], with slight modifications. Rituximab (1 mL, 10 mg/mL) was conjugated with p-SCN-Bn-NOTA at two molar ratios: 1 : 10 and 1 : 50 (Rituximab: p-SCN-Bn-NOTA). The conjugation reaction was carried out in 0.2 M sodium bicarbonate buffer (NaHCO3), pH 9.0. The mixture was allowed to react for 2 hours at room temperature, followed by overnight incubation at 4°C with continuous shaking. Then, the NOTA-Rituximab was purified using preparative-HPLC to remove unreacted and excess of p- SCN-Bn-NOTA. Subsequently, the NOTA-rituximab was radiolabeled with ($^{68}$Ga eluted from a ($^{68}$Ge/$^{68}$Ga generator, and the labelled product was purified using a PD-10 column. To perform the purification, 500 $\mu$L of the reaction mixture was applied to the column, followed by adding 500 $\mu$L L of saline into the PD-10 and each fraction collected and activity determined by dose calibrator. The collected tubes with highest activity of $^{68}$Ga-NOTA-Rituximab were mixed in a pool. The radiochemicalpurity (RCP) of the preparation was determined before and after purification by Instant Thin Layer Chromatography (ITLC).

## 3 Results and Discussion

### 3.1 Determination of retention time (RT) of p-SCN-Bn-NOTA and Rituximab with preparative-HPLC

The successful conjugation of rituximab with p-SCN-Bn-NOTA was confirmed through preparative-HPLC with distinct retention times for the rituximab and p-SCN-Bn-NOTA. The radiolabeling of NOTA- rituximab with $^{68}$Ga was conducted at molar ratios of 1:10 and 1:50, followed by purification using a PD-10 column. Figure 1 presented for preparative-HPLC profile of rituximab and p-SCN-Bn-NOTA, showing their retention times (RT) under specific conditions. A series volume of rituximab from 5−100 $\mu$L has been injected to the preparative-HPLC and the RT appeared at 10.157–10.168 minutes, while p- SCN-Bn-NOTA was appeared at 14.099 minutes. These results confirmed that the two substances have distinct retention times, allowing for the effective separation of Rituximab from the chelator p-SCN-Bn-NOTA during the labeling process.

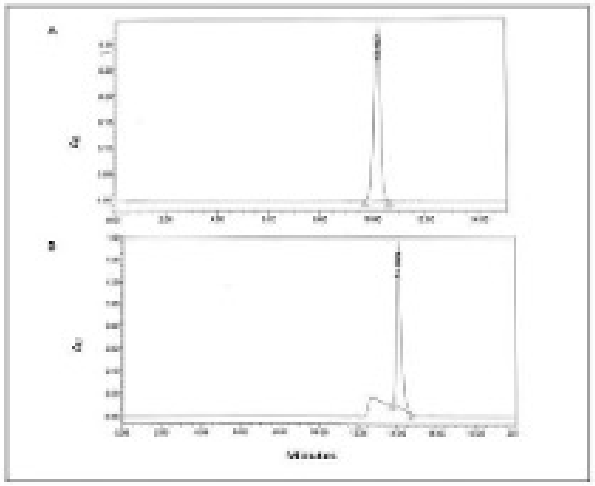


Figure 1: Preparative-HPLC profile (UV, 280 nm) showing A) The retention time (RT) of injected 5µl of rituximab (10 mg/mL) at 10.157 minutes and B) retention time (RT) of injected 5µl of p-SCN-Bn-NOTA at 14.099 minutes. (Flow rate 0.5 mL/min; Solvent 0.05M PBS (pH 6.8) containing 0.05% sodium azide.

### 3.2 Determination of RCP (%) of purified and non-purified radiolabelled Rituximab

The RCP of $^{68}$Ga-NOTA-Rituximab at a 1:10 ratio was determined to be 97.34 ± 0.16% before purification, improving to 99.63 ± 0.16% post-purification. Similarly, for the 1:50 ratio, the RCP was 89.02 ± 2.24% before purification and increased to 99.06 ± 0.01% after purification. This demonstrates that the purification process efficiently removed the free gallium and other impurities, yielding a highly pure radiolabelled rituximab and it showed can be used for in-vivo applications. These findings confirm the efficiency of the radiolabeling and purification processes in producing high-purity $^{68}$Ga-NOTA-Rituximab, making it suitable for potential clinical applications.

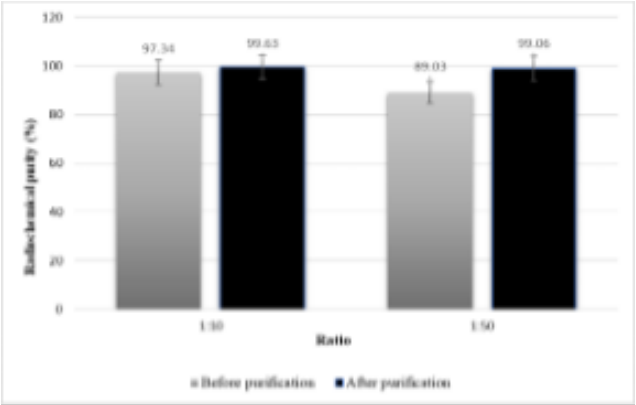



Figure 2: RCP (%) of $^{68}$Ga-NOTA-Rituximab before and after purification with PD-10 column at ratio 1:10 and 1:50

## 4 Conclusions

This study successfully optimized the radiolabeling and purification of $^{68}$Ga-NOTA-Rituximab, demonstrating high RCP, stability, and suitability for further development in radioimmunotherapy applications. These results provide a strong foundation for subsequent preclinical studies, paving the way for potential clinical translation.

## References

Gilles Salles, Martin Barrett, Robin Foà, Joerg Maurer, Susan O'Brien, Nancy Valente, Michael Wenger, and David G Maloney. 2017. Rituximab in b-cell hematologic malignancies: a review of 20 years of clinical experience. *Advances in therapy*, 34:2232–2273.

Martina Steiner and Dario Neri. 2011. Antibody-radionuclide conjugates for cancer therapy: historical considerations and new trends. *Clinical Cancer Research*, 17(20):6406–6416.

Claudia Stolz and Martin Schuler. 2009. Molecular mechanisms of resistance to rituximab and pharmacologic strategies for its circumvention. *Leukemia & lymphoma*, 50(6):873–885.

Shishu Kant Suman, Mythili Kameswaran, Usha Pandey, Haladhar Dev Sarma, and Ashutosh Dash. 2019. Preparation and preliminary bioevaluation studies of 68ga-nota-rituximab fragments as radioimmunoscintigraphic agents for non-hodgkin lymphoma. *Journal of Labelled Compounds and Radiopharmaceuticals*, 62(12):850–859.

Individual Research Contribution Review, 2024: 87–88
*ISSN: 3083-922X*

# Schiff Based Manganese Nanoparticles (MN-L2) As Radiosensitizer On Neutron Therapy Against Breast Cancer Cell

**Siti Selina Abdul Hamid**
Department of Medical Technology, Malaysian Nuclear Agency
43000 Kajang, Selangor
selina@nm.gov.my

## Abstract

Radiotherapy may harm nearby healthy tissues, so radiosensitizers like nanoparticles are used to increase radiation effectiveness on cancer cells while reducing exposure to surrounding healthy areas. This study aims to evaluate the effects of the Schiff-based manganese complex (Mn-L2) as a radiosensitizer in neutron therapy for MCF-7 breast cancer cells. In this study, MCF-7 cells were treated with Mn-L2 NPs, and the optimal concentration was determined through cytotoxicity assay. The cells were then irradiated with neutrons at the TRIGA PUSPATI reactor. The results showed that the optimal non-toxic concentration of Mn-L2 NPs for MCF-7 cells was 0.025 mg/mL and 0.05 mg/mL Irradiated cells treated with Mn-L2 NPs exhibited a significant reduction in colony formation. The SER at 0.025 mg/mL was 2.49, while at 0.05 mg/mL, it was 3.17. These values indicate that the presence of Mn-L2 NPs enhances the radiosensitivity of MCF-7 cells. These findings suggest that Mn-L2 NPs have the potential to act as an effective radiosensitizer in neutron therapy for breast cancer by enhancing the radiation effect on cancer cells while protecting healthy tissues.

**Keywords:** Schiff based manganese nanoparticles, radiosensitizers, neutron therapy, radiotherapy

## 1 Introduction

Breast cancer remains a major global health issue and is the most common cancer among women. In Malaysia, it affects 1 in 19 women, with an incidence rate of 34.1 per 100,000—lower than the 1 in 8 rate reported in the US and Europe. Radiotherapy is a key cancer treatment, but its effectiveness is limited by the maximum dose healthy tissues can tolerate, as higher doses can cause severe radiation toxicity. (Abshire and Lang, 2018). Metal-based nanoparticles are emerging as effective radiosensitizers in cancer treatment, enhancing radiotherapy by increasing tumor damage with minimal side effects. Their small size and biocompatibility make them ideal for targeted therapy. Schiff-based metal complexes have drawn interest among other nanoparticles because of their capacity to strengthen radiosensitization and anticancer effects (Goyal et al., 2021).

## 2 Methods

### 2.1 *Nanoparticles preparation*

The Schiff-based Manganese (Mn-L2) were synthesized in the form of gray-green colour nano-powder. Stock solutions (2mg/mL) of the metal salts Mn (II) and the ligand L2 were prepared by dissolving Schiff based manganese nanoparticles (Mn- L2 NPs) in solvent.

### 2.2 *Cell culture*

MCF-7 cell line was maintained in Dulbecco's Modified Eagle's Medium (DMEM) supplemented with 10% of fetal bovine serum and L-Glutamine in humidified and 5% CO2 at 37 °C.

### 2.3 *Cytotoxicity assay*

The study evaluated cell viability using various Mn-L2 NP concentrations (0.025–0.6 g/mL) and incubation times (24, 48, and 72 hours). Cells were plated in 96-well plates, treated with PrestoBlue Cell Viability Reagent, and absorbance was measured using a Multiskan$^{TM}$ FC Microplate Reader.

### 2.4 *Cells irradiation and Cologenic assay*

MCF-7 cells were treated with 0.025 mg/mL and 0.05 mg/mL concentrations of Mn-L2 NPs and exposed to neutron irradiation at the TRIGA PUSPATI Reactor, Agensi Nuklear Malaysia, with a constant dose rate and radiation doses ranging from 0 to 3 Gy. After irradiation, the cells were re-cultured in 6-well plates for 4 days, then fixed and stained with crystal violet. Visible colonies were counted to assess cell survival.

### 2.5 *Cell survival and data analysis*

The cell survival was analyzed by calculating the survival fraction from the cell colonies according to equation (1). The survival fraction for samples with and without Mn-L2 NPs were then plotted and fitted according to the linear quadratic model (LQ) model using OriginPro 2024 software. The sensitization enhancement ratio (SER) was determined from the survival curves by comparing the radiation dose required for 80% survival in control cells versus those treated with Mn-L2 NPs, as shown in Equation (2).

$$\text{Survival fraction} = \frac{\text{Number of irradiated cell colonies}}{\text{Number of control cell colonies}} \quad (1)$$

$$\text{SER}_{80} = \frac{D8_0 \text{ control}}{D8_0 \text{ Mn-L2 NPs}} \quad (2)$$

## 3 Results & Discussion

The cytotoxic effects of Mn-L2 NPs on MCF-7 cells are presented in Figure 1. After 24 hours of incubation, percentages of cell viability are 99.36%, 100%, and 102.27% for concentrations of 0.025 mg/mL, 0.05 mg/mL, and 0.1 mg/mL, respectively. However, cell viability declined after 48 and 72 hours. Based on the cytotoxicity assessment, the optimal concentrations of Mn-L2 NPs for MCF- 7 cells are 0.025 mg/mL and 0.05 mg/mL, as both maintain cell viability within the range of 80% to 100%. In contrast, 0.1 mg/mL exceeded 100% viability at 24 hours, falling outside the desired range. Although its viability later declined. Mn-L2 NPs at 0.025 mg/mL and 0.05 mg/mL are considered the most suitable, as they are biocompatible and do not exhibit substantial long-term cytotoxic effects on MCF-7 cells.

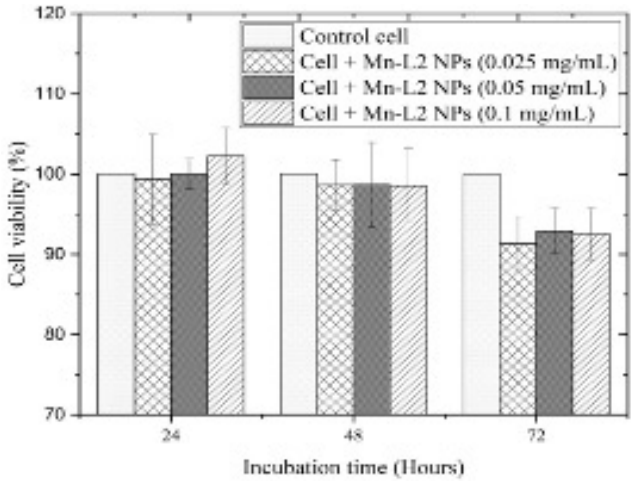



Figure 1: Percentage of cell viability measured for different concentration of Mn-L2 NPs of incubation.

Figure 2 shows that cell survival decreases with increasing radiation dose, with a greater reduction in cells treated with Mn-L2 NPs. The steeper survival curve at 0.05 mg/mL compared to 0.025 mg/mL indicates stronger radiosensitization at the higher concentration.

The results indicate that Mn-L2 NPs effectively enhance radiosensitivity in MCF-7 cells, with SER values obtained for treated cells at concentrations of 0.025 mg/mL and 0.05 mg/mL are 2.49 and 2.80, respectively. A higher SER value at 0.05 mg/mL suggests a more effective radiosensitization effect, as it requires a lower radiation dose to achieve the same level of cell survival. These findings confirm that Mn-L2 NPs play a significant role in enhancing the radiation response of breast cancer cells in neutron therapy.

## 4 Conclusion

This study highlights the potential of Schiff based manganese nanoparticles (Mn-L2 NPs) as effective radiosensitizers in neutron therapy for MCF-7 breast cancer cells. In vitro experiments demonstrated that Mn-L2 NPs effectively increase cancer cell sensitivity to neutron radiation. The combination

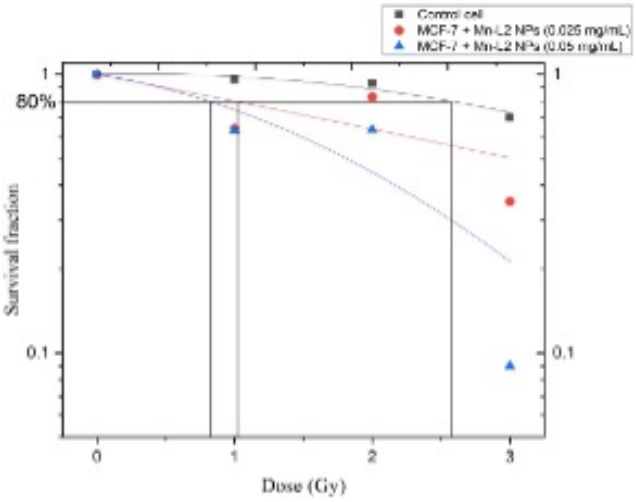



Figure 2: Cell survival curve with SER 80% extrapolation.

of Mn-L2 NPs with neutron irradiation enhances radiotherapy efficiency at lower doses, reducing potential side effects.

## References

D. Abshire and M. K. Lang. 2018. The evolution of radiation therapy in treating cancer. *Seminars in Oncology Nursing*, 34(2):151–157.

Serhat Aras. 2024. Radiation protection and radiobiology. *Radiology and Molecular Imaging*, 1(2):26–30.

Samta Goyal, Usha Bansal, and Swati Agrawal. 2021. Biologically active schiff base nanoparticles: A review. *Eur. J. Biomed. Pharm. Sci*, 8:244–252.

Individual Research Contribution Review, 2024: 89–90
*ISSN: 3083-922X*

# Functionalization Of Gold Nanoparticles with Irradiated Chitosan ($^{68}$Ga-DOTA-CHITOSAN-AuNPs) For Tumor Imaging

**Wan Hamirul Bahrin Wan Kamal**
Medical Technology Division, Malaysian Nuclear Agency
43000 Kajang, Selangor
mirul@nm.gov.my

## Abstract

Functionalization of gamma radiation-treated chitosan with, gold nanoparticles (AuNPs), and 1,4,7,10- Tetraazacyclododecane-1,4,7,10-tetraacetic acid mono-N- hydroxysuccinimide ester (DOTA-NHS) affords an innovative new imaging agent with potential applications in molecular imaging and therapy. The preparation involves the production and full characterization of gamma-treated chitosan (MW; 10,000 Da), via gamma ($\gamma$) rays (100 kGy) irradiation, followed by encapsulation of gold nanoparticles to produce Chitosan-AuNPs (CHI-AuNPs). CHI-AuNPs were then conjugated with DOTA-NHS to yield DOTA-CHI-AuNPs followed by purification process and finally radiolabelling with Ga-68. Percentage of Radiochemical Purity (%RCP) of $^{68}$Ga-DOTA-CHI-AuNPs were found to be > 90% for up to five hours analyzed by using radio-UHPLC.

**Keywords:** gamma radiation treated chitosan, gold nanoparticles (AuNPs), DOTA conjugation, radiolabelling, radio-UHPLC

## 1 Introduction

Cancer cases and mortality in Malaysia and globally will continue to rise. These increases in cancer mortality rates are due to a lack of early detection and subsequent treatment. AuNPs are attractive as materials for use in medicine, since they are inert, biocompatible and can be easily modified with surface capping ligands. The coating of AuNPs with chitosan is advantageous as it can improve colloidal stability as well as impart desirable properties like non-toxic, biodegradability, and biocompatibility. Furthermore, these surface modifications allow for further functionalization with bioactive moieties, therapeutics and imaging agents. Chitosan molecules contain high numbers of reactive hydroxyl (-OH) and amino (-$NH_2$) groups. Its hydroxyl and amine groups make it an ideal carrier material in the construction of chitosan-drug conjugates. Hence it has been used as a gold nanoparticles coating, applied during synthesis or after synthesis, for various biomedical applications such as photothermal therapy, drug delivery, gene delivery and sensing.

## 2 Methods

Two types of gold nanoparticles (AuNPs), 20 and 50 nm, were coated with 0.002% chitosan solution at pH 3.0 and 5.5, which had previously been irradiated with a gamma ray source at varying radiation doses of 25, 50, and 100 kGy. Chitosan's molecular weights were 43, 28, and 10 kDa, respectively. A chemical reduction procedure at 85 °C for four hours was used to coat a mixture of chitosan solution and AuNPs solution, which was regulated by a silicone oil-based synthesis reactor heating equipment. The mixed solution was filtered and transferred to a centrifuge tube and the centrifuge process was carried out for at least three hours at a speed of 5000 rpm. The supernatant was dried by using the freeze-drying method to obtain the chitosan coated AuNPs (CHI-AuNPs) product. The filtered mixed solution was examined for its properties using a dynamic scattering technique to characterize the size and charge of the material formed. The synthesis of DOTA-CHI-AuNPs derivative was then carried out by mixing the CHI-AuNPs and DOTA-NHS at molar ratio of CHI-AuNPs:DOTA-NHS (1:2). The adding of TEA (30 µL) into the CHI-AuNPs solution first and sonicated for fifteen minutes was to activate the NH2 ankle at the chitosan site. DOTA-NHS solution was added into the CHI-AuNPs. The mixture was regulated to pH 8-9 by using the 1.0 M HCl, followed by stirring over night at 4 °C. The mixture has undergone the purification process by using the MWCO 3,500 Da membrane cassette for three days with LC-MS water changed (every day). The final purified solution of DOTA-CHI-AuNPs was extracted from the cassette for further step. The purified DOTA-CHI-AuNPs was radiolabeled with Ga- 68 as follow: 0.34 mg of dried DOTA-CHI-AuNPs was dissolved with 1000 µl LC-MS water and vortexed as stock solution. 50 µl of the stock solution was mixed with 55.5 - 62.9 MBq (1.5-1.7 mCi) in 1.0 ml of [$^{68}$Ga]GaCl3 fresh eluate from the $^{68}$Ge/$^{68}$Ga generator. The solution was added with 60.0 µl of 1.0 M sodium acetate (NaOAc), stirred and measured the pH as 3.9-4.0. The mixture was then heated at 95 °C for fifteen minutes. The filtered radiolabelled DOTA- CHI-AuNPs (20-30 µl) was then



Figure 1: $^{68}$Ga-DOTA-CHI-AuNPs injection into the radio-UHPLC with radioactivity detector

injected into the radio- UHPLC (Waters Acquity Arc UHPLC connected with Elysia Gabi radioactivity detector, Empower 3 software) to gain the percentage of Radiochemical Purity (% RCP) at hourly incubation at room temperature (Fig. 1).

## 3 Results

The study's findings revealed that the pH parameter of the chitosan solution played a significant effect in the development of the chitosan-coated AuNPs. In chitosan solution with pH 3.0, the size was approximately 42-47 nm, whereas in chitosan solution with pH 5.5, the size was around 75-78 nm. Finally, the ideal volume for the creation of chitosan-coated AuNPs was 0.002% chitosan solution due to the consistency of the nanoparticle size at the variety of the molecular weight and the size of the AuNPs. These nanoparticles were also positively charged at 26-30 mV (Fig. 2).

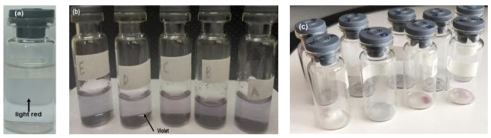



Figure 2: The process of preparing samples and producing chitosan coated AuNPs: (a) mixed solution of chitosan and AuNPs; (b) chitosan coated AuNPs solution; (c) chitosan coated AuNPs freeze-dried powder

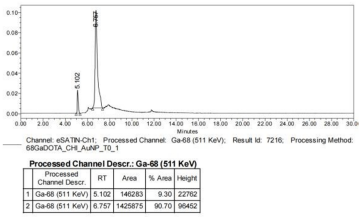



Figure 3: The radio-UHPLC chromatogram of free $^{68}$Ga at retention time (RT) of 5.103 min (9.30%) and $^{68}$Ga-DOTA-CHI- AuNPs at 6.757 min (RCP; 90.70%).

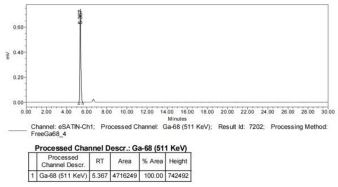



Figure 4: The radio-UHPLC chromatogram of free $^{68}$Ga at RT of 5.367 min.

Figure 3 showed good peak separation obtained from the radio-UHPLC chromatogram between the free Ga-68 at 5.103 minutes and $^{68}$Ga-DOTA-CHI-AuNPs at 6.757 minutes. At separate injection intervals, only free Ga-68 solution was injected into the radio-UHPLC, which gave the RT of 5.367 minutes (Fig. 4). The calculation of the %RCP for the labelled compound is done by the percentage of AUC (area under curve) of radiolabeled compound over the total peaks available (stated as % Area in the chromatogram table, Fig. 3&4).

Table 1 showed the %RCP stability data was conducted for up to five hours. The %RCP remains > 90% of up to five hours stored at room temperature.

| **Stability study** | **% RCP, Hr (s)** | | | | | |
|---|---|---|---|---|---|---|
| | **0** | **1** | **2** | **3** | **4** | **5** |
| $^{68}$Ga-DOTA-CHI-AuNP | 90.70 | 91.47 | 92.06 | 91.72 | 91.65 | 93.47 |

Table 1: Stability study of $^{68}$Ga-DOTA-CHI-AuNP over time

## 4 Discussion

The most suitable CHI-AuNPs with certain characteristics have been selected from the experiment based on molecular weight (MW), which in this study was 10,000 Da. Both gamma irradiation and electron beam have been used, and the most optimum MW treatment was found to be by using the gamma irradiation.

Producing the final product of CHI-AuNPs has its own challenge, especially in terms of the yield. Few attempts have been carried out, but only to gain about 0.3 to 0.8 mg per cycle.

The conjugation work followed by the purification process using the MWCO membrane cassette was time-consuming (2-4 days). Few attempts were done by using the preparative HPLC, but due to the low concentration of DOTA-CHI-AuNPs, the final product was found to be too diluted and failed to proceed to the next step.

The radiolabelling work was successfully done with > 90% of RCP. In this study, we have established the gradient method (radio-UHPLC) by changing the ratio mixing between the acetonitrile (ACN) and water (LC-MS water), both added 0.1% TFA. Good peak separation between free Ga-68 and labelled compound was seen, and the labelled compound peak presented as one solid peak without any other impurities detected (Fig. 3). The stability study also proved that the labeled compound was stable for up to five hours (five half-lives of the Ga-68).

## 5 Conclusion

This preliminary work has demonstrated that the gamma irradiation was feasible to produce the optimum MW (10,000 Da) of the chitosan, followed by the encapsulation process with AuNPs to produce CHI-AuNPs.

The CHI-AuNPs were easy to conjugate with the DOTA linker and provided a good %RCP radiolabeled with Ga-68. The %RCP was found to be > 90% for up to five hours, indicating the potential to be a good radiopharmaceutical preparation.

Further investigation needs to be done, such as mass quantification (LC-MS) and chemical structure analysis (NMR) on the DOTA-CHI-AuNPs. It is also recommended to add in a feature of targeting to this compound, such as peptide (PSMA, somatostatin, etc.) or antibody (rituximab, trastuzumab, etc.), and it will make it possible to reach the cancer site.

To add in, the use of the radio-UHPLC method was so much more convenient, with high accuracy, reproducible data, and the ability to reduce a significant amount of radiation exposure to the researcher as compared to the radio-TLC method.

Individual Research Contribution Review, 2024: 91–92
*ISSN: 3083-922X*

# Exploring the Potential of Gamma Irradiation for Effective Newcastle Disease Virus (NDV) Inactivation

**Zainah Adam**
Medical Technology Division, Malaysian Nuclear Agency
43000 Kajang, Selangor
zainah@nm.gov.my

## Abstract

Inactivated vaccines often rely on chemical agents like formaldehyde and beta-propiolactone, which are associated with safety concerns and reduced immunogenicity. Gamma irradiation offers a promising alternative for viral inactivation. This study investigated the effects of gamma irradiation (0 – 25 kGy) on the Newcastle disease virus (NDV) titer. Hemagglutination (HA) assays revealed a twofold reduction of NDV titer at gamma dose of 5 kGy and a fourfold reduction at higher doses (10 – 25 kGy). Hemagglutination inhibition (HI) assays showed no inhibition in either irradiated or non-irradiated NDV, potentially due to anti-NDV antibody specificity limitations. These findings highlight gamma irradiation as a viable method for NDV inactivation, warranting further optimization for in-activated vaccine development.

**Keywords:** Inactivated vaccine, Newcastle disease virus, gamma radiation

## 1 Introduction

Vaccines are biological preparations that stimulate the immune system to recognize and combat pathogens, providing active acquired immunity against specific diseases. Various vaccine types, including inactivated, live-attenuated, mRNA, subunit, recombinant, and conjugated vaccines, have been developed to address diverse infectious disease (Saxena and Rawat, 2013);(World Health Organization (WHO), 2023). Inactivated vaccines are widely utilized for their safety and stability, often achieved through chemical inactivation using agents like formaldehyde and beta- propiolactone. However, these methods present limitations, such as potential residual toxicity, allergic reactions, and reduced immunogenicity due to alterations in antigenic structures. These drawbacks highlight the need for safer, more effective inactivation methods (Delrue et al., 2012). Gamma irradiation has emerged as a promising alternative, capable of inactivating pathogens by damaging their nucleic acids without compromising antigenic properties. This method preserves critical protein structures essential for immune recognition, ensuring effective immune responses (Seo, 2015). In this study; we used the Newcastle disease virus (NDV) as the pathogen model to prove that gamma radiation is capable of inactivating the pathogen, and can subsequently be used as the vaccine candidate.

## 2 Methods

### 2.1 Propagation and gamma irradiation of NDV

Newcastle disease virus (NDV) seed from Universiti Putra Malaysia was propagated in 10-day-old embryonated chicken eggs by inoculating 20 HAU into the allantoic cavities and incubating at 37 °C for 48 hours. Harvested NDV was pooled, stored at −80 °C, and divided into seven groups. Each group was irradiated with cobalt-60 gamma rays at doses of 0, 3, 5, 10, 15, 20, and 25 kGy at the SINAGAMA facility (Seo, 2015).

### 2.2 Hemagglutination assay (HA)

A serial dilution of NDV was performed in a V-shaped microtiter plate using 25 $\mu$L of phosphate-buffered saline (PBS, pH 7.5). NDV (25 $\mu$L) was added to well 1 and serially transferred through well 11, discarding 25 $\mu$L from the final well. Each well received 25 $\mu$L of PBS and 1% red blood cell (RBC) suspension. After 30-minute incubation, hemagglutination (HA) was identified by a hazy film, while a sharp RBC button indicated no HA (World Organization for Animal Health (OIE), 2021).

### 2.3 Hemagglutination inhibition assay (HI)

Phosphate-buffered saline (PBS, pH 7.5, 25 $\mu$L) was added to all wells of a V-shaped microtiter plate. Antibody suspension (25 $\mu$L) was serially diluted from well 1 to 11, discarding 25 $\mu$L from well 11. Virus suspension (4 HA units, 25 $\mu$L) was added to each well and incubated for 30 minutes. Following this, 1% red blood cell (RBC) suspension (25 $\mu$L) was added and incubated. Hemagglutination inhibition (HI) was indicated by a sharp RBC button (World Organization for Animal Health (OIE), 2021).

## 3 Results and Discussion

Hemagglutination assay was conducted to quantify the active NDV after irradiation process. Figure 1 presents the results of hemagglutination (HA) analysis of NDV following gamma irradiation at various doses. Clear hemagglutination indicates active NDV, while a sharp red button signifies inactivated NDV. In the control and at 3 kGy, hemagglutination was observed up to a 1:1024 dilution, corresponding to an NDV titer of 40,960 HAU/mL. At 5 kGy, hemagglutination was detected up to a 1:512 dilution, indicating an NDV titer of 20,480 HAU/mL. At higher doses (10 – 25 kGy), hemagglutination was limited to a 1:256 dilution, yielding an NDV

titer of 10,240 HAU/mL. These findings demonstrate that low doses of gamma irradiation (5 kGy) reduce the NDV titer by 2-fold, while higher doses (10 – 25 kGy) result in a 4-fold reduction in NDV titer.

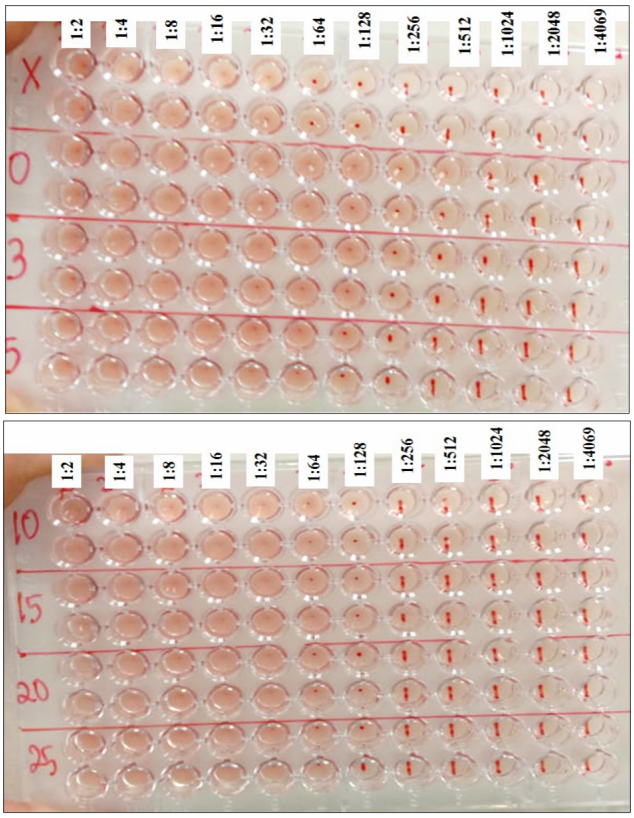



Figure 1: Hemaglutination assay results of the irradiated NDV. (Virus used 25 $\mu$L)

The hemagglutination inhibition (HI) assay was performed to evaluate the presence and integrity of the hemagglutinin-neuraminidase (HN) protein, a key antigenic determinant of Newcastle disease virus (NDV). The assay is based on the principle that anti-NDV antibodies bind specifically to the HN protein, preventing viral attachment to red blood cells (RBCs) and resulting in the formation of a red button at the bottom of the well. The results of the HI assay for NDV irradiated with gamma rays at doses ranging from 0 to 25 kGy are presented in Figure 2. No red button was observed in any well across all dose groups, indicating hemagglutination inhibition in all cases. At 0 kGy, the absence of a red button was unexpected, as the HN protein should remain intact. This anomaly may be attributed to the non- specificity of the anti-NDV antibodies used in the assay. Similarly, the absence of a red button at 3 – 25 kGy may result from the same issue of antibody non-specificity or potential degradation of the HN protein due to gamma irradiation. The degradation of the HN protein at higher doses is particularly concerning, as this protein is crucial for inducing protective immunity in vaccines. The loss of HN protein integrity undermines the immunogenic potential of the virus, rendering the inactivation process unsuitable for vaccine production. To conclusively determine the integrity of the HN protein post- irradiation, further validation through Western blot analysis is necessary. This step is essential to confirm the structural preservation of the HN protein and assess the feasibility of gamma-irradiated NDV for vaccine applications.

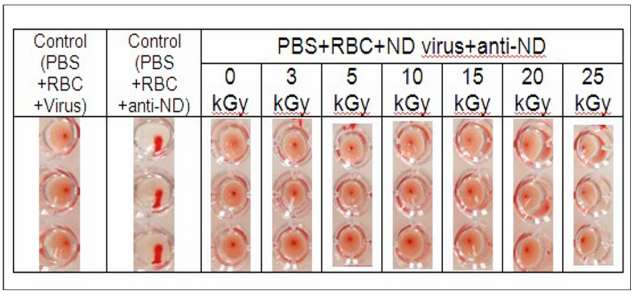



Figure 2: Hemagglutination inhibition analyses of irradiated NDV

## 4 Conclusion

The study demonstrates that gamma irradiation effectively reduces NDV titer, with higher doses causing greater reductions. However, the absence of hemagglutination inhibition across all doses raises concerns about HN protein integrity, likely due to antibody non-specificity or protein degradation. Further confirmation via Western blot is crucial for confirmation of findings

## References

Delrue, Dieter Verzele, Annemieke Madder, and Hans J Nauwynck. 2012. Inactivated virus vaccines from chemistry to prophylaxis: merits, risks and challenges. *Expert Review of Vaccines*, 11(6):695–719, DOI: 10.1586/erv.12.38.

Jyoti Saxena and Shweta Rawat. 2013. Edible vaccines. *Advances in biotechnology*, pages 207–216. doi: 10.1007/978–81– 322–1554–712. PMCID: PMC7120417.

HS. Seo. 2015. Application of radiation technology in vaccines development. *Clin Exp Vaccine Res.*, 4(2):145–148.

World Health Organization (WHO). 2023. Vaccine development process and types. Accessed: 2025-06-17.

World Organization for Animal Health (OIE). 2021. Manual of diagnostic tests and vaccines for terrestrial animals: Hemagglutination and hemagglutination inhibition test. Accessed: 2025-06-17.

Individual Research Contribution Review, 2024: 93–94
*ISSN: 3083-922X*

# Physicochemistry Studies on Irradiation-Induced Biochar Recovery from Empty Fruit Bunch via Microwave Pyrolysis

**Ahmad Zuhdi Mohd On**
Radiation Processing Technology Division, Malaysian Nuclear Agency
43000 Kajang, Selangor
zuhdi@nm.gov.my

## Abstract

This study explores the physicochemical transformations of biochar derived from empty fruit bunches (EFB) using microwave pyrolysis and gamma irradiation. FTIR spectroscopy highlights significant functional group modifications during carbonization and irradiation, including the reduction of O-H and C=O groups due to dehydration and decarboxylation. The biochar exhibits increased aromaticity, with stable aromatic C=C bonds and enhanced inorganic functional groups such as Si-O-Si at higher irradiation doses. These findings demonstrate the potential of combining microwave pyrolysis with irradiation to optimize biochar properties for environmental and industrial applications, contributing to sustainable agricultural waste valorisation.

**Keywords:** Biochar, Empty Fruit Bunch, Physicochemistry.

## 1 Introduction

Biochar derived from agricultural residues like empty fruit bunches (EFB) offers a sustainable solution for waste management and environmental applications, including carbon sequestration and pollutant adsorption. Microwave pyrolysis, a thermal decomposition method characterized by rapid and uniform heating, has shown promise in optimizing biochar yield and quality (Lam et al., 2017; Demirbas, 2009). However, enhancing biochar properties for specific applications often requires post-treatment methods. Gamma irradiation, which can modify surface chemistry, increase porosity, and introduce functional groups, has been successfully applied to other carbon-based materials to improve their adsorptive capacities and chemical reactivity (Ahmed and Hameed, 2018; Fan et al., 2020). Integrating electron beam irradiation with microwave pyrolysis offers a novel approach to producing high-performance biochar, yet this combination remains underexplored. This study investigates the physicochemical changes induced by gamma irradiation on microwave-pyrolyzed biochar from EFB, contributing to sustainable waste valorization technologies.

## 2 Materials and Methods

Empty fruit bunches, an abundant byproduct of the palm oil industry, were pretreated and subjected to microwave pyrolysis under controlled conditions to produce biochar. Post-pyrolysis, the biochar samples were irradiated with electron beam irradiation at varying doses from 0-15kGy of interval 5kGy. The physicochemical properties of the irradiated biochar, including surface area, porosity, thermal stability, elemental composition, and functional groups, were analyzed using techniques such as Scanning Electron Microscope, FTIR spectroscopy, and Thermal Gravimetric Analysis.

## 3 Results and Discussion



Figure 1: Physical appearance of EFB at 0 kGy for: a) 1 mins b) 2 mins c) 3 mins d) 4 mins

Figure 1 shows that the physical appearance of biochar of EFB after undergo pyrolysis. Based on the physical appearance, the EFB biochar was started to undergo pyrolyzed at 2 mins where the sample was partially pyrolyzed until 3 minutes. The sample depicted to fully pyrolyzed at 4 minutes. The pyrolysis process beyond 4 minutes leads to the formation of ash where the carbon might undergo degradation and the collapse of lignin structure.

| **Residence time for pyrolysis (min)** | **Percentage weight loss at range of dose (%)** | | | |
|---|---|---|---|---|
| | **0 kGy** | **5 kGy** | **10 kGy** | **15 kGy** |
| 1 | 12.27 | 15.41 | 16.42 | 17.99 |
| 2 | 19.15 | 20.06 | 21.22 | 22.30 |
| 3 | 18.56 | 19.06 | 20.44 | 21.01 |
| 4 | 17.18 | 18.10 | 18.92 | 19.73 |
| 5 | 16.50 | 17.71 | 18.48 | 19.35 |

Table 1: Residence time for pyrolysis with the effect of irradiation dose

The analysis of weight loss yielded significant findings re-

garding both the impact of irradiation and the types of materials used. Table 1 demonstrate that the increase in weight loss percentage correlates with the duration of the sample's residence time in the pyrolysis process. Longer residence times indicate higher process temperatures, which in turn result in greater weight loss. This relationship indicates that the absorption of electromagnetic waves by the samples triggers intense molecular collisions, thereby elevating sample temperatures. The optimal residence time for pyrolysis of EFB was found to be 2 minutes where the biochar produced was fully pyrolyzed and the weight depicted as the highest at 4 minutes. Additionally, higher levels of irradiation led to increased weight loss due to the breakdown of molecular weight, indicating that the samples underwent degradation prior to the pyrolysis process.

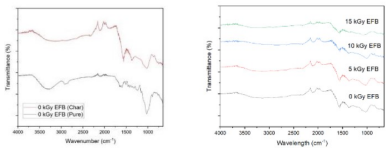



Figure 2: FTIR spectrum of controlled EFB pure and biochar and FTIR spectrum of dose exposure range of EFB Biochar.

The FTIR analysis reveals significant changes in the functional groups of EFB and its derived biochar, emphasizing the transformations occurring during carbonization and irradiation. In pure EFB, prominent peaks corresponding to functional groups such as O–H (3500–3000 $cm^{-1}$), C–H (3000–2750 $cm^{-1}$), C=O (1750–1700 $cm^{-1}$), and C–O (1250–1000 $cm^{-1}$) were observed are present. These groups, associated with organic compounds, diminish or disappear upon carbonization, with the reduction in O-H and C=O intensities indicating dehydration and decarboxylation processes (Arshad et al., 2019). For biochar irradiated at varying doses, the aromatic C=C peak near 1600 $cm^{-1}$ remains consistent, while the O–H stretching intensity around 3500 $cm^{-1}$ shows noticeable variation decreases with increasing dose, reflecting the removal of hydroxyl groups through dehydration (Larasati et al., 2019).

Notable changes in biochar from different biomass sources are observed. For example, rice husk biochar shows the disappearance of O-H and aliphatic C-H stretching bands due to pyrolytic decomposition of reactive hydroxyl groups and aliphatic compounds. Peaks at approximately 1600–1700 $cm^{-1}$ indicate aromatic C=O and lignin C=C stretching, signifying the development of stable carbon structures during pyrolysis. Unique peaks in rice husk biochar, such as 1090 $cm^{-1}$ (Si–O–Si) and 788 $cm^{-1}$ (Si–H), highlight the presence of silica-derived functional groups (Kalaivani, 2019).

Across varying biochar doses, significant alterations in functional group intensity are minimal, though Si–O–Si bonds within 1250–1000 $cm^{-1}$ exhibit proportional increases with higher irradiation doses. These results suggest that irradiation enhances specific inorganic functional groups without drastically altering the overall biochar structure, supporting its potential for tailored applications.

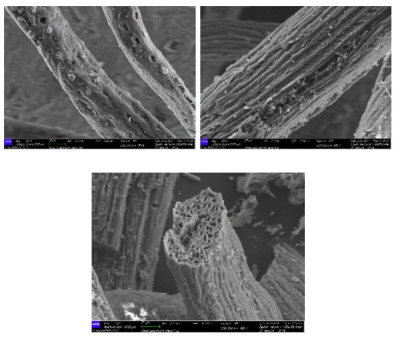


Figure 3: The SEM for pure and biochar EFB with various irradiation dose ; a) pure EFB b) biochar 0kGy c) biochar 15kGy

The corrugated morphological surface for both type of materials was observed in the FESEM image to compared with untreated fibre. The irradiation treatment was clearly seen at the 15kGy of RH where expected cellulose part was disappear leading to the wavy morphological surface.

## 4 Conclusions

The integration of microwave pyrolysis and gamma irradiation effectively enhances the physicochemical properties of biochar derived from EFB. FTIR analysis confirms structural transformations, such as decreased hydroxyl and carboxyl groups, increased aromaticity, and the development of inorganic functional groups, particularly at higher irradiation doses. These modifications improve biochar's stability and functionality, making it suitable for applications in carbon sequestration, pollutant adsorption, and soil enhancement. This study underscores the viability of this combined approach as a sustainable strategy for agricultural waste management and high-value biochar production.

## References

M. J. Ahmed and B. H. Hameed. 2018. Effect of gamma irradiation on adsorption and surface properties of activated carbon. *Radiation Physics and Chemistry*, 151:94–101.

A. Demirbas. 2009. Agricultural waste as a biomass resource for energy and chemical products. *Energy Sources, Part A: Recovery, Utilization, and Environmental Effects*, 31(16):1450–1461.

S. Fan, X. Li, Q. Chen, et al. 2020. Surface functional group modification of biochar with gamma-ray irradiation for improved heavy metal adsorption. *Environmental Research*, 182:109092.

T. Kalaivani. 2019. Structural analysis of silica-rich biochar from rice husks using ftir and xrd techniques. *Environmental Science and Pollution Research*, 26(12):11587–11596.

S. S. Lam, R. K. Liew, A. Jusoh, et al. 2017. Microwave pyrolysis valorization of waste palm shell into biochar with optimized surface area for solid fuel applications. *Bioresource Technology*, 246:167–172.

Individual Research Contribution Review, 2024: 95–96
*ISSN: 3083-922X*

# Innovative UV-Blocking Packaging Materials Derived from Banana Peel Waste Using Radiation Crosslinkings

**Farah Fadzehah Hilmi**
Radiation Processing Technology Division, Malaysian Nuclear Agency
43000 Kajang, Selangor
farah@nm.gov.my

## Abstract

This study focuses on the development of UV-blocking bioplastic packaging made from banana peel waste and polyvinyl alcohol (PVA). The film was crosslinked using electron beam radiation. A polyvinyl alcohol /sago starch film was also prepared for comparison purposes. The addition of the banana peel in the film was compared in terms of visual observation and UV blocking properties. the banana peel bioplastic exhibits high absorbance in the UV range (200–400 nm) and visible light, with a notable value of 0.97 at 671 nm, indicating strong light-blocking capabilities. This property makes it ideal for preserving the quality of light-sensitive products throughout their shelf life. The use of agricultural waste and radiation technology enhances its biodegradability, mechanical strength, and sustainability, offering a cost-effective and eco-friendly alternative to conventional plastic packaging.

**Keywords:** Radiation crosslinked, UV block packaging, Banana peel waste.

## 1 Introduction

The increasing environmental concerns about conventional plastic waste and its adverse impacts on ecosystems have driven global efforts toward the development of sustainable and biodegradable alternatives. Bioplastics, derived from renewable sources, offer a promising solution to address these challenges. Among various biopolymer materials, polyvinyl alcohol (PVA) has gained attention due to its biodegradability, non-toxicity, and excellent film-forming properties (Hilmi et al., 2019). However, the enhancement of its mechanical, thermal, and functional characteristics remains a critical area of research. This study introduces an innovative approach to fabricating UV-blocking bioplastics by leveraging banana peel waste as a sustainable additive and utilizing electron beam for crosslinking. Banana peel, an agricultural by-product often considered waste, is rich in bioactive compounds such as polyphenols, flavonoids, and antioxidants. These compounds exhibit intrinsic UV-blocking properties, making banana peel an excellent candidate for enhancing the functionality of PVA-based bioplastics (Ahmed and Abbas, 2019). Additionally, the use of banana peel aligns with the principles of circular economy and waste valorization, turning an underutilized resource into a value-added material. Integrating banana peel extracts into PVA not only improves the film's UV resistance but also contributes to the overall biodegradability of the composite material. The crosslinking process is a critical step in the development of bioplastics to improve their mechanical strength and thermal stability.

Traditional chemical crosslinking methods often require hazardous agents, posing risks to health and the environment. In contrast, radiation-induced crosslinking using electron beam offers a cleaner, more sustainable alternative. Radiation facilitates the formation of stable covalent bonds between polymer chains without the need for chemical additives, ensuring the safety and eco-friendliness of the process. Furthermore, this method allows precise control over the degree of crosslinking, enabling tailored properties for specific applications. In this study, we explore the synergistic effects of banana peel waste incorporation and radiation crosslinking on the properties of PVA-based bioplastics. The developed bioplastic films were characterized for UV-blocking efficiency. Our findings demonstrate that the addition of banana peel significantly enhances the UV resistance of the films, while radiation crosslinking improves their structural integrity and performance under various conditions. These improvements make the fabricated bioplastic suitable for applications in packaging, agriculture, and other fields requiring UV protection.

## 2 Materials and Methods

### 2.1 Fabrication of the biodegradable plastic packaging

The banana peel waste was thoroughly cleaned and patted dry using tissue paper to eliminate any contaminants or debris. The clean peel was then cut into small pieces and dried in an oven at 60°C for 24 hours. Once dried, the banana peel waste was ground using a fine grinder to obtain a fine powder. This powder was subsequently mixed with distilled water to prepare a 10% (w/v) aqueous solution.The resulting banana peel solution was combined with a 10% (w/v) polyvinyl alcohol (PVA) solution at a ratio of 70:30 (banana peel solution:PVA). The PVA was incorporated to enhance the mechanical properties of the biodegradable plastic. The mixture was then cast onto a petri dish and subjected to electron beam irradiation at 30kGy using an EPS 3000 system. The process is illustrated as below Figure 1.

Figure 1 shows that the physical appearance of biochar of EFB after undergo pyrolysis. Based on the physical appearance, the EFB biochar was started to undergo pyrolyzed at 2 mins where the sample was partially pyrolyzed until 3 minutes. The sample depicted to fully pyrolyzed at 4 minutes.



Figure 1: Preparation process of banana peel waste

The pyrolysis process beyond 4 minutes leads to the formation of ash where the carbon might undergo degradation and the collapse of lignin structure.

### 2.2 Evaluation of the UV-Vis properties

The UV-Vis properties of the film were characterized using a UV-Vis spectrophotometer over the wavelength range of 200–800 nm. The casted film was cut in the dimensions of 1 cm x 3 cm was placed in a film holder to ensure optimal light penetration and minimize scattering effects. Baseline correction was performed using an empty film holder as a reference. Absorbance spectra were recorded to evaluate the film ability to filter UV and visible light. The cast film then was compared to the polyvinyl alcohol/sago starch film.

## 3 Results and Discussion

The physical properties of PVA/SS (polyvinyl alcohol/sago starch) and PVA/BP (polyvinyl alcohol/banana peel) films differ significantly based on visual observation as in below Figure 2.

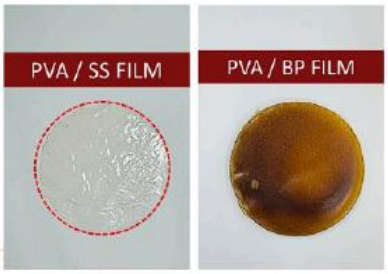



Figure 2: Observation of physical properties of PVA/SS and PVA/BP film.

The PVA/SS film appears transparent with a smooth surface, indicating good miscibility between PVA and sago starch, though slight surface wrinkles suggest minor phase separation during drying. In contrast, the PVA/BP film is opaque with a brownish hue, attributed to pigments and polyphenolic compounds from banana peel waste, indicating possible chemical interactions within the matrix. The presence of fibrous content from the banana peel likely enhances the mechanical strength and rigidity of the PVA/BP film, making it more robust than the PVA/SS film.

The UV-Vis absorption spectrum of the PVA/SS and PVA/BP film was shown in Figure 3.

From the Figure 3, it can be shown that PVA/BP exhibit light-blocking efficiency, particularly in the UV range (200–400 nm), with significantly higher absorbance value

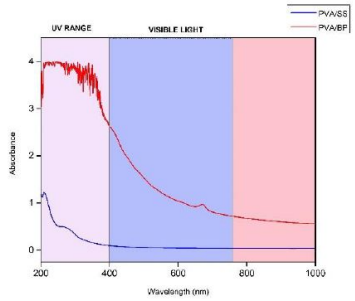



Figure 3: Observation of physical properties of PVA/SS and PVA/BP film.

compared to the PVA/SS film. The strong UV-blocking efficiency of the PVA/BP film can be attributed to natural compounds present in banana peel, particularly polyphenols and flavonoids (Silva et al., 2020). These bioactive compounds are well-known for excellent UV-absorbing properties. In addition, the PVA/BP film achieves an absorbance of 0.97 at 671 nm in the visible range, balancing UV protection with partial light transmission.This dual functionality makes the PVA/BP film an ideal candidate for packaging applications that require shielding against harmful UV radiation while maintaining some level of visibility. It is particularly suited for preserving the quality of light-sensitive products, including pharmaceuticals, cosmetics, and perishable foods, by minimizing photodegradation during storage.

## 4 Conclusions

In conclusion, the PVA/BP film shows UV-blocking efficiency due to the presence of natural polyphenols and flavonoids from banana peel. These compounds enhance the film's ability to absorb and block harmful UV radiation, making it highly suitable for applications requiring protection against photodegradation.

## References

M. A. Ahmed and A. E. Abbas. 2019. Utilization of banana extract for eco-friendly functional finishing of textile materials: a review. *Gezira Journal of Engineering and Applied Sciences*, 13(2):1–18.

F. Hilmi, M. Wahit, N. Shukri, Z. Ghazali, and A. Zanuri. 2019. Physico-chemical properties of biodegradable films of polyvinyl alcohol/sago starch for food packaging. *Materials Today: Proceedings*, 16:1819–1824.

V. D. M. Silva, M. C. C. Macedo, C. G. Rodrigues, A. N. dos Santos, A. C. d. F. e Loyola, and C. A. Fante. 2020. Biodegradable edible films of ripe banana peel and starch enriched with extract of eriobotrya japonica leaves. *Food Bioscience*, 38:100750.

Individual Research Contribution Review, 2024: 97–98
*ISSN: 3083-922X*

# FLOODCOM: Floating Flood Disaster Command Center

**Khairil Nor Kamal Umar**
Radiation Processing Technology Division, Malaysian Nuclear Agency
43000 Kajang, Selangor
kn_kamal@nm.gov.my

## Abstract

FLOODCOM: Floating Flood Disaster Command Centre is a floating structure built from bio-composite material and RX-HDPE floating module and will be functioning as a flood disaster command centre. This floating structure are placed in a strategic area at Kampung Bantal, Ulu tembeling, Jerantut, Pahang and will be used by Civil Defense Emergency response Team (CDERT) under Malaysian Civil Defense Force (Angkatan Pertahanan Awam Malaysia) to assist rescue operation, evacuation and humanitarian aid to flood victim. Malaysian Nuclear Agency has the technology and expertise in the construction of floating disaster command center from bio-composite material. The expertise of Malaysian Nuclear Agency in the field of bio-composite material, polymer material and composite processing equipment has been proven in previous projects, mostly community projects such as aquacultural floating bio-composite cage, bio-composite floating jetty and anchovy catching floating bio-composite barge (bagang terapung biokomposit). The successfulness of the project was a proof that the technology was well accepted by the community.

**Keywords:** FLOODCOM, Floating, bio-composite, RX-HDPE

## 1 Introduction

Mukim Ulu Tembeling is located at the head of Sungai Tembeling, in Jerantut district, Pahang. Ulu Tembeling is located at the entrance of the National Park in Pahang. This area consisting 5 main villages namely Kampung Bantal, Kampung Pagi, Kampung Kuala Sat, Kampung Gusai and Kampung Bukit Mat Daling. The five villages are inhabited by about 2595 people who mostly were self-employed. The location of these villages is isolated, where it involves a long distance and takes a long time to reach. Furthermore, Kampung Bantal, which is inhabited by the largest population, is separated by the Tembeling River and a boat service must be used to cross the river to the village. All of these villages are located in areas that are very vulnerable to flood and every time a flood occurs, the village will be cut off from any communication road resulting in the aid delivery process being blocked as well as rescue operations and the evacuation of victims being delayed or taking a long time to arrive. Furthermore, the operation of delivering aid through the river route are very costly and endangers the Malaysian Civil Defense Force (APM) personnel and there have been several incidents of overturned boats.



Figure 1: Kampung Bantal's condition during flood season



Figure 2: Capsized boat

The Malaysian Nuclear Agency has the technology and expertise in the field of manufacturing floating structures from bio-composite materials. In this project, a floating structure consisting of bio-composite material and RX-HDPE modules will be built which will serve as a floating disaster command center (Design, ). This floating command center will be placed in a strategic location for use by the Malaysian Civil Defense Force (APM) of the State of Pahang for rescue operations, evacuation and delivery of humanitarian aid to flood victims. In addition, this command center will act as a first responder preparedness center for search and rescue operations in the event of an accident along the river. In a normal situation, this floating center will be a standby station that will be used by the APM CDERT (Unit Maritim, ). This floating bio-composite technology has already been used and applied in previous projects, namely as a bio-composite floating jetty for the MSI project in Semporna, Sabah and as a floating anchovy fishing station for the MySI project in Kota Belud, Sabah (Patent, nd). The same technology has been used by the Malaysian Armed

Forces through the Joint Forces Headquarters in Sabah as a jetty for the movement and operation of the quick response force in the responsibility of safeguarding the security of the country's waters from foreign invasion.

## 2 Materials and Methods

a) Preparation of bio-composite compound with the addition of additive using a compounding machine at the Malaysian Nuclear Agency.

b) Production of bio-composite structure component through compression molding method.

c) Production of floating module from radiation-modified polymeric material RX-HDPE by extrusion blow molding technique.

d) Pre-assembly of framing structure, bio-composite decking, and floating module.

e) Installation of the FLOODCOM structure.

## 3 Results and Discussion

The development and preparation of FLOODCOM involving 4 stages.



Figure 3: Stage 1: Procurement of framing materials, floating modules, bio-composite decking, anchoring materials and fastening materials.

## 4 Conclusions

The use of a floating flood disaster operation center is very important in helping the Malaysian Civil Defense Force carry out rescue operations, the evacuation of flood victims and the delivery of humanitarian aid during a flood disaster. The usage of bio-composite materials and RX-HDPE floating modules in the FLOODCOM structure has given good performance and its durability has been proven in previous floating structure projects.

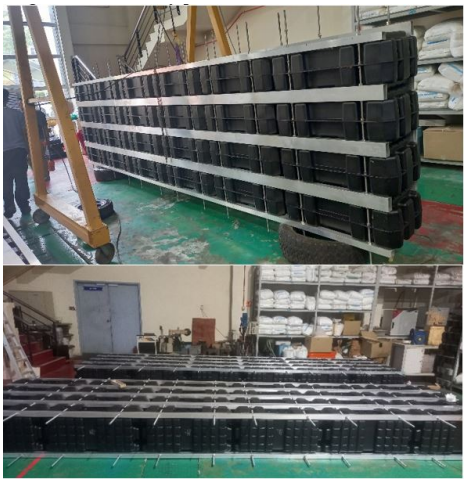


Figure 4: Stage 2: Pre-assembly process



Figure 5: Stage 3: Assembly process at site.



Figure 6: Stage 4: Installation completion and Anchoring.

## References

Malaysian Industrial Design. Marine floating module unit. MY-20-E0735-0101. Malaysian Industrial Design.

Malaysian Patent. n.d. Composition of an armor unit and method of fabrication thereof. Malaysian Patent.

Ibu Pejabat JKR Malaysia Unit Maritim, Cawangan Pangkalan Udara dan Maritim. Marina design guidelines. Internal Publication. JKR Malaysia.

Individual Research Contribution Review, 2024: 99–100
*ISSN: 3083-922X*

# Synthesis and Properties of Waterborne Polyurethane Acrylate (WPUA) Dispersions: A Comparative Study of PPG and Palm Oil-Based Polyol

**Khairul Azhar Abdul Halim**
Radiation Processing Technology Division, Malaysian Nuclear Agency
43000 Kajang, Selangor
azharhalim@nm.gov.my

## Abstract

This study explores waterborne polyurethane acrylate (WPUA) dispersions synthesized from polypropylene glycol (PPG) and palm oil-based polyol (PE135). Both dispersions were successfully prepared and analyzed for pH, solid content, and particle size. The PE135 dispersion had a slightly lower pH and a solid content close to 40%, similar to PPG. It appeared murkier and had higher viscosity due to its larger median particle size of 354 nm with a dual-peak distribution. In comparison, the PPG dispersion had a median particle size of 104 nm with a uniform distribution, resulting in lower viscosity. These findings demonstrate how polyol composition impacts the physical properties of WPUA dispersions, with palm oil-based polyols offering potential for customized formulations.

**Keywords:** Radiation curing, bio-based polyols, polyurethane dispersion

## 1 Introduction

Conventional polyurethane (PU) coatings often require organic solvents to enhance application properties, but these solvents contribute to environmental and health issues due to hazardous air pollutants and volatile organic compounds. Waterborne PU coatings have emerged as an eco-friendly alternative but face challenges, such as slower curing times at room temperature compared to solvent-based systems. Radiation curing technology offers a solution, providing fast, energy-efficient, and environmentally friendly drying. The pursuit of sustainable coatings has led to exploring bio-based polyols from vegetable oils like soybean, castor, and linseed. However, the potential of palm oil-based polyols for radiation-curable waterborne polyurethane acrylates (WPUAs) remains underexplored. This study investigates the synthesis and properties of WPUA dispersions using PPG, a petrochemical polyol, and PE135, a palm oil-based polyol, to understand the impact of polyol composition on the dispersions' characteristics.

## 2 Materials and Methods

### 2.1 Synthesis of WPUA

WPU dispersion was synthesized with an NCO:OH molar ratio of 2.0, calculated using isophorone diisocyanate (IPDI): PE135 polyol, and dimethylol propionic acid (DMPA). PE135 and DMPA were mixed with N-methyl-2-pyrrolidone as a co-solvent at 80°C and 250 rpm until homogenous. IPDI was added dropwise, followed tin catalyst to form an NCO-terminated prepolymer. The reaction was monitored via titration (ASTM D2572) until the NCO content reached 5%. The DMPA was neutralized with triethylamine at 40°C for 30 minutes, after which hydroxyethyl acrylate was added dropwise to introduce vinyl groups, reacting until all NCO was consumed. The prepolymer was dispersed in deionized water to achieve 40% solid content. The process was repeated with PPG as a control.

### 2.2 WPUA dispersion characterization

The pH of the WPUA dispersions was measured at room temperature using a pH meter, with the probe rinsed between measurements for accuracy. Viscosity was measured with a rotational viscometer (DV2T, AMETEK Brookfield) at 10 rpm for 60 seconds. Solid content was determined by drying a 1.0 g sample at 80°C until constant weight, calculated using the formula: (weight of dried sample/initial weight) × 100. Particle size was analyzed using a laser particle size analyzer (MicrotracX100).

## 3 Results and Discussion

### 3.1 WPUA characterization

The study successfully synthesized waterborne polyurethane acrylate (WPUA) dispersions using both PPG (petrochemical-based polyol) and PE135 (palm oil-based polyol) as shown in Figure 1. As listed in Table 1, both dispersions had solid content near the targeted 40% and differed slightly in pH, with PE135 showing a lower value due to its distinct chemical structure.

Visually, the PE135 dispersion was more opaque and exhibited higher viscosity compared to the PPG dispersion. This difference was attributed to the larger molecular structure of PE135 (Figure 2), leading to a higher median particle size (354 nm) with a dual-peak distribution (Figure 3). In contrast, the PPG dispersion displayed a lower median particle size (104 nm) and a more uniform single-peak distribution (Figure 4), correlating with its lower viscosity and clearer appearance.

These observations indicate that the choice of polyol affects not only the dispersion's particle size distribution but also its overall rheological and visual properties. The higher viscosity and more complex particle structure of the PE135 dispersion

suggest potential implications for film-forming properties and application processes in radiation-cured coatings.

| WPUA Dispersion Properties | Polyol | |
|---|---|---|
| | PPG | PE135 |
| Viscosity (cp), 10rpm, 25°C | 36 | 98 |
| pH | 7.79 | 7.27 |
| Particle size, mean diameter, nm | 104 – single peak | 354 – dual peak |
| Solid content % | 37.5 | 42.2 |

Table 1: WPUA dispersion properties

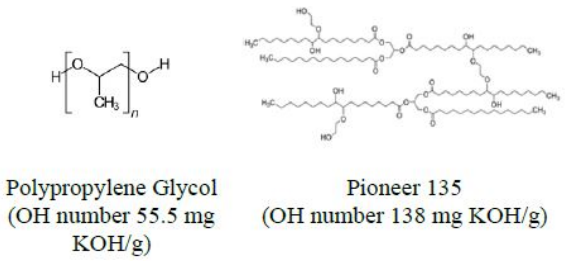



Figure 1: Molecular structures of PPG and PE135 polyols (Ismail et al., 2018)

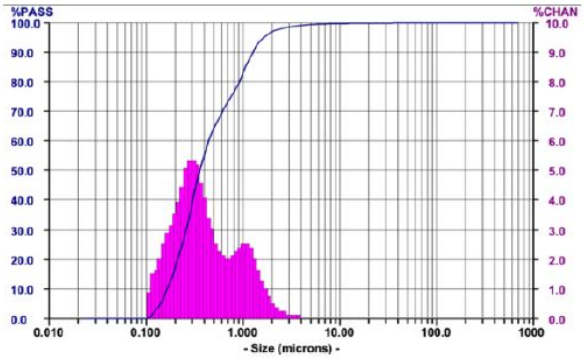



Figure 2: Particle size distribution of PE135 PUA dispersion.

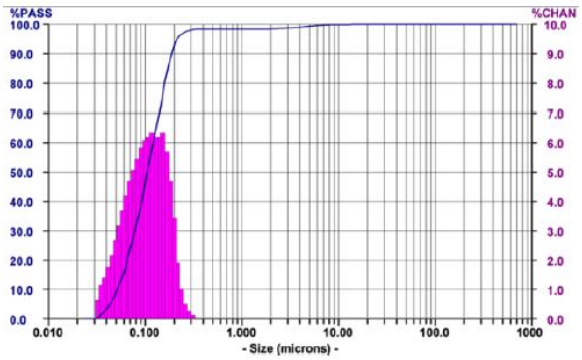



Figure 3: Particle size distribution of PPG PUA dispersion.

## 4 Conclusions

This study demonstrated the successful synthesis of water-borne polyurethane acrylate (WPUA) dispersions using PPG and PE135 polyols. The findings revealed that PE135-based dispersions exhibit higher viscosity, greater particle size, and murkier appearance compared to PPG-based dispersions, attributed to the bulkier molecular structure of PE135. These differences underscore the significant impact of polyol selection on the physicochemical properties of WPUA dispersions, providing insights into tailoring dispersion formulations for specific applications.

## References

T. N. M. Tuan Ismail, N. A. Ibrahim, M. A. Mohd Noor, S. S. Hoong, K. D. Poo Palam, S. K. Yeong, Z. Idris, C. M. S. I. Sendijarevic, E. Abd Malek, N. Zainuddin, and V. Sendijarevic. 2018. Oligomeric composition of palm olein-based polyols: The effect of nucleophiles. *European Journal of Lipid Science and Technology*, 120(4):1700354.

Individual Research Contribution Review, 2024: 101–102
*ISSN: 3083-922X*

# Electron Beam Irradiation Induced Degradation Mixture of Diclofenac, Gliclazide, Metformin and Amlodipine in STP Effluent

**Khomsaton Abu Bakar**
Radiation Processing Technology Division, Malaysian Nuclear Agency
43000 Kajang, Selangor
khomsaton@nm.gov.my

## Abstract

A study used electron beam irradiation (EBI) to degrade Diclofenac (DEC), Gliclazide (GLZ), Metformin (MET), and Amlodipine (AML) added in STP effluents. EBI at 1MeV, 3 mA and 9 mA current, and 2–20 kGy irradiation dosages observed DEC, GLZ, MET, and AML deterioration. The degradation of DEC, GLZ, MET, and AML at 100ug/l at 2–20 kGy irradiation dosages was considerable. All pharmaceuticals substances in the research disintegrate more quickly in acidic environments, while phosphate prevents decomposition. At dosage 2kGy, COD, TOC, and $NH_3$-N reduced 35.33%, 12.23%, and 8.33%.

**Keywords:** STP effluent, Diclofenac, Gliclazide, Irradiation

## 1 Introduction

Studies indicate a significant presence of pharmaceutical residues in Malaysia's wastewater treatment systems, particularly in sewage treatment plants (STPs) and wastewater treatment plants (WWTPs). Research by previous reseracher highlighted the detection of pharmaceutical substances, including metformin and gliclazide, in the Langat River due to effluent from nearby STPs . To address this issue, ionizing radiation has been proposed as a potential solution for degrading pharmaceutical residues in sewage effluents. This method utilizes reactive radical intermediates generated during the radiolysis of water, which effectively decompose organic molecules without producing harmful byproducts, making it a greener remediation technique.

## 2 Materials and Methods

The research employed pharmaceutical compounds like Diclofenac Sodium (DEC), Gliclazide (GLZ), Metformin (MET), and Amlodipine (AML) as spike reagents in STP effluent samples. Samples were obtained from a sewage treatment plant (STP) in Kuala Lumpur and infused with these chemicals. The samples containing phosphates were utilized to examine the impact of phosphates on the degradation of medicinal compounds following exposure to electron radiation. Electron beam irradiation was conducted utilizing EPS 3000, with radiation dosages of 2, 5, 10, 15, and 20 kGy. The degradation of DEC, AML, MET, and GLZ was assessed using UV-Vis spectrophotometry, and studies of organic and inorganic anions were performed.

## 3 Results

### 3.1 Degradation of DCF, GLZ and Mixture of DCF/GLZ in STP Effluent by Irradiation

Figure 1 demonstrates the removal of DEC, AML, MET, and GLZ in STP effluent after EBI at 1 MeV, with varying irradiation levels indicated by the absorbance of each substance. The absorbance values for DEC, AML, MET, and GLZ are 275, 367, 234, and 228, respectively. As radiation dosages rise, there is a corresponding decrease in the efficacy of all medications. Following 20 kGy doses of DEC, AML, MET, and GLZ, the elimination percentages recorded were 22.04%, 8.10%, 11.53%, and 3.56%, respectively. The linear graph in Fig. 1 indicates that the GLZ presents the greatest removal challenge, whereas the DEC exhibits superior removal efficiency compared to the other substances.

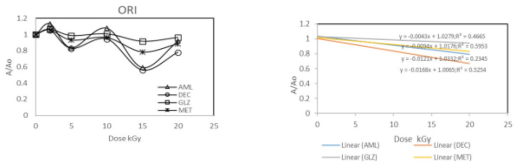



Figure 1: Degradation of DEC, AML, GLZ and MET in STP effluent at original pH (6.65).

### 3.2 Effect of pH and on degradation DEC, AML, MET and GLZ in STP effluent by irradiation

Figure 2 shows that DEC, AML, MET, and GLZ are degraded easily by EBI when the pH is around 5.0. It works next best when the pH is neutral (6.65) Fig. 1 and finally when the pH is 8.0.

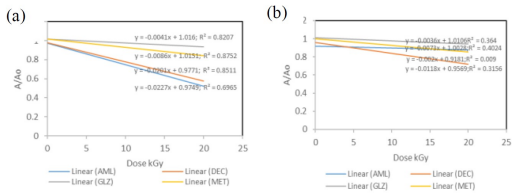



Figure 2: Degradation of DEC, AML, GLZ and MET in STP effluent at original pH (6.65).

### 3.3 Effect of phosphate anion ($PO_4^{3-}$) on DEC, AML, MET, and GLZ degradation

Samples with phosphate addition of 7 mg/l and without addition were irradiated at doses of 5 kGy. As shown in Fig. 3, phosphate inhibits pharmaceutical degradation in STP effluent when irradiated at 5 kGy. Without additional phosphate, DEC, AML, MET, and GLZ degrade effectively in STP effluents. The breakdown rates for DEC, AML, MET, and GLZ are 17.32%, 16.21%, 6.92%, and 4.28%, respectively. However, when STP effluent contains $PO_4^{3-}$, these degradation efficiencies drop to 3.16 %t, 4.15 %, 2.06 %t, and 0.01% respectively.

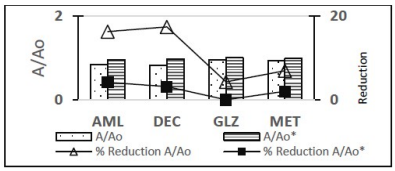



Figure 3: DEC, AML, MET and GLZ degradation in the presence and without of anion phosphate $PO_4^{3-}$ irradiated at 5 kGy in STP effluent. Note: * [$PO_4^{3-}$] added in sample.

### 3.4 Effect of irradiation on COD, TOC, and inorganic ammonia nitrogen ($NH_3$-N) in STP effluent containing pharmaceutical compounds under study

Fig. 4(a) illustrates the degradation of studied pharmaceutical compounds in STP effluent caused by electron beam irradiation in terms of COD and TOC levels. Pharmaceutical compounds containing STP effluent show rapid reduction upon EBI at 2 kGy doses. Meantime, the reduction rate steadily slowed at 5-20 kGy. At an irradiation dose of 2 kGy, the COD reduction percentage attained was approximately 35.33%. However, at an irradiation dose of 5- 20 kGy the COD reduction percentage had shown little significant changes in the range of 49.33%-73.33%. The significant reduction in COD after a dosage of 2 kGy as compared to 5–20 kGy. Fig. (b) shows the changes in $NH_3$-N content upon EBI. $NH_3$-N level decreases after EBI for pharmaceutical substances containing STP effluent samples. The recorded ammonia nitrogen reduction percentage was 8.33% at dose 2 kGy while, 25.00% - 80.83% were achieved at dose 5-20 kGy.

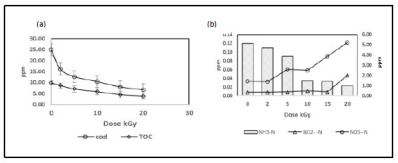



Figure 4: Effect of absorbed dose on COD and TOC(a) and the conversion of $NH_3$-N to $NO_2{}^-$ and subsequently to $NO_3{}^-$ in the sample

## 4 Discussion

Hydroxyl radicals (·OH), hydrated electrons ($e^-_{aq}$), and hydrogen atoms (·H) are primarily responsible for the degradation of pharmaceuticals spiked into secondary treatment plant (STP) effluent samples.

At acidic pH, $e^-_{aq}$ reacts with $H^+$ to form hydrogen atoms (·H), reducing the recombination between $e^-_{aq}$ and ·OH, and thereby increasing the effective concentration of ·OH. Under alkaline conditions, ·OH may convert into $O^-$, which is less reactive.

Although phosphate radicals (e.g., $PO_4^{\cdot 2-}$) can oxidize pollutants, they do not significantly contribute to the degradation of diclofenac (DEC), amlodipine (AML), metformin (MET), and glipizide (GLZ). The phosphate radical reacts with ·OH (rate constant $\approx 1.0 \times 10^7\,\mathrm{L \cdot mol^{-1} \cdot s^{-1}}$), thereby depleting the available ·OH required for pharmaceutical degradation.

Significant reductions in COD and TOC after 2 kGy irradiation are attributed to reactive species (·OH, $e^-_{aq}$, ·H) generated via radiolysis of water. Hydroxyl radicals, in particular, degrade organic pollutants primarily through hydrogen abstraction and hydroxylation.

The degradation rate of pharmaceuticals decreased with increasing radiation dose, likely due to competition among the parent analyte, its byproducts, and matrix components for the reactive species.

Ammonia nitrogen ($NH_3$) reacts with hydroxyl radicals forming amino radicals ($\cdot NH_2$) as follows (Pagsberg, 1969):

$$NH_3 + \cdot OH \rightarrow \cdot NH_2 + H_2O \quad (1)$$

$$\cdot NH_2 + H_2O_2 \rightarrow \cdot NHOH + H_2O \quad (2)$$

$$\cdot NH_2 + \cdot OH \rightarrow NH_2OH \quad (3)$$

Subsequent oxidation produces unstable species like $NH_2O_2$, which decompose into $NO_2^-$, and are further oxidized to $NO_3^-$ by either ·OH or $H_2O_2$, thereby reducing ammonia-nitrogen content.

Dissolved oxygen also contributes to ammonia oxidation, as shown (Purwono et al., 2017):

$$NH_4^+ + 1.5\,O_2 \rightarrow NO_2^- + H_2O + 2H^+ \quad (4)$$

$$NO_2^- + 0.5\,O_2 \rightarrow NO_3^- \quad (5)$$

As illustrated in Fig. 4(b), after 20 kGy radiation exposure, $NH_3$-N concentration decreased from 0.12 ppm to 0.02 ppm, while $NO_3^-$ increased from 1.42 ppm to 5.20 ppm, indicating the effectiveness of electron beam irradiation (EBI) in facilitating nitrogen transformation.

## 5 Conclusions

The EBI technique is capable of degrading 100 ug/l mixture of DEC, AML, MET and GLZ in STP effluent. However, complete degradation cannot be achieved at a dose ranging from 2kGy to 20kGy. The pharmaceuticals mixture is more likely to be removed in acidic conditions and in minimal/free phosphate content. The COD, TOC, and NH3-N decreased by 35.33%, 12.23%, and 8.33% at dose 2kGy.

## References

P. Pagsberg. 1969. Pulse radiolysis of ammonia in aqueous solutions in presence of nitrous oxide. In *Radiation Research*, 2021 Spring Rd, Ste 600, Oak Brook, IL 60521. Radiation Research Society.

Rezagama A. Purwono, M. Hibbaan, and M. A. Budihardjo. 2017. Ammonia-nitrogen ($nh_3$-n) and ammonium nitrogen ($nh_4{}^+$-n) equilibrium on the process of removing nitrogen by using tubular plastic media. *Journal of Materials and Environmental Science*, 8:4915–4920.

Individual Research Contribution Review, 2024: 103–104
*ISSN: 3083-922X*

# Chemical composition and morphology observation of cellulose from sago pith waste

**Mahathir Mohamed**
Radiation Processing Technology Division, Malaysian Nuclear Agency
43000 Kajang, Selangor
mahathir@nm.gov.my

## Abstract

This study focuses on the preparation and characterization of acrylonitrile butadiene styrene (ABS) and epoxidized natural rubber (ENR) membranes using the casting method. ABS was chosen for its excellent mechanical properties and chemical resistance, making it a promising material for various applications. The casting method was selected for its simplicity and efficiency compared to techniques such as electrospinning. Membranes with varying ABS/ENR ratios, thicknesses, and water bath immersion durations were prepared and analyzed. Morphology was examined using optical microscopy and field emission scanning electron microscopy (FESEM), while water absorption capacity was evaluated to assess performance. The findings contribute to understanding ABS/ENR membranes and their potential applications in material science and engineering.

## 1 Introduction

Porous membranes are increasingly explored for water separation due to their tunable structures and performance. Composite membranes from acrylonitrile butadiene styrene (ABS) and epoxidized natural rubber (ENR) combine high mechanical strength, chemical resistance, and adjustable pore size. Membrane casting, a simple and scalable method, forms a thin polymer film on a substrate, followed by phase separation to create a porous structure. ABS, a copolymer of acrylonitrile, butadiene, and styrene, offers chemical resistance, toughness, and processability (Campos et al., 2016). Its hydrophobic nature enables pore size control by adjusting polymer concentration, solvent, viscosity, and evaporation time (Guillen et al., 2011).

ENR, a modified natural rubber, improves flexibility, tensile properties, and oil/gas resistance (Othaman, 2016). Its elasticity increases chain mobility, producing larger pores. In ENR/PVDF membranes, higher ENR content lowers tensile strength but increases strain, showing its value for tailoring performance.Top-layer porosity strongly affects water flux; higher polymer content reduces porosity due to increased viscosity, limiting macrovoid formation. By optimizing polymer ratios and processing conditions, membranes can be tuned for specific needs. This study prepares and characterizes ABS/ENR membranes via casting, examining morphology and water absorption under varied polymer ratios, thicknesses, and immersion times.

## 2 Materials and Methods

### 2.1 Materials

In this research, industrial grade Toyolac ABS (Acrylonitrile Butadiene Styrene) was used as the host polymer due to its high thermal and mechanical properties. Epoxidized natural rubber (ENR, 50 mol % conversion) was used as the modifier supply by Guthrie Malaysia. Degradation of ENR via UV irradiation to form low molecular weight liquid epoxidized natural Rubber (LENR). Acetone as solvent was purchased from Sigma Aldrich Chemical Co.

### 2.2 Preparation of the ABS/ENR Formulation

Epoxidised natural rubber (ENR) was added to ABS solutions at concentrations of 16%, 18%, and 20% in order to generate ABS/ENR formulations. The ABS:ENR ratios were 90:10, 70:30, and 50:50. Each solution was formulated with a total mass of 50 g. Initially, liquid ENR was subjected to heating and stirring at 150 rpm on a hotplate magnetic stirrer for a duration of 2 hours, or until it attained a dark yellow colour and demonstrated enhanced viscosity. The viscous ENR was subsequently dissolved in acetone, followed by the gradual addition of ABS beads over a period of one hour. The mixture was stirred continuously at 200 rpm and held at a temperature of 45 – 50 °C overnight to ensure complete dissolution of the ABS beads. The solution was stored in an airtight container to maintain its concentration and inhibit acetone evaporation over time.

### 2.3 Casting of ABS/ENR

In the casting process, a pipette was used to dispense the polymer solution onto a glass plate, ensuring the volume was sufficient to uniformly cover the surface. The solution was spread using clean rods of varying thicknesses (100, 150, and 200 $\mu$m) for uniformity. After air drying for 60 seconds to allow partial solvent evaporation, the cast was immersed in a water bath for 60 seconds, 8 hours, or 24 hours for solvent exchange, forming a white cast film. The film was then dried in a vacuum oven at 80 °C for 2 hours.

## 3 Results and Discussion

### 3.1 Water absorption

Table 1 presents the water absorption percentages of ABS/ENR cast films with a thickness of 150 $\mu$m, tested to identify the concentration and ratio yielding the highest absorption. None of the samples exceeded 50%. The 18%

50:50 ABS/ENR ratio exhibited the highest water absorption at 48%, while the 18% 90:10 ratio showed no absorption. Consequently, casting was continued with the 50:50 ratio for ABS/ENR solutions at concentrations of 16%, 18%, and 20%, using thicknesses of 100, 150, and 200 $\mu$m and immersion durations of 8 and 24 hours.

| ABS/ENR | Average percentage of water absorption (%) | | |
|---|---|---|---|
| | 90:10 | 70:30 | 50:50 |
| 16% | 26 | 8 | 18 |
| 18% | 0 | 23 | 48 |
| 20% | 15 | 28 | 20 |

Table 1: Average percentage of water absorption of ABS/ENR for ratios 90:10, 70:30, and 50:50

Table 2 summarizes the average water absorption percentages of ABS/ENR membranes (50:50 ratio) at varying concentrations, thicknesses (100, 150, and 200 $\mu$m), and immersion durations (8 and 24 hours). The 18% 50:50 membrane showed the highest absorption overall, prompting further tests at different thicknesses and durations to analyze their effects. High absorption is linked to increased membrane porosity. At 24 hours, membranes with 16%, 18%, and 20% ABS at 100 $\mu$m, and 16% and 18% at 200 $\mu$m, showed significant absorption. Notably, the 20% 50:50 membrane (100 $\mu$m, 24 hours) exhibited 125% absorption, likely due to swelling exceeding the film's dry weight. No absorption values were observed for 18% 50:50 (100 $\mu$m, 8 hours: 0%) and 20% 50:50 (200 $\mu$m, 24 hours: 0%), possibly due to high ABS content, as butadiene and styrene contribute to hydrophobicity.

| Sample | Average percentage of water absorption (%) | | | | | |
|---|---|---|---|---|---|---|
| | 100 $\mu$m | | 150 $\mu$m | | 200 $\mu$m | |
| | 8h | 24h | 8h | 24h | 8h | 24h |
| 16%:50:50 | 13 | 13 | – | – | 7 | 14 |
| 18%:50:50 | 0 | 23 | 32 | 17 | 19 | 28 |
| 20%:50:50 | 5 | 125 | – | – | 18 | 0 |

Table 2: Average percentage of water absorption of ABS/ENR for ratio 50:50 and immersion duration of 8 and 24 hours

### 3.2 Porosity

Table 3 highlights the porosity percentages of ABS/ENR cast films (50:50 ratio) under different thicknesses and immersion durations. The 16% 50:50 cast film with a thickness of 100 $\mu$m exhibited significantly higher porosity (>50%) compared to the 200 $\mu$m film, which showed 28%. For the 18% 50:50 cast film, porosity remained consistent at approximately 15% across all thicknesses, except for the 100 $\mu$m film immersed for 24 hours, which achieved a porosity of 65%. The 20% 50:50 cast film demonstrated high porosity levels, ranging from 45% to 55% for films of 100 $\mu$m and 200 $\mu$m thicknesses, except for the 200 $\mu$m film immersed for 8 hours, which had a porosity of only 13%. Overall, thinner films (100 $\mu$m) displayed higher porosity than thicker ones (200 $\mu$m), and longer immersion durations (24 hours) resulted in greater porosity compared to shorter durations (8 hours).

| Sample | Average percentage of porosity (%) | | | | | |
|---|---|---|---|---|---|---|
| | 100 $\mu$m | | 150 $\mu$m | | 200 $\mu$m | |
| | 8h | 24h | 8h | 24h | 8h | 24h |
| 16%:50:50 | 51 | 54 | – | – | 28 | 28 |
| 18%:50:50 | 15 | 65 | 11 | 13 | 13 | 15 |
| 20%:50:50 | 54 | 54 | – | – | 13 | 48 |

Table 3: Average porosity (%) of ABS/ENR (50:50) at varying thicknesses and immersion durations.

### 3.3 FESEM

Field Emission Scanning Electron Microscope (FESEM) analysis was conducted on ABS/ENR cast films: 16% 50:50 (200 $\mu$m, 24 hours), 18% 50:50 (150 $\mu$m, 8 hours), and 20% 50:50 (200 $\mu$m, 8 hours). Figure 1(a) showed no visible pores and an uneven surface, attributed to ENR agglomeration In contrast, Figure 1(b) displayed more circular pores of random sizes, while Figure 1(c) showed fewer pores with both circular and irregular shapes. The pores formed during the solvent-exchange process between acetone and water.

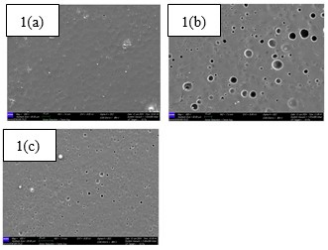



Figure 1: Morphology of ABS/ENR, (a). 16%50:50, (b). 18%50:50, (c), 20%50:50, magnification x 500

## 4 Conclusions

In conclusion, ABS/ENR membranes were successfully prepared using the casting technique, demonstrating the feasibility of blending acrylonitrile butadiene styrene (ABS) with epoxidized natural rubber (ENR) for membrane applications. The addition of ENR was critical in inducing pore formation, as ABS alone resulted in non-porous films. Among the tested ratios, the 50:50 blend at an 18% concentration exhibited the highest water absorption (48%), highlighting the importance of ENR in enhancing hydrophilicity. These findings suggest that careful control of formulation ratios, film thickness, and processing conditions can optimize membrane performance for specific applications.

## References

M.D Campos et al. 2016. Plos one. *PloS One*, 11(8):e0160728.

G. R. Guillen, Y. Pan, M. Li, and E. M. V. Hoek. 2011. Preparation and characterization of membranes formed by nonsolvent induced phase separation: a review. *Industrial & Engineering Chemistry Research*, 50(7):3798–3817.

R. Othaman. 2016. Preparation and characterization of epoxidised natural rubber (enr)/poly (vinylidene fluoride) (pvdf) (enr/pvdf) composite membrane. *The Malaysian Journal of Analytical Sciences*, 20(5):1090–1094.

Individual Research Contribution Review, 2024: 105–106
*ISSN: 3083-922X*

# Polyethylene Glycol Diacrylate/ Epoxidized Palm Oil Acrylate by Stereolithography 3D Printing for Tissue Scaffold Application

**Marina Talib**
Radiation Processing Technology Division, Malaysian Nuclear Agency
43000 Kajang, Selangor
marina@nm.gov.my

## Abstract

This study addresses these challenges by leveraging stereolithography (SLA) 3D printing to fabricate a novel hybrid scaffold integrating Polyethylene Glycol Diacrylate (PEGDA) and Epoxidized Palm Oil Acrylate (EPOLA). Characterization techniques, including Fourier Transform Infrared Spectroscopy (FTIR), compressive strength testing, and Scanning Electron Microscopy (SEM), are employed to evaluate the mechanical properties, and surface morphology of the scaffolds. The optimized PEGDA/EPOLA scaffolds exhibit superior mechanical strength, a uniform pore structure conducive to tissue ingrowth, and supporting robust cell proliferation and controlled biodegradation. This research underscores the potential of SLA 3D printing technology to fabricate intricate, high-resolution scaffolds tailored for applications in tissue engineering, drug delivery systems, and regenerative medicine. By addressing current limitations in biomaterial design, this study paves the way for advancements in scaffold-based therapies, potentially revolutionizing the field of biomaterials and enhancing outcomes in tissue regeneration and medical treatment.

**Keywords:** Polyethylene Glycol Diacrylate, EPOLA, FTIR.

## 1 Materials and Methods

The optical contact angle (OCA) was performed to study the scaffold tendency towards water whether it is hydrophobic or hydrophilic. It is measured by a sessile drop using water. The wettability of a scaffold should be compatible with the surrounding tissues and fluids. FTIR (Tensor II, Brucker) is used to confirm the presence of EPOLA functional group after the crosslinking process of EPOLA and PEGDA (Bouti et al., 2022). Mechanical properties of the scaffolds in term of compressive strength were determined and measured using SHIMADZU Autograph AGX-V Series with a 50 mm/min cross speed according to the ASTM D638. Morphology of the studied scaffolds were examined using FEI Quanta 400 scanning electron microscopy (SEM).

## 2 Results and Discussion

The results of the gel fraction test, conducted to determine the effect of EPOLA on the crosslinking percentage of PEGDA/EPOLA, are summarized in Figure 1.

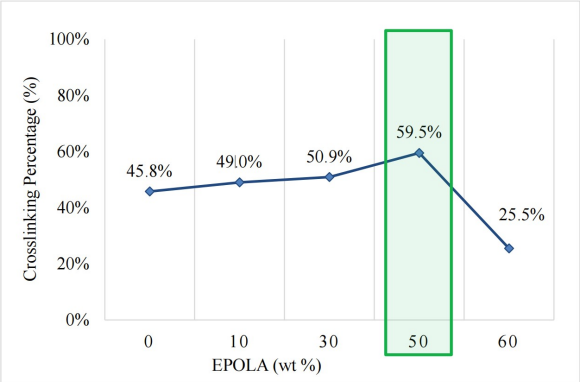



Figure 1: Crosslinking Percentage of PEGDA/EPOLA with addition of EPOLA by wt % ratio.

Figure 1 illustrate the crosslinking percentage of PEGDA/EPOLA mixtures with varying weight percentages of EPOLA. The crosslinking percentage appears to increase initially with the addition of EPOLA. The highest crosslinking percentage is observed at a formulation of 50 wt% EPOLA and 50 wt% PEGDA, reaching a peak value of 59.5%. However, further increasing the EPOLA content to 60 wt% results in a significant drop in the crosslinking percentage. Fourier Transform Infrared (FTIR) spectroscopy analysis was performed onboth PEGDA and PEGDA/EPOLA to analyse the presence of EPOLA after UV crosslinking process. The initial structure of EPOLA consists of C=C stretching, C-H bending, -OH bending, C-O-C, C=C, C=O stretching from acrylate group (Lebedevaite et al., 2019).

Compressive strength, which indicates the load-bearing capacity of the scaffolds under compressive forces, was evaluated. Table 1 provides a comparative analysis of the compressive strength between PEGDA and PEGDA/EPOLA scaffolds.

| Scaffold | Compressive Strength (kPa) |
|---|---|
| PEGDA | 342.0 |
| PEGDA / EPOLA | 536.5 |
| | Increase of 56.5% |

Table 1: Compressive Strength of PEGDA and PEGDA/EPOLA.

The trend observed shows a substantial enhancement in mechanical properties when EPOLA is integrated with PEGDA.

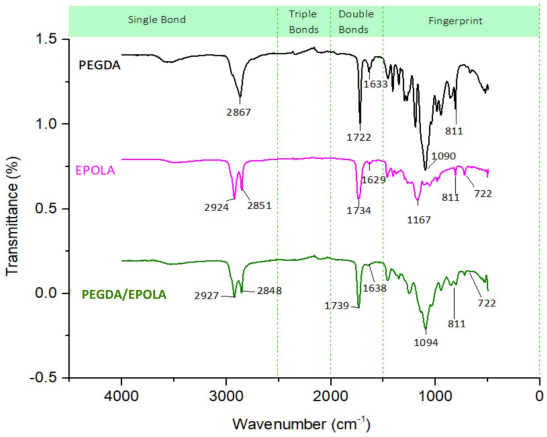



Figure 2: Spectral Analysis of PEGDA, EPOLA, and PEGDA/EPOLA

The compressive strength of the scaffolds increased markedly, suggesting that the combination of these materials results in a scaffold with superior load-bearing capacity. This trend highlights the potential advantages of using hybrid materials to achieve better mechanical performance in tissue engineering scaffolds (Tajau et al., 2017).

The microstructure test was performed to verify the presence and appearance of EPOLA on the scaffold morphological surface. Figure 3 presents SEM images at 2500x magnification that illustrate the morphological changes in the PEGDA scaffold before (a) and after (b) incorporation with EPOLA.

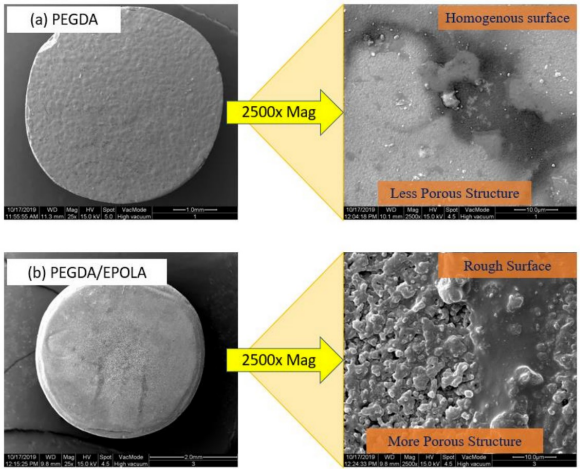



Figure 3: SEM images at 2500x magnification for morphological changes in the PEGDA scaffold before (a) and after (b) incorporation with EPOLA.

## 3 Conclusions

The study successfully developed a novel PEGDA/EPOLA resin formulation optimized for 3D printing using stereolithography. The optimized formulation demonstrated improved compressive strength and structural integrity, essential for supporting tissue growth and regeneration. Furthermore, the study demonstrated the feasibility of using stereolithography (SLA) to fabricate complex 3D scaffolds with the novel PEGDA/EPOLA resin. The high-resolution printing capability of SLA allowed for precise control over scaffold architecture, ensuring reproducibility and scalability for potential clinical application.

## References

M. Bouti, R. Irinislimane, and N. Belhaneche-Bensemra. 2022. Properties investigation of epoxidized sunflower oil as bioplasticizer for poly (lactic acid). *Journal of Polymers and the Environment*, 30(1):232–245.

M. Lebedevaite, J. Ostrauskaite, E. Skliutas, and M. Malinauskas. 2019. Photoinitiator free resins composed of plant-derived monomers for the optical micro-3d printing of thermosets. *Polymers (Basel)*, 11(1).

R. Tajau, R. Rohani, W. Wan Isahak, and M. Z. Salleh. 2017. Palm oil-based precursors for development of polymeric delivery system. *Malaysian Journal of Analytical Sciences*, 21:496–511.

Individual Research Contribution Review, 2024: 107–108
*ISSN: 3083-922X*

# Molecular Weight Effects of Gamma-Irradiated κ-Carrageenan on Plant Growth Enhancement

**Maznah Binti Mahmud**
Radiation Processing Technology Division, Malaysian Nuclear Agency
43000 Kajang, Selangor
maznah@nm.gov.my

## Abstract

Carrageenan, a versatile natural polymer, has demonstrated its effectiveness in a wide range of applications. Studies have shown that carrageenan, at specific molecular weights, can promote plant growth. However, the effect of different molecular weights on plant growth promotion is not fully understood. Therefore, in this study, commercial κ-carrageenan was degraded to achieve various molecular weights by subjected to gamma radiation at doses of 25, 50, 75, and 100 kGy, resulting in a reduction of its initial molecular weight, Mw from 45.77 kDa to 20.38, 9.48, 5.78, and 3.18 kDa, respectively. The irradiated carrageenan powders were subsequently dissolved in a sodium salt solution at a concentration of 100 ppm, prior to being used to treat rice seeds. The impact on rice growth during the nursery stage was then investigated.

**Keywords:** plant growth promoter; low molecular weight carrageenan; gamma radiation.

## 1 Introduction

Carrageenans are linear, sulfated polysaccharides derived from various marine red algae species. These compounds consist of a chain of D-galactose units connected by β-(1, 3) and β-(1, 4) glycosidic linkages, with ester sulfate groups attached to every two repeating galactose units (San et al., 2021). Research has demonstrated that κ-carrageenan has bio-stimulatory effects on a variety of crops, including legumes, rice, maize, fruits, and vegetables. The application of low molecular weight κ-carrageenan also helps reduce fertilization costs, as it optimizes fertilizer use by plants (Malbataan et al., 2023). The reduction of κ-carrageenan can be controlled by adjusting the radiation dose, material form, and by adding chain degradation accelerators, such as hydrogen peroxide. (Naeem et al., 2015).

In addition to molecular weight, the concentration of κ-carrageenan has also been found to influence its growth-promoting activity. Tecson et al. (Tecson et al., 2021) suggests that at concentrations below 800 ppm, κ-carrageenan helps plants produce alkaloids that promote growth, phytohormones that enhance immunity, and improve micronutrient absorption. Thus, the aim of this study was to investigate whether foliar application with irradiated κ-carrageenan affects growth activity of rice seeds. The irradiated κ-carrageenan with various molecular weights were obtained through gamma radiation-induced chain scission reaction.

## 2 Materials and Methods

**2.1** The commercial κ-carrageenan powder purchased from the local supplier was subjected to gamma ray irradiation at doses of 25, 50, 75, and 100 kGy.

**2.2** The molecular weight of κ-carrageenan and irradiated κ-carrageenan was determined using SEC-MALLS (Size Exclusion Chromatography with Multi-Angle Laser Light Scattering), with 0.1 M sodium nitrate as the mobile phase.

**2.3** The FT-IR spectra of κ-carrageenan and irradiated κ-carrageenan were characterized using FTIR CARY 630 ATR.

**2.4** The irradiated κ-carrageenan solutions, each at 100 ppm in a sodium salt-based solution with an adjusted pH around 5.0–5.5, were prepared and stored under chilled conditions.

**2.5** Rice seeds were immersed in 100 ppm irradiated κ-carrageenan solution for 24 hours and planted the following day. The seedlings were then sprayed with the irradiated κ-carrageenan solutions twice a week for 28 days. All parameters were fixed for all treatments; only the molecular weight of κ-carrageenan was varied. The treatments are listed in Table 1.

**2.6** The data collected on the (i) germination; (ii) seed survival; (iii) plant height; (iv) number of leaves per plant and (v) dry biomass, from day 5 until day 28.

## 3 Results and Discussion

Figure 1 shows the reduction in the molecular weight of carrageenan after being irradiated at 25, 50, 75, and 100

| No. | Treatment Code | Description |
|---|---|---|
| 1 | C | No CarraPGP |
| 2 | T25 | CarraPGP 1 (Mw = 20.38 kDa) |
| 3 | T50 | CarraPGP 2 (Mw = 9.48 kDa) |
| 4 | T75 | CarraPGP 3 (Mw = 5.78 kDa) |
| 5 | T100 | CarraPGP 4 (Mw = 3.18 kDa) |

Table 1: Description of the treatments

kGy. The gamma rays cause chain degradation, where the initially long chains of carrageenan break down into low molecular weight fragments (Naeem et al., 2015). The graph shows the highest rate of molecular weight reduction at 25 kGy, with the reduction rate slowing down at higher doses.

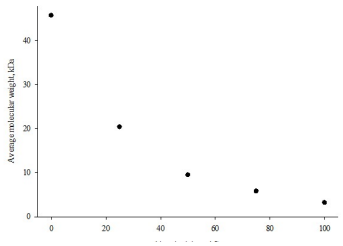



Figure 1: Effect of gamma ray on $\kappa$-carrageenan Mw

The structure of $\kappa$-carrageenan was analyzed using FT-IR spectroscopy, which identifies functional groups based on their spectral absorption as shown in Fig. 2. Strong absorption is indicated by high peak intensity, while weak absorption is reflected by low peak intensity $\kappa$-carrageenan easily degraded when exposed to radiation at room temperature, without the need for any chemical additives. This degradation occurs due to the rearrangement of radicals, leading to the formation of a stable product after chain scission As the absorbed gamma ray increased, the breakage of glycosidic C-O-C bonds increased. However, the chain breakage rate becomes insignificant after certain dose.

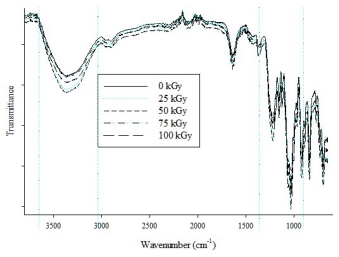



Figure 2: IR spectra of carrageenan and irradiated carrageenan

Table 2 shows the results on rice growth after being

Table 2: Results on rice during nursery stage with treatments

| DAY | CRITERIA | TREATMENT | | | | |
|---|---|---|---|---|---|---|
| | | C | T25 | T50 | T75 | T100 |
| 5 | Average number of seed germinate | 25.67 | 19.33 | 20.67 | 23.00 | 26.00 |
| 28 | Average number of seeds survive | 35.67 | 38.00 | 37.67 | 35.30 | 37.00 |
| 28 | Average plant height (cm) | 13.11 | 23.43 | 23.10 | 20.12 | 23.80 |
| 28 | Average number of leaves per plant | 2.15 | 2.12 | 2.15 | 2.19 | 2.25 |
| 28 | Average dry biomass (g) | 0.67 | 0.70 | 0.57 | 0.70 | 0.67 |

*N = 50 seeds with 3 replications

treated with irradiated carrageenan at different molecular weight compared with C, the treatment without growth promoter. According to Table 2, survival of grown seed is better with treatment than without growth promoter, C. Carrageenan produces multiple primary and secondary metabolites can have high impact in agriculture crops that improve seed germination and survival. In terms of average leaves number and dry biomass weight, the effect of treated seeds with C are insignificant. The treated seeds also indicated higher height compared to C.

## 4 Conclusions

$\kappa$-carrageenan can be broken down into smaller fragments through gamma radiation. The use of different doses of gamma rays results in varying molecular weight ranges, although gamma radiation does not affect the backbone structure of $\kappa$-carrageenan. The irradiated $\kappa$-carrageenans show a positive impact on rice seed survival and plant height but have no significant effect on the number of leaves or dry biomass. Based on these results, further studies are necessary, and additional research on plant growth should be conducted in the future.

## References

C. J. M. Malbataan, F. F. Carandang, and M. F. O. Mercado. 2023. Efficacy evaluation of irradiated carrageenan as plant growth promoter in cowpea (vigna unguiculata l.) walp. and bush sitao (vigna unguiculata (l.) walp. ssp sesquipedalis (l.) verdc. x v. unguiculata (l.) walp. ssp unguiculata) production. *International Journal of Agricultural Technology*, 19(4):1669–1680.

M. Naeem, M. Idrees, T. Aftab, M. M. Alam, M. M. A. Khan, M. Uddin, and L. Varshney. 2015. Radiation processed carrageenan improves plant growth, physiological activities, and alkaloids production in catharanthus roseus l. *Advances in Botany*, pages 1–11.

P. T. San, C. M. Khanh, H. H. N. Khanh, T. A. Khoa, N. Hoang, P. D. Thinh, and T. D. Nguyen. 2021. Impacts of - oligocarrageenan application on photosynthesis, nutrient uptake and bean yield of coffee (coffea robusta). *Sains Malaysiana*, 50(11):3171–3179.

M. G. Tecson, L. V. Abad, V. D. Ebajo, and D. H. Camacho. 2021. Ultrasound-assisted depolymerization of kappa-carrageenan and characterization of degradation product. *Ultrasonics Sonochemistry*, 73:105540.

Individual Research Contribution Review, 2024: 109–110
*ISSN: 3083-922X*

# Analysis of PE Irradiation Tubes for High-Performance PTS and RR Systems in PUSPATI TRIGA Research Reactor

**Mohammed Iqbal bin Shueb**
Radiation Processing Technology Division, Malaysian Nuclear Agency
43000 Kajang, Selangor
iqbal@nm.gov.my

## Abstract

This study focuses on the development of high-density polyethylene (HDPE) irradiation tubes for the Pneumatic Transfer System (PTS) and Rotary Rack (RR) within the TRIGA Mark II research reactor, Malaysia's sole nuclear research reactor, operational since 1982 under the Malaysian Nuclear Agency. This versatile reactor supports neutron activation analysis (NAA), radioisotope production, neutron radiography, and small-angle neutron scattering (SANS), playing a pivotal role in scientific and industrial applications. The newly developed HDPE tubes offer a cost-effective and reliable alternative to imported irradiation tubes, significantly reducing reliance on foreign suppliers while fostering local expertise in nuclear technology. Designed to integrate seamlessly with the PTS and RR systems, the tubes ensure optimal neutron moderation and gamma ray transparency. Performance evaluations using an Americium-Beryllium (Am-Be) neutron source and a Barium-133 (Ba-133) gamma source confirmed the suitability of the tubes for their intended applications. Results demonstrated that the PTS tube enhances neutron interaction for isotope production, while the RR tube maintains stable neutron flux for precise activation analysis. This innovation reduces costs by 90% and strengthens Malaysia's self-reliance in nuclear reactor operations.

**Keywords:** TRIGA Mark II, HDPE irradiation tubes, neutron activation analysis, gamma shielding

## 1 Introduction

The TRIGA Mark II reactor as displayed in Figure 1, commissioned on 28 June 1982 and located at the Malaysian Nuclear Agency, is a vital asset for Malaysia's nuclear research and applications (Malaysian Nuclear Agency, 2022). The reactor's versatility is underscored by its use in neutron activation analysis (NAA), delayed neutron activation analysis (DNA), radioisotope production, neutron radiography, and small-angle neutron scattering (SANS). TRIGA, which stands for Training, Research, Isotope Production, and General Atomic, is globally recognized for its operational flexibility and inherent safety features. Figure 2 (a) (b) represent The Pneumatic Transfer System (PTS) and Rotary Rack (RR) which are integral facilities of the reactor, designed for sample irradiation under controlled neutron and gamma flux conditions. These systems rely on irradiation tubes to ensure sample containment, optimal radiation exposure, and safety. Previously, Malaysia relied on imported irradiation tubes, which posed challenges of high costs and supply chain reliability. This study introduces high-density polyethylene (HDPE) irradiation tubes as shown in Figure 3 as a locally manufactured alternative, produced by the Radiation Processing Technology Division of the Malaysian Nuclear Agency. HDPE's hydrogen content makes it an excellent material for neutron moderation, while its low gamma attenuation ensures effective radiation delivery. These tubes are strategically positioned in the reactor's central thimble, a region of maximum neutron and gamma flux, to maximize irradiation efficiency.



**Figure 1**

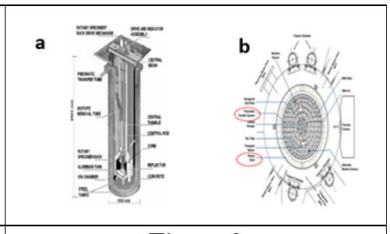



**Figure 2**

Figure 1: Nuklear Malaysia's PUSPATI TRIGA Research Reactor. Figure 2: (a) Pneumatic Transfer System (PTS) and (b) Rotary Rack (RR) tube positions in the reactor.

Figure 2: (a) Pneumatic Transfer System (PTS) and (b) Rotary Rack (RR) tube positions in the reactor.

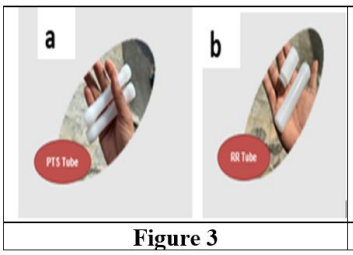



**Figure 3**

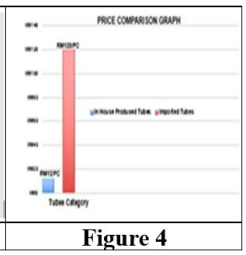



**Figure 4**

Figure 3: Locally manufactured high-density polyethylene (HDPE) irradiation tubes for the PTS and RR systems.

Figure 4: (Cost savings achieved by using locally manufactured HDPE tubes compared to imported alternatives.

## 2 Materials and Methods

The development and evaluation of HDPE irradiation tubes involved four stages: material selection, fabrication, radiation performance testing, and operational integration within the TRIGA Mark II reactor (International Atomic Energy Agency (IAEA), 2020). Material selection prioritized properties critical to reactor operations, including neutron moderation, gamma transparency, and mechanical stability. Injection-grade HDPE was selected for its excellent radiation interaction properties and structural durability. The tubes were fabricated using an injection molding process with a Battenfeld HM800/350 machine, ensuring dimensional precision and consistency. After fabrication, the tubes were subjected to radiation shielding tests. Neutron radiation shielding was evaluated using an Americium-Beryllium (Am-Be) source, with neutron flux measured by a Helium-3 (He-3) detector to assess moderation effectiveness (Lewis, 2019). Gamma shielding tests utilized a Barium-133 (Ba-133) gamma source to determine the material's attenuation and transparency properties (Stansbury, 2018). Subsequent integration into the reactor's PTS and RR systems allowed for live operational testing. Neutron flux and gamma transmission were measured to validate the tubes' performance under operational conditions. A comparative analysis was conducted against imported irradiation tubes to evaluate cost efficiency and long-term sustainability.

## 3 Results and Discussion

The results validated the high performance of the HDPE irradiation tubes across all tested parameters. Neutron flux measurements indicated that the RR tube provided stable flux levels closely matching background neutron counts, making it ideal for applications requiring consistent irradiation, such as NAA. Conversely, the PTS tube exhibited enhanced neutron flux, suitable for high-intensity isotope production. Gamma shielding tests confirmed that HDPE allowed consistent gamma penetration with minimal attenuation, ensuring reliable radiation delivery to samples. The comparative performance of the PTS and RR tubes is summarized in Table 1.

| **Tube Type** | **Neutron Count** | **Gamma Count** | **Performance Highlights** |
|---|---|---|---|
| RR Tube | 3209 (near 2390 background) | 4500 | Stable neutron flux ensures uniform NAA results |
| PTS Tube | 3463 (higher than background) | 4500 | Enhanced neutron flux supports rapid isotope production |

Table 1: Neutron and Gamma Performance of HDPE Tubes

Economic analysis as represented by Figure 4 revealed that locally manufactured HDPE tubes cost only 10% of imported alternatives, representing a significant cost saving. This innovation also mitigates supply chain risks, ensuring consistent availability of critical components while advancing local expertise in nuclear materials engineering. Operational validation confirmed the compatibility of HDPE tubes with the PTS and RR systems. The RR tube supports uniform activation of multiple samples, while the PTS tube facilitates rapid irradiation and transfer of short-lived isotopes.

## 4 Conclusions

The development of HDPE irradiation tubes for the TRIGA Mark II reactor demonstrates a successful transition toward cost-effective and sustainable solutions for nuclear reactor operations. The RR tube provides stable neutron flux for precise NAA applications, while the PTS tube's enhanced neutron interaction supports efficient isotope production. Radiation shielding tests validated HDPE's dual capabilities for neutron moderation and gamma transparency, confirming its reliability under operational conditions. This innovation reduces costs by 90%, enhances Malaysia's self-reliance in nuclear technology, and establishes a foundation for future advancements in reactor components. Further research will focus on optimizing HDPE formulations for improved radiation resistance and expanding the tubes' applications to high-flux environments.

## References

International Atomic Energy Agency (IAEA). 2020. *TRIGA Reactor Overview and Applications*. IAEA, Vienna.

G. N. Lewis. 2019. Neutron interaction with hydrogen-rich materials in research reactors. *Nuclear Science Journal*.

Malaysian Nuclear Agency. 2022. Innovation in reactor component production: Hdpe applications. Technical report, Malaysian Nuclear Agency.

E. Stansbury. 2018. Gamma radiation attenuation properties of hdpe materials. *Radiation Physics Review*.

Individual Research Contribution Review, 2024: 111–112
*ISSN: 3083-922X*

# Characterization of Recycled Electron Beam Irradiated Polyethylene terephthalate (PET) flakes for Potential Synthesis of Carbon Nanomaterials as Functional Fillers for Radiation Curable Radon Mitigation Coating and Antiviral Coating

**Mohd Hamzah Harun**
Radiation Processing Technology Division, Malaysian Nuclear Agency
43000 Kajang, Selangor
hamzah@nm.gov.my

## Abstract

Research is underway to identify novel uses for recycled plastic, with polyethylene terephthalate (PET) emerging as the most promising option for recycling. One strategy is to upcycle recycled plastic to create a better material by using electron beam irradiation. In this study, PET was irradiated with six different doses of electron beam irradiation and the purpose is to investigate the physicochemical changes occurring in PET flakes in comparation with virgin recycled plastic (PET) flakes. This was accomplished by the use of characterization techniques, which can be found in the next section The results of the comparative study between the virgin and the irradiated PET flakes concluded that electron beam irradiation can be used to improve the properties of PET. However, the effects of the irradiation are complex and depend on the irradiation doses.

**Keywords:** recycled PET, microplastics, electron beam irradiation

## 1 Introduction

The abundance of waste disposal in the plastics industry is a major environmental problem. Polyethylene terephthalate being one of the most widely used plastics, and it can take hundreds of years to decompose in a landfill. Electron beam irradiation is a promising technology for upcycling PET waste, which can be used to create structural defect within PET and improve its mechanical properties. In this study, we will evaluate the effects of electron beam irradiation on PET used as an upcycling material in comparison with the virgin recycled PET flakes. PET flakes are produced by sorting, washing, grinding, drying, and other processes from PET bottle wastes. The findings of this research will aid in our understanding of the possibilities of electron beam irradiation to be a useful tool for lowering the environmental impact of the plastics industry (Lee et al., 2023).

## 2 Materials and Methods

The PET bottles were crushed into flaky fragments using a crusher machine as part of a mechanical recycling process. The crushed PET size ranges between 1-10 mm. The PET is prepared in 6 plastic bags, with approximately a teaspoon of PET flakes in each packet. 1 of the packets will be the control virgin PET and 5 packets for the electron beam irradiated PET flakes. The Alurtron Malaysian Nuclear Agency's EPS 3000 electron beam equipment is used for the sample preparation of electron beam irradiation. The five samples were irradiated at five different dosages (20, 40, 80, 120, 160 and 200 kGy), respectively.

### 2.1 Materials

Polyethylene terephthalate (PET) flakes used in this study was sourced from recycled water bottles. Before utilization, recycled PET microplastic flakes were recovered and crushed by a crusher machine. The crushed PET flakes' size ranges between 1-5 mm.

### 2.2 Characterization

The samples were thoroughly characterized using a range of analytical methods following irradiation. The X-ray Diffraction (XRD) method was utilized to ascertain alterations in the PET samples' crystallinity. Any changes in the chemical structure were examined using Fourier Transform Infrared Spectroscopy (FTIR). Differential Scanning Calorimetry (DSC) was also used to evaluate changes in the thermal characteristics of the PET that had been exposed to radiation.

## 3 Data/Results

### 3.1 Fourier Transform Infrared spectroscopy (FTIR)

The FTIR spectra of PET samples irradiated with electron beam doses (0–200 kGy) show transmittance (%) as a function of wavenumber $cm^{-1}$. At 1715 $cm^{-1}$, the ester group peak slightly decreases with higher radiation doses, suggesting scission or alteration. The 1245 $cm^{-1}$ ester bond peak shows minor intensity changes, while the 1103 $cm^{-1}$ ether linkage peak varies, indicating structural changes. The 870 $cm^{-1}$ peak, linked to aromatic rings, remains stable, suggesting minimal impact on aromatic structures. Similarly, the 732 $cm^{-1}$ benzene ring peak shows minor changes, indicating resistance to radiation. Variations in ester and ether peaks (1245 $cm^{-1}$ and 1103 $cm^{-1}$) point to chain scission or cross-linking. Minor shifts in aromatic ring peaks (870 $cm^{-1}$ and 732 $cm^{-1}$) indicate potential alterations in ring structures or substitutions.

### 3.2 X-Ray Diffraction Analysis (XRD)

X-ray Diffraction (XRD) is used to analyze the crystalline structure of PET, which significantly influences its mechanical, thermal, and barrier properties (Chikaoui, 2019). PET

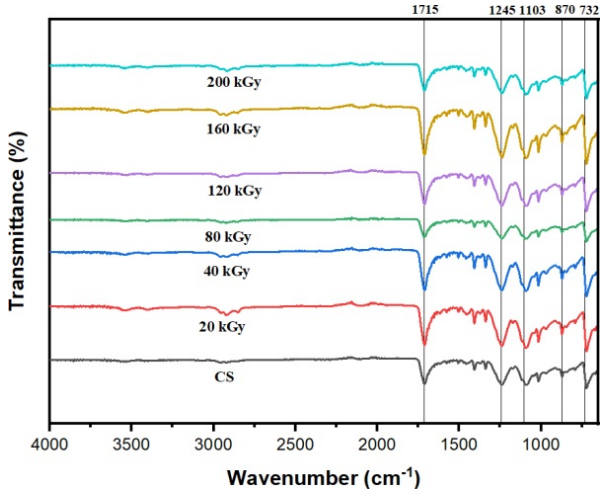



Figure 1: FTIR graph shows the transmittance (%) of PET samples exposed to different doses of electron beam irradiation (from 0 kGy to 200 kGy)

typically exhibits distinct peaks at $2\theta \approx 17°$, corresponding to the (010) plane, and $2\theta \approx 26°$, corresponding to the (100) plane, both indicative of crystalline regions in the polymer. The characteristic peaks at $2\theta \approx 17°$ and $2\theta \approx 25°$ confirm the presence of crystalline regions in PET. The control sample shows sharp and high-intensity peaks, indicating a well-defined crystalline structure. However, as the radiation dose increases, peak intensities decrease, and the peaks become less sharp, indicating a reduction in crystallinity. Peak broadening, particularly at $2\theta \approx 25°$, is observed with higher doses, suggesting increased structural disorder and a reduction in crystallite size. There is no significant shift in peak positions, indicating that the lattice parameters remain relatively unchanged. These changes suggest that radiation induces amorphization and disrupts the crystalline regions, potentially affecting the physical and mechanical properties of PET.

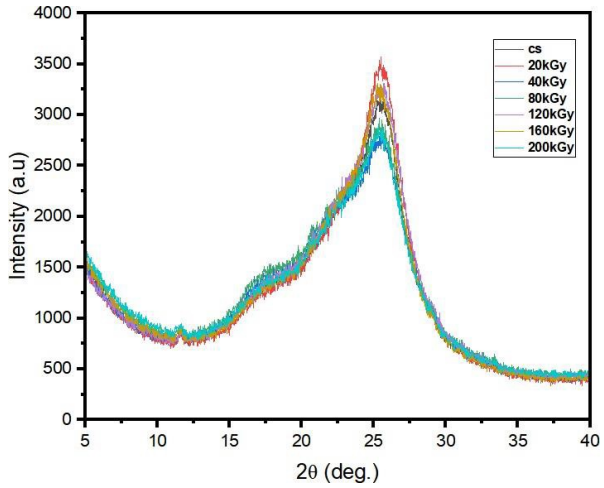



Figure 2: XRD graph; The x-axis represents the diffraction angle ($2\theta$), and the y-axis represents the intensity of the diffracted X-rays (in arbitrary units, a.u.)

### 3.3 Differential Scanning Calorimeter (DSC)

The DSC analysis of PET samples irradiated with electron beam doses (0–200 kGy) reveals significant insights into the effects of radiation on thermal behavior. Tg, observed as a step change in the DSC graph, marks the transition from a rigid to a flexible state. A $\Delta C_p$ value of 0.159 J/(g·K) highlights the change in molecular mobility at Tg. Tc, identified as an exothermic peak, shifts in onset, peak, and end temperatures with higher radiation doses. These changes indicate modifications in the crystallization behavior, likely caused by structural changes in the polymer from radiation-induced crosslinking or chain scission. The broad crystallization peak (-1.7 J/g) suggests changes in energy release and reorganization of crystalline domains. Tm, represented by an endothermic peak at 247.0°C, reflects the melting of crystalline regions. Higher radiation doses result in broader and less distinct Tm peaks, indicating a range of crystal sizes, imperfections, and decreased crystallinity. The enthalpy of fusion (-33.99 J/g) and peak width (19.5°C) further confirm these changes.

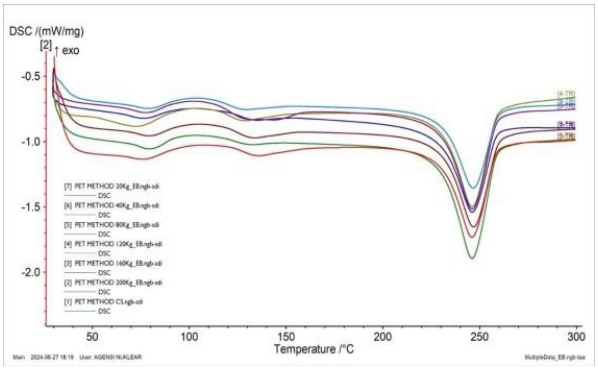



Figure 3: A DSC graph subjected to different dose of electron beam radiation

## 4 Discussion/Conclusion

Electron beam radiation induce significant structural modifications in PET, including chain scission, cross-linking, and oxidation, as evidenced by FTIR, XRD, and DSC analyses. FTIR revealed changes in ester (C=O) and alkyl (C-H) groups, while XRD indicated reduced crystallinity and increased amorphous regions. DSC showed variations in Tg, Tc, and Tm, reflecting altered thermal stability and crystallinity. Higher radiation doses decrease crystallinity, enhancing flexibility and affecting thermal properties.

## References

K. Chikaoui. 2019. Gamma rays irradiation effects in thin film polyethylene terephthalate polymer. *Radiation Physics and Chemistry*, 162:18–22.

Y. Lee, J. Cho, J. Sohn, and C. Kim. 2023. Health effects of microplastic exposures: Current issues and perspectives in south korea. *Yonsei Medical Journal*, 64(5):301–308.

Individual Research Contribution Review, 2024: 113–114
*ISSN: 3083-922X*

# The Effects of Gel Content and Swelling Ratio of Irradiation and Chemically Crosslinked Optimized Plasticized Gelatin Biopolymer Films

**Mohd Shahrulnizam Ahmad**
Radiation Processing Technology Division, Malaysian Nuclear Agency
43000 Kajang, Selangor
m_shahrulnizam@nm.gov.my

## Abstract

The effects of gel content and swelling ratio of the biopolymer are crucial to determine the crosslinking percentage. From 250 bloom, the maximized formulation is 8 g with 30% glycerol (optimized Ts) and 10 g with 40% glycerol (optimized EB). These optimized formulations are being crosslinked with chemical crosslinking (glutaraldehyde, GTA) and irradiation-induced crosslinking. Crosslinking percentage for GTA crosslinking can achieved up to 64% at 2% GTA. However, irradiation modification has achieved up to 70% at 15 kGy of biopolymer films.

**Keywords:** biopolymer, gelatin, glutaraldehyde, glycerol, irradiation

## 1 Introduction

Biodegradable materials break down through the enzymatic action of bacteria, fungi, and algae when placed in bioactive environments (Folino et al., 2020). A group of proteins known as gelatin has been carefully studied and has the ability to form films (Suderman et al., 2018). Plasticizers can reduce gelatin's brittle and easy crack properties (Vieira et al., 2011). A plasticiser's function minimises gelatin's natural brittleness by lowering intermolecular pressures. Crosslinking to protein structure is another solution that can drive stiffer and less permeable films. Several pieces of research have investigated the enhancement of functional properties, such as mechanical properties and thermal stabilities, through crosslinking induced by heat (irradiation modification) and chemical agents or enzymes (Buchert et al., 2010).

## 2 Materials and Methods

The film's optimized formulations were crosslinked with 0.5, 1.0, 1.5 and 2.0% (weight of GTA/weight of gelatin) of glutaraldeyhyde (GTA) with 12 minutes of mixing time. The films were then dried in an oven for 48 hours at 45 °C. For electron beam irradiation crosslinking, the optimized formulations were irradiated in liquid form using electron beam accelerator Model EPS 3000 in a dose range of 0, 5, 10, 20 and 25 kGy. This method was proposed by Bigi et al. (2004) with little modification, where the crosslinked gelatin films were weighed at room temperature (approximately 0.5 g). They were then immersed in reverse osmosis (RO) water for 24 hours. Wet samples were wiped to remove excess liquid and weighed. The amount of adsorbed water was calculated as Equation 1:

The swelling ratio (%) was calculated using the following equation:

$$\text{Swelling Ratio (\%)} = \frac{W_w - W_i}{W_i} \times 100\% \quad (1)$$

where $W_w$ and $W_i$ are the weights of the wet sample and the initial dry sample before immersion in RO water, respectively.

To determine the gel content of the crosslinked films, the swelled samples were dried. GTA-crosslinked samples were dried in an oven at 60 °C for 24 hours, and irradiated samples were dried in a vacuum oven at 30 °C for 24 hours. The gel content was then calculated using the following equation:

$$\text{Gel Content (\%)} = \frac{W_d}{W_i} \times 100\% \quad (2)$$

where $W_d$ is the weight of the dried sample after swelling, and $W_i$ is the initial weight before immersion in RO water.

## 3 Results and Discussion

Generally, the yield of crosslinking modification can be estimated from gel content determination. Otherwise, this crosslinking modification can also measure the swelling ratio as an independent cross-linking evaluation. Figures 1 and 2 show the effects of gel content and swelling ratio at different GTA contents and various irradiation doses, respectively. A gradual increase in gel content was observed as the GTA content increased from 0.5 to 2.0% (w/w) for optimized Ts and optimized EAB formulations of gelatin, as shown in Figure 1. Figure 1 shows that the cross-linking fraction can be achieved up to around 64% from 55% for 2.0% and 0.5% of GTA, respectively. Concurrently, this crosslinking treatment can also considerably increase the swelling ratio and the capability of the crosslinked films to sustain water in the polymer matrix. The results from Figure 1 show that GTA crosslinking induces a significantly decreased swelling ratio. This might be attributed to the ability to sustain water in the polymer matrix dropping when the crosslinking percentage increased as the crosslinker contents increased.

Figure 2 shows the effects of irradiation doses (5 to 25 kGy) on gel content and swelling ratio of the optimized content gelatin/glycerol films, as discussed previously. In the irradiation treatment, plasticized gelatin films must be irradiated in liquid (after gelatin powder is immersed in water) to

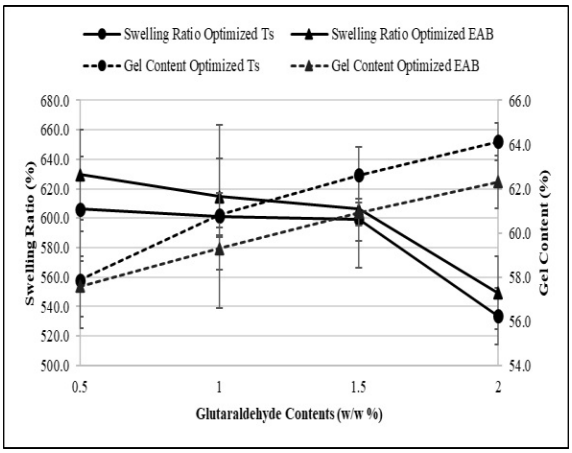



Figure 1: Effect of GTA contents on gel content and swelling ratio of the crosslinked plasticized fish gelatin films

induce a crosslinking reaction in a polymer matrix (Haema et al., 2014). The gel content increased rapidly from 5 kGy to 15 kGy, up to 70% for both gelatin contents. However, the gel content was not a significant difference between these two contents of fish gelatin (¡8% difference). After 15 kGy of irradiation dose, the gel content dropped drastically due to the degradation of plasticized gelatin films by irradiation modification. Vieira and Mastro (Vieira et al., 2011) reported that the viscosities of films decrease in response to an irradiation dose. This might correlate to the degradation stage at this higher dosage of irradiation. Moreover, this decrease in viscosities also correlated to the decrease in molecular weight of gelatin (Kimura et al., 2021) especially dose up to 100 kGy and can caused degradation.

Kimura et al. (2021) introduced at lower irradiation dose (20 Gy) obtained around 90% of crosslinking percentage. Figure 2 also shows the swelling ratio of irradiated plasticized fish gelatin films. As Haema et al. (2014) mentioned, the swelling ratio is a measurement of the tendency of the polymer matrix to build up a three-dimensional (3D) structure after being cross-linked. Furthermore, this 3D network also recognized the capability to sustain water where the low irradiation dose absorbs more water than the higher dose because the crosslinking density is lower. The results show that the swelling ratio decreased rapidly from 5 kGy to 25 kGy. As confirmed, the plasticized gelatin films were successfully irradiated in liquid condition at room temperature without any chemical crosslinkers. Irradiation is revealed to be a superior option, capable of achieving high moisture content and effectively inducing crosslinking at lower doses while maintaining a lower swelling ratio. This method is considered more sustainable and environmentally friendly as it avoids using chemical additives, thereby enhancing the sustainability of the production process.

The gel content and swelling ratio are increased and decreased, respectively, for crosslinked plasticized fish gelatin films. This is attributed to the fact that the GTA crosslinking successfully built a 3D network in the biopolymer matrix and reduced water retention. However, the irradiation-induced crosslinking has achieved a crosslinking percentage of up to 70% at 15 kGy. Then, crosslinking percentage dropped at 20 and 25 kGy due to the degradation. Even though, degradation is dominated at 20 and 25 kGy, the swelling ratio decreased from 0 to 25 kGy.

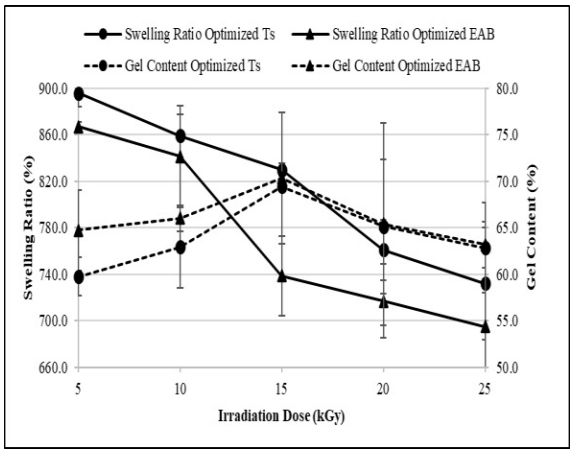



Figure 2: Effect of irradiation dose (kGy) on gel content and swelling ratio of the crosslinked plasticized fish gelatin films

## 4 Conclusions

In summary, crosslinking modification has successfully enhanced the crosslinking percentage and swelling ratio in the plasticized gelatin biopolymer films. The crosslinking percentage can be achieved around 64% at 2% GTA. However, the crosslinking for irradiation modification has achieved up to 70% at 15 kGy.

## References

J. Buchert, D. Ercili Cura, H. Ma, C. Gasparetti, E. Monogioudi, G. Faccio, M. Mattinen, H. Boer, R. Partanen, E. Selinheimo, R. Lantto, and K. Kruus. 2010. Crosslinking food proteins for improved functionality. *Annual Review of Food Science and Technology*, 1:113–138.

A. Folino, A. Karageorgiou, P. S. Calabrò, and D. Komilis. 2020. Biodegradation of wasted bioplastics in natural and industrial environments: A review. *Sustainability*, 12(15):6030.

K. Haema, T. G. Oyama, A. Kimura, and M. Taguchi. 2014. Radiation stability and modification of gelatin for biological and medical applications. *Radiation Physics and Chemistry*, 103:126–130.

A. Kimura, F. Yoshida, M. Ueno, and M. Taguchi. 2021. Application of radiation crosslinking technique to development of gelatin scaffold for tissue engineering. *Radiation Physics and Chemistry*, 180:109287.

N. Suderman, M. I. N. Isa, and N. M. Sarbon. 2018. The effect of plasticizers on the functional properties of biodegradable gelatin-based film: A review. *Food Bioscience*, 24:111–119.

M. G. A. Vieira, M. A. Silva, L. O. Santos, and M. M. Beppu. 2011. Natural-based plasticizers and biopolymer films: A review. *European Polymer Journal*, 47(3):254–263.

Individual Research Contribution Review, 2024: 115–116
*ISSN: 3083-922X*

# X-ray diffraction (XRD) analysis for Graphene Oxide as Corrosion Agent Preventive In POBUA

**Mohd Sofian Alias**
Radiation Processing Technology Division, Malaysian Nuclear Agency
43000 Kajang, Selangor
sofian@nm.gov.my

## Abstract

This study investigates the structural properties of graphene oxide (GO) as a corrosion agent preventive in palm oil-based urethane acrylate (POBUA) coatings through X-ray diffraction (XRD) analysis. The integration of GO into the POBUA matrix was analyzed to evaluate its effect on the material's crystallinity, a key factor influencing its barrier and anti-corrosion performance. XRD measurements were performed over a $2\theta$ range of 5° to 60° using a copper X-ray source. The crystallinity index (CI) of POBUA with GO (POBUA-gO) was calculated using the Segal equation, revealing a significant enhancement in crystallinity compared to the pure POBUA and POBUA with graphite (POBUA-g). The sharper and more intense diffraction peaks in POBUA-gO indicate improved structural order due to the effective dispersion and interaction of GO within the polymer matrix. This increased crystallinity is expected to enhance the coating's mechanical stability and impermeability, making POBUA-gO a promising material for corrosion prevention applications.

**Keywords:** X-ray diffraction, POBUA-gO, polymer, Graphene oxide

## 1 Introduction

Graphene oxide (GO) has emerged as a promising material in the field of corrosion prevention due to its remarkable chemical, mechanical, and barrier properties. Its ability to form a protective layer on surfaces makes it an excellent candidate for enhancing the durability of various materials. This study focuses on the application of GO as a corrosion agent preventive in polyurethane-based urethane acrylate (POBUA) films, a widely used material in protective coatings. The structural characterization of GO, crucial for understanding its interaction with the POBUA matrix, was conducted using X-ray diffraction (XRD) analysis. XRD provides detailed insights into the crystallographic properties of GO, including its interlayer spacing and degree of oxidation, which directly influence its effectiveness as a corrosion inhibitor. By investigating the structural properties of GO and its integration within POBUA, this research aims to establish a foundation for the development of high-performance anti-corrosion coatings.

## 2 Materials and Methods

X-ray diffraction (XRD) analysis was performed to determine the crystallinity percentage of polyurethane-based urethane acrylate (POBUA) coatings with graphene oxide filler (POBUA-gO). The experiment utilized an XRD instrument (PANalytical, X'Pert PRO MPD PW 3040/60). Diffraction data were collected over a $2\theta$ range of 5° to 60° using a copper X-ray source, operated at a voltage of 50 kV and a current of 120 mA. The recorded diffraction spectra for POBUA-gO were analyzed using High Score Plus X'Pert Plus Version 2.2b (2.2.2) software. The crystallinity index (CI) of the POBUA-gO sample was calculated using the Segal equation:

$$CI\ (\%) = \left[\frac{I_{02} - I_{\text{am}}}{I_{02}}\right] \times 100$$

## 3 Results and Discussion

The resulting diffraction patterns, shown in Figure 1, revealed a broad, amorphous halo characteristic of POBUA coatings. Meanwhile The addition of GO enhanced the crystallinity of POBUA, likely due to the formation of nucleation sites by the GO particles. GO, a two-dimensional graphene derivative, has been shown to increase polymer nucleation density, leading to smaller and more numerous crystalline regions (Jang et al., 2021). The long-chain acrylate structure of POBUA and its crosslinking network contribute to its crystallinity. Previous studies have indicated that longer polymer segments exhibit better crystallinity, potentially due to reduced segment mobility (Nissenbaum et al., 2020).However, increased crystallinity may compromise certain coating properties, such as surface adhesion.

The incorporation of GO into the POBUA matrix enhances crystallinity by increasing packing density and providing nucleation sites through its surface functional groups (OH, COOH) (Jang et al., 2021). As the GO content increases, the amorphous halo intensity decreases, and a sharp peak appears at $2\theta = 26.4°$, corresponding to the (002) crystallographic planes of graphite structures. This shift in the diffraction peak is consistent with previous findings (Sang et al., 2018). Figure 1 also illustrates the correlation between GO content and the crystallinity index (CI) of the cured POBUA film.

## 4 Conclusions

The XRD analysis demonstrates that the incorporation of graphene oxide (GO) into palm oil-based urethane acrylate (POBUA) coatings significantly enhances the crystallinity of

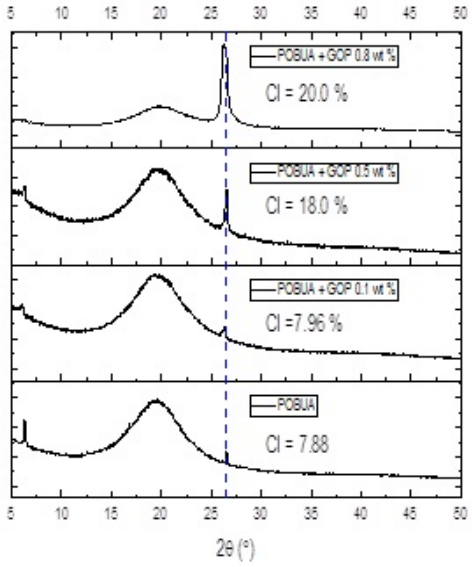



Figure 1: XRD graph of POBUA and POBUA with 0.1-0.8 wt% GOP

the material. GO serves as a nucleating agent, increasing the density of crystalline regions through its functional groups (OH, COOH) and improving the packing density within the polymer matrix. This enhancement is evidenced by the reduction of the amorphous halo and the emergence of a sharp diffraction peak at$2\theta = 26.4°$, corresponding to the (002) crystallographic planes of graphite structures. The findings align with previous studies, confirming that GO promotes nucleation and structural ordering in polymer matrices. However, it is essential to consider the trade-off between increased crystallinity and potential changes in coating properties, such as reduced surface adhesion. Overall, the study highlights the potential of GO to improve the structural and anti-corrosion performance of POBUA coatings by modulating their crystallinity.

## References

J.-H. Jang, B. Oh, and E.-J. Lee. 2021. Crystalline hydroxyapatite/graphene oxide complex by low-temperature sol-gel synthesis and its characterization. *Ceramics International*, 47(19):27677–27699.

A. Nissenbaum, I. Greenfeld, and H.D. Wagner. 2020. Shape memory polyurethane - amorphous molecular mechanism during fixation and recovery. *Polymer*, 190:122226–122234.

L. Sang, W. Hao, Y. Zhao, L. Yao, and P. Cui. 2018. Highly aligned graphene oxide/waterborne polyurethane fabricated by in-situ polymerization at low temperature. *Polymer Bulletin*, 18(1):75–84.

Individual Research Contribution Review, 2024: 117–118
*ISSN: 3083-922X*

# Gamma-Induced Synthesis of Silver Nanoparticles

**Mohd Yusof Hamzah**
Radiation Processing Technology Division, Malaysian Nuclear Agency
43000 Kajang, Selangor
m_yusof@nm.gov.my

## Abstract

A novel method of producing silver nanoparticles (AgNPs) using gamma ray-induced process has been proposed. This method has been proven to be simple, fast, and economical; it does not require reducing agents; it employs water as the solvent, thus greener, while enabling simultaneous synthesis and sterilization; it produces AgNPs of homogeneous distribution and allows control of their size by adjusting the experimental conditions. The rapid production of AgNps at larger volumes, thus enabling an economic advantage. Herein, AgNPs with size ranging from 5 to 50nm have been successfully produced. Its antimicrobial properties has also been demonstrated.

**Keywords:** gamma radiation; silver nanoparticles

## 1 Introduction

AgNPs can be synthesized using physical, chemical, and biological methods. Conventionally, physical methods involve evaporation-condensation using a tube furnace at atmospheric pressure(Pucelik et al., 2022). They also include spark discharging and pyrolysis processes. Chemical methods, on the other hand, rely on water or organic solvents silver nanoparticles synthesis. They usually employ three main components–metal precursors, reducing agents, and stabilizing/capping agents. Meanwhile, biological methods depend on bio-sorption of metals by gram-negative and gram-positive bacteria as reduction agents. While these methods are proven to produce AgNPs of intended quality, they require multiple steps and involve addition of excessive hazardous reducing agent such as sodium borohydride ($NaBH_4$). Some may involve bacteria that are borderline pathogenic and maybe not economically viable due to prolonged processing time that may take more 5 days to complete (Sood and Chopra, 2018). Additionally, due to production in small batches, economic advantage is not met.

A novel method of producing NPs from silver and other metal salts employs gamma ray-induced process (Sood and Chopra, 2018). This method has been proven to be simple, fast, and economical; it does not require reducing agents; it employs water as the solvent, thus greener, while enabling simultaneous synthesis and sterilization (Medici et al., 2019); it produces AgNPs of homogeneous distribution and allows control of their size by adjusting the experimental conditions. Herein, AgNps with size ranging from 5 to 50nm have been successfully produced using the gamma-induced reaction pathway. Its antimicrobial properties was also demonstrated.

## 2 Materials and Methods

### 2.1 Materials

$AgNO_3$, 99% and PVP, 99%, were purchased from Sigma-Aldrich and used without prior purification. Ultrapure water (UPW) was used throughout this work for all solution preparations.

### 2.2 Synthesis of AgNPs

$AgNO_3$ and PVP were dissolved in water at suitable molar ratios. The mixture was aliquoted into several vessels and purged with $N_2$ 30m before irradiation. Each vessel was irradiated at 5, 10, 15 and 20 kGy. Then, the AgNPs were collected and analyzed without prior purification.

Changes in chemical structures were monitored using a Shimadzu Uv-vis spectrosphotometer, and the particle size was monitored using a Sympatec particle size analyzer.

## 3 Results

Formation of AgNPs

Figure 1 Shows the surface plasmon resonance (SPR) properties of the resulting AgNPs/PP with peaks around 410–420 nm, clear indication of AgNPs formation.

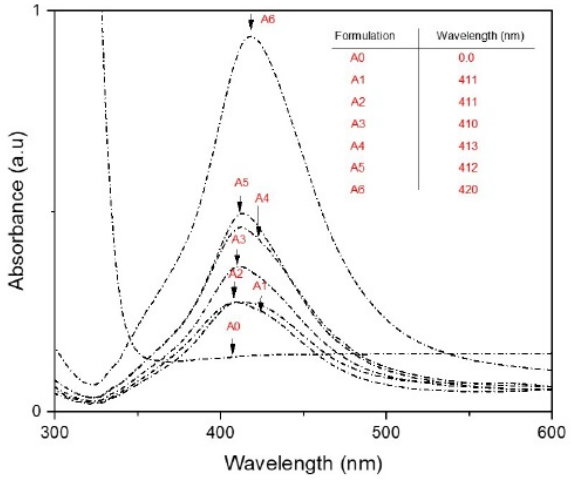



Figure 1: FTIR spectrums of unirradiated monomers and nanogels irradiated at 20 kGy.

## 4 Discussion

In the dilute solution regime, upon absorption of the ionizing energy, the aqueous media absorbed the energy from the irradiation source, which then led to the formation of several species of radicals (1):

$$H_2O \rightarrow e^-_{aq},\ \cdot OH,\ H^{\cdot},\ H_2O_2,\ H_2,\ H^+,\ OH^- \qquad (1)$$

For context, solvated electrons are one of the most abundance radicals formed as product of water radiolysis, typically 2.7 of it are produced for each 100eV absorbed bye the water molecules. They are highly efficient reducing radicals. Another redcutamt are the hydrogen radicals, H. Both types of tadicals were expected to induce radiolytic reduction of $Ag^+$ ions in PVP solutions as in figure 2. The transition was indicated by formation of yellow colored colloids

$$Ag^0 + Ag^+ \rightarrow Ag_2^+,$$
$$Ag_{n-1} + Ag^+ \rightarrow Ag_n^+,$$
$$Ag_n + Ag^+ \rightarrow Ag_{n+1}^+$$
$$Ag_{n+1}^+ + e_{aq}^- \rightarrow Ag_{n+1}$$
$$Ag_{n+1}^+ + H^{\cdot} \rightarrow Ag_{n+1} + H^+$$

Figure 2: Proposed reaction pathways for the formation of the AgNPs

Figure 3. Shows typical size data. The minimum size of AgNPs was obtained at 20kGy, while the largest was at 5kGy.

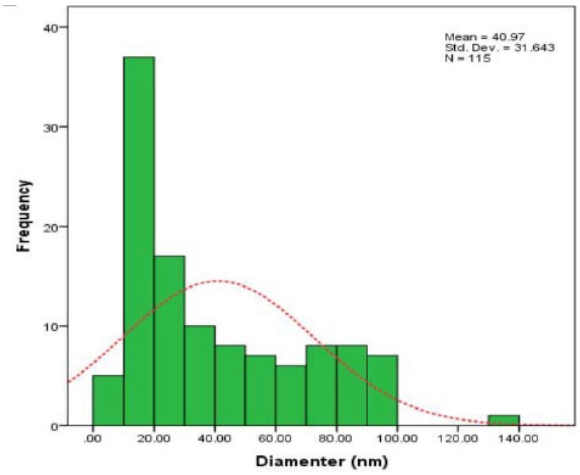



Figure 3: The AgNPs size at 5kGy.

Figure 4. Shows the inhibition properties of the AgNPs against gram-positive *Staphylococcus aureus (S.aureus)*.

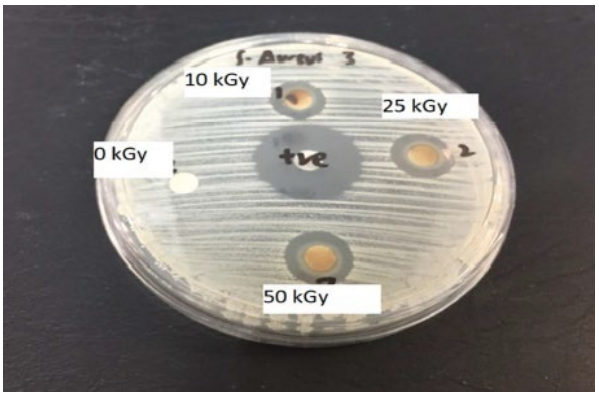



Figure 4: The produced AgNps shows good microb inhibition.

## 5 Conclusions

A novel method of producing silver nanoparticles (AgNPs) using gamma ray-induced process has been proposed. This method has been proven to be simple, fast, and economical; it does not require reducing agents; it employs water as the solvent, thus greener, while enabling simultaneous synthesis and sterilization. AgNPs with size ranging from 5 to 50nm have been successfully produced. Its antimicrobial properties has also been demonstrated against *S.aureus*.

## References

S. Medici, M. Peana, V. M. Nurchi, and M. A. Zoroddu. 2019. Medical uses of silver: history, myths, and scientific evidence. *Journal of Medicinal Chemistry*, 62:5923–5943.

B. Pucelik, A. Sulek, M. Borkowski, A. Barzowska, M. Kobielusz, and J. M. Dabrowski. 2022. Synthesis and characterization of size-and charge-tunable silver nanoparticles for selective anticancer and antibacterial treatment. *ACS Applied Materials & Interfaces*, 14:14981–14996.

R. Sood and D. S. Chopra. 2018. Regulatory approval of silver nanoparticles. *Applied Clinical Research, Clinical Trials and Regulatory Affairs*, 5:74–79.

Individual Research Contribution Review, 2024: 119–120
*ISSN: 3083-922X*

# Gamma Radiation-Induced Synthesis of Tin Oxide ($SnO_2$) Nanoparticles: Investigating Concentration and Dose-Dependent Yield for Scalable Production

**Muhammad Aidell Amir**
Radiation Processing Technology Division, Malaysian Nuclear Agency
43000 Kajang, Selangor
aidell@nm.gov.my

## Abstract

$SnO_2$ nanoparticles are widely used in sensors, energy storage, and catalysis due to their unique properties. However, the traditional methods to produce nanoparticles require high temperatures, toxic chemicals, and complex setups, thus making them costly and harming the environment. The following study explores a simpler, greener method of gamma radiation synthesis of $SnO_2$ nanoparticles. The process is done at room temperature, using no hazardous chemicals, and it uses water radiolysis to create nanoparticles of consistent size and purity. Using the SINAGAMA irradiation facility, this research is going to test how scalable and reliable this method will be for larger production. It is expected to be demonstrated that gamma radiation represents an alternative, more effective, ecological, and cheaper means for producing $SnO_2$ nanoparticles in comparison with the current conventional procedures for industrial applications.

**Keywords:** Tin Oxide, Nanoparticle, Radiation, Free Radicals

## 1 Introduction

Tin oxide ($SnO_2$) nanoparticles have emerged as a vital material in various industries due to their exceptional properties, including high electrical conductivity, optical transparency, and catalytic activity (Das et al., 2021). These characteristics have enabled their use in diverse applications such as gas sensors, photocatalysts, lithium-ion batteries, and solar cells. However, conventional methods for synthesizing$SnO_2$ nanoparticles, including sol-gel processes, chemical vapor deposition (CVD), and solvothermal techniques, often pose significant challenges. These methods generally involve high temperatures, long processing times, and the use of hazardous chemicals, which raise energy costs, environmental concerns, and scaling-up problems (Tsega and Dejene, 2017; Takami et al., 1999; Saegusa et al., 2023). Besides, it is difficult to achieve a consistent size distribution and purity with these techniques, which makes them unsuitable for industrial production.

Recently, radiation-induced synthesis, especially using gamma radiation, has been considered a novel alternative in the production of nanoparticles. This method applies the ionizing power of gamma radiation to induce water radiolysis and produce radicals that will drive nanoparticle formation under ambient conditions. In contrast to conventional methods, synthesis by gamma radiation does not require high temperatures or toxic chemicals and is, therefore, an energy-saving and more environmentally benign process. Moreover, its high penetration ability allows gamma rays to provide uniform treatment throughout the material and therefore easily produce nanoparticles of consistent quality (Ken et al., 2022). Additionally, by precisely controlling the dosage of radiation, it has enabled the fine-tuning of nanoparticle characteristics-size and morphology-which becomes really essential for their performance in use.

Application on a larger scale is limited with regards to availability and the high costs incurred in the operation of an irradiation facility. This work tries to address these challenges by exploring the feasibility of gamma radiation-induced synthesis for scalable and reliable production of$SnO_2$ nanoparticles using the SINAGAMA irradiation facility. In particular, this research investigates the effect of sample concentration and radiation dose on scalability and assesses batch-to-batch consistency in order to ensure reproducibility. These findings intend to show how gamma radiation is a cost-effective, sustainable, and easily scalable production method for $SnO_2$ nanoparticles, leading to wide industrial applications, hence an advanced nanotechnology study.

## 2 Materials and Methods

### 2.1 Materials

Materials Tin(II) chloride dihydrate ($SnCl_2{\cdot}2\,H_2O$, ≥ 99% purity, sigma-aldrich) and polyvinylpyrrolidone (PVP, sigma-aldrich) were used as precursors and stabilizing agents, respectively. Deionized water was used as the solvent for all preparations. All chemicals were used without further purification.

### 2.2 Preparation of Tin Chloride Solutions

Aqueous solutions of tin chloride with varying concentrations (0.05 M, 0.1 M, 0.3 M, and 0.5 M) were prepared by dissolving $SnCl_2{\cdot}2\,H_2O$ in deionized water. For selected samples, PVP was added as a stabilizer at concentrations of 1%, 2%, and 3% (w/v) relative to the solution. The solutions were mixed thoroughly until complete dissolution was achieved. Each solution was transferred into sealed glass vials to minimize contamination and evaporation during irradiation.

### 2.3 Gamma Irradiation Procedure

SINAGAMA gamma irradiation facility using a cobalt-60 source. The total absorbed dose was set at 100 kGy, delivered at a dose rate of approximately 1.5 kGy/hour under ambient temperature and pressure. This dose was chosen based on preliminary studies to ensure the generation of sufficient radicals for nanoparticle formation. The irradiation process causes the radiolysis of water, producing reactive species such as hydroxyl radicals •OH, hydrogen atoms H•, and solvated electrons $e^-_{aq}$, which are responsible for the reduction of $Sn^{2+}$ ions to $SnO_2$ nanoparticles.

## 3 Data and Results

### 3.1 Concentration of $SnO_2$ Nanoparticles vs yield percentage

The synthesis method using gamma radiation was able to produce $SnO_2$ nanoparticles for all concentrations of the solutions of tin chloride. The percentage of yield increased with the increase in precursor concentration, as obtained in Table 1, where the solution at 0.05 M gave a yield of 62.3%, while the solution at 0.5 M gave a yield of 89.7% as shown in Table 1.

| Concentration (M) | Yield (%) |
|---|---|
| 0.05 | 62.3 ± 3.2 |
| 0.1 | 78.5 ± 2.8 |
| 0.3 | 85.2 ± 2.4 |
| 0.5 | 89.7 ± 3.0 |

Table 1: Concentration and yield of $SnO_2$ nanoparticle

### 3.2 Effects of Radiation Dose vs yield percentage

The influence of radiation dose on nanoparticle properties was investigated using 0.1 M solutions irradiated at doses of 50 kGy, 100 kGy, and 150 kGy.

| Dose (kGy) | Yield (%) |
|---|---|
| 50 | 71.2 ± 3.5 |
| 100 | 78.5 ± 2.8 |
| 150 | 79.3 ± 3.0 |

Table 2: Dose rate and yield of $SnO_2$ nanoparticles.

## 4 Discussion

nanoparticles increased with higher sample concentrations, where the 0.1 M solution yielded significantly less compared to the 0.3 M and 0.5 M solutions. Such a trend can be attributed to more precursor molecules being available in higher concentrations, which facilitated more effective radiolysis and subsequent nanoparticle formation. However, a plateauing effect at the highest concentration suggests that above a certain threshold, the radiation's ability to drive further conversion becomes limited, possibly due to self-shielding effects or saturation of reactive species.

Similarly, the relationship between radiation dose and yield indicates that higher doses promote greater nanoparticle formation, likely due to increased generation of radicals from water radiolysis. For example, increasing the dose from 50 kGy to 100 kGy significantly increased the yield, but doses in excess of 100 kGy did not continue this upward trend, seeming to flatten out and perhaps pointing toward some maximum in the process efficiency for these experimental conditions. This could reflect that all precursors were exhausted or that secondary effects, like aggregation of particles, could now start to dominate at higher doses.

## 5 Conclusions

In conclusion, the results project the potential of gamma radiation-induced synthesis for efficient production of $SnO_2$ nanoparticles, with yield optimization achieved through careful control of concentration and dose. Future studies will focus on detailed characterization and application-specific evaluations to validate the broader utility of this method.

## References

L. Das, L. D. Koonathan, A. Kunwar, S. Neogy, A. K. Debnath, and S. Adhikari. 2021. Nontoxic photoluminescent tin oxide nanoparticles for cell imaging: deep eutectic solvent mediated synthesis, tuning and mechanism. *Materials Advances*, pages 4303–4315.

S. Ken, A. Srivastava, A. Debnath, S. Adhikari, and M. Rath. 2022. One-step synthesis of tin oxide nanoparticles in aqueous solution induced by free radicals. *Materials Chemistry and Physics*.

S. Saegusa, K. Sakurai, I. Okada, K. Yamada, M. Shima, Y. Utsumi, and A. Yamaguchi. 2023. The effect of ph on x-ray-radiolysis-induced synthesis of nickel nanoparticles on lithium niobate substrates. *Materials Science and Engineering: B*, page 116093.

A. Takami, H. Kurita, and S. Koda. 1999. Laser-induced size reduction of noble metal particles. *The Journal of Physical Chemistry B*, 103:1226–1232.

M. Tsega and F. Dejene. 2017. Influence of acidic ph on the formulation of $tio_2$ nanocrystalline powders with enhanced photoluminescence property. *Heliyon*, 3(7):e00246.

Individual Research Contribution Review, 2024: 121–122
*ISSN: 3083-922X*

# Determination of Factor Influence on Irradiated Waste Polyethylene Terephthalate (PET) as a Filler for Construction Material

**Muhammad Hazim Muhammad Sayuti**
Radiation Processing Technology Division, Malaysian Nuclear Agency
43000 Kajang, Selangor
hazim@nm.gov.my

## Abstract

This project explores the use of recycled PET (RC-PET) obtained from bottle preform manufacturing waste, which is irradiated with 3.0 MeV Electron Beam (EB) to produce RC-PET. The absorbed radiation doses, ranging from 0 to 200 kGy, are studied to assess their effects on crystallization and molecular weight. Characterization of the irradiated PET aims to determine the optimal dose for use as a filler in construction materials. The irradiated samples undergo mechanical, thermal, and morphological testing. The RC-PET is then used in concrete mixed with nano silica, and mixing parameters like filler percentage and radiation dose are optimized for better compressive strength and cost-effectiveness. The project evaluates the changes in various properties of the concrete, including compressive strength and ultrasonic pulse velocity.

**Keywords:** Polyethylene Terephthalate, Electron Beam, Irradiated Waste.

## 1 Introduction

This project focuses on studying the Electron Beam Radiation Crystallization (RC) technique for recycling PET (Polyethylene Terephthalate), commonly used in plastic bottles. PET is known for its recyclability and safety, often marked with the number "1" on water bottles. The project investigates how Electron Beam irradiation can enhance the crystallization phase of recycled PET (RC-PET) by applying various radiation doses to find the optimum level for crystallization. The resulting RC-PET will then be used in concrete preparation. Finally, the physical and mechanical properties of the concrete will be characterized to assess the impact of RC-PET.

## 2 Materials and Methods

Figure 1 shows the process flow for the development and testing of PET- reinforced concrete - crystallized.

## 3 Results and Discussion

The irradiated samples showed some increment in their mechanical properties after being bombarded with electron beam. Tensile strength with different dose was summarized in Figure 2. Tensile strength of the PET increased with increasing of irradiation dose. Tensile strength of pure PET was 30.1 MPa.

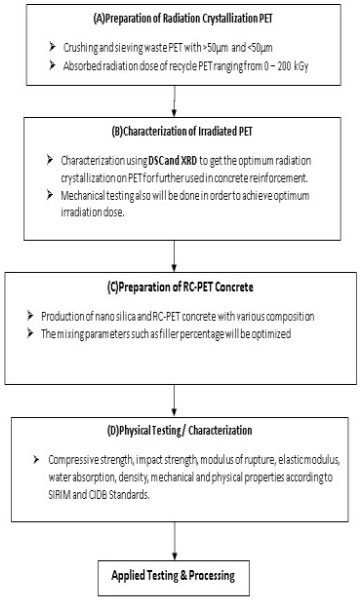



Figure 1: Process Flow for the Development and Testing of Radiation-Crystallized PET-Reinforced Concrete

When undergo the irradiation dose from 50 up to 200kGy, the tensile strength increasing to 30.3, 31.3, 32.2 and 32.1 MPa respectively. This occurred due to the cross linking of the PET (Meza et al., 2021). The highest tensile strength recorded is 32.2 MPa with irradiation dose of 150 kGy.

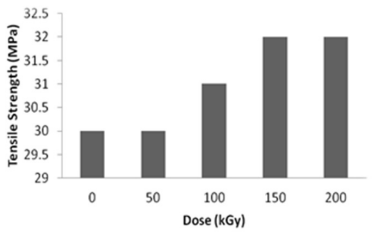



Figure 2: Tensile Strength

The hardness test was carried out and the results shown in the figure 3 below. From the figure, the hardness of cross-linked PET showed at 150 kGy achieved the highest value and decreasing when being radiated with 200 kGy.

From the graph shown in Figure 4, the degree of crosslinking was increased with increasing of irradiation dose. From

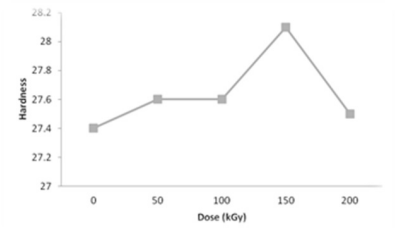



Figure 3: Hardness

0% of gel content degree, it is increased up to 42% when being irradiated with electron beam with dose of 50, 100, 150 and 200kGy respectively. This showed PET undergoes the crosslinking process throughout the irradiation using electron beam (Nkomo et al., 2022).

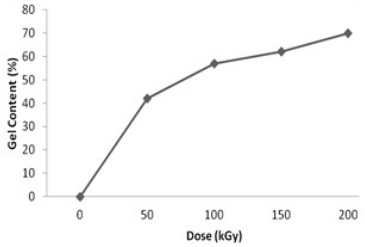



Figure 4: Gel Content

The thermal properties of samples were determined by DSC analysis. The value of melting temperature, Tm, glass transition temperature, Tg and degree of crystallinity, %Xc of each samples were summarized in Table 1.

| **Sample Description** | $T_m$ (°C) | $T_g$ (°C) | $X_c$ (%) |
|---|---|---|---|
| PET pure | 131.38 | 67.34 | 54.41 |
| PET 50 | 131.98 | 66.70 | 55.62 |
| PET 100 | 131.98 | 66.28 | 55.51 |
| PET 150 | 132.41 | 66.45 | 56.78 |
| PET 200 | 131.82 | 65.67 | 55.97 |

Table 1: Thermal properties of PET samples subjected to different treatments.

The $T_m$ (melting temperature) of pure PET increases with irradiation dose, but decreases when exposed to 200 kGy. The $T_g$ (glass transition temperature) of pure PET decreases after electron beam irradiation. The reduction in $T_g$ could also be linked to enthalpy relaxation effects from the thermal history of the samples (Piątek-Hnat et al., 2020).

Despite this, the concrete still meets medium-strength specifications, indicating that the inclusion of PET flakes does not compromise its suitability for use. UPV values remain consistent over 7, 14, and 28 days, demonstrating that the PET flakes do not negatively impact the long-term performance or structural integrity of the concrete.

The compressive strength results for concrete with different types of PET show distinct trends over time. On day 7, the control concrete achieved a strength of 13 MPa, while concrete with pure PET had 12 MPa, and irradiated PET showed

| **Pulse velocity (km/s)** | |
|---|---|
| Control | 3.6264 (Good) |
| PET Concrete | 3.2269 (Medium) |
| rPet Concrete | 3.4481 (Medium) |

Table 2: Ultrasonic Pulse Velocity

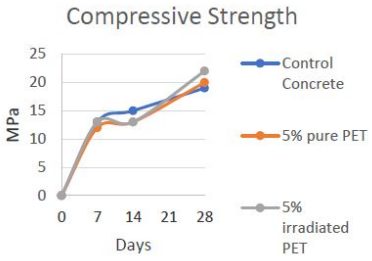



Figure 5: Compressive Strength

13 MPa, indicating that irradiation may help mitigate the negative effects of PET flakes. By day 14, the control concrete reached 15 MPa, concrete with pure PET improved to 13 MPa, and irradiated PET maintained 13 MPa, showing comparable strength. By day 28, the control reached 20 MPa, pure PET reached 19 MPa, and irradiated PET significantly improved to 22 MPa, surpassing both pure PET and control samples, demonstrating the long-term benefits of irradiated PET in enhancing compressive strength.

## 4 Conclusions

In conclusion, the optimal irradiation dose for PET is 150 kGy, which significantly enhances the mechanical and thermal properties of recycled PET. This irradiated PET, used as a substitute for fine sand in concrete, improves its strength by better bonding with cement and promoting even distribution of PET particles. This reduces porosity, increasing the concrete's density and durability. Additionally, this method is environmentally friendly as it recycles plastic waste, reducing the reliance on natural sand. Overall, replacing some sand with irradiated PET results in stronger, more durable, and sustainable concrete.

## References

A. Meza, P. Pujadas, L. M. Meza, F. Pardo-Bosch, and R. D. López-Carreño. 2021. Mechanical optimization of concrete with recycled pet fibres based on a statistical-experimental study. *Materials (Basel)*, 14(2):240.

Nkosilathi Nkomo, L. M. Masu, and P. K. Nziu. 2022. Effects of polyethylene terephthalate fibre reinforcement on mechanical properties of concrete. *Advances in Materials Science and Engineering*, pages 1–9.

M. Piątek-Hnat, K. Bomba, J. Pęksiński, A. Kozłowska, J. G. Sośnicki, and T. J. Idzik. 2020. Effect of e-beam irradiation on thermal and mechanical properties of ester elastomers containing multifunctional alcohols. *Polymers (Basel)*, 12(5):1043.

Individual Research Contribution Review, 2024: 123–124
*ISSN: 3083-922X*

# The Effectiveness of Ultraviolet Germicidal Irradiation (UVGI) in Eradicating the Fomite Transmission ESKAPE Pathogen

**Naurah Mat Isa**
Radiation Processing Technology Division, Malaysian Nuclear Agency
43000 Kajang, Selangor
naurah@nm.gov.my

## Abstract

The emergence of hospital-acquired or nosocomial infection caused by ESKAPE pathogens (*Enterococcus faecium, Staphylococcus aureus, Klebsiella pneumoniae, Acinetobacter baumannii, Pseudomonas aeruginosa,* and *Enterobacter sp.*) that are resistant to antibiotics poses public healthcare concern. Transmission of the pathogens to patients and healthcare workers can occur through various types of fomites. Pathogens can be eradicated by using germicidal irradiation treatment. In this study, fomite samples such as fabric, paper, and leather stained with pathogens were treated with UVC for germicidal treatment. The effectiveness was evaluated by comparing the bacterial growth on the fomite samples before and after irradiation. The results show that UVC radiation has 90-100% average efficiency in pathogen eradication against several different ESKAPE strains.

**Keywords:** ESKAPE; fomite; UVC irradiation; disinfection

## 1 Introduction

Fomites are inanimate objects or surfaces that can be contaminated with infectious agents including bacteria, viruses, fungi and parasites. Hospital patient care devices are the examples of fomite that can cause hospital acquired infection (HAI) as they are practically of sharing basis (Kraay and others, 2018). Typically, 0.14% of hospitalized patients will get this infection [3] where the spread has involved millions of patients each year as the pathogens were easily transmitted to low and compromised immune systems, including those undergoing invasive procedures and surgeries (Raoofi and others, 2023).

Infections caused by ESKAPE pathogens are more critical as they are resistant to various antibiotics treatment (Tacconelli and others, 2018). To combat the spread, good hygiene practice was usually promoted among the healthcare workers. However, this practice is short if the pathogen is resistant to the conventional cleaning method.

In this study, an improved disinfection practice is evaluated for its effectiveness against ESKAPE pathogen. Widely proven ultraviolet germicidal irradiation method was proposed to be incorporated into the routine to treat several fomite samples (fabric, paper, and leather) to simulate the real hospital situation.

## 2 Materials and Methods

### 2.1 Bacteria Culture

*E. coli* and *K. pneumoniae* were isolated from clinical samples. Methicillin-resistant *S. aureus* (MRSA) and *P. aeruginosa* were obtained from the American Type Culture Collection (ATCC) numbered ATCC 33591 and ATCC 27853, respectively. *A. baumannii* strain was a Carbapenem-resistant strain isolated from clinical samples. All bacterial strains were cultured on nutrient agar. Only one colony was picked and put into nutrient broth for incubation at 37 °C, 24 hours.

### 2.2 UVGI Disinfection

UVGI disinfection was done using the LembayUVng® (Model L4). Minimum UV lamp (254 nm) intensity was 2700 $\mu$W/cm$^2$ at the holder level giving an irradiation exposure of 0.5, 1.0 and 1.5 J/cm$^2$ when irradiated at 3, 6 and 9 minutes.

### 2.3 Bacterial Viability Test on Nutrient Agar Against Direct UV Germicidal Irradiation

The test was performed according to the modified AATCC 100-2014 standard laboratory protocol (Nicoloro and others, 2020). The standard inoculum concentration of bacteria was determined using a spectrophotometer (625 nm), equated to a density value of 0.08-0.10 to produce a bacterial concentration of 108 CFU/mL. Serial dilutions were performed up to a dilution of 10-3. From each dilution tube, 10 $\mu$L of bacterial inoculum was inoculated onto the nutrient agar using the spread plate method. Each culture was directly exposed to UVC radiation for periods of 0 (control), 3, 6, and 9 minutes without a lid cover. It was later incubated at 37 °C for 24 hours and followed by colony counting (CFU/mL).

### 2.4 Bacterial Viability Test on Fomites Against UVC Radiation

The test was performed based on a modified ASTM E2149 standard laboratory protocol (Campos and others, 2016). The fomite sheet was cut to a size of 20 mm × 20 mm coupon. A total of 200 $\mu$L of inoculum that has been equalized to a bacterial concentration of 108 CFU/mL was inoculated onto the coupon surface and incubated at 37 °C for 4 hours. Then, the coupon was directly exposed to UVC radiation for a period of 0 (control), 3, 6, and 9 minutes. The treated coupons were later immersed in a centrifuge tube containing 20 mL of 0.85% normal saline solution and vortexed to extract the bacteria from the fomites. Serial dilutions were performed

up to a dilution of 10-3. From each dilution tube, 10 $\mu$L of bacterial inoculum was inoculated onto the nutrient agar using the spread plate method. All nutrient agar cultures were incubated at 37 °C for 24 h and followed by colony enumeration (CFU/mL).

## 3 Results

### 3.1 Bacterial Viability Test on Nutrient Agar Against Direct Exposure to UVC Radiation

These bacterial viability tests were conducted to test the UVC disinfection effect on agar as a control surface. A reduction of 5 $\log_{10}$ equivalent to 99.999-100% was recorded for all bacteria at all exposure time periods.

### 3.2 Bacterial Viability Tests on Fomites Against UVC Radiation

From the UVGI disinfection treatment on the selected fomites, all the stained ESKAPE pathogenic bacteria recorded 2 log reduction (99%) at the 3rd minute and 5 log reduction (99.999-100%) at the 6th minute. A 9-minute exposure time was not performed since no pathogenic bacterial colony growth was observed at 6 minutes. This indicates that the complete decontamination process of pathogenic bacteria on all types of fomites occurred during the exposure time of 6 minutes (Figure 1-3).

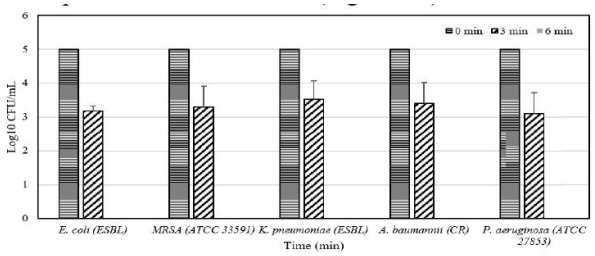



Figure 1: $\log_{10}(x)$ number of bacteria on fabric fomite against UVC radiation.

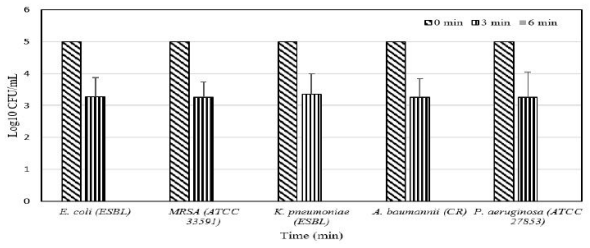



Figure 2: $\log_{10}(x)$ number of bacteria on paper fomite against UVC radiation.

## 4 Discussion

Disinfection using the UVC method has effectively eradicate fomite transmission ESKAPE pathogen. This process efficiently kills pathogens and prevents their transmission through contaminated surfaces. The results are comparable to other studies on UVC irradiation against MRSA, VRE

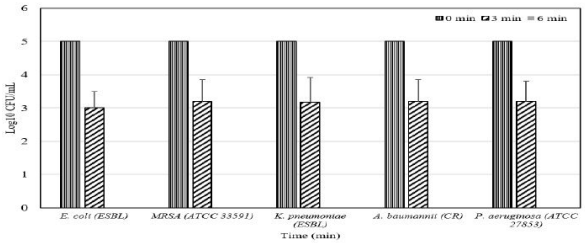



Figure 3: $\log_{10}(x)$ number of bacteria on leather fomite against UVC radiation.

(*Vancomycin-resistant Enterococcus*), and *C. difficile* in hospital rooms (Boyce and others, 2016).

Fomites characteristics can also affect the UVGI sterilization where the log reduction of influenza virus was shown differing depending on the type of fomite [13]. The ability of UV rays to penetrate a surface depends on the light emitting of a material. Liquids with high light emissivity can be effectively treated using UV radiation while liquids with low light emissivity, due to materials, particles or organic compounds, may create obstacles to receive the effects of UV irradiation.

Effective sterilization whether using UVC or gamma radiation depends on the dose and exposure time of UVC radiation. Different microorganisms require different doses of UV radiation for effective sterilization [15]. Bacterial strains with more effective dimer repair mechanisms may have a lower reduction percentage after exposure to UV light [16]. In overall, the effectiveness of UVC sterilization is influenced by the material being treated, the characteristics of the UV light, and the resistance mechanisms of the targeted microorganisms.

## 5 Conclusions

This study has successfully demonstrated an effective decontamination of ESKAPE pathogen with a 99.999-100% reduction as early as 3 minutes of exposure. The decontamination effect of each pathogen on all three types of test fomites showed that the ability of UVC irradiation was the same even when tested on different types of composition and matrix of materials.

## References

J. M. Boyce et al. 2016. Inf. ctrl. & hosp. epidemiology. *Infection Control & Hospital Epidemiology*, 37(6):667–672.

M. D. Campos et al. 2016. Plos one. *PloS One*, 11(8):e0160728.

A. N. M. Kraay et al. 2018. Bmc infectious diseases. *BMC Infectious Diseases*, 18(1):540.

J. M. Nicoloro et al. 2020. J. microbiological methods. *Journal of Microbiological Methods*, 173:105937.

S. Raoofi et al. 2023. Plos one. *PloS One*, 18(1):e0274248.

E. Tacconelli et al. 2018. The lancet. infectious diseases. *The Lancet Infectious Diseases*, 18(3):318–327.

Individual Research Contribution Review, 2024: 125–126
*ISSN: 3083-922X*

# Thermogravimetric Analysis of Electron Beam-Irradiated Polypropylene waste

**Noora'tiqah Mohamad Fauzi**
Radiation Processing Technology Division, Malaysian Nuclear Agency
43000 Kajang, Selangor
nooratiqah@nm.gov.my

## Abstract

This study investigates the thermal degradation behavior of polypropylene (PP) waste subjected to varying doses of electron beam irradiation. Thermogravimetric analysis (TGA) was employed to evaluate the weight loss patterns and thermal stability of irradiated samples. The primary objective was to identify the optimal irradiation dose to enhance the pyrolysis process. Results indicate a significant shift in degradation temperatures with distinct variations observed across doses.

**Keywords:** Polypropylene, Electron Beam Irradiation, Thermogravimetric Analysis

## 1 Introduction

The increasing accumulation of plastic waste has become a critical environmental challenge prompting the need for innovative recycling methods and material recovery techniques (Wong, 2024). Polypropylene (PP) a widely used thermoplastic is particularly prevalent in various applications ranging from packaging to automotive components. However its durability and resistance to degradation also contribute to its persistence in the environment and leading to significant ecological concerns. One promising approach to address this issue is the conversion of polypropylene waste into valuable resources through pyrolysis, a thermal decomposition process that breaks down organic materials in the absence of oxygen. To enhance the efficacy of the pyrolysis process, understanding the thermal properties of polypropylene waste is crucial. Thermogravimetric analysis (TGA) is a powerful technique that measures the mass change of a material as a function of temperature and time, providing insights into its thermal stability, decomposition behavior and the kinetics of thermal degradation.

Recent advancements in polymer modification techniques such as electron beam irradiation have shown promise in enhancing the thermal properties of polypropylene waste. Electron beam irradiation involves exposing materials to high energy electrons resulting in cross-linking and structural changes that can improve thermal stability and mechanical performance (Ponomarev et al., 2022). By subjecting polypropylene waste to electron beam irradiation, it is possible to improve its reactivity during pyrolysis and potentially leading to higher yields of valuable products such as fuels and chemical feedstock (Gorbarev et al., 2019). This process not only aids in the recycling of polypropylene but also open avenues for the development of new materials with tailored properties. This study aims to investigate the thermal properties of electron beam irradiated polypropylene waste through thermogravimetric analysis, providing essential data that can inform and optimize the subsequent pyrolysis process. Understanding these properties will contribute to the development of more sustainable methods for the recycling and valorization of polypropylene waste, ultimately aiding in the reduction of plastic pollution and the promotion of a circular economy.

## 2 Materials and Methods

Polypropylene (PP) waste was sourced from Alam Flora Sdn Bhd. The waste was first cleaned thoroughly to remove contaminants such as dirt, grease and foreign materials. The cleaned PP waste was then air-dried at room temperature to ensure complete removal moisture. After drying, the samples were irradiated using an electron beam at doses of 100, 200, 300, 400 and 500 kGy (applied in increments of 5 kGy per pass). Following irradiation, the samples were subjected to thermogravimetric analysis (TGA) by using Netzsch equipment. The TGA analysis was carried out under a nitrogen atmosphere to evaluate the thermal stability and degradation profile of the irradiated PP waste.

## 3 Results and Discussion

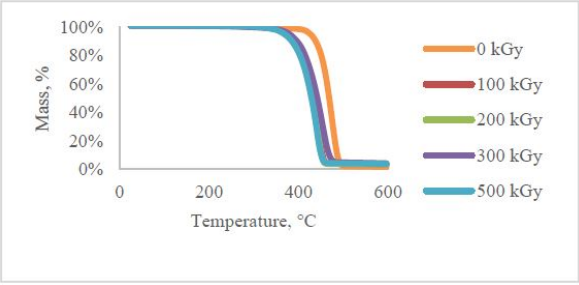



Figure 1: TGA Thermogram for PP Waste

The thermogravimetric analysis of PP waste irradiated at different doses reveals a clear dose-dependent effect on thermal stability. At lower doses (100-200 kGy), the onset degradation temperature decreased slightly compared to non-irradiated PP which is indicated initial chain scission. The medium dose of 300 kGy resulted in a significant reduction in thermal stability as evidenced by a sharper degradation peak

| **Irradiation** Dose | **Onset Temp** (°C) | **Temp$_{15\%}$** (°C) | **Temp$_{50\%}$** (°C) | **Temp$_{100\%}$** (°C) | **Temp$_{max}$** (°C) | **Peak Height** (wt%/min) |
|---|---|---|---|---|---|---|
| 0 kGy | 438.24 | 445.00 | 468.33 | 596.67 | 474.17 | 23.89 |
| 100 kGy | 406.23 | 398.33 | 433.33 | 596.67 | 445.00 | 21.25 |
| 200 kGy | 395.05 | 398.33 | 427.50 | 596.67 | 445.00 | 20.46 |
| 300 kGy | 398.70 | 404.17 | 439.17 | 596.67 | 450.83 | 16.57 |
| 500 kGy | 421.66 | 392.50 | 427.50 | 596.67 | 439.17 | 22.37 |

Table 1: TGA Data for PP Waste

and lower onset temperature. This suggests enhanced chain cleavage making the material more amenable to pyrolysis. At higher doses (400-500 kGy), the degradation profile showed stabilization indicating that structural modifications reached a saturation point. The residual weight at the end of degradation decreased slightly at higher doses possibly due to the formation of cross-linked structures or volatile by-products. These observations align with the goal of optimizing irradiation doses to improve the efficiency of pyrolysis. The results indicate that a medium dose of 300 kGy achieves a balance between sufficient chain scission and avoiding excessive cross-linking. This dose minimizes the energy required for thermal degradation and is likely to maximize oil yield during pyrolysis.

## 4 Conclusions

This study demonstrates the effectiveness of electron beam irradiation in modifying the thermal properties of PP waste. TGA analysis shows a dose-dependent reduction in thermal stability with the 300 kGy dose emerging as the most favorable for enhancing pyrolysis efficiency. By optimizing irradiation parameters, this approach provides a practical pathway for improving waste to oil conversion processes.

## References

I. N. Gorbarev, S. I. Vlasov, V. N. Chulkov, A. V. Bludenko, and A. V. Ponomarev. 2019. Degradation of plastics via electron beam distillation. *Russian Academy of Sciences*, 158:64–67.

A. V. Ponomarev, U. Gohs, C. T. Ratnam, and C. I. Horak. 2022. Keystone and stumbling blocks in the use of ionizing radiation for recycling plastics. *Radiation Physics and Chemistry*, 201:110397.

P. Y. Wong. 2024. Exporting pollution, colonizing health. In *Exporting Pollution, Colonizing Health*, pages 259–289. Springer.

Individual Research Contribution Review, 2024: 127–128
*ISSN: 3083-922X*

IRCR

# Case study assessment of microplastic pollution on agricultural soil in Malaysia

**Nor Azwin Shukri**
Radiation Processing Technology Division, Malaysian Nuclear Agency
43000 Kajang, Selangor
azwin@nm.gov.my

## Abstract

Over the years, researchers have become increasingly interested in microplastics' (MP) distribution and environmental behaviour in the ocean. However, human consumption of agricultural products represents a more significant exposure route to microplastics than exposure in marine environments. Since most plastic waste is disposed of on land, plastic pollution extensively affects the soil environment. Consequently, soils will likely serve as long-term sinks for MP debris through various routes. However, the impact of MP pollution on agricultural soil has received scant attention and has not been adequately addressed in publications. Therefore, this study aims to provide a case study assessment of MP pollution in agricultural soil in Malaysia. This includes the source, pollution status, and toxic effect of MP on the soil community. According to data compiled from the research manuscript between 2018 and 2023, mismanaged plastic waste in the agricultural sector contributed to the presence of MP particles in soil. In addition to affecting soil fertility and plant productivity, these contaminants can also enter the food chain, posing a serious threat to human health.

**Keywords:** microplastic pollution, agricultural soil, Malaysia.

## 1 1 Introduction

The extensive use of plastics in agriculture has created a critical environmental issue such as microplastic pollution. In Southeast Asia, the use of agricultural plastics is substantial, with an estimated 4.1 million tons consumed in 2018 and projected to rise to 7 million tons by 2030. Since most plastic waste ends up in landfills,it becomes a key source of microplastic pollution in soils. Microplastics, are defined as plastic particles smaller than 5 mm that pose significant threats to ecosystems and human health. Malaysia, a rice-dependent nation are susceptible to these MP contaminations through dietary rice consumption. In addition, MPs disrupt soil structure, reduce water retention, and interfere with microbial activities essential for nutrient cycling which threatens agricultural sustainability. Despite the rising concern, research focusing on the impact of microplastics on Malaysian agricultural soils is limited. Thus, this research aims to evaluate the potential sources of MP contamination in paddy fields in Sabak Bernam, Selangor, and establish a benchmark for future research and policy interventions.

## 2 Materials and Methods

The study employs a case study approach to assess MP pollution in agricultural soil, particularly in the rice paddy fields of Sabak Bernam, Selangor, Malaysia. This site was chosen due to its extensive use of agricultural plastics and potential for MP contamination. Figure 1 illustrated the site description for site decription of paddy field in Sabak Bernam, Selangor. In addition, this study also incorporated a review of existing literature on MP contamination in agricultural soils in Malaysia to establish a benchmark for comparison.

## 3 Data/Result

Compressive strength, which indicates the load-bearing capacity of the scaffolds under compressive forces, was evaluated. Table 1 provides a comparative analysis of the compressive strength between PEGDA and PEGDA/EPOLA scaffolds.

## 4 Discussion/Conclusions

Polyethylene (PE) and polypropylene (PP) were identified as the dominant polymers. The size of the detected MPs, typically ranging from 50 to 100 $\mu$m, indicates their potential to interfere with soil structure and ecosystem functions. MPs were found to disrupt soil water retention properties. This disruption affected nutrient availability, leading to lower crop yields and compromised soil health. It was reported that potential contamination pathways included direct plastic waste dumping, degradation of agricultural plastics, artificial irrigation systems, and




Figure 1: Site description of paddy field in Sabak Bernam, Selangor

| Site Resources | Site Location | Type of Microplastic | Ref |
|---|---|---|---|
| Vegetable farm | Semenyih and Puchong | PVC, HDPE, PS, PC | (Shanmugam et al., 2024) |
| Vegetable farm | Gombak, Serdang and Cyberjaya | HDPE, LDPE, ABS, PVC | (Moeck et al., 2023) |
| River basin | Rawang, Kerling and Tinggi River | PP, PE, Polyester | (Praveena et al., 2023) |
| Pig farm effluent | Melaka | Not reported | (Zaki et al., 2023) |
| Mixed landuse area | Semenyih | SBR, Nylon, PS, LDPE, HDPE, PP | (Chen et al., 2022) |

Table 1: Previous studies on microplastic contamination related to soil in Malaysia

atmospheric deposition. Discarded fertilizer bags, waste tyres and plastic bottles were commonly found near agricultural plots, potentially releasing smaller plastic particles into the soil. These findings confirm the inadequate waste management and agricultural practices that

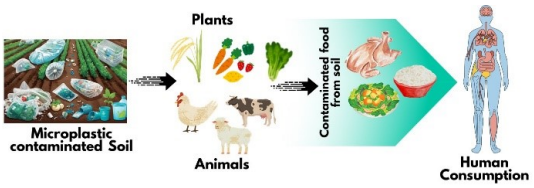



Figure 2: Pathway of microplastic from soil to human



Figure 3: Site assessment of paddy field in Sabak Bernam, Selangor

can contribute to MP pollution in Sabak Bernam.

## References

H.L. Chen, S.B. Selvam, K.N. Ting, K.Y. Tshai, and C.N. Gibbins. 2022. Relative contributions of different local sources to riverborne microplastic in a mixed landuse area within a tropical catchment. *Environmental Research*, 210:112972.

C. Moeck, G. Davies, S. Krause, et al. 2023. Microplastics and nanoplastics in agriculture—a potential source of soil and groundwater contamination? *Grundwasser - Zeitschrift der Fachsektion Hydrogeologie*, 28:23–35.

S.M. Praveena, M.A.F.I. Hisham, and A.L. Nafisyah. 2023. Microplastics pollution in agricultural farms soils: preliminary findings from tropical environment (klang valley, malaysia). *Environmental Monitoring and Assessment*, 195:650.

S.D. Shanmugam, S.M. Praveena, S.A. Wahid, et al. 2024. Occurrence and characteristics of microplastics pollution in tropical agricultural soils in klang valley, malaysia. *Environmental Monitoring and Assessment*, 196:144.

M.R.M. Zaki, F.F. Sukatis, M.Q.J. Roslan, et al. 2023. Microplastic pollution in freshwater sediments: Abundance and distribution in selangor river basin, malaysia. *Water, Air, and Soil Pollution*, 234:474.

Individual Research Contribution Review, 2024: 129–130
*ISSN: 3083-922X*

# A Dual Approach: Super Water Absorbents and Plant Growth Promoters on Vegetable Crop Performance

**Norhashidah Talip**
Radiation Processing Technology Division, Malaysian Nuclear Agency
43000 Kajang, Selangor
norhashidah@nm.gov.my

## Abstract

This study examines the synergistic effects of super water absorbent (SWA) and plant growth promoter (PGP) on vegetable plants. SWA, made from sago waste, and PGPs, derived from chitosan and carrageenan, were prepared using gamma radiation. In the experiments, 0.1% SWA was mixed into the soil, while 100 ppm PGPs were sprayed onto plants twice a week. Results showed that the combined application of SWA and PGPs significantly enhanced plant weight compared to the control group.

**Keywords:** Super water absorbent, plant growth promoter, gamma irradiation

## 1 Introduction

Agricultural productivity is significantly influenced by soil moisture and plant growth regulators. In regions where water shortage poses a challenge, the use of Super Water Absorbent and Plant Growth Promoters can play a vital role in enhancing plant growth and yield. SWA is hydrophilic material capable of absorbing and retaining large amounts of water, thus mitigating drought stress. On the other hand, PGPs, such as oligochitosan and oligocarrageenan, have been shown to improve plant growth, increase resistance to pathogens, and stimulate immune responses. This study investigates the synergistic effects of SWA and PGPs on vegetable plants, specifically mustard aiming to determine whether the combination of these two substances can improve plant growth parameters such as height, weight, leaf area, and root length

## 2 Materials and Methods

### 2.1 Preparation and characterization of super water absorbent

The details of the preparation of super water absorbent (SWA) from sago waste and its characterizations have been reported in (Talip et al., 2023). In summary, sago waste was mix with other polymers and exposed to gamma radiation. The swelling properties, a key characteristic of super water absorbents, were evaluated.

### 2.2 Preparation and characterization of plant growth promoter

The preparation of oligochitosan and its characterizations have been discussed in (Mahmud et al., 2023). In summary, the preparation of oligochitosan oligocarrageenan follows a similar process, where chitosan and carrageenan powder were irradiated to reduce their molecular weight to levels that are beneficial for plant growth. One key characteristic of an effective plant growth promoter is its molecular weight; measured using Gel Permeation Chromatography (GPC).

### 2.3 Synergistic study of SWA and PGP

Approximately 1kg of soil was used in each pot (poly bag). First, 600g of soil was placed into the pot, followed by the addition of swollen SWA at a concentration of 0.1%. The pot was then filled with an additional 400g of soil, making it ready for plant transplantation. Mustard which have been germinated for two weeks and were of similar heights, were transferred into the pots, with one plant per pot. The plants were irrigated once a week, fertilizer was applied directly to soil daily. PGPs were sprayed onto the plants on days 1 and 4 of each week. This experiment was carried out in control environment.

## 3 Results and Discussion

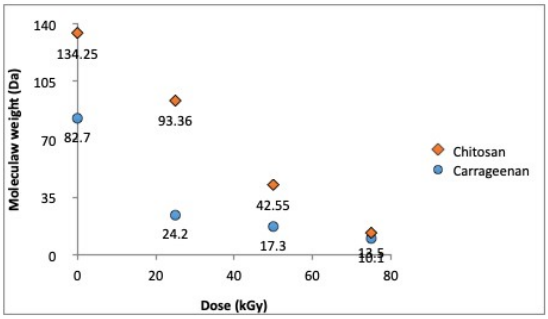



Figure 1: Molecular weight of chitosan and carrageenan before and after irradiation a different dose

Figure 1 illustrates the effect of Gamma 60Co irradiation on the molecular weight of chitosan and carrageenan at different doses. Both natural polymers, when irradiated in solid (powder) form, show a gradual decrease in molecular weight as the irradiation dose increases. This reduction in molecular weight is a result of chain scission or degradation, which also leads to a decrease in viscosity. According to studies by Sabharwal et al. and others researchers (Sabharwal et al., 2004; Czechowska-Biskup et al., 2005; **?**), irradiation causes chain scission in chitosan and carrageenan, which can occur

in various physical forms, including solid, suspension, paste, or solution. Radiation processing can be used to produce chitosan and carrageenan at various molecular weights.

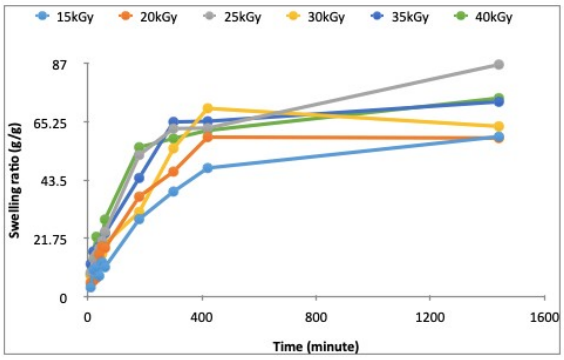



Figure 2: Swelling ration of SWA at different soaking time

Figure 2 shows the swelling ratio of SWA exposed to different gamma irradiation doses (15 kGy to 40 kGy) and soaking times. The results indicate that the swelling ratio increases with longer soaking times. SWA irradiated at 15 kGy exhibited the lowest swelling ratio, while SWA irradiated at 25 kGy showed the highest swelling ratio (87 g/g) after soaking for 1400 minutes. As the irradiation dose increased beyond 25 kGy, the swelling ratio decreased. This behavior is attributed to the optimal network density formed at 25 kGy, which creates suitable pores for better water absorption. At higher doses, increased crosslinking density reduces pore size, limiting water absorption (Talip et al., 2021).

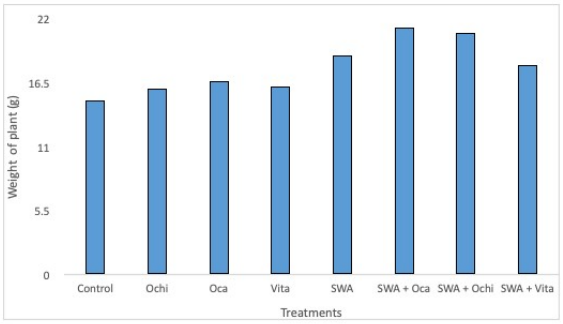



Figure 3: Weight of mustard plants at different treatment

Figure 3 presents the results for plant weight, highlighting the synergistic effects of Super Water Absorbent (SWA) and Plant Growth Promoters (PGP) compared to plants treated with only SWA or PGP. It shows that plants without SWA or PGP (control) performed the worst. When only PGP (oligochitosan, oligocarrageenan, or Vita) was applied, the average plant weight was 16g. However, when both SWA and PGP were applied, plant weight increased significantly, with the highest weight of 21.2 grams observed in plants treated with SWA and oligocarrageenan. Oligochitosan and oligocarrageenan have been shown to effectively promote growth in various plants, including maize, paddy, chili, tomato, and vegetables, likely due to increased chlorophyll content in the leaves (Mondal et al., 2012; Pham et al., 2021). Additionally, chitosan application has been shown to enhance biochemical activity in plants (Mondal et al., 2012).

## References

R. Czechowska-Biskup, B. Rokita, S. Lotfy, P. Ulanski, and J. M. Rosiak. 2005. Degradation of chitosan and starch by 360-khz ultrasound. *Carbohydrate Polymers*, 60(2):175–184.

M. Mahmud, N. Talip, N. Yacob, and S. Idris. 2023. Application interval and concentration effect of gamma degraded chitosan on mulberry plant. *Food Research*, 7(Suppl.2):94–100.

M. M. A. Mondal, M. A. Malek, A. B. Puteh, M. R. Ismail, M. Ashrafuzzaman, and L. Naher. 2012. Effect of foliar application of chitosan on growth and yield in okra. *Australian Journal of Crop Science*, 6(5):918–921.

T. S. Pham, M. K. Chau, H. H. Nhu Khanh, A. K. Truong, H. Nguyen, D. T. Pham, and T.-D. Nguyen. 2021. Impacts of $\kappa$-oligocarrageenan application on photosynthesis, nutrient uptake and bean yield of coffee (coffea robusta). *Sains Malaysiana*, 50(11):3171–3179.

S. Sabharwal, L. Varshney, A. D. Chaudhari, and S. P. Ramnani. 2004. Radiation processing of natural polymers: Achievements & trends. Retrieved from Vienna.

N. Talip, A. Muhammad Afifi, M. Y. Hamzah, M. Mahmud, and S. Idris. 2021. Radiation modified cs/pva film with pvp coating as cu adsorbent material. *Pertanika Journal of Science and Technology*, 29(2).

N. Talip, M. Mahmud, N. Yacob, and S. Idris. 2023. Effect of gamma irradiated super water absorbent from sago waste on vegetables. *Food Research*, 7(Suppl.2):155–159.

Individual Research Contribution Review, 2024: 131–132
*ISSN: 3083-922X*

# Performance of Radiation-Induced Grafted Polyethylene (PE) Filter Cartridges as Adsorbent for Heavy Metal Removal

**Norliza Ishak**
Radiation Processing Technology Division, Malaysian Nuclear Agency
43000 Kajang, Selangor
norliza@nm.gov.my

## Abstract

Heavy metals contamination in water resources poses significant environmental and public health challenges, necessitating the development of cost-effective adsorbent for sustainable remediation. The study explores the use of the radiation-induced grafting technique for the modification of the surface of polymeric materials as adsorbent for heavy metal removal. Therefore, the main objective of this study is to determine the adsorption performance and adsorptive properties of modified polyethylene (PE) filter cartridge via radiation-induced grafting (RIG) process with Glycidyl Methacrylate (GMA) by employing gamma irradiation and followed by subsequent chemical functionalization with different aliphatic amine group. This modification technique to enhance the surface properties and increasing adsorption efficiency of the material as an adsorbent for addressing heavy metal pollution.

**Keywords:** radiation-induced grafting, PE filter cartridge, gamma irradiation, adsorption

## 1 Introduction

The industrialization and economic advancement in emerging nations have resulted in pollution, specifically the discharge of harmful metal ions into aquatic environments. Responding to the issues, extensive research has been conducted concentrating on cellulosic biofibers and biopolymers as adsorbent in removing metal ions due to their abundance, biodegradability, and hydrophilicity (Kolya and Kang, 2023). The development and cost-effectiveness of polymeric materials as adsorbents are noteworthy considering their versatility and ability for chemical modification to meet particular applications (Mahdaoui et al., 2024).

The main aim of the polymer modification is to introduce and enhance a specific characteristic that acts as a precursor in improving adsorption efficiency for removal of metal ions from water. Among various monomers, GMA is particularly advantageous due to the presence of epoxide rings, which facilitate subsequent modification with a wide range of functional groups.

This research focuses on the adsorption behavior in term of performance and efficiency of the modified PE filter cartridge by the RIG technique using gamma. Batch adsorption tests were performed to evaluate the suitability of the modified PE filter cartridge as an adsorbent for the removal of metal ions from actual industrial effluents.

## 2 Materials and Methods

The research aims to determine adsorption performance and adsorptive capacity of the modified PE filter cartridge using radiation induced grafting via gamma irradiation for metal ions removal.

### 2.1 Grafting and Functionalization of Grafted PE Filter Cartridge

The grafted PE filter cartridge was modified through RIG with GMA and amine functionalization. The grafting process involves immersing PE cartridge in a GMA solution and irradiated with gamma rays at optimum dose which is 25 kGy. The degree of grafting was calculated based on weight changes. For functionalization, the grafted PE cartridge was chemically functionalized using 3 types of amine groups (Ethylene diamine (EDA), Dimethyl Amine (DMA) and Triethylenetetramine (TETA)) with a solvent. The functionalization processes will be at temperature of 15°C for 1 hour.

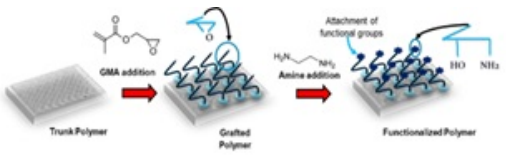



Figure 1: Mechanism of the modified PE filter cartridge

### 2.2 Batch Adsorption Process

A batch adsorption experiment will be carried out to determine the adsorption capacity of the modified PE filter cartridge. A known mass of modified PE filter cartridge was immersed in the metal ions solution under acidic conditions for 5 hours at room temperature. UV-Vis spectrometer was used to measure the remaining metal ions in the solution after it has been filtered from the adsorbent.

## 3 Data/Results

### 3.1 Adsorption Performance of modified PE Filter Cartridge

The chemical composition of sago pith waste and its cellulose is shown in Table 1. It is shown from the table that sago pith waste contains a high amount of sago starch (38.41%). Meanwhile, sago pith waste also contains cellulose (14.31%), hemicellulose (17.45%) and lignin (4.83%). Upon bleaching, the cellulose content increased to 91 wt% whereas, lignin and starch was extensively removed.

| **Material (Industrial PE Filter Cartridge)** | **Contact Angle, CA (°)** | **Corrected Contact Angle, CAc (°)** |
|---|---|---|
| Raw | 139.09 | 93.75 |
| Grafted | 133.57 | 92.76 |
| DMA | 122.53 | 92.51 |
| EDA | 114.11 | 91.96 |
| TETA | 131.72 | 92.42 |

Table 1: Optical Contact Angle and Corrected Contact Angle of industrial raw, grafted, and functionalized PE filter cartridges.

The table shows the contact angle (CA) and corrected contact angle (CAc) of raw, grafted and functionalized PE filter cartridges. CAc measured by considering the surface roughness and provides more accurate assessment of wettability of the material. Functionalization of EDA, significantly reduces the contact angle indicating the hydrophilicity of the adsorbent surface was improved. These results demonstrate that functionalization process, particularly EDA effectively improves surface wettability of the surface material. This enhancement is crucial for adsorption process, as increased wettability promotes better interaction between adsorbent surface and aqueous solutions containing metal ions.

The graph illustrates the comparison of the adsorption performance of iron (Fe) ions using different aliphatic amines (EDA, DMA and TETA). EDA shows the highest removal efficiency and adsorption capacity which 70% and 40.85mg/g respectively, followed by DMA (60%, 33.94mg/g) and TETA (55%, 19.34mg/g). The superior performance of EDA can be attributes to its molecular structures, which likely provides an optimal balance of functional groups for strong interaction with Fe ions on the adsorbent surface. DMA demonstrates moderate efficiency and TETA's lowest performance due to complex structure and potentially less exposed for effective binding toward Fe ions. The results highlight EDA the most effective functional group for enhancing the adsorption performance of the modified adsorbent.

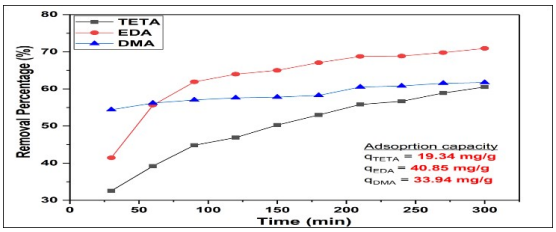



Figure 2: Adsorption capacity of Fe ions using modified PE filter cartridge with different aliphatic amines (EDA, DMA and TETA)

## 4 Conclusions

The modification of an industrial PE filter cartridge as an adsorbent was evaluated for heavy metal adsorption. Herein, EDA functionalized cartridges demonstrated the best performance with the highest adsorption capacity for Fe ions. The improved adsorption capacity supported by reduced contact angle that indicating enhanced surface hydrophilicity. These findings highlight the structure and accessibility of functional groups on the adsorbent play a critical role in the adsorption mechanism.

## 5 Acknowledgements

The authors would like to thank the Radiation Processing Technology Division (BTS), Malaysian Nuclear Agency for the support in providing facilities for the experiments. This Project was set as a non-funding of internal project (NM-R&D-23-01) in Nuclear Malaysia.

## References

H. Kolya and C. H. Kang. 2023. Next-generation water treatment: Exploring the potential of biopolymer-based nanocomposites in adsorption and membrane filtration. *Journal of Polymers*, 15(16):3421.

A. E. Mahdaoui, S. Radi, A. Elidrissi, M. A. F. Faustino, M. G. P. M. S. Neves, and N. M. M. Moura. 2024. Progress in the modification of cellulose-based adsorbents for the removal of toxic heavy metal ions. *Journal of Environmental Chemical Engineering*, 12(5):113870.

Individual Research Contribution Review, 2024: 133–134
*ISSN: 3083-922X*

IRCR

# Thermal Properties of Repetitive Hot Compression Cycle in Plasticized PVC

**Norshafarina Ismail**
Radiation Processing Technology Division, Malaysian Nuclear Agency
43000 Kajang, Selangor
norshafarina@nm.gov.my

## Abstract

In this work, the effect of the hot compression molding cycle on plasticized PVC was evaluated through thermal gravimetric analysis (TGA), differential scanning calorimetry (DSC), and dynamic mechanical analysis (DMA). The objective was to determine the thermal degradation potential of PVC upon repetitive hot compression cycles. Compression molding was conducted at 170°C for 4 minutes of full compression, repeated up to three times. Compressed PVC sheets were tested for thermal properties. TGA shows a melting point of 220°C for all samples, with no other property changes, and 70% weight loss at 700°C. DSC revealed consistent thermal behavior across heating and cooling cycles (30-200°C), indicating stability below 150°C and reversible transitions. DMA shows significant damping properties. Overall, thermal analysis suggests insignificant changes in thermal degradation after three cycles; however, for applications involving vibration or repetitive movement, multiple hot compression cycles should be considered.

**Keywords:** DMA, DS, hot press, PVC, TGA

## 1 Introduction

Polyvinylchloride (PVC) is widely used in wire and cable for its non-conductive and flexible properties. As a thermoplastic, it can be remelted, but thermal degradation may occur during cycles, especially under load. Ensuring thermal stability is critical for maintaining performance in applications exposed to cyclic thermal loads. Thermal Gravimetric Analysis (TGA) measures mass changes under controlled heating or cooling, revealing thermal stability, composition, and decomposition behavior. Differential Scanning Calorimetry (DSC) assesses the effects of repetitive heating, offering insights into degradation mechanisms such as dehydrochlorination, hydrogen chloride release, and glass transition shifts from plasticizer loss, all affecting flexibility (Wang et al., 2018). Analyzing PVC's response to repeated heating is essential for quality control and performance prediction. DSC provides key data for ensuring long-term reliability (Szarka and Iván, 2013). Dynamic Mechanical Analysis (DMA) measures viscoelastic behavior under load and temperature, with storage modulus ($E'$), loss modulus ($E''$), and Tan $\delta$ ($E''/E'$) indicating stiffness, viscous, and damping properties. This work evaluates thermal properties of plasticized PVC after multiple hot compression cycles.

## 2 Materials and Methods

### 2.1 Materials

Plasticized PVC with a melt flow index of 7.27 g/10 min at 175°C/min 20kg, and density of 1.1 g/cm$^3$ was supplied by Nam Ah Sdn. Bhd. The samples were identified as follows: PVC1, PVC2 and PVC3 for 1-time, = 2 times hot compression molding, 3 times hot compression molding.

### 2.2 Thermal gravimetric Analysis (TGA)

Thermogravimetric analysis (TGA) was performed on Netzsch TG. Plasticized PVC weighing around 2.00 mg was put into the crucible. The temperature was set from room temperature to 600°C at 10.0°C/min heating rate, under a nitrogen flow of 50 mL/min.

### 2.3 Differential Scanning Calorimetric (DSC)

The differential scanning calorimetry (DSC) analysis was conducted by using a DSC 300 Caliris (NETZSCH) to study three PVC samples (PVC 1, PVC 2, PVC3). The study aimed to investigate the thermal behavior of the samples after repetitive heat application. The heating was 10.0°C/min, covering a temperature range from 330-200°C under a nitrogen atmosphere.

### 2.4 Dynamic Mechanical Analysis (DMA)

The compression molded PVC with a thickness of 1 mm was cut into 10mm x 1mm and subjected to DMA using the Perkin Elmer D8000. The measurements were carried out in the 3-point bending mode of the equipment, and corresponding viscoelastic properties were determined as a function of temperature. The temperature range used was between 30°C and 100°C, with a heating rate of 2°C/

min. The samples were scanned at a fixed frequency of 1 Hz.

## 3 Discussion/Conclusions

### 3.1 Thermal gravimetric Analysis (TGA)

The results are presented in Figure 1 and Table 1, showing the decomposition temperature at respective weight loss. The onset temperature of T20 and T50 referring to 20% and 50% weight loss were used to indicate thermal stability. At T50, 3-time hot compression has reduced temperature from 349.92°C to 346.63°C, about (1.00%). No significant changes were observed in PVC1, PVC2, and PVC3, suggesting thermal stability in all samples.

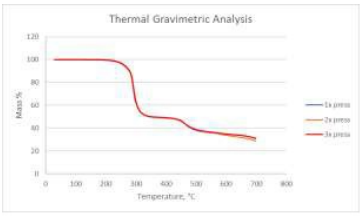



Figure 1: TGA graph of PVC1, PV2, PVC3

| Sample | Glass transition temperature, $T_g$ (°C) | Melting temperature, $T_m$ (°C) | Weight Loss $T_{20}$ | Weight Loss $T_{30}$ |
|---|---|---|---|---|
| PVC 1 | 62.0 | 182.0 | 287.42 | 349.92 |
| PVC 2 | 62.5 | 181.7 | 287.45 | 347.45 |
| PVC 3 | 61.9 | 183.0 | 286.63 | 346.63 |

Table 1: Thermal data of PVC1, PVC2, and PVC3

### 3.2 Differential Scanning Calorimetric (DSC)

The results, shown in the endothermic thermogram (Figure 2) and Table 1, revealed no significant changes in Tg or Tm among PVC1, PVC2, and PVC3. Tg was around 62°C and Tm about 182°C. The plateau region indicates that repeated heating had little effect on PVC's thermal properties. These findings suggest good thermal stability, with minimal changes in glass transition and melting temperatures (Yu et al., 2021), likely due to stabilizers or the polymer's inherent resistance to thermal stress.

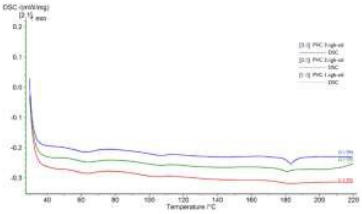


Figure 2: TGA graph of PVC1, PV2, PVC3

### 3.3 Dynamic Mechanical Analysis (DMA)

Figure 3 shows the variation of storage modulus with temperature for PVC1, PVC2, and PVC3. All samples exhibit a significant decrease in modulus with increasing temperature. PVC2 initially has the highest modulus, which drops sharply before stabilizing at higher temperatures. At lower temperatures, molecular segments have low kinetic energy, limited oscillations, and restricted motion, resulting in high stiffness. As temperature rises, free volume increases, allowing greater molecular mobility. This increased motion produces more strain under load, causing the modulus to decrease from room temperature to 100°C for all samples.

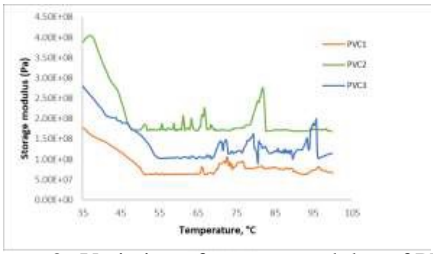



Figure 3: Variation of storage modulus of PVC

## 4 Conclusions

PVC samples exhibit stable thermal properties, with a consistent Tg around 50 to 70°C indicating a stable amorphous phase. For Tm, it shows a prominent melting peak around 170 to 180°C, which suggests that the PVC has a well-defined crystalline phase that melts within this temperature. The insignificant changes in thermal properties with repeated heating indicate good thermal stability, which is desirable in many applications. This shows that this PVC is reliable in maintaining its thermal characteristics under repeated thermal cycling.

## References

G. Szarka and B. Iván. 2013. Thermal properties, degradation and stability of poly (vinyl chloride) predegraded thermooxidatively in the presence of dioctyl phthalate plasticizer. *Polymer-Plastics Technology and Engineering*, 50(2):208–214.

Z. Wang, R. Wei, X. Wang, J. He, and J. Wang. 2018. Pyrolysis and combustion of polyvinyl chloride (pvc) sheath for new and aged cables via thermogravimetric analysis-fourier transform infrared (tg-ftir) and calorimeter. *Multidisciplinary Digital Publishing Institute*, 11(10):1997–1997.

Y. Yu, Z. Cao, and H. Li. 2021. Mechanical properties of four types of pvc-coated woven fabrics at high temperatures and after exposure to high temperatures. *Polymer Testing*, 33:830–840.

Individual Research Contribution Review, 2024: 135–136
*ISSN: 3083-922X*

# Chemical composition and morphology observation of cellulose from sago pith waste

**Norzita Yacob**
Radiation Processing Technology Division, Malaysian Nuclear Agency
43000 Kajang, Selangor
norzita@nm.gov.my

## Abstract

Cellulose from agricultural waste has gained more attention owing to its high aspect ratio, reinforcing effect and abundance. In this study, cellulose was extracted from sago pith waste (SW) which was recovered after sago starch extraction. The SW was treated through sodium hydroxide treatment, followed by bleaching. Results revealed cellulose content, thermal stability and crystallinity increased bleaching treatment.

**Keywords:** Cellulose, morphology, extraction.

## 1 Introduction

Natural fibers can be categorized according to their source (e.g., plant, animal, or mineral). Plant/vegetable fibers can be additionally categorized into subgroups based on their origin (e.g., stem fibers, leaf fibers, seed fibers, or fruit fibers). The chemical chemical composition of plant fibers is influenced by the type, age, and source of the fiber, along with the extraction technique. The characteristics of natural fibers rely on their chemical composition.

Cellulose is the most abundant renewable biopolymer, where it exists as a structural element in the cell walls of plants and various algae species. Besides being a potentially sustainable material, cellulose enables multiple functions and applications derived from its multidimensional structure (Zhu and others, 2016). Cellulose fibers can be separated into fibrils from micrometer to nanometer (Figure 1).

Sago (*Metroxylon Sago spp.*) palm is one of the crops widely planted in Malaysia that belongs to the Palmae family. The residue left behind in the sago starch extraction is called sago pith waste. In Malaysia, according to the Malaysia Statistic Department, over 200,000 metric tonnes of sago starch were produced in 2017. It was reported that one tonne of sago pith waste was formed from every tonne of sago starch produced (dry weight basis) (Bujang and Ahmad, 1999).

## 2 Materials and Methods

The sago pith waste (SW) was treated with 4% NaOH at 125°C for 2 h, followed by bleaching with 1.7 w/v% $NaClO_2$ at pH 4.5 and 125°C for 4 h. cellulose (CS) was successfully extracted. Each step was repeated several times, and the leaves were washed with distilled water after each treatment.

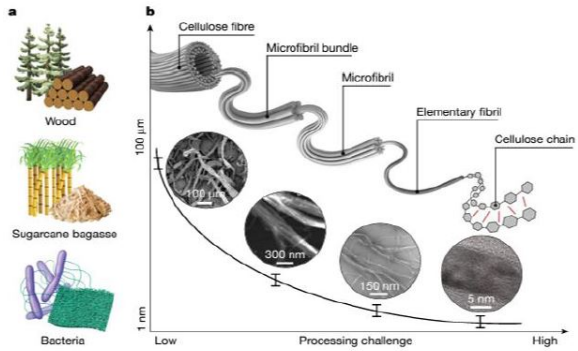



Figure 1: Common source for cellulose (a). A diagram illustrating the hierarchical structure and production difficulties of fibrillated cellulose. The level of fibrillation indicates the degree to which the fibers have been split longitudinally into finer fibrils (b).

## 3 Results and Discussion

Extraction of cellulose from sago pith waste was done by chemical treatment (Gopi et al., 2019). Figure 2(a) displays a photograph of the dried sago pith waste while Figure 2(b) shows a photograph of extracted cellulose. The dried sago pith waste exhibited a light brown color. The colour changed to white after bleaching. The FESEM micrograph of the sago pith waste surface is shown in Figure 2(c). The surface of the sago pith waste appears non-smooth and has an evenly corrugated coating. As measured by a particle size analyzer, the average size of the sago pith waste revealed around 300 – 600 $\mu$m. After bleaching (Figure 2d), the SW bundles were dispersed into individual fibers with diameters in the range of 5 – 80 $\mu$m.

The chemical composition of sago pith waste and its cellulose is shown in Table 1. It is shown from the table that sago pith waste contains a high amount of sago starch (38.41%). Meanwhile, sago pith waste also contains cellulose (14.31%), hemicellulose (17.45%) and lignin (4.83%). Upon bleaching, the cellulose content increased to 91 wt% whereas, lignin and starch was extensively removed.

| | Starch (%) | Cellulose (%) | Hemicellulose (%) | Lignin (%) |
|---|---|---|---|---|
| SW | 38.41 ± 1.36 | 14.31 ± 1.48 | 17.45 ± 0.90 | 4.83 ± 1.04 |
| CS | - | 91.26 ± 2.84 | 7.84 ± 1.32 | - |

Table 1: Compositional analysis data

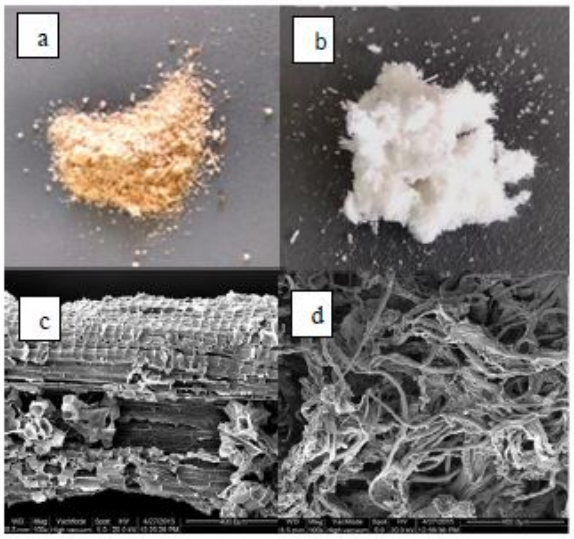



Figure 2: Photograph of (a) sago pith waste, (b) cellulose, (c) FESEM micrograph of sago pith waste and (d) cellulose.

## 4 Conclusions

Cellulose was successfully extracted from sago pith waste using NaOH, followed by $CH_3COOH/NaClO_2$ treatment. Determination of the chemical composition and microscopic observation showed the effects of chemical treatments on the surface and components of sago pith waste. In accordance with these results, the characteristics of the extracted cellulose from SW were well studied and its potential applications could be expanded.

## References

K. B. Bujang and F. B. Ahmad. 1999. Production, properties and utilization of sago starch in malaysia. In *Sago. Sustainable small-scale sago starch extraction and utilization: Guidelines for the sago industry. The Regional Round Table Meeting*, pages 9–11.

S. Gopi, A. Amalraj, S. Jude, K. T. Benson, P. Balakashnan, J. T. Haponiuk, and S. Thomas. 2019. Isolation and characterization of stable nanofiber from turmeric spent using chemical treatment by acid hydrolysis and its potential as antimicrobial and antioxidant activities. *Journal of Macromolecular Science, Part A*, 56(4):327–340.

H. Zhu et al. 2016. Wood-derived materials for green electronics, biological devices, and energy applications. *Chemical Reviews*, 116:9305–9374.

Individual Research Contribution Review, 2024: 137–138
*ISSN: 3083-922X*

# Investigation of mechanical properties of self-healing coating based on jatropha oil resin

**Nurul Huda Mudri**
Radiation Processing Technology Division, Malaysian Nuclear Agency
43000 Kajang, Selangor
nurul_huda@nm.gov.my

## Abstract

Self-healing coatings offer a number of advantages, such as increased material longevity and reduced operating expenses due to the elimination of planned maintenance, particularly in remote areas. One method that is frequently employed in the creation of self-healing coatings is the microcapsule. With this method, an active healing agent was kept in the microcapsule. The prior study used a polyurea formaldehyde (PUF) microcapsule to encapsulate pure jatropha oil (JO) and its derivatives, known as jatropha oil-based polyurethane acrylate (JPUA). In this study, the JPUA-TDI-based coating was loaded with JO and JPUA-IPDI-based microcapsules. It was discovered that when the microcapsules were added to the coating formulation in 5% and 10% JPUA, the hardness value decreased. As the coating in the self-healing coating with microcapsules thickened from 50 $\mu$m to 100 $\mu$m, 150 $\mu$m, and 200 $\mu$m, this trend steadily decreased. In conclusion, when compared to the control sample, the self-healing coating with a 5% loading of JO and JPUA-IPDI-based microcapsule with a 50 µm thickness has preserved the hardness, adhesion, haze, and transmittance properties.

**Keywords:** self-healing; microcapsule; mechanical properties; thickness; hardness

## 1 Introduction

The performance and longevity of self-healing coatings are largely determined by their mechanical characteristics. However, adhesion, hardness, and bending and compression tests are still the only mechanical properties covered in the report on microcapsule-based systems (Jiang et al., 2023; Pongmuksuwan et al., 2023). For example, research was done on the melamine-formaldehyde wall of a microcapsule, while the core was composed of a combination of multiwalled carbon nanotubes and carbonyl iron powder. The study found that the gloss and adhesion of the coatings declined with increasing microcapsule addition. When microcapsules were added to the coatings, the hardness, impact resistance, and tensile properties tended to increase before trending downward. Notwithstanding the research done in the past, little is known about the extent of transmittance and haze characteristics on self-healing coatings. Thus, it is crucial to research these characteristics, particularly in relation to self-healing coatings used on transparent surfaces like glass. The mechanical characteristics of a self-healing coating made with pure jatropha oil and its modified form, polyurethane acrylate based on jatropha oil, as a healing agent in PUF microcapsules are the main focus of this study. The study looks at important factors like coating thickness and microcapsule loading in connection to mechanical characteristics like haze, pendulum hardness, adhesion, and transmittance. These mechanical characteristics are regarded as useful guidelines for the durability and application of the product.

## 2 Materials and Methods

Using a mechanical stirrer, microcapsules loaded at 5 and 10 weight percent were distributed throughout the coating formulation until a homogenous mixture was achieved. A bar applicator was used to apply the self-healing coating formulation with thicknesses of 50 $\mu$m, 100 $\mu$m, 150 $\mu$m, and 200 $\mu$m to a steel plate measuring 100 mm by 100 mm by 1.5 mm. After that, the wet film was exposed to UV light until it had completely dried. The cured self-healing coating was subjected to mechanical tests, including the Pendulum Hardness Test (ASTM D4366), Cross-cut Adhesion Test (ASTM D3359-09), Transmittance Test (ASTM E1348), and Haze Test (ASTM D1003). The self-healing coating's mechanical characteristics were contrasted with those of the control coating, which did not have microcapsule loading. Figure 1 shows the instrument that being used to investigate the mechanical properties.

## 3 Data/Results

### 3.1 Pendulum Hardness

Pendulum damping tests were performed to assess the flexibility and hardness of the coatings containing microcapsules, as presented in Figure 2. As the microcapsules were added to the coating formulation in 5% JO, 10% JO, 5% IPDI, and 10% IPDI, the hardness value decreased. As the coating thickness increased from 50 $\mu$m to 100 $\mu$m, 150 $\mu$m, and 200 $\mu$m in each coating containing microcapsules, this trend steadily decreased. This is because there is a chance that the microcapsules will impede the curing process. In this study, the microcapsule was added by physical mixing without forming a chemical bond with the coating's polyurethane network. Epoxy-based coating can be used to increase the PUF-based microcapsule's compatibility with the coating (Pongmuksuwan et al., 2023). Furthermore, it was shown by Paquet

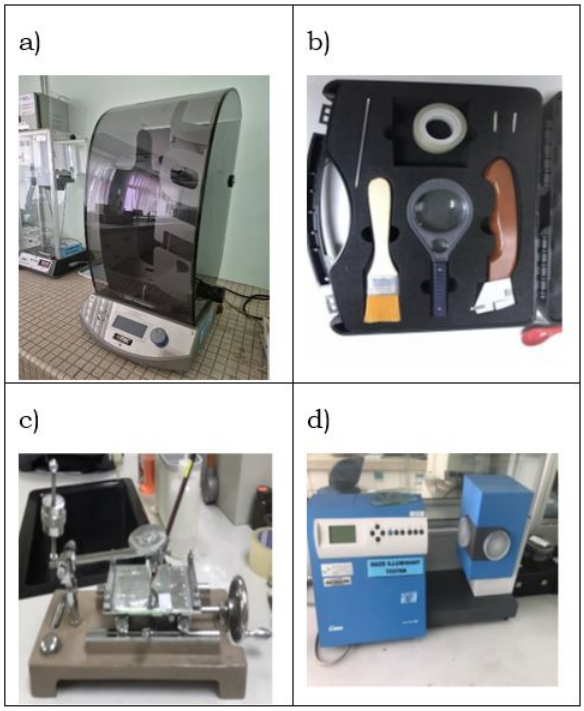



Figure 1: a) Pendulum hardness tester b) Cross hatch adhesion kit c) Pencil hardness tester d) Haze and transmittance tester

et al. (Paquet et al., 2020) that the hardness of the self-healing coating material was enhanced by the introduction of hydrogen bonding between the coating matrix and microcapsule shell. When tested at 50 µm thickness, the 5% JO and 5% IPDI film performs similarly in terms of hardness to the Control (about 80 seconds).

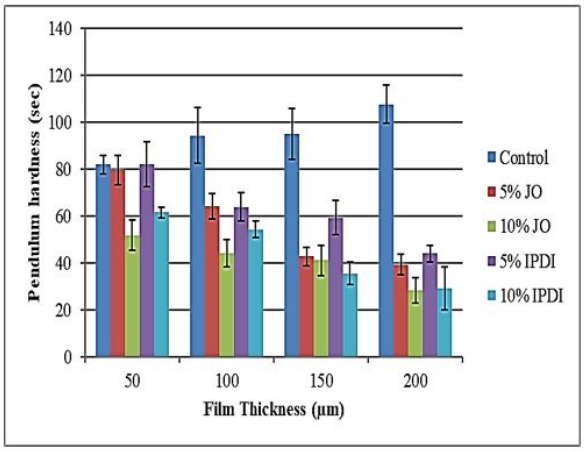



Figure 2: Pendulum hardness test for coating loaded with JO and JPUA-IPDI -based microcapsules

## 4 Conclusions

The self-healing coating's mechanical performance have deteriorated due to the addition of microcapsule loading and increased coating thickness. When compared to the control sample, the self-healing coating based on jatropha oil retained its mechanical properties up to a 5% microcapsule loading with a 50 $\mu$m film thickness. After being exposed to UV light before the curing process, the 5% JO and 5% IPDI preserved the microcapsule's spherical shape under an optical microscope, showing no signs of destruction.

## References

B. Jiang, C. F. Yu, L. Yuan, K. Lu, W. Tao, H. Lin, and Y. Zhou. 2023. Investigation on oxidative pyrolysis characteristics of bituminous coal through thermal analysis and density functional theory. *Applied Energy*, (349):121680.

C. Paquet, T. Schmitt, J. E. K. Sapieha, J. F. Morin, and V. Landry. 2020. Self-healing uv curable acrylate coatings for wood on self-healing efficiency. *Coatings*, 10(8):770.

P. Pongmuksuwan, T. Jangmee, and W. Kitisatorn. 2023. Microencapsulated epoxidized palm oil: A self-healing coating solution. *Applied Surface Science Advances*, 18:100458.

Individual Research Contribution Review, 2024: 139–140
*ISSN: 3083-922X*

# Study on The Stability of TPE With Silica Using Various Mixing Method

**Pairu bin Ibrahim**
Radiation Processing Technology Division, Malaysian Nuclear Agency
43000 Kajang, Selangor
pairu@nm.gov.my

## Abstract

This research aimed to study the effect of mixing method on the properties of TPE composite filled silica. Two methods of mixing were applied which are direct mixing and latex latex mixing. FESEM analysis has proven that the surface of latex blending was smooth compared to the direct mixing method. TGA analysis revealed the increasing of degradation temperature for the sample latex mixing indicated that this method help to increase the thermal stability of composite TPE.

**Keywords:** hydro, nanosilica, grafting

## 1 Introduction

Method of mixing materials in the blending system plays a role in influencing the uniformity of the distribution of filler materials. According to Yrieix and Majesté (Yrieix and Majesté, 2017), the effect of fillers on dispersion or reinforcement may not relies on the nature, properties andcontent of the silane only but also on the mixing conditions. Normally, the integration of large amount of silica content into polymer exhibited low dispersion and processibility. Hence, a new material produced by a new technology suitable for manufacturing highly silica filled rubber compound is required. One such material is silica wetmasterbatch (WMB), which is manufactured by simultaneously solidifying silane coupling agent treated silica and either rubber latex or solution (Kim et al., 2020). Wet masterbatch (WMB) technology is studied to develop high-content and highly disperse silica-filled compounds. This technology refers to the solidification of surface-modified silica with a rubber solution or latex which also known as latex blending technique. Latex blending offers the possibility of finer scale dispersion leading to improvement in processing as well as the ultimate properties of the blends (Prasertsri et al., 2013). It has been reported that latex blending offers the possibility of finer scale dispersion leading to improvement in processing as well as the ultimate properties of the blends.

## 2 Materials and Methods

There are three steps involved in this method:

i. **Direct mixing:** HDPE, natural rubber, and silica were mixed directly in a mixing chamber and blended at the specified temperature and speed.

ii. **Latex mixing:** Silica was mixed with latex at various compositions and continuously stirred for 4 hours. The dried rubber was then mixed with HDPE using a hot two-roll mixer.

## 3 Data/Results

SEM

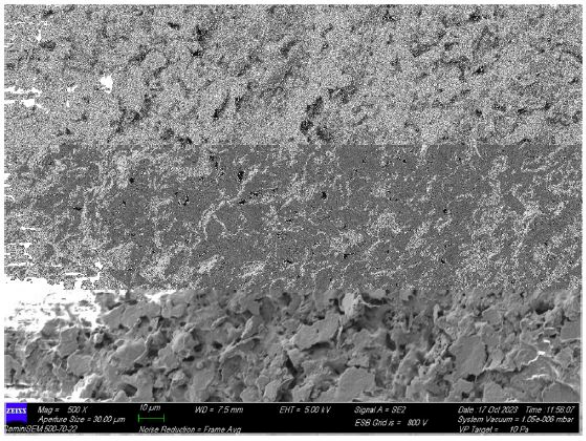


Figure 1: Sample : Control (100KGy)

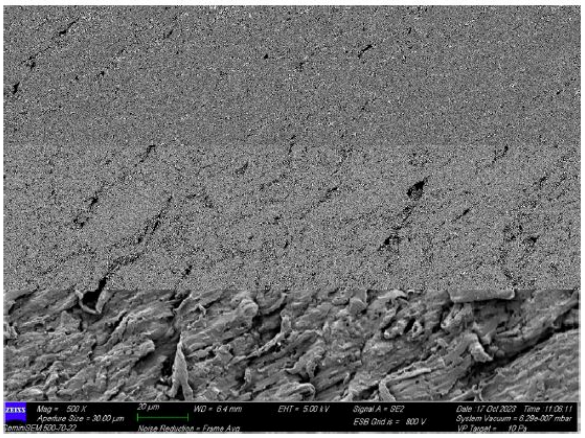


Figure 2: Sample : Direct blend (100KGy)

| Sample | $T_{5\%}$ (°C) | $T_{50\%}$ (°C) | $T_{max1}$ (°C) | $W_{loss1}$ (%) | $T_{max2}$ (°C) | $W_{loss2}$ (%) |
|---|---|---|---|---|---|---|
| Direct blend 0.5% nanosil | 334.93 | 390 | 375 | 470 | – | – |
| Direct blend 1.0% nanosil | 336.60 | 400 | 374.6 | 465 | – | – |
| Direct blend 1.5% nanosil | 324.94 | 400 | 370 | 455 | – | – |
| Direct blend 2.0% nanosil | 335.50 | 410 | 375 | 457 | – | – |
| Direct blend 2.5% nanosil | 336.50 | 410 | 375 | 464 | – | – |
| Latex blend 0.5% nanosil | 337.50 | 395 | 375 | 470 | – | – |
| Latex blend 1.0% nanosil | 334.95 | 400 | 375 | 470 | – | – |
| Latex blend 1.5% nanosil | 339.98 | 410 | 375 | 490 | – | – |
| Latex blend 2.0% nanosil | 337.50 | 410 | 380 | 490 | – | – |
| Latex blend 2.5% nanosil | 334.98 | 410 | 380 | 490 | – | – |

Table 1: Thermogravimetric analysis (TGA) results of direct and latex blend samples with various nanosilica content.

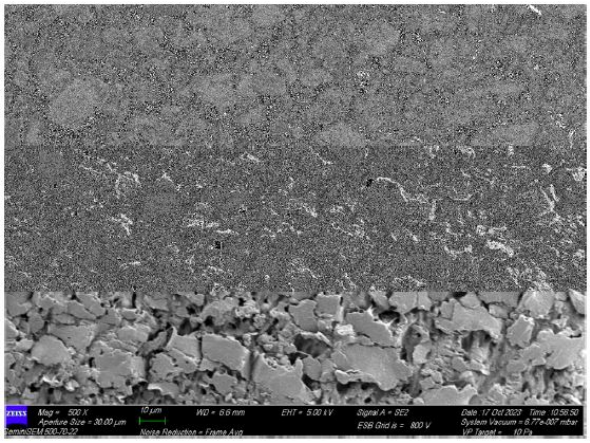


Figure 3: Sample : Latex blend (100KGy)

## 4 Discussion/Conclusions

In this study, we successfully prepared composite TPE using two methods of mixing i.e direct and latex mixing. From the results obtained, we concluded that the latex mixing produced more homogenous distribution of silica fillers compared to direct mixing with higher thermal stability.

## References

W. Kim, E. Yu, G. Ryu, D. Kim, C. Ryu, Y. Seo, and W. Kim. 2020. Silica dispersion and properties of silica filled esbr/br/nr ternary blend composites by applying wet masterbatch technology. *Polymer Testing*, 84:106350. Published online October 2019.

S. Prasertsri, F. Lagarde, N. Rattanasom, C. Sirisinha, and P. Daniel. 2013. Raman spectroscopy and thermal analysis of gum and silica-filled nr/sbr blends prepared from latex system. *Polymer Testing*, 32(5):852–861.

M. Yrieix and J. C. Majesté. 2017. Correlation of silane grafting density with rheological properties of silica filled rubber: Coupling of flow and temperature. *Polymer Testing*.

Individual Research Contribution Review, 2024: 141–142
*ISSN: 3083-922X*

# Performance Evaluation of Palm Oil-Based UV Curable Coatings for Diverse Environmental Applications

**Rida Tajau**
Radiation Processing Technology Division, Malaysian Nuclear Agency
43000 Kajang, Selangor
rida@nm.gov.my

## Abstract

Palm oil-based UV-curable resins can potentially serve as wood coating materials. In this study, the wood coating products were exposed to outdoor weather and room temperature. The durability and resilience of the palm oil-based coatings in ambient weather in Malaysia were investigated.

**Keywords:** Cellulose, morphology, extraction.

## 1 Introduction

Nuclear Malaysia has been developing radiation-curable palm oil-based coatings for over 30 years utilizing UV/EB radiation curing techniques (Mahmood et al., 1994). The technology's product and process research relied on local expertise. The base material of the coating is a natural polymer synthesized from palm olein. The curing method used in this coating process is a green technology that emits less Volatile organic compounds (VOC) gases than conventional methods, thereby lowering the carbon footprint on the environment. The palm oil-based UV-curable coating is waterproof, anti-scratch, and has good thermal characteristics (Figure 1). The coatings are waterproof with hydrophobic properties of a contact angle of up to 90°. It can withstand the friction force of scratches around 2-3 Newton (N) and has high thermal properties up to 310 °C (Tajau et al., 2024b; Tajau et al., 2024a).

Nanofillers, such as titanium dioxide (TiO2) nanoparticles (NPs), can increase the coating's anti-scratch, thermal, and antimicrobial properties (Tajau et al., 2024b) (Figure 2). As a result, this coating has the potential to serve as a surface finish for wood products such as furniture and handicrafts.

The usability of this coating material in different environments was evaluated to determine the product's quality level. The durability of the coating material on the surface of rubber wood was evaluated at room temperature and in an open ground area that was directly exposed to sunlight, rain, and environmental humidity.

## 2 Materials and Methods

The palm oil-based UV curable resin was applied to the rubber wood. The radiation curing technique employed an IST-UV Dryer (Switzerland) UV irradiator and a 200 Watt/cm mercury vapor lamp. The conveyor speed was set at 10 m/min for each pass. This coating product is evaluated in a room at 20 – 25 °C for a year and a half, as well as on open ground for 30 days.

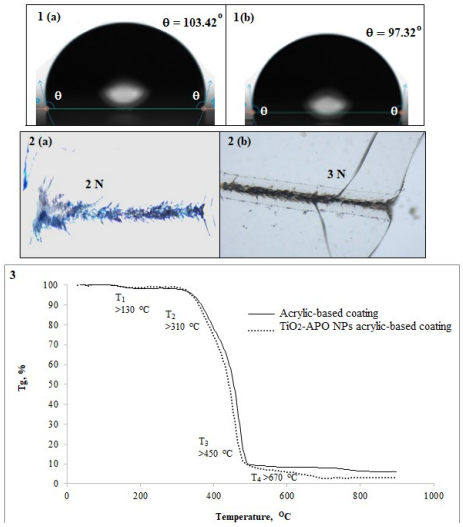



Figure 1: Water contact angle (1) and scratch tester measurements (2) of palm oil-based coatings: (a) acrylic-based coating and (b) TiO2-APO NPs-based acrylic coating, as well as the thermogravimetric analysis (TGA) curves (3).

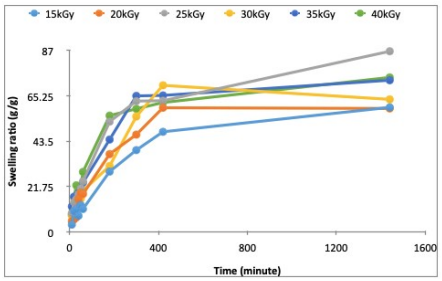



Figure 2: The silane-modified $TiO_2$-APO NPs synthesized using the sol-gel method (a), as well as the hybrid composite coating of $TiO_2$-APO NPs with acrylic resin (b).

## 3 Results and Discussion

Palm oil-based coatings are very resistant to moisture and atmospheric dirt for interior applications. UV-curing cross-linking considerably improved the coating's surface characteristics, resulting in extremely effective and long-lasting antimicrobial properties (Tajau et al., 2024b; Tajau et al., 2024a). The cross-linked coatings were extremely robust after one and a half years of indoor exposure (Figure 3). After a year and

a half of exposure to room temperature, the coated hardwood surface retained its water resistance and exceptional adhesive properties. This study also discovered that degradation of the coatings at room temperature was caused by the decay of the carbonyl, ester, carbon double bonds, and alkane functional groups of the film coating, resulting in deterioration of film coating quality (Figure 4).

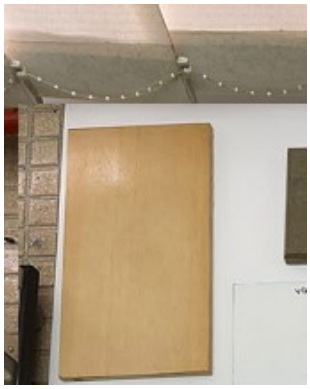


Figure 3: The physical state of the coated rubber wood samples after a year and a half in the indoor environment.

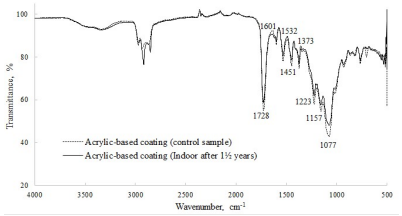



Figure 4: The chemical functional group that contributed to the coating's deterioration at room temperature for over a year.

Outdoor exposure impacts include coating deterioration caused by external environmental conditions such as humidity, heat, and sunlight. After 30 days of exposure to natural weathering, the weathering impact caused severe damage to the film coatings. Tajau et al. (Tajau et al., 2024a) describe coating deterioration as a combination of physical and chemical processes. The alternating dry and wet circumstances caused the formation of osmotic molecules in the coating, degrading coating systems while increasing substrate degradation and mould growth (Figure 5).

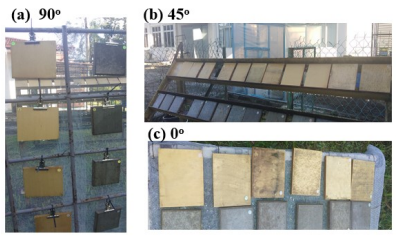



Figure 5: The physical condition of the coated rubber wood samples after 30 days of exposure to natural weathering at different angles (0°, 45° and 90°).

Long-term exposure of coated wood to sunlight or UV rays contributed to the photo-oxidation phenomenon on the coating system, which accelerated the deterioration process. Meanwhile, hydrolysis degradation causes water molecules to absorb into the coating system, attack the functional groups of the polymer chains, and cleave the chemical structure network, resulting in a primary deterioration of the protective coating layer that allows water molecules to interact with the substrate surface (Tajau et al., 2024a). The findings also show that the coatings' chemical functional groups, such as carbonyl, ester, carbon double bonds, alkane, and hydroxyl peaks, lead to deterioration under outdoor conditions (Figure 6).

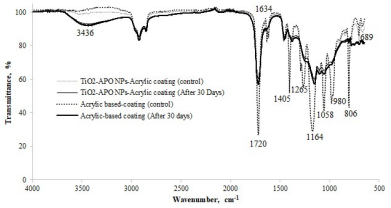



Figure 6: FTIR test findings for palm oil-based coatings after 30 days of natural weathering exposure. The chemical functional group that reacted to the degradation of the coating.

## 4 Conclusions

The palm oil-based UV-curable coatings are waterproof, UV resistant, antimicrobial, and enhances the aesthetics of wood in interior applications. For outdoor applications, the quality of this coating requires further improvement.

## 5 Acknowledgements

The author expresses his appreciation to the Malaysian Nuclear Agency and the Radiation Curing and Synthesis Group for their support and facility throughout the process of this study.

## References

M. H. Mahmood, H. Mohd Nor, and R. Ismail. 1994. The development of palm oil based acrylated resins and their applications. In *Compilation of Research Papers, Malaysian Institute for Nuclear Technology Research (MINT)*, Bangi, Kajang, Malaysia.

R. Tajau, M. S. Alias, M. H. Harun, N. H. Mudri, F. F. Hilmi, S. M. Faisal, R. C. Ismail, A. M. Sani, C. R. C. Hak, and W. S. Paulus. 2024a. Natural weathering effects on the surface morphological and physicochemical properties of radiation curable coatings in tropical climate. In *IOP Conference Series: Materials Science and Engineering*, volume 1308, page 012009.

R. Tajau, M. S. Alias, N. H. Mudri, F. F. Hilmi, S. M. Faisal, R. C. Ismail, A. M. Sani, C. R. C. Hak, W. S. Paulus, B. C. Jong, W. Y. Liew, J. N. Hing, N. M. Mat Rapi, and N. N. Halipah. 2024b. Modification of silane modified $tio_2$ nanoparticles as an antimicrobial additive for palm oil-based surface coatings. *Jurnal Sains Nuklear Malaysia*, 36(1):81–98.

Individual Research Contribution Review, 2024: 143–144
*ISSN: 3083-922X*

# Characteristics of treated shrimp shells for agricultural component

**Sarada Idris**
Radiation Processing Technology Division, Malaysian Nuclear Agency
43000 Kajang, Selangor
sarada@nm.gov.my

## Abstract

This current article studies the properties of shrimp shells treated with acidic and alkaline solutions in demineralization and deproteination processes to form chitin. Gamma irradiation was used as a pre-treatment to facilitate the deproteination and demineralization processes. Shrimp shells were irradiated by gamma rays at dosage 0 - 100 kGy and demineralized under acidic conditions to remove calcium carbonate and other minerals. The removal of proteins was carried out using an alkaline solution. The FESEM-EDX revealed the composition of macro- and micro nutrients in shrimp shell and chitin. The mild acidic solution for demineralization process was able to remove several elements, including K, Mg, P, Na, Al and $CaCO_3$. Deproteination, together with the demineralization process, facilitate chitin extraction reactions. Thermogravimetric Analysis (TGA) elaborates on the composition of chitin, protein, and calcium carbonate in shrimp shells treated with acidic and alkaline condition.

**Keywords:** shrimp shell, gamma irradiation, chitin.

## 1 Introduction

Security of the food supply is one of the most serious challenges in our society due to the rapidly increasing population. The agricultural sector is facing the intimidating challenge of feeding this rapid burst in population by applying chemical fertilizers. However, the application of chemical fertilizer results in the degradation of the soil environment and contamination of groundwater. Chemical fertilizer applications have depleted the soil's fertility, led to a decrease in biodiversity, and resulted in nutrient and pesticide runoff, posing health and environmental risks. Furthermore, chemical fertilizers can contribute the climate change and global warming as they release greenhouse gases like nitrous oxide. Numerous reported experiments have shown that $CH_4$ and $CN_2O$ emissions are primarily controlled by the type of fertilizer (Chen et al., 2014), and therefore it is essential to look for alternatives to chemical fertilizers. This study discuss the extraction of chitin from shrimp shells using demineralization and deproteination processes. Initially, the pre-treatment process used gamma irradiation as a tool to aid in demineralization and deproteination. Milder organic acid and alkaline replaced strong acid and alkaline solution, to remove calcium carbonate, minerals, and proteins from shrimp shells instead of the traditionally used of strong HCl and NaOH in the chitin extraction process. The use of gamma irradiation at a 25 kGy irradiation dose aids in the removal of minerals and proteins with less harmful chemicals.

## 2 Materials and Methods

Shrimp shell waste was purchased from a local market in Selangor. The samples then irradiated with gamma irradiation at 25 kGy. The samples were crushed and then stored in a closed container prior to use. The irradiated shrimp shell was treated with acid condition to removed calcium carbonate and other minerals. Another condition involved treating the shrimp shell with an alkaline solution to remove proteins. The combination of acidic and alkaline-treated shrimp shell was also studied to complete the process. The pristine shrimp shell and extracted shrimp shell were analyze by FESEM, TGA and FTIR for morphology and structural analysis.

## 3 Results and Discussion

### 3.1 Morphology and Elemental Analyses

The surface morphology and elemental composition of deproteinized and demineralized shrimp shells were analyzed by FESEM-EDX. The surface morphology of irradiated shrimp shells treated with alkaline solutions was rougher, which contributed to the minerals and $CaCO_3$. The elemental component demonstrated that shrimp shells treated with alkaline solutions retained more nutrients compared to those treated with acid solutions. This is because protein removal by an alkaline solution cannot remove most of the element adhered to the shells. On the other hand, the irradiated shrimp shell treated with an acid solution has lower mineral content because it was removed during the demineralization process. During the mineralization process, the elemental components of Mg, P, K, Na and $CaCO_3$ vanished, in contrast to the deproteination process using an alkaline solution. Combining demineralization and deproteination with acidic and alkaline solutions resulted in the removal of more nutrients from the shells, as evidenced by elemental analysis EDX (Figure 1).

### 3.2 Thermal analysis

The DTG and TGA thermogram of shrimp shells treated with alkaline solution show that the shell cuticles degraded in four stages, contributing to the shell's main component. The first transition from 50 to 180°C was due to the release of adherent and inevitable water molecules in the cuticles.

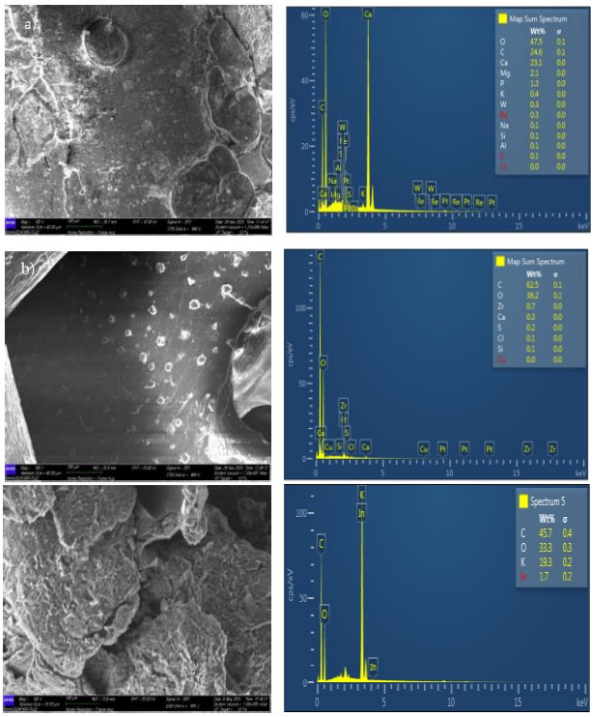


Figure 1: The FESEM-EDX analysis on shrimp shells treated with a) alkaline, b) acidic, and c) acidic-alkaline conditions (Magnification 150x)

The second phase between 195 and 400°C was contributed to the decomposition of chitin (chitinous materials) and the third transition between 400 and 600°C is the traced of remaining protein on the shrimp shells. At higher temperatures (600 to 800°C), the decomposition of calcium carbonate into calcium oxide and carbon dioxide and other minerals were detected. The thermal stability and the decomposition behavior exhibited a different trend after shrimp shell was treated with an acidic solution. The decomposition of calcium carbonate at the final stage revealed that less calcium carbonate was detected in shrimp shells as it was eliminated during the demineralization process by an acidic condition. Meanwhile, the combination of acid alkaline treatments was able to exclude both proteins and minerals, including $CaCO_3$ from the shrimp shell. When the shrimp shell was heated to 900°C the TGA/DTG thermogram showed the transition curve of chitin pyrolysis (Figure 2c). This meant that there was no proteins or minerals left on the shell treated with acid-alkaline. This is align with study done by Mahlous et al., (Mahlous et al., 2007) which proved that gamma irradiation aided chitin extraction from prawn shells.

### 3.3 FTIR analysis

The optimal conditions for deprotenation and demineralization were selected and compared with the pristine shrimp shell. From the IR spectra (Figure 3), bands belonging $CaCO_3$ at 867 $cm^{-1}$ is no longer detectable for shrimp shell treated with acid and the diminished of Amide I and II bands between 1500 to 1700 $cm^{-1}$ in alkaline treated shrimp shell as compared to the pristine shrimp shell.

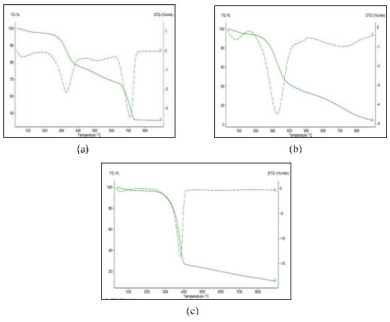


Figure 2: Thermogravimetric Analysis (TGA) on shrimp shells treated with a) alkaline, b) acidic, and c) acidic-alkaline conditions

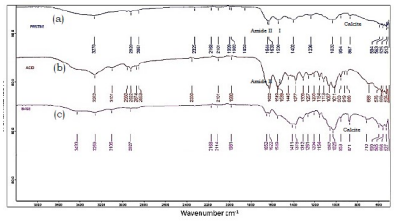


Figure 3: FTIR spectra for a) pristine shrimp shell and shrimp shells treated with b) acid and c) alkaline conditions

## 4 Conclusions

Shrimp shell treated with gamma irradiation, acidic and/or alkaline solution is a waste product that has the potential for useful applications including as an organic fertilizer. An efficient and green approach for extracting chitin from shrimp shells has been developed using mild organic acid and alkaline with the aid of gamma irradiation. Further study on application of treated shrimp shell as organic fertilizer will be explore and discuss in other publication.

## References

X. Chen, Z. Cui, M. Fan, P. Vitousek, M. Zhao, W. Ma, Z. Wang, W. Zhang, X. Yan, and J. Yang. 2014. Producing more grain with lower environmental costs. *Nature*, 514:486–489.

M. Mahlous, D. Tahtat, S. Benamer, and A. N. Khodja. 2007. Gamma irradiation-aided chitin/chitosan extraction from prawn shells. *Nuclear Instruments and Methods in Physics Research Section B: Beam Interactions with Materials and Atoms*, 265:414–417.

Individual Research Contribution Review, 2024: 145–146
*ISSN: 3083-922X*

# Preliminary study on gamma irradiation-aided treated shrimp shell as soil conditioner

**Sarada Idris**
Radiation Processing Technology Division, Malaysian Nuclear Agency
43000 Kajang, Selangor
sarada@nm.gov.my

## Abstract

This current article studies the properties of shrimp shells treated with acidic and alkaline solutions in demineralization and deproteination processes to form chitin. Gamma irradiation was used as a pretreatment method to facilitate the deproteination and demineralization processes. Shrimp shells were irradiated by gamma rays at 25 kGy and demineralized under acidic conditions to remove calcium carbonate and other minerals. The removal of proteins was carried out using an alkaline solution. Deproteination, in conjunction with the demineralization process, facilitate the improvised removal reactions. A large number of beneficial microbes in soil with added treated shrimp shell enhanced soil fertility, as presumed in N, P, K, EC and pH analyses. The absence of pathogenic bacteria in the soil is a good indicator that the soil with treated shrimp shells is safe as soil conditioner with plant disease protection.

**Keywords:** Keywords: shrimp shell, gamma irradiation, chitin.

## 1 Introduction

Chitin extracted from crustacean shells, including shrimp shells, can be beneficial as an organic fertilizer, primarily due to its effects on soil health and plant growth. Chitin is considered the second most plentiful biopolymer in nature after cellulose (Mao et al., 2017). Shrimp shells primarily consist of 15–40% chitin. The shrimp shell also contains two major components; 20–40% proteins and 20–50% $CaCO_3$ (Pakizeh et al., 2021), which are useful in organic fertilizer and have always been discarded during the chitin extraction process. In this study, chitin was extracted from shrimp shells using demineralization and deproteination processes with the aid of gamma irradiation. Treated shrimp shell were then use to determine soil fertility.

## 2 Materials and Methods

Shrimp shell waste was purchased from a local market in Selangor. The samples then irradiated with gamma irradiation at 25 kGy. The samples were crushed and then stored in a closed container prior to use. The irradiated shrimp shell was treated with acid condition to removed calcium carbonate and other minerals. Another condition involved treating the shrimp shell with an alkaline solution to remove proteins. Total population (bacteria) was analyzed using serial dilution and plate count methods for nitrogen fixation bacteria, as well as phosphate and potassium solubilization bacteria. The pathogenic microbes (*E.coli, Enterococcus, Proteus, A. aureus, Citrobacter* and *S.saprophyticus*) were analyzed using serial dilution and Chor Magar plate count methods.

## 3 Results and Discussion

### 3.1 Soil fertility study

Soil fertility is the ability of soil to sustain plant growth and optimize crop yield, which can be enhanced through organic and inorganic fertilizers in the soil. In this study, the addition of treated shrimp shell to the soil improved the soil fertility, as shown in Table 1. The addition of treated shrimp shell to the soil resulted in an improvement in N, P, K, EC and pH values. The addition of treated shrimp shell to the soil resulted in an increase in N, P, and K levels to 105, 148 and 352 ppm, respectively, compared to the initial levels of 3, 3 and 8 ppm. As shown in Table 1, soil with treated shrimp shell increases electrical conductivity (EC), as well as pH values which represents the amount of nutrient increases.

| Soil | N ppm | P ppm | K ppm | EC mS/m | pH |
|---|---|---|---|---|---|
| Untreated | 3 | 3 | 8 | 0.07 | 4.90 |
| With irradiated SS in alkaline | 105 | 148 | 352 | 0.94 | 6.36 |
| With irradiated SS in acid | 68 | 103 | 243 | 0.80 | 7.55 |
| With irradiated SS in neutral solution | 84 | 119 | 239 | 0.59 | 7.37 |

*Note: SS = shrimp shell.*

Table 1: Nitrogen (N), Phosphorous (P), Potassium (K), Electrical conductivity (EC) and pH of soil

### 3.2 Beneficial microbes and pathogen evaluation

Beneficial microorganisms benefit from abundance of macro- and micronutrients found in shrimp shells. Shrimp shells contain nutrients that feed microbes in the soil. These microscopic organism are capable of improving plant nutrition, primarily by increasing plant nutrient availability in soil and enhancing plant nutrient uptake (Singh et al., 2022). By looking at the good microbes in the soil, we found that adding treated shrimp shells to the soil increased the number of bacteria that fix nitrogen and bacteria that dissolve phosphate and potassium (Table 2). Nitrogen fixation in soil is important

for agriculture because it provides a digestible form of nitrogen for crop health. Plants apply phosphorus (P), a major essential macronutrient, to the soil in the form of phosphate fertilizers. The presence of phosphate-solubilizing bacteria in treated shrimp shells allows inorganic phosphorus to solubilize from insoluble compounds. Although the soil is a huge reservoir of potassium ion, 98% of its total contents exist in fixed form; only 2% are present in plant-available form (Jalali et al., 2021). Therefore, potassium-solubilizing bacteria are essential to improving the growth and productivity of plants grown under salt-affected conditions by breaking down of complex K compounds into simpler ones, making them available to plants (Bahadur et al., 2019).

| **Soil** | **Nitrogen fixation bacteria** | **Phosphate solubilization bacteria** | **Potassium solubilization bacteria** | **Pathogenic microbes** |
|---|---|---|---|---|
| Untreated | × | | × | × |
| With irradiated SS in alkaline | ✓ | ✓ | ✓ | |
| With irradiated SS in acid | ✓ | | × | × |
| With irradiated SS in neutral solution | × | ✓ | | |

*Note: SS = shrimp shell.*

Table 2: Beneficial and pathogenic microbes in soil

On the other hand, there was no population of pathogenic microbes including *E.coli, Enterococcus, Proteus, A. aureus, Citrobacter* and *S.saprophyticus* (Table 2), indicating the efficacy of this material as organic fertilizers. The potential health intricacies linked to organic fertilizers relate to their origin and their treatment. Adegoke et al. (Adegoke et al., 2016) indicated that pathogens from wastes like *E. coli, Salmonella sp., Listeria sp., Cryptosporidium sp.* and *Campylobacter sp.* among others are usually conveyed to the farmland through poorly composted organic fertilizers. Crop plants can acquire pathogens through direct contact, surface deposition, or splash contamination. Shrimp shells, originating from marine crustaceans, minimized the risk of pathogenic microbes. Additionally, treatment with gamma irradiation and alkaline and acidic conditions has proven to further diminish or eliminate the pathogenic microbes from the shrimp shells.

## 4 Conclusions

Shrimp shell treated with gamma irradiation, acidic and/or alkaline solution is a waste product that has the potential to serve as organic fertilizer. This preliminary study indicated the use of treated shrimp shell as a promising environmentally-friendly natural alternative to chemical fertilizer in order to control plant diseases caused by pathogens and enhance soil fertility. The absence of pathogenic microbes in the soil with treated shrimp shell is a good indicator to further explore this material as organic fertilizer. The presence of beneficial microbes (nitrogen fixation bacteria, phosphate and potassium solubilizing bacteria) in treated shrimp shells is a valuable resource for developing environment-friendly conditions to meet crop nutrient requirements. Beneficial soil microbes capable of enhancing plant nutrient acquisition, providing environmentally benign solutions to meet plant nutrition requirements in a cost-effective, environmentally friendly and sustainable manner.

## References

A. A. Adegoke, O. O. Awolusi, and T. A. Stenström, 2016. *Organic Fertilizers: Public Health Intricacies*. InTech.

I. Bahadur, R. Maurya, P. Roy, and A. Kumar. 2019. Potassium-solubilizing bacteria (ksb): a microbial tool for k-solubility, cycling, and availability to plants. In *Plant Growth Promoting Rhizobacteria for Sustainable Agriculture: From Theory to Practice*, pages 257–265. Agric. Sustain. Theory Pract.

M. Jalali, V. Antoniadis, and S. Najafi. 2021. Assessment of trace element pollution in northern and western iranian agricultural soils: a review. *Environmental Monitoring and Assessment*, 193:1–30.

X. Mao, N. Guo, J. Sun, and C. Xue. 2017. Comprehensive utilization of shrimp waste based on biotechnological methods: A review. *Journal of Cleaner Production*, 143:814–823.

M. Pakizeh, A. Moradi, and T. Ghassemi. 2021. Chemical extraction and modification of chitin and chitosan from shrimp shells. *European Polymer Journal*, 159:110709.

S. K. Singh, X. Wu, C. Shao, and H. Zhang. 2022. Microbial enhancement of plant nutrient acquisition. *Stress Biology*, 2:3.

Individual Research Contribution Review, 2024: 147–148
*ISSN: 3083-922X*

# Preparation of an adsorptive membrane of polyvinylidene fluoride incorporated functionalized boron nitride nanosheets for arsenic removal

**Sarala Selambakkannu**
Radiation Processing Technology Division, Malaysian Nuclear Agency
43000 Kajang, Selangor
sarala@nm.gov.my

## Abstract

Incorporating nanomaterials into membranes improves wastewater treatment by enhancing permeability, thermal stability, hydrophilicity, and fouling control. This study grafted polyethylene glycol (PEG) onto boron nitride modified with phosphoric acid (PA/BN) and blended it with polyvinylidene fluoride (PVDF) at different ratios. The resulting composite membranes were tested for chemical composition, crystallinity, morphology, and thermal properties. Water permeability, anti-fouling resistance, and solute rejection (including arsenic) were evaluated. The highest arsenic removal was observed in the 93:7 BN blend, where arsenic ion adsorption occurred via complexation with PA/BN, confirmed by various analyses.

**Keywords:** Membrane, boron nitride, arsenic removal, adsorption.

## 1 Introduction

Membrane separation is widely used in industrial processes for its simplicity and sustainability. Recent advancements have improved membrane efficiency in removing pollutants, such as organic matter and heavy metals. Membrane technologies like microfiltration, ultrafiltration, and reverse osmosis are commonly used for heavy metal removal (Abdullah et al., 2019). Adsorptive membranes, which combine adsorption and filtration, have gained attention for their low operating pressure, high removal capacity, and reusability. Incorporating nanomaterials like boron nitride (BN) into polymer membranes enhances performance, but challenges like nanomaterial agglomeration can affect efficiency (Fadila et al., 2022). This study explores the incorporation of modified BN into polyvinylidene fluoride (PVDF) membranes via melt blending and phase inversion. The resulting membranes' performance in arsenic removal, water permeability, anti-fouling resistance, and solute rejection was thoroughly evaluated. This approach represents a novel method for fabricating PVDF-PA/BN membranes for water purification.

## 2 Materials and Methods

### 2.1 Materials

All chemicals were of analytical grade. Polyvinylidene fluoride (PVDF), Arkema Kynar® 6000 HD (melting point: 120 – 130 °C), was used as the membrane support material. h-BN (BNNS) powder (purity 98%, density ~ 2.29 $g \cdot cm^{-3}$, size ~ 1 $\mu$m) from Sigma Aldrich, polyethylene glycol (PEG) (Mn = 6000), and dibenzoyl peroxide (BPO, 75%) from Aldrich were utilized. N-Methyl-2-pyrrolidone (NMP) from Merck served as the casting solvent, and ethanol (Merck) was used for grafting. Arsenic standard solution for AAS (999 $mg \cdot L^{-1}$) from Sigma Aldrich was used as a model pollutant. Reverse osmosis (RO) water (Sartorius) was used throughout.

### 2.2 Grafting

PEG was grafted onto PA/BN using BPO as an initiator. PA/BN (100 mg) was dissolved in 50 ml ethanol and stirred. PEG (1 g) was added and stirred for 1 hour, followed by addition of BPO (1 g). The mixture was heated to 60 °C for 5 hours with continuous shaking (250 $r \cdot min^{-1}$). After grafting, the dispersion was centrifuged at 5000 $r \cdot min^{-1}$ for 30 minutes, filtered, and dried overnight at 50 °C before use in membrane fabrication.

### 2.3 Melt Blending

PVDF resin and PEG-g-BN were melt-blended in an internal mixer (Haake Rheomix OS, Germany) at 130 °C with 80 $r \cdot min^{-1}$ rotor speed for 10 minutes. Both PVDF and PEG-g-PA/BN were dried at 50 °C for 24 hours before blending. Torque versus time was recorded to monitor the blending process. Five different blends were prepared: 100% PVDF, 3% PEG-g-PA/BN + 97% PVDF, 5% PEG-g-PA/BN + 95% PVDF, 7% PEG-g-PA/BN + 93% PVDF, and 7% PEG-g-PA/BNNS + 93% PVDF for evaluating arsenic removal.

### 2.4 Composite Membrane Preparation

The melt-blended samples were cast into thin membranes using the phase inversion technique. A dope solution was prepared by mixing 15% melt blend with 85% NMP, followed by 1-hour ultrasonication for homogeneous dispersion. The solution was stirred at 60 °C for 24 hours and degassed for 1 hour using a bath sonicator. The solution was cast onto a glass plate with a thickness of 300 $\mu$m, and phase inversion occurred by immersing the plate in pure water at 25°C. The composite membranes were stored in RO water for 24 hours to remove residual solvents. Finally, the membranes were cut into 47 mm discs and stored in pure water for further use.

### 2.5 Membrane Properties

#### 2.5.1 Membrane Flux and Compaction

A dead-end filtration setup was used to measure the pure water flux of the membranes. Membranes with a 30 mm diameter were stabilized at 15 psi (1 psi = 6.895 kPa) trans-membrane pressure for 1 hour. After stabilization, the pressure was reduced to 10 psi, and pure water flow was measured continuously for 1 hour. The flux for each of the five prepared membranes was calculated using the following equation:

$$J = \frac{V}{A \times t} \tag{1}$$

where $J$ is the membrane flux in $\mathrm{L \cdot m^{-2} \cdot h^{-1}}$ and $A$ is the area of filtration membrane and t is the time required to fill volume, $V$.

### 2.6 Removal of Arsenic by Membrane

The removal of arsenic from the solution was evaluated by filtering arsenic solutions at different concentrations (3, 7, 10 $\mathrm{mg \cdot L^{-1}}$) through the prepared membranes. The amount of arsenic adsorbed at equilibrium (qeq_eqe, $\mathrm{mg \cdot g^{-1}}$) was measured. The adsorption mass was calculated based on the material balance during the adsorption process. The arsenic removal efficiency (RRR, %) was calculated using the following equation:

$$R = \frac{C_0 - C_e}{C_0} \times 100\%$$

where $C_0$ ($\mathrm{mg \cdot L^{-1}}$) is the initial arsenic concentration, and $C_e$ ($\mathrm{mg \cdot L^{-1}}$) is the equilibrium arsenic concentration in the solution.

## 3 Results and Discussion

### 3.1 Preparation of PVDF/BN-based Composite Membranes

PVDF resin was loaded into the mixing chamber of an internal mixer set at 130 °C. After 8 minutes of melting, PEG-g-PA/BN was added. Figure 3 shows the torque versus time graph from the combination of PVDF resin and PEG-g-PA/BN. Upon adding PEG-g-PA/BN, a slight decrease in torque was observed (Fig. 1), which was attributed to the initial low viscosity and high density of the mixture. After 8 minutes, the addition of PEG-g-PA/BN required less energy to blend both materials. Once the PVDF and PEG-g-PA/BN were completely fused, the torque increased to the usual level. Blends of PVDF and PEG-g-PA/BN at different compositions showed similar torque trends due to their comparable molecular weights. However, when BNNS was added to the melted PVDF, a significant decrease in torque was observed. This was attributed to the bulk density and surface area of BNNS.

### 3.2 Arsenic Removal

The maximum arsenic removal efficiency for the different membranes at an initial concentration of 3 ($\mathrm{mg \cdot L^{-1}}$) was as follows: PVDF (3.9%), 97:3 BN (94.2%), 95:5 BN (98.2%), 93:7 BN (99.4%), and 93:7 BNNS (11.1%) as shown in Fig. 2. At 10 ($\mathrm{mg \cdot L^{-1}}$), the arsenic removal efficiencies were

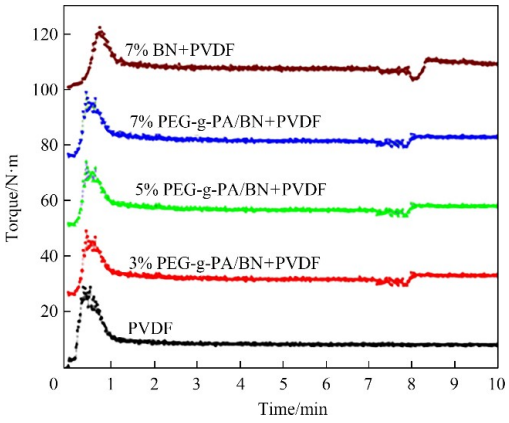



Figure 1: Real-time torque vs time of the PVDF/PA/BN blends

approximately 1.1% for PVDF, 81.8% for 97:3 BN, 82.8% for 95:5 BN, 88.1% for 93:7 BN, and 5.9% for 93:7 BNNS. This trend, with lower efficiency in PVDF and 93:7 BNNS membranes and higher efficiency as the composition of PEG-g-PA/BN increases.

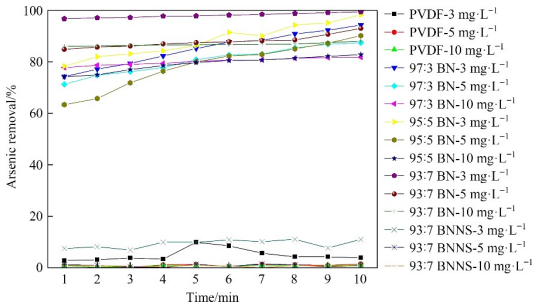



Figure 2: Arsenic removal efficiencies of PVDF/PEG-g-PA/BN blends.

## 4 Conclusions

Water remediation using adsorptive membranes has proven to be an efficient method for removing a wide range of emerging pollutants from wastewater. In this study, a novel nanomaterial-incorporated membrane was successfully developed for arsenic adsorption through ultrafiltration. Future studies could focus on evaluating the metal ion removal mechanism further by conducting kinetics studies to better understand the adsorption process and optimize membrane performance.

## References

N. Abdullah, N. Yusof, W. J. Lau, J. Jaafar, and A. F. Ismail. 2019. Recent trends of heavy metal removal from water/wastewater by membrane technologies. *Journal of Industrial and Engineering Chemistry*, 76:17–38.

C. R. Fadila, M. H. D. Othman, M. R. Adam, R. Takagi, T. Yoshioka, W. Khongnakorn, M. A. Rahman, J. Jaafar, and A. F. Ismail. 2022. Adsorptive membrane for heavy metal removal: Material, fabrication, and performance. *Materials Today: Proceedings*, 65:3037–3045.

Individual Research Contribution Review, 2024: 149–150
*ISSN: 3083-922X*

# Effect of Radiation Sensitizer on the Friction Behaviour of Electron Beam cured FKM-PTFE Composite

**Sivanesan Appadu**
Radiation Processing Technology Division, Malaysian Nuclear Agency
43000 Kajang, Selangor
siva@nm.gov.my

## Abstract

Friction coefficient behaviour of electron beam cured vinylidene fluoride-hexafluoropropylene copolymer fluorocarbon rubber (FKM) with 30% weight loading of polytetrafluoroethylene micro-powder (PTFEMP) irradiated at 250 kGy dose were studied by using a pin-on-disk tribometer. The same tests were done with the addition of radiation sensitizers n,n-1,3 phenylene bismaleimide (HVA2), trimethylol propane triacrylate (TMPTA) and tripropylene glycol diacrylate (TPGDA). The average friction coefficient ($\mu$) value of all the composites with sensitizer decreased with the TMPTA system recording the lowest $\mu$ value which reduced by almost half compared to the pure composite due to better crosslinking density of the vulcanizate.

**Keywords:** Fluorocarbon rubber, polytetrafluoroethylene, radiation sensitizer, electron beam,

## 1 Introduction

Fluorocarbon rubber (FKM) made of vinylidene fluoride-hexafluoropropylene copolymer are a type of synthetic rubber widely used in many industrial applications for products such as O-rings, gaskets and seals due to its outstanding resilience to heat, oil, and chemical solvents (Ajalesh Balachandran et al., 2013; Maiti and Bhowmick, 2006). Currently, there is demand from various industries for specialized polymer composites with reduced friction properties for better wear protection. Therefore, a potential solution for the preparation of FKM rubbers with improved tribological and overall properties, with the added cost-benefit advantages is by blending polytetrafluoroethylene micro-powder (PTFEMP) in FKM rubbers (Friedrich, 2018).

## 2 Materials and Methods

FKM A-401C-CC a dipolymer of vinylidine fluoride (VF2) and hexafluoropropylene (HFP) obtained from The Chemours Chenguang Fluoromaterials (Shanghai) Co., Ltd was melt-blended with 30 wt% PTFEMP produced in-house with an average particle size of around 30 $\mu$m and density of 2.2 g/cm$^3$. The samples were irradiated at 250 kGy with an electron beam machine (EBM). Radiation sensitizers used, namely, trimethylol propane triacrylate (TMPTA), tripropylene glycol diacrylate (TPGDA) and n,n-1,3 phenylene bismaleimide (HVA2) were obtained from Sigma-Aldrich. Friction coefficient properties of the samples were investigated with an Anton Paar TRB3 pin-on-disk tribometer according to the ASTM G99 testing method at room temperature of 24°C and a relative humidity of 40%. Hardened carbon balls made of steel 100Cr6 with a diameter of 6 mm and average roughness, Ra of 0.45 $\mu$m served as counterpart. The ball slid against the samples and the tests were done without lubrication for a total distance of 360 m at a sliding speed and applied normal load (FN) of 0.05 m/s and 1 N respectively.

## 3 Results and Discussion

Friction coefficient behaviour against sliding distance of FKM rubber and FKM-PT30 composite with radiation sensitizer are shown in Figures 1(a) and 1(b). The friction coefficient of elastomeric material sliding against a hard counter-surface can be articulated mainly in terms of the contribution of the adhesive and deformation components. The adhesion component derives from the adhesive junctions formed on the spots of real contact between the mating surfaces, while the deformation component of friction results from the resistance of the polymer to "ploughing" by the asperities of the harder counter-surface. However, for composite systems with PTFE micro-powder used as a solid lubricant filler, special consideration is required for the micro-powder transfer films to the counter-surface being a key factor which would determine the tribological behaviour of the composite (Bogoeva-Gaceva et al., 2018).

The graphs show clearly the influence of PTFEMP fillers on the friction behaviour of FKM vulcanizate. For pure FKM vulcanizate, the friction coefficient shows increasing fluctuations in the beginning and reduces slightly towards the end of measurement at around $\mu$=1.7. From the friction coefficient behaviour curve of FKM-PT30 composite, we can observe that there is a sudden fluctuation in the beginning but reduces gradually up to the 1500 cm distance and stabilizes at the end of measurement at around $\mu$=1.1. The lower friction value in the composite is due to the transfer film of PTFE micro-particles from the rubber matrix on to the surface of the counter-body. For elastomeric materials in general, compatibility as well as the dispersion or agglomeration of PTFE filler particles in the matrix would critically influence the friction coefficient behaviour of the tested sample (Khan et al., 2009).

For the composites added with radiation sensitizer, lower friction coefficient values were observed compared to the pure

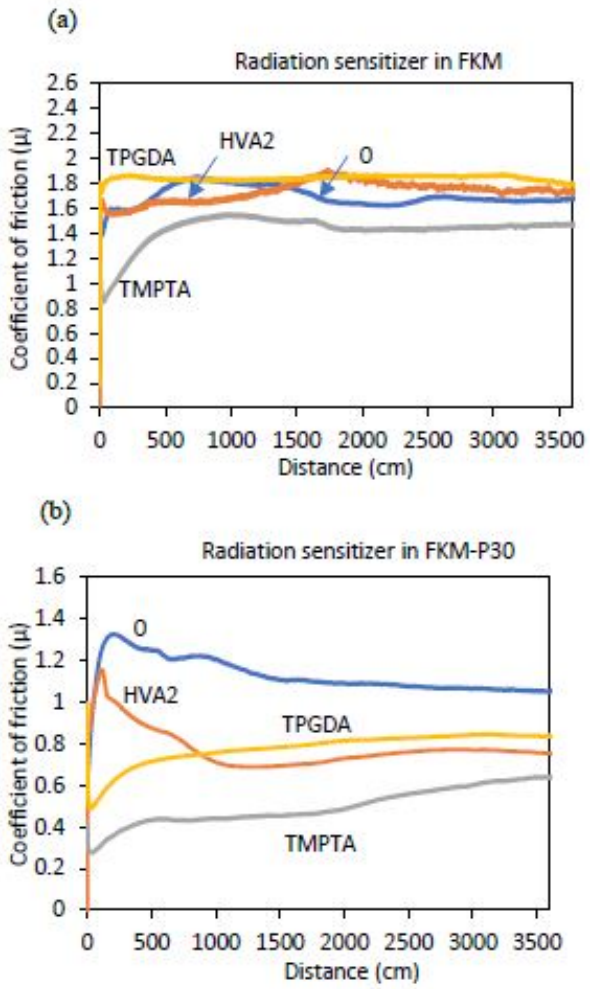



Figure 1: Comparison of the friction behaviour of (a) FKM and (b) FKM-PT30 blends with radiation sensitizer as a function of sliding distance

composite. Therefore, higher crosslinking density in the matrix as well as the synergistic effect by chemical coupling of the filler-matrix system through irradiation, have resulted in a decrement of the adhesive friction and better resistance to surface deformation, resulting in lower coefficient of friction with radiation sensitizers. We can observe that in the TMPTA and TPGDA composite, the graph shows and increasing friction trend from an initial low value, while HVA2 composite recorded an initial high value but shows a reducing trend versus distance. This shows HVA2 promotes better synergistic effect and miscibility of PTFEMP in the FKM matrix, resulting in a more efficient micro-particle transfer film to the counter-body as it slides against the surface. Therefore, lower friction values will be shown for the remaining testing time (Khan et al., 2009).

## 4 Conclusions

The study shows that the friction coefficient value of electron beam cured FKM-PTFE composite can be reduced with the addition of radiation sensitizer due to the higher crosslinking density in the matrix as well as the synergistic effect by chemical coupling of the filler-matrix system through irradiation.

## References

N. Ajalesh Balachandran, K. Philip, and J. Rani. 2013. Effect of expanded graphite on thermal, mechanical and dielectric properties of ethylene-propylene-diene terpolymer/hexa fluoropropylene-vinylidinefluoride dipolymer rubber blends. *European Polymer Journal*, 49(1):247–260.

G. Bogoeva-Gaceva, D. Dimeski, and V. Srebrenkoska. 2018. Friction mechanism of polymers and their composites. *Macedonian Journal of Chemistry and Chemical Engineering*, 37(1):1–11.

K. Friedrich. 2018. Polymer composites for tribological applications. *Advanced Industrial and Engineering Polymer Research*, 1(1):3–39.

M. S. Khan, D. Lehmann, G. Heinrich, U. Gohs, and R. Franke. 2009. Structure-property effects on mechanical, friction and wear properties of electron modified ptfe filled epdm composite. *Express Polymer Letters*, 3(1):39–48.

M. Maiti and A. K. Bhowmick. 2006. Structure and properties of some novel fluoroelastomer/clay nanocomposites with special reference to their interaction. *Journal of Polymer Science, Part B: Polymer Physics*, 44(1):162–176.

Individual Research Contribution Review, 2024: 151–152
*ISSN: 3083-922X*

# PGEC-18 Participant Dosimetry Report: Monthly Analysis for August 2024

**Ahmad Bazlie Bin Abdul Kadir**
Radiation Health and Safety Division, Malaysian Nuclear Agency
43000 Kajang, Selangor
bazlie@nm.gov.my

## Abstract

Nuclear Malaysia is hosting the 2024 IAEA Post Graduate Educational Course (PGEC-18) in Bangi. The six-month program has 25 participants from 17 countries working in fields like medical physics and nuclear technology. SSDL Nuclear Malaysia gives each PGEC-18 participant an Optically Stimulated Luminescence Dosimeter (OSLD) badge. Participants wear these badges for one month to monitor their radiation exposure. They then return the badges to SSDL for analysis.

**Keywords:** PGEC-18, OSLD, Dose Report

## 1 Introduction

The Secondary Standards Dosimetry Laboratory (SSDL) at Nuclear Malaysia stands as one of the providers of individual radiation monitoring services. As an established monitoring service provider, SSDL Nuclear Malaysia offers two advanced types of dosimeters: Optically Stimulated Luminescence Dosimeters (OSLD) and Thermoluminescent Dosimeters (TLD). These monitoring devices are essential tools in measuring and tracking radiation exposure levels received by workers in various sectors, including medical facilities, industrial applications, research institutions, and nuclear facilities throughout Malaysia.

## 2 Methods

### 2.1 OSLD (XA Type)




Figure 1: OSLD (XA Type)

In this OSLD, it consists of 4 units of tissue equivalent detector materials Aluminum Oxide doped with elemental carbon ($Al_2O_3$:C), which layer $Al_2O_3$:C will be attached in the second polyester layer having a thickness of 0.3mm.This OSL holder consists of 2 parts, front and back and each side has one open window types and 3 types of filters. The thickness of the open window to the front is 29 mg/cm$^2$ and 134 mg/cm$^2$ backsides. Filters for OSL holders are 275 mg/cm$^2$ thick plastic filters to the front and to the rear of 283-mg/cm$^2$, 375 mg/cm$^2$ thick aluminum filter to the front and to the rear of 383-mg/cm$^2$, 545mg/cm$^2$ thick copper filter to the front and to the rear of 553-mg/cm$^2$. To get the data stored in the OSL, it should be exposed to light at wavelength of 540 nm.

### 2.2 Flow Chart of Supply and Evaluation of OSL Dosimeter

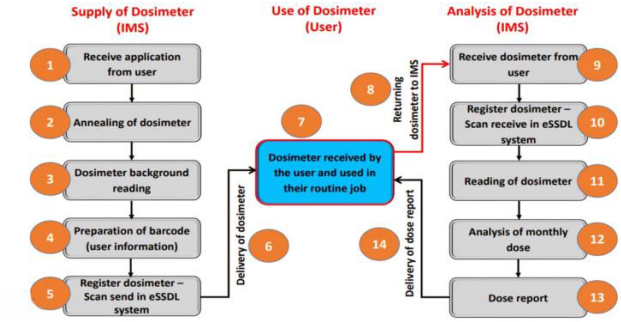


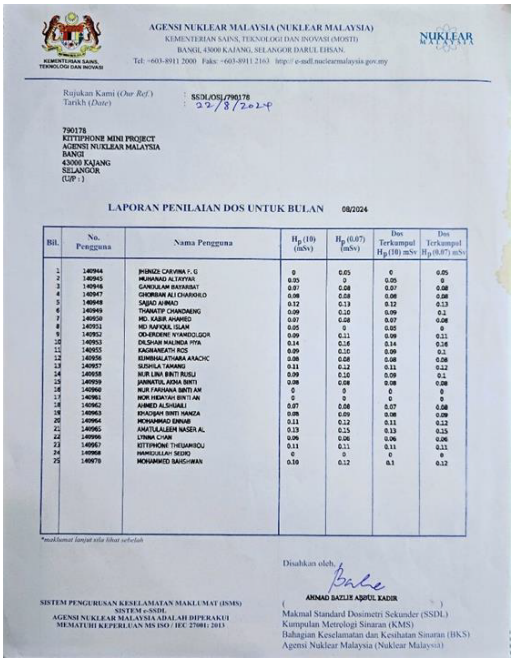

Figure 2: Flow Chart of Supply and Evaluation of OSL Dosimeter

The process begins with SSDL receiving an application from the user. Once received, the dosimeter undergoes an annealing process, followed by a background reading to establish baseline measurements. The next step involves preparing a barcode containing the user's information. The dosimeter is then registered in the eSSDL system through a scanning process. After registration, the dosimeter is delivered to the user (PGEC-18) participant, who wear it during their routine job activities. When the monitoring period is complete, the user returns the dosimeter to SSDL for analysis.

The analysis phase begins when SSDL receives the returned dosimeter from the user. Upon receipt, the dosimeter is registered and scanned in the eSSDL system. The dosimeter then undergoes a reading process to measure the accumulated radiation exposure. This is followed by an analysis of the monthly

dose. Finally, SSDL generates a dose report, which is delivered back to the user to inform them of their radiation exposure levels. This cyclical process ensures proper monitoring and documentation of radiation exposure for individuals working in radiation-controlled environment.

## 3 Results



AGENSI NUKLEAR MALAYSIA (NUKLEAR MALAYSIA)
KEMENTERIAN SAINS, TEKNOLOGI DAN INOVASI (MOSTI)
BANGI, 43000 KAJANG, SELANGOR DARUL EHSAN.
Tel: +603-8911 2000 Faks: +603-8911 2163 http:// e-ssdl.nuclearmalaysia.gov.my

Rujukan Kami (*Our Ref.*) : SSDL/OSL/790178
Tarikh (*Date*) : 22/8/2024

790178
KITTIPHONE MINI PROJECT
AGENSI NUKLEAR MALAYSIA
BANGI
43000 KAJANG
SELANGOR
(UP : )

LAPORAN PENILAIAN DOS UNTUK BULAN 08/2024

| Bil. | No. Pengguna | Nama Pengguna | $H_p(10)$ (mSv) | $H_p(0.07)$ (mSv) | Dos Terkumpul $H_p(10)$ mSv | Dos Terkumpul $H_p(0.07)$ mSv |
|---|---|---|---|---|---|---|
| 1 | 140944 | INGNZE CARVINA F. G | 0 | 0.05 | 0 | 0.05 |
| 2 | 140945 | MUHAMAD ALIFFYAR | 0.05 | 0 | 0.05 | 0 |
| 3 | 140946 | GANJULAM BAYARBAT | 0.07 | 0.08 | 0.07 | 0.08 |
| 4 | 140947 | GHORBANI ALI CHAHOOLD | 0.08 | 0.08 | 0.08 | 0.08 |
| 5 | 140948 | SAJJAD AHMAD | 0.12 | 0.13 | 0.12 | 0.13 |
| 6 | 140949 | THANATIP CHANDAENG | 0.09 | 0.10 | 0.09 | 0.1 |
| 7 | 140950 | MD. KABIR AHAMED | 0.07 | 0.08 | 0.07 | 0.08 |
| 8 | 140951 | MD RAFIQUL ISLAM | 0.05 | 0 | 0.05 | 0 |
| 9 | 140952 | OD-ERDENE NYAMDOLGOR | 0.09 | 0.11 | 0.09 | 0.11 |
| 10 | 140953 | DILSHAN MALINDA PIYA | 0.14 | 0.16 | 0.14 | 0.16 |
| 11 | 140955 | KAGIANEATH ROS | 0.09 | 0.10 | 0.09 | 0.1 |
| 12 | 140956 | KUMBHALATHARA ANACHC | 0.08 | 0.08 | 0.08 | 0.08 |
| 13 | 140957 | SUSHILA TAHANG | 0.11 | 0.12 | 0.11 | 0.12 |
| 14 | 140958 | NUR LINA BINTI RUSLI | 0.09 | 0.10 | 0.09 | 0.1 |
| 15 | 140959 | JANNATUL AKMA BINTI | 0.08 | 0.08 | 0.08 | 0.08 |
| 16 | 140960 | NUR FARAHA BINTI AH | 0 | 0 | 0 | 0 |
| 17 | 140961 | NOR HIDAYAH BINTI AN | 0 | 0 | 0 | 0 |
| 18 | 140962 | AHMED ALSHAALI | 0.07 | 0.08 | 0.07 | 0.08 |
| 19 | 140963 | KHADIJAH BINTI HANIZA | 0.08 | 0.09 | 0.08 | 0.09 |
| 20 | 140964 | MOHAMMAD EMNUR | 0.11 | 0.12 | 0.11 | 0.12 |
| 21 | 140965 | AMATULALEEM NASER AL | 0.13 | 0.15 | 0.13 | 0.15 |
| 22 | 140966 | LYMAN CYAN | 0.06 | 0.06 | 0.06 | 0.06 |
| 23 | 140967 | KITTIPHONE THISAMBOU | 0.11 | 0.11 | 0.11 | 0.11 |
| 24 | 140968 | HAMIDULLAH SEDIQ | 0 | 0 | 0 | 0 |
| 25 | 140979 | MOHAMMED SAKSHAAN | 0.10 | 0.12 | 0.1 | 0.12 |

*maklumat lanjut sila lihat sebelah

Disahkan oleh,
AHMAD BAZLIE ABDUL KADIR
Makmal Standard Dosimetri Sekunder (SSDL)
Kumpulan Metrologi Sinaran (KMS)
Bahagian Keselamatan dan Kesihatan Sinaran (BKS)
Agensi Nuklear Malaysia (Nuklear Malaysia)

SISTEM PENGURUSAN KESELAMATAN MAKLUMAT (ISMS)
SISTEM e-SSDL
AGENSI NUKLEAR MALAYSIA ADALAH DIPERAKUI
MEMATUHI KEPERLUAN MS ISO / IEC 27001: 2013

Figure 3: PGEC-18 Participant Dosimetry Report

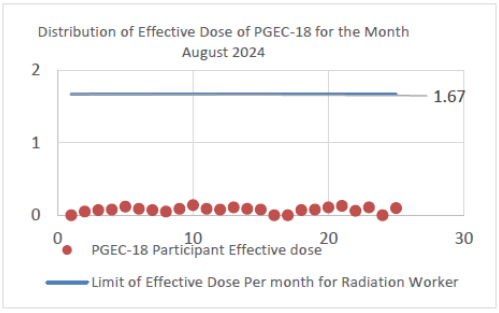



Figure 4: Distribution of Effective Dose of PGEC-18 for the Month August 2024

## 4 Discussion

The radiation exposure monitoring for PGEC-18 participants in August 2024 demonstrates effective implementation of radiation protection principles. Individual dose measurements were recorded using OSLD badges for both deep dose [Hp(10)] and shallow dose [Hp(0.07)]. The maximum recorded deep dose was 0.16 mSv, while the highest shallow dose was 0.25 mSv. These values are significantly below the monthly dose limit of 1.67 mSv, representing less than 15% of the permitted monthly exposure. The low dose readings suggest that participants followed proper radiation safety protocols, including time, distance, and shielding principles during their practical training sessions.

## 5 Conclusion

The personal dose monitoring results for August 2024 confirm that all PGEC-18 participants received radiation exposures well within safe limits. Both deep dose [Hp(10)] and shallow dose [Hp(0.07)] measurements remained considerably below the monthly dose limit of 1.67 mSv, indicating successful implementation of radiation protection measures during the training program. These results demonstrate Nuclear Malaysia's commitment to maintaining high safety standards in radiation protection education and training. The monitoring program effectively ensures participant safety while providing practical experience in radiation protection practices.

## References

https://e-ssdl.nuclearmalaysia.gov.my.

Individual Research Contribution Review, 2024: 153–154
*ISSN: 3083-922X*

IRCR

# Enhancing Safety Culture Practice through Conducting Safety Culture Self-Assessment Based on IAEA Guidelines

**Andy Kong Shin Shyen**
Radiation Health and Safety Division, Malaysian Nuclear Agency
43000 Kajang, Selangor
andy_kong@nm.gov.my

## Abstract

This paper explores the critical role of safety culture in improving organizational safety performance, particularly within nuclear facilities. Drawing on the International Atomic Energy Agency (IAEA) guidelines, this research emphasizes the utilization of self-assessment to identify the key elements that contribute to effective safety culture. This research contributes to the understanding of safety culture dynamics and provides practical recommendations for organization aiming to enhance its' safety practices.

**Keywords:** safety culture, self-assessment, questionnaire, document review, observation, descriptive analysis, normative analysis

## 1 Introduction

Safety culture is a critical component of organizational effectiveness, particularly in high-risk industries like nuclear power, where safety lapses can have dire consequences. A strong safety culture not only enhances operational efficiency but also promotes employee well-being by encouraging proactive safety behaviors. Despite advancements in safety culture initiatives, challenges remain in the assessment and enhancement of these practices, often due to a lack of standardized methods and actionable insights. Recognizing this gap, the International Atomic Energy Agency (IAEA) has developed guidelines under Safety Reports Series No. 83 to facilitate systematic safety culture self-assessments. This research proposal aims to implement these guidelines within Nuclear Malaysia, focusing on the evaluation and improvement of safety culture practices. By leveraging IAEA's comprehensive framework, organizations can better understand their safety culture dynamics, identify improvement areas, and foster an environment that prioritizes safety, ultimately leading to reduced accident rates and enhanced employee morale.

## 2 Methods

The research will adopt a multiple-methods approach based on the IAEA Safety Culture Assessment Methodology, which encompasses several key methods to comprehensively evaluate safety culture within the organization:

### 2.1 Questionnaire

The first method involves the utilization of the IAEA Safety Culture Perception Questionnaire. This structured survey is designed to measure various dimensions of safety culture, capturing employees' perceptions and attitudes towards safety practices within the organization. The questionnaire consists of a series of carefully crafted questions that align with the IAEA's normative framework for strong safety culture. By distributing this questionnaire to a representative sample of employees, including management and operational staff, the research aims to gather quantitative data that reflects the overall safety climate. The results will not only highlight areas of strength but also identify potential weaknesses in the organization's safety culture, enabling targeted interventions.

### 2.2 Document Review

The second method focuses on document review, where specific types and quantities of organizational documents will be selected for analysis. This review will include safety policies, incident reports, training materials, and internal communications. By examining these documents, the research aims to uncover how the organization represents itself in writing and what shared values and basic assumptions are reflected in its documentation. This qualitative analysis will provide insights into the alignment between documented safety practices and actual behaviors observed within the organization. The findings from this document review will complement the quantitative data obtained from the questionnaire, offering a more holistic view of the organization's safety culture.

### 2.3 Observation

The third method involves observation of selected situations within the workplace. This observational approach aims to provide information regarding employee behavior in realtime contexts. By identifying specific scenarios that are critical to safety operations, researchers can observe how employees interact with safety protocols and each other. This method allows for an assessment of actual practices versus stated policies, revealing discrepancies that may exist between formal safety culture and its enactment on the ground. Observational data will be invaluable in understanding the nuances of organizational behavior related to safety.

### 2.4 Sampling

For all methods employed in this research, convenience sampling will be utilized based on availability and willingness to participate among employees. This approach allows for practical data collection while ensuring that diverse perspectives are captured across different departments and levels within the organization. While convenience sampling may introduce

some bias, it is deemed appropriate in this context due to logistical constraints and the need for timely data collection.

By integrating these three methods, i.e., questionnaires, document reviews, and observations — the research aims to create a comprehensive assessment of safety culture within Nuclear Malaysia, aligned with IAEA guidelines. This multi-faceted approach ensures that both quantitative and qualitative dimensions of safety culture are explored, facilitating a deeper understanding of organizational dynamics related to safety practices.

### 2.5 Data Analysis

This study employs a comprehensive data analysis approach to extract cultural themes across various qualitative methods. Initially, cultural themes are identified from each method, revealing distinct insights into the underlying values and beliefs that shape cultural narratives. Following this, conclusions are developed for each method, highlighting the unique contributions of each analytical approach to understanding cultural dynamics.

The overarching analysis encompasses both descriptive and normative evaluations. The descriptive analysis identifies overarching themes that emerge from the data, providing a holistic view of the cultural landscape. In contrast, the normative analysis evaluates the existing culture against the IAEA Safety Culture Framework, assessing how well current practices align with established principles of safety culture. This dual approach not only enriches our understanding of cultural themes but also offers critical insights into areas for improvement in fostering a robust safety culture.

## 3 Data/Results

The study is in its preparatory phase, and as such, empirical data remains to be gathered.

## 4 Discussion/Conclusions

Given that the research is still in its initial stages, conclusions and discussions are forthcoming and will be addressed in subsequent publications.

## References

Federal Highway Administration. 2019. Organizational safety culture self-assessment for transportation agencies. Retrieved from https://highways.dot.gov/media/56616.

International Atomic Energy Agency. 2016. Performing safety culture self-assessments. *Safety Reports Series*, No. 3.

S. Gadd and A. Collins. 2013. Literature review of safety culture. Sandia National Laboratories.

Safety and Quality in Health Care. n.d.. Safety culture assessment in health care: A review of the literature on safety culture assessment modes. *Safety Reports Series*, Retrieved from https://www.safetyandquality.gov.au/sites/default/files/migrated/Safety-Culture- Assessment-in-Health-Care-A-review-of-theliterature- on-safety-culture-assessmentmodes. pdf.

Individual Research Contribution Review, 2024: 155–156
*ISSN: 3083-922X*

# Comparison of air kerma measurements between Medical Physics Laboratory (MPL) and the IAEA Dosimetry Laboratory for X-radiation qualities used in general diagnostic radiology

**Asmaliza Hashim**
Radiation Health and Safety Division, Malaysian Nuclear Agency
43000 Kajang, Selangor
asmaliza@nm.gov.my

## Abstract

A comparison of the air kerma standards for X-radiation qualities used in general diagnostic radiology was performed between the IAEA Dosimetry Laboratory and the Medical Physics Laboratory (MPL). The comparison was conducted through the calibration of transfer chamber received from the IAEA. Four radiation qualities were selected in this comparison. The results shown the calibration coefficients of both laboratories to be in good agreement (1.001-1.008) within the standard uncertainty of the comparison of about 2.2%.

**Keywords:** Comparison, radiation quality, calibration coefficient, uncertainty

## 1 Introduction

The Medical Physics Laboratory (MPL), accredited under MS ISO/IEC 17025 (SAMM No: 275) for calibration in diagnostic radiology, ensures the validity and accuracy of its results by complying with requirement clause 7.7 of the standard. This is achieved through active participation in interlaboratory comparison programs, which helps maintain the quality of its calibration services in line with international standards.

The objective of this interlaboratory comparison is to demonstrate that the measurement and calibration services provided by the MPL align with international standards, verify the consistency and validate the calibration procedures implemented, and ensure compliance with clause 7.7 of MS ISO/IEC 17025:2017.

## 2 Methods

The comparison was conducted by calibrating transfer chamber Exradin A3 in terms of air kerma ($K_a$) according to the MPL laboratory procedure. Meanwhile MPL was using the PTW Model TW34060 chamber, connected to a PTW UNIDOS Model T10005 electrometer. The comparison parameters were the calibration coefficients of the transfer chamber. The X-ray source used was a Philips MG165, manufactured by YXLON International X-Ray GmbH with capability kV up to 160 kV. For filtration, aluminum (Al) was applied for RQR quality, while a combination of aluminum (Al) and copper (Cu) with 99.9% purity was used for RQT quality. A total of four radiation qualities were selected for the assessment.

The calibration coefficients for the transfer chamber were provided in terms of air kerma per charge, expressed in units

Table 1:

| Radiation Qualities | kV | 1st. HVL | Tube Current (mA) |
|---|---|---|---|
| RQR2 | 40 | 1.42 | 7.0 |
| RQR5 | 70 | 2.52 | 2.5 |
| RQR10 | 150 | 6.62 | 1.5 |
| RQT9 | 120 | 8.15 | 2.5 |



Figure 1: Transfer chamber Exradin A3




Figure 2: MPL chamber and electrometer PTW Model TW34060 and T10005

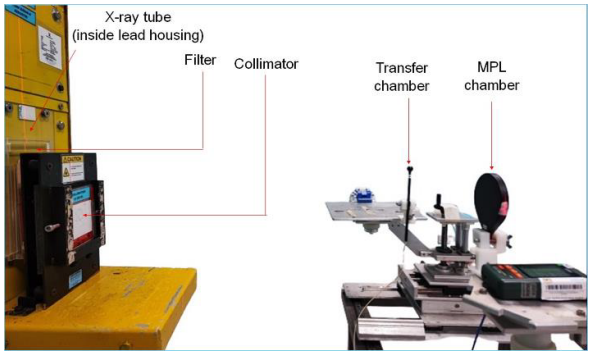



Figure 3: Set-up of comparison

Table 2: Result of comparison

| Beam code | Participant | | | | | | IAEA | | | | | | Comparison result | |
|---|---|---|---|---|---|---|---|---|---|---|---|---|---|---|
| | HVL (mm Al) | Air kerma rate (mGy/min) | $N_{k(SSDL)^*}$ | U (k-2) | Tracebility | Tracebility date | HVL (mm Al) | Air kerma rate (mGy/min) | $N_{k(IAEA)^*}$ | U (k-2) | Tracebility | Tracebility date | R = $N_{k(SSDL)}$/ $N_{k(IAEA)}$ | $U_k$ (k=2) (%) |
| RQR-2 | 1.42 | 9 | 7.99 | 1.7 | IAEA | 2023-09-28 | 1.42 | 42 | 7.96 | 1.3 | PTB | 2019-10-18 | 1.003 | 2.2 |
| RQR-5 | 2.52 | 11 | 7.97 | 1.7 | IAEA | 2023-09-28 | 2.57 | 38 | 7.91 | 1.3 | PTB | 2019-10-18 | 1.008 | 2.2 |
| RQR-10 | 6.62 | 18 | 7.92 | 1.7 | IAEA | 2023-09-28 | 6.71 | 40 | 7.89 | 1.3 | PTB | 2019-10-18 | 1.003 | 2.1 |
| RQT-9 | 8.15 | 11 | 7.91 | 1.8 | IAEA | 2023-09-28 | 8.47 | 41 | 7.90 | 1.3 | 43756.0 | 2019-10-18 | 1.001 | 2.2 |

of mGy/nC, and normalized to standard conditions of air temperature and pressure (T = 293.15 K, P = 101.325 kPa). The relative air humidity was maintained between 30% and 70% during the calibrations. The focus-to-chamber distance and beam diameter were 100 cm and 16 cm, respectively, to ensure uniform irradiation of the transfer and MPL chambers. The mark on the stem of the Exradin A3 and MPL chambers was positioned to face the X-ray tube. The comparison was performed by the substitution method. The calibration was repeated twice. Between these repeated calibrations, the chambers were removed from the beam and repositioned. The uncertainty estimations for the comparison measurements was calculated.

## 3 Results

The IAEA calibration coefficients, $N_{k(IAEA)}$, were the comparison reference values. The result of the comparison was $R = N_{k(MPL)}/N_{k(IAEA)}$, where $N_{k(MPL)}$ was the calibration coefficient determined by the MPL. The comparison result R was considered acceptable if $0.975 \leq R \leq 1.025$.

Table 2 shown the results of comparison in term of $N_k$.

## 4 Discussion

The results showed R to be in reasonable agreement (1.001 - 1.008), with a standard uncertainty of about 2.2%. The comparison results were acceptable, thus fulfilling the MS ISO/IEC 17025:2017 requirements. The measurements and calibration services provided by the MPL were equivalent to international standards. The result of this comparison was valid for 5 years.

## 5 Conclusion

The comparison results serve as a crucial mechanism for validating the precision and accuracy of MPL's measurement capabilities. The favorable outcomes confirm that MPL consistently upholds a high standard of measurement and calibration, aligning with international benchmarks.

## References

IEC 61267, 2005: Medical Diagnostic X-Ray Equipment – Radiation Conditions for Use in the Determination of Characteristics:1 –14, 17 – 18.

Technical Reports Series (TRS) No 457, 2007: Dosimetry in Diagnostic Radiology: An International Code of Practice:7 – 14, 41 – 52, 55 – 75.

MS ISO/IEC 17025:2017 General requirements for the competence of testing and calibration laboratories.

SSDL Newsletter, Feb 2021, No. 73, ISSN 1001 – 2669.

Individual Research Contribution Review, 2024: 157–158
*ISSN: 3083-922X*

# Radiological and Nuclear Emergencies Exercise at Malaysia Nuclear Agency

**Azimawati binti Ahmad**
Radiation Health and Safety Division, Malaysian Nuclear Agency
43000 Kajang, Selangor
azima@nm.gov.my

## Abstract

Malaysia Nuclear Agency conducted a comprehensive Radiological and Nuclear Emergency Exercise to assess and improve its emergency preparedness and response capabilities. The agency recognized the critical importance of effective emergency management for public safety and environmental protection. The exercise employed a structured, multi-phase approach simulating real-life emergency scenarios involving chemical, fire, and radiological incidents. Through careful planning, simulation, observation, and evaluation, the exercise aimed to test the readiness of emergency responders and identify potential gaps in existing protocols. Key findings highlighted several areas for improvement, including decontamination procedures, emergency communication, personal protective equipment, logistical support, and training methodologies. The exercise successfully demonstrated the agency's commitment to continuous improvement in emergency response, emphasizing the need for periodic training, clear communication, and well-defined organizational structures.

**Keywords:** radiological preparedness, emergency management, incident simulation, organization readiness

## 1 Introduction

At Nuclear Malaysia, the the Sub-Committee of Emergency (JKK) under the Committee Environmental Safety and Health (JKSHE) is responsible for managing and implementing emergency management and response. In order to comply license requirements (LPTA/A/724, LPTA/A/1026 and LPTA/A/3233) for radiological emergency and preparedness, JKK in process and continuous to strengthening the emergency preparedness and response at Nuclear Malaysia.

At Nuclear Malaysia, there are 12 main facilities, and more than 700 radioactive sources are used for research, instrument calibration, sterilization, medicine and other activities. And various chemical and biological laboratories in the agency. Within this variety of sources, there is a range of radionuclides, forms and quantities of radioactive material that need to be considered in emergency response. The potential for emergencies is a critical concern for public safety, health and environment. To mitigate these risks, it is essential for response team and organization are well prepared to handle the emergencies swiftly and effectively.

A Radiological and Nuclear Emergency Exercise provides a comprehensive platform for testing the readiness of responders, identifying potential gaps in plans and procedures, and ensuring that the key players are equipped with the necessary skills to manage these high-stakes situations.

## 2 Methods

The method for conducting a Radiological and Nuclear Emergency Exercise involves a structured, multi-phase approach designed to simulate real-life emergency scenarios, with controlled environment and assess the effectiveness of response strategies. This method ensures that all responder is able to practice their roles in managing an emergency while identifying strengths and areas for improvement.

The phases and activities involved in the exercise:

i. Planning and preparation: Objective setting, scenario development, roles and responsibilities, logistic and resources,

ii. Training and briefing: pre-exercise briefing and safety consideration,

iii. Exercise simulation: activation of the scenario, real-time decision making, simulation of communication and using tools,

iv. Observation and evaluation: observation teams, real-time feedback and documentation,

v. Debriefing and after-action review: post exercise review, after-action report and lesson learn and

vi. Continuous Improvement and Follow-Up: Action plan, regular drills and update procedure and protocol.

## 3 Results and Discussion

In Nuclear Malaysia planning, preparation and response to radiological emergencies involved many parties. From the security department, radiological responder, chemical and biological responder, engineering section, administrative department, technical laboratories and etc. The new emergency response structure organization was review and this organization is more structured for the response to each type of accident and the resources that will be needed.

For 2024, the scenario for the emergency drill involve chemical, fire emergency and radiological emergency and injuries.

From the drill exercise and incident reported, we identified some the following issues in management of chemical, fire and radiological emergencies is:

a) Chemical contamination decontamination procedures need to be reviewed.

b) Emergency number improvements, including the addition of emergency contact numbers for the Dengkil location.

c) Improvements to firefighting squad safety attire, requiring new and appropriate clothing.

d) Requiring appropriate personal protective equipment for each responder.

e) No headcount of occupants was conducted during evacuation.

f) Each officer must identify hazards at the location to ensure emergency response is conducted safely.

g) Need to further refine training for emergency response team members.

h) Logistics need to be streamlined, with vehicle shortages during the emergency.

i) Communication issues, with emergency information between ECC and ED, OSC and squads being unclear.

j) Established emergency response organization with a command structure that is clearly defined and integrated.

k) Clear information and communication within responds squad and emergency director.

l) Use of the compatible methodologies to response for the radiological emergencies

m) Appropriated training of the related personnel involved.

n) Safety equipment and facilities is always at risk for malfunction during the emergency.



Figure 1: Radiation screening



Figure 2: Radioactive decontamination

## 4 Conclusions

The chemical, fire, radiological and nuclear emergency exercise successfully demonstrated the preparedness and coordination capabilities of all involved responders in managing the emergencies. The exercise allowed participants to assess and refine their response procedures, enhance communication between emergency squad, and identify areas for improvement in both individual and collective readiness.

The lessons learned from this exercise will be instrumental in refining the emergency response protocols and ensuring that all involved parties are better equipped to handle a chemical, fire, radiological or nuclear incident in the future. Continued collaboration and periodic training will ensure that all squad maintain a high level of preparedness, and minimizing harm in the event of a real emergency.

## References

Jabatan Tenaga Atom. 2023. Panduan Penyediaan dan Pengujian Pelan Kecemasan Radiologi Jabatan Tenaga Atom. LEM/TEK/66 Sem.3.

IAEA. 2002. Safety standards series: Preparedness and response for a nuclear or radiological emergency. IAEA Safety Standards series, GS-R-2, IAEA, Vienna.

IAEA. 2015. Safety standards :Preparedness and response for a nuclear or radiological emergency. IAEA Safety Standards General Safety Requirement GSR Part 7, IAEA, Vienna.

IAEA. 2018. Safety standards: Occupational radiation protection. IAEA Safety Standards Series No. GSG-7, IAEA, Vienna.

IAEA. August 2000. Safety standards: IAEA-TECDOC-1162, Generic procedures for assessment and response during a radiological emergency. Vienna, Austria.

IAEA. July 2003. Safety standards: IAEA-TECDOC-1134 Categorization of radiation sources. Vienna, Austria.

IAEA. June 1999. Safety standards: IAEA-TECDOC-1092 Generic procedures for monitoring in a nuclear or radiological emergency. Vienna, Austria.

SHE/WP/06 Emergency Preparedness and Response.

Individual Research Contribution Review, 2024: 159–160
*ISSN: 3083-922X*

# Flexi Rad Joint Compound as Architectural Radiation Shielding Materials

**Azuhar bin Ripin**
Radiation Health and Safety Division, Malaysian Nuclear Agency
43000 Kajang, Selangor
azuhar@nm.gov.my

## 1 Introduction

The healthcare and industrial sectors rely heavily on radiation shielding to ensure safety, with traditional materials like lead and concrete dominating the field. However, these conventional solutions face significant challenges, including radiation leakage at critical points such as door frames, glass frames, and wall joints, as well as environmental concerns associated with lead-based products. This research introduces an innovative solution: The Flexi Rad Joint Compound, a flexible, environmentally friendly, and efficient radiation shielding material.

The proposed material addresses the shortcomings of traditional shielding by leveraging locally sourced minerals such as kaolin, barite, and bauxite. Enhanced with polymeric binders, the compound exhibits superior flexibility and adhesion, making it ideal for applications requiring precise sealing or broad coverage on irregular surfaces. Its lightweight nature significantly reduces the structural load on facilities, while its durability minimizes the need for frequent maintenance, lowering long-term costs.

## 2 Objectives

Key objectives of this research include:

1. Optimizing the formulation of the Flexi Rad Joint Compound to maximize its radiation shielding efficiency, mechanical integrity, and adaptability.
2. Validating its performance against national (MOH/JTA) and international (ISO/IEC) standards through rigorous testing of its Radiation Protection Efficiency (RPE), Half-Value Layer (HVL), and Lead Equivalence Testing (LET).
3. Demonstrating its practical application in sealing radiation leaks in real-world settings, such as X-ray room joints and door frames.

The project builds upon prior successes with Mullite Barite Ceramic (MBC), a rigid radiation shielding material, adapting its formulation to create a more versatile compound. The integration of polymeric binders allows the Flexi Rad Joint Compound to maintain its shielding properties while offering the flexibility needed for modern healthcare and industrial facilities.

**Methodology** involves mineral refinement, binder integration, formulation optimization, and iterative testing. The compound will be produced in two functional forms:

sealant for precise application wall putty for broader use.

Real-world validation will ensure its practical efficacy and ease of deployment.

## 3 Outputs

Expected outputs include:

1. A validated flexible shielding material tailored for radiation facilities.
2. Prototypes in sealant and putty forms.
3. Comprehensive application guidelines.
4. Dissemination of findings through scientific publications and potential intellectual property filings.

By transforming rigid ceramic shielding into a flexible, adaptable solution, the Flexi Rad Joint Compound not only enhances safety but also simplifies construction and repair processes, marking a significant leap in radiation shielding innovation. This development promises to redefine the design and functionality of radiation facilities, ensuring safety, sustainability, and operational efficiency.

## References

ISO/IEC 2919:2012. Radiation protection—sealed radioactive sources—general requirements and classification. (International standard for evaluating radiation protection materials).

Ahmad S. et al. 2018. Lightweight and durable radiation shielding materials. *International Journal of Advanced Materials Research*, 234:78–85. (Covers advancements in lightweight and sustainable shielding materials).

Abdullah M. Z. et al. 2019. Utilization of local minerals in eco-friendly construction materials. *Sustainable Materials and Technologies*, 23:e00127. (Investigates the use of kaolin and bauxite in environmentally friendly materials).

Singh V. P. et al. 2020. Radiation shielding materials: A review. *Radiation Physics and Chemistry*, 175:108511. (A comprehensive review of current radiation shielding materials, including polymers and ceramics).

Alaboodi A. S. et al. 2021a. Development of polymer composite materials for radiation shielding applications. *Materials Science and Engineering: C*, 123:112053(Focuses on the integration of polymers with other materials to improve flexibility and radiation shielding properties).

Shahbazi-Gahrouei D. et al. 2021b. Development of flexible and high-density radiation shielding materials. *Radiation Protection Dosimetry*, 195(2):189–197. (Focuses on flexible shielding applications in medical and industrial settings).

Reis J. M. L. et al. 2022. Clay-based composites for radiation shielding: A sustainable approach. *Journal of Building Engineering*, 49:104028. (Explores the use of local clays in developing sustainable shielding solutions).

Ripin A. et al. 2023. Evaluation of lead equivalent thickness of x-ray rooms in health clinics in Kelantan. *Presented at the Nuclear Technical Convention 2023*, (Discusses issues of radiation leakage and lead equivalence in X-ray rooms, forming the baseline problem for this research).

Azis F. and Salmi M. 2020. The role of barite in enhancing radiation shielding properties in construction materials. *Advances in Material Science*, 15(4):12–21. (Discusses the effectiveness of barite in shielding applications).

Kaplan M. F. 2013. Concrete radiation shielding: Nuclear power applications. John Wiley & Sons. (Examines conventional shielding methods and their limitations).

Individual Research Contribution Review, 2024: 161–162
*ISSN: 3083-922X*

# Radon Concentration in Hot Springs of Peninsular Malaysia

**Faizal Azrin Bin Abdul Razalim**
Radiation Health and Safety Division, Malaysian Nuclear Agency
43000 Kajang, Selangor
faizal_azrin@nm.gov.my

## Abstract

Radon concentration in hot springs across several areas of Peninsular Malaysia was measured using a RTM1688-2 radon/thoron monitor at sampling sites. Results showed an average radon concentration of 5.3 Bq/L (range 0.1 - 15.8 Bq/L). These values are significantly lower than the World Health Organization's (WHO) reference level for drinking water of 100 Bq/L. If users consume water containing radon at 500 L/year, the average effective dose received is still low at 9.3 $\mu$Sv/year (range 0.2 - 27.7 $\mu$Sv/year).

## 1 Introduction

Radon is a naturally occurring radioactive gas produced from uranium decay in rocks and soil. In the context of hot springs, radon's presence becomes an interesting scientific subject with health implications for the public. Radon is colorless, odorless, and tasteless. It forms naturally when uranium in rocks and soil undergoes radioactive decay. This gas can seep into groundwater and subsequently into hot spring pools.

Hot springs are an interesting geological phenomenon in Peninsular Malaysia, with more than 60 locations identified. Scientific research conducted by researchers from the Malaysian Nuclear Agency aims to study natural hot spring radon gas concentrations, which may have health implications for local residents and visitors.

## 2 Methods

The study methodology involved sampling hot water from 14 locations spread across Peninsular Malaysia, focusing on igneous rock areas with high natural radioactivity potential.

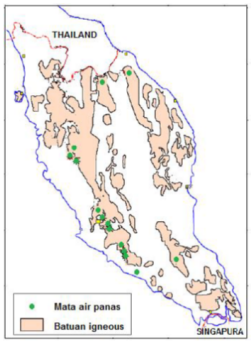



Figure 1: Radon study area in hot springs



Figure 2: RTM1688-2 radon/thoron monitor

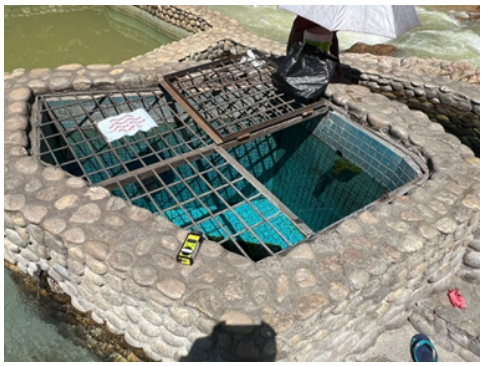


Figure 3: Hot Spring Lubok Timah, Perak

## 3 Data/Results

Results revealed that radon concentration in Malaysian hot springs is low, with an average of 5.3 Bq/L and range between 0.1 to 15.8 Bq/L. These levels are well below WHO reference limit of 100 Bq/L for drinking water. More than half of the hot spring locations have radon concentrations less than 5 Bq/L, indicating high safety levels.

Results revealed that radon concentration in Malaysian hot springs is low, with an average of 5.3 Bq/L and range between 0.1 to 15.8 Bq/L. These levels are well below WHO reference limit of 100 Bq/L for drinking water. More than half of the hot spring locations have radon concentrations less than 5 Bq/L, indicating high safety levels.

Table 1: Radon concentration of various hot springs.

| No | Location | Temperature (°C) | Average Concentration Rn (Bq/L) |
|---|---|---|---|
| 1 | Lubuk Timah (Simpang Pulai), Perak | 44 | 15.1 |
| 2 | Kuala Woh (Tapah), Perak | 60 | 3.7 |
| 3 | Klah River (Sungkai), Perak | 90 | 3.8 |
| 4 | Jeli, Kelantan | 44 | 5.6 |
| 5 | Tok Bok (Machang) Kelantan | 42 | 15.8 |
| 6 | Gersik (Muar), Johor | 47 | 1.2 |
| 7 | Labis, Johor | 55 | 0.1 |
| 8 | Cherana Putih (Alor Gajah), Melaka | 50 | 2.3 |
| 9 | Gadek (Alor Gajah), Melaka | 43 | 1.0 |
| 10 | Bt.16 (Hulu Langat), Selangor | 40 | 1.5 |
| 11 | Sg. Serai (Hulu Langat), Selangor | 48 | 5.4 |
| 12 | Selayang, Selangor | 48 | 10.4 |
| 13 | Setapak, Kuala Lumpur | 44 | 2.8 |
| 14 | Rembau, Negri Sembilan | 42 | 5.7 |
| | | **Average** | **5.3 ± 5.0** |

## 4 Discussion/Conclusions

The effective dose received by hot spring users was also found to be very low, averaging 9.3 $\mu$Sv/year with a range between 0.2 to 27.7 $\mu$Sv/year. This means health risks from radiation exposure due to radon in hot springs are minimal and pose no significant danger to users.

Various factors influence radon concentration, including local geology, rock structure, natural radioactivity levels, water temperature, and radon gas release rate. Researchers found that radon concentration decreases with increasing temperature, and natural hot springs have slightly higher concentrations compared to artificial pools.

The location with the highest radon concentration was identified at Tok Bok hot springs, Machang, Kelantan, while the lowest concentration was in Labis, Johor. This observation shows natural variation in geological characteristics and radioactivity across different areas of Peninsular Malaysia.

The study concludes that Malaysian hot springs are safe for recreational use and bathing. Radiation doses received are far below levels that could pose health risks. This study provides important scientific perspective on Malaysian hot springs conditions, giving public confidence about the safety of these natural water sources. It also opens opportunities for tourism potential development and hot springs-related infrastructure development in our country, similar to Japan's use of hot springs as their tourism industry.

## References

H. Baioumy, Nawawi. M., K. l. Wagner, and M. H Arifin. 2014. Geochemistry and geothermometry of non-volcanic hot springs in West Malaysia. *Journal of Volcanologyand Geothermal Research*, doi:10.1016/j.jvolgeores.2014.11.014.

W.S. Chow, S. Irawan, and M.T Fathaddin. 2010. Hot springs in Peninsula Malaysia. *Proceedings of the World Geothermal Congress, Bali, Indonesia*, 25-29 April 2010.

Individual Research Contribution Review, 2024: 163–164
*ISSN: 3083-922X*

# Dose Mapping of OB-Servo Ignis Gamma Irradiator

**Hasan bin Sham**
Radiation Health and Safety Division, Malaysian Nuclear Agency
43000 Kajang, Selangor
hasansham@nm.gov.my

## Abstract

Dose mapping of OB-Servo Ignis Gamma Irradiator (Cobalt-60) with activity 444 TB (12,000 Ci) in Bilik Gamma Cell (37B3004), Block 37, Malaysian Nuclear Agency was carried after the installation of the gamma source on 21 October 2024. Ceric-cerous dosimeters was used to estimate the dose distribution at certain position in 3 different level inside the sample holder. Dose Uniformity Ratio (DUR) was determined using ceric-cerous dosimeters from maximum and minimum dose location.

**Keywords:** Dose mapping; Gamma Irradiator; Ceric-Cerous dosimeter, DUR

## 1 Introduction

The Gammacell OB-Servo Ignis supplied by Izotop, Institute of Isotopes Co. Ltd., Hungary (Figure 1), was commissioning in October 21, 2024 with Co-60 source. The activity was 12,000 Ci (444 Tbq) and dose rate of 82.83 Gy/min.



Figure 1: OB-Servo Ignis Gamma Irradiator

## 2 Method

The ceric-cerous dosimeter contains 0.02 mol/litre ammonium cerium (IV) sulphate dihydrate and dilute with 0.4 mol/litre Sulphuric acid. It has been prepared using distilled water from Thermo's water distillation system, Barnstead Smart2Pure. The dosimeters are calibrated against Fricke dosimeters and traceable to IAEA. The useful range of the ceric-cerous dosimeter is 5 – 50 kGy.

Ceric-cerous dosimeter in 2 ml ampoule is placed in the position as in Figure 2 in the polystyrene holder. This polystyrene holder is then placed into the sample holder with 3 different heights (Figure 3). The height of the sample holder is 280 mm and the diameter is 150 mm. A total of 9 dosimeters are placed on each level and a total of 27 dosimeters are used. The irradiation time was 3 hours and the estimated dose was 15 kGy.

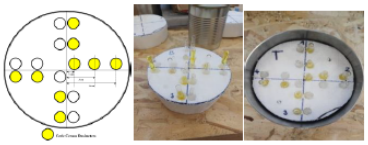


Figure 2: Placement of ceric-cerous dosimeters fixed in polystyrene holder

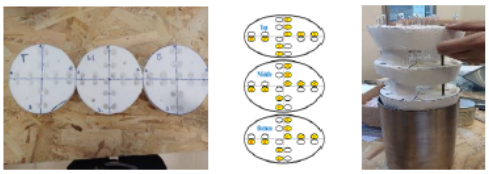


Figure 3: The position of polystyrene holder at 3 different level

## 3 Result

Table 1: Dose values in the sample holder at different positions and levels

| Top | | Position 1 | | Position 2 | | Position 3 | | Position 4 | |
|---|---|---|---|---|---|---|---|---|---|
| | | Dosimeter No. | Dose (kGy) | Dosimeter No. | Dose (kGy) | Dosimeter No. | Dose (kGy) | Dosimeter No. | Dose (kGy) |
| Radius (cm) | 1 | T1 | 15.8 | - | - | - | - | - | - |
| | 2 | T2 | 15.5 | T4 | 15.9 | T6 | 16.3 | T8 | 16.4 |
| | 3 | T3 | 15.0 | T5 | - | T7 | 16.6 | T9 | 16.6 |
| Middle | | Position 1 | | Position 2 | | Position 3 | | Position 4 | |
| | | Dosimeter No. | Dose (kGy) | Dosimeter No. | Dose (kGy) | Dosimeter No. | Dose (kGy) | Dosimeter No. | Dose (kGy) |
| Radius (cm) | 1 | M1 | 18.5 | - | - | - | - | - | - |
| | 2 | M2 | 18.9 | M4 | 18.7 | M6 | 18.8 | M8 | 18.8 |
| | 3 | M3 | 19.4 | M5 | 19.4 | M7 | 19.6 | M9 | 19.6 |
| Bottom | | Position 1 | | Position 2 | | Position 3 | | Position 4 | |
| | | Dosimeter No. | Dose (kGy) | Dosimeter No. | Dose (kGy) | Dosimeter No. | Dose (kGy) | Dosimeter No. | Dose (kGy) |
| Radius (cm) | 1 | B1 | 14.5 | - | - | - | - | - | - |
| | 2 | B2 | 15.2 | B4 | 14.6 | B6 | 14.2 | B8 | 14.1 |
| | 3 | B3 | 15.9 | B5 | 14.7 | B7 | 14.5 | B9 | 14.4 |

## 4 Discussion

The maximum dose in the Gammacell OB-Servo Ignis irradiator using ceric-cerous dosimeter was 19.6 kGy at the middle location M7 and M9 respectively. While the minimum dose was 14.1 kGy at the bottom location B8.

Dose Uniformity Ratio (DUR) can be calculated using formula below:

$$\text{DUR} = \frac{D_{max}}{D_{min}} \tag{1}$$

Table 2: Result for Dose Uniformity Ratio (DUR)

| Dose (kGy) | | **Dose Uniformity Ratio (DUR)** |
|---|---|---|
| **Dose Maximum $D_{max}$** | **Dose Minimum $D_{min}$** | |
| 19.6 | 14.1 | 1.39 |

## 5 Conclusion

From the results, the Dose Uniformity Radio (DUR) inside gamma sample holder of OB-Servo Ignis gamma irradiator was 1.39.

## References

H. Jameel. 2000. The dose distribution inside the irradiation chamber of the gamma cell 220 at KACST using MCNP4B. *Journal of Nuclear Science and Technology*, Supplement 1:402–405.

H.S. Seungwoo, Kihong S., Chang Y.L., Kum B.K., Haijo J., and Young. 2010. Dose distribution of gamma. *2010 Spring Conference: Proceedings of Korean Society for Radiation Protection S*, pages 62–63.

Individual Research Contribution Review, 2024: 165–166
*ISSN: 3083-922X*

# Monitoring Radiation in Working Area: Annual Dose Trend in Selected Facility Within Malaysia Nuclear Agency from 2020 to 2023

**Hasbi Husein Bin Sulkifli**
Radiation Health and Safety Division, Malaysian Nuclear Agency
43000 Kajang, Selangor
hasbi@nm.gov.my

## 1 Introduction

Workplace monitoring is an important tool to ensure workers' safety in any nuclear facility. Workplace monitoring is one of the fundamental in radiation protection program and can be utilise to improve individual monitoring (Schuhmacher, 2011). Malaysia Nuclear Agency, the primary centre of Nuclear Science and Technology in Malaysia operate few facilities for research and commercial use. Following this, a strict radiation protection program has been imposed in these facilities which involve the classification of working area into 3 categories, clean area (<0.5 $\mu$Sv/hr), supervise area (0.5 – 3.0 $\mu$Sv/hr) and control area (>3.0 $\mu$Sv/hr) (JTA, LEM/TEK/65 Sem.2 Pin. 1). In this study, annual dose variation for SSDL (Block 32) and WASTEC (Block 30/31) has been documented and analyse to understand the trend throughout the 4 years period.

## 2 Methods

Data use in this study are collected from the monthly dose report produce by Secondary Standard Dosimetry Lab (SSDL), Radiation Metrology Group of the Radiation Safety and Health Division. However, only the annual cumulated Hp(10) dose from all monitoring station within the facility are used since this study only concern the year-to-year variation.

Table 1: Dose reading variation from SSDL (Block 32)

| **Monitoring Station** | **2020** | **2021** | **2022** | **2023** |
|---|---|---|---|---|
| STN 1 | 0.89 | 0.62 | 0.75 | 1.82 |
| STN 2 | 0.81 | 0.67 | 0.72 | 1.72 |
| STN 3 | 0.64 | 0.53 | 0.50 | 1.20 |
| STN 4 | 0.55 | 0.36 | 0.48 | 1.01 |
| STN 5 | 0.98 | 0.69 | 0.68 | 1.60 |

## 3 Result and Discussion

Table 1 and Figure 1 show dose variation between 2020 and 2023 for SSDL (Block 32). In general, SSDL record a consistently low dose in radiation working area, below 2 mSv/year throughout the period. However, two distinct trends can be observed where in 2021 the reading is decreasing for at least 0.3 mSv/year compared to previous year before increasing dramatically in 2023 with the highest reading is 1.82 mSv/year (station 1). Covid-19 and source replacement in 2023 could be the reason behind this variation, the source in Co-60 bunker had been replaced in January 2023, prior to that the activity of the old source already weak and combine with limited operation during Covid-19 explain the decreasing trend. In 2022, Covid-19 restriction had been eases and operation slowly back to normal thus the increase in 2022. After source replacement in January 2023, with a higher activity source the radiation exposure also increases.

Table 2: Dose reading variation from WASTEC (Block 30/31)

| Monitoring Station | 2020 | 2021 | 2022 | 2023 |
|---|---|---|---|---|
| STN1 | 1.57 | 1.24 | 0.93 | 2.04 |
| STN2 | 1.89 | 1.33 | 1.01 | 2.13 |
| STN3 | 1.83 | 1.24 | 0.79 | 2.25 |
| STN4 | 1.88 | 1.70 | 1.52 | 3.37 |
| STN5 | 1.73 | 1.98 | 1.00 | 2.51 |
| STN6 | 1.71 | 2.79 | 1.59 | 4.25 |
| STN7 | 2.73 | 7.06 | 3.15 | 8.21 |
| STN8 | 1.56 | 1.34 | 0.85 | 2.04 |
| STN9 | 0.29 | 1.40 | 1.33 | 1.68 |
| STN10 | 0.54 | 1.14 | 1.28 | 2.98 |
| STN11 | 0.28 | 1.02 | 0.76 | 2.40 |

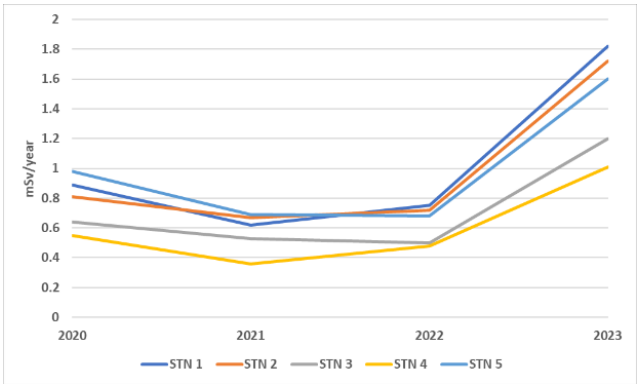



Figure 1: Graph showing the variation of dose reading in SSDL (Block 32)

Data for WASTEC (Block 30/31) is represented by Table 2 and Figure 2. This facility handled and stored radioactive waste which require bigger space, hence there are more monitoring station installed. This facility also shows a consistently low dose level for the four years period (below 10 mSv/year) but overall display a slightly increasing trend especially in 2023 where the reading across all monitoring stations are the

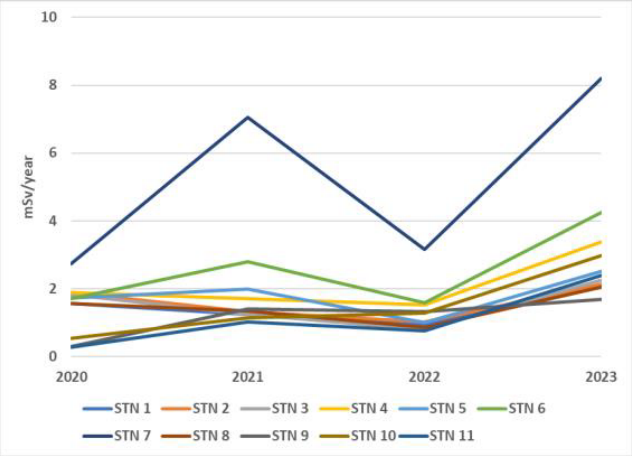



Figure 2: Graph showing dose variation in WASTEC (Block 30/31)

highest. Considering the activity conducted in this facility, the elevated reading is expected. Even so, there is no immediate danger to workers because the monitored area in the facility are only occasionally occupied for usually less than 8 hours a day.

## 4 Conclusion

From the data presented, it shows dose level for both SSDL (Block 32) and WASTEC (Block 30/31) are consistently low from 2020-2023. The lowest recorded dose level in SSDL is 0.36 mSv/year (Station 4 in 2021) while the highest is 1.82 mSv/year (Station 1 in 2023) and the lowest for WASTEC (Block 30/31) is 0.28 mSv/year (Station 11 in 2020) while the highest is 8.21 mSv/year (Station 7 in 2023). This is evident that radiation protection program in Malaysia Nuclear Agency is effective in protecting the workers. It is also important to note that all radiation work area in Malaysia Nuclear Agency is limited to authorised personnel only and heightened security measures are in place to prevent any malicious act.

## References

Jabatan Tenaga Atom. 2022. Panduan pengelasan kawasan kerja menurut peraturan-peraturan pelesenan tenaga atom (perlindungan sinaran keselamatan asas) 2010. LEM-TEK-65 Sem.2 Pin.1.pdf.

H. Schuhmacher. 2011. Workplace monitoring of mixed neutron-photon radiation fields and its contribution to external dosimetry. *Radiation Protection Dosimetry*, 144(1-4):599–604. https://doi.org/10.1093/rpd/ncq588.

Individual Research Contribution Review, 2024: 167–168
*ISSN: 3083-922X*

# Self-Assessment of Nuclear Security Culture in Malaysian Nuclear Agency

**Hasfazilah binti Hassan**
Radiation Health and Safety Division, Malaysian Nuclear Agency
43000 Kajang, Selangor
asfa@nm.gov.my

## Abstract

The goal of nuclear security culture is to provide assurance that the entire nuclear security program will accomplish its functions of preventing, detecting, delaying, and responding to theft, sabotage, unauthorized access, illegal transfer or other malicious acts involving radioactive material in use, storage or transport. Each organization already has an existing nuclear security culture. However, this nuclear security culture can be enhanced. An enhanced nuclear security culture will increase the stakeholder's ability to maintain effective nuclear security and support the continuous improvement of nuclear security. Humans can be the strongest but also the weakest point within an attackscenario. In order to strengthen the awareness of the staff, Nuclear Security Culture Self-Assessment (NSC SA) is an efficient and effective approach. The assessment will include all main facilities including reactor operations, waste management center, and support services like IT and human resources. This survey aimed to assess the nuclear security culture within Malaysian Nuclear Agency, providing valuable insights into our current practices and areas needing attention.

**Keywords:** Nuclear Security, Nuclear Security Culture, Self-assessment

## 1 Introduction

Nuclear security culture is crucial for safeguarding nuclear materials and facilities. Understanding and improving this culture through assessments helps organizations evaluate the effectiveness of their security practices and identify areas needing enhancement. This paper presents the findings from a Nuclear Security Culture Self- Assessment (NSCSA) conducted at Agensi Nuklear Malaysia. The survey, administered via Google Form, consisted of 30 questions designed to evaluate nuclear security culture across three key areas: management, supervisors, and personnel. By conducting this selfassessment, facilities can enhance awareness of nuclear security among both employees and management, identify necessary improvements, and implement more effective security practices. Additionally, these assessments can improve internal communication about security issues, reducing the risk of misunderstandings and promoting better cooperation across all levels of staff.

## 2 Methods

In designing the NSCSA survey, demographic considerations were included, with questions covering age, department, position, gender, education, and work experience. These demographic questions aimed to identify specific areas requiring detailed improvements. A pilot survey was then conducted to assess the feasibility of the survey. This pilot involved a select group of employees representing each department to ensure that the language was clear, the chosen indicators were appropriate, and the analysis process and timeline were suitable. After obtaining approval from senior management, the full survey was implemented using Google Forms and distributed to all staff via the agency's official email. The survey was open for a duration of one week to allow sufficient time for responses.

**Average Score Calculation**: The average score for each question was determined by dividing the weighted sum by the total number of valid responses (160 in this case). The formula used was:

$$\text{Avg}_j = \frac{\sum_{i=1}^{160} x_{ji}}{160} \tag{1}$$

Where:

- $x_{ij}$ is the response from participant i to question j.
- $\sum_{i=1}^{160} x_{ji}$ is the sum of all responses for question j.
- 160 is the total number of valid responses.

## 3 Results and Discussion

### 3.1 Demographic Data

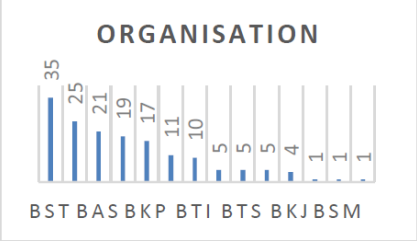



Figure 1: Distribution of Employees by Organization

### 3.2 Survey Questions Indicators Data

The graphs below represent the aggregated average scores from the survey responses, highlighting the relative strengths and areas for improvement across the different aspects of nuclear security culture.

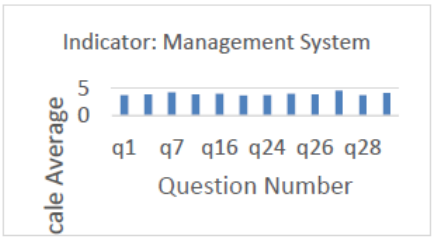



Figure 2: Average Scores for Management System

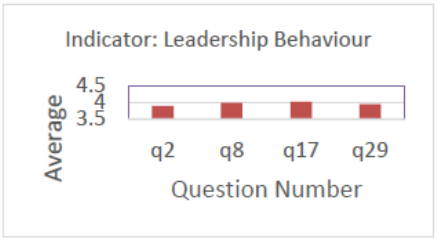



Figure 3: Average Scores for Leadership Behaviour

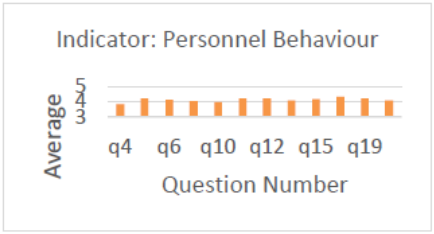



Figure 4: Average Scores for Personnel Behaviour

#### 3.2.1 Management System Indicators

Questions: Q1, Q3, Q7, Q15, Q16, Q21, Q24, Q25, Q26, Q27, Q28, Q30

Insights:

- **Strong Agreement**: Questions like Q7 (”Nuclear security is one of the priorities in my agency”) and Q27 (”Measures are taken when security equipment is taken out of service for maintenance or when breakdowns occur”) received high scores, with averages of 4.33 and 4.57 respectively. This indicates that employees generally believe in the prioritization of nuclear security within the management system and the effectiveness of measures taken during critical times.

**Recommendations**:

- Enhance Coordination Mechanisms
- Proactive Performance Management

#### 3.2.2 Personnel Behavior Indicators

Questions: Q2, Q8, Q17, Q29

Insights:

- **Consistent Agreement**: The questions in this category showed fairly consistent scores, with averages ranging from 3.91 to 4.04. This indicates that personnel generally have a positive view of their behavior in relation to nuclear security.

**Recommendations**:

- Continuous Training Programs
- Behavioral Reinforcement

#### 3.2.3 Supervisor (Management Behavior) Indicators

Questions: Q4, Q5, Q6, Q9, Q10, Q11, Q12, Q14, Q15, Q18, Q19, Q20

Insights:

- **High Levels of Compliance**: Questions such as Q11 (”I strictly follow nuclear security procedures rather than taking shortcuts”) and Q18 (”I understand that adherence to the security policy is expected of all personnel”) received high average scores of 4.21 and 4.32. This suggests that supervisors are effectively enforcing nuclear security procedures and that personnel understand the expectations set by management.
- **Areas of Potential Improvement**: Q15 (”I am confident in my ability to detect and report security incidents”) scored slightly lower (4.16), indicating that while confidence is generally high, there may be room for improvement in ensuring that all personnel feel equally capable of detecting and reporting incidents.

**Recommendations**:

- Leadership Training
- Enhanced Incident Reporting Systems

## 4 Conclusion

The survey findings show a widespread dedication to nuclear security in the organization, as most answers demonstrate a strong consensus on important security measures. Workers acknowledge the significance of nuclear security and have trust in the organization’s capability to uphold its security infrastructure, specifically when dealing with and looking after security tools.

In summary, the survey depicts an organization with a strong security culture, supported by strict adherence to procedures and a collective dedication to upholding high standards in nuclear security.

## References

IAEA. 2008. Nuclear security culture: Implementing guide - Nuclear security. Series No. 7. Vienna.

IAEA. 2017. Self-assessment of nuclear security culture in facilities and activities. Vienna.

Individual Research Contribution Review, 2024: 169–170
*ISSN: 3083-922X*

# Remediation of Contaminated Norm Site

**Khairuddin Mohamad Kontol**
Radiation Health and Safety Division, Malaysian Nuclear Agency
43000 Kajang, Selangor
khairuddin-m@nm.gov.my

## Abstract

Recycling of naturally occurring radioactive material (NORM) residue, or it use in other applications rather than disposing of it as waste, should be considered. Besides the recycle option, methods and ways are being sought out to overcome the problem related to the contaminated land due to past activities and the future disposal of the waste. Tin slag produced during tin production contains NORM. The overall remediation process of NORM contaminated land due to past activities involves four main activities: i) initial site characterization and selection of remediation criteria ii) identification of remediation options and their optimization followed by subsequent development and approval of the remediation plan iii) implementation of the remediation plan and iv) post–remediation management. In this case of land contaminated by NORM past activities (e.g. tin slag residue), will be assessed using RESRAD computer code and remediation option of source removal has been considered and the site/land will be release for unrestricted use.

**Keywords:** Remediation, RESRAD

## 1 Introduction

Tin has, at one time been the number one export commodity for Malaysia. However, nowadays the overall trend of tin ore concentrate production has been declining. Price decreases, depletion of high grades reserves and rising production costs contribute to this declining trend. Naturally Occurring Radioactive Material (NORM) residue (e.g. tin slag) can also be extracted to obtain precious and important metals such as Niobium, tantalum, manganese, iron, aluminium, titanium, etc. Generally, recycling of NORM residue, or it use in other applications rather than disposing of it as waste, should be considered. Besides the recycle option, methods and ways are being sought out to overcome the problem related to the contaminated land due to past activities and the future disposal of the waste.

## 2 Contaminated Site

As contaminated sites can ultimately lead to undesired health effects for local people, appropriate actions must be taken. Remediation of contaminated land areas-or other contaminated media, such as surface or groundwater- is applied in two ways:

i) By applying actions to the contamination itself. This can lead to isolation, immobilization or removal of the actual source of radiation, for example by means of decontaminating area, surfaces and environmental media.

ii) Evaluating risk related to radiation exposure to people and thinking of ways of breaking the pathways between the radiation source and people. This approach may lead to evacuation, area isolation or changing land use and the local population's living habits.

## 3 Remediation Process

The overall remediation process shown in Figure 1 involves four main activities (IAEA, 2007):

i) Initial site characterization and selection of remediation criteria

ii) Identification of remediation options and their optimization followed by subsequent development and approval of the remediation plan

iii) Implementation of the remediation plan and

iv) Post–remediation management.

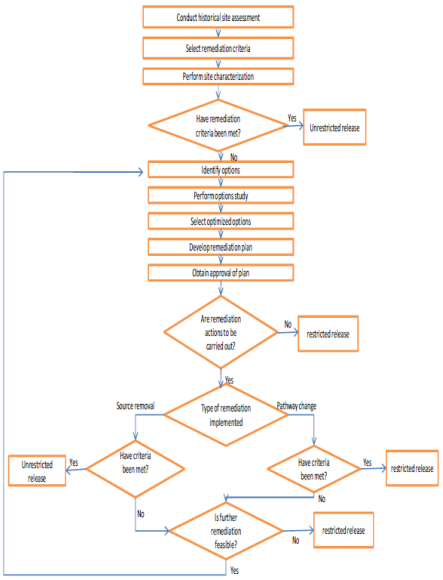



Figure 1: The Remediation Process

## 4 RESRAD ONSITE

RESRAD computer code (RESRAD 7.2) developed by Argonne National Laboratory, USA was used. It is the only code designated by Department of Energy (DOE), USA for the evaluation of radioactively contaminated site. The code was designed to estimate radiation doses and risks from residual radioactive materials (in this case, residual radioactive materials are from NORM contaminated land).

## 5 Input Parameter

### 5.1 Source Term

In this case study, contaminated soil (Tin slag residue) is the source of exposure. The amount of radioactive material in tin slag residue is called the source term. The source term is the most important parameter to be used in the remediation process study. In determining the source term, there were 10 tin slag residue samples taken from the contaminated land and the background Malaysian soil radioactivities are taken from UNSCEAR 2000 report. The concentrations of contaminated soil (tin slag) analysed was 950 Bq/kg of $^{238}$U, 420 Bq/kg of $^{232}$Th, 4575 Bq/kg of $^{226}$Ra and 1112 Bq/kg of $^{228}$Ra. NAA technique was used for analyzing $^{238}$U and $^{232}$Th while high energy gamma spectrometry for analysing $^{226}$Ra and $^{228}$Ra.

### 5.2 Regulatory Criteria

The annual dose limit to the member of public is less than 1 mSv/y and collective dose of 1 man.Sv. Dose constraint of 0.3 mSv/y was also used in this assessment. If the calculated public dose is less than 0.3 mSv/y, the site is exempted from regulatory control. On the other hand, if the public dose is greater than 0.3 mSv/y (but still < 1 mSv/y), then the site is controlled under the regulation and environmental monitoring may be required to be conducted for a specific period decided by regulatory authority.

### 5.3 Pathway

Critical pathways for the estimation of dose to the critical groups by different migration patterns and modes of transport of radionuclides in passing through the environment have been identified. The critical pathways considered in the assessment would be external radiation, inhalation of dust (including radon and thoron daughters) and intake through food chain (leafy vegetables, drinking water, aquatic and meat). The critical group who will be affected by the past activities have been identified. They include the people who will live or work at the contaminated site and around the site before and after the remediation process have been successfully completed.

### 5.4 Scenario

In order to assess the dose received by the critical groups, worst case scenario was selected. The scenario involves the contaminated land used for residential purposes. It was assumed people (critical group) built houses and lives on the contaminated site. They were exposed to external radiation, inhaling airborne dust and radon and thoron progenies emitted by the contaminated soil (tin slag residue). They were also relied on ground water onsite as a source of drinking water, cooking, irrigation and for livestock which will give internal exposure.

## 6 Results and Conclusion

The maximum dose received by the critical group was 13.6 mSv/y (refer Figure 2). This value is well above the limit of the regulatory body of 1 mSv/y and dose constraint of 0.3mSv/y. This implies that the contaminated area cannot be used for restricted or unrestricted release purpose and source removal or evaluating further the risk exposure/scenario should be considered as an option.

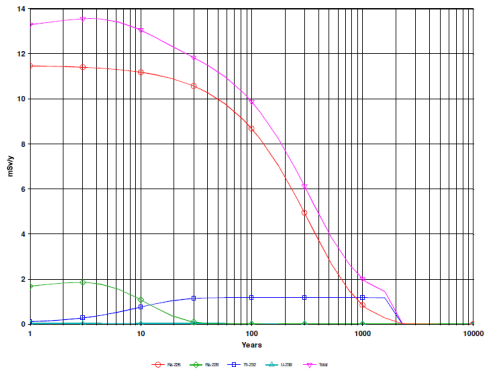



Figure 2: Dose Received by Critical Group

The radionuclide which gives significant contribution (83.94%) to the total dose received is $^{226}$Ra due to its higher radioactivity concentration compared with other radionuclides (e.g. 228Ra-13.52%, $^{238}$U-0.19% and $^{232}$Th 2.35%).

## References

Edited by Leo van Velzen. Environmental remediation and restoration of contaminated nuclear and NORM sites. *Woodhead Publishing Series in Energy*, Number 71.

IAEA. 2007. Safety standards series no. WS-G-3.1, Remediation process for areas affected by past activities and accidents.

Argonne National Laboratory. March 2018. User's guide for RESRAD ON-SITE code. ANL/EVS/TM 18/1.

Individual Research Contribution Review, 2024: 171–172
*ISSN: 3083-922X*

# Strengthening Emergency Preparedness And Response In Malaysian Nuclear Agency

**Mohd Fazlie bin Abdul Rashid**
Radiation Health and Safety Division, Malaysian Nuclear Agency
43000 Kajang, Selangor
fazlie@nm.gov.my

## Abstract

Malaysian Nuclear Agency (Nuklear Malaysia) plays a critical role in managing radiation sources across various sectors, including research, industrial, and medical applications. Given the potential threats posed by radiological hazards, it is vital for Nuklear Malaysia to have a robust emergency preparedness and response program. This study evaluates the effectiveness of Nuklear Malaysia's current protocols by conducting a survey among its staff. The findings contribute to understanding the effectiveness of emergency management practices in the radiation field and provide recommendations for future improvement.

**Keywords:** Emergency preparedness, survey, SPSS

## 1 Introduction

Radiation sources are essential components in various fields, including healthcare, industry, and research. However, with such reliance comes the significant responsibility to manage these sources safely to prevent accidents. Given the potentially disastrous nature of radiological events - stemming from accidental exposure or nuclear incidents - effective emergency preparedness and response mechanisms are critical. The aim of this study is to assess the effectiveness of these procedures within Nuklear Malaysia, focusing on identifying strengths and areas requiring improvement.

The crucial nature of this work highlights the agency's need to ensure that all staff members are adequately prepared and informed about emergency protocols. By thoroughly evaluating current practices, Nuklear Malaysia can enhance its emergency management strategies and ensure the well-being of the public and the environment.

## 2 Methods

To evaluate the effectiveness of the emergency preparedness and response program, a quantitative approach was employed. Participants were selected from Nuklear Malaysia's staff to ensure a representative sample. An online survey was developed to specifically assess five critical categories:

i. Awareness of workers

ii. Training programmes

iii. Regulatory compliance

iv. Communication system

v. Leadership

Each category contained ten statements rated on a 7-point Likert scale, allowing staff to express their levels of agreement or disagreement with various assertions regarding their preparedness and training. The survey was administered using Google Forms and gathered 480 responses from the total workforce of 775 employees.

Data analysis involved testing the validity and reliability of responses using SPSS software version 26. This analysis allowed for the extraction of meaningful insights, ensuring that the findings would be actionable and credible.

## 3 Results

Based on the distribution of the age, years of working experience, type of work and work position, the highest number of respondents were in the groups of 40-49 years old, have working experience of 11-20 years, work in R&D program and work as support staff.

The scores by each categories of the survey were analysed, and the result are shown in Figure 1.

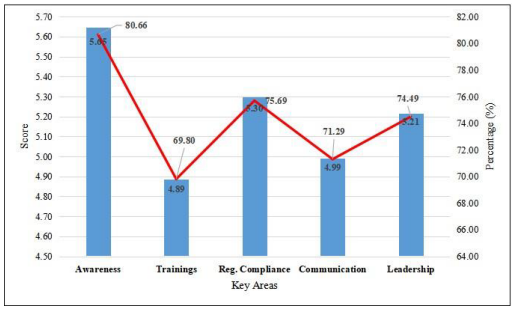



Figure 1: Scores by categories

Based on the analysis, the category of awareness of workers had the highest score (5.65), followed by regulatory compliance (5.30), leadership (5.21), communication system (4.99) and training programmes (4.89).

## 4 Discussion

The highest score of the survey came from the category of awareness of workers (5.65), whilst the lowest score was from training programmes (4.89). According to the DeVellis, R.F. (2016), common interpretation for 7-point Likert scale, 5-7

score is considered as agreement or positive sentiment, score 4 is considered as neutral or mixed response and 1-3 score is considered as disagreement or negative sentiment.

### 4.1 Awareness of workers

Employees reported a commendable level of awareness regarding safety protocols and regulatory standards. This demonstrates that Nuklear Malaysia has effectively communicated its core values and safety practices.

### 4.2 Training programmes

Although awareness levels are high, many staff members indicated shortcomings in practical training opportunities. They expressed a desire for more comprehensive training sessions that incorporate hands-on experiences and recent technological advancements.

### 4.3 Regulatory compliance

The survey results show strong adherence to regulations, reflecting Nuklear Malaysia's commitment to maintaining safety standards. Staff members generally feel confident that regulatory practices are well implemented.

### 4.4 Communication systems

A notable gap was identified in Nuklear Malaysia's communication protocols. Employees raised concerns about the clarity and consistency of messages during past emergency drills and real incidents, indicating a need for a more robust communication strategy.

### 4.5 Leadership

Survey respondents recognized the effectiveness of Nuklear Malaysia's leadership, particularly in fostering an environment conducive to safety and compliance. The positive leadership ratings suggest that the management is perceived as supportive and proactive in addressing safety concerns.

These results underline Nuklear Malaysia's strengths while highlighting critical areas for improvement. By actively working on enhancing training programs and communication systems, Nuklear Malaysia can significantly improve its overall readiness for potential radiological emergencies.

## 5 Conclusion

While Nuklear Malaysia exhibits commendable leadership and regulatory adherence in its emergency management protocols, there remain significant areas that require enhancement. Specifically, by developing more comprehensive training programs and fortifying communication strategies, Nuklear Malaysia can better prepare its staff for emergency scenarios. The findings of this study not only celebrate Nuklear Malaysia's accomplishments but also pave the way for constructive changes that can lead to higher standards of safety and preparedness. This pathway towards improvement will ultimately contribute to the protection of public health and well-being in Malaysia.

## References

H. B. Bahari, A. andHassan and R. Ahmad. 2011. Emergency preparedness amongst emergency response team in managing accidents at the workplace. https://www.researchgate.net/publication/260555527.

R. F. DeVellis. 2016. Scale development: Theory and applications. (4th ed.).

K. L. Hashim. 2022. Enhancing innovative work behaviour of malaysian public sector employees. *Malaysian Journal of Social Sciences and Humanities. (MJSSH)*, 6(2):253–265. doi: 10.47405/mjssh. v6i2.665.

H. Ibrahim and M. L. Mohd Zin. 2020. The influence of individual characteristics, training content, and manager support on on-the-job training effectiveness. *Journal of Asian Finance, Economics and Business*, 7(11):499–506.

A. Janati Esfahani, R. Mehrabi, N. Gheibi, R. Paydar, M. Aliakbari, F. S. Bagheri, S. Heshmati, E. Mohammadi, Z. S. Seyedi Gilavan, and M. Gangi. 2020. The effectiveness of a radiation safety training program in increasing the radiation safety knowledge of physicians: A pilot study. *The Journal of Qazvin University of Medical Sciences*, 24(1):32–43.

Individual Research Contribution Review, 2024: 173–174
*ISSN: 3083-922X*

# Development of Comprehensive Safety Analysis Report for the JS10000 Gamma Irradiator: Design, Risk Assessment and Regulatory Compliance Based on IAEA Guidelines (Technical Cooperation IAEA MAL 9019)

**Mohd Khairul Azfar Bin Ramli**
Radiation Health and Safety Division, Malaysian Nuclear Agency
43000 Kajang, Selangor
khairulazfar@nm.gov.my

## Abstract

The Safety Analysis Report (SAR) for the JS10000 gamma irradiator, developed using the IAEA recommendation template and the manufacturer's manual, ensures regulatory compliance. This paper addresses briefly the information provided in the SAR includes design, shielding, and safety systems while incorporating risk assessments and emergency preparedness. The SAR highlights robust safety methodologies and operational excellence for irradiation facility.

## 1 Introduction

The Safety Analysis Report (SAR) for the JS10000 gamma irradiator at the Malaysian Nuclear Agency is developed using the "Recommended Template for SAR Gamma Irradiator," formulated based on an expert mission by the International Atomic Energy Agency (IAEA) under the Technical Cooperation Project IAEA MAL 9019.

This template was developed to standardize safety documentation for industrial irradiators, focusing on regulatory review, safety assessment, and safety analysis. The SAR comprehensively addresses the irradiator's design, operation, and safety mechanisms, providing a framework for evaluating compliance with international standards.

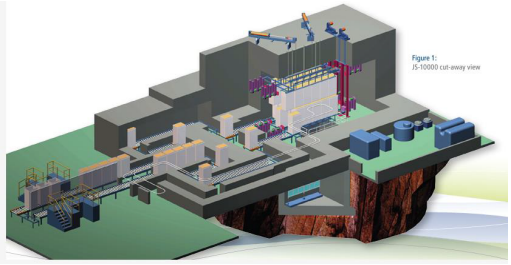


Figure 1: A Typical JS 10000 Design

## 2 Facility Description

### 2.1 Basic Description

Classified as a Category III gamma irradiator, the JS10000 accommodates diverse irradiation needs with a maximum design activity of 2,000,000 curies. It integrates advanced automation and modular features to optimize both routine and experimental irradiations.

### 2.2 Radioactive Sources

The SAR details the recommended working life of the sources, ISO classification, and IAEA compliance for transportation. The Internal Design Features includes:

- Source Transport Mechanism
- Product Positioning System
- Pool Design and Water Treatment
- Ventilation System

### 2.3 Shielding

The irradiator's shielding consists of 2-meter-thick concrete walls, designed to limit radiation exposure. The SAR predicts radiation levels outside the shielding will not exceed 0.25 mR/hr.

#### 2.3.1 Special Features

- **Maze Design**: Reduces scattered radiation, ensuring negligible exposure near the entry point.
- **Roof Plug**: Prevents radiation escape during operations by sealing the source loading aperture.

#### 2.3.2 Interlocks, Sensors, and Radiation Monitoring

Interlocks and sensors ensure protection against operational errors. The system includes:

- Source Transport Sensors
- Access Door Interlocks
- Heat and Smoke Detectors
- Water Pool Level Control

Radiation monitoring systems in the irradiator room, product exit detectors, and water circuit monitors ensure compliance with safety standards.

## 3 Risk Assessment and Safety Procedures

The SAR uses scenario-based analysis to evaluate risks and mitigation strategies. Identified risks include (example):

- Loss of Pool Water
- Interlock Failures
- Radiation Leakage

Safety procedures include comprehensive operator training, dosimetry monitoring, and regular inspections to ensure compliance with radiation safety standards.

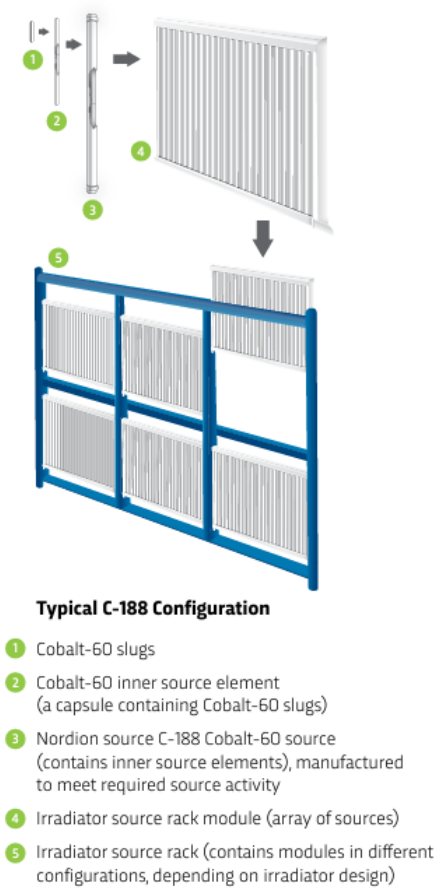



Figure 2: Cobalt-600 C-188 Source Model

## 4 Methodology for Developing the SAR

The SAR is developed using a structured methodology that integrates multiple sources of information and safety techniques:

- Reference to Manufacturer's Manual
- IAEA Guidelines and Best Practices
- Risk Assessment Techniques

The SAR combines manufacturer guidelines, IAEA standards, and advanced safety methodologies, providing a comprehensive and regulatory-compliant safety document.

## 5 Conclusion

The SAR for the JS10000 gamma irradiator exemplifies a robust approach to safety, leveraging the "Recommended Template for SAR Gamma Irradiator" provided under the IAEA MAL 9019 Technical Cooperation Project. This collaboration underscores the facility's alignment with international standards and best practices, providing a benchmark for industrial irradiator safety and performance. By addressing all elements of design, operation, and risk management, the SAR ensures the JS10000 irradiator's role as a safe, reliable, and versatile asset for irradiation applications operated at Nuclear Malaysia.

## References

AELB. Code of practice on radiation protection of non-medical gamma and electron irradiation facilities. LEM/TEK/57.

Nordion (Canada). JS10000 gamma irradiator operator manual.

Nuklear Malaysia. Nuclear Malaysia emergency plan and response plan. SHE.WP.06.

Individual Research Contribution Review, 2024: 175–176
*ISSN: 3083-922X*

# Quality Control in Mammography System: HVL and Image Quality Test

**Mohd Khalid Matori**
Radiation Health and Safety Division, Malaysian Nuclear Agency
43000 Kajang, Selangor
khalid_matori@nm.gov.my

## Abstract

Mammography equipment used for breast examination must undergo quality control testing as a prerequisite for obtaining operational licenses. This study compares digital and conventional mammography systems, revealing that digital mammography has more consistent Half-Value Layer (HVL) values, higher image resolution, lower noise, and a wider dynamic range, making it superior in quality and performance.

**Keywords:** Mammography, Quality Control, Half Value Layer and Image Quality

## 1 Introduction

Mammography uses low-energy X-rays to create detailed breast images, crucial for early cancer detection. Quality control (QC) ensures the safety and accuracy of mammography equipment by enforcing standards that optimize image quality and reduce radiation doses. In Malaysia, QC certification is required for licensing, supporting reliable diagnoses and minimizing misdiagnoses.

## 2 Objective

This study evaluates the Half-Value Layer (HVL) to balance X-ray penetration and contrast, essential for minimizing radiation while maximizing image quality for accurate breast cancer diagnosis in digital and conventional mammography.



Figure 1: Mammography equipment used in this study: (Hologic Selenia Dimensions digital mammography system and Bennett MF-150G conventional mammography system

## 3 Material and Method

This study compares digital and conventional mammography systems in terms of quality control for Half-Value Layer (HVL) and image quality. Using a Hologic Selenia Dimensions digital machine and a Benneth MF-150G conventional machine (see Figure 1) at the Malaysian Nuclear Agency, researchers measured HVL to balance X-ray penetration and contrast. HVL was tested with different target-filter combinations (W/Rh for digital, Mo/Mo for Conventional), and the RMI-156 phantom simulated breast tissue for image quality assessment. The tests analysed image clarity, brightness, and contrast, using ImageJ software for detailed analysis, ensuring accurate calibration and optimizing diagnostic quality across both systems.

## 4 Result and Discussion

The Half-Value Layer (HVL) in mammography refers to the thickness of a material, usually aluminum, needed to reduce the X-ray beam's intensity by half. This measurement is vital in mammography to:

i. Protect Against Radiation

ii. Determine Beam Quality

iii. Enhance Image Contrast

iv. Quality Control

HVL in mammography is influenced by the X-ray tube's anode and filter materials, affecting image quality and radiation dose. Digital systems, typically using tungsten-rhodium or tungsten-silver combinations, show higher HVL values (0.53–0.57 mm Al) compared to conventional systems (0.31–0.36 mm Al), which often use molybdenum or rhodium. These HVL ranges align with optimal standards for safe, high-quality imaging.

Analyzing X-ray images of the RMI-156 phantom (Figure 4) helps assess digital and conventional mammography image quality. With specific fiber, speck, and mass sizes, both systems meet ACR standards, but digital mammography provides superior image quality.

Using ImageJ to analyze RMI-156 phantom images (Figure 6) reveals contrast differences between digital and conventional mammography. Conventional systems show higher grayscale values and irregular background noise, while digital systems demonstrate higher grayscale values from B to D, indicating a greater dynamic range and finer detail capture.

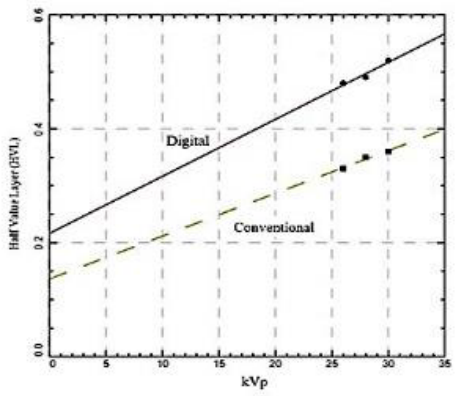



Figure 2: Graph of HVL versus kVp for both mammography

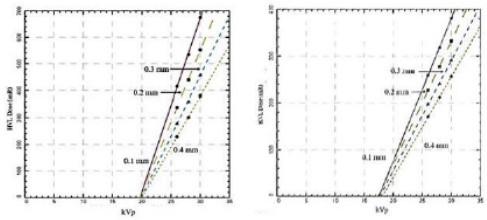


Figure 3: Graph of HVL radiation dose against kVp for conventional & digital mammography

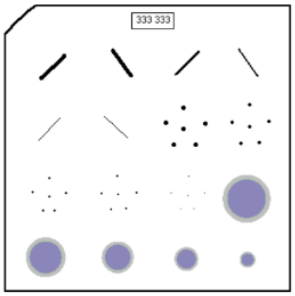



Figure 4: Mammography phantom RMI-156 image diagram: 6 fibers, 5 speck groups, and 5 masses

Digital mammography provides higher grayscale values and brightness (Figure 6) compared to conventional mammography, enhancing contrast and detail detection, especially for smaller samples. This improvement is due to digital mammography's higher dynamic range, which is critical in accurately capturing subtle tissue differences and aiding accurate diagnosis.

## 5 Conclusion

The study concludes that digital mammography has a higher HVL than conventional systems, using higher-energy X-rays for improved image quality and diagnostic accuracy. Digital mammography also offers higher resolution, lower noise, and a wider dynamic range, showing superior performance in image quality assessments with RMI-156 phantom tests.

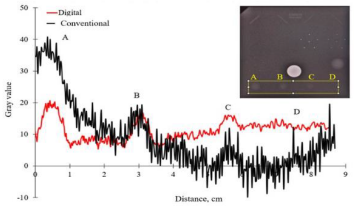



Figure 5: Graph of gray value against distance for both mammograms

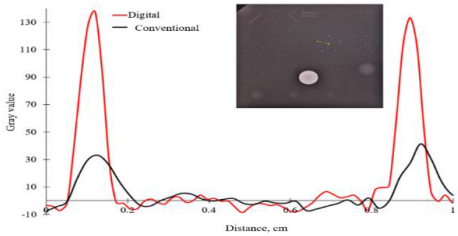



Figure 6: Graph of gray value against distance for two points in RMI-156 phantom image

## References

R. Ishii, A. Yoshida, M. Ishii, S. Fujimoto, and N. Henmi. 2011. Precision of half-value layer measurement on mammography. *Nihon Hoshasen Gijutsu Gakkai zasshi*, 67(12):1533–1539.

N Jamal, K.H Ng, and D Mclean. 2003. A study of mean glandular dose during diagnostic mammography in Malaysia and some of the factors affecting it. *The British Journal of Radiology*, 76:238–245.

April 2009. Commissioning and routine testing of full fill digital mammography system. *NHSBSP Equipment Report 0604*, version 3.0.

Ministry Of Health (MOH) Malaysia Radiation Health & Safety Section. 2014. Technical quality control protocol handbook for mammography system (Screen film and full field digital mammography).

C. Reis, A. Pascoal, T. Sakellaris, and M. Koutalonis. 2013. Quality assurance and quality control in mammography: A review of available guidance worldwide. *Insights into Imaging*, 4(5):539–553.

G. Scielzo and S. Maggi. 1993. Physics, dosimetry, and quality control in mammography. *Radiol Med*, 86(5):687–694.

K. C. Young, R. v. Engen, H. Bosmans, J. Jacobs, and F. Zanca. 2010. Quality control in digital mammography. *Digital Mammography*, pages 33–54. https://doi.org/10.1007/978–3–540–78450–03.

Individual Research Contribution Review, 2024: 177–178
*ISSN: 3083-922X*

# Radiation Metrology Group (KMS); Technical Service Achievements Throughout Its Establishment

**Mohd Khalid Matori**
Radiation Health and Safety Division, Malaysian Nuclear Agency
43000 Kajang, Selangor
khalid_matori@nm.gov.my

## Abstract

The Radiation Metrology Group (KMS), established in 2015 by merging the Medical Physics Laboratory (MPL) and the Secondary Standard Dosimetry Laboratory (SSDL), offers accredited ionizing radiation standards and dosimetry services. Recognized as national standard laboratories, KMS supports Acts 304, 514, and 675, contributing substantially to the Malaysian Nuclear Agency's revenue by providing high-quality services for domestic and international clients.

**Keywords:** Metrology, SSDL, Calibration, Standard

## 1 Introduction

The Radiation Metrology Group (KMS), established in 2015, is the result of a merger between the Medical Physics Laboratory (MPL) and the Standard Secondary Dosimetry Laboratory (SSDL) where the objective of the merger is to provide quality technical services in radiation metrology on par with international laboratories. MPL and SSDL laboratories are laboratories recognized as national standard laboratories for ionizing radiation to meet the requirements of Act 304 (Atomic Energy Licensing Act 1984), Act 514 (Occupational Safety and Health Act 1994), and Act 675 (National Measurement System Act 2007). Nuklear Malaysia is the only government agency responsible for providing facilities for ionizing radiation standards, class H license services, and offering various dosimetry services such as calibration of radiation measuring devices and personal dosimetry in this country.

## 2 Objective

This paper details the services and achievements of KMS throughout its establishment.

## 3 Material and Method

The KMS is a group under the Radiation Safety and Health Division (BKS) that is heavily involved in providing technical services and training in the field of radiation metrology. BKS provide technical support services to domestic and foreign customers. Table 1 show the technical services offered by the MPL and SSDL respectively.

## 4 Result and Discussion

Table 1: Services offered by the Radiation Metrology Group (KMS)

| |
|---|
| MPL |
| i. Calibration Services;<br>• dosimeters used in diagnostic radiology<br>ii. Testing and verification;<br>• all types of Medical X-ray modalities and irradiation room (MOH class H license)<br>iii. Radiation Protection Service;<br>• PPE integrity testing<br>• Radiation protection monitoring<br>iv. Nuclear Medicine Calibration Service;<br>• Thyroid counter calibration<br>• Dose calibrator<br>v. Medical Physics Consultation |
| SSDL |
| i. Calibration Services;<br>• Calibration of Survey Meters and Dosimeters (Protection Level)<br>• Calibration of Ionization Chambers ( Protection Level and Therapy Level)<br>• Calibration of Personal Dosimeter (Pocket & Alarm)<br>ii. Supply and evaluation of Personal and Area Dosimeter Services;;<br>• TLD Service<br>• OSL Service<br>iii. High Dose Dosimetry Services;<br>• Ceric-cerous dosimeter service<br>• Fricke dosimeter service<br>iv. SSDL Service Quality Assurance;<br>• National Inter Laboratory Dose Comparison<br>• ISO Quality Management System Consultant |

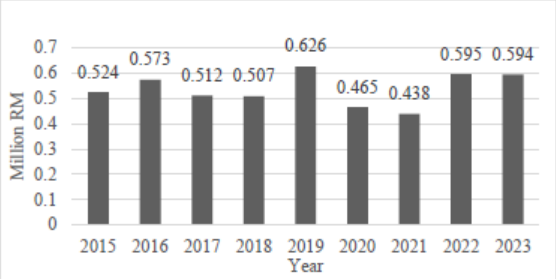



Figure 1: Income from MPL services

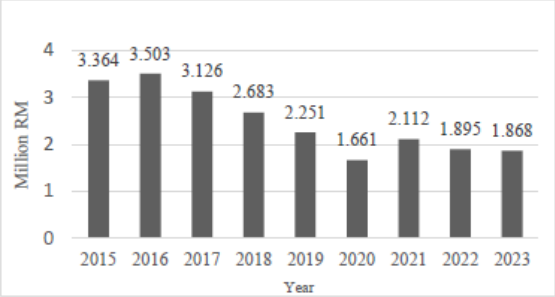



Figure 2: Income from SSDL services

Figures 1 and 2 show the annual income achievement for services obtained for MPL and SSDL for 2015 - 2023. MPL recorded an average annual income of around RM 0.54 million, while SSDL was RM 2.50 million. SSDL's service centre is one of the service centres in Nuclear Malaysia that generates the highest income compared to other service centres in Nuclear Malaysia.

KMS is also heavily involved in training domestic and foreign trainees in dosimeter calibration, personal dosimeters, and high-level dosimeters. Throughout 2015 - 2019, 19 trainees from various countries, namely Syria, Indonesia, UAE, Myanmar, Nepal, Cambodia, Vietnam, Pakistan, Qatar, and Afghanistan, underwent training at SSDL. Eight IAEA expert missions have been carried out by SSDL staff abroad from 2017 - 2023. These missions aim to help countries such as Cambodia, Myanmar, Oman, Nepal, Kuwait, Indonesia, and the Philippines with radiation protection for workers regarding using OSL as a personal dosimeter.

In addition to the accomplishments outlined earlier, KMS serves as a key hub for IPTA students undertaking industrial training, as well as a venue for executing final-year projects for Bachelor's degrees, Master's theses, PhD research, and PGEC initiatives. Between 2015 and 2023, over 150 students participated in internships at KMS, engaging in training activities primarily focused on the operations of MPL and SSDL facilities.

## 5 Conclusion

KMS, a top revenue generator in Nuclear Malaysia, plays a vital role in advancing radiation metrology, serving over 3,000 domestic and international organizations across industries, medicine, and research. As a Designated Institute (DI) for ionizing radiation measurement, KMS strengthens national standards while contributing to Malaysia's economy, education, health, and international reputation in radiation metrology.



## References

R. Ishii, A. Yoshida, M. Ishii, S. Fujimoto, and N. Henmi. 2011. Precision of half-value layer measurement on mammography. *Nihon Hoshasen Gijutsu Gakkai zasshi*, 67(12):1533–1539.

N Jamal, K.H Ng, and D Mclean. 2003. A study of mean glandular dose during diagnostic mammography in Malaysia and some of the factors affecting it. *The British Journal of Radiology*, 76:238–245.

April 2009. Commissioning and routine testing of full fill digital mammography system. *NHSBSP Equipment Report 0604*, version 3.0.

Ministry Of Health (MOH) Malaysia Radiation Health & Safety Section. 2014. Technical quality control protocol handbook for mammography system (Screen film and full field digital mammography).

C. Reis, A. Pascoal, T. Sakellaris, and M. Koutalonis. 2013. Quality assurance and quality control in mammography: A review of available guidance worldwide. *Insights into Imaging*, 4(5):539–553.

G. Scielzo and S. Maggi. 1993. Physics, dosimetry, and quality control in mammography. *Radiol Med*, 86(5):687–694.

K. C. Young, R. v. Engen, H. Bosmans, J. Jacobs, and F. Zanca. 2010. Quality control in digital mammography. *Digital Mammography*, pages 33–54. https://doi.org/10.1007/978–3–540–78450–03.

Individual Research Contribution Review, 2024: 179–180
*ISSN: 3083-922X*

# Validation of The Current Measurement for FAC-LO2 Free Air Chamber in Low-Energy X-Ray

**Mohd Taufik Bin Dolah**
Radiation Health and Safety Division, Malaysian Nuclear Agency
43000 Kajang, Selangor
taufik@nm.gov.my

## Abstract

This study validates the current measurement of a Free Air Chamber (FAC) for low-energy X-ray radiation at 50 kV using a comparative analysis between the Secondary Standard Dosimetry Laboratory (SSDL) Nuklear Malaysia and the Korean Institute of Standard and Science (KRISS). The measurement focused on measuring ionization current using a custom-designed FAC-LO2 chamber with a volume of 1.22863 $cm^3$. The comparison revealed a 9.68% deviation in current measurements between the two laboratories.

**Keywords:** Free Air Chamber (FAC), Current

## 1 Introduction

A Free Air Chamber (FAC) is used to measure the dose of ionizing radiation with high accuracy and precision. It works by creating a uniform electric field and measuring the resulting ionization of the air as radiation passes through the chamber.

The basic primary quantity for measuring the X-ray dose for radiation protection is air kerma. The air kerma standard for the X-ray beam can be measured using the FAC, known as the primary standard device. In this paper, only the current measured by the FAC-LO2 was compared.

The comparison has been made between the current measured by SSDL Nuklear Malaysia and the Korean Institute of Standard and Science (KRISS) in the 50 kV lowenergy x-ray using the FAC-LO2. The FAC-LO2 low-energy xray FAC was fabricated by KRISS with their design because they are not commercially available. The current and the correction factors were measured by KRISS before the FACLO2 summited to Nuklear Malaysia.

## 2 Method

Measurements were performed with an X-ray irradiator model MGC 325, it has a tungsten anode target, a 5.5 mm focal field and inherent 3 mm beryllium (Be) filtration.

With Aluminium (Al) additional filtration with 1.000 mm thickness and tube voltage at 50 kV X-ray with 2 mA current, the X-ray was measured using the FAC-LO2 (air volume 1.22863 $cm^3$) placed at 1 m from the center of the x-ray tube. The laser pointer was used to align between the X-ray tube and FAC-LO2. The FAC-LO2 was connected to the Keithley series 2290 high voltage power supplier and was set 2000 V (positive polarity) to the HV plate for the operating voltage.

Electrometer Keithley model 6517B connected to the FACLO2 was used for the current measurement. The measurement method consists of 10 current readings of 60 seconds each. Two sets of data were taken from this measurement. The temperature, pressure and humidity before and after irradiation were recorded to determine the correction factors that contribute to the current readings. The setup for the current measurement as shown in Figure 1.



Figure 1: The set-up of the FAC-LO2 to measure 50 kV the low energy X-ray at SSDL Nuklear Malaysia

The same FAC was used by the KRISS to measure the current at their laboratory. The CCRI(I)-BIPM beam quality has been used for the validation. The tube voltage is 50 kV and the tube current is 2 mA. The additional filtration condition of 1.009 mm Al with the inherent filter of 3 mm Be. The measuring distance is 1 m.

## 3 Result

The comparison results are given in Table 1. The current values were corrected for the influence of the temperature and pressure during measurement.

Table 1: The percentage deviation of current measurement between KRISS and SSDL Nuklear Malaysia.

| **Laboratory** | **KRISS** | **SSDL Nuklear Malaysia** |
|---|---|---|
| Average Current (pA) | 6.7923 | 6.1346 |
| % Deviation | 9.68 | |

## 4 Discussion

When measuring current in a FAC, a 9.68% current deviation indicates that the measured current deviates from the expected or nominal value by nearly 10%. In high-precision measurements, even small deviations can be problematic. This deviation can arise due to a variety of factors such as measurement technique or setup, the thickness of additional filtration and environmental influences. One of the parameters that can contributed this deviation is the thickness of the additional Al filter used at KRISS which is thicker about 0.0082 mm compared to the filter used by SSDL Nuklear Malaysia.

## 5 Conclussion

Measurement current is a critical aspect of the operation of a free air chamber, enabling the accurate calibration of radiation measurement instruments. It ensures that the measurements of radiation dose are precise and reliable, which is vital for various applications in radiation protection, medical treatments, and scientific research. A 9.68% current deviation is noteworthy and requires investigation.

## References

CY Yi, YH Kim, and DY Jeong. 2022. Effective volume of the Korean research institute of standards and science free air chamber L1 for low-energy x-ray measurement. *Progress in Medical Physics*, 33(1).

Individual Research Contribution Review, 2024: 181–182
*ISSN: 3083-922X*

IRCR

# Evaluation of Nuclear Security Architecture Design Training Workshop

**Muhamad Zahidee Taat**
Radiation Health and Safety Division, Malaysian Nuclear Agency
43000 Kajang, Selangor
zahidee@nm.gov.my

## Abstract

Nuclear security is a critical component of ensuring the safety and protection of nuclear materials, facilities, and personnel. As security threats become increasingly sophisticated, it is essential for nuclear security professionals to stay up-to-date with the latest design strategies and technological advancements.

**Keywords:** Nuclear Security

## 1 Introduction

Nuclear security is an essential component of safeguarding nuclear facilities and materials from threats such as theft, sabotage, and terrorism. As global nuclear infrastructures evolve, so must the security measures that protect them. One of the key components in strengthening nuclear security is the training of professionals responsible for designing, implementing, and evaluating security systems.

This paper presents an evaluation of a Nuclear Security Architecture Design Training Workshop, which aims to enhance the capacity of nuclear security professionals in designing and evaluating security architectures. The workshop covers various aspects of nuclear security, including risk assessment, architectural design, threat modeling, and the integration of modern security technologies. The evaluation assesses the effectiveness of the workshop in meeting its objectives, identifying gaps in participants' understanding, and suggesting improvements for future training initiatives.

## 2 Methods

The evaluation of the Nuclear Security Architecture Design Training Workshop was conducted using a mixed-methods approach.

i. **Pre- and Post-Training Surveys**: To assess changes in participants' knowledge and understanding, surveys were administered before and after the workshop. These surveys focused on key topics such as risk assessment methodologies, security system integration, and the application of advanced technologies in nuclear security design.

ii. **Focus Groups**: After the workshop, a series of focus group discussions were held with participants to gather qualitative feedback on the training content, delivery methods, and practical applicability of the knowledge gained.

iii. **Observational Analysis**: The facilitator's observations were also used to assess participant engagement and interaction during hands-on activities, such as designing sample security architectures.

iv. **Follow-Up Evaluation**: A follow-up survey was conducted after the workshop end to assess impact on participants' performance and application of the skills learned during the training.

## 3 Results

The evaluation of the training workshop produced several key findings regarding its effectiveness and areas for improvement:

i. **Improvement in Knowledge**: Participants demonstrated a significant increase in knowledge related to nuclear security architecture design, particularly in areas such as risk assessment models, threat analysis, and the integration of cybersecurity measures with physical security systems.

ii. **Practical Application**: Participants reported high levels of satisfaction with the hands-on design exercises. Many were able to develop more comprehensive security designs incorporating advanced technologies such as AI-based surveillance, block chain for access control, and adaptive response mechanisms.

iii. **Gaps in Knowledge**: Despite improvements, some participants still felt unclear on certain aspects of integrating new technologies into existing nuclear security systems. There were also concerns regarding the applicability of the training to facilities with limited resources or those in developing countries.

iv. **Training Delivery**: The workshop's interactive elements, including group discussions and collaborative design activities, were highly valued by participants. However, some participants suggested that more time be allotted for case study analysis and practical problem-solving.

v. **Long-Term Impact**: Follow-up results indicated that a majority of participants had begun implementing aspects of the workshop's teachings into their daily work, although further training on specific technologies was requested.

## 4 Conclusion

The evaluation of the Nuclear Security Architecture Design Training Workshop shows that it was successful in significantly enhancing participants' understanding of nuclear security design principles and the integration of advanced technologies. The workshop effectively improved participants' ability to assess and design security architectures that are resilient to evolving threats. However, there are areas for improvement, such as the need for more focused training on integrating modern technologies into resource-constrained environments and allowing more time for practical problem-solving exercises. Moving forward, the workshop can be refined to address these gaps, ensuring that nuclear security professionals are better equipped to manage the increasingly complex and dynamic threats facing nuclear facilities worldwide.

## References

IAEA. Nuclear security system and measures for the detection of nuclear and other radioactive material out of regulatory control. Nuclear Security Series No. 21.

Individual Research Contribution Review, 2024: 183–184
*ISSN: 3083-922X*

IRCR

# Online Permit to Work Process: Transition from Manual to Digital

**Muhamad Zahidee Taat**
Radiation Health and Safety Division, Malaysian Nuclear Agency
43000 Kajang, Selangor
zahidee@nm.gov.my

## Abstract

The Permit to Work (PTW) system is a vital safety tool used to control high-risk work activities across industries such as construction, oil and gas, and manufacturing. Traditionally, PTW processes are paper based, resulting in inefficiencies and challenges in tracking, communication, and compliance. This paper explores the transition from a manual to an online PTW process, highlighting the benefits of digitalization, such as increased efficiency, improved safety, and enhanced compliance. It discusses key features of an online PTW system, its advantages over traditional methods, and implementation considerations. The results demonstrate that digital PTW systems significantly streamline workflows, improve real-time communication, and provide better documentation for regulatory compliance.

**Keywords:** Permit to work

## 1 Introduction

The PTW system is a safety protocol used to ensure that high-risk activities are conducted safely, with proper precautions in place. The traditional manual PTW process involves paper-based permits, manual approvals, and physical records. While effective, this approach has several limitations, including slow processing times, risk of human error, and difficulty in tracking compliance. Transitioning to an **online PTW system** offers several advantages, such as enhanced speed, real-time communication, better risk management, and streamlined documentation. This paper examines how moving to an online PTW system can improve overall workplace safety, efficiency, and regulatory adherence.

## 2 Methods

The paper explores the features and operational structure of online PTW systems by analyzing case studies and industry best practices. Key aspects of the transition process include:

i. **System Design:** Development or selection of an online platform that allows the creation, approval, and management of PTWs.

ii. **Customization:** Customization of permit templates for different types of work (RTP, Radiation and non radiation)

iii. **Integration:** Integration of the online PTW system with existing safety management

iv. **Training and User Adoption:** Providing training and support to ensure workers, supervisors, and safety officers effectively use the system.

v. **Data Management:** Ensuring secure, cloud-based storage of permit records, audits, and safety reports.

vi. **Notifications and Alerts:** Implementation of real-time alerts for permit approvals, expiration, and safety-related updates.

## 3 Results

Transitioning to an online PTW system leads to several positive outcomes:

### 3.1 Improved Efficiency

i. The PTW process is streamlined, with automated permit creation, approval workflows, and notifications, reducing administrative burdens.

ii. Supervisors can review and authorize permits remotely, speeding up approval times and minimizing delays.

### 3.2 Enhanced Safety

i. Real-time risk assessments and hazard identification features help workers to stay informed of potential risks and safety measures before beginning work.

ii. Safety briefings can be conducted online, with quizzes or acknowledgments confirming that workers understand the safety protocols.

### 3.3 Better Compliance

i. The online system generates an audit trail that automatically records every action taken on the PTW, ensuring transparency and simplifying regulatory inspections.

ii. Compliance with industry standards and regulatory requirements is easier to track and report.

### 3.4 Increased Accessibility

i. The system could be accessed remotely through mobile devices, allowing workers and supervisors to manage permits in real-time, especially on-site or at remote locations.

### 3.5 Cost Savings

i. Reduction in paper-based processes and physical storage leads to cost savings in administrative tasks, record-keeping, and document management.

## 4 Conclusion

The shift to an online PTW system provides numerous advantages over traditional paper based methods. Some key benefits include:

### 4.1 Operational Efficiency

i. The online system reduces bottlenecks associated with paper based approvals, allowing faster issuance of permits. This efficiency directly contributes to reduced downtime and improved productivity.

### 4.2 Safety Improvements

i. Real-time updates ensure workers are always aware of the latest safety protocols. The online system's integration with hazard and risk management tools allows for better decision-making before work begins, reducing the likelihood of accidents or safety breaches.

### 4.3 Compliance and Accountability

i. The digital PTW system provides comprehensive records and audit trails, which simplify compliance with both internal safety protocols and external regulations. Detailed reports can be generated quickly for inspections, and issues can be easily traced to their source.

### 4.4 Challenges and Considerations

i. While the benefits are clear, implementation can face challenges such as resistance to change, the need for system integration, and initial setup costs.

ii. Cybersecurity is also a concern, and the system must include strong data encryption and access controls to protect sensitive information.

## References

HSE (Health and Safety Executive). 2013. Permit to work: A guide to the safe system of work. *[Online]*.

Individual Research Contribution Review, 2024: 185–186
*ISSN: 3083-922X*

# Radiation Safety Assessment for Consumer Products

**Noor Ezati Shuib**
Radiation Health and Safety Division, Malaysian Nuclear Agency
43000 Kajang, Selangor
noorezati@nm.gov.my

## Abstract

Consumer products containing radioactive materials are widely available, and their safety is a growing concern. This study aimed to evaluate the radiation exposure levels and safety assessment of several consumer products. Using a radiation survey meter, the skin dose rate ($H_{skin}$) and effective dose rate (E) were measured for each product. The annual effective dose was calculated based on different usage scenarios (16 and 24 hours per day). The results showed a significant variation in radiation levels among the products. While most products, including cards A, B, C, and panty liners, were found to be below the regulatory exemption limit of 10 $\mu$Sv per year, pillow A exceeded this limit. These findings highlight the importance of ongoing monitoring and regulation of consumer products containing radioactive materials. It is crucial to inform consumers about potential risks and encourage responsible usage. Further research is needed to assess the long-term health implications of low-level radiation exposure and to develop stricter regulations for products that exceed safety limits.

## 1 Introduction

Consumer product defined as a device an article or a thing that contains the amount of radioactive materials (AELB, 2016). Radiation safety assessments are crucial for optimizing radiation protection. They involve estimating potential doses during normal use, accidents, and disposal, and comparing these estimates to regulatory limits. The annual effective dose limit for any individual must be less than 10 millisievert, mSv (IAEA, 2016). The assessed doses are then compared to regulatory dose limits to ensure compliance and identify areas for improvement.

In considering safety of consumer product, the product defined by International Atomic energy Agency (IAEA) as a device or manufactured item into which radionuclides have been incorporated or produced by activation, or which generates ionizing radiation, and being sold or made available to members of public without special surveillance or regulatory control after sale (IAEA, 2016). A variety of consumer products which has been added with small amount of radionuclides are readily available for use by members of the public worldwide. The study aims to evaluate the radiation exposure levels and safety assessment for consumer products that containing radionuclides.

## 2 Methods

The radiation measurement by using radiation survey meter to measure dose rate of radiation and recorded as in Table 1.



Figure 1: Survey meter used to measure dose rate from consumer product sample

The dose to the public is limited to the dose of external exposure received from radiation sources. The calculation of the annual effective dose, E, to the whole body is derived from the following formula:

$$E = H_{skin} \times W_r \times \frac{Area\ exposed}{Total\ area} \times t_{use} \qquad (1)$$

$H_{skin}$ is surface area irradiated, $W_T$ is the tissue weighting factor ($10^{-2}$) and tuse is total time usage per annual. The total area for man is $10^4$ cm$^2$. The potential dose estimated by assuming that only one product used each day and the product placed on the head, hands, shirt pocket (left or right), and pants pocket (left and right) for a minimum of 16 hours per day and a maximum of 24 hours per day for 365 days, (AELB, 2016).

## 3 Results

There is a significant variation in radiation levels among the different products. The results of annual effective dose for consumer products as in Table 1 shown that the effective dose value obtained for the consumer products are between 0.19 $\mu$Sv - 4.97 $\mu$Sv and up to 15.62 $\mu$Sv for pillow A for a usage period of between 16-24 hours per day for one year (365 days).

Table 1: Result for the calculation of annual effective dose

| Consumer product (Dimensions in centimeter (cm)) | $H_{skin}$($\mu$Sv/h) | E ($\mu$Sv/h) | Annual Effective Dose ($\mu$Sv/h) | |
|---|---|---|---|---|
| | | | 16 h | 24 h |
| Card A (8.5×5.3) | 12.6 | $5.7\times10^{-4}$ | 3.31 | 4.97 |
| Card B (8.5×5.3) | 4.11 | $1.8\times10^{-4}$ | 1.08 | 1.62 |
| Card C (8.5×5.3) | 1.82 | $0.8\times10^{-4}$ | 0.47 | 0.71 |
| Panty Liner | 0.59 | $0.3\times10^{-4}$ | 0.19 | 0.29 |
| Pillow A (40×30) | 1.48 | $1.8\times10^{-3}$ | 10.62 | 15.62 |

## 4 Discussion/ Conclusions

It was observed that the annual effective dose increases with increased usage duration as recorded by comparing the 16-hour and 24-hour exposure values for each product. The authority has set a basic criterion of 10 $\mu$Sv per year effective dose for exempt consumer products, following the guidelines in "Assessment and Licensing of Consumer Product Containing Radioactive Material" (LEM/TEK/69). This radiological safety assessment shows that the annual effective dose from using the smart card on the body is below the regulatory exemption limit of 10 $\mu$Sv per year and exceeded the limit for pillow A. The data obtained offers a valuable opportunity to assess the safety and potential risks associated with consumer products containing radioactive materials.

The assessed products, comply with the regulatory exemption limit of 10 $\mu$Sv per year. However, product pillow A exceeds this limit, indicating a potential safety concern.

Further investigation and potential regulatory action may be necessary for products that exceed the regulatory limits. Consumers should be informed about the potential risks and benefits of using such products, and how to minimize exposure.

## References

AELB. 2016. Assessment and licensing of consumer product containing radioactive material. Panduan Teknikal LEM/TEK/69 Sem.1, 24 November 2016.

IAEA. 2016. Radiation safety for consumer products. IAEA Safety Standard Series No.SSG-36.

Individual Research Contribution Review, 2024: 187–188
*ISSN: 3083-922X*

# Assessing Wholebody Counting Accuracy for Internal Dosimetry

**Noor Fadilla binti Ismail**
Radiation Health and Safety Division, Malaysian Nuclear Agency
43000 Kajang, Selangor
fadilla@nm.gov.my

## Abstract

A team of researchers from the Radiation Safety and Health Division at the Malaysian Nuclear Agency has recognized the need to harmonize internal dose assessment procedures. This study was conducted using a wholebody counter (WBC) bed type and a thyroid counter in the WBC laboratory, which has been in operation since 2012. The primary aim is to establish comprehensive guidelines to standardize the assessment of radionuclide intake and internal doses, with a particular focus on occupational exposure in Nuclear Malaysia.

**Keywords:** Internal dose, Wholebody counter (WBC), occupational exposure

## 1 Introduction

The internal doses assessment can be considered into two categories, namely the determination of the intakes of radionuclides in the human body by direct method measurements and/or by indirect methods such as excretion analysis. Numerous influencing factors and assumptions, including the physical and chemical properties of the radioactive substances, the mode of intake, the biokinetic and energy absorption processes are taken into consideration when interpreting monitoring data in terms of intake or internal dose (Doerfel et al., 2007). In this study, the WBC bed type was used to assess occupational radionuclide exposure within the entire body at the time of measurement. The WBC system consist of HPGe detectors, shielding, data processing and analysis units. It applicable to measure the radionuclides emitting $\beta$ and $\gamma$ (Kalef-ezra et al., 2012). The technique is a preferred choice for large scale screening and monitoring during radiological emergencies (Park et al., 2020). Usually, there are some radionuclides such as $^{137}$Cs, $^{131}$I and $^{60}$Co were highlighted for internal dosimetry assessment. This study supports the development of an effective measurement protocol using WBC and thyroid counters and offers a valuable reference point for establishing internal dosimetry in Malaysia.

## 2 Materials and Method

### 2.1 WBC system

The WBC bed type with HPGe model GEMFX8530P4 used in this was shielded with steel and lead frame in order to minimize the background radiation as shown in Figure 1. During counting time, the individual need to lying on the moving bed by facing the surface of the detector for about 30 mins.

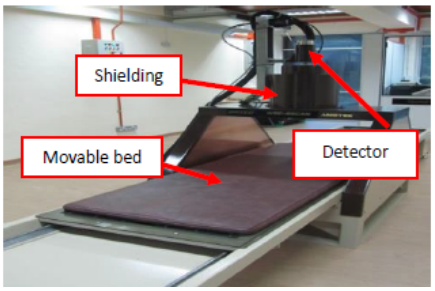



Figure 1: WBC bed type for internal dosimetry

### 2.2 Energy and Efficiency Calibration

The energy and efficiency calibration of a detector system were conducted by placed the standard mixed source in static positioned under the detector. The mixed standard source that used in this calibration is consist of radionuclides detection in ranged of 50 to 1800 keV The energy calibration was conducted by align the accurate photopeak energy of each radionuclide to match with the operating channel number (Dararutana, 2021). The energy calibration graph of the detector is shown in Figure 2.

The efficiency calibration of the detector was performed using a standard mixed gamma radiation source, and it also can be estimated using Equation 1 (Taha, 2024).

$$\varepsilon = \frac{C}{A \times P} \tag{1}$$

Where:

- $\varepsilon$ is a calibration efficiency.
- C is net counts per second
- A is disintegration per second and
- P is gamma ray emission probability

## 3 Results and Discussion

This study validated the WBC method used for rapid and accurate assessment of the internal radiation dose for occupational. Regarding to the validation of the WBC measurement,

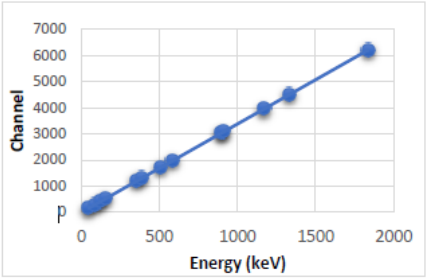



Figure 2: Energy calibration of the detector

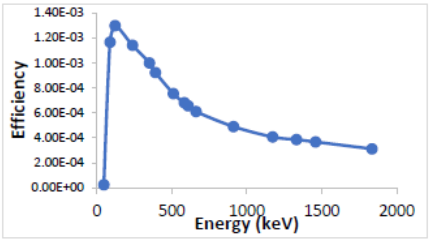



Figure 3: Efficiency calibration of the detector

specific requirements should be evaluated such as selectivity energy of radionuclides, linearity, efficiency, sensitivity and measurement range (Park et al., 2020).

## 4 Conclusion

Based on this study, the reliable and the validation results indicated that the WBC can accurately measure the concentration of radionuclides in the human body and the internal dosimetry for assessment of radiation dose for occupational especially in the event of nuclear or radiological emergency.

## References

C. Dararutana. 2021. Calibration of whole body counter for assessment of internal dose in the human body. https://doi.org/10.1088/1742-6596/1719/1/012044.

H. Doerfel, A. Andrasi, M. Bailey, V. Berkovski, E. Blanchardon, C. M. Castellani, R. Cruz-Suarez, C. Hurtgen, B. Leguen, I. Malatova, J. Marsh, J. Stather, and J. Zeger. 2007. A structured approach for the assessment of internal dose: The IDEAS guidelines. *Radiation Protection Dosimetry*, 127(1–4):303–310. https://doi.org/10.1093/rpd/ncm405.

J. Kalef-ezra, S. Valakis, and S. Pallada. 2012. HNPS advances in nuclear physics applications of a novel whole body counter in radiation protection and human body composition studies. 20:62–65.

M. Park, M. Kim, J. Yoo, and M. Jo. 2020. Validation of the whole-body counting measurement in a radiation emergency. *Applied Radiation and Isotopes*, September, 109476. https://doi.org/10.1016/j.apradiso.2020.109476.

T. M. Taha. 2024. Internal dosimetry for individuals following inhalation of radionuclides. 0–6.

Individual Research Contribution Review, 2024: 189–190
*ISSN: 3083-922X*

# Comparison of Dose-Response and Performance Between OSL Reader in Secondary Standard Dosimetry Laboratories (SSDL), Malaysia Nuclear Agency (MNA) & Nuclear Medicine Department, National Cancer Institute (NCI)

**Noor Fatin Shuhada Binti Ab Hamid**
Radiation Health and Safety Division, Malaysian Nuclear Agency
43000 Kajang, Selangor
fatin@nm.gov.my

## Abstract

This study to evaluates the performance and dose-response of two Optically Stimulated Luminescence (OSL) readers, the InLight® LANDAEUR MicroStar, used at the Secondary Standard Dosimetry Laboratories (SSDL) of the Malaysia Nuclear Agency (MNA) and the Nuclear Medicine Department of the National Cancer Institute (NCI). The main goals are to compare the reader performance in term of linearity and accuracy of the two OSL readers. Two tests were conducted with radiation doses of 1, 3, 5, 7, and 10 mSv for linearity test. The relationship between measured dose (Dmeas) and delivered dose (Ddel) was plotted, showing an $R^2$ value of 0.965 for SSDL and 0.994 for NCI, indicating high linearity. An accuracy test using the ICRP 1991 trumpet graph, the experimental values for all doses fell within the acceptable upper and lower limits.

**Keywords:**OSL, EX, Reader OSL

## 1 Introduction

Secondary Standard Dosimetry Laboratories (SSDL) are responsible for calibrating radiation detectors and ensuring the accuracy of radiation measurements, often through standardized procedures and protocols. In Malaysia, the Malaysia Nuclear Agency (MNA) and the Nuclear Medicine Department of the National Cancer Institute (NCI) are two key institutions that utilize OSL readers for various radiation measurement applications, including patient monitoring and environmental dosimetry.

This study aims to compare the performance and dose-response characteristics of OSL readers used at the MNA's SSDL and the NCI's Nuclear Medicine Department. Specifically, it evaluates the consistency, accuracy, and precision of the OSL readings obtained from these two institutions in response to known radiation doses. Given the critical role of accurate radiation measurement in both medical and research settings, understanding the performance of OSL readers across different laboratories is essential for maintaining high standards of radiation protection and patient safety.

## 2 Methods

### 2.1 Comparison of two (2) OSL Reader performance

In this study, 15 Optically Stimulated Luminescence (OSL) dosimeters were prepared and exposed to gamma radiation from a Cs-137 source. The dosimeters were grouped in sets of three and irradiated at five different radiation doses: 1 mSv, 3 mSv, 5 mSv, 7 mSv, and 10 mSv.

During the readout process, dosimeters were analyzed using Inlight LANDAEUR Microstar Dosimetry System and Reader at both the SSDL and the NCI. Calibration factors were applied before readings. The results were analyzed for linearity and accuracy by plotting the measured against the delivered dose and fitting a linear regression. An ideal relationship would have an $R^2$ value close to 1, indicating a strong linear correlation between the measured and delivered doses.

### 2.2 Irradiation Protocol

OSL dosimeters encased in holder and were positioned in front on an ISO 4037 water phantom. The dosimeter was irradiated subjected to gamma (Cs-137). The distance was fixed at 5 meters.

## 3 Data and Discussion

### 3.1 Comparison of two (2) OSL Reader performance

Table 1: Dose Response for OSL Reader at SSDL and NCI

| $D_{del}$ (mSv) | $D_{meas} \pm \Delta D_{meas}$ for readers | | Percentage Deviation, Δ (%) | |
|---|---|---|---|---|
| | SSDL | NCI | SSDL | NCI |
| 1 | 0.947 ± 0.075 | 1.243 ± 0.186 | -5.333 | 24.333 |
| 3 | 2.843 ± 0.146 | 3.947 ± 0.308 | -5.222 | 31.556 |
| 5 | 4.706 ± 0.028 | 6.420 ± 0.537 | -5.042 | 28.400 |
| 7 | 8.805 ± 0.007 | 9.665 ± 0.219 | 20.500 | 38.071 |
| 10 | 13.565 ± 0.219 | 12.450 ± 1.245 | 26.281 | 24.500 |

From Table 1, all the readers give out the readings of $D_{meas}$ closer to the $D_{del}$ with standard error, SE in the range 0.007 to 1.245. The percentage deviation, $\Delta$ % of $D_{meas}$ for reader SSDL is from 5.333 to 26.281%. For reader NCI, the values $\Delta$ % of the $D_{meas}$ is within the range of 24.333 to 24.500%.

### 3.2 Linearity

A linear graph of the measured dose, $D_{meas}$ versus delivered dose, $D_{del}$ was plotted to get the linear equation y=mx+c. From here, R2 was obtained.

Linearity is defined as the degree of deviation of an instrument from its ideal straight-line performance. The linear regression coefficient, $R^2$, as stated by Douglas et al. (2008), describes the strength of the linear relationship between two

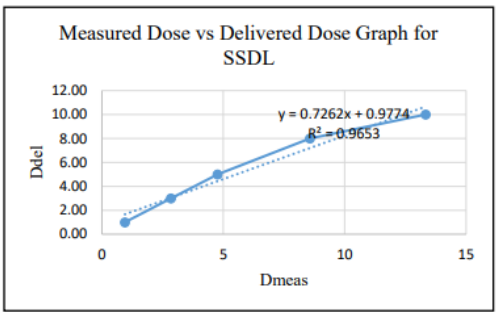



Figure 1:

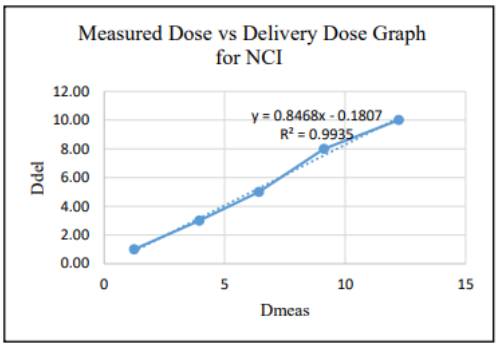



Figure 2:

variables, which in this case refers to the relationship between $D_{meas}$ and $D_{del}$ for each reader. The ideal $R^2$ should equal 1.

Based on the Figure 1 and Figure 2, the $R^2$ value for the OSL reader from SSDL is 0.965, while for NCI it is 0.994. The linear fit between Dmeas and Ddel demonstrates good linearity, with $R^2$ values for both OSL readers close to 1.

### 3.3 Accuracy

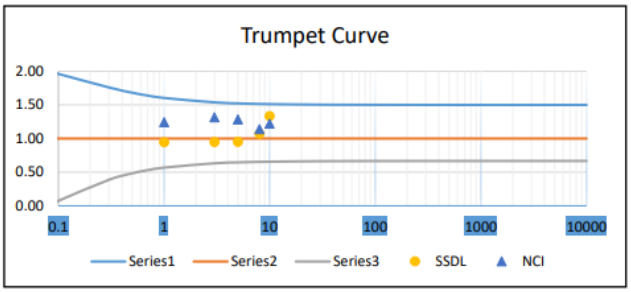



Figure 3: Accuracy graph

A dose measurement accuracy test was conducted for this study to determine whether the $D_{meas}$ was accurate. The ratio of $D_{meas}$ to the known $D_{del}$, referred to as R, was calculated to achieve this.

The best value for R is 1. A trumpet graph, as recommended by the ICRP (1991), was utilized to assess the accuracy of $D_{meas}$. The value of R should fall within the established lower limit (LL) and upper limit (UL). The dose is considered accurate if R lies between the UL and LL calculated for each dose. The values of UL and LL vary for each dose, as they depend on $D_{del}$. The value of R must lie between LL $\leq$ R $\leq$ UL. All the values of R in Table 1 are then plotted in the trumpet graph as in Figure 3, to see whether the R is in the acceptance limit for doses 1, 3, 5, 7, and 10 mSv. The trumpet graph above shows that the value of R for both OSL readers lies within the LL to the UL for each dose.

## 4 Conclusion

This comparative study demonstrates that both the OSL readers used in the Secondary Standard Dosimetry Laboratory (SSDL) at the Malaysia Nuclear Agency (MNA) and the Nuclear Medicine Department at the National Cancer Institute (NCI) perform well in terms of dose-response, accuracy, and precision. However, slight differences in dose-response curves and accuracy were noted, suggesting that further standardization and calibration harmonization may be needed to ensure consistent results across different laboratories.

The findings of this study highlight the importance of routine calibration and cross-institutional comparisons in maintaining high standards of radiation dosimetry. To enhance the reliability of OSL dosimetry practices in Malaysia, it is recommended that both institutions adopt a more unified approach to calibration procedures and performance monitoring.

## References

V. E. Aleinikov and W. Böhmer. 2020. Calibration of dosimeters: Theory and practice. *Journal of Radiation Protection*, 40(1):23–45.

L. Bøtter-Jensen, S.W.S. McKeever, and A.G. Wintle. 2003. Optically stimulated luminescence dosimetry. *Elsevier, Amsterdam*.

IAEA. 2018. Guidance for secondary dosimetry laboratories and calibration facilities. International Atomic Energy Agency, Vienna.

Individual Research Contribution Review, 2024: 191–192
*ISSN: 3083-922X*

# Preliminary study on lens of eye dose measurement using head phantom and nanodots

**Norriza Mohd Isa**
Radiation Health and Safety Division, Malaysian Nuclear Agency
43000 Kajang, Selangor
norriza@nm.gov.my

## Abstract

Ionizing radiation is used in medical fields could be contributed to occupational exposure and considered major risk factor for cataract formation among personnel who work in a close distance to the X-ray source especially in interventional cardiology procedures. Because of this reason, the International Commission of Radiation Protection (ICRP) significantly decreased the previous annual dose limit for radiation worker's lens of the eyes from 150 mSv to 20 mSv in a year for 5 years and no single annual dose exceed 50 mSv (ICRP, 2011). Currently, even though Malaysia does not yet implement the new limit for eye lens dose. The purpose of the study is to find out Hp (3) conversion coefficient for a head phantom using standard X-ray narrow spectrum as a preparation to monitor Malaysian radiation worker in the future. Nanodots were used and located at different inner layer of the head phantom and with 3 mm thickness from out surface of the head phantom to estimate the effective dose of lens of eye dose. The results were compared with the air kerma measured by calibrated ion chamber to obtained conversion coefficients (cf) for Hp (3). The result of cf obtained from the study in range of 0.792 to 1.777.

**Keywords:** Lens of eye dose, Head Phantom, Radiation Worker, Nanodots

## 1 Introduction

Application of X-ray image-guided procedures has rapidly increased in a wide range of medical field (neurosurgery, cardiology, urology). Brain cancer & cataract cases increasing among medical specialist because they were operating the equipment especially interventional cardiology and radiology. In 2011, The International Commission on Radiological Protection (ICRP) recommended a reduction for occupational exposure of eye lens from 150 mSv to 20 mSv. It was endorsed and recommended by The International Atomic Energy Agency (IAEA) to revised the eye lens dose limit for other countries. But nowadays, Malaysia had not yet implemented the new dose limit for eye lens for worker which is 20 mSv. As preparation for next future personnel dosimetry in Malaysia, the preliminary study on that matter was conducted. The aim of the study is to determine conversion coefficients of Hp (3) in air for monoenergetic photons (narrow spectrum standard X-ray beams).

## 2 Methods

The cylindrical phantom from Nagase Landauer, Japan was used in this study composes of 40 polymethyl methacrylate (PMMA) slice rings (20 cm in diameter and 0.5 cm in slice thickness). The nanodot dosimeters (Landauer Inc., USA) were used in the study. The data measurements were read out by a microStar mobile reader (Landauer Inc., USA). A calibrated ion chamber was irradiated with standard X-ray beam qualities to measure air kerma doses without the head phantom. Its position was similar with the location where nanodots will be located in the head phantom. Then the phantom with embedded nanodots were irradiated with standard X-ray beam of qualities N-40, N-60, N80, N-100, N120 and N-150. The Measurement set-up for the measurement is shown in Figure 1.



Figure 1: Measurement set-up for the test

## 3 Results

The conversion coefficients (cf) of different air kerma (mGy) for different X-ray standard beam quality and effective doses (mSv) are shown in Table 1.

## 4 Discussion

Based on the data and result obtained, the cf values for different beam qualities, point location (layer) and air kerma dose (0.15, 1.5 & 3.0 mGy) in the range between 0.792 to 1.777.

Table 1: Conversion coefficients (cf) for different beam qualities for dose in air kerma with 0.15, 1.5 and 3 mGy.

| **Bean Quality** | **mGy** | **Dose, mSv (L1)** | | **Dose, mSv (L2)** | | **Dose, mSv (L3)** | |
|---|---|---|---|---|---|---|---|
| | | mSv | cf | mSv | cf | mSv | cf |
| N-40 | 0.15 | 0.264 | 1.761 | 0.256 | 1.704 | 0.267 | 1.277 |
| | 1.5 | 2.284 | 1.523 | 2.570 | 1.713 | 2.422 | 1.615 |
| | 3 | 4.926 | 1.642 | 4.716 | 1.572 | 4.653 | 1.551 |
| N-60 | 0.15 | 0.264 | 1.761 | 0.263 | 1.752 | 0.258 | 1.723 |
| | 1.5 | 2.519 | 1.679 | 2.462 | 1.642 | 2.536 | 1.691 |
| | 3 | 5.103 | 1.701 | 5.008 | 1.669 | 5.052 | 1.684 |
| N-80 | 0.15 | 0.251 | 1.672 | 0.254 | 1.695 | 0.252 | 1.679 |
| | 1.5 | 1.841 | 1.227 | 1.921 | 1.281 | 2.025 | 1.350 |
| | 3 | 3.922 | 1.307 | 4.156 | 1.385 | 3.952 | 1.317 |
| N-100 | 0.15 | 0.198 | 1.320 | 0.193 | 1.287 | 0.195 | 1.300 |
| | 1.5 | 1.198 | 0.799 | 1.215 | 08.10 | 1.213 | 0.809 |
| | 3 | 2.399 | 0.800 | 2.209 | 0.736 | 2.404 | 0.801 |
| N-120 | 0.15 | 0.161 | 1.073 | 0.160 | 1.067 | 0.166 | 1.107 |
| | 1.5 | 1.298 | 0.865 | 1.473 | 0.982 | 1.248 | 0.832 |
| | 3 | 2.517 | 0.839 | 2.605 | 0.868 | 2.588 | 0.863 |
| N-150 | 0.15 | 0.140 | 0.933 | 0.143 | 0.953 | 0.126 | 0.840 |
| | 1.5 | 1.190 | 0.793 | 1.196 | 0.797 | 1.188 | 0.792 |
| | 3 | 2.618 | 0.873 | 2.629 | 0.876 | 2.638 | 0.879 |

These shown that cf are depend on the air kerma dose, location of nanodots and beam qualities used in the study.

The dedicated cf of this beam quality will be used to estimate the effective dose received by eye lens of radiation worker, The cf will be multiplied with the estimated air kerma dose produced by dedicated beam quality to quantify the effective dose for eye lens of radiation worker. This method can be applied if the beam is direction to the eye of radiation worker.

In the study, entrance surface dose on the surface of the head phantom and other angles of radiation source are not considering. These are the limitation in the study and will be carried out in the future to obtain comprehensive results.

## 5 Conclusion and attention

From this study, Hp (3) could be calculated by knowing the conversion coefficients (cf) for certain X-ray beam quality with air kerma dose. Nanodot dosimeters were selected in the study because their small size which can be attached on lead glasses worn by radiation worker and can be calibrated directly at the depth of 3 mm in the cylindrical head phantom.

## References

ISO 4037-3. 1999. Calibration of area and personal dosimeters and the measurement of their response as a function of energy and angle of incidence.

J Esor et al. 2017. Comparing Hp (3) evaluated from the conversion coefficients from air kerma to personal dose equivalent for eye lens dosimetry calibrated on a new cylindrical PMMA phantom. *J. Phys.: Conf.*, Ser. 860 012045.

IAEA. 2018a. Occupational radiation protection (2018). IAEA Safety Standard Series No. GSG-7.

IAEA. 2018b. Radiation protection and safety in medical uses of ionizing radiation (2018). Specific Safety Guide No. SSG-46.

International Commission on Radiological Protection (ICRP). 2011. Statement on tissue reactions. *International Commission on Radiological Protection (ICRP)*.

Individual Research Contribution Review, 2024: 193–194
*ISSN: 3083-922X*

# Determination of the Need for Internal Exposure Monitoring of Radiation Workers

**Nur Khairunisa Zahidi**
Radiation Health and Safety Division, Malaysian Nuclear Agency
43000 Kajang, Selangor
khairunisa@nm.gov.my

## Abstract

Radiation workers in nuclear medicine are not only exposed to ionizing radiation externally but also internally. The widespread use of unsealed radioactive sources in nuclear medicine poses a potential for internal exposure of radiation workers in the field of nuclear medicine. External radiation monitoring using a dosimeter has been developed in Malaysia since 1985. However, assessment of the need for individual internal dose monitoring has not yet been developed in Malaysia. The purpose of this study is to compare determination value of the need individual internal exposure monitoring of radiation workers in nuclear medicine department. This study involves radiation workers by observation, survey forms and calculation of decision factor of the need for internal exposure monitoring based on IAEA dose criteria. The results show that the highest risk is during the use of radiopharmaceuticals for diagnosis and treatment of disease through inhalation process for lung scan as well as the preparation and oral administration to patient, especially radiopharmaceutical containing I-131 and I-124. A total of 12 out of 16 workers need internal monitoring involving biochemists, pharmacists, and technologists while physicist do not require internal monitoring. Overall, data obtained from this study is the first step in establishing a comprehensive internal exposure framework.

**Keywords:** Internal dose, Wholebody counter (WBC), occupational exposure

## 1 Introduction

The basic concept of internal exposure is when radioactive materials enter the body through several main routes, through respiration and wounds (UNSCEAR, 2008). The work routines of nuclear medicine workers cause them to be exposed to higher radiation doses when compared to other healthcare workers (Krajewska et al., 2023; Alashban and Shubayr, 2021). Currently, radiation worker exposure monitoring in Malaysia is done externally using Optically Stimulated Luminescence Dosimeters (OSLD). Collecting data on the requirements for monitoring the internal dose of radiation workers is the initial step in developing a comprehensive internal exposure monitoring program for radiation workers.

## 2 Methods

This study was conducted at the one of the nuclear medicine facility in Malaysia. This study involves radiation workers by observation, survey forms and calculation of decision factor of the need for internal exposure monitoring based on IAEA dose criteria.

### 2.1 Determination of Internal Exposure Requirements

A total of 16 radiation workers who work with unsealed radioactive materials are considered in this determination assessment. This method is used to determine whether radiation workers need to undergo internal exposure dose monitoring based on the calculation of dose criteria issued by the IAEA (IAEA, 1999) as shown in Equation 1.

$$d_{j_scenario} = \frac{A_j e(g)_{j.inh}\, f_{fs}\, f_{hs}\, f_{ps}}{0.001} \tag{1}$$

Where:

- $d_j$ = decision factor based on operation and radionuclide
- $A_j$ = cumulative activity of radionuclide $j$ present in the workplace over the course of the year
- $e(g)_{j.inh}$ = dose coefficient (Sv/Bq) for inhalation of radionuclide, j
- $f_{fs}$ = physical form safety factor based on the physical and chemical properties of the material being handled
- $f_{hs}$ = handling safety factor
- $f_{ps}$ = protection safety factor
- 0.001 = conversion factor from Sv to mSV

The calculation of the final decision factor for each radiation worker is sum of all decision factor, dj, obtained for each radiation worker as shown in Equation 2.

$$D = \sum_j d_j \tag{2}$$

## 3 Results and Discussion

There are 12 workers, who have final decision values, D, exceeding 1 mSv means require individual internal exposure monitoring while 4 workers have D values below 1 mSv that do not require individual internal exposure monitoring. Only 1 worker, does not require internal exposure monitoring for

Ga-68 due to the assessment value, D, for this radionuclide below 0.1 mSv. In general, 75% of the workers involved in this study need to undergo individual internal exposure monitoring. Similar studies conducted showed that 71.9% and 100% of the workers in their studies (Bento et al., 2011; Krajewska et al., 2023), respectively, needed individual internal exposure monitoring. The findings of this study are supported by a similar study where individual internal exposure monitoring should be included in the radiation protection plan for workers handling I-131 due to its high risk (Dantas et al., 2008). The same study has also been carried out in Chile and China, where workers handling I-131 and Tc-99m need to undergo individual internal exposure monitoring (Astudillo et al., 2015; Wang et al., 2016). Biochemists have the lowest decision factor. Biochemist also involved in RIA techniques (of Health of Malaysia, 2018), where this process only involves external radiation exposure. The findings of this study also indicate that all physicist do not require individual internal exposure monitoring as they are not directly involved in the production, preparation, or administration of radiopharmaceuticals. Physicist involved with checking for any contamination on vials before it sent to customers. However, physicist also have the risk of individual internal exposure when there is any contamination during the test. Additionally, the involvement of physicist in radiological emergency response and decontamination activities could pose a risk of individual internal exposure. Therefore, physicist need to undergo immediate individual internal exposure monitoring when deemed necessary.

## 4 Conclusion

High risk assessments occur during the use of radiopharmaceuticals for the diagnosis and treatment of diseases, especially in the administration of doses through vapor or inhalation for lung scans, as well as the preparation and oral administration of doses to patients, particularly for radiopharmaceuticals containing I-131 and I-124. The research findings indicating that a total of 12 workers, consisting of biochemists, pharmacists and technologists require individual internal exposure monitoring, while 4 physicists are exempt. This situation is due to the varying risk levels associated with their roles and potential exposure to hazardous materials. Targeting monitoring efforts towards these at-risk individuals is crucial for effective occupational health and safety management.

## References

Yazeed Alashban and Nasser Shubayr. 2021. Occupational dose assessment for nuclear medicine and radiotherapy technologists in Saudi Arabia. *Radiation Protection Dosimetry*, 195(1):50–55.

R. Astudillo, A. Hermosilla, G.Diaz-Londono, and M. Garcia. 2015. Assessing the need for a routine monitoring program in three nuclear medicine centers in Chile. *Radioprotection*, 50(2):141–144.

J. Bento, P. Teles, M. Neves, A. I. Santos, G. Cardaso, A. Baretto, F. Alves, C. Guerreiro, A. Rodrigues, J. a. M. Santos, R. Parafita, and B. Matins. 2011. *Study of Nuclear Medicines Practices in Portugal from an Internal Dosimetry Perspective*, 149(4):438–443.

B. M. Dantas, E. a. D. Lucena, and A. L. a. B. Dantas. 2008. Internal exposure in nuclear medicine: Application of IAEA criteria to determine the need for internal monitoring. *Archives of Biology and Technology*, 51.

IAEA. 1999. Assessment of occupational exposure due to intakes of radionuclides – IAEA safety guide No.RS-G-1.2. Vienna, International Atomic Energy Agency.

Krajewska, Grażyna, and Pawe l Krajewski. 2023. Evaluation of internal exposure of nuclear medicine staff working with radioiodine in Poland. *Int J Occup Med Environ Health*, 36(5):587–595.

Ministry of Health of Malaysia. 2018. Operational policy in nuclear medicine services, Ministry of Health of Malaysia.

UNSCEAR. 2008. Sources and effects of ionizing radiation. Volume I: Sources Report to the General Assembly Scientific Annexes a and B. New York: United Nations.

H.-B. Wang, Q.-Z. Zhang, Z. Zhang, C.-S. Hou, W.-L. Li, H. Yang, and Q.-F. Sun. 2016. Necessity of internal monitoring for nuclear medicine staff in a large specialized Chinese hospital. *International Journal of Environmental Research and Public Health*, 13(418).

Individual Research Contribution Review, 2024: 195–196
*ISSN: 3083-922X*

# Estimates of Collective Dose due to the Discharging of Radioactive Substances to the Environment using IAEA Generic Model

**Raymond Yapp Tze Loong**
Radiation Health and Safety Division, Malaysian Nuclear Agency
43000 Kajang, Selangor
raymond@nm.gov.my

## Abstract

This study conducted to estimate the collective dose of the public due to the discharging of radioactive substance to the environment from Malaysian Nuclear Agency Reactor TRIGA PUSPATI in 2023. The results showed that the public around Malaysian Nuclear Agency is estimated received up to 1.39 $\mu$ Sv in 2023.

**Keywords:** Public Dose, Discharging of Radioactive Substance

## 1 Introduction

The potential risks of radionuclides in the environment, stemming from uranium mining, nuclear waste storage, routine and accidental nuclear plant discharges, nuclear weapons, and "dirty bombs," are a pressing issue of significant public concern. Events such as the 2011 Fukushima-Daiichi nuclear accident highlighted the importance of effective systems for managing and mitigating ionizing radiation's impact on humans and the environment.

The International Atomic Energy Agency (IAEA) has published a Safety Report outlines a method for assessing public radiation doses as part of environmental impact analyses for predicted radioactive discharges. It utilizes screening models that mathematically represent environmental processes to generate quantitative results. The report supports and builds upon Safety Standards Series No. WS-G-2.3 (2000) and replaces Safety Series No. 57 (1982) by providing updated models and parameters for evaluating radionuclide transfer in the environment.

This paper presented the result of estimated collective dose due to the discharging of radioactive substances to the environment by Malaysian Nuclear Agency (Nuklear Malaysia) Reactor TRIGA PUSPATI (RTP) in the year of 2023 using IAEA generic model described in Safety Report Series 19 (SRS 19).

## 2 Methods

The methods used is outlined in SRS 19.

### 2.1 Determination of Source Term

The source term is provided by stack monitoring RTP Nuklear Malaysia and the data is used to calculate the annual average discharge rate for radionuclide i, $Q_i$ (Bqs$^{-1}$). The assumption of radionuclide discharge to the environments are $^{60}$Co (particulate), $^{131}$I (iodine) and $^{41}$Ar (noble gas).

### 2.2 Measurement of Wind Speed and Wind Direction

The wind speed and wind direction are measured using RM Young Ultrasonic Anemometer to determine the geometric mean of the wind speed at the height of release representative of a year, $U_a$ ($ms^{-1}$) and the fraction of the time during the year that the wind blows toward the locations surrounding Nuklear Malaysia, $P_p$ (unitless).

### 2.3 Assess Location Identification and Measurement of Distance from Release Point

The assess location is identified based on the human activity in the location. The distance between RTP release point to assess location is measured using Google Maps to determine the the Gaussian diffusion factor appropriate for the height of release $H$ and the downwind distance to the location being consider, $F(m^{-2})$.

### 2.4 Determination of Ground Level Air Concentration and Total Daily Average Deposition Rate on the Ground

The ground level air concentration at the location, $C_A$ (Bqm$^{-3}$) is given by:

$$C_A = \frac{P_p F Q_i}{U_a} \tag{1}$$

where $U_a$ is the average of the wind speed at the height of release (ms$^{-1}$).

The total daily average deposition rate on the ground of a given radionuclide $I$ from both dry and wet processes, including deposition either on to impervious surfaces or on to both vegetation and soil, $d_i$ (Bqm$^{-2}$d$^{-1}$) is given by:

$$d_i = (V_d + V_w) C_A \tag{2}$$

where $V_d$ is the dry deposition coefficient for a given radionuclide (md$^{-1}$) and $V_w$ is the wet deposition coefficient for a given radionuclide (md$^{-1}$).

### 2.5 Calculation of External Doses from Airborne Radionuclide

The annual effective dose from immersion in the atmospheric discharge plume $E_{im}$ (Sv year$^{-1}$) is given by:

$$E_{im} = C_A D F_{im} O_f \tag{3}$$

where $DF_{im}$ is the effective dose coefficient for immersion (Sv year$^{-1}$ per Bqm$^{-1}$) and $O_f$ is the fraction of the year for which the public is exposed to this particular pathway, assuming the public only exposed to this particular pathway during RTP operation time, $O_f$ will be given by RTP operation time in hour per 8760 hours.

### 2.6 Calculation of External Doses from Deposited Activity

The annual effective dose from ground deposition $E_{gr}$ (Sv year$^{-1}$) is given by:

$$E_{gr} = C_{gr} DF_{gr} O_f \tag{4}$$

where $DF_{gr}$ is the dose coefficient for exposure to ground deposits (Sv year$^{-1}$ per Bqm$^{-2}$) and $C_{gr}$ is the deposition density of radionuclide i (Bqm$^{-2}$). $C_{gr}$ is obtained according to the equation:

$$C_{gr} = \frac{d_i[1 - e^{-\lambda_{E_i^s} t_b}]}{\lambda_{E_i^s}} \tag{5}$$

where $\lambda_{E_i^s}$ is the effective rate constant for reduction of the activity in the top 10 to 20 cm of soil (d$^{-1}$), where $\lambda_{E_i^s} = \lambda_i + \lambda_s$, $\lambda_s$ is the rate constant for reduction of soil activity owing to processes other than radioactive decay, $\lambda_i$ is the decay constants of radionuclide I and $t_b$ is refers to a 30 years exposure period (d).

### 2.7 Calculation of Internal Doses due to Intake by Inhalation

The annual effective dose from inhalation $E_{inh}$ (Sv year$^{-1}$) is given by:

$$E_{inh} = C_A R_{inh} DF_{inh} \tag{6}$$

where $R_{inh}$ is the inhalation rate (m$^3$year$^{-1}$), $DF_{inh}$ is the inhalation dose coefficient (SvBq$^{-1}$).

### 2.8 Estimation of Collective Dose

The collective dose is then estimated by summation of $E_{im}$, $E_{gr}$ and $E_{inh}$ of all radionuclide.

## 3 Data/Results

The result show that the estimated collective dose to the public is ranged in between 0.17 to 1.39 $\mu$Sv in 2023. Figure 1 shows the collective dose estimated for each selected assess location around RTP Nuklear Malaysia.

## 4 Conclusions

This study successfully estimated the collective dose of the public resulting from the discharge of radioactive substances into the environment by Nuklear Malaysia RTP in 2023. Utilizing the IAEA generic model, the results indicated that the collective dose to the public ranged between 0.17 and 1.39 $\mu$Sv. These findings underscore the importance of continuous monitoring and adherence to safety standards to minimize the radiological impact on surrounding communities and the environment.

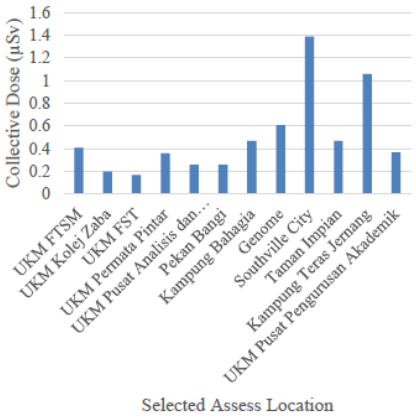



Figure 1: Estimated collective dose for each selected assess location around RTP Nuklear Malaysia

## References

IAEA. 2001. Generic models for use in assessing the impact of discharges of radioactive substances to the environment. Safety Report Series No. 19.

Karoplina Stark, José M. Goméz-Ros, Jordi Vives i Batlle, Elisabeth Lindbo Hansen, Karine Beaugelin-Seiller, Lawrence A. Kapustka, Michael D. Wood, Clare Bradshaw, Almudena Real, Corynne McGuire, and Thomas G. Hinton. 2017. Dose assessment in environmental radiological protection: State of the art and perspectives. *Journal of Environmental Radioactivity*, 175–176:105–114.

Individual Research Contribution Review, 2024: 197–198
*ISSN: 3083-922X*

# Radiofrequency Electromagnetic Field (RF- EMF) Exposure Assessment For Occupational Workers of Telco Industry in Malaysia

**Roha Binti Tukimin**
Radiation Health and Safety Division, Malaysian Nuclear Agency
43000 Kajang, Selangor
roha@nm.gov.my

## Abstract

Workers in telecommunication industry, whom are frequently involved in radiocommunication infrastructure (RCI) erection, installation of equipment, servicing and maintenance, are exposed to radio frequency electromagnetic field (RF-EMF) while working. Due to this concern, safety measurement and assessment of the RF-EMF exposure level is vital to ensure that the RF-EMF exposure for occupational workers in telecommunication industry in Malaysia is in accordance to permissible exposure limit (PEL) established by the regulator. The main objective of this project is to assess and measure the RF-EMF emission level for occupational workers environment at twenty RCIs in Malaysia. The key outcome of the project is a baseline data of RF-EMF exposure level for occupational workers in telecommunication industry in Malaysia. The study for occupational RF-EMF exposure were conducted at twenty (20) selected RCI in Klang Valey, Penang, Perak and Johor. The RCIs were selected with various characteristics taken into consideration, which include different morphologies, types of physical structure, and different equipment load from various network service providers (NSP) and network facility provider (NFP). The measurement results shows that workers are exposed to significantly high level of RF-EMF above PEL when working right in front of an actively radiating antenna which is in the near-field region. In some cases, this can exceed ten times of the occupational PEL. For workers working further away from the actively radiating antenna, which is in the far-field region, the measured RF-EMF levels were mostly lower than the PEL. This will be used as reference to propose a framework for occupational safety RF-EMF exposure compliance guideline for telecommunication industry in Malaysia.

**Keywords:** RF-EMF , Occupational, Permissible Exposure limit (PEL)

## 1 Introduction

Workers in telecommunication industry, whom are frequently involved in radiocommunication infrastructure (RCI) erection, installation of equipment (e.g., antenna and radio), servicing and maintenance, are exposed to radio frequency electromagnetic field (RF EMF) while working. This scenario has triggered occupational and general public fear, especially on the long-term health effects for those working and living in the vicinity of RCIs. Owing to this concern, safety measurement and assessment of the RF-EMF exposure level is vital to ensure that the RF-EMF exposure for occupational workers in telecommunication industry in Malaysia is in accordance to permissible exposure limit (PEL) established by the industry regulator. Malaysian Communications and Multimedia Commission (MCMC) has recently determined a mandatory standard entitled "Commission Determination on the Mandatory Standard for Electromagnetic Field Emission from Radiocommunications Infrastructure" to regulate the RF-EMF emission limit from RCI.

## 2 Methods

This study has been included of near-field and far-field occupational RF-EMF exposure for RF and non-RF workers scenarios through on-site measurement campaign at twenty (20) selected RCI in Klang Valey, Penang, Perak and Johor. The RCIs were selected with various characteristics taken into consideration, which include different morphologies, types of physical structure, and different equipment load from various network service providers (NSP) and network facility provider (NFP). The measurement procedure adopted in this project in accordance with the Technical Code for Prediction and Measurement of RF- EMF Exposure from Base Station –MCMC MTFSB TC G032:2021. Measurement has been conducted and recorded for 6 minutes by using broadband and selective spectrum analyser with appropriate probe (according to frequency used by each service provider); m. Results obtained during the measurement process will be recorded in E-field strength (V/m), power density ($\mu$Watts) and H-field strength (A/m). n. Data analysis will be separately conducted for broadband and narrowband measurement equipment (Figure 1).

This study is focused on near-field and far-field RF-EMF exposure level for occupational workers around the selected RCIs. In order to get real exposure for workers who are working very close to the telecommunication equipment as depicted in Figure 2, measurements were carried out in close proximity to the RF-EMF transmitter source, replicating the typical working scenario for workers who are doing the installation, servicing and maintenance jobs at RCIs. In addition, the far-field exposure for non-RF workers (e.g., air-condition system maintenance worker, cleaners, etc) working around the



Figure 1: Measurement equipment for occupational RF-EMF exposure

RCIs were also assessed.



Figure 2: Example of position for occupational exposure measurement

The measurement were carried very close to the antenna and other equipment, which sometimes we were using sky-lift and also climbed the RCI structure.

Table 1: Types and distribution of the 20 selected RCI sites

| No. | Type of RCI Structure | Rural | Suburban | Urban |
|---|---|---|---|---|
| 1. | Rooftop | | 2 sites<br>• Bkt. Bendera Carpark, Penang<br>• Bkt. Bendera Upper Station, Penang | 3 sites<br>• Amazing Height Apartment, Klang<br>• Puncak Hijauan Condominium, Bangi<br>• Simfoni Apartment, Eco Majestic, Semenyih |
| 2. | Mono-pole | | 1 site<br>• Hospital Sg. Siput, Perak | 1 site<br>• Design Village, Penang |
| 3. | Smart -pole | | 1 site<br>• Tmn. Pelangi, Johor | 4 sites<br>• Jln. Permata, Subang<br>• Jln. Delima, Subang Hi-Tech<br>• Bandar Rimbayu, Selangor<br>• Jln. Kelawai, Penang |
| 4. | Three-legged tower | 1 site<br>• Kg. Ulu Chepor, Chemor, Perak | 1 site<br>• Tmn. Nusa Bayu, Johor | 1 site<br>• Bayan Bay, Sg. Nibong Highway, Penang |
| 5. | Four- legged tower | | 1 site<br>• Tmn. Jesselton, Penang | - |
| 6. | Billboard | | | 1 site<br>• Marina Island, Lumut, Perak |
| 7. | Minaret | 1 site<br>• Tmn. Klebang Jaya, Perak | 1 site<br>• Masjid Tmn. Bukit Mutiara, Johor | |
| 8. | Water Tank | | 1 site<br>• Jln. Jagong, Tmn Uda, Johor | |
| | **Total** | **2 sites** | **8 sites** | **10 sites** |

The distribution of the samples are including 20 selected RCI located in Perak, Johor, Penang and Selangor. It was particularly in Urban, Sub-urban and rural area. It also considered eight of RCI structure namely rooftop, mono-pole, smart-pole, three and four – legged structure, billboard, minaret and water tank.

## 3 Permissible exposure limit (PEL)

The PEL values stipulated in the MCMC Mandatory Standard and the ICNIRP guideline are adopted in this project, as shown in Table 2.

M is frequency in MHz. while N/A signifies not applicable and does not need to be taken into account when determining compliance. Permissible Exposure Limit (PEL) calculation for shared sites is determined by using the lowest frequency used by the shared service provider.

Table 2: PEL for occupational workers (100kHz – 300GHz)

| Exposure scenario | Frequency range | Incident E-field strength, $E_{inc}$ (V m$^{-1}$) | Incident H-field strength, $H_{inc}$ (A m$^{-1}$) | Incident power density, $S_{inc}$ (W m$^{-2}$) |
|---|---|---|---|---|
| Occupational workers | 0.1 MHz - 30 MHz | $660/f_M^{0.7}$ | $4.9/f_M$ | N/A |
| | > 30 MHz - 400 MHz | 61 | 0.16 | 10 |
| | > 400 MHz - 2 000 MHz | $3\ f_M^{0.5}$ | $0.008\ f_M^{0.5}$ | $f_M/40$ |
| | > 2 GHz - 300 GHz | N/A | N/A | 50 |

## 4 Results and discussion

The measured RF-EMF exposure level right in front of actively radiating antennas were significantly higher than the PEL for occupational workers as listed in MS for EMF and ICNIRP guidelines. In this region, the workers will be in the near-field region of the radiating antennas. The measured RF-EMF exposure level right at the back of actively radiating antennas were below the PEL for occupational workers as listed in MS for EMF and ICNIRP guidelines. In this region, the workers will be in the near field region of the radiating antenna, but the majority of the RF-EMF energy from the antenna will be radiated away from the workers whom are working at the back of the radiating antennas. For short distance (i.e., 1 to 2 meters) away from the actively radiating antennas, e.g., at the middle of smart pole where utility lighting is installed, the RF workers or non-RF workers will be in the far field region of the radiating antennas. In this region, the RF-EMF exposure level dropped significantly below PEL in most measurement cases. For distance further (i.e., above 4 meters) away from the actively radiating antennas, the typical RF workers or non-RF workers will be in the far field region of the radiating antennas, and can be assessed as non-RF workers or general public accessible areas. In this region, the RF-EMF exposure level were far below PEL in all measurement cases.

## 5 Conclusion

RF-EMF exposure level right in front of actively radiating antennas were significantly higher than the PEL for occupational workers while; RF-EMF exposure level right at the back of actively radiating antennas were below the PEL for occupational workers.

## References

ICNIRP. 2020. Guidelines for limiting exposure to electromagnetic fields (100khz to 300 ghz). 118(5):483–524.

MCMC. 2017. MCMC(T)13-TDD/170/001 Jld.1 (02); 2017 Guideline on the mandatory standard for electromagnetic field emission from radio communications infrastructure.

MCMC. 2021a. MCMC Mandatory standards for electromagnetic field emission for radio communications infrastructure. Determination No. 5 of 2021.

MCMC. 2021b. Technical code for prediction and measurement of RF- EMF exposure from base station. MCMC MTFSB TC G032:2021.

Individual Research Contribution Review, 2024: 199–200
*ISSN: 3083-922X*

# Performance Characteristics of Nanodot Optically Stimulated Luminescence Dosimeter (OSLD)

**Rozaimah Binti Abdul Rahim**
Radiation Health and Safety Division, Malaysian Nuclear Agency
43000 Kajang, Selangor
rozaimah@nm.gov.my

## Abstract

This study explores the performance characteristics of Nanodot Optically Stimulated Luminescence Dosimeters (OSLDs) in monitoring radiation exposure, focusing on their linearity and energy response under varying conditions of X-rays and gamma radiation. The objective is to ensuring their effectiveness for accurate dose measurement, which is crucial for enhancing radiation safety. The study concludes that nanodot OSLD exhibit excellent linearity ($R = 1$) and a robust energy response with normalized readings closely aligning with ideal standards. In conclusion, the findings suggest that nanodot OSLDs can significantly enhance radiation safety protocols in medical, industrial, and environmental settings. This research can provide an alternative to other older dosimetry system for radiation protection and monitoring.

**Keywords:** linearity, energy response, dose accuracy

## 1 Introduction

OSLD is the most widely used material in dosimetry. Meanwhile, the OSLD OSLD nanodots has a great potential to be used in clinical dosimetry because of its prevailing advantages in both handling and application. OSLD nanodots (Landauer, Glenwood, Illinois, USA), consisting of aluminium oxide doped with carbon (Al2O3:C) with sensitive material placed in a plastic disk. The dimension of the plastic disk is 10 × 10 × 2 mm thickness. Their compact size and lightweight make them suitable to use in small spot area. OSLD nanodots was found to be a very good dosimeter for point dose measurements (Journal of Physics: Conference Series 2021). The effectiveness of nanodot OSLDs for dose measurement can only be ensured if the performance and characteristics of the dosimeters are appropriate.

The objective of this study is to evaluate the performance of OSLD nanodots using diagnostic X-rays and high-energy photons such as those emitted by Cesium-137 (Cs-137). The aspects that are being studies were the energy response and the dose accuracy. Result will analysed using microStar reader (Landauer, Inc., Glenwood, IL).

## 2 Methods

### 2.1 Dose Linearity for Cs-137

Linearity test utilized five different delivered doses, specifically on 1, 5, 10, 20 and 50 mGy. For each delivered dose, three nanodot OSLDs were irradiated, and the average reading was utilized. For specific dose, half-life of Cs-137 and kerma rate were measured. From latest rate of delivered dose, the irradiation time can be calculated using this formula:

$$K_{latest} = K_{old} \times \frac{e^{(-\ln 2 \times \Delta \text{ days})}}{t_{1/2}} \quad (1)$$

From latest rate of delivered dose, $K_{del}$, the irradiation time can be calculated using the formula:

$$t(min) = \frac{K_{del}}{K_{latest}} \quad (2)$$

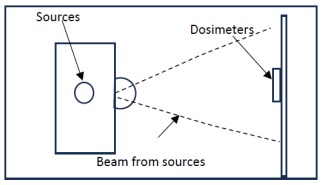



Figure 1: Illustrates the schematic diagram for the setup of this experiment

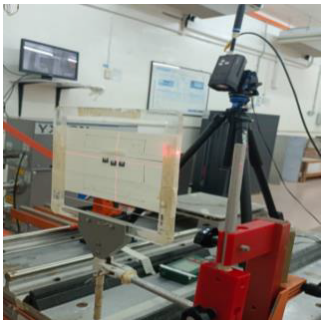


Figure 2: Setup of experiment

### 2.2 Energy Response

The delivered dose Kdel for this fixed at 1.5mGy. Nanodot OSLDs were irradiated using X-ray or gamma radiation machine to delivered 1.5mGy dose. Eight(8) photon energies 40, 50, 60, 70, 100, 150, 662(Cs-137) and 1250(Co-60) keV were utilized. Three nanodot OSLDs were irradiated, and the average reading was utilized. The distance between the source and dosimeter was 1 meter except 0.5 meter for Co-60. After irradiation process, all dosimeters need to store for 24 hours.

This process to ensure electron trapping process to be stabilized and the Nanodot OSLDs were analysed using MicroStar InLight reader.

## 3 Result and Discussion

### 3.1 Dose Linearity for Cs-137

A graph of measured dose against delivered dose was plotted to determine the linearity characteristic of nanodot OSLDs. Linearity was defined as the amount of deviation of an instrument from its own ideal straight-lined performance (Amdan, 2014). Figure 3 clarifies the relationship between measured dose and delivered dose. Nanodot OSLDs response was found to be in linear in the entire dose range. The linear fit of the measured dose and the delivered dose and demonstrated a good linearity with linear regression coefficient, $R^2$ were equal to 1.

Figure 4 shown a trumpet graph of ratio for against $K_{del}$ was plotted to show the yielding ratio, *R(K)* with the ICRP's upper and lower limits for Cs-137. All the values of the ratio, *R* lie within the limited for delivered dose $K_{del}$. All readings obtained from OSL dosimeter comply with the trumpet acceptance limit curve.

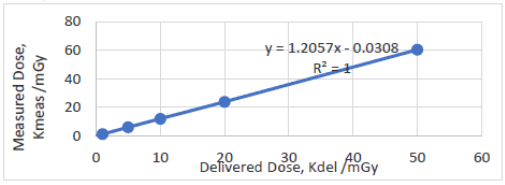



Figure 3: Graph of Measured Dose, $K_{meas}$ against Delivered Dose, $K_{del}$ for Cs-137

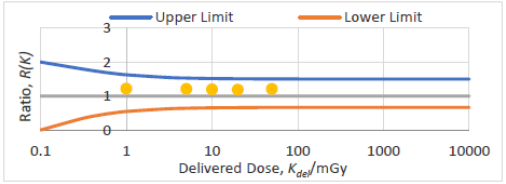



Figure 4: Trumpet curve of Ratio Kerma, *R(K)* against delivered dose, $K_{del}$ for Cs-137

### 3.2 Energy response

Energy response was defined as the variation of response that depends on the energy range that requires correction. Based on the graph of energy response, the curve will give information about the performance of the nanodot OSLDs whether it is close to ideal case or not. For energy response graph, ideally, the response must be flat as dosimeters should be independent of energy for a certain range quality (Abdul Karim et al., 2021).

However, in Figure 5, the curves were slightly over response which indicates that the nanodot OSLDs might have minor error in dose measurement. This might be caused by overused of nanodot OSLDs. The inconsistent of the curve also caused by the charges for each energy. This affected the air kerma rate which also influenced the time for nanodot OSLDs exposed for irradiation. Therefore, nanodot OSLDs signal released were low in certain photon energies.

In Figure 6, there were eight points of ratio, *R(K)*. It can be seen that all eight points lie within the trumpet curve. This means all of them showed a good degree of agreement as they cluster within the trumpet curve.

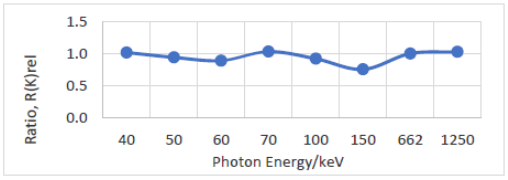



Figure 5: $R(K)_{rel}$ against Photon Energy, E

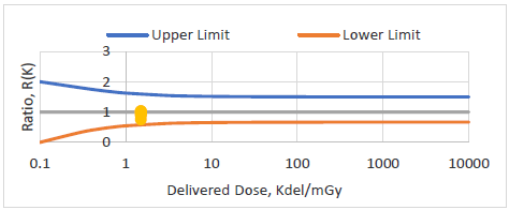



Figure 6: Trumpet curve of Ratio Kerma, *R(K)* against delivered dose, $K_{del}$ for energy response

Table 1 shown a percentage deviation subjected 662 keV. The percentage deviation $R(K)_{rel}$ for Nanodot OSLDs was found to be below 5%.

Table 1: $R(K)_{rel}$ normalized to 662 keV and percentage deviation

| Source/ keV | < Measured dose > (mGy) | Average measured dose (mGy) | $R(K)_{std}$ = Dose meas/ Dose delivered | $R(K)_{rel}$ |
|---|---|---|---|---|
| 40 | 1.846 | 1.231 | 1.016 | |
| 50 | 1.782 | 1.188 | 0.980 | |
| 60 | 1.619 | 1.079 | 0.891 | |
| 70 | 1.871 | 1.248 | 1.030 | |
| 100 | 1.672 | 1.115 | 0.920 | |
| 150 | 1.371 | 0.914 | 0.755 | |
| 662 | 1.817 | 1.212 | 1.000 | |
| 1250 | 1.880 | 1.253 | 1.034 | |

## 4 Conclusion

In conclusion, these findings can contribute to the establishment of updated standards for radiation exposure monitoring in clinical environments. Nanodot OSLDs was found to be a very good candidate for point dose measurements. This is an indication that nanodot OSLDs could be utilized for point dose measurement with an accuracy over a period of time. The study should improve experiment for energy dependence by using new nanodot OSLDs rather than overused of nanodot OSLDs to avoid minor error in dose measurement.

## References

M. K. Abdul Karim, N. S. Mohd Haniff, A. B. Abdul Kadir, Kamal, and Y. Musa. 2021. Energy response, accuracy and linearity of Optically Stimulated Luminescence (OSL) dosimeters. *Physics and Technology in Medicine*, 2(1 & 2).

Individual Research Contribution Review, 2024: 201–202
*ISSN: 3083-922X*

# Navigating Laser Safety in Industrial and Medical Setting

**Shamesh Raj Parthasarathy**
Radiation Health and Safety Division, Malaysian Nuclear Agency
43000 Kajang, Selangor
shamesh@nm.gov.my

## Abstract

In both industrial and medical settings, Laser technology plays a crucial role in various applications. With these, ensuring the safety of personnel and patients are paramount when working with lasers. Each applications of lasers are very diversified and consequently their power and precision also pose unique safety challenges. Understanding and adhering to laser safety procedures are essential to prevent accidents and protect both individuals and surroundings. The paper describes the challenges faced by industrial and medical/healthcare personnel in ensuring laser safety. Among the important aspects that will be covered are the importance of ensuring a correct laser safety goggles or laser eye protection with the right Optical Density (OD) and the corresponding wavelength is worn. In addition, the classification of Laser Controlled Area (LCA) will be highlighted. Finally, the essential engineering and administrative control measures especially on the usage of Class 3B and Class 4 laser systems will be emphasized.

**Keywords:** Industrial Laser, Medical Laser, Laser Safety

## 1 Introduction

Lasers continue to shape our world, bridging medicine and industry. As technology evolves, we can expect even more exciting breakthroughs. Lasers play a crucial role in various industrial processes. Some of the key laser applications in industries are laser marking, engraving, surface texturing, and drilling. As for the medical field, lasers are utilized during various surgeries to cut, vaporize, or coagulate tissue. In addition, lasers correct refractive errors in vision by reshaping the cornea, allowing patients to reduce or eliminate their dependence on glasses or contact lenses. In summary, industrial and medical lasers offer versatility, precision, and improved patient outcomes across various specialties. Their continued development contributes to advancements in healthcare and numerous industries. The primary hazard from lasers is eye and skin exposure to the laser beam itself. The concentrated energy in a laser beam can cause permanent damage to the retina and cornea of the eye, including blindness, as well as potentially severe skin burns. Even relatively low-powered laser beams are hazardous to eye safety due to the eye's focusing geometry. In order to gauge the challenges faced by personnel directly dealing with lasers, a discussion session consisting of enquiries and investigations was conducted.

## 2 Methods

A discussion session comprising of an exchange of opinions on laser safety was implemented with key personnel, specifically the Safety Health Officers (SHO) and Laser operators. For this survey and investigation, a total of 20 personnel from different organizations consisting of industrial and medical field were enquired on the important aspects of laser safety. The purpose of the discussion was to identify risks and to improve laser safety protocols. The session was initiated with enquiring the relevant personnel about the classification of laser. Next, queries on the personal protective equipment (PPE) specifically on the correct usage and specifications of the laser safety glasses were asked. In terms of this stated query, the personnel were questioned on the method of choosing the right Optical Density (OD) number or designation for each laser safety glasses for the respective laser. In addition, the personnel were asked on the maintenance of the laser safety glasses. The third point of discussion was on the identification of Laser Controlled Area. The terms Maximum Permissible Exposure (MPE), Nominal Hazard Zone (NHZ) and Nominal Ocular Hazard Distance (NOHD) were also highlighted in this section. Finally, a debate on the usage of engineering control focusing on the laser protective barrier and laser safety window film was deliberated.

## 3 Results/Discussion

Based on first part of the discussion session, all personnel (20 participants) were able to identify the laser classes of the Laser that is being used in their respective field. The important fragment of this point of discussion was to clearly identify laser classification based on the potential hazards. The classification system ranges from Class 1 (safe) to Class 4 (high-risk) (ANSI, 2022). The brief overview of laser classification is as following:

1. Class 1: Safe under normal operating conditions; no risk of eye or skin damage.

2. Class 2: Low-power lasers (visible light) that pose minimal risk; blink reflex protects the eyes.

3. Class 3R: Low to moderate risk; avoid direct eye exposure.

4. Class 3B: Moderate to high risk; can cause eye and skin injuries.

5. Class 4: High-power lasers with severe risks; protective measures are essential.

For the second part, only 2 out of 20 participants (10%) were aware on the type of Optical Density (OD) number or designation for the laser safety glasses that is to be utilized during laser operations. Laser safety glasses play a critical role in protecting the eyes from harmful laser radiation. To ensure their effectiveness, it's vital to understand optical density (OD) and how it relates to laser safety. Optical density measures how much a lens or filter blocks light at a specific wavelength. OD quantifies the reduction in laser intensity (ANSI, 2022). For example, an OD of 2 attenuates the laser by a factor of 100 (102), and an OD of 3 attenuates the laser by a factor of 1000 (103), and so on. In addition, 10 out of 20 participants (50%) were alert on the proper maintenance and storage of the laser safety glasses. Laser eye protection should be visually inspected for defects prior to use. Laser safety goggles should be inspected to ensure that the head band is not permanently overstretched, the ventilation ports are intact, and for other obvious defects such as crack and pigment changes (Barat, 2019).

For the third point of discussion, only 4 out of 20 participants (20%) were able to correctly identify the Laser Controlled Area (LCA). An LCA refers to a designated space where laser operations occur, and safety requirements are strictly enforced. Safety measures within these controlled area help mitigate risks associated with laser use. Speaking about LCA, another important term is the Nominal Hazard Zone (NHZ). Nominal Hazard Zone (NHZ) refers to the space within which exposure to a direct, reflected, or scattered laser beam exceeds the Maximum Permissible Exposure (MPE). Mirrors, optics, and reflective materials in the beam path may result in diffuse or specular reflections in unintended directions (Barat, 2019).

For the fourth point of discussion, 15 out of 20 participants (75%) were well aware on the usage of proper engineering control when dealing with open beam laser. The discussed engineering control comprises of the usage of laser safety curtain, laser barrier and laser safety window film. Laser safety curtains serve as specialized barriers designed to shield individuals and surroundings from laser hazards, especially in areas where class 3B or higher lasers operate. Different lasers (wavelengths, power) demand specific curtain materials and installation. Laser safety window films are essential for protecting workers and equipment from laser glare. The films are chosen based on OD and wavelength. Laser safety curtains and laser safety window film are essential in any setting where lasers are used and this makes them indispensable in maintaining a safe and secure work environment (Shenkenberg, 2009).

## 4 Conclusions

In the intricate landscapes of industrial and medical settings, lasers illuminate the path toward progress. Based on the discussion session, main crucial elements on laser safety have been raised and discussed. An emphasis was given to four main essentials on laser safety, first on the awareness of OD calculations, next on the proper maintenance of the laser safety glasses. The third element is on the identification of LCA and the classification of NHZ. The final component is on the usage of engineering control especially during open beam laser operations. Raising awareness about laser safety is crucial to prevent accidents and protect both professionals and the public.

## References

American National Standards Institute ANSI. 2022. Safe use of lasers. ANSI Z136.1-2022.

K. Barat. 2019. Laser safety: Practical knowledge and solutions. *Institute of Physics Publishing*.

D.L. Shenkenberg. 2009. Making laser safety a priority. *Photonics Spectra*.

Individual Research Contribution Review, 2024: 203–204
*ISSN: 3083-922X*

# Occupational UVR Exposure: Case Study from A UV Disinfection System

**Shamesh Raj Parthasarathy**
Radiation Health and Safety Division, Malaysian Nuclear Agency
43000 Kajang, Selangor
shamesh@nm.gov.my

## Abstract

The paper highlights the UVR measurement conducted on the UV Disinfection System focusing on the UV intensity and the type of UV emitted from this system. The measurement was conducted in measuring the UV intensity in $\mu$W/cm$^2$ from UV lamp installed in the system from the surface up to 6 meters. The intensity was calculated according to distance to classify the safe zone while the system is operational. In addition, the maximum effective time was calculated in order to gauge the maximum number of seconds any personnel could operate this system at a very close distance. Finally, the safety control measures in terms of engineering, administrative and PPE will be emphasized.

**Keywords:** UV Disinfection system, UV Safety, UV Exposure, Control Measures

## 1 Introduction

UV radiation is known to cause adverse health effects that can manifest over both short and long term. UV radiation is absorbed in the skin and the adverse health effects are mostly confined to the skin and eyes. Protection against UVR emitted from artificial sources is generally straightforward where sources are used in a controlled work environment (on Non-Ionizing Radiation Protection in Collaboration with International Labour Organization and (WHO), 2007). A comprehensive analysis of the intensity of ultraviolet (UV) radiation from portable disinfectants could be of great interest to employees, especially for industries that frequently consume such devices.

## 2 Methods

The assessment on the level of UVR from the UV Disinfection unit was performed using the Spectrometer and UV Radiometers. The Spectrometer was used to measure the peak UV wavelength emitted from the UV Lamp, while the UV Radiometers were utilized to measure the UVR irradiance. The wavelength detected by the spectrometer is stored in the data logger, and the results from the UV Radiometers are stored in the device itself. The measurement of UV intensity was divided into 4 sections which are front, back, left and right. The measurement distance was recorded at the surface (0cm) up to 600 cm (6m) from each location. Each measurement was taken for an average of 1-2 minutes until the reading becomes stable (Gardner and Shama, 1999). The UVR strength level was recorded in microwatts per square centimetre ($\mu$W/cm$^2$). The method of measurement is as shown in Figure 1.

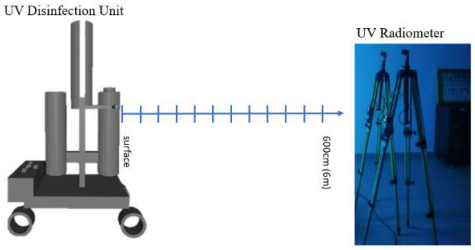



Figure 1: Method on the measurement of UV Intensity from the UV Disinfection Unit

## 3 Results/Discussion

Based on the wavelength measurement, 3 peaks were detected from the UV lamp of the UV Disinfection Unit, with the highest peak detected at the wavelength 254nm, which is in the region of UVC. Based on the measured data obtained during this assessment, the average irradiance of UVR from the UV lamp (UV disinfection unit) was found ranging from 0 microwatts per square centimetre ($\mu$W/cm$^2$) to 7,709 $\mu$W/cm$^2$ at the distance of 0cm (surface) to 600cm (6m). The highest averaged irradiance was detected at the front (location/facing) of the with the effective irradiance of 9.11 W/m$^2$. The effective irradiance (Eeff), is calculated in order to determine the permissible exposure duration (teff) in minutes and seconds for exposure to UVR incident upon the unprotected skin or eye (D'Orazio et al., 2013). Based on this effective irradiance, the maximum permissible exposure duration should not exceed 0.05 minutes or 3 seconds from this particular UV Disinfection unit location/facing. In addition, from the UVR safety assessment, it was found that the minimum distance from each side of the UV disinfection system where the irradiance drops to 0 $\mu$W/cm$^2$ is 600 cm or 6m. The permissible exposure duration is based on the effective irradiance in which it may be computed by dividing 30 J/m$^2$ by the value of Eeff in W/m$^2$ (on Non-Ionizing Radiation Protection (ICNIRP) Guideline, 2004). In the case where the effective irradiance (W/m$^2$) is at 0, then the permissible exposure duration is not applicable.

## 4 Conclusions

The highest averaged irradiance was detected at the front of the stated unit operating at UVC. The study also revealed differences in the UV intensity among the four sides of the device. These differences could be due to the design and installation of the UV lamps, as well as potential shadowing effects on the device structure. Based on the worst-case exposure, the minimum distance of any operators or users not wearing any Personal Protection Equipment (PPE) should at least be 600 cm (6m) away from this UV Disinfection System during operation. PPE in terms of full-face UV Shield and UV protection gloves should be worn if the operators or users are operating the stated Disinfection Unit directly (Lopes and McMahon, 2015).

## References

J. A. D'Orazio, S. G. Jarrett, A. Amaro-Ortiz, and T. Scott. 2013. UV radiation and the skin. *International Journal of Molecular Sciences*, 14(6):12222–12248.

D. W. M. Gardner and G. Shama. 1999. UV intensity measurement and modelling and disinfection performance prediction for irradiation of solid surfaces with UV light. *Food and Bioproducts Processing*, 77(3):232–242.

D. M. Lopes and S. B. McMahon. 2015. Ultraviolet radiation on the skin: A painful experience? *CNS Neuroscience and Therapeutics*, 22(2):118–126.

International Commission on Non-Ionizing Radiation Protection (ICNIRP) Guideline. 2004. Guidelines on limits of exposure to ultraviolet radiation of wavelengths between 180 nm and 400 nm (incoherent optical radiation). *Health Physics*, 87(2):171–186.

International Commission on Non-Ionizing Radiation Protection in Collaboration with International Labour Organization and World Health Organization (WHO). 2007. Protecting workers from ultraviolet radiation. *ICNIRP 14/2007*.

Individual Research Contribution Review, 2024: 205–206
*ISSN: 3083-922X*

# Roles of Radiation Protection Officer Malaysian Nuclear Agency in Supporting Global Radium-226 Management Initiative

**Suzilawati Muhd Sarowi**
Radiation Health and Safety Division, Malaysian Nuclear Agency
43000 Kajang, Selangor
suzie@nm.gov.my

## Abstract

Malaysian Nuclear Agency (Nuclear Malaysia) is an organisation consists of several nuclear facilities such as reactor, radiopharmaceutical laboratory, gamma greenhouse and electron beam. It is a leading agency in introducing and promoting the application of nuclear science technology and have various classes of license with our regulatory body. To ensure activities in the agency are comply with regulator requirements, Radiation Protection Officer (RPO) with secretariat assistance plays a critical role in ensuring safety and operational efficiency within the agency. This paper describes an involvement of RPO in supporting Global Radium-226 ($^{226}$Ra) Management Initiative which is received invitation to join by International Atomic Energy Agency (IAEA) in 2022.

**Keywords:** Role, Radiation Protection Officer, Regulatory compliance, Radium-226

## 1 Introduction

Nuclear Malaysia is a leading agency in introducing and promoting the application of nuclear science technology in Malaysia. It consists of several nuclear facilities such as reactor, radiopharmaceutical laboratory, gamma greenhouse, electron beam and serve as National Radioactive Waste Treatment Centre (WasTec). Numerous activities within the agency make Nuclear Malaysia as the biggest licensee by having various classes of license with our regulatory body. Realised that many member states including Malaysia have legacy stocks of Radium-226 ($^{226}$Ra) which may present a long-term management challenge for some of them. The IAEA understands this challenge presented by long-lived radionuclides and continues to seek suitable solutions for the stored legacy $^{226}$Ra. Conversely, the secretariat notes that several member states may have a use for such legacy $^{226}$Ra stocks, particularly, in the field of targeted alpha therapy in nuclear medicine. The treatment of cancer cells through the application of radiotracers with Actinium-225 shows very promising results and using $^{226}$Ra as a feedstock material is an effective production route for the Actinium. In light of the above, the Secretariat is coordinating an activity focussing on $^{226}$Ra recycling referred as the "Global Radium-226 Management Initiative". In the frame of this initiative a platform to facilitate information exchange between member states possessing legacy $^{226}$Ra sources and member states with capabilities and suitable recycling facilities has been established (IAEA, 2023) In Malaysia $^{226}$Ra were deposited in WasTec, Nuclear Malaysia. As $^{226}$Ra need a long term of storage, hazardous and can be use as a feedstock for recycling, proper management is needed (IAEA, 2018). This matter involves responsibility of the RPO which is cover the movement and registration of radioactive waste and Disused Sealed Radioactive Sources (DSRS). This task was carried out together with the Radioactive Waste Management Officer (RWMO).

## 2 Methods

The steps are describe below:

1. Determination of $^{226}$Ra inventory in WasTec, Nuclear Malaysia
2. Nuclear Malaysia agree to join the Global $^{226}$Ra Management Initiative in 2022
3. 1$^{st}$ Technical Meeting Global $^{226}$Ra Management Initiative in June, 2023.

## 3 Results

The legacy of $^{226}$Ra in the inventory (1984 -2017) are used in different applications namely conditioned stainless steels capsules and cemented in 2 drums radium needles for medicine, check sources, lightning arrester and smoke detectors. There are $^{226}$Ra in the WasTec, reported total activity are 1,962.52 mCi (S and M.Z, 2023) By the justification to remove liability and contribute to the public health globally. Nuclear Malaysia agree to join the Global $^{226}$Ra Management Initiative in 2022 and send out the legacy of $^{226}$Ra to recipient country with no additional course. The discussion online has made after the 1st Technical Meeting Global $^{226}$Ra Management Initiative in 2023 with the potential and interested company to receive the $^{226}$Ra. One company is really interested and have good reputation in recycling program was determined as the recipient.

## 4 Discussion

RPO has a responsible in this initiative as it will involve ensuring safety; dose monitoring not only to the workers but also the area of workplace as the radium needles has to be retrieve from the conditioned stainless steels capsules and cemented in 2 drums, repackaging, shipment and transportation between two different countries. Meeting with the regulator body was arranged then we learn that:

i. DSRS or waste is not allow to be ship; the $^{226}$Ra have to be register one by one as in used in the license

ii. Investigate carefully import and export requirements as it might be involved the transit so that aware and prepare on delay and denial issue.

iii. Ensure the safety of workers and workplace monitoring

Operation i-ii above has to be made through the e-license system to the regulator. This system only can be access and manage by the RPO and the secretariat. The involment of RPO in this project is very important.

## 5 Conclusion

Malaysia through Nuclear Malaysia are underway to provide a feedstock of $^{226}$Ra to the recipient country which has a capability to recycle the $^{226}$Ra for the use in nuclear medicine under the Global $^{226}$Ra Management Initiative. As $^{226}$Ra has very long half-life which is 1600 years, therefore it has to be managed properly and systematic. RPO have a responsible in ensuring safety and regulatory compliance. Key responsibilities include developing comprehensive radiation protection programs, implementing personal protective equipment protocols and maintaining rigorous documentation standards aligned with national and international regulatory frameworks.

## References

IAEA. 2018. Guidance on the management of disused radioactive sources, iaea, vienna.

Zakaria N. 2023. The role of international programmes for the effective management of disused sources during a technology transition. *IAEA slide presentation, Workshop on End-of-life Management In Support Of Radiological Security And Technology Transition, France*.

Muhd Sarowi S and Ibrahim M.Z. 2023. Management of radioactive sources in Malaysian Nuclear Agency. *Slide Presentation, Technical Meeting Global Radium-226 Management Initiative, Vienna.*

Individual Research Contribution Review, 2024: 207–208
*ISSN: 3083-922X*

# Occupational and Environmental Monitoring for Reactor TRIGA PUSPATI 2023

**Syed Asraf Fahlawi Wafa bin Syed Mohd Ghazi**
Radiation Health and Safety Division, Malaysian Nuclear Agency
43000 Kajang, Selangor
asraf@nm.gov.my

## Abstract

This paper presents a comprehensive analysis of both occupational radiation exposure and environmental monitoring conducted at the TRIGA PUSPATI reactor facility throughout 2023. The monitoring program encompassed two main components: internal radiological safety monitoring for facility staff and visitors, and environmental surveillance within a 25 km radius of the facility. Occupational exposure monitoring demonstrated all personnel remained well below annual dose limits, with a maximum individual dose of 0.70 mSv. Environmental sampling at eleven locations showed stable levels of natural and artificial radionuclides, with soil samples averaging 113.31 Bq/kg for $^{226}$Ra and 128.69 Bq/kg for $^{228}$Ra. Water samples consistently showed radionuclide levels below detection limits, while external radiation levels averaged 0.85 mSv/year within the facility complex. Facility monitoring recorded a maximum accumulated dose of 3.32 mSv in operational areas. These results confirm effective radiation protection measures and minimal environmental impact of facility operations.

**Keywords:** Radiation protection, environmental monitoring, occupational exposure, TRIGA reactor, dosimetry, radioactivity surveillance

## 1 Introduction

The comprehensive monitoring program at the TRIGA PUSPATI reactor facility serves dual purposes: ensuring occupational safety through personnel radiation monitoring and assessing environmental impact through systematic environmental surveillance. This integrated approach is crucial for maintaining regulatory compliance and public safety assurance. The program encompasses both internal facility monitoring and environmental sampling within a 25 km radius, providing a complete picture of the facility's radiological impact on both workers and the environment.

## 2 Methods

### 2.1 Occupational Exposure Monitoring

- **Personnel monitoring** using Optically Stimulated Luminescence (OSL) badges and Thermoluminescent Dosimeter (TLD) rings for staff
- **Pen dosimeters** for visitors and non-radiation workers
- **Continuous monitoring** at strategic locations within the facility across all levels

### 2.2 Environmental Surveillance

- Systematic sampling at eleven locations within 25 km radius
- Environmental media sampled:
  - Soil (collected at 5 cm depth using soil auger)
  - Sediment (obtained using sediment scoops)
  - Flora (harvested using cutting tools)
  - Water (direct transport to laboratory)
- Analysis of natural radionuclides ($^{226}$Ra, $^{228}$Ra) and artificial radionuclides ($^{137}$Cs)
- External radiation measurement using Optically Stimulated Luminescence Dosimeters (OSLD

## 3 Results

The analysis revealed that the levels of radioactivity in river water and pond water remained low and below detectable limits throughout the year. Specific findings included:

- **Soil Samples**: Average concentrations were 113.31 Bq/kg for $^{226}$Ra, 128.69 Bq/kg for $^{228}$Ra, and less than 1.00 Bq/kg for $^{137}$Cs.
- **Sediment Samples**: Similar trends were observed, with average values of 104.31 Bq/kg for $^{226}$Ra and 102.28 Bq/kg $^{228}$Ra.
- **Flora Samples**: Recorded average concentrations were lower than those in soil and sediment.
- **Water Samples**: All tested radionuclides were below the minimum detection limits.

External radiation levels measured within the Nuclear Malaysia complex averaged 0.85 mSv year, indicating no significant increase in radiation exposure attributable to agency activities.

For occupational exposure, monitoring results for 2023 at TRIGA PUSPATI reactor were within safety limits, with staff receiving a maximum dose of 0.70 mSv (well below the 20 mSv annual limit), facility areas showing highest reading of 3.32 mSv in the East Hall, and 199 visitors collectively receiving 0.67 mSv total exposure.

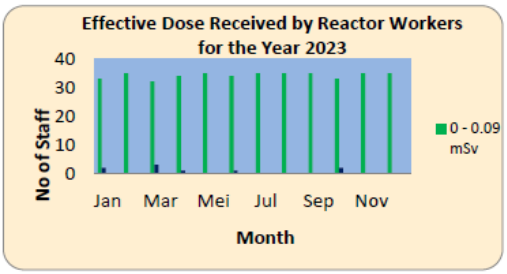



Figure 1: Dose received by reactor personnel

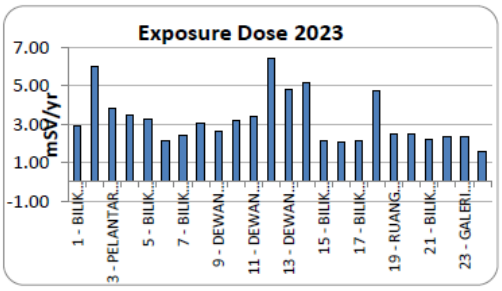



Figure 2: Radiation exposure at each location

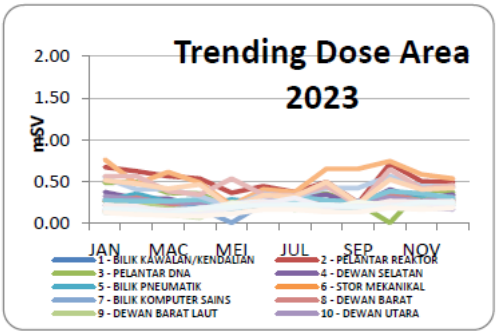



Figure 3: Trending radiation exposure at each location

## 4 Discussion

The monitoring results demonstrate consistent compliance with radiation protection standards across both occupational and environmental domains. Personnel doses remained well below the annual limit, with no staff member exceeding one-third of the annual dose limit. The historical comparison from 2013-2023 shows stable dose trends, with occasional variations remaining within acceptable ranges. Environmental monitoring results align with historical data, indicating no significant impact from facility operations on the surrounding environment. The comprehensive nature of the monitoring program, covering both occupational and environmental aspects, provides robust verification of the facility's safety measures.

## 5 Conclusion

The 2023 monitoring program demonstrates effective radiation protection at the TRIGA PUSPATI reactor facility, with all occupational exposures and environmental measurements well within regulatory limits. The dual approach of personnel monitoring and environmental surveillance provides comprehensive assurance of safety for both workers and the surrounding environment. The results support the conclusion that facility operations maintain appropriate radiation protection standards while having minimal environmental impact. Continued monitoring remains essential for maintaining these safety standards and public confidence in nuclear operations.

## References

Atomic Energy Licensing Regulations (Basic Radiation Protection) 2010 P.U.(A) 46.

IAEA. 2001. Generic models for use in accessing the impact of discharges of radioactive substances to environment. Safety Reports Series No.19, Vienna.

Individual Research Contribution Review, 2024: 209–210
*ISSN: 3083-922X*

# Radiation-Induced Bystander Effect: Molecular Mechanisms and Its Clinical Implications

**Tengku Ahbrizal Tengku Ahmad**
Radiation Health and Safety Division, Malaysian Nuclear Agency
43000 Kajang, Selangor
ahbrizal@nm.gov.my

## Abstract

For many years, DNA damage caused by direct exposure of cells to ionizing radiation has been considered the primary cause of various biological effects. However, various studies have shown that non-irradiated cells experience the same effects as irradiated cells. The radiation-induced bystander effect (RIBE) is a phenomenon in which non-irradiated cells respond to irradiation due to signals received from nearby irradiated cells. Understanding the mechanism of this bystander effect is important for basic biomedical research and clinical applications, to ensure the accuracy of cancer treatment and protection of normal cells in the patient's body.

**Keywords:** Ionizing radiation, soluble factors, GJIC, hypoxia

## 1 Introduction

responds only occur in irradiated cells, where DNA damage is the primary target of radiation caused by direct deposition of radiation energy. However, recent studies have shown that biological effects also occur in non-targeted cell or not directly exposed to ionizing radiation (IR). Radiation-induced bystander effect (RIBE), is a phenomenon in which irradiated cells signal their neighbours (non-irradiated cells) and induce a cellular response that resembles those of the irradiated cells. It was first described by Nagasawa and Little in 1992 and is considered an important phenomenon related to radioprotection, especially for cancer patients undergoing radiotherapy. This is because the location of normal cells surrounding the tumor area allows for a bystander response to be experienced by normal cells in the patient's body. Responses of non-irradiated cells include changes in gene/protein expression, cell proliferation, apoptosis and cell death. The complex cancer microenvironment not only induces multiple cellular defence pathways in irradiated cancer cells, but also influences the neighbouring non-irradiated cells. Therefore, it is important to understand the mechanisms behind RIBE induction, to achieve precise cancer treatment without affecting normal cells in the patient's body.

## 2 Mechanisms of Bystander Effects

There are two (2) basic mechanisms that may induce the bystander effect:(i) Gap junctional intercellular communications (GJIC) which allows physical contact between irradiated and non-irradiated cells, and generates intercellular communication between both cell types, and (ii) release of soluble signaling molecules from irradiated cells to non-irradiated cells which generates extracellular commination between cell types.

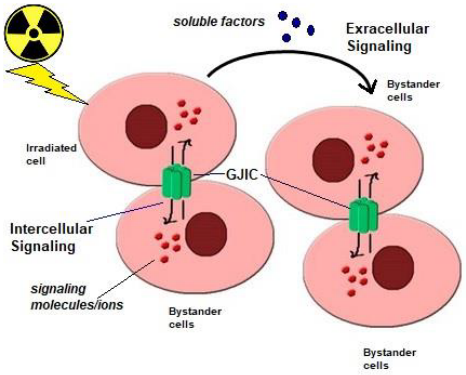



Figure 1: A modal of radiation induced bystander responses (RIBE)

GJIC is a unique structure in cell membranes that allows direct transfer of small molecules such as protein signaling molecules, ions and transmission of electrical impulses involved in metabolism and cell growth under normal conditions. Previous studies have shown that cell survival rates decrease due to the receipt of damage signals from irradiated cells. However, some studies showing that signal flow can occur in both directions by sending a survival signals to irradiated This situation may be one of the reasons why irradiated cells become resistant to IR and continue to grow. Meanwhile, the second bystander factor which is a soluble signaling molecules; reactive oxygen species (ROS) and secondary messengers such as nitric oxide (NO), protein kinases and cytokines such as TGF-$\beta$ and TNF-$\gamma$ have been identified to play an important role in induction of RIBE in different type of cells exposed to IR.

## 3 Bystander Effects Influence Cancer Treatment Accuracy

The main goal of radiotherapy is to eliminate cancer cells without affecting normal cells in the human body. However, previous studies have shown that genetic damage occurs due to factors released by the irradiated cells into the medium and not necessarily direct damage by the X-rays. This causes normal

cells around the cancer tumour to be damaged. The situation is more critical when most of the cancer cells are in a state of oxygen deprivation or called hypoxia. This condition occurs when cancer cells are far from blood vessels and located in the centre of the tumour. This condition affects the accuracy of cancer treatment, especially when using low-LET (linear energy transfer) such as photon radiation, where the main mechanism of damage is due to the presence of free radicals. Indirectly, this condition also affects the bystander effect on non-irradiated cancer cells, and it is possible that cancer cells may regrow and lead to secondary malignancy.

## 4 Conclusion

Understanding the mechanisms underlying the bystander effect is important in assessing radiation risk and protocols for cancer treatment using ionizing radiation. This understanding may also indirectly help in protecting normal cells in the human body.

## References

N. Autsavapromporn, C. Liu, A. Kobayashi, T.A.F. Tengku Ahmad, M. Oikawa, N. Dukaew, J. Wang, A. Wongnoppavich, and T. Konishi. 2018. Emerging role of secondary bystander effects induced by fractionated proton microbeam radiation. *Radiation Research*, 191. DOI: 10.1667/RR15155.1.

N. Autsavapromporn, A. Kobayashi, C. Liu, C. Jaikang, TAF. Tengku Ahmad, M. Oikawa, and T. Konishi. 2022. Hypoxia and proton microbeam: Role of gap junction intercellular communication in inducing bystander responses on human lung cancer cells and normal cells. *Radiat Res.*, doi: 10.1667/RADE-21-00112.1.

N. Autsavapromporn, A. Kobayashi, C. Liu, A. Duangya, M. Oikawa, T.A. Tengku Ahmad, and T. Konishi. 2023. Primary and secondary bystander effects of proton microbeam irradiation on human lung cancer cells under hypoxic conditions. Biol.12:1485. https://doi.org/10.3390/biology.

N. Autsavapromporn, T. Mamiya, A. Kobayashi, C. Liu, A. Duangya, TAF. Tengku Ahmad, M. Oikawa, and T. Konishi. 2024. Bystander effects on hypoxic cells exposed to FLASH irradiation using the SPICE-QST proton microbeams. *Int. J. Part. Ther.*, 12:100113. Proceedings to the 62nd Ann. Conf. Part. Ther. Coop. Group (PTCOG).

S. Desai, A. Kobayashi, T. Konishi, M. Oikawa, and B.N. Pandey. 2014. Damaging and protective bystander cross-talk between human lung cancer and normal cells after proton microbeam irradiation. *Mutation Research*, 763–764, 39–44.

A. Kobayashi, TAF. Tengku Ahmad, N. Autsavapromporn, M. Oikawa, S. Homma-Takeda, Y. Furusawa, J. Wang, and T. Konishi. 2017. Enhanced DNA double-strand break repair of microbeam targeted A549 lung carcinoma cells by adjacent Wi38 normal lung fibroblast cells via bidirectional signaling. *Mutat Res Fund Mol Mech Mutagen*, 803–805,1–8.

A. Kobayashi, N. Autsavapromporn, T. A. F. Tengku Ahmad, M. Oikawa, S. Homma-Takeda, Y. Furusawa, J. Wang, and T. Konishi. 2018. Bystander WI-38 cells modulate DNA double-strand break repair in microbeam-targeted A549 cells through gap junction intercellular communication. *Radiation Protection Dosimetry*, 1–5. DOI:10.1093/rpd/ncy249.

T. Konishi, A. Kobayashi, T. A. F. Tengku Ahmad, and J. Wang. 2018. Enhanced DNA double strand break repair triggered by microbeam irradiation induced cytoplasmic damage. *Journal of Radiation and Cancer Research*, 9(4):183–189. DOI: 10.4103/jrcr.jrcr_21_18.

M. Taisei, I. Qona'atun, TAF. Tengku Ahmad, N. Autsavapromporn, T. Kusumoto, R. Hirayama, S. Kodaira, K. Kurita, and T. Konishi. 2024. Cell killing effect of heavy ion track structure. *QST Annual Report 2024*, 21J347.

Individual Research Contribution Review, 2024: 211–212
*ISSN: 3083-922X*

# Study on the accuracy of optically stimulated luminescence dosimeter (OSLDs) dose measurement using MicroStar reader calibrated for low dose diagnostic range at Nuklear Malaysia

**Wan Hazlinda Binti Ismail**
Radiation Health and Safety Division, Malaysian Nuclear Agency
43000 Kajang, Selangor
linda@nm.gov.my

## Abstract

The MicroStar reader that were use to read the optically stimulated luminescence dosimeter (OSLDs) for diagnostic range are usually calibrates using the nanoDot kit 80 kV calibrated of dose range 0 mSv, 5 mSv, 30 mSv, 500 mSv, 1,000 mSv provided by the manufacture. This study investigates the accuracy of dose measurement using microstar reader calibrated for low dose diagnostic range of 0 mSv, 0.5 mSv, 1 mSv, 2 mSv to 30 mSv using RQR 6 beam quality established in Malaysian Nuclear Agency standard laboratory. The methodology involved 30 Landauer nanoDot$^{TM}$OSLDs exposed to RQR 6 beam quality of 80 kV with dose range from 0 mSv to 30 mSv to generate a linear calibration on two (2) MicroStar reader. Additional 36 nanoDot$^{TM}$OSLDs were used to measure dose output from various diagnostic modality of general x-ray, mobile C-arm, intra oral dental x-ray and digital mammography x-ray with tungsten target. Dose measured were from a single exposure and accumulated dose of 3 dan 5 exposures for dose linearity response. A calibrated solid-state dosimeter were use to measure the output dose and compared to the dose measured by the nanoDot$^{TM}$OSLDs. The results showed linear response for all measurement. However, the MicroStar reader (1) measurement displays a maximum 2% difference from the solid-states dosimeter output whereas MicroStar reader (2) measurement displays a maximum 4% difference from the solid-states dosimeter output. For accumulated dose measurement MicroStar reader (1) & MicroStar reader (2) measurement displays a maximum 8% and 9% difference from the solid-states dosimeter output respectively.

In conclusion, this study shows that the MicroStar readers calibrated for low dose diagnostic range accuracy are tolerable.

**Keywords:** Calibration, OSLDs, Microstar reader, Diagnostic modality, Diagnostic x-ray

## 1 Introduction

Optical simulated luminescent dosimeter (OSLD) were introduced in medical dosimetry as point based dosimeters and were commonly used for patient dose measurement in radiation therapy and then broaden the usage to diagnostic energy range. Over the years many studies have been made. In the early studies made by by Jursinic et al., the OSLD dosimeters shows high precision and accuracy in measuring dose in radiation therapy energy range and shows no energy. However, the study made by Al-Senan and Hatab, they found out that the OSLD dosimeters were energy dependence when using in diagnostic range and recommended to acquire correction factors. In recent study by Jeannie et al, they discussed the challenges of using OSLD in diagnostic range because of their energy dependence (ED) and variability of element sensitivity factor (ESF). In this study, they introduce ESF and ED correction to reduce the uncertainty of dose measurements in diagnostic range.

This study focuses on the calibration of the MicroStar reader that were used to read the optically stimulated luminescence dosimeter (OSLDs) for diagnostic range. Manufacture usually provide a nanoDot kit calibrated at 80 kV for dose range 0 mSv, 5 mSv, 30 mSv, 500 mSv, 1,000 mSv to calibrate the user MicroStar reade. However, this study investigates the accuracy of dose measurement using microstar reader calibrated for low dose diagnostic range of 0 mSv, 0.5 mSv, 1 mSv, 2 mSv to 30 mSv using RQR 6 (80kV) beam quality established in Malaysian Nuclear Agency standard laboratory.

## 2 Methods

30 Landauer nanoDot$^{TM}$OSLDs exposed to RQR 6 beam quality of 80 kV established in Nuklear Malaysia Standard calibration laboratory with dose range of 0, 0.5, 1, 2,5, 8,10, 15, 20 and 30 mSv (as shown in Figure 1) to generate a linear calibration curve on two (2) MicroStar reader at SSDL.

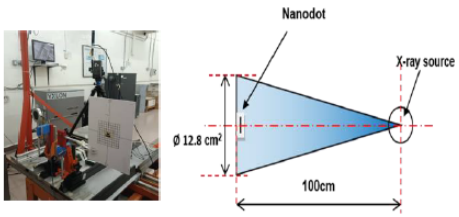



Figure 1: Calibration Set-up using Beam Quality: RQR 6 (80 kV) of total Filtration: 3.2 mm Al (HVL: 3.07 mmAl)

Additional 36 nanoDot$^{TM}$OSLDs were used to measure dose output from various diagnostic modality of general x-ray, mobile C-arm, intra oral dental x-ray and digital mammography x-ray with tungsten target. Dose measured were

from a single exposure and accumulated dose of 3 dan 5 exposures for dose linearity response. A calibrated solid-state dosimeter RTI Piranha 657 with probe were use to measure the output dose and compared to the dose measured by the nanoDot$^{TM}$OSLDs.

## 3 Data/Results

The calibration response curve obtained was a linear curve as shown in Figure 2 was use to calibrate the MicroStar readers with $R^2$ of 0.9998.

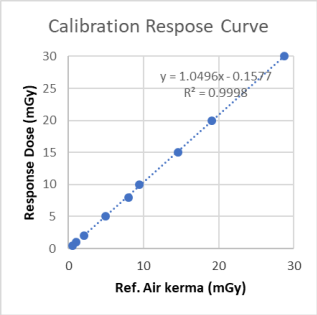



Figure 2: calibration response curve

Table 1 shows the result of the dose measurement for various diagnostic modality of general X-ray machine and dental X-ray machine. The MicroStar reader (1) and (2) measurement displays a maximum 2% difference from the solid-states dosimeter output for these two modalities. For accumulated dose of 5 times exposure record a maximum difference of 2%.

Table 1: The difference between between nanoDot$^{TM}$OSLDs t output measurement from the solid-states dosimeter output for General X-ray system and Intra Oral X-ray unit

| No. of Exposure | TYPE | General x-ray | Dental |
|---|---|---|---|
| | MODEL | Toshiba DRX-3724HD | Extend Myray |
| | HVL | 3.0 mmAl | 1.97mmAl |
| | Potential Energy | 80 kV | 70 kV |
| | Dose Range (mGy) | 1.6 - 8.0 | 0.5 - 2.6 |
| 1 | Reader 1 | 0% | 2% |
| | Reader 2 | 2% | 1% |
| 3 | Reader 1 | 0% | 1% |
| | Reader 2 | 2% | 1% |
| 5 | Reader 1 | 2% | 1% |
| | Reader 2 | 2% | 0% |

Table 2 shows the result of the dose measurement for for a C-Arm X-ray system and full-field digital mammography X-ray unit. For C-Arm system the dose measurement between MicroStar reader (1) and (2) measurement displays a maximum 3% difference from the solid-states dosimeter output for a single dose however for accumulated dose the difference increases significantly for reader (2), whilst for reader (1) only shows a slight increase. For the full-field digital mammography X-ray dose measurement the dose measurement between

Table 2: The difference between between nanoDot$^{TM}$OSLDs output measurement from the solid-states dosimeter output for a C-Arm X-ray system and full-field digital mammography X-ray unit.

| No. of Exposure | TYPE | C-Arm | Mammo |
|---|---|---|---|
| | MODEL | Toshiba 5XG-1000A | Hologic Selenia Dimensions |
| | HVL | 2.84mmAl | 0.610mmAl |
| | Potential Energy | 80 kV | 39 kV |
| | Dose Range (mGy) | 2.3 - 11.6 | 3.1 - 15.9 |
| 1 | Reader 1 | 3% | 4% |
| | Reader 2 | 2% | 2% |
| 3 | Reader 1 | 5% | 5% |
| | Reader 2 | 9% | 7% |
| 5 | Reader 1 | 3% | 0% |
| | Reader 2 | 8% | 3% |

MicroStar reader (1) and (2) measurement displays a maximum 4% difference from the solid-states dosimeter output from a single exposure and both reader measurement varies from accumulated dose measurement.

## 4 Discussion/Conclusions

From the results obtained in this study shows that the MicroStar readers calibrated for low dose diagnostic range accuracy are below 10% calibrated with the nanodot calibration kit provided by Nuklear Malaysia. This study did not consider any correction for the measurement. Either with energy dependence correction factor or the element sensitivity factor (ESF) was considered as recommended by Jeannie et al. Introducing the correction factors may reduce the uncertainty of measurement accuracy. In conclusion, further investigation should be carried out for this study and consideration of the correction factors should be included. However, from this study shows that the MicroStar readers calibrated for low dose diagnostic range accuracy are tolerable.

## References

Jursinic PA. 2007. Characterization of optically stimulated luminescent dosimeters, OSLDs, for clinical dosimetric measurements. *Med Phys*, 34(12):4594–4604.

Al-Senan RM and Hatab MR. 2011. Characteristics of an OSLD in the diagnostic energy range. *Med Phys*, 38(7):4396–4405.

Jeannie Hsiu Ding Wong and Wan Hazlinda Ismail. 2024. Addressing challenges in diagnostic x-ray dosimetry: Uncertainties and corrections for Al2O3:C-based optically stimulated luminescent dosimeters. *Journal of the Australasian College of Physical and Science*, Volume 47:821–832.

Clifford J. Yahnke. June 10, 2009. Landauer microstar inlight system, Calibrating the microstar. Rev. 2.

Individual Research Contribution Review, 2024: 213–214
*ISSN: 3083-922X*

# Study on the Irradiance Level of Ultraviolet (UV) Radiation from Environment

**Wan Syazlin Wan Yunoh**
Radiation Health and Safety Division, Malaysian Nuclear Agency
43000 Kajang, Selangor
wan_syazlin@nm.gov.my

## Abstract

Ultraviolet (UV) radiation is found almost everywhere in the environment. The source of UV radiation could be artificial or natural and the strongest source of UV radiation in the environment is the sun. UV radiation has been classified as an established human carcinogen. The well-known effect from the UV radiation is sunburn and many other health effects towards skin and eyes. It is important to know the irradiance level and the UV Index of UV radiation from the sun to manage our daily activity to avoid any excessive exposure toward the sun. According to Malaysian Meteorological Department, UVA and about 10atmosphere. The measurement in this study was conducted using spectrometer and radiometer. Radiometer device can measure which type of UV radiation had passed through. The parameter involved in this study are irradiance, wavelength and time at selected location. The irradiance measured from the study was compared with the permissible exposure limit to the members of public by International Commission on Non Ionizing Radiation Protection (ICNIRP). Based on the data collected from this study, a further study on UV radiation from the environment will be recommend.

**Keywords:** UV, Exposure Limit, Radiation Safety, Environment

## 1 Introduction

We should aware on the health effect from the UV radiation because this type of radiation just located next to x-ray in the electromagnetic spectrum. Besides that, it is not possible to protect ourselves totally from UV radiation exposure because the main source is from the sun. Preventative method from over exposure to the sun should be taken especially for those having special condition of skin and eyes. Therefore, it is important to conduct a study on the level of UV radiation in the environment and came out with recommendation for public safety. This study is a preliminary study and should be continue for further study on the level of radiation from the environment. The objective of this study were to study the type of UV radiation from the sun that passed through to the atmosphere and to analyse the irradiance level of the UV radiation from the sun and compare with exposure limit from the International Commission on Non-Ionising Radiation Protection (ICNIRP) guidelines.

## 2 Methods

Five location was selected at Putrajaya based on the availability of space to conduct the measurement. All selected location was public attraction place. The types of equipment used in this study are given in Table 1 and Figure 1.

Table 1: Type of equipment used in the study

| **Equipment** | **2020 Detection range (nm)** |
|---|---|
| Radiometer GenUV 1 | 220 – 280 (UVC) |
| Radiometer GenUV 2 | 250 (UVC) |
| Radiometer GenUV 3 | 230 – 395 (UVA) |
| Radiometer GenUV 4 | 220 – 320 (UVB) |
| Avantes Spectrometer | 200 - 1100 |



Figure 1: Measurement Equipment

The spectrum of UV radiation was capture by using the Avantes Spectrometer at four interval time. The irradiance level was measured using 5 types of equipment stated in Table 1. Avantes Spectrometer able to capture the spectrum and the irradiance level. The measurement was conducted from 9:30 am until 12:30 pm with 15 minutes interval. All measured UV radiations were assessed and evaluated against the exposure limits based on the guideline by ICNIRP. The duration to record the data from the 5 equipment was in 10 seconds. Therefore, the duration of 10 seconds as the value to compare with the exposure limit of UV radiation.

## 3 Data/Result

The level of irradiance and spectrum of UV radiation at 5 locations was plotted in Figure 2 to Figure 6.

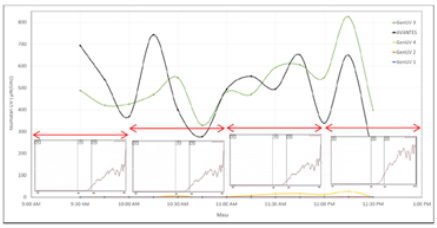


Figure 2: A plot of Irradiance of UV Radiation against time and the spectrum of UV radiation at Taman Saujana Hijau

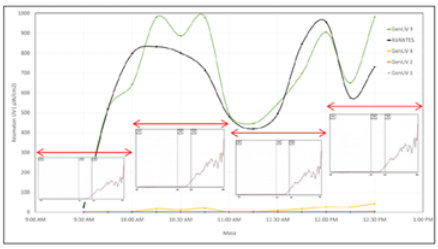


Figure 3: A plot of Irradiance of UV Radiation against time and the spectrum of UV radiation at Medan Selera

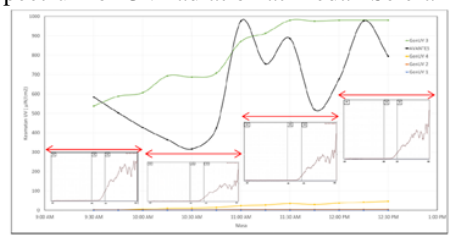


Figure 4: A plot of Irradiance of UV Radiation against time and the spectrum of UV radiation at Taman Tasik Putrajaya

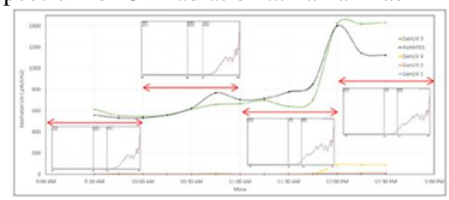


Figure 5: A plot of Irradiance of UV Radiation against time and the spectrum of UV radiation at Taman Pancarona

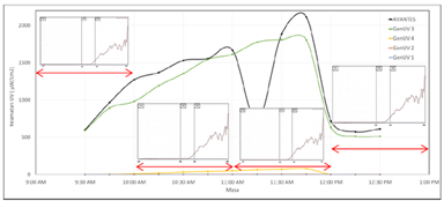


Figure 6: A plot of Irradiance of UV Radiation against time and the spectrum of UV radiation at Taman Warisan Pertanian

Based on the spectrum that captured at 5 locations, only UVA and UVB were passed through the atmosphere (refer Figure 2 to Figure 6). Measurement using the radiometer GenUV 1 and 2 which measure UVC irradiance level also measure no value. Table 2 show the maximum irradiance level and the comparison to the public exposure limit of UV for 10 seconds duration also included.

Table 2: Maximum irradiance level at 5 selected location

| Equipment ($\mu$ W/m$^2$) and Comparison with Exposure Limit (%) | Location (Putrajaya Area) | | | | |
|---|---|---|---|---|---|
| | Taman Saujana Hijau Presint 11 | Medan Selera Presint 11 | Taman Tasik Putrajaya Presint 2 | Taman Pancarona Presint 18 | Taman Warisan Pertanian Presint 16 |
| GenUV 3 | 616.40<br>205.47 | 825.71<br>275.24 | 981.70<br>327.23 | 981.00<br>327.00 | 1066.00<br>355.33 |
| GenUV 4 | 10.95<br>3.65 | 26.67<br>8.89 | 42.12<br>14.04 | 47.10<br>15.70 | 57.58<br>19.19 |
| Spectrometer Avantes | 442.08<br>147.36 | 743.81<br>247.94 | 956.01<br>318.67 | 977.47<br>325.82 | 1145.90<br>381.97 |

## 4 Discussion/Conclusions

From the data in this study, it was confirmed only UVB and UVA passed through the atmosphere. The irradiance level of UVA also dominant compare to UVB. The exposure limit of UV radiation for duration of 10 seconds is vary from 3.65% to 381.97%. The maximum reading was capture between 12:15pm to 12:30pm. This mean, public was over expose to UV radiation at noon. To avoid the harmful health effects from UV radiation, we should protect ourselves by stay in the shade but if need to, we should wear sunscreen for UVA and UVB, sunglasses and clothes that cover the skin from over expose to the sun.

## References

Centres for Disease Control and Prevention C. 2015. The electromagnetic spectrum: Non ionizing radiation.

Canadian Centre for Occupational Health and Safety C. 2022.

International Ultraviolet Association (IUVA). 2017. Method for the measurement of the output of Monochromatic (254 nm) Low-pressure UV lamps.

International Commision on Non-Ionizing Radiation Protection (ICNIRP). 2004. Guidelines on limits of exposure to ultraviolet radiation of wavelentghs between 180 nm and 400 nm (Incoherent optical radiation). *Health Physics*, 87(2):171–186.

International Commission on Non-Ionizing Radiation Protection in Collaboration with International Labour Organization and World Health Organization. 2007. Protecting workers from ultraviolet radiation, ICNIRP 14/2007. SBN 978-3-934994-07-2 (DCM, Meckenheim).

Australian Radiation Protection and Nuclear Safety Agency A. 2020. Ultraviolet radiation. 20 Jun 2020.

Eastern Washington University. 2017. Ultraviolet radiation. *Environment Health Safety, Revision 1 27/4/2017*.

Individual Research Contribution Review, 2024: 215–216
*ISSN: 3083-922X*

# Development of IoT Platform using Thingsboard for Nuklear Malaysia

**Ahmad Adib bin Abdul Rahman**
Technical Support Division, Malaysian Nuclear Agency
43000 Kajang, Selangor
adib@nm.gov.my

## Abstract

In recent years, Internet of Things (IoT) has emerged rapidly in evolving technology nowadays that has revolutionized various industries. Internet of Things (IoT) is an emerging network which joins physical things and people together with software via internet. This paper explores the development of IoT platform using Thingsboard on premise. In this project, establishing robust IoT platform is important to ensure the effectiveness of device integration and data analysis. Thingsboard was selected as it offers a scalable and flexible architecture that can be deployed on premise, allowing organization to maintain complete control over their data and infrastructure. The development of the IoT platform involves several key components such as device management, data collection, processing, and visualization. Parameters such as temperature, humidity and light intensity were monitored on the Thingsboard's dashboard as the results of this project. This project emphasized the advantages of Thingsboard to achieve efficient data collection and system monitoring revolutionizing smart and cost-effective approach to the industry.

**Keywords:** Internet of Things (IoT), Thingsboard, on premise, robust IoT platform

## 1 Introduction

IoT has been developed as a modern technology purposely to ensure our daily life activities more efficient. As we noticed, there are many devices which connected to the internet while they also communicating with each other to assist human's work by reducing human-to-human and human-to-computer interaction to only computer-to-computer interaction. The promise of Internet of Things (IoT) is where a technology that rapidly transforming industries by linking physical devices which equipped with sensors and software. The sensors and software can integrate and shares data with each other will enable smarter operation across various fields. However, there are challenges in managing of massive amounts of data from the IoT devices. In order to harness the full potential of IoT, we do need a robust platform that can handle device management, data collection, data processing and also visualization smoothly. An ideal platform should integrate devices smoothly to ensure reliable data collection, process information in real-time, and user-friendly visualization to present the data to be understand. As referred to Wawasan Nuklear Malaysia, IoT has been included as an important KPI that need to be achieved within the period of 2023 to 2030. The IoT is focusing on the demonstration of the cyber security that could protect any IoT initiatives supporting smart system for scientific research activities. Therefore a framework IoT for user and system centric should be established so that any IoT requirements from any research projects and group can use a standard, centralized and secure IoT platform in Nuclear Malaysia that comply with current ISMS/ISO 27001 and Government of Malaysia 's legal and regulations.

## 2 Method

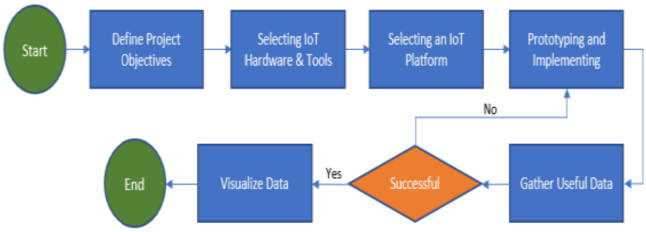



Figure 1: Methodology

The flow chart in Figure 1 illustrates the essential steps taken in the development of IoT platform for Nuklear Malaysia according to the ultimate guide to implementing IoT by Kuilenberg (2024). Method used in this project can be assumed as development method. This project driven by the objectives started with the selection of IoT hardware and tools includes microcontroller device, sensors and data server (Bassi et al., 2013). An IoT platform which is Thingsboard (ThingsBoard, 2020) was chosen as it supports various data collection protocols, offers robust data processing capabilities through its rule engine, and provides customizable dashboards for data visualization. Prototyping and implementing of IoT devices and Thingsboard application are the step by step procedure includes the establishment of sensor devices and Thingsboard UI. The integration between device and software will gather useful data such as temperature, humidity and light intensity. As shown in Figure 1, if the data collection was unsuccessful, there are issues occurred while establishing either sensor device or Thingsboard UI. If it was successful, we can visualize the data on using various widgets on Thingsboard dashboard.

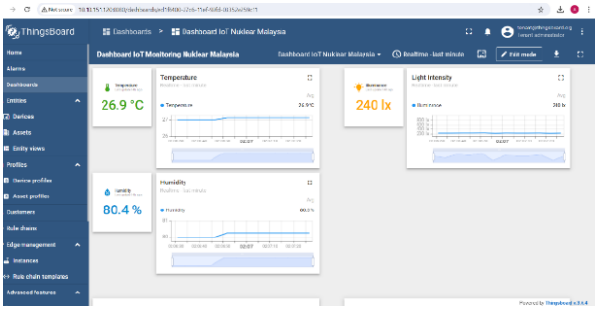



Figure 2: Thingsboard Dashboard

## 3 Result and Discussion

Figure 2 shows the Thingsboard dashboard created based on the method above. Several parameters were displayed such as temperature, humidity and light intensity. The visualization cards were manually added from widget features. The sensor device must be integrated with Thingsboard via access token to enable the communication between device and application software.

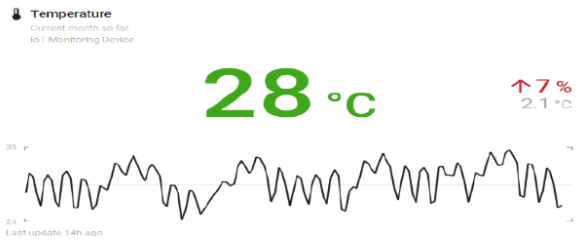



Figure 3: Temperature graph

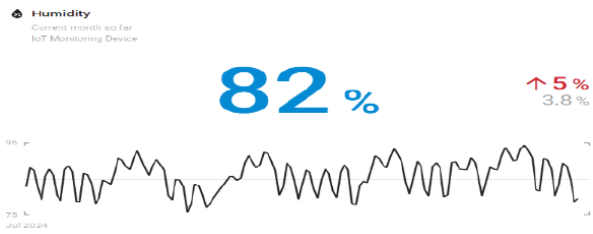



Figure 4: Humidity graph

Graphs in Figure 3, Figure 4 Figure 5 shows the temperature, humidity and illuminance measured in the whole month of July 2024 in ISG laboratory at Blok 15, Nuklear Malaysia. The data were measured by DHT 11 sensor and LDR sensor programmed with NodeMCU ESP-8266 microcontroller as a single prototype. The graphs pattern generally affected by working hours and non-working hours whereas in working hours, the AC and lights are on so the temperature decreased and light intensity increased while in non-working hours, the AC and lights are off causing the temperature increased and light intensity decreased.

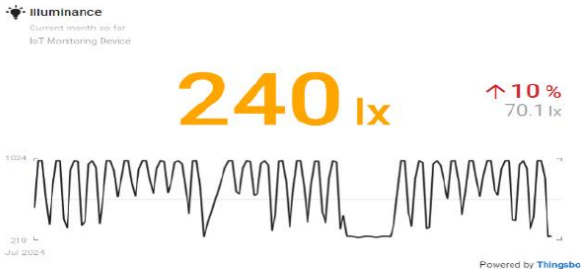



Figure 5: Light intensity graph

## 4 Conclusion

The real-time reading of measured parameters such as temperature, humidity and light intensity displayed on Thingsboard dashboard indicates that integration between device prototype and application software worked smoothly. The platform used was installed in Nuklear Malaysia local server complying the purpose of this project which is to develop IoT platform on premise. To be concluded, the implementation of method in establishing IoT platform in Nuclear Malaysia were successful and the objective of this project was achieved. Future project could emphasize the security in IoT devices and connection in order achieved robust and secure IoT platform.

## References

A. Bassi, M. Bauer, M. Fiedler, T. Kramp, R. van Kranenburg, S. Lange, and S. Meissner. 2013. *Enabling Things to Talk: Designing IoT solutions with the IoT Architectural Reference Model*. Springer Berlin Heidelberg.

J. V. Kuilenberg. 2024. The ultimate guide to implementing iot. `https://www.cloudcredential.org/blog/the-ultimate-guide-to-implementing-iot`.

ThingsBoard. 2020. ThingsBoard Documentation. `https://thingsboard.io/docs`.

Individual Research Contribution Review, 2024: 217–218
*ISSN: 3083-922X*

IRCR

# Sustaining Cyber and ICT Security Preparedness Through Disaster Recovery Testing and Simulations

**Amy Hamijah Ab. Hamid**
Technical Support Division, Malaysian Nuclear Agency
43000 Kajang, Selangor
amyhamijah@nm.gov.my

## Abstract

This paper examines and highlights both challenges and success factors in Cyber and Information Security Incident Management at the Malaysian Nuclear Agency (Nuclear Malaysia) by implementing simulation exercises using a ”walkthrough” approach for disaster recovery testing of Information and Communication Technology (ICT). Effective cyber and information security incident management is essential for ensuring compliance and monitoring ICT governance, particularly through the certification of the Cyber and ICT Security Management System (ISMS, ISO/IEC 27001), including the Business Continuity Management System (BCMS, ISO 22301). The goal of these simulations is to evaluate the achievement of disaster recovery objectives and identify potential improvements in ICT disaster recovery strategies at Nuclear Malaysia. The exercises have successfully identified critical achievement levels of Nuclear Malaysia's Information Center (PTM) incident management, based on Business Impact Analysis (BIA) objectives, through detailed ICT incident management simulation workflows. In conclusion, these simulation exercises verified the BIA objectives achievement levels, ensuring that Nuclear Malaysia's cybersecurity and ICT management are robust and capable of smooth operational normalization. Additionally, they reveal vulnerabilities and weaknesses in current security controls and operational systems, leading to continuous improvements in Nuclear Malaysia's ICT incident management planning.

**Keywords:** preparedness, security, incident management, disaster recovery plan, business continuity plan

## 1 Introduction

Nuclear Malaysia's Cyber and Information Security Incident Management is a critical requirement in implementing compliance and monitoring of ICT governance according to various regulations and procedures. Nuclear Malaysia's ISMS certification has been focusing on eSSDL System credentials located at our data center for the provision of data management, web application services, and, in managing eSSDL servers and network management (Malaysia, 2023)(Hamid, 2018). Meanwhile the BCMS provisions are focusing on sustaining efficient and effective ICT management in competence of the critically acclaimed eSSDL web services and application (for Standardization (ISO), 2019)(Malaysia, 2021).

## 2 Problem Statements and Analysis Methods

Previous research has highlighted various challenges in developing the Business Continuity Plans (BCP) and Disaster Recovery Plans (DRP), stemming from inaccurate and inappropriate assumptions about cyber threats due to lack of expertise, differing perspectives and priorities, insufficient reference sources and inadequate readiness levels as in Hamid (2018).

Hence, Nuclear Malaysia's BCMS effectiveness validation focuses on how-to achieve organizational resilience is based on BIA strategy charts for the critically acclaimed processes and activities of the dedicated eSSDL web services and application as mentioned in Zalil (2019).

Meanwhile, the Nuclear Malaysia's ISMS effectiveness validation based on DRP according to the act of maintaining and minimizing system downtime during any disaster and crises that must be restored within 48-hour Recovery Time Objective (RTO) for system applications (i.e. eSSDL system) and 14 days restoration for network and storage credentials (Malaysia, 2023). Essentially, the RTO and Recovery Level Objective (RLO) are determined by evaluating the time requirements (or lead time) and minimum operational needs of the eSSDL system to function effectively following the simulated disaster scenario as explained in (for Standardization (ISO), 2013).

## 3 Results and Discussion

Figure 1 indicated the simulation drill ”walkthrough” scenario is based on hardware failures at the Bangi Data Center, which results in eSSDL web access disruption and database server malfunction. As a result, recent simulation drills adhered to the estimated RTO timeline of less than a day during regular work hours, with completion times of 3 hours and 20 minutes in 2021, 6 hours and 12 minutes in 2022, 13 hours and 45 minutes in January 2024, which includes, 5 hours and 39 minutes in November 2024. Each simulation exercise met the expected RLO, demonstrating that 100% of the data was successfully retrieved (dan Aplikasi (PTM), 2021)(dan Aplikasi (PTM), 2022)(dan Aplikasi (PTM), 2024).

## 4 Conclusions

In conclusion, these simulation exercises have enhanced the validation of DRP and BIA objectives, ensuring that Nuclear

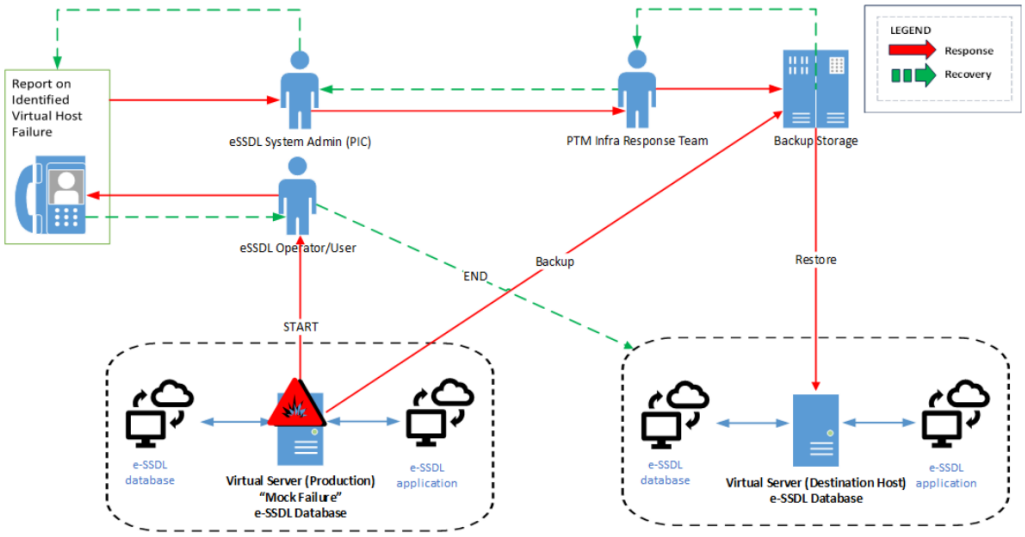



Figure 1: eSSDL System "Walkthrough" Simulation Drill Workflow

Malaysia's cybersecurity and ICT management are effectively maintained through the smooth normalization of ICT governance and operations. They also expose vulnerabilities and weaknesses in security controls and operational systems. Consequently, PTM's cybersecurity and ICT incident management planning at Nuclear Malaysia can be continuously refined and improved. Looking ahead, our team plans to advance these simulation exercises by integrating a digitization module for large-scale consolidation across multiple departments within Nuclear Malaysia.

## References

Unit Teknologi Maklumat dan Aplikasi (PTM). 2021. Laporan pengujian pemulihan bencana ict essdl. Technical report, Agensi Nuklear Malaysia.

Unit Teknologi Maklumat dan Aplikasi (PTM). 2022. Laporan pengujian pemulihan bencana ict essdl. Technical report, Agensi Nuklear Malaysia.

Unit Teknologi Maklumat dan Aplikasi (PTM). 2024. Laporan pengujian pemulihan bencana ict essdl. Technical report, Agensi Nuklear Malaysia.

International Organization for Standardization (ISO). 2013. *ISO/IEC 27001:2013 Information security, cybersecurity and privacy protection — Information security management systems — Requirements*. International Organization for Standardization, Geneva, Switzerland.

International Organization for Standardization (ISO). 2019. *ISO 22301:2019 Security and resilience — Business continuity management systems — Requirements*. International Organization for Standardization, Geneva, Switzerland.

AHA Hamid. 2018. Limitations and challenges towards an effective business continuity management in nuklear malaysia. In *IOP conference series: materials science and engineering*, volume 298, page 012050. IOP Publishing.

Kerajaan Malaysia. 2021. Penjenisan kod bagi hasil dan perbelanjaan. Technical Report PS 1.1, Kerajaan Malaysia.

Agensi Nuklear Malaysia. 2023. Dokumen isms. `https://sp-kms.nuclearmalaysia.gov.my/teknikal/bst/itc/isms/SitePages/DokumenISMS.aspx`.

Nurain Fitri Zalil. 2019. Predictive analytics: Analysing effectiveness of the business continuity recovery response simulation system (bcrrss) in nuklear malaysia [practicum report]. Technical report, Universiti Utara Malaysia.

Individual Research Contribution Review, 2024: 219–220
*ISSN: 3083-922X*

# UV Irradiation on Coagulated Latex Film

**Chai Chee Keong**
Technical Support Division, Malaysian Nuclear Agency
43000 Kajang, Selangor
chai@nm.gov.my

## Abstract

Ultraviolet (UV) radiation is widely used across various fields, including polymer modification, and specifically latex vulcanization. The properties of UV vulcanized latex are comparable to gamma vulcanized latex. UV irradiator has smaller form factor and flexibility for integration to latex product manufacturing lines. To further explore the capability of UV radiation in rubber vulcanization, experiments were conducted to study the effect of UV irradiation on coagulated latex film. Results revealed that UV radiation is capable of inducing crosslinking in coagulated latex film, and its mechanical properties were comparable to UV irradiated latex.

## 1 Introduction

UV radiation can be categorized into UVA, UVB and UVC based on its wavelength. It has been used in various applications including water disinfection, coating curing, food sterilization, photolithography in semiconductor and air purification. There is an increasing interest in using UV radiation to cure or vulcanize latex. Previous researches focused on the latex formulation for UV vulcanization which involved the use of photoinitiator, diacrylate monomer coagents and peroxides, and irradiation apparatuses such as thin-layer photoreactor and falling film photoreactor (Schlogl et al. (2014), Wiroonpochit et al. (2017),Ibrahim et al. (2023)). The potential of UV vulcanization should be explored further to benefit the latex dipped product manufacturing industries. Compares to ionizing radiation, UV irradiator is non-ionizing that does not as hazardous than the former, and does not require bulky shielding. With its versatility, UV irradiator can be integrated to latex dipped product manufacturing facility and help to reduce production cost. The integration can be applied in latex compounding stage and product dipping stage, where UV can be used to vulcanize and dry the latex gel film. However, there is no research finding on the effect of UV irradiation on dry latex film that can proof the viability of this idea. Hence, it was the aim of this paper to report experimental findings on the effect of UV irradiation on coagulated latex film by looking into the change of its tensile properties and crosslink density with different type of UV radiation and irradiation condition. Comparisons were also made between latex sample irradiated on glass plate and in plastic bag.

## 2 Materials and Methods

Materials used in this experiment comprised of high ammonia latex concentrate, 1,6-hexanediol diacrylate (HDDA) as sensitizer, Octosperse KL20 as stabilizer and 2 hydroxy-2-methyl-1-phenylpropanone (Irgacure 1173) as photoinitiator. All these materials were used as received. The Experiment workflow was shown in Figure 1. The formulation of radiation prevulcanized natural rubber latex (RVNRL) was prepared according to Table 1. The samples were prepared in the forms of coagulated latex film on glass plate and formulated latex packed in plastic bags. Theses samples were subjected to UVA and UVC irradiation by using a UV irradiator as shown in Figure 2. After irradiation, the rubber film samples were subjected to leaching and drying before tensile test and linear swelling test.

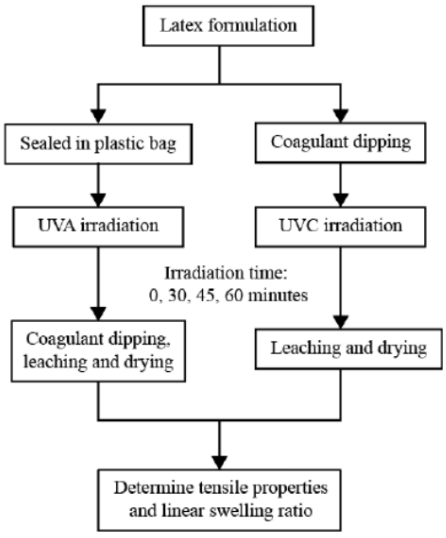



Figure 1: Experiment flow diagram

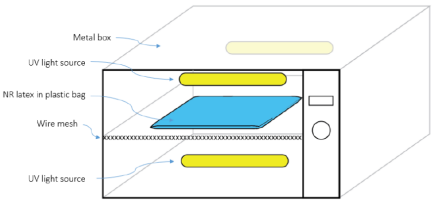



Figure 2: UV irradiator used to irradiate formulated latex in plastic bag and coagulated latex film.

| Ingredient | amount, part per hundred rubbers (phr) |
|---|---|
| Latex concentrate | 100 |
| HDDA | 3 |
| Photoinitiator | 3 |
| Potassium Laurate | 0.06 |
| Water | For dilution to 45% total solid content |

Table 1: RVNRL formulation

## 3 Results and Discussions

The effect of UV irradiation on coagulated latex film was evaluated by changes in modulus at 500% elongation (M500), tensile strength, and linear swelling ratio of the irradiated latex films. Figure 3 shows M500 results for latex on glass plates and in plastic bags, irradiated with UVA and UVC. Modulus reflects stiffness, proportional to crosslink density from vulcanization . M500 increased with UV irradiation, rising with exposure time. The effect followed UVA > UVC and glass plate > plastic bag, with the best result from UVA + glass plate. Both UVA and UVC induced crosslinking in latex containing photoinitiators (Irgacure 1173) and acrylate monomers (HDDA), but UVA outperformed UVC due to greater penetration, explaining the stronger effect on samples without the plastic bag barrier.

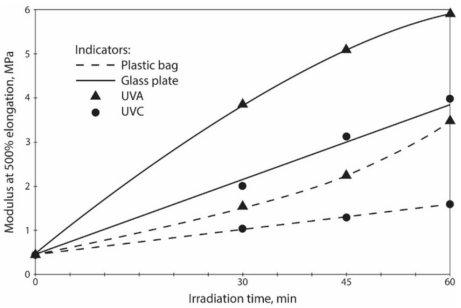



Figure 3: Modulus at 500% elongation of latex irradiated at various durations.

Tensile strength results shown in Figure 4 also showed a positive correlation with irradiation time. No decline from over-crosslinking was observed within the studied range , though a wider time range may identify the optimum. UVA again gave higher tensile strength than UVC, likely due to penetration power.

Linear swelling ratio results in Figure 5 matched M500 trends, decreasing with irradiation time, confirming UV-induced crosslinking.

## 4 Conclusions

The results of this study give evidence to the following:

i Both UVA and UVC radiation are capable of inducing crosslink in coagulated latex film.

ii Based on the context of this study, UVA radiation is more effective than UVC radiation due to higher penetration power of the former.

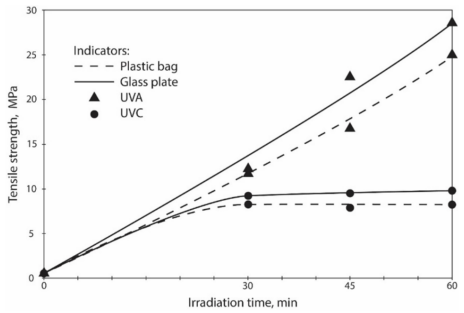



Figure 4: Tensile strength of latex irradiated at various durations.

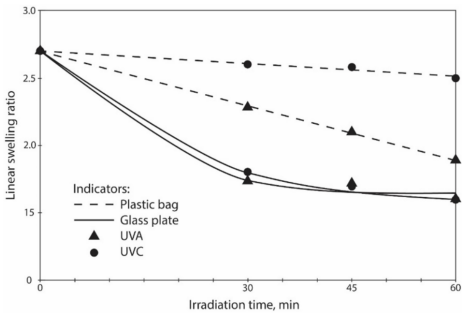



Figure 5: Linear swelling ratio of latex irradiated at various durations.

iii UV irradiation on coagulated latex film is more effective than latex in plastic bag, which may be due to the barrier effect of the plastic bag.

iv The effects of UV radiation on tensile properties and linear swelling ratio increase with the duration of irradiation.

In conclusion, UV irradiation on coagulated latex film is potentially viable. However, much work is needed in many important expects such as aging resistance, film thickness and irradiation parameter, before it can really benefit the latex dipped product industries.

## References

Sofian Ibrahim, Chai Chee Keong, Muhammad Hannan Bahrin, Hasan Sham, Mohd Noorwadi Mat Lazim, Anwar Abdul Rahman, Ahmad Bazlie Abdul Kadir, and Noor Hasni M Ali. 2023. Sulphur-free prevulcanization of malaysian natural rubber latex using a hybrid ultraviolet-peroxide vulcanization method. *Jurnal Sains Nuklear Malaysia*, 35(2):38–48.

Sandra Schlogl, Marie-Luise Trutschel, Walter Chasse, Ilse Letofsky-Papst, Raimund Schaller, Armin Holzner, Gisbert Riess, Wolfgang Kern, and Kay Saalwachter. 2014. Photovulcanization using thiol-ene chemistry: Film formation, morphology and network characteristics of uv crosslinked rubber latices. *Polymer*, 55(22):5584–5595.

Panithi Wiroonpochit, Kittaporn Uttra, Kanokwan Jantawatchai, Nanthiya Hansupalak, and Yusuf Chisti. 2017. Sulfur-free prevulcanization of natural rubber latex by ultraviolet irradiation in the presence of diacrylates. *Industrial and Engineering Chemistry Research*, 56(25):7217–7223.

Individual Research Contribution Review, 2024: 221–222
*ISSN: 3083-922X*

# Assessment of Structural Integrity of Biological Shielding Structure at RTP

**Hasniyati Md binti Md Razi**
Technical Support Division, Malaysian Nuclear Agency
43000 Kajang, Selangor
hasniyati@nm.gov.my

## Abstract

Reaktor TRIGA PUSPATI (RTP) is a crucial research facility for nuclear science and technology, relying on a robust biological shielding structure to contain radiation and ensure the safety of personnel and the environment. Over time, factors such as aging, radiation exposure, and environmental conditions can degrade the structural integrity of this vital shielding. The aim of this project is to evaluate and assess the condition of the biological shielding structure at the RTP. The overall average value of the rebound number across the walls of the RTP (excluding the results from the rebound test on the thermal column) amounts to 39.2. This finding indicates that, on average, the concrete quality of the RTP wall aligns with the characteristics of a highly durable and resilient hard layer, signifying its quality as being very good. These findings are in line with theoretical expectations and provide valuable insights into the structural integrity of the TRIGA PUSPATI Reactor.

**Keywords:** Biological shielding, Structural integrity, Non-destructive testing, Research reactor

## 1 Introduction

Reaktor TRIGA PUSPATI (RTP) is Malaysia's research reactor, operated by the Malaysian Nuclear Agency. Commissioned in 1982, this TRIGA Mark II reactor has a nominal power of 1 MW and supports nuclear research, education, and applications. Its compact core ensures high neutron fluxes with exceptional safety. The pool-type design, with the core in a 7 m deep aluminum tank and concrete biological shield, enhances reliability.

RTP facilities include in-core dry tubes, central thimble, and rotary rack for isotope production, neutron activation analysis, neutron beam research (e.g., SANS, NuR), and neutron/gamma studies. The high-density biological shield protects personnel and the environment from radiation, using layered concrete for optimal neutron and gamma attenuation. Additionally, the reactor pool, filled with water, acts as an additional shielding layer.

Over time, aging factors such as concrete degradation, reinforcement corrosion, and seismic risks may affect the shield. To ensure the continued safety and reliability of the RTP, comprehensive monitoring and inspection assessment are essential. These programs involve regular assessments of the biological shield's structural integrity, including concrete strength testing, reinforcement condition evaluation, and overall structural analysis. Understanding the structural behavior of the biological shielding is essential for ensuring reactor safety and extending its operational lifespan.

The rebound (Schmidt) hammer, a non-destructive tool, estimates concrete strength by measuring rebound distance of a spring-loaded mass. It offers portability, rapid results, and cost-effectiveness, but readings are influenced by age, moisture, and surface condition. Accurate calibration is essential, and it mainly measures surface hardness, not core condition.

Effective use requires a detailed test protocol, defined locations, multiple readings, and data analysis. Combining rebound hammer results with other methods like ultrasonic pulse velocity improves accuracy. This research assesses RTP biological shield integrity by considering material properties, loading, and aging effects.

## 2 Methodology

The rebound hammer used to measure surface hardness, providing an estimate of surface compressive strength, uniformity, and concrete quality. Calibration of the rebound hammer adheres to ISO/DIS 8045, EN 12 504-2, and BS 1881 Part 202 standards. The rebound hammer operates on the principle that an elastic mass rebounds based on concrete surface hardness. When pressed against the concrete, the hammer's spring-controlled mass rebounds, with the rebound distance correlating to concrete hardness. During the assessment of biological shielding surface at RTP, the rebound hammer technique will be employed. The testing process involves pressing the rebound hammer at 40 cm intervals on the selected biological shielding surface as in Figure 1.

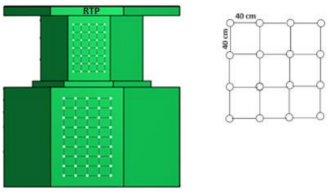



Figure 1: Various points for inspection at biological shielding concrete surface structure of RTP

The hammer is held perpendicular to the surface and pushed until the spring is fully compressed. Once the spring reaches its maximum extension, the latch is released, and the spring pulls the mass towards the surface. As the mass strikes the

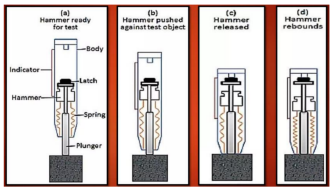



Figure 2: A cutway schematic view of the Schmidt rebound number

plunger rod, it rebounds due to the resistance from the concrete. During this rebound, a slide indicator moves along with the hammer mass and comes to a stop at the maximum distance the mass reaches after rebounding as shown in Figure 2.

Based on (Patil et al., 2015), the quality of the concrete was evaluated by referring to Table 1.

| Average Rebound Number | Quality of Concrete |
|---|---|
| > 40 | Very Good Hard Layer |
| 30 to 40 | Good layer |
| 20 to 30 | Fair |
| < 20 | Poor Concrete |
| 0 | Delapidated |

Table 1: Quality of concrete different values of rebound number (Patil et al., 2015).

## 3 Results and Discussions

A comprehensive assessment of the RTP's biological shielding concrete surface was conducted using the rebound hammer test. A total of 344 test points was evaluated. Table 2 shows the rebound values obtained from rebound hammer test at various points at biological shielding concrete surface structure of RTP.

Table 2: Test location with average rebound number and quality of the concrete.

| Test Location | Average Rebound Number | Quality of Concrete |
|---|---|---|
| **Ground Level** | | |
| Beam Port 1 | 43.6 | Very Good Hard Layer |
| Beam Port 2 | 44.2 | Very Good Hard Layer |
| Beam Port 3 | 42.9 | Very Good Hard Layer |
| Beam Port 4 | 42.2 | Very Good Hard Layer |
| Sample Storage | 42.0 | Very Good Hard Layer |
| **Level 1** | | |
| Beam Port 1 | 37.8 | Good Layer |
| Beam Port 2 | 32.7 | Good Layer |
| Beam Port 3 | 34.3 | Good Layer |
| Beam Port 4 | 34.1 | Good Layer |
| Sample Storage | 33.0 | Good Layer |
| Thermal Column | 33.0 | Good Layer |

The test locations were measured at Ground Level and Level 1 of RTP structure. The average rebound number for the Ground Level was between 42.0-44.2 indicates very good hard layer of concrete. The highest and lowest rebound numbers were recorded on the Beam Port 2 and Sample Storage surface structure, suggesting variations in concrete properties. Minor surface damage was observed at one location at the Beam Port 4 surface structure, resulting in a low rebound number value. However, the overall concrete integrity at this point remains acceptable. Theoretically, the presence of porosity should not adversely affect the concrete's suitability as a biological shield, given that concrete requires a minimum thickness of 60 cm to effectively mitigate gamma radiation and thermal neutron radiation (Sarkawi et al., 2018)

The overall average rebound number for the RTP wall is 39.2, indicating a highly durable and resilient concrete layer. This value exceeds the average rebound number reported for the Dhruva research reactor (Rai et al., 2019), potentially due to differences in operational history and concrete composition. The estimated compressive strength of the RTP concrete is approximately 39.5 $\mathrm{N\,mm^{-2}}$, surpassing the value reported for the JMTR (Ohto et al., 2011). While the upper segment exhibits lower average rebound numbers, indicative of excellent concrete quality, the lower segment demonstrates higher values, suggesting a good concrete layer. This discrepancy may be attributed to the greater concrete thickness in the lower segment, which compensates for lower rebound readings.

## 4 Conclusion

This investigation assessed the condition of the RTP wall primarily through rebound hammer testing. Results indicate that the concrete generally meets or exceeds required standards for its role as a biological shield within the TRIGA PUSPATI reactor. While minor damage and rebound value variations were observed, the overall structural integrity of the wall appears satisfactory. Nevertheless, considering the potential long-term degradation of concrete, especially within a nuclear reactor environment, continuous monitoring and maintenance are crucial. A regular inspection regime should be implemented, focusing on critical areas like the TC wall. Further research into concrete deterioration under these specific conditions would enhance our understanding of concrete behavior and inform future maintenance strategies. Ultimately, these efforts contribute to the long-term safety and reliability of the RTP and similar facilities.

## References

Tsutomu Ohto, Tadashi Kimura, Akitomi Fukasaku, and Tsuyoshi Kusunoki. 2011. Investigation on integrity of jmtr reactor building. Technical Report 2010-066, Japan Atomic Energy Agency.

Hitesh Patil, Dhaval Khairnar, and Rupali Thube. 2015. Comparative study of effect of curing on compressive strength of concrete by using ndt & dt. *International Journal for Science and Advance Research in Technology*, 1(6).

K. Rai, C. Satheesh, and P. Verde. 2019. Nondestructive evaluation of concrete structures: A case study of 36 years old reinforced concrete in research reactor dhruva. In *e-Journal of Nondestructive Testing*, volume 24.

Muhammad Syahir Sarkawi, Muhammad Rawi Mohamed Zin, Mohamad Hairie Rabir, Faridah Mohamad Idris, and Jasman Zainal. 2018. Radiation shielding properties of ferro-boron concrete. In *IOP Conference Series: Materials Science and Engineering*, volume 298, page 012037. IOP Publishing.

Individual Research Contribution Review, 2024: 223–224
*ISSN: 3083-922X*

IRCR

# Development of Neutron Radiography and CT(NuRCT) facility at RTP

**Khairiah Yazid**
Technical Support Division, Malaysian Nuclear Agency
43000 Kajang, Selangor
khairiah@nm.gov.my

## Abstract

The neutron digital radiography computed tomography facility has been set up at research TRIGA PUSPATI reactor (RTP) Beamport 3. The facility consists of a collimator, a rotation stage for the sample, an imaging system, a control system, and other components. The rotation stage for the sample is used to rotate the sample during imaging. The imaging system incorporates a CCD camera and a LiF-ZnS scintillator. To enhance the signal-to-noise ratio of the CCD imaging system, a Peltier cooler is used to maintain the CCD temperature below −30 °C. A front surface coated with aluminum (Al) and titanium dioxide ($TiO_2$) as a protective layer shields the CCD from direct neutron irradiation. A light-tight box made of aluminum (Al) is used to prevent long-term activation. In the control system, a C++ program has been developed to improve facility automation and enhance radiation shielding for researchers and instruments.

**Keywords:** Computed Tomography, Image reconstruction algorithm, neutron imaging detector, Two-dimensional projections, CT images, CT automated control systems

## 1 Introduction

Neutron radiography (NR), a non-destructive imaging technique that utilizes neutron radiation to probe the internal structure of objects, similar to X-ray radiography. This imaging technique excels in materials characterization, defect detection, and analysis of various opaque objects particularly useful for imaging materials that are difficult to penetrate with X-rays, such as metals or materials with high atomic numbers. Neutrons have high penetration capabilities into all types of materials, including heavy metals, and sensitive to many light elements, especially hydrogen (Kardjilov et al. (2018), Lehmann and Mannes (2018), Tengattini et al. (2021)). The high penetration of neutrons through metals compared to X-rays and relatively high attenuation by light elements such as hydrogen can be exploited for the study of several applications.

Computed Tomography (CT) is a tomography technique that generates digital image data from multiple angles and uses a computer to combine the data, revealing the internal structure of an object in detail. A CT image is commonly referred to as a slice, where the gray levels represent the radiation attenuation coefficient in the corresponding section of the object.

CT has become one of the most exciting modalities in the field of imaging. Its advantages lie in its non-invasive nature and its ability to capture detailed parameters across an entire cross-section. While CT is widely used in the medical field for diagnostic radiology, it is also applied to imaging non-biological systems, such as engine performance diagnostics, materials research, and geology. The upgraded neutron radiography (NuR) facility at the research TRIGA PUSPATI reactor (RTP) was constructed at the one of the radial Beamport 3. Neutron radiography at RTP had some preliminary success with imaging objects (Muhammad Rawi Mohamed Zin et al., 2022). However, NR only provide 2D image. Therefore, neutron 3D tomography is proposed at NuR facility. The primary aim of this study is to add a new neutron CT system at the NuR facility. To achieve this goal, the study focuses on two main objectives:

1. Developing computer-based programs to control the existing sample manipulator and imaging detector.

2. Integrating the detector system with the sample manipulator system.

## 2 Neutron Radiography Facility at RTP

Figure 1 shows the new upgraded neutron radiography and CT facility (NuRCT) at Beamport 3. Since the neutron entrance aperture diameter is 3 cm and the distance between the inlet aperture to the image plane is 312 cm, this gives the L/D ratio of approximately is 104. The measured neutron flux at this position is 104 $n/cm^2s$ at a reactor power of 500 kW. The imaging detector is CCD/scintillator type, using 16-bit cooled CCD camera. The neutron beam strikes a 0.1 mm thick green scintillation screen. The lights produced by the scintillation screen were recorded on the CCD comprising of $2200 \times 2750$ active pixels. A double surface coated was used to keep the camera away from the direct neutron beam. Additional shielding was used to protect the electronic parts from the direct neutron beam.

Implementation: Complete set of projection images after full rotation at 360° from the neutron imaging detectors are acquired for all volume scan. The CT scans were conducted in October 2024. In this study, all acquired neutron images were processed using open source ImageJ software to remove the significant noise mainly added during acquisition. Then



(a) Inside Biological Shielding; second beam shutter, linear and rotation stages for sample positioning and digital imaging detector



(b) Outside the biological shielding: control system to control automation manipulators and imaging detector

Figure 1: NuRCT system at Beamport 3

the low dynamic range image contrast is adjusted to widen the dynamic range.

## 3 Results and Discussions

In the following, we present experimental results obtained using the developed NuRCT system. Achieving perfect tomography typically requires numerous projections and well-illuminated images. However, in this study, only 60 projections were captured over a full rotation. Due to low dynamic range, the integration time for each projection was 3 minutes. Figure 2 shows a small, compact digital camera was selected for this experiment. The sample was positioned on a sample holder located between the detector and the outer collimator. The total scanning time was approximately 3 hours, with the RTP operating at 500 kW.

After image acquisition, the projections (2D radiography) of the sample were reconstructed using the OCTOPUS cone beam reconstruction software, which is based on the FDK algorithm. The raw projection data underwent normalization procedures to correct the influence of the dark current and to adjust the center of rotation. No further image processing was applied. Finally, 2D cross-sectional images of the sample were obtained as consecutive slices throughout the sample.

Using these reconstructed slices, a 3D volume rendering of the sample was performed, providing a comprehensive visualization of the sample's internal structure. Figure 3 shows the

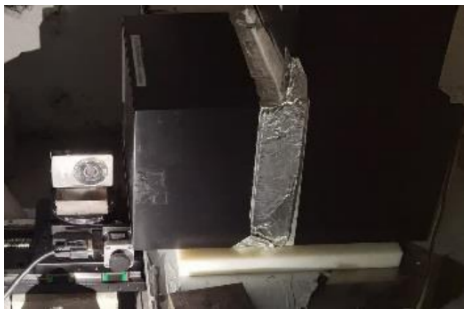


Figure 2: Compact digital used for test sample.

3D volume rendering using opensource dragonfly program.

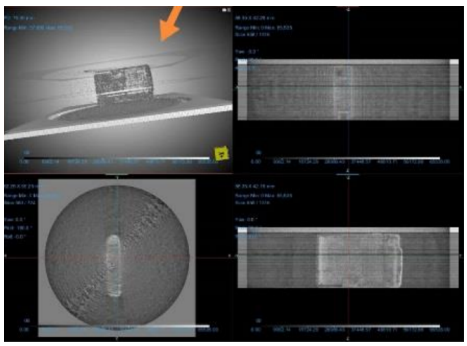


Figure 3: CT slices & 3D volume rendering using dragonfly.

## 4 Conclusions

In conclusion, the development of an automated neutron CT system at the RTP successfully enhances imaging capabilities by integrating automated control programs, improving sample manipulation, and optimizing detector performance. This system provides a reliable and efficient tool for obtaining high-quality neutron tomography images, supporting various research and industrial applications

## References

Nikolay Kardjilov, Ingo Manke, Robin Woracek, André Hilger, and John Banhart. 2018. Advances in neutron imaging. *Materials Today*, 21(6):652–672.

Eberhard H Lehmann and David Mannes. 2018. Neutron radiography and tomography. *The Encyclopedia of Archaeological Sciences*, pages 1–6.

Muhammad Rawi Mohamed Zin, Hishamuddin Hussain, Khairiah Yazid1, Na'im Syauqi Hamzah, Muhamad Faiz Azizan, Nirmala Sharippudin, and Zaifol Samsu. 2022. Applications of neutrons from triga puspati reactor for investigation of cultural heritage objects. In *Nuclear Technique Applications in Cultural Heritage Object Investigation*, pages 40–47. Malaysian Nuclear Agency.

Alessandro Tengattini, Nicolas Lenoir, Edward Andò, and Gioacchino Viggiani. 2021. Neutron imaging for geomechanics: A review. *Geomechanics for Energy and the Environment*, 27:100206.

Individual Research Contribution Review, 2024: 225–226
*ISSN: 3083-922X*

# High voltage and battery charging circuits for the G2TAG RADIGMETER V2

**Lojius Lombigit**
Technical Support Division, Malaysian Nuclear Agency
43000 Kajang, Selangor
lojius@nm.gov.my

## Abstract

The G2TAG RADIG meter, developed for radiation survey applications by Malaysian Nuclear Malaysia, experienced inconsistent performance due to high-voltage circuit issues and excessive power consumption. To address these challenges, a new high-voltage circuit (HV) and printed circuit board (PCB) were designed, enhancing operational stability and reliability. A rechargeable lithium-ion (Li-ion) battery was introduced as an alternative power source to reduce power-related issues, supported by a custom-designed charger with a built-in protection circuit for safety and efficiency. This paper discusses the design and implementation of these improvements, demonstrating significant enhancements in performance consistency and energy efficiency for dependable radiation monitoring applications.

**Keywords:** radiation survey meter, high voltage circuit, front-end amplifier

## 1 Introduction

Radiation survey meters are crucial in monitoring radiation levels across various applications, including environmental safety, industrial processes, and medical diagnostics. The G2TG RADIG meter, developed by Malaysian Nuclear Malaysia, is designed to provide accurate and reliable measurements of radiation levels. However, the meter's performance has been hindered by technical challenges, particularly with its HV circuit and power system. These issues have led to inconsistencies in dose readings and operational inefficiencies, compromising its effectiveness in critical applications. The HV circuit, a critical component for the proper functioning of radiation detectors, has shown instability, leading to inconsistent dose readings and reduced reliability. Additionally, two AAA batteries cannot support the meter's high power consumption, limiting operational duration and requiring frequent battery replacements. Commercial radiation survey meters typically need at least 600 - 800 hours of stand-by operation, a performance standard the current design fails to meet.

This paper comprehensively redesigns the high-voltage circuit and printed circuit board (PCB) to address these issues to enhance performance stability. Moreover, a rechargeable lithium-ion (Li-ion) battery was identified as a sustainable alternative power source, supported by a custom-designed charging and protection circuit. These improvements aim to resolve the identified challenges, ensuring the G2TAG RADIG meter's reliability and efficiency.

## 2 Methods

The redesign of the G2TAG RADIG meter focused on addressing the instability of the HV circuit and optimising the power system. The HV circuit, a critical component for enabling consistent radiation dose readings, was developed using the Linear Technology LT1615 micropower step-up DC-DC converter (Linear Technology Corporation, 1998). In conjunction with a voltage multiplier, this converter effectively boosts the 5 VDC input voltage to approximately 600 VDC output, ensuring the required operational voltage for the radiation detection system.

The Li-ion battery charger circuit was designed using the TP4056 constant current and linear voltage charger IC (NanJing Top Power ASIC Corp., 2024). This charger accepts a 5VDC input through a Type-C USB connector and provides a fixed 3.7 VDC at 1A. The TP4056 was selected for its simplicity, reliability, and integrated protection features, ensuring safe charging and discharge management for the battery. This configuration provides a stable and efficient power source, addressing the limitations of the original design and reducing dependency on disposable batteries.

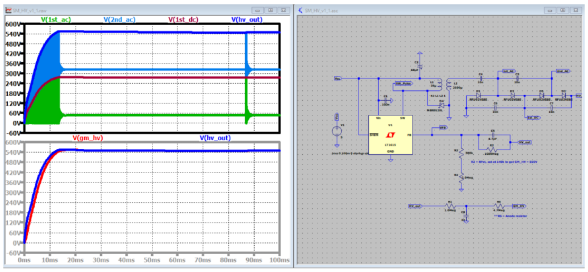
The high-voltage (HV) circuit design was simulated and optimised using the LTSPICE circuit simulator to ensure the circuit's efficiency and reliability. This platform enabled precise modelling of the circuit's behaviour under varying conditions, allowing for fine-tuning component values and configurations to minimise voltage ripple and maximise output stability. Key performance parameters, including voltage regulation, power consumption, and thermal behaviour, were thoroughly analysed to address inconsistencies in the original design. The HV and Li-ion charger circuits' printed circuit boards (PCBs) were designed using EasyEDA software (EasyEDA, 2024), incorporating small footprint components to achieve compact designs. The HV PCB measures $11 \times 54$ mm, while the Li-ion charger PCB measures $20 \times 42$ mm, ensuring efficient use of available space.

## 3 Data/Results

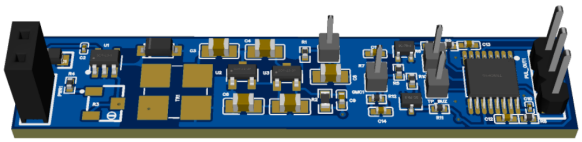
### 3.1 High-voltage circuit and PCB

The high-voltage (HV) circuit simulation results in Figure 1b indicate stable operation and efficient voltage boosting from

the 5V input to approximately 550V output. The voltage multiplier and LT1615 step-up DC-DC converter perform consistently, as shown in the upper graph, where the output voltage (V(hv out)) stabilises with minimal ripple after an initial transient phase. The second graph highlights the gradual ramp-up of the HV output (V(gm hv)) to the target value, confirming the circuit's ability to achieve the required voltage levels within 10–20 ms. Additionally, the LT1615 requires only 20 µA of quiescent current in active mode, ensuring low-power operation and making it suitable for portable applications.



(a) HV simulation



(b) 3D visualisation of the HV PCB

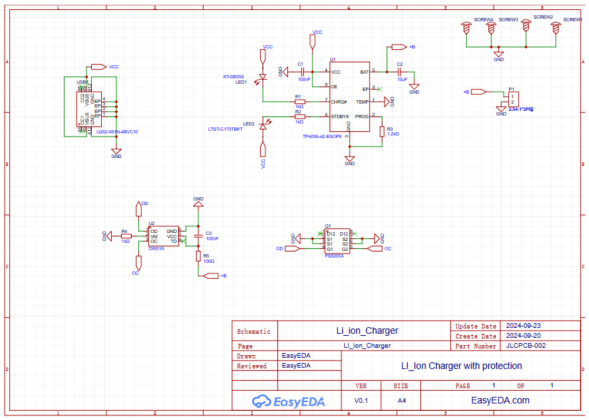
Figure 1: LTspice simulation of the proposed new HV circuit and the 3D visualisation of the PCB

### 3.2 Li-ion charger circuit and PCB

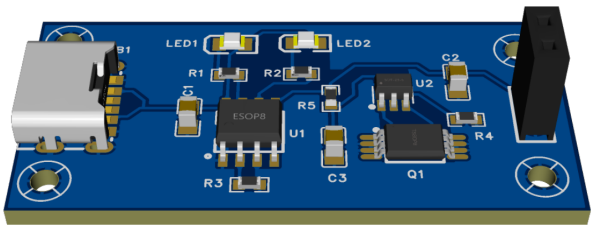
The Li-ion battery charging circuit (see Figure 2a) is based on TP4056 (NanJing Top Power ASIC Corp., 2024), provide a constant current (1A) and fixed (3.7 VDC) output from 5VDC power source via a Type-C USB connector. Combined with the DW01A battery protection IC and FS8205A dual N-channel power provides overcharging protection to the Li-ion batteryand prolongs its lifetime. The 3D visualisation of the Li-ion charging circuit PCB is shown in Figure 2b.

## 4 Discussion/Conclusions

In conclusion, the redesigned high-voltage circuit and Li-ion charger system significantly improve the performance and reliability of the G2TAG RADIG meter. Addressing issues with voltage instability and high power consumption, the proposed solutions enhance operational efficiency, extend battery life, and meet commercial standards for standby duration. The LT1615 DC-DC converter, optimised through LTSPICE simulations, ensures stable high-voltage output with low power requirements. Furthermore, the compact PCB designs, created using EasyEDA, demonstrate effective space utilisation. These advancements make the G2TAG RADIG meter more robust and sustainable, reinforcing its suitability for critical radiation monitoring applications




(a) Li-ion charging with output protection circuit




(b) Li-ion charger PCB

Figure 2: Li-ion battery charging circuit and their PCB

## References

EasyEDA. 2024. Easyeda: web-based eda tool suite. https://www.easyeda.com.

Linear Technology Corporation. 1998. Lt1615/lt1615-1: Micropower step-up dc/dc converters in thinsot. https://www.analog.com/media/en/technical-documentation/data-sheets/16151fas.pdf.

NanJing Top Power ASIC Corp. 2024. Tp4056 (1a standalone linear li-ion battery charger). http://toppwr.com/uploadfile/file/20240130/65b892bb04a3c.pdf.

Individual Research Contribution Review, 2024: 227–228
*ISSN: 3083-922X*

# Predicting Insider Threats for Nuclear Security: A New Method for Quantifying Personnel Trustworthiness Using a Combination of Organizational and Social Media Data

**Maizura Ibrahim**
Technical Support Division, Malaysian Nuclear Agency
43000 Kajang, Selangor
maizura@nm.gov.my

## 1 Introduction

The threat of nuclear terrorism has been a matter of concern for all States. The responsibility of ensuring the security of nuclear material, other radioactive material, associated facilities and associated activities under its jurisdiction lies entirely with the State. One of the critical elements in the fight against nuclear terrorism is addressing the threat of insiders. Most organizations implement a background check process to assess personnel trustworthiness in containing insider threats. This process is typically manual and involves the screening of background data by security personnel. However, this method raises issues due to human intervention, leading to potential bias based on the evaluator's perception or their relationship with the personnel being evaluated.

To overcome these challenges, this article presents a novel technique aimed at combating nuclear terrorism by predicting insider threats using an artificial intelligence (AI) system. The methodology integrates advanced AI algorithms with behavioral analysis to autonomously evaluate personnel trustworthiness, thus eliminating human bias. Using data from employee activity, access patterns, communication logs, and social media data, our approach develops predictive models that calculate the value of the personnel trustworthiness matrix (TMV) and preemptively flag suspicious behavior indicative of insider threats. This technique offers a proactive and efficient solution to mitigate the risks associated with nuclear terrorism and to ensure robust protection against insider threats.

## 2 Methods

Creating a new method that is not readily available involves imagination and a projection process. To create this method, the projection of the implementation scenario is necessary. Figure 1 shows the implementation of the suggested projection scenario of the proposed method in a personnel security system. As depicted in the figure, a new method is created to quantify the trustworthiness of personnel for the prediction of insider threat, namely the Trustworthiness Metrics Value(TMV) calculation.

### 2.1 TMV Parameters

Two categories of parameters are used in the TMV calculation, namely the organizational parameters and the social media parameters.

The organizational parameters are those with values that can be obtained from the data within the organization's information system. Meanwhile, the social media parameters are the values that can be obtained from the social media data. The specific parameters, that is, the organizational and social parameters of the media, are encapsulated with general parameters that are related to the evaluation scenario. Figure 2 shows the source and description of the parameter used in the TMV calculation. In this case, we identified that the evaluation of trustworthiness must be performed as a timely basis, therefore a temporal parameter must be considered in the prediction model. The prediction algorithm will be exposed and explained in detail in the next section.

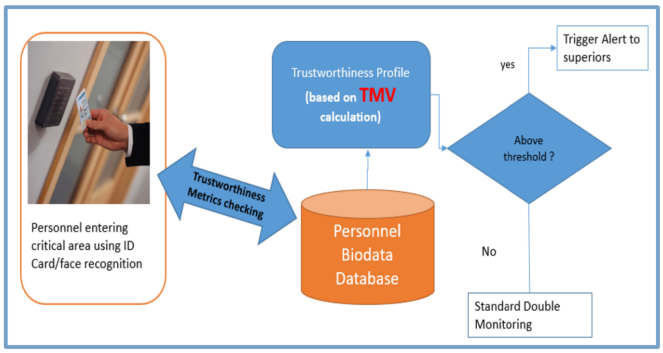



Figure 1: Projection scenario implementation of the proposed technique in personnel security systems.

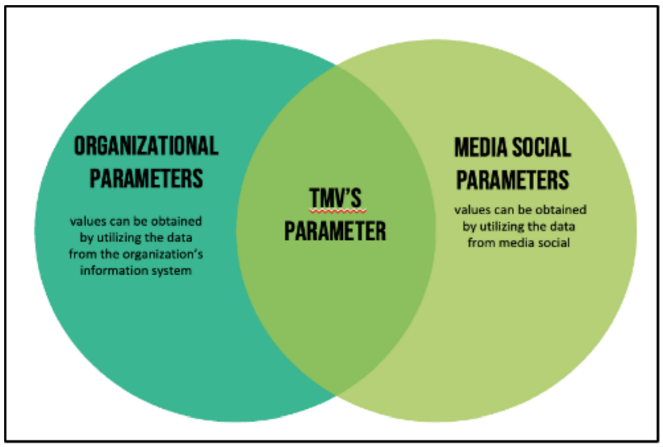



Figure 2: Parameter used in TMV

## 3 The TMV Algorithm

The general mathematical expression model is shown in Equation 1.

### 3.1 Mathematical Model

**Equation 1: Probability of Insider**

$$P_{ins} = R_{ins} + SMT_{ins} \tag{1}$$

where,

$P_{ins}$ is the probability of insiders

$R_{ins}$ is the reliability matrix, and

$SMT_{ins}$ is the Social Media Trustworthiness Metrics.

### 3.2 Components of the Model

Incorporating the temporal elements in the prediction model, the equations are elaborated in the equation 2 and 3.

**Equation 2: Reliability Metrics**

$$R_{ins} = A \sum_{t=1}^{n} DW_t + B \sum_{t=1}^{n} NFR_t + C \sum_{t=1}^{n} WS_t \tag{2}$$

where,

$A$, $B$, and $C$ are constant numbers represent the weight assigned to each parameters,

$\sum_{t=1}^{n} DW_t$ is the Disengaged Workforce of the personnel at a time $t = 1$ to $n$,

$\sum_{t=1}^{n} NFR_t$ is the Numbers of fulfilling of assigned $t = 1$ responsibilities of the personnel measured at a time $t = 1$ to $n$, and

$\sum_{t=1}^{n} WS_t$ is the Work Satisfaction score for the personnel at a time $t = 1$ to $n$.

**Equation 3: Social Media Trustworthiness Metrics**

$$SMT_{ins} = X \sum_{t=1}^{n} RH_t + Y \sum_{t=1}^{n} MF_t + Z \sum_{t=1}^{n} TL_t \ldots \tag{3}$$

where,

$X$, $Y$, and $Z$ are constant numbers represent the weight assigned to each parameters,

$\sum_{t=1}^{n} RH_t$ is the Relative Happiness of the personnel at a time $t = 1$ to $n$,

$\sum_{t=1}^{n} MF_t$ is the Motive Force score of the personnel measured at a time $t = 1$ to $n$,

$\sum_{t=1}^{n} TL_t$ is the Trustworthiness Lexicon score for the personnel at a time $t = 1$ to $n$.

## 4 Discussion/Conclusions

The person who is trustworthy is known to not let down expectation by always fulfilling the assigned responsibilities so that the trust placed is not betrayed (IAEA, 2020). Based on that statement, three measurable parameters related to these qualities are identified, namely: 1. Disengaged Workforce; 2. Numbers of fulfilling of assigned responsibilities; 3. Work satisfaction.

The disengaged workforce (DW) could be measured using data from the organization's internal KPI evaluation system. The number of responsibilities assigned (NFR) could utilize the organization's internal task monitoring system. In addition, work satisfaction (WS) can be obtained from an organization's personnel satisfaction survey. It is said that a happy person is more trusted. Therefore, Relative Happiness (RH) is considered one of the important parameters for the Social Media Trustworthiness Metrics. Calculating the RH, involved the process of emoticon mining of social media comments. In addition to that, adversaries can be described by motive force (IAEA, 2020). The Motivation Force (MT) of the personnel can be traced in the social media profile, the likes and sharing done on social media, and comments. In addition to that, the value of personnel behaviors evaluated with the Trustworthiness Lexicon (TL) also contributed to the calculation of the TMV.

The presented method has laid a fundamental work toward a proactive solution to mitigating nuclear terrorism risks, via a method that eliminates the human bias to evaluate personnel trustworthiness using AI-driven models.

## Acknowledgment

This research is supported by The International Atomic Energy Agency (IAEA) under the Coordinated Research Project (CRP) contract number RC22165.

## References

IAEA. 2020. *Preventive and Protective Measures Against Insider Threats: Implementing Guide*. Number 8-G in Nuclear Security Series. International Atomic Energy Agency.

Individual Research Contribution Review, 2024: 229–230
*ISSN: 3083-922X*

# Lesson Learnt In Operating RN42 Station Located In Equatorial Doldrum Area For Stable Electrical Power Supply

**Mohamad Suhaimi Yahaya**
Engineering Division, Malaysian Nuclear Agency
43000 Kajang, Selangor
m.suhaimi@nm.gov.my

## Abstract

RN42 station is located in Cameron Highlands, Malaysia which is a hilly area surrounded by the forest. The station is situated in the equatorial doldrum area, which is rainy and sunny throughout the year. The humidity is relatively high which is around 80 to 90% RH. It is quite challenging in order to operate and maintain the power system from electrical substation to the stations' equipment such air sampler, gamma detector, local server and mechanical and electrical system especially to overcome the threat come from insect and animal pest. The insect and animal pest such as ant and mouse like to bite the wiring insulation and electronic component that can cause electrical short circuit. Other than that, the bad weather could also affect the operation of RN42 station. This paper will describe the countermeasures taken to prevent damage to the RN42 station's power transmission line and electronic components caused by the threat of insects and pests and also challenging operating the station in bad weather. The measures taken were successfully prevent severe damage on electronic component cause by insect, minimized the downtime and prolong the lifespan of the RN42 station.

**Keywords:** equatorial, power transmission line, insect, bad weather

## 1 Introduction

The Radionuclide Monitoring Station RN42 is one of International Monitoring System (IMS) station owned by Comprehensive Nuclear-Test-Ban Treaty Organization (CTBTO) and managed by Malaysian Nuclear Agency as a liaison agency to CTBTO. RN42 station is used for monitoring and sampling radionuclides resulting from nuclear weapons tests or nuclear radiological accident. The station is located on the highland "spine" of Peninsular Malaysia which is in Cameron Highlands, Pahang Malaysia (latitude: 4.4843°, longitude: 101.3713°) about 200km far away from Kuala Lumpur.

RN42 station is located at hilly area surrounding by the forest in the equatorial doldrum area, South East Asia. The local climate is equatorial which is rainy and sunny throughout the year. The humidity is relatively high which is around 80 to 90% RH, meanwhile the mean annual temperature is 18 degC. The average annual rainfall is 3108 mm, one of the wettest areas in Malaysia. In addition, the study shows the lightning seems to happen more often closer to the equator.



Figure 1: RN42 station located in Cameron Highlands

The station received the electrical power supplied by Tenaga Nasional Berhad (TNB). The electricity supplied to the RN42 station through an underground cable from substation. There is a diesel generator for backup power supply. For equipment itself, there is an uninterruptible power supply (UPS) for short-term power supply when the main power source fails.

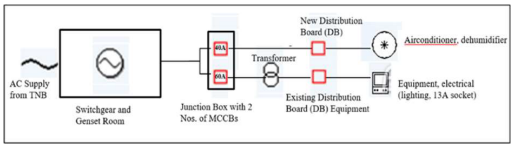



Figure 2: Single line drawing the power supply to RN42 station

## 2 Discussion

### 2.1 Challenges and Issues

One of the challenges is the threat come from insect and animal pest. The insect and animal pest such as ant and mouse like to bite the wiring insulation and electronic component that can cause electrical short circuit. There is a case which the dead mouse is found inside air conditioning's blower. As a result, this might cause major problem to air conditioning and finally can cause interruption the station operation.

Another challenge is to operating the station in bad weather such as heavy rain and thunderstorms which can cause flooding and landslides in areas leading to the station. This such as event may disrupt power transmission lines that will cause power outage to the RN42 station. In addition, the station is located in hilly side that attract the lightning strikes occurred and can damage the electronic component with excessive current. The transient voltage surges that generated from lightning can exceed the voltage limits of electronic components,



Figure 3: Wound wire found in trunking



Figure 4: Dead mouse found in air conditioning's air blower.



Figure 5: Air conditioner pipe insulation damaged suspected due to mouse biting

leading to failure or permanent damage to electronic equipment. Moreover, the uncertain weather in station which is hot during sunny day and cold during night and rainy season can possibly cause the cable brittle and electrical supply component broken much frequent. Therefore, it can lead the power outage or may lead to fire in the electrical system.



Figure 6: Landslides occurred in 2021 Jalan Tapah-Cameron Highlands



Figure 7: Cable insulation brittle found in transformer



Figure 8: Cut-out and supply incoming cable insulation from electric utility company was found melting

### 2.2 Solution

The operator and maintenance team are using pest control pill or poison to kill mouse and ant as part of pest control. It is very effective to control the ant and mouse from entering the station in order to protect the electrical cabling and other equipment. Moreover, the maintenance team had fully sealed or closed any holes and opening on the station wall, floor and roof including electrical board in order to prevent the animal such as mouse or lizard from entering the station.



Figure 9: Mouse pill used to kill the mouse



Figure 10: The opening has been fully sealed

Besides that, the operator and maintenance team are practicing good engineering practice such as designing a proper earthing for sensitive equipment, using proper type of cable suitable for extreme weather and using galvanized iron (GI) conduit for outdoor electrical wiring. Meanwhile for underground wiring, HDPE solid wall cable pipe has been used for protection from underground water and surface loading. Furthermore, the maintenance team has good maintenance schedule to monitor and do the preventive maintenance on electrical supply system and generator every 3 months. Likewise, the team clean regularly the electrical board and its components. Additionally, the maintenance team is very responsive to repair and replace damage part of station such as roof to prevent the rainy water goes inside the station.



Figure 11: The cleaning activity on electrical board



Figure 12: The generator has been inspected during preventive maintenance

As known, the station is surrounded by the trees and bush that can be habitat for animal pest and also wild animal. The operator and maintenance team did the house keeping regularly in order to make sure the surrounding area is always clean and free of bushes. Other than that, the operator and maintenance team always monitor the station condition frequently using CCTV for video surveillance and assessment to ensure electrical power at the station working properly. Fortunately, the station is well located which is just beside the tall metrological tower that can protect the station itself from lightning strike that can damage the electrical and electronic equipment.

## 3 Conclusion

The challenges in operating the RN42 station in the Equatorial Doldrums can cause power outages at the station. Therefore, several measures taken such as pest control, comprehensive monitoring, good engineering practices and maintenance activities have successfully reduced the possibility of electrical power outages and also prevented severe damage to electronic components caused by insects and other animals and extreme weather.

## References

F. A. Abdul Razalim, B. Baharuddin, N. K. Zahidi, R. Yapp, and M. S. (n.d.) Yahaya. Knowledge document series: Radionuclide Monitoring Station (rn42), Tanah Rata, Cameron Highlands as part of comprehensive nuclear- test-ban treaty gizmo, Malaysian Nuclear Agency.

M. S. Yahaya, F. A.n Abdul Razalim, H. Abu Bakar, M. N. Othman, M. F. A. Abdol Azis, M. I. Sabar, M. H. Chik, and I. Mustpha. 2017. Technical report: Mechanical and electrical troubleshoot works at radionuclide monitoring station RN42 Cameron Highlands Malaysia, Malaysian Nuclear Agency. NUKLEARMALAYSIA/L/2017/13.

Individual Research Contribution Review, 2024: 231–232
*ISSN: 3083-922X*

# Studying on Cost Saving After Installation of Solar PV in Complex Bangi Malaysian Nuclear Agency

**Mohamad Suhaimi Yahaya**
Engineering Division, Malaysian Nuclear Agency
43000 Kajang, Selangor
m.suhaimi@nm.gov.my

## Abstract

Malaysian Nuclear Agency (MNA) is one of the government agencies that has a high monthly electricity bill. According to record, the electricity bill in 2022 and 2023 are RM4.992 million and RM6.362 million respectively for both the Bangi and Dengkil complexes. The solar panels have been installed in Bangi Complex since the end of 2020 and started to fully operational in July 2022 under the Supply Agreement with Renewable Energy (SARE) programme involving Tenaga Nasional Berhad (TNB), GSPARX Sdn. Bhd. and MNA. This paper will study how much cost saving in electricity bill can be achieved with solar PV installation in Malaysian Nuclear Agency. The study has focused on electricity bills in the Bangi Complex from January to November 2024. Based on this study, the cost saving for electricity bill in 2024 is RM140,694.18 with a monthly average of RM12,790.38.

**Keywords:** electricity bill, solar PV

## 1 Introduction

Malaysian Nuclear Agency (MNA) is an agency under Ministry of Science, Technology and Innovation (MOSTI) Malaysia that focuses on research and development (R&D) activities in the field of nuclear science and technology. MNA has 2 complexes, namely Bangi Complex and Dengkil Complex, which are located 3km away. With over 70 buildings, the electricity bill for both complexes is RM4.992 million in 2022 and RM6.362 million for 2023 as one of the government agencies with high electricity bills. For this reason, the minister of the Ministry of Energy, Science, Technology, Environment and Climate Change (MESTECC) requested MNA to study the possibility to install solar photovoltaic (PV) under Supply Agreement with Renewable Energy (SARE) programme. The purpose of installation of solar PV is mainly to reduce electricity bill and also to promote renewable energy used in Malaysia.

GSPARX Sdn. Bhd. has been appointed as solar PV installer in MNA with 21 years contract for repayment through TNB bill. Through this solar leasing project, there are no initial costs incurred by MNA with all costs borne by GSPARX Sdn. Bhd.. The project has started the installation of solar PV at the end of 2020 and became fully operational in July 2022. The solar PV has been installed in parking lot near to Block 15, Bangi Complex with total capacity of 460kWp. The energy generated from solar PV will be used directly for MNA's use, however if there is excess energy generated it will be sold directly to the TNB grid at rate of RM 0.365 per kWh since there is no battery system installed to store energy from solar. The objective of this study is to determine the cost saving in electricity bill for Complex Bangi from January until November 2024 after installation of solar PV.



Figure 1: The solar PV installed in parking lot near to Block 15 Complex Bangi

## 2 Methods

The study focused on the electricity bill of the Bangi Complex from January to November 2024. The monthly electricity consumption was studied including the power generated from solar PV. The total cost of electricity consumption will be calculated using the actual rates charged by TNB assuming no solar PV is installed in the MNA. The cost will then be compared to the actual electricity bill to determine how much cost savings has been achieved by using solar PV in the MNA.

## 3 Result and Discussion

The average energy generated by solar PV from January until November 2024 is 50936 kWh with the maximum energy generated being 60513 kWh in March 2024. The total energy solar generated is 560291 kWh with the excess energy that has been sold to TNB is 981 kWh which is about 0.18% from total energy generated. However, the energy generated from solar PV is only about 8% from total electricity consumption in Bangi Complex. The energy generated and used as well as the surplus is shown in Figure 2 below.

The usage of electrical power in Bangi Complex is shown in Table 1 below from January until November 2024. TNB has imposed a C2 commercial tariff for the Bangi Complex with 2 different rates applied, namely peak rate which is RM0.365/kWh (C2p) and RM0.224/kWh (C2o) for off-peak rate from 10.00 pm to 8.00 am.

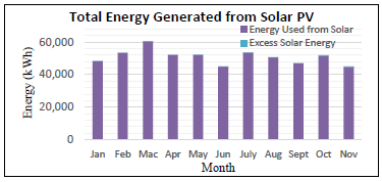



Figure 2: Total energy generated from solar PV from January until November 2024

Table 1: Electrical energy used in Complex Bangi

| Month | Peak Hour Usage, kWh (A) | Off Peak Usage, kWh (B) | Energy used from solar Peak hour, kWh (C) | Total Energy Used, kW (D) = (A) + (B) + (C) |
|---|---|---|---|---|
| Jan | 342,492 | 204,135 | 48,320 | 594,947 |
| Feb | 328,683 | 195,433 | 53,388 | 577,504 |
| Mac | 338,133 | 210,907 | 60,478 | 609,518 |
| Apr | 324,415 | 199,382 | 52,093 | 575,890 |
| May | 373,743 | 218,967 | 52,231 | 644,941 |
| June | 326,117 | 196,783 | 44,989 | 567,889 |
| July | 352,453 | 200,486 | 53,637 | 606,576 |
| Aug | 335,724 | 192,697 | 50,600 | 578,621 |
| Sept | 311,163 | 169,656 | 46,903 | 527,722 |
| Oct | 348,490 | 198,569 | 51,797 | 598,856 |
| Nov | 337,141 | 193,185 | 44,874 | 575,200 |

In the electricity bill especially for commercial consumer, there are additional charges imposed by TNB such as maximum demand (MD), Imbalance Cost Pass-Through (ICPT) and RE fund (KWTBB). MD is the highest level of electrical demand monitored in a particular period usually for a month period as shown in Table 2 below. Currently the MD rate is RM45.1 per kW. Meanwhile, ICPT is a mechanism to reflect changes in fuel and other related costs in the electricity power plant. In addition, the ICPT rate is reviewed every 6 months. For example, the ICPT rate is RM0.17 per kWh for the first 6 months in 2024 and has been reduced to RM0.16 per kWh for July onwards. On the other hand, the Renewable Energy Fund (KWTBB) is a fund collected by the Government to be used to promote growth of electricity generation from renewable energy resources. For time being, KWTBB rate is 1.6%.

Table 2: Maximum Demand (MD) every month

| Month | Maximum Demand, kW | Maximum Demand Charge, RM |
|---|---|---|
| Jan | 1671 | 75,362.10 |
| Feb | 1720 | 77,572.00 |
| Mac | 1698 | 76,579.80 |
| Apr | 1792 | 80,819.20 |
| May | 1822 | 82,172.20 |
| June | 1790 | 80,729.00 |
| July | 1702 | 76,760.20 |
| Aug | 1641 | 74,009.10 |
| Sept | 1678 | 75,677.80 |
| Oct | 1715 | 77,346.50 |
| Nov | 1694 | 76,399.40 |

For this study, the estimated total electricity bill was calculated for the total energy used assuming electricity supplied entirely from TNB. The detailed calculation is tabulated in Table 3 below. The cost saving is calculated by the difference between the estimation electricity bill with the actual bill as shown in Table 4 below with total is RM140,694.18 with average saving is RM12,790.38 monthly.

Table 3: Detailed calculation assuming energy is supplied by TNB in RM

| Month | Peak Hour (G)= [(A) + (C)] x C2p | Off Peak (H) = (B) x C2o | ICPT (I)=(D)xICPT | KWTBB (J)=[(G)+ (H) + (F)] x 1.6% |
|---|---|---|---|---|
| Jan | 142,646.38 | 45,726.24 | 101,140.99 | 4,219.76 |
| Feb | 139,455.92 | 43,776.99 | 98,175.68 | 4,172.88 |
| Mac | 145,493.02 | 47,243.17 | 103,618.06 | 4,309.06 |
| Apr | 137,425.42 | 44,661.57 | 97,901.30 | 4,206.50 |
| May | 155,480.51 | 49,048.61 | 109,639.97 | 4,587.22 |
| June | 135,453.69 | 44,079.39 | 96,541.13 | 4,164.19 |
| July | 148,222.85 | 44,908.86 | 97,052.16 | 4,318.27 |
| Aug | 141,008.26 | 44,275.62 | 93,437.28 | 4,148.69 |
| Sept | 130,694.09 | 38,002.94 | 84,435.52 | 3,910.00 |
| Oct | 146,104.76 | 44,479.46 | 95,816.96 | 4,286.89 |
| Nov | 139,435.48 | 43,273.44 | 92,032.00 | 4,145.73 |

Table 4: Cost saving

| Month | Estimation Bill without solar, RM (K) | Actual Bill, RM (L) | Saving Amount, RM (K)-(L) |
|---|---|---|---|
| Jan | 369,095.47 | 356,729.05 | 12,366.42 |
| Feb | 363,153.47 | 349,490.45 | 13,663.02 |
| Mac | 377,243.10 | 361,767.60 | 15,475.50 |
| Apr | 365,013.99 | 351,680.35 | 13,333.64 |
| May | 400,928.51 | 387,565.65 | 13,362.86 |
| June | 360,967.41 | 349,455.75 | 11,511.66 |
| July | 371,262.34 | 358,069.75 | 13,192.59 |
| Aug | 356,878.94 | 344,429.70 | 12,449.24 |
| Sept | 332,720.35 | 321,178.60 | 11,541.75 |
| Oct | 368,034.56 | 355,282.65 | 12,751.91 |
| Nov | 355,286.05 | 344,240.45 | 11,045.60 |

However, if the saving from reduction of MD is taken into consideration, the total saving every month would be higher as shown in Figure 3 below. Before the implementation of solar PV, the average MD was 1843kW monthly. After the solar PV used in MNA, the MD reading generally has been dropped to below 1800kW as can be seen in Table 2.

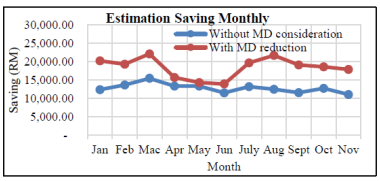



Figure 3: Estimation saving with and without MD consideration

## 4 Conclusions

With the presence of solar PV at Bangi Complex, the total electricity bill cost savings from January to November 2024 is RM140,694.18 with a monthly average of RM12,790.38. However, if savings from maximum demand (MD) are taken into account, the total savings per month will be higher. Additionally, the saving will be higher after SARE contract completed in 2043.

## References

Bahagian Pengurusan Maklumat (BPM). 2022. Kad laporan 2022 agensi nuklear malaysia: Pelaksanaan projek solar leasing. ISBN 978-967-9970-81-4:29.

Individual Research Contribution Review, 2024: 233–234
*ISSN: 3083-922X*

# Monte Carlo Studies on Depth Penetration of the Low Energy Electron Accelerator using PHITS in Difference Distance of PTFE Material

**Mohd Azhar Ahmad**
Bahagian Sokongan Teknikal, Malaysian Nuclear Agency
43000 Kajang, Selangor
mohdazhar@nm.gov.my

## Abstract

Particle and Heavy Ion Transport Code System (PHITS) is a Monte Carlo simulation program used for transport and interactions of nearly all particles over wide energy range. One of its useful features for accelerator design is the calculation of depth dose profile. This paper describes depth dose measurement of Low Energy Electron Accelerator (LEEA) by using PHITS. The penetration dose was obtained during the simulation process on PTFE materials in different distance from 5 cm, 7cm to 9 cm from window to the sample.

**Keywords:** Low Energy Electron Accelerator; Depth Dose Profile, PHITS

## 1 Introduction

Low-energy electron accelerators are widely utilized in various scientific and industrial applications, including surface treatment, radiation therapy, and material analysis. The ability of these accelerators to deliver precise doses of energy to specific depths within a material makes them invaluable in fields such as medical physics and materials science. However, understanding and predicting the penetration depth and energy deposition of low-energy electrons within different materials is crucial for optimizing these applications (Chulan et al., 2020).

Malaysian Nuclear Agency has successfully developed a Low Energy Electron Accelerator (LEEA) with the maximum energy of 250 keV and beam current output of 30 mA (Wah et al., 2020). For this device to work properly, it needs to go into the commissioning process to ensure the reliability of the resulting radiation dose. There are several parameters to be tested and studied and one of them is the depth penetration profiles of electrons in material after passing through titanium foil and the air.

PHITS, which stands for Particle and Heavy Ion Transport Code System, has been developed by JAEA. It is a general-purpose Monte Carlo particle transport simulation code and is used in many studies and one of them is on accelerator technology studies (Wah et al., 2021). The interaction of low-energy electrons with matter is complex, involving multiple scattering events, ionization, and energy loss through various mechanisms. As a result, computational approaches, particularly Monte Carlo simulations, have become essential tools for modeling electron transport and understanding depth penetration (Zin et al., 2019).

In this study, we use PHITS to perform Monte Carlo simulations of low-energy electron penetration in PTFE materials. By simulating various scenarios, including different distance we aim to enhance the understanding of electron-matter interactions and provide data that can be used to optimize the design and application of LEEA.

## 2 Objectives

The objective of the study is:

1. To investigate how low-energy electrons penetrate into polytetrafluoroethylene (PTFE) material
2. To determine the depth penetration profiles of low-energy electrons penetrate into PTFE material.
3. To analyze the effect of distance by examine the distance between the scanning window and the PTFE material affects the penetration depth of electrons.

## 3 Methodology

The methodology for this study involves several key steps. PTFE (polytetrafluoroethylene) samples with 1 cm thickness is select for this simulation to study the penetration depth. The geometry setup is design based on the dimensional size of LEEA, including the vacuum inside accelerator tube, 25 µm titanium scanning window and positioning of the PTFE samples varying distances (5 cm,7 cm,9 cm) from the scanning window. The geometry of this simulation in PHITS software for 9 cm distance as shown in Figure 1.

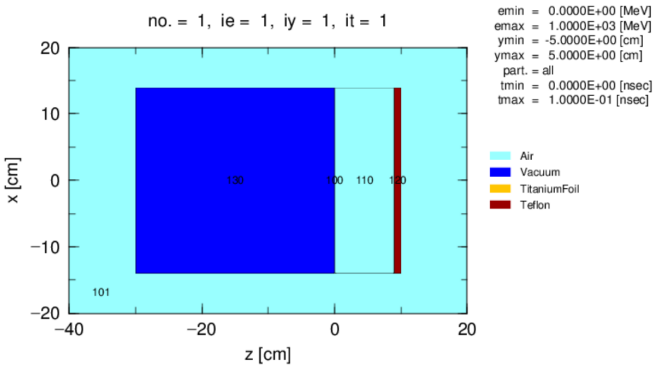



Figure 1: Geometry in PHITS for 9 cm distance.

For PHITS simulation process, the Monte Carlo simulations is run for each distance setting, generating data on electron penetration depth, energy deposition, and scattering within the PTFE. The depth penetration profiles generated by the simulations is analyze to determine how deep the electrons penetrate into the PTFE material at each distance and identify the maximum penetration depth and compare it changes with varying distances from the scanning window. The penetration depths and energy deposition patterns across the different distances is compare to determine the influence of distance on electron-material interactions.

## 4 Results and Discussions

The study is confirming that increasing the distance between the scanning window and the sample PTFE material leads to a decrease in penetration depth. Figure 2 shows that distance of 5 cm give the highest depth penetration around 80 µm compare with 70 µm and 60 µm for 7 cm and 9 cm, respectively.

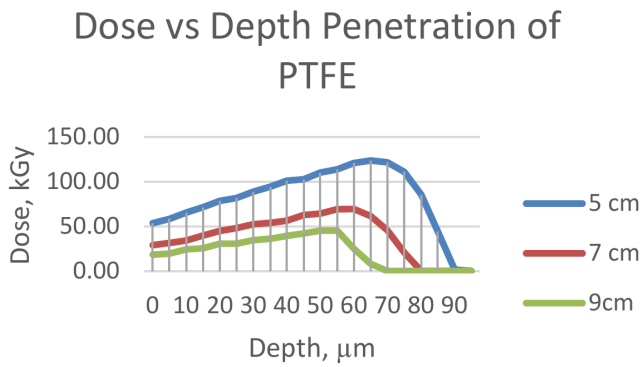



Figure 2: Graph of Dose vs Depth Penetration of PTFE

This observation is due to the loss of energy electrons experience through scattering and interactions with the medium between distance of air and the target material. It is likely that energy deposition will be concentrated near the surface of the PTFE material, with a rapid falloff in energy as the electrons travel deeper into the material. This could indicate that low-energy electron beams are more suitable for surface modifications or treatments, as most of the energy does not penetrate deeply.

The simulation results are expected to closely match theoretical models of electron penetration in materials like PTFE. The experimental results align with the experimental data in paper (Wah et al., 2023) confirming the accuracy of the PHITS simulation in modeling electron-material interactions.

## 5 Conclusion

This study successfully employed the Monte Carlo simulation method using PHITS to investigate the depth penetration of low-energy electrons in PTFE materials in different distance from 5 cm, 7 cm to 9 cm from window to the sample. The findings demonstrate that the penetration depth of low-energy electrons is highly dependent on the distance and material's density. Energy deposition profiles indicate that low-energy electrons deposit most of their energy near the material's surface, with rapid attenuation as depth increases. This characteristic makes low-energy electrons particularly useful for applications requiring surface-level treatments.

## References

Mohd Rizal Md Chulan, Mohd Faiz Mohd Zin, Leo Kwee Wah, Mukhlis Mokhtar, Mohd Azhar Ahmad, Rokiah Mohd Sabri, Khaidawaton Abd Malik, et al. 2020. Electron range after titanium foil window from low energy electron accelerator. In *IOP Conference Series: Materials Science and Engineering*, volume 785, page 012003. IOP Publishing.

Leo Kwee Wah, M Azhar, RM Chulan, SA Hashim, M Mokhtar, H Baijan, RM Sabri, et al. 2020. Development of the scanning power supply for 300 kev electron accelerator. In *IOP Conference Series: Materials Science and Engineering*, volume 785, page 012037. IOP Publishing.

Leo Kwee Wah, M Azhar, RM Chulan, SA Hashim, M Mokhtar, H Baijan, RM Sabri, et al. 2021. Study the dose profile of low energy electron accelerator. In *IOP Conference Series: Materials Science and Engineering*, volume 1106, page 012023. IOP Publishing.

Leo Kwee Wah, M Mokhtar, M Azhar, RM Chulan, SA Hashim, MN Shafeek, H Baijan, and RM Sabri. 2023. Study the depth dose profile of the low energy electron accelerator. *JOURNAL of NUCLEAR and Related TECHNOLOGIES*, pages 13–18.

Mohd Faiz Mohd Zin, Mohd Rizal Md Chulan, Leo Kwee Wah, Rokiah Mohd Sabri, Mohd Azhar Ahmad, Mukhlis Mokhtar, Khaidawaton Abd Malik, et al. 2019. Monte carlo studies for the radiation shielding in the bunker of the electron beam accelerator using phits. In *IOP Conference Series: Materials Science and Engineering*, volume 555, page 012020. IOP Publishing.

Individual Research Contribution Review, 2024: 235–236
*ISSN: 3083-922X*

# Development of Rogowski Coil Diagnostics for the MNA Plasma Focus and Characterization of Its Focus Mode

**Mohd Faiz Bin Mohd Zin**
Technical Support Division, Malaysian Nuclear Agency
43000 Kajang, Selangor
faizzin@nm.gov.my

## Abstract

This work presents the development of diagnostic tools for the Malaysian Nuclear Agency Plasma Focus (MNA-PF) device and its characterization as operating in the slow focus mode. Using argon as the filling gas, experiments were conducted to identify the optimal operational parameters. Four Rogowski coil designs were tested to measure discharge current, highlighting the impact of response frequency on signal resolution. Results from a 630 MHz Rogowski coil and Lee Model Code simulations identified 1.5 mbar argon at 12 kV as the optimal pressure for achieving a good pinch. The speed factor ($84\,\mathrm{kA/cm.torr^{1/2}}$) confirmed the slow focus mode. This study demonstrates the utility of diagnostics in optimizing plasma focus operations and provides insights into future device enhancements.

**Keywords:** Plasma Focus, Rogowski coil, Lee Model Code, plasma diagnostics

## 1 Introduction

The MNA-PF device, a 3.37 kJ Mather-type plasma focus, generates multi-radiation sources including X-rays, ions, and neutrons, depending on the filling gas. With interest in neutron and ion beam applications, its operation in slow focus mode is of particular relevance for material science and nanotechnology (Damideh et al., 2012) (Salehizadeh et al., 2013). The study aims to validate the device's operational mode and optimize its performance through advanced diagnostic tools, particularly Rogowski coils and Lee Model Code simulations.

## 2 Methods

### 2.1 Experimental Setup

The MNA Plasma Focus (MNA-PF) device is a Mather-type plasma focus system powered by a 30 µF capacitor bank charged up to 15 kV. It consists of:

- A stainless-steel experimental chamber with a gas inlet and vacuum system.
- A central copper anode and six rod cathode assembly.
- Diagnostic tools: magnetic probe, voltage probe, and Rogowski coils for measuring current and voltage waveforms.

The experiments were conducted with argon gas pressures ranging from 0.5 mbar to 5.5 mbar. Signals were recorded using a 1 GHz oscilloscope.

### 2.2 Rogowski Coil Development

Four types of Rogowski coils were designed with varying geometry, materials, and measurement locations. The final coil (23 turns wound around a plastic tube) achieved the best time resolution of 1.6 ns. Measurements at the collector plate were found to be the clearest.

### 2.3 Lee Model Code Simulations

The Lee Model Code was employed to simulate current waveforms and determine the optimal operating parameters of the MNA-PF device. Experimental data was fitted to the code to validate the slow focus mode of operation.

## 3 Results and Discussions

### 3.1 Current Waveform Analysis

The discharge current waveforms measured using the four Rogowski coil designs revealed the influence of coil geometry, material, and placement on signal clarity and resolution. The fourth coil design, which consisted of 23 turns wound on a plastic tube and placed at the collector plate, provided the clearest and most noise-free signal. Its high response frequency (630 MHz) allowed for a time resolution of 1.6 ns, which was critical for accurately capturing rapid current changes in the plasma focus discharge.

The current waveforms were consistent with theoretical predictions, confirming the accuracy of the Rogowski coil design in diagnosing plasma dynamics. Signals taken from the collector plate produced better waveform integrity compared to those taken from single high-voltage cables, likely due to reduced interference and noise at this location.

### 3.2 Optimal Operational Operators

Through a series of tests using argon as the filling gas, the optimal pressure for operation was determined to be 1.5 mbar at 12 kV. At this setting, the plasma focus device achieved a stable and well-defined pinch. Key parameters derived from Lee Model Code fitting include:

- Static Inductance (L): 320 nH, higher than the typical value (110 nH) for similar devices, indicating the MNA-PF's unique design.

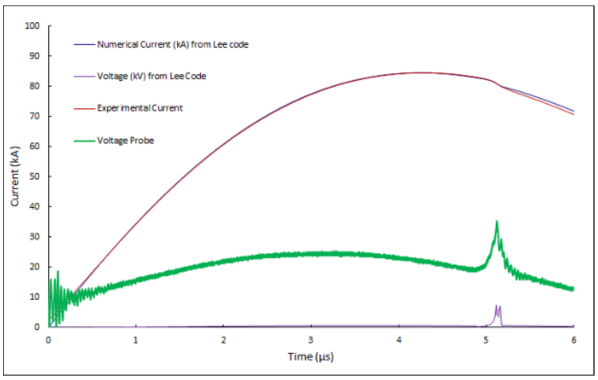



Figure 1: Caption

- Speed Factor: 84 kA/cm·torr 2 84 kA/cm.torr$^{1/2}$, confirming slow focus mode operation (Al-Hawat et al., 2012).
- Mass Swept Factors: Axial phase ( $f_m$ = 0.0223) and radial phase ($f_{mr}$ = 0.37).

These values highlight the MNA-PF's slower dynamics, which are attributed to its high circuit inductance. The slow focusmode is particularly beneficial for material science applications as it enables better control over plasma compression and energy transfer (Shafiq et al., 2014).

### 3.3 Pressure Dependence and Plasma Behavior

Tests conducted over a pressure range from 0.5 mbar to 5.5 mbar showed significant variation in device performance:

- Low Pressure (0.5–1.0 mbar): Higher inductance values (420 nH) were observed, resulting in incomplete plasma compression and reduced pinch quality.
- Optimal Pressure (1.5 mbar): The best fits between experimental and simulated current traces were achieved in Fig. **??**. The pinch current peaked at 56 kA, with strong plasma confinement.
- High Pressure (> 2.0 mbar): Plasma parameters, including speed and temperature, declined significantly, leading to weaker compression and broader pinch radii.

The observed pressure-dependent behavior emphasizes the importance of fine-tuning gas pressure to maintain optimal plasma characteristics. Beyond 1.5 mbar, the increasing resistance and inductance within the system led to reduced pinch intensity, as confirmed by the Lee Model Code.

### 3.4 Challenges in High-Inductance Systems

The MNA-PF's relatively high inductance is a result of its design, particularly the long high-voltage cables connecting the capacitor bank to the collector plate. This high inductance limits the device's speed factor, which directly impacts the efficiency of plasma focus compression. Future improvements could involve: 1. Replacing the current cables with low-inductance alternatives (Akel and Lee, 2012), 2. Optimizing the capacitor bank configuration to reduce energy losses, 3. Exploring advanced electrode geometries to enhance current sheath dynamics.

### 3.5 Simulation and Validation

The Lee Model Code simulations validated the experimental results, providing accurate predictions of plasma behavior. The fitting process revealed the device's suitability for slow focus mode applications. Additionally, the results demonstrated the robustness of the diagnostic approach, particularly the Rogowski coil, in capturing high-resolution data for computational modeling.

## 4 Conclusions

A Rogowski coil made by using single wire with 23 turns wounded around a plastic tube and used to measure the current of all cables produced the best signal time resolution. This coil will be used to for diagnostic purposes in latter exercises. We have also verified that MNA-PF is working on slow focus mode due to the high inductance that may have come from the modifications made on the connecting cables. Using the Lee Model Code, the operating characteristics of the system in argon gas for the MNA-PF were obtained and will be used to run for further experiments.

## Acknowledgements

This project is supported by Ministry of Science, Technology, and Innovation (MOSTI) through RMK11 RP1 budget, managed by Malaysian Nuclear Agency.

## References

M Akel and S Lee. 2012. Dependence of plasma focus argon soft x-ray yield on storage energy, total and pinch currents. *Journal of fusion energy*, 31(2):143–150.

Sh Al-Hawat, M Akel, S Lee, and SH Saw. 2012. Model parameters versus gas pressure in two different plasma focus devices operated in argon and neon. *Journal of fusion energy*, 31:13–20.

V Damideh, AA Zaeem, A Heidarnia, A Sadighzadeh, MA Tafreshi, F Abbasi Davani, M Moradshahi, M Bakhshzad Mahmoudi, and R Damideh. 2012. Design and fabrication of 11.2 kj mather-type plasma focus ir-mpf-1 with high drive parameter. *Journal of fusion energy*, 31:47–51.

A Salehizadeh, A Sadighzadeh, M Sedaghat Movahhed, AA Zaeem, A Heidarnia, R Sabri, M Bakhshzad Mahmoudi, H Rahimi, S Rahimi, E Johari, et al. 2013. Preliminary results of the 115 kj dense plasma focus device ir-mpf-100. *Journal of Fusion Energy*, 32:293–297.

Muhammad Shafiq, G Amjad Hussain, Lauri Kütt, and Matti Lehtonen. 2014. Effect of geometrical parameters on high frequency performance of rogowski coil for partial discharge measurements. *Measurement*, 49:126–137.

Individual Research Contribution Review, 2024: 237–238
*ISSN: 3083-922X*

IRCR

# Preliminary Study on the Relationship Between Be-7 Concentration and Northeast Monsoon Dynamics: Insights from Indices of Monsoon Activity

**Mohd Fauzi Haris**
Bahagian Sokongan Teknikal, Malaysian Nuclear Agency
43000 Kajang, Selangor
fauziharis@nm.gov.my

## Abstract

Establishing several radionuclide stations by the Comprehensive Nuclear Test-ban Treaty (CTBT) along wind pathways during the Northeast Monsoon season has provided a unique opportunity for this study to investigate and further utilize Be-7 concentration. Beryllium-7 (Be-7), a cosmogenic radionuclide also detected by these stations, serves as a tracer for atmospheric processes, particularly precipitation dynamics influenced by monsoonal patterns. This research explores the initial correlation between Be-7 concentration and two types of surges during the Northeast Monsoon in Malaysia: Easterly surges (ES) and Meridional surges (MS). The Northeast Monsoon, a significant climatic phenomenon in Southeast Asia, impacts regional weather patterns and precipitation levels. Understanding the correlation between Be-7 concentration and these two surges could provide insights into atmospheric transport mechanisms, rainfall variability, and potential implications for climate and environmental studies. Granger Causality tools is used for this purpose. Initial findings suggest a potential linkage between Be-7 concentration and the intensity or duration of the Northeast Monsoon, highlighting avenues for further research to elucidate these interactions more comprehensively.

**Keywords:** Be-7 intensity, Granger causality test, Easterly surge, Meridional surge

## 1 Introduction: Climate Influence on Be-7 Concentration

Understanding the dynamics of the Northeast Monsoon is crucial for predicting weather patterns and mitigating the impacts of extreme weather events. The northeast monsoon season, or winter season in Malaysia, starts in October or November and usually ends in March next year. During the season, the amount of rainfall is very intense compared to other seasons in Malaysia (Suhaila et al., 2010). About half of the yearly precipitation in Peninsular Malaysia's east coastline regions, which face the South China Sea (SCS), falls during the first half of the northeast monsoon season, from November to December. These two months may account for up to 70% of the annual total rainfall in some years with a vigorous monsoon (Moten et al., 2014). This phenomenon can create catastrophic events in the exposed area, such as heavy floods and landslides, and the amount of losses in terms of cost reaches up to millions of ringgit annually.

This preliminary study explores the relationship between Be-7 concentration and the ES an MS. By analyzing historical data, we seek to determine whether variations in Be-7 levels can serve as a predictive marker for monsoon intensity and behavior. Previous research has suggested a link between Be-7 and monsoon activity, such as a study by Terzi et al. (2019) to predict monsoon onset and withdrawal in Kerala, India, providing a foundation for our investigation. Understanding this relationship could help identify the CTBT radionuclide stations that most interact with easterly and meridional surges, thus enhancing our ability to forecast monsoon events effectively and improving preparedness for their associated impacts.

## 2 Methodology

The following flowchart illustrates the key steps undertaken to investigate the relationship between Be-7 concentration and the Northeast Monsoon Index. This process begins with identifying and shortlisting the CTBTO's radionuclide station for data collection and preprocessing, followed by applying statistical methods such as the Granger causality test. It concludes with the analysis and interpretation of the results. Each stage is designed to systematically address the research objectives, ensuring a robust and thorough examination of the data. The flowchart in Figure 1 below visually summarizes the entire process, highlighting the sequence and interconnection of each step.

## 3 Results & Discussions

| | **Meridional Surge** | | **Easterly Surge** | |
|---|---|---|---|---|
| | P-value | Optimum lag value | P-value | Optimum lag value |
| JPP37 | 0.0008* | 6 | 0.0001* | 3 |
| MNP45 | 0.0246* | 11 | 0.1128 | 4 |
| PHP52 | 0.0059* | 11 | 0.0071* | 4 |
| USP77 | 0.7341 | 6 | 0.0069* | 2 |
| USP78 | 0.3800 | 6 | 0.0017* | 4 |
| USP79 | 0.4321 | 6 | 0.0920 | 3 |
| USP80 | 0.7666 | 11 | 0.0306* | 5 |

Statistically significant, $p < 0.005$

Table 1: Granger Causality test result

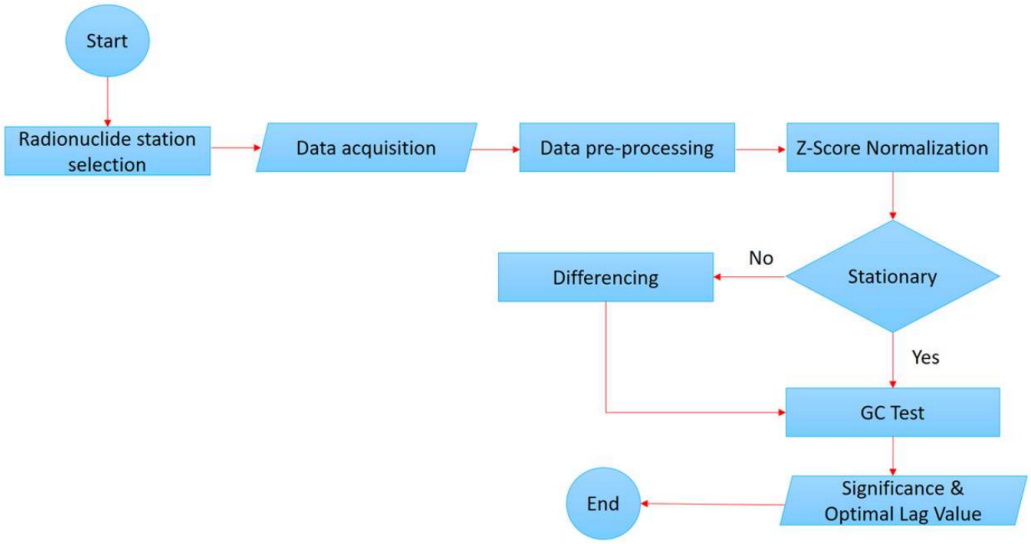



Figure 1: Flowchart of the study.

Our Granger causality analysis explored the relationship between MS and ES with Be-7 concentrations in Table 1. There is evidence that past values of both surges have Granger predictive value for Be7 intensity, which is evidence of a Granger causal relationship. These findings further emphasize the impact of atmospheric surges on Be-7 levels across various locations.

## References

Subramaniam Moten, Fariza Yunus, Munirah Ariffin, Norazura Burham, Diong Jeong Yik, Mat Kamaruzaman Mat Adam, and Yip Weng Sang. 2014. Statistics of northeast monsoon onset, withdrawal and cold surges in malaysia. *Petaling Jaya*.

Jamaludin Suhaila, Sayang Mohd Deni, WZ Wan Zin, and Abdul Aziz Jemain. 2010. Trends in peninsular malaysia rainfall data during the southwest monsoon and northeast monsoon seasons: 1975–2004. *Sains Malaysiana*, 39(4):533–542.

Lucrezia Terzi, Martin Kalinowski, Michael Schoeppner, and Gerhard Wotawa. 2019. How to predict seasonal weather and monsoons with radionuclide monitoring. *Scientific reports*, 9(1):2729.

Individual Research Contribution Review, 2024: 239–240
*ISSN: 3083-922X*

# Dust Collector System Design Consideration for Analytical Chemistry Application Group (ACA)

**Mohd Rizal Mamat bin Ibrahim**
Technical Support Division, Malaysian Nuclear Agency
43000 Kajang, Selangor
m_rizal@nm.gov.my

## Abstract

Analytical Chemistry Application Group (ACA) has requested the assistance from Prototype and Plant Development Centre (PDC) in determining and specifying the appropriate dust collector system for their use in the handling of homogenized powdered samples. ACA has planned to procure a dust collector system to replace the existing in-house dust exhaust system. This extended abstract outlines the main design consideration of the dust collector system.

**Keywords:** dust collector system, main design consideration

## 1 Introduction

In 2024, the Analytical Chemistry Application Group (ACA) group received funding for procurement of dust collector system to be installed in block 18. The ACA has requested a consultancy service from the Plant and Prototype Development Center (PDC) group to determine and specify the appropriate dust collector system in the market suited for their need and usage.

Previously, the handling of powdered samples was done under a flexible hose attached to the extraction fan installed at the window. There was still a risk of dust exposure/inhalation to the worker and the powdered samples were just released to outside environment without any proper trap/collector mechanism.

Dust collection systems are designed to capture airborne particles generated during industrial operations. These systems play a crucial role in maintaining workplace safety, improving air quality, reducing environmental impact, and ensuring regulatory compliance.

The new installed dust collector (Figure 1) would provide a better system to collect or trap the airborne sample particulates while protecting the worker and also improve the air quality.

## 2 Dust Collector Selection Consideration

The selection of a dust collector takes into account several main factors to ensure optimal performance which include dust characteristics and load, selecting the right type of dust collection system, determining the appropriate airflow capacity, determining the appropriate filter area, choosing the best filtration media, and consideration of ease of maintenance (ACGIH, 2019).




Figure 1: Downdraft Bench Dust Collector (DUSTHOG Model VB-1500) installed in grinding laboratory (Room 18125)

### 2.1 Dust Characteristics and Load

The samples that need to be handled are homogenized powder samples of 200 - 300 micron size that are produced from grinding process using ball mill grinder. The types of samples include environment samples (soil, sediment, rock,mineral), plants, etc. The samples are for Neutron Activation Analysis after being irradiated in the Reactor TRIGA PUSPATI. The weight of the sample is about 500 g per sample and about 30 – 50 samples are prepared per month. The dust collector is intended to be used during the handling of the samples that have been grinded. Therefore the dust load should not be as high as during the grinding process (roughly about 70% less). The dust collector system selected needs to be able to sufficiently cater for the dust load expected.

### 2.2 Type of Dust Collector System Selected

There are many types/categories of dust collector system in the market that cater for various industries and activities which include Baghouse Dust Collectors, Cyclone Dust Collectors, Electrostatic Precipitators, Wet Scrubbers and Cartridge Collectors. The initial design of the dust collector system focused on the Baghouse Dust Collector system that involved long ducting/piping and much higher space requirement with much bigger capacity. However, finally after having taking into account the medium work load, medium sample size, limited size of the grinding laboratory and cost, downdraft bench cartridge dust collector has been chosen.

### 2.3 Minimum Air Flow Capacity Calculated

Since the type of dust collector system that has been selected is an integrated downdraft bench dust collector unit, it has no long ducting/piping (from the point of dust generation to the point of dust collection) that is typically associated with other dust collector system such as Baghouse Dust Collectors or Cyclone Dust Collectors. In this case, no system pressure loss and fan capacity/power need to be calculated. The only main parameter to be calculated is the air flow capacity of the downdraft bench collector unit.

Airflow capacity and velocity are crucial to the design of an efficient dust collection system. The system must be able to capture dust at the point of generation, requiring a precise balance between airflow and collection efficiency.

The minimum air flow capacity has been calculated from the minimum air face velocity of 200 FPM multiplied by the cross-sectional area of the estimated working area which is 6 $ft^2$. The calculated minimum air flow capacity is 600 CFM.

### 2.4 Filter Surface Area Calculated

The efficiency of the dust collector also depends on the filtration area, which should be large enough to handle the dust load without causing excessive pressure drops. The total filtration area required can be calculated by dividing the airflow capacity (600 CFM) with the filter velocity (roughly 2.5 FPM). The calculated total filtration area is 240 $ft^2$.

### 2.5 Filtration Media Selected

The selection of filtration media plays a central role in the efficiency of the dust collector. The media must be capable of handling the particle size distribution of the dust, as well as any chemical or thermal properties that may affect its performance. Common filtration materials include polyester, polypropylene, and PTFE for standard applications, while more specialized materials like ceramic or metal may be required for high-temperature or highly abrasive dusts.

The filtration media selected is HEPA filter of MERV 15 specifications. These high-efficiency filters trap over 95% of particles sized 3.0-10.0 microns.

### 2.6 Consideration of Ease of Maintenance

The dust collector selected must incorporate ease of maintenance to ensure long-term performance. Regular filter cleaning or replacement, monitoring of system performance, and inspections of components such as fans are essential to maintaining efficient operation.

Pulse-jet as the dust load and filter cleaning mechanisms has been considered as additional feature to the selected dust collector system as it can minimize maintenance downtime and extend filter life. The pulse-jet works by injecting pulses of compressed air (6-7 bar of pressure) to the filter so that the dust would fall to the drawer usually located at the bottom of the dust collector unit. The dust drawer would then be removed and the dust would be appropriately disposed of.

## 3 Conclusion

Selecting the right dust collector system for an application involves considering several factors that ensure optimal performance, safety, and also cost. A well-chosen dust collector can help maintain air quality, meet regulatory requirements, and improve overall operational efficiency.

The dust collector unit that has been selected based upon all the consideration discussed before is DUSTHOG VB-1500 downdraft bench dust collector unit from Parker that comes with HEPA MERV 15 cartridge (and dust drawer), acrylic cover and wheel.

The main speciation of the DUSTHOG VB-1500 (Corporation, 2020) downdraft bench dust collector unit is listed below:

**Model** VB-1500

**Nominal Airflow (CFM)** 1500

**Filter Area ($ft^2$)** 283

**Sound Level (dBA)** 77

**Motor (HP)** 3

**Drawer Capacity ($ft^3$)** : 1.242

**Size** 1340mm (L) x 762mm (W) x 1189mm (H)

## References

ACGIH. 2019. *Industrial Ventilation : A Manual of Recommended Practice*. American Conference of Governmental Industrial Hygienists, 30 edition.

Parker Hannifin Corporation. 2020. Versatile/portable cartridge (v-series) dust collectors. `https://www.parker.com/content/dam/Parker-com/Literature/IGFG/IAF/DustHog\_V-Series\_Brochure.pdf`.

Individual Research Contribution Review, 2024: 241–242
*ISSN: 3083-922X*

# Review on Slam Methods for Unmanned Ground Vehicle Autonomous Mapping

**Mohd Shafiq Bin Sazali**
Technical Support Division, Malaysian Nuclear Agency
43000 Kajang, Selangor
mohdshafiq@nm.gov.my

## Abstract

Simultaneous Localization and Mapping (SLAM) is vital for enabling Unmanned Ground Vehicles (UGVs) to autonomously navigate and map unknown environments, with applications spanning search and rescue, agriculture, and logistics. This paper reviews three prominent SLAM methods—GMapping, Hector SLAM, and Cartographer—analyzing their mapping accuracy, computational efficiency, and robustness in varied scenarios. It evaluates their suitability for diverse operational requirements and highlights advancements in sensor technology and artificial intelligence integration. The findings aim to guide researchers and industry professionals in selecting optimal SLAM solutions to advance autonomous navigation.

**Keywords:** Simultaneous Localization and Mapping (SLAM), Unmanned Ground Vehicles (UGVs), Autonomous Mapping

## 1 Introduction

SLAM technology empowers UGVs to create real-time maps of unknown environments while localizing themselves (Shafiqul Islam et al., 2022). Based on Bayesian filtering, SLAM involves prediction and measurement updates, leveraging sensors like LiDAR, cameras, and IMUs. Historically, SLAM faced challenges in handling complex environments due to limited sensors and computational capabilities. Advances in algorithms, high-performance computing, and machine learning now enable SLAM to tackle intricate environments, offering adaptability to dynamic conditions (Dhaoui et al., 2025). However, achieving high accuracy, efficiency, and robustness across diverse conditions remains a critical challenge.

## 2 SLAM Methods Overview

This review examines three SLAM methods(Table 1), each suited for specific applications such as GMapping employs a particle filter to construct 2D occupancy grids, excelling in handling noisy data but demanding high computational resources for complex environments. Hector SLAM uses scan matching, enabling efficient real-time mapping without relying on odometry, but struggles with featureless or sparse sensor data environments. Cartographer combines laser scans and IMU data to support 2D and 3D mapping, offering high accuracy and adaptability for large-scale operations, albeit with significant computational demands (Dhaoui et al., 2025).

| **Feature** | **GMapping** | **Hector SLAM** | **Cartographer** |
|---|---|---|---|
| **Year** | 2007 | 2011 | 2016 |
| **Algorithm Type** | RBPF (Rao-Blackwellized particle Filter) | Graph-based SLAM | Hybrid approach (Laser+IMU) |
| **Type of LIDAR** | 2D LIDAR | 2D LIDAR | 2D or 3D LIDAR |
| **Performance** | Good for indoor and outdoor environments | Fast and accurate for indoor environments | High accuracy and performance |
| **Odometry** | Uses odometry for pose estimation | Does not require odometry | uses IMU for pose estimation |
| **Computational Load** | Moderate | Low | High |
| **Ease of Use** | Easy to set up and use | Requires careful tuning | Requires calibration and tuning |
| **Applications** | Indoor and outdoor mapping, robotics | Indoor mapping, small scale environments | Large-scale environments, autonomous vehicles |

Table 1: Features of SLAM Methods

## 3 Performance Comparison

Performance evaluation focuses on three criteria which are Mapping Accuracy, Computational Efficiency and Robustness. All of these criteria are compared with the ground truth (1) which symbolize as the actual environment mapping. For the first criteria which is Mapping Accuracy, GMapping (2) performs well in structured indoor environments, but it's accuracy will be affected by complex configuration citedhaoui2025benchmarking, Hector SLAM (3) excels in dynamic settings, but may struggle due to poor reflectivity where it mostly relies on high-frequency LiDAR data, and Cartographer (4) provides superior accuracy for complex terrains

which is relevant for UGV applications (Shafiqul Islam et al., 2022).

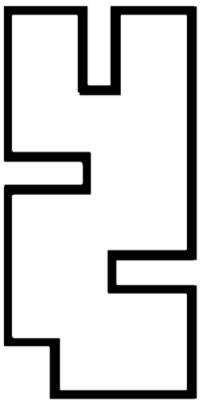


Figure 1: Ground Truth (Dhaoui et al., 2025)

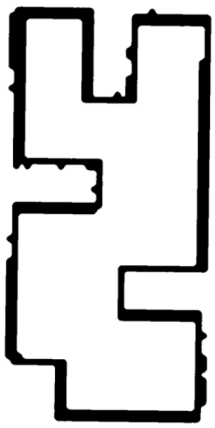


Figure 2: GMapping (Dhaoui et al., 2025)

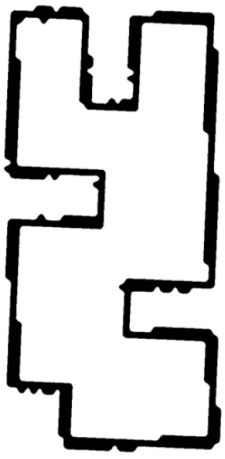


Figure 3: Hector SLAM (Dhaoui et al., 2025)

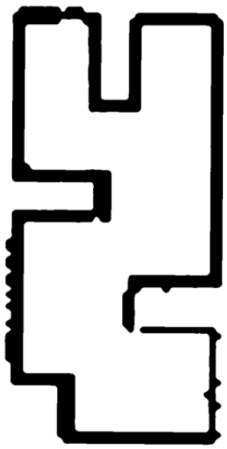


Figure 4: Cartographer (Dhaoui et al., 2025)

For Computational Efficiency, GMapping tends to be less computational efficient due to the method which it uses called particle filter-based approach that involves maintain and updating large number of particles to represent the UGV position. Hector SLAM is the most resource-efficient because it uses scan matching approach which simplifies the computational and reduces the processing power required, while Cartographer balances computational demands with accuracy.

GMapping's particle filter approach is resource-intensive and for Robustness, GMapping is versatile but less effective in dynamic environments. Hector SLAM adapts quickly to changes, and Cartographer demonstrates robustness in varied topologies (Svishchev et al., 2024).

## 4 Discussion

The selection of a SLAM method should align with application-specific needs such as GMapping offers precision in structured settings but is computationally taxing for real-time use. Hector SLAM is efficient and well-suited for dynamic conditions but limited to 2D mapping. Cartographer delivers high-quality maps and adaptability for diverse environments but requires advanced computational resources.

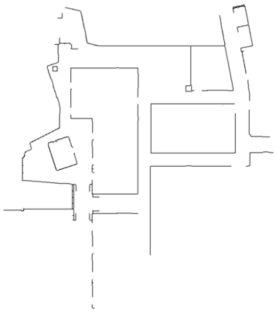


Figure 5: Ground Truth (Dhaoui et al., 2025)

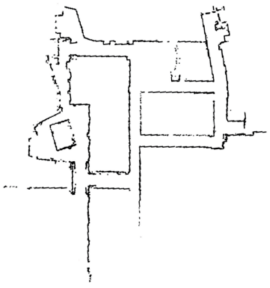


Figure 6: GMapping (Dhaoui et al., 2025)

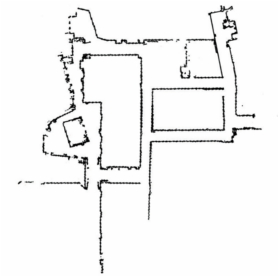


Figure 7: Hector SLAM (Dhaoui et al., 2025)

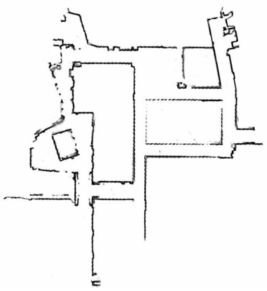


Figure 8: Cartographer (Dhaoui et al., 2025)

## 5 Conclusion

This review underscores SLAM's significance in advancing UGV autonomy. GMapping, Hector SLAM, and Cartographer cater to varied requirements, balancing accuracy, efficiency, and robustness. The integration of emerging technologies like AI holds promise for enhancing SLAM capabilities, making this review a valuable resource for researchers and practitioners.

## References

Riadh Dhaoui, Zuhair A Ahmed, Taha Houda, and Chaher Dhaoui. 2025. Benchmarking 2d laser-based slam algorithms: a novel framework for assessing occupancy grid map quality. *International Journal of Intelligent Robotics and Applications*, pages 1–15.

Md Shafiqul Islam, Md Tarequl Islam, and Mohammad Gazi Golam Faruque. 2022. A survey on lidar-based slam technique for an autonomous model using particle filters. In *Soft Computing for Security Applications: Proceedings of ICSCS 2021*, pages 227–240. Springer.

Nikolai Svishchev, Paolo Lino, Guido Maione, and Iskandar Azhmukhamedov. 2024. A comprehensive survey of advanced slam techniques. In *E3S Web of Conferences*, volume 541, page 05004. EDP Sciences.

Individual Research Contribution Review, 2024: 243–244
*ISSN: 3083-922X*

IRCR

# Comparative Analysis of Commercial Robots for Radiation Mapping

**Muhammad Izzuan bin Mohd Ghazali**
Technical Support Division, Malaysian Nuclear Agency
43000 Kajang, Selangor
izzuan@nm.gov.my

## Abstract

Radiation mapping is essential for safety in nuclear facilities, environmental monitoring, and emergency response. Autonomous robots improve safety, efficiency, and flexibility compared to manual methods. This paper evaluates four robots for radiation mapping: Elios 2 RAD, PackBot, Spot, and Go2 Edu Plus, based on mobility, sensor integration, mapping accuracy, environmental adaptability, and cost-effectiveness. Elios 2 RAD excels in aerial mobility for confined spaces, Spot in terrain adaptability, PackBot in durability for hazardous environments, and Go2 Edu Plus in affordability and customization. The aim is to guide decision-makers in selecting the most suitable platform based on operational needs, budget, and conditions.

**Keywords:** Autonomous Robot, Mapping, Safety

## 1 Introduction

In radiation-prone environments like nuclear plants or disaster zones, traditional detection is limited by access and risks to workers. Autonomous robots with radiation sensors can safely perform mapping tasks in hazardous areas, collecting precise data from dangerous or confined spaces. They are used in facility monitoring, environmental surveys, and emergency response.

Robots such as Elios 2 RAD, PackBot, Spot, and Go2 Edu Plus offer varied features for these tasks, including mobility, sensor integration, and environmental adaptability. This paper compares their suitability for radiation mapping based on mobility, sensor capabilities, mapping performance, environmental resilience, and cost.

## 2 Methods

This study compares four commercially available robots for radiation mapping: Elios 2 RAD, PackBot, Spot, and Go2 Edu Plus. Evaluation covers mobility, sensor integration, mapping capabilities, environmental adaptability, and cost-effectiveness. Mobility is assessed by the ability to navigate varied terrains, including confined spaces, rugged areas, and high-radiation zones. Sensor integration is evaluated for precision, real-time data collection, and platform compatibility.

Mapping capabilities are examined through each robot's use of LiDAR or specialized software to produce detailed radiation maps. Environmental adaptability considers performance in extreme conditions such as high temperatures, restricted access, and radiation-heavy areas. Costs, including base models and payloads, are converted to Malaysian Ringgit for local affordability analysis.

Data is sourced from technical datasheets, manufacturer specifications, case studies, and performance reviews, enabling a comprehensive comparison of each platform's strengths and limitations for radiation mapping in various scenarios.

## 3 Data/Results

### 3.1 Elios 2 RAD (Flyability

**3.1.1 Key Features:** The Elios 2 RAD is a drone designed for use in tight spaces, equipped with Geiger-Müller sensors to measure radiation levels. Its ability to fly in confined spaces such as reactor buildings or underground facilities makes it valuable for inspecting hazardous area (dronelife, 2021)

**3.1.2 Strengths:** It excels in environments that are difficult for humans or ground-based robots to access. Its aerial capability allows for quick and flexible radiation surveys in tight or dangerous locations.

**3.1.3 Limitations:** While the drone can map radiation levels in small areas, it is limited by its small payload capacity and may not be ideal for large-scale mapping

**3.1.4 Price:** Approximately MYR 325,000



Figure 1: Elios 2 RAD by Flyability

### 3.2 PackBot (Endeavor Robotics)

**3.2.1 Key Features:** The PackBot is a tracked robot capable of navigating rugged terrain and hazardous environments. Equipped with various sensors for radiation detection, it is designed to perform tasks in environments that are too dangerous for humans (Xiao et al., 2021)

**3.2.2 Strengths:** It is highly durable and can perform well in challenging terrains. Its tracked design ensures stability in environments where other robots might struggle.

**3.2.3 Limitations:** The PackBot is more focused on mobility and direct radiation detection rather than generating detailed radiation maps.

**3.2.4 Price:** Approximately MYR 300,000 which estimated from similar models)



Figure 2: PackBot by Endeavor Robotics

### 3.3 Spot with Radiation Payload

**3.3.1 Key Features:** Spot is a quadruped robot with high agility, capable of traversing difficult terrains. With customizable payloads, it can be equipped with radiation sensors for detailed data collection (Raj and Kos, 2022).

**3.3.2 Strengths:** It is extremely versatile, able to navigate stairs, rough terrain, and complex environments. Its payload flexibility makes it suitable for both radiation detection and mapping tasks.

**3.3.3 Limitations:** The primary limitation is its high cost, which includes customization for radiation-specific tools, making it less accessible for smaller projects or budgets.

**3.3.4 Price:** Approximately MYR 352,000 (base model without radiation payload)



Figure 3: Spot by Boston Dynamics

### 3.4 Go2 Edu Plus (Unitree Robotics)

**3.4.1 Key Features:** The Go2 Edu Plus is an affordable quadruped robot with a 4D LiDAR for 360° mapping and autonomous navigation. It supports various payloads, including radiation sensors for research purposes (xd4solutions, 2024)

**3.4.2 Strengths:** Its affordability makes it ideal for educational and research environments. It is also highly customizable, offering versatility for different types of radiation mapping tasks.

**3.4.3 Limitations:** While affordable, the Go2 Edu Plus is smaller and may not support high-end radiation sensors. It is best suited for research applications rather than large-scale industrial deployment.

**3.4.4 Price:** Approximately MYR 20,000 to 25,000 for the Edu Plus version



Figure 4: GO2 Edu Plus by Unitree

## 4 Conclusions

This comparative study highlights the strengths and limitations of four commercial robots used for radiation mapping. The Elios 2 RAD is an ideal choice for inspecting confined spaces and areas where human access is limited, while Spot offers superior adaptability in diverse terrains but comes at a premium cost. PackBot excels in durability and mobility, making it a reliable choice for hazardous environments, though it is less suited for detailed mapping tasks. The Go2 Edu Plus, with its affordability and customization potential, provides a strong solution for research and educational purposes, offering a cost-effective option for radiation monitoring. Ultimately, the selection of the appropriate robotic platform depends on the specific requirements of the radiation mapping task, environmental conditions, and available budget.

## References

dronelife. 2021. Flyability launches elios 2 rad for remote indoor radiation detection by drone. `https://dronelife.com/2021/08/09/flyability-launches-elios-2-rad-for-remote-indoor-radiation-detection-by-drone/`.

Ravi Raj and A. Kos. 2022. A comprehensive study of mobile robot: History, developments, applications, and future research perspectives. *Applied Sciences*, 12:6951, 07.

xd4solutions. 2024. Advanced ai: The brain behind the unitree go 2. `https://xd4solutions.com.br/advanced-ai-brain-unitree-go-2/`.

Xuesu Xiao, Jan Dufek, and Robin R. Murphy. 2021. Autonomous visual assistance for robot operations using a tethered uav. In Genya Ishigami and Kazuya Yoshida, editors, *Field and Service Robotics*, pages 15–29, Singapore. Springer Singapore.

Individual Research Contribution Review, 2024: 245–246
*ISSN: 3083-922X*

# Wireless Transmission of Radiation Pulse Data Using NRF24L01 Modules

**Nabilah Ramli**
Technical Support Division, Malaysian Nuclear Agency
43000 Kajang, Selangor
nabilah@nm.gov.my

## Abstract

This project presents the implementation of a wireless communication system using NRF24L01 modules. The system comprises a transmitter unit coupled to a scintillation detector and a receiving unit. The data was successfully transmitted in real time.

**Keywords:** NRF24L01, Transmitting, Receiving

## 1 Introduction

Wireless communication is a key component that enables the integration of current embedded systems, which are used in applications such as industrial monitoring systems and home automation. For short and medium range wireless communications, the NRF24L01 module as shown in Figure 1 is among the most suitable low-cost, low-power, and dependable wireless modules available (Zhu et al., 2023).



Figure 1: NRF24L01 module

In this paper, a wireless communication system using NRF24L01 was explored in transmitting and receiving pulse data in real time. It was implemented in the design of the system that pulse data generated by radiation detectors are sent via a transmitting unit wirelessly to a receiving unit for processing. It emphasizes simplicity, accuracy, and reliability within the construction process making it universally applicable for a number of embedded systems. The complete specifications are as given in Table 1.

| | |
|---|---|
| Frequency Range | 2.4 – 2.5Hz ISM band |
| hline Data Rates | 250Kbps / 1Mbps / 2 Mbps |
| Max. Output Power | 0dBm |
| Operating Voltage | 1.9 – 3.6V |
| Max. Operating Current | 12.3 mA |
| Standby Current | $22\mu A$ |
| Logic Inputs | 5V tolerant |
| Communication Range | 100m (open space) |

Table 1: NRF24L01 specifications

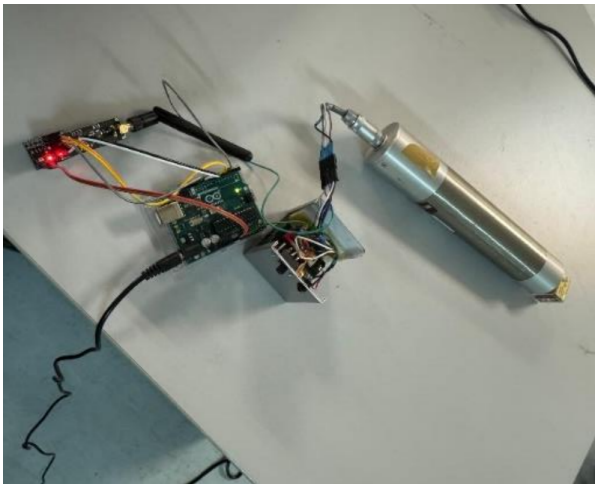


Figure 2: Transmitting unit connected to scintillation detector

The aim of this study is to implement an effective wireless data transmission and reception system using NRF24L01 modules for pulse detection. The objectives of the project include the design and real time transmission through an active pulse transmitter and receiving system.

## 2 Methods

The experiment was conducted with a distance of 15 meters between the two units to test the NRF24L01 module operating wirelessly. Figure 2 showed the transmitting unit that was placed inside the lab along with the detector and check source (Co-60). While Figure 3 showed the receiving unit was positioned in the officer's room.

A configuration of NRF24L01 for transmitting the counter value wirelessly used the `radio.write()` function at spec-

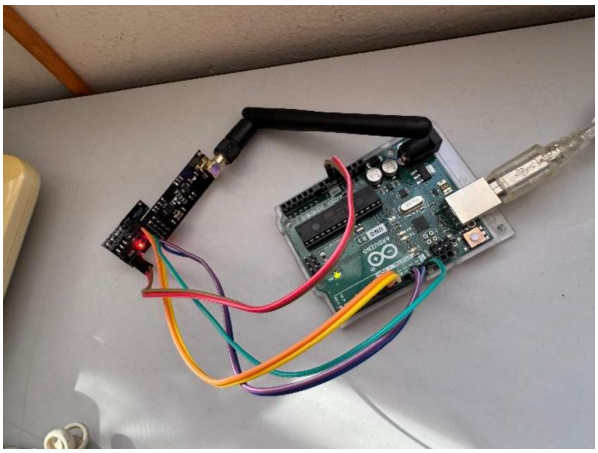


Figure 3: Receiving unit

ified intervals. On the receiving side, another microcontroller interfaced with the module is set to reading mode, using the same address and configuration settings. The receiver operates in a passive listening mode enabled by the `radio.startListening()` function. When data becomes available, the transmitted value can be retrieved using the `radio.read()` function.

## 3 Results

The results successfully displayed on the serial monitor that operated from the receiving unit in Figure 4. It demonstrates the wireless transmission of data from the detector to the receiver.

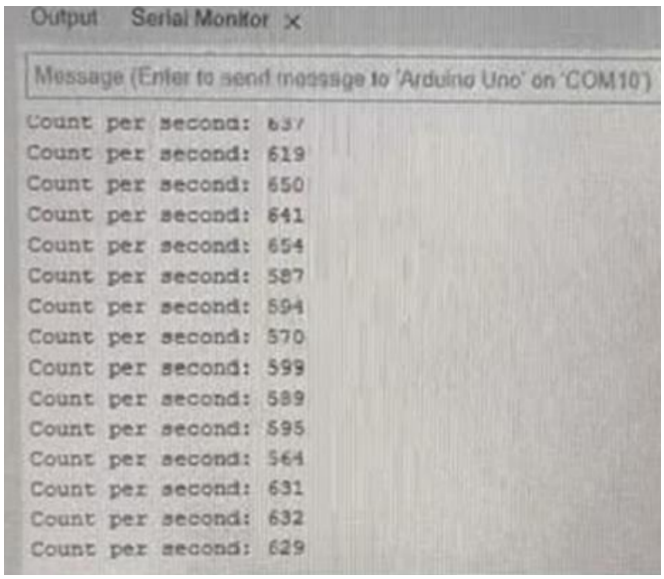



Figure 4: Result display in Serial Monitor of Arduino IDE

The ”Count per second” values indicate the number of radiation events or pulses detected by the detector within one-second intervals. This reading reflects the real-time radiation level captured by the detection system. The data shown on the serial monitor confirms that the transmitting unit is successfully sending the detected counts wirelessly to the receiving unit, where the microcontroller processes and displays the information. The consistency in receiving and displaying the data on the serial monitor highlights the effectiveness of the NRF24L01 module in maintaining reliable communication between the two units.

## 4 Conclusion

As a conclusion, the wireless communication system employing NRF24L01 modules was integrated and tested with the capability of real time pulse data transmission and receiving. The pulse generating unit which is programmed to detect the pulse using interrupt system was successful in counting the pulses produced by the input detector.

## 5 Acknowledgments

This project is part of the “Development of A Semi-Automated Gamma-Ray Detection System for In-Situ and Rapid Density Prediction on Timber Products: NM-R&D-23-10” project led by Dr. Soleha. I would like to express my gratitude to Dr. Soleha for providing the opportunity and resources to contribute to this work.

## References

Lipeng Zhu, Wenyan Ma, and Rui Zhang. 2023. Movable antennas for wireless communication: Opportunities and challenges. *IEEE Communications Magazine*, 62(6):114–120.

Individual Research Contribution Review, 2024: 247–248
*ISSN: 3083-922X*

IRCR

# Probabilistic Framework for Radiation Source Localization and Anomaly Detection Using Gaussian Mixture Models

**Nolida Yussup**
Technical Support Division, Malaysian Nuclear Agency
43000 Kajang, Selangor
nolida@nm.gov.my

## Abstract

Gaussian Mixture Models (GMMs) are widely recognised for their effectiveness in modelling multi-modal distributions. This study investigates the application of GMMs in radiation source localisation and anomaly detection, two critical aspects of radiation monitoring. Traditional methods often fall short in environments with multiple sources or irregular distributions. We applied GMMs to cluster radiation data and identify anomalies to address this. The study demonstrates GMMs' capability to accurately localise three distinct radiation sources and detect deviations in radiation levels. These results highlight the potential for GMMs to enhance autonomous radiation monitoring and mapping systems, providing a robust framework for safety and security applications.

**Keywords:** Gaussian Mixture Models, source localisation, anomaly detection, radiation monitoring, radiation mapping

## 1 Introduction

Gaussian Mixture Models (GMMs) are a machine learning method used to model data as a probabilistic combination of multiple Gaussian distributions (Goodfellow et al., 2016). They belong to unsupervised learning algorithms, where they can analyse unlabelled data and infer underlying patterns or distributions. GMMs have been widely applied in diverse fields such as image segmentation, speech recognition, and anomaly detection due to their ability to capture complex and multi-modal distributions.

In mathematical terms, a GMM represents the probability density function (p.d.f.) as:

$$P(x) = \sum_{k=1}^{K} \pi_k \mathcal{N}(x|\mu_k, \Sigma_k) \tag{1}$$

where $K$ is the number of Gaussian components, $\pi_k$ is the weight of the $k-$th component, $\mu_k$ is its mean vector, $\Sigma_k$ is the covariance matrix, and $\mathcal{N}$ refers to the multivariate Gaussian function. The model parameters are optimised using the Expectation-Maximization (EM) algorithm, which iteratively refines the likelihood function to find the best fit for the data. In radiation monitoring, the spatial and intensity distributions of radiation often exhibit complex patterns influenced by factors such as source type, environmental interference, and detector noise. GMMs are particularly well-suited to address these challenges because they can model overlapping distributions and identify hidden structures in the data. Their probabilistic foundation allows for robust predictions even in noisy environments, which is critical for applications in nuclear safety.

GMMs are powerful radiation detection and monitoring tools that offer a probabilistic approach to modelling spatial and intensity distributions. Morelande and Skvortsov (2009) used GMMs to estimate radiation fields, reducing noise sensitivity and improving accuracy in spatial distribution modelling. Quirós and Wilson (2012) extended GMMs to source separation tasks, showing flexibility in handling multivariate dependencies for radiation detection scenarios.

GMMs have also been applied to real-time monitoring. Simms et al. (2018) used GMM-based classifiers for gamma-neutron pulse shape discrimination, achieving high accuracy at low energies. Blair et al. (2019) demonstrated GMMs' ability to classify particles in neutron detectors, even with unlabelled data. Abdulaziz et al. (2022) further enhanced pulse discrimination by integrating GMMs with variational autoencoders, which enabled better performance in mixed datasets. These advancements highlight GMMs' versatility in addressing challenges in both software and hardware implementations for radiation monitoring.

This study aims to establish a GMM-based framework for radiation source localisation and anomaly detection. This study seeks to enhance the accuracy and adaptability of radiation monitoring systems, providing deeper insights to support their development and integration into autonomous operations.

## 2 Methodology

The localisation task incorporates spatial and intensity correlations by modeling simulated radiation data as a probabilistic mixture of multivariate Gaussian components, where each component represents a potential source. Using GMMs, the task involves clustering radiation data from three distinct sources. Fig. 1 shows the simulated radiation data, consisting of three distinct sources, with overlaid anomalies represented as outliers to the primary distributions.

The EM algorithm iteratively estimates the parameters, enabling precise identification of source locations. Key steps include:

1. Initialisation: K-means clustering for parameter initialisation.

2. EM Iterations:

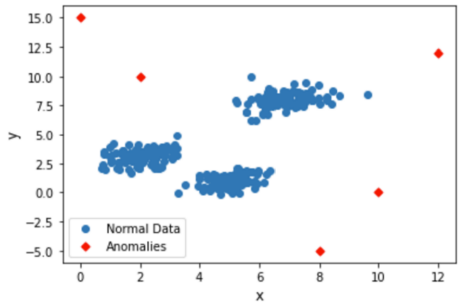



Figure 1: Simulated radiation data with anomalies.

a) Expectation Step: Compute posterior probabilities of data points.
b) Maximisation Step: Update component parameters.

3. Termination: Convergence of the log-likelihood function.

To detect anomalies, data points with low probabilities under the fitted GMM model were flagged as potential anomalies, ensuring the detection of irregular radiation levels. We evaluated data points against the fitted GMM using Mahalanobis distance:

$$D^2 = (x - \mu_k)^T \Sigma_k^{-1} (x - \mu_k) \tag{2}$$

where points with high $D^2$ were flagged as anomalies. This method ensures robustness to varying noise distributions. Using a confusion matrix, we evaluated the anomaly detection performance metrics, which are accuracy, precision, and sensitivity.

## 3 Results and Discussions

Fig. 2 shows the results of the GMM fitted model applied to the simulated data, illustrating its effectiveness in capturing the underlying patterns.

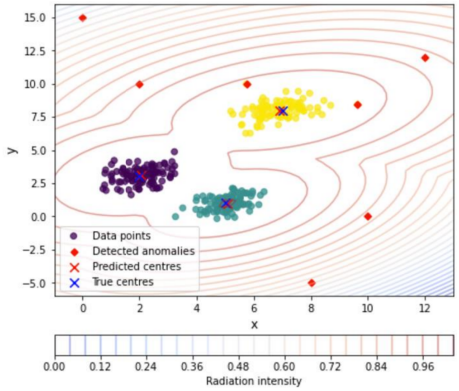



Figure 2: GMM results showing clustered sources and detected anomalies.

The GMM framework achieved a mean localisation error below 1%, successfully identifying three distinct radiation sources. The approach proved effective in clustering the data points and accurately identifying the source locations at the centres of the clusters. The contour lines in Fig. 2 represent the probability density of each Gaussian component in the GMM, plotted based on Eq. 1. However, in the context of this study, we manipulated the contour lines to illustrate the radiation intensity.

The anomaly detection module identified subtle deviations where seven anomalies were detected instead of just five, yielding over 99% accuracy and sensitivity, and 71.43% the GMM model to minimise false positives and false negatives in anomaly detection to ensure reliability in dynamic environments.

This combined localisation and anomaly detection framework supports smooth integration into autonomous radiation monitoring systems. It addresses critical needs in nuclear safety and environmental surveillance. While effective, the Gaussian assumption of GMMs limits their adaptability in highly non-linear scenarios. To overcome these limitations, we can explore hybrid models that integrate GMMs with deep learning techniques, such as variational autoencoders or employ alternative mixture models using non-Gaussian distributions like the Student's t-distribution to capture complex data patterns better.

## 4 Conclusions

This study established a probabilistic framework for radiation source localisation and anomaly detection using GMMs. By leveraging their machine learning capabilities, the framework demonstrates high accuracy and adaptability, offering significant potential to advance autonomous radiation mapping and monitoring. Further research will focus on enhancing robustness and exploring hybrid models to extend GMM applicability.

## References

Abdullah Abdulaziz, Jianxin Zhou, Angela Di Fulvio, Yoann Altmann, and Stephen McLaughlin. 2022. Semi-supervised gaussian mixture variational autoencoder for pulse shape discrimination. In *ICASSP 2022-2022 IEEE International Conference on Acoustics, Speech and Signal Processing (ICASSP)*, pages 3538–3542. IEEE.

Brenton Blair, Cliff Chen, Andrew Glenn, Alan Kaplan, Jaime Ruz, Lance Simms, and Ron Wurtz. 2019. Gaussian mixture models as automated particle classifiers for fast neutron detectors. *Statistical Analysis and Data Mining: The ASA Data Science Journal*, 12(6):479–488.

Ian Goodfellow, Yoshua Bengio, Aaron Courville, and Yoshua Bengio. 2016. *Deep learning*, volume 1. MIT press Cambridge.

Mark R Morelande and Alex Skvortsov. 2009. Radiation field estimation using a gaussian mixture. In *2009 12th International Conference on Information Fusion*, pages 2247–2254. IEEE.

Alicia Quirós and Simon P Wilson. 2012. Dependent gaussian mixture models for source separation. *EURASIP Journal on Advances in Signal Processing*, 2012:1–11.

Lance M Simms, Brenton Blair, Jaime Ruz, Ron Wurtz, Alan D Kaplan, and Andrew Glenn. 2018. Pulse discrimination with a gaussian mixture model on an fpga. *Nuclear Instruments and Methods in Physics Research Section A: Accelerators, Spectrometers, Detectors and Associated Equipment*, 900:1–7.

Individual Research Contribution Review, 2024: 249–250
*ISSN: 3083-922X*

# Real-Time IoT-Based Temperature Monitoring System for High Purity Germanium (HPGe) Detectors

**Noor Farhana Husna A. Aziz**
Technical Support Division, Malaysian Nuclear Agency
43000 Kajang, Selangor
farhanahusna@nm.gov.my

## Abstract

High-Purity Germanium (HPGe) detectors are widely used in nuclear research and radiation detection due to their superior resolution. However, these detectors require precise temperature control, as their operational efficiency is highly dependent on achieving a stable cryogenic state at approximately −160 °C. This project introduces a real-time IoT based temperature monitoring system designed to monitor temperature variations during the maintenance of HPGe detectors . The system employs Arduino-based hardware, specifically the WeMos D1 WiFi UNO ESP8266 , an OLED display, and an RTC DS3231 module, integrated with the Blynk platform (Kamarudin et al. (2022), Kumar et al. (2024), Seman et al. (2020), Visan and Diaconu (2021)).

**Keywords:** IoT, HPGe Detectors, Temperature Monitoring, Arduino, Blynk

## 1 Introduction

In the rapidly evolving industry of automation and smart infrastructure, the integration of real time monitoring systems is an essential requirement. A key challenge arises when the cooling process fails, preventing the detector from reaching the required −160 °C, which is critical for reducing thermal noise and minimizing leakage current. Damaged HPGe detectors often require extended cooling times, necessitating continuous temperature monitoring, which disrupts routine tasks. To address this, this paper presents the design and development of an Arduino-based automated temperature monitoring via a Blynk application enabling more efficient and uninterrupted workflows.

## 2 Methods

The developed monitoring system consists of the WeMos D1 WiFi UNO ESP8266, an OLED display and an RTC DS3231 module for timekeeping. The input from the sensor is resistance readings converted to temperature using a formula derived from an interpolated graph of the manufacturer's temperature data, as outlined in Equation 1.

$$\text{Temperature}(^\circ\text{C}) = 0.506 \times (\text{Resistance}) - 256.19 \quad (1)$$

The data is processed in real-time and transmitted wirelessly to the Blynk application, allowing for access to live updates and graphical visualizations. Blynk provides a user-friendly interface for visualizing data and interacting with the hardware.

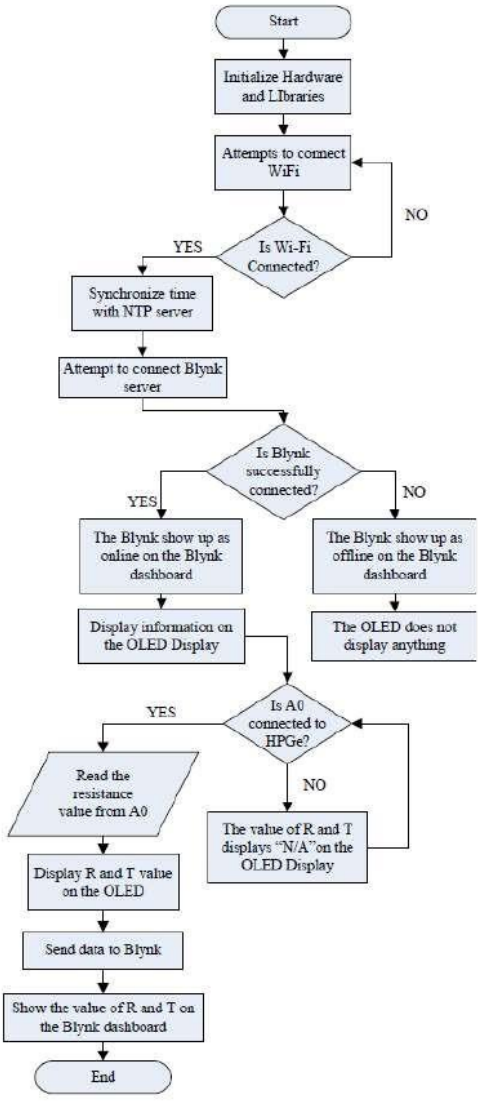



Figure 1: Flowchart of the software implementation.

The firmware, developed using the Arduino IDE, runs on the WeMos D1 WiFi UNO ESP8266 and responsible for initializing hardware, reading sensor data, and communicating with the Blynk platform. The flowchart in Figure 1 shows the

temperature monitoring system process from the start until the end. Successful code deployment to the WeMos D1 WiFi UNO ESP8266 requires the inclusion of various libraries, as outlined in Table 1.

| Library | Function |
|---|---|
| U8g2lib | For controlling the OLED display. |
| RTClib | For real-time clock functionalities. |
| U8g2lib | For controlling the OLED display. |
| RTClib | For real-time clock functionalities. |
| U8g2lib | For controlling the OLED display. |
| RTClib | For real-time clock functionalities. |
| ESP8266WiFi | For WiFi connectivity. |
| BlynkSimpleEsp8266 | For integrating with the Blynk platform. |
| NTPClient | For synchronizing time with an NTP server. |
| WiFiUdp | For handling UDP communication. |

Table 1: Libraries utilized in the project.

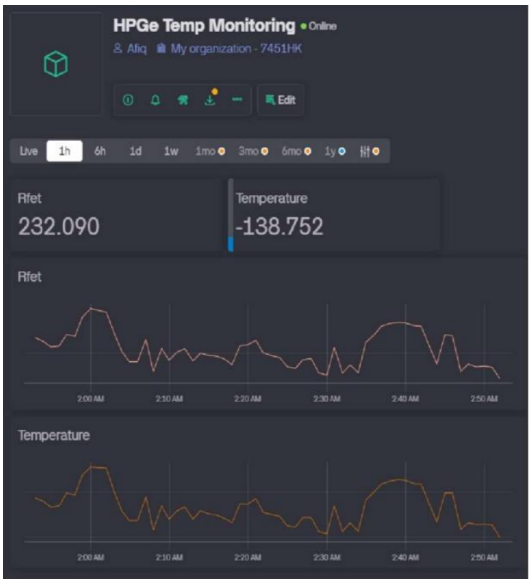


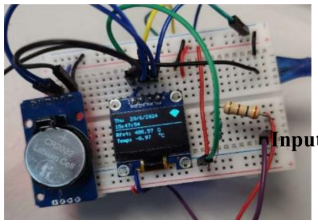

Figure 3: The Blynk dashboard for data monitoring

## 3 Results

The connection of the system's hardware components was carried out. Input A0 of the WeMos D1 WiFi UNO ESP8266 microcontroller board was connected directly to the sensor pin on the HPGe detector, as shown in Figure 2a and 2b.



(a)




(b)

Figure 2: (a) HPGE sensor pin (b) Input to A0

The testing of the Arduino program code was carried out successfully. Figure 3 shows the resistance and temperature values and graph obtained from the sensor and displayed clearly on the Blynk platform. This result highlights the successful integration of the sensor, WeMos D1 WiFi UNO ESP8266, and Blynk platform, showcasing the system's effectiveness in real-time temperature monitoring and data presentation.

## 4 Conclusion

The developed IoT-based temperature monitoring system successfully addresses the need for accurate and real-time temperature management during maintenance of HPGe detectors. By utilizing Arduino-based hardware and the Blynk platform, the system provides automated solution that minimizes manual monitoring efforts and reduces workflow disruptions. The integration of components like the WeMos D1 WiFi UNO ESP8266, RTC DS3231 module, and an OLED display ensures reliable operation and user-friendly data visualization. Future improvements will focus on designing a suitable casing for better durability and usability and transitioning to the ThingsBoard platform, developed by the Information Technology Center.

## References

Muhammad Amiruddin Kamarudin, Noor Hidayah Mohd Yunus, Mohd Raziff Abd Razak, Mohd Shahrul Mohd Nadzir, and Kemal Maulana Alhasa. 2022. Development of blynk iot platform weather information monitoring system. In *Advanced Materials and Engineering Technologies*, pages 295–305. Springer.

Jella Bharath Kumar, Banothu Charan, Guglavanth Vinod Kumar, Choudhary Sunil, and P. Sumithabhashini. 2024. Iot based temperature monitoring system using esp8266 and blynk app. *International Journal For Multidisciplinary Research*, 6(1):1–5.

MTA Seman, MN Abdullah, and MK Ishak. 2020. Monitoring temperature, humidity and controlling system in industrial fixed room storage based on iot. *J. Eng. Sci. Technol*, 15(6):3588–3600.

I Visan and EM Diaconu. 2021. Home automation system using esp8266 microcontroller and blynk application. *The Scientific Bulletin of Electrical Engineering Faculty*, 21(2):59–62.

Individual Research Contribution Review, 2024: 251–252
*ISSN: 3083-922X*

# Energy Dependence Evaluation from Model 001 of G2Tag Radig Meter

**Nor Arymaswati Abdullah**
Technical Support Division, Malaysian Nuclear Agency
43000 Kajang, Selangor
arymas@nm.gov.my

## Abstract

Energy dependence for G2Tag Radig Meter is one of significant factor to ensure an accurate measurement when exposed to radiation. This experiment had been done at SSDL, Malaysian Nuclear Agency. Few step and procedure had been taken care during the experiment including distance, collimator size, shielding, level of photon energy, temperature and pressure. Three types of photon energy were utilized for calibration purposes. There are x-ray, Co-60 and Cs-137. This paper will discuss on for only Model 001 of G2Tag Radig Meter. It showed that Model 001 of the G2Tag Radig Meter showed the stable response for energy over 200 keV.

**Keywords:** energy dependence, energy effective, photon energy

## 1 Introduction

There are two main elements in energy dependence of radiation dosimeters; intrinsic energy dependence and absorbed-dose energy dependence. Intrinsic energy dependence indicates how a detector's reading relates to the average dose of the sensitive detective element. This approach is primarily influenced by the beam quality (Q). For example, in ion chambers, this relationship is often assumed constant due to the proportionality of charge released to the dose. Variations in intrinsic energy dependence are notable in detectors like thermoluminescent dosimeters (TLDs), which can exhibit 5–15% response differences for low-energy photons. The intrinsic energy dependence, $k_{bq}(Q)$ can be described as (Rogers, 2009) (Hermida-López et al., 2014);

$$f(Q) = D_{med}(Q)/D_{det}(Q) \tag{1}$$

Where $D_{med}(Q)$ is the dose to the medium at the point of measurement in the absence of the detector. In general, energy dependence of a detector is the product of these two components, forming the calibration coefficient used in clinical and research applications. This dependence must be carefully analyzed and adjusted using models or simulations to ensure accurate dosimetry across varying energy conditions. In this study, an evaluation of energy dependence of G2Tag Radig Meter (G2TRM) at various level energies with different type irradiations has been done. The investigation were based on photon energy level and the measurement of the G2TRM.

## 2 Methodology

The calibration of the G2TRM has been done at Secondary Standard Dosimetry Laboratory (SSDL) in Malaysian Nuclear Agency. Seven level photon energies were used to investigate energy dependence of G2TRM. Irradiations were performed under following conditions of energies;

- Five levels of x-ray
- One level of Co-60
- One level of Cs-137

The six levels energy of x-ray included 60 kV (equivalent to 47keV), 100kV (equivalent to 84keV), 150kV (equivalent to 121keV), 200kV (equivalent to 171keV) and 250kV (equivalent to 218keV), whereas Co-60 at 1250keV and Cs-137 at 662keV. The experiment was performed start with low background. The G2TRM was fixed at three-meter distance from the source. At this stage, a proper alignment is critical between the source and G2TRM besides a proper collimator and shielding to ensure accurate energy delivery. After exposed the G2TRM to the source, the total charge, current, temperature, pressure and G2TRM reading were recorded for 60 seconds. This experiment was repeated for each energy levels and recorded. The result of the experiment from Model 001 was discussed in next section.

## 3 Results and Discussion

The calculation of energy effective at each photon energy is shown in Table 1 and plotted in Figure 1. These showed that the G2TRM's Model 001 response varies with photon energy, revealing the efficiency at detecting radiation across a range of energies. At the low level, which is below 200 keV, G2TRM shows over-response energy effectively due to being highly sensitive. However, at 218 keV G2TRM demonstrated a stable detection response and later under response followed by over response at 1250 keV.

## 4 Conclusion

The over response of G2TRM for below 200 keV is due to uncompensated GM tube utilized in the prototype. To overcome this issue, the compensated GM tube has to be substituted.

Table 1: Calculated energy effective for Model 001

| Photon Energy (keV) | Energy Effective (keV) |
|---|---|
| 47 | 2.873 |
| 84 | 3.279 |
| 121 | 2.212 |
| 171 | 1.397 |
| 218 | 1.046 |
| 662 | 0.754 |
| 1250 | 1.168 |

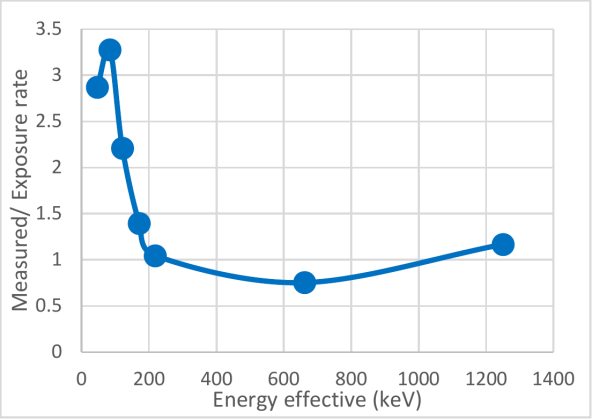



Figure 1: Energy effective for Model 001

## References

M Hermida-López, L Lüdemann, A Flühs, and L Brualla. 2014. Influence of the phantom material on the absorbed-dose energy dependence of the ebt3 radiochromic film for photons in the energy range 3 kev–18 mev. *Medical Physics*, 41(11):112103.

DWO Rogers. 2009. General characteristics of radiation dosimeters and a terminology to describe them. *Clinical dosimetry measurements in radiotherapy*, pages 137–146.

Individual Research Contribution Review, 2024: 253–254
*ISSN: 3083-922X*

IRCR

# Computational Modeling of Neutron Flux for Boron Neutron Capture Therapy Applications

**Norfarizan Mohd Said**
Technical Support Division, Malaysian Nuclear Agency
43000 Kajang, Selangor
norfarizan@nm.gov.my

## Abstract

Boron Neutron Capture Therapy (BNCT) is a cancer treatment modality that leverages the high linear energy transfer (LET) particles produced from the nuclear reaction between Boron-10 and thermal neutrons to selectively destroy cancer cells. Computational modeling of neutron flux is a critical component in the optimization and effectiveness of BNCT. This paper reviews the methods and techniques used in the computational modeling of neutron flux for BNCT applications. The use of Monte Carlo simulations, deterministic methods, and hybrid approaches to accurately predict neutron flux distributions in complex geometries are discussed. The importance of accurate cross-section data, patient-specific anatomical modeling, and the integration of advanced computational techniques to enhance the precision and efficacy of BNCT treatments are emphasised. The review highlights recent advancements in computational tools and their application in preclinical and clinical settings, providing insights into the challenges and future directions for research in this field. The aim is to improve the therapeutic ratio of BNCT, minimizing damage to healthy tissues while maximizing the dose delivered to cancerous cells.

**Keywords:** Computational Modeling, Boron Neutron Capture, research reactor, cancer treatment

## 1 Introduction

BNCT implementation involves two steps. First is the administration of a drug containing Boron-10 that will selectively be accumulating in tumor cells. The effectiveness of BNCT hinges on the selective accumulation of boron-10 in tumor cells while maintaining low concentrations in normal tissues. Various boron-containing compounds have been developed, which include Sodium Borocaptate (BSH), Boronophenylalanine (BPA) and nanoparticle-based boron carriers. Secondly, the patient is exposed to low-energy neutrons, causing the Boron-10 to release alpha particles and lithium nuclei that destroy the cancer cells from within. The nuclear reaction can be written as:

$$^{10}\mathrm{B} + n \longrightarrow {}^{4}\mathrm{He} + {}^{7}\mathrm{Li} + 2.79\,\mathrm{MeV} \quad (1)$$

In this reaction, boron-10, when exposed to low-energy neutrons (thermal neutrons), captures a neutron and undergoes fission. This reaction releases high-linear energy transfer (LET) particles which are an alpha particle and a lithium ion, both of which have a very short path length ($\approx$ 5–9 µm), roughly the diameter of a single cell. These particles deposit their energy over a confined region, causing double-strand DNA breaks and other molecular damage, leading to cell death. Due to the short range, the damage is confined primarily to the boron-containing cells, minimizing the impact on surrounding normal tissues.

## 2 Methods

Computational modeling of neutron flux is essential for treatment planning, as it helps determine the optimal neutron energy and flux distribution required to deliver a therapeutic dose to the tumor while sparing healthy tissue. Commonly, the modeling approaches consist of deterministic, stochastic, machine learning and hybrid. The key elements considered for a good computational model are the accuracy, computational cost, clinical applicability and flexibility.

## 3 Results

Table 1: Summary of modeling approaches performance according to the key elements.

| Methods or Techniques | Key Elements | | | |
|---|---|---|---|---|
| | Accuracy | Compute Cost | Clinical Applicability | Flexibility |
| Monte Carlo Simulation (MC) | High | High | High | High |
| Finite Element Method (FEM) | Moderate | Moderate | Moderate | Moderate |
| Hybrid Methods | High | Moderate | High | High |
| Machine Learning | Variable | Low After Training | Moderate | High |

Table 1 summarized the performance of modeling approaches according to the key elements specified. Monte Carlo (MC) represents the stochastic approach, while Finite Element Method (FEM) represents deterministic approach.

MC is widely used in BNCT treatment planning for high accuracy, clinical applicability and flexibility to predict the energy deposition from neutron interactions and optimize boron delivery, such as in Table 2. Ongoing research interest are on hybrid methods combine with MC to improve algorithms and computational efficiency on beam optimization and characterization, and the biological effects are important factors need to be considered in biological aspects.

Table 2: Modeling approaches used in BNCT treatment systems

| System or Model | Developer | Modeling Approach |
|---|---|---|
| NCTPLAN | Zamenhof et al. (1996) (Harvard & MIT) | Monte Carlo |
| BNCT_RTPE | Nigg et al. (1997) (INEEL & Montana State University) | Monte Carlo + non-uniform rational B-spline (NURBS) |
| SERA | Nigg et al. (1999) (INEEL & Montana State University) | Monte Carlo + pixel by pixel uniform-volume element ("univel") reconstruction of the patient geometry |
| JCDS | Kumada et al. (2005) (JAERI) | Numerical model + Monte Carlo |
| CARONTE | Cerullo and Daquino (2001) (Genova & Pisa University) | Monte Carlo (MCNP-4A) |
| BTPS | Jung et al. (2008) (Ulsan University Hospital + KAERI) | Monte Carlo (MCNPX) |
| MC-RD | Nojiri et al. (2024) (Kyoto University & Kansai BNCT Medical Centre) | Monte-Carlo + Removal Diffusion |

## 4 Conclusions and Future Work

In BNCT, computational modeling of neutron flux is essential for treatment planning, as it helps determine the optimal neutron energy and flux distribution required to deliver a therapeutic dose to the tumor while sparing healthy tissue. Monte Carlo models excel in precision, while deterministic models stand out in speed. Therefore, hybrid methods combining the strengths of both techniques are the best option to achieve high accuracy while reducing computational overhead. Continued advancements in computational techniques and the integration of machine learning will likely play a pivotal role, enabling more efficient and precise neutron flux modeling in future applications.

## References

N Cerullo and G Daquino. 2001. "caronte", a treatment planning system based on real macroscopic boron distribution and mcnp-4a code: Results and discussion. In *Frontiers in Neutron Capture Therapy: Volume 1*, pages 225–230. Springer.

Sang Hoon Jung, Ik Soo Choi, Sung Ho Park, Kyung-O Kim, and Jong Kyung Kim. 2008. A new gui based patient-specific treatment planning system for boron neutron capture therapy. *Journal of Nuclear Science and Technology*, 45(sup5):201–204.

Hiroaki Kumada, Kazuyoshi Yamamoto, Akira Matsumura, and Yoshinobu Nakagawa. 2005. Development of computational dosimetry system'jcds'for neutron capture therapy. *Hoshasen*, 31.

David W Nigg, Floyd J Wheeler, Daniel E Wessol, Jacek Capala, and Manjeet Chadha. 1997. Computational dosimetry and treatment planning for boron neutron capture therapy. *Journal of neuro-oncology*, 33:93–103.

D W Nigg, C A Wemple, D E Wessol, F J Wheeler, C Albright, M Cohen, M Frandsen, G Harkin, and M Rossmeier. 1999. Sera – an advanced treatment planning system for neutron therapy and bnct. *Transactions of the American Nuclear Society*, 80:66–68, 09.

Mai Nojiri, Takushi Takata, Naonori Hu, Yoshinori Sakurai, Minoru Suzuki, and Hiroki Tanaka. 2024. Neutron flux evaluation algorithm with a combination of monte carlo and removal-diffusion calculation methods for boron neutron capture therapy. *Medical Physics*, 51(5):3711–3724.

R Zamenhof, E Redmond II, G Solares, D Katz, K Riley, S Kiger, and O Harling. 1996. Monte carlo-based treatment planning for boron neutron capture therapy using custom designed models automatically generated from ct data. *International Journal of Radiation Oncology Biology Physics*, 35(2):383–397.

Individual Research Contribution Review, 2024: 255–256
*ISSN: 3083-922X*

# Migration of the AMoRA Algorithm Implementation from ROS1 to ROS2

**Nur Aira binti Abd Rahman**
Technical Support Division, Malaysian Nuclear Agency
43000 Kajang, Selangor
nur_aira@nm.gov.my

## Abstract

The Autonomous Mobile Robot for Accurate Radiation Detection and Mapping (AMoRA) algorithm enables unmanned ground vehicles (UGVs) to autonomously map radiation in designated areas. This study presents the migration of AMoRA from ROS1 on TurtleBot 2 to ROS2 on TurtleBot 4. The new implementation leverages a ROS2 *radmapper* package, featuring components for waypoint generation, path planning, navigation, radiation data logging, and visualization. Integration with existing ROS2 packages for SLAM and motion control ensures robust functionality. Experimental results validate the system's ability to generate a 2D map, grid segmentation, sampling points, and optimized path planning for autonomous radiation mapping. The upgrade demonstrates improved performance and highlights the algorithm's adaptability to other UGV platforms.

**Keywords:** ROS2, autonomous radiation mapping, coverage radiation mapping, mobile robot

## 1 Introduction

The AMoRA algorithm enables UGVs to perform radiation mapping in designated areas, a critical function in nuclear safety and security operations. Originally, AMoRA was implemented on the TurtleBot 2 platform using Robot Operating System 1 (ROS1) Kinetic Kame on Ubuntu 16.04 LTS. However, ROS1 Kinetic Kame reached its end-of-life in April 2021, ceasing official support and updates. This deprecation necessitated a transition to a more current and supported framework.

The acquisition of the TurtleBot 4 platform, compatible with Robot Operating System 2 (ROS2) Humble Hawksbill on Ubuntu 22.04 LTS, presented an opportunity to upgrade the AMoRA system. ROS2 Humble, offers support extending until May 2027. This migration not only ensures continued support but also demonstrates the adaptability of the AMoRA algorithm across different UGV platforms and ROS versions.

To implement the AMoRA algorithm on the TurtleBot 4, the *radmapper* package, responsible for radiation mapping functionalities, required modification to align with ROS2 syntax and protocols. This paper details the components of the *radmapper* package, outlines the upgrade process, and presents experimental verification results, highlighting the system's enhanced capabilities and adaptability following the migration.

## 2 Comparison of TurtleBot 2 and TurtleBot 4

Table 1 summarizes the key specifications of both platforms:

| Feature | Turtlebot 2 | Turtlebot 4 |
|---|---|---|
| Platform | Kobuki base | iRobot Create 3 base |
| Operating System | ROS1 (Kinetic Kame, Ubuntu 16.04) | ROS2 (Humble, Ubuntu 22.04) |
| Processor | External laptop | Raspberry Pi 4B |
| Camera | Kinect RGB-D | OAK-D |
| LiDAR | Convert RGB-D data to point cloud | 2D, 360$^o$ field of view |
| Navigation Sensors | Wheel encoders,bumper sensors, cliff sensors, IMU | Wheel encoders, bumper sensors, cliff sensors, IMU |
| Payload Capacity | Up to 5 kg | Up to 9 kg |

Table 1: Comparison of Turtlebot 2 and Turtlebot 4 key specifications

## 3 Methods

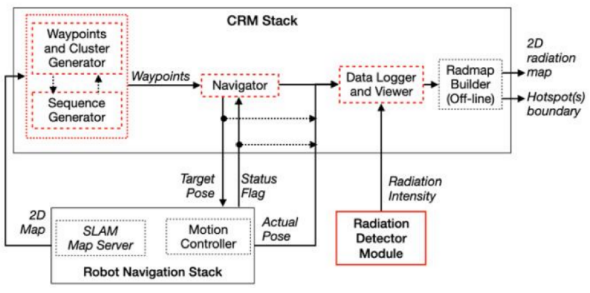



Figure 1: CRM stack architecture which implements AMoRA algorithm

Implementation of the AMoRA algorithm on Turtlebot4 necessitated the development of a new ROS 2 package with updated structures and protocols (Open Robotics, 2024). As

highlighted in the algorithm architecture in Figure 1, this package encompasses the following components:

**Waypoints and Cluster Generator** Generate sampling points and clusters the points for efficient mapping.

**Sequence Generator** Determines the optimal sequence for the UGV to navigate through waypoints.

**Navigator** Directs the UGV along the planned path, interfacing with ROS 2's navigation stack.

**Data Logger and Viewer** Records radiation data and provides visualization tools for online monitoring and analysis.

**Radiation Detector Module** Interfaces with radiation sensors to collect and process data.

The migration preserved the original Coverage Radiation Mapping (CRM) process (Abd Rahman et al., 2022) maintaining the system's core functionality. For Simultaneous Localization and Mapping (SLAM) and motion control, the system integrates existing ROS 2 packages i.e. *turtlebot4_navigation slam* package for synchronous and asynchronous mapping capabilities and the *nav2* package for motion control and obstacle avoidance. The radiation map builder is executed offline to process logged data files.

The migration to ROS 2 was performed in the following steps:

1. **Initialize ROS 2 Package** Created a new *radmapper* package to establish the foundational structure.

2. **Develop Component Nodes** Created each system component as individual Python program (**.py*). Updated existing codebases to replace ROS 1 dependencies with ROS 2 equivalents.

3. **Build with Colcon** Compiled the package using *colcon* build.

4. **Conduct Individual Component Testing** Performed isolated testing on each node to validate functionality and performance.

5. **Execute System Integration Testing** Assessed internode communication, functionality, and data accuracy.

## 4 Results and Discussion

The execution of the new ROS 2 *radmapper* package on TurtleBot 4 is summarized in Figure 2. The process began with the generation of a 2D occupancy map of the target environment. Next, this map was segmented into a uniform grid, with each cell measuring 50 cm × 50 cm. A total of 156 sampling points were generated at the centroids of unoccupied cells, ensuring complete coverage of the mapped area. These points were clustered into partitions to optimize path planning. The visitation sequence for the sampling points was generated using a combination of boustrophedon path planning and nearest neighbor algorithms, which minimized traversal distance and time.

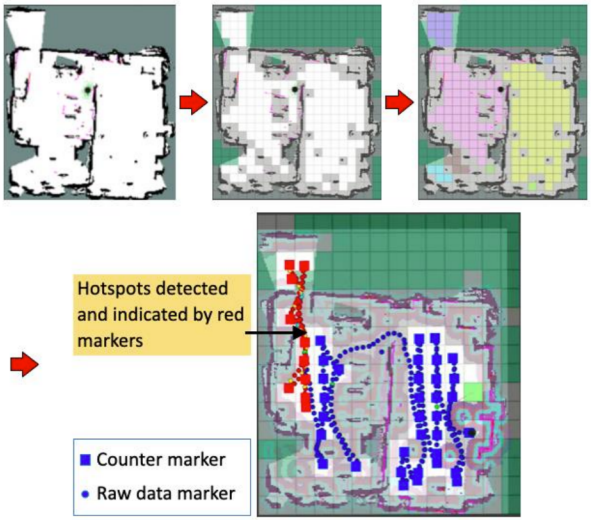



Figure 2: AMoRA algorithm progression and results executed on the Turtlebot 4 and ROS2 *radmapper* package

## 5 Conclusion

The migration of the AMoRA system to ROS 2 and its deployment on TurtleBot 4 significantly improved its autonomous radiation mapping capabilities with the ROS 2 *radmapper* package. This work also demonstrates the algorithm's adaptability across different robotic platforms.

## References

Nur Aira Abd Rahman, Khairul Salleh Mohamed Sahari, Nasri A Hamid, and Yew Cheong Hou. 2022. A coverage path planning approach for autonomous radiation mapping with a mobile robot. *International Journal of Advanced Robotic Systems*, 19(4):17298806221116483.

Open Robotics. 2024. Ros 2 documentation - humble hawksbill. https://docs.ros.org/en/humble/index.html.

Individual Research Contribution Review, 2024: 257–258
*ISSN: 3083-922X*

# Study of Existing Shielding for Malaysian Nuclear Agency - Dense Plasma Focus (MNA-PF) using Monte Carlo PHITS

**Puteri Nuraliah Husna binti Mohd Tajuddin**
Technical Support Division, Malaysian Nuclear Agency
43000 Kajang, Selangor
puteri@nm.gov.my

## Abstract

This study evaluates the effectiveness of existing shielding for the Dense Plasma Focus (DPF) neutron source at the Malaysian Nuclear Agency using the Monte Carlo simulation capabilities of the Particle and Heavy Ion Transport code System (PHITS). By modeling the current shielding configuration, we assess its performance in attenuating neutron and radiation dose. The simulation results provide insights into the spatial distribution of radiation. This analysis aims to study the current shielding uses to ensure the safety of personnel when conducting the experiment inside the room and optimize shielding designs for future upgrades.

**Keywords:** PHITS, shielding, neutron, plasma focus

## 1 Introduction

Paraffin is often employed as a neutron shielding material in plasma focus devices due to its high hydrogen content. Paraffin has the ability to moderate neutrons due to its high macroscopic cross-section and its ability to absorb them (Sardjono et al., 2022). This process, known as neutron moderation, is crucial in plasma focus devices where neutron radiation is a significant by-product of fusion reactions. The effectiveness of paraffin in neutron shielding lies in its ability to slow down fast neutrons to thermal energies, which can then be more easily absorbed or captured by other materials. Additionally, paraffin is relatively inexpensive, easy to shape and handle, making it a practical choice for constructing neutron shields in various experimental and industrial applications involving plasma focus devices (O'Brien, 2006).

This study aims to evaluate the existing shielding of the Malaysian Nuclear Agency-Plasma Focus (MNA-PF) using the Monte Carlo Particle and Heavy Ion Transport code System (PHITS). The PHITS code, renowned for its versatility and accuracy, provides a robust framework for simulating the transport and interaction of particles within complex geometries. By leveraging PHITS, this research seeks to model the neutron emission and transport processes within the DPF facility, identify potential weak points in the current shielding, and propose enhancements where necessary (Iwamoto et al., 2017).

## 2 Methods

Before running the simulation, the 'cave' design shielding of MNA-PF used in the Malaysian Nuclear Agency needs to be measured. Figure 2 shows the schematic view of the shielding of MNA-PF. The length and width of the shielding is 104 cm and 91 cm respectively. The height of the shielding is 189 cm. The outer part of the shield is made of stainless steel and the inner part of the shielding is poured with paraffin with composition of 14.86% of hydrogen and 85.14% of oxygen. The composition of shielding has been defined in the Material section.

Next, we have to define the source. The collision of plasma for D-D reaction causes the neutrons to produce. In the simulation, the neutron yield is 7500 neutrons/shot. It has been defined using totfact. The value of neutron yield in the MNA-PF is being obtained from the previous study and experiment that had been done in the paper of Preliminary results of Malaysian Nuclear Agency Plasma Focus (MNA-PF) as a slow focus mode device for deuterium filling gas in correlation with Lee model code (Zin et al., 2017).

The results are obtained from the output file. Several output files have been created. The neutron flux, effective dose rate, and dose mapping in the plasma focus device were obtained using the T-Track in the PHITS. To determine the effective dose rate, the T-Track has been configured to convert the unit from pSv $s^{-1}$ pSv/sec to µSv $s^{-1}$. The results have displayed the effective dose rate spectrum. To reduce the relative inaccuracy, the number of batches (maxbch) and the history number per batch (maxcas) have been set high. This is a result of the uncertainty being reliant on the total number of historical events. Less than 5% relative error is given in the results.

## 3 Discussion

The results will consist the neutron distribution around the MNA-PF and paraffin shielding. These results obtain after run the PHITS simulation and obtain from the output file.

The neutron distribution for the Dense Plasma Focus (DPF) device at the Malaysian Nuclear Agency (MNA-PF) has been assessed using Monte Carlo PHITS simulations, as illustrated in the Figure 1 and Figure 2. Figure 1 presents the neutron distribution around the MNA-PF with paraffin shielding from -100 cm to 100 cm. From the figure, it shows the centre of MNA-PF consists of highest neutron flux that has been indicated by the red and yellow regions. The peak flux reaches values on the order of 105 neutrons/cm2/source particle. This indicates that the flux is highest near the source.

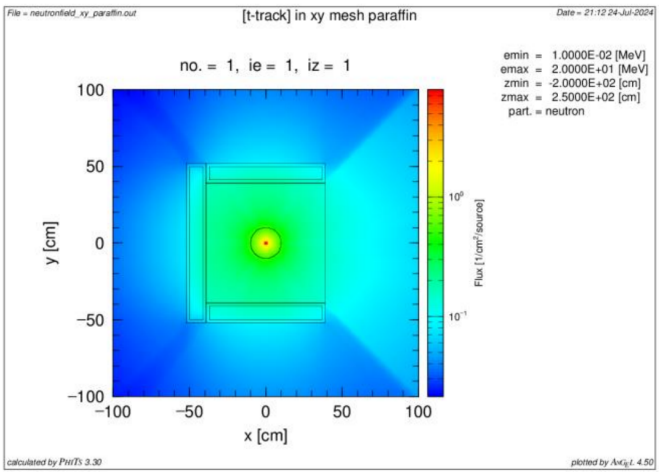



Figure 1: Neutron distribution around MNA-PF and paraffin shielding.

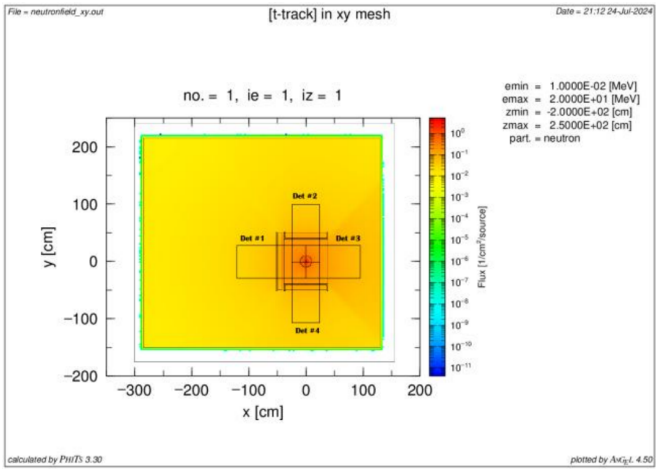



Figure 2: Neutron distribution in the MNA-PF's lab.

The maximum effective dose rate from the output file of PHITS for plasma focus device is $1.03 \times 10^{-3} \mu$Sv per shot. To meet the occupational safety limit of 20 mSv/year, it would require approximately 6 million shots. This calculation ensures that the cumulative exposure stays within the safety threshold set for occupational radiation exposure, thereby protecting workers from exceeding the annual dose limit. By carefully monitoring the number of shots and adhering to this limit, safety protocols can be maintained effectively in the operational environment of the plasma focus device.

## 4 Conclusion

The study of the existing shielding for the Malaysian Nuclear Agency's Dense Plasma Focus (MNA-PF) using Monte Carlo PHITS simulations has provided critical insights into the effectiveness and optimization of the current shielding configuration. By simulating neutron flux and energy distribution, the study identified key areas where the shielding performs adequately and highlighted potential vulnerabilities that could be addressed to enhance safety and efficiency. The neutron yield of $7.5 \times 10^3$ served as a significant parameter, ensuring the simulations accurately represented the operational conditions of the MNA-PF. Overall, the results emphasize the necessity of ongoing evaluation and adjustment of shielding materials and geometries to maintain compliance with safety standards and to support the high neutron output applications of the plasma focus device. These findings will guide future improvements in the facility's shielding design, ensuring both the protection of personnel and the optimization of experimental outcomes.

## References

Yosuke Iwamoto, Tatsuhiko Sato, Shintaro Hashimoto, Tatsuhiko Ogawa, Takuya Furuta, Shin-ichiro Abe, Takeshi Kai, Norihiro Matsuda, Ryuji Hosoyamada, and Koji Niita. 2017. Benchmark study of the recent version of the phits code. *Journal of Nuclear Science and Technology*, 54(5):617–635.

Robert James O'Brien. 2006. Shielding and radiation dose analysis for a dense-plasma focus neutron source. Master of science, University of Nevada, Las Vegas.

Y Sardjono, R Walhikmah, R Widiatmono, RSN Mahmudah, GS Wijaya, IM Triatmoko, et al. 2022. Safety analysis of paraffin wax based biological shielding for cancer therapy with bnct method on piercing beamport of kartini nuclear reactor yogyakarta. In *Journal of Physics: Conference Series*, volume 2190, page 012014. IOP Publishing.

MFM Zin, AH Baijan, V Damideh, SA Hashim, and RM Sabri. 2017. Preliminary results of malaysian nuclear agency plasma focus (mna-pf) as a slow focus mode device for argon and deuterium filling gas in correlation with lee model code. In *AIP Conference Proceedings*, volume 1824. AIP Publishing.

Individual Research Contribution Review, 2024: 259–260
*ISSN: 3083-922X*

# Gel Content and Hot Set Test as Main Requirements for Heat Shrink Tube Irradiation at ALURTRON

**Ruzalina Baharin**
Technical Support Division, Malaysian Nuclear Agency
43000 Kajang, Selangor
ruzalina@nm.gov.my

## 1 Introduction

The automotive industry is constantly evolving, with manufacturers seeking new and innovative ways to improve the performance, reliability, and safety of vehicles. One area of focus in this evolution is the crosslinking effect on wire, cables, and tubes through electron beam irradiation. Crosslinking, the process of chemically bonding polymer chains to form a three-dimensional network, has been widely studied and implemented in various industries. The use of electron beam irradiation for crosslinking in the automotive industry offers several advantages over traditional methods. Firstly, electron beam irradiation produces non-residue and non-carcinogenic gas, resulting in a fast and efficient crosslinking process. No after process treatment or quarantine needed. Secondly, the application of electron beam radiation from the high energy accelerator provides quick turnaround time production. Then, electron beam irradiation is a clean with on/off technology that gives good acceptance to the public.

Wire, cables, and tubes play a critical role in connecting various electrical and electronic systems within the vehicle, ensuring smooth operation and communication between different components. As a country becomes increasingly reliant on electronic components for its automotive needs, the need for efficient and reliable wiring becomes even more crucial. The process of crosslinking, particularly through electron beam irradiation, has emerged as an effective method for enhancing the properties and performance of automotive wiring. Electron beam irradiation has been developed as a method of crosslinking polymeric materials for various applications in the automotive industry.

When exposed to the electron beam radiation, heat shrink tube polymer undergoes crosslinking that can be observed through gel content percentage and hot set value. They become the main element for ALURTRON, the electron beam irradiation facility in Nuclear Malaysia to confirm the crosslinking process of the customer product. Hot set test was done to measure the elongation of samples for static load at a fixed temperature. Gel content analysis is performed to determine the percentage of crosslink fraction in polymer (Sharif et al., 2000)(Isa et al., 2010)(A'iasah et al., 2010).

Therefore, in this work, we carried out a study on gel content and hot set data from heat shrink tubes that were irradiated at ALURTRON. The gel content value required by the customer fall within 65% to 75% while the hot set range is set at 60% to 98%. Correlation were made between both set of data from year 2017 to 2022.

## 2 Method

Data measurement on hot set and gel content of heat shrink tube were collected from year 2017 to 2022. All data were tabulated in Excel software and analyzed on hot set data with numbers of outlier data from 65% to 75% of gel content measurement. The main point is to get the percentage of correlation between hot set and gel content data.

Heat shrink tube used in this work was made from polyethylene as a main component by one of the pioneer manufacturers of tubing and cable in Malaysia. Tube was irradiated at 160 kGy with accelerator energy of 2.0 MeV and beam current of 30 mA. Speed of product handling system is within the rage of 270 to 380 m/min with 54 turns of capstan under the beam.

Hot set test measurements were carried out in an oven at 200 °C with normal air conditions. The irradiated tubes (sample) loading was $20\,\mathrm{N\,cm^{-1}}$. The elongation between two marks was determined after 15 minutes heating of the sample. For gel content test, percentage of crosslinked gel fraction was determined from the weight loss measurement during the extraction.

## 3 Results and Discussions

From this work, there are 642 data were analyzed. Hot set test requirements between 60% to 98% have been met. This requirement was overcome during the irradiation process because the hot set test was performed at the beginning of the process around the first 100m of the tube. The irradiation process will be stopped pending QC confirmation that the hot set reading is in the 60% to 98% range. Adjustments to product handling speed will be made accordingly so that the correct hot set requirements will be achieved.

As above, figure 1 shows hot set measurement data with correlation to gel content requirements in the range of 65% to 75%. It was found that 97% of the irradiation work had met the gel content requirements. There are 21 data that are out of the required range but have been accepted by the customer. They did a physical test verification at their premises and it was successful.

## 4 Conclusions

Taking advantage of being the only electron beam irradiation facility in Malaysia that provides irradiation services to the wire, cable and tube industry, ALURTRON has established both physical tests, namely hot set and gel content tests. The hot set test is used as an indicator that the dose absorbed by the

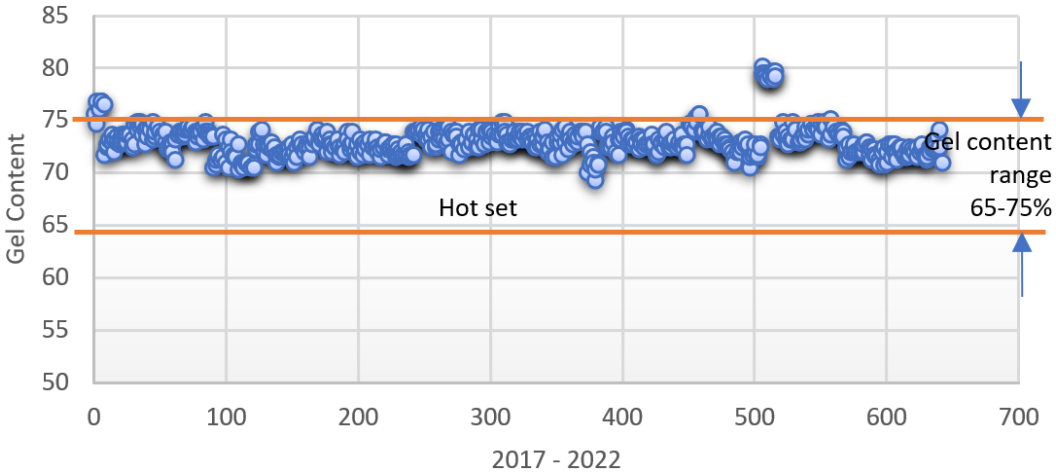



Figure 1: Hot set and gel content data collected within year 2017 to 2022 for heat shrink tube irradiated at ALURTRON.

product is sufficient for the product to crosslink. It is related to electron beam machine parameters and product handling system. Meanwhile, the percentage of gel content represents the effect of crosslinking, which is the change in the bond among the polymer chains from the irradiation process. Both tests are key to the specifications required by the customer depending on the application.

In 5 years (2017-2022), 97% of heat shrink tube irradiation work at ALURTRON has met the gel content requirement. These findings highlight three key components which is uniformity of heat shrink tube components, accurate physical testing and correct irradiation process.

## References

Siti A'iasah, Mohd Sidek Othman, Shari Jahar, Sarada Idris, Naurah Md. Isa, and Muhamad Zahidee Taat. 2010. Commercializing alurtron's electron beam irradiation service. In *Research and Development Seminar 2010*, number INIS-MY–2012-062.

Naurah Mat Isa, Siti Zulaiha Hairaldin, Mohd Yusof Hamzah, and Zulkafli Ghazali. 2010. Gamma irradiation effect on thermoshrink polyethylene tube: Case study. In *Research and Development Seminar 2010*, number INIS-MY–2012-038.

Jamaliah Sharif, Zulkafli Ghazali, and Khairul Zaman Mohd Dahlan. 2000. Development of radiation croslinked heat shrinkable compounds. In *Seminar Research and Development 2000 MINT*, number INIS-MY–051.

Individual Research Contribution Review, 2024: 261–262
*ISSN: 3083-922X*

# Ageing Management of EPS-3000

**Shalina Sheik Muhamad**
Technical Support Division, Malaysian Nuclear Agency
43000 Kajang, Selangor
shalina@nm.gov.my

## Abstract

This paper focuses on the development of ageing management programs for ALURTRON, an electron beam irradiation facility at the Malaysian Nuclear Agency. The facility has two electron beam machines: 3.0 MeV machine (EPS-3000) and the 1 MeV machine (ELV 4). The report covers topics such as physical ageing of structures, systems, and components (SSCs) and ageing management techniques of EPS-3000 machine. The first elements of ageing management are identified the system, structure and components of the machine. The paper concludes by highlighting the importance of ageing management in the operation of EPS-3000, highlighting the need for effective strategies to manage technological obsolescence and ensure the safety of the facility's operations.

**Keywords:** Ageing management, EPS 3000, Degradation

## 1 Introduction

An Ageing Management Programs (AMP) is a set of plant activities relating to the understanding, prevention, detection, monitoring and mitigation of a specific ageing effect on a structure, component or group of components. Plant activities include maintenance, in-service inspection, testing and surveillance, as well as technical support programs (IAEA, 2020).

Ageing is defined as a general process in which the characteristics of SSCs gradually change with time or use. Two kinds of time dependent changes which are: (1) Degradation of SSCs (physical ageing), i.e. gradual deterioration in their physical characteristics; (2) Obsolescence of SSCs (non-physical ageing), i.e. their becoming out of date in comparison with current knowledge, standards and technology.

Effective ageing management throughout the lifetime of SSCs requires the use of a systematic approach to managing the effects of ageing that provides a framework for coordinating all activities relating to the understanding, prevention, detection, monitoring and mitigation of ageing effects on the plant's structures and components. This approach is illustrated in Figure 1, which is an adaptation of Deming's 'plan–do–check–act' cycle to the ageing management of SSCs.

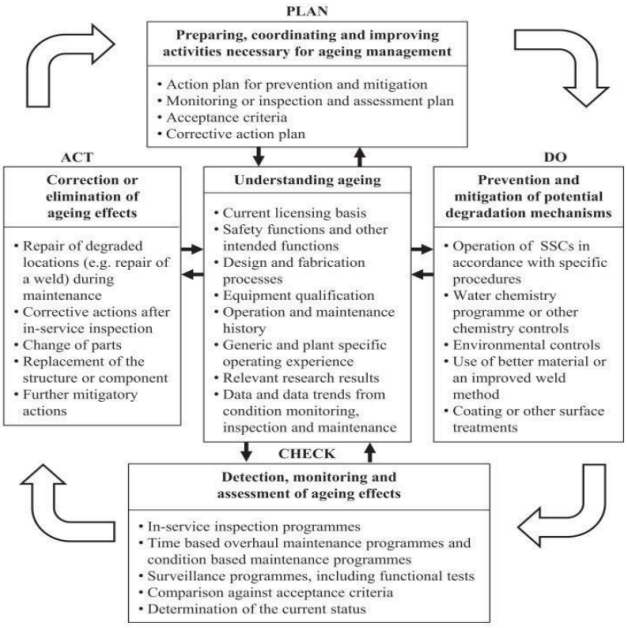



Figure 1: Systematic approach to ageing management (IAEA, 2018)

## 2 Methods

The ageing management methods involve the following actions:

1. Identification of the SSCs that are candidates for comprehensive ageing management.
2. Assessment of design, material and construction information.
3. Assessment of the facility's operating history.
4. Assessment of age-related degradation of selected SSCs:
5. Effects of stressors (chemical, electrical, mechanical, radiation);
6. Inspection, surveillance, maintenance, repair, etc.

## 3 Discussions

### 3.1 Identification of The SSCs

The SSCs, divided into commodity groups. SSCs belonging to the same commodity group are identified by the similarity

of function. These similarities result in the same ageing mechanisms for all components of each group, allowing also their ageing to be managed similarly. Table 1 defines structures, systems and components used in the EPS 3000.

Table 1: Structures, systems and components

| Systems | Components |
|---|---|
| High Voltage Power Supply | Inverter |
| | High Frequency Transformer |
| | High Voltage Circuit - Silicon Rectifier, Oil Filled Capacitor, Resistor and Sparks Gap |
| | Generating Voltage Meter (GVM) |
| | M-G for electron source-motor and a generator coupled by an insulated shaft |
| Accelerator Assembly | Filament Assembly - heated cathode,cooling fin and filament transformer |
| | Accelerator Tube Assembly - accelerating cathodes |
| Scanning Assembly | Beam Scanning Equipment - magnetic scanning coils |
| | Scanning Chamber - scanning horn, window foil, metallic O ring, windows flange and cooling air duct |
| Control System | Programmable Logic Controller (PLC) - CPU unit, Output and input devices and analog and digital converter unit |
| | Scanner Power Supply |
| | Vacuum Controller |
| | Control Unit |
| | Control Terminal |
| | Focus Power Supply |
| | Shorting Rod Controller |
| Gas Handling System | Gas compressor |
| | Vacuum pump |
| | Surge tank |
| | Oil mist filter |
| | Gas filter |
| | Filter |
| | Control panel |

### 3.2 Identification of ageing related degradation mechanisms

An ageing effect is a phenomenon that could lead to a loss of function of a component or structure. An ageing effect is a consequence of one or more degradation mechanisms affecting a component or structure. The list below identifies the degradation mechanism of EPS-3000.

1. Changes of properties due to electron irradiation
2. Changes of properties due to temperature
3. Stress or creep (due to pressure and temperature)
4. Motion, fatigue or wear (resulting from cycling of temperature, flow and/or load, or flow induced vibrations)
5. Corrosion
6. Chemical processes
7. Erosion (due to water and air)
8. Changes of technology
9. Changes of regulations
10. Obsolescence of documentation
11. Time dependent degradation due to normal service conditions
12. Electrical connections oxidizing

The record keeping of facility operating history, maintenance history is an important element to carry out the ageing program. Several activities such as obtaining information on preventive and corrective maintenance of the SSCs of the EPS-3000. The data should be recorded for monitoring and analyses. The next stages of AMP are assessment of the facility's operating history.

## 4 Conclusion

The aging management program is focused on identifying the structures, systems, and components (SSCs) and identify the mechanisms that can affect the SSCs of EPS-3000.

Ageing management of SSCs shall implemented proactively throughout the plant's lifetime, i.e. in design, fabrication and construction, commissioning, operation (including long term operation and extended shutdown) and decommissioning. EPS3000 machine has been in use for a long time and often suffers from breakdown, it is suggested that major improvements should be made, namely system upgrades, comprehensive overhauls (overhauls) and conducive training for staff.

The in-depth review of ageing management shall ensure that plant programs and practices that support the management of ageing effects during long term operation are reviewed and consistent with the generic attributes of an effective ageing management program such as mitigating ageing effects- Operations, maintenance, repair and replacement of parts and consumables to control ageing degradation of the structure or component.

## References

IAEA. 2018. *Ageing Management and Development of a Programme for Long Term Operation of Nuclear Power Plants*. Number SSG-48 in Safety Standards Series. International Atomic Energy Agency.

IAEA. 2020. *Ageing Management for Nuclear Power Plants: International Generic Ageing Lessons Learned (IGALL)*. Number 82 in Safety Reports Series. International Atomic Energy Agency.

Individual Research Contribution Review, 2024: 263–264
*ISSN: 3083-922X*

# Effect of Hydroxyacetone On Mechanical Properties of Hybrid Ultraviolet-Peroxide Prevulcanized Natural Rubber Latex

**Sofian Ibrahim**
Technical Support Division, Malaysian Nuclear Agency
43000 Kajang, Selangor
sofian_ibrahim@nm.gov.my

## Abstract

In recent years, researchers have explored UV vulcanization combined with peroxide to improve the mechanical properties of natural rubber latex without ionizing radiation. By adding an activator, peroxide decomposition and cross-linking are enhanced. This study examines how varying hydroxyacetone (HAC) levels affect the mechanical properties of hybrid UV-peroxide vulcanized latex. Using a specific formulation and a 60-minute UVA exposure, the latex film achieved a tensile strength of 24.6 MPa and over 90% gel content, a significant improvement over the25% in the control.

**Keywords:** UV, vulcanization, latex, crosslink

## 1 Introduction

Natural rubber latex is typically vulcanized using sulfur, ionizing radiation, or peroxide, but UV vulcanization has gained attention in the past 15 years. Schlogl et al. (2010) demonstrated that adding a photoinitiator to latex, which forms free radicals under UV, creates crosslinks. Her method required two UV cycles with different photoinitiators for comparable strength to sulfur vulcanization. Later, Wiroonpochit et al. (2017) improved this by combining photoinitiators with co-agents like hexanediol diacrylate (HDDA), achieving strong UV-vulcanized latex in just one cycle. Based on these methods, Ibrahim et al. (2023) found that adding organic peroxide and an activator like hydroxyacetone (HAC) to accelerate peroxide decomposition improves mechanical properties and cross-linking without ionizing radiation. This study focuses on HAC's impact on the mechanical properties of hybrid UV-peroxide prevulcanized natural rubber latex.

## 2 Materials and Methods

### 2.1 Materials

The natural rubber latex (NRL) utilized in this work was a high ammonia type (HA latex) supplied by Getahindus (M) Sdn. Bhd., Malaysia. The sensitizers used were hexanediol diacrylate (HDDA) supplied by Allnex, China and tert-butyl hydroperoxide (t-BHPO) supplied by Fluka. The photo initiator, 2 hydroxy-2-methyl-1-phenylpropanone (Irgacure 1173) was purchased from Sigma Aldrich (M) Sdn. Bhd., Malaysia. The stabilizer used was Potassium laurate supplied by Tiarco Chemical (M) Sdn. Bhd., Malaysia. The activator used was Hydroxyacetone (HAC) supplied by Sigma Aldrich (M) Sdn. Bhd., Malaysia. All the stated materials were used as received.

### 2.2 Preparation of Ultraviolet Prevulcanized Natural Rubber Latex (UVNRL) formulations

A 500 g latex formulation was prepared by weighing NRL into a beaker. Then the beaker was covered using aluminum foil before slowly adding stabilizer, acrylate, photoinitiator and water within 5 minutes interval (with gentle stirring) at room temperature in the dark as shown in Table 1 [Lazim et al. (2021), Hansupalak et al. (2016), Wiroonpochit et al. (2017) & Ibrahim et al. (2023)]. Once the addition of the materials was completed, the latex mixture was left stirring for one hour. Then 500 g from the prepared latex mixture was transferred into a 250 × 350 mm polyethylene bag and then sealed (thickness of the latex sample < 10 mm). Latex sample then exposed to UVA light for 60 minutes. After exposure, the latex was made into a film by the coagulant dipping method and mechanical properties and gel content tests were performed.

| Materials | Part perhundred gram of rubber (Pphr) |
|---|---|
| NR Latex (62% *TSC) | 100.0 |
| Stabilizer | 0.1 |
| HDDA | 2.0 |
| Irgacure 1173 | 2.0 |
| tBHPO | 0.5 |
| Water | Add to 52% TSC |

*TSC- Total solid content

Table 1: Compounding formulation of UVNRL (control)

The experiment was repeated by adding 0.1, 0.3 and 0.5 pphr of HAC respectively into the 500 g latex formulation as formulated in Table 2. Once the addition of the materials was completed, the latex mixture was left stirring for one hour. It was then transferred into a 250 × 350 mm polyethylene bag and then sealed. Latex sample then exposed to UVA light for 60 minutes.

| Materials | Part perhundred gram of rubber (Pphr) |
|---|---|
| NR Latex (62% *TSC) | 100.0 |
| Stabilizer | 0.1 |
| HDDA | 2.0 |
| Irgacure 1173 | 2.0 |
| tBHPO | 0.5 |
| HAC | 0.1/0.3/0.5 |
| Water | Add to 52% TSC |

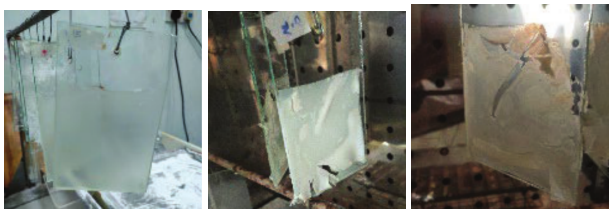
Table 2: Compounding formulation of Hybrid UV-peroxide prevulcanized natural rubber latex.

## 3 Results and Discussions

### 3.1 Effect of HAC activator on mechanical properties of hybrid UV-peroxide prevulcanized natural rubber latex

Peroxide decomposition in natural rubber latex was activated by hydroxyacetone (HAC) under UVA irradiation (60 minutes, 11 148.6 mJ $cm^{-2}$, 70-74 °C) generating radicals that initiate cross-linking. The mechanism involves three steps: (1) HAC reacts with tert-butyl hydroperoxide (t-BHPO) to form an acyl peroxy radical, (2) the radical propagates, initiating a chain reaction, and (3) free radicals cross-link polymer chains.

Observations in Fig. 1 revealed that latex films with higher HAC levels (0.3 and 0.5 pphr) developed cracks, likely due to over-curing. The film with 0.1 pphr HAC demonstrated a tensile strength of 24.63 MPa, more than double that of the control, due to increased cross-link density from UV and peroxide vulcanization.



(a) 0.1 pphr HAC (b) 0.3 pphr HAC (c) 0.5 pphr HAC

Figure 1: Observation of latex film.

Gel content testing showed that higher HAC levels led to greater cross-link density, but starting from 0.3 pphr, the films began cracking, likely due to stiffened C-C bonds that became brittle under stress.

## 4 Conclusion

In the preparation of hybrid UV-peroxide prevulcanized natural rubber latex, HAC acts as an activator to decompose organic peroxide, facilitating a uniform vulcanization process. The combination of UV and peroxide vulcanization improved the latex's mechanical properties. Using UVA (10 cm lamp-sample distance, 60 minutes), a formulation with HDDA, IRGACURE 1173, potassium laurate, tBHPO, and HAC produced a latex film with a tensile strength of 24.6 MPa and over 90% gel content, a significant improvement over the 25% gel content in the control.

## 5 Acknowledgments

The authors would like to express their deepest appreciation to Malaysian Ministry of Science, Technology and Innovation (MOSTI) for financial support under Technology Development Fund 1 (TDF07211421(A)) and Malaysian Nuclear Agency for providing research facilities for this work.

## References

Nanthiya Hansupalak, Sirinapa Srisuk, Panithi Wiroonpochit, and Yusuf Chisti. 2016. Sulfur-free prevulcanization of natural rubber latex by ultraviolet irradiation. *Industrial & Engineering Chemistry Research*, 55(14):3974–3981.

Sofian Ibrahim, Chai Chee Keong, Muhammad Hannan Bahrin, Hasan Sham, Mohd Noorwadi Mat Lazim, Anwar Abdul Rahman, Ahmad Bazlie Abdul Kadir, and Noor Hasni M Ali. 2023. Sulphur-free prevulcanization of malaysian natural rubber latex using a hybrid ultraviolet-peroxide vulcanization method. *Jurnal Sains Nuklear Malaysia*, 35(2):38–48.

M Noorwadi M Lazim, A Faiza Mohd, C Keong Chai, and Norazura Ibrahim. 2021. The effects of hdda and n-ba & tmptma on the physical and thermal properties of uv irradiation vulcanization natural rubber latex. *International Transaction Journal of Engineering, Management, & Applied Sciences & Technologies*, 12(9):1–11.

S Schlogl, Armin Temel, Raimund Schaller, Armin Holzner, and Wolfgang Kern. 2010. Prevulcanization of natural rubber latex by uv techniques: a process towards reducing type iv chemical sensitivity of latex articles. *Rubber chemistry and technology*, 83(2):133–148.

Panithi Wiroonpochit, Kittaporn Uttra, Kanokwan Jantawatchai, Nanthiya Hansupalak, and Yusuf Chisti. 2017. Sulfur-free prevulcanization of natural rubber latex by ultraviolet irradiation in the presence of diacrylates. *Industrial and Engineering Chemistry Research*, 56(25):7217–7223.

Individual Research Contribution Review, 2024: 265–266
*ISSN: 3083-922X*

# Ludlum 44-7 HV Plateau Analysis Through Responding with SR-90

**Syirrazie Shaari**
Technical Support Division, Malaysian Nuclear Agency
43000 Kajang, Selangor
syirrazie@nm.gov.my

## Abstract

This study investigates the characteristics of the high voltage (HV) plateau in a radiation detector system to determine the optimal operational range. By varying HV bias voltage from 13 V to 1000 V, count rates were analyzed to identify a stable operating region. Results indicate a plateau between 700 V and 850 V, ensuring consistent and reliable detection performance. This work is essential for calibrating radiation detectors and optimizing measurement accuracy.

## 1 Introduction

Establishing an accurate HV operational range is crucial for ensuring the reliability of radiation detection systems (Reyes-Almanza et al. (2019), Ghazali et al. (2013), Abdullah et al. (2014)). The high voltage plateau represents a stability region where count rates remain unaffected by minor changes in voltage. For radiation detectors, determining this plateau is essential to avoid detector saturation or inefficiencies (Dyakonova et al. (2016), Buckles et al. (2018)). This study focuses on evaluating the HV plateau for optimal detector performance.

## 2 Methodology

The experimental setup was designed to evaluate the HV plateau of a radiation detection system. A Strontium-90 (Sr-90) radioactive source with an activity of 19.62 kBq (0.5302$\mu$Ci ) was used. The system consisted of a Ludlum 44-7 Geiger-Muller (GM) detector powered by a high-voltage power supply, with count rates recorded in counts per minute (cpm) using a counter.

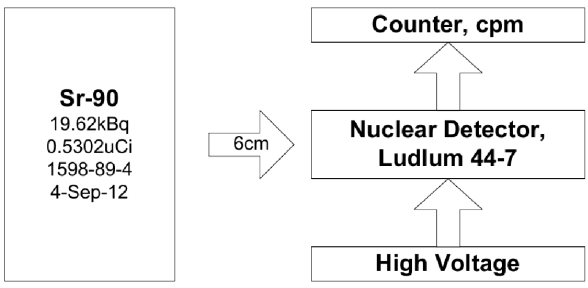



Figure 1: GM Detector Response with SR-90

The HV bias voltage was varied incrementally from 13 V to 1000 V. At each voltage setting, three measurements of count rates (C1, C2, and C3) were recorded and averaged. Background radiation levels were measured separately and subtracted to isolate the effective signal from the Sr-90 source.

The figure of the experimental setup (Figure 1) illustrates the process, showing how the Sr-90 source was connected to the GM detector and counter. The resulting data were plotted to identify the HV plateau, a range where the detector output remained stable, indicating optimal operating conditions for reliable measurement.

## 3 Result and Discussions

Results demonstrated a stable HV plateau between 700 V and 850 V, where count rates remained consistent despite voltage fluctuations as shown in Figure 2.

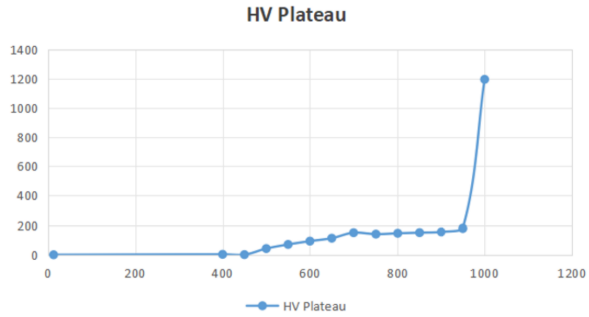



Figure 2: Ludlum 44-7 HV Plateau

At voltages above 900 V, count rates increased sharply, indicating noise interference or detector saturation. These findings highlight the importance of maintaining operational settings within the plateau range for accuracy and reliability.

## 4 Conclusion

The identified HV plateau provides a practical guide for optimizing radiation detector performance. By operating within the 700 V to 850 V range, users can ensure consistent measurement accuracy. Further studies could explore implementation of distance variation between the detector and Sr-90 to determine global best solution for HV configuration of the nuclear detector.

## References

Nor Arymaswati Abdullah, Lojius Lombigit, and Nur Aira Abd Rahman. 2014. High voltage stability perfor-

mance of a gamma ray detection device. In *AIP Conference Proceedings*, volume 1584, pages 73–76. American Institute of Physics.

RA Buckles, I Garza, JN Bellow, KJ Moy, GA Chandler, CL Ruiz, and BM Jones. 2018. Superlinearity, saturation, and the pmt—tailoring and calibration methodology for prompt radiation detectors. *Review of Scientific Instruments*, 89(10).

N Dyakonova, P Faltermeier, DB But, Dominique Coquillat, SD Ganichev, Wojciech Knap, K Szkudlarek, and G Cywinski. 2016. Saturation of photoresponse to intense thz radiation in algan/gan hemt detector. *Journal of Applied Physics*, 120(16).

AB Ghazali, TS Ahmad, and NA Abdullah. 2013. Characterization of a pulsed mode high voltage power supply for nuclear detectors. In *IOP Conference Series: Earth and Environmental Science*, volume 16, page 012137. IOP Publishing.

R Reyes-Almanza, A Dimitrov, Alexis Fagot, Muhammad Gul, Christos Roskas, Michael Tytgat, Nikolaos Zaganidis, S Fonseca De Souza, A Santoro, F Torres Da Silva De Araujo, et al. 2019. High voltage calibration method for the cms rpc detector. *Journal of Instrumentation*, 14(09):C09046.

Individual Research Contribution Review, 2024: 267–268
*ISSN: 3083-922X*

# Dose Mapping Process of Old Books for Cultural Heritage Preservation at Sinagama

**Syuhada Ramli**
Technical Support Division, Malaysian Nuclear Agency
43000 Kajang, Selangor
syuhada@nm.gov.my

## Abstract

The use of gamma irradiation is an excellent alternative tool to the traditional process of decontamination of cultural and historical materials, mainly because of its biocidal action. This works aims to define the product loading pattern (PLP) through product dose mapping procedure and the effects of irradiation absorbed dose for the treatment of cultural heritage disinfection, respecting the ethical principles of conservation activities.

**Keywords:** gamma irradiation, product dose mapping, cultural heritage preservation

## 1 Introduction

The preservation of world cultural heritage is crucial for conserving cultural traditions and national identities. Cultural heritage artifacts are often threatened bio deteriorating agents such as microorganisms, insects' pest which can cause severe physical and chemical damages, leading to the degradation of cultural heritage materials and posing health risks to restorers, archivists and operators.

Gamma radiations offer an effective solution for eradicating insects and removing microorganisms from degraded archived materials or cultural heritage artifacts (D'Orsi et al., 2024)(Nagai et al., 2021).

Product dose mapping are used to determine the validity of dose acceptance against the distribution of the minimum dose and the maximum dose of the entire product in the tote during irradiation process. Product loading pattern (PLP) will be obtained from the product dose mapping.

PLP summary will be issue in the dose mapping report to be a reference for next irradiation materials or product as it would be carried out to verify compliance with the PLP process specification.

## 2 Methods

Requirements for the treatment using gamma irradiation is referring to Sinagama Production and Service Provision procedure explained through process flowchart in Figure 1.

Receiving process have to follow specification that product must be sealed in air-tight packaging to prevent recontamination. Then followed by irradiation process was in air, at room temperature and humidity conditions at absorbed dose within the range 6 kGy to 10 kGy, with the ability of the

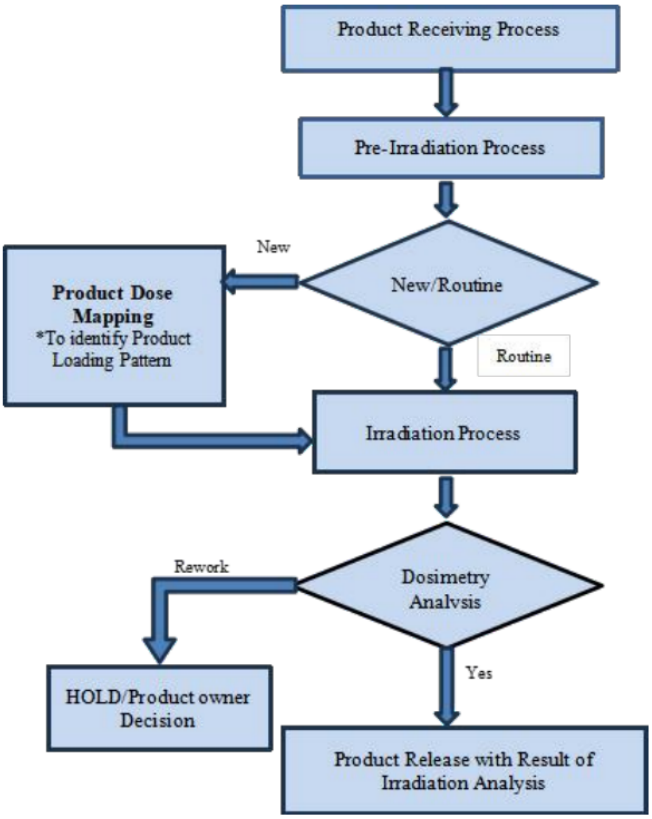



Figure 1: Flowchart of the process of irradiation at Sinagama

Sinagama irradiation plant operating on JS1000 (IR219) that irradiating various different doses simultaneously.

All absorbed dose was measured using ceric-cerous dosimeter. The characterization measurements were conducted immediately after irradiation for all samples. After irradiation, materials should be stored in an environment protected from heat and high humidity.

## 3 Results and Discussions

As a result of the dose mapping process of old books for heritage culture preservation conducted, product loading pattern (PLP) experiment for boxes arrangement in the tote were designed and illustrated in Figure 2 and Figure 3.

In this study, Figure 2 PLP A showed box position layout 4 cartons per tote with cartons dimension $(30 \times 30 \times 41)$cm and weight $(16.06 \pm 0.5)$kg. Referring to Sinagama work-

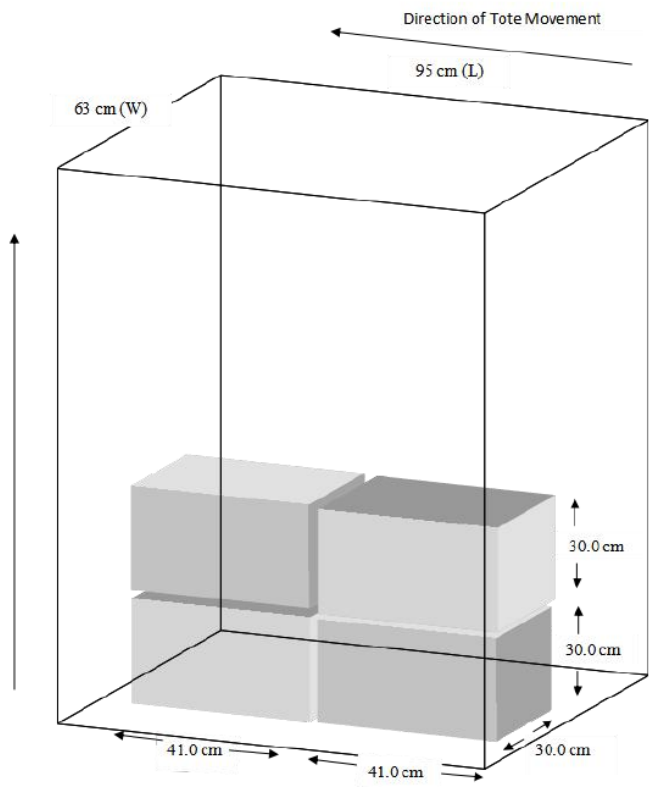



Figure 2: PLP A for box position layout 4 cartons per tote (4 ctns/tote)

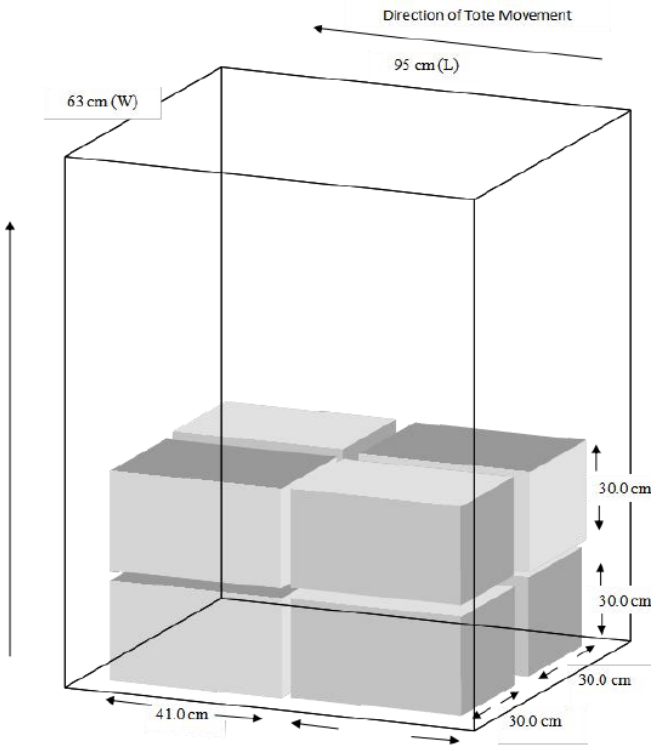



Figure 3: PLP B for box position layout 8 cartons per tote (8 ctns/tote)

ing instruction calculation of bulk density, the bulk cartons density of a product as part of requirement for dose mapping activity should be in tolerance level between the boxes density measurement:

**For dimension:** +1 cm

**For weight:** +0.5 kg

The result obtained dose minimum $D_{min}$ = 6.9 kGy and dose maximum $D_{max}$ = 8.7 kGy, which is within the dose specification. Instead of result from Figure 3 PLP B showed box position layout 8 cartons per tote with cartons dimension (30 × 30 × 41)cm and weight (15.61 ± 0.5)kg. The result obtained $D_{min}$ = 5.7 kGy and $D_{max}$ = 8.3 kGy revealed dose achieved lower than minimum dos requirement which is 6 kGy. This is identified by the higher density factor which is 0.13 g/cc for PLP B compared to 0.07 g/cc for PLP A that influenced the penetration of gamma radiation dose absorbed.

## 4 Conclusions

In conclusion, the experimental results obtained in this work provide conclusive evidence of the impact of gamma irradiation on different PLP of old books materials for cultural heritage preservation purposes. These results may guide the selection of PLP for similar or different cultural heritage materials without requiring a destructive approach in optimizing for the preservation treatment of cultural heritage artifacts.

## Acknowledgment

The authors are grateful to the staff of Sinagama as irradiator facility and team of Industrial Technology Division (BTI) and Perpustakaan Muzium Perak that have provided the old books employed for radiated, also Agriculture and Bioscience Division.

## References

B D'Orsi, R Carcione, I Di Sarcina, G Ferrara, M Oliviero, T Rinaldi, J Scifo, A Verna, and A Cemmi. 2024. Gamma irradiation for cultural heritage conservation: Comparison of the side effects on new and old paper. *Journal of Cultural Heritage*, 70:335–344.

Maria Luiza Emi Nagai, Paulo de Souza Santos, and Pablo Antonio Vasquez Salvador. 2021. Irradiation protocol for cultural heritage conservation treatment. *Brazilian Journal of Radiation Sciences*, 9(1A).

Individual Research Contribution Review, 2024: 269–270
*ISSN: 3083-922X*

# Surface Analysis of Silicon Dioxide Thermally Grown on Atomically Flat Silicon Surface at Different Oxidation Time

**Umi Zulaikha Mohd Azmi**
Technical Support Division, Malaysian Nuclear Agency
43000 Kajang, Selangor
umizulaikha@nm.gov.my

## Abstract

Dry thermal oxidation method is the common method to grow the oxide layer on substrate. This study utilized silicon (Si) wafer as a substrate and thermally grown the silicon dioxide ($SiO_2$) at 1000 celsius with different oxidation time (15, 30, 60, and 120 mins). The thickness of the $SiO_2$ surfaces were determined using spectral reflectance and color chart, then compared both results. The results show that the determination of thickness using spectral reflectance is more accurate compare to color chart. The thickness of $SiO_2$ layer was increased as the oxidation time increased. The chemical bonding of $SiO_2$ on Si substrate was confirmed by Fourier Transform Infrared (FTIR). The roughness of $SiO_2$ surfaces were investigated by using Atomic Force Microscopy (AFM). This study shows that the thickness and surface roughness of $SiO_2$ was influenced by the oxidation time.

**Keywords:** Dry oxidation, surface roughness, Atomic Force Microscopy

## 1 Introduction

Silicon dioxide ($SiO_2$) have been used extensively in integrated circuits (ICs), as well as in microelectromechanical systems (MEMS). They are employed as not only the passivation layer or mask layer, but also the structural layer, such as the dielectric of field-effect transistors (TFTs) (Hashim et al., 2015) for various applications.

The $SiO_2$ layers can be grown using the thermal method (diffusion furnace) either vertical or horizontal type and also can be grown in a Rapid Thermal Processor (RTP). RTP is a cost-effective method where it can grow the $SiO_2$ layers on single wafer in a very short time. However, it suffers from a lack of precise thickness control. Thermally grown silicon oxide is using a high temperature that is ranging from 800 °C - 1200 °C either a "Wet" or "Dry" growth method. Dry thermal oxide uses only pure oxygen, where the wet thermal oxide uses the pyrogenic steam as the oxidation gas. Meanwhile, dry oxidation will produce more uniform and denser thermal oxide and also have higher dielectric strength compared to wet oxide. This is because of the gas that are being used in the oxidation process. The critical difference in the growth of wet and dry oxide is the growth rate, dry oxide grows much slower than wet oxide. For this reason, dry oxides normally used for thin gate and capacitor oxides where high uniformity and high dielectric strength are needed. Where the wet oxide will be grown a thick layer of an isolation layer.

Surface roughness at the oxide surface is play an important role as it could deteriorate the uniformity of the oxide thickness. The non-uniformity would cause the dispersion of the leakage current, and lowers production yield (Ohsawa et al., 2009). Therefore, in this study, the dry oxidation method with fixed temperature (1000 °C) but different oxidation time was applied in order to study the effect of oxidation time towards the thickness and roughness of $SiO_2$ layer.

## 2 Methods

### 2.1 Sample Preparation

The double-side polished, 2cm × 2cm, < 111 > orientation, N-type Si wafers were used. Prior to oxidation process, the Si wafers were cleaned by organic solvent, RCA-1, and finally dipped with hydrofluoric acid (HF) to remove inorganic and organic residues, as well as native oxide (Hashim et al., 2015). Then, the cleaned Si wafers were stored in a desiccator for further used.

In this study, the dry oxidation process was performed by using a split tube furnace (VT Tube Furnace, STF-1200- 450-100, Malaysia). Firstly, the tube furnace was flushed using nitrogen gas until temperature reached 800 °C. Then, the cleaned Si wafer was placed vertically in a slotted quartz wafer boat and pushed to the middle of tube furnace using quartz rod. The nitrogen gas was continuously flown until reached the temperature of 1000 °C. Subsequently, the nitrogen gas was stopped and replaced with oxygen gas at constant temperature for various temperatures (15, 30, 45, 60 and 90 mins), and we called it as oxidation time. The oxygen and nitrogen gas were set at direct reading scale of 60.

### 2.2 Sample Characterization

The $SiO_2$ layer appeared different colour indicates the different thickness. The determination of $SiO_2$ colour based on red, green and blue (RGB) by a handheld spectrophotometer (China), then compared with $SiO_2$ colour chart (BYU, 2025). The other method for thickness determination was based on spectral reflectance by using Filmetric F20-UV. The structural characterization was studied by Agilent Cary 630 FTIR Spectrometer with spectral resolution of 2 $cm^{-1}$ over a spectral range from 4000 – 700 $cm^{-1}$. Atomic Force Microscopy (AFM) (Park Systems, XE-70, Korea) was used to determine

the root mean square (RMS) roughness at different oxidation time.

## 3 Results and Discussions

The color of the $SiO_2$ layer on Si wafer depends on the incident angle of the light source, the luminance of the source, the thickness of the dielectric film, and the dielectric material. This study used two different methods to determine the thickness of $SiO_2$; (i) handheld spectrophotometer and (ii) spectral reflectance. The handheld spectrophotometer gave the red, green and blue (RGB) readings and can be converted into a specific colour. The colour obtained were compared with the colour chart retrieved from BYU (2025) by using naked eye. For the spectral reflectance, the thickness of $SiO_2$ was determined by using the light and it is reflected perpendicular to the film. The reading of thickness was obtained directly from the software of instrument. As shown in Table 1, both methods provide the same trend, the thickness of $SiO_2$ increases as the oxidation time increases. However, the results obtained from spectral reflectance remains promising compared to color chart.

Table 1: The comparison data of thickness determination using color chart and spectral reflectance

| Oxidation time (min) | Estimation thickness based on color chart (nm) | Thickness determination from spectral reflectance (nm) |
|---|---|---|
| 15 | 80 | 67.41 ± 1.25 |
| 30 | 100 | 141.52 ± 0.18 |
| 60 | 200 | 193.57 ± 0.88 |
| 90 | 225 | 209.50 ± 1.05 |

The structure of $SiO_2$ layer was characterized by FTIR spectroscopy. From the IR spectra, the peaks around 1070 $cm^{-1}$ and 1200 $cm^{-1}$ were observed which related to the stretching peaks of Si–O and Si–O–Si, respectively. The Si–O bending mode are observed at around 700 – 800 $cm^{-1}$. It has been The structure of $SiO_2$ layer was characterized by FTIR spectroscopy. From the IR spectra, the peaks around 1070 $cm^{-1}$ and 1200 $cm^{-1}$ were observed which related to the stretching peaks of Si–O and Si–O–Si, respectively. The Si–O bending mode are observed at around 700 – 800 $cm^{-1}$. It has been noticed that the IR spectra of bare Si wafer appears almost similar to the $SiO_2$ layers, but the peaks are weaker than $SiO_2$ layer, which indicates that the Si wafer have native oxide layer prior to oxidation.

The roughness of $SiO_2$ surfaces were further characterized using AFM. At 0 min, unoxidized sample shows the highest roughness of 0.403 nm. This is quite reasonable to expect because, prior to oxidation, the silicon surface may retain some imperfections due to processing, handling, or cleaning steps. Without an oxide layer on top, these imperfections contribute to higher roughness. Starting from 15 mins of oxidation time until 90 mins, the RMS values are quite fluctuated. For 15 min oxidation time sample, RMS decreases significantly to 0.137 nm, indicating that the initial $SiO_2$ layer forms a smoother, more even surface that effectively reduces surface roughness by covering the native defects or imperfections on the silicon wafer. However, when the oxidation time was 30 mins, the RMS was increased, about 0.195 nm, while the RMS for 60 and 90 mins were 0.175 and 0.327 nm, respectively. Therefore, further study needs to be done such as varies other parameters (temperature and gas flow rate) that might affect the surface roughness of $SiO_2$/Si wafer.

## 4 Conclusion

Dry thermal oxidation process is a common process for growing the oxide layer on Si wafer with utilization of pure oxygen. Different oxidation times were applied in this study in order to study the effect of $SiO_2$ surface. The thickness of $SiO_2$ layer was determined accurately using spectral reflectance and it shows the thickness was increased as the oxidation time increased. However, the surface roughness of $SiO_2$ shows uncertain result. Even though the obtained RMS values are difficult to be concluded, but it still shows that the oxidation time have the potential to influence the surface roughness. Therefore, further study needs to be done by study other parameters such as oxidation temperature and gas flow rate.

## References

BYU. 2025. Silicone dioxide color chart. `https://cleanroom.byu.edu/color_chart`.

U Hashim, AH Azman, RM Ayub, MK Md Arshad, S Norhafiezah, MFM Fathil, MZ Kamarudin, R Adzhri, and MNM Nuzaihan. 2015. Comparison of deal grove model growth rate with dry thermal oxidation process for ultra-thin silicon dioxide film. In *2015 2nd International Conference on Biomedical Engineering (ICoBE)*, pages 1–4. IEEE.

Keichiro Ohsawa, Yusuke Hayashi, Ryu Hasunuma, and Kikuo Yamabe. 2009. Roughness increase on surface and interface of sio2 grown on atomically flat si (111) terrace. In *Journal of Physics: Conference Series*, volume 191, page 012031. IOP Publishing.

Individual Research Contribution Review, 2024: 271–272
*ISSN: 3083-922X*

# Comparison of Uranium $^{238}$U and Thorium $^{232}$Th Isotopes in Minerals from Two Industrial Sources

**Azian Hashim**
Waste Technology and Environment Division, Malaysian Nuclear Agency
43000 Kajang, Selangor
azian@nm.gov.my

## Abstract

This study evaluates uranium (U-238) and thorium (Th-232) activity concentrations in 54 mineral samples from two industrial sources, including zircon sands, zircon flour, and related products. Using Neutron Activation Analysis (NAA), the samples were categorized into six groups based on radionuclide levels: Extremely High, High, Moderate, and Low U-238 and/or Th-232 Levels, with Wollastonite included in the Low category. The highest U-238 concentration was recorded in Sample 22: Zircon Low Contents (2023) at 16,750 Bq/kg, which also had the highest Th-232 concentration at 8,960 Bq/kg. While U-238 dominated in some categories, Th-232 was comparable or higher in others, reflecting variability in isotopic distribution. This study provides key data on the radiological characteristics of mineral products, contributing to industrial optimization and environmental safety efforts.environment and public health.

**Keywords:** Neutron Activation Analysis, minerals, uranium-238, thorium-232

## 1 Introduction

Uranium-238 (U-238) and Thorium-232 (Th-232) are naturally occurring radionuclides found in minerals like zircon sands and zircon flour, which are used in various industries, including ceramics, refractories, and nuclear technology. These isotopes, part of the uranium and thorium decay series, contribute to natural radioactivity and have implications for radiological safety, environmental health, and industrial processing. The presence of U-238 and Th-232 in industrial minerals raises concerns about occupational exposure, environmental contamination, and compliance with radiological standards. Accurate characterization of these isotopes is essential for safe handling, storage, and usage, and can help optimize industrial processes, reduce waste, and minimize environmental impacts. Mineral products with high U and Th activity concentrations have a negative impact on the price of these mineral products (Hazin et al., 2008). This study investigates U-238 and Th-232 concentrations in 54 mineral samples from two industrial sources, analyed using neutron activation analysis (NAA). The samples were categorized into six groups based on radionuclide content, allowing for a comparison of isotopic distribution between sources. In this regard, the Analytical Chemistry Application group at the Malaysian Nuclear Agency provides sample analysis services for the measurement of uranium (U) and thorium (Th). The findings aim to enhance understanding of the radiological properties of these materials, supporting industrial optimization and ensuring compliance with environmental safety standards.

## 2 Methods

A total of 54 mineral samples, including zircon sands, zircon flour, zirconium silicate opacifiers, and related mineral products, were obtained from two industrial sources. The samples were finely ground, weighed (approximately 0.1g), and sealed in polyethylene containers to ensure homogeneity and prevent contamination. Each sample was prepared in triplicate for accuracy. Uranium (U-238) and thorium (Th-232) activity concentrations were measured using neutron activation analysis (NAA), a non-destructive technique. The process involved the following steps:

- Irradiation: Samples and certified reference materials (CRM) were irradiated in the TRIGA PUSPATI Mark II reactor (750 kW) for 3 hours at a neutron flux of 3.0 x $10^{12}$ n cm$^{-2}$ s$^{-1}$. The samples were placed in a rotating rack to ensure uniform irradiation.
- Cooling: After irradiation, samples were allowed to cool for 3 to 4 days to allow short-lived isotopes to decay.

Gamma Spectrometry: Gamma counting was performed using an Ortec HPGe detector (25% efficiency, 1.9 keV resolution at 1.33 MeV). The detector was calibrated with a certified multi-radionuclide standard source. Counting occurred in two stages:

- First stage: Uranium content was measured at 228 keV and 278 keV.
- Second stage: Thorium content was measured at 312 keV after a 10-day cooling period.

Activity concentrations of U-238 and Th-232 were recorded in Bq/Kg by comparing sample values with standard materials.

## 3 Results and Discussion

The results show significant variation in the U-238 and Th-232 concentrations across the 54 samples. The highest concentrations were observed in Sample 22 (Zircon Low Contents, 2023), which was categorized in Category 1 (Extremely



Figure 1: Examples of Mineral Samples from Industrial Sources Analysed for U-238 and Th-232 Activity

High Levels). This is consistent with the natural variation in radionuclide content typically found in different mineral products. The study reveals that U-238 concentrations are generally higher than Th-232 in most samples. However, in Category 5 (Low U-238, Moderate Th-232 Levels), Th-232 concentrations are more prominent. These findings are important for assessing radiological safety, as minerals with higher concentrations of both isotopes, particularly in Category 1 and Category 2, may present greater occupational and environmental risks. Understanding these variations is crucial for ensuring the safe handling, storage, and usage of industrial minerals.

Table 1: Ranges of U-238 and Th-232 Activity Concentrations for Each Category Based on 54 Mineral Samples

| **Category** | **U-238 Range (Bq/kg)** | **Th-232 Range (Bq/kg)** | **Description** |
|---|---|---|---|
| Category 1: Extremely HighU-238 and Th-232 Levels | 16340 - 18720 | 2120 - 8960 | Extremely elevated levels of both U-238 (>10,000) and Th-232 (>2,000). |
| Category 2: High U-238 and Th-232 Levels | 5550 - 9970 | 1000 - 4460 | U-238 levels between 5,000 - 10,000 and Th-232 levels between 700 - 5,000. |
| Category 3: Moderate U-238 and Th-232 Levels | 3120 - 5240 | 560 - 1460 | U-238 levels between 3,000 - 5,000 and Th-232 levels between 500 - 2,000. |
| Category 4: Moderate U-238 and Low Th-232 Levels | 2710 - 4470 | 512 - 747 | U-238 levels between 3,000 - 5,000 and Th-232 levels less than 1,000. |
| Category 5: Low U-238 and Moderate Th-232 Levels | 2590 - 6170 | 523 - 2980 | U-238 levels below 3,000 with Th-232 between 1,000 - 3,000. |
| Category 6: Low U-238 and Low Th-232 Levels (Includes Wollastonite) | 1810 - 3270 | 433 - 858 | Both U-238 and Th-232 levels are below 3,000 and 1,000, respectively, including Wollastonite. |

## 4 Conclusions

This study provides a comprehensive comparison of U-238 and Th-232 concentrations in industrial minerals, offering valuable data for radiological safety, regulatory compliance, and process optimization.

## References

C. A. Hazin, M. H. P. Gazineu, and de Farias E. E. G. 2008. Uranium and thorium in zircon sands processed in northeastern brazil. *In Proceedings of International Congress of the International Radiation Protection Association (IRPA): Strengthening Radiation Protection Worldwide*, Buenos Aires (Argentina), IPRA.

Individual Research Contribution Review, 2024: 273–274
*ISSN: 3083-922X*

# Radiological Impact of Natural Radioactivity in Malaysian Building Bricks

**Engku Mohd Fahmi Engku Chik**
Waste Technology and Environment Division, Malaysian Nuclear Agency
43000 Kajang, Selangor
mohdfahmi@nm.gov.my

## Abstract

Indoor radionuclide exposure is significantly affected by the concentration of isotopes present in outdoor soil and building materials. Building materials derived from rocks and soils can elevate health risks for occupants due to higher radionuclide concentrations. This study aims evaluating the natural concentrations of radionuclides in Malaysian bricks used for construction. Gamma-ray spectroscopy with a high-purity germanium (HPGe) detector was used to determine the activity concentrations of $^{238}$U, $^{232}$Th and $^{40}$K radionuclides in 20 brick samples. The mean activity concentrations of $^{238}$U, $^{232}$Th and $^{40}$K in the brick samples were 93.95 ± 18.82Bqkg$^{-1}$, 80.66 ± 15.03Bqkg$^{-1}$ and 693.13 ± 123.24 Bqkg$^{-1}$, respectively, which are well below the maximum limits. Our study indicates that most of the studied samples pose minimal health risks to Malaysian occupants. This research provides baseline information from a radiological perspective on bricks and can contribute to the development of guidelines for monitoring building materials in Malaysia's construction industry.

**Keywords:** Malaysia's bricks, radionuclide identification, elemental analysis

## 1 Introduction

Building materials play a crucial role in the construction of buildings, with the choice of materials impacting their structural integrity, safety, and environmental impact. Several factors such as cost-effectiveness, durability, functionality, and aesthetics need to be considered when selecting materials that are safe, specially from any harmful radiation hazard. Malaysia benefits from a variety of natural resources, resulting in a diverse range of building materials used in construction. Among the commonly used building materials in Malaysia are bricks. Bricks, an essential construction material, are commonly used in building construction. They come in various types and sizes, influenced by cultural and practical considerations. Bricks are made from clay or a mixture of clay and other materials like sand and cement. When selecting building materials, it's crucial to consider potential radiation exposure from unavoidable sources, such as radon in homes, natural environmental radiation, and naturally occurring radioactive materials (NORMs) present in the materials. In general, radiation exposure situations can be classified based on the level of exposure and its impact on health. One such classification is known as "existing exposure situations." Radiation exposure from building materials falls under this category. These exposures are typically ongoing and long-term, posing health risks to those affected. Since it is impossible to avoid radiation exposure from natural radioactivity in building materials, it is essential to monitor the radiological properties of these materials, especially those made with naturally occurring radioactive materials (NORMs).

The purpose of this study is to investigate the activity concentration levels of $^{238}$U, $^{232}$Th and $^{40}$K in Malaysian bricks. Besides, it also includes evaluating the element composition that can serve as preliminary information for guiding the selection of suitable construction materials, ensuring the minimization of prolonged health risks for individuals.

## 2 Methods

This research involved analyzing 20 brick samples, including cement, red and light-weight. All samples are manufactured locally in Malaysia. All the brick samples were crushed into small pieces, ground to fine grain size, and sieved using a 0.63mm mesh to homogenize the sample's particle size. Subsequently, the samples were dried at 105°C for 24 hours to ensure complete moisture removal (Ahmed, 2005). Following this, the samples were transferred to a standard Marinelli beaker, sealed hermetically with adhesive tape and left for a minimum of 28 days. This duration ensured that the daughter products of $^{238}$U up to $^{210}$Pb and those of $^{232}$Th up to $^{208}$Pb reached secular equilibrium with their respective parent radionuclides. The sample masses were weighed and they varied between 0.36 ± 0.01kg and 0.96 ± 0.01kg, depending on the type of brick.

The concentrations of $^{238}$U, $^{232}$Th and $^{40}$K radioactivity in the brick samples were determined using an ORTEC GEM Series P-type coaxial high-purity germanium (HPGe) spectroscopy. Each sample underwent a counting period of 86,400 seconds.

## 3 Results and Discussions

### 3.1 Radioactivity concentrations

The activity concentrations ($A$) of the radionuclides $^{238}$U, $^{232}$Th and $^{40}$K contained in each brick samples, measured in Bqkg$^{-1}$, were determined using the Equation 1:

$$A = \frac{N}{\varepsilon_\gamma \times P_\gamma \times m \times t} \quad (1)$$

where $N$ is the corrected peak under photo peak at energy $E$ (keV), $\varepsilon_\gamma$ is the efficiency of the detector at particular gamma-ray energy, $P_\gamma$ is the gamma-ray emission probability at energy $E$, $m$ is the sample mass (kg) and $t$ is the counting time (seconds). The variation in primordial activity concentrations among these samples can be attributed to differences in the content of radioactive minerals, as well as the geological, geochemical and geographical origins of the bricks.

The activity concentration levels of $^{238}$U, $^{232}$Th and $^{40}$K measured in brick samples ranged from 16.08 ± 3.41 to 259.49 ± 50.85Bqkg$^{-1}$ with a mean of 93.95 ± 18.82Bqkg$^{-1}$, 13.00 ± 2.58 to 211.92 ± 39.02Bqkg$^{-1}$ with a mean of 80.66 ± 15.03Bqkg$^{-1}$ and 78.96 ± 14.35 to 1,362.11 ± 241.84 with a mean of 693.13 ± 123.24Bqkg$^{-1}$, respectively. The highest average activity concentration of 259.49 ± 50.85, 211.92 ± 39.02 and 1,362.11 ± 241.84Bqkg$^{-1}$ for $^{238}$U, $^{232}$Th and $^{40}$K, respectively. However, these values are lower than those obtained from similar studies in Kenya and Namibia (Endjambi et al., 2024). Moreover, the mean activity concentration level of $^{238}$U measured in the subcategory of cement brick at 140.69 ± 27.81 Bqkg$^{-1}$ was greater than in red bricks and AAC blocks, which were 78.06 ± 15.74 and 41.40 ± 8.73 Bqkg$^{-1}$, respectively. Similarly, the mean activity concentrations of $^{232}$Th and $^{40}$K measured were higher in subcategory of cement bricks compared to the red brick and AAC block sample subcategories.

The maximum values of clay brick's activity concentration for $^{238}$U, $^{232}$Th and $^{40}$K reported in ICRP Publication 142 are 200, 200 and 2000 Bqkg$^{-1}$, respectively (ICRP, 2019). Samples BC4, BC6 and BC7 were recorded to exceed the maximum value for the $^{238}$U radionuclide. Sample BC7 exceeded the maximum value for the $^{232}$Th radionuclide and none of the studied samples were found to exceed the maximum value for the $^{40}$K radionuclide. The elevated activity concentration could be attributed to the use of locally sourced materials such as clay, sand and cement in brick production (Manap et al., 2016). Peninsular Malaysia is well-known for its extensive granite regions and significant levels of natural radioactivity (Metcalfe, 2013). Nevertheless, the mean activity concentrations of these radionuclides are lower than those found in other similar study (Endjambi et al., 2024).

### 3.2 Radionuclide identification and element analysis

Radionuclides $^{232}$Th, were identified by using a calibrated portable detector (Identifinder R425, FLIR), in all of the measured brick samples. Then, the element concentrations in two brick samples which are BC2 and BC7 were further analyzed by the WDXRF spectrometer. From the analysis, the primary element in the sample BC7 is Si, with a mean fraction of 38.35 ± 0.49 mass%. This is followed by Ca, Fe, Al and Sc, with a mean fraction of 25.00 ± 0.28, 10.20 ± 0.28, 9.75 ± 0.06 and 6.22 ± 0.14 mass%, respectively. While the primary element in the sample BC2 is Ca, with a mean fraction of 51.90 ± 0.00 mass%. This is followed by Sc, Si, Mg and Fe, with a mean fraction of 21.85 ± 0.49, 11.70 ± 0.14, 5.86 ± 0.35 and 3.30 ± 0.00 mass%, respectively. The high concentration of Si in the materials might contribute to enhanced radiation emission (Dickson and Scott, 1997), possibly accounting for the elevated dose rate in sample BC7 when compared to sample BC2.

In terms of NORMs elements of U, Th and K in the brick samples, it was revealed that element K consists of a higher fraction compared to elements U and Th. This reflects the higher activity concentration of radionuclide $^{40}$K, comparable to the trends for radionuclide activity concentration. The concentrations of K, U and Th in sample BC7 were recorded as higher than in sample BC2, with values of 6.33 ± 0.02, 0.03 ± 0.01 and 0.03 ± 0.01 mass% compared to 0.98 ± 0.06, 0.01 ± 0.01 and 0.01 ± 0.01 mass% respectively. A higher of elements fraction in the sample leads to an increased activity concentration, indicating that the presence of larger amounts of specific elements correlates directly with levels of radioactive activity.

## 4 Conclusions

This study aimed to investigated the radioactivity concentration, radionuclide identification and elemental analysis of randomly selected Malaysian building bricks samples. Results showed that the activity concentration of $^{238}$U in samples BC4, BC6 and BC7 exceeded the 200 Bqkg$^{-1}$ limit, while only BC7 exceeded the limit for $^{232}$Th. None of the samples surpassed the limit for $^{40}$K. High activity could be due to bricks made from local sources like clay, sand and cement. Element concentration analysis revealed that silicon was more prevalent in sample BC7 than in BC2. Additionally, both samples contained trace amounts of radioactive isotopes such as uranium, thorium and potassium, with the highest concentration also found in sample BC7 compared to BC2.

## References

N. K. Ahmed. 2005. Measurement of natural radioactivity in building materials in qena city, upper egypt. *Journal of Environmental Radioactivity*, 83(1):91–99.

B. L. Dickson and K. M. Scott. 1997. Interpretation of aerial gamma-ray surveys-adding the geochemical factors. *AGSO Journal of Australian Geology and Geophysics*, 17.

T. Endjambi, R. Mapani, B.and Shikangalah, K. Caspah, and M. Zivuku. 2024. Radiological hazards assessment of building materials used in swakopmund, namibia. *Journal of African Earth Sciences*, 213:105227.

ICRP. 2019. *Radiological Protection from Naturally Occuring Radioactive Material (NORM) in Industrial Processes*. Publication 142: SAGE.

N. Manap, R. A. A. R. Bedali, K. Sandirasegaran, M. A. N. Masrom, and M. Y. Yahya. 2016. Strength of brick made from dredged sediments. *Jurnal Teknologi*, 78:7–3.

I. Metcalfe. 2013. Tectonic evolution of the malay peninsula. *Journal of Asian Earth Sciences*, 76:195–213.

Individual Research Contribution Review, 2024: 275–276
*ISSN: 3083-922X*

# Post-closure Safety Assessment Calculation Using AFRY Intelligent Scenario Modeling (AISM) for Borehole Disposal in Malaysia

**Esther Phillip**
Waste Technology and Environment Division, Malaysian Nuclear Agency
43000 Kajang, Selangor
esther@nm.gov.my

## Abstract

Post-closure safety assessment of Malaysian borehole disposal facility for disused sealed radioactive sources (DSRS) was performed using AFRY Intelligent Scenario Modeling. The safety assessment evaluates the performance of the borehole disposal facility by calculating dose received by human from the release of radionuclides. Preliminary calculational results show that the dose received by human is below the dose constraint of 0.3 mSv/y.

**Keywords:** Borehole; Disused sealed radioactive sources (DSRS); Safety assessment; AFRY Intelligent Scenario Modeling

## 1 Introduction

The constructed borehole planned for disposal of DSRS is currently used as demonstration borehole as it is found to be unsuitable for disposal purpose due to engineering defect of the HDPE casing. Upcoming project to construct a new disposal borehole is currently underway. In this project, the previous design was updated to include the use of carbon steel casing replacing the HDPE casing. Previously, IAEA BDC Scoping Tool and AMBER were used to model the release of radionuclide to the biosphere where human and other biotas reside. Following the acquisition of AFRY Intelligent Scenario Modeling from the IAEA, safety assessment calculations for the new borehole are conducted using this software.

## 2 Methods

For the purpose of safety assessment of the disposal borehole, AFRY Intelligent Scenario Modeling is used as a tool to create dynamic compartmental models and to perform deterministic or probabilistic simulations. Endpoint for the safety assessment is shown as dose received by human residing near a river located 1300 m from the borehole. Other endpoint also include dose obtained from drinking of water abstracted from the river.

Example of user interfaces of the model are given in Figure 1.

## 3 Results

Results obtained from preliminary safety assessment calculations are presented in Figure 2 and 3.

Calculational results showed that the dose exposure is below the dose constraint of 0.3 mSv/y.

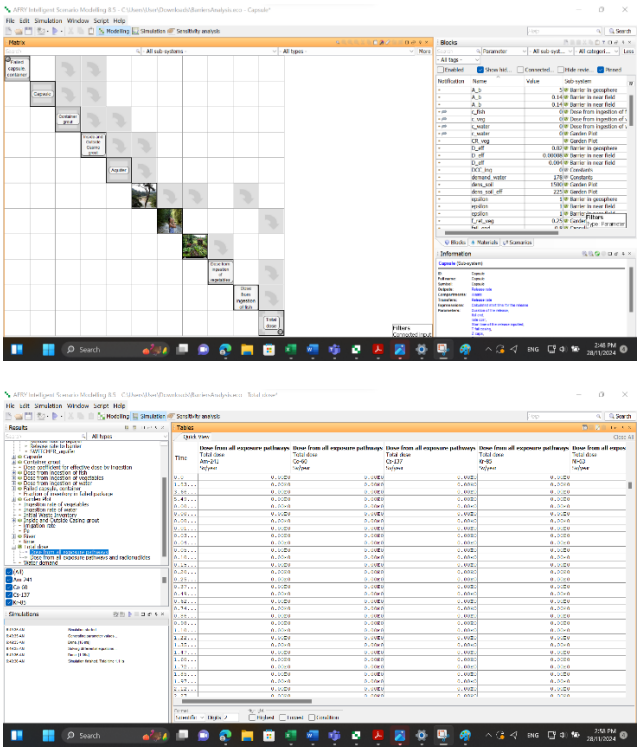


Figure 1: User interfaces of the model

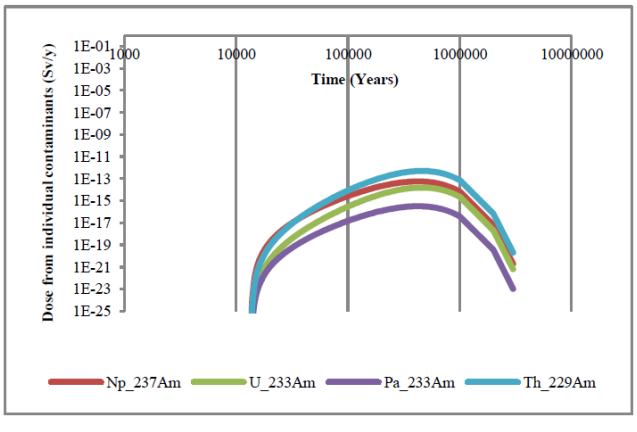



Figure 2: Dose from individual contaminants (Sv/y)

## 4 Conclusions

Preliminary calculational results show that the dose received by human is below the dose constraint of 0.3 mSv/y. This

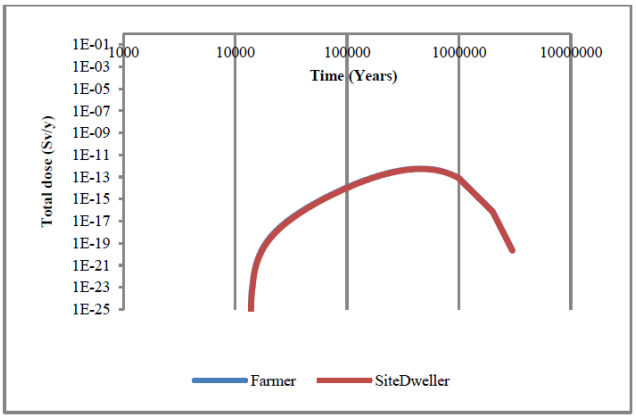



Figure 3:

finding thus supports the performance of the borehole disposal facility as a safe approach in the long-term management of DSRS.

## References

INTERNATIONAL ATOMIC ENERGY AGENCYS. December 2012. Generic Post-Closure Safety Assessment for Borehole Disposal of Disused Sealed Sources. *IAEA-TECDOC (Draft), IAEA*.

NECSA. October 2004. *Site Specific Safety Assessment for the Borehole Disposal Concept, GEA 1625*. NECSA, Pretoria.

Individual Research Contribution Review, 2024: 277–278
*ISSN: 3083-922X*

# Development of a Predictive Model for Terrestrial Gamma Radiation Based on Weathered Soil and Rock Characteristics in Sarawak, Malaysia

**Hairul Nizam Idris**
Waste Technology and Environment Division, Malaysian Nuclear Agency
43000 Kajang, Selangor
hairul_nizam@nm.gov.my

## Abstract

This study investigates the feasibility of predicting TGR dose rates using a linear regression model based on surface-weathered soils and rocks in Sarawak, Malaysia. Sarawak's geology, shaped by a complex tectonic history, comprises 93% sedimentary rocks and 7% igneous and metamorphic rocks. A total of 1044 TGR dose rate measurements were collected, ranging from 7 to 320 nGy $h^{-1}$, with a mean of 100 nGy $h^{-1}$. Statistical analyses confirmed significant differences among six categories of weathered soils and between sedimentary and igneous rocks. The derived regression model, TGR (nGy $h^{-1}$) = 0.992Dsoil – 0.816Drock + 109, demonstrated reliable predictive capability. Spatial mapping and semivariogram analysis validated the model, making it a valuable tool for estimating TGR dose rates in unsampled regions with similar geology, supporting radiation exposure assessment and environmental monitoring.

**Keywords:** Terrestrial Gamma Radiation, TGR Dose Rate, Isodose, Sarawak

## 1 Introduction

Terrestrial gamma radiation (TGR) baseline data is essential for assessing public exposure to natural radiation and calculating annual effective doses. While TGR exposure is generally low, cumulative radiation from multiple sources can be significant. Spatial TGR distribution mapping aids in evaluating public doses from anthropogenic sources, such as nuclear fallout events and TENORM contamination from mining industries (Kleinschmidt and Watson, 2016). This data is crucial for epidemiological studies of hereditary cancer risks and health impacts of elevated background radiation (ICRP, 2007).

Radiological Although several countries have completed national TGR mapping, including Canada, Croatia, Spain, and China, comprehensive mapping requires extensive in-situ gamma surveys, which are costly and time-consuming, particularly in inaccessible areas (Sanusi et al., 2014). This study explores TGR dose rate estimation using a linear regression model based on dose rates from surface-weathered soils and rocks in Sarawak, Borneo, Malaysia.

## 2 Methods

Measurement survey location points were determined based on geological background, soil distribution, and accessibility, using Sarawak's physical, topographic, geology, and soil maps. A total of 1044 points were selected via the stratified sampling method. Navigation to these points was guided by a GPS device. Terrestrial gamma radiation (TGR) dose rates were measured using a NaI(Tl) scintillation detector (Ludlum-19 Micro R survey meter) at approximately 1 meter above ground level. An isodose map of Sarawak was generated through Kriging spatial analysis using ArcGIS 10.5 software.

This study employed regression analysis to explore a linear model for TGR based on soil and rocks information, with the aim of quantifying the strength of the correlation between these two variables. The results obtained from this model will be used for predicting values at unsampled points. The goal of fitting the linear regression model is to estimate the regression coefficients that minimize the sum of squared differences between the predicted values of dose rates and the actual observed values of the measured dose rates. seconds.

## 3 Results

As shown in Table 1, the unstandardized regression coefficients ($\beta$ coefficients) were chosen to represent the prediction model or direct change based on raw values (or original units), instead of standardized coefficients, which express the relative effects in terms of standard deviations or regardless of original units. The TGR dose rate predictor model consisted of one positive predictor variable (0.992 for weathered soil) and one negative predictor variable (-0.816 for geological rocks). The observed negative beta coefficient suggests an inverse relationship between the predictor (geological rocks) and response variables (TGR dose rate), while keeping the soil variable constant. The developed linear independent variable model based on the estimator coefficients (dependent variables) can be expressed as: -

$TGR$ (nGy $h^{-1}$) = $0.992Dsoil - 0.816Drock + 109$

where 109 nGy $h^{-1}$ is a constant.

Table 1: The linear regression model of TGR dose rate based on weathered soil and geological rock groups

| Model | Unstandardized Coefficients | | Standardized Coefficients |
|---|---|---|---|
| | B | Std. Error | Beta |
| (Constant) | 108.576 | 17.915 | |
| rock | -.816 | .132 | -.133 |
| soil | .992 | .031 | .697 |

Meanwhile, Figure 1 shows two spatial maps of TGR dose rates developed based on: (a) in-situ TGR dose and (b) linear regression dose predictive model. Graphically, the maps

showed similarities in terms of regional dose rate contour, where 50 nGy $h^{-1}$ to 100 nGy $h^{-1}$ dose rate dominated the coastal and recent rock developments i.e. Quaternary and Pleistocene age of rock regions (gleysols, thionic, alluvial, and organic), whereas the upper dose rate range 110 – 320 nGy $h^{-1}$ dominated the sedentary formation (e.g., skeletal and podzolic). To analyse the variability of these spatial maps, two semivariogram plots analysis were given in Figure 2.

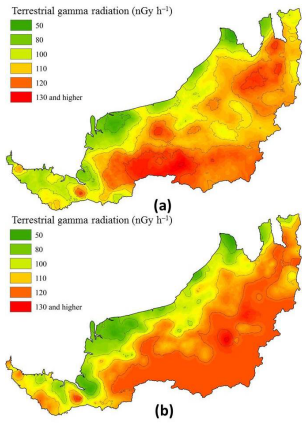



Figure 1: Distribution of TGR dose rates in Borneo Sarawak based Ordinary Kriging of (a) in-situ TGR dose rate and (b) linear regression dose predictive model

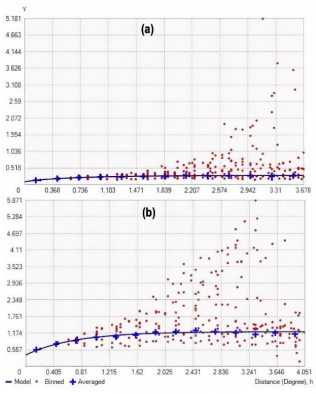



Figure 2: Semivariogram model of Kriging interpolation for comparison between (a) in-situ and (b) predicted TGR dose rates

## 4 Discussions

The semivariogram model (Figure 2) based on a linear regression predictive model suggests that the correlation between data points decreases and eventually becomes flat (i.e., no longer correlated) at a distance of approximately 1.62 degrees. In contrast, the in-situ data indicates that the correlation between data points decreases and becomes flat at a distance of around 1.47 degrees. Comparable sill and nugget values indicated from both semivariogram plots suggest that the developed regression prediction model provides an adequate estimator for TGR dose rate prediction. Such prediction and its consistent variation are considered acceptable at environmental levels, allowing one to build an empirical, methodological basis for spatial inference. The presented model also applicable for long-term use and will not be affected by heavy rainfall and flood. For tropical climates, soil develops slowly over millions of years, and the weathering process by rain, flood, and climates may require a long time to alter the U, Th, and K distribution in soil bodies (Sanusi et al., 2017).

## 5 Conclusions

This study successfully developed a regional predictive model for terrestrial gamma radiation (TGR) dose rates using a linear regression approach based on data from superficial-weathered soils and rocks. Nonparametric statistical analyses of variance demonstrated significant differences among six groups of weathered soils, and as well as between two distinct groups of sedimentary and igneous rocks. The predictive model, expressed as TGR dose rate (nGy $h^{-1}$) = 0.992Dsoil – 0.816Drock + 109, is applicable to regions with similar rock and soil types within the Sundaland-Borneo tectonic block. While the model predicts unsampled values based on random nearby sampled points – an assumption that may not universally hold true for all environmental data – it provides an acceptable and practical methodological framework. This model establishes an empirical methodological foundation for spatial inference of TGR dose rate levels in unmeasured locations with similar geological and soil characteristics, offering valuable insights for radiation exposure assessment and environmental monitoring.

## References

103 ICRP. 2007. Recommendations of the international commission on radiological protection. *International Commission on Radiological Protection ICRP Publication 103, Annals of the ICRP 37*.

R. Kleinschmidt and D. Watson. 2016. Terrestrial gamma radiation baseline mapping using ultra low-density sampling methods. *J. Environ. Radioact*, 151(3):609–622.

M.S.M. Sanusi, A.T. Ramli, H.T. Gabdo, N.N. Garba, A. Heryanshah, H. Wagiran, and M.N. Said. 2014. Isodose mapping of terrestrial gamma radiation dose rate of Selangor State, Kuala Lumpur and Putrajaya, malaysia. *J. Environ. Radioact*, 135:67–74.

M.S.M. Sanusi, A.T. Ramli, M.N. Said, A. Izham, M.H. Lee, A. Heryanshah, and H. Wagiran. 2017. Assessment of impact of urbanisation on background radiation exposure and human health risk estimation in Kuala Lumpur, Malaysia. *Environ. Int*, 109:91–101.

Individual Research Contribution Review, 2024: 279–280
*ISSN: 3083-922X*

# The depth distribution of Beryllium-7 in different land uses study

**Jalal Bin Sharib@Sarip**
Waste Technology and Environment Division, Malaysian Nuclear Agency
43000 Kajang, Selangor
jalal@nm.gov.my

## Abstract

This paper aims to study the depth penetration of Beryllium-7 as a tracer onto the soil surface. The use of this tracer is still not widespread in local studies due to its short half-life compared to other tracers. Hence, the study was conducted in various land uses in the Sembrong catchment, Kluang involving two different seasons. The distribution of the soil depth profile onto the soil surface or ho value varies between 2.53 – 4.89 $kgm^{-2}$ and 3.11 - 5.12 $kgm^{-2}$ for dry and wet seasons. The results of this study have given a value that is not much different from other studies. In conclusion, Beryllium-7 which is used as a short-term tracer is very suitable to be used in this study to determine the value of depth penetration onto the soil surface in different land uses.

**Keywords:** Paper, Depth penetration, Beryllium-7, soil surface, Short-term

## 1 Introduction

The environmental isotope refers to the isotopes that are usually widely distributed in the environment or in the landscape. In most cases, these isotopes are naturally occurring but in some cases is a man-made. It is also known as Fallout Radionuclides (FRNs) such as $^{137}Cs$, $^{210}Pb_{ex}$ and $^{7}Be$ which have been widely used as tracer sediments in soil erosion studies and sedimentation by scientists all over the world. $^{7}Be$ is a naturally occurring radionuclide that is produced by the bombardment of the earth's atmosphere by cosmic radiation (Lal and Peters, 1967). $^{7}Be$, a radioactive isotope, with a half-life 53.29 days is produced when nuclear spallation processes interact with oxygen and nitrogen in the upper troposphere and lower stratosphere (Lal and Suess., 1968). Furthermore, $^{7}Be$ is rapidly and strongly absorbed by soil particles in most environments (Hawley et al., 1986). Moreover, the $^{7}Be$ has been shown to offer considerable potential to provide information over shorter timescales in depth distribution study.

## 2 Methods

This sampling activity has taken a total of twenty (20) core soil samples from several different land uses using a metal corer. All soil samples that have been sliced to increments of 2 mm to the inner 4 cm and taken to the Laboratory of the Radiochemistry and Environment Group (RAS), Nuclear Malaysia in Bangi, Selangor for further treatment. The samples before being counted using gamma spectrometry should be dried in the oven at a temperature of 45 - 60°C for several days until the weight becomes constant or stable and were put into a 6 ml vial tube for counting using Gamma Spectrometry.

The $^{7}Be$ concentrations or activity from the samples was calculated using equation 1 as below:

$$A = \frac{N}{\varepsilon p_{\gamma} m t} \tag{1}$$

Where;
N was the net count under the peak of 477.6 keV gamma line energy that characterized $^{7}Be$ (in counts)
$\varepsilon$ was the efficiency of the detection system for the 477.6 keV gamma line energy (in counts.$Bq^{-1}.s^{-1}$) obtained from equation 1,
$p_{\gamma}$ was the absolute probability transition for 477.6 keV gamma line for $^{7}Be$,
m and t were the mass (in kg) and time of counting in second.

Meanwhile, the depth distribution of $^{7}Be$ is represented by an exponential decline with depth,

$$C(x) = Ce^{\frac{-x}{h_o}} \tag{2}$$

Where;
C(x) is the mass activity density of $^{7}Be$ at mass depth x, $Bqkg^{-1}$
$h_o$ is the coefficient describing profile shape $kgm^{-2}$ and also known as the relaxation mass depth.

If the value of $h_o$ increases, the penetration of the $^{7}Be$ can be assumed to be greater into the soil profile depth.

## 3 Results and Discussion

The results of the distribution of soil depth profile onto the soil surface or $h_o$ value of the six land uses are shown in Table 1. Thus, the results that vary between the two study seasons are 2.53 - 4.89 $kgm^{-2}$ and 3.11 - 5.12 $kgm^{-2}$. Meanwhile, it shows that the penetration of $^{7}Be$ decreases exponentially the decay in the soil depth as presented in the literature (Matisoff et al., 2002a; Blake, 2000). However, the two results from these two seasons were not significantly different for all land use diversity. Furthermore, value $h_o$ on two seasons for modern agriculture is 3.14 $kgm^{-2}$ and 3.32 $kgm^{-2}$, each respectively.

It may be due to the relatively high concentration of $^{7}$Be in rainwater which has a low volume and can then seep more onto the soil surface during the rainy season when compared to the dry season. However, some other factors such as the type of soil where there is likely to be a stony soil content in the mixed crop area that can cause some obstacles for more rainwater percolation to occur on the soil surface.

Table 1: The $h_o$ ( $kgm^{-2}$) and depth increment (cm) values in different land use

| | **Land Use** | **$h_o$ value ( $kgm^{-2}$)** | | **depth increment (cm)** | |
|---|---|---|---|---|---|
| | | Dry season | Wet season | Dry season | Wet season |
| 1. | Modern agriculture | 3.14 | 3.32 | 2.1 | 2.5 |
| 2. | Mixed crop | 4.89 | 5.12 | 2.4 | 2.3 |
| 3. | Oil palm plantation | 3.12 | 3.86 | 1.5 | 2.2 |
| 4. | Rubber tree plantation | 2.53 | 3.11 | 2.3 | 2.7 |
| 5. | Fruit orchard | 3.68 | 3.92 | 1.8 | 2.4 |
| 6. | Forest | 3.25 | 3.87 | 1.6 | 2.1 |

Furthermore, the two values of $h_o$ are not significantly different even though the frequency of precipitation occurs in the wet rainy season compared to the dry season (p value > 0.05). The depth penetration of $^{7}$Be or the $h_o$ value from the overall results of this study is slightly higher when compared to the study reports in Valdivia, Chile and Brazil 1.28 to 2.15 $kgm^{-2}$, respectively (Walling and Collins, 2008).

## 4 Conclusions

The depth distribution of $^{7}$Be from this study for all land uses for both seasons has decreased exponentially with depth and is limited in the top few centimeters and similar to other work has been reported. Meanwhile, this study also found that the value of $h_o$ and the increase in depth were not completely affected by the two seasons during the study period although there was a slight difference that was not significant. In conclusion, $^{7}$Be as a short-term tracer is very suitable to be used in this study to determine the value of depth penetration or $h_o$ onto the soil surface in different land uses.

## References

W.H. Blake. 2000. The use of $^{7}$be as a tracer in sediment budget investigations. *Geography Department, University of Exeter*.

N. Hawley, J.A. Robbins, and B.J. Eadie. 1986. The partitioning of 7-beryllium in fresh water. *Geochim. Cosmochim.*, Acta 50:1127 – 1131.

Lal and Peters. 1967. Cosmic ray produced radioactivity on the earth. *Handbuch der Physik B XLVI, Springer Verlag, Berlin/Heidelberg/New York*, pages 551–612.

D. Lal and H.E. Suess. 1968. The radioactivity of the atmosphere and hydrosphere. *Annu. Rev. Nucl. Sci.*, 18:407 – 434.

G. Matisoff, E.C. Bonniwell, and P.J. Whiting. 2002a. Soil erosion and sediment sources in an ohio watershed using beryllium-7, cesium-137, and lead-210. *J. Environ. Qual.*, 31:54 – 61.

D.E. Walling and A.l. Collins. 2008. The catchment sediment budget as a management tool. *Environmental Science and Policy*, 11:136–143.

Individual Research Contribution Review, 2024: 281–282
*ISSN: 3083-922X*

# Seepage Water Study in Pedu Dam, Kedah

**Jeremy Andy Anak Dominic Daung**
Waste Technology and Environment Division, Malaysian Nuclear Agency
43000 Kajang, Selangor
jeremy@nm.gov.my

## Abstract

The study was conducted at Pedu Dam which is located in Padang Terap District, Kedah. The aim of this study is to identify qualitatively the potential sources of seepage water at the seepage inspection chamber dam using water stable isotopes and multi-element composition signatures. A total of twenty-seven water samples for stable isotope and multi-element analysis were collected from five selected locations comprises of the open standpipe piezometer, reservoir, seepage inspection chamber, left groin seepage point and downstream river. The seepage water from the right-side seepage inspection chamber, RSC01, RSC02 and RSC03 comprises mixtures between the reservoir and groundwater with higher proportion of groundwater mixtures in the seepage water from RSC01. The seepage water from the left-side seepage inspection chamber, LSC01, LSC02 and LSC03 comprises mixtures between the reservoir and groundwater with higher proportion of groundwater mixtures in the seepage water from LSC03. The result also indicates that the proportion of groundwater mixture in the left seepage inspection chamber is relatively higher than that of the right inspection chamber. The left groin seepage water at SP01 is most likely originated from the groundwater.

**Keywords:** Stable isotope, seepage water

## 1 Introduction

Environmental isotopes consist of both stable and radioactive, occur in the atmosphere and the hydrosphere in varying concentrations. The most commonly used stable isotope in hydrological study are those of oxygen and hydrogen. Variations in stable isotope ratios of natural compounds are governed by chemical reactions and phase changes because of the energy difference between chemical bonds involving different isotopes of an element. Such energy differences are caused by the relative mass difference between isotopes. Stable isotope ratios in hydrology are conventionally reported as per mil (‰) deviation from those of a standard using the $\delta$ (delta) notation:

$$\delta(‰) = \frac{R_{sample} - R_{standard}}{R_{standard}} \times 1000 \qquad (1)$$

where $R_{sample}$ and $R_{standard}$ denote the ratios in the sample and standard, respectively, of the heavy to light isotope ($^{18}O/^{16}O$ or $^{2}H/^{1}H$). The isotopic standard used for hydrogen and oxygen isotopes is the Vienna Standard Mean Ocean Water (VSMOW) Clark and Fritz (1997).

Inductively coupled plasma mass spectrometry (ICP-MS) is an advanced analytical technique used to identify the presence of many metals and some non-metals in a material. The aim of this study is to identify qualitatively the potential sources of seepage water at the seepage inspection chamber dam using water stable isotopes and multi-element composition signatures.

## 2 Methods

The study was conducted at Pedu Dam which is located in Padang Terap District, near the border with Thailand. It was built in 1969, together with the Muda Dam, under the Muda Irrigation Scheme for the purpose of providing irrigation water to the Muda Irrigation area. The scope of study comprises of water sample collection from the open standpipe piezometer, reservoir, seepage inspection chamber, seepage point source and downstream river. In-situ physical parameter measurement of water sample, stable isotope and multi-element analysis and data interpretation. A total of twenty-seven water samples for stable isotope and multi-element analysis were collected from five selected locations comprises of the open standpipe piezometer, reservoir, seepage inspection chamber, left groin seepage point and downstream river (Figure 1).




Figure 1: Sampling locations

## 3 Data/Results

The $\delta^{18}O$ and $\delta^{2}H$ values of the water samples were plotted near the Alor Setar Local Meteoric Water line (LMWL). The $\delta^{18}O$ and $\delta^{2}H$ values of reservoir water samples collected from both surface (BS and CS) and deeper level (A1, A2, A3, B1, B2, B3, B4, C1, C2, C3, C4 and CS1) were relatively enriched than that of the other sampling locations. The $\delta^{18}O$ and $\delta^{2}H$ values of the surface water samples collected from BS and CS were relatively enriched than that of the deeper water, thus indicates that fractionation of the stable water isotopes are most likely occur on water surface due to evaporation. Similarly, the $\delta^{18}O$ and $\delta^{2}H$ values of water sample collected at shallower water depth, B1 and C1 (Figure 2) were relatively enriched.

The $\delta^{18}O$ and $\delta^{2}H$ values of water samples collected from RSC02 and RSC03 of the right seepage inspection chamber were relatively higher than that of the water samples collected from RSC01 (Figure 2). This indicates that seepage water from RSC02 and RSC03 conduits comprises of mixtures between the reservoir and ground water with a relatively higher proportion of reservoir water. The seepage water from the RSC01 conduit comprises of mixtures between the reservoir and ground water with a relatively higher proportion of groundwater.

The $\delta^{18}O$ and $\delta^{2}H$ values of water samples collected from LSC01 and LSC02 of the left seepage inspection chamber were relatively higher than that of the water samples collected from LSC03 (Figure 2). This indicates that seepage water from LSC01 and LSC02 conduits comprises of mixtures between the reservoir and ground water with a relatively higher proportion of reservoir water. The seepage water from the LSC03 conduit comprises of mixtures between the reservoir and ground water with a relatively higher proportion of groundwater. Based on visual observation the seepage water flow rate from the LSC01 conduit was relatively higher compared to other discharge points in both inspection chamber. The element concentrations of water sample collected from PZ06 shows a significantly moderate correlation with water samples collected from LSC03 and RSC01. The results also indicates that the correlation of element concentrations between PZ06 and LSC03 are relatively stronger than RSC01 (Figure 3 and 4).

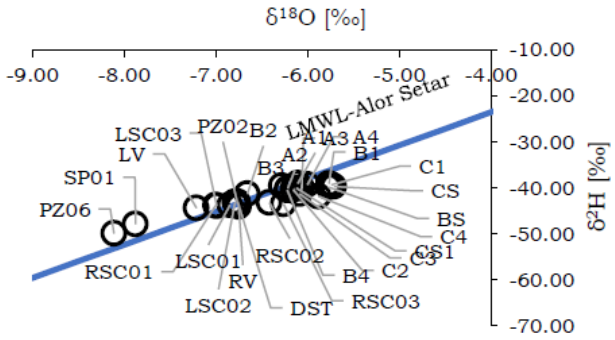



Figure 2: $\delta^{18}O$ ‰ vs $\delta^{2}H$ ‰ graph plot

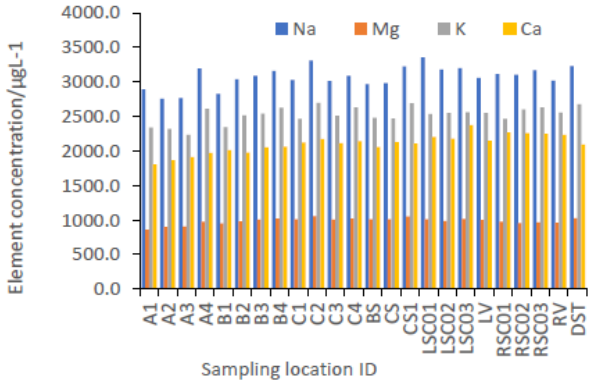



Figure 3: Element concentration in surface water samples

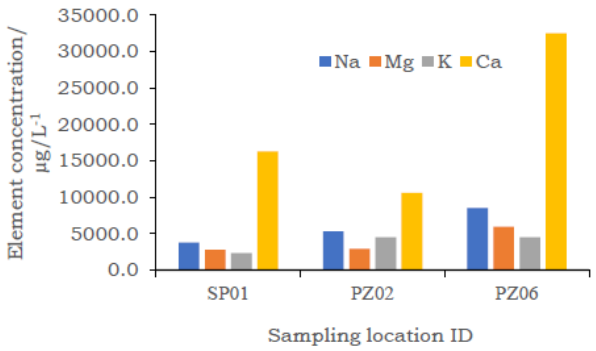



Figure 4: Element concentration in groundwater samples

## 4 Discussion/Conclusions

The seepage water from the right-side seepage inspection chamber, RSC01, RSC02 and RSC03 comprises mixtures between the reservoir and groundwater with higher proportion of groundwater mixtures in the seepage water from RSC01. The seepage water from the left-side seepage inspection chamber, LSC01, LSC02 and LSC03 comprises mixtures between the reservoir and groundwater with higher proportion of groundwater mixtures in the seepage water from LSC03. The result also indicates that the proportion of groundwater mixture in the left seepage inspection chamber is relatively higher than that of the right inspection chamber. The left groin seepage water from SP01 is most likely originated from the groundwater.

## References

Clark I and Fritz P. 1997. Environmental isotopes in hydrology. *CRC Press.*

Individual Research Contribution Review, 2024: 283–284
*ISSN: 3083-922X*

# Groundwater potential investigation using resistivity imaging and isotope hydrology at Universiti Malaysia Sabah Campus, Sabah

**Lakam Anak Mejus**
Waste Technology and Environment Division, Malaysian Nuclear Agency
43000 Kajang, Selangor
lakam@nm.gov.my

## Abstract

A field survey consisting of resistivity imaging investigation and isotope hydrology was conducted near the Universiti Malaysia Sabah (UMS) campus. The survey aimed to investigate the possible presence of underground aquifer systems and determine the origin of groundwater. Three 800 m electrical resistivity tomography (ERT) lines were conducted at designated locations. The ERT profiles provided subsurface information to a depth of 160 m and showed promising evidence of aquifers. Contrasting electrical properties were used to characterize stratigraphic units, classified into four main resistivity ranges. Several positions along the survey lines were interpreted as potential groundwater sources and proposed for extraction drilling. Stable isotope analysis showed groundwater and surface water directly interact with rainwater. Additionally, groundwater extracted for domestic use in the UMS campus originates from two different unconfined aquifers.

**Keywords:** Resistivity, stable isotope

## 1 Introduction

Exploration and exploitation of aquifer systems containing groundwater is often pursued to meet rising water demand for agricultural, domestic, and industrial use. Proper investigation tools are essential to assess groundwater potential and sustainability as a major future water source. Surface geophysical techniques have proven effective in hydrogeological studies by linking physical and hydrological properties. Resistivity imaging investigates subsurface physical properties to differentiate and characterize lithological units, sometimes linking them to hydrological processes. Conversely, isotope hydrology, based on water and environmental isotope variations, provides key information for hydrological and environmental studies.

A field survey combining resistivity imaging and isotope hydrology was conducted near Universiti Malaysia Sabah (UMS) at 6°01'52.1" N, 116°07'01.6" E, about 10 km from Kota Kinabalu. The objectives were to investigate possible underground aquifers and determine groundwater sources. Resistivity imaging helps identify potential drilling sites, while isotope hydrology using stable isotopes oxygen-18 ($^{18}$O) and hydrogen-2 ($^{2}$H or deuterium) analyzes relationships between groundwater, surface water, rainwater, and tap water. The study area lies within the Crocker Formation (upper Eocene to lower Miocene), consisting of deep-sea lithic greywacke sandstone with thin shale layers, along with faults and fractures. Expected resistivity responses range from 10 to 1,000 Ωm. Figure 1 show the survey line locations and geological map, respectively.

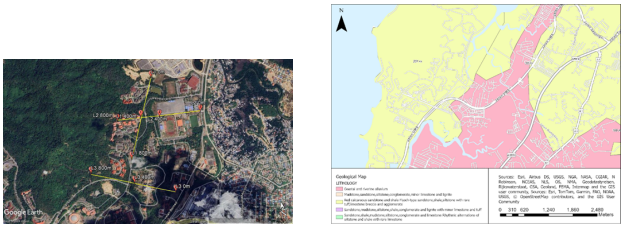


Figure 1: (a) and (b) show the Universiti Malaysia Sabah area and its geological context for the resistivity survey.

## 2 Methods

### 2.1 Electrical Resistivity Tomography (ERT)

A total of 3 ERT profiles with a length of 800m each were collected by employing a Schlumberger quadrapole configuration. The ERT survey were carried out with a 61 electrodes ABEM Terrameter LS2 (Guideline Geo, Stockholm, Sweden). The Schlumberger quadrapole configuration can gather a total of 748 data points. Each data obtained by inserting certain amount of electrical current (10-50mA) into the ground through a pair of electrodes and the resulting voltage (potential) measured at a different pair of electrodes on the ground surface. To observe a good data quality, the standard deviation of the measured voltage was set at ±3% with a maximum 3 stacking cycles. The collected resistance magnitude data will be used as the input data and recalculate using Res2Dinv inverse solution for a 2-D resistivity distribution based on computation of current flow in a quadrilateral or triangular mesh (Loke and Barker, 1996; Loke, 1999).

### 2.2 Water sampling

A variety of water samples including surface water, groundwater, rainwater and tap water were collected (Table 1). The water samples for stable isotope analysis were kept in a 100ml polyethylene plastic bottle and closed tightly to avoid the presence of air bubbles in the sample bottle. The presence of air bubbles may cause evaporation process and will affect the actual stable isotope delta value of the water samples. The

water samples were analyzed using a Los Gatos Research (LGR) liquid water isotope analyzer (LWIA) at the Malaysian Nuclear Agency for the determination of Oxygen-18 ($^{18}$O) and Deuterium ($^{2}$H).

Table 1: Location of water sampling within the UMS campus and surrounding areas

| No | Sampling location | Sample ID | Type of water |
|---|---|---|---|
| 1 | Residence College E | UMS01 | Groundwater |
| 2 | Residence College E | UMS02 | Groundwater |
| 3 | Residence College E | UMS03 | Reservoir water |
| 4 | Residence College Tun Mustapha (in front of the bus stop) | UMS04 | Groundwater |
| 5 | Residence College Tun Mustapha (Blok F) | UMS05 | Groundwater |
| 6 | Tun Fuad Residence College | UMS06 | JANS tap water |
| 7 | Tun Fuad Residence College | UMS07 | Groundwater |
| 8 | Faculty of Sciences & Natural Resources | UMS08 | Reservoir water |
| 9 | SFERA @ UMS | UMS09 | Rain water |
| 10 | Saga Village | UMS10 | River water |

## 3 Results and discussion

Figure 2 presents the inversion results of the ERT surveys, showing variations in topography and proposed drilling locations. Sharp resistivity contrasts in all three 2D sections indicate inhomogeneous subsurface materials, divided into four categories: <20Ωm, 20–150Ωm, 150–3000Ωm, and >3000Ωm. The main feature is the contrast between conductive zones (<200Ωm) and resistive units (>200Ωm). In ERT1, a continuous conductive zone (<20Ωm) from 10–280 m along the line, up to 100 m deep, is interpreted as a water-saturated layer likely influenced by surface water infiltration; drilling is proposed at 290 m and 580 m. ERT2 shows a conductive top layer over a resistive layer, with a potential fracture zone proposed for drilling. In ERT3, low resistivity values (10–200Ωm) dominate, suggesting infiltration effects, with drilling recommended at 360 m and 480 m.

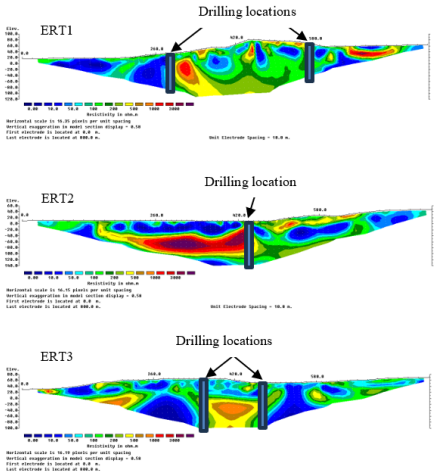



Figure 2: The inversion results of the ERT surveys. The contrasting resistivity values indicate the inhomogeneous subsurface materials

Table 2 and Figure 3 summarize water stable isotope analysis results. $\delta^{2}$H and $\delta^{18}$O values for ground and surface water ranged from –62.1‰ to –36.8‰ and –9.61‰ to –6.06‰, respectively, separating groundwater into two source groups. Samples from UMS01, UMS02, and UMS07 shared values of –53.9‰ to –51.3‰ ($\delta^{2}$H) and –8.57‰ to –8.45‰ ($\delta^{18}$O), while UMS04 and UMS05 ranged from –47‰ to –45.7‰ and –7.5‰ to –7.48‰, respectively. The values plotted near the Kota Kinabalu Local Meteoric Water Line (KKLMWL) [$\delta^{2}$H=(7.58±0.14)$\delta^{18}$O+(8.97±0.28)], derived from GNIP rainfall data, indicating that ground and surface water likely mix with meteoric water.

Table 2: Result of the water stable isotope analysis

| Sample ID | Type of water | $\delta^{2}$H (‰) | $\delta^{18}$O (‰) | Electrical conductivity ($\mu$S/cm) |
|---|---|---|---|---|
| UMS01 | Groundwater | -51.3 | -8.45 | 127.33 |
| UMS02 | Groundwater | -53.4 | -8.77 | 1574.00 |
| UMS03 | Reservoir water | -50.0 | -8.00 | 144.00 |
| UMS04 | Groundwater | -45.7 | -7.50 | 480.00 |
| UMS05 | Groundwater | -47.0 | -7.48 | 504.67 |
| UMS06 | JANS tap water | -43.4 | -6.87 | 98.00 |
| UMS07 | Groundwater | -53.9 | -8.57 | 508.67 |
| UMS08 | Reservoir water | -49.9 | -7.67 | 362.00 |
| UMS09 | Rain water | -62.1 | -9.61 | 4.00 |
| UMS10 | Rain water | -36.8 | -6.06 | 36966.67 |

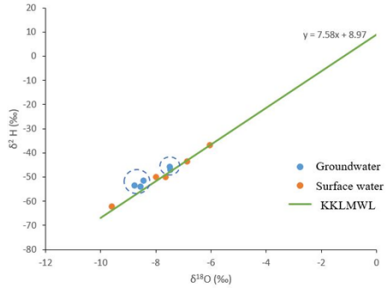



Figure 3: Plot of $\delta^{2}$H versus $\delta^{18}$O for river water. Blue circle indicates the groundwater can be separated into two groups of sources

## 4 Conclusions

The electrical resistivity tomography technique has been able to delineate an aquifer system in the UMS campus. The inversion results showed the existence of deeper potential groundwater zones or layers. The positions for drilling investigation along the survey line has also been marked to assist the concerned parties in making appropriate decisions. The result of stable isotope analysis revealed two different source of groundwater that being used on the UMS campus. Also, noticeable that the groundwater has direct influence from rainwater and interpreted as groundwater from the unconfined aquifer type. Worth-mentioning here that further investigation is needed to ensure the sustainability/continuity of the aquifer systems.

## References

M.H Loke and R.D. Barker. 1996. Rapid least-squares inversion of apparent resistivity pseudosection by quasi-newton method. *Geophysical Prospecting*, 44:131–152.

M.H Loke. 1999. Electrical imaging surveys for environmental and engineering studies. http://www.georentals.co.uk/Lokenote.pdf.

Individual Research Contribution Review, 2024: 285–286
*ISSN: 3083-922X*

# Distribution of Rare Earth Elements (REEs) Concentration in Soil Samples from Kapar Industrial Area

**Md Suhaimi Elias**
Waste Technology and Environment Division, Malaysian Nuclear Agency
43000 Kajang, Selangor
mdsuhaimi@nm.gov.my

## Abstract

Studies of Rare earth elements (REEs) pollution in the soil were collected from the Kapar industrial area to determine the concentration and distribution in that area. The average concentration of REEs for Tb, Dy, Yb and Lu in the soil of the Kapar industrial area exceeded the average concentration in the upper continental crust (UCC).

**Keywords:** Rare earth element, soil, Kapar, neutron activation analysis

## 1 Introduction

Nowadays, the release of REEs into the environment has become an issue. In general, sources of REEs pollution in soil mainly originate from two sources, namely anthropogenic activities and geogenic processes. The anthropogenic sources of REE pollution were derived from industrial waste, mining, mineral processing, logging, land clearing, processing and manufacturing of metal. Meanwhile, the geogenic process occurs with weathering of soil and rocks, soil erosion, terrestrial runoff and atmosphere deposition (S. et al., 2020). Studies of REE contamination in the soil of Malaysia are still limited. The objective of this study is to determine the concentration and distribution level of REEs in the soil sample from the Kapar Industrial area. The study of REEs and pollution levels in the soils is vital due to their capability to be uptake by plants, vegetation and crops. REEs can be transferred through the food chain and could have an adverse effect on human health at high concentrations.

## 2 Methods

### 2.1 Sampling and analysis of soil samples using Neutron Activation Analysis (NAA) technique

Fourteen locations (area A to area R) in the Kapar industrial areas were selected for the sampling of soil samples. The soil samples were collected at 0 – 15 cm depth using an auger and dried at 60°C in an oven, followed by ground using agate mortar. Approximately 0.20 grams of soil samples were weighed and placed into polyethylene vials. The soil samples, standard reference materials and blank were irradiated for six hours at the PUSPATI TRIGA Research Reactor at the Malaysian Nuclear Agency and allowed for a decay process of two to four days, followed by one hour of counting. The counting process of the irradiated soil samples, SRM, and blank was performed using a gamma spectrometer.

### 2.2 Contour Map

The contour maps of REEs concentrations were generated using Surfer software. Kriging interpolations were applied to illustrate the contour map of REEs concentrations in the Kapar Industrial area.

## 3 Results and Discussion

### 3.1 Concentration of REEs in the soil samples industrial area

The Rare earth elements (REEs) concentration and (average) of La, Ce, Nd, Sm, Eu, Tb, Dy, Yb and Lu were ranged from 14.73 - 61.43 (31.08), 30.59 – 132.8 (62.0), 11.71 – 44.02 (23.9), 2.12 – 9.6 (4.48), 0.37 – 1.43 (0.66), 0.03 – 1.57 (0.68), 2.20 – 7.45 (4.11), 1.99 – 4.15 (2.73), 0.28 – 0.81 mg/kg (0.44 mg/kg), respectively Figure 1 and the distribution of RRE in soil of Kapar industrial area was depicted in Figure 2. The average concentrations of Tb, Dy, Yb and Lu were higher than the upper continental crust (UCC) of the respective element (UCC: La=32.2, Ce=65.7, Nd=25.9, Sm=4.7, Eu=0.95, Tb=0.50, Dy=2.9, Yb=1.5 and Lu=0.27mg/kg) (H., 1995). This indicates the additional and accumulation of Tb, Dy, Yb and Lu in the soil of the Kapar industrial area. The sources of Tb, Dy, Yb and Lu likely originated from anthropogenic activities and natural land-based activities (landslides and terrestrial runoff).

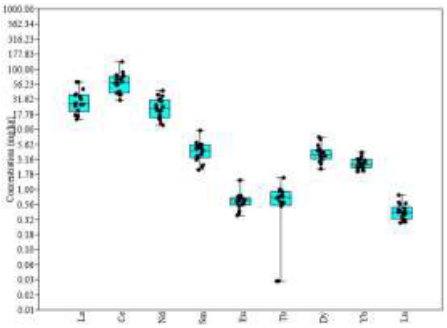


Figure 1: The concentration of REEs in the soil of the Kapar industrial area

### 3.2 Contour map for distribution of REEs concentration in soil

The contour maps of the distribution of REEs concentrations in the soil of the Kapar industrial area are depicted in Figure 3. The groups of REEs (La, Ce, Nd, Sm, Eu, and Dy) and

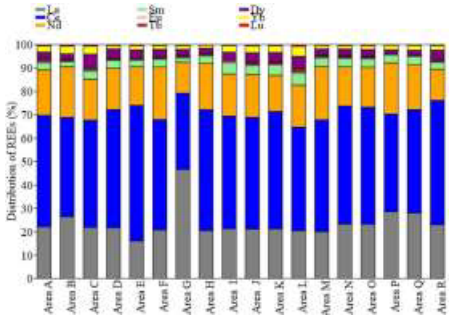



Figure 2: Bar graph for distribution of REE in the soil of Kapar Industrial Area

(Lu and Yb) were shown a similar trend in the contour map. All rare earth elements showed higher concentrations in the N area compared to other areas.

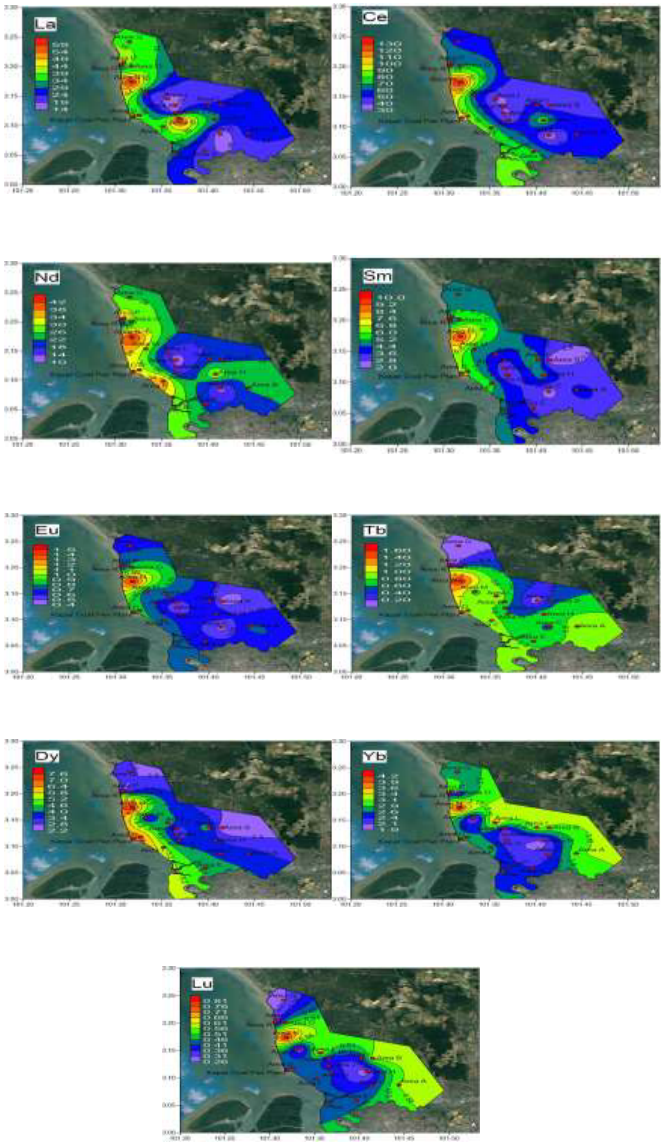



Figure 3: Contour map for distribution of REEs in soil from Kapar Industrial Area

## 4 Conclusions

The REEs such as Eu, La, Sm, Tb, Dy, Ce, Nd, Lu, and Yb showed higher in Area N compared to other areas, which are located food industry, manufacturing, wood, furniture, plastic, and coating industries.

## References

Wedepohl K. H. 1995. The composition of the continental crust. *Geochim. Cosmochim*, Acta 59(7):1217–1232.

Elias M. S., Ibrahim S., Samuding K., Daung J. A. D., Kantasamy N., Rahman S. A., and Hashim A. 2020. Distribution, sources and modified degree of contamination of trace elements in Linggi estuary surface sediments, Malaysia. *Journal of Sustain. Sc. and Management*, 15(4):109–119.

Individual Research Contribution Review, 2024: 287–288
*ISSN: 3083-922X*

# Radon in Water as a Tracer to Identify Connection Between Surface Water and Groundwater in Melaka River Basin

**Mohamad Syahiran Bin Mustaffa**
Waste Technology and Environment Division, Malaysian Nuclear Agency
43000 Kajang, Selangor
syahiran@nm.gov.my

## Abstract

Radon-222 is a natural radioactive tracer increasingly used to study the interactions between surface water and groundwater. This study investigates the hydraulic connectivity between surface water and groundwater in the Melaka River Basin, Malaysia, using radon as a tracer. Groundwater, enriched in radon due to its contact with radon-rich rocks and sediments, can influence radon levels in surface water where discharge occurs. Radon activity was measured at multiple locations along the river during different hydrological conditions to identify discharge zones and quantify groundwater contributions. Supplementary parameters such as water temperature, pH, and conductivity were also recorded. The findings reveal significant spatial and temporal variability in radon concentrations, correlating with potential groundwater discharge zones. This research provides valuable insights for sustainable water resource management and highlights the utility of radon as a tracer in hydrological studies.

**Keywords:** Radon in Water, Radon, Groundwater

## 1 Introduction

Understanding the interaction between surface water and groundwater is crucial for sustainable water resource management, especially in river basins like the Melaka River Basin, where increasing water demand and environmental pressures threaten water availability. Natural tracers such as offer an effective means to investigate these interactions due to their sensitivity to groundwater discharge. Radon is a noble gas with a half-life of approximately 3.8 days, making it suitable for tracing recent groundwater inputs to surface water. This study aims to utilize radon as a tracer to identify areas of hydraulic connectivity in the Melaka River Basin, providing a scientific basis for integrated water resource management.

### 1.1 Study Area

The Melaka River Basin is in the southern region of Peninsular Malaysia, characterized by a tropical climate with distinct wet and dry seasons. The study area covers approximately 270 km$^2$ and is an important water source for domestic, agricultural, and industrial use. The river flows through a mix of urban, agricultural, and forested areas, each potentially influencing water quality and hydrological connectivity.

Geological formations in the basin, consisting of granite and sedimentary rocks, contribute to varying radon levels in groundwater. These geological and hydrological conditions make the Melaka River Basin an ideal site for studying surface water-groundwater interactions as in Figure 2.

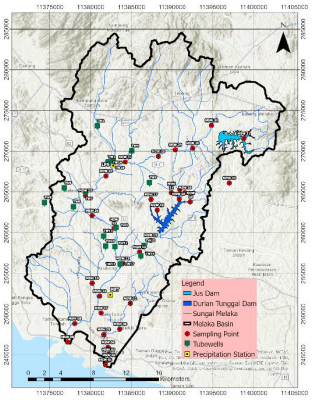



Figure 1: Sampling location for Radon in Water in Melaka River Basin

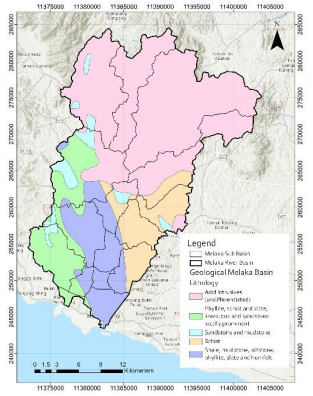



Figure 2: Geological information in Melaka River Basin

## 2 Methods

### 2.1 Sampling and Analysis

Fieldwork was conducted to collect water samples from both groundwater and surface water at selected point along the Melaka River Basin September 2024. Sampling points were chosen based on hydrological features, including tributary confluences, river bends, and visible seepage zones. Sea-

sonal sampling campaigns were performed to capture temporal variability in radon concentrations. Groundwater was sampled from wells and boreholes using submersible pumps. To minimize degassing, water samples were collected directly into radon-tight bottles. Surface water samples were collected from the river and its tributaries using a grab sampling method. Care was taken to avoid disturbance of sediments, which could alter radon concentrations. In situ measurements of temperature, pH, and electrical conductivity were performed at each sampling site to complement the radon data. These parameters help identify groundwater signatures in surface water.

### 2.2 Radon Measurement

Radon activity in water samples was measured using a DURRIDGE RAD7 radon detector. The RAD7 setup onsite involved a RAD H2O accessory for water sample analysis, which extracts radon gas into a closed air loop, with results reported in becquerels per liter (Bq/L).

### 2.3 Data Analysis

A radon mass balance approach was applied to estimate groundwater contributions to the river. This method incorporates radon inputs from groundwater discharge, atmospheric evasion, and decay to quantify the exchange dynamics between surface water and groundwater.

## 3 Results and Discussion

Field measurements of radon activity were conducted at strategic locations along the river, targeting potential groundwater discharge zones such as river bends, tributary confluences, and areas with visible upwelling. Radon concentrations varied significantly across sites, with higher levels observed near known groundwater discharge points. Seasonal analysis showed increased radon activity during the dry season, likely due to reduced dilution from surface runoff.

Supplementary parameters, including temperature, pH, and conductivity, supported the radon data, revealing distinct chemical signatures associated with groundwater inputs. A radon mass balance model was applied to quantify groundwater contributions, revealing that groundwater accounted for a significant portion of the river's flow in certain segments. These findings underscore the importance of groundwater in maintaining river flow, particularly during dry periods. The study also highlights the impact of human activities, such as urbanization and agriculture, on hydrological connectivity and water quality.

## 4 Conclusion

This study demonstrates the effectiveness of radon as a tracer for identifying and quantifying surface water-groundwater interactions in the Melaka River Basin. The spatial and temporal variability in radon concentrations provides critical insights into the dynamics of groundwater discharge. These findings can inform sustainable water management strategies, particularly in regions experiencing increasing water stress. Further research integrating isotopic and geochemical data is recommended to refine the understanding of hydrological processes in the basin.

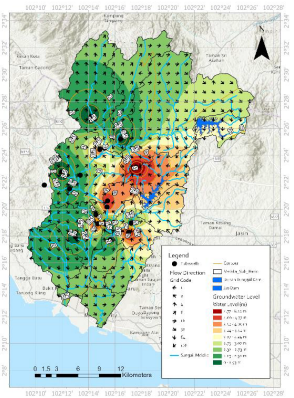


Figure 3: Groundwater Flow Direction in Melaka River Basin

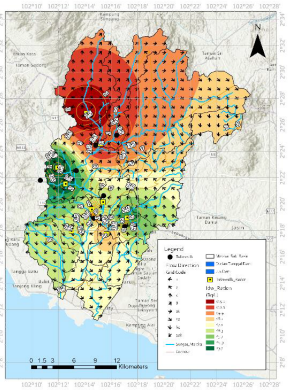


Figure 4: Radon Concentration Across groundwater and Surface Water in Melaka River Basin

## References

W. C. Burnett and H. Dulaiova. 2003. Estimating the dynamics of groundwater input to the coastal zone via continuous radon-222 measurements. *Journal of Environmental Radioactivity*, 69(1-2):21–35.

I. Clark and P. Fritz. 1997. Environmental isotopes in hydrogeology. *CRC Press*.

P. G. Cook and A. L. Herczeg. 2000. Environmental tracers in subsurface hydrology. *Springer*.

N. T. Dimova, W. C. Burnett, K. Speer, and W. Jing. 2013. Application of radon-222 to investigate groundwater discharge into small shallow lakes. *Journal of Hydrology*, 486:112–122.

H. Dulaiova, W. C. Burnett, C. E. Stringer, and P. W. Swarzenski. 2010. Assessment of groundwater discharge into West Neck Bay, New York, via natural tracers. *Continental Shelf Research*, 30(5):552–565.

M. Schubert, A. Paschke, E. Lieberman, and W. C. Burnett. 2012. Assessment of groundwater–surface water interactions using radon and radium isotopes. *Hydrogeology Journal*, 20(4):613–631.

Individual Research Contribution Review, 2024: 289–290
*ISSN: 3083-922X*

# Distribution of Natural Radionuclide Radioactivity in soil near Kuala Selangor Nature Park (KSNP), Selangor.

**Mohd Izwan Bin Abdul Adziz**
Waste Technology and Environment Division, Malaysian Nuclear Agency
43000 Kajang, Selangor
izwan@nm.gov.my

## Abstract

The increase in natural radioactive materials, particularly in soil, needs attention, as it is one of the pathways of exposure to humans and communities. Studies and monitoring of the distribution and determination of the activity of natural radionuclides can be used as guidance and reference, especially during unplanned exposure. Surface soil samples from several identified locations around the Kuala Selangor Nature Park (KSNP) were taken for analysis. Radioactive concentration measurements in soil samples were carried out using a gamma spectrometry counting system equipped with a High Purity Germanium (HPGe) detector. The results showed that the average radioactivity concentrations for $^{238}$U, $^{226}$Ra, $^{228}$Ra, $^{232}$Th and $^{40}$K were 24.64 Bqkg$^{-1}$, 32.18 Bqkg$^{-1}$, 23.85 Bqkg$^{-1}$, 26.70 Bqkg$^{-1}$, and 30.20 Bqkg$^{-1}$, respectively. The values of radioactivity concentrations of these radionuclides were found to be low or equivalent to values reported in previous studies.

**Keywords:** Gamma Spectrometry, Soil, Natural Radioactive Material, HPGe detector.

## 1 Introduction

In Malaysia, data on the activity, concentration, and distribution of Naturally Occurring Radioactive Materials (NORM) is limited. There is a particular need for more detailed information on terrestrial radionuclide concentrations and the development of databases for analysing radiological and health risks. Scientific research on the potential health and environmental impacts of these materials is critical for supporting government decisions on future development plans. This study seeks to evaluate the levels of NORM radioactivity in soil and sediment samples collected from various locations within the study area. The results will provide valuable baseline data on terrestrial radioactivity in Malaysia, which can serve as a reference for environmental monitoring. Additionally, this information will help in identifying and addressing potential contamination issues in the future, particularly in sensitive areas such as nature parks and conservation zones.

## 2 Methods

The sampling site for this study is located in the Kuala Selangor Nature Park (KSNP), Selangor, and its surrounding areas. This location was selected due to the wide range of activities occurring within its watershed. These activities include small and large scale agricultural practices, mangrove ecosystem management, tourism, and river estuaries connected to densely populated areas. A total of 12 sampling stations were strategically identified to represent the various environments within the study area. The locations of these stations are illustrated in Figure 1. Each sample weighed approximately 1–2 kg and was carefully packed in polyethylene bags for transport to the laboratory, where they underwent processing and analyze using a calibrated HPGe Gamma Spectrometry.




Figure 1: Study area map indicating the positions of 12 sampling station around KSNP

## 3 Results

The analysis revealed that the average radioactivity concentrations of $^{238}$U, $^{226}$Ra, $^{228}$Ra, $^{232}$Th and $^{40}$K were 24.64 Bqkg$^{-1}$, 32.18 Bqkg$^{-1}$, 23.85 Bqkg$^{-1}$, 26.70 Bqkg$^{-1}$, and 30.20 Bqkg$^{-1}$, respectively.

These values were found to be low or comparable to those reported in previous studies.

Table 1: Comparison of average specific radionuclides activity in the study are with other location in Malaysia

| **Sample** | **Activity of specific radionuclides (Bqkg$^{-1}$)** | | | | | **Reference** |
|---|---|---|---|---|---|---|
| | $^{238}$**U** | $^{226}$**Ra** | $^{228}$**Ra** | $^{232}$**Th** | $^{40}$**K** | |
| KSNP, Selangor | 24.64 | 32.18 | 23.85 | 26.70 | 30.20 | This study |
| Sembrong, Johor | 21 | 24 | 27 | 28 | 24 | (Abdul Adziz et al., 2024) |
| Repository Facility Bukit Kledang, Perak | - | 21 | - | 33 | 21 | (Abdul Adziz and Khoo, 2018) |
| Kinta District, Perak | 12–426 | - | - | 246 | - | (Lee et al., 2007) |
| Pulau Pinang | - | 64 - 799 | - | 16 - 667 | - | (Almayahi et al., 2012) |
| Dengkil, Selangor | 31.64 – 449.15 | - | - | 27 - 103 | - | (Yasir et al., 2006) |
| Malaysia | 66 | 67 | - | 82 | 310 | (UNSCEAR, 2000) |

## 4 Discussions

This study shows that the average activity concentrations of $^{238}$U, $^{226}$Ra, $^{228}$Ra and $^{232}$Th were found to be comparable to Malaysia average values. However, the concentration of $^{40}$K was lower (30.2 Bqkg$^{-1}$) than the average for Malaysia (310 Bqkg$^{-1}$). Additionally, the study showed that the average concentrations of $^{226}$Ra and $^{232}$Th were similar to those found in previous research in Peninsular Malaysia, including areas such as Johor (Sembrong) and Perak (Kinta and Bukit Kledang), and were lower than the average values reported in earlier studies for certain regions (Dengkil, Selangor and Pulau Pinang) in Peninsular Malaysia.

## References

M. I. Abdul Adziz and K.S. Khoo. 2018. An assessment of absorbed dose and radiation hazard index from soil around repository facility at Bukit Kledang, Perak, Malaysia. *IOP Conf. Ser.: Mater. Sci. Eng.*, 298:012001.

M. I. Abdul Adziz, J. Sharib, D.F. Ahmad Tugi, and M.T. Ishak. 2024. Study on the distribution of naturally occurring radioactive materials (NORM) in the surrounding areas of water catchment in sembrong, johor. *Malaysia Journal of Analytical Sciences (submitted for review)*.

B.A. Almayahi, A.A. Tajuddin, and M.S. Jaafar. 2012. Radiation hazard indices of soil and water samples in northern malaysian peninsular. *International Journal of Applied Radiation and Isotopes*, 70(11):2652–2660.

Siak Kuan Lee, W. Husin, R. Ahmad Termizi, and H.A. Nursama. 2007. Natural gamma background radiation dose rate and its relationship with geological background in the Kinta district, Perak, Malaysia. *pplied Radiation and Isotopes*, 54:327–333.

UNSCEAR. 2000. Radiation sources and effects of ionizing radiation. *New York: United Nations Scientific Committee on the Effect of Atomic Radiation.*

M. S. Yasir, Majid A.A., M.S.Q. Tap, and M.R.Z. Abidin. 2006. Analisis $^{238}$U, $^{226}$Ra, $^{228}$Ra, $^{232}$Th dan $^{40}$K dalam sampel amang, tanah dan air di dengkil, selangor menggunakan spektometri sinar gama. *Malaysia Journal of Analytical Sciences*, 10(1):35–40.

Individual Research Contribution Review, 2024: 291–292
*ISSN: 3083-922X*

# Application of 2-D geoelectrical resistivity tomography for subsurface geological investigation at Blok 33, Malaysian Nuclear Agency

**Mohd Muzamil Bin Mohd Hashim**
Waste Technology and Environment Division, Malaysian Nuclear Agency
43000 Kajang, Selangor
muzamil@nm.gov.my

## Abstract

A geoelectric resistivity study was carried out at block 33, Malaysian Nuclear Agency. The purpose of this study was to obtain geological subsurface information in the study area. This subsurface information is necessary to find the suitable location for the construction of the borehole disposal concept project. An 800m-long survey line has been stretched from west to east to produce a 2D profile of electrical resistance as deep as 160m. Based on the 2D profile produced, the subsurface geological information of the area has been classified according to three ranges of electrical resistivity values: less than 30 Ωm, between 30 Ωm and 2000 Ωm, and above 2000 Ωm.

**Keywords:** electrical resistivity, borehole disposal

## 1 Introduction

Radioactive waste has been produced as a result of the usage of radioactive materials in industrial, medical, and scientific settings. Safe management and disposal of the many kinds of radioactive waste are required. Therefore, investigation must be done to determine the best location for disposal. Borehole disposal is one of the disposal options. The proposed site should be investigated to learn more about the subsurface condition before a borehole disposal may be built there. Electrical Resistivity Imaging Technique is one of the Geophysical methods that are used in the site characterizations based on electrical resistant of composition of the materials below ground.

## 2 Objectives

The objectives of this project are to map subsurface profiles at the Block 33 and to identify suitable location for borehole construction project.

## 3 Study Location

The project was conducted at Blok 33 of the Malaysian Nuclear Agency. The orientation of the line survey was west-east. The survey's 0m and 800m are situated at Block 11 and Kampung Bahagia, Bangi, respectively.

## 4 General Geology

Generally, the geology of the study area is overlaid by metasedimentary rocks from the Kenny Hill Formation. The original sedimentary rocks have changed slightly to form schist and phyllite. Due to the active tropical weathering process, the residual soil layer is quite thick; Therefore, it is difficult to obtain fresh rock outcrops along the study area. However, in certain areas there are remnants of schistosity and phyllitic textures as well as secondary structures such as fault zones that are still visible. The geological map of the study area is shown in Figure 2.




Figure 1: Location of 800m survey line at Blok 33, Malaysian Nuclear Agency

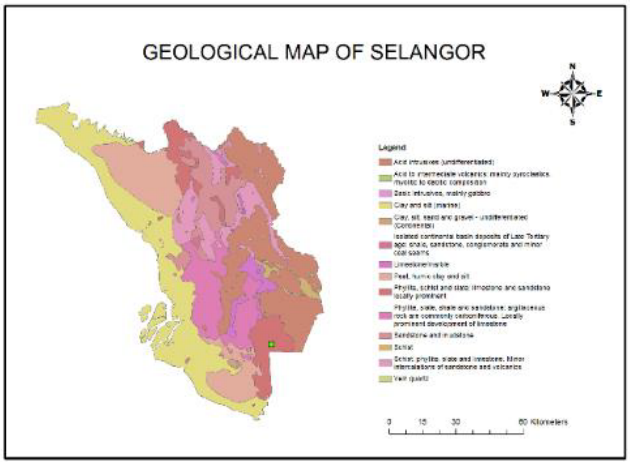



Figure 2: Geological map of Selangor

## 5 Methods

In this survey, field data were obtained using ABEM Terrameter LS2 Schlumberger configuration (Figure 3). This equipment was linked to the 800m multicore cables. 61 electrodes were connected to the cables with a fixed distance of 10m spacing for each electrode (Figure 4). The depth of the 2D profile produced using this electrode configuration is approximately 160m from the surface with a total of 748 data points obtained. The data obtained is pseudo-data and needs to be recalculated by modeling using Res2Dinv software (Loke and Barker, 1996) to obtain a 2-dimensional resistivity profile.

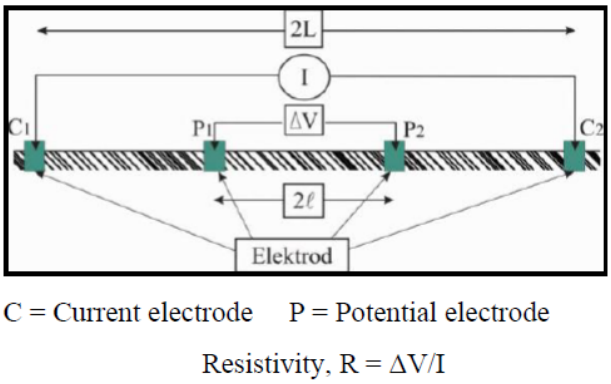



Figure 3: Schlumberger configuration on resistivity survey

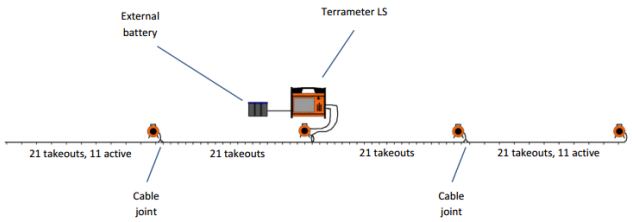



Figure 4: Configuration of equipment on site

## 6 Result

The data obtained was processed and subsequently plotted using RES2DINV software in a two-dimensional form where the x-axis represents the distance on the earth's surface and the y-axis refers to the depth of the subsurface in meter units. The contours shown in various colors represent the value of the resistance of the material under the subsurface. The resilience values obtained can be classified into three main resilience values, namely, less than 30 Ωm, between 30 Ωm and 2000 Ωm and exceeding 2000 Ωm. A resistance value of less than 30 Ωm is believed to be a water-containing layer or a weak zone. Resistance values between 30 Ωm and 2000 Ωm are classified as weathered rocks while those above 2000 Ωm are bedrock / hard rock layer.

## 7 Discussion

According to the 2D electrical resistivity profile, the hard layer zone located at 420 m on the survey line is considered

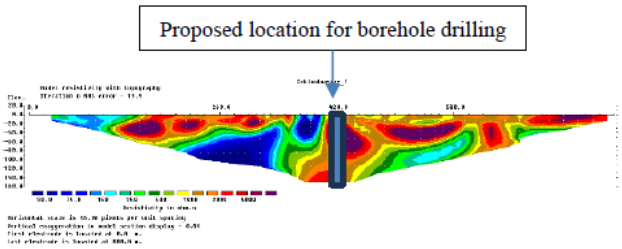



Figure 5: 2D electrical resistivity profile

the most suitable location for borehole construction. It was not recommended to construct the borehole in the water-saturated area and highly weathered zone due to the stability of the rock formation.

## 8 Conclusion

Generally, the subsurface profile at Block 33 was obtained by using the electrical resistivity technique. The subsurface geological information of the area has been classified according to three ranges of electrical resistivity values: less than 30 Ωm, between 30 Ωm and 2000 Ωm, and above 2000 Ωm.

## References

M.H Loke and R.D. Barker. 1996. Rapid least-squares inversion of apparent resistivity pseudosection by quasinewton method. *Geophysical Prospecting*, 44:131–152.

M.H Loke. 1999. Electrical imaging surveys for environmental and engineering studies. http://www.georentals.co.uk/Lokenote.pdf.

Individual Research Contribution Review, 2024: 293–294
*ISSN: 3083-922X*

# Global Radium-226 Management Initiative

**Mohd Zaidi Ibrahim**
Waste Technology and Environment Division, Malaysian Nuclear Agency
43000 Kajang, Selangor
mohd_zaidi@nm.gov.my

## Abstract

Implementing Global Radium-226 Management Initiative project in Malaysia started in 2022 with objective to eliminates a waste liability by send out legacy Ra-226 source to recipient country for reprocessing with zero cost to Malaysia, and at the same time contributes to global healthcare. Implementation is conducting through collaboration Malaysian Nuclear Agency (Nuklear Malaysia) on behalf of government Malaysia and Canadian Nuclear Laboratories (CNL). Material Transfer Agreement between government Malaysia and CNL was finalized on second week of November 2024 and will be submitted to MOSTI together with cabinet paper for cabinet approval purposes.

**Keywords:** Radium-226, global management

## 1 Introduction

Many countries are involved in implementation of Global Ra-226 Management Initiative project. Only Thailand and Slovenia were reported successfully removed their Ra-226 sources. Malaysia joins this initiative program a year after Thailand, and the second country in this region. According to the plan setup by CNL and Nuklear Malaysia, the sources will be sent to Canada in one year period, together with Thailand.

Malaysia only has 1.07 curie (Ci) of Ra-226 sources, much smaller compared to Thailand which have 6.69 Ci of Ra-226 sources. But due to different government policy, Malaysia need much longer time to implement this program compared to Thailand. In Malaysia, Nuklear Malaysia's Director General, even MOSTI's Minister need approval from cabinet before they can sign agreement with foreign entities. It's taken more than a year to reach the cabinet through MOSTI because the agreement needs to go through a thorough review via the ministry's law advisor and attorney general department. With the final version of Material Transfer Agreement getting ready on November 2024, the cabinet approval is supposed to be received before June 2025.

## 2 Methods

This project or activities will be implemented in three (3) phases as follows:

### 2.1 Phase 1 - Contracting

a) Malaysia will be dismantled and sent to CNL a list of dismantled Ra-226 sources in full details. Status: completed.

b) CNL will send draft template nondisclosure for review by Nuklear Malaysia. Status: completed.

c) Nuklear Malaysia will sign NDA for information sharing by CNL. Status: completed.

d) CNL will send draft template contract for review by Nuklear Malaysia and Ministry's Legal Advisor. Status: Completed.

e) Contract will be sent to the Ministry OR Cabinet Approval. Status: on-going.

f) Contract signing between Nuklear Malaysia and CNL.

g) Finalized the list under the project after visiting by CNL and communication with regulatory body. Status: completed.

### 2.2 Phase 2 - Preplanning

a) CNL will send procedures to Nuklear Malaysia.

b) CNL advance team site visit.

c) Updating the statement of ownership

d) CNL apply for import permit.

e) Nuklear Malaysia apply for export permit and declaration participation in Global Ra-226 Management Initiative as undertaking letter will be provided to regulatory body.

### 2.3 Phase 3 – Execution

a) CNL deliver shipping containers to Nuklear Malaysia.

b) Local packaging operations by CNL.

c) Shipping the packages to CNL.

d) CNL and Nuklear Malaysia updating the statement of ownership.

## 3 Results

Currently activities 2.1 (a – d) were completed and the material transfer agreement or contract will be sent together with cabinet paper to the cabinet through ministry's office for approval. Usually, under normal conditions the process for the cabinet approval will take about 6 months.

This project was delayed for more than a year because the review process of the material transfer agreement by the ministry's law advisor and attorney general department takes about 14 months to complete. It involves a thorough reviewing by ministry's law advisor because this agreement involved government of Malaysia and foreign entity, and this type of activities is first time implemented in this country.

IAEA are highly encouraging member countries to take this opportunity to remove their liability to manage radium-226 by joining this project, and at the same time IAEA advises member countries who already joined this project not to delay sending their radium-226 sources to recipients to ensure they have enough radium-226 stock for studies and Ac-225 production for commercial purposes. There are also possibilities that isotope production companies will switch to other raw materials or process when the cost for radium-226 increases, uneconomical to recycle and unavailable.

## 4 Discussion/Conclusions

Global radium-226 management initiative can be considered as pilot project for sending out DSRS to other countries for reprocessing. Beside eliminating a waste liability and contributes to global healthcare, this project also will establish the procedure for export of DSRS to other country for reprocessing. Malaysia have capability in term of technical and enough legal instruments to send out DSRS, but government procedure not allowed government agency to sign any agreement with foreign parties is greatly affect the project timeline. Power delegation from government to the agency will reduce the project timeline significantly.

## References

Richard Dufour and Peter D'Amico. 2023. Turning waste into medicine: International radium 226 turnkey recovery program. canadian national laboratories. *A presentation to Nuklear Malaysia*.

EVT2205305. Technical meeting on the global radium-226 management initiative. *IAEA's Headquarters, Vienna, Austria, from 5 to 9 June 2023*.

Mohd Zaidi Ibrahim. Global radium-226 management initiative. *A presentation to Nuklear Malaysia's Top Management.*

Mohd Zaidi Ibrahim. 2 – 6 December 2024. Current progress on implementation of global radium-226 management initiative project in malaysia. *Invited Presentation: Technical Meeting on the implementation of the Global Radium-226 Management Initiative. IAEA Headquarters, Vienna, Austria.*

Archara Phattanasub. 2 – 6 December 2024. Successfully completed project on ra226 sources removal. thailand. challenges and experience to share. *Invited Presentation: Technical Meeting on the implementation of the Global Radium-226 Management Initiative. IAEA Headquarters, Vienna, Austria.*

Simona Susic. 2 – 6 December 2024. Successfully completed project on ra226 sources removal. slovenia. challenges and experience to share. *Invited Presentation: Technical Meeting on the implementation of the Global Radium-226 Management Initiative. IAEA Headquarters, Vienna, Austria.*

Individual Research Contribution Review, 2024: 295–296
*ISSN: 3083-922X*

# LEXSYG SMART- Thermoluminescence Optically Stimulated Luminescence (TL OSL) Reader At Nuclear Dating Laboratory, Malaysia Nuclear Agency

**Mohd Zuhair bin Mohd Sanusi**
Waste Technology and Environment Division, Malaysian Nuclear Agency
43000 Kajang, Selangor
zuhair@nm.gov.my

## Abstract

LEXSYG SMART is an advance Thermoluminescence Optically Stimulated Luminescence (TL OSL) reader for dating in application of variety of fields. The main advantages of this reader is it can perform luminescence measurement up to 40 sample at once. In addition, this reader is equipped with an irradiation source, which has high activity. The beta sources with an activity 1.85 GBq delivery dose rate range 120 mGy/s is placed on reader. For thermal luminescence stimulation (TL) a plated ceramic contact heater reaching up to 700°C is implement to this reader. Optical stimulation can be achieved by equipped laser diode/LED which has different wavelength as infrared, violet and blue in range of 400-950 nm. Thus, LEXSYG SMART provide on development of dating technique for crystal mineral sample based such as ceramic, rock and sediment.

**Keywords:** Thermoluminescence, Optical Stimulated Luminescence, LEXSYG SMART

## 1 Introduction

Nuclear Dating Laboratory located at Malaysian Nuclear Agency aim to conduct a study on dating mineral based material. This laboratory is located at Block 19 under the supervision of Radiochemistry Environment Group (RAS), Waste Technology and Environment Division (BAS).

This laboratory was established in 1983 via collaboration between Isotope Hydrology Unit with International Atomic Energy Agency (IAEA), Australian Atomic Energy Commission (AAEC) and Pusat Penyelidikan Atom Tun Ismail (PUSPATI). In 2003, BAS took over this laboratory after being advised by the management. Due to several critical problems regarding the equipment, the laboratory cannot fully function in order to provide service. Therefore, further initiative was taken to redevelop this laboratory under Rancangan Malaysia 11 (RMK-11) RP4 2020 (Abdullah et al., 2021). The budget allocation was used to purchased advance thermoluminescence (TL) Optically Stimulated Luminescence (OSL) reader from Freiburg, Germany and the reader was fully installed in November 2021. All basic training was successfully conducted in December 2021 to meet the scope of human capital development under this budget. This paper aims to discuss the technical aspect related to LEXSYG SMART reader.

## 2 The Advance LEXSYG SMART

The advance LEXSYG SMART reader is the combination TL and OSL for luminescence measurement. This combination can provide advantages in the application of dating minerals. This reader system is very sensitive to changes, up to several millimeter scale through depth-luminescence profile (Ageby et al., 2022). Thus, the reader can provide dating age from 100 years up to 200,000 years or even older with precision range 5-10% (Feathers, 2008). In addition, this reader only requires small aliquot sample in preservation of archeology material (Brill and Tamura, 2020). Therefore, the advantages this reader can be fully utilize to perform luminescence measurement in the nuclear dating laboratory.

## 3 Component of LEXSYG SMART System

LEXSYG SMART is developed by Freiburg Instrument. It is used to determine luminescence profile efficiently for a large number of samples. The sample wheel in the reader can run the measurement up to 40 sample simultaneously. This factor considered as an advantage in terms of time saving and efficient.

### 3.1 Radiation Source

LEXSYG SMART reader is capable to execute variety protocol in luminescence measurement. Among the crucial procedure in SAR protocol is the irradiation of sample using ionizing radiation. Therefore, this reader is equipped with a beta radiation source for absorbed dose purpose. The beta source itself has been stored in radiation source module. It is fixed permanently and only control shutter movement for function of irradiation. The main objective of this concept is for accuracy of radiation dose applied to sample. The technical specification of the beta sources is shown in Table 1.

Table 1: Technical aspect on irradiation source

| Technical Aspect | Specification |
|---|---|
| Type of radiation | Beta |
| Radioisotope | Strontium-90 (Sr-90) |
| Activity | 1.85 GBq |
| Form | Sealed (302 capsule) |
| Factory | Eckert & Ziegler Nuclite GmbH |

### 3.2 Thermal stimulation

The reader is equipped with heating ceramic plate for thermal stimulation. The heating ceramic plate on the reader can reach a temperature operational up to 700°C. The advantages of this heating plate is to allow the sample to gain thermal stimulation homogenously, repeatably and definitively. A part of the main concern in stimulation is to ensure the heating from plat necessity to penetrate sample in disc approximately 0.5 mm thickness. However, disc sample is a heat conductor because it is made with aluminum and stainless steel. Thus, its allowed a stable heating to sample in order to assure the stimulation consistently.

### 3.3 Optical stimulation

LEXSYG SMART reader system is equipped with an OSL stimulation for optical stimulation. It consists of several unit of variance wavelength that acquire the usage up to three difference wavelengths as a choice either LED or laser diode. The optical stimulation unit incorporate of a total 15 LED/laser diode position that execution as optical source to implement a high unity of light excitation. All these optical stimulations are presented in Table 2.

Table 2: The optical stimulation including variance of wavelength and type

| Colour | Wavelength (nm) | Type |
|---|---|---|
| Blue | 445/458 | Laser diode/LED |
| Green | 525 | LED |
| Yellow | 590 | LED |
| Infrared | 850 | Laser diode/LED |
| Violet | 405 | Laser diode |

## 4 Conclusions

The LEXSYG SMART reader system is an advance tool for luminescence measurement. This is due to numerous advantages in technical aspect. The major component has higher activity of radiation sources about 1.85 GBq. The equipped of heating plate is capable to generate an operational temperature up to 700°C and variance of wavelength of OSL stimulation ranging 400 to 950 nm in order to accomplish required thermal and optical stimulation. Thus, existence of this advance TL OSL reader is adequate to develop dating technique at Malaysia Nuclear Agency for sample such as ceramic, rock and sediments.

## References

N. Abdullah, N.@Muhammad Mohamed, M.Z. Mohd Sanusi, Salahuddin Muhamad, M.N. Sawon, M.T. Ishak, and M.I.M. Ramli. 2021. Pembangunan aliran sintesis benzena di makmal tentu umur radiokarbon, Agensi Nuklear Malaysia. *Seminar NTC 2021*, 26 – 28 Oktober 2021.

L. Ageby, D. E. Angelucci, D. Brill, F. Carrer, H. Brückner, and N. Klasen. 2022. Dating dry-stone walls with rock surface luminescence: A case study from the Italian Alps. *Journal of Archaeological Science*, 144:105625.

D. Brill and T. Tamura. 2020. Chapter 32 - Optically stimulated luminescence dating of tsunami and storm deposits. In M. Engel, J. Pilarczyk, S. M. May, D. Brill, E. Garrett (Eds.). *Geological Records of Tsunamis and Other Extreme Waves*, pages 705–727.

J. Feathers. 2008. LUMINESCENCE DATING. In D. M. Pearsall (Ed. *Encyclopedia of Archaeology*, pages 1590–1592.

Individual Research Contribution Review, 2024: 297–298
*ISSN: 3083-922X*

# Assessment of Heavy Metal and Toxic Elements in Industrial Zones in Nilai 3

**Muhammad Azfar Azman**
Waste Technology and Environment Division, Malaysian Nuclear Agency
43000 Kajang, Selangor
m_azfar@nm.gov.my

## Abstract

Human activities, especially those near the heavy industries in the Negeri Sembilan, are major contributors to environmental and health issues in populated areas. This study focuses on identifying the presence of actinides, heavy metals, and rare earth elements in soil samples using the Neutron Activation Analysis technique. By analyzing these elements, we aim to understand their impact on the environment and public health.

**Keywords:** Elemental Analysis, Heavy Metals, Neutron Activation Analysis, Environmental Analysis

## 1 Introduction

Negeri Sembilan, located in Malaysia, is experiencing significant environmental and health challenges due to various human activities, including urbanization, industrialization, and transportation. These activities have led to an increase in heavy metal and toxicity levels in the environment. This study focuses on the concentration of heavy and toxic elements, as they pose potential risks to human health. A total of 10 elements will be analyzed in this study, including heavy metals and toxic elements.

## 2 Methods

Location for sampling were determined based on the criteria of industrial area as targeted area, near to industrial area and residential area as control area. Therefore, for the first phase locations are around Nilai 3 have predetermined based on those criteria. Soil samples were collected to understand the possible contamination of elements in the soils. This study used Neutron Activation Technique (NAA) technique and counted using Hyper-Pure Germanium Gamma Spectrometer. The obtained results were then calculated to get concentration of the elements.

### 2.1 Sample Collection

Soil samples were collected throughout 5 multiple area in each Nilai 3 locations to get distribution of elements in the soil using an auger.

### 2.2 Sample Preparation

The collected samples were cleaned and dried using an oven at 65°C until dried before ground into powder using a ball mill. Samples were then sieved using 0.2 mm sieve and were weighted approximately 0.10 g for a soil sample. Each sample was prepared in duplicate to better analytical results. For each batch of irradiation, certified reference materials were co irradiated to get viable results.

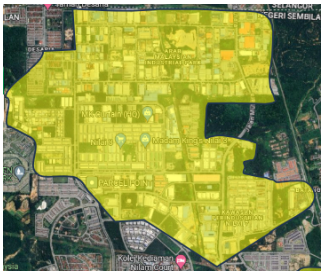


Figure 1: Sampling location throughout Nilai 3

### 2.3 Sample Irradiation

The samples were irradiated using the Pneumatic Transfer System of Triga Mark II Puspati Research Reactor operated at 750 kW with thermal neutron flux of about 2.0 x $10^{12}$ n.cm$^{-2}$.s$^{-1}$. Each polyethylene vial was inserted into each rabbit tube. The rabbit tube was then inserted into the PTS chamber before setting it off to the reactor. The travel time from the chamber to the PTS port in the reactor is 3 seconds. Each sample was irradiated for 30 seconds and was cooled down for 10 minutes behind lead brick inside the fume hood. To determine long lived radionuclide another batch of samples were irradiated for 5 hours through Rotary Rack (RR) After irradiation, samples were cooled down for 3-4 days in a lead storage container before counted.

### 2.4 Sample Counting

For short lived radionuclides, the samples were then counted using the ORTEC HPGe detector of a high-resolution gamma spectrometry system for 5 minutes using GammaVision software. The detector has a relative efficiency of 20% with a resolution of 2.0 keV at 1332 keV. The ADC system connected to the PC analyzed the output signal from the detector. For long lived radionuclide, after cooling of 3-4 days, the samples were counted using ORTEC HPGe detector for 1 hour. Samples will then later counted after 21 days since irradiation to determine long lived radionuclides.

### 2.5 Sample Analysis

Equation 1 shows the mathematical calculation of elemental concentrations in the sediment sample (Joel et al., 2018).

$$C_{sample} = \frac{A_{sample}}{A_{standard}} \times \frac{W_{sample}}{W_{standard}} \times C_{standrad} \quad (1)$$

where $C_{sample}$ is the concentration of element in sample (mg/kg), $A_{sample}$ is the net area count of an element in sediment sample, $A_{standard}$ is the net area count of an element in a standard, $W_{standard}$ is the standard weight, $W_{sample}$ is the sediment sample weight and $C_{standard}$ is the concentration of an element in standard (mg/kg).

## 3 Results and Discussion

In the study, Table 1 show the concentration of Toxic and Heavy Metals element for Nilai 3 area.

Table 1: Toxic Elements

| Location | Toxic Elements | | |
|---|---|---|---|
| | As | Br | Sb |
| N1S01 | 10.5 ± 0.5 | 4.1 ± 0.9 | 8.7 ± 1.1 |

Table 2: Heavy Elements

| Location | Heavy Metal Elements | | | | |
|---|---|---|---|---|---|
| | Ba | Co | Cr | V | Zn |
| N1S01 | 373 ± 10 | 1.64 ± 0.09 | 64.6 ± 1.2 | 183 ± 1 | 24 ± 2 |

From Table 1 and 2, the enrichment factor (EF) and Geo-accumulative Index ($I_{Geo}$) could be determine to understand the correlation between concentration of the elements and its impact to the environmnet. The Enrichment Factor (EF) is a useful indicator for distinguishing between natural and anthropogenic contributions to element concentrations in the soil. Table 2 presents EF values for various toxic elements, providing insights into the extent of anthropogenic influence (Reimann and Caritat, 2020).

- Be the secretary for the management of the kenaf tree plantation in Tambunan, Sabah
- EF < 2 : Minimal enrichment (natural origin)
- 2 ≤ EF < 5 : Moderate enrichment (minor anthropogenic influence)
- 5 ≤ EF < 20 : Significant enrichment (considerable anthropogenic contributions)
- 20 ≤ EF < 40 : Very high enrichment (strong anthropogenic influence)
- EF ≥ 40 : Extremely high enrichment (predominantly anthropogenic sources)

From Table 3, there is extremely high enrichment of Sb which are most likely contributed from the electronic and battery industries as well as plastics industries which is the majority of the industry in Nilai 3. There are some moderate enrichment of As, Br and V in the area which might also contributed from the plastics industries.

Table 3: Enrichment Factor (EF)

| Location | As | Br | Sb | Ba | Co | Cr | V | Zn |
|---|---|---|---|---|---|---|---|---|
| N1S01 | 6.0 | 7.1 | 59.4 | 1.6 | 0.3 | 1.9 | 5.2 | 1.0 |

Table 4: Geo-accumulative Index ($I_{Geo}$)

| Location | As | Br | Sb | Ba | Co | Cr | V | Zn |
|---|---|---|---|---|---|---|---|---|
| N1S01 | 0.5 | 0.8 | 3.9 | -1.3 | -4.0 | -1.1 | -0.1 | 0.1 |

The Geo-accumulation Index ($I_{Geo}$) is a critical tool for assessing the degree of soil contamination by comparing current element concentrations to pre-industrial levels. The $I_{Geo}$ values provided in Table 3 offer insights into the pollution status of different elements across the sampling sites (Müller, 1969).

- $I_{Geo} \leq 0$: Practically uncontaminated
- $0 < I_{Geo} \leq 1$: Uncontaminated to moderately contaminated
- $1 < I_{Geo} \leq 2$: Moderately contaminated
- $2 < I_{Geo} \leq 3$: Moderately to heavily contaminated
- $3 < I_{Geo} \leq 4$: Heavily contaminated
- $4 < I_{Geo} \leq 5$: Heavily to extremely contaminated
- $I_{Geo} > 5$: Extremely contaminated

From Table 4, it is determined that Sb are heavily contaminating the soil in the Nilai 3 area from the contribution of the industries.

## 4 Conclusions

From the study done in Nilai 3, it is known that Sb is extremely high in the area which could be contributed from the industries in it, thus more research need to be done by collection flora samples to know the soil-plant uptake to understand thethe impact of the contamination to public health. More locations need to be done to know the concentration of the toxic and heavy metals elements near the area.

## References

E. S. Joel, O. Maxwell, O. O. Adewoyin, C. O. Ehi-Eromosele, C. O. Embong, and F. Oyawoye. 2018. Assessment of natural radioactivity in various commercial tiles used for building purposes in Nigeria. *MethodsX 5*, 8 – 19.https://doi.org/10.1016/J.MEX.2017.12.002.

G. Müller. 1969. Index of geoaccumulation in sediments of the rhine river. *Geojournal*, 2(3):108–118.

C. Reimann and P. d. Caritat. 2020. Intrinsic Flaws of Element Enrichment Factors (EFs) in Environmental Geochemistry. *Environmental Science Technology*, 34(24):508.

Individual Research Contribution Review, 2024: 299–300
*ISSN: 3083-922X*

# Level of Cadmium (Cd) in Clam Tissues from Selected Coastal Areas in Peninsular Malaysia

**Munirah binti Abdul Zali**
Waste Technology and Environment Division, Malaysian Nuclear Agency
43000 Kajang, Selangor
munirahzali@nm.gov.my

## Abstract

This study investigates the cadmium (Cd) levels in clam tissues collected from four coastal areas in Peninsular Malaysia: Melaka, Pahang, Johor, and Selangor. Clams, as filter feeders, are susceptible to accumulating heavy metals, making them crucial indicators of aquatic contamination and potential health risks. The clam samples were microwave-digested and quantified using inductively coupled plasma-mass spectrometry (ICP-MS). Results revealed the highest Cd concentration in clams from Melaka and the lowest in Johor, attributed to differences in industrial activities and urbanization levels near the sampling sites. All Cd concentrations were below the Malaysian Food Act 1985's permissible limit of 2 mg kg-1, indicating the safety of the sampled clams for consumption. Further research is recommended to assess bioaccumulation potential across trophic levels.

**Keywords:** clam, cadmium, pollution, food safety

## 1 Introduction

Cadmium (Cd) is a toxic heavy metal that poses significant risks to human health and the environment due to its widespread presence in industrial activities and pollution. It has been well-established that cadmium can accumulate in various organisms, including marine species, through the food chain, leading to potential health hazards for consumers (Hossen et al., 2015). Clams, being filter feeders, are particularly susceptible to accumulating cadmium in their tissues from contaminated aquatic environments. Monitoring the level of Cd in clam tissue samples is crucial for assessing the extent of contamination and potential human health risks associated with consuming contaminated seafood.

Numerous studies have highlighted the bioaccumulation of Cd in clam tissues and its implications for public health. For example, research by Nour et al. (2020) demonstrated elevated levels of Cd in clam tissues collected from polluted coastal areas, highlighting the need for ongoing monitoring and regulatory measures to protect human health. Furthermore, studies by Hossen et al. (2015) and Gagné et al. (2022) have shown that the concentration of Cd in clam tissues can vary based on environmental factors and locations, emphasizing the importance of targeted sampling and analysis to understand the extent of contamination in different regions. Evaluating the level of Cd in clam tissue samples is essential for assessing the potential risks associated with consuming contaminated seafood and informing regulatory actions to mitigate these risks. This study aims to determine the Cd concentration in the clam tissue samples and compare its level with the Malaysian Food Act 1985.



Figure 1: Common clam found in Peninsular Malaysia

## 2 Methods

### 2.1 Sample Pretreatment and Digestion

In this study, the clam samples were collected from Melaka (Kuala Sungai Baru), Pahang (Kuantan), Johor (Pontian) and Selangor (Kuala Selangor) states (Figure 2) in between July to November 2023. The clam samples were stored in plastic zip locked bag and kept chill during transportation, In the laboratory, the clam samples were kept frozen prior to extraction and analysis.




Figure 2: Selected sampling locations in Peninsular Malaysia

The soft edible tissues of the clams were dissected and pooled for 20 samples. The soft tissues were ground and homogenized using stainless steel grinder. The soft tissues were digested according to the Association of Analytical Collaboration (AOAC) Official Method 2015.01 Heavy Metals in Food. In brief, 1.0 g of wet-weight soft clam tissues (n=20) were added with 10 ml of concentrated nitric acid and allowed to stand for 10 minutes. The tissue samples were digested using microwave digester (MARS 6, USA). The digestion program was set at 200°C for 15 minutes ramping followed by 15 minutes holding times. The pressure was set at 800 psi and the power was between 900 - 1050 W during the digestion. The digested tissue samples were allowed to cool and mark up to 25 ml using ultrapure water.

In every batch of digestion procedure, two method blanks and standard reference materials (SRMs) were digested for method performance analysis. The SRM used in this study are trace elements and methylmercury in mussel tissue (National Institute of Standard and Technology (NIST) SRM 2976), Dogfish liver certified reference material (CRM) for trace metals and other constituents (National Research Council Canada (NRCC) DOLT-5) and oyster tissue (NIST SRM 1566b). The limit of detection (LOD) was determined through the analysis of 23 method blanks and calculated as 3 times the standard deviation (SD) of the method blanks results.

### 2.2 Quantification of Cd using ICP-MS

The quantification of Cd in the clam samples was performed using inductively coupled plasma-mass spectrometer (ICP-MS) and iridium as internal standard. Three calibration points consisted of 0.010 mg $L^{-}1$, 0.025 mg $L^{-}1$, and 0.050 mg $L^{-}1$ were established with correlation coefficient (R2) of more than 0.995. Calibration verification (quality control standards) was analyzed for every ten samples and the values ranged between 90 and 110%. The concentration of samples was reported in mg $kg^{-}1$ (wet weight) unit.

## 3 Results and Discussion

From the quantification result, the LOD of Cd in clam samples is 0.001 mg $kg^{-}1$ (wet weight). The digestion and quantification recovery percentage (%) of the three SRMs in this study was between 83% and 121%. Table 1 displays the concentration of Cd (wet weight) in four different coastal areas in Peninsular Malaysia. The highest Cd level in clam samples was identified from Kuala Sungai Baru, Melaka. On the other hand, the clams from Pontian, Johor were the lowest level of Cd compared to clams from Melaka, Pahang and Selangor.

The spatial difference of Cd level in all coastal areas may due to the land used activities. Melaka coastal area was nearby petroleum industries and industrial activities. Meanwhile, Pontian, Johor was among the less urbanized coastal areas in Peninsular Malaysia (Sohaili et al., 2014).

Based on the Malaysian Food Act 1985, the maximum permitted level for Cd in mollusc samples (i.e. clam) is 2 mg $kg^{-}1$. Based on this study, the Cd level in all clam samples from four sampling locations was lower than the maximum permitted level.

Table 1: Level of Cd wet weight (mg $kg^{-}1$) in the clam samples

| **Sampling location** | **Melaka (n=20)** | **Pahang (n=20)** | **Johor (n=20)** | **Selangor (n=20)** |
|---|---|---|---|---|
| Clam Tissue wet weight (mg $kg^{-}1$) | 0.35 ± 0.02 | 0.33 ± 0.14 | 0.19 ± 0.01 | 0.22 ± 0.02 |

## 4 Conclusions

In the present study, the Cd level was varied between sampling locations due to land-used activities. Based on the Malaysian Food Act 1985, the clams in the sampling locations were safe for consumption. There is also a need to study the potential bioaccumulation of Cd in the clam samples and across trophic levels.

## References

F. Gagné, C. André, S. Turgeon, and N. Ménard. 2022. Spatio-temporal variation of elemental contamination and health of Mya arenaria clam in the Saguenay–St. Lawrence Marine Park. *Applied Sciences*, 12(3):1106.

M. F. Hossen, S. Hamdan, and M. R. Rahman. 2015. Review on the risk assessment of heavy metals in malaysian clams. *The Scientific World Journal*, 1:905497.

H. E. S. Nour. 2020. Distribution and accumulation ability of heavy metals in bivalve shells and associated sediment from Red Sea coast. *Egypt. Environmental Monitoring and Assessment*, 192(6):353.

J. Sohaili, N. A. Kasan, Z. Ibrahim, and N Hashim. 2014. The integrated biological indicator as a tool for detection of river pollution. in Brunei. *International Conference on Engineering and Technology*, pages 1–9.

Individual Research Contribution Review, 2024: 301–302
*ISSN: 3083-922X*

# Total and Isotope Carbon in Indigenous Rice from Kota Belud, Sabah

**Nazaratul Ashifa Abdullah Salim**
Waste Technology and Environment Division, Malaysian Nuclear Agency
43000 Kajang, Selangor
shifa@nm.gov.my

## Abstract

This study investigates the total carbon and stable carbon isotopic composition ($\delta^{13}$C) in indigenous rice from Kota Belud, Sabah. The carbon analysis and isotopic ratio mass spectrometry were applied in assessing the variations across different rice varieties. The results show significant differences ($p<0.05$) in carbon content and $\delta^{13}$C, reflecting the impact of local environmental factors and traditional farming practices. These findings contribute to understanding the carbon dynamics in rice cultivation and offer insights into crop sustainability in the face of climate change.

**Keywords:** carbon, isotope, rice

## 1 Introduction

Rice is a staple food globally, and understanding its carbon composition is critical for addressing food security and environmental challenges. Indigenous rice varieties, particularly those cultivated in traditional systems, often exhibit unique biochemical and isotopic signatures influenced by soil type, water management, and microclimatic conditions (Smith et al., 2020). Kota Belud, Sabah, is known for its indigenous rice varieties, which are cultivated using traditional methods that emphasize sustainability.

Stable carbon isotopes ($\delta^{13}$C) have been widely used as markers to study plant physiology and environmental stress, as they reflect photosynthetic pathways and water-use efficiency (Farquhar et al., 1989). Thus, this study aims to elucidate the total carbon content and $\delta^{13}$C profiles in indigenous rice varieties from Kota Belud, providing baseline data for future agronomic and ecological research.

## 2 Methods

Approximately, 1 kg of rice from four different varieties were sampled. The rice namely;

i. beras wangi keladi putih (BWKP),

ii. beras wangi keladi merah (BWKM),

iii. beras wangi keladi hitam (BWKH) and

iv. beras keladi putih (BKP)

### 2.1 CHNS Analyzer

Total carbon of samples was determined by an elemental combustion analyzer (EA2400, Perkin Elmer, USA). Dried samples of 3mg and reference material (SRM 1537a Tomato Leaves) were weighed into tin capsules.

### 2.2 Isotope Ratio Mass Spectrometry (IRMS)

The isotope ratio analysis was performed in an IRMS (Isoprime, Elementar, UK) coupled to an elemental analyzer for carbon. Approximately 1mg of sample was weighted onto tin capsule. Samples were analyzed in triplicate. Isotopic composition was expressed in relative units (‰) or per mil). The international standard for carbon is V-PDB (Vienna Pee Dee Belemnite).

### 2.3 Data Analysis and Chemometric

The mean and standard deviation of total carbon and stable isotope were calculated. Differences in varieties were analyzed by one-way analysis of variance (ANOVA) at a significant level of $p<0.05$. The univariate analysis was performed using the freeware PAST4 (ver. 4.17, Hammer et al., 2001).

## 3 Results

The indigenous rice varieties showed total carbon content ranging between 39.02% and 40.40%. Table 1 shows a significant different ($p < 0.05$) among the varieties. BWKP is the highest in carbon content. This variation may contribute from soil organic carbon levels and the organic farming practices used by local farmers.

Table 1: The compositions of total and isotopic carbon in indigenous rice varieties

| Variety | Total C (%) | $\delta^{13}$C (‰) |
|---|---|---|
| BWKP | $40.17 \pm 0.24^{a}$ | $-27.67 \pm 0.10^{a}$ |
| BWKM | $40.12 \pm 0.10^{a}$ | $-28.59 \pm 0.16^{b}$ |
| BWKH | $40.09 \pm 0.25^{a}$ | $-27.50 \pm 0.07^{a}$ |
| BKP | $39.52 \pm 0.48^{b}$ | $-27.99 \pm 0.08^{b}$ |
| *p*-value | 0.01 | <0.0001 |

Note: BWKP- beras wangi keladi putih, BWKM-beras wangi keladi merah, BWKH- beras wangi keladi hitam, BKP- beras keladi putih Different letters in the same row represent the significant difference between at $p<0.05$.

The $\delta^{13}$C values ranged from -28.75‰ to -27.39‰, indicative of variability in photosynthetic efficiency and envi-

ronmental conditions. Isotopic carbon showed a significant different ($p < 0.05$) among rice varieties. Certain varieties exhibited lower $\delta^{13}C$ values, suggesting higher water-use efficiency under drought-prone conditions.

However, there was no significant correlation ($p > 0.05$) observed between total carbon content and $\delta^{13}C$ values. This is due to $\delta^{13}C$ , which largely reflects isotopic fractionation processes and is not necessarily directly related to total carbon content.

## 4 Discussion and Conclusions

The results highlight the intricate relationship between environmental factors and carbon dynamics in rice plants. The observed $\delta^{13}C$ variability aligns with findings from other studies on C3 crops under variable water conditions (Cernusak et al., 2013). The indigenous rice varieties with higher carbon content and lower $\delta^{13}C$ values demonstrate an adaptive strategy to mitigate water stress, which could be attributed to traditional water management practices in Kota Belud.

Additionally, these findings provide insights into carbon sequestration potential in paddy fields, contributing to sustainable agricultural practices. Previous research emphasizes the importance of such studies for understanding the role of traditional farming systems in mitigating climate change impacts (Gupta and Seth, 2021).

This study provides valuable data on total carbon and $\delta^{13}C$ in indigenous rice varieties from Kota Belud, Sabah. The significant variation in carbon content and isotopic composition underscores the role of traditional farming practices and environmental factors in shaping these biochemical traits. Future research should focus on extending this analysis to other regions and exploring the implications for rice productivity and resilience under changing climate scenarios.

## References

L. A. Cernusak, K. Winter, and B. L. Turner. 2013. Plant $\delta^{13}C$ - $\delta^{15}N$: Nutritional ecology in a changing world. *Trends in Ecology and Evolution*, 28(3):121–131.

G. D. Farquhar, M. H. O'Leary, and J. A. Berry. 1989. On the relationship between carbon isotope discrimination and the intercellular carbon dioxide concentration in leaves. *Australian Journal of Plant Physiology*, 9(2):121–137.

R. Gupta and A. Seth. 2021. Role of indigenous farming practices in carbon sequestration: A review. *Environmental Sustainability*, 4(1):22–31.

P. Smith, J. F. Soussana, and R. Lal. 2020. The role of soils in addressing climate change. *Nature Sustainability*, 3(11):967–977.

Individual Research Contribution Review, 2024: 303–304
*ISSN: 3083-922X*

# Spatial Distribution of Heavy Metal and Land Use Assessment Using Fallout Radionuclides (FRNs) Technique

**Nurrul Assyikeen binti Md. Jaffary**
Waste Technology and Environment Division, Malaysian Nuclear Agency
43000 Kajang, Selangor
assyikeen@nm.gov.my

## Abstract

This study examines heavy metals and radionuclides in the Kuala Selangor mangrove ecosystem using Fallout Radionuclides (FRNs) as natural tracers. It assesses the impact of human activities on sediment quality and pollution. Sediment cores were collected, and radionuclide activity ($^{210}$Pb, $^{226}$Ra, and $^{210}$Pb$_{ex}$) was measured to estimate sedimentation rates. Heavy metal concentrations (e.g., Mg. Al, Mn, Cr, Fe. Zn) were analyzed via Neutron Activation Analysis (NAA), while geoaccumulation indices, $I_{geo}$ quantified pollution levels. Results emphasize the critical role of mangroves in retaining contaminants and the need for targeted pollution management.

**Keywords:** Radionuclides, heavy metals, geoaccumulation index, mangrove ecosystem, sediment quality

## 1 Introduction

Mangrove ecosystems protect coastlines but are increasingly affected by human activities, including land-based pollution (Jusoff, 2013). Heavy metals are a major concern due to their persistence, bioaccumulation, and toxicity (Mohd Ilman Che et al., 2020). The Kuala Selangor mangroves, important for biodiversity and coastal defense, face similar threats. This study examines heavy metal distribution using fallout radionuclides (FRNs) to understand pollution patterns and support sustainable management.

## 2 Methods

This study combined field sampling, laboratory analysis, and spatial data integration to assess heavy metal and radionuclide levels in the Kuala Selangor mangroves. Sediment cores (20–80 cm depth) were collected from multiple sites. Key radionuclides ($^{210}$Pb, $^{226}$Ra, and $^{210}$Pb$_{ex}$) were analyzed to estimate sedimentation rates and sediment mixing. Heavy metal concentrations (Mg, Al, Mn, Cr, Fe, and Zn) were determined *via* Neutron Activation Analysis (NAA) followed by gamma spectrometry measurement.

Geoaccumulation indices ($I_{geo}$) were calculated to evaluate pollution levels and sediment quality, helping determine human contributions to contamination (Mohd Ilman Che et al., 2020). The $I_{geo}$ formula follows (Müller, 1979):

$$I_{geo} = log_2(\frac{C_n}{1.5B_n}) \quad (1)$$

$C_n$ is the measured element concentration, and $B_n$ is the background concentration. The coefficient 1.5 accounts for geological variations in the background.

## 3 Results and Discussion

The study found that $^{210}$Pb$_{ex}$ distribution in sediment layers indicated significant mixing, which could impact sedimentation rate accuracy. Table 1 shows key parameters and their spatial trends. Heavy metal contamination varied, with higher levels near aquaculture areas and estuaries due to human activities.

The geoaccumulation indices, $I_{geo}$ showed varying heavy metal contamination, ranging from unpolluted to strongly polluted. As pollution increases, identifying a precise background value ($B_n$) becomes challenging. In this study, the lowest element concentrations were used as the background value. Sediment quality was classified using Müller's categories (Table 2), and Table 3 compares $I_{geo}$value between aquaculture and mangrove areas.

## 4 Conclusion

This study shows that mangroves effectively retain metals like Mn, highlighting their role in mitigating pollution. It offers insights into the distribution and behavior of heavy metals and radionuclides in the Kuala Selangor mangrove ecosystem. Identifying pollution hotspots and assessing sediment quality emphasize the need for targeted monitoring and mitigation. These findings lay the groundwork for future research to strengthen mangrove resilience against pollution and climate change.

## References

K Jusoff. 2013. Malaysian mangrove forests and their significance to the coastal marine environment. *Polish Journal of Environmental Studies*, 22(4):979 – 1005.

A. Mohd Ilman Che, S.R.M.S. Amir, and H Hazzeman. 2020. Geoaccumulation index and enrichment factor of arsenic in surface sediment of Bukit Merah Reservoir, Malaysia. *https://. Tropical Life Sciences Research*, 31(3):109 – 125.

G. Müller. 1979. Schwermetalle in den sediments des rheinsveran-derungen seitt 1971. *Umschan*, 79:778–783.

Table 1: Key parameters and distribution trends of heavy metal and land use

| **Parameter** | **Aquaculture area** (3°20.137"N, 101°14.149"E) | **Mangrove Covered Area** (3°20.137"N, 101°14.149"E) | **Mangrove flat area** (3°19'49.80"N, 101°13'43.40"E) | **Estuary area** (3°20'20.60"N, 101°13'18.87"E) | **Boating area** (3°21'11.82"N, 101°14'29.10"E) | **Key Observations** |
|---|---|---|---|---|---|---|
| Pb-210$_{ex}$ (Bq/kg) | 24.08-45.11 (Mean: 34.5) | 18.17-34.56 (Mean: 25.3) | 16.23-28.39 (Mean: 23.2) | 19.27-33.95 (Mean: 26.1) | 1.32-53.47 (Mean: 27.5) | Higher input indicates receives higher sediments |
| Ra-226 (Bq/kg) | 31.96-65.76 (Mean:51.9) | 30.67-47.70 (Mean:40.4) | 27.56-44.13 (Mean: 34.7) | 28.91-40.14 (Mean: 33.8) | 0.68-36.50 (Mean: 29.1) | Reflecting natural background levels |
| Mg (ppm) | 14287.6-20744.96 (Mean: 17457.0) | 11657.2-41610.4 (Mean: 16409.6) | 11354.7-19579.5 (Mean: 14727.4) | | | Indicates anthropogenic input from land use |
| Al (ppm) | 113044.1-137645.2 (Mean: 128373.4) | 45765.9-251705.5 (Mean: 99514.0) | 62868.2-107344.3 (Mean: 83749.2) | | | Elevated near aquaculture zones |
| Mn (ppm) | 221.83-764.51 (Mean: 290.5) | 172.1-984.5 (Mean: 387.8) | | 62.7-120.7 (Mean: 78.8) | (Mean: 75.6) | Higher in mangroves, indicating retention |
| Cr (ppm) | 65.5-77.05 (Mean: 70.1) | 59.9-134.2 (Mean: 86.1) | 44.2-99.7 (Mean: 79.0) | 38.9-143.7 (Mean: 85.2) | (Mean:94.5) | Higher in mangroves, indicating retention |
| Fe (ppm) | 31525.33-44534.09 (Mean: 35718.3) | 21875.2- 33353.6 (Mean: 28777.9) | 18085.8- 32384.2 (Mean: 26774.7) | 19136.3-37285.6 (Mean: 29613.8) | (Mean: 34702.5) | Indicates anthropogenic input from land use |
| Zn (ppm) | 64.46-153.37 (Mean: 127.1) | 67.9-112.4 (Mean: 93.7) | 68.1-118.1 (Mean: 92.5) | 69.2-136.3 (Mean: 105.6) | (Mean:112.8) | Indicates anthropogenic input from land use |
| Silt and Clay (%) | (Mean:98.3) | (Mean:95.2) | | | | Influences radionuclide and metal retention |

Table 2: Sediment Quality Classification Based on $I_{geo}$

| $I_{geo}$ | **value Class** | **Designation of sediment quality** |
|---|---|---|
| $I_{Geo} \leq 0$ | 0 | Unpolluted |
| $0 < I_{Geo} \leq 1$ | 1 | Unpolluted to moderately polluted |
| $1 < I_{Geo} \leq 2$ | 2 | Moderately polluted |
| $2 < I_{Geo} \leq 3$ | 3 | Moderately to strongly polluted |
| $3 < I_{Geo} \leq 4$ | 4 | Strongly polluted |
| $4 < I_{Geo} \leq 5$ | 5 | Strongly to extremely polluted |
| $I_{Geo} > 5$ | 6 | Extremely polluted |

Table 3: $I_{geo}$ Values and Müller Classification

| **Element** | $I_{geo}$ | **Class** | **Sediment quality** |
|---|---|---|---|
| **Location:** Aquaculture area | | | |
| Mg | 0.036 | 1 | Unpolluted-moderately polluted |
| Al | 0.90 | 1 | Unpolluted-moderately polluted |
| Mn | 1.63 | 2 | Moderately polluted |
| Cr | 0.079 | 1 | Unpolluted-moderately polluted |
| Fe | 0.40 | 1 | Unpolluted-moderately polluted |
| Zn | 0.40 | 1 | Unpolluted-moderately polluted |
| **Location:** Mangrove-covered area | | | |
| Mg | -0.054 | 0 | Unpolluted |
| Al | 0.54 | 1 | Unpolluted-moderately polluted |
| Mn | 2.04 | 3 | Moderately to strongly polluted |
| Cr | 0.38 | 1 | Unpolluted-moderately polluted |
| Fe | 0.09 | 1 | Unpolluted-moderately polluted |
| Zn | -0.045 | 0 | Unpolluted |

Individual Research Contribution Review, 2024: 305–306
*ISSN: 3083-922X*

# Seasonal Variations in Elemental Concentrations in Putrajaya Constructed Wetland System: Implications for Sedimentation and Water Quality Standards

**Nurul Fairuz Diyana Bahrudin**
Waste Technology and Environment Division, Malaysian Nuclear Agency
43000 Kajang, Selangor
nurulfairuz@nm.gov.my

## Abstract

This study investigates seasonal variations in elemental concentrations in a constructed wetland system, focusing on its role in wastewater treatment and environmental management. Data were collected across three seasons: two dry seasons (September 2023 and April 2024) and one wet season (January 2024) at Putrajaya Constructed Wetlands. The analysis reveals significant seasonal differences, with lower concentrations in most elements during the wet season due to dilution from rainfall and runoff. In contrast, slight increases in elements like barium (Ba) and potassium (K) were observed during the dry season, likely due to evaporation. The results also highlight the impact of sedimentation and desilting processes on elemental dynamics, emphasizing the importance of sediment management for maintaining system functionality.

**Keywords:** constructed wetland, elemental concentrations, seasonal variability

## 1 Introduction

Constructed wetlands are man-made ecosystems designed to treat wastewater, manage stormwater, and recycle nutrients (Rousseau et al., 2022). They are inspired by natural wetlands but are built to improve processes like sedimentation, nutrient removal, and contaminant filtering. Seasonal changes, such as rainfall and evaporation, strongly affect sediment movement and the cycling of elements in these systems. These changes influence how wetlands grow, change, and function over time, impacting their long-term stability (Zhang et al., 2023). Understanding these seasonal variations is important for improving wetland performance and sustainability. This study examines how elemental concentrations change during two dry seasons (September 2023 and April 2024) and one wet season (January 2024) at Putrajaya Constructed Wetlands, using the average concentrations from 34 sampling points across the wetland. The Putrajaya Constructed Wetlands (101.68830E and 2.9363610N) were designed to manage surface runoff from upstream development and agriculture before reaching the 400-hectare Putrajaya Lake (Majizat et al., 2010). The study focuses on the effects of dilution, concentration changes, and desilting on wetland functionality.

## 2 Methods

Sampling was conducted during three distinct periods: September 2023 (dry season), January 2024 (wet season), and April 2024 (dry season) at Putrajaya Constructed Wetlands. The average concentrations from 34 sampling points were analyzed for 20 elements, including aluminium (Al), silicon (Si), sodium (Na), barium (Ba), and calcium (Ca), using Wavelength Dispersive X-Ray Fluorescence (WDXRF). The seasonal variations in elemental concentrations were studied to explore the relationships between hydrological conditions, sedimentation, and elemental dynamics, with a focus on desilting activities and sediment management.

## 3 Data/Results

The seasonal analysis of elemental concentrations, based on the average of 34 sampling points, revealed distinct trends influenced by hydrological changes (Table 1). During the wet season (January 2024), most elements, including aluminium (Al), silicon (Si), and sodium (Na), exhibited significant reductions in concentration due to dilution effects from increased rainfall and runoff, which flushed sediments and dissolved elements from the wetland. In contrast, the dry season (April 2024) showed slight increases in elements such as barium (Ba) and potassium (K), likely driven by evaporation and concentration effects as water levels declined. Comparing the two dry seasons (September 2023 and April 2024), higher concentrations were observed in September 2023, indicating that sedimentation before the wet season led to the accumulation of elements like Al and Si. These findings highlight the critical roles of sedimentation and desilting processes in shaping elemental dynamics within the constructed wetland system.

### 3.1 Discussion

The seasonal trends observed in the constructed wetland, based on the average of 34 sampling points, are influenced by a combination of hydrological and sedimentation processes:

a) Dilution in the Wet Season: Increased rainfall and runoff during the wet season lead to significant flushing of sediments, resulting in reduced concentrations of particulate-bound elements like Al and Si.

b) Concentration in the Dry Season: During the dry season, reduced water flow and evaporation contribute to increased concentrations of dissolved elements, as observed with Ba and K.

Table 1: Seasonal variations in elemental concentrations (September 2023, January 2024, April 2024) from Putrajaya constructed wetlands

| Standard Parameter | Unit (mg/l) | Sept 2023 (mg/l) | Jan 2024 (mg/l) | April 2024 (mg/l) |
|---|---|---|---|---|
| Al | 0.05* | 1.78 | 0.74 | 0.53 |
| Sb | 0.03* | 0.52 | 0.31 | 0.31 |
| As | 0.05* | 0.52 | 0.25 | 0.25 |
| Ba | 1* | 0.52 | 0.26 | 0.27 |
| Cd | 0.002* | 0.54 | 0.31 | 0.30 |
| Ca | 200** | 0.54 | 0.26 | 0.26 |
| Cr | 0.05* | 0.51 | 0.27 | 0.27 |
| Co | 0.05** | 0.51 | 0.24 | 0.24 |
| Cu | 0.02* | 0.50 | 0.25 | 0.25 |
| Fe | 1* | 0.66 | 0.37 | 0.30 |
| Pb | 0.05* | 0.50 | 0.28 | 0.26 |
| Mg | 150** | 1.23 | 0.29 | 0.28 |
| Mn | 0.1* | 0.52 | 0.27 | 0.26 |
| Ni | 0.02* | 0.49 | 0.25 | 0.25 |
| K | 200** | 0.52 | 0.27 | 0.27 |
| Se | 0.01** | 0.51 | 0.25 | 0.26 |
| Si | 50*** | 1.99 | 0.94 | 0.59 |
| Ag | 0.05*** | 0.47 | 0.32 | 0.32 |
| Na | 200** | 1.06 | 0.27 | 0.27 |
| Zn | 5* | 0.50 | 0.25 | 0.25 |

* Putrajaya Lake Water Quality Standard
** National Lake Water Quality Standard
*** Department of Environment, Class IIB

c) Sedimentation and Desilting Effects: The differences in elemental concentrations between the two dry seasons suggest the role of sediment management practices. The higher concentrations in September 2023 may reflect the accumulation of sediments prior to the wet season, emphasizing the importance of regular desilting in maintaining optimal wetland performance.

The results emphasize the essential role of sedimentation and desilting in regulating elemental dynamics within constructed wetlands, significantly influencing the system's efficiency in retaining and processing nutrients and contaminants. Similarly, Mereta et al. (2020) reported the critical role of sedimentation and desilting in regulating nutrient retention and sediment dynamics in wetlands, aligning with the findings on the importance of effective management practices to maintain wetland functionality.

This study investigates seasonal variations in key elements such as Al, Si, Na, Ba, and K, in a constructed wetland, focusing on sedimentation, nutrient cycling, and hydrological processes. Al and Si concentrations decreased during the wet season due to runoff and sediment flushing, while Na showed dilution in the wet season and concentration in the dry season due to evaporation. Ba and K exhibited slight seasonal increases, reflecting sediment interactions and evaporation. These findings highlight the connection between seasonal hydrology, sedimentation, and elemental cycling in wetland management.

## 4 Conclusions

This study provides valuable understandings into the seasonal variations in elemental concentrations in constructed wetland systems. By focusing on key elements such as Al, Si, Na, Ba, and K, the research highlights how sedimentation, nutrient cycling, and hydrological processes influence wetland functioning. The wet season is dominated by dilution due to rainfall and runoff, while the dry season sees concentration effects driven by evaporation and sedimentation. These findings underscore the importance of understanding seasonal changes and sediment dynamics for effective wetland management and optimization.

## References

A. Majizat, R. Sahat, N. Noordin, N.A. Rahaman, and Y. Muhamad. 2010. Tasik Putrajaya and Wetlands, Putrajaya, lake brief. in: Managing lakes and their basins for sustainable use in Malaysia (lake briefs report series i). *Akademi Sains Malaysia, Kuala Lumpur*, page 139–169.

S.T. Mereta, L. De Meester, P. Lemmens, W. Legesse, P.L. Goethals, and P. Boets. 2020. Sediment and nutrient retention capacity of natural riverine wetlands in Southwest Ethiopia. *Frontiers in Environmental Science*, 8:122.

National water quality standards for malaysia. https://environment.com.my/wp-content/uploads/2016/05/River.pdf.

2015. National lake water quality system. https://enviro2.doe.gov.my/ekmc/wp-content/uploads/2021/01/National-Lake-Water-Quality-Criteria-and-Standards-PRINTED.pdf.

Perbadanan Putrajaya. Catchment development and management plan for Putrajaya lake. 1(Main Report).

Diederik P.L. Rousseau, Flor Louage, Qintong Wang, and Rui Zhang. 2022. Constructed wetlands for urban wastewater treatment: An overview. *Encyclopedia of Inland Waters (Second Edition)*, 4:272–284.

X. Zhang, Y. Liu, W. Zhao, J. Li, S. Xie, C. Zhang, X He, D. Yan, and M. Wang. 2023. Impact of hydrological changes on wetland landscape dynamics and implications for ecohydrological restoration in Honghe National Nature Reserve, Northeast China. *Water*, 15(19):3350.

Individual Research Contribution Review, 2024: 307–308
*ISSN: 3083-922X*

# Studies on Optimum Mix Design for Immobilization of Spent Resin from Low Level Effluent Treatment Plant (LLETP), Malaysian Nuclear Agency Using Fly Ash Based Geopolymer

**Nurul Wahida Ahmad Khairuddin**
Waste Technology and Environment Division, Malaysian Nuclear Agency
43000 Kajang, Selangor
nwahida@nm.gov.my

## Abstract

Radioactive waste management is a key issue in Malaysia's use of atomic energy. Since the 1960s, radioactive materials have been used in research, medicine, and industry, leading to waste in gas, liquid, or solid forms. The Malaysian Nuclear Agency's Waste Technology Development Centre (WasTeC) is responsible for handling all radioactive waste in the country, including its collection, transportation, treatment, and storage. Immobilization is a crucial method for managing this waste. This project aims to assess the effectiveness of geopolymer, a new technology in Malaysia, for immobilizing radioactive waste. The project will focus on immobilizing spent resin from the Low-Level Effluent Treatment Plant (LLETP) using geopolymer made from fly ash, a by-product of coal plants. Spent resin, after repeated use, becomes radioactive and needs to be safely disposed of. This study will help find a safe and effective method for immobilizing spent resin, ensuring long-term safety in waste management.

**Keywords:** geopolymer, radioactive waste, spent resin

## 1 Introduction

Radioactive waste is produced in fields like agriculture, medicine, and industry. In Malaysia, the Waste Technology Center (WasTeC) is the main agency managing this waste, including its collection, treatment, and storage. WasTeC's facilities, operational since 1984, include the Low-Level Effluent Treatment Plant (LLETP), which treats and stores liquid radioactive waste.

In 2019, Tank 3A was added to the LLETP to handle liquid waste with alpha emitters from a new project recovering thorium, uranium, and rare earth elements from mining by-products. The processes involved create wastewater that exceeds pollution limits. This waste is treated using flocculation-coagulation, where chemicals help particles clump for easier removal. Ion exchangers are also used to reduce pollutants and meet safety standards.

Spent ion exchange resins, which become highly radioactive, require special handling. Around 640 kg of this waste is stored at WasTeC, posing risks of leaks and contamination. Safer treatment and disposal methods are being explored.

Geopolymers are made by mixing aluminosilicates with alkali solutions, which then polymerize at room temperature. First introduced in 1978, geopolymers differ from regular cement as they use silica and alumina to provide strength instead of calcium silicate-hydrates. Geopolymers are environmentally friendly compared to energy-intensive Portland cement, which releases $CO_2$. They are recommended for applications like encapsulating radioactive and hazardous waste and can replace materials like bricks and tiles.

## 2 Methods

Spent resin samples from the LLETP water treatment process were collected and placed in sealed 3L plastic containers for testing. In this study, the spent ion exchange resins were directly immobilized and encapsulated. Fly ash, sourced from the Sultan Salahuddin Abdul Aziz Power Plant in Selangor, was used to create the geopolymer. To activate the silica and alumina in the fly ash, sodium hydroxide and sodium silicate were added, along with a super plasticizer for better workability.

### 2.1 Particle Analysis

The particle size of the samples was analyzed using a digital microscope and a particle size analyzer. Phase identification was done with X-ray diffraction.

### 2.2 Radionuclide Content

Fly ash and spent resin samples were packed in plastic containers and analyzed using a gamma spectrometer. The concentrations of radionuclides like $^{226}$Ra and $^{232}$Th were measured by analyzing specific gamma-ray energies.

### 2.3 Mixture Proportions

Experiments were conducted to test how variables like workability, the ratio of chemicals, and the addition of water and superplasticizer affect the strength of the geopolymer. The optimum mixture was determined by casting geopolymer cubes and testing their compressive strength. The materials were mixed and compacted, then cured for up to 28 days. Nine cube samples were tested at 3 different curing times (7, 14, and 28 days).

## 3 Results and Discussion

### 3.1 Particle Distribution

The particle size of Kapar fly ash was measured using a laser diffraction analyzer. The particles ranged from 1.06 to 209.3 $\mu$m, with a median size of 20.64 $\mu$m. For optimal binding, 80-90% of fly ash particles should be smaller than 45 $\mu$m.

### 3.2 Mineralogy composition

Fly ash is classified as Class F or Class C based on its chemical composition. Kapar fly ash is Class C, with a combined $SiO_2$, $Al_2O_3$, and $Fe_2O_3$ content below 70% and $SO_3$ under 5%. For optimal binding, fly ash should have low calcium, $Fe_2O_3$ below 10%, and silica content between 40-50%.

### 3.3 Radionuclides Content

The radionuclide activity in Kapar fly ash ranges from 96.5–338.5 Bq/kg for $^{226}$Ra, 139–422.7 Bq/kg for $^{232}$Th, and 251.8–422 Bq/kg for $^{40}$K, all below regulatory limits of 1000 Bq/kg for $^{226}$Ra and $^{232}$Th, and 10,000 Bq/kg for $^{40}$K. Thus, the fly ash complies with safety standards for Naturally Occurring Radioactive Material (NORM).

### 3.4 Optimum Mix Design for Immobilization of Spent Resin using Geopolymer Based Fly Ash

Table 1 highlights the optimal mix proportions for geopolymer production, including fly ash-to-alkaline solution ratio, $Na_2SiO_3$-to-NaOH ratio, NaOH molarity, water content, and superplasticizer volume. The geopolymer achieved a compressive strength of 15.4 MPa on day 7, compared to 6.1 MPa in a previous study. This meets the IAEA and CERN-NN standards for radioactive waste immobilization (minimum 10 MPa at 28 days). A higher NaOH molarity improved early strength by enhancing aluminosilicate dissolution. The spent resin content was 14% by weight, staying below the 20% limit to prevent cracking and ensure stability in water.

Table 1: The Optimum Mix Design for Immobilization of Spent Resin using Geopolymer Based Fly Ash

| Details of Mix Proportion | | |
|---|---|---|
| **Parameter** | **(Nurul Wahida et al., 2015)** | **Current study** |
| Ration fly ash to alkaline activator | 2.0 | 2.5 |
| Ratio $Na_2SiO_3$ to NaOH | 2.5 | 3.0 |
| NaOH (M) | 12 | 14 |
| Distilled water (%) | - | 8 |
| Superplasticizer (%) | 6.0 | 2.0 |
| Spent resin (%) | 10 | 14 |
| Curing Temperature | Room temperature | Room temperature |
| Curing time (hrs) | 24 | 24 |
| Compressive strength (MPa) on $7^{th}$th day | 6.1 | 15.4 |

Adding water as a new parameter improved the compressive strength of the geopolymer compared to earlier studies. Water enhances workability and facilitates the reactions essential for geopolymer formation but too much can weaken compressive strength. The optimal water content was 8%. Superplasticizer also improved workability, strength, and durability but adding more than 2% caused segregation and reduced compressive strength.

## 4 Conclusions

Results from the study shows that conditioning of the spent resin together with fly ash at room temperature can produce geopolymer with reasonable strength properties. The composition of the spent resin that make up the monolith geopolymer

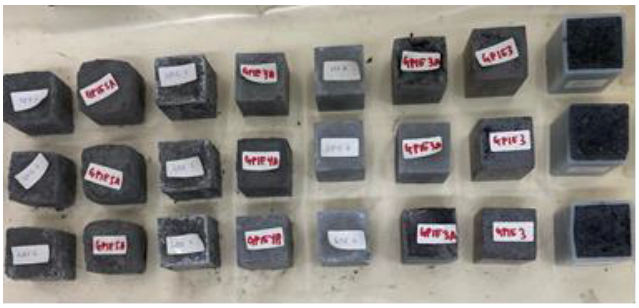


Figure 1: Samples of Monolith Geopolymer

was 14% (wt.), with the monolith geopolymer compressive strength of 15.4 MPa is well within the internationally acceptable value. Adding water in the geopolymer mixture can increase the compressive strength of the monolith geopolymer. This research should be put in a continuous effort in other method of testing such as leaching and durability test. In this way, more reliable data could be produced to support the use of geopolymer technology as an option for immobilization of radioactive waste. Furthermore, immobilization could enhance the handling and transportation of radioactive waste. Solidified waste is less prone to leakage, spillage, or accidental release during handling and transport operations, could reduce the risks to the workers and environment.

## References

P. Chindaprasirt, T. Chareerat, and V. Sirivivatnanon. 2007. Workability and strength of coarse high calcium fly ash geopolymer. Cem. Concr. Compos.

Nurul Wahida A. K., Muhamad Samudi Y., Amran Ab. M., Mohd A. W., Nik Marzukee, Wilfred P., Esther P., Thanaletchumy, and Irwan M.N. 2015. Immobilization of spent ion exchange resin from puspati triga reactor using fly ash-based geopolymer. *Malaysian Journal of Analytical Sciences*, 19(3):472–480.

Nurul Wahida A. K., Ahmad Khairulikram Z., Esther P., and Muhammad Fathi S. 2021. Coal power plant fly ash characterization assessment for geopolymerization process.

Comissão Nacional De Energia Nuclear. 2002. Critérios de aceitação para deposição de rejeitos radioativos de baixo e médio nível de radiação. *CNEN-NN6.09, Rio de Janeiro, Brasil,*.

Individual Research Contribution Review, 2024: 309–310
*ISSN: 3083-922X*

# 2024 Annual Report on Radioactive Waste Disposal and Inventory Management in Malaysia

**Nurul Wahida Ahmad Khairuddin**
Waste Technology and Environment Division, Malaysian Nuclear Agency
43000 Kajang, Selangor
nwahida@nm.gov.my

## Abstract

Waste Technology Development Centre (WasTeC) is Malaysia's National Radioactive Waste Management Centre, designated by the government to manage radioactive waste in the country. This centre provides comprehensive services for the collection, dismantling, conditioning, storage, and disposal of radioactive waste generated from various sectors including the manufacturing industry, hospitals, educational institutions, and research laboratories. This paper is intended to report the status of radioactive waste in Malaysia form January to November 2024, with a focus on Disused Sealed Radioactive Sources (DSRS), solid and liquid radioactive waste.

**Keywords:** Inventory, radioactive waste

## 1 Introduction

In Malaysia, radioactive waste management is established by the Malaysian Nuclear Agency (Nuclear Malaysia) under the Atomic Energy Licensing Act 1984 and the Regulations for Radioactive Waste Management. The country's radioactive waste inventory mainly comprises waste from the medical, industrial, research, and nuclear energy sectors. This inventory tracks the generation, handling, treatment, and storage of radioactive waste to ensure compliance with safety standards and regulatory requirements.

WasTeC offers a variety of services for the disposal of different types of radioactive waste, including solid waste, liquid waste, and disused sealed radioactive sources (DSRS). Additional services include the disposal of lightning arrestors and smoke detectors, along with the collection, dismantling, conditioning, transportation, storage, and disposal of radioactive waste. These services ensure the safe management, handling, and disposal of waste, contributing to the protection of public health and environmental safety.

In 2024, WasTeC provided radioactive waste disposal services to 54 companies, institutions, schools, and research laboratories under Nuclear Malaysia. Financially, WasTeC contributed RM 190,123.35 to Nuclear Malaysia's revenue, marking a 189.6% increase from RM 100,265.38 in 2023.

Figure 1 below shows a comparison of WasTeC's revenue from 2019 to November 2024.

As of November 2024, WasTeC delivered a total of 54 services, comprising 26 external services and 4 internal services. Additionally, 24 services were offered free of charge to schools, highlighting Nuclear Malaysia's dedication to corporate social responsibility (CSR) and community contributions (as shown in Table 1).

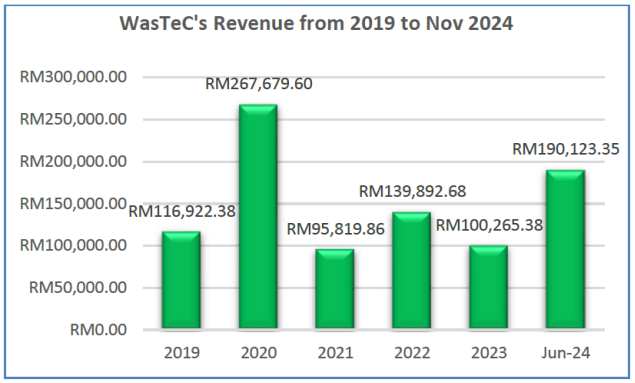



Figure 1: Comparison of Total Revenue Earned by WasTeC from 2019 to Nov 2024

Table 1: Type of Services Offered to Client in 2024

| Type of Services | 2024 |
|---|---|
| External Services | 26 |
| Internal Services | 4 |
| Schools | 24 |
| Total | 54 |

## 2 Inventory of Radioactive Waste

The inventory of radioactive waste is critical for ensuring the safe and compliant management of waste materials containing radioactive substances.

Table 2 highlights the types of radioactive waste collected by WasTeC from 2022 to November 2024, with inventory data routinely reported to the Jabatan Tenaga Atom. Maintaining an accurate inventory ensures the safe management of radioactive waste, safeguarding human health and the environment while adhering to national and international regulations. Table 2 presents the various types of radionuclides collected in 2024.

The DSRS are typically categorized based on their radioactivity levels, uses, and associated risks. These categories help determine the appropriate management and disposal methods for these sources. Based on the recorded inventory, most of

Table 2: Type of Radioactive Waste Collected from 2022 – November 2024

| SourceType of Radioactive Waste | 2022 | 2023 | Nov 2024 |
|---|---|---|---|
| DSRS (Unit) | 341 | 224 | 265 |
| Nuclear Material (Unit) | 0 | 86 | 18 |
| Depleted Uranium (kg) | 0 | 1595.79 | 15 |
| Solid (kg) | 36.16 | 263.61 | 4940.26 |
| Liquid (L) | 66.13 | 1.67 | 0.06 |
| Gas (ml) | 10 | 0 | 0 |
| Lightning Arrester (Unit) | 5 | 28 | 4 |

the DSRS collected were from Category 4 and Category 5, which are considered to have lower radiation levels and associated risks. For DSRS with an unknown category, further assessment will be carried out to determine their radioactivity levels, uses, and associated risks. This will ensure proper classification and the application of appropriate management and disposal methods. Table 3 presents the DSRS categories for DSRS collected in 2024. While Table 4 shows the total activity for radioactive waste collected in 2024.

Table 3: Categories of DSRS Collected from January to November 2024

| DSRS Category | Unit |
|---|---|
| Category 4 | 8 |
| Category 5 | 215 |
| Not Available | 42 |
| Total | 265 |

Table 4: Inventory of DSRS from January to November 2024

| Radionuclide | Half-life (years) | DSRS (Units) | Current Activity (mCi) (Nov 2024) |
|---|---|---|---|
| Co-60 | 5.27 | 53 | 1.32E+00 |
| Cd-109 | 462.6 | 1 | NA |
| Ra-226 | 1600 | 42 | 6.75E-01 |
| H-3 | 12.33 | 8 | NA |
| Mn-54 | 312.3 | 1 | NA |
| C-14 | 5730 | 2 | NA |
| Cf-252 | 2.645 | 1 | 9.30E-01 |
| Ba-133 | 10.51 | 2 | NA |
| Ge-68 | 270.8 | 8 | 1.09E+00 |
| Kr-85 | 10.7 | 2 | 1.36E+02 |
| Ir-192 | 73.831 | 1 | NA |
| Sr-90 | 29.1 | 39 | 3.99E+00 |
| Cs-137 | 30 | 39 | 2.32E+02 |
| Am-241 | 432 | 40 | 5.02E+02 |
| Co-57 | 221.7 days | 10 | 7.10E+00 |
| Ni-63 | 96 | 4 | 4.81E+01 |
| Tl-204 | 3.78 | 3 | 0.00E+00 |
| Po-210 | 0.379 | 3 | 9.41E-37 |
| Na-22 | 2.6 | 6 | 1.24E-03 |
| **Total DSRS** | **265** | | |
| **Total Activity (mCi)** | **9.34E+02** | | |

## 3 Conclusions

The Annual Report on Radioactive Waste Disposal Services and Inventory for 2024 highlights the significant contributions of WasTeC in managing and disposing of radioactive waste in Malaysia. With a total of 54 services provided, including both external and internal services, WasTeC has continued to play a vital role in ensuring the safe handling and disposal of radioactive waste. Through accurate inventory tracking and adherence to safety standards, WasTeC contributes to protecting public health and the environment, while ensuring compliance with both national and international regulations. As the volume of services continues to grow, WasTeC remains integral to Malaysia's efforts in managing radioactive waste effectively and responsibly.

## References

International Atomic Energy Agency. 2005. Categorization of radioactive source.

Individual Research Contribution Review, 2024: 311–312
*ISSN: 3083-922X*

# Study on Agro-contaminants Distribution in Selangor North-West Integrated Agriculture Development Area (IADA) Using Stable Isotope Approach

**Roslanzairi Mostapa**
Waste Technology and Environment Division, Malaysian Nuclear Agency
43000 Kajang, Selangor
roslanzairi@nm.gov.my

## Abstract

Significant decline of rice production yield from the paddy field over the past few years in some of the IADA areas has led to the investigation of this study. Bagan Terap and Pancang Bedena are the areas that experienced the lowest production which is about 1 to 2 tons per hectare of average yield compared to other areas (Sungai Nipah, Pasir Panjang, Sungai Leman, Sekinchan, Sungai Burong and Sawah Sempadan) that can reach up to 8 tons per hectare. Several factors have been identified as the contributors to the decline in yield such as low soil fertility, pest and diseases infestation, low water quality and natural disasters such as flooding. However, water quality is expected to be the main factor contributing to yield reduction in Bagan Terap and Pancang Bedena areas. Thus, this study will use the integrated isotopic approaches with conventional methods to study surface water and groundwater interactions; characterizing and determining the sources, movement and fate of the contaminants to effectively assessing issues related to wide area contamination problems.

**Keywords:** Stable isotope, precipitation, Malaysian meteoric water line

## 1 Introduction

Human activities are identified as the primary causes of water, soil and ecosystem pollutions. Those include manufacturing, urbanization, deforestation and intensive agriculture activities which lead to accumulation of contaminants and suspended particles ending up in rivers (sedimentation), resulting aquatic ecosystems damage and water quality impair. Major pollutants (either from point or non–point sources or both) include organic matter and disease-causing organisms from waste water discharges, fertilizer and pesticide residue from agricultural land, acid rain resulting from air pollution and heavy metals released from mining and industrial activities. In order to address this important issue, a comprehensive study must be conducted. The study area proposed in this study is the Selangor North-west Integrated Agriculture Development Area (IADA) located in Sungai Bernam Irrigation Scheme. This area is one of an important rice production area in Malaysia providing economic resources to more than 10,000 farmers. The entire area of IADA Barat Laut water resource for irrigation comes from Sungai Bernam which is then divided into two rivers, namely Sungai Tengi and Sungai Haji Dorani (located further down from Sungai Tengi). Sungai Tengi supplies water to high yielding areas while Sungai Haji Dorani supplies water to Bagan Terap and Pancang Bedena areas (low yield areas). Data from a study conducted in 2021 confirmed that water quality of Sungai Haji Dorani was low compared to Sungai Tengi. (Baharudin et al., 2021). The proposed investigation includes the assessment of surface water and groundwater, source and origin of contaminants (point and non–point sources) in the selected study site based on the isotope signature and hydro-chemical constituents. These data will be useful to the local and other concerned authorities to plan and undertake actions for better agricultural production management and long-term impact assessment of pollution to the natural environment.

## 2 Methods

Surface water and groundwater samples will be collected for stable isotope analysis ($\delta^2$H and $\delta^1$8O) seasonally i.e., dry season and wet season for the period of 2 years (January 2024 to December 2025) from 44 sampling points located in the study area as illustrated in Figure 1 and Figure 2.

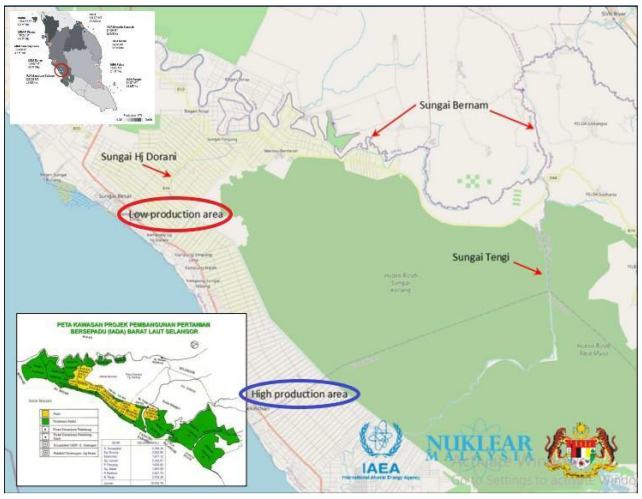



Figure 1: Study area

## 3 Preliminary and Expected Results

In general, all the water samples fall quite uniformly on the Local Meteoric Water Line (LMWL) except for some groundwater samples (Figure 3). P1 which is the control point was




Figure 2: Sampling points

found to have a significantly depleted water isotope value. However, this could possibly due to the high intensity rain-event happened (4 hours, > 100mm) during the sample collection which has caused the rain-amount effect. In contrast, the quite enriched value for P1 and P2 indicate the possibility of mixing process with seawater due to the seawater intrusion. Nevertheless, this also could be due to the natural geological condition of the study area due to the existence of marine clay. All these preliminary findings are to be investigated further and verified by other techniques.

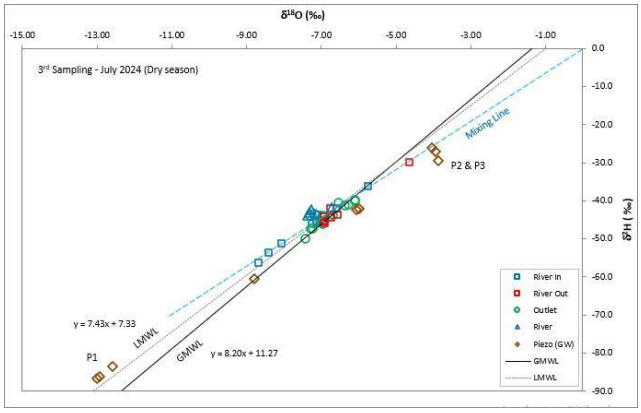



Figure 3: Sampling points

Based on the future results and findings, this project is anticipated to identify and assess the agro–contaminants distributions in the study area using isotopic tools integrated with conventional techniques.

## References

Fauzi Baharudin, Jalina Kassim, Siti Nurulhuda Mohd Imran, and Mahyun Ab Wahab. 2021. Water Quality Index (WQI) classification of rivers in agriculture and aquaculture catchments. *IOP Conf. Ser.: Earth Environ. Sci*, 646:012023.

Individual Research Contribution Review, 2024: 313–314
*ISSN: 3083-922X*

# Method for quick screening $^{226}$Ra level in water samples

**Yii Mei-Wo**
Waste Technology and Environment Division, Malaysian Nuclear Agency
43000 Kajang, Selangor
yii@nm.gov.my

## Abstract

Present of $^{226}$Ra in water is of concern due to its radiotoxicology. Limits were set for $^{226}$Ra concentration in waters by authorities to ensure public safety. Ra-226 measurement can be performed by various methods such as through gamma spectrometry after secular equilibrium or via alpha/beta energies after chemical purification and measured with alpha spectrometry or liquid scintillation counter. These methods were either time consuming or required chemical separation before measurement. A new approach is discussed here to screen $^{226}$Ra quickly without neither have to wait for secular equilibrium nor involve complicated chemistry process.

**Keywords:** $^{226}$Ra, secular equilibrium, liquid scintillation counter

## 1 Introduction

Radium-226 ($^{226}$Ra), a naturally occurring radioactive materials (NORMs) from uranium decay series, poses health risks due to its decay into radon gas, known to cause lung cancer and other diseases. Geochemical behavior of radium in the environment allow its presence in water as $Ra^{2+}$ ions or $RaSO_4$ compounds. The study reviews current methods for measuring radium activity in water, such as by gamma spectrometry and/or alpha spectrometry, which typically require waiting for secular equilibrium with radon prior to measurement. The study introduces a quicker approach using liquid scintillation counters (LSC), allowing rapid but accurate determination of radium activity in water without needing to wait for equilibrium, thereby improving monitoring capability of radium contamination in water sources.

## 2 Methods

### 2.1 Reagents and materials

20 mL glass vials with airtight foil-lined caps from Perkin-Elmer are used for counting. Perkin-Elmer ULTIMA Gold F scintillation cocktail with a 65% counting efficiency for 3H was used as scintillator. The $^{226}$Ra standard solution (15.0618 Bq/g) was supplied by Eckert & Ziegler Isotope Products, also with distilled water serving as the blank.

### 2.2 Standards set preparation and counting

A standard set was prepared to check the secular equilibrium between $^{226}$Ra and $^{222}$Rn, consisting of one blank and five different $^{226}$Ra concentrations. The standards were made by mixing $^{226}$Ra with distilled water and scintillation cocktail, then shaking and leaving them in the dark for five hours to separate into two phases. After phase separation, the vials were counted for up to 47 days, and all sample preparation details were recorded.

### 2.3 Sample preparation and counting

Each sample and a blank distilled water were mixed with 10 mL of scintillation cocktail, shaken, and left in the dark for five hours to allow phase separation. After four days, the vials were counted multiple times until secular equilibrium was reached, with all preparation details recorded.

### 2.4 Counting System

Counting system used in this study was Perkin-Elmer Tri-Carb 5110TR analyser. This system was monitored frequently using unquenched LSC conventional size (20mL) standard set that consists of Background Standard (blank), $^{3}$H Standard (~4100 Bq) and $^{14}$C Standard (~1600 Bq) to optimise the LSC settings and to check the long-term stability of the instrument.

### 2.5 Counting protocol and activity calculation

All vials were counted using a preset counting protocol on the counting instrument. Each vial will be counted for 60 minutes. Repetition and cycle counting were performed whenever necessary to confirm the stability of the count rate.

The current $^{226}$Ra standard activity can be calculated with the equation below:

$$A_t Ra = A_0 Ra e^{-\lambda_1 t_1} \quad (1)$$

Where:

$A_t$Ra: current $^{226}$Ra activity in the vial

$A_0$Ra: initial $^{226}$Ra activity on reference date

$\lambda_1$: Decay constant (ln 2 / (1600 years))

$t_1$: Time different between $^{226}$Ra reference date and counting date.

As the increase in count/min, cpm (hence cps, Bq) counting is expected due to the ingrowth of Radon-222 ($^{222}$Rn) gas from the $^{226}$Ra decays in the aqueous phase, therefore, using the assumption of secular equilibrium, the net cps (hence Bq) expected after subtracting the blank (instrument noise) at the secular equilibrium can be estimated using the equation as below: [Remark: For sample counted after reaching secular equilibrium, this step is excluded.]

$$E_{cps} = \frac{M_{cps}}{1 - e^{-\lambda_2 t_2}} \quad (2)$$

Where:

$E_{cps}$: estimated cps at equilibrium

$M_{cps}$: net cps after subtract blank

e: exponential

$\lambda_2$: decay constant (ln 2 / (3.8232 days))

$t_2$: time different preparation-counting

Calculation for the $^{226}$Ra specific activity in the sample (at present time) can be determined using the equation below:

$$A_{Spec} = \frac{cps_S \times 1000}{\varepsilon \times w_S} \quad (3)$$

Where:

$A_{Spec}$: sample activity (in Bq/L at present)

$cps_S$: net sample count rate (in cps)

1000: convert the volume from mL to L

$\varepsilon$: detector efficiency (in nominal)

$w_S$: weight of sample used (g)

The $^{226}$Ra specific activity in the sample at reference date can be back calculated using Equation 1 above.

## 3 Data/Results/Discussions

Count rate (in cps) for each sample was normalised over the sample and scintillator weight. Experiment showed that the count rate increased over time for vials spiked with $^{226}$Ra, while the blank vial's count rate remained constant, indicating the ingrowth of $^{222}$Rn. Count rate reached a maximum after 27 days, suggesting achieving secular equilibrium between $^{226}$Ra and $^{222}$Rn, as confirmed by Yu et al. (2011).

The experimental data were compared with theoretical values, showing that the ingrowth of $^{222}$Rn followed the expected growth curve. The experimental values closely matched the theoretical ones, confirming that $^{226}$Ra radioactivity could be estimated without waiting for equilibrium. However, to minimize counting error, sample should be counted only after day 4 (after one $^{226}$Ra half-life). As the $^{226}$Ra concentration increased, the experimental and theoretical values aligned more closely, with differences remaining within ±4%, an acceptable error margin for activity measurement.

## 4 Conclusions

This study concludes that the proposed method effectively screens $^{226}$Ra activity in water, especially for high concentrations, though it may face challenges with very low concentrations. By using a higher detection limit, it remains useful for screening and eliminates the need to wait for long secular equilibrium, making it ideal for urgent decision-making.

## References

W. Abdellah. 2019. Determination of radium-226 in rock samples by liquid scintillation counter. *J. Appl. Sci.*, 9:270–284.

Dickson B.L. 1990. Radium in groundwater. In: The environmental behaviour of radium (vol. 1). *Tech. Rep. Series No.310*, International Atomic Energy Agency, Vienna(8A):335–372.

Sill C.W. 1987. Determination of radium-226 in ores, nuclear wastes and environmental samples by high-resolution alpha spectrometry. *Nuclear and Chemical Waste Management*, 7(3-4):239–256.

M. Dowdall, Selnaes Ø. G., Gwynn J.P., and Davids C. 2004. Simultaneous determination of ra-226 and u-238 in soil and environmental materials by gamma-spectrometry in the absence of radium progeny equilibrium. *J. Radioanal. Nucl. Chem*, 261:513–521.

Bolton D.W. 2000. Occurrence and distribution of radium, gross alpha-particle activity, and gross beta-particle activity in ground water in the Magothy formation and Potomac group aquifers, Upper Chesapeake bay area, Maryland. *Report of investigations No. 70*, pages Department of Natural Resources, Maryland.

Diab H.M and Abdellah W.M. 2013. Validation of ra-226 and ra-222 measurements in water samples using gamma spectrometric analysis. *J. Water Resource Prot.*, 5(8A):53–57.

Yu. L., Mallants D., and Olyslaegers G. 2011. Assessment of radon release from concrete components in the Dessel low-level waste near surface disposal facility. *External Report SCK•CEN-ER-118*, SCK•CEN, Mol.

Q. Li, S.L. Wang, Zhao Y.G., Liu S.J., Fan Y.Q., Shi J.F., Jia H.M., and Yu W.X. 2015. Determination of ra-226 activity using gamma spectrometry with ra-226 -rn-222 disequilibrium. *Health Phys.*, 109(2):113–116.

H.P. Moreno, Vioque I., and G. Manjón. 1999. An easy method for ra-226 determination in river waters by liquid-scintillation counting. *Czech J. Phys.*, 49(Suppl 1):467 – 472.

Krishnaswami S., Cochran J.K., and editor(s). 2008. U-th series nuclides in aquatic system. *Elsevier, Oxford*, page 458pp.

M.W. Yii, Abdullah N., and Muhammad S. 2024. Quick screening method for ra-226 determination in water samples. *Seminar RD 2024, Nuclear Malaysia.*

Individual Research Contribution Review, 2024: 315–316
*ISSN: 3083-922X*

# Comprehensive Characterization of Radioactive Source Casings Using Multi-Technique Methods for Nuclear Forensics

**Zalina Laili**
Waste Technology and Environment Division, Malaysian Nuclear Agency
43000 Kajang, Selangor
liena@nm.gov.my

## Abstract

This study provides a comprehensive analysis of radioactive source casings for nuclear forensic applications, utilizing advanced techniques such as XRF, XRD, SEM, and X-ray imaging, alongside visual inspection and physical characterization. The findings provide valuable details about the materials, manufacturing processes, and origins of the casings, highlighting essential nuclear forensic signatures. These methods significantly enhance nuclear forensic capabilities by supporting the tracing of radioactive sources, improving detection and control of unauthorized materials, and mitigating risks associated with unregulated nuclear substances.

**Keywords:** nuclear forensics, radioactive source casings, signatures, advanced analytical techniques

## 1 Introduction

Radioactive sources are widely used in applications such as material testing, non-destructive evaluation in construction, and manufacturing process control. However, incidents like the 2018 Iridium-192 case have raised concerns about the risk of these materials being misused in nuclear terrorism New Straits Times, 2018). Between 2005 and 2019 (AELB, Retrieved March 15 2024) at least 18 cases of missing radioactive sources were reported, with some being improperly disposed of or recycled as scrap metal. Nuclear forensics, which focuses on determining the origins and history of such materials, is crucial for mitigating these risks. This study aims to improve the characterization of radioactive source casings using multi-technique methods, to develop a robust framework for evaluating the material composition, structural integrity, and potential forensic signatures of these casings.

## 2 Methods

The study involved collecting radioactive source casings from the Waste Technology Development Centre (WasTeC) and selecting diverse samples based on isotopes (e.g., $^{137}$Cs, $^{60}$Co, $^{241}$Am), manufacturers, and design variations to ensure comprehensive representation (see Figure 1). Physical characterization included visual inspection, weight, dimensions, and surface texture analysis using tools like calipers, scales, and survey meters to identify damage or contamination. Material composition was analysed using SEM-EDX, XRF, and XRD to assess microstructure, elemental, and crystalline properties. X-ray imaging with a portable XRS4 system provided high-resolution images of casings, enabling detailed examination of internal structures and shielding materials. These methods collectively supported the forensic investigation of radioactive source casings.

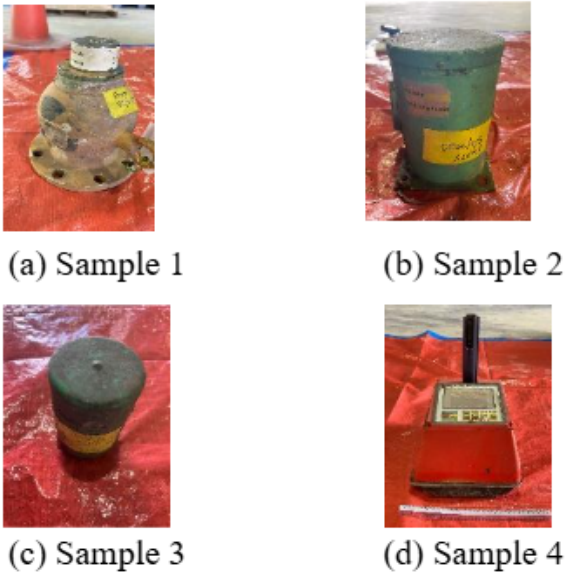



Figure 1: Types of radioactive source casings for for characterization study: Sample 1 (a) and Sample 2 (b) Nuclear Density Gauge, Sample 3 (c) Lead Pot Container, Sample 4 (d) Nuclear Moisture Density Gauge.

## 3 Results

The physical characterization of radioactive source casings revealed significant wear, corrosion, and degradation across various designs, including cylindrical, spherical, and rectangular containers. Damage such as peeling paint, flaking metal, faded or missing labels, and structural wear pose risks to safety and forensic tracking. SEM and EDX analyses highlighted surface degradation, including corrosion, oxidation, and contamination, with elements like iron, oxygen, and trace metals indicating environmental exposure and material wear (Figure 2). X-ray imaging offered non-destructive evaluation, confirming structural integrity and identifying internal features in lead pots and nuclear moisture density gauges with-

out anomalies or tampering, emphasizing its utility in forensic investigations.




Figure 2: (a) and (b) Example of significant wear, corrosion, and degradation observed in the radioactive source casings during physical characterization.

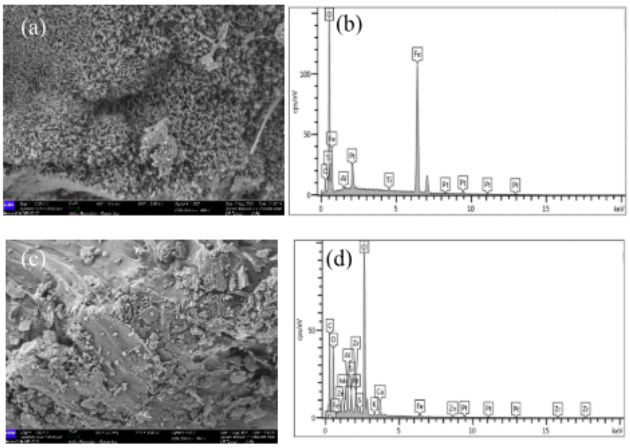



Figure 3: SEM Images and EDX Results of Metal Powder Obtained from Scraping Samples 1 and 2

## 4 Discussion

The findings underscore the importance of integrating physical, morphological, and non-destructive analytical techniques to understand the condition of radioactive source casings and their implications for nuclear forensics. Physical characterization highlights significant degradation in container surfaces, such as corrosion and fading labels, which could hinder the safe handling and tracking of radioactive materials. SEM and EDX analyses reveal details of surface corrosion, contamination, and material wear, reflecting environmental exposure and mechanical stress. X-ray radiography, as a non-invasive method, confirms structural integrity and internal features, enabling effective evaluation without altering the object (Figure 3). These results collectively demonstrate the value of combining multiple methods to enhance the evaluation and forensic tracking of degraded radioactive source containers, ensuring their safety and traceability.

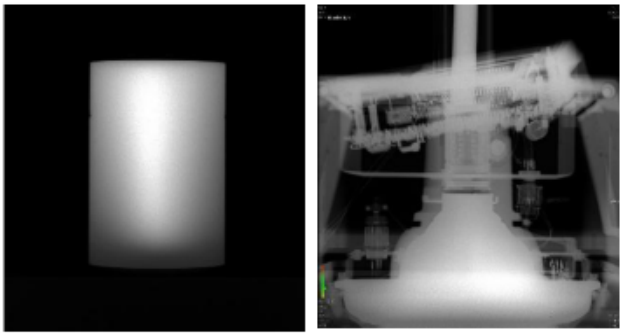


Figure 4: X-ray images of the lead pot container and nuclear moisture density gauge

## 5 Conclusions

This study utilized a comprehensive laboratory approach, combining techniques like visual inspection, physical characterization, XRF, XRD, SEM-EDX, and X-ray radiography, to analyse radioactive source casings for nuclear forensic purposes. The analysis revealed critical physical and chemical properties, including signs of wear, corrosion, and oxidation, which serve as key forensic markers for tracking and managing radioactive materials. The findings enhance nuclear security by supporting material tracking and forensic investigations, providing a foundation for improved radioactive source regulation.

## References

AELB. Retrieved March 15, 2024. Radiological incident/accident statistics. *AELB*, https://www.aelb.gov.my/v2/index.php/en/radiological-incident-accident-statistics/.

New Straits Times. August 11, 2018. Exclusive: Radioactive device missing. new straits times. *New Straits Times 2018*, https://www.nst.com.my/news/nation/2018/08/403235/exclusive-radioactive-device-missing.

Individual Research Contribution Review, 2024: 317–318
*ISSN: 3083-922X*

IRCR

# Pioneer On Phosphate Leaching From Monazite Mineral Using Alkaline Treatment

**Abdul Rahman Norazumin**
Industrial Technology Division, Malaysian Nuclear Agency
43000 Kajang, Selangor
abdrahman@nm.gov.my

## Abstract

Monazite is an orthophosphate mineral that contains rare earth elements that can be obtained from various other minerals in the world. The high demand for rare earth elements and phosphates as by-products has increased in the use of high technology and consumer products. After mining, monazite minerals are comminuted and ore refined before the next process, namely hydrometallurgy and pyrometallurgy, is carried out for phosphate recovery. The cracking process is an important process to breakdown the mineral structure into elements of rare earth elements and concentrated phosphate. This method can be carried out by autoclave leaching, atmospheric leaching, mechanical decomposition dan fusion. The concentration of cracking produces a phosphate solution that is dissolved through the solid-liquid extraction method. This paper reviews cracking discovery to recover phosphate from monazite to facilitate further REE processes.

**Keywords:** Monazite, Rare earth elements, Phosphate recovery, Solid-liquid extraction

## 1 Introduction

Monazite is a remarkable rare earth phosphate mineral that plays a significant role in geological and industrial contexts. Characterized by its complex chemical composition of (Ce, La, Nd, Th)($PO_4$, $SiO_4$), this mineral represents an important source of rare earth elements and thorium, making it economically and technologically valuable.

Typically occurring as small, discrete grains, monazite is predominantly found embedded within various igneous and metamorphic rock formations. These host rocks include granite, pegmatite, schist, and gneiss, reflecting the mineral's diverse geological origins and formation conditions. The mineral's unique physical and chemical properties contribute to its widespread distribution and resilience.

One of monazite's most distinctive characteristics is its exceptional weathering resistance. Unlike many minerals that readily break down when exposed to environmental conditions, monazite grains remain structurally stable. This durability enables them to persist and become dispersed from their original host rock, ultimately accumulating in downslope soils and sedimentary deposits.

The mineral's significance extends beyond its geological occurrence. Monazite is critically important in the extraction of rare earth elements and thorium, materials with numerous high-technology and industrial applications. Researchers and mining industries are particularly interested in monazite for its potential to supply these strategically important elements.

This introduction sets the stage for a comprehensive exploration of monazite's geological, chemical, and economic characteristics, highlighting its unique position in mineral science and resource extraction.

## 2 Methods

### 2.1 Autoclave Leaching

The autoclave leaching technique represents a groundbreaking approach to rare earth and thorium extraction, with its origins tracing back to a seminal discovery by G. Calkins and his colleagues at the Battelle Memorial Institute in 1950 (Calkins et al., 1950). This innovative method revolutionized the processing of monazite sand, offering an efficient mechanism for separating valuable rare earth elements and thorium from mineral matrices.

The process is characterized by its precise operational parameters. Researchers utilize a highly concentrated 30% caustic solution to interact with finely ground monazite sand. The particle size specification is critical, with all material required to pass through a 0.0075mm (200 mesh) screen to ensure optimal surface area and reaction efficiency. The reaction conditions are equally specific, involving a carefully controlled temperature of 200°C and a sustained reaction time of 4 hours.

A key aspect of the methodology is the carefully calculated chemical ratio. The technique employs a weight ratio of 2:1 for caustic to sand, translating to 150 g of caustic solution precisely combined with 75 g of monazite sand. This specific proportion ensures maximum chemical interaction and extraction efficiency.

The extraction process involves multiple critical stages. After the initial high-temperature reaction, the mixture undergoes filtering and thorough water washing to remove trisodium phosphate. Subsequently, hydrochloric acid is introduced to dissolve the mixed hydroxide, completing the separation process.

The remarkable efficacy of this technique is evident in its extraction performance, with the method successfully digesting more than 98% of the processed sand. This high efficiency makes autoclave leaching a cornerstone technology in rare earth element extraction, demonstrating the sophisticated

chemical engineering approaches developed in mid-20th century metallurgical research.

The breakthrough represented by this method not only advanced rare earth extraction technologies but also laid the groundwork for future developments in mineral processing and strategic material recovery.

### 2.2 Atmospheric Leaching

The atmospheric leaching technique, developed by Rohden et al. at the Battelle Memorial Institute in 1957, represented a significant advancement in monazite processing and trisodium phosphate extraction. This method introduced an open digestion approach that differed from previous autoclave techniques, offering a novel pathway for rare earth element recovery. The process was meticulously designed, involving a precise combination of 1 ton of sodium hydroxide with 1 ton of finely ground monazite sand, specifically requiring all particles to pass through a 0.075mm (200 mesh) screen to ensure optimal reaction conditions.

The operational parameters of this atmospheric leaching method were carefully controlled to maximize extraction efficiency. The sodium hydroxide solution was prepared at a 65% concentration and subjected to heating between 140°C and 145°C for a duration of 2 to 5 hours. Research demonstrated remarkable effectiveness, with the process capable of breaking down up to 98% to 100% of the monazite's original composition within just 3 to 4 hours of treatment. The culmination of this sophisticated chemical process resulted in the production of 1.5 tons of trisodium phosphate, highlighting the method's significant industrial potential and chemical transformation capabilities. This approach not only advanced mineral processing techniques but also provided a scalable solution for extracting valuable chemical compounds from complex mineral sources.

### 2.3 Mechanochemical Decomposition

The breakdown of monazite with caustic soda and monazite grinding in one step were the subjects of a study by Mcerson et al. in 1957. In comparison to alternative caustic exchanges, the use of ball milling eliminates the generation of reaction products that surround mineral grains and further reduces caustic use by 50% (Kim et al., 2009). In a ball mill that had been heated to 130 °C, Mcerson et al.(1957) broke down monazite using solid sodium hydroxide. In the following stage, the undissolved residue is subjected to a second reaction in a ball mill with a 650 $gL^{-1}$ sodium hydroxide solution.

### 2.4 Fusion

Caustic fusion techniques employing sodium hydroxide was initially investigated and it was reported in United States Patent 617,636 (1899) (Calkins et al., 1957). With the usage of high temperature, the reaction products are too hard, the making the solid mass difficult to manipulate, which is one flaws in this pyrometallurgical process. For this reason, the possibility of carrying out the reaction in an aqueous solution was investigated.

## 3 Conclusion

From the review study, it was found that caustic conversion decomposition is mostly used for phosphate treatment on monazite. Phosphate removed at an early stage for further rare earth cracking processes, potentially as a commercial by-product. The known uses of phosphate produced are cleaning agent, sugar, food additive, lubricant, stain remover, textile, fertilizer, and degreaser.

## References

G. Calkins, R. Filbert Jr, A. Bearse, and J.Clegg. 1950. Recovery of thorium and uranium from monazite sand. *Final Report Volume II from Battelle Memorial Institute*.

G. Calkins, Ohio, and E.G.Bohimann. 1957. Processing of monazite sand. *United States Patent*.

W. Kim, I. Bae, S. Chae, and H. Shin. 2009. Mechanochemical decomposition of monazite to assist the extraction of rare earth elements. *Journal of Alloys and compounds*, 486:610–614.

Individual Research Contribution Review, 2024: 319–320
*ISSN: 3083-922X*

# Review: Advances in PLLA/CMS/$\beta$-TCP Nanofiber Scaffolds for Biomedical Applications

**Abul Adli bin Anuar**
Industrial Technology Division, Malaysian Nuclear Agency
43000 Kajang, Selangor
abuladli@nm.gov.my

## Abstract

Poly-L-lactic acid (PLLA)-based nanofibers have received significant attention in the field of regenerative medicine due to their tuneable mechanical properties and biodegradability. The addition of carboxymethyl starch (CMS) and $\beta$-tricalcium phosphate ($\beta$-TCP) into the PLLA matrix increases the wettability, degradation rate, and osteoconductivity of the scaffold. This review discusses fabrication methods, material properties, and biomedical applications of PLLA/CMS/$\beta$-TCP nanofibers, with emphasis on recent findings on composition optimization and post-processing techniques such as electron irradiation. These improvements make the PLLA/CMS/$\beta$-TCP scaffold a versatile solution for bone tissue engineering and related applications, with future directions focusing on clinical translation.

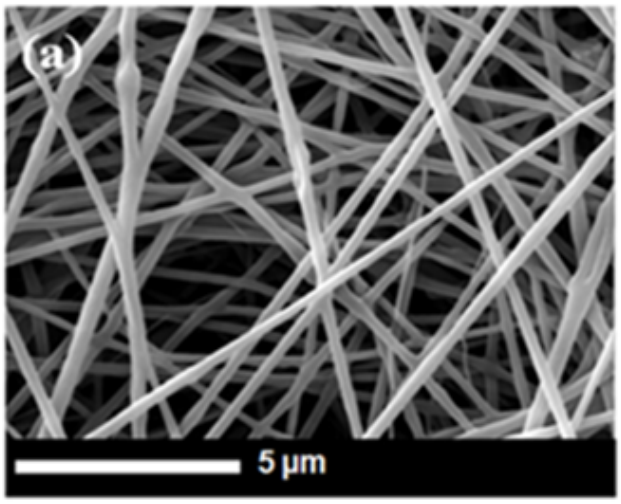



Figure 1: SEM micrographs of the morphology and fiber diameter (M.R Yusof et.al, 2020)

## 1 Introduction

The demand for innovative biomaterials in tissue engineering has prompted research into scaffolds produced by electrospinning with properties tailored for specific applications. PLLA appears as a promising material due to its mechanical strength, but its hydrophobic nature and slow degradation rate limit its effectiveness as a single material (Wojtasinski et al., 2013; Spasova et al., 2014).

To overcome these limitations, composite scaffolds containing CMS and $\beta$-TCP have been developed. CMS, a biocompatible starch derivative, improves wettability and degradation, while $\beta$-TCP, a bioactive ceramic, promotes osteoconductivity and mechanical bonding (Mansourizadeh et al., 2014). This review synthesizes findings on PLLA/CMS/$\beta$-TCP scaffolds, focusing on fabrication, material properties, and applications, while identifying gaps for future exploration.

## 2 Method

### 2.1 Fabrication Technique

PLLA/CMS/$\beta$-TCP scaffolds are usually produced by electrospinning. The choice of solvent, such as a mixture of dichloromethane (DCM) and dimethylformamide (DMF), has a large effect on the uniformity and morphology of the fibers. Studies suggest a polymer concentration of 5–10% w/w and a voltage setting of 10–17.5 kV for optimal results (Wojtasinski et al., 2013; Mansourizadeh et al., 2014). Key parameters include flow rate, nozzle diameter, and collector spacing, which ensure uniform fiber deposition.

### 2.2 Material Properties

#### 2.2.1 Hydrophilicity and Biodegradable

The addition of CMS increases water absorption, and facilitates cell attachment and proliferation. $\beta$-TCP accelerates scaffold degradation by neutralizing acidic products, overcoming the hydrophobic nature of PLLA (Mansourizadeh et al., 2014; Salifu et al., 2017).

#### 2.2.2 Mechanical Strength

$\beta$-TCP increases scaffold strength, supporting load-bearing applications. However, high filler content can cause cracking, emphasizing the need for a balanced composition (Spasova et al., 2014; Mansourizadeh et al., 2014).

#### 2.2.3 Enhancement Through Post-Processing

Electron-beam irradiation is a promising technique for tailoring scaffold properties:

1. Morphological Stability: Low-dose radiation preserves fiber structure while increasing wettability.

2. Degradation Control: Higher doses increase the rate of degradation, allowing customization of the scaffold for

different clinical needs (Wojtasinski et al., 2013; Salifu et al., 2017)

## 3 Conclusion

The PLLA/CMS/$\beta$-TCP scaffold represents a significant advance in regenerative medicine, offering a balance between mechanical strength, wettability, and biodegradability. Electron radiation has improved these properties, enabling tailored solutions for applications such as bone tissue engineering. Future research should focus on optimizing filler ratios to improve mechanical and degradation profiles, investigating hybrid materials combining CMS and $\beta$-TCP with other bioactive components, and conducting in vivo studies to confirm clinical efficacy. This progress will pave the way for the clinical translation of PLLA/CMS/$\beta$-TCP scaffolds in regenerative medicine.

## References

Wojtasinski R. et al. 2013. Electrospinning of plla solutions: Effects of viscosity on fiber morphology and degradation properties. *Biomedical Engineering*.

Mansourizadeh F. et al. 2014a. Plla/ha composite scaffolds for bone tissue engineering. *International Journal of Plant, Animal, and Environmental Sciences*.

Spasova M. et al. 2014b. Plla/peg nanofibers: Morphology and biomedical applications. *Advanced Polymer Technologies*.

Salifu A. et al. 2017. Multifunctional plla composite scaffolds for bte and drug delivery. *Materials Today*.

M.R.Yusof. et al. 2020. Electron-beam irradiation of the plla/cms/-tcp composite nanofibers obtained by electrospinning. *MDPI*.

Individual Research Contribution Review, 2024: 321–322
*ISSN: 3083-922X*

# Characterization and Silica Aerogel Performance in Solvent-based Paint

**Ahmad Hambali Ismail**
Industrial Technology Division, Malaysian Nuclear Agency
43000 Kajang, Selangor
hambali@nm.gov.my

## Abstract

Using nuclear gauging as an inspection tool in the industrial area requires proper training to ensure the workers are inspecting effectively and efficiently. The harm of the radioactive can be reduced using appropriate radiation protection procedures. However, the exposure of electronic parts to high-temperature surroundings may affect their functionality. Applying an insulative coating can be an alternative solution. Therefore, in this study, silica aerogel had been identified and incorporated (1%, 3%, 5% and 7%) into solvent-based paint. It shows that the addition of aerogel increased the viscosity of the paint. It also shows a rougher surface coat due to undispersed aerogel. Fourier Transform Infrared (FTIR) characterization was used to determine the effect on the chemical structure of the paint. It shows that 7% of aerogel had changed its chemical structure.

**Keywords:** Silica aerogel, solvent-based paint, FTIR

## 1 Introduction

Conducting plant or process evaluation using nuclear gauging can be practical in determining the integrity or any malfunctions. Radioactive sources and detectors can provide the density profile of the inspected part and can be used to determine the efficiency and integrity inside the pipes, columns or vessels. The harmful effects of radioactive sources used can be reduced by following the radiation protection guidelines such as the use of appropriate personal protective equipment (PPE), shielding material and practising as low as reasonably achievable "ALARA" concept. However, other concerns about the electronic parts have been highlighted. The high temperature surrounding the inspection site might affect the electronics parts especially the detectors and the scaler ratemeter. Therefore, applying a heat-protective layer would be appropriate for the parts.

Applying a coating on the detector's surface material is considered an alternative. Furthermore, a coating with a mixture of good thermal insulative material would produce more effective protection against heat. Aerogel is a good thermal insulative material and will be reinforced with the paint to produce heat insulation paint. Aerogel is a material with low densities (0.003 – 0.15 kg/m$^3$) (Smirnova and Gurikov., 2018). Furthermore, aerogel also possesses large porosity and surface area that make it exist with low thermal conductivity. In this study, silica aerogel will be added to the solvent-based paint to produce a thermal insulative paint. However, studies related to the introduction of silica aerogel and solvent-based paint are still lacking in the literature. Therefore, the compatibility of the newly formulated mixture will be assessed. The recently formulated mixture will also be characterized using Fourier Transform Infra-Red (FTIR) to determine any structural changes.

## 2 Materials and Methods

### 2.1 Material

The solvent-based paint (9000 Gloss Finish) Nippon Paint brand used in this study was a commercial type and purchased from the existing market. Silica aerogel (ENOVA® Aerogel Particles (IC3120)) was purchased from the supplier.

### 2.2 Preparation of Formulation and Performance Evaluation

In this part, the newly mixed silica aerogel and solvent-based paint were prepared. Approximately 300 grams of solvent-based paint undergo vigorous stirring using an electronic mixer. The aerogel was added to the solvent-based paint simultaneously during the stirring. The amount of silica aerogel added to the solvent-based paint was 1%, 3%, 5% and 7% wt. The well-mixed paint was evaluated by observing the appearance of the mixture and then applying a coat on a plate. The coating appearance had also been assessed.

### 2.3 Characterization

#### 2.3.1 Fourier Transform Infrared (FTIR)

The newly formulated solvent-based paint was characterized using FTIR (Agilent: Cary 630 FTIR Diamond ATR) to observe any changes in the chemical bonding from the original formulation.

#### 2.3.2 Energy Dispersive X-Rays Flourescence

The purity and elemental composition of the purchased silica aerogel were evaluated using ED-XRF (Shimadzu: ED-X-7000).

## 3 Data/Results

The composition of the silica aerogel had been evaluated using ED-XRF. It is to ensure that the silica aerogel has higher purity. Hence, it exhibits low thermal conductivity properties. The composition of the Enova Aerogel is shown in Table 1.

Table 1: Composition of Silica Aerogel using ED-XRF

| Analyte | Result, % | [3-sigma] |
|---|---|---|
| Si | 92.350 | 0.597 |
| P | 3.817 | 0.111 |
| Ca | 3.361 | 0.029 |
| Ba | 0.159 | 0.037 |
| Cu | 0.086 | 0.005 |
| Os | 0.073 | 0.008 |
| Ir | 0.064 | 0.008 |
| Fe | 0.040 | 0.004 |
| Cr | 0.025 | 0.005 |
| Ge | 0.022 | 0.003 |
| Zn | 0.005 | 0.001 |

The mixing paint had shown a similar trend for every amount of silica aerogel added. The viscosity of the paint is increasing as the amount of silica aerogel increases. Other than that, paint with a higher amount of silica aerogel also shows a rougher surface after being applied to the metal plate. The observation is shown in Figure 1.

The structural changes on the paint had been assessed using FTIR equipment. The FTIR spectrum is shown in Figure 2. The result shows that only a mixture of 7% wt amount of aerogel had shown a new peak that resembles pure aerogel with the formation of the Si-O-Si bond.

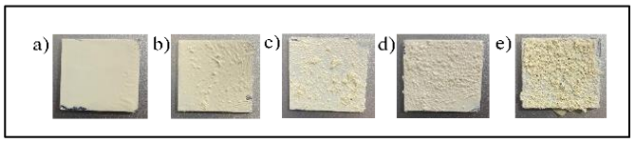



Figure 1: Appearance of the a) original paint, b) 1% aerogel, c) 3% aerogel, d) 5% aerogel, e) 7% aerogel on plate.

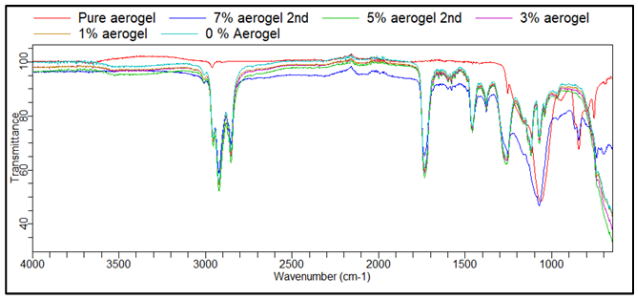



Figure 2: FTIR spectra on silica aerogel, original paint and mixture of solvent-based point and silica aerogel.

## 4 Discussion

The incorporation of silica aerogel into the solvent-based paint produced a thicker paint as the amount increased. Even with the thickening of the mixture, it managed to be used to coat a plate. It is observed that the surface of the plate shows a rougher surface as the amount increases. It shows that the silica aerogel is not fully dispersed into the paint and remains as solid particles within the solvents.

The FTIR spectrum shows that the 1%, 3%, and 5% wt show a similar pattern with the original paint formulation. Silica aerogel shows a peak at 844 and 1254 $cm^{-1}$, which indicates the Si-C bond and at 1071 $cm^{-1}$, which refers to the Si-O-Si bond. As for the 7% wt mixture of aerogel, different findings were detected on the spectrum. New peaks formed at 844 and 1256 $cm^{-1}$ and 1071 $cm^{-1}$ indicate the Si-C and Si-O-Si bond. The latest peak formation suggested that the 7% silica aerogel had modified the original solvent-paint chemical structure.

## 5 Conclusions

In conclusion, the incorporation of silica aerogel into the solvent based paint had been well prepared. The amount of silica aerogel added was 1%, 3%, 5% and 7%. It concluded that the amount of silica aerogel will affect the flow and viscosity of the paint and the coating appearance on the plate. Other than that, the incorporation of 7% silica aerogel indicates that aerogel was well-incorporated into the solvent-based paint as it shows an interference in the chemical bonding of the paint. This study will continue with heat penetration testing to determine the effectiveness of silica aerogel as an additive in solvent-based paint.

## References

Irina Smirnova and Pavel Gurikov. 2018. Aerogel production: Current status, research directions, and future opportunities. *The Journal of Supercritical Fluids*, 134:228–233.

Individual Research Contribution Review, 2024: 323–324
*ISSN: 3083-922X*

IRCR

# Impact of Focal Spot Size on Film Image Quality by using YXLON Y.XMB 225 X-ray system: A Comparative Study

**Amer Hazreq Bin Haron**
Industrial Technology Division, Malaysian Nuclear Agency
43000 Kajang, Selangor
amer@nm.gov.my

## Abstract

Radiographic non-destructive testing (NDT) detection of construction defects requires X-ray equipment. Study found that 14 mm and 15 mm steel plates had sharper pictures with 0.4 mm focal points. While 1.0 mm images were soft and less detailed, this size allowed high-resolution imaging and structural analysis. The small focal spot proved appropriate for high-resolution quality control and industrial structural inspections. The larger 1.0 mm focus spot is suitable for clear and comprehensive industrial imaging. The study emphasizes matching focal spot size to imaging needs and material properties.

**Keywords:** X-ray, focal spot, film density, Yxlon Y.XMB 225

## 1 Introduction

Non-destructive testing (NDT) is a method employed to identify internal and external defects in constructions. The most prevalent non-destructive testing (NDT) procedures include radiographic testing (RT), thermal/infrared testing (IR), dye penetrant testing (PT), magnetic particle testing (MT), electromagnetic testing (ET), acoustic emission testing (AE), and ultrasonic testing (UT). RT is extensively utilized across multiple sectors owing to its exceptional reliability. X-ray machines are fundamental to radiographic testing, generating radiographs that reveal internal imperfections or faults. YXLON Copenhagen has created sophisticated X-ray systems, including the Y.XMB transportable X-ray system, tailored for challenging situations such as power plants and aircraft constructions. The focal point size, which dictates image resolution, is essential for identifying intricate features and imperfections. This experiment seeks to examine the influence of imaging parameters on film quality and aid in the advancement of more effective and efficient non-destructive testing procedures.

## 2 Methods

The experiment was conducted at the bunker of Blok 59, Malaysian Nuclear Agency, using different steel plates with thicknesses of 14 and 15 mm. Lead letters were used for radiographic identification, and an Image Quality Indicator (IQI) was employed to ensure accuracy and consistency in the imaging process. Film preparation was done in a controlled dark room to prevent exposure to white light. The film was carefully inspected, cleaned, and loaded between lead screens to avoid introducing artifacts.

The X-ray equipment was set up for precise imaging of the welded structure, with the focal-to-film distance (FFD) set to 700 mm. A laser pointer was installed to guide accurate alignment, and the sample was placed beneath it to ensure the welded structure was aligned with the focal spot.

The YXLON Y.XMB 225 X-Ray System was used to capture the radiographic image of the steel plate. The exposure parameters, including voltage, current, and exposure time, were documented and positioned accurately under the X-ray focal spot. The X-ray beam penetrated the steel plate, transferring varying degrees of radiation to the film, creating a latent image representing the internal structure of the steel plate and its weld.

| Thickness (mm) | Voltage (kV) | Current (mA) | Exposure time (sec) |
|---|---|---|---|
| 14 | 180 | 4.4 | 27 |
| 15 | | | 34 |

Table 1: System parameters for image quality determination.

Film analysis was performed in a controlled dark room environment to prevent damage to the film. The film was washed, dried, and analyzed using a densitometer to determine the film's exposure levels and quality. Any deviations from the expected density readings indicated areas for potential adjustment in the exposure process.

## 3 Results

The study's goal was to look at how well X-ray photos work at taking clear pictures of steel plates. At focus points of 0.4 mm and 1.0 mm, density readings were taken for samples that were 14 and 15 mm thick, respectively. The density readings showed that both films did a good job of showing what the steel plates were made of on the inside. The films met the standards for optical density, which showed that the exposure settings were right for the medium and the results that were wanted.

The 0.4 mm focal spot size gave slightly more consistent density readings and might have made the images clearer, which was especially helpful for seeing small features in thinner materials. On the other hand, the bigger 1.0 mm focal spot size was able to penetrate and image thicker steel samples, though the density values were slightly higher because the beam covered more area.

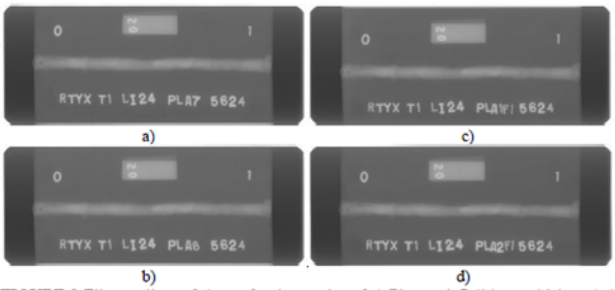



**FIGURE 1** Film quality at 0.4 mm focal spot size of a) Plate – A 7 (14 mm thickness), b) Plate – A 8 (14 mm thickness) and at focal spot size 1.0 mm of c) Plate – A1 F1 (14 mm thickness), d) Plate – A2 F2 (14 mm thickness)

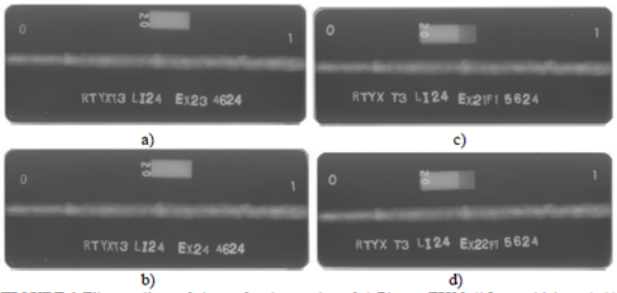



**FIGURE 2** Film quality at 0.4 mm focal spot size of a) Plate – EX23 (15 mm thickness), b) Plate – EX24 (15 mm thickness), and at 1.0 mm focal spot size of c) Plate – EX21 F1 (15 mm thickness), d) Plate – EX22 F1 (15 mm thickness)

The optical density readings from the 0.4 mm focal spot size constantly fell within the acceptable range for the 14 mm thick steel samples. This suggests that the smaller focal spot size produced sharp, high-resolution images that showed the intricate details inside the steel. The films' ability to keep picture clarity and detail even as the material thickness went up was further supported by the fact that the densities were the same across both the 14 mm and 15 mm samples.

| Sample | Voltage (kV) | Current (mA) | Time (sec) | Density | | | Thickness (mm) | Conclusion |
|---|---|---|---|---|---|---|---|---|
| Plate A-7 | 180 | 4.4 | 27 | 2.10 | 2.21 | 2.28 | 14 | Film accepted |
| Plate A-8 | | | | 2.05 | 2.14 | 2.14 | | Film accepted |
| Ex2-3 | | | 34 | 2.79 | 2.29 | 2.34 | 15 | Film accepted |
| Ex2-4 | | | | 2.59 | 2.39 | 2.34 | | Film accepted |

Table 2: Density for sample with different thickness at focal spot = 0.4 mm

| Sample | Voltage (kV) | Current (mA) | Time (sec) | Density | | | Thickness (mm) | Conclusion |
|---|---|---|---|---|---|---|---|---|
| Plate A-1 F1 | 180 | 4.4 | 27 | 1.90 | 2.21 | 2.19 | 14 | Film accepted |
| Plate A-2 F1 | | | | 2.14 | 2.25 | 2.28 | | Film accepted |
| Ex2-1 F1 | | | 34 | 2.22 | 2.53 | 2.30 | 15 | Film accepted |
| Ex2-2 F1 | | | | 2.31 | 2.34 | 2.30 | | Film accepted |

Table 3: Density for sample with different thickness at focal spot = 1.0 mm

The experiment shows how tricky it can be to get enough X-ray penetration while still keeping image quality good. The smaller focus spot size (0.4 mm) showed better results in making clear, detailed pictures, which is important for tasks that need to analyze fine structures. On the other hand, the 1.0 mm focal spot size gave strong images that could be used for thicker materials, even though they were a little less sharp. These results show how important it is to find the best focal spot size and exposure settings to improve the quality of X-ray images and make sure they meet the exacting standards needed by industry for clarity and precision.

## 4 Conclusion and attention

The study compared X-ray imaging quality for steel plates with varying focal spot sizes, revealing that a 0.4 mm focal spot size yielded sharper and more detailed images for both 14 mm and 15 mm thick steel samples. This size was highly suitable for high-resolution imaging and precise structural analysis, while a larger 1.0 mm size produced slightly softer and less detailed images. Both focal spot sizes maintained optical density readings within acceptable standards, indicating that the exposure parameters were appropriate for imaging steel samples of these thicknesses. The findings suggest that the 0.4 mm focal spot size is particularly advantageous for applications requiring high detail resolution, such as quality control or detailed structural inspections in industrial settings. The larger 1.0 mm focal spot size is better suited for general industrial imaging tasks where overall clarity and coverage are important. The study emphasizes the importance of aligning the choice of focal spot size with specific imaging requirements and material properties. Future research could explore varying focal spot sizes and exposure parameters across a broader range of material thicknesses to further refine the X-ray imaging process and optimize it for diverse industrial applications.

## References

A. K. Dey. 2024. Radiographic testing: Principle, procedure, standards, advantages, and disadvantages. what is piping.

G. Peruń. 2004. Advances in non-destructive testing methods. 17(3).

M. I. Silva, E. Malitckii, T. G. Santos, and P. Vilaça. 2023. Review of conventional and advanced non-destructive testing techniques for detection and characterization of small-scale defects. 138(101155).

Individual Research Contribution Review, 2024: 325–326
*ISSN: 3083-922X*

IRCR

# Simulating Qualitative Phased Array Ultrasonic Testing Defect Indication on Flange Face Using CIVA

**Amry Amin Abas**
Industrial Technology Division, Malaysian Nuclear Agency
43000 Kajang, Selangor
amry@nm.gov.my

## Abstract

Flanges are a component that joins two section of pipes together to achieve a contained flow of product through it. However flanges are susceptible to flange face corrosion due to various factors. One of the methods of Non-destructive testing that has potential to detect FFC is phased array ultrasonic testing (PAUT). In this article, the method of simulating PAUT inspection of flanges to detect FFC using CIVA software is discussed. The objective of this research is to optimize inspection parameters and Probability of Detection (POD) without compromising on practicality of inspection.From the initial simulation, it is found that a model has been successfully established that enables further optimisation work to be furthered.

**Keywords:** Flange Face Corrosion, Phased array ultrasonic testing, Non-destructive testing

## 1 Introduction

Flanges are components which joints two pipes together without the need to weld them together. The purpose is for easiness of fitting and ability to service sections of the pipeline. There are many types of flanges such as weld neck, slip on, threaded and etc with different flange face such as raised joint, flat face and ring type (Didik, 2017). Between the flanges, a layer of gasket is placed to ensure tightness and prevent loss of containment. However, due to the closed air environment, there is a high possibility of crevice corrosion occurring especially at the flange face in contact with the gasket surface. Material investigation showed that the chemical composition and mechanical properties of the flange were all in accordance with the corresponding parameter requirements, and the corrosion phenomenon was mainly attributed to $CO_2$ corrosion. High temperature and high medium flow rate also had a big influence on the acceleration of the corrosion process. Corrosion of the sealing groove end face was attributed to galvanic corrosion, the corrosion potential difference between the flange and gasket was the main reason for the galvanic corrosion (Nan et al., 2023).

Currently there are no methods of detecting FFC. It is only discovered during maintenance or when a loss of containment (LOCA) occurs. PAUT has been proposed as the technique to be able to detect FFC and could potentially reduce down time of production.

## 2 Methods

A model of a carbon steel flange was developed using a CAD software as dimensional accuracy is required to achieve reliable results. The model is then imported into the CIVA UT 2023 version in 3D format. The flange used in this simulation is made of carbon steel with weld neck and a raised face with 8 inches face diameter. This model is based on the readily available flange specimen which will be used to validate this simulation results. The inspection parameters are then selected based on the range that has been decided based on the relevant codes and standards such as ASME BPVC 2023. The probe selected is 5L16A10 with a SA10-0L wedge attached. Sectorial scanning is utilised to ensure sufficient coverage while the optimized resolution shall be determined from the simulation results in accordance to the interval range input. A side drilled hole reflector with diameter of 5 mm was placed at the raised face inner surface.

The inspection strategy is to utilise surfaces that are accessible to contact of a probe. There are two areas which are accessible which are the flange neck and thickness. In this study, simulations were developed to obtain the amplitude response from flat bottom holes with different depths from the surface of flange face.

## 3 Results and Discussion

The model has been successfully developed in 3D format and with the inspection setup visualised as in Figure 1. The model also shows the beam profile and provides information on coverage of scan.



Figure 1: Model of flange inspection setup with a side drilled hole (red) and indication of beam coverage (green)

When the probe is positioned at the flange thickness, it was found that indication from the flat bottom hole appears on the sectorial scan as in Figure 2. Therefore detection of reflectors at the flange face is possible when the probe is placed at this position.

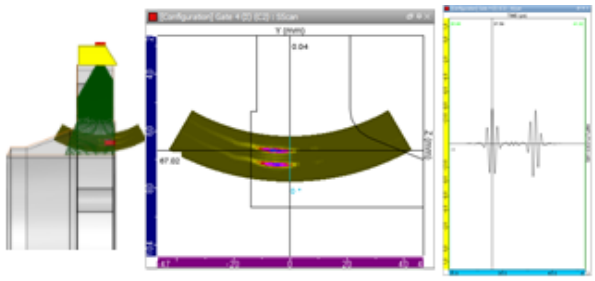


Figure 2: Indication from reflection of waves from the flat bottom hole

Due to the placement of holes for bolt fittings on the flange, there are several areas that are inaccessible for inspection when the probe is placed at the flange thickness. Therefore, another approach was required for full coverage of flange face inspection. For flanges with weld necks, the probe is able to be placed at the weld neck. Thus, areas that do not have coverage when the probe is placed on the flange thickness can be overcome.

In Figure 3, when the probe is placed at the weld neck and the beam steered to the flange face, it is found that the echo amplitude response from a flat bottom hole with 2 mm depth and 5 mm diameter can be detected. When the depth of the flat bottom hole is increased, the echo amplitude response from the hole increased.

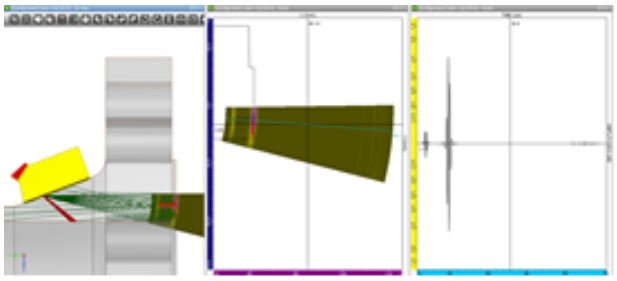


Figure 3: Indication from reflection of waves from the 2 mm depth flat bottom hole

In Figure 4, when the probe is placed at the weld neck and the beam steered to the flange face, it is found that the echo amplitude response from a flat bottom hole with 2 mm depth and 5 mm diameter can be detected.

It shows that detection of flat bottom holes are feasible using both of this scan strategies. The next step would be to validate the simulation using actual inspection. Successful validation would enable various dimension of flanges to be simulated to without the need for actual flanges to be validated.

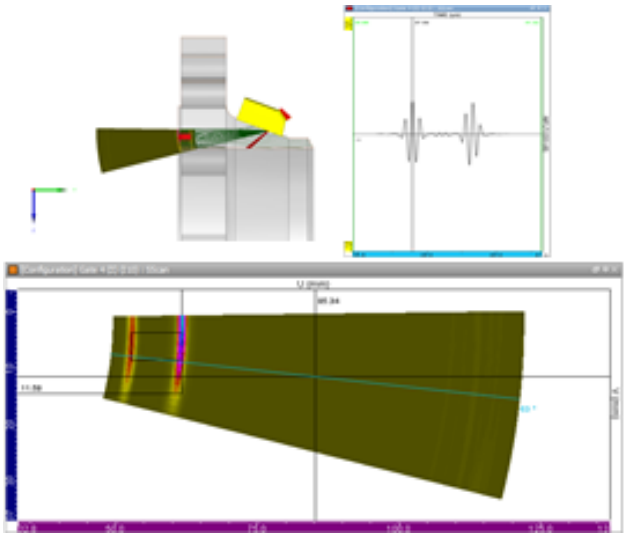


Figure 4: Indication from reflection of waves from the 2 mm depth flat bottom hole

## 4 Conclusion

Simulating inspection of flanges for detection of FFC using CIVA simulation software has been demonstrated to be useful in this research. Inspection parameters can be optimised while ensuring high POD.

## References

F. A Didik. 2017. Phased array ultrasonic testing for internal corrosion detection on the flange joint. *Proceedings Indonesian Petroleum Association Forty First Annual Convention Exhibition*, IPA17-83-F.

J. Nan, L. Changliang, W. Peng, Z. Lijuan, and F. Chun. 2023. Corrosion cause analysis of a surface pipeline flange. *Journal of Physics: Conference Series*, 2468 012171.

Individual Research Contribution Review, 2024: 327–328
*ISSN: 3083-922X*

# Emissivity Evaluation Using Thermography for Different Composites

**Asyraf Arif Bin Abu Bakar**
Industrial Technology Division, Malaysian Nuclear Agency
43000 Kajang, Selangor
asyrafarif@nm.gov.my

## Abstract

Thermal emissivity is a critical material property, significantly influencing heat transfer and energy efficiency in various applications. This study evaluates the emissivity of composites, including aluminum, Kevlar/Kenaf hybrids, fiberglass, and carbon fiber-reinforced polymers (CFRP), using thermographic methods within the framework of non-destructive testing (NDT). Results demonstrate the versatility of thermography for emissivity characterization, with Kevlar/Kenaf hybrids exhibiting the highest emissivity (0.89), making them ideal for high-radiation applications. The findings underscore the relevance of NDT in composite material evaluation, suggesting future avenues for expanding this approach.

**Keywords:** composites, emissivity, NDT, thermography

## 1 Introduction

Thermal emissivity is a fundamental parameter in determining a material's efficiency in emitting thermal radiation. Its significance spans industries such as aerospace, automotive, and renewable energy, where optimized heat management is crucial. Traditional methods for emissivity measurement often require invasive and time-intensive procedures, limiting their applicability in sensitive or high-precision environments.

Non-destructive testing (NDT) techniques, particularly infrared thermography, offer an efficient and non-invasive alternative for evaluating thermal properties (Maldague, 2001). By integrating thermography into emissivity studies, this research aims to enhance the understanding of composite materials' radiative behavior and support their selection for advanced applications, such as heat shields, thermal insulation, and energy systems.

## 2 Methods

The experimental methodology consisted of several key steps. First, the setup involved using an infrared camera, a thermal probe, and a heat gun as shown in Figure 1. Emissivity settings were adjusted by heating the objects to steady-state temperatures at least 10°C above the ambient temperature. The contact temperature was measured, and the emissivity values were fine-tuned to ensure alignment between the infrared camera readings and the contact measurements (E1933-14, 2019).

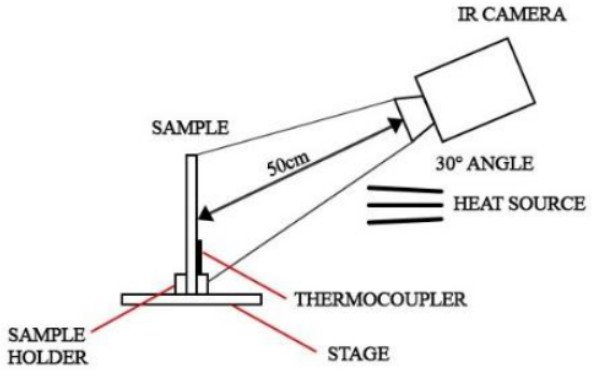



Figure 1: Experimental Setup

Environmental parameters were carefully controlled, with an ambient temperature maintained at 24°C, relative humidity at 30%, and a reflective angle of 30°. The samples were positioned 50 cm away from the camera lens to ensure accurate thermal imaging. The tested materials included various composites, such as Kevlar-Kenaf hybrids, CFRP, aluminum and fiberglass.

Thermal data were collected for each material in three trials to ensure reliability. The emissivity values obtained from these trials were then averaged to provide a consistent and representative measurement for each composite material.

## 3 Results and Discussion

The emissivity results for the tested materials are summarized in Table 1.

Table 1: Average Emissivity for Different Composites

| Material | Avg. Emissivity |
|---|---|
| Kenaf/Kevlar | 0.89 |
| CFRP | 0.80 |
| Fiberglass | 0.76 |
| Aluminium | 0.20 |

Thermal emissivity is a fundamental parameter in determining a material's efficiency in emitting thermal radiation.

Its significance spans industries such as aerospace, automotive, and renewable energy, where optimized heat management is crucial. Traditional methods for emissivity measurement often require invasive and time-intensive procedures, limiting their applicability in sensitive or high-precision environments.

Non-destructive testing (NDT) techniques, particularly infrared thermography, offer an efficient and non-invasive alternative for evaluating thermal properties. By integrating thermography into emissivity studies, this research aims to enhance the understanding of composite materials' radiative behavior and support their selection for advanced applications, such as heat shields, thermal insulation, and energy systems.



Figure 2: From left Aluminum and Fiberglass

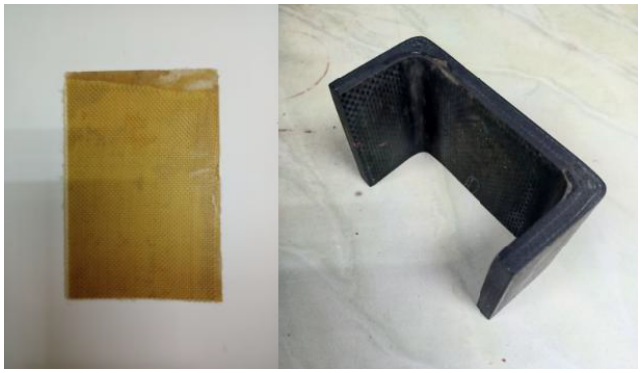


Figure 3: From left Kenaf/Kevlar and CFRP

The layered structure of hybrid materials, such as Kevlar-Kenaf, enhances their radiative heat emission capabilities. On the other hand, the lower emissivity values of aluminum suggest limitations in radiative heat transfer, favoring its use in reflective or low-radiation applications.

## 4 Conclusion

This study demonstrates the application of thermography as a non-destructive testing (NDT) method for evaluating the thermal emissivity of composite materials. The results highlight the technique's effectiveness in differentiating materials based on their emissivity, providing insights into their thermal performance without the need for invasive procedures. Kevlar/Kenaf composites exhibited the highest emissivity, making them suitable for high-radiation thermal applications, while CFRP and fiberglass demonstrated versatility for moderate heat transfer requirements. Aluminum's low emissivity indicates its potential for reflective or low-radiation applications.

## References

ASTM Standard E1933-14. 2019. Standard test methods for measuring and compensating for emissivity using infrared imaging radiometers. *ASTM International*.

X.P.V Maldague. 2001. Theory and Practice of Infrared Technology for Non-Destructive Testing. *John Willey Son Inc. New York*.

Individual Research Contribution Review, 2024: 329–330
*ISSN: 3083-922X*

# A Preliminary Characterization of Graphene-Enhanced Aluminium: Effects on Hardness and Electrical Resistance

**Azlan Shah Nerwan Shah @ Nintin**
Industrial Technology Division, Malaysian Nuclear Agency
43000 Kajang, Selangor
azlanshah@nm.gov.my

## Abstract

This study evaluates the impact of graphene (G) enhancement on the electrical and mechanical properties of aluminium (Al), concentrating on three sample types: pure aluminium, aluminium with 0.15% graphene (Al + 0.15% G), and aluminium with 0.25% graphene (Al + 0.25% G). Results indicated that hardness soared with increasing graphene content, while electrical resistance reduced, indicating improved conductivity. However, no significant hardness difference was seen between pure aluminium and Al + 0.15% G, suggesting a threshold amount for efficient reinforcing. Overall, the findings highlight graphene's promise as an improvement material for aluminium, delivering greater hardness and conductivity, with implications for electrical wiring and advanced materials. Further study is needed to enhance graphene amount and processing processes.

**Keywords:** aluminium, graphene, hardness, resistance

## 1 Introduction

In today's world, the importance of energy efficiency and environmental sustainability is growing, leading to a heightened emphasis on finding alternative materials to replace traditional ones. Copper (Cu) is widely preferred for electrical wiring due to its exceptional conductivity and reliability. Nevertheless, due to the expensive price of copper and its heavy nature, researchers and industries have been investigating alternative materials such as aluminium (Al) for wire applications. With its advantages of lightweight properties, resistance to corrosion and recyclability, aluminium emerges as a viable candidate for replacing copper as conductor materials. However, there is a limitation to Al when compared to Cu, as its electrical conductivity and mechanical strength are significantly lower. Consequently, a substantial improvement in the electrical and mechanical properties of aluminium can be attained by incorporating reinforcing phase materials such as graphene into the aluminium matrix. Graphene, one of the allotropic types of carbon with very high electrical and thermal conductivity and mechanical strength, creates great opportunities for designing and producing new materials. Graphene has good physical properties including strength, electrical conductivity and thermal conductivity and stable chemical properties. By incorporating graphene into aluminium, it is expected that the electrical conductivity and mechanical strength of the aluminium can be enhanced, making the aluminium-graphene mixed alloy a potential candidate for wire cable material in future.

## 2 Methods

The influence of graphene enhancement on the electrical and mechanical properties of aluminium were evaluated using three sample types: pure aluminium (Al), Al with 0.15% graphene, and Al with 0.25% graphene. The samples were prepared by melting Al granules at 680 °C before adding the graphene powder, to ensure optimal dispersion. The molten mixture was then cast into specimens for mechanical testing and molded into wire for electrical resistance testing. Mechanical properties were tested using the Vickers hardness test, where a diamond indenter delivered a particular load, and the resulting indentation dimensions were measured to calculate the Vickers hardness number (HV). Electrical properties entailed measuring resistance using a Keithley Source Meter, which supplied a constant current to determine voltage across the samples.

## 3 Results and Discussion

Table 1 shows the result of hardness and resistance value for respective samples. The results of this research demonstrate a definite association between graphene content and the mechanical and electrical properties of aluminium (Figure 1). Specifically, the hardness of the aluminium samples revealed a substantial rise with the addition of graphene. This enhancement could be owing to the reinforcement effect of graphene, which is recognized for its exceptional strength and rigidity. The integration of graphene into the aluminium matrix likely increases the load-bearing capacity and overall structural integrity of the material, leading to better hardness values.

Table 1: Hardness and resistance value of samples.

| Sample | Hardness (HV) | Resistance (kΩ) |
|---|---|---|
| Pure Al | 28.9 | 1.28 |
| Al + 0.15% G | 29.0 | 1.04 |
| Al + 0.25% G | 54.7 | 0.98 |

However, it is crucial to highlight that no significant variation in hardness was seen between the pure aluminium and the aluminium with 0.15the lower amount of graphene does not adequately enhance the mechanical properties in a statis-

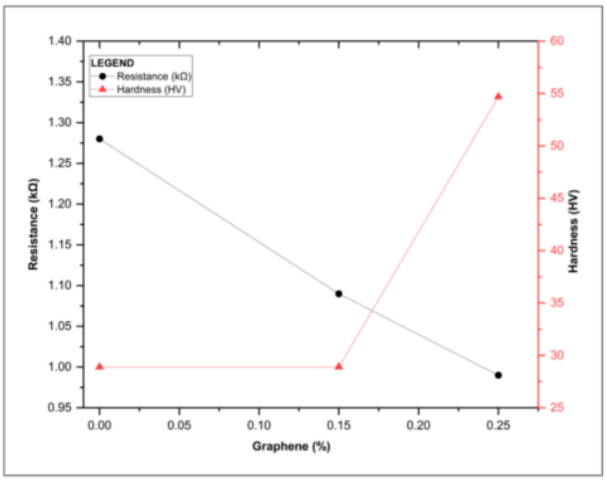



Figure 1: The trend of resistance and hardness with different amounts of graphene in Al samples.

tically significant manner compared to pure aluminium. It is possible that a threshold amount is necessary for graphene to impart significant gains in hardness.

Interestingly, whereas the hardness continuously increased with higher graphene amounts, the electrical resistance of the samples demonstrated a decreasing tendency with increasing graphene content. This shows that the inclusion of graphene promotes greater electrical conductivity within the aluminium matrix. Graphene's high conductivity enables for enhanced electron mobility, which is useful for applications needing efficient electrical performance. The research demonstrated only a modest decrease when graphene was introduced to the aluminium matrix, particularly at the 0.15%. This slight reduction may imply that while graphene begins to boost conductivity, the effect is not evident until a larger amount is obtained, such as in the 0.25% graphene sample. The small change in resistance at lower graphene levels implies that the distribution and interaction of graphene inside the aluminium matrix are significant elements controlling its conductivity.

## 4 Conclusion

In summary, the data illustrate the twofold benefit of graphene reinforcement: greater hardness and higher electrical conductivity. However, the lack of significant changes between pure aluminium and the 0.15% graphene sample underlines the need for more study into the appropriate amount of graphene required to generate major benefits. Future studies could focus on adjusting the graphene content further or exploring other processing procedures to maximize the benefits of graphene in aluminium composites, particularly for use in electrical wiring and high-performance materials.

## References

İrfan Ay and Sare Celik. 1999. Comparison of properties of friction and diffusion welded joints made between the pure aluminium and copper bars. *BAÜ Fen Bilimleri Enstitüsü Dergisi*, 1(2):88–102.

D.D.L. Chung. 2001. Materials for thermal conduction. *Applied Materials Science: Applications of Engineering Materials in Structural, Electronics, Thermal, and Other Industries (1st ed.).Boca Raton: CRC Press.*

X. Cui, Y. Wu, G. Zhang, Y. Liu, and X. Liu. 2017. Study on the improvement of electrical conductivity and mechanical properties of low alloying electrical aluminum alloys. *Composites Part B: Engineering*, 110(6):381–387.

T. Knych, A. Mamala, P. Kwaśniewski, G. Kiesiewicz, B. Smyrak, G. Gnie lczyk, A. Kawecki, K. Korzeń, and E. Sieja-Smaga. 2022. New graphene composites for power engineering. *Materials (Basel)*, 15(3):715.

R. Sharma, K. Sharma, and B.K. Saraswat. 2023. A review of the mechanical and chemical properties of aluminium alloys aa6262 t6 and its composites for turning process in the cn. *Materials Today: Proceedings. United Kingdom: Elsevier Ltd.*

Individual Research Contribution Review, 2024: 331–332
*ISSN: 3083-922X*

# In Situ Synthesis and Deposition of Palladium Nanoparticles on Gas Diffusion Layers via Gamma Radiolysis for Cathode Electrodes in Proton Exchange Membrane Fuel Cells

**Choo Thye Foo**
Industrial Technology Division, Malaysian Nuclear Agency
43000 Kajang, Selangor
ctfoo@nm.gov.my

## Abstract

This study investigates gamma radiolysis technique for synthesizing and depositing palladium (Pd) nanoparticles on gas diffusion layers (GDLs). The Pd-coated GDLs were then used to fabricate MEAs, which were evaluated for their single-cell performance. The fabricated PEMFCs with Pd-loaded GDLs successfully generated potential and produced electricity, with the PEMFC with a Pd loaded GDL prepared using a 0.05 M Pd precursor solution and 50 KGy dose achieved performances comparable to the PEMFC with commercial gas diffusion electrodes (GDEs). This study represents the first demonstration of a functional PEMFC using a novel gamma radiolysis-synthesised Pd catalyst GDL as the cathode electrode.

**Keywords:** In situ synthesis, palladium, nanoparticles, gamma radiolysis, gas diffusion layer, PEMFC

## 1 Introduction

In previous research, we successfully synthesised and deposited palladium (Pd) nano particles onto graphene oxide (GO) (Choo et al., 2023b) and carbon nanotubes (CNT) (Choo et al., 2023a) using gamma radiolysis. The resulting materials were used as electrocatalysts for oxygen reduction reaction (ORR), and excellent electrochemical performance was reported in half cell tests. Given the excellent electrocatalytic performance of Pd nanoparticles and the simplicity of the gamma radiolysis technique, this method was proven viable for preparing catalyst electrodes for the MEA in PEMFCs. This study employed gamma radiolysis to synthesise and deposit Pd nano particles onto gas diffusion layers (GDLs) to create catalyst electrodes. The resulting catalyst electrodes were fabricated into MEAs, and their single-cell performance was evaluated.

## 2 Methods

A precursor solution with a total volume of 50 mL was prepared by mixing isopropyl alcohol (IPA, 99.8%, HmbG Chemicals) and ultrapure water (resistivity of 18.3 MΩ, Synergy Water Purification System) in a 1:1 vol ratio, along with a precise amount of palladium chloride ($PdCl_2$, R&M Chemicals). This mixture was stirred vigorously in a glass container until all solid components were wholly dissolved.

A gas diffusion layer (GDL), measuring 3 cm x 3 cm, was subsequently immersed in the precursor solution. Three distinct concentrations of the precursor solution—0.05 M, 0.005 M, and 0.0005 M Pd—were prepared for the study. Before gamma irradiation using a Co-60 source, the solutions were purged with nitrogen gas ($N_2$) for 15 min. The gamma irradiation was conducted at a dose of 50 kGy with a dose rate of 2 kGy per hour. Following irradiation, the GDLs were extracted from the solutions, thoroughly washed with ultrapure water, and dried in an oven at 80°C for 2 h. In producing the membrane electrode assembly (MEA), the anode layer utilised a commercially available gas diffusion electrode (GDE) featuring a 60% Pt/C catalyst loading of 0.5 mg/cm$^2$, sourced from the Fuel Cell Store. The cathode layer was constructed using the synthesised GDL. Both the anode and cathode layers possessed an active area of 2.5 cm x 2.5 cm. Nafion 212 membranes were employed as the proton exchange membrane (PEM). During the assembly of the MEA, the cathode and anode layers were positioned on the top and bottom surfaces of the PEM, respectively. The layers were then subjected to hot pressing at 30 bar and 120°C for 3 min to ensure the effective fusion of the layers into a cohesive MEA. Following assembly, the MEA was integrated into a single-cell test setup. During testing, hydrogen and oxygen gases were introduced into the cell at flow rates of 0.08 L/min and 0.16 L/min, respectively. The single cell's polarisation curve and maximum power output were obtained using the Fuel Cell Monitor Pro U104 (H-Tec Education) and Fuel Cell Monitor 3.4 data acquisition software. An MEA consisting of GDEs (60% Pt/C catalyst loading of 0.5 mg/cm$^2$) for the cathode and anode layers was also fabricated for comparative analysis.

## 3 Results

Fig. 1 shows the polarization and power curves of the PEMFC using commercial GDEs (60 loading of 0.5 mg cm$^{-2}$) for both the cathode and anode catalyst electrodes. The PEMFC with commercial GDEs recorded an open circuit voltage (OCV) of 0.782 V and a maximum power density of 12.28 mW cm$^{-2}$. The PEMFC with MEAs incorporating Pd-loaded GDL, prepared with 0.05 M Pd precursor solution, recorded an OCV of 0.763 V and a maximum power density of 8.20 mW cm$^{-2}$. These values are comparable to those obtained from the PEMFC with commercial GDEs.

For the PEMFC with MEAs incorporating Pd-loaded GDLs prepared with a 0.005 M Pd precursor solution. Despite using ten times less concentrated Pd precursor solution, the PEMFC

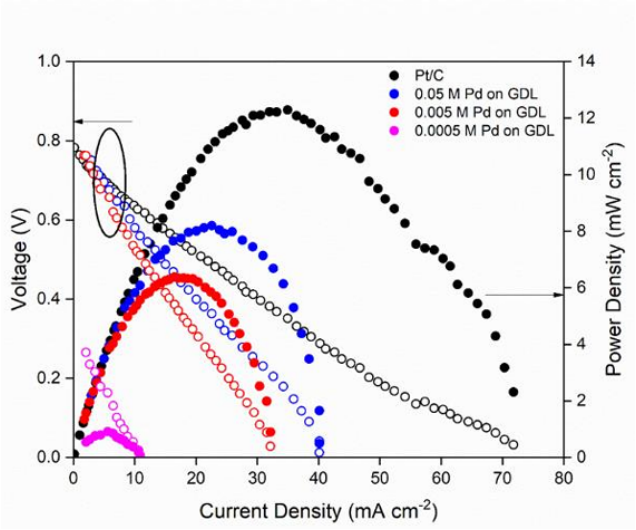



Figure 1: Polarization and power curves of the PEMFC with commercial GDE (60% Pt/C catalyst) and PEMFCs with various synthesised-Pd GDL as cathode electrodes.

only recorded a slight reduction in OCV and maximum power density compared to the PEMFC prepared with a 0.05 M Pd precursor solution. Specifically, the PEMFC achieved an OCV of 0.751 V and a maximum power density of 6.38 mW $cm^{-2}$. The PEMFC prepared with a 0.0005 M Pd precursor solution, achieved an OCV of 0.266 V and a maximum power density of 0.92 mW $cm^{-2}$, which are the lowest values among all the PEMFCs with Pd loaded GDL.

## 4 Discussion

Table 1 summarises the catalyst loading, OCV, maximum current density, and maximum power density of the PEMFCs. Among the PEMFCs with MEAs incorporating Pd-loaded GDLs, the one prepared with a 0.05 M Pd precursor solution recorded the highest maximum current density of 40.13 mW $cm^{-2}$. Interestingly, despite having a much lower amount of Pd, the PEMFC with a Pd-loaded GDL prepared with a 0.005 M Pd precursor solution still recorded a respectable maximum current density of 32.15 mW $cm^{-2}$. This suggests that catalyst loading can be compensated using smaller catalyst particles. Smaller particles typically have a higher surface area-to-volume ratio, increasing the active surface area for reactions. This can enhance catalytic activity even with a lower overall mass of catalyst. Additionally, well-dispersed smaller particles can improve the uniformity of the catalyst layer, potentially leading to better performance.

Table 1 also shows that although the Pd loading of 0.67 $mg/cm^2$, achieved using the 0.05 M Pd precursor solution, exceeds the 0.5 $mg/cm^2$ catalyst loading of the commercial Pt/C GDE, its maximum current density remains lower. This can be attributed to the superior performance of the Pt/C catalyst, where Pt particles are highly dispersed on a high-surface-area carbon support. This dispersion significantly increases the number of exposed Pt active sites, enhancing the catalytic efficiency without needing a large amount of Pt. This suggests that the Pd-loaded GDL could be further improved by introducing high-surface-area carbon as the support for Pd particles, increasing the number of active sites available for catalysis and improving overall efficiency.

Table 1: The OCV, maximum current density and maximum power density of the PEMFCs

| **MEA** | **Loading** ($mg/cm^2$) | **OCV** (V) | $\mathbf{J_{max}}$ ($mA/cm^2$) | $\mathbf{P_{max}}$ ($mW/cm^2$) |
|---|---|---|---|---|
| Commercial GDE | 0.50* | 0.782 | 71.82 | 12.28 |
| GDL Pd (0.05 M) | 0.67 | 0.763 | 40.13 | 8.20 |
| GDL Pd (0.005 M) | 0.22 | 0.751 | 32.15 | 6.38 |
| GDL Pd (0.0005 M) | 0.12 | 0.266 | 10.91 | 0.92 |

*provided by the manufacturer

## 5 Conclusion

This study demonstrates the effectiveness of gamma radiolysis as a one-step, in-situ method for synthesizing and depositing Pd nanoparticles on GDLs, simplifying the MEA fabrication process. The fabricated PEMFCs with the Pd-loaded GDLs exhibited the ability to generate potential and produce electricity. This pioneering demonstration of a functional PEMFC utilising a gamma radiolysis-synthesized Pd GDL as the cathode electrode underscores the potential of gamma radiolysis as a promising and cost-effective approach for producing catalyst electrodes in PEMFCs.

## References

T.-F. Choo, N. Mat Zali, N.U. Saidin, and K.-Y. Kok. 2023a. Gamma radiolysis-synthesized carbon nanotube supported palladium as electrocatalyst for oxygen reduction reaction. *Electrocatalysis*, 14(3):418–428.

T.-F. Choo, N. Mat Zali, N.U. Saidin, K.-Y. Kok, and N. Azhar. 2023b. Gamma irradiation synthesis and modification of palladium supported on graphene oxide as oxygen reduction reaction electrocatalyst. *Chem. Phys. Lett.*, 830:140822.

Individual Research Contribution Review, 2024: 333–334
*ISSN: 3083-922X*

# Characterization of physico-chemical properties of gold nanoparticles

**Cik Rohaida Che Hak**
Industrial Technology Division, Malaysian Nuclear Agency
43000 Kajang, Selangor
rohaida@nm.gov.my

## Abstract

Particle size and size distribution are two of the most vital parameters of nanomaterials since their physical properties as well as applications are highly dependent on these key factors. The objective of this work is to study the particle size and size distribution of gold nanoparticles. Surface morphology analysis was carried out on microscopic images to observe the dimension of the AuNPs. The particle size, size distribution, polydispersity and the zeta potential of the gold solution was measured using zeta sizer. Elemental analysis was performed using energy dispersive X-Ray (EDX) spectrometer to determine the gold composition. FE-SEM results showed that gold nanoparticles were in spherical shape with the size in the range of 20– 40 nm. The zeta potential value was -23.3 mV indicating gold nanoparticles were not stable as dispersion in water, resulting in larger diameter and polydisperse because of agglomeration. EDX analysis confirmed the presence of AuNPs.

**Keywords:** Gold nanoparticles, particle size, polydispersity, nanomaterials.

## 1 Introduction

Gold nanoparticles (AuNPs) are composed of nanosized colloidal gold particles suspended in water or other liquids that come in various shapes such as spherical, rods, stars, cubes, triangles, clusters and shells with a unique set of properties and applications. These nanoparticles eexhibited unique optical, and electronic properties which can be fine-tuned to obtain desired effect by adjusting the size, shape, and surface chemistry (Acharya et al., 2017). There is a strong relationship between the morphology and dimensions of AuNPs and their potential applications (Allen et al., 2017). For example, rod-like structure AuNPs are widely used in the diagnosis and treatment of cancer (Allen et al., 2017; JHuang et al., 2012), spherical morphology is useful for antibacterial, antiviral, and catalytic activities, while triangular and prism-like structures are good for catalysis and sensing applications (Alabbad et al., 2014). The particle size and size distribution of AuNps can be measured using numerous techniques either via dry powders or dispersion. In this study, we used the latter technique using two methods; direct measurement on microscopic images and utilizing relationship between particles' behaviour and its size which implies an assumption of equivalent spherical size developed using a size-dependent property of the particle and relating it to a linear dimension. Equivalent spherical diameters are the diameters of spheres that have the same or equivalent length and volume as irregular particles themselves. For microscopic techniques we used scanning electron microscope field emitter type (FE-SEM) and for the equivalent spherical size we used zeta sizer with dynamic light scattering principles.

## 2 Experimental method

In this study, AuNPs were received from a university that requested physico-chemical characterization and analysis services in MTEG. The samples received were shown in figure 1a. For microscopic imaging and elemental composition analysis, the AuNPs solution was pipetted onto a glass cover slip and dried at room temperature as shown in figure 1b. Prior to analysis, the AuNPs specimen on cover slip was platinum coated using sputtering technique. For zeta sizer analysis, 1 uL of the AuNPs solution was diluted in 1mL of deionized water and was measured in a disposable capillary type cuvette using 630 nm laser. The microscopic analysis was performed with FE-SEM (Carl Zeiss, GeminiSEM 500) and the elemental composition was measured with EDX (Oxford Instrument, X-Max 80). Particle size, size distribution and zeta potential were determined by zeta sizer (Malvern, NanoZs).

## 3 Results and Discussion

### 3.1 Particle size

Figure 1c shows the surface morphology of AuNPs captured at different magnifications. It is clearly seen that the AuNPs are spherical and slightly agglomerated. The particle size was determined at 23.45 to 36.84 nm as shown in figure 1d. However, the average size of AuNPs calculated by zeta sizer is 121 nm, a lot larger than determined from microscopic image. This is explained by the high polydispersity value which is 0.6 and in agreement with the inhomogeneous particle size distribution as shown in figure 1e.

Furthermore, the surface charge of the AuNPS excerpt from the zeta measurement is negative and the zeta potential values are (-)23.3 mV. This low value of zeta potential indicates that the AuNPs dispersed in water is not stable, prone to agglomeration and this is agreed by the polydispersity value. This shows that the size determined using microscopic images are more reliable and precise than the hydrodynamic size measured using DLS technique.

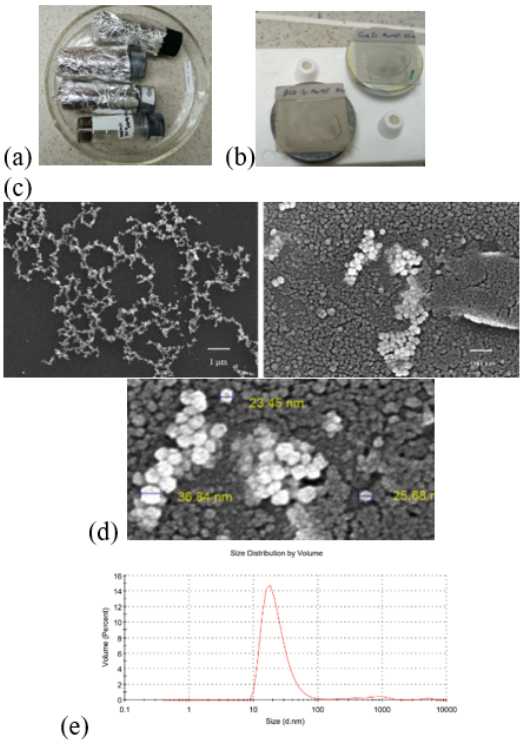



Figure 1: (a) Samples received; (b) samples ready for microscopic imaging; (c) electron images; (d) particle size of AuNPs; (e) particle size distribution of AuNPs.

### 3.2 Elemental composition

The elemental composition of gold was analyzed using elemental mapping mode. Figure 2a shows the EDX spectrum indicating the presence of Au in the sample. Other elements such as Si and Al are from the glass cover slip. The elemental mapping in figure 2b confirmed that the spherical shape particles are gold. The elemental composition in Table 1 indicates the concentration of Au is 5.16 wt.%. The major element is Si referring to the glass cover slip. These results confirmed that the spherical shape particles on the cover slip are AuNPs.

Table 1: Element composition of AuNPs

| Element | Wt.% | sigma wt.% |
|---|---|---|
| Au | 5.16 | 0.17 |
| Si | 35.87 | 0.10 |
| Al | 1.30 | 0.03 |
| Na | 1.23 | 0.03 |
| O | 56.45 | 0.13 |

## 4 Conclusion

The physico-chemical properties of AuNPs were successfully analyzed. The nanoparticles are conformed as Au element, spherical shape, sizes between 20–40nm, negative surface charges with 23.3mV zeta potential, unstable and agglomerated when dispersed in water.

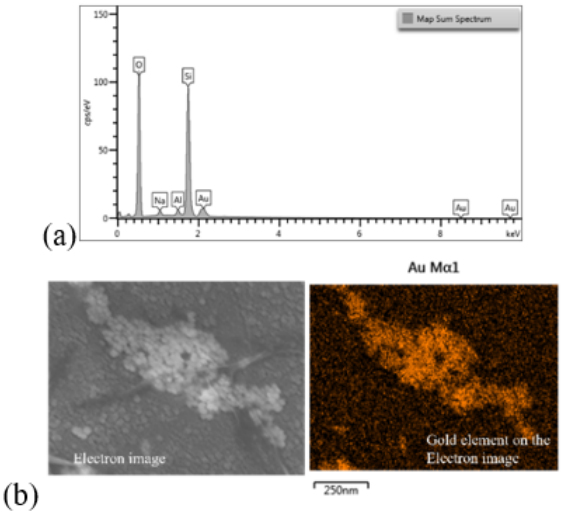



Figure 2: (a) EDX spectrum of AuNPs; (b) Electron image and element mapping of samples on the glass cover slip shows that it was gold.

## References

Gayathri Acharya, Ashim K. Mitra, and Kishore Cholkar. 2017. Emerging nanotechnologies for diagnostics, drug delivery and medical devices. *Micro and Nano Technologies*, pages 217–248.

Saad Alabbad, S.F. Adil, M.E. Assal, Mujeeb Khan, Abdulrahman Alwarthan, and M. Rafiq H. Siddiqui. 2014. Gold silver nanoparticles supported on manganese oxide: synthesis, characterization and catalytic studies for selective oxidation of benzyl alcohol. *Arab J Chem*, 7(6):1192–1198.

Joshua M. Allen, Junpeng Xu, Maria Blahove, Stephanie A. Canonico-May, Taylor J. Santaloci, and John W. Stone Martha E. Braselton. 2017. Synthesis of less toxic gold nanorods by using dodecylethyldimethylammonium bromide as an alternative growth-directing surfactant. *J Colloid Interface Sci*, (505):1172–1176.

Zhao JHuang, Yan Liu, Fangyun Xie, Yingchun Fu, Yong He, Ming Ma, Qingji Xie, and Shouzhuo Yao. 2012. Au-supported pt–au mixed atomic monolayer electrocatalyst with ultrahigh specific activity for oxidation of formic acid in acidic solution. *Chem Commun*, 48(99):12106–12108.

Individual Research Contribution Review, 2024: 335–336
*ISSN: 3083-922X*

IRCR

# Room Temperature Synthesis and Characterization of HKUST-1, Metal-Organic Frameworks (MOFs)

**E. M. Mahdi**
Industrial Technology Division, Malaysian Nuclear Agency
43000 Kajang, Selangor
mahdiezwan@nm.gov.my

## Abstract

In the present work, HKUST-1 has been synthesised at room temperature with 1:0, 1:1, and 0:1 ratios of ethanol and water. Various reaction conditions were explored to understand solvent and temperature effects. It was discovered that multiple precursors yielded products with various BET-specific surface areas. Therefore, the effect of water may be explained by the decrease in reaction rate with an increasing concentration of reactants. The XRD data and SEM analysis showed that both MOFs were crystalline in the product.

## 1 Introduction

Metal-organic frameworks (MOFs) are sponge-like materials that are crystalline and very porous and trap, store, and distribute gases. Their structures comprise metal ions and organic molecules called "linkers,". Beneficial properties, particularly selectivity and capacity, can be altered by selecting the appropriate metal and linker for the MOF (Kandiah, 2010; Sharanyakanth and Radhakrishnan, 2020). MOFs are coordinated compounds composed of metal ions correlated to organic molecules that are often rigid to produce one-, two-, or three-dimensional structures that can be porous. In the observation, these metals provide metallic coordination environments with various geometries. The development of coordination bonds between the metal ions and the organic linkers can also be reversible, which is possible because of the standard liability of metal complexes.

Chui et al. made the initial discovery of HKUST-1 (Hong Kong University of Science and Technology), one remarkable type of MOF, in 1999. The reported findings concern the synthesis, structure, and preliminary physical and chemical properties of HKUST-1, a highly porous open-framework metal coordination polymer $[Cu(TMA)(H_2O)_3]_n$. This polymer crystallises into face-centred cubic crystals with a massive square-shaped network of intersecting three-dimensional (3D) pores. The HKUST-1 framework comprises dimeric metal units linked together using benzene-1,3,5-tricarboxylate linker molecules. The paddle wheel unit, also known as the secondary building unit (SBU) of the HKUST-1 structure, is a structural motif often used to define the coordination environment of metal centres. Benzene-1,3,5-tricarboxylate linkers molecules connect two metal centres in the paddle wheel, four molecules. Two metal centres on the paddle wheel unit are linked by one water molecule when hydrated, which is usually found if the material is handled in the air.

## 2 Results and Discussion

The structures of the synthesised HKUST-1 are illustrated in Figure 1, where a (synthesised with 1:0 ethanol: water ratio), b (synthesised with 1: ethanol: water ratio), and c(synthesised with 0: 1ethanol: water ratio). It was observed that in Fig. 1a, HKUST-1 appear in octahedral and cubic. Figure 1b shows octahedral, cubic and monoclinic structures. The grain of the freshly prepared sample emerges from the crystalline crystal with sharp edges, and both have an uneven size of particles, which are in the range of an average length of 0.5-1.2 um for HKUST-1. Kareem et al. say that the process of crystallinity slows down when water is present during synthesis. Hence, the structures of b and c have a monoclinic crystal structure, which indicates the crystallisation of HKUST-1 is decreasing. A study by Kuen et al. shows that a low-temperature synthesis yields cubic crystals with sharp edges while a high-temperature synthesis yields spherical particles. The unreacted chemicals must be thoroughly washed out of the as-synthesized MOF before removal; otherwise, they will remain in the crystals. All the samples were characterised using X-ray diffraction (XRD).The diffraction peaks are present between two theta ranges, 5° and 20°; it was found that the highest peak formed at 1. 74° is the copper element (JCPDS card No. 96-230-0382). The intensity is higher than the band because of the increment in crystallinity. This is due to the presence of water during the synthesis of b and c, implying these materials' excellent crystallinity.

The maximum Langmuir-specific surface area (259 m2 g-1) was achieved for the HKUST-1. As given in Table 24.1, as the volume of ethanol increased, the Langmuir and BET-specific surface areas increased for HKUST-1. This figure is still much below the measurement made by Kuen et al. (1558 m2 g-1). Sample activation, or the elimination of amorphous or nonporous impurity phases, must be supervised for this problem. According to Kuen and his colleague, it is possible to post-treat a material to eliminate guest molecules trapped inside its pores after manufacturing. The following average pore size values for the three samples indicate that the samples created in this study are microporous materials. The three HKUST-1 samples' pore textural characteristics became identical with increasing ethanol volume. Typically, the produced MOFs include many solvent molecules such as H2O, ethanol, DMF, and the like. They are employed to manufacture MOF

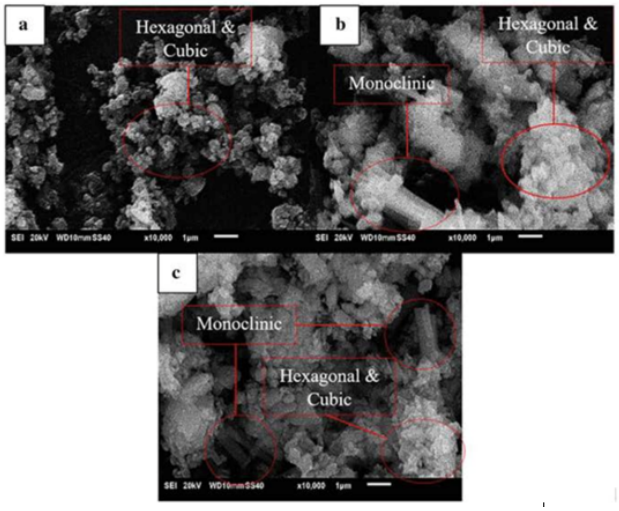



Figure 1: SEM images of HKUST-1

or reactant compounds or by-products within their pores. The pore channels may also get blocked due to these impurities. Therefore, various procedures can be used to remove those solvent molecules or impurities.

## 3 Conclusion

In the current study, HKUST-1 was synthesised. To comprehend the effects of solvent, SEM, XRD, and BET analyses were performed to explore its characteristics. It was observed that several precursors created a product with diverse surface areas. It was observed that HKUST-1 has an irregular shape and various nanostructures, including octahedral, cub octahedral, and monoclinic structures. The samples were analysed by X-ray diffraction, and the patterns of synthesised HKUST-1 exhibited and implied good crystallinity of these materials. The results of the average pore size of all samples show that the samples generated in this work are microporous materials.

## References

Mathivathani Kandiah. 2010. Synthesis and stability of tagged 010-66 zr-mofs. *Chem. Mater*, 22(24):6632–6640.

P.S. Sharanyakanth and M. Radhakrishnan. 2020. Synthesis of metal-organic frameworks (mofs) and its application in food packaging: a critical review. *Trends Food Sci. Technol.*, 104(June):102–116.

Individual Research Contribution Review, 2024: 337–338
*ISSN: 3083-922X*

# Bibliometric Analysis of Research on Hydrometallurgy Process on Rare Earth Extraction Based on SCOPUS Database

**Fazila binti Said**
Industrial Technology Division, Malaysian Nuclear Agency
43000 Kajang, Selangor
fazila@nm.gov.my

## Abstract

The purpose of this study is to reveal the status of scientific publications on simulation of hydrometallurgy process on rare earth elements from the past to the present in terms of bibliometric indicators. A total of 442 publications on the subject between the years 2000–2023 were found in the search using keywords after various screening processes. Publications were revealed through descriptive and research field mapping based on network analyses (bibliometric analysis). In the study, the distribution of publications by years and citation numbers, the most published journals on the subject, the most local cited publications, the most prolific authors, affiliations, and countries were examined. In addition, the cooperation between the authors and countries that publish on the subject was mentioned and a network structure was created for the relations between the keywords. It has been determined that research in this field has progressed and the number of publications and citations has increased over the years. As a result of the bibliometric analysis, it was concluded that the most influential countries in the field for both samples are China, USA, and Australia. The Chulalongkorn University and Central South University as the most prolific institutions in terms of the number of publications. According to the keyword co-occurrence analysis, rare earths, rare earth elements, leaching, extraction and recycling keywords stand out in the field of hydrometallurgy process on rare earth elements. This paper helps in objectively understanding the efficient separation techniques of rare earth elements, various types of acid leaching and provides a valuable reference for the simulation software use in metallurgy process.

## 1 Introduction

Since the first issue of Hydrometallurgy 45 years ago, Science Direct has accumulated over 4500 articles related to this field by the end of 2019. Researchers find it increasingly challenging to manually gather, organize, and analyze such vast amounts of information through traditional reading methods. Consequently, scientists are turning to computer-based solutions (Jensen et al., 2006; Lok, 2010) to address this issue. One effective approach is the use of scientific knowledge mapping, which originated from a seminar organized by the National Academy of Sciences of the United States in 2003. This method involves analyzing, structuring, and visually presenting the vast literature data for easy comprehension with the assistance of computer technology. Several science mapping analysis tools are available, such as Sci2, SciMAT, VOSviewer, and CiteSpace. In this study, the authors have chosen to employ the knowledge tool, CiteSpace, to capture and identify the development trends of hydrometallurgy based on the articles available in the database.

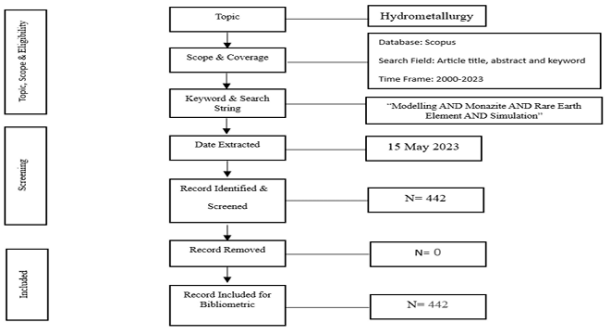



Figure 1: Flow chart for conducting Bibliometric Evaluation

## 2 Results and Discussion

In this study, the distribution of publications on hydrometallurgy on rare earth elements in the Scopus database by years and citation numbers was examined. The results are shown in Figure 2. Analyzing Figure 2, it is seen that basic research on hydrometallurgy started in 2010. For this reason, publications made between 2010–2023 were included in the scope of bibliometric analysis.

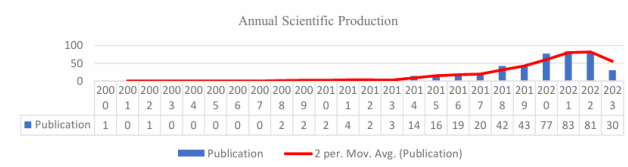



Figure 2: Annual Scientific Production

Table 1 shows the 10 most prolific countries/regions were examined in the study. Publications by countries/regions factor, it was evaluated with 4 indicators, namely the total number of publications (TP), the total number of citations (TC), the average number of citations per publication (TC/TP), the single

Table 1: The 10 Most Prolific Countries

| Rank | Country/Region | TP | TC | TC/TP | SCP | MCP |
|---|---|---|---|---|---|---|
| 1 | China | 76 | 2465 | 32.43 | 60 | 16 |
| 2 | USA | 38 | 740 | 19.47 | 35 | 3 |
| 3 | Egypt | 35 | 320 | 9.14 | 34 | 1 |
| 4 | India | 22 | 502 | 22.82 | 17 | 5 |
| 5 | Iran | 22 | 228 | 10.36 | 19 | 3 |
| 6 | Canada | 19 | 402 | 21.16 | 17 | 3 |
| 7 | Germany | 19 | 598 | 31.47 | 13 | 6 |
| 8 | Brazil | 13 | 126 | 9.69 | 10 | 3 |
| 9 | Korea | 13 | 268 | 20.64 | 10 | 3 |
| 10 | France | 12 | 172 | 14.33 | 7 | 5 |

country production (SCP) and the multiple country production.

These indicators, which are widely used in bibliometric analysis, reflect the general status of publications by country.

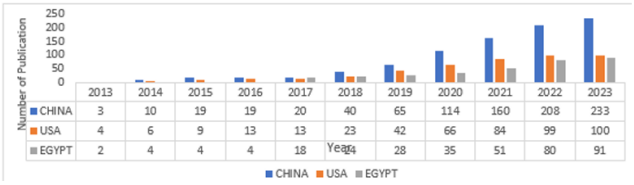



Figure 3: Annual publications from the top three countries

Figure 3 shows three most productive countries in hydrometallurgy research are China, the United States of America, and Egypt, the numbers of publications these countries were compared for the period of 2013–2023.

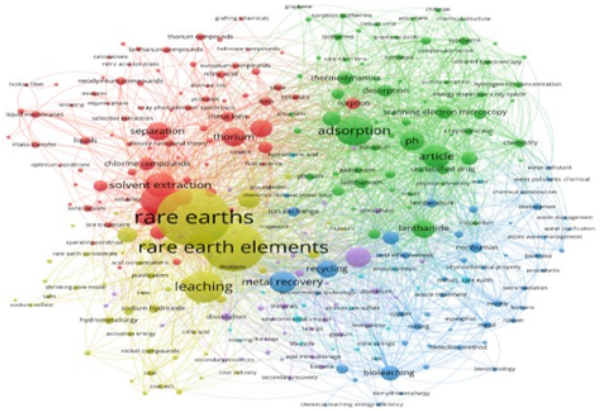



Figure 4: The co-occurrence network of keywords

Figure 4 shows the most discussed topic, and the yellow areas show the updated topics. It is seen that many keywords such as rare earths, rare earth elements, adsorption, leaching, extraction, pH, lanthanide are frequently used according to the size of the circle and the number of links. Therefore, in general, rare earths study are carried out with extraction (cluster 1), adsorption (cluster 2) and metal recovery (cluster 3). These keywords are concepts that have been studied together with other clusters. They have been determined as the most frequently encountered keywords.

## 3 Conclusion

This paper presents a systematic analysis of the research progress of hydrometallurgy based on the information collected from 422 articles published in 2000–2023. This study fills the gap in applying bibliometric methods to rare earth research to some extent, and the results can help researchers in the hydrometallurgy field to quickly determine the research frontier and the overall situation.

## References

L. J. Jensen, J. Saric, and P. Bork. 2006. Literature mining for the biologist: from information retrieval to biological discovery. *Nature reviews genetics*, 7(2):119–129.

C. Lok. 2010. Speed reading. *Nature*, 7280(463):416–418.

Individual Research Contribution Review, 2024: 339–340
*ISSN: 3083-922X*

# Bibliometric Analysis on the Research Trends of Dust Explosions from the Year 2001 to 2023

**Fazila binti Said**
Industrial Technology Division, Malaysian Nuclear Agency
43000 Kajang, Selangor
fazila@nm.gov.my

## Abstract

Highly destructive combustible dust explosions, which is prone to cause secondary explosion, has been a concern in industrial processes. To understand the current development and status of research on dust explosions, 244 publications related to dust explosions from 2001 to 2023 were indexed through the Scopus database. All the articles resulted in the Scopus database were then screened based on selected keywords, open access, year, subject area, document type, publication stage, source type and language. The selected articles were then further sorted by availability to access the full article and issues regarding dust explosions. RStudio were used to visualize and analyze the collected literature information. China, United States of America, and United Kingdom are the major contributors in this field. Henan Polytechnic University, Delft University of Technology and National Institute for Occupational Safety and Health are the top instutions that are carrying out the dust explosion research. In the year 2021 is the most annual scientific production regarding dust explosions followed by the year 2022 and 2017. Journal of Loss Prevention in the Process Industries, Powder Technology, Journal of Hazardous Materials, and Process Safety and Environmental Protection are the major sources of publications related to dust explosions. The research topic of dust explosions mainly evolves into three aspects: explosion characteristics and influencing factors, explosion suppression, and types of dust particles. New research hotspots have appeared related to gas–dust hybrid mixtures, nanomaterials, and powder suppressants. The results can help researchers in the dust explosion field to quickly determine the research frontier and the overall situation.

## 1 Introduction

More academics are incorporating bibliometrics into their fields of study since it offers a comparatively objective perspective on the findings of researchers. For instance, Wang and Lu (Huang et al., 2020) used bibliometrics to determine the most important books, popular frontiers, and important research areas in the area of big data research. Using bibliometrics, Huang et al. (Wang and Lu, 2020) examined the emergency evacuation literature from 2008 to 2018.

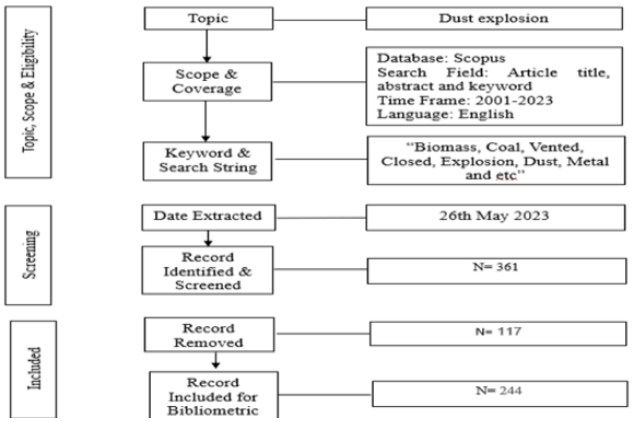



Figure 1: Process flow chart for conducting bibliometric evaluation.

## 2 Results and Discussion

The annual number of publications in the topic of dust explosions is statistically analyzed, which helps to understand the field's evolution through time. Figure 1 displays the cumulative results and the annual number of published articles. The development of linked research can be roughly split into three phases, as indicated in Figure 1: the initial phase, the fluctuating growth stage, and the rapid development stage.

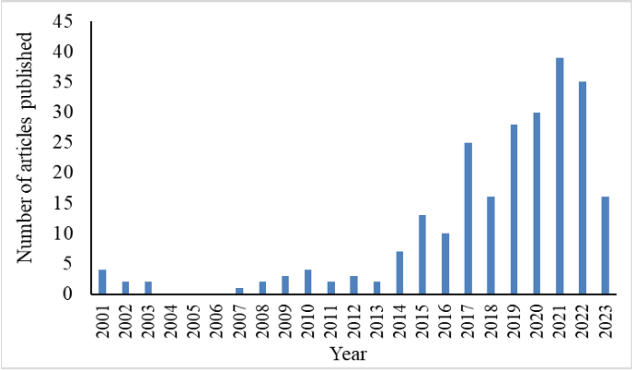



Figure 2: Trends in the yearly publication of studies on dust explosions.

The number of publications from China, United States of America, and United Kingdom were compared for the years 2007 through 2023 because these three nations are the most productive in dust explosion research. Figure 2 shows that

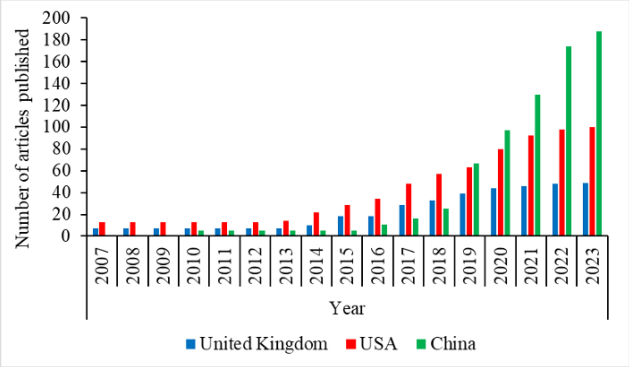



Figure 3: Articles each year on dust explosion research from the top three countries.

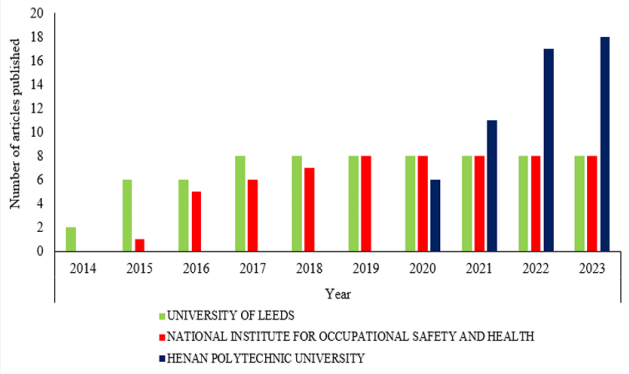



Figure 4: Top 3 institutions in dust explosion research.

there were significantly more documents published in China between 2011 and 2021. Moreover, China produces the highest number of publications annually regarding dust explosion followed by United States of America, and United Kingdom.

In the period from 2001 to 2023, a total of 340 institutions were actively involved in dust explosion research. Figure 4 illustrates the total number of articles published by the top three institutions over the years.

There are 49 keywords related to the subject. The size of the circle shows the most discussed topic. In Figure 5, the visualization of term clusters pertaining to dust explosion research reveals the presence of two prominent main clusters. The first cluster is centered around experimental dust explosion research, encompassing a range of terms related to various aspects of conducting experiments, studying explosion characteristics, and analyzing dust behavior during explosions. The second main cluster revolves around terms related to humans and explosions, suggesting a strong emphasis on research concerning human factors, safety protocols, and the impact of dust explosions on individuals and the environment.

## 3 Conclusion

These trends and research focuses collectively demonstrate the evolving nature of the field of dust explosion research, with researchers exploring innovative approaches and advanced technologies to address the challenges posed by dust explosions and improve safety measures in various industrial settings.

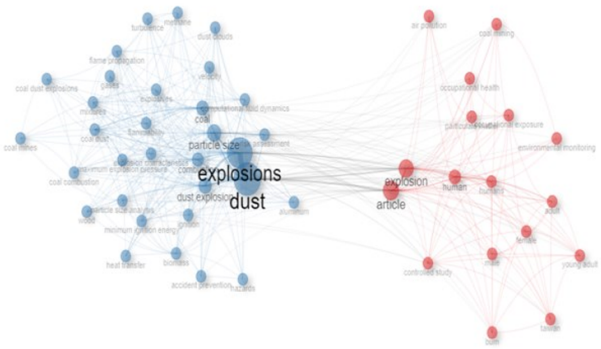



Figure 5: Terms in average publication year on dust explosion research

## References

J. Huang, J.X. You, H.C. Liu, and M.S. Song. 2020. Failure mode and effect analysis improvement: a systematic literature review and future research agenda. *Reliab. Eng. Syst. Saf.*, 199(12).

W.H. Wang and C. Lu. 2020. Visualization analysis of big data research based on citespace. *Soft Comput.*, 24:8173–8186.

Individual Research Contribution Review, 2024: 341–342
*ISSN: 3083-922X*

# Small Angle X-ray Scattering Technique (SAXS) Analysis of BAM (Cat. Number 2005) Standard Sample

**Hafizal Yazid**
Industrial Technology Division, Malaysian Nuclear Agency
43000 Kajang, Selangor
hafizal@nm.gov.my

## Abstract

We have demonstrated the significant use of the Small Angle X-ray Scattering (SAXS) technique in elucidating the surface area of BAM standard sample. This sample is typically used for calibrating the BET instrument. The SAXS instrument resolution is 0.035 $nm^{-1}$, known as q min. The success of the technique was dictated by its capability to reveal a comparable result with the BET technique.

**Keywords:** SAXS, BAM standard sample, BET

## 1 Introduction

Surface area is vital in most of the chemical reaction. Knowing this information will allow materials scientists to improve their experimental work effectively. A sample scatters X-rays, and the resulting scattering patterns reveal important details about the material's atom or molecular structure. Further calculation will reveal the surface area of the sample.

## 2 Methods

The samples were characterised using a point collimation SAXS instrument from Anton Paar. The X-ray source was Ni-filtered CuK$\alpha$ radiation with a wavelength of 0.154nm. The instrument was operated at 50 kV and 1 mA, coupled with an Eiger CMOS 2-D detector. The scattering vector q covered from 0.035 to 5$nm^{-1}$. All measurements were corrected for sample thickness, transmission, and background scattering.

Table 1: Samples

| No. | Sample |
|---|---|
| 1 | BAM standard sample |

## 3 Results

Figure 1 shows the result of BAM sample. Isotropic scattering profile was found for this sample.

Figure 2 shows the result of 1D profile after data reduction. From this profile, Porod region was selected for the calculation of the surface area (Yazid et al., 2022).

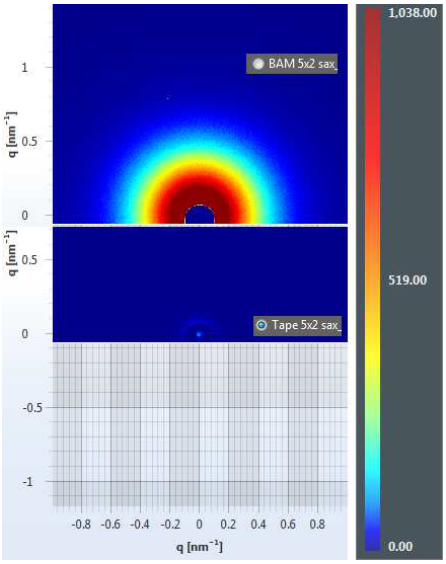



Figure 1: 2D scattering profile of tape (holder) & BAM sample (SAXS)

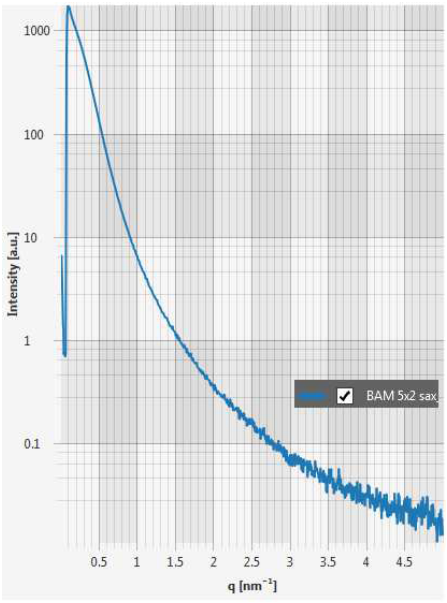



Figure 2: 1D scattering profile of BAM sample (SAXS) after subtraction.

## 4 Conclusion

In conclusion, SAXS and BET results are very close. Thus, both are complimentary methods that are essential for char-

| Table 2: Surface area of BAM by SAXS and BET | |
|---|---|
| Samples | Specific surface area ($m^2/g$) |
| SAXS | 107.6 |
| BAM (reference value) by BET | 105.0 |

Table 2: Surface area measurement results by SAXS and BET

acterising a variety of materials and providing information on their specific surface area.

## References

Hafizal Yazid, Umar A. Anwar, A. Siti Zaubidah, M. Nurulizzati, Maria Sabtu, M. Julie Andrianny, M.Z. Nurazila, M. Rawi M. Zin, R.S. Chen, and Sahrim Ahmad. 2022. A combined method to probe the behaviour of the filler in polymer blend nanocomposites via x-ray diffraction and thermal measurement. *Nano-Structures Nano-Objects*, 32:100906.

Individual Research Contribution Review, 2024: 343–344
*ISSN: 3083-922X*

# Development of Gamma Densitometry Scanning System for Multiphase Column Analysis

**Hanafi Ithnin**
Industrial Technology Division, Malaysian Nuclear Agency
43000 Kajang, Selangor
hanafi_i@nm.gov.my

## Abstract

This study presents the development of an automated gamma densitometry scanning system for analyzing multiphase columns. The system uses a gamma-ray source, such as Ba-133 or Cs-137, paired with a 1-inch sodium iodide (NaI) scintillation detector mounted on motorized actuators for synchronized vertical and horizontal scanning. Controlled via LabVIEW, the setup provides real-time data acquisition and precise phase distribution measurements. The system was tested on a 50 mm inner diameter, 2 m high column containing carborundum and varying flows of water and air, successfully capturing detailed density profiles. These results demonstrate the system's capability to enhance the understanding and optimization of hydrodynamic behavior in multiphase processes.

**Keywords:** Gamma densitometry, Multiphase flow analysis, Density profiling.

## 1 Introduction

Gamma densitometry is a powerful non-invasive technique used to characterize the phase distribution within multiphase systems, such as those found in chemical reactors, distillation columns, and fluidized beds. By determining the density variations across a column, gamma densitometry provides valuable insights into hydrodynamic behavior and process efficiency. The density profiles reveal how different phases such as solids, liquids, and gases are distributed and interact within the column, offering a clear understanding of flow patterns and phase transitions. This information is critical for diagnosing issues like maldistribution, channeling, or uneven holdup, which can hinder optimal performance (Toukan et al., 2024; Rahman et al., 2023). As a non-invasive technique, gamma densitometry not only enables accurate evaluation of multiphase systems but also supports real-time monitoring and optimization of industrial processes. The objective of this study is to develop a fully automated gamma densitometry scanning system that integrates precision motion control and data acquisition to enhance the accuracy and efficiency of column analysis.

## 2 Methods

The proposed system comprises a gamma-ray sealed source, a sodium iodide (NaI) scintillation detector, motorized linear actuators, and a data acquisition and control unit. The gamma-ray source, which can be varied between isotopes such as Barium, Ba-133 or Cesium, Cs-137 based on the column size and required penetration depth, is paired with a 1-inch Sodium Iodide, NaI scintillation detector. Both the source and detector are mounted on motorized linear actuators, allowing synchronized vertical and horizontal scanning across the column for comprehensive density profiling. This system was inspired by Gamma-Spider system (Abdullah et al., 2015). Figure 1 illustrate the gamma densitometry system developed in this study.

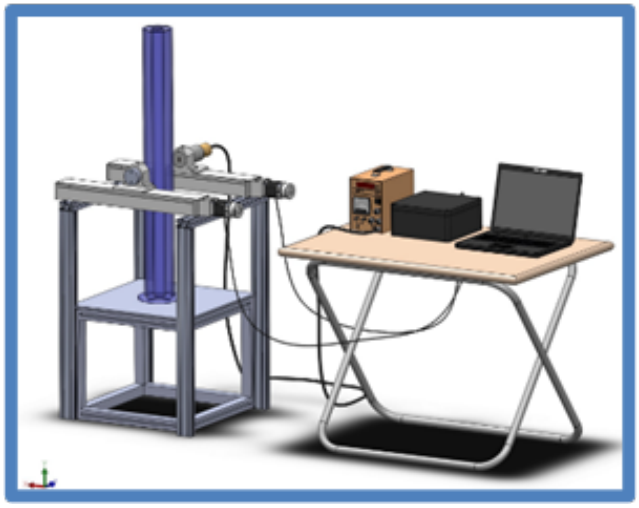


Figure 1: Illustration for gamma densitometry system.

The detector is connected to a Ludlum 2200 scaler rate meter, which processes the radiation counts. Both the motors and the scaler rate meter are interfaced with a PC or laptop via a control system designed in LabVIEW. This software facilitates automated control of the scanning process, allowing the system to execute predefined scanning patterns while simultaneously acquiring data in real-time. The automation streamlines the workflow, reduces human intervention, and minimizes error. Figure 2 shows the GUI of the control system developed using LabVIEW software.

## 3 Results

### 3.1 System Performance

To evaluate the system's performance, a multiphase column with a 50 mm inner diameter (ID) and a height of 2 m was

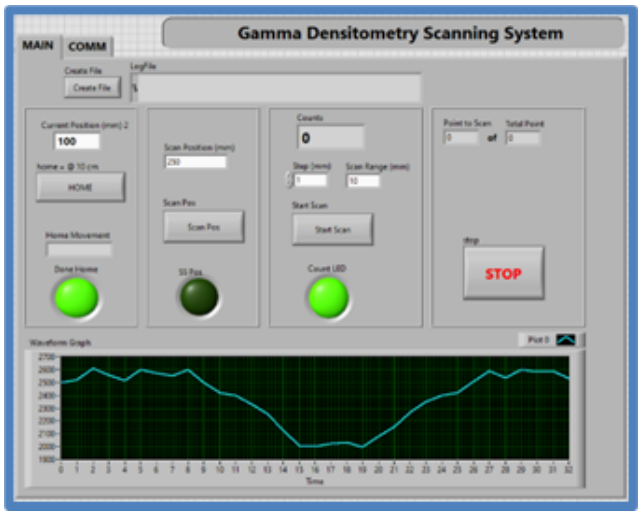



Figure 2: The graphical user interface for Gamma Densitometry control system.

scanned. The column contained carborundum particles as the solid phase, with varying flows of water and air to simulate multiphase conditions. A Ba-133 gamma-ray source was selected for this experiment due to its suitability for penetrating the column dimensions.

The scanning process involved dividing the column into multiple planes along its height, with the gamma-ray source and detector traversing horizontally across each plane. The synchronized motion of the actuators ensured consistent alignment of the source-detector pair during data acquisition. Density profiles obtained from the scans revealed distinct regions corresponding to the distribution of solid, liquid, and gas phases. For instance, areas of high density indicated zones predominantly occupied by carborundum and liquid, while regions of lower density corresponded to air-filled spaces. Figure 3 demonstrates the results from the one of the measurements made using this system. These results demonstrated the system's capability to capture detailed phase distributions and highlight flow dynamics within the column.

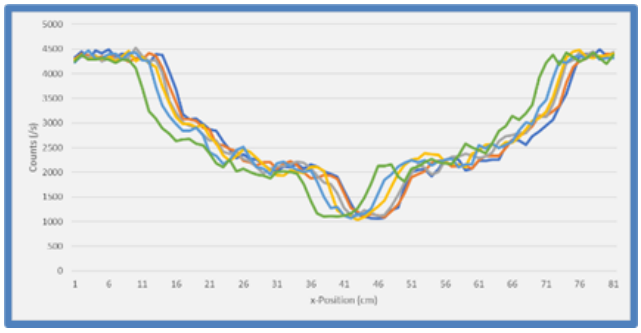



Figure 3: The gamma-ray profile plotting example acquired from the developed gamma densitometry system.

## 4 Conclusions

In this study, three different arrangements of the iSPECT system were modeled and simulated to assess their capability in mapping static single and two point-source images. The findings indicate that all three arrangements successfully detect the single point source at the origin (0,0), 5 cm from the origin (5,10), and near the edge of the ROI at (0,10). Among the three systems, the reconstructed images of the hexagonal arrangement exhibit less noise. Concurrently, despite the presence of noise, the nonagonal arrangement demonstrates superior overall image resolution compared to the other two systems. Based on these results, it can be concluded that the nonagonal arrangement of the iSPECT system is optimal for imaging a 20 cm ROI for point-source detection. Further studies will explore the detection process with different radiotracer sources and source shapes to enhance the applicability of the iSPECT system in industrial environments.

## References

J. Abdullah, H. Hassan, M. R. Shari, M. M. Ibrahim, N. Yussup, H. Ithnin, and A. A. Mahmood. 2015. Development and implementation of a portable nucleonic computed tomography system for engineering inspection. *Jurnal Teknologi*, 77(17).

M. F. A. Rahman, H. Ithnin, N. H. Azahar, A. A. Mahmod, H. Hasan, and N. Abdullah. 2023. Density profile comparison of different build-up using gamma transmission. *Journal of Nuclear and Related Technologies*, pages 19–25.

A. Toukan, A. Jasim, V. Alexander, H. AlBazzaz, and M. Al-Dahhan. 2024. Experimental investigation of liquid holdup in a co-current gas–liquid up flow moving packed bed reactor with porous catalyst using gamma-ray densitometry. *Chem Engineering*, 8(3):54.

Individual Research Contribution Review, 2024: 345–346
*ISSN: 3083-922X*

# The IAEA Technical Cooperation Project RAS1027 - Improving the Utilization of Nuclear Techniques for Cultural Heritage Characterization, Consolidation, and Preservation

**Hishamuddin Husain**
Industrial Technology Division, Malaysian Nuclear Agency
43000 Kajang, Selangor
hishamuddin@nm.gov.my

## Abstract

The IAEA Technical Cooperation Project RAS1027, titled "Improving the Utilization of Nuclear Techniques for Cultural Heritage Characterization, Consolidation, and Preservation" has started in 2022. It focuses primarily on enhancing nuclear and radiation techniques for the characterization and preservation of cultural heritage. This regional project is designed to support the use of nuclear techniques for cultural heritage characterization, consolidation, and preservation. About 21 IAEA Member States in the region involved in this project. These included Bangladesh, Cambodia, Indonesia, Iran, Iraq, Jordan, Malaysia, Mongolia, Myanmar, Oman, Pakistan, Philippines, Sri Lanka, Thailand, and Vietnam. The project's activities include regional training courses/workshops, scientific visits, meetings, and fellowships.

**Keywords:** Cultural heritage, characterization, preservation and consolidation

## 1 Introduction

Nuclear technology has proven to be safe to use, non-destructive, and accurate in the characterization and preservation of tangible cultural heritage artifacts. In the Asia and the Pacific region, awareness of the use of nuclear techniques for cultural heritage preservation has increased. Currently, several nuclear and radiation facilities within the region can facilitate the use of these techniques for cultural heritage characterization, consolidation, and preservation. With the variety of cultural heritage artifacts from different materials, various nuclear techniques are needed to be explored. This regional project aims to improve the utilization of nuclear facilities for these purposes. The project aligns with the regional community's interest in broadening awareness of the cultures, histories, and values of the past. Furthermore, the project strategically contributes to the application of nuclear science and technology for a better regional community.

Through the implementation of the project, it is expected that the knowledge and technical experiences of the participating countries in applying nuclear techniques for cultural heritage purposes will be significantly enhanced. Additionally, end users can benefit from using nuclear technology in their work.



Figure 1: The Regional Coordination Meeting of RAS 1027 in Jakarta, Indonesia

## 2 Involvement of Malaysia

Under the IAEA RAS 1027, Malaysia has successfully conducted the IAEA Regional Training Course (RTC) On "The Application Of Nuclear Techniques For Characterization And Preservation Of The Artifacts Obtained From The Shipwreck" which was held in UNESCO Historical city of Melaka. At the national level, Malaysian Nuclear Agency and the Department of Museums Malaysia are working together with the Department of National Heritage and the Melaka Museums corporation (PERZIM) involving the agenda of training and identification of sites for demonstration. This has involved collaboration among three different ministries and one state government. Malaysia also participated in the Regional Training Course on Cultural Heritage: "From Excavation Site to Museum Display" organized by IAEA and the Jordan Atomic Energy Commission (JAEC) in Amman, Jordan.

Malaysian Nuclear Agency (Nuclear Malaysia) has strengthened the collaboration with the Department of Museums Malaysia and the Department of National Heritage involving several activities related to characterization of artifacts, organizing training workshop, joint exhibitions in outreach programs and joint publications. The outreach programs found to be an effective way of creating awareness and promoting the use of nuclear techniques to the public. Several states museums have shown their interest and started to request for training and characterization of their artifacts using nuclear techniques.

In the capacity building, Malaysia is ranked the highest number of participation in the project activities. The high contribution of capacity building participants from Malaysia is due to the involvement of local participants in the RTC in



Figure 2: Technical demonstration at shipwreck site during the Regional Training course in Melaka



Figure 3: The exhibition in conjunction to the International Museums Day 2024 in Penang. The outreach programs found to be an effective way of creating awareness and promoting the use of nuclear techniques to the public.

Malaysia as a host country.

In preservation of artifacts, Malaysia has successfully started to apply the gamma irradiation for disinfection of rare books at a small scale. We hope that the capacity will increase in the future. We also hope that we can further enhance our capability in the application of nuclear techniques in disinfection and consolidation with the supports from the IAEA. In characterization, there are several techniques which are commonly used. These include XRD, XRF, NAA, SEM/EDX, Neutron and X-ray imaging, as well as the other Non-destructive techniques (NDT) and the use of Ground Penetrating Radar (GPR) for surveying subsurface materials and structures.

## 3 Conclusion

RAS1027 project successfully accomplished planned deliverables since its inception in 2022. Malaysia has proven to be an active member state through involvement in several major activities designed in this project. Participation of Malaysia includes scientist, curator, conservator as well as archaeologist. There are member states with the advanced facilities such as synchrotrons. Through the existing networking, we need to gain knowledge of advanced characterization and analysis to obtain valuable and more accurate data. Considering the increased awareness of the importance of preserving cultural heritage, where the potential of nuclear and radiation techniques has not yet been fully explored, along with the new political and social situations worldwide and global environmental challenges, the member states' representatives recommend that the IAEA consider launching new projects in upcoming cycles.

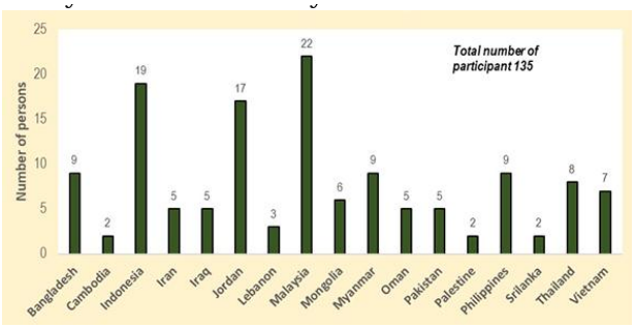



Figure 4: Distribution of capacity building by RAS1027 participating countries




Figure 5: Disinfected rare books using gamma irradiation at Sinagama facility in Malaysian Nuclear Agency

Individual Research Contribution Review, 2024: 347–348
*ISSN: 3083-922X*

# Acoustic Emission Analysis of Gate Valve Performance Using Machine Learning Clustering Techniques

**Ismail Bin Mustapha**
Industrial Technology Division, Malaysian Nuclear Agency
43000 Kajang, Selangor
ismail@nm.gov.my

## Abstract

The integrity of pipeline systems relies heavily on the performance of valves, which are critical components in fluid transport. However, faults within these valves can lead to significant financial losses due to fluid waste and adverse environmental impacts. This study explores the application of acoustic emission (AE) techniques, which utilize stress wave detection to identify discontinuities and assess valve performance. The research aims to investigate the relationship between acoustic emission parameters and the pressure differential across gate valves and to analyze experimental data using K-Means clustering and K-Nearest Neighbors (K-NN) methods facilitated by NOESIS software. By leveraging AE as a diagnostic tool, this study seeks to enhance the understanding of valve performance and leakage behavior, contributing to improved maintenance strategies and reduced environmental risks in fluid handling systems.

**Keywords:** Acoustic emission, Internal leakage, Gate Valve

## 1 Introduction

Valve leakage is a common challenge in industrial environments, leading to significant operational difficulties and financial repercussions. Despite advancements in valve technology, including those claiming to be "zero leakage" or "bubble tight," the reality is that these assurances may not guarantee absolute leak-proof performance. Leakage can manifest in two primary forms: internal and external. Internal leakage occurs when a valve, despite being fully closed, still allows the medium to escape from its outlet pathway. This failure often indicates issues such as improper sealing due to medium erosion, impurities, or wear. Even with the valve stem fully engaged, gaps may develop between the valve body and its components, resulting in fluid flow and undermining system integrity (Kinsler et al., 2000).

In contrast, external leakage happens during the operation of the valve specifically during opening or closing when the medium escapes through inadequate sealing at the interfaces, such as flanges or threaded connections. Factors contributing to external leakage include loose connections, wear on the valve body, and degradation of packing seals (Zhao and Yan, 2022). To effectively detect and assess these issues, the acoustic emission (AE) technique presents a promising non-destructive testing solution. By capturing and analyzing transient elastic waves generated by local energy releases in fluid leakage AE offers high sensitivity for diagnosing the condition of mechanical components (Gupta and Kumar, 2021). Research has demonstrated that AE signals correlate with fluid leakage, characterized by high-frequency stress waves induced by turbulence as fluids navigate through leaks. This innovative approach can enhance maintenance and operational efficiency in valve systems, ultimately leading to improved reliability and reduced environmental impacts (Smith and Lei, 2019).

## 2 Methods

The objective of this project is to detect leakage in a gate valve using acoustic emission (AE) techniques. This study focuses on employing AE as a non-destructive testing (NDT) method to identify leaks within the gate valve system. The AE testing employs continuous method. The continuous method captures all AE activity within a set time interval. Data acquisition and analysis are conducted using AEwin software for real-time waveform visualization and NOESIS for advanced pattern recognition and classification, enhancing the capability to analyze and interpret AE data effectively. For this study, four PZT (lead zirconate titanate) sensors strategically positioned on a galvanized pipe to monitor acoustic signals resulting from leakages. Sensor placements include positioning one sensor before the gate valve, two sensors directly at the valve, and one following the valve, ensuring comprehensive coverage of the potential leak sites. A pressure meter will be incorporated within the piping system to monitor water pressure accurately as the experiment progresses. The pipeline used will be filled with high-pressure water from a water pump, achieving a maximum pressure of 6 bar (600 kPa), while the gate valve will be gradually opened to induce controlled leakage conditions simulating real-world scenarios. As the pressure difference decreases, the amplitude continues to diminish. This observation indicates that the amplitude is directly proportional to the pressure difference associated with water flow leakage. The data analyzed comes from a sensor strategically placed at the point of leakage and is equipped with low-frequency capabilities.

## 3 Result and Discussion

This section discusses all the results obtained during the experiment. The analysis of the results was conducted using the AEwin software and NOESIS software, focusing on various

parameters that highlight the conditions and characteristics of the leakage detected in the gate valve.

The parameters analyzed include the percentage of leakage at the valves, which affects the flow of liquid within the pipeline. As liquid passes through the valves with internal leakage, it results in variations in amplitude measurements corresponding to different leakage rates. Specifically, the percentage of valve opening was significantly varied at 1.0 percent, 2.0 percent, and 3.0 percent. This range provides insights into the relationship between valve opening and the corresponding acoustic emission characteristics.

As the pressure difference decreases, the amplitude continues to diminish. This observation indicates that the amplitude is directly proportional to the pressure difference associated with water flow leakage. The data analyzed comes from a sensor strategically placed at the point of leakage and is equipped with low-frequency capabilities. Notably, the maximum amplitude recorded is 81, which corresponds to a maximum pressure difference range of 300-349 kPa (Figure 1).

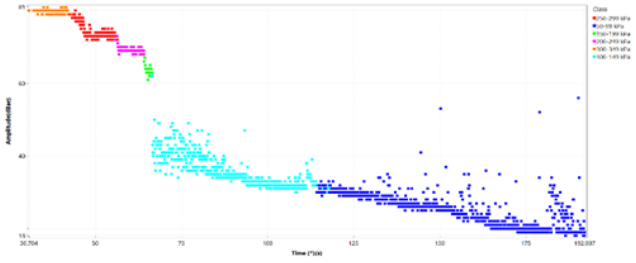


Figure 1: Analyzing Pressure vs Amplitude Relationships through K-NN Clustering at 1% Leakage

According to the data shown in Figure 2, the amplitude decreases as the pressure difference declines. This suggests a direct proportionality between the amplitude and the pressure difference in the context of water flow leakage. The values are derived from a sensor located precisely at the leakage point, utilizing low-frequency measurement capabilities. The graph indicates a maximum amplitude of 68, which corresponds to a maximum pressure difference range of 300-349 kPa.

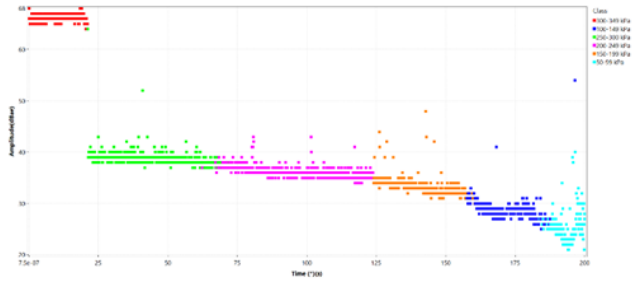


Figure 2: Analyzing Pressure vs Amplitude Relationships through K-NN Clustering at 2% Leakage

As a result shows in Figure 3, the pressure difference decreased, the amplitude continued to decrease. This shows that the amplitude is directly proportional to the pressure difference of the fluid flow leakage. The maximum value of

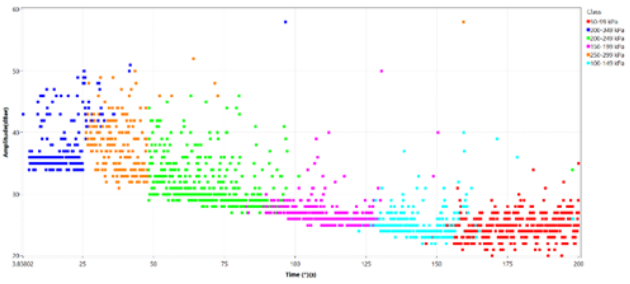


Figure 3: Analyzing Pressure vs Amplitude Relationships through K-NN Clustering at 3% Leakage

amplitude in this graph is 38, and the maximum pressure range is from 300-349 kPa.

## 4 Conclusion

This section summarized the results of the experiment conducted on leakage detection in gate valves, utilizing AEwin and NOESIS software for comprehensive analysis. The investigation focused on various parameters that illuminate the conditions and characteristics of leakage in the fluid flow through the valves. Key parameters included the percentage of leakage and valve opening, revealing a clear relationship between valve opening and acoustic emission characteristics. Specifically, the valve openings were systematically varied at 1.0 percent, 2.0 percent, and 3.0 percent, demonstrating how these variations impact the amplitude measurements associated with different leakage rates. Crucially, the data indicated that as the pressure difference decreases, the amplitude diminishes as well. This correlation suggests a direct proportionality between amplitude and pressure difference in fluid flow leakage scenarios. The experiments utilized a strategically positioned low-frequency sensor at the leakage site, with maximum recorded amplitudes of 81, 68, and 38 corresponding to pressure difference ranges of 300-349 kPa. Overall, these findings underscore the significance of monitoring acoustic emissions and pressure differentials in understanding and diagnosing leakage conditions within gate valves, offering valuable insights into the relationship between system parameters and leakage behavior in fluid systems.

## References

R. Gupta and S Kumar. 2021. Detection of leakage in hydraulic systems using acoustic emission techniques. *Journal of Sound and Vibration*, 490(115724).

L. E. Kinsler, A. R. Frey, A. B. Coppens, and J.V Sanders. 2000. Fundamentals of acoustics. *John Wiley Sons*.

J. P. Smith and X. Lei. 2019. Innovative techniques in acoustic emission for valve integrity assessment. *Proceedings of the International Conference on Acoustic Emission Testing*, pages 231–238.

Y. Zhao and X Yan. 2022. Acoustic emission monitoring of valve leakage: A review. *Journal of Petroleum Science and Engineering*, 215(110202).

Individual Research Contribution Review, 2024: 349–350
*ISSN: 3083-922X*

# Elemental Analysia Using XRF on Rare Books

**Izura Izzuddin**
Industrial Technology Division, Malaysian Nuclear Agency
43000 Kajang, Selangor
izura@nm.gov.my

## Abstract

Paper is one of the main components of rare books that should be studied. Understanding the properties of the paper used can provide valuable insights into the history of the book. In this study, XRF was employed to analyze the paper's properties. The elemental data obtained allows for the identification of the additives used. The main additive for the rare books paper is calcium carbonate ($CaCO_3$), while modern books primarily contain kaolinite ($Al_4Si_4O_{14}$).

**Keywords:** rare books, XRF

## 1 Introduction

Rare books, classified as those exceeding a century in age, represent irreplaceable and invaluable treasures, especially for preserving the nation's heritage. Gaining a comprehensive understanding of a rare book's core components such as the paper, pigments, and inks not only unveils valuable insights into its history but also elevates its intrinsic value as a historical artifact. This can be achieved by studying the material properties of the core component through physical characterizations. Moreover, understanding the material properties also plays a crucial role for effective preservation and conservation strategies to extend the rare books lifespan.

However, the challenge of physically characterizing rare books lies in ensuring that the methods are non-destructive and do not alter the original properties of the materials. Proper handling of these fragile items is essential, often requiring operators to spend more time on the characterization process. Moreover, limitations of the instruments, such as sample holder constraints, may restrict the types of characterizations that can be performed.

Paper production involves a wide range of additives, both organic and inorganic, that are mixed together. Each additive plays a specific role such as coating additives, sizing, wet and dry strength agents, chelating agents, colorants, optical brighteners and process chemicals (Ginebreda et al., 2012; Hubbe, 2004). Ultimately, the purpose of incorporating these additives is to improve the quality of the paper and optimize the efficiency and cost-effectiveness of the production process.

One viable method for analyzing element is X-ray fluorescence (XRF) characterization. While it is not commonly used for characterizing organic materials, it can effectively identify inorganic elements present in the paper, pigments, and inks. For this study, the XRF characterization only focused on the paper of the rare books.

## 2 Methods

XRF characterization was conducted on two rare books paper, labeled as Sample A and Sample B, which were randomly selected from the rare book collection of Department of Museums Malaysia. This book housed in Museum Taiping library. Additionally, a current book that used modern paper was labeled as a Reference to serve as a comparison with the two rare books. The characterization was performed using an EDXRF Shimadzu model EDX-7000. The analysis was carried out on the paper at two distinct locations: (i) one on the written portion and the other (ii) on the clean surface.

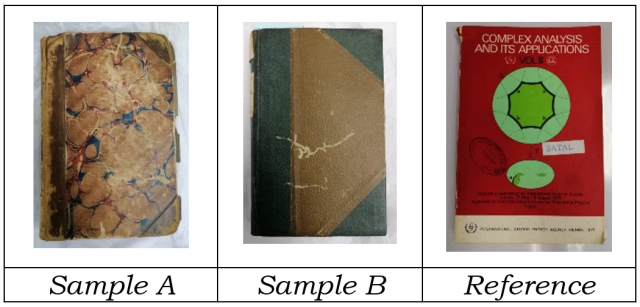



Figure 1: Image of the books

## 3 Results and Discussion

Tables 1, 2, and 3 display the results of XRF characterization for the Sample A, Sample B and Reference sample respectively. The data provided shows the percentage of elements present in the tested paper. Readings from two different spots for every sample did not show significant differences between them.

Table 1: XRF result for *Sample A*

| Element | Clean surface | On word |
|---|---|---|
| Ca | 67.178 | 66.910 |
| S | 27.899 | 27.778 |
| Cl | 2.464 | 2.584 |
| Fe | 1.363 | 1.410 |

The elements detected are additives used in papermaking, as XRF only identifies inorganic elements. This is due to

Table 2: XRF result for *Sample B*

| Element | Clean surface | On word |
|---|---|---|
| Ca | 34.634 | 36.223 |
| Cl | 22.171 | 21.393 |
| S | 11.092 | 8.922 |
| Fe | 9.794 | 10.571 |
| K | 8.265 | 9.303 |
| Mn | 4.596 | 4.982 |
| Hg | 2.790 | 1.910 |
| Si | 2.247 | 1.970 |
| Br | 1.405 | 1.334 |
| P | 1.039 | 1.003 |

Table 3: XRF result for *Reference*

| Element | Clean surface | On word |
|---|---|---|
| Si | 34.138 | 33.087 |
| Al | 22.418 | 22.113 |
| K | 9.074 | 9.240 |
| Fe | 7.875 | 7.754 |
| Cl | 6.103 | 6.463 |
| Ca | 6.040 | 6.052 |
| Ti | 5.805 | 5.728 |
| S | 4.599 | 5.444 |
| P | 2.288 | 2.398 |
| Cu | 0.537 | 0.558 |
| Ir | 0.295 | 0.293 |
| V | 0.158 | 0.170 |
| Rb | 0.157 | 0.146 |
| Os | 0.104 | 0.138 |
| Cr | - | 0.123 |

the fact that the primary material in paper production is pulp, which is cellulose, a type of organic material.

The total elements detected show that rare books paper contains fewer elements compared to modern paper. This can be attributed to the more complex modern paper production process, which benefits from advanced technology. In contrast, the production of rare books paper involved a simpler process with fewer additives. Both rare books show a high percentage of calcium (Ca) elements as displayed in Table 1 and Table 2 . This suggests that one of the main additives used is calcium carbonate ($CaCO_3$). It is typically used as a coating material. More specifically, $CaCO_3$ is used to grade paper according to specific requirements for opacity, brightness, smoothness, and strength. In line with the evolution of paper production, the use of $CaCO_3$ has decreased, as evidenced by the lower Ca content detected in the Reference sample, which is only around 6%. The high concentrations of silicon (Si) and aluminum (Al) in the reference sample suggest that the additive material used in the paper is kaolinite ($Al_4Si_4O_{14}$), which also serves as a coating agent, similar to $CaCO_3$.

## 4 Conclusion

Based on the XRF results, the evolution of papermaking can be inferred. However, this conclusion should be verified and supplemented with additional characterization techniques. Therefore, further analysis is required on the paper samples studied.

## References

A. Ginebreda, D. Guille´n, D. Barcelo, R. M. Darbra, and B. Bilitewski. 2012. Global risk-based management of chemical additives i: Production, usage and environmental occurrence. *Hdb Env Chem*, 18:11–34.

M .A. Hubbe. 2004. Pulping. *Chemical Additives*, pages 933–939.

Individual Research Contribution Review, 2024: 351–352
*ISSN: 3083-922X*

# Recovery of Cerium, Neodymium, Lanthanum and Thorium from Monazite

**Jacqueline Kones**
Industrial Technology Division, Malaysian Nuclear Agency
43000 Kajang, Selangor
jacqueline@nm.gov.my

## Abstract

Monazite contains phosphate, light rare earth elements (LREE) namely cerium (Ce), neodymium (Nd), and lanthanum (La) apart from other rare earth elements (REE) as well as thorium (Th) and uranium (U). REE can be separated from other elements and components found in monazite so that the elements can be used for other application.

**Keywords:** Rare earth, cerium, neodymium, lanthanum

## 1 Introduction

Monazite contains light rare earth elements (LREE) namely cerium (Ce), neodymium (Nd), and lanthanum (La) apart from other rare earth elements (REE) as well as other related elements. Processing monazite involves a series of steps that eventually separate the elements found the raw monazite. This study will demonstrate the overall process to retrieve Ce, Nd, La and Th concentrate from alkali digestion of monazite.

Separation of the elements is essential to ensure maximum concentration of the element of interest by minimizing the presence of other elements. Then, purification can follow after. RE separation can be done by using the selective precipitation method. It means, the elements will be removed through precipitation from the solution by neutralisation at a certain pH level. This method can also be used to separate REEs from thorium and uranium that are also present in monazite. Another way that can be used to separate REE is to manipulate the property of the oxidation state. REEs have the oxidation state of +3 but in the case of cerium, it can also form +4 oxidation state. This is due to Ce have four valence electrons while others have three. Hence, Ce can be taken away without affecting other elements. It is important to remove Ce from the mixed RE compound before other elements can be purified because Ce presence will interfere the purity of the final products (T. and C.A., 2016).

## 2 Methods

Details in the process used in this study were as described below:

### 2.1 Alkali Digestion

Ground monazite (>325 mesh) reacted with sodium hydroxide 50% (w/v) at 120 °C for four hours. The slurry product then added with water to dissolves the phosphate. While hot, the phosphate solution filtered and more hot water added while filtering to rinse any leftover loose phosphate and excess sodium hydroxide. The solution obtained then kept in a storage container, while the solid particle was dried in the oven.

### 2.2 Acid Leaching and Separation of Thorium

The dried digested particles in 2.1 then was reacted with concentrated hydrochloric acid. The yellow pregnant leach solution formed then added with water to dilute the solution and filtered from the undigested particles. Ammonia solution then added until pH 5.8 to precipitate thorium and uranium. After filtration, more ammonia solution added into the acidic solution to precipitate the remaining elements until not further precipitation observed – usually at around pH 10.5. At this step, the precipitate is identified as rare earth hydroxides ($RE(OH)_3$ which was then washed to remove excess ammonia and dried at 120 °C.

### 2.3 Separation of Ce

The dried $RE(OH)_3$ obtained in 2.2 was dissolved in concentrated nitric acid. Water then added to dilute the solution. 5% sodium carbonate ($Na_2CO_3$) solution added to adjust the pH to pH 3. Potassium permanganate solution added while continue to add $Na_2CO_3$until the purple colour did not disappear. After that, more $Na_2CO_3$ added to precipitate the remaining Ce (IV) until pH 4. $Ce(CO_3)_2$ concentrate produced then filtered and dried.

### 2.4 Separation of Nd and La

Filtrate from 2.3 then added with ammonia solution until pH 7.5 to precipitate Nd. After filtering the Nd concentrate, more ammonia solution was added to retrieve La concentrate. Both precipitates were filtered, washed to remove excess ammonia and dried.

### 2.5 Analysis and characterisation

The precipitates formed were analysed by using ED-XRF for its elemental constituents.

## 3 Results

Analysis of the elemental concentration obtained from each precipitate formed were as described in Table 1 while the precipitates obtained were illustrated in Figure 1 below:

Table 1: Elemental concentration of the precipitates obtained

| **Precipitate** | **Main elements** | **Other elements** (> 7 %) |
|---|---|---|
| pH 5.8 (Th concentrate) | Th (>50%); Fe (>15 %); Nd (> 7 %) | Cl, Ba, Ce, Ba, U, Se, P, Ca, As, Yb, Sc |
| Ce (IV) carbonate | Ce (>60 %), Nd (>15 %), Mn (>10 %) | Y, P, Cl, Dy, Tm, Ca |
| $Nd(OH)_3$ | Nd (>50 %), Sm (> 15 %), Y (>7%) Gd (>7%) | La, V, Dy |
| $La(OH)_3$ | La (>50 %) Nd (>25%) Pr (>10 %) | P, Cl, Ca, Y |

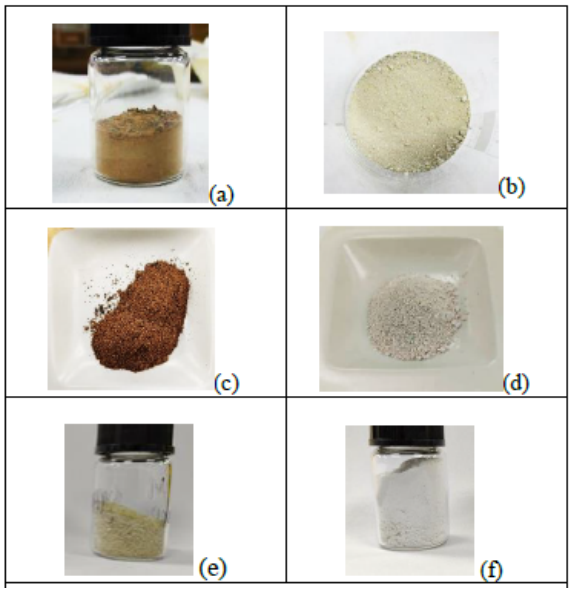



Figure 1: (a) Th concentrate obtained at pH 5.8; (b) Mixed $RE(OH)_3$ before Ce separation; (c) Ce (IV) concentrate; (d) Mixed $RE(OH)_3$ after Ce separation; (e) $Nd(OH)_3$ concentrate; (f) $La(OH)_3$ concentrate

## 4 Discussion

Presence of Th and U in monazite has made this mineral to be identified as radioactive mineral. Fortunately, Th and U can be separated through selective precipitation by neutralization as patented by Calkins (Calkins, 1952). This method was proven to be able to separate Th from Malaysian monazite. Once these elements can be separated, the RE concentrate is non-radioactive.

In separating Ce from mixed RE concentrated, Ce (III) was oxidized by addition of $KMnO_4$ solution. At this step, basic $Na_2CO_3$ was needed to maintain the pH of the solution as the oxidation process will produce extra H+ ion that can reduce the pH. It is important to maintain the pH for the oxidation to take place as $KMnO_4$ is more stable at a pH more than 2.5. The process of oxidation of Ce was illustrated in the equation below.

$$3Ce^{3+} + MnO^{4-} + 10H_2O \leftrightarrow 3Ce(OH)_4\,(s) + MnO_2\,(s) + 8H^+\,(aq) \quad \text{(Equation 1)}$$

$$3Ce(NO_3)_3 + KMnO_4 + 2H_2O \leftrightarrow 2Ce(NO_3)_4 + Ce(OH)_4 + KNO_3 + MnO_2 \quad \text{(Equation 2)}$$

$$Ce(NO)_3 + 4H_2O \leftrightarrow Ce(OH)_4 + 4HNO_3 \quad \text{(Equation 3)}$$

$$HNO_3 + Na_2CO_3 \leftrightarrow NaNO_3 + H_2O + CO_2 \quad \text{(Equation 4)}$$

$$2MnO^{4-} + 8H^+ + 6Cl^- \leftrightarrow 2MnO_2 + 3Cl_2 + 4H_2O \quad \text{(Equation 5)}$$

Recovery of the other RE can be done by selectively precipitate the elements at different pH. It was found that Nd and La has different preferred pH for reaction with ammonia. From the result, $La(OH)_3$ concentrate still contain >25 % Nd which is considerably high. Further study is needed to identify the suitable pH for this reaction so that the purity of La in $La(OH)_3$ can be maximized.

## 5 Conclusion

The demonstrated in this paper was found to separate Th from other elements. Ce can also be separated from the mixed RE hydroxide with purity at around 70 %. Further study is needed to produce higher purity of Ce, Nd, and La by minimizing the co-precipitation of Nd in $Ce(CO_3)_2$ and $La(OH)_3$.

## References

G.D. Calkins. 1952. Recovery of uranium and thorium from aqueous solutions. *United States Patent Office.*, 2838370.

Formiga T. and Morais C.A. 2016. Cerium separation from light rare earth concentrate by liquid-liquid extraction. *World Journal of Engineering and Technology*, 4:129–137.

Individual Research Contribution Review, 2024: 353–354
*ISSN: 3083-922X*

# Study on Neutron Flux of Different Shielding Materials at reactor TRIGA PUSPATI (RTP)

**Julie Andrianny Murshidi**
Industrial Technology Division, Malaysian Nuclear Agency
43000 Kajang, Selangor
julie@nm.gov.my

## Abstract

Neutron flux measurement of five different shielding materials namely water, baryte colemanite, lead, cadmium and paraffin were done using Radial Piercing Beamport at reactor TRIGA PUSPATI (RTP) in Malaysian Nuclear Agency. This beamport is installed with highly oriented pyrolytic graphite (HOPG) mosaic crystals as monocromator. The flux of thermal neutron and fast neutron of these materials were measured using two types of neutron detectors. The first detector is a liquid scintillator of type NE213 for detecting neutrons with energies from 800 keV to 20 MeV. The second detector is the 3He gas that is suitable to detect spectrum of thermal neutrons up to 1.5 MeV neutrons. The effect of different type of shielding materials and their combination to the neutron fluxes will be studied to provide suitable arrangement for effective shielding for use in neutron beam installation at RTP.

**Keywords:** Neutron Flux, Shielding Materials, RTP

## 1 Introduction

Understanding the fundamentals of the interactions of neutrons with matter is an important step in working safety in areas where neutron radiation may be encountered (McAlister, 2016). Neutron shielding materials are typically constructed from low atomic number elements (H, C and O) with high scattering cross sections to moderate incident neutrons. Elements with high capture cross sections (B, Cd and Gd) are often dispersed in the shielding materials to capture these moderated neutrons. Elements with high atomic weight (Pb, Bi and W) or layers of higher atomic weight shielding material are also incorporated to reduce dose from secondary gamma production. In view of this, different shielding material and their combinations are study to estimate their neutron fluxes. To study neutron flux of different shielding materials and its dependence on material properties.

## 2 Methods

1. One type shielding material.
   *Baryte, Parafin, Cadmium, Lead*
2. Two shielding materials combinations.
   *Parafin* + *Baryte*
   *Parafin* + *Cadmium*
   *Parafin* + *Lead*
   *Baryte* + *Parafin*
   *Baryte* + *Cadmium*
   *Baryte* + *Lead*
3. Three shielding materials combinations.
   *Parafin* + *Lead* + *Baryte*
   *Parafin* + *Baryte* + *Lead*
   *Baryte* + *Parafin* + *Lead*
   *Baryte* + *Lead* + *Parafin*
4. Experimental set-up.




Figure 1: Experimental set-up for neutron flux measurement of different shielding materials combination.

### 2.1 Characterization

Neutron spectrometer is an instrumental system that can measure the neutron energy spectrum from neutron sources such as research reactors or radioactive materials. The spectrum covers the thermal neutrons energy range as well as the fast neutrons energy range. Therefore, it must have at least two types of detectors to cover these ranges of neutron energies, for instance 3He detector for thermal neutrons and organic scintillator detector for fast neutrons. This spectrometer is a powerful and portable spectroscopic survey system for the detection, identification, and measurement of ionizing radiation. This rugged system features multiple modes to address a broad range of missions, including dosimetry, spectroscopy, and radiation mapping.




Figure 2: MOBILE MICROSPEC is a spectroscopic system for detection, identification and measurement of ionizing radiation.

## 3 Data/Results

Table 1: Neutron flux value for one type shielding material.

| MATERIALS | THERMAL NEUTRON ($ncm^2s^{-1}$) | FAST NEUTRON ($ncm^2s^{-1}$) |
|---|---|---|
| Open shutter (background) | – | 34000 |
| $H_2O$ | 4.55 | 74.1 |
| Baryte | 142.0 | 610.5 |
| Parafin | 154.5 | 642.0 |
| Cadmium | 177.5 | 913.0 |
| Lead | 541.0 | 6280.0 |

Table 2: Neutron flux value for two shielding materials combinations.

| MATERIALS | THERMAL NEUTRON ($ncm^2s^{-1}$) | FAST NEUTRON ($ncm^2s^{-1}$) |
|---|---|---|
| Parafin + Baryte | 17.0 | 137 |
| Parafin + Cadmium | 41.8 | 205.5 |
| Parafin + Lead | 51.0 | 232.5 |
| Baryte + Parafin | 17.0 | 136.5 |
| Baryte + Cadmium | 26.5 | 168.0 |
| Baryte + Lead | 35.0 | 197.5 |

Table 3: Neutron flux value for three shielding materials combinations.

| MATERIALS | THERMAL NEUTRON ($ncm^2s^{-1}$) | FAST NEUTRON ($ncm^2s^{-1}$) |
|---|---|---|
| Parafin + Lead + Baryte | 9.0 | 55.5 |
| Parafin + Baryte + Lead | 10.0 | 64.5 |
| Baryte + Parafin + Lead | 10.0 | 64.0 |
| Baryte + Lead + Parafin | 10.0 | 73.0 |

## 4 Discussion/Conclusions

Neutron flux measurement for different shielding materials and their combinations were conducted using a 750 keV beam at RTP. $H_2O$ is the most effective due to its high H content. Combination of paraffin and barite shows the lowest flux value due to their scattering cross section elements. Combination of low and high atomic number, high scattering cross sections and high capture cross sections elements results lower flux value compared to 34000 $ncm^{-2s-1}$ before shielding. Neutron flux for both fast and thermal neutrons become lower as the shielding materials combination increases.

## References

D. R. McAlister. 2016. Neutron shielding materials. *PG Research Foundation, Inc. 1955 University Lane Lisle, IL 60532, USA*.

Jr. Robert C. Singleterry and Sheila A Thibeault. 2000. Materials for low-energy radiation shielding. *NASA/TP-2000-210281*.

Individual Research Contribution Review, 2024: 355–356
*ISSN: 3083-922X*

# Selective Precipitation and Recovery of Rare Earth Elements from Monazite Concentrate

**Khaironie Mohamed Takip**
Industrial Technology Division, Malaysian Nuclear Agency
43000 Kajang, Selangor
khaironie@nm.gov.my

## Abstract

The recovery of REEs is an important development that would cushion REE supply challenges and require significant consideration. The REE supply must be increased to meet the rising demand. There are a wide range of techniques to recover REEs from either primary or secondary resources. Monazite is the rare earth mineral most utilized in the production of LREEs due to its high content. This paper investigates the recovery of La, Ce, and Nd from Malaysian monazite concentrates by using a selective precipitation technique. The experiments used $NaCO_3$ and $NH_4OH$ as precipitation agents and $KMnO_4$ as an oxidation agent. The study aimed to ascertain the possible selectivity of REEs from monazite for their recovery under specific experimental circumstances.

**Keywords:** Rare earth elements, monazite, selective precipitation

## 1 Introduction

Monazite is a phosphate mineral that commonly containing about 24.0-29.0% phosphate, 55-60% rare earth elements (REEs), 5-10% thorium (Th) and 0.2-0.4% uranium (U) (Zhang and Liu, 2017). It is a reddish-brown phosphate, containing abundance of light rare earth elements (LREEs) and heavy rare earth elements (HREEs) (Bahri et al., 2016). According to Möller and Williams (Möller and Williams, 2003), among the most abundant LREEs in monazite are cerium (Ce), lanthanum (La), and neodymium (Nd).

Selective precipitation is a frequently used separation technique in the REE recovery because of its ability to separate and concentrate specific elements from complex mixtures. The process exploits differences in the solubility and chemical properties of REEs under various conditions, allowing for their selective precipitation from solution. It is commonly combined with other techniques, such as solvent extraction, ion exchange, and crystallization, to maximize the recovery and purification of REEs (Liu and Chang, 2019).

The focus of this study is on the recovery of REEs from mineral resource through selective precipitation technique. The objective is to investigate the recovery of La, Ce and Nd as the uppermost abundant REEs in the Malaysian monazite mineral.

## 2 Methods

Monazite concentrates was obtained from the mining factory in Perak which had been undergone beneficiation process prior to further study. All chemicals and reagents used were of analytical grade and their solutions were prepared with distilled water. All samples were determined by the Wavelength Dispersive X-Ray Fluorescence (WDXRF) Spectrometry of Rigaku Supermini 200.

### 2.1 Alkaline digestion and acid leaching

A 100g sample of monazite mineral concentrate (95% purity) was digested in a 50% sodium hydroxide solution with continuous stirring at 140°C for about 3 to 4 hours. After heating, the mixture was diluted with hot water, filtered to collect a hydrous mixed-metal oxide cake, and the filtrate underwent sodium phosphate crystallization. The cake was washed until the pH was constant, dried overnight, and then leached with hydrochloric acid (HCl) The slurry was stirred for 1 hour at 80°C before filtration, yielding a filtrate containing Th, U, and REE in mixed hydroxide form.

### 2.2 Selective precipitation of uranium and thorium

Both Th and U were selectively precipitated with 10% ammonium hydroxide ($NH_4OH$) solution at pH-5.8. The solution was filtered to separate the precipitation of Th and U hydroxide from the filtrate, and dried overnight.

### 2.3 Selective precipitation of rare earths hydroxide

10% of $NH_4OH$ was repoured into the filtrate until precipitate was formed at pH-11. Discarded the filtrate and oven dried the hydroxide cake overnight.

### 2.4 Separation of Ce from La and Nd

The anhydrous cake was leached using nitric acid ($HNO_3$)and heated for 30 minutes. Deionized water was added, and the mixture was reheated until cerium hydroxide $Ce(OH)_3$ precipitated, which was then filtered out. Potassium permanganate ($KMnO_4$) was added to the filtrate in a certain ratio to oxidize Ce from Ce(III) to Ce(IV). The mixture was further leached at 120°C for about 2 hours and diluted with deionized water. The pH was adjusted to 3.6 using 15% sodium carbonate ($Na_2CO_3$), causing cerium (IV) hydroxide ($Ce(OH)_4$) to precipitate. The $Ce(OH)_4$ cake was filtered and dried overnight.

## 3 Data/Results

The chemical composition of the working monazite mineral concentrate of about 95% purity is presented in Table 1. From this table, it is shown that concentration of $RE_2O_3$, $P_2O_5$, $ThO_2$ and $U_3O_8$ in the sample was determined as 70.27%, 13.30%, 9.25% and 0.30% respectively.

Table 1: Chemical composition of monazite concentrates

| Elements | Wt.% | Elements | Wt.% |
|---|---|---|---|
| $RE_2O_3$ | 70.27 | $Fe_2O_3$ | 1.45 |
| $P_2O_5$ | 13.30 | $Al_2O_3$ | 1.03 |
| $ThO_2$ | 9.25 | CaO | 0.67 |
| $SiO_2$ | 1.72 | $ZrO_2$ | 0.51 |
| TiO | 1.49 | $U_3O_8$ | 0.30 |

The chemical composition of REE in monazite is detailed in Table 2, showing LREE (Ce, La, Nd, Sm, Pr) ranging from 2.59% to 32.0%, and HREE (Y, Gd, Dy, Er, and Tm) ranging from 0.39% to 1.91%. The highest concentrations are found in Ce, followed by La and Nd. These findings align with previous studies by Bahri et al. (Bahri et al., 2016) and Purwani et al. (Purwani et al., 2019).

Table 2: REEs composition in monazite

| Elements | Wt.% | Elements | Wt.% |
|---|---|---|---|
| Ce | 32.0 | Y | 4.31 |
| La | 12.2 | Gd | 1.91 |
| Nd | 11.7 | Dy | 1.03 |
| Sm | 2.59 | Er | 0.66 |
| Pr | 3.47 | Tm | 0.39 |

Selective separation of Th and U from a mixed hydroxide solution was achieved using 10% $NH_4OH$ at pH 5.8, resulting in the formation of a yellowish cake. Elemental composition analysis, shown in Table 3, confirmed the complete separation of Th and U from REE. It was concluded that precipitating Th and U under the studied conditions (10% $NH_4OH$ at pH 5.8) is the optimal approach for this study.

This investigation work will be combined with the solvent extraction technique by using organic extractant in diluent. The resulting solution will undergo a further purification process for higher purity of the selected REE. The preferred organic extractant used for individual element separation is di(2-ethylhexyl) phosphoric acid (D2EHPA) (Mackenzie and McLean, 2020).

Table 3: Element composition after Th and U removal

| Elements | Before Th and U removal Wt.% | After Th and U removal Wt.% |
|---|---|---|
| Ce | 32.0 | 38.0 |
| La | 12.20 | 18.20 |
| Nd | 11.70 | 15.40 |
| Th | 9.25 | 0.0 |
| U | 0.30 | 0.0 |
| Other REEs | 14.36 | 9.34 |
| Other associated elements | 6.87 | 0.76 |

## 4 Discussion/Conclusions

This study focused on the selective separation of three major REEs (Ce, La, Nd) and two radioactive elements (Th, U) from the hydrous mixed oxide cake of monazite concentrate after alkaline digestion. Th and U were almost completely separated from the leach solution using selective precipitation with 10% $NH_4OH$ at pH 5.8. Ce was removed by oxidizing $Ce^{3+}$ to $Ce^{4+}$ with $KMnO_4$ and followed by precipitating $Ce(OH)_4$ using 15% $Na_2CO_3$ at pH 3.6, though further optimization is needed for Ce recovery. Nd and La will be recovered further by solvent extraction from the REOH filtrate, to achieve high purity yield through multistage extraction.

## References

C. N.A. C. Z. Bahri, W. M. AL-Areqi, A. A. Majid, and M. I. F. M. Ruf. 2016. Production of rare earth elements from malaysian monazite by selective precipitation. *Malaysian Journal of Analytical Sciences*, 1(20):44 – 50.

S. Liu and X. Chang. 2019. Study on the selective precipitation of rare earth elements in leachate solutions. *Hydrometallurgy*, (185):140–148.

L. C. Mackenzie and J. L. McLean. 2020. Advances in rare earth extraction and separation processes: A review of current technologies. *Separation and Purification Reviews*, 3(49):160–177.

P. Möller and P. A. Williams. 2003. Monazite: A source of rare earth elements. geology and resources of rare earth elements. 3(22):12–18.

M. V. Purwani, K. Trinopiawan, H. Poernomo, Suyanti, N. D. Pusporini, and R.A. Amiliana. 2019. Separation of ce, la and nd in rare earth hydroxide (reoh) by oxidation with potassium permanganate and precipitation. *Journal of Physics*, 1(20).

Y. Zhang and C. Liu. 2017. Monazite: Occurrence, mineralogy, and geochemistry. *Minerals*, 7(3):54.

Individual Research Contribution Review, 2024: 357–358
*ISSN: 3083-922X*

# Evaluation of Radiographic Testing - Digital (RT-D) in NDT: A Comparative Analysis of Modulation Transfer Function (MTF) and Basic Spatial Resolution ($SR_b$)

**Khairul Anuar Mohd Salleh**
Industrial Technology Division, Malaysian Nuclear Agency
43000 Kajang, Selangor
khairul_anuar@nm.gov.my

## Abstract

Radiographic Testing - Digital (RT-D) has revolutionized Non-Destructive Testing (NDT) by replacing conventional film-based methods with enhanced image quality and faster inspection capabilities. This paper explores the roles of Modulation Transfer Function (MTF) and Basic Spatial Resolution ($SR_b$) in evaluating RT-D systems. While MTF provides a detailed, quantitative image quality assessment, $SR_b$ offers a more practical and accessible metric for defect detection. The paper also discusses why ISO 17636-2 prioritizes $SR_b$ over MTF, emphasizing its practical advantages and relevance to industrial radiography standards. This paper highlights the trade-offs between MTF and $SR_b$, emphasizing $SR_b$'s increasing importance in practical, reliable RT-D applications across various industries.

**Keywords:** Non-Destructive Testing (NDT), Radiographic Testing – Digital (RT-D), Modulation Transfer Function (MTF), Basic Spatial Resolution ($SR_b$)

## 1 Introduction

Radiographic Testing (RT) is a widely used Non-Destructive Testing (NDT) technique in industrial applications that evaluates the internal integrity of materials and structures. Radiographic Testing – Digital (RT-D), including Computed Radiography (CR) and Digital Detector Arrays (DDAs), has replaced traditional film-based methods due to superior image quality, faster processing, and better inspection capabilities. Among the various parameters used to assess the quality of digital radiographic images, Modulation Transfer Function (MTF) and Basic Spatial Resolution ($SR_b$) are two critical metrics. While MTF quantitatively evaluates an imaging system's ability to reproduce spatial frequencies, $SR_b$ focuses on the system's ability to resolve small, closely spaced objects. This paper aims to explore the applications, similarities, and differences between these two parameters and examine why ISO 17636-2, a key standard in radiographic testing, does not emphasize MTF as a primary evaluation tool.

## 2 Methods

### 2.1 Modulation Transfer Function

The Modulation Transfer Function (MTF), denoted as $M(u)$, is commonly used to assess the spatial resolution of imaging systems, including screen-film systems (ICRU, 1986). According to Rossmann (Rossmann, 1964), $M(u)$ quantifies image degradation resulting solely from optical factors, such as the scattering of image-forming radiation. It indicates the sharpness of the imaging system, typically expressed in cycles per millimeter (cycles/mm) or line pairs per millimeter (lp/mm). Additionally, MTF characterizes how sinusoidal signals are transferred within the spatial frequency domain. Mathematically, $M(u)$ is the Fourier transform of the Line Spread Function (LSF), shown in equation 1, representing the response of an imaging system to a single-line input. It is mathematically defined as the derivative of the Edge Spread Function (ESF), denoted as $e(x)$:

$$l(x) = \frac{d}{d(x)}(e(x)) \tag{1}$$

The $e(x)$ is obtained by using a sharp-edge image generated from radiographed phantoms. The equation for $M(u)$ is then defined as follows:

$$M(u) = \left| \int_{-\infty}^{\infty} l(x) e^{-2\pi i u x} d(x) \right| \tag{2}$$

### 2.2 Basic Spatial Resolution

The Basic Spatial Resolution ($SR_b$) of an imaging system is also an important metric to assess the image quality of an RT-D system. $SR_b$ is typically determined using a duplex wire phantom or an Image Quality Indicator (IQI). Resolution refers to the minimum distance between two points or lines that can be distinguished separately. In other words, it represents the smallest spacing of two lines that can be resolved. The duplex wire IQI was introduced to NDT in 1976 and adopted in the British Standard in 1980. It was introduced as European Norm 462-5 in 1982 (Halmshaw, 1995) and is commonly used to evaluate image resolution, including its adoption in ISO 17636-2. Figure 1 shows the duplex wire with a resolution range from 0.8 line pairs per millimeter (cycles/mm) to 0.05 cycles/mm.




Figure 1: EN462-5 duplex wire IQI

### 2.3 Key Differences

Table 1 summarizes the key differences between MTF and $SR_b$, two important metrics for evaluating imaging system performance. MTF is a complex quantitative measure that assesses how well an imaging system reproduces spatial details across a range of frequencies, covering fine and coarse details. In contrast, $SR_b$ is a more straightforward and practical metric, typically measured using a duplex IQI wire, focusing on the ability to resolve fine details such as small separations between lines. While MTF provides a broad understanding of system performance, $SR_b$ is more straightforward to measure and directly relevant for defect detection in RT-D applications.

Table 1: Summary of key differences between MTF and Basic Spatial Resolution $SR_b$

| **Aspect** | **MTF** | **$SR_b$** |
|---|---|---|
| **Definition** | Measures how well an imaging system reproduces spatial details. | Measures the smallest distance between two points that can be resolved. |
| **Measurement Method** | Derived from the Fourier transform of the line spread function (LSF). | Measured using a duplex wire phantom or IQI. |
| **Nature** | Quantitative, frequency-based metric. | Simplified, practical measure of resolution. |
| **Focus** | Assesses the system's ability to handle different spatial frequencies. | Focuses on resolving small or closely spaced features. |
| **Scope** | Covers all spatial frequencies, from coarse to fine details. | Primarily concerned with fine details (high-frequency). |
| **Unit of Measurement** | Cycles per millimeter (cycles/mm) or cycles per pixel (c/p). | Minimum resolvable distance, typically in millimeters. |
| **Complexity** | Requires detailed analysis and advanced equipment. | Easier to measure, often with visual inspection. |
| **Application** | Helps understand overall system performance. | More practical for direct resolution assessment in industry. |
| **Noise Sensitivity** | Sensitive to noise across all frequencies. | It is affected mainly by high-frequency noise and image clarity. |

## 3 ISO 17636-2 and the Emphasis on MTF

ISO 17636-2 is the international standard for RT-D of weldments. It does not emphasize MTF as a primary metric, like ASTM E2597, but focuses on practical aspects such as defect visibility and the compliance of inspection criteria. The $SR_b$, being easier to measure and more relevant to defect detection, is prioritized. While MTF provides a detailed image quality assessment, it is often complex and difficult for non-expert users. $SR_b$, introduced as a more accessible alternative, directly relates to defect detection, making it more practical for industrial applications. In 2007, $SR_b$ was introduced as a simpler alternative, representing the effective pixel size of the system. The 10% MTF value can be converted to $SR_b$ using $SR_b = 1/2 \times MTF_{10\%}$, making it more accessible for industrial users. As a result, $SR_b$ is emphasized in ISO 17636-2 for its practicality in industrial settings.

## 4 Conclusion

MTF and $SR_b$ are both essential for evaluating RT-D systems in NDT. While MTF offers detailed insights into system performance, $SR_b$'s simplicity and direct relevance to defect detection make it the preferred metric in ISO 17636-2. As industries prioritize user-friendly methods, $SR_b$ will continue to play a central role in the practical application of RT-D.

## References

R. Halmshaw. 1995. Industrial radiology. *Pondicherry: Springer-Science+Business Media, B.V.*

ICRU. 1986. ICRU Report 41, Modulation Transfer Function of Screen- Film Systems. *International Commission on Radiation Units Measurements (ICRU), Bethesda.*

K. Rossmann. 1964. Measurement of the modulation transfer function of radiographic systems containing fluorescent screens. *Phys. Med. Biol*, 9(4):551–557.

Individual Research Contribution Review, 2024: 359–360
*ISSN: 3083-922X*

# Study of Multiphase Hold-Up of Packed Bed Reactor Using Gamma Densitometry with Varying Flow Rates

**Lahasen Dahing**
Industrial Technology Division, Malaysian Nuclear Agency
43000 Kajang, Selangor
shah@nm.gov.my

## Abstract

Flow rates play a significant role in influencing phase hold-up in packed bed reactors. Increased gas and liquid flow rates result in higher hold-up for their respective phases, impacting phase distribution and flow dynamics. Understanding these effects is essential for accurately predicting reactor behavior under different operational conditions. This study explores the application of gamma densitometry to determine the density profiles of phase hold-up (gas, liquid, and solid) at varying flow rates in a Plexiglas packed bed reactor. A gamma ray source and detector were positioned at two axial locations, allowing for non-invasive measurements.The effects of flow rates on phase hold-up were analyzed. The findings indicate that solid hold-up remains stable regardless of flow conditions, while gas and liquid hold-up increase with higher flow rates. These results highlight the effectiveness of gamma densitometry as a tool for characterizing multiphase hold-up in packed bed columns, offering valuable insights for reactor design and optimization.

**Keywords:** Gamma Densitometry, Multiphase Hold-up, Flow rates, Packed Bed

## 1 Introduction

The behaviours of multiphase hold-up in packed bed reactors is inherently complex, influenced by factors such as flow rates, packing geometry, particle size, and interfacial interactions. Among these, flow rates play a critical role in shaping phase distribution, directly affecting reactor efficiency and stability. Higher gas and liquid flow rates increase the hold-up of their respective phases, altering phase distributions, flow dynamics, and the interactions among gas, liquid, and solid phases in the packed bed column. Understanding these interactions is essential for accurately predicting reactor performance and optimizing its design and operation under varying conditions.

Quantifying multiphase hold-up in packed beds, however, poses significant challenges due to their opaque nature. Traditional methods like pressure drop analysis cannot distinguish between gas, liquid, and solid phases. Invasive techniques such as sampling and tracer methods disrupt natural flow, leading to errors.

These limitations have led to the development of non-invasive techniques like gamma densitometry, which provides greater accuracy without disrupting flow dynamics. This method quantifies hold-up by measuring the attenuation of gamma rays as they pass through the reactor. Each phase (gas, liquid, and solid) exhibits unique gamma-ray attenuation properties, enabling precise phase identification and quantification.

The applicability of gamma densitometry was first demonstrated by Kumar et al. (Kumar1 et al., 2012; Kumar et al., 1995) for bubble columns and later by Van Baten and Krishna (Van Baten and Krishna, 2001) for trickle bed reactors, both of whom reported strong agreement between gamma densitometry and invasive measurement techniques. Although gamma densitometry has been widely applied to bubble and trickle beds, its use in fully gas-liquid-solid packed bed reactors remains underexplored. Past studies have focused on: 1. Investigating phase interactions in simpler two-phase systems. 2. Understanding the effects of particle size, shape, and packing arrangement on flow dynamics. Few studies have systematically analyzed the combined impact of flow rates and packing geometry on multiphase hold-up in three-phase packed beds.

This study seeks to fill these gaps by utilizing gamma densitometry to investigate the density profiles and hold-up of gas, liquid, and solid phases in a packed bed reactor under varying flow rates. By examining how flow rate variations influence phase distributions and interactions in three-phase systems, the research aims to provide critical insights for optimizing packed bed reactor design. The findings will contribute to improving reactor efficiency and facilitating the scalability of gamma densitometry for industrial applications.

## 2 Methods

The experimental setup featured a Plexiglas column, 2 meters in height and 5 cm in inner diameter. The column was filled with carbonate particles, each 5 mm in diameter, creating a packed bed with a height of 1.5 m. A 1.58 mCi 133 Barium gamma-ray source and a sodium iodide (NaI) scintillation detector were positioned at two axial points along the column to measure gamma-ray attenuation.

The gas and liquid flow rates entering the column were regulated using rotameters. Air served as the gas phase, and water was used as the liquid phase. Experiments were conducted with 5 difference flow rates of water (liquid) with range from 23.53 to 157 ml/min and air flow rates from 34 to 226.212 scph. For each flow rate, the scanning position at the same level to a void the geometry and particle size effect. The data

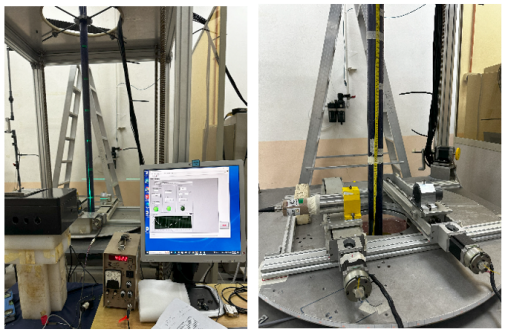


Figure 1: Gamma densitometry system and scanning position.

acquisition and motor control for synchronizing the movement of the detector and the gamma-ray source were implemented using LabVIEW software. This setup ensured precise coordination of both components during the experimental sequence. Figure 1 shows the Gamma densitometry system and scanning position.

## 3 Results and Discussion

The Figure 2 to Figure 4 presents the density profile of gas, liquid and solid holdup across scanning points in a packed bed column under five different flow rates.

The Figure 2 shows that, as flow rates increase, the gas hold-up values generally increase. This indicates that higher gas flow rates introduce more gas into the packed bed, raising the proportion of gas in the multiphase system.

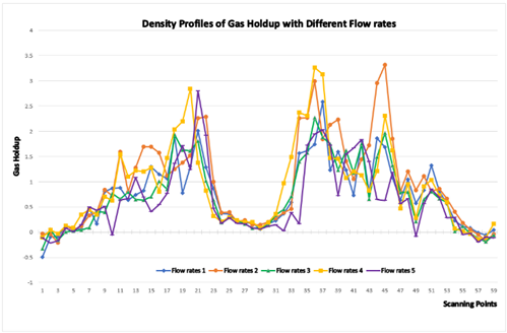



Figure 2: Graph of Gamma densitometry Profile of Gas hold-up Plexiglas packed bed column with difference flow rates of gas and liquid.

Figure 3 shows that, the liquid hold-up generally increases with higher flow rates, showing more liquid accumulation in the column.

The graph 4 demonstrates that the distribution of solid material in the packed bed column remains consistent regardless of flow rate changes. Its suggesting minimal impact of flow rates on solid phase distribution.

## 4 Conclusion

In summary, experimental results indicate that the solid phase remains stable regardless of flow rate changes, serving as

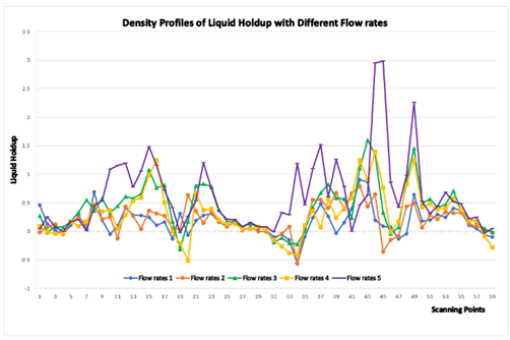



Figure 3: Graph of Gamma densitometry Profile of Liquid hold-up Plexiglas packed bed column with difference flow rates of gas and liquid

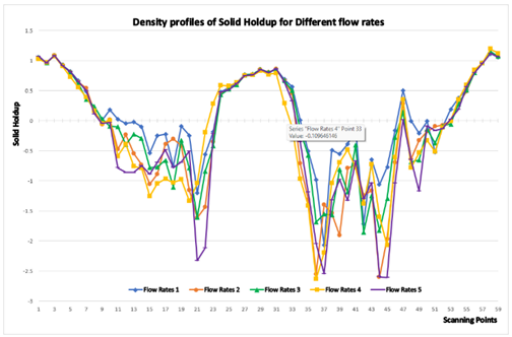



Figure 4: Graph of Gamma densitometry Profile of Solid hold-up Plexiglas packed bed column with difference flow rates of gas and liquid.

a consistent structural component in the packed bed. Conversely, liquid and gas hold-up increase with rising gas flow rates, highlighting the significant impact of flow rates on phase distribution within the reactor. These findings highlight the importance of flow rate control for optimizing reactor performance. They also demonstrate that gamma densitometry is a reliable, non-invasive tool for characterizing multiphase hold-up in packed beds.

## References

S.B. Kumar, M.P. Dudukovic, and B.A. Toseland. 1995. Measurement techniques for local and global fluid dynamic quantities in two and three phase systems. *Non-Invasive Monitoring of Multiphase Flows*, pages pp.1–78.

R. Kishore Kumar1, A.V. Raghavendra Rao1, T. Sankarshana2, and Ahamed Khan1. 2012. Liquid holdup in concurrent gas liquid upflow through packed column with random and corrugated structured packing. *Proceedings of the World Congress on Engineering and Computer Science 2012 Vol II WCECS 2012*, pages 24–26.

J.M. Van Baten and R. Krishna. 2001. Cfd simulations of mass transfer from taylor bubbles rising in circular capillaries. *Chemical engineering science*, 56(4):pp.1117–1126.

Individual Research Contribution Review, 2024: 361–362
*ISSN: 3083-922X*

# Collaboration Program: Capacity Development of RSA Academy Sdn. Bhd. to Implement Electromagnetism Testing Courses to Industry

**Dr. Mahmood Dollah**
Industrial Technology Division, Malaysian Nuclear Agency
43000 Kajang, Selangor
mahmooddollah@nm.gov.my

## Abstract

The Research, Innovation, and Strategic Engagement (RISE) program, in partnership with the industry, is dedicated to enhancing the capacity and capability of RSA Academy Sdn. Bhd. to conduct electromagnetism testing courses. This initiative is designed to improve the skills of local personnel working in the petroleum and gas industries, as well as in power stations, through targeted training program. The project is anticipated to be completed within a timeframe of 8 to 12 months, following established milestones and Key Performance Indicators (KPIs).

**Keywords:** RISE Program; Electromagnetism Testing; Training Programs; Key Performance Indicators (KPIs)

## 1 Introduction

Almost all critical engineering components in industrial plants are tested for integrity before they operate or after prolonged operation. Generally, inspections are conducted using non-destructive testing techniques, which do not damage the components being tested. Heat exchangers (HE) are one of the main components in industrial plants, primarily functioning to transfer heat generated from one process in the plant from the primary cooling system to the secondary cooling system. A heat exchanger typically contains thousands of tubes through which liquid from the primary cooling system flows. The efficiency of the heat transfer process depends on the integrity of each of the thousands or tens of thousands of tubes within each heat exchanger. Therefore, it is essential to conduct courses such as Eddy Current testing and RFECT to ensure that companies can undertake quality inspections to confirm that there are no defects in the tubes.

One of the primary methods used for inspecting the integrity of tubes is the Eddy Current testing method and RFECT, which are also known as electromagnetism courses. However, the involvement of skilled local personnel has not developed as expected. Recognizing the importance of this need, RSA Academy Sdn. Bhd. is a training and certification company that aims to develop human resources in this industrial sector in collaboration with staff from the Malaysian Nuclear Agency (Nuklear Malaysia). The training to be developed will enable inspections of tubes in the gas and petroleum industries, as well as power stations. The capability to develop these courses will allow the company to offer services more efficiently and quickly to meet customer demands. Nuklear Malaysia will provide advisory services in identifying equipment needs, training, certification, signal/data analysis, human resources, and standards, as well as developing a planning program for the company to implement the aforementioned tests




Figure 1: Flowchart project

## 2 Methods

The methodology for the project involves a structured approach to developing the capacity of RSA Academy Sdn. Bhd. to conduct electromagnetism testing courses (Figure 1). The company will allocate sufficient financial resources for training development and ensure a comfortable working environment for researchers to carry out their tasks effectively. The project will follow a Gantt chart that outlines specific tasks and timelines, ensuring that all activities are monitored and evaluated throughout the implementation period. Key activities include initial briefings, discussions on laboratory requirements, and the identification of necessary equipment and training needs.

Researcher will provide guidance on identifying equipment needs, training requirements, and certification processes, ensuring that the training meets industry standards. The collaboration with Nuclear Malaysia is crucial, as it will facilitate the development of a certification training program that enhances the skill set of personnel capable of performing integrity tests on heat exchanger tubes in the oil and gas industry. Regular monitoring and feedback sessions will be conducted to assess progress and make necessary adjustments to the training programs, ensuring that the objectives are met within the projected timeline of 8 to 12 months.

## 3 Results and Discussion

The successful execution of this project will result in a certification training program that enhances the skill set of personnel capable of performing integrity tests on heat exchanger tubes

in the oil and gas industry. The collaboration with Nuclear Malaysia will ensure that the training meets industry standards and addresses the specific needs of the sector. Regular monitoring and feedback sessions will be conducted to assess progress and make necessary adjustments to the training programs.

The RSA Academy Sdn. Bhd. has the right to decide whether to proceed with the implementation of the electromagnetism course development project. The collaboration with Nuclear Malaysia is crucial for achieving the desired outcomes, and the project is expected to significantly contribute to the development of skilled personnel in the industry. The final report will be presented to both RSA Academy Sdn. Bhd. and Nuclear Malaysia, outlining the achievements and future directions of the initiative.

## References

Mahmood Dollah. 2024. Pembangunan kapasiti syarikat RSA Academy Sdn. Bhd. untuk melaksanakan kursus ujian electromagnetism kepada industri, program kerjasama pegawai penyelidik Agensi Nuklear Malaysia (Nuklear Malaysia) dengan pihak industri.

Individual Research Contribution Review, 2024: 363–364
*ISSN: 3083-922X*

# Burstein-Moss Effect on the Optical Properties of Zr Doped $TiO_2$ Nanorods Thin Films

**Masliana Muslimin**
Industrial Technology Division, Malaysian Nuclear Agency
43000 Kajang, Selangor
masliana@nm.gov.my

## Abstract

This research examines the impact of Zr doping into the $TiO_2$ matrix on crystal defects. This work used a simple hydrothermal approach with low temperatures and a short time frame. The enhanced optical characteristics of Zr doped $TiO_2$ nanorod thin film for photocatalytic applications necessitate further investigation. The synthesized samples are analyzed using ultraviolet visible (UV Vis) spectrometers. The direct band gap of undoped $TiO_2$ (3.0 eV) increased dramatically to 3.17 and 3.24 eV for 150-Zr$TiO_2$ and 200-Zr$TiO_2$, respectively.

**Keywords:** $TiO_2$ nanorods thin films, Zr dopant, band gap

## 1 Introduction

Titanium dioxide ($TiO_2$) has emerged as a material of immense interest due to its remarkable photocatalytic activity, chemical stability, non-toxicity, and abundance (Lagopati et al., 2014). These properties have positioned $TiO_2$ as a promising candidate for applications in environmental remediation (Shahrezaei et al., 2017), solar energy conversion (Chenyu et al., 2022) and self-cleaning surfaces (T. and Padmanabhan, 2020). However, pure $TiO_2$ exhibits certain limitations, such as a wide bandgap (~3.2 eV for anatase), which restricts its activity to the ultraviolet (UV) region of the solar spectrum, accounting for only ~5% of sunlight. This limits its efficiency in utilizing visible light for practical applications.

To overcome these limitations, doping with metal ions has been widely explored as a strategy to modify the electronic structure of $TiO_2$ (Pan et al., 2015). Extend its light absorption into the visible region, and enhance its photocatalytic performance. Among the various dopants, zirconium (Zr) has garnered attention due to its ability to introduce localized states within the bandgap, reduce recombination of photogenerated charge carriers, and maintain the crystallinity of the $TiO_2$ matrix. Furthermore, Zr-doping is known to influence the optical, structural, and electronic properties of $TiO_2$, making it a versatile modifier for thin-film applications (Sunil et al., 2024).

Thin films of $TiO_2$ have unique advantages, such as high surface area-to-volume ratio, tunable thickness, and ease of integration into devices, which make them ideal for optoelectronic and photocatalytic applications. Investigating the optical properties of Zr-doped $TiO_2$ thin films using UV-Vis spectroscopy provides critical insights into the bandgap modifications and light-harvesting efficiency introduced by Zr doping. Such analysis not only elucidates the impact of doping on the electronic structure but also aids in optimizing the material for specific applications.

This study focuses on the synthesis and characterization of Zr-doped $TiO_2$ thin films and evaluates their optical properties through UV-Vis spectroscopy. By analyzing the bandgap energy and optical absorption characteristics, we aim to understand the effect of Zr doping on the performance of $TiO_2$ thin films for potential applications in photocatalysis and solar energy harvesting.

## 2 Methods

$TiO_2$ nanorods were produced on an FTO substrate using a simple hydrothermal process. To prepare a growth solution for $TiO_2$ nanorods, 10 mL of concentrated hydrochloric acid (HCl) was dissolved in 10 mL of deionized (DI) water. Then, 0.7 ml of titanium butoxide was added using a micropipette and rapidly agitated for 15 minutes. Next, various volume percentages of zirconium butoxide (50, 150, and 200%v/v) were added to the growth solution. The hydrothermal process was then initiated by placing the solution into an autoclave with a Teflon liner. The hydrothermal reaction occurs at 170 °C for 30 minutes. The autoclave was then taken from the oven and allowed to cool till room temperature. The sample was then washed with DI water and heated using a hotplate for 5 minutes at 100 °C. UV Vis analysis was conducted using Perkin Elmer Lambda 900 spectrometer in the range of 300 nm to 800 nm at 100-240V keywords.

## 3 Results

Figure 1 shows the optical absorption spectra of undoped and $TiO_2$ nanorods with varying Zr doping percentages (x-Zr/$TiO_2$). From the Figure 1 the band gap (Eg) value for Zr-doped $TiO_2$ were calculated. The Eg value for each sample was derived by creating a graph using the Tauc equation, which is $(\alpha h\nu)^2$ versus photon energy. It is obvious that an increase in Zr concentration has resulted in two conditions: widening and contraction of Eg in comparison to the undoped sample. For example, attenuation occurred in 50-Zr/$TiO_2$ samples. Eg broadening has occurred in the 150-Zr/$TiO_2$ and 200-Zr/$TiO_2$ samples. This is known as the Burstein-Moss phenomenon. The apparent band gap widening is explained by the Burstein-Moss effect (Moss., 1959). The photon energy needed for inter-band transitions from the valence band to the

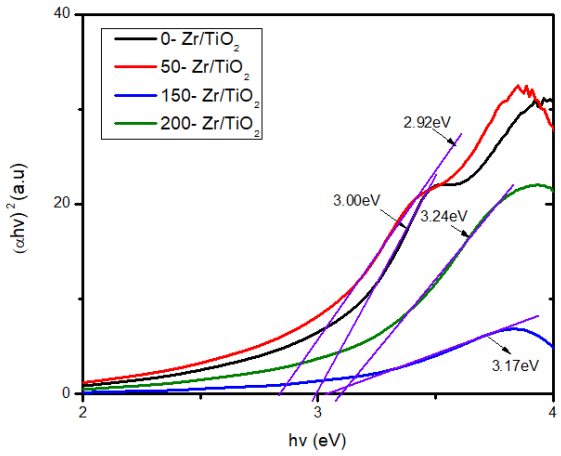



Figure 1: Band gap value (Eg) for undoped and Zr doped $TiO_2$

higher energy empty states in the conduction band is increased by the electron accumulation caused by Zr donors, which fills the electronic states in the conduction band.

## 4 Conclusion

Zr doped $TiO_2$ thin films were effectively deposited on FTO using a simple hydrothermal technique. The effect of Zr doping concentration on optical characteristics was studied. The addition of Zr to the $TiO_2$ matrix results in considerable changes in crystal defect and energy band gap. Future characterization studies will be done for photoelectrocatalytic water splitting utilizing this samples.

## References

Z. Chenyu, X. Zhaoyi, J. Dario, and M. L. Stacchiola. 2022. Application of ultrathin tio2 layers in solar energy conversion devices. *Special Issue:10th Anniversary of Energy Science Engineering*, 5(10).

N. Lagopati, E.P. Tsilibary, P. Falaras, P. Papazafiri, E.A. Pavlatou, E. Kotsopoulou, and P. Kitsiou. 2014. Effect of nanostructured tio2 crystal phase on photoinduced apoptosis of breast cancer epithelial cells. *Int. J. Nanomed.*, (9):3219–3230.

T.S. Moss. 1959. Optical property of semiconductor. *Butterworths Scientific Publications, London, and Academic Press, New York*, page 279.

J. W. C. Pan, Y.F. Li, R.X. Zhao, Y.Y. Liu, L.Y. Gong, X.J. Niu, and B.Q. Chi. 2015. Electronic properties of tio2 doped with sc, y, la, zr, hf, v, nb and ta. *Chem. Phys. Lett.*, 8(62):43–48.

M. Shahrezaei, A.A. Babaluo, and M.H. Habibzadeh. 2017. Photocatalytic properties of 1d tio2 nanostructures prepared from polyacrylamide gel–tio2 nanopowders by hydrothermal synthesis. *Eur. J. Inorg. Chem.*, (3):694–703.

A. Sunil, M.S. Gopika, S. Jayasudha, and Prabitha B. N. 2024. Multifunctional applications of tio2 thin films synthesized by sol–gel dip coating technique. *J Sol-Gel Sci Technol*, (110):346–362.

Nisha T. and H. J. Padmanabhan. 2020. Titanium dioxide based self-cleaning smart surfaces: A short review. *Journal of Environmental Chemical Engineering*, 5(8):104211.

Individual Research Contribution Review, 2024: 365–366
*ISSN: 3083-922X*

# A Study on Detection of Water Detection in Process Pipeline in Oil & Gas Plant using Neutron Backscattered Technique

**Md Fakarudin Ab Rahman**
Industrial Technology Division, Malaysian Nuclear Agency
43000 Kajang, Selangor
fakarudin@nm.gov.my

## Abstract

The detection of liquid in gas pipelines is critical for maintaining operational efficiency and preventing potential hazards in industrial applications. Neutron Backscatter Scanning (NBT) has emerged as a viable non-destructive testing (NDT) method for assessing moisture levels within pipeline systems. This study focuses on the implementation of NBT to detect liquid within the horizontal pipeline system at Petrochemicals plants. The primary objective was to verify the water trapped in pipeline during normal operations, thereby informing maintenance strategies.

**Keywords:** Neutron Backscattered, fast neutrons

## 1 Introduction

Three sources can produce neutrons: isotope sources, nuclear reactors, and neutron generators. Consequently, in the absence of any interaction with the electric fields of electrons or nuclei, neutrons can penetrate matter relatively deeply. Fast neutron will be thermalized when collide directly with an atom of a light element, like a hydrogen nucleus. This is due to very light neutrons preferentially exchange momentum and energy with similar sized particles. Rapid neutrons with energies between 0.5 and 11 MeV have the potential to "thermalize," or slow down, and lose energy to become thermal neutrons, which have energies of 0.25 eV.

The thermal neutron that was created during the thermalization process had a brief travel path but was dispersed in all directions. The detector counts the neutrons that are scattered back towards the scanning head from among these thermal neutrons. Higher concentrations of hydrogen will reflect more neutrons back to the detector. Any hydrogenous substance, such as water, hydrocarbons and concrete can be determined.

Several industrial processes like petroleum, chemical and power generation industries require continuous measurement of interface level to operate efficiency and guarantee uniform product quality. Determination of moisture exists in certain location of the wall in process vessel or storage tank is also considered as extremely important for the assessment and improvement of the plant performance. The technology used in measurement of interface level is known as the 'neutron backscattered' technique which is based on measuring the hydrogen concentration of material. This technique is a non-destructive method where a slow-level radioactive source is used to generate the high-energy neutrons, collide with hydrogen atom, slowed down, and the backscattered neutron (part of thermal neutron) bounced back toward the source and measured by a thermal neutron detector. The detector response is recorded as count rate on the portable electronics gauging system.

## 2 Methods

The Am-Be 241, 50mCi fast neutron produced during the thermalization process had a short travel path but was scattered in all directions. Among these thermal neutrons, the detector counts the neutrons that are scattered back towards the scanning head. The scattering process is responsible for energy loss and slowing down of neutrons. If neutron energy before collision is denoted by $E_1$, neutron energy after collision is denoted by $E_2$, and A is the mass number of nucleus, it is possible to show that the energy transferred to the nucleus in a head-on collision is (Md Fakarudin Ab Rahman, 2012):

$$\frac{E_2}{E_1} = \left(\frac{A-1}{A+1}\right)^2 \quad (1)$$

From Equation (1), it can be seen that it is possible for a nucleus to lose all its kinetic energy in head-on collision with hydrogen nucleus. It is clear that the hydrogen is the major factor in the slowing down of fast neutrons (Md Fakarudin Ab Rahman, 2012). When in use, the measuring probe (comprising fast neutrons) positioned adjacent to slow neutron detector is suspended at the material. The detector will count the resulting flux. The detector count rate displayed on the electronic unit depends directly on hydrogen concentration of the surrounding medium. The equipment used for NBT is portable Hydrotector which uses Americium- 241/Beryllium (Am/Be) as the neutron source.

### 2.1 Device

Portable electronics gauging system has been used for this experimental including:

i) Detector: CPN MCM2- DETECTOR
ii) Radioactive source: Americium-241: Beryllium
iii) Type of radiation: neutron
iv) Survey meter calibration
v) Height marking tools
vi) Measuring tape

### 2.2 Procedures

The scanning procedure involved the following steps:

i) Area Preparation: Establishment of a controlled inspection area with radiation warnings to ensure safety protocols.

ii) Pipeline Measurements: Recording the dimensions of the pipeline (height, diameter, wall thickness) to configure effective scanning operations.

iii) Data Collection: Conducting spot measurements at 2-meter intervals, with each measurement taken over a duration of 8 seconds to ensure reliable data.

iv) Probe Utilization: A portable NBT probe allowed for real-time data collection and rapid identification of moisture content in the pipeline system.highest position from the surface.

## 3 Data/Results

The standards an air counts refer to slow neutron counts/8sec have been taken as references measurement.

### 3.1 Standard and air counts

Table 1: Neutron count rate indicator

| Count rate / 8 sec | Level of Hydrogen Concentration | Color of Indicator |
|---|---|---|
| 0 to 1500 | Low condition (Gas or ambient air) | Low |
| 1500 to 2500 | Moderate condition (Low moisture concentration) | Moderate |
| Above 2500 | High condition (High moisture concentration) | High |

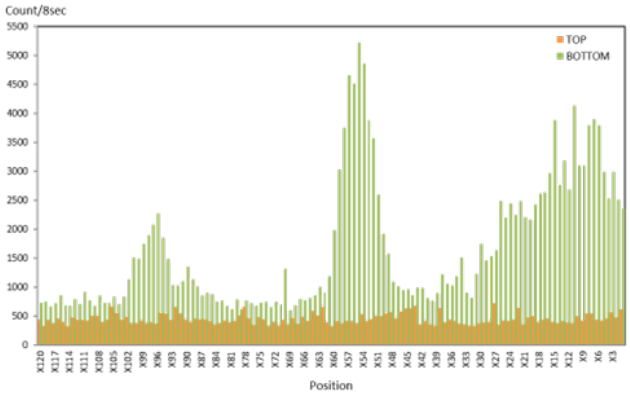



Figure 1: Pipeline Measurements Result

## 4 Discussion/Conclusions

### 4.1 Discussion

The results from the scanning campaign indicated clear distinctions in moisture levels based on the positional orientation of the measurements. The top positions (0°) generally revealed low neutron counts that aligned with expectations for gas-only conditions, thereby supporting the assumption of effective gas flow without significant liquid interference. Conversely, the increased counts recorded from the bottom positions (180°) raised concerns regarding the potential accumulation of moisture, especially at the identified points of interest (points #X5 to #X18).

The elevated moisture levels could correlate with external environmental influences, such as humidity levels and water ingress due to poor drainage. This highlights a necessity for integrated monitoring systems that not only measure moisture levels but also assess external conditions affecting pipeline integrity.

### 4.2 Conclusion

The findings support the efficacy of Neutron Backscatter Scanning as a reliable method for detecting moisture in gas transfer pipeline. The validation of moisture levels at various points provides actionable intelligence for maintenance practices, ensuring operational integrity and safety.

Going forward, the study proposes several recommendations such as Periodic Monitoring and Baseline Data Creation.

## References

D. J. Abdullah. 2005a. Gamma scanning can aid in troubleshooting and optimisation of distillation columns. *Malaysian Institute for Nuclear Technology Research*, pages 1–4.

D. J. Abdullah. 2005b. Poliscanner, neutron backscatter technique. *Malaysian Institute for Nuclear Technology Research*, pages 1–4.

Neutron Backscatter Scanning for Detection of Liquid Inside Piping 750-15-Vh-2350 at BAGSF Complex in Bintulu Integrated Facility (BIF). 2019. *NUKLEAR-MALAYSIA/L/2019/95(R)*.

I. M. Md Fakarudin Ab Rahman. 2012. Detection of pipeline by neutron device. *Jurnal Sains Nuklear Malaysia*, pages 35–42.

P. Priyada, M. Margret, R. Ramar, and Shivaramu. 2012. Intercomparison of gamma ray scattering and transmission techniques for fluid-fluid and fluid-air interface levels detection and density measurements. 70(3):462–469.

Individual Research Contribution Review, 2024: 367–368
*ISSN: 3083-922X*

IRCR

# Research and Commercial Opportunities in Developing Artificial Intelligence Assisted NDT Micro-SaaS System

**Megat Harun Al Rashid Megat Ahmad**
Industrial Technology Division, Malaysian Nuclear Agency
43000 Kajang, Selangor
megatharun@nm.gov.my

## Abstract

The integration of Artificial Intelligence (AI) with the widespread adoption of Software as a Service (SaaS) creates transformative opportunities for Non-Destructive Testing (NDT) inspection companies, which are critical across various industries such as aerospace and manufacturing. By leveraging AI-driven micro-SaaS platforms, NDT professionals can enhance the efficiency and accuracy of data analyses related to material integrity assessments. These platforms facilitate real-time insights and automate routine tasks through advanced machine learning algorithms, thereby expediting evaluation times and improving precision. The adoption of AI in NDT not only addresses common industry challenges such as rapid result generation and compliance with regulatory standards but also fosters innovation and elevates overall service quality. This convergence of technologies represents a significant evolution in NDT methodologies, positioning the industry to meet increasing demands for reliable assessment and quality assurance.

**Keywords:** AI, Saas, Flask, Python.

## 1 Introduction

The advent of an AI-assisted system for evaluating Non-Destructive Testing (NDT) inspection data presents a groundbreaking opportunity to enhance analytical thoroughness while significantly reducing the potential for human error. Traditional NDT practices often rely heavily on the expertise and interpretation skills of human inspectors, which can lead to inconsistencies and oversights in data analysis. By deploying this system as a micro-SaaS application, NDT professionals can gain wider access to advanced analytical tools, democratizing the capabilities of effective inspection methods across diverse industries such as aerospace, automotive, and infrastructure. However, the successful development of such a system hinges not only on crafting a user-friendly web service that caters to various user levels but, more crucially, on implementing a sophisticated and well-trained AI model capable of accurately analyzing complex NDT data from sources like ultrasonic testing, radiography, and thermography. This introduction sets the stage for an in-depth exploration of the feasibility and technical requirements for creating this AI-driven solution, highlighting the potential benefits, challenges, and innovative approaches necessary to produce a robust and effective tool that can significantly elevate the standards of NDT evaluation processes. With an increasing demand for quality assurance and safety in critical applications, the implications of integrating AI into NDT workflows could redefine industry practices, contributing to safer and more reliable operational environments.

## 2 Framework and Technologies for AI-Driven NDT Data Analysis

The development of the AI-assisted platform designed for evaluating Non-Destructive Testing (NDT) inspection data centers around a well-structured implementation utilizing Flask, a popular micro web framework known for its flexibility and simplicity. This framework will support a rich user interface, enabling professionals to easily upload their inspection data—typically stored in formats such as CSV or Excel. Upon submission, the data will be processed using the Pandas library to ensure proper formatting and preprocessing, which is critical for accurate analysis. The heart of the platform lies in its integration with Keras, which allows us to harness powerful machine learning capabilities. By employing a pre-trained model or training a new one based on a curated dataset of NDT outcomes, we will enable the AI to analyze the uploaded data and generate meaningful predictions that can aid in decision-making processes for users. Moreover, the application will feature interactive data visualizations using JavaScript libraries like Plotly, allowing users to gain insights through dynamic charts and graphs that represent trends or anomalies identified by the AI. This adds an essential layer of accessibility to complex data, making it easier for users to understand the outcomes of their inspections at a glance. Furthermore, to streamline the user experience, the interface will incorporate essential widgets such as sliders for adjusting analysis parameters and dropdown menus for selecting specific types of investigations.

Payment processing is another critical aspect of the service, whereby we will integrate Stripe to facilitate subscription management. This allows users to securely manage their payments in a smooth, hassle-free manner while accessing the platform's features without interruption. Throughout the development process, we will keep user feedback at the forefront, ensuring that every feature added enhances usability and meets the needs of NDT professionals. Ultimately, the goal is to create a robust, intuitive web service capable of transforming how NDT inspection data is processed and an-

alyzed, thereby empowering professionals to achieve higher levels of accuracy and efficiency in their work. This comprehensive approach will not only improve validation and predictive capabilities within the NDT field, but also foster a more informed decision-making culture across various applications of the technology. Through iterative enhancements and a commitment to adaptability in response to user needs, the platform aspires to become an indispensable tool for the NDT community.

## 3 Discussion and Conclusion

As the project remains in its developmental phase, no source codes have been released at this time. The scattered nature of the codebase presents a logistical challenge for both the development team and potential users interested in the project's progress. However, this situation also highlights an important opportunity to consolidate efforts and streamline the code into a more organized, accessible format for future dissemination.

A pivotal aspect of the work is the integration of artificial intelligence, heavily inspired by foundational research, as referenced in prior work (et.al Suhairy, 2020). Yet, there is a significant hurdle: the limitations of the current dataset do not provide enough variety or quantity for effective training of the machine learning models. This insufficiency presents both a challenge and an opportunity for innovation. By focusing on the generation of quality synthetic datasets, it is possible to create robust inputs that replicate the statistical patterns and properties of real-world NDT inspection data.

The generation of synthetic datasets is not merely about filling a gap; it is a strategic endeavor that leverages advanced algorithms and modeling techniques to produce artificial data capable of training AI in a reliable and relevant manner. This approach enhances the training capabilities of the models while also addressing broader industry needs. The commercial potential of synthetic datasets is notable; as industries increasingly seek scalable and privacy-preserving solutions for data analysis, synthetic data generation can serve as a viable business model. This opportunity allows for the exploration of dual possibilities: augmenting the own dataset and offering synthetic datasets to other organizations grappling with similar issues of data insufficiency.

In conclusion, as the complexities of this ongoing project are navigated, addressing the limitations posed by the current dataset remains a priority. The development of synthetic datasets serves as a promising pathway that not only enhances the efficacy of the AI models but also opens up new avenues for commercialization. Continued research and development will be crucial in refining processes, ensuring that high-quality datasets are produced that meet the rigorous demands of NDT inspection data analysis. The ultimate goal is to advance this project into a fully operational platform that benefits a wide array of stakeholders in the industry while contributing to a growing understanding and appreciation for the role of synthetic data in enhancing machine learning applications.

## References

et.al Suhairy. 2020. *Defence S and T Technical Buletin*, 17(1):37.

Armando Fox and David A. Patterson. 2020. Engineering software as a service: An agile approach using cloud computing. *Pogo Press ISBN 978-1-7352338-0-2*.

Individual Research Contribution Review, 2024: 369–370
*ISSN: 3083-922X*

# Acoustic Emission Testing on Cargo Oil Tank

**Mohamad Ridzuan Ahmad**
Industrial Technology Division, Malaysian Nuclear Agency
43000 Kajang, Selangor
ridzuan_a@nm.gov.my

## Abstract

The formation of turbulence flow from internal leaks in closed valves that generates Acoustic Emission (AE) noise is used in determining whether there is leakage in the valves. Therefore, an open valve should be closed for a while to inspect whether there is a leak when the valve is closed. Inspection for valve passing has been performed on the pump room valve. In determining the valve passing situation, generated AE noise at the body of the valves is compared to the background noises at the upstream and downstream of the valves. The higher noise at the body of the valves indicates internal leaks that cause the turbulence flows.

**Keywords:** Acoustic Emission, Valve

## 1 Introduction

Acoustic Acoustic Emission testing (AET) is a nondestructive testing method that has been applied in the petrochemical industry since the early 1980s with several well-proven codes and standards. In shipping and marine industry, the method has been applied in oil tankers and containerships.

The Acoustic Emission process begins when forces acting on a body that result in changes in the stress field and localized deformation at defect sites. These localized deformations produce Acoustic Emissions, elastic waves that travel outward from the source, echoing through the body until they arrive at a remote sensor. The elastic waves manifest themselves as in-plane and out-of-plane displacements that cause the sensor to produce an electrical signal, which is passed to electronic equipment for further processing.

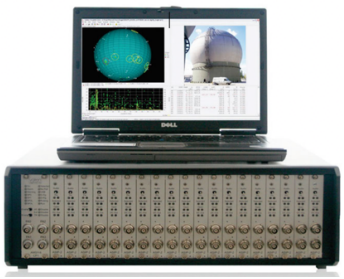


Figure 1: Acoustic Emission System – Vallen Systeme AMSY-6 38 Channels

## 2 Methods

The system uses ASIP-2 which is a dual channel AE-signal processor board which can be mounted in any of the chassis. Each ASIP- 2 board and each channel on the board is processing data independent of each other. There are two versions of the ASIP-2:

- ASIP-2/S: Standard Version
- (17 cards total of 34 channels)
- ASIP-2/A: Advanced Version
- (2 cards total of 4 channels)

Both ASIP-2 versions can be used simultaneously within the same chassis. The ASIP-2/A has ability beyond the standard version of ASIP-2/S. Following tables describe ASIP-2/S Signal Processing, Hit Assembly, and Feature Extraction:



Figure 1: Port Side View – Red Square Indicates Location of Marine Valves Inspected within vicinity of Cargo Oil Tank 4 Centre (COT4C)

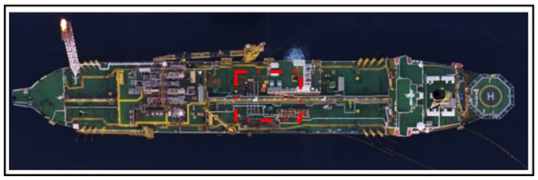


Figure 2: Plan View – Red Square Indicates Location of Marine Valves Inspected within vicinity of Cargo Oil Tank 4 Centre (COT4C)

## 3 Results and Discussion

AE signals at upstream, body, and downstream of the valves are recorded to identify the internal valve passing as in Figure 10. The sensors on the body of the valve are used to measure the pressure noise and the rest used to monitor the background noises. Minimum of 3 AE sensors are used for the inspections where 1 sensor are placed on the body of the valves with 2 sensors have been attached on each of upstream and downstream of the valves. AE parameters including ASL

value are recorded during the inspections of the valves. Since the formation of turbulence flow from internal leaks in closed valves that generates Acoustic Emission (AE) noise, it is used in determining whether there is leakage in the valves.

| Photos of Probe Placement on Valve | |
|---|---|
|  | Description:<br>Acoustic emission sensor placed at downstream and upstream of the valve. |
|  | Description:<br>General view of more valves to be inspected using AET |
|  | Description:<br>General view of more valves to be inspected using AET |
|  | Description:<br>General view of more valves to be inspected using AET |
|  | Description:<br>Side View of initial placement of AE Sensors |

The measured pressure noise at body of the valve recorded

| | |
|---|---|
|  | Description:<br>General view of more valves to be inspected using AET |
|  | Description:<br>AE Sensors placed on valve body |

lower RMS signal compared to the background noise at the downstream of the valve. Hit signal at body is lower compared to hit signal to upstream and downstream indicating there are no turbulence flow occurred, the valve in good condition.

## 4 Conclusion and attention

AE sensors are used to determine valve passing from the measured pressure noise and background noise of the inspected valves. Eight valves consist of pump room valve No 20, 22,46,61,64,73,75 and 76 have been inspected for the valve passing test. Average signal level (ASL) for the measured noise in body of the valve is used to determine the event of valve passing. As the result, valve passing has been identified at the pump room valve 61 and 64 while the other valve is tight.

## References

Vinamra Bhushan et al Sharma. 2024. A comprehensive study of techniques utilized for structural health monitoring of oil and gas pipelines. *Structural Health Monitoring*, 23(3):1816–1841.

Sascha Schieke, Mark Geisenhoff, and Ke Wang. 2024. Nde in oil, gas, and petrochemical facilities. *Handbook of Non-destructive Evaluation 4.0.*, pages 1–21.

Individual Research Contribution Review, 2024: 371–372
*ISSN: 3083-922X*

# Development of International Standard (ISO) for Residence Time Distribution (RTD) Formulation and Applications Using Industrial Radioactive Tracer

**Mohd Amirul Syafiq Mohd Yunos**
Industrial Technology Division, Malaysian Nuclear Agency
43000 Kajang, Selangor
syafiq@nm.gov.my

## Abstract

Stimulated by an increasing demand from the large production plants, radioactive tracer methods have been evolved to provide fast and effective solutions by utilizing competitive tools for process optimizations and investigations. There is lack of standards in the area of radiotracers techniques to enhance related nuclear techniques and ensure the sustainability and quality of the technology. A working group (WG7) on tracer methods of subcommittee (SC 5) on velocity and mass methods was created by the International Organization of Standardization (ISO) Technical Committee (TC 30) on measurement of fluid flow in closed conduits in 2020 has been convened to develop, validate and finalize the ISO 25056 – Methods for residence time distribution using radioactive tracer project supported by International Atomic Energy Agency (IAEA). The ISO standard in this subject will for sure encourage industrialists to take full advantage of the technology.

**Keywords:** Residence Time Distribution, Radioactive Tracer, ISO Standard, RTD Model

## 1 Introduction

The concept of RTD has become a crucial tool for diagnosing industrial processing vessels and reactors. The RTD of mass flow within these vessels plays a key role in assessing their performance. Short-lived radiotracers are commonly used to obtain the RTD. Radioactive tracers are predominantly employed for real-time RTD measurement. This method is non-invasive, allowing for online measurements in harsh industrial environments, conducted externally while the process is operational.

Although RTD technology is applicable to a wide array of industries, it is especially beneficial in sectors such as petrochemical, mineral processing, and wastewater treatment. RTD techniques are used to optimize processes, address operational issues, enhance product quality, conserve energy, and minimize pollution. The technical, economic, and environmental advantages of RTD have been widely acknowledged by both industrial and environmental sectors. The objective of this study was to validate the RTD formulation experimentally and establish international standard that describes the radioactive tracer method for the measurement of residence time distribution for mass flow characterization in industrial process equipment.

## 2 Methods

The residence time distribution (RTD) experiments test is carried out in a bubble column reactor. The radioactive tracer can be monitored continuously once injected into the system. The radiation detection system consists of a radiation detector coupled to data analyzer. For online in-situ radiotracer applications, detection system normally consists of many gamma radiation detectors connected to a multichannel analyzer (MCA).

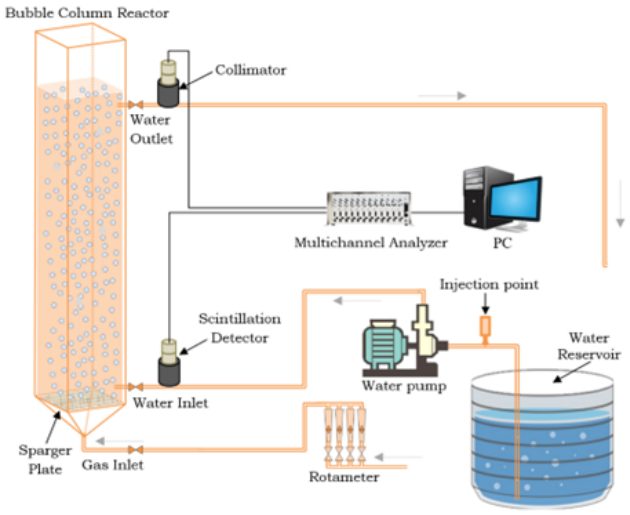



Figure 1: The RTD experimental setup.

### 2.1 Radiation Detectors

Two detectors were used and placed at the feed inlet and top outlets using lead collimated NaI(Tl) scintillation detectors were connected to a multichannel to record radiotracer concentration data at frequency of 50ms for further analysis.

### 2.2 Radioisotope Tc-99m

The amount of radiotracer required for a radiotracer test depends on the accuracy, efficiency of radiation detector, level of dilution, half-life of radiotracer and background radiation level. A series of experiments was carried out using 4 mCi radioisotope Tc-99m eluted as sodium pertechnetate solution extracted from Mo-99/Tc-99m generator.

Table 1: Properties of Tc-99m radiotracer.

| Radionuclide | Half-life (hours) | $\gamma$ Radiation of Interest (MeV) | Chemical Form in Aqueous |
|---|---|---|---|
| Tc-99m | 6 | 140 (98.6%) | $C_{13}H_{25}N_4O_3Tc$ |

## 3 Results and Discussion

Residence Time Distribution (RTD) is a probability distribution function defined as the amount of time that a fluid element could spend inside a vessel. The developed model by IAEA helps to understanding of a process or hydrodynamic model parameters, modeling a flow from RTD raw data is required to represent the experimental curve by a theoretical function E(t).

### 3.1 RTD Data Treatment

The RTD experimental data contain statistical fluctuations need to be treated before further data analysis. To obtain cleaned curve, dead time, background radiation, radioactive decay, starting point, data filtering, and data extrapolation correction must be done first before area normalization executed for RTD modeling.

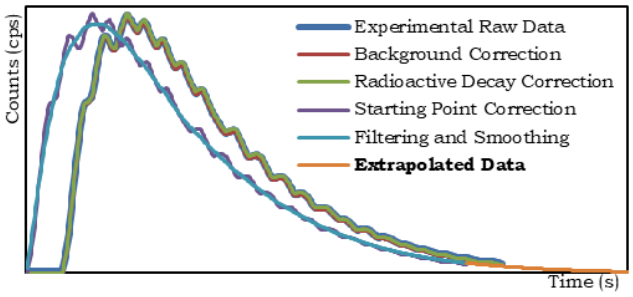



Figure 2: The corrected signal after curve treatment.

### 3.2 RTD Model Analysis

Parameters of the model were determined by optimizing experimental RTD curve with 6 different types of RTD mathematical models. The value of sum of the squares of the errors (SSE) between experimental and model can determine the most ideal RTD mathematical model where optimal value of parameters can be obtained by using the following equation (IAEA, 1996; Sugiharto et al., 2009):

$$SSE = \sqrt{\frac{1}{N_p}\int_0^{\infty}\left[E_{\exp}(t) - E_{\text{model}}\,(t,\ \text{parameter})\right]^2 dt} = \text{Minimum} \quad (1)$$

where $E_{\exp}(t)$ is the experimental measured RTD curve, $E_{\text{model}}$ (t,parameter) is the simulated RTD model and $N_p$ is the number of data points. After simulation has been completed, the best fitted model was chosen based on the smallest value of differences between measured experimental data and the mathematical model as suggested by IAEA (IAEA, 2008). The acceptable fitted model for current bubble column study was best described by perfect mixers in series with exchange model (PMSE) as shown in Figure 3. Thus, the capability of radioactive tracer to maintain its stability in ambient temperature and fluid flow media against chemical degradation and oxidation during RTD measurement was successfully validated.

Table 2: Optimal parameter values of simulated model

| RTD Model | $\tau$ | Pe | N | J | Tm | K | $\tau$2 | J2 | SSE Value | Seq. |
|---|---|---|---|---|---|---|---|---|---|---|
| ADM | 624 | 2 | | | | | | | $1.645 \times 10^{-8}$ | 5 |
| ADME | 358 | 2 | 1 | 1 | | | | | $0.976 \times 10^{-8}$ | 4 |
| PMS | 445 | | | 1.9 | | | | | $0.028 \times 10^{-8}$ | 3 |
| PMSE | 442 | | | 2 | 176 | 0.94 | | | $0.023 \times 10^{-8}$ | **1*** |
| PMP | 444 | | | 1.9 | | | 9.7 | 1 | $0.160 \times 10^{-8}$ | 2 |
| PMR | Optimization Failed | | | | | | | | | |

*Minimum sum of the square of error (highest goodness of fit to RTD curve)

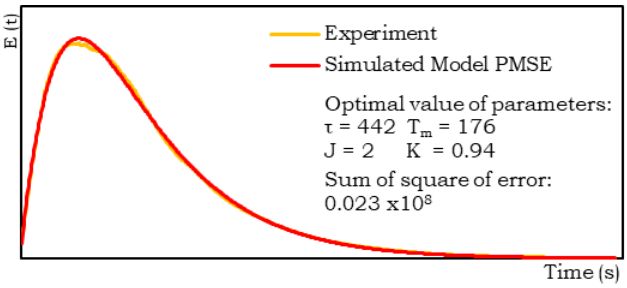



Figure 3: The RTD simulated PMSE model.

### 3.3 Conclusion

The current investigations to measure residence time distribution (RTD), including the data treatment process and validation of mean residence time using dedicated RTD mathematical models by the IAEA, have been successfully completed. The ISO Working Draft (WD) document was prepared on time and of high quality. Continuous work is ongoing to formulate, review, and finalize ISO documents at every stage of the ISO procedures. Once the WD document is approved by the P Member States of SC 5, the finalization process continues until the ISO document is published, which may take up to two years.

## References

IAEA. 1996. Residence time distribution software analysis. *International Atomic Energy Agency, Vienna, Austria*, Computer Manual Series(No.11).

IAEA. 2008. Radiotracer residence time distribution method for industrial and environmental applications. *Training Course Report*, Series 31, Vienna.

S. Sugiharto, Z. Suud, R. Kurniadi, W. Wibisono, and Z. Abidin. 2009. Radiotracer method for residence time distribution study in multi-phase flow system. *Applied Radiation Isotopes*, 67:1445–1448.

Individual Research Contribution Review, 2024: 373–374
*ISSN: 3083-922X*

# Concrete Slab Detection Using Ground Penetrating Radar

**Mohd Fajri Bin Osman**
Industrial Technology Division, Malaysian Nuclear Agency
43000 Kajang, Selangor
fajri@nm.gov.my

## Abstract

Ground Penetrating Radar (GPR) uses electromagnetic microwaves to detect and locate materials with varying dielectric constants. It is popular for non-destructive methods in civil engineering, geotechnical investigations, and monitoring concrete flaws. In an experiment, GPR surveys were conducted on concrete slabs to determine fracture causes, with most radargrams showing water penetration into the slab.

**Keywords:** GPR, Conrete Slab, Water Penetration

## 1 Introduction

Ground Penetrating Radar (GPR) uses electromagnetic The electromagnetic microwave used by Ground Penetrating Radar (GPR) is comparable to sound in an ultrasonic pulseecho technique. Its foundation is the idea that electromagnetic energy travels through materials with varying dielectric constants, much like acoustic impedance in sound. The amount of electromagnetic energy reflected at an interface between two materials increases with the difference in their dielectric constants. In non-destructive methods for detecting pipes and utilities, locating tanks and drums, inspecting concrete and rebar, sinkholes, geology and geologic hazards, landfill and burial pits, cemetery and grave sites, and archaeological research, GPR is growing in popularity.

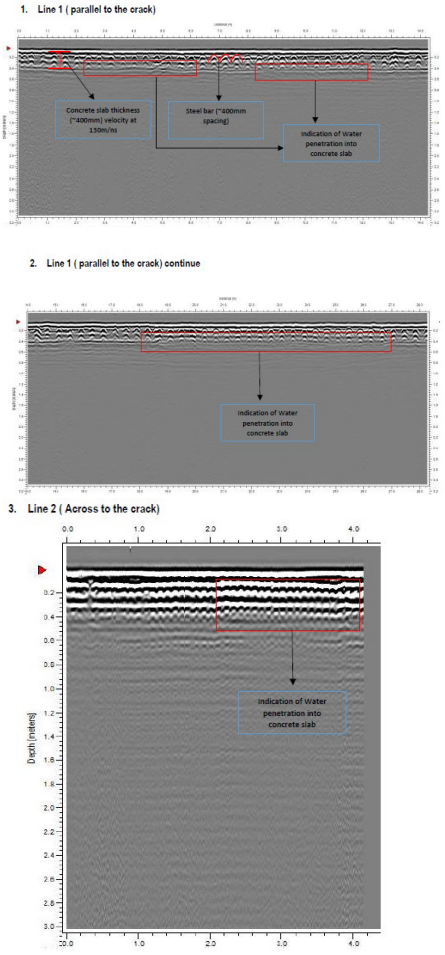
A continuous cross-sectional profile of several subsurface structures is produced. Parameters like bar position, void detection, and asphalt layer thickness are made possible in civil engineering. On the other hand, GPR scanning can provide crucial data for geotechnical investigations, including the depth to bedrock, various soil layers, and subsurface cavities. Through the use of an antenna, GPR sends radio wave pulses into the ground. High frequencies—typically between 300 MHz and 2.5 GHz—are employed for civil engineering applications. For the nondestructive detection of reinforcement bars, slab/asphalt layer thickness measurements, delaminations, voids, and other concrete flaws, radar provides a practical and quick method. It also has a lot of promise for additional uses, such as tracking the cement's hydration or strength development in concrete, analyzing how different admixtures affect concrete curing, figuring out how much water is in fresh concrete, and measuring the thickness of concrete members.

## 2 Methods

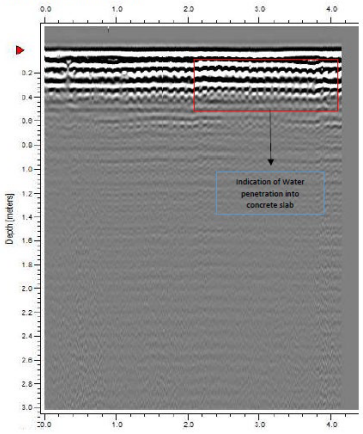
The experiment aims to do GPR surveys on concrete slabs in order to ascertain the underlying cause of the fracture at MEX toll Plaza, Putrajaya, Selangor. The survey made use of MALA GeoScience, Sweden's 800 MHz antenna RAMAC/GPRequipment.

Survey was done across the crack at approximately 4 meter as in Figure 1 with 5 line. Another whole line survey was performed in 28 meter along the crack as reference and comparison to the individual survey.

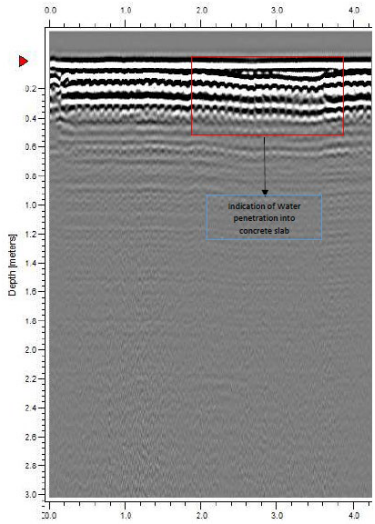
## 3 Results



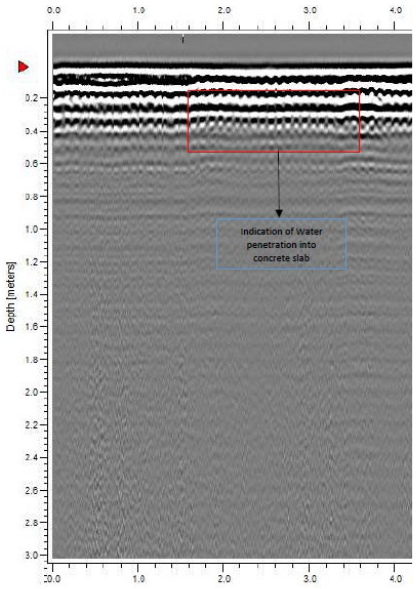
3. Line 2 ( Across to the crack)



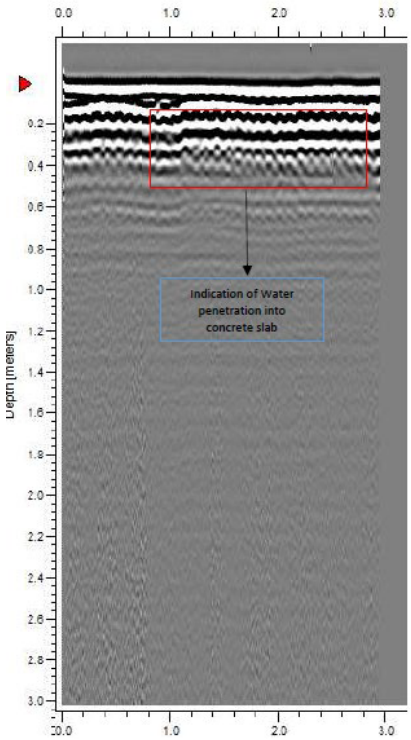

4. Line 3 ( Across to the crack)




Line 4 ( Across to the crack)




6. Line 5 ( Across to the crack)




## 4 Discussion and Conclusion

The total 4 line scan across crack and 1 line along the line has been scan using GPR antenna 800Mhz. From most of the radar grams show the indication of water penetration into concrete slab.

## References

Vienna (IAEA) International Atomic Energy Agency. 2002. Guidebook on non-destructive testing of concrete structures, training course. (17).

Mohamad Pauzi Ismail, Mohd. Azmi Ismail, Amry Amin Abas, and Suhairy Sani. 2004. Application of gpr in concrete inspection and geotechnical studies.

Individual Research Contribution Review, 2024: 375–376
*ISSN: 3083-922X*

# Effect of Internal Gas Hold-up on Packed Bed Reactor Using Gamma Densitometry

**Mohd Fitri Abdul Rahman**
Industrial Technology Division, Malaysian Nuclear Agency
43000 Kajang, Selangor
fitri@nm.gov.my

## Abstract

Gas holdup studies are important to determine the distribution inside the packed bed column. This study used gamma radiation (Cesium-137) to measure gas distributions in a 5 cm inner diameter of a packed bed reactor. The measurements were taken cross-sectionally along a 2.5m reactor filled with carborundum particles. Higher gas flows increased gas content while reducing liquid on catalyst surfaces. The method proved effective for the noninvasive measurement of phase distributions, benefiting reactor design and operation.

**Keywords:** Hold-up, Packed Bed, Gamma Densitometry

## 1 Introduction

Holdup is a phase distribution in a packed bed reactor. Determination of holdup is a crucial part of hydrodynamic studies, specifically in chemical engineering. A packed bed reactor is sometimes designed with internals and without the internals. The internals function as a heat probe to give heat to the packed bed reactor. However, this study focuses on hydrodynamics compared to chemical reactions as it was more of an interesting subject to explore.

The study of the effect of internal on phase holdup has been conducted by Ramesh et al. (Ramesh et al., 2009) for a three-phase fluidized bed. The method used was pressure drop measurement. The other study on multiple holdup equilibria was done for the pipe flows (Johannsson et al., 2024). Sun et al, study hydrodynamics of structured packing, mainly for liquid holdup (Sun et al., 2024).

The study on cross-sectional gas holdup was done on a photobioreactor using computed tomography techniques (Sabri et al., 2019). Other researchers Jasim et. al, studied the influence of tube diameter in the bubble column on the gas holdup and bubble dynamics (Jasim et al., 2019). Based on the literature reviews, studies are still needed for the cross-sectional holdup on packed bed reactors. The importance of the capability of using gamma densitometry can penetrate the packed bed reactor while the process is still online. The present work will benefit the packed bed reactor hydrodynamics studies and aid in reactor designs.

## 2 Methods

The multiphase column of 2m tall was designed with plexiglass packed with carborundum as a catalyst up to a height of 1.5m. The inner diameter is 5cm. The internal is a thermowell diameter of 0.5cm and a length of 1.5m which can be installed and un-installed.

The gas and liquid flow rates were used to control the flow rates applied to the column. Air was used as a gas phase and water as a liquid phase. The experiments were conducted with gas velocities from 0.05 to 0.5 m/s and liquid velocities from 0.02 to 0.1 m/s.

A 10 mCi of 137 Cesium gamma-ray source and a NaI Scintillation detector were installed at two axial locations along the column. Gamma-ray attenuation was measured in a 1-second measurement time. Then, the data acquisition was acquired from different flow conditions. The data acquisition and motor control for the simultaneous movement of the detector and source were designed by LabVIEW software. Figure 1 shows the schematic diagram of the experiment.

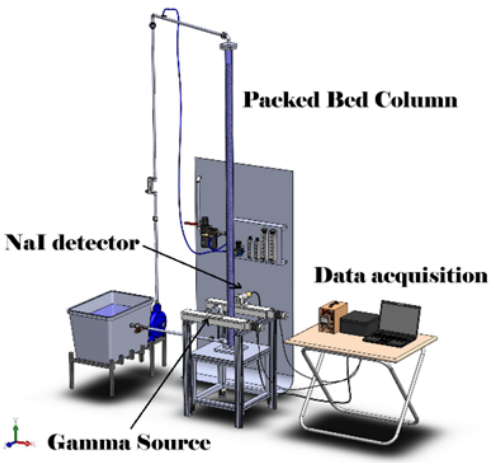



Figure 1: Gamma densitometry with Plexiglas packed bed column

Figure 2 shows the schematic diagram for the position of the source, detector, and column with rod/internal and without internal.

## 3 Results and Discussion

The gas holdup will be plotted using the raw data acquired from the data acquisition. Figure 3 shows the trend of the gas holdup.

In reference to the graph, the internal plays a pivotal role in the flow of the hydrodynamics. It shows that with the internal,

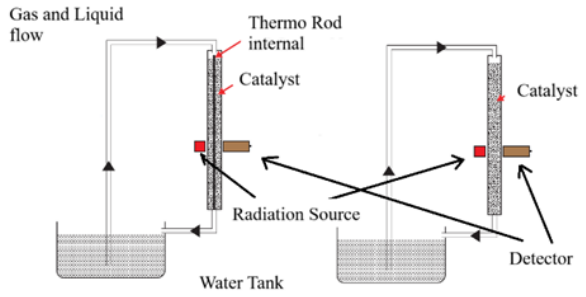



Figure 2: Schematic diagram of packed bed column with internal/rod and without internals.

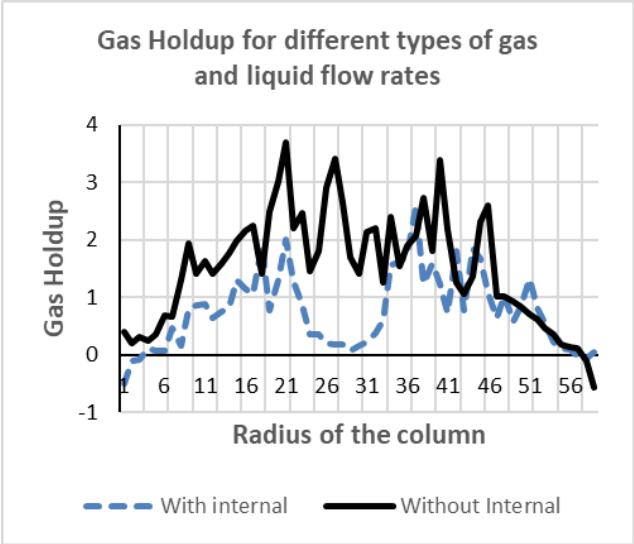



Figure 3: Gas holdup for the different gas and liquid flow rates.

the distribution of gas holdup is more homogenous compared to gas holdup without the internal. However, the gas and liquid flow rate will depend on the distribution of gas holdup. The higher gas and flow rate will result in a more homogenous distribution for the gas holdup based on columns with and without the internal.

With lower conditions in the flow rate of gas and liquid, liquid and gas channeling will be observed due to the liquid flow being confined to the wall sides. This indicates that further studies or experiments are needed to find the ideal condition of gas and liquid flow rate to receive the optimal homogenous conditions flow.

Figure 4 shows the liquid holdup of the different gas and liquid flow rates. It indicates that a quite homogeneous conditions.

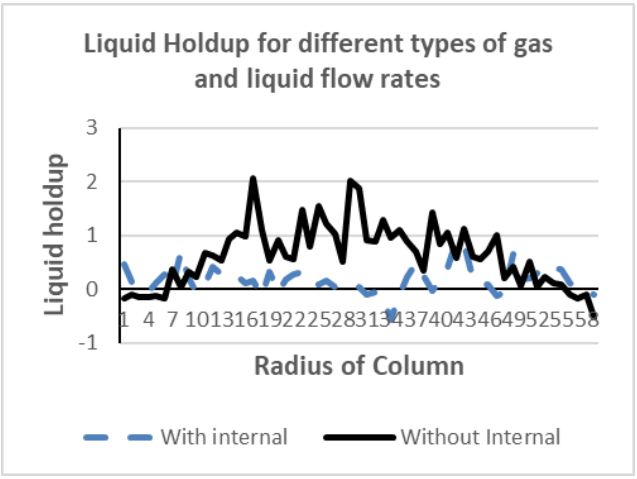



Figure 4: Liquid holdup for the different gas and liquid holdup

## 4 Conclusions

Hydrodynamics studies are fundamental in designing the best column conditions and operations parameters such as gas and liquid flow rates. Based on the findings, it is evident that with the inclusion of the internals, a more homogenous gas holdup and flow distribution will be observed. Overall, this study demonstrates the capability of gamma densitometry to indicate gas holdup with multiple types of columns. Further studies could explore other factors such as packing materials and types of internals.

## References

A.A. Jasim, A.J. Sultan, and M.H. Al-Dahhan. 2019. Influence of heat-exchanging tubes diameter on the gas holdup and bubble dynamics in a bubble column. *Fuel*, 236:1191–1203.

P.S. Johannsson, Z. Yang, D. Larrey, R. Belt, and L. Liu. 2024. Multiple holdup equilibria and hydraulic gradients in stratified gas-liquid flows. *Gas Science and Engineering.*, 131:205–461.

K.V. Ramesh, G.M.J. Raju, G.V.S. Sarma, and C. Bhaskara Sarma. 2009. Effect of internal on phase holdups of a three-phase fluidized bed. *Chemical Engineering Journal*, 145:393–398.

L.S. Sabri, A. J. Sultan, and M.H. Al-Dahhan. 2019. Investigating the cross-sectional gas holdup distribution in a split internal-loop photobioreactor during microalgae culturing using a sophisticated computed tomography (ct) technique. *Chemical Engineering Research and Design*, 149:13–33.

B. Sun, W.S. Tan, T. Bhatelia, and V.K. Pareek. 2024. Study on the hydrodynamics of structured packing: Liquid holdup and pressure drop of a novel 3d printed packing. *Chemical Engineering Research and Design*, 206:200–209.

Individual Research Contribution Review, 2024: 377–378
*ISSN: 3083-922X*

# Development of Hybrid Nanofibers

**Mohd Reusmaazran bin Yusof**
Industrial Technology Division, Malaysian Nuclear Agency
43000 Kajang, Selangor
reusmaazran@nm.gov.my

## Abstract

Nanofiber were produced using the electrospinnig technique to obtain the nanofibers diameter in the range of 100 – 350 nm. PLLA and PCL were use as synthetic polymer whereas the natural polymer from sago waste know as CMS and CMC were incorporated in the range of 10 to 40%. The nanofibers then undergo the number of characterizations including the morphology, chemical interaction, mechanical integration, thermal analysis and biodegradation. The study investigates the properties migration of synthetic polymer with present the natural polymer in the nanofiber mat.

## 1 Introduction

The nanofiber has being used in very wide range of application presently including water filtration, energy storage, drug delivery, biomedical applications and protective clothing. Hybrid nanofibers becoming a greater attention to many investigators to explore the new properties of the materials in the nanofibers in the way to be functionalize to different applications.

## 2 Investigation Procedures

System parameter were obtained by the hybrid polymer solution between natural and synthetic polymers at different composition. Natural polymer was extracted from a sago waste and undergo the carboxymethylation process to improve the solubility. The hybrid polymer solution were electro spin at 10 to 15 kV with the flowrate 0.05 ml/min. The distance from the polymer solution source to the collector were fix to 16 cm (Figure 1). CMC were extracted from the sago waste whereas CMS extracted from a Sago Palm. Nanofiber mat were collected at the collector for further characterization which morphology, chemical interaction, mechanical and biodegradation.

## 3 Findings

Refer Figure 2, 3 and 4.

## 4 Conclusion

The study indicates the potential use of natural polymer of CMS to incorporate either with the PLLA or other synthetic polymers. This would initiate the further investigation to comply with biomedical applications. In vitro degradation,

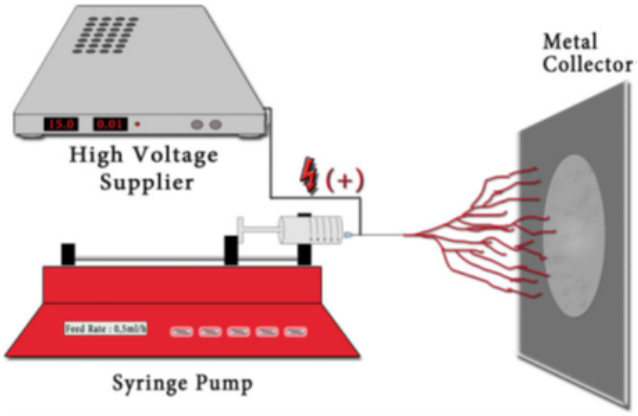



Figure 1: Schematic diagram of needle electrospinning

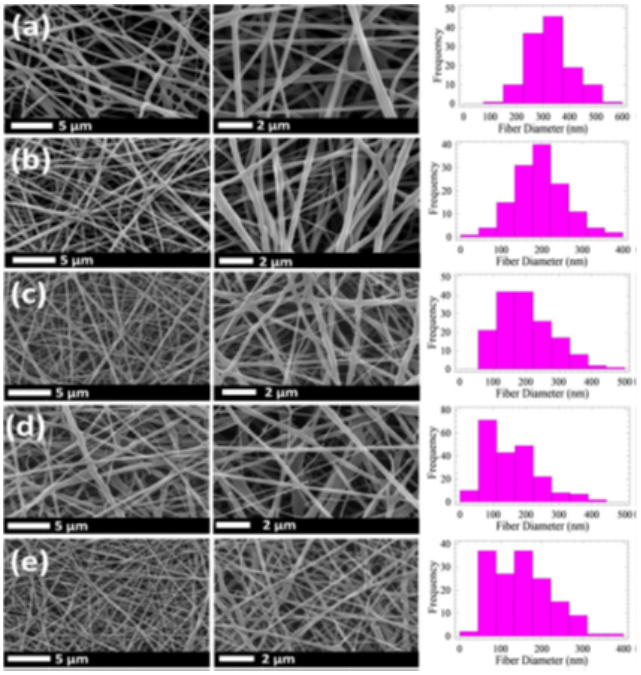



Figure 2: Scanning electron microscope images of the nanofibers at ×5000 and ×10 000 of magnification and the distribution of fiber diameter from (a) to (e) the increasing of natural polymer (CMS) in PLLA

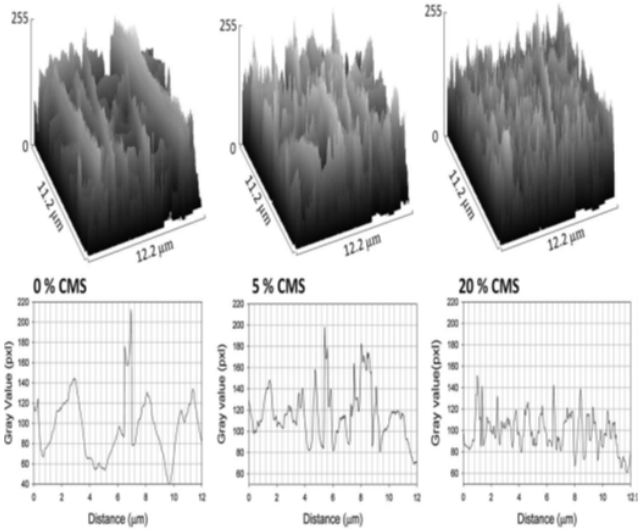



Figure 3: Topography of the surface texture and surface profile of neat poly(L-lactide acid) (PLLA), 5%, and 20% of carboxymethyl starch (CMS) in PLLA nanofibers obtained by image J of gray value from scanning electron microscope images

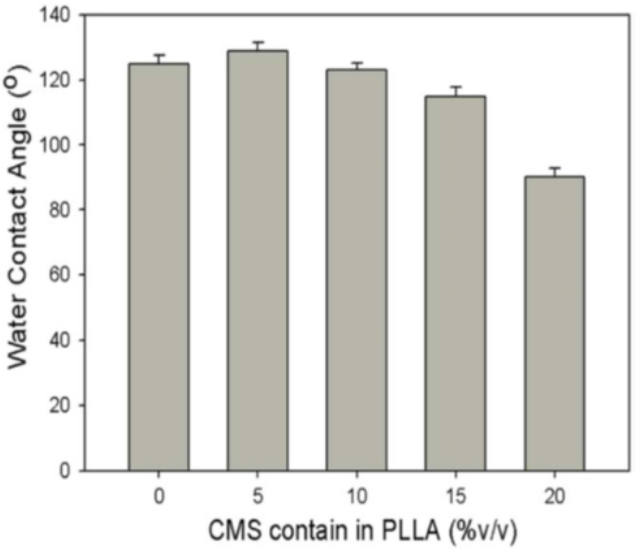



Figure 5: Water contact angle indicates the surface wettability

surface architecture, cell material interactions, and the performance of this composite PLLA/CMS nanofiber in vivo need to be investigated.

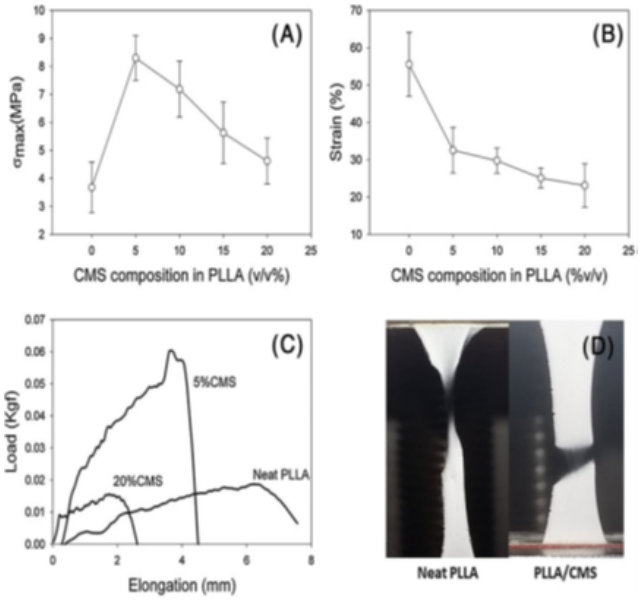



Figure 4: Mechanical properties of the neat poly(L-lactide acid) (PLLA) and composite PLLA/carboxymethyl starch (CMS) nanofibers: (A) tensile strength, (B) tensile strain, (C) tensile behavior, and (D) image of fracture behavior

Individual Research Contribution Review, 2024: 379–380
*ISSN: 3083-922X*

# Potential Application of Laser Shearography for Analysis of Corrosion in Petroleum Pipeline

**Mohd Yusnisyam Bin Yusof**
Industrial Technology Division, Malaysian Nuclear Agency
43000 Kajang, Selangor
yusnisyam@nm.gov.my

## Abstract

This paper aims at assessing of corrosion defects in standard petroleum pipelines by using shearography method. Shearography technique reveals the stress-affected zone due to additional loading that can be realized by the laser speckle correlation on the inspected object.

**Keywords:** Phase, Fringe Pattern, Phase Shift

## 1 Introduction

Shearography can be used for fast and nondestructive inspection of large components, because local defects in components generally cause little additional strain on its surface (Hung, 1982). This paper deals with the application of shearography for nondestructive inspection of petroleum pipeline. The principle is based on measuring the surface deformation of the pipe to be inspected, which can be employed by changes the magnitude of applied pressure in the pipe.

## 2 Methods

In pipeline inspection, shearography shows the effect of a local strain concentration due to mechanical loading if a defect present, on the visible surface of this component. The petroleum pipeline to be inspected is internally loaded by pressurized the pipe, this will produce the internal stress of the pipe wall. In the areas of weakened wall caused by corrosion, the wall of the pipeline is deformed more than the areas of without defects (see Figure 1, state 1 and state 2). The phase change difference of a loaded and unloaded state provides information about the deformation of the wall of the pipeline.

The area to be inspected is illuminated with laser light at a define illumination angle and the amount of shearing. An image of the inspected area is recorded by charge coupled device (CCD) camera and stored as a master image on an image frame. The following video images are recorded and subtracted pixel by pixel in real time from this master image, result displays as contour line of the phase change on the surface of the pipeline as bright and dark fringes. This correspond to isostrain lines, e.g. a local strain concentration will produce a typical fringe pattern as shown on the far right of Figure 1.

In phase-shifted interferometry technique, three and four phase shifted sinusoidal fringe patterns are shifted onto an object surface with phase shifted by $2\pi/3$ and $\pi/2$ respectively. The following algorithms (Equation 1 and 2) are used to represent successive intensity distributions with phase shift between each frame.

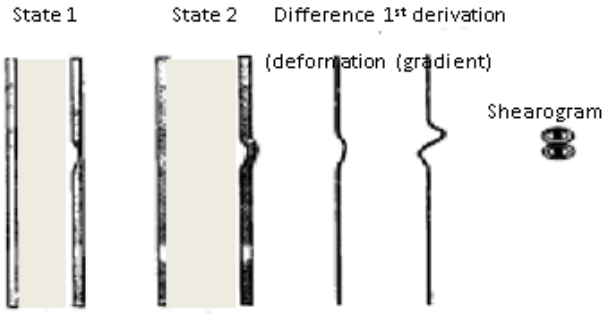



Figure 1: Principle of Shearographic Pipeline Inspection.

**3 Phase Step Image Frame Intensity**

$$I_1(x,y) = a(x,y) + b(x,y) + cos\varphi(x,y)$$
$$I_2(x,y) = a(x,y) + b(x,y) + cos[\varphi(x,y) + \frac{2\pi}{3}]$$
$$I_3(x,y) = a(x,y) + b(x,y) + cos[\varphi(x,y) + \frac{4\pi}{3}] \quad (1)$$

**4 Phase Step Image Frame Intensity**

$$I_1(x,y) = a(x,y) + b(x,y) + cos\varphi(x,y)$$
$$I_2(x,y) = a(x,y) + b(x,y) + cos[\varphi(x,y) + \frac{\pi}{2}]$$
$$I_3(x,y) = a(x,y) + b(x,y) + cos[\varphi(x,y) + \pi] \quad (2)$$
$$I_4(x,y) = a(x,y) + b(x,y) + cos[\varphi(x,y) + \frac{3\pi}{2}]$$

**3 Phase Step Image Frame Technique**

$$\varphi(x,y) = \arctan\sqrt{3}\frac{I_1(x,y) - I_3(x,y)}{2I_1(x,y) - I_2(x,y) - I_3(x,y)}$$

**4 Phase Step Image Frame Technique**

$$\varphi(x,y) = \arctan\frac{I_4(x,y) - I_2(x,y)}{I_1(x,y) - I_3(x,y)} \quad (3)$$

Where a(x,y) is the average intensity, b(x,y) is the intensity modulation, and $\varphi$(x,y) is the optical phase. By solving Equation 1 and 2 simultaneously, the phase $\varphi$(x,y) at point (x,y) in the image can be obtained as given by the Equation 3.

The phase $\varphi(x,y)$ results in a principal value of $2\pi$ phase shifted regardless of the actual value of the phase.

## 3 Data and Results

In this experiment, radiography testing method and shearography technique powered by 15mWatts Nd:YAG (532nm) laser was used. The vertical shearing ($\delta x$) amount of the interferometer was set at 10mm. The stress mechanism was applied into pipeline using air pressure at about 0.5MPa. The measurement taken from the density profile in the radiographic image was measured in gray value. An example of Series A at positions 1, 2 and 3 of film density profile is given in Figure 2.

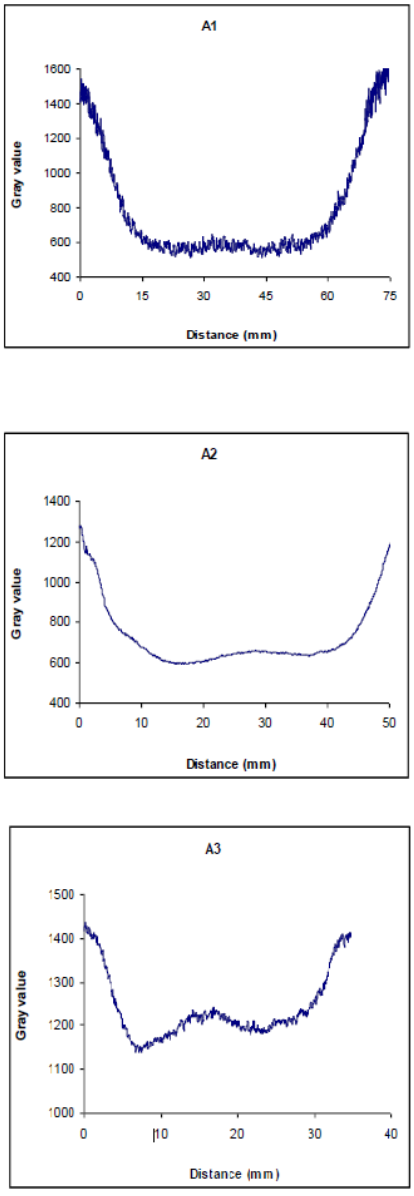



Figure 2: Film density profile (gray value) at the corrosion area in the pipe a) corrosion area A1 b) corrosion area A2 and c) corrosion area A3

Figure 3 shows the wrapped phase image of corrosion series A1, which represent the strain distribution at the corrosion area and compared to the profile of corrosion area from gray value digital radiography.

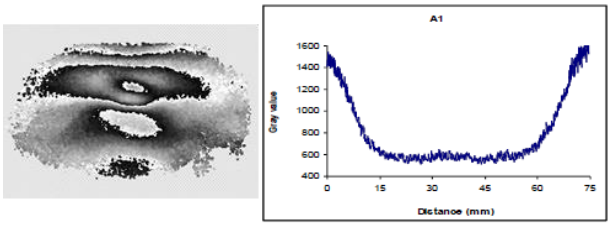



Figure 3: Corrosion area of 5mm depth at position A1 of inner pipe wall a) wrapped phased map by shearography techniques represent the stress pattern due to change of pressure $\triangle$P=0.24MPa, b) image density profile represent the depth and shape of corrosion by radiography techniques.

## 4 Discussion and Conclusion

Radiography and shearograhy techniques were used to inspect the corrosions in test pipeline. The study indicated that radiography is capable to provide information about the profile of depth, size and shape of the corrosion in pipeline. Whereas laser shearography was found potential for estimation of the severity and criticality, size and shape of the corrosion. Data generated from shearography techniques could be more meaningful since it provided information about the criticality of corrosion compared to radiography techniques which only provide physical information of corrosion. This experiment proposed that the shearograhy has potential application for nondestructive inspection of corrosion in steel petroleum pipelines.

## References

W.S. Wan Abdullah. 2019. Analysis of error functions in speckle shearing interferometry.

Y.Y Hung. 1982. Shearography: a new optical method for strain measurement and nondestructive testing. *Opt. Eng.*, 21(3):391–395.

Y.Y Hung. 1999. Applications of digital shearography for testing of composite structures. *Composites Part B*, 30:765–773.

Individual Research Contribution Review, 2024: 381–382
*ISSN: 3083-922X*

# Development of Image Reconstruction and Analysis for Gamma Process Computed Tomography

**Muhamad Noor Izwan Bin Ishak**
Industrial Technology Division, Malaysian Nuclear Agency
43000 Kajang, Selangor
noorizwan@nm.gov.my

## Abstract

Gamma-ray computed tomography (CT) is a vital non-destructive evaluation tool, especially for industrial applications like packed bed column scanning. Current systems rely on FORTRAN for data acquisition and image reconstruction but lack a user-friendly interface for non-experts. This project aims to upgrade the existing system by developing algorithms for data acquisition and image reconstruction, optimizing image accuracy, and creating an intuitive user interface. Using open-source tools like Python, C/C++, Fortran, and LabView, the project will improve the system's efficiency and accessibility. The results will enhance industrial applications and contribute to further research in material inspection and process monitoring.

**Keywords:** Gamma-ray computed tomography, image reconstruction, data acquisition, user interface, packed bed column scanning, tomography optimization, process monitoring

## 1 Introduction

Gamma-ray computed tomography (CT) is a powerful non-destructive evaluation (NDE) technique used in industrial applications to inspect and analyze complex internal structures, particularly for packed bed column scanning. It enables the detection of process and mechanical faults and provides critical insights into material distribution and flow dynamics in reactors. This real-time imaging technology is essential for ensuring quality control, safety, and performance in industries like chemical engineering and nuclear technology.

However, current gamma-process tomography systems are hindered by outdated FORTRAN-based software and computationally intensive reconstruction algorithms, requiring specialized knowledge to operate. This lack of user-friendliness limits the broader application of the technology.

This study aims to modernize the gamma-process tomography system by developing efficient software that integrates advanced image reconstruction techniques with a user-friendly graphical interface (GUI). Using open-source tools like Python, C/C++, Fortran, and LabView, the project will focus on optimizing image reconstruction accuracy and simplifying the system for use by non-expert industrial users.

## 2 Methods

This research takes a systematic approach to improve gamma-ray computed tomography (CT) for industrial use. Key stages include software development, system calibration, data acquisition, image reconstruction, user interface design, and optimization. methodology:

### 2.1 Code Development

The project focuses on developing algorithms for data acquisition and image reconstruction using Python, selected for its strong libraries for image processing. Key considerations include gamma-ray attenuation and detector characteristics, with the Expectation Maximization (EM) algorithm being central for iterative image reconstruction.

### 2.2 Lab Testing and Calibration

Extensive calibration is conducted to ensure accuracy, including baseline measurements of the gamma-ray source and detectors in a controlled environment to correct for artifacts in the data.

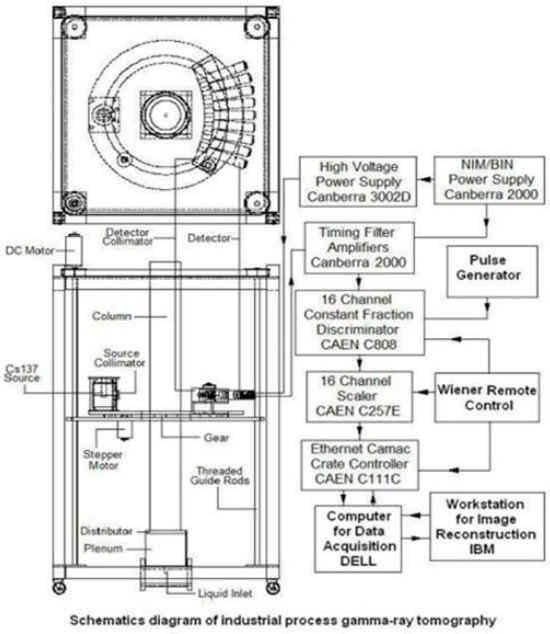



Figure 1: Gamma Process Tomography setup

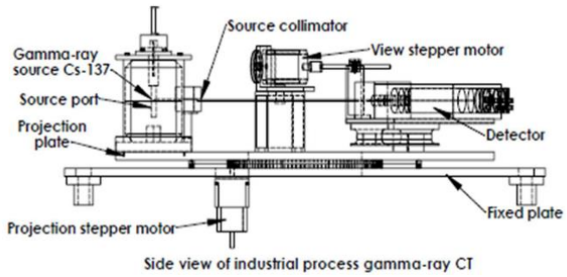



Figure 2: Setup Table



Figure 3: Gamma Process Tomography machine

### 2.3 Data Acquisition

Initial data acquisition involves capturing projection data from NaI(Tl) detectors as the object rotates. Test datasets are collected under various conditions and processed to minimize noise.

### 2.4 Image Reconstruction

The EM algorithm will refine images based on gamma-ray attenuation. The reconstruction process will focus on improving image accuracy and efficiency, addressing data quality variations.

### 2.5 User Interface Development

An intuitive graphical user interface (GUI) will be developed for non-expert users, featuring data visualization, image manipulation, and easy export options, using Python frameworks like Tkinter or PyQt.

### 2.6 System Optimization and Software Refinement

Post-testing, the system will be refined for better performance and usability based on user feedback. Continuous calibration will enhance reliability and reduce artifacts.

### 2.7 Data Analysis and Validation

Reconstructed images will be validated against benchmark datasets to assess accuracy and reliability, particularly in detecting internal defects for industrial applications.

### 2.8 Report and Publication

Results will be compiled in a report detailing system performance and optimizations, which will be shared in a peer-reviewed journal or at conferences to highlight advancements in gamma-ray tomography systems.

## 3 Data/Results

The project is expected to achieve accurate density profiles using the gamma-process tomography system, with improved image reconstruction quality and reduced computational time. Preliminary results should demonstrate enhanced image resolution, fewer artifacts, and optimized processing speed. The new user interface is anticipated to allow easy operation by non-experts, while calibration tests will minimize errors and improve accuracy. Data analysis will validate the system's ability to detect defects and material variations, ensuring reliable performance for industrial applications.

## 4 Discussion/Conclusions

This project aims to enhance the gamma-process tomography system by improving image reconstruction accuracy, optimizing processing speed, and creating a user-friendly interface. The expected outcomes include more reliable density profiles, faster data processing, and increased accessibility for non-expert users. Ultimately, these advancements will make the system a more effective tool for industrial applications, contributing to improved material inspection and process monitoring. Further refinements will be made based on initial testing and user feedback.

## References

A. Jaafar, M. K. Said, A. Mahmood, and 8 others. 2011. Development of a gamma-ray process tomography system for hydrodynamic characterisation of multiphase reactors. *Applied Mechanics and Materials*, 6:1–5.

Individual Research Contribution Review, 2024: 383–384
*ISSN: 3083-922X*

# Evaluation of Impact Damage in Carbon/Carbon Composites Using Piezoelectric transducer-based Vibrothermography

**M.Z. Umar**
Industrial Technology Division, Malaysian Nuclear Agency
43000 Kajang, Selangor
zaki@nm.gov.my

## Abstract

This study demonstrates the application of an advanced thermal non-destructive testing technique known as piezoelectric transducer-based vibrothermography for finding hidden defects in a carbon/carbon (C/C) composite. The C/C sample, which contained twelve 5 J impact damage was ultrasonically stimulated using four ultrasonic devices at frequencies of 22, 40, 60, and 100 kHz. The surface temperature elevations produced by the defects were recorded and quantitatively analysed by using an infrared imager. The effect of stimulation frequency and power efficiency of all ultrasonic devices employed on defect detection was investigated.

**Keywords:** impact damage, carbon/carbon, piezoelectric transducer, vibrothermography

## 1 Introduction

The potential of VT technique in the detection of subsurface defects in composites have been proven by many researchers (Vavilov et al., 2014; Rantala et al., 1997). Typical VT technique using piezoelectric and magnetostrictive transducers encounters the problem of reproducibility. In this study, we investigate the efficiency of four different ultrasonic transducers operating at the frequencies of 22, 40, 60 and 100 kHz in application to the detection of impact damage in C/C composite. The following issues have been considered: 1) efficiency of ultrasonic devices concerning acoustic power absorbed by a test sample, 2) efficiency of ultrasonic devices in regard to total electric power, 3) quality of contact between a transducer and a sample, 4) distance between a stimulation point and a defect.

## 2 Experimental setup and sample

A classical experimental setup shown in Figure 1 was used in this study. The electrical power of the ultrasonic units was set to 200 W (the maximum power of the unit – 400 W). Experiments were carried out on a 440×350×10 mm bi-directional C/C plate containing 12 areas of 5 J impact damage (Figure 2), which were placed by concentric circles at different radii from the stimulation points. The defects were introduced in the sample by using a semi-spherical 1-inch-radius impact tip (INSTRON Dynatup 9250HV machine). The impact of such low power produced no visible defect indications on the

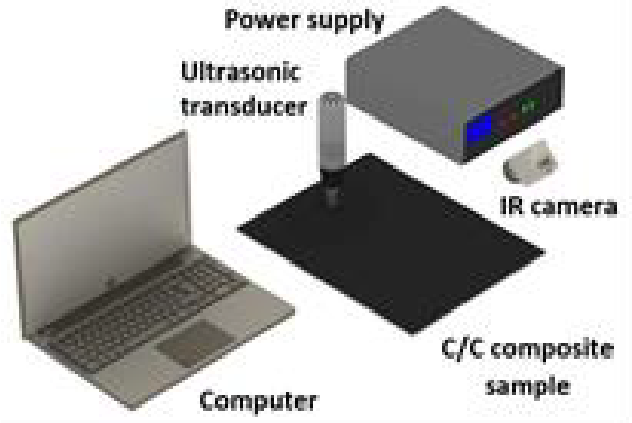



Figure 1: Simplified VT experimental setup

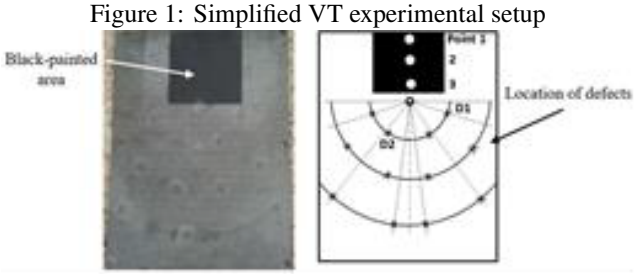



Figure 2: Bi-directional C/C composite sample with 12 impact damage (5J energy) areas

sample surface. A square area on the sample surface was painted black to analyze C/C composite emissivity and the influence of surface clutter on test results. The test plate was ultrasonically stimulated by using 4 piezoelectric transducer-based ultrasonic devices operating at the frequencies of 22, 40, 60 and 100 kHz. Ultrasound was inputted in the sample at Points 1-3, as shown in Figure 2. In further analysis, two defect areas called D1 and D2 were chosen for quantitative evaluation of detection parameters. The distance between D1 and D2 defects located by the first concentric circle and the stimulation Point 1 was 150 mm, Point 2 – 110 mm and Point 3 – 90 mm. As it will be shown below, only faint temperature indications were observed in the case of defects located by the second (210 mm from Point 1) and third (270 mm from Point 1) circles.

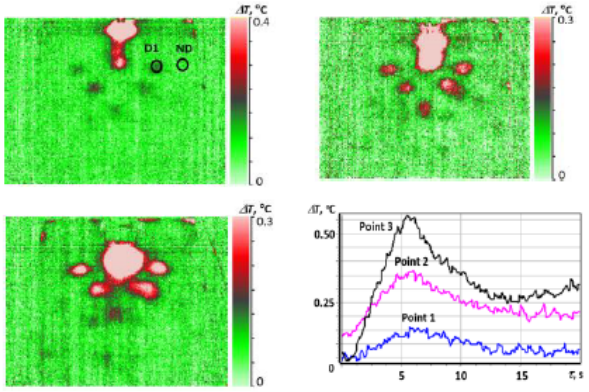



Figure 3: IR thermograms at the end of stimulation and evolutions of ΔT vs. $\tau$.

## 3 Results and Discussion

As mentioned above, the C/C sample was stimulated at four frequencies for 5 seconds at 3 points located at different distances from the defect sites, see Figure 2: The ultrasonic transducers were pressed to the sample surface employing a robotic manipulator, which ensured the same clamping force of 3.5 kg. One of the defect areas (D1) was chosen to calculate SNR values concerning the nearby sound area (ND), see the IR thermogram obtained when stimulating Point 1. The test results are presented in Figure 3 as the IR thermograms at the end of stimulation and evolutions of ΔT vs. $\tau$. Only the defects in the first circular row and one defect in the second row are detected thus proving the strong influence of distance on defect signals because of the damping of ultrasound in C/C composite. The maximal values of ΔT, which occurred at the end of stimulation, are given in Table 1. In general, temperature signals over the defect D1 grow up with shorter distances between the defect and the stimulation point, although such consistency was not observed in all test cases. We explain this with the fact that the quality of the contact between the transducer and the material that strongly affects absorbed acoustic energy can hardly be controlled from one test to another, even if the constant clamping force was provided.

Table 1: Maximal ΔT values (four frequencies, three surface points)

| Point | ΔT, °C (ΔT/$Q_u$, °C/W) | | | |
|---|---|---|---|---|
| | 22 kHz | 44 kHz | 60 kHz | 100 kHz |
| 1 | 0.09 (0.0029) | 0.16 (0.0091) | 0.49 (0.022) | 0.22 (0.025) |
| 2 | 0.31 (0.0098) | 0.37 (0.021) | 0.41 (0.018) | 0.34 (0.039) |
| 3 | 0.23 (0.0073) | 0.57 (0.032) | 0.15 (0.0066) | 0.11 (0.013) |

Another way of optimizing thermoacoustic parameters is using signal-to-noise ratio (SNR) as a figure of merit:

$$T = \frac{\overline{T_d} - \overline{T_{nd}}}{\sigma_{nd}} \quad (1)$$

, where $\overline{T_d}$ - $\overline{T_{nd}}$ are the mean temperatures in chosen defect and non-defect areas (such areas are shown in Figure 3 for the defect D1). SNR varies in time in tact with the corresponding

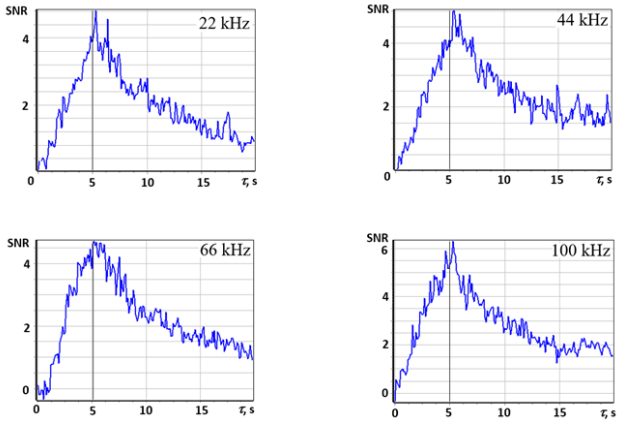



Figure 4: Signal-to-noise (SNR) vs. time (stimulation at Point 2)

ΔT($\tau$) values, see some examples in Figure 4. Since a mean value of noise is constant in time, maximal SNR values appear at the end of stimulation, i.e. at 5 seconds. These values are shown in Table 2 for all 12 test cases analyzed.

Table 2: Maximal SNR values (four frequencies, three surface points)

| Point | SNR | | | |
|---|---|---|---|---|
| | 22 kHz | 44 kHz | 60 kHz | 100 kHz |
| 1 | 2.0 | 2.8 | 8.3 | 3.9 |
| 2 | 5.5 | 5.0 | 4.7 | 6.3 |
| 3 | 5.2 | 7.1 | 2.9 | 0.7 |

## 4 Conclusion

In this study, the attractiveness of the VT technique for detecting low energy impact damage defects was demonstrated. VT is considered as a fast and reliable inspection technique that can be used for the assessment of technical conditions of various types of composite structures. However, there is still a lack of understanding of the physics governing the heat generation process in defective zones. Further studies are needed to help explain the heating mechanisms and their correlation with the resonant features of the structure, especially as complex geometries are considered. This will lay the base for the development of more reliable theoretical and numerical models allowing calculation of the surface temperature produced by buried heat sources.

## References

J. Rantala, D. Wu, A. Salerno, and G.. Busse. 1997. Lock-in thermography with mechanical loss angle heating at ultrasonic frequencies. *Proc. Conference on Quantitative Infrared Thermography (QIRT'97), Eurotherm Seminar*, 50:388–393.

VP. Vavilov, A.O. Chulkov, and D.A. Derusova. 2014. Ir thermographic characterization of low energy impact damage in carbon/carbon composite by applying optical and ultrasonic stimulation. *Proc. SPIE*, 9105(91050J).

Individual Research Contribution Review, 2024: 385–386
*ISSN: 3083-922X*

# Evaluation of Gamma Radiation Disinfection of Rare Books

**Nadira Kamarudin**
Industrial Technology Division, Malaysian Nuclear Agency
43000 Kajang, Selangor
nadira@nm.gov.my

## Abstract

This study demonstrates effective gamma radiation disinfection of total of 341 rare books from the Museum Perak Library collection, eliminating microbial contamination while preserving structural integrity, aesthetics, and chemical composition. Analysis confirmed gamma radiation at optimum dose provides a safe and reliable method for disinfecting and conserving valuable cultural heritage artifacts.

**Keywords:** Gamma Radiation, Rare Books Preservation, Cultural Heritage Conservation

## 1 Introduction

Rare books represent invaluable cultural heritage but are vulnerable to microbial contamination and structural damage over time. To ensure their preservation, 341 rare books from the Perak Museum Library were disinfected using gamma radiation. This innovative approach focused on eliminating harmful microorganisms while preserving the books' original physical and aesthetic properties. The International Atomic Energy Agency (IAEA) has highlighted the application of radiation techniques in cultural heritage conservation as an effective and non-invasive method. Their publication, Radiation and Cultural Heritage, provides insights into the safe application of radiation for disinfection and preservation purposes (IAEA, 2002). Comprehensive pre- and post-irradiation evaluations confirmed the method's effectiveness and safety, making it a viable solution for protecting historical collections. The study highlights gamma radiation's potential to maintain the integrity of rare materials without causing degradation, supporting its use in cultural heritage conservation. The primary aim of this study is to disinfect total of 341 rare books from the Perak Museum Library using gamma radiation and assess its effects on the books' structural, aesthetic, and chemical properties.

## 2 Methods

This study utilized a systematic approach to evaluate the effectiveness of gamma radiation for disinfecting rare books. The methods were designed to ensure sterility while preserving the books' structural and aesthetic properties. The process included careful preparation of materials, precise application of radiation doses, and rigorous pre- and post-irradiation analyses to assess the impact on microbial contamination, color stability, and chemical integrity.

### 2.1 Material Preparation

Prior to irradiation, the books were assessed for condition and prepared by sealing them in plastic to prevent contamination. This sealing method, although not mandatory, it ensured sterility throughout the disinfection process. Additionally, the books were organized into totes, and their volumes measured to optimize dose penetration during irradiation. Detailed records of these preparations were maintained to ensure accuracy and reproducibility of the process.

### 2.2 Gamma Radiation Procedure

The SINAGAMA facility performed irradiation under controlled conditions. Subjected to dose mapping to ensure accurate radiation levels (6–10 kGy) was applied. Dose mapping was done to verify uniform distribution.

### 2.3 Evaluation Techniques

Pre- and post-irradiation analyses included evaluations to ensure the gamma radiation effectively eliminated microbial contamination without compromising the structural, chemical, or aesthetic integrity of the books. The techniques used for evaluating are:

1. Microbial sampling for colony formation.
2. Colorimetric analysis using a spectrophotometer (CIELAB colour space).
3. Structural examination with X-ray Diffraction (XRD).
4. Chemical assessment through Fourier Transform Infrared Spectroscopy (FTIR).

## 3 Results

The results of this study highlight the effectiveness of gamma radiation as a disinfection method for rare books. The findings demonstrate its success in eliminating microbial contamination while maintaining the books' structural integrity, colour stability, and chemical composition. Each aspect was meticulously analysed to validate the preservation of the rare books' original characteristics.

### 3.1 Microbial growth

Heavy microbial growth (too numerous to count, TNTC) was observed before irradiation. Post- irradiation sampling revealed no microbial growth, confirming effective disinfection.

Table 1: Colony formation before irradiation.

| Sample | Agar (Cfu/ML) | Dilution Factor | | | | |
|---|---|---|---|---|---|---|
| | | $10^{-1}$ | $10^{-2}$ | $10^{-3}$ | $10^{-4}$ | $10^{-5}$ |
| 940 | PDA | TNTC | | | | 66 |
| | NAA | TNTC | | | | 75 |
| 910 | PDA | TNTC | | | | 75 |
| | NAA | TNTC | | | | 47 |

### 3.2 Color stability

The colour changes were calculated from random sampling techniques at the same location for pre- and post-irradiation. Changes in $\triangle E^*$ values indicated negligible visible colour differences, with most $\triangle E^* \leq 1$, except for slight changes in one sample ($\triangle E^* = 1.6$).

### 3.3 Structural changes

XRD analysis showed minimal changes in cellulose crystallinity, with primary peaks remaining consistent, indicating negligible damage.

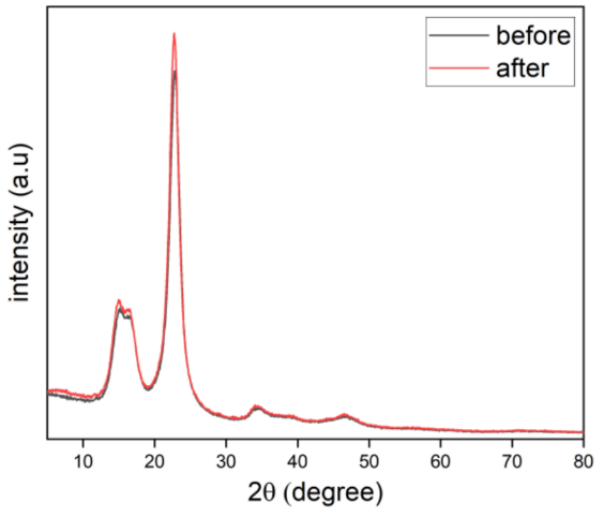



Figure 1: XRD spectrum for a random sample taken at the same location, pre- and post-irradiation

### 3.4 Chemical changes

FTIR revealed minor chemical changes, such as slight increases in carbonyl groups and reductions in hydroxyl groups, without significant structural degradation. These changes, while indicative of mild oxidative processes, do not translate into visible or functional damage to the books. This confirms that gamma irradiation is a safe and effective method for disinfection without compromising the chemical integrity of rare materials.

## 4 Discussion/Conclusions

Gamma irradiation at optimized doses effectively disinfected the rare books while preserving their aesthetic and material properties. The method is confirmed to be safe and effective

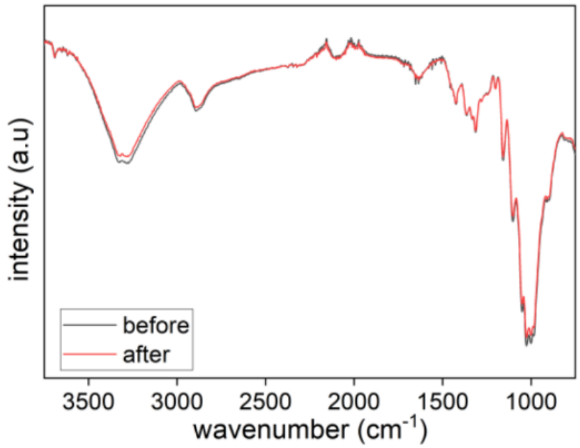



Figure 2: FTIR spectrum for a random sample taken at the same location, pre- and post-irradiation

for cultural heritage conservation. The thorough pre- and post-irradiation evaluation techniques employed, including microbial, structural, and chemical analyses, substantiate that the applied dose was adequate for effective disinfection. The detailed assessment methodologies provided a comprehensive understanding of the impact, confirming no significant damage to the books. This study aligns with findings by Tormey and Rooney (Tormey and Rooney, 2018), which also emphasize gamma radiation's efficacy for disinfecting manuscripts without harmful effects. To enhance preservation, complementary measures such as environmental control and periodic monitoring are suggested. This ensures the long-term protection and usability of rare books in archives and libraries.

## References

IAEA. 2002. Radiation and cultural heritage. *IAEA-TECDOC-1276*.

L. Tormey and D. Rooney. 2018. Gamma radiation for the disinfection of books and manuscripts. *Journal of Cultural Heritage Conservation*, 15(3):123–125.

Individual Research Contribution Review, 2024: 387–388
*ISSN: 3083-922X*

# Enhancing Neutron Shielding: Investigating The Absorption Properties Of Mortar With Colemanite Mineral

**N.M. Azreen**
Industrial Technology Division, Malaysian Nuclear Agency
43000 Kajang, Selangor
noorazreen@nm.gov.my

## Abstract

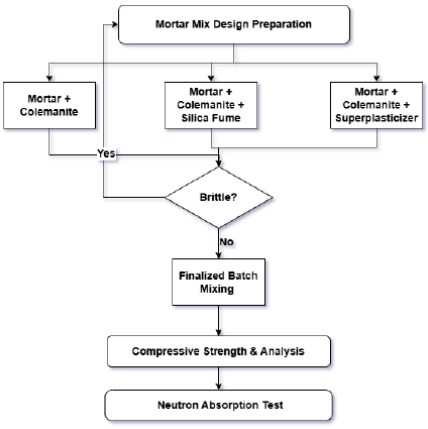
This research examines the synergistic impacts of silica fume (SF) and superplasticizer (SP) on the characteristics of concrete, prioritizing aspects such as workability, compressive strength, brittleness, and neutron attenuation. The findings indicate that SP alone exhibits superior performance in rebound hammer evaluations; however, mixtures of SF and SP successfully endure drop tests without exhibiting cracks, reflecting their resilience. Workability, evaluated through Ultrasonic Pulse Velocity (UPV), demonstrates that mixtures containing SF surpass the 4500 m/s benchmark, signifying enhanced workability in comparison to SP alone. Compressive strength assessments indicate that SF + SP mixtures consistently yield higher and more stable strength over time. Furthermore, neutron attenuation studies reveal that the SF + SP combination significantly improves neutron shielding efficacy, surpassing the performance of SP when used independently of SF. In summary, while SP alone delivers commendable performance in specific mechanical properties, the amalgamation of SF and SP yields superior overall characteristics of concrete, encompassing enhanced workability, augmented compressive strength, and better radiation shielding capabilities. This investigation highlights the critical role of mix design in optimizing concrete for structural and radiation-sensitive applications, thereby providing significant insights into materials science and engineering.

**Keywords:** silica fume; superplasticizer; concrete; rebound hammer; ultrasonic pulse velocity

## 1 Introduction

The escalating demand for nuclear technology has intensified the necessity for sophisticated materials that can effectively mitigate neutron radiation. Neutron radiation poses a considerable challenge due to its penetrative characteristics, which can adversely affect both the environment and human health. Although conventional concrete is frequently employed for radiation shielding, its effectiveness in neutron attenuation is somewhat restricted. The incorporation of boron-rich minerals, such as colemanite, into concrete formulations emerges as a viable solution, as boron's capacity to capture thermal neutrons significantly bolsters radiation shielding performance. This research is dedicated to the development of novel mortar formulations with varied proportions of colemanite to tackle this challenge. The aim is to engineer a material that integrates robust mechanical properties with efficient neutron absorption, rendering it suitable for nuclear applications such as waste management facilities. Nonetheless, a significant challenge arises as elevated concentrations of colemanite in mixtures tend to adversely affect mechanical properties, particularly ductility and brittleness, thereby constraining their structural applicability. Beyond addressing material challenges, this study illuminates a deficiency in Malaysia's scientific landscape, where participation in nuclear energy projects remains minimal. By concentrating on neutron shielding materials, this research endeavors to contribute not only to global advancements in radiation protection but also to the evolution of nuclear research within Malaysia. Motivated by a commitment to applied sciences, this project prioritizes empirical experimentation to explore the relationship between mechanical and radiation absorption properties in mortar mixtures. By harnessing the chemical interactions of minerals like colemanite and amalgamating them with synergistic additives, the research aims to augment concrete's essential attributes, including ductility, strength, and radiation shielding efficacy. The outcomes of this study possess the potential to address critical concerns in neutron shielding while fostering practical applications in construction and nuclear safety. The research accentuates the significance of interdisciplinary strategies in advancing material science and resolving tangible real-world challenges.

## 2 Methods



## 3 Results & Discussion

In the initial mix design process, numerous singular cube samples were created through trial and error to achieve the first objective of testing brittleness. Some samples underwent drop tests and rebound hammer (RH) tests to assess their brittleness and refine the mix design accordingly. The drop test was performed on all samples. In some cases, particularly with higher colemanite replacement, cracks appeared as the samples were removed from the mould. In Table 1 it is shown that after CM7 none of the three mixture design had passed the drop test showcasing that higher colemanite replacement is directly affecting the integrity of sample. Similarly (Figure 2), to the drop test, the already cracked samples indicated that rebound hammer tests were unnecessary, as applying them caused further damage. The samples that survived the drop test were subjected to the rebound hammer test, yielding five readings each to produce average values. In special cases like CM10, only one or two rebound hammer readings were obtained, but they were too low to be considered valid, and thus were deemed null.

| | REF | CM1 | CM3 | CM5 | CM7 | CM10 | CM13 | CM15 | CM20 | CM30 |
|---|---|---|---|---|---|---|---|---|---|---|
| M+C | Pass | Pass | Pass | Pass | Pass | Fail | Fail | Fail | Fail | Fail |
| M+C+SF | Pass | Pass | Pass | Pass | Pass | Fail | Fail | Fail | Fail | Fail |
| M+C+SF+SP | Pass | Pass | Pass | Pass | Pass | Fail | Fail | Fail | Fail | Fail |

Table 1: Drop Test Result

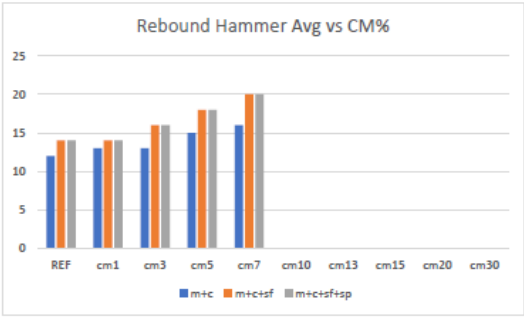



Figure 1: RH (avg) vs Colemanite Replacement

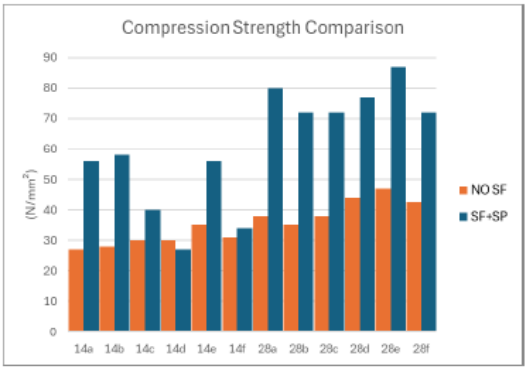



Figure 2: Comparison of MPa of SP + SF and No SF

The graph highlights the superior performance of the SF + SP mixture in terms of compressive strength, particularly

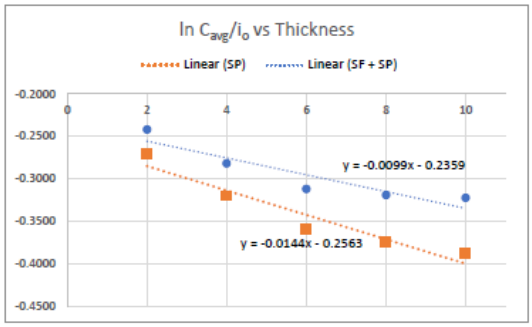



Figure 3: Comparison of Linear Graph Between the Two Mixture

with extended curing times. While the No SF mixture shows consistent strength development, it does not reach the levels achieved by the SF + SP mixture. This suggests that adding silica fume into the mixture enhances the overall strength and durability of the concrete, making it a more suitable choice for applications requiring high compressive strength.

## 4 Conclusion

The initial mix design phase played a crucial role in shaping the direction of this study. Through iterative experimentation and analysis, it was determined that incorporating silica fume (SF) and superplasticizer (SP) into concrete mixtures yielded significant improvements across multiple parameters. This led to the formulation of two main mixtures: SF + SP and SP (No SF). This study investigated the effects of silica fume (SF) and superplasticizer (SP) on various properties of concrete mixtures. The research began by evaluating brittleness through drop and rebound hammer tests. Workability, assessed by Ultrasonic Pulse Velocity (UPV), demonstrated that mixtures with silica fume exceeded the 4500 m/s threshold, indicating excellent workability compared to SP alone. Compression strength results showed that both mixtures improved with longer curing periods, but SF + SP consistently exhibited higher and more stable strengths over time compared to SP alone. Neutron attenuation tests revealed that SF + SP significantly enhanced neutron absorption rates across different thicknesses, highlighting its superior radiation shielding capability compared to SP without SF. In conclusion, the addition of Silica Fume (SF + SP) enhances overall concrete performance. SF + SP shows superior workability, higher and more consistent compression strengths, and enhanced neutron attenuation capabilities. These findings underscore the importance of incorporating silica fume and superplasticizer in concrete mix designs for applications requiring both structural integrity and radiation shielding properties

## 5 Research Context

This research was conducted at Block 60, Agensi Nuclear Malaysia, in collaboration with a degree student from Universiti Tenaga Nasional (UNITEN), and the findings have been published as an undergraduate thesis (Abdul Hannan Bin Che Nordin).

Individual Research Contribution Review, 2024: 389–390
*ISSN: 3083-922X*

# Impact of Scanning Time Delay on Radiographic Image Quality in Computed Radiography for Non-Destructive Testing

**Noorhazleena Azaman**
Industrial Technology Division, Malaysian Nuclear Agency
43000 Kajang, Selangor
hazleena@nm.gov.my

## Abstract

The evaluation of radiographic image quality in Radiographic Testing - Digital (RT-D) is essential for accurately interpreting and assessing discontinuities in Non-Destructive Testing (NDT). This study investigates the impact of scanning time delay on the radiographic images produced by a Computed Radiography (CR) imaging plate under consistent exposure conditions. Scans were conducted immediately after exposure using the white CR imaging plate and at intervals ranging from 10 minutes to 64 hours. The plates were securely stored in a cassette and an imaging plate box post- exposure. Radiographic image quality was assessed in accordance with the ISO 17636-2 standard. The findings underscore the critical role of timely processing and careful handling in preserving the integrity of radiographic image quality in CR imaging. This research provides valuable insights into best practices for optimizing image quality in NDT applications.

**Keywords:** Non-Destructive Testing (NDT), Radiographic Testing - Digital, Image Quality, Computed Radiography (CR), Scanning Time Delay

## 1 Introduction

In Malaysia, Digital Radiographic-Testing (RT-D) is increasingly being adopted in Non-Destructive Testing (NDT) due to its efficiency and accuracy. The Malaysian Nuclear Agency (Nuklear Malaysia) and the Malaysian Society for Non-Destructive Testing (MSNT) are at the forefront of providing training for RT-D and promoting. RT-D nowadays is widely used in various fields and it is one of the advanced NDT technique where it helps to ensure the integrity and safety of materials and structures. Digital imaging technology used in x-ray radiography. Unlike conventional radiography, CR uses photostimulable phosphor plates to capture and store x-ray images. When these plates are exposed to x-rays, they store the image as a latent image. This latent image is then read by a laser scanner, which releases the stored energy as visible light. The light is measured and converted into a digital image that can be viewed on a computer screen.

## 2 Methods

In this study, the radiation used is X-ray. The X-ray machine is a GE & Isovolt Titan E 225. It has a maximum tube voltage of 225 kV and a current of 13 mA. The focal spot size ranges from 0.4 mm to 3.0 mm, and it uses an aluminum (Al) filter with a thickness of 2 mm. The detector specification for the Computed Radiography system includes the DURR NDT 35 model. It features a 16-bit A/D conversion and a scanning mode of 100 micrometers. The imaging plate used is a Standard IP (White). The radiographic image quality required is according to ISO 17636-2:2022. The required radiographic image quality includes a grey value of 50-80% of ADC, which corresponds to 32,768 to 52,429. The testing class is A, with a single wire IQI of W12 and a duplex wire IQI of D8. The SNRN (Signal to-Noise Ratio Normalized) for parent metal/HAZ (Heat-Affected Zone) is 98. The test object is a welded plate made of stainless steel, with dimensions of 300 x 300 mm. The parent metal thickness is 15.3 mm, and the weld penetrated thickness is 12.0mm. The radiographic exposure was performed with a tube voltage of 160 kV and a current of 3 mA. The exposure time was 19 seconds, with a focal spot size of 3.0 mm. The source-to-detector distance (SDD) was 700 mm. The scanning time delay for the Imaging plate includes various intervals as below:

Table 1: Scanning time delays parameter

| **Scanning time delay** |
|---|
| 0 minute |
| 0.17 hour (10 minutes) |
| 0.33 hour (20 minutes) |
| 0.5 hour (30 minutes) |
| 0.67 hour (40 minutes) |
| 0.83 hour (50 minutes) |
| 1 hour (60 minutes) |
| 2 hours (120 minutes) |
| 4 hours (240 minutes) |
| 8 hours (480 minutes) |
| 16 hours (960 minutes) |
| 32 hours (1920 minutes) |
| 64 hours (3840 minutes) |

These intervals can be used to capture different levels of detail and changes in the imaging plate over time.

## 3 Results

The data is collected from the 13 radiographic images. The analysis of the radiographic image digital starts with the recorded grey values. Single wire IQI, the wires shall be

directed perpendicular to the weld and its location shall ensure that at least 10 mm of the wire length. The basic spatial resolution of digital images is based on the determination of the first duplex wire pair (smallest number) withless than 20% modulation depth (dip). $SNR_N$ determined in a window of Region of Interest (ROI) 20 × 55 pixels and shall be determined preferably beside the weld near the wire.

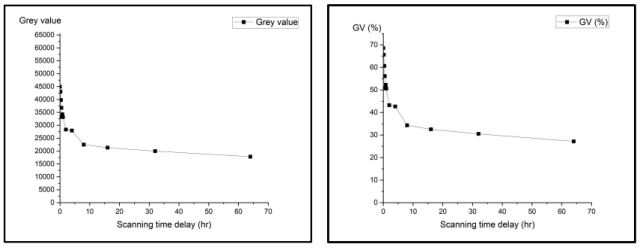



Figure 1: Graph of Image Grey Value versus Scanning time

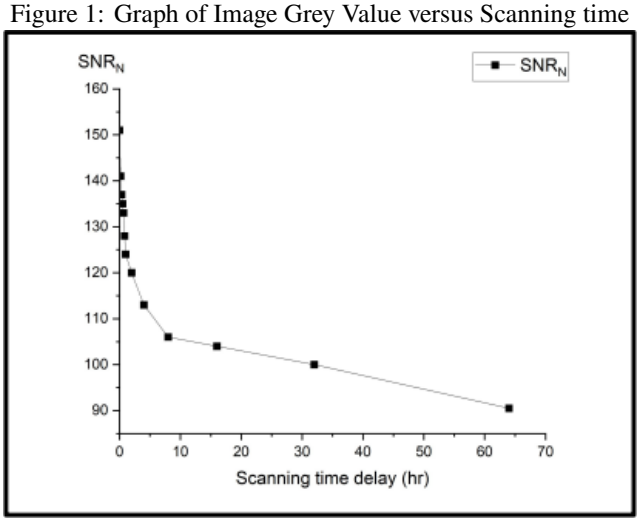



Figure 2: Graph of $SNR_N$ versus Scanning time delay

## 4 Discussion

The results demonstrated a significant decrease in grey values with increased scanning time delay. After 1 hour delay, the gray value was reduced to less than 50% of the 16 bit of ADC. The $SNR_N$ also decreased with longer scanning delays, indicating a decline in image quality. At 64 hours the $SNR_N$ is below than 98. The single and duplex wire image quality indicators (IQIs) showed no significant changes from 0 to 64 hours of scanning delay. Change the time between exposure and read-out will be affected to the GV, $SNR_N$ and IP fading.

## 5 Conclusion

The delay between exposure and scanning can affect the quality of the radiographic image due to phosphor fading. Based on this study, it is recommend to read the IP less than 1 hour. After 1 hour delay, the grey value was reduced to less than 50% of the 16 bit of ADC. These findings highlight the importance of minimizing scanning time delays in CR to maintain optimal image quality for accurate RT-D assessments.

## References

ISO 17636-2:2022. 2018. Part 2: X- and gamma-ray teschniques with digital detectors. *Non-destructive testing of welds - Radiographic testing*.

Individual Research Contribution Review, 2024: 391–392
*ISSN: 3083-922X*

# Investigation of Process Flow inside Demineralizer Using Radiotracer Technique: A Qualitative Analysis

**Noraishah Othman**
Industrial Technology Division, Malaysian Nuclear Agency
43000 Kajang, Selangor
noraishah@nm.gov.my

## Abstract

This document provides a preliminary work on radiotracer intervention in a demineralizer, a filtration column to ensure the water inlet into a research reactor is well maintained with high purity. A qualitative analysis has been conducted to map out the radiotracer distribution in the resin as means of efficient filtration substrate.

**Keywords:** Radiotracer, Demineralizer, Resin

## 1 Introduction

Radiotracer approach was introduced in order to map out the demineralization process and diagnose the process anomalies inside the demineralizer column located at PUSPATI TRIGA Reactor (RTP), Malaysian Nuclear Agency. The column acts as a fixed bed column whereby the upper part of the column is filled with water whereas the lower part is occupied with Amberlite IRN 150 resin respectively. The work was carried out during reactor maintenance week when reactor was experiencing shut down. Radiotracer technique is an excellent method to diagnose and identify process plant anomalies without plant shut down (IAEA, 2008; IAEA, 2001).

## 2 Methods

Some modifications were made in this work to ensure radiotracer material did not compromise with the reactor operation. The column inlet flow rate was assigned to 5gpm instead of 10gpm whereby the outlet was isolated from being recycled to reactor pool. Instead of using water from reactor pool as the input, tap water was used as continuous input to the column and the outlet was not recycled to reactor but discharged to reactor pit. Room temperature was adopted whereby $T_{inlet}$ is 27°C instead of 49°C. Moreover, monitoring of dose rate was still made to the discharged water before channeling to radioactive aquifer. The detected dose rate was 3$\mu$Sv/h during the running of experiment and kept in the reactor pit. About 138MBq (3.72mci)/4ml 68Ga-NOTA-NHS was prepared to be injected inside the demineralizer. $^{68}$Ga was eluted from commercial $^{68}$Ge and chelated with NOTA-NHS as chelating agent with 1M Sodium Acetate anhydrous (NaOAc) as buffer in order for $^{68}$Ga to be water tracing material. 12 sodium iodide (NaI) detectors were arranged accordingly around the column. Detector which was assigned at the outlet of column was analyzed for residence time distribution (RTD) measurement. Detector 1 and 2 were installed at the upper part (water area) whereas the remaining detectors were installed at the lower part (resin space) around the column.Figure 1 shows four detectors were assigned for Resin Upper Level (RUL) from D3-D6 whereas for Resin Lower Level (RLL) another four detectors denoted as D7-D10 were installed respectively. D11 was assigned for isolated discharged to reactor whereas D12 was meant for outlet at pit.

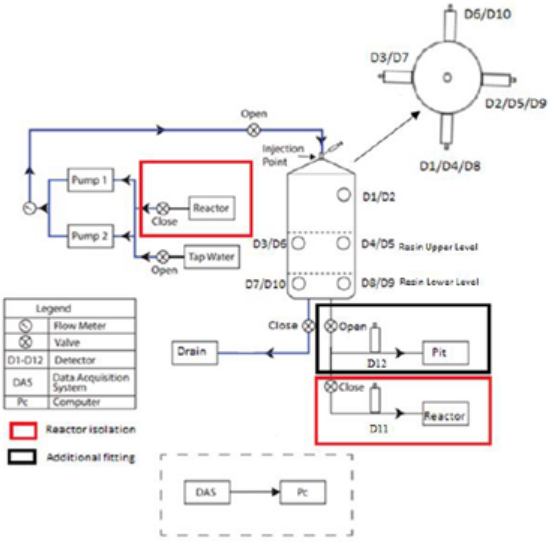



Figure 1: Schematic diagram of demineralizer system and assignment of detectors

### 2.1 Preparation of $^{68}$Ga-NOTA-NHS

In order to ensure Ga-68 acts as water tracer, buffer solution comprises of 1 M sodium acetate anhydrous (NaOAc) was prepared together with NOTA-NHS ester (2-[4-(carboxymethyl)-7-[2-(2,5-dioxopyrrolidin-1-yl) oxy-2-oxoethyl]-1,4,7-triazonan-1-yl] acetic acid with molecular formula of $C_{16}H_{24}N_4O_8$. NOTA-NHS ester is a bi-functional chelating agent that is used for labeling biomolecules with radiometals such as gallium-68. In acidic condition, $^{68}$Ga exists as a free stable ion ($68Ga^{3+}$). At a higher pH, it is hydrolyzed to form insoluble trihydroxide. Hence, to avoid this colloidal formation, a suitable buffer with weak metal complexing properties shall be incorporated. Therefore, the optimal condition for $^{68}$Ga complexation with NOTA-NHS is achieved at pH of 3.9 in room temperature. Ge/Ga-68 generator from Eckert-Ziegler that uses use titanium dioxide ($TiO_2$)

as column resin is available for this study. The radiolabeling takes place by adding 400$\mu$l formulation buffer containing 1.0M sodium acetate to 4.0ml Ga-68 eluate. Ga-68 is eluted from the generator using 5.0 ml 0.1 M hydrochloric acid and slow process which takes about 5minutes elution process is involved in order to ensure the integrity of resin is restored. The following formulation is adopted to produce 3.72mCi/4ml Ga-68-NOTA-NHS with optimized pH of 3.9

80$\mu$l(1.028mg) NOTA-NHS + 400$\mu$l of 1M NaOAc + 3.72mlGa-68

## 3 Data/Results

Figure 2 shows that D1 and D2 received radioactive signals with comparable intensity (inset) and the overlapping data indicate that injected radiotracer distributed evenly at its individual location as anticipated. Moreover, the highest peaks which are picked up by detector imply the radioactive materials are highly concentrated once injection commences and reduces in counts due to continuous supply of water. Initially, no active signals are observed before radiotracer injection as shown by background readings.

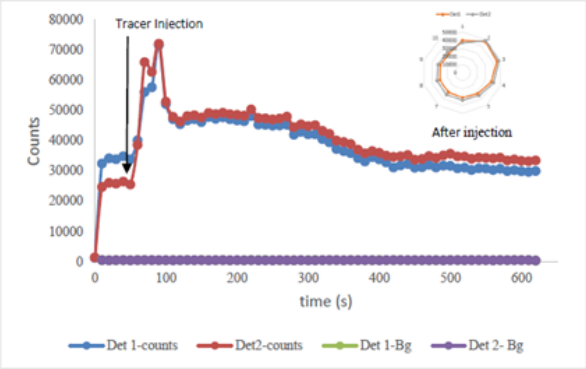



Figure 2: Radiation counts at water area (Upper level).

### 3.1 Qualitative Analysis

It can be observed that each detector at Resin Upper Level (RUL) receives significant and comparable amount of radiation which is sufficient for analysis as shown in Figure 3 whereas Figure 4 provides pattern of concentration of $^{68}$Ga received by individual detector at Resin Upper Level (RUL). It shows that background reading is higher at D5 before injection that can be implied the resin is accumulated more at that area and provides more void for fluid occupancy for area D3-D4-D6. During injection (50-120s), the water-68Ga radiotracer has the tendency to occupy the area at D3-D4-D6 which has less amount of resin deposition. However, as the process progresses, the distribution of water-$^{68}$Ga radiotracer is well dispersed and concentrated more at the center of the column although the end streamline is towards D5 which is due to the similar location with outlet D12 (i.e. on the right hand side of tank bottom) that creates pressure drop as shown in Figure 1. On top of that, it can be observed that D3-D4-D6 is unswept and acts as dead zone.

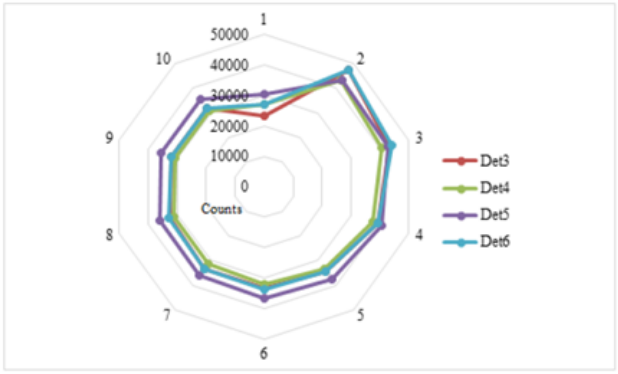



Figure 3: Concentration of radioactive 68Ga at Resin Upper Level (RUL)

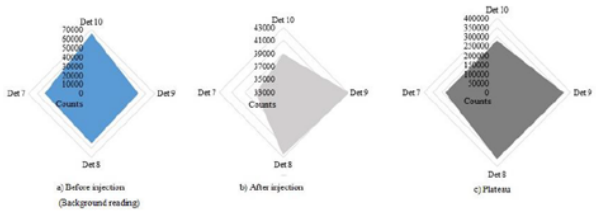


Figure 4: Radiation counts at water area (Upper level).

## 4 Conclusions

In conclusions, radiotracer technology has successfully executed in the demineralizer column at Reactor TRIGA PUSPATI (RTP), Malaysian Nuclear Agency. Nevertheless, some *adjustments have to be made prior conducting the radiotracer works to ensure reactor operation is not compromised.

* Tap water was used to supply the continuous flow to demineralizer and not water from reactor pool outlet and 10 minutes was the allowable duration to complete the works due to pit constraint. Thus, the results might not be fully representative for actual reactor operation.

## References

IAEA. 2001. Radiotracer technology as applied to industry, vienna, austria.

IAEA. 2008. Radiotracer residence time distribution method for industrial and environmental applications, vienna, austria.

Individual Research Contribution Review, 2024: 393–394
*ISSN: 3083-922X*

# Relative Difference in Mass Attenuation Coefficient of Synthesized Glasses: XCOM Software Analysis and Experimental Lead Equivalent Testing at Makmal Fizik Perubatan Nuklear Malaysia

**Nor Hayati Alias**
Industrial Technology Division, Malaysian Nuclear Agency
43000 Kajang, Selangor
norhayati@nm.gov.my

## Abstract

XCOM analysis was conducted on five produced samples of $[PbO]x[(TeO_2)0.7(B_2O_3)0.3]_{1-x}$ with x = 0, 5, 10, 15, and 20 mol%. The XCOM software was used to calculate the theoretical values of the mass attenuation coefficients ($\mu$m) of the samples at low energy photon levels. Experimental mass attenuation was determined via LET (Lead Equivalence Thickness) measurements performed at the Makmal Fizik Perubatan Nuklear Malaysia. XRD analysis confirmed the amorphous phase of the fabricated glasses.

## 1 Introduction

XCOM software and experimental LET measurements were employed to determine the mass attenuation coefficients of lead-doped borotellurite glasses at low energy levels (0.1 MeV).

## 2 Method

The WinXCOM software was utilized to theoretically calculate the attenuation coefficients of the synthesized samples. The mass attenuation coefficients ($\mu$m) of the glasses at 0.1 MeV were calculated using the mixture rule (Berger et al., 2010):

$$\mu_m = \sum_i w_i (\mu_m)_i \tag{1}$$

where $w_i$ represents the fractional weight of the elements (Pb, B, O, and Te) derived from the XCOM software. Experimental mass attenuation coefficients were obtained using LET analysis. The lead thickness for each glass was determined by extrapolating the natural logarithm of the dose rate against the glass thickness on a calibration curve for LET evaluation. All measurements were repeated three times to ensure an experimental error of less than 6%.

The shielding properties of the glasses were evaluated at low photon energy (0.1 MeV) using the Lambert-Beer law:

$$I = I_0 e^{-\mu t} \tag{2}$$

where t is the glass thickness, I is the transmitted photon intensity, and $I_0$ is the incident photon intensity.

The mass attenuation coefficient (MAC) was calculated using the relation:

$$MAC = \frac{\mu}{\rho} \tag{3}$$

where $\rho$ represents the glass density.

## 3 Results and Discussion

Reduced structural connectivity was observed in higher-doped samples, as evidenced by dual-phase transformation peaks in the XRD patterns (Figure 1). This result aligns with findings by Kaur et al. (Kaur et al., 2016; Kaur et al., 2020), which demonstrated that introducing metal oxides into borotellurite glass can lead to dual peaks in XRD patterns, indicating multiphase structures and structural modifications.

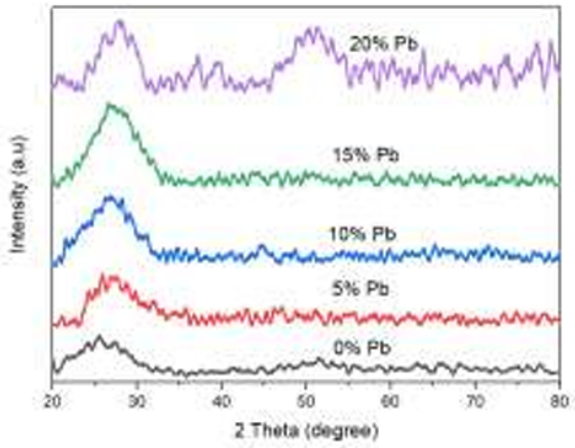



Figure 1: XRD patterns of synthesized glasses with varying Pb mol% concentrations.

Experimental and theoretical XCOM-calculated MAC values against lead dopant concentrations are shown in Figure 2. Theoretical MAC values exhibit a linear decreasing trend, from 1.67 $cm^2/g$ at 0 mol% to 1.24 $cm^2/g$ at 20 mol%. Experimental LET derived MAC values, however, show a polynomial trend, with the lowest value (0.16 $cm^2/g$) at 20 mol%. Relative differences between experimental and theoretical MAC values (Figure 3) are significantly higher for doped samples (79.3% - 87.3%).

The larger relative differences in doped samples may arise from structural and compositional factors. Studies by Kurtulus & Kavas (Kurtulus and Kavas, 2022) revealed that varying heavy metal oxide content in barium borotellurite glasses significantly impacts mass attenuation coefficients. The introduction of high-Z elements like Pb increases atomic number and electron density variations, leading to nonlinear interactions with radiation and deviations from XCOM predictions.

Similarly, Nasuha et al. (Nasuha et al., 2021) reported that doping yttrium lead borotellurite glasses with neodymium

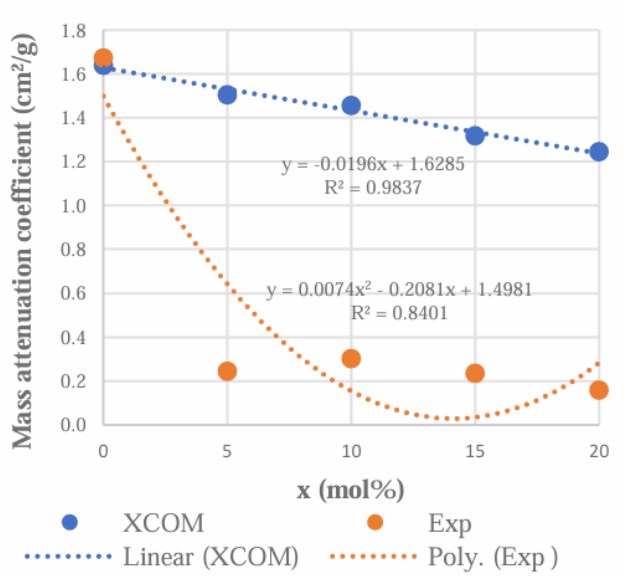



Figure 2: Mass attenuation coefficients (MAC) from experimental and theoretical values.

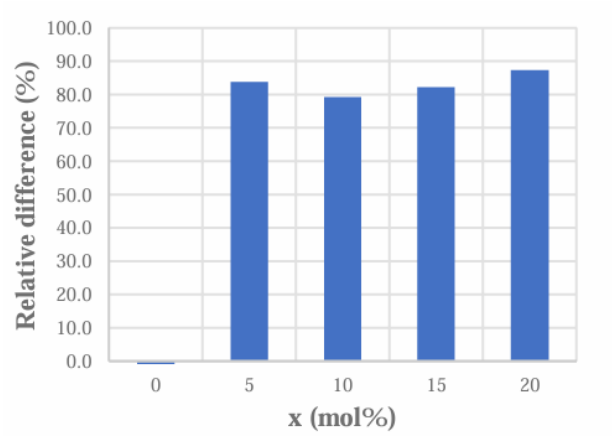



Figure 3: Relative differences between experimental and theoretical MAC values.

oxide ($Nd_2O_3$) altered their optical and structural properties, contributing to heterogeneity. Structural non-uniformities such as phase separation and microdomain formation were noted by Kothan et al. (Kothan et al., 2016), further explaining the observed polynomial trends in MAC values.

## 4 Conclusion

The high relative differences (%) between experimental and theoretical MAC values in doped samples, compared to undoped glasses, suggest that structural heterogeneity introduced by doping is not accurately captured by XCOM theoretical evaluations. Experimental LET measurements reveal a polynomial trend in MAC values, indicating enhanced structural heterogeneity in doped glasses. This study highlights the importance of understanding structural and compositional effects on attenuation properties. The findings provide valuable insights for optimizing glass materials in radiation shielding applications.

## References

Hubbell J. H. Seltzer S. M. Chang J. Berger, M. J., J. S. Coursey, R. Sukumar, K. Zucker, and D. S. Olsen. 2010. Xcom: Photon cross sections database. nist standard reference database (xgam).

A. Kaur, K. Singh, and K. S. Thind. 2016. Dsc and raman studies of silver borotellurite glasses. *Journal of Applied Physics*.

A. Kaur, J. C. McLaughlin, and A. M. Smith. 2020. Structure of strontium tellurite glass, anti-glass, and crystalline phases by high-energy x-ray diffraction, reverse monte carlo, and rietveld analysis. *Acta Crystallographica Section B: Structural Science, Crystal Engineering and Materials*, 76(1):1–12.

S. Kothan, T. Thongtem, and J. Kaewkhao. 2016. Influence of heavy metal oxides on the structural and optical properties of barium-borotellurite glasses. *Journal of Non-Crystalline Solids*, 452(1):9.

M. Kurtulus and T. Kavas. 2022. Calculation of lac and hvl values of newly developed barium borotellurite glass containing different heavy metal oxides using phy-x/psd. *Pamukkale University Journal of Engineering Sciences*, 30(1):1–10.

N. Nasuha, Z. Ahmad, and M. R. Sahar. 2021. Structural and elastic properties studies of yttrium lead borotellurite glass doped with neodymium oxide. *Chalcogenide Letters*, 18(1):1–10.

Individual Research Contribution Review, 2024: 395–396
*ISSN: 3083-922X*

# Fuel Cell Electrode Preparation: Transfer Efficiency and Morphology at Different Catalyst's Ink Concentrations

**Norhazirah Azhar**
Industrial Technology Division, Malaysian Nuclear Agency
43000 Kajang, Selangor
norhazirah@nm.gov.my

## Abstract

Efficient catalyst ink's deposition onto a substrate's surface is essential in the fabrication of fuel cell electrodes. The way the catalyst is applied to the substrate and the morphology resulting from it have an effect on the proton exchange membrane fuel cell's (PEMFC) performance. This study used a direct catalyst ink spraying technique to examine surface morphology and transfer efficiency over different ink concentrations. With a fixed loading of 1.0 mg/cm2, the concentrations of catalyst ink employed in the spraying process are 0.5, 1.0, 1.5, 2.0, and 2.5 mg/ml. Human error while spraying was not taken into account when calculating the catalyst inks' transfer efficiency. Using a Field Emission Scanning Electron Microscope (FESEM), the coating thickness and dispersion of the formed catalysts were evaluated.

**Keywords:** Spray, Ink, Concentration, Particle size, FESEM, PEMFC

## 1 Introduction

Several types of fuel cells include solid oxide fuel cells, direct liquid fuel cells, proton exchange membrane fuel cells and bio fuel cells(Gencoglu and Ural, 2009) . The heart of a fuel cell is the membrane electrode assembly (MEA), which includes the membrane, the catalyst layer, and gas diffusion layer (GDL). MEA manufacturing processes are mainly divided

into the catalyst-coated membrane (CCM) and the catalyst-coated substrate (CCS) methods (Lim et al., 2021) . Performance of CCS

where the catalyst layer was sprayed onto the GDL has been studied. Spraying is a straightforward but some ink loss might be resulted from this technique, either into the air or out of the targeted areas. This study aims to identify ink loss effect based on different ink concentrations used when using direct spraying method. There are limited studies on the catalysts ink loss via spray deposition technique related to PEMFC preparation. These resulting data can be used in future's PEMFC ink preparation after take into account on percentage of ink loss. This studies hopefully will be able to assist in enhancing PEMFC performance. Through this work, the effect of catalyst ink concentration on the loss will be studied. The ink loss was measured via weight different of the substrate before and after being applied.

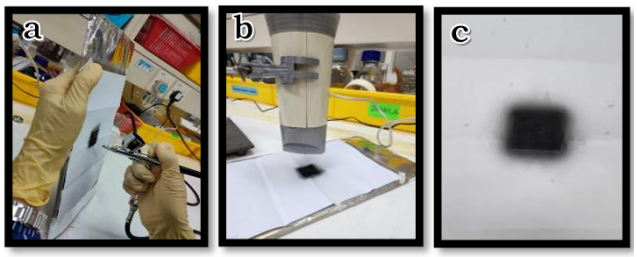



Figure 1: Preparation of catalysts loaded electrode via spraying.

## 2 Methods

- **Catalyst ink component:** Graphite powder + Nafion + isopropyl alcohol + deionized water
- **Catalyst loading:** 1.0 mg/cm$^2$
- **Catalyst ink concentration:** 0.5, 1.0, 1.5, 2.0, 2.5 and 3.0 mg/ml
- **Electrode area:** 6.25 cm$^2$

1. Catalyst ink component was sonicated for 20 minutes until the powder dispersed homogenously. The initial mass of GDL was weighted and recorded.
2. The catalyst ink was sprayed at constant pressure. A distance between substrate and the gun's tip was approximate to 20 mm as in Figure 1(a).
3. The ink was allowed to dry before spraying another layer (Figure 1(b)).
4. The prepared catalyst layer was annealed at 60°C for 60 minutes and cool down to room temperature (Figure 1 (c)).
5. The prepared electrode was weighted and recorded.
6. Finally, the ink loss was calculated using Equation 1 and Equation 2.

$$Gp_f = \quad Cp_b - Cp_a \tag{1}$$

$$\text{Ink Loss (\%)} = \frac{Gp_f - Gp_i}{Gp_i} \times 100 \tag{2}$$

Where, G$p_i$ = Actual weight of graphite powder used, G$p_f$ = Weight of graphite powder on carbon paper, C$p_b$ = Weight of carbon paper before spraying, C$p_a$ = Weight of carbon paper after spraying

## 3 Data/Results

Figure 2 shows that at 0.5 mg/ml ink concentration resulted in the least ink (59.98%) followed by 1.0 (69.39 %), 2.0 (70.57%), 1.5 (77.45%), 3.0 (79.77%) and 2.5 mg/ml (83.81%). The trend shows increasing percent of ink loss as the concentration of ink increased.

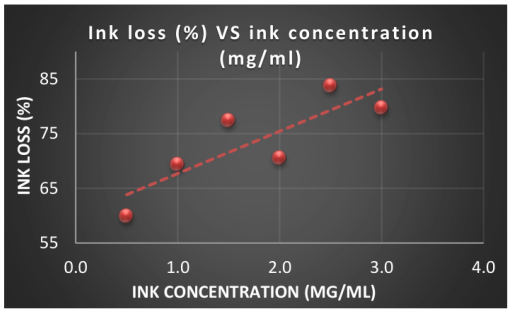



Figure 2: Effect of inc concentration toward ink loss percentage.

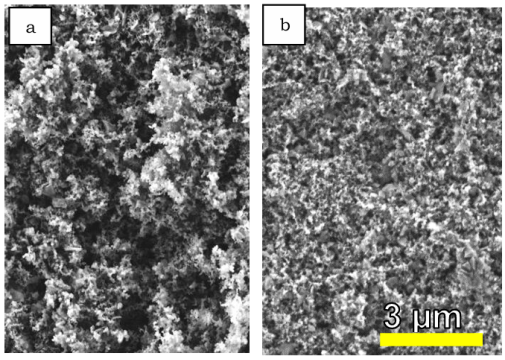



Figure 3: FESEM morphology of ink loading at 0.5 (a), 1.5 (b) and 3.0 (c) mg/ml

The FESEM morphology shows that the spreading appears homogeneous at ink concentrations of 0.5, and 3.0 mg/mL. This indicates that the concentration does not have a significant effect on the spread of the ink on the substrate. However, there are still losses that can arise from losses into the air.

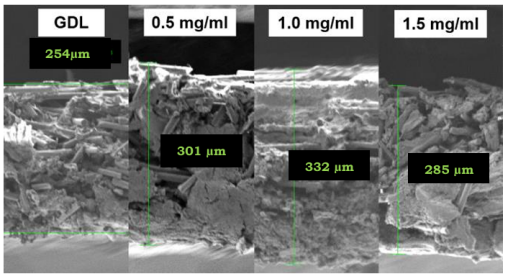



Figure 4: Comparison on thickness of plain GDL with catalysts coated GDL

FESEM photos of the cross-section of the created catalyst layer demonstrate that the thickness of the catalyst layer increases with the concentration of the catalyst ink. CCS concentrations of 0.5 and 1.0 mg/ml, exhibiting minimal ink loss,

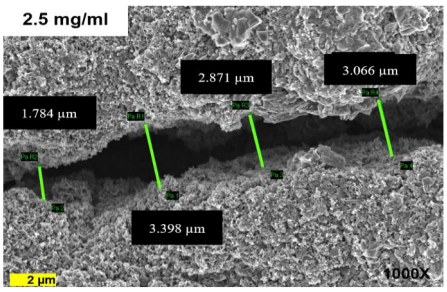



Figure 5: Surface profile of substrates at 1000X

result in a larger catalyst layer deposition. Concentrations of 2.5 and 3.0 mg/ml yield the greatest ink loss, resulting in a diminished catalyst layer. Increased ink loading was effectively deposited into the substrate with a 0.5 mg/ml ink concentration. The graphite powder seemed crushed due to its impact with the substrate at elevated spraying velocities. Cracks have emerged on the surface of substrates, as illustrated in Fig. 5, with a greater number of cracks found at 2.5 mg/ml than at lower concentrations. Cracks on 2.5mg/ml substrate were deeper and wider crack.

Liu (Liu et al., 2022) states that ink with a high solid concentration may dry more slowly than ink with a low solid concentration, owing to a reduced contact area and limited surface exposure for air drying. Furthermore, if the distance between the nozzle and the GDL is insufficient (less than 30mm), it will induce excessive ink liquid, ultimately resulting in the creation of cracks. Cracks on the substrate are classified as flaws, which may adversely affect fuel cell performance. Consequently, employing a low solid concentration (low ink concentration) may mitigate fracture formation, performance.

## 4 Discussion/Conclusions

The best concentration for catalyst ink with a loading of 1.0 mg/cm2 is 0.5 mg/ml, which resulted in 59.98% ink loss and was demonstrated by the thickness increase using FESEM analysis. In addition, the distribution of ink particles on GDL appears to be homogeneous for each concentration indicates an even spreading despite different ink concentrations were applied. Further studies can be conducted to investigate the ink loss effect with different catalyst types and loadings.

## References

M. T. Gencoglu and Z. Ural. 2009. Design of a pem fuel cell system for residential application. *International Journal of Hydrogen Energy*, 34(12):5242–5248.

Bee Huah Lim, Edy Herianto Majlan, Ahmad Tajuddin, Teuku Husaini, Wan Ramli Wan Daud, Nabilah Afiqah Mohd Radzuan, and Md. Ahsanul Haque. 2021. Comparison of catalyst-coated membranes and catalyst-coated substrate for pemfc membrane electrode assembly: A review. *Chinese Journal of Chemical Engineering*, 33:1–16.

H. Liu, L. Ney, N. Zamel, and X. Li. 2022. Effect of catalyst ink and formation process on the multiscale structure of catalyst layers in pem fuel cells. *Applied Sciences (Switzerland)*, 12(8).

Individual Research Contribution Review, 2024: 397–398
*ISSN: 3083-922X*

# Removal of Inorganic Element of Rare Earth Oxalates by Preliminary Scrubbing

**Nur Aqilah binti Sapiee**
Industrial Technology Division, Malaysian Nuclear Agency
43000 Kajang, Selangor
nuraqilah@nm.gov.my

## Abstract

The separation of rare earth element is difficult due to their chemical properties similarities. Usually, separation process of rare earth includes extraction, scrubbing and stripping. This study focus on scrubbing process that had been applied to rare earth oxalates before undergo separation process to remove inorganic element (calcium, phosphorus and silica). The parameter that had been studied in this paper is contact time and ratio of rare earth oxalate to deionized water.

**Keywords:** Scrubbing, inorganic, rare earth.

## 1 Introduction

Nowadays, Rare Earths (REs) are seemly increase as important sources of advanced materials with the recent drastic advancement in technology. Example usage of REs is in a field such as electronic, environmental, optical, magnetic and catalytic technologies. REs processing requires chemical treatment, which is known as cracking process. Acid treatment and alkaline treatment are the two routes in chemical treatment. Both routes are used in order to increase REs concentration and to remove impurities. There are various hydrometallurgy techniques that had been applied in the world for RE separation process such as precipitation, solvent extraction and ion chromatography. Usually, the techniques that had been selected need to review or examine to understand its limitation and advantages. In addition, the process selection with regards to the feed properties, waste management of the separated radioactive elements, and how they can be treated to produce valuable co-products are also need to consider (García et al., 2020).

## 2 Methodology

Rare Earth Oxalate is obtained from Mineral Laboratory stockpile of Nuklear Malaysia where Xenotime and sodium hydroxide is fused at 350°C (MS. et al., 2015). Rare earth oxalate is then mixed up with deionized water and stirred at different time and ratios. Sample is then separated by using filter funnel and aqueous sample is sent for XRF analysis.

## 3 Result and Discussions

Refer Figure 1 and 2.

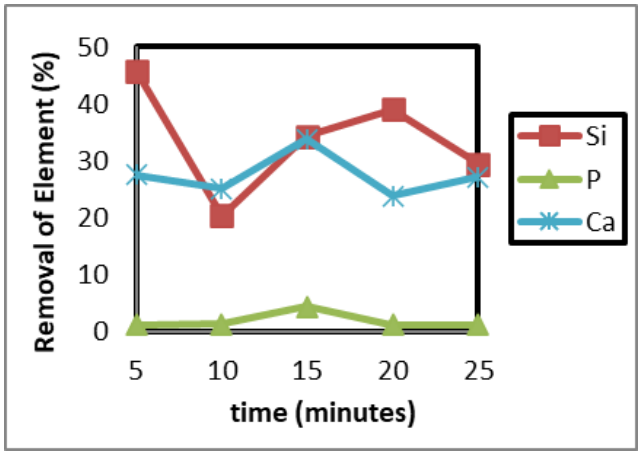



Figure 1: Percentage of removal on element at different time of scrubbing.

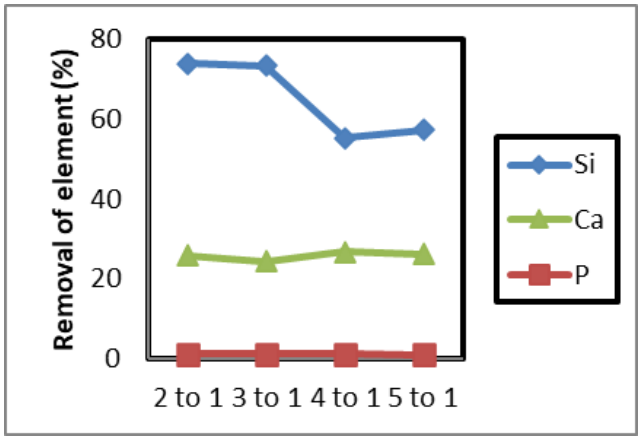



Figure 2: Effect of elemental removal at different ratio of deionized water to rare earth oxalate.

## 4 Conclusion

Preliminary scrubbing process can be applied to rare earth oxalates before solvent extraction route is determined. From results, it shows that preliminary scrubbing helps to remove inorganic element at certain time and ratio.

## References

Adrián Carrillo García, Mohammad Latifi 1, Ahmadreza Amini 1, and Jamal Chaouki. 2020. Separation of radioactive elements from rare earth element-bearing minerals. *Metals*, 10:1524.

AMeor Yusoff MS., Khaironie MT., Nursaidatul K., Ahmad Khairulikram Z., and Nuraqilah S. 2015. An alternative alkaline fusion process for the production of heavy rare earth, thorium, uranium and phosphate from malaysian xenotime. *Recent Advances in Environment, Ecosystem and Development.*, pages 163–167.

Individual Research Contribution Review, 2024: 399–400
*ISSN: 3083-922X*

# Characterization of Cobalt Oxide Nanoparticles Prepared by Co-precipitation Method

**Nurazila Mat Zali**
Industrial Technology Division, Malaysian Nuclear Agency
43000 Kajang, Selangor
nurazila@nm.gov.my

## Abstract

Recent studies show a great interest in the production of metal oxide nanoparticles. Cobalt oxide nanoparticles caught a lot of attention due to their wide applicability in high-technology industries. In this work, cobalt oxide nanoparticles ($Co_3O_4$) were synthesized by co-precipitation method and calcination at various temperatures (300°C - 600°C). The prepared nanoparticles were characterized using X-ray Diffraction (XRD) and Field Emission Scanning Electron Microscopy (FESEM). The results show that the properties of cobalt oxide depend on heat treatment. $Co_3O_4$ nanoparticles show an increase in size with increasing calcination temperature. The nanoparticles produced are in the range of 96 nm to 100 nm.

**Keywords:** Cobalt oxide, Nanoparticles, Characterization

## 1 Introduction

Over the past few years, cobalt oxide nanoparticles have been employed in a wide range of applications, including nanosensors, nanoelectronics devices, and catalysts due to its distinctive electrical, catalytic, magnetic, and optical properties (Lakra et al., 2021). Many methods of synthesizing cobalt oxide nanoparticles have been reported by various researchers. Wet chemical reactions such as co-precipitation method are one of the most common synthesis techniques used. This is mostly due to the advantage of a simple and low-cost approach. This method also allows the production of high yield and purity of cobalt oxide which makes it easier to produce large quantities of nanoparticles. The particle size and morphology of nanoparticles can be controlled by adjusting the reaction conditions like pH, temperature, and concentration of reactant (Iravani and Varma, 2020; Xu et al., 1998; Haase et al., 2022; Christoskova et al., 1999). This research aims to produce cobalt oxide nanoparticles by using co-precipitation method and to characterize it by using XRD and FESEM.

## 2 Methods

### 2.1 Synthesis of materials

Cobalt (II) chloride and sodium hydroxide were used as the main component in the production of cobalt oxide nanoparticles. The synthesis process started with the preparation of mixture solutions by dissolving both cobalt (II) chloride and sodium hydroxide in DI water and each solution was magnetically stirred for 1 hour. Then, the cobalt solution was dropped into NaoH solution while stirring. Olive green color precipitated was collected by filtration and the precipitate was washed several times with DI water. The collected precipitate was dried in oven at 80°C for 24 hours. The end product, cobalt hydroxide was then calcined in the furnace for 2 hours at different temperatures of 300°C to 600°C.

### 2.2 Characterization

Structural characterization of the samples was performed using XRD PANalytical X'Pert PRO. This instrument was operated at 40 kV and 30mA at scanning step of 0.03 with 2 theta in the range of 5°-80°. Surface morphology and elemental composition of the samples were investigated using Field Emission Scanning Electron Microscopy (FESEM), Carl Zeiss (GeminiSEM 500) and Energy Dispersive X-ray (EDX) analysis.

## 3 Results

The data from X-ray Diffraction (XRD) were analyzed by using X'Pert Highscore plus software. The XRD diffractogram of the synthesis product at various calcination temperatures can be observed in Figure 1. The results show that pure cobalt oxide, $Co_3O_4$ can be formed at temperatures as low as 300°C with cubic crystal structure. The diffraction peaks of the sample with calcination temperature of 300°C- 600°C confirm the formation of $Co_3O_4$ nanoparticles where it matches the pattern of JCPDS 98-000-8298. We can see well- defined diffraction peaks at 19.24°, 31.23°, 36.99°, 44.97°, 59.96°, 65.47° where these peaks correspond to the (111), (022), (113), (004), (115), (044) planes of cobalt oxide crystals, respectively.

Figure 2 (a-d) displays the morphology of $Co_3O_4$ nanoparticles at 300°C-600°C calcination temperatures from FESEM micrographs with 50000x magnification. $Co_3O_4$ nanoparticles which have plate-like shapes show an increase in size with increasing calcination temperature. The nanoparticles produced are in the range of 96 nm to 100 nm.

## 4 Conclusion

Cobalt oxide nanoparticles were successfully synthesized and characterized using XRD and FESEM. The XRD results show that pure cobalt oxide ($Co_3O_4$) can be formed at low calcination temperature of 300°C with cubic crystal structure. $Co_3O_4$ nanoparticles which have plate-like shapes show an increase

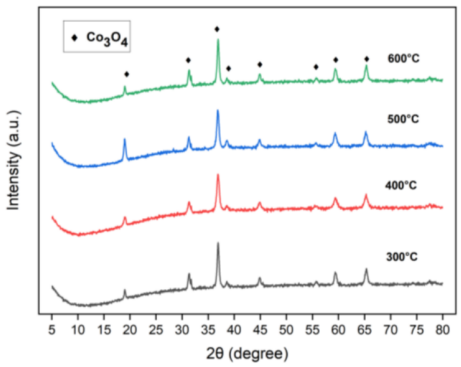



Figure 1: XRD patterns for $Co_3O_4$ at various calcination temperatures

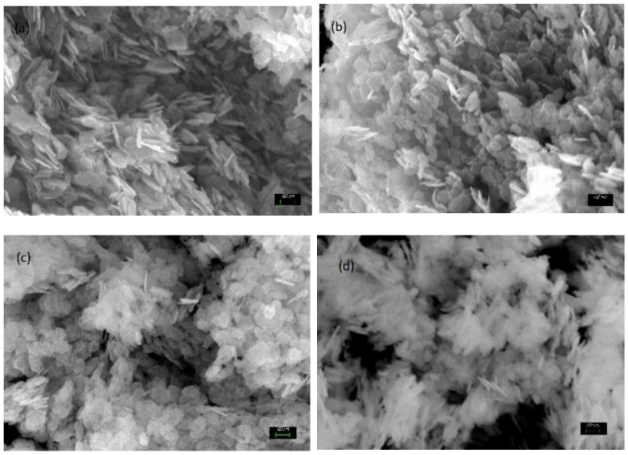



Figure 2: FESEM micrograph of $Co_3O_4$ at 300°C- 600°C calcination temperatures

in size with increasing calcination temperature. The nanoparticles produced are in the range of 96 nm to 100 nm. Therefore, it is proven that this technique is capable of producing high-purity metal oxide nanoparticles ideal for a variety of applications.

## References

S. G. Christoskova, M. Stoyanova, M. Georgieva, and D. Mehandjiev. 1999. Preparation and characterization of a higher cobalt oxide. *Materials Chemistry and Physics*, 60(1):39–43.

F. T. Haase, A. Bergmann, T. E. Jones, J. Timoshenko, A. Herzog, H. S. Jeon, C. Rettenmaier, and B. R. Cuenya. 2022. Size effects and active state formation of cobalt oxide nanoparticles during the oxygen evolution reaction. *Nature Energy*, 7(8):765–773.

S. Iravani and R. S. Varma. 2020. Sustainable synthesis of cobalt and cobalt oxide nanoparticles and their catalytic and biomedical applications [10.1039/d0gc00885k]. *Green Chemistry*, 22(9):2643–2661.

R. Lakra, R. Kumar, D. Nath Thatoi, P. Kumar Sahoo, , and A. Soam. 2021. Synthesis and characterization of cobalt oxide (co3o4) nanoparticles. *Materials Today: Proceedings*, 41:269–271.

P. Xu, Z., and H. C. Zeng. 1998. Thermal evolution of cobalt hydroxides: a comparative study of their various structural phases [10.1039/a804767g]. *Journal of Materials Chemistry*, 8(11):2499–2506.

Individual Research Contribution Review, 2024: 401–402
*ISSN: 3083-922X*

# Solvent Extraction of Cerium from Acidic Chloride Medium using Synergist Extractant

**Nurliana Roslan**
Industrial Technology Division, Malaysian Nuclear Agency
43000 Kajang, Selangor
nurliana_r@nm.gov.my

## Abstract

This study focuses on the extraction of light rare earth elements (LREEs) especially cerium (Ce) using four formulated synergist extractants and the extraction efficiency was compared with that using the single extractants. Therefore, the synergistic solvent extraction of Ce from acidic chloride medium was investigated using the mixture of trihexyl(tetradecyl) phosphoniumbis(2,4,4 trimethylpentyl)phosphinate (Cyphos IL), di-(2-ethyl hexyl) phosphoric acid (D2EHPA), tributyl phosphate (TBP) and trioctylmethylammonium chloride (Aliquat 336) in kerosene. The experiment is expected to identify the best synergist extractants with higher extraction efficiency of Ce compared to the use of single extractants and to overcome the environmental issue of undesired volatile organic compounds (VOCs). The study of solvent extraction was carried out by mixing synergist extractant with aqueous phase of Ce in the ratio of 1:1 under room temperature. The results show that the synergistic extraction system enhanced the extraction efficiency compared to the single extraction system. Synergist extractant between the mixture of Cyphos IL/D2EHPA (S08) appeared to be the most positive in the extraction of Ce based on a 94.1% increase in the extraction efficiency followed by Cyphos IL/TBP (66.2%), Aliquat 336/D2EHPA (51.6%), Aliquat 336/Cyphos IL (51.2%) and Aliquat 336/TBP (42.0%). In conclusion, the synergist extractant of Ce is more efficient compared to single extractant under room temperature.

**Keywords:** Rare earth elements, Cerium, Synergist, Single extractant, Efficiency

## 1 Introduction

Monazite mineral is one of the major sources for REEs including thorium and uranium. Monazite contains a high amount of REEs which contribute about 54 – 60%, 3.1 – 11.34% of thorium and a small amount of uranium (0.2 – 0.4%) (Mohd Salehuddin et al., 2019). Solvent extraction is a conventional technique that applies various types of organic extractants which are expected to produce high purity single REEs solutions or compounds. However, these extractants offer several drawbacks such as the tendency of extractant loss into the aqueous phase due to the acts of multiple contacts and the formation of emulsion due to a high viscosity of extractant that declines the extraction efficiency (Hidayah and Zainal Abidin, 2019; Gupta and Krishnamurthy, 2005).

Therefore, synergistic extraction with the mixed extractants has been developed as the promising method, which could improve the extraction capability and durability as well as to produce high selectivity of REEs. The research is expected to identify the optimum parameters of the synergist extractant in extracting Ce using solvent extraction Furthermore, the synergist extraction efficiency of Ce more than 59% was achieved at laboratory level.

## 2 Methods

### 2.1 Materials

Four types of selected commercial extractants including trihexyl(tetradecyl)phosphonium bis(2,4,4 trimethylpentyl)phosphinate (Cyphos IL), di-(2-ethyl hexyl) phosphoric acid (D2EHPA), tributyl phosphate (TBP) and trioctylmethylammonium chloride (Aliquat 336) were purchased from Sigma-Aldrich Chemical Company. Commercially available kerosene (Sigma Aldrich Chemical Company) was used as an organic phase diluent. Rare earth chloride acidic media (ReCl) was prepared by dissolving some amount of dried hydroxide powder in concentrated hydrochloric acid. All the chemicals used in this study are of analytical reagent grade and no further purification is required on every chemical used.

### 2.2 Extraction Procedure

The solvent extraction experiments were carried out by shaking the mixture of equal volumes (15 mL) of organic and aqueous phases (O/A=1) in beaker for 10 minutes using a mechanical shaker at room temperature (298 K), which is enough to reach equilibrium. After equilibration, the mixture was left to stand for at least 10 minutes to allow the phases to separate. The concentration of Ce in the aqueous phase before and after the extraction was measured spectrometrically using Energy dispersive X-ray fluorescence (ED-XRF). Synergist extractant between Cyphos IL, D2EHPA, TBP and Aliquat 336 was prepared with ratio of 1:1 as shown in Table 1.

The concentrations of Ce(IV) in the aqueous phase before and after extraction were obtained by analysis with XRF. The Ce extraction efficiency, E of synergist extractant was determined using Equation 1.

$$\text{Efficiency of Ce extraction} = \frac{C_{\text{before}} - C_{\text{after}}}{C_{\text{before}}} \quad (1)$$

where $C_{\text{before}}$ is the initial concentration of Ce in aqueous phase and $C_{\text{after}}$ is the final concentration of Ce in aqueous phase.

Table 1: Synergist extractant system for the chloride solution.

| Sample ID | Ratio | Extractant 1 | Extractant 2 |
|---|---|---|---|
| S01 | - | Cyphos IL | - |
| S02 | - | D2EHPA | - |
| S03 | - | TBP | - |
| S04 | - | Aliquat 336 | - |
| S05 | 1:1 | TBP | D2EHPA |
| S06 | 1:1 | TBP | Aliquat 336 |
| S07 | 1:1 | TBP | Cyphos IL |
| S08 | 1:1 | Aliquat 336 | Cyphos IL |
| S09 | 1:1 | Aliquat 336 | D2EHPA |
| S10 | 1:1 | D2EHPA | Cyphos IL |

## 3 Results

The experiments were carried out under acidic chloride solution (0.2 M) at organic-to-aqueous (O/A) phase ratio of 1. The efficiency of Ce extraction is presented in Table 2. It is obviously seen that the chemical composition of Ce extraction was increased after the synergistic extraction compared to single extraction.

Table 2: Efficiency of Ce extraction

| Sample ID | Ratio | Extractant 1 | Extractant 2 | Efficiency of Ce (%) |
|---|---|---|---|---|
| S01 | - | TBP | - | 2.4 |
| S02 | - | D2EHPA | - | 46.2 |
| S03 | - | Cyphos IL | - | 73.2 |
| S04 | - | Aliquat 336 | - | 39.7 |
| S05 | 1:1 | TBP | D2EHPA | 72.7 |
| S06 | 1:1 | TBP | Cyphos IL | 66.2 |
| S07 | 1:1 | TBP | Aliquat 336 | 42.0 |
| S08 | 1:1 | D2EHPA | Cyphos IL | 94.1 |
| S09 | 1:1 | D2EHPA | Aliquat 336 | 51.6 |
| S10 | 1:1 | Cyphos IL | Aliquat 336 | 52.2 |

## 4 Discussion

The results show that the synergistic extraction system enhanced the extraction efficiency compared to the single extraction system. From the results in Table 2, it was found that the extraction of Ce from acidic chloride medium using synergist extractants between D2EHPA and Cyphos IL gives the highest extraction efficiency of 94.1%, followed by TBP/D2EHPA (70.7%), TBP/Cyphos IL (66.2%), D2EHPA/Aliquat 336 (51.6%), Cyphos IL/Aliquat 336 (51.2%) and TBP/Aliquat 336 (42.0%).

## 5 Conclusion

Extraction of rare earth chloride from monazite mineral was successfully achieved. Synergist extractants in extracting cerium from acidic chloride medium using solvent extraction techniques at laboratory scale was successfully achieved. Synergist extractant of D2EHPA/Cyphos IL gave the highest Ce extraction efficiency (94.1%) compared to other extractants. The synergist extractant of Ce is more efficient compared to single extractant under room temperature.

## References

C.K. Gupta and N. Krishnamurthy. 2005. Chapter 3: Resource processing. *Extractive Metallurgy of Rare Earths, CRC Press*, pages 172–174.

N.N. Hidayah and S. Zainal Abidin. 2019. Extraction of light, medium and heavy rare- earth elements using synergist extractants developed from ionic liquid and conventional extractants. *Comptes Rendus Chimie*, 22(11-12):728–744.

AH.J. Mohd Salehuddin, A. Fazli Ismail, C.N.A. Che Zainul Bahri, and E.S. Aziman. 2019. Economic analysis of thorium extraction from monazite. *Nuclear Engineering and Technology*, 51:631–640.

Individual Research Contribution Review, 2024: 403–404
*ISSN: 3083-922X*

# Tannic Acid-based Rust Inhibitor with Metal Fillers for Corrosion Protection of Mild and Low Carbon Steel

**Nur Ubaidah Saidin**
Industrial Technology Division, Malaysian Nuclear Agency
43000 Kajang, Selangor
ubaidah@nm.gov.my

## Abstract

Corrosion is a major issue in many industries, resulting is a large economic loss. Traditional corrosion inhibitors frequently raise environmental concerns and have limited long-term performance capabilities. This work aims to develop eco-friendly and effective corrosion inhibitors based on tannic acid, a natural polyphenol molecule. To improve the performance of tannic acid-based coatings, metal fillers of boron carbide ($B_4C$), silica ($SiO_2$), graphene oxide (GO), copper (Cu) and alumina ($Al_2O_3$) were used on both mild and low carbon steel. The corrosion protection performance of developed coatings was evaluated using electrochemical characterization. Tannic acid and metal fillers have been shown to have a synergetic impact by performing protective layers in the metal surface. This study presents a viable way to generate long-term and effective corrosion protection solutions especially for low carbon steel.

**Keywords:** Corrosion, tannic acid, filler.

## 1 Introduction

Corrosion, a natural process that deteriorates metals, presents substantial hurdles to a variety of sectors. It causes significant economic losses and environmental problems. Traditional corrosion inhibitors, which are generally based on harmful chemicals, have aroused environmental concerns, necessitating the search for eco-friendly and sustainable alternatives.

Tannic acid, a naturally occurring polyphenol molecule, has emerged as a promising corrosion inhibitor due to its superior chelating and film-forming capabilities. However, the performance of tannic acid-based coatings can be improved by adding metal fillers. These fillers, including $B_4C$, $SiO_2$, GO, Cu and $Al_2O_3$, can serve as sacrificial anodes, physical barriers, and catalysts for the development of protective films.

This fundamental study will investigate the synergistic effect of tannic acid and metal fillers in the development of high-performance corrosion inhibitors for mild and low carbon steel. The coatings will be studied using a variety of physicochemical and electrochemical techniques.

## 2 Methods

Tannic acid solution was added with various fillers, $B_4C$, $SiO_2$, GO, Cu and $Al_2O_3$, at a concentration of 0.05 and 0.2 wt.%. The solutions were stirred for an hour. Next, 100 $\mu$L of each coating solution was applied to 9 $cm^2$ area of corroded mild and low carbon steel substrate and allow to dry for 48 hours. Prior to coating, the rusted steel surfaces were extensively cleaned to removed loose rust.

The developed coating solution was then characterized using thermogravimetric analysis/differential scanning calorimetry (TGA/DSC), Fourier Transform Infrared (FTIR) and X-ray diffraction (XRD). The morphology of the coated samples was evaluated using field emission scanning electron microscopy (FESEM). Electrochemical Impedance Spectroscopy (EIS), polarization testing, and Tafel analysis were performed to evaluate the coatings' corrosion performance in 3.5 wt.% NaCl solution. Additionally, immersion test in the same solution were carried out to evaluate the coatings' long-term corrosion resistance. This extended abstract will reveal the results on Tafel polarization analysis.

## 3 Results and Discussion

Table 1 shows the elemental analysis of mild and low carbon steel used in this work. Results shows that both materials have specific elemental compositions and relative amounts of these elements can influence their properties and applications.

Table 1: Comparison of Elemental Composition in Mild Steel and Low Carbon Steel

| Element | Mild steel (%) | Low carbon steel (%) |
|---|---|---|
| C | 0.1650 | 0.0300 |
| Si | 0.4490 | <0.005 |
| Mn | 0.4550 | 0.2000 |
| Cr | 0.0456 | 0.0165 |
| Ni | 0.0970 | 0.0261 |
| Al | 0.2570 | 0.0504 |
| Cu | 0.04530 | 0.0198 |
| Co | <0.0100 | 0.0024 |
| Fe | Balance | Balance |

Figure 1 shows the Tafel polarization curves of coated steel samples in 3.5 wt.% NaCl solution. The addition of metal fillers to the tannic acid-based coating resulted in a considerable reduction in corrosion current densities. Notably, low carbon steel provided more corrosion resistance than mild steel, especially when $Al_2O_3$ filler was used. Future research will investigate the use of $Al_2O_3$ as a possible filler material for improving the corrosion resistance of tannic acid-based coatings.

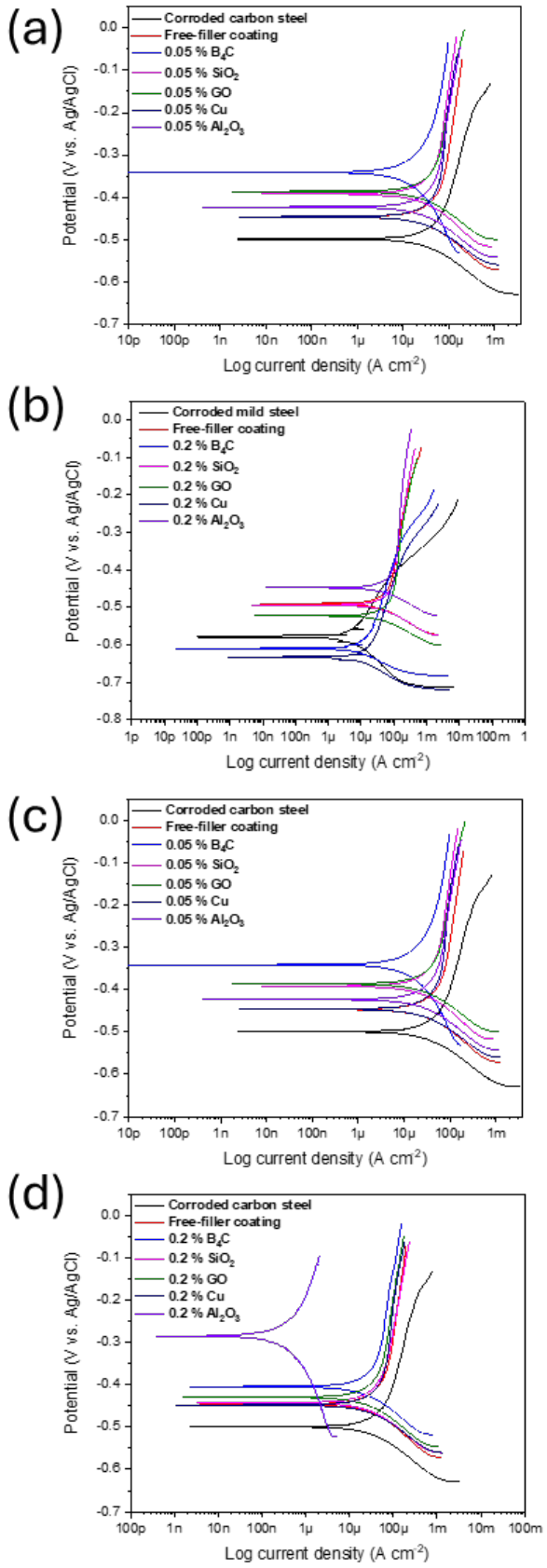



Figure 1: : Tafel polarization plots for various coatings with and without metal fillers (a) 0.05 wt.% of fillers on corroded mild steel, (b) 0.2 wt.% of fillers on corroded mild steel, (c) 0.05 wt.% of fillers on corroded low carbon steel, and (d) 0.2 wt.% of fillers on corroded low carbon steel.

## 4 Conclusion

This study found that the tannic acid-based coatings with metal fillers are effective at protecting mild and low carbon steel from corrosion. The addition of metal fillers significantly increased the corrosion resistance of the coatings when compared to tannic acid alone for low carbon steel. Tannic acid's synergistic impact with metal fillers was attributed to the formation of protective layers on the metal surface, as well as the sacrificial protection provided by the fillers. Future research may focus on refining the compositions and application techniques of these coating to improve their performance and broaden their applications in a range of industries.

Individual Research Contribution Review, 2024: 405–407
*ISSN: 3083-922X*

# Experimental Investigation of Time Domain Pulsed Eddy Current Technique on Non-Ferromagnetic Conductivity Plates

**Nurul A'in Binti Ahmad Latif**
Industrial Technology Division, Malaysian Nuclear Agency
43000 Kajang, Selangor
nurul_ain@nm.gov.my

## Abstract

Pulsed eddy current (PEC) is an advanced non-destructive testing (NDT) technique based on the electromagnetic principle. The excitation consists of a broad frequency spectrum for detection of defects in various depths of specimens. This paper details out the experimental investigations in determining the correlation between PEC signals and conductivity of five different non ferromagnetic plates. Specimens with high conductivities generate high current density within the specimen, which increases the net magnetic field acquired from the specimen. From the results, it shows that there is an increment in the amplitude of the net magnetic field acquired from specimens with different conductivity values.

## 1 Introduction

Pulsed eddy current (PEC) uses a time domain square waveform to drive an excitation coil, which significantly improves its penetration. During the inspection, the excitation coil carrying the square waveform induces transient eddy currents and resultant magnetic fields in the specimen (Sha et al., 2021; Xie et al., 2020). The square waveform consists of a series of frequency contents where its excitation allows for deeper eddy current penetration, resulting in higher robustness of anti-interference and decreasing power consumption during operations. In addition, the wideband pulse consists of frequency ranges of components leading to the potential for gathering information about defects that occur in both ferromagnetic and non ferromagnetic materials. Furthermore, this technique does not require a specific saturation magnetisation device for ferromagnetic material inspection (Han et al., 2022; Johnston et al., 2018; Piao et al., 2019). One advantage of PEC over ET is the use a magnetic sensor to replace the function of the pick-up coil. The magnetic sensor offers a high range of magnetic field detection over wideband frequencies (Angani et al., 2016; Li et al., 2017; Rocha et al., 2015).

## 2 Methods

Figure 1 shows the PEC system developed for the test. A basic PEC system comprising of a function generator, power amplifier, power supply and PEC coil was used to experiment on multiple conductivity plates. A 5 V output from a power supply was used to operate the magnetic sensor. The function generator provided the rectangular input current to drive the excitation coil and the 5 ms pulse width used for current excitation. For signal processing, all of the signals detected by the PEC coil were transferred, displayed and processed using a computer installed with a data acquisition card.

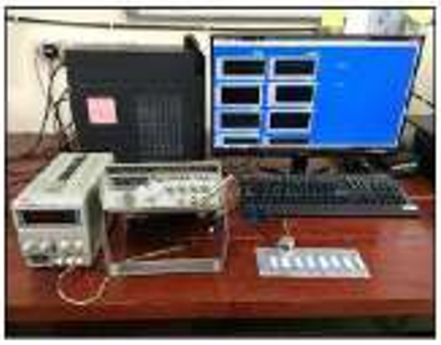


Figure 1: The PEC system developed for the experimental work.

Figure 2 shows the schematic diagram of the PEC coil fabricated for the experiment, with dimensions of 18 mm outer diameter, 12 mm inner diameter and 30 mm height, made up of 300 turns of copper wire. In order to replace the function of the pick-up coil and for magnetic field detection, a magnetic sensor (Hall) was installed at the center of the ferrite core.

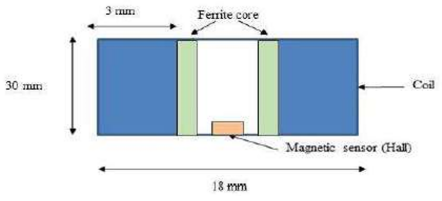



Figure 2: Schematic diagram of PEC probe.

The specimens evaluated were tungsten, Al-7075-T6, Al-6061-T3, Al-1100-F and copper with their conductivities listed in Table 1. The specimens were cut into square plates with dimensions of 50 mm x 50 mm and 5 mm thick. For the experiment, a PEC coil is positioned above the plate with a 2 mm lift-off distance.

The magnetic field of the PEC within the vicinity of a

Table 1: Conductivity and resistivity values of specimens used in experimental work.

| Specimen | Conductivity (S/m) | Resistivity (Ω/m) |
|---|---|---|
| Tungsten | $1.856\text{x}10^{7}$ | $5.388\text{x}10^{-8}$ |
| Al-7075-T6 | $1.890\text{x}10^{7}$ | $5.291\text{x}10^{-8}$ |
| Al-6061-T3 | $2.459\text{x}10^{7}$ | $4.066\text{x}10^{-8}$ |
| Al-1100-F | $3.445\text{x}10^{7}$ | $2.903\text{x}10^{-8}$ |
| Copper | $5.800\text{x}10^{7}$ | $1.724\text{x}10^{-8}$ |

conductive sample can be determined using the following equation:

$$B_z = B_{ze} - B_{zm} \tag{1}$$

where $B_z$ denotes the magnetic field at the z-axis of the specimen, $B_{ze}$ is the field produced by the coil, and $B_{zm}$ is the field change caused by the specimen. The magnitude of change in the acquired magnetic field, $B_z$ is relatively minimal. Thus, in order to observe the magnetic field changes acquired from each plate, the differential net magnetic field was calculated by taking the difference between the magnetic field acquired, $B_z$, and the reference signal of each specimen. The $\triangle B_z$ of each plate can be mathematically defined using the following equation:

$$\Delta B_z = B_{zref} - B_z \tag{2}$$

where $B_{zref}$ is the reference magnetic field acquired while the PEC coil is held in the air.

## 3 Results and Disccusion

Figure 3 shows the normalised transient magnetic field, $B_z$ acquired by the PEC coil from the experiment. It can be seen from the results that air has the highest $B_z$ as compared to the rest of the specimens. Meanwhile, the second highest $B_z$ is acquired from tungsten, followed by Al-7075-T6, Al-6061-T3, Al-1100-F and copper. These net magnetic fields were obtained by taking the difference between the magnetic fields of the coil, $B_{ze}$ and specimen, $B_{zm}$. $B_{zm}$ of air is acquired while the coil is holding in the air. Air has the lowest $B_{zm}$ because the Hall sensor measures the magnetic field that exists in the ambience without any field change from the specimen. This in turn causes air to have the highest $B_z$ as mathematically calculated according to Equation 1.

Figure 4 shows the net magnetic field, $\triangle B_z$ for each specimen with various conductivities. Copper exhibits the highest $\triangle B_z$, followed by Al-1100-F, Al-6061-T3, Al-7075-T6 and tungsten. Consequently, it can be observed that as the conductivity increases, the amplitude of the respective profiles increases. As copper has smaller resistance, more currents are allowed to pass within it. The specimen with higher conductivity will allow for more current flow, increasing the magnetic field. Each specimen's conductivity influences the eddy current's path, phase and distribution. In addition, the strength of the magnetic field depends on the strength of the induced current density within the specimens.

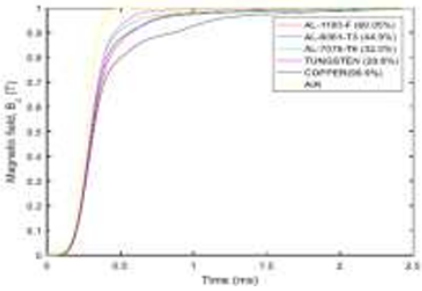


Figure 3: Normalised transient magnetic field, $B_z$ acquired from the specimen with different conductivity values

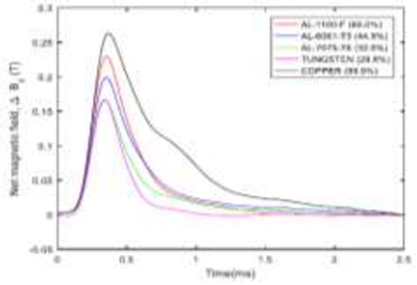


Figure 4: Net magnetic field, $\triangle B_z$ acquired from the specimen with different conductivity values.

## 4 Conclusion

This paper detailed out the experimental and simulation works for PEC and the correlation between the acquired PEC transient signals with non-ferromagnetic materials having different conductivities. The secondary magnetic field's strength depends on the induced eddy current inside the specimen. Therefore, with increasing conductivities, the induced current density also increases, thus increasing the magnetic field density in the specimen.

## References

C. S. Angani, H. G. Ramos, A. L. Ribeiro, and T. J. Rocha. 2016. Evaluation of transient eddy current oscillations response for thickness measurement of stainless steel plate. *Measurement: Journal of the International Measurement Confederation*, 90:59–63.

Y. Han, Y. chun Tao, C. bing Shao, H. Yan, and Z. zhen. Peng. 2022. Pulsed eddy currents in ferromagnetic pipes with cladding in nuclear power plants. *Energy Reports*, 8:104–111.

D. P. Johnston, J. A. Buck, P. R. Underhill, J. Morelli, and T. W. Krause. 2018. Pulsed eddy current detection of loose parts in steam generators. *IEEE Sensors Journal*, 18(6):2506–2512.

Y. Li, B. Yan, W. Li, H. Jing, Z. Chen, and D. Li. 2017. Pulse modulation eddy current probes for imaging of external corrosion in nonmagnetic pipes. *NDT and E International*, 88:51–58.

G. Piao, J. Guo, T. Hu, Y. Deng, and H Leung. 2019. A novel Pulsed Eddy Current method for high-speed pipeline inline inspection, journal = Sensors Actuators: A. Phisycal, volume = 295, pages = 244–258,.

T. J. Rocha, H. G. Ramos, A. Lopes Ribeiro, D. J. Pasadas, and C. S Angani. 2015. Studies to optimize the probe response for velocity induced eddy current testing in aluminium. *Measurement: Journal of the International Measurement Confederation*, 67:108–115.

J. Sha, M. Fan, B. Cao, and B. Liu. 2021. Noncontact and nondestructive evaluation of heat-treated bearing rings using pulsed eddy current testing. *Journal of Magnetism and Magnetic Materials*, 521(P2):167516.

S. Xie, L. Zhang, Y. Zhao, X. Wang, Y. Kong, Q. Ma, and Z. Chen. 2020. Features extraction and discussion in a novel frequency-band selecting pulsed eddy current testing method for the detection of a certain depth range of defect. *NDT and E International*, page 102211.

Individual Research Contribution Review, 2024: 408–409
*ISSN: 3083-922X*

# Morphology Changes of Single Crystal Silicon Electrode (100 and 111) By an Ex-Situ Operando Synchrotron Tomography Imaging

**Rafhayudi Jamro**
Industrial Technology Division, Malaysian Nuclear Agency
43000 Kajang, Selangor
rafhayudi@nm.gov.my

## Abstract

In-operando synchrotron tomography imaging combined with impedance spectroscopy as well as scanning electron microscopy were used to investigate and visualise the morphology changes of lithium ion batteries (LIBs) based on single crystal silicon electrode at room temperature based on (100) and (111) silicon anode electrodes. This technique is a one of crucial tools to visualise and examine of internal morphological changes and evaluation during lithiation and delithiation mechanism for limited cycling behaviour at room temperature. The study found that the crystal orientation of the silicon electrode has a significant impact on the morphology changes of LIBs. The (100) silicon electrode cracked perpendicular to the electrode surface, while the (111) silicon electrode cracked propagate to the electrode surface. The study also found that the size of the cracks was larger for the (100) silicon electrode than for the (111) silicon electrode. These findings suggest that the (111) silicon electrode is a more promising material for LIBs than the (100) silicon electrode.

**Keywords:** Li-Si, ex-situ synchrotron tomography, SEM, single crystal silicon electrode, separator, LIBS

## 1 Introduction

Study on silicone electrodes based on lithium battery was widely performed since many years ago. Silicon is basically considered as a potential electrode material for next generation lithium ion batteries (LIBs) due to high specific capacity where it has a theoretical capacity ~10 times of graphite: up to 4200 mAh/g (Ronneburg et al., 2021). Moreover, silicon storage ability is approximately 1 order of magnitude higher than current graphite electrode (Ashuri et al., 2016) and also it's have been considered as a promising candidate because of their extremely abundant reserves, low cost, easy to synthesis, environmental friendly, not harmful and is non-toxicity material.

Silicone is promising electrode anode material for lithium battery system but however suffer by extremely major obstacle for Si battery systems is microstructure degradation which seriously influences performance and lifetime. The major challenges and drawback which is including gigantic maximum volume expansion during cycling process up to about 400%, low electrical conductivity, morphology changes such as cracking and instability of the solid electrolyte interface (SEI). The enormous volume expansion resulted in particle pulverization, large mechanical stress and fracture, loss of electrical contact with the conductive addictive or current collector and even peeling off from the current collector surface and also creates internal stress in the silicon and introduces cracks (Zhang et al., 2020) within electrode which leads to capacity fading phenomena. The repeated of huge amount of volume expansion and shrinkage lead to fracture and cracking and re-formation of the SEI layer around Si particles resulting in continuous consumption of the electrolyte an increasing impedance behaviour, loss mass and capacity fading phenomenon in lithium-ion batteries (LIBs).

## 2 Material Characterization Using Synchrotron Tomography Imaging Method

The ex-situ synchrotron tomography experiments were conducted at Petra 3 Desy laboratory, Hamburg Germany. Since 2010, PETRA III has been one of the brightest storage-ring-based X-ray radiation sources in the world. The facility offers optimum experimental capabilities at 25 beamlines with almost 60 measuring stations (Deutsches Elektronen-Synchrotron DESY: A Research Centre of the Helmholtz Association 2023). Moreover, synchrotron tomography of the Imaging Beamline P05 was providing high quality, absorption contras tomogram with ultra high density resolution (Wilde et al., 2016). Synchrotron radiation based techniques are powerful tools for battery research and allow probing a wide range of length scales, with different depth sensitivities and spatial/temporal resolutions. Operando experiments enable characterization during functioning of the cell and are thus a precious tool to elucidate the reaction mechanisms taking place (Black et al., 2023). The battery samples on the rotating sample holder were exposed to a monochromatic X-ray beam. This technique also beneficial for investigating very small samples or requiring tightly collimated and very short-wavelength X-rays for their experiments-ranging from medical research to nanotechnology research.

The spatial resolution in this experiment the pixel size was set to have a spatial resolution of 1.28µm. Meanwhile, for this synchrotron tomography measurement set-up with hard synchrotron white beam, the energy is set to 29.99 kV. Source-to-detector distance (SDD) was set to 29.99 mm. A schematic illustration of the tomography x-ray imaging set-up are given in Figure 2. A set of 1000 projections along a 360° rotation angle with 450 second of exposure per projection was acquired

for each synchrotron computed tomography scan.

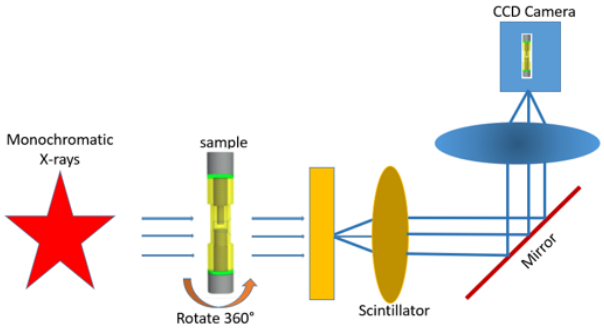



Figure 1: Schematic illustration of the synchrotron tomography imaging technique.

## 3 Results and Discussion

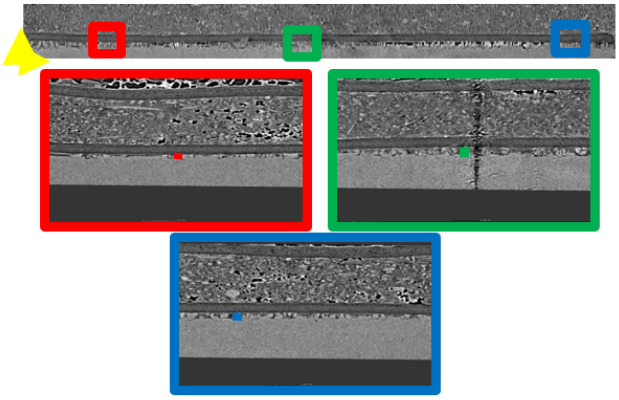


Figure 2: Morphology of cracks for Si wafer (100) images is not visible for 20 cycles by ex-situ operando synchrotron tomography in XZ plane

Figure 2 (b-c) clearly illustrates on the crack depth of the same cycles on the ZY and ZX planes. The maximum crack depth was observed in the centre (22.27 µm) of the anode cell along the ZY plane. The cracks depths were approximately 12.40 µm and 18.61 µm on the left and right for the Si (100) for 20 cycles. On the XZ plane, the crack depths were 26.75 µm, 22.67 µm and 27.04 µm from the left to the right of the Si anode.

However, upon examining the ZY and ZX planes in the Figure 6(b-c), the crack depth of Si (111) remains obscured. This could potentially be attributed to the small depth dimensions being beyond the imaging resolution or the propagation of the crack's orientation.

## 4 Conclusion

To sum up, structure evaluation of morphological changes in single crystal silicon electrode for (100) and (111) are clearly visualised by in operando synchrotron imaging technique as well as SEM method. The orientation of cracking behaviour

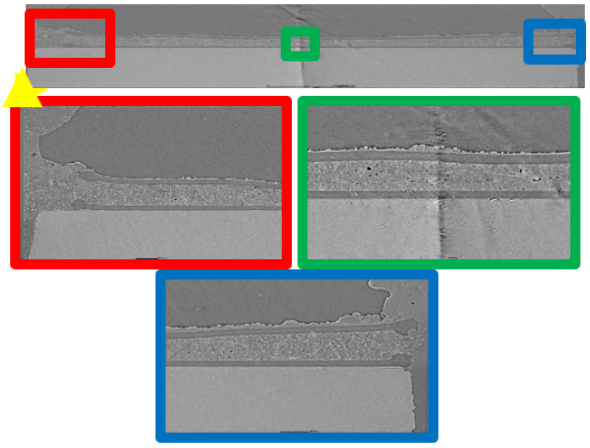


Figure 3: Morphology of cracks for Si wafer (111) images is not visible for 20 cycles by ex-situ operando synchrotron tomography in XZ plane

of Si electrodes with different crystal plane or orientation can be revealed by in operando technique where the Li-Si alloying reaction of Si (111) electrode is carried out along the <121> direction and meanwhile Si (100) tend to proceed perpendicular to the <100> surface as reported by (Shi et al., 2019).

## References

M. Ashuri, Q. He, and L.L. Shaw. 2016. Silicon as a potential anode material for li-ion batteries: Where size, geometry and structure matter. *Nanoscale*, 8:74–103.

A. P. Black, A. Sorrentino, F. Fauth, I. Yousef, L. Simonelli, C. Frontera, A. Ponrouch, D. Tonti, and M. R. Palacin. 2023. Synchrotron radiation based operando characterization of battery materials. *Chem. Sci.*, 14:1641.

A. Ronneburg, L. Silvi, J. Cooper, K. Harbauer, M. Ballau, and S. Risse. 2021. Solid electrolyte interphase layer formation during lithiation of single-crystal silicon electrodes with a protective aluminum oxide coating. *ACS Appl Mater Interfaces.*, 13(18).

Y. Shi, J. Wan, J.Y. Li, X.C. Hu, S.Y. Lang, Z.Z. Shen, G. Li, H.J. Yan, K.C. Jiang, Y.G. Guo, R. Wen, and L.J. Wan. 2019. Elucidating the interfacial evolution and anisotropic dynamics on silicon anodes in lithium-ion batteries. *Nano Energy*, 61:304–310.

F. Wilde, M. Ogurreck, I. Greving, J. U. Hammel, F. Beckmann, A. Hipp, L. Lottermoser, I. Khokhriakov, P. Lytaev, T. Dose, H. Burmester, M. Müller, and A. Schreyer. 2016. Micro-ct at the imaging beamline p05 at petra iii. *AIP Conference Proceedings*.

K. Zhang, Y. Zhang, J. Zhou, Y. Li, B. Zheng, F. Yang, and Y. Kai. 2020. A stress-based charging protocol for silicon anode in lithium-ion battery: Theoretical and experimental studies. *Journal of Energy Storage*, 32.

Individual Research Contribution Review, 2024: 410–411
*ISSN: 3083-922X*

# The Utilisation of Alkaline Fusion for the Removal of Phosphates from Xenotime Minerals

**Roshasnorlyza Hazan**
Industrial Technology Division, Malaysian Nuclear Agency
43000 Kajang, Selangor
roshasnorlyza@nm.gov.my

## Abstract

In Malaysia, heavy rare earth elements (HREE) are extracted from xenotime minerals. This study examined the phosphate removal procedure from xenotime by alkaline fusion, which entails fusing the minerals with sodium hydroxide pellets. The xenotime mineral was fused with sodium hydroxide in a 1:2 ratio at 350 °C for 3 hours to facilitate mineral extraction. The subsequent phase entailed rinsing the fused mixture with deionised water, accompanied by agitation and filtration procedures. The fused mixes were further modified with and without washing using hot water (~80 °C) until achieving a neutral pH (pH 6 to pH 8). The combined substance and its filtrate were examined by X-ray fluorescence (XRF) for elemental analysis. The solid sample is subjected to an acid leaching process to clarify the impact of the washing method on the leaching of fused xenotime. These findings together emphasise alkaline fusion methods for the effective extraction of phosphate from xenotime minerals by hot water rinses.

**Keywords:** Alkaline Fusion, Phosphate, Rare Earth Element (REE), Xenotime

## 1 Introduction

A growing number of high-tech applications, such as applications in the electronics, defence, and renewable energy sectors, rely on rare earth elements (Chang et al., 2020). Together with yttrium (Y) and scandium (Sc), it includes gadolinium (Gd), terbium (Tb), dysprosium (Dy), holmium (Ho), erbium (Er), thulium (TM), ytterbium (Yb), and lutetium (Lu) (Akademi Sains Malaysia, 2013). Heavy rare earth elements, such as yttrium, dysprosium, and terbium, are very rare and in high demand (Hoshino et al., 2016) as essential components of cutting-edge technologies (Xu et al., 2024). In order to overcome this difficulty, scientists have looked into non-traditional sources of heavy rare earth elements, such as peralkaline igneous rocks (Hoshino et al., 2016).

Previous research has demonstrated that alkaline fusion is a promising method for recovering rare earth elements from a variety of resources, including xenotime ores (Hazan et al., 2024a), monazite ores and wasted zeolites (Alfiyan, 2021; Mendonça et al., 2007). The ideal parameters for the alkaline fusion process, encompassing reagent type, reagent-to-mineral ratio, temperature, and fusion duration, must be meticulously examined to ensure full phosphate elimination and to optimise the recovery of rare earth elements (Wu et al., 2018). A 2023 article indicates that the alkaline fusion technique may be employed to extract phosphate from apatite and monazite, as well as other phosphate-containing minerals (Merzeg et al., 2023). The presence of phosphate in xenotime minerals hindered the recovery of rare earth elements by diminishing the efficacy of acid leaching. Consequently, further investigation is required to improve the phosphate removal procedure. Thus, the purpose of this work is to investigate the use of an alkaline fusion process to achieve total phosphate removal from xenotime minerals.

## 2 Methods

Mineral cracking was done by mixing xenotime minerals with NaOH beads and fused in the furnace at 300 °C for 3 hours. Detail procedure were followed from NUKLEAR-MALAYSIA/M/2024/43 (Hazan et al., 2024b).

Shidmadzu's EDXRF 7000 performed the elemental analysis for both liquid and solid samples. For morphology of the samples, Field Emission Scanning Electron Microscope (FESEM), Carl Zeiss, GeminiSEM 500 equipped with Energy Dispersive X-Ray Spectrometer (EDXs), X-Max 80 by Oxford Instrument were used. We have selected three points to pinpoint the presence of the element in a particular morphology.

## 3 Results

Table 1 shows that the amounts of most of the elements in the raw xenotime and fused mixture were clearly different after alkaline fusion process. The phosphorus content was one of the most noticeable differences and not detected in mixture after rinsed with hot water.

The fused mixture obtained after the alkaline fusion experiment was observed under FESEM. Figure 1a and b, respectively, show FESEM micrographs of the fused samples without and with hot water rinsing. Therefore, Figure 1a clearly displays the fibre structure. Elemental analysis on these fibres was further analysed with EDAX, and the results are shown in Table 3. It was observed that the fibre morphology consists mainly of phosphorus elements.

## 4 Conclusion

The removal of phosphate from xenotime minerals is essential for the efficient extraction and purification of rare earth elements. The alkaline fusion process presents a viable approach

to achieve total phosphate removal, but the process parameters need to be carefully investigated and optimised for xenotime minerals.

Table 1: Composition of raw xenotime and after alkaline fusion process. *ND= Not Detected

| Element (%) | Raw xenotime | Rinse without hot water | Rinse with hot water |
|---|---|---|---|
| **Rare Earth elements (REE)** | | | |
| Y | 22.0 | 51.5 | 50.7 |
| Gd | 1.4 | 2.8 | 3.3 |
| Tm | ND | 3.9 | 4.8 |
| Ho | 0.7 | 2.0 | 2.2 |
| Yb | 5.6 | 8.0 | 8.8 |
| Nd | 2.0 | 4.4 | 5.1 |
| Ce | 1.8 | 3.0 | 4.6 |
| **Radioactive elements** | | | |
| Th | 0.5 | 1.1 | 1.1 |
| U | 0.4 | 0.8 | 0.8 |
| **Inorganic elements** | | | |
| P | 41.9 | 4.9 | ND |
| Other elements | 24.0 | 17.6 | 18.5 |

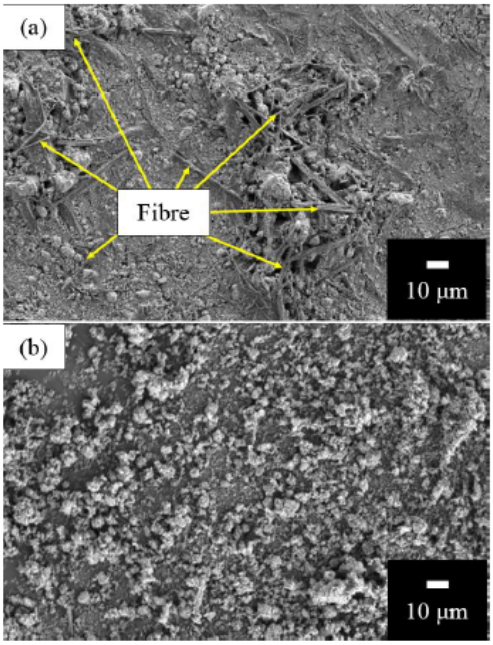



Figure 1: FESEM image on sample (a) without and (b) with hot rinse water.

Table 2: Element identification with EDAX for samples in Figure 1.

| Element | Without hot water rinse | With hot water rinse |
|---|---|---|
| Y | 23.3 | 36.3 |
| Dy | 1.7 | 5.8 |
| P | 44.3 | 0 |
| Other | 30.8 | 57.9 |

## References

M. Alfiyan. 2021. Implementation of bapeten chairman regulation no. 16 years 2013 for extracting rare earth elements from tenorm materials. *American Institute of Physics (AIP) Conference Proceedings*, 2374(060007).

S. Chang, K. Tseng, T. Yang, D. Chao, J. Yeh, and J. Liang. 2020. Irradiation-induced swelling and hardening in hfnbtatizr refractory high-entropy alloy. *Materials Letters*, 272:127832–127832.

R. Hazan, M. Ahmad, M. F. Rosdidi, M. I. Idris, K. Mohamed Takip, N. A. Sapiee, N. Azhar, J. Kones, and W. Paulus. 2024a. Yttrium and other rare earth elements (ree) recovery from chloride solution via carbonate and peroxide precipitation. *AIP Conf. Proc.*, 2925(020006).

R. Hazan, K. Mohamed Takip, N. A. Kamarudin, N. Asri, N. A. Sapiee, N. Azhar, W. Paulus, and J. Kones. 2024b. Improvement process for phosphate removal from malaysian xenotime using alkaline fusion digestion method. *NUKLEARMALAYSIA/M/2024/43.*

M. Hoshino, K. Sanematsu, and Y. Watanabe. 2016. Ree mineralogy and resources in handbook on the physics and chemistry of rare earths. b. jean-claude and k. p. vitalij (eds.). *Elsevier.*, pages 129–291.

L A D. Mendonça, R. Adamian, and J C. Afonso. 2007. Parâmetros operacionais no processamento de zeólitas desativadas por fusão com khso4. *Brazilian Chemical Society*, 30:476–480.

F. A. Merzeg, N. Bezzi, N. Bouzidi, S. Narsis, N. Bait, R. Ladji, and K. Bachari. 2023. Solid state physics mineral processing. 1(61).

S. Wu, L. Wang, L. Zhao, P. Zhang, El-Shall, Moudgil H., X. B., Huang, and L. Zhang. 2018. *Chemical Engineering Journal*, 335(774).

C. Xu, A. Shi, M. Brenna, P. Li, Q. Li, and C. A. Fan. 2024. Degassing-driven oxidation promotes hree enrichment in south china granites. *Journal of Petrology*, 65(064).

Individual Research Contribution Review, 2024: 412–413
*ISSN: 3083-922X*

# Image Optimization Using Predetermined Voltage and Filter on the 1172 Micro Computed Tomography (MicroCT) System

**Roslan Yahya**
Industrial Technology Division, Malaysian Nuclear Agency
43000 Kajang, Selangor
roslan_y@nm.gov.my

## Abstract

In MicroCT systems, selecting the appropriate voltage and filter settings is essential for obtaining optimal image quality and contrast across different samples. Although past studies often provide guidance, variations between MicroCT systems can limit the accuracy of these references. As a result, researchers frequently rely on a time-intensive trial-and-error approach. To overcome this challenge, systematic studies are needed to identify the ideal settings for specific samples and imaging objectives. By methodically adjusting parameters and analyzing the resulting images, researchers can reduce the reliance on trial and error, streamline the scanning process, and improve the efficiency of MicroCT imaging research.

**Keywords:** Micro Computed Tomography (MicroCT)

## 1 Introduction

Micro computed tomography (MicroCT) is a non-destructive imaging technique that enables detailed three-dimensional exploration of the internal structures of small objects. It is based on the principles of conventional computed tomography (CT) but offers significantly higher resolution. The SKYSCAN 1172 MicroCT, now produced by Bruker, is a widely used model in scientific research and industrial applications for analyzing diverse materials.

The MicroCT process involves capturing multiple x-ray transmission images of a sample from various angles. Positioned between an x-ray source and a detector, the sample modulates the x-ray attenuation or absorption based on its density and composition, producing a series of shadow images. Advanced computational algorithms then reconstruct these images into cross-sectional slices, revealing the internal structure layer by layer. By stacking these slices, a detailed 3D representation or volume rendering of the sample is generated, allowing an in-depth examination of its intricate internal features.

## 2 Methods

In order to optimize MicroCT imaging, the goal is to develop a comprehensive database that includes voltage settings ranging from 20 kV to 100 kV, along with corresponding filter usage details. This database aims to provide researchers and operators with a reliable resource to achieve optimal image quality and contrast for specific sample types. Once completed, the secondary goal is to apply the database in practical image optimization. By consulting this resource, users can efficiently select the most suitable voltage and filter settings based on their characteristics of sample, significantly reducing reliance on time-consuming trial-and-error methods.

A critical component of the project involves fabricating a set of phantom with specialized material. This phantom is designed with materials of varying densities, ranging from 0.46 g/ml to 2.70 g/ml (Table 1), likely representing different compositions or structural variations encountered in MicroCT samples.

Table 1: Phantom number with specific density

| Serial no. | Phantom no. | Density $\rho$ (g/cm$^3$) |
|---|---|---|
| QSA-926.1 | 1 | 0.46 ± 0.02 |
| QSA-926.2 | 2 | 1.08 ± 0.02 |
| QSA-926.3 | 3 | 1.47 ± 0.02 |
| QSA-926.4 | 4 | 1.88 ± 0.02 |
| QSA-926.5 | 5 | 2.70 ± 0.02 |

Beyond density variations, the phantom also possesses distinct dimensions, measuring 33mm in length. Notably, the diameter of the phantom exhibits a staggered pattern, starting wider at one end (20mm) and gradually tapering down to a narrower end (2mm). This design enables the phantom to mimic the diverse geometric characteristics encountered in actual microCT samples. Overall, the development of such a phantom serves as a crucial tool for ensuring accurate calibration and quality control in microCT imaging systems.

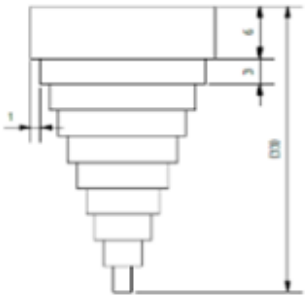


Figure 1: Phantom dimension in millimeter (mm)

## 3 Results

Results were obtained for Phantom 1 through Phantom 5 to evaluate the percentage of x-ray radiation transmitted through each phantom at specific densities and sizes. The tests were conducted at voltages of 40kV, 60kV, and 80kV under different filter configurations: no filter, 0.5mm aluminum filter, and a combination of 0.5mm aluminum filter with 0.5mm copper filter. The recorded results are presented in Figures 2 through Figures 6, corresponding to Phantoms 1 to 5, respectively.

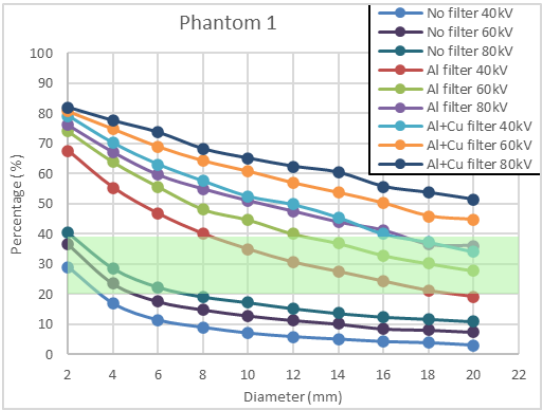



Figure 2: Percentage of x-ray passing through Phantom 1

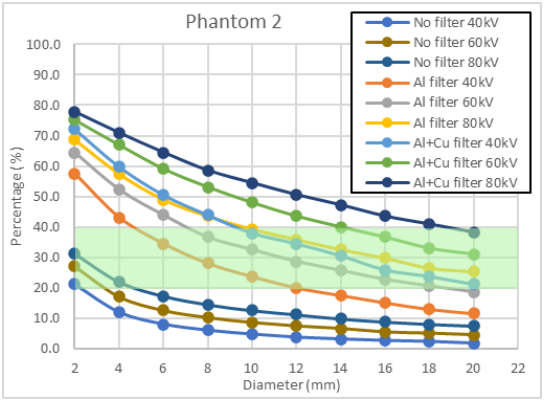



Figure 3: Percentage of x-ray passing through Phantom 2

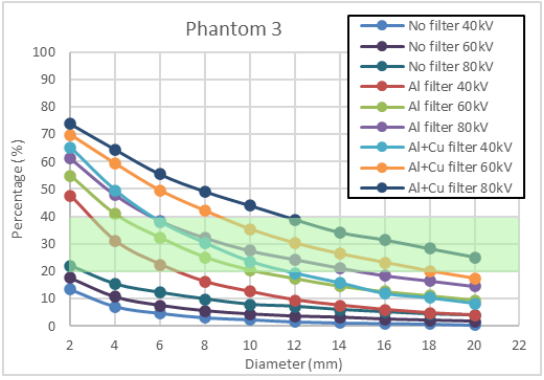



Figure 4: Percentage of x-ray passing through Phantom 3

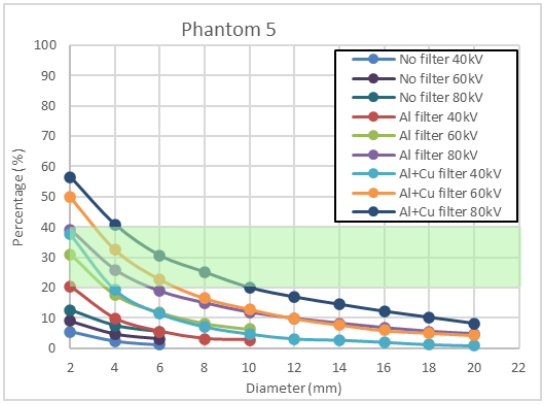



Figure 5: Percentage of x-ray passing through Phantom 4

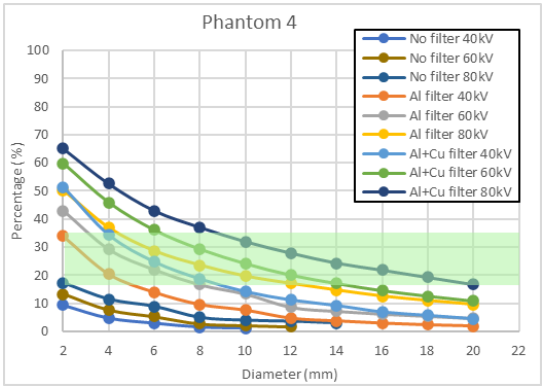



Figure 6: Percentage of x-ray passing through Phantom 5

## 4 Discussion

The findings indicate that introducing a filter increases the percentage of x-rays passing through a specific phantom diameter. Among the phantoms analyzed, Phantom 5 shows the highest attenuation, while Phantom 1 has the lowest. To achieve good image reconstruction, the recommended percentage of x-rays ranges between 20% and 40%. Based on the results, an 8 mm diameter with a material density of 2.7 g/cm$^3$ is considered the maximum size and density, while a 2 mm diameter with a density of 0.46 g/cm$^3$ is considered the minimum size and density for effective imaging. In summary, the data reveal key relationships between x-ray beam attenuation, filters, phantom density, and voltage. For sample sizes and densities within the specified maximum and minimum ranges, appropriate kV and filter settings can be identified using the corresponding graphs.

## References

Bruker MicroCT method note: Flat-field corrections (MCT-129).

Bruker MicroCT method note: SkyScan 1172 microCT.

Individual Research Contribution Review, 2024: 414–415
*ISSN: 3083-922X*

# Development of an Electrolysis System for Rust Removal

**Siti Aishah Ahmad Fuzi, Dr.**
Industrial Technology Division, Malaysian Nuclear Agency
43000 Kajang, Selangor
aishahfuzi@nm.gov.my

## Abstract

Corrosion is a common problem faced by ferrous metals. There are various methods to remove the rust. One of them is through electrolysis method. Although this method is the most commonly used, but further studies are needed to determine the optimal values of voltage, time and concentration to remove the rust properly.

**Keywords:** Electrolysis, ferrous

## 1 Introduction

Rust removal is an important aspect in preservation and conservation of the cultural heritage artifacts. In conservation works, the aim is to preserve and protect the artifacts through proper cleaning, restoration and maintenance.

Electrolysis is a common method used for removing rust from metal objects (Letardi, 2013). The process involves using a direct electrical current to break down the rust on the object leaving the metal underneath intact (Zalaffi et al., 2020). Electrolysis is a process that involves charging the electrode and the rust material in an electrolyte. During electrolysis, an electric current is passed through an electrolyte. The rust material (as cathode) can remove the oxide layer that flows to the electrode (as anode) that receives the oxide.

Electrolysis is also used for electroplating, the extraction of reactive metals, metal purification, and the manufacture of compounds. Electrolysis has some limitations, including the fact that it does not work on coated or painted surfaces and may produce harmful gas. However, electrolysis is the most efficient, effective, and cost-effective method of cleaning iron artefacts because it can clean rust in the smallest of corners and crevices, does not harm the metal, and avoids producing scratches while cleaning (Singh et al., 2021; Siham Mohammed, 2018).

## 2 Methods

The rust samples are prepared using soaking in seawater for 1 day and dry it for 3 days. Then, remove the rust using electrolysis process with different voltage, time duration and concentration of electrolyte. After the electrolysis process, the prepared samples will be characterized using stereo microscope, hardness tester and X-Ray Diffraction (XRD).

## 3 Result and Discussions

Figure 1 shows images of the original, rust, 5V, 10V and 15V samples under a stereo microscope. The image in Fig. 1 signified that removing rust using the electrolysis method is successful.



Figure 1: Image for original, rust, 5V, 10V and 15V samples under stereo microscope

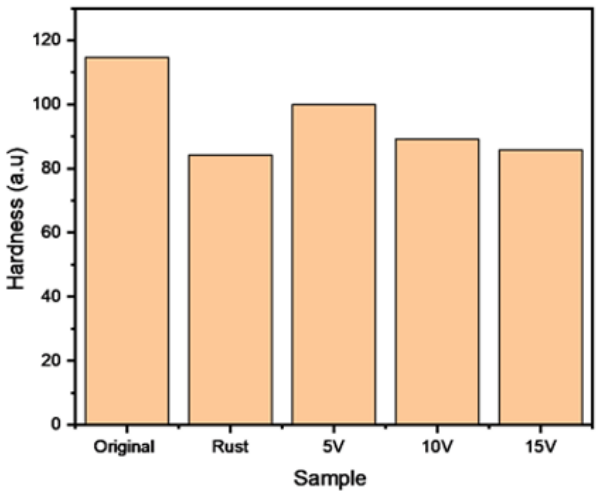



Figure 2: Hardness tester for each sample

Figure 2 shows the hardness graph for each sample. Based on Figure 2, the original sample has the highest hardness value of 114.6 while the rust sample has the lowest hardness value of 84.1. This hardness value represents the hardness level for each sample where, the higher the hardness value, the stronger the sample. Whereas, the lower the hardness value, the more fragile the sample. This finding shows that the voltage at 5V provides the highest hardness value of the sample compared to other voltage. This finding also shows that the optimum voltage is at 5 V, which represent most likely same hardness value as original ferrous metal.

Figure 3 represent XRD data for original, rust, 5V, 10V and 15V samples, respectively. The success of the electrol-

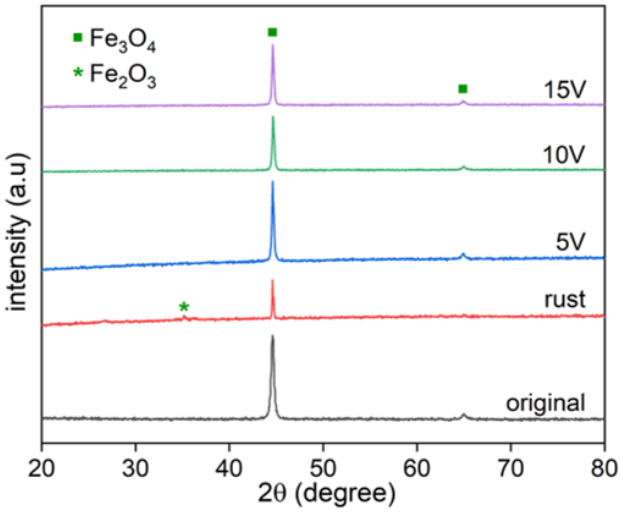



Figure 3: XRD Data

ysis process is further evidenced by the disappearance of the Fe2O3 peak from the XRD spectrum as low as 5V.

## 4 Conclusion and attention

Based on XRD and hardness tester analysis, the electrolysis process exhibited minimal variation across different voltages. However, the hardness of the material significantly decreased at higher voltages (e.g., 10V and 15V). To mitigate this reduction in hardness, which is critical for heritage samples, the optimal electrolysis voltage was determined to be 5V.

## References

P. Letardi. 2013. Electrochemical measurement in the conservation of metallic heritage artefacts; an overview. *European Federation of Corrosion (EFC) Series*, pages 126–148.

M. E. Siham Mohammed. 2018. The structural properties of iron oxides using raman spectroscopy. *Journal of Scientific and Engineering Research*, pages 183–187.

Gurmider Singh, Sunpreet Singh, Chander Prakash, and Seeram Ramakrishna. 2021. On investigating the soda-lime shot blasting of az31 alloy: Effects on surface roughness, material removal rate, corrosion resistance, and bioactivity. *Journal of Magnesium and Alloys*, 9:1272–1284.

Maria Sole Zalaffi, Najmeh Karimian, and Paolo Ugo. 2020. Review-electrochemical and sers sensors for cultural heritage diagnostics and conservation: Recent advances and prospects. *Journal of The Electrochemical Society*, 167:037548.

Individual Research Contribution Review, 2024: 416–417
*ISSN: 3083-922X*

# Preliminary Work on Automated Defect Recognition for Thermography Impact Damage Defects

**Siti Madiha Muhammad Amir**
Industrial Technology Division, Malaysian Nuclear Agency
43000 Kajang, Selangor
madiha_amir@nm.gov.my

## Abstract

Industrial Revolution 4.0 (IR 4.0) is about using modern technology to make industries smarter and working more efficiently. The revolution involves smart manufacturing, predictive maintenance, supply chain optimization, digital twin technology, 3D printing, autonomous robots, energy efficiency and sustainability and artificial intelligence. In this work, Artificial Intelligence (AI) algorithms are employed for the automated defect recognition process of the defects due to low velocity impact damage. Python coding is implemented and the tensor flow method is used in classifying the defects of the images. The data sets are non-defect and defect images of the damaged hybrid composites. It is found that the method employed in this work has the ability in recognizing the defects. Hence, AI plays a significant role in recognizing defect without human intervention.

**Keywords:** Composite defects, Impact damage, Python, Automated Defect Recognition, Artificial Intelligence

## 1 Introduction

The advancement of computer technology has contributed to the rapid progress in Industrial Revolution 4.0 (IR 4.0). IR 4.0 consists of wide range of modern advancement such as Big Data and Analytic, Artificial Intelligence (AI) and Machine Learning, Additive Manufacturing (Meynard, 2019), Robotics and Autonomous System and many more. These technologies not limited to only manufacturing industry (Ling et al., 2020) but also Non Destructive Testing (NDT) has also applied the concept of IR 4.0 in the NDT sector and it is known as NDT 4.0. NDT 4.0 is an integration of IR 4.0 into NDT methods. The purpose of NDT 4.0 is to improve inspection performance, integrity engineering, classification of defects and quality control (Schulenburg, 2021).

Manually identifying composite defects on thermographic images is time consuming. Manual interpretation is prone to errors and inconsistencies. Hence, there is a need for an automated solution to improve efficiency and accuracy. This work focus on the classification of defects from thermographic images using Artificial Intelligence (AI) to improve the efficiency and accuracy during defect interpretation. In employing AI for defect interpretation, Nicolai (Nicolai et al., 2021) in his work employed Machine Learning method to identify the defectiveness of mechanical parts from fluorescent penetrant inspection.

## 2 Methods

Tensorflow framework and Keras through the Tensor flow framework is employed in this work. Data sets which are the images from the thermography experiments and digital camera images. The images comprise of images with defects and non defects. The defects only limited to holes and cracks as shown in Figure 1.

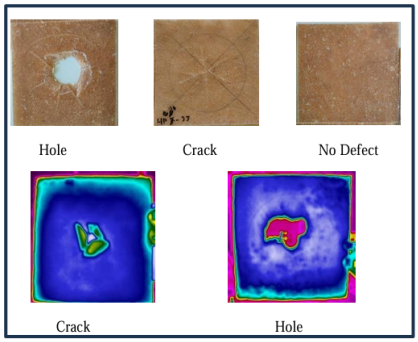



Figure 1: Examples of data sets used in the work

Open source Phython is used in developing the code. The work flow of the programme is given in Figure 2.

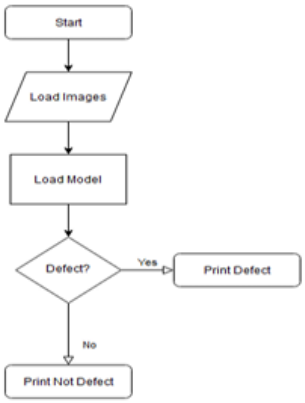



Figure 2: The work flow of the programming code

## 3 Results and Discussion

The precision and accuracy in classifying the defects using the model is evaluated and tabulated in Table 1.

Table 1: The precision of the developed model

| Class | Precision | Recall |
|---|---|---|
| Crack | 0.98 | 0.99 |
| Hole | 1.00 | 0.90 |
| No Defect | 0.95 | 0.95 |

The results in Table 1 show that crack defects have the highest precision and recall. This indicates that very few false positives and false negatives. Hole defects have prefect precision but slightly lower recall indicating some false negatives. The images with no defects also have high precision and recall which indicate few false positives and false negatives. The results of the trained developed model are shown in Figure 3.

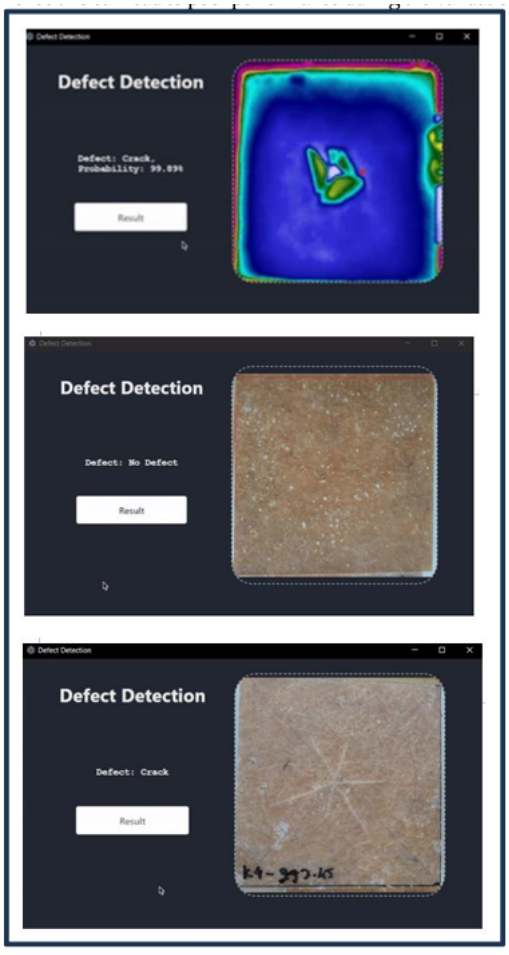



Figure 3: The classification of images using developed model

The main challenge in training the developed model is limited datasets. This can result in lack of diversity in training data which can affect the model's ability in generalizing the new unseen data. Besides, the limited data sets, the model may learn the noise and details of the training data hence this can lead to poor performance during the validation.

## 4 Conclusion

The developed machine learning model for defect recognition using thermography images is efficient and significantly reduces defect interpretation time compared to manual execution. The developed model shows promising results, however, future work is suggested to improve the model. Improvements could include expanding the datasets and enhancing the model's ability to detect multiple defects in a single image.

## References

Yong M. Ling, Nor A.A. Hamid, and Lee T. Chuan. 2020. Is malaysia ready for industry 4.0? issues and challenges in manufacturing industry. *International Journal of Integrated Engineering*, 12(7):134–150.

Philippe Meynard. 2019. NDT 4.0:robotics and defects recognition for automated quality control. *11th International Symposium NDT in Aerospace*.

Alessandro Nicolai, Davide Caputo, Leonardo Chieco, Francesco Grimaccia, and Marco Musetta. 2021. Machine learning-based detection technique for NDT in industrial manufacturing. *MDPI Mathematics*, 9:1251.

Lennart Schulenburg. 2021. NDT 4.0 - a technology overview. *13th International Symposium on NDT in Aerospace*.

Individual Research Contribution Review, 2024: 418–419
*ISSN: 3083-922X*

# Effect of the Elevated Temperatures on the Corrosion Behaviour of the Nurust-Coated Samples

**Siti Radiah Mohd Kamarudin**
Industrial Technology Division, Malaysian Nuclear Agency
43000 Kajang, Selangor
radiah@nm.gov.my

## Abstract

The impact of elevated temperatures on the corrosion behaviour of the heat-treated NuRust coated samples has been investigated using Tafel extrapolation and open circuit potential (OCP) measurement. Preliminary results have shown that heat treatment of the coated samples has shifted the corrosion potential, Ecorr and OCP to a more noble value in 3.5 wt% NaCl solution compared to the uncoated sample. Heat treatment of the coated samples especially at 50°C to 100°C seemed to significantly increase the corrosion properties of the NuRust-coated sample.

**Keywords:** NuRust-coated, $E_{corr}$, OCP, corrosion properties

## 1 Introduction

NuRust is a water-based compound that coats over rusty ferrous-based metals. It chemically converts rust into a more stable protective layer that seals out moisture and protects against future corrosion. However, since NuRust is an organic water-based compound, it might not be suitable for use in higher temperature environments. Thus, this work aims to assess the performance of NuRust as a coating material for high-temperature applications.

## 2 Methods

The Tafel curve and OCP measurements were carried out by using the corrosion analyser model Gamry Reference 600. Prior to testing, heat treatment of the coated samples was carried out at 50°C, 100°C, 150°C and 200°C for 24 hours in a laboratory oven. For the measurements, a standard three-electrode system was used i.e.; a graphite electrode as the counter electrode, a silver/silver chloride (Ag/AgCl) electrode as the reference electrode, and samples as the working electrode. All measurements were carried out in a 3.5 wt% sodium chloride (NaCl) solution. Samples used for measurements were carbon steel with the composition; C 0.0303%, Mn 0.2%, Cr 0.0165%, Ni 0.0261%, Al 0.0504%, Cu 0.0198%, Co 0.0024% and Fe 99.5%.

## 3 Result and Discussions

Figure 1 shows the Tafel curves of the samples, whereas the corrosion parameters of all samples are shown in Table 1.

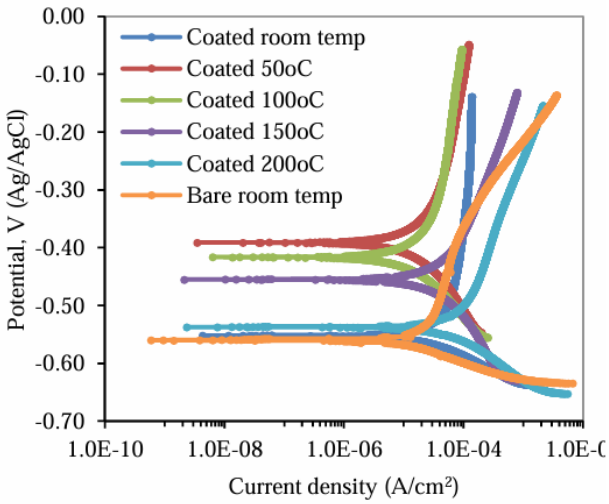



Figure 1: Tafel curve of the NuRust-coated samples treated at elevated temperatures

Generally, the Tafel curve shapes of all samples are very similar, indicating similar corrosion behaviour. This was maintained throughout the test period, suggesting that there was an almost unchanged corrosion mechanism for all samples. A slight increase in current density toward the end of the experiment for the bare uncoated sample at room temperature indicates more active sample dissolution.

Clearly observed in Table 1, the corrosion potentials ($E_{corr}$) of heat-treated samples are more noble than not heat-treated and uncoated samples.

Table 1: Corrosion parameters of the samples

| Sample | Corrosion rate ($x10^{-3}$) | $I_{corr}$ ($\mu A/cm^2$) | $E_{corr}$, V (Ag/Ag Cl) |
|---|---|---|---|
| Bare room temp (uncoated) | 701.3 | 70.2 | -0.560 |
| Coated room temp. | 146.0 | 11.5 | -0.550 |
| Coated 50C | 198.8 | 16.9 | -0.390 |
| Coated 100C | 261.0 | 22.2 | -0.416 |
| Coated 150C | 279.7 | 23.8 | -0.455 |
| Coated 200C | 697.9 | 67.0 | -0.540 |

Significant differences in corrosion rate and corrosion current ($I_{corr}$) values were observed for bare at room temperature as well as coated samples treated at 200°C. The most noble is -0.390 V for coated heat treated at 50°C. As expected, uncoated bare metal displayed a more electronegative OCP value of -0.64 V, indicating lower corrosion resistance compared to the coated samples. Fig. 2 shows the OCP curves of the

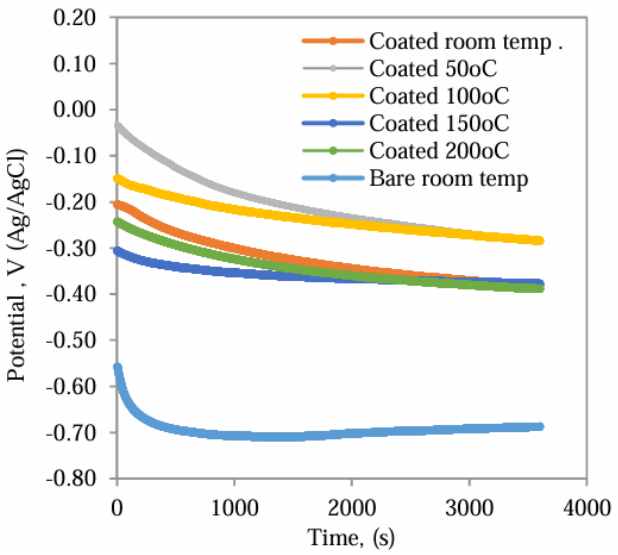



Figure 2: Open circuit potential curves of the coated samples and bare metal in 3.5wt% NaCl solution

coated heat-treated, coated and bare metal (uncoated) at room temperature samples. In general, all samples displayed unstable OPC values for the first 1000 s and achieved relatively stable potentials after 3600 s.

Table 2 shows the final OCP values of the samples after 3600 s immersion in 3.5 wt% NaCl solution. The results displayed a similar trend with the Tafel extrapolation where the uncoated sample recorded the most negative OCP value of -0.64 V, indicating the sample was naturally in an active state with no significant formation of a stable passive layer. The most noble OCP values of -0.29 V and -0.28 V were recorded for the coated samples heat-treated at 50°C and 100°C respectively, while coated at room temperature and coated heat-treated at 150°C and 200°C displayed slight negative OCP values of 0.38V and -0.39 V respectively. The trend shows that decrease in OCP values after 100°C.

Table 2: Open circuit potential (OCP) in 3.5% NaCl

| **Sample** | **OCP at 3600 s (V vs. Ag/AgCl)** |
|---|---|
| Bare room temp (uncoated) | -0.68 |
| Coated room temp. | -0.38 |
| Coated 50°C | -0.29 |
| Coated 100°C | -0.28 |
| Coated 150°C | -0.38 |
| Coated 200°C | -0.39 |

The Tafel extrapolations and OCP results revealed that the elevated temperatures significantly affect the thermal behaviour of the NuRust-coated layer. It suggests that the NuRust-coated surfaces can withstand operating temperatures up to 100°C before undergoing thermal degradation towards higher temperatures as evidenced by the OCP results in Table 2. The low thermal stability of the NuRust can be associated with the evaporation of water and volatile compounds in the NuRust formulation at 100°C. Therefore, at temperatures higher than this, a significant OCP drop was expected due to the breaking of the protection layer resulting from these occurrences. Evaporation of moisture and solvents at approximately 100°C was also reported by other researchers (Kumar et al., 2023). However, when the temperature increases to more than 100°C, the OCP starts to decrease to -0.35 V and -0.41 V at 150°C and 200°C respectively, indicating the adverse effect of higher temperature on the NuRust-coated samples. These OCP results display the influence of heat treatment and coating application on the corrosion property of carbon steel. Since coating enhances the corrosion protection of the samples, it is therefore expected to produce higher OCP values for the coated samples. Seemingly, results also showed that the heat treatment helped to increase higher OCP values for the coated samples, especially at 50°C and 100°C. When temperatures increase, thermal degradation of the coated film becomes observable, leading to the damage and degradation of the coated film, consequently, lowering its protection against corrosion attack. Hence, resulting in lower OCP values and corrosion parameters.

## 4 Conclusion and attention

concluded that the NuRust-coated surface is performing well at temperatures of 50°C to 100°C. Exceeded these temperatures will result in a decrease in corrosion resistance due to the thermal degradation of NuRust largely corresponds to its composition which contains water and volatile compounds. This has resulted in low thermal stability at higher temperatures. Therefore, when exposed to higher temperatures, the coating will thermally degrade, consequently contributing to the deterioration of corrosion resistance. Nevertheless, the NuRust-coated samples still displayed better corrosion behaviours; OCP, $E_{corr}$, corrosion rate and $I_{corr}$ as compared to the bare metal (uncoated), indicating better corrosion protection of NuRust.

## References

S. S. A. Kumar, N. B. Mohammed, O. Alduhaish, K. Ramesh, and M. Khan. 2023. Anticorrosion, thermal degradation, and hydrophobic performances of graphene/tio2 nanocomposite coating. *Polymers*, 15(11):2428.

Individual Research Contribution Review, 2024: 420–421
*ISSN: 3083-922X*

# Effect of Heating Temperature on Properties of Titanium Dioxide Nanoparticles

**Siti Salwa Zainal Abidin**
Industrial Technology Division, Malaysian Nuclear Agency
43000 Kajang, Selangor
sitisalwa_za@nm.gov.my

## Abstract

The effect from different heat treatment on structural properties of titanium dioxide nanoparticles, $TiO_2$ was studied. These materials were produced by using synthetic rutile with the hydrothermal method via the alkaline fusion process. The samples were characterized with X-ray diffraction (XRD).

**Keywords:** Heat treatment, XRD

## 1 Introduction

Titanium dioxide nanoparticles, $TiO_2$ is an n-type semiconductor material with particles size less than 100 nm. These materials also have thermal stability, low-cost materials, high photo reactive and sensitivity. Based on its special properties this material has attracted so many researchers and are widely used in many applications and various field in industries such as sensors, photocatalysts, electronic, medical, antimicrobial activity, self-cleaning, water purification, degradation of pollutant, dielectric properties, optical, solar cell and electrical properties. (Jule et al., 2021; L.Velardi et al., 2020; Haq et al., 2018) Titanium dioxide nanoparticles produced from the more common methods such as sol-gel method (widely used commercially), the hydrothermal, chemical precipitation and solvothermal methods. (E.M et al., 2013; Yusoff et al., 2014; rosli et al., 2018).

It has three main polymorphs like anatase, rutile and brookite (Jule et al., 2021; E.M et al., 2013). The crystalline structure of anatase and rutile are tetragonal and Brookite has orthorhombic crystal structure. The anatase is metastable with the suitable photocatalytic activity, and will convert to rutile phase at high temperature heating which is the most stable phase. verlardi et al. calcined $TiO_2$ nanoparticles at 100°C, 450°C and 800°C for 4 h and observed a transformation from anatase to rutile at 450°C to 800°C. Jule et al. (Jule et al., 2021) suggested that anatase to rutile phase transformation occurred at temperature greater than 800°C after annealing proses. This titanium dioxide nanoparticles also annealed at 120°C, 300°C, 600°C and 900°C by S. Haq et al. showed phase transformation at which the rutile phase dominated at 900°C. At this work, we use the sample of titanium dioxide nanoparticles, $TiO_2$ to study the effect of heat treatment with different temperature (from 0°C- uncalcined, 600°C, 800°C and 1000°C) on structural of the materials.

## 2 Experimental methods

The titania nano powder or titanium dioxide nanoparticles was produced from synthetic rutile which was derived from the mineral ilmenite ($FeTiO_3$). The hydrothermal method via alkaline fusion was used to prepare the samples by using synthetic rutile where the process includes with fusion, washing, filtration and leaching process. First, the synthetic rutile and Sodium Hydroxide, NaOH supplied by R&M Chemical with ratio (1:2) were mixed and calcined in a furnace at 550°C for 3 hours. Then the product was washed with distilled water and its precipitate collected after the fusion process. The precipitate was added with 2M Sulfuric Acid, $H_2SO_4$ at 80°C for 4 hours for leaching process. After leaching, the precipitate was dried in an oven at 80°C. Then the samples were grinded to produce a fine powder (E.M et al., 2013; Yusoff et al., 2014; rosli et al., 2018). In this study, these samples of ($TiO_2$) nano powder was prepared and calcined in the furnace at temperatures of 600°C, 800°C and 1000°C and with another sample set as the control (0°C- uncalcined). The crystalline phases composition of the samples was analyzed by X-ray Diffractometer (XRD, XPert Pro MPD, Cu K$\alpha$ irradiation, $\lambda$= 1.5405 Å).

## 3 Results and discussion

The titanium dioxide nanoparticles, $TiO_2$ were characterized by using X-ray diffraction analysis. Fig. 1 shows the XRD patterns of all the samples $TiO_2$ powders treated at different temperatures of 0°C (uncalcined), 600°C, 800°C and 1000°C. More crystalline phase of anatase in $TiO_2$ sample at 0 °C was detected, while in the other samples calcined at 600°C it is still in anatase phase (start to mixture of both anatase and rutile phases) was found. Samples of $TiO_2$ was calcined from temperature 800°C and 1000°C (each sample) were shown in rutile phases mostly. The diffraction peak with three sharp peaks at 25.34°, 38.42°and 47.92°which corresponding to (011), (004) and (020) (ICSD code: 98- 009-4632) for anatase and peaks at 27.44°, 36.06°, 41.22°, 44.03°, 54.30°and 56.61°and which corresponding to (110), (011), (111), (120), (121) and (220) (ICSD code: 98-009-4409) for rutile, respectively. Both anatase and rutile phase with tetragonal geometry. Transformation phase from anatase to rutile due to increase the temperature (D.K.Muthee and B.F.Dejene., 2021).

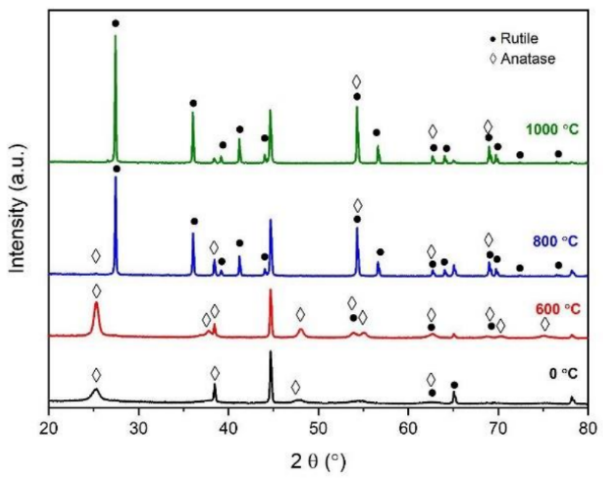



Figure 1: X-Ray diffraction pattern of $TiO_2$ nanoparticles at various temperatures.

## 4 Conclusion

In conclusion, this work has shown how the heating with different temperatures influences the crystalline phase composition of titanium dioxide, $TiO_2$ nanoparticles which produced by hydrothermal method via alkaline fusion. The synthesized $TiO_2$ nanoparticles were characterized by X-ray Diffraction (XRD. The heat treatment initially from unheated 0°C and heated 600°C were results in anatase phases, while sample heated from temperature 800°C and 1000°C were mostly dominant in rutile phases. All these results obtained from characterized of XRD analysis.

## References

D.K.Muthee and B.F.Dejene. 2021. Effect of annealing temperature on structural, optical, and photocatalytic properties of titanium dioxide nanoparticles. *Heliyon*, 7.

Mahdi E.M, M. Hamdi, M. S. M. Yusoff, and Wilfred P. 2013. Xrd and edxrf analysis of anatase nano-tio2 synthesized from mineral precursors. *Advanced Mat. Research.*, 620(179185).

S. Haq, W. Rehman, M. Waseem, R. Javed, M ur Rehman, and M. Shahid. 2018. Effect of heating on structural and opyical properties of tio2 nanoparticles: antibacterial activity. *App. Nanoscience*, 8:11–18.

L.T. Jule, K. Ramaswamy, B. Bekele, A. Saka, and N. Nagaprasad. 2021. Experimental investigation on the impacts of annealing temperatures on titanium dioxide nanoparticles structure, size and optical properties synthesized through sol-gel methods. *Mat. Today Procedd.*, 45:5752–5758.

L.Velardi, L. Scrimieri, A. Serra, D. Manno, and L. Calcagnile. 2020. Effect of temperature on physical, optical and photocatalytic properties of tio2 nanoparticles. *SN.Applied Sciences*, 2(707).

N. S. rosli, C. A. C. Abdullah, and R. Hazan. 2018. Synthesis, characterization and investigation of photocatalytic activity of nano-titania from natural ilmenite with graphite for cigarette smoke degradation. *Results in Physics*, 11:72–78.

M. S. M. Yusoff, E.M. Mahdi, P.Wilfred, and M. Masliana. 2014. Photocatalytic active nanorutile tio2: synthesis characterization and photocatalysis tests. *Journal of Nano Research.*, 26:17–23.

Individual Research Contribution Review, 2024: 422–423
*ISSN: 3083-922X*

# Development of data collection system from scaler ratemeter using open source software

**Soleha Binti Mohamat Yusuff**
Industrial Technology Division, Malaysian Nuclear Agency
43000 Kajang, Selangor
soleha@nm.gov.my

## Abstract

This study presented the development of a data collection system from a scale ratemeter using open-source software. The objective of this study is to reduce operational time using cost-effective software. The Python library packages and Visual Studio Code software were used in the development process. The developed system featured a graphical user interface (GUI) that provides meaningful data visualization and operates smoothly for three hours with a short data collection interval. In conclusion, this system represents a significant advancement in optimizing time management during gamma-ray measurements.

**Keywords:** data collection, gamma-ray, Python

## 1 Introduction

Gamma rays play a vital role in medicine, industry, agriculture, scientific research, and security due to their high energies (above 100 keV) and short wavelengths (less than 10 pm), allowing them to interact quickly with material electrons. Beigzadeh et al. (Beigzadeh et al., 2019) developed a nuclear densitometer using the gamma transmission method with a NaI(Tl) scintillation detector and Cs-137 source to measure the density of various wood types, achieving accurate and non-destructive results compared to traditional methods. Aung and Tun ((Aung and Tun, 2019) used a similar approach to analyze gamma radiation shielding properties of seven wood species from Myanmar.

Advancements in nuclear applications also rely on software development for efficient instrumentation. Python has emerged as a popular programming language for this purpose due to its open-source nature, simple syntax, and extensive libraries.

This paper aims to create a data collection system for a gamma radiation instrument. The system utilizes the NaI(Tl) scintillation detector to measure gamma-ray signals. The development was carried out using Python and Visual Studio Code softwares.

## 2 Methods

A data collection system for measuring gamma rays was developed using a Ludlum Model 2200 scaler ratemeter, a computer with Windows 10, a detector (thallium doped sodium iodide (NaI(TI)) scintillation crystal optically coupled to a 38 mm diameter photomultiplier tube (PMT)), an alternating current (AC) power cable, and an RS-232 to USB cable. The scaler ratemeter connects to the computer via a 9-pin RS-232 port and allows adjustments for high voltage and other settings. It can operate on AC power or batteries and supports various detectors. The study used a computer with an Intel Celeron CPU, 20 GB RAM, and a 64-bit operating system.

The system performs three main functions: data acquisition, calculating intensity and density, and generating graphs. Figure 1 shows the flow process in the development of the coding of the data collection system.

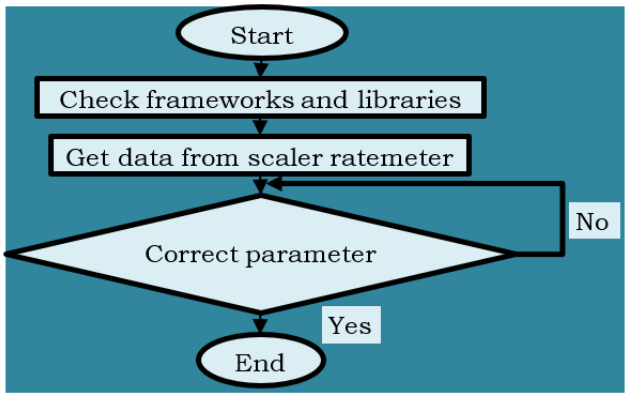



Figure 1: Process in development of data collection system.

The system was built using Python in Visual Studio Code, utilizing libraries such as Datetime, Serial, Threading, Numpy, Pandas, Tkinter, and Matplotlib for data manipulation and visualization. To communicate with the scaler, RS-232 parameters like Baud Rate, Data Bits, Parity, and Stop Bit must be set. Commands ”SS” and ”RS” are used for data requests. The code includes formulas while taking inputs like the operator’s name, sample’s name, sample thickness, attenuation parameter, and count time. The Tkinter-based GUI facilitates navigation and configuration, with options for RS-232 settings, operator info, sample input, data logging, and graph visualization.

## 3 Results and Discussion

The user interface named ’Ludlum 2200 Scaler Ratemeter’ was created using Python and Visual Studio Code (see Figure 2). It contains a menu bar, a settings panel, a data entry section, and a visual data display.

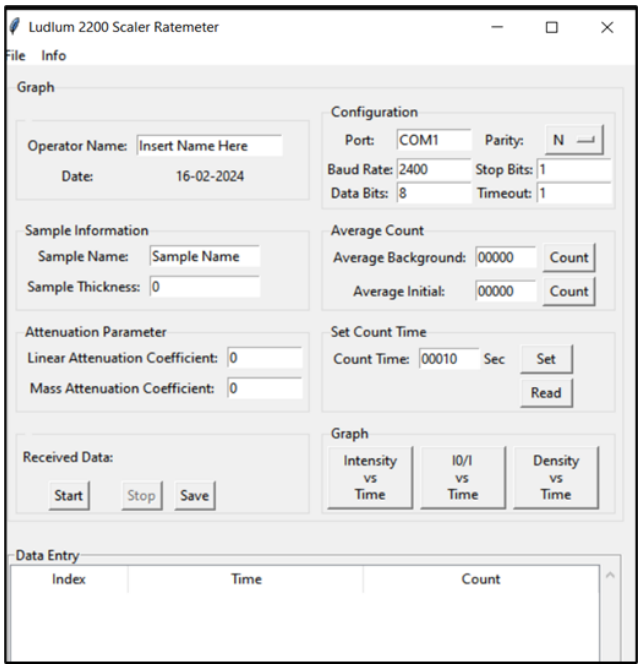



Figure 2: The developed graphical user interface of 'Ludlum 2200 Scaler Ratemeter'.

After setting up the hardware, users can open the GUI to configure it by entering the port, parity, baud rate, stop bit, data bit, and timeout values. They can create a new project by entering the operator name, sample name, sample thickness, and counting time. The interface displays the current date and time and allows users to start, stop, and save count data in a Microsoft Excel table. Users can also enter linear or mass attenuation coefficients, calculate background averages and initial counts, and view real-time count data along with graphs of Intensity vs. time, Io/I vs. time, and Density vs. time.

Key functions are divided into smaller parts for easier execution. The system combines user interface design and graphing functionality. This separation improves code readability. The main Python packages used are Tkinter, Pandas, and Matplotlib. The data collection system met the user's requirements and operated continuously for 3 hours without error.

## 4 Conclusions

This study developed a system to collect gamma-ray measurement data using Python and Visual Studio Code. This open-source software enables cost-effective development and improves safety when handling radioactive sources. We recommend integrating the system with cloud computing for mobile support and remote operation.

## References

Y. Y. Aung and K.T. Tun. 2019. Investigation of gamma radiation shielding characteristics for various wood slabs by using gamma attenuation method. *International Research Journal of Advanced Engineering and Science.*, 4(3):99.

A. M. Beigzadeh, M. R. R. Vaziri, Z. Soltani, and H. Afarideh. 2019. Design and improvement of a simple and easy-to-use gamma-ray densitometer for application in wood industry. *Measurement*, 138(157).

Individual Research Contribution Review, 2024: 424–425
*ISSN: 3083-922X*

# Preliminary Study on the Properties of Diverse Tropical Woods

**Suhaila Hani Ilias**
Industrial Technology Division, Malaysian Nuclear Agency
43000 Kajang, Selangor
suhaila_hani@nm.gov.my

## Abstract

Malaysia tropical wood stands out as the most crucial natural organic material in human history, being among the first materials utilized by humans. It has been used to create crucial items such as shelters, tools, furniture, weapons, boats, coaches, and religious or symbolic works of art. This makes it exceptionally significant for cultural heritage conservation in Malaysia. A preliminary study of Malaysian tropical wood includes a variety of species such as Balau, Resak, Pine, Getah, Keruing, Kelampaian, Merbau, Meranti Merah, Meranti Putih, and Cengal. Tropical wood is a complex composite of biopolymers, with cellulose being the most vital component, making up 40–50% by weight. Cellulose, a linear polymer of glucose, can form ordered assemblies at the nanoscale, such as crystallites, fibrils, and fibers. This high degree of organization, along with its hydrophilic nature, makes cellulose the primary constituent of wood's cellular structure. Lignin, another significant macromolecule, is present in wood at concentrations of 25–30% and contributes to the wood's strength and rigidity (Cortella et al., 2011). Fourier Transform Infrared Spectroscopy (FTIR) is an analytical technique used to identify organic, polymeric, and, in some cases, inorganic materials. By analyzing tropical woods using FTIR, we can gain a comprehensive understanding of their properties and behaviors. FTIR provides valuable information about the chemical composition, structure, and properties of the wood. These absorption bands offer insights into the wood's chemical structure. The microscopic morphologies of cellulose in tropical woods were characterized using Field Emission Scanning Electron Microscopy (FESEM).

**Keywords:** Tropical Wood, Fourier Transform Infrared Spectroscopy (FTIR)

## 1 Introduction

Wood stands out as the most crucial natural organic material in human history, being among the first materials utilized by humans. Throughout history, it has served as the primary material for crafting vital objects such as shelters, tools, furniture, weapons, boats, coaches, and religious or symbolic works of art. Consequently, it holds exceptional significance for cultural heritage conservation. Tropical woods produced by the vascular cambium. Variations in the chemical composition, structure, morphology, and properties of the wood are induced by the habitat of trees and affect the end utility properties.

Wood constitutes a complex composite cellulose as its most vital component, comprising 40–50% by weight. Cellulose, a linear polymer of glucose, possesses the ability to form ordered assemblies at the nanoscale, including crystallites, fibrils, and fibers. This high degree of organization, coupled with its hydrophilic nature, qualifies cellulose as the primary constituent of wood's cellular structure. Lignin, another macromolecule, is present in wood at a concentration of 25–30%. It serves various functions within the wood structure, contributing to its strength andrigidity. Understanding the functional groups present in tropical woods can enhance research into their behavior, including aspects such as cellulose composition and structural properties.

## 2 Methods

In this study, analyzing tropical woods using Fourier Transform Infrared Spectroscopy (FTIR), we can gain a comprehensive understanding of their properties and behaviors. FTIR provides valuable information about the chemical composition, structure, and properties of the wood. These absorption bands offer insights into the wood's chemical structure. The microscopic morphologies of cellulose in tropical woods were characterized using Field Emission Scanning Electron Microscopy (FESEM).

## 3 Results

The FTIR spectra were measured using direct transmittance using Cary FTIR Diamond ATR. The identified functional groups are listed in the table below.

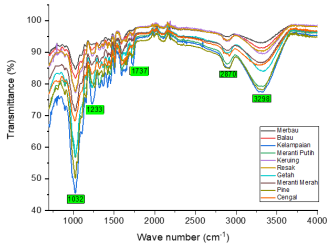



Figure 1: FTIR Spectra of tropical woods.

Table 1: Functional groups and its quantified frequencies. Data was adopted from reference (Coates, 2011)

| Exp. | Literature | Functional Group | Band Assignment | Possible Nutrient Type | Tropical woods |
|---|---|---|---|---|---|
| 1032 | 1045-1053 | Methylene | C-O component | Carbohydrate | A,B,C, D,E,F, G,H,I,J |
| 1233 | 1230-1238 | Ether and oxy compound | C-H component | Protein (Amide III) | A,B,D, E,F, G,H,I,J |
| 1737 | 1740-1720 | Carbonyl compound | C=O stretching | Lipids | A,B,C, D,E,F, G,H,I,J |
| 2870 | 2853-2860 | Ether and oxy compound | CH2 Lipids | Amine Salt | A,B,D, E,F, G,H,I,J |
| 3298 | 3273-3293 | Common inorganic ions | $O_H symmetric$ | Water | A,B,D, E,F, G,H,I,J |

The surface morphology of tropical woods was characterized by using FESEM.

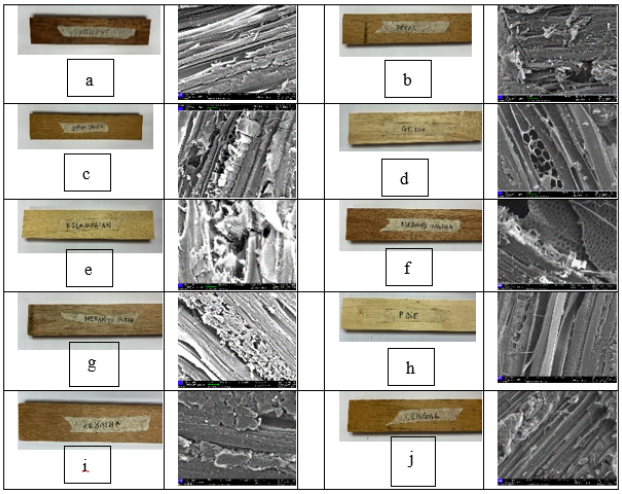



Figure 2: FESEM micrographs of tropical woods of (a) Merbau, (b) Balau, (c) Kelampaian, (d) Meranti Putih, (e) Keruing, (f) Resak, (g) Getah, (h) Meranti Merah, (i) Pine and (j) Cengal

Table 2: EDS analysis of the tropical woods

| Tropical Woods | % Carbon | % Oxygen |
|---|---|---|
| Merbau | 56.2 | 4.69 |
| Balau | 54.1 | 39.6 |
| Kelampaian | 55.5 | 36.5 |
| Meranti Putih | 51.5 | 40.6 |
| Keruing | 59.6 | 31.6 |
| Resak | 55.6 | 36.2 |
| Getah | 54.3 | 38.2 |
| Meranti Merah | 52.6 | 40.4 |
| Pine | 51.4 | 41.2 |
| Cengal | 54.1 | 38.1 |

Table 2 shows the summarized data of EDS analysis of the tropical woods in terms of carbon content (atomic %) and oxygen content (in atomic %).

## 4 Conclusion

Generally, O-H stretching absorption bands (around 3306 $cm^{-1}$) and C-H absorption bands (around 2896 $cm^{-1}$) are observed in all types of tropical wood.

## References

J. Coates. 2011. Interpretation of infrared spectra, a practical approach. *Encyclopedia of analytical chemistry*, 12:10815–10837.

Laurent Cortella, Quoc Khoi Tran, Wojciech Gluszewski, Ion Valentin Moise, and Corneliu Catalin Ponta. 2011. *Nuclear Techniques for Preservation of Cultural Heritage Artifacts.*, 16(2).

Individual Research Contribution Review, 2024: 426–427
*ISSN: 3083-922X*

IRCR

# Ultrasonic Signals Fusion Datasets for Enhanced Weld Defect Classification Using Convolutional Neural Networks Models

**Suhairy bin Sani**
Industrial Technology Division, Malaysian Nuclear Agency
43000 Kajang, Selangor
suhairy@nm.gov.my

## Abstract

This study explores the application of convolutional neural networks (CNN) for ultrasonic signal weld defect classification using fusion datasets. The research focuses on evaluating the performance of different CNN architectures, specifically VGG19, VGG16, and ResNet50, in classifying weld defects from image datasets. The fusion datasets, namely iCont, iOl, and iA, are derived from ultrasonic signals and are used to enhance the accuracy and reliability of defect classification. The VGG19 model, when combined with the iCont dataset, demonstrates superior performance with an accuracy of 99.81%, showcasing its effectiveness in identifying various defect types. This paper provides insights into the potential of CNN models in improving weld defect classification through data fusion techniques.

**Keywords:** Fusion Datasets; Weld Defect Classification; Convolutional Neural Networks (CNN); Transfer Learning.

## 1 Introduction

Ultrasonic testing (UT) is a widely adopted non-destructive testing (NDT) technique for detecting and characterizing weld defects due to its ability to provide valuable information on weld joints. However, the precise classification of weld defects remains a complex task due to the subtle differences in data patterns for different defect types. Convolutional neural networks (CNN) have been extensively studied for their effectiveness in pattern recognition and classification tasks, including weld defect classification.

This study aims to address the effectiveness of fusion datasets extracted from ultrasonic signals of different types of weld defects; i.e., 1) center crack (CCr); 2) slag inclusion (SI); 3) lack of fusion (LOF); 4) cluster porosity (Po); 5) lack of penetration (LOP); and 6) normal conditions (N - no defects) in improving the accuracy and reliability of CNN models for weld defect classification. The research focuses on evaluating the performance of CNN models, specifically VGG19, VGG16, and ResNet50 by using fusion datasets to enhance defect classification accuracy (Figure 1). VGG16 and VGG19 are part of the VGG family, known for their simplicity and depth, with VGG16 having 16 layers and VGG19 having 19 layers. These models use pre-trained weights from the ImageNet dataset to extract features from images, which enhances their ability to classify complex patterns. ResNet50, on the other hand, is part of the ResNet family and consists of 50 layers, utilizing residual learning to address the vanishing gradient problem in deep networks.

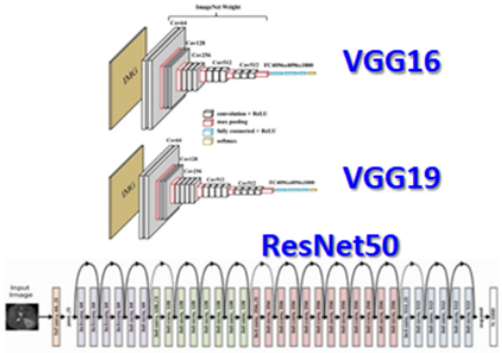



Figure 1: CNN models (VGG19, VGG16 and ResNet50)

## 2 Methods

The study employs three categories of image datasets (Figure 2) for CNN: iA, iOl, and iCont. The iA dataset consists of images from side A only, while the iOl dataset is fused in overlap from side A and side B. The iCont dataset is fused continuously from side A and side B, providing a comprehensive view of the weld. The CNN models, VGG16, VGG19, and ResNet50, are utilized to extract features from 128x128-pixel images with three color channels. The models are evaluated based on transfer learning (accuracy and loss), confusion matrix and classification report (precision, recall and F1-score) to determine their effectiveness in classifying weld defects (Figure 3).

## 3 Results and Discussion

The performance of three CNN models (VGG19, VGG16, and ResNet50) on test datasets iA, iOl, and iCont are shown in Figure 4. The iCont dataset achieved the best results, with the highest accuracy (97.2–99.8%) and lowest loss (1.7–8.8%), followed by the iOl dataset with slightly lower accuracy (93.0–97.8%) and higher loss (6.6–21.0%). The iA dataset performed the worst, showing lower accuracy (86.3–89.6%) and significantly higher loss (27.6–47.2%). Among the models, VGG19 consistently outperformed VGG16 and ResNet50, particularly on the iCont dataset, where it achieved the highest accuracy (99.81%) and lowest loss (1.71%). The superior performance of VGG19 is attributed to its deeper architecture,

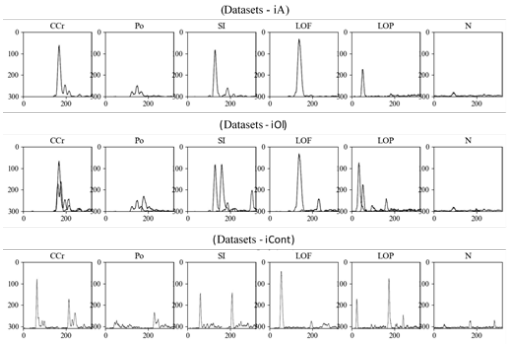



Figure 2: CNN datasets (iA, iOl, and iCont).

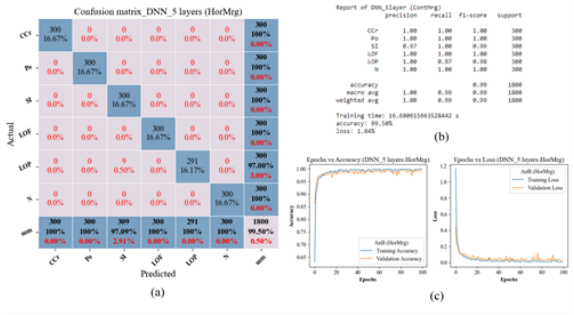



Figure 3: (a) Confusion matrix, (b) classification report and (c) transfer learning plot.

which enhances its ability to capture complex patterns, reducing underfitting while managing overfitting through regularization. Overall, VGG19 with the iCont dataset demonstrated the best classification performance.

The transfer learning performance of the VGG19 model over 100 epochs on the test datasets iCont, iOl, and iA is depicted in Figure 5. The iCont dataset displayed the most stable performance, with training and validation accuracy exceeding 99% within the first 5 epochs and remaining consistent thereafter. Its loss curve also dropped sharply to approximately 0.1% early on and stabilized. In contrast, the iA dataset exhibited significant fluctuations, concluding with lower training accuracy (around 88%) and clear signs of overfitting. The iOl dataset performed better than iA, achieving about 97% validation accuracy with slight overfitting. Overall, the iCont

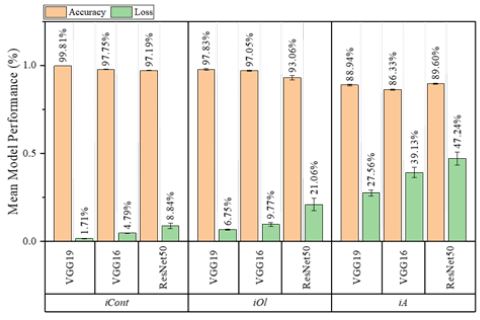



Figure 4: CNN model performance of accuracy and loss results for different pre-trained models and datasets.

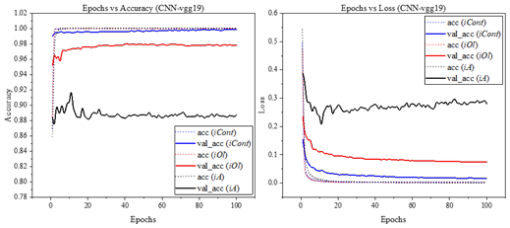



Figure 5: CNN transfer learning for the VGG19 model with different datasets.

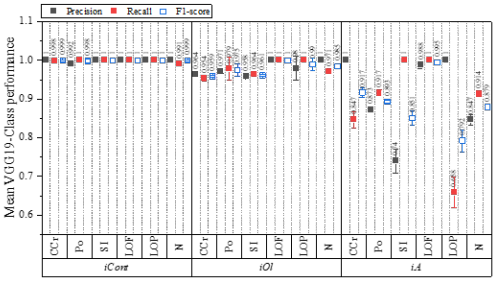



Figure 6: CNN class performance of VGG19 pre-trained model with different datasets.

dataset demonstrated the fastest learning rate and the most reliable performance for the VGG19 model.

The class performance of the VGG19 model on the three datasets (iCont, iOl, and iA), evaluated using precision, recall, and F1-score, highlights distinct trends. The iCont dataset demonstrated consistently high metrics (approximately 1.0) across all classes, reflecting excellent classification accuracy. The iOl dataset also showed strong performance, with metrics exceeding 0.95 for most defect types, although slightly lower scores were observed for CCr, Po, and SI compared to LOF and LOP. In contrast, the iA dataset exhibited more variability, achieving perfect recall (1.0) for SI and LOF but struggling with CCr (recall: 0.847) and LOP (recall: 0.658). Overall, the iCont dataset delivered the most reliable results, followed by iOl and iA with some performance differences.

## 4 Conclusion

The fusion datasets generated from ultrasonic signals hold considerable promise as a practical alternative for defect classification with CNN models. The VGG19 model, when combined with the iCont dataset, consistently outperforms the VGG16 and ResNet50 models in terms of accuracy and loss metrics, showcasing its effectiveness in identifying various defect types. The study demonstrates the potential of CNN models in improving weld defect classification through data fusion techniques, providing valuable insights for future research and development in this field.

## References

et al. Suhairy Sani. 2024. Fusion datasets for ultrasonic weld defect classification with transfer learning in neural networks. *Defence ST Technical Bulletin*, 17(1):1–12.

Individual Research Contribution Review, 2024: 428–429
*ISSN: 3083-922X*

# Ensuring Safety in Industrial Inspection: A Focus on Gamma Ray Tomography

**Susan Maria Sipaun**
Industrial Technology Division, Malaysian Nuclear Agency
43000 Kajang, Selangor
susan@nm.gov.my

## 1 Introduction

Gamma-ray computed tomography (CT) is a non-destructive inspection technique that utilises gamma radiation to generate detailed cross-sectional images of an object's internal structure. Unlike conventional X-ray CT, gamma-ray CT employs radioactive isotopes like Cobalt-60, Caesium-137 or Barium-133 as radiation sources. These isotopes emit high-energy gamma rays that can penetrate dense materials, making them ideal for inspecting thick or dense components.

Additionally, gamma ray sources are encapsulated and not reliant on external power sources, making gamma-ray CT systems portable and suitable for on-site inspections. However, the use of radioactive materials necessitates stringent safety protocols to mitigate potential radiation risks, especially when operating outside of controlled laboratory environments. This work investigates the safe implementation of gamma-ray tomography for on-site and field inspections, emphasising adherence to established safety guidelines.

## 2 Methods

Two radiation survey meters were utilised: a multipurpose meter (RDS-110) and a general-purpose meter (Ludlum Model 3) paired with a pancake detector (Ludlum Model 44-9). Dose rates, measured in units of Sieverts per hour (Sv/h) or Roentgens per hour (R/h), were recorded at each meter. Two encapsulated radioactive materials, 1480MBq (40mCi) Cs-137 and 370MBq (10mCi) Ba-133 were placed in tungsten and lead source holders respectively. The tungsten holder has 5mm opening and the lead holder has 5mm x 15mm opening. Gamma rays escape from the openings and are directed towards the object of investigation during CT scanning as well as the survey meter during dose mapping. A background radiation measurement was obtained and recorded as a reference. Additionally, an optically stimulated luminescence (OSL) badge was worn to monitor occupational dose. Theoretical dose rate values were calculated using following formula; $\dot{D}$=Γ.A/ ($r^2$) where $\dot{D}$= dose rate, A = current activity, Γ= specific gamma constant and r = distance. The specific gamma constant, $\wp$, allows the calculation of exposure rate for a point source of a gamma-emitting radionuclide for a given activity at a specified distance from the source. Typically, $\wp$ is measured in R/hr at one meter from a 1 Ci source. It is expressed in units such as roentgens per hour per curie (R/h/Ci) at one meter or Sieverts per hour per Becquerel (Sv/h/Bq). This constant is used to calculate the radiation dose rate in various applications such as determining safe distances and shielding requirements around gamma emitting sources.

## 3 Results

### 3.1 Dose Mapping

Dose mapping ensures the portable gamma CT system operates safely by identifying high-radiation areas, assessing shielding, and defining safe zones. Table 1 shows the estimated and experimental dose rates values for both Cs-137 and Ba-133 sources.

Table 1: Dose rate values for Cs-137 and Ba-133 at several distances.

| Distance (meter) | Cs-137 Dose Rate (ΓSv/h) | | Error (%) | Ba-133 Dose Rate (ΓSv/h) | | Error (%) |
|---|---|---|---|---|---|---|
| | Theory | Exp | | Theory | Exp | |
| 1.0 | 152.7 | 126.0 | 17.5 | 45.6 | 16.1 | 64.7 |
| 2.0 | 38.2 | 35.5 | 7.0 | 11.4 | 5.6 | 50.6 |
| 5.0 | 6.1 | 6.7 | 8.8 | 1.8 | 0.9 | 49.5 |
| 10.0 | 1.5 | 1.6 | 5.9 | 0.5 | 0.3 | 36.1 |

Comparing theory and actual dose rate values, it is found that results for Cs-137 is closer to the theoretical estimation whereas for Ba-133 it is showing a huge difference. This difference is attributed to 370MBq Ba-133 being less penetrative compared to 1480MBq Cs-137 and is mostly attenuated by the lead source holder hence the much lower experimental dose rate values. The maximum difference between theory and actual is at 1.0 meter, i.e. 17.5% for Cs-137 and 64.7% for Ba-133. However, as the distance increases, the actual dose values tend to become closer to the calculated values (Figure 1). At the 10-meter radius, the radiation absorbed dose rates are 14.0 and 2.6 millisievert per year for Cs-137 and Ba-133 respectively (Table 1). These values are considered still within the acceptable limit for radiation workers.

Figure 2 shows the calculated distance radius for control (<7m), supervised (7m<area<17.5m) and clean (>17.5m) areas when using the Cs-137. For Ba-133, control area is within the 3.9-meter radius, supervised area is between 3.9- and 9.5-meter radius, and clean area is 9.5 meters and beyond. Ba-133 requires less stringent safety measures than Cs-137 due to its lower energy and activity levels. This results in smaller radiation footprints, necessitating less shielding and shorter safety distances. Consequently, Ba-133 offers a safer alternative for industrial applications.

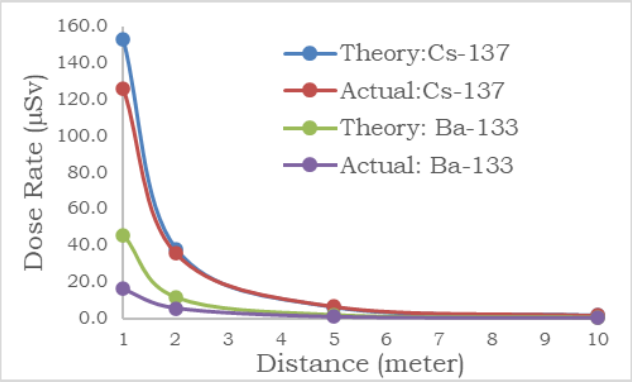



Figure 1: Estimation of dose rate values at several distances.

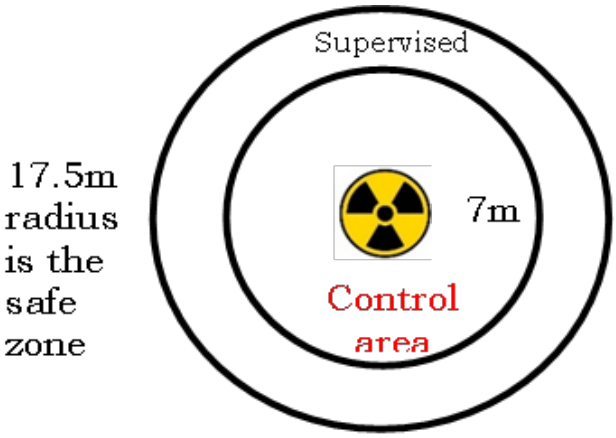



Figure 2: Defining Cs-137 work area and safe zones by calculation; assuming annual dose limit for radiation worker is 20mSv/year and public dose limit at 1mSv/year. Number of working hours per year is 2080 hours.

### 3.2 CT Scanning Parameters

The CT scanning parameters, time and source type, were investigated using a phantom that consists of an insulated 6-inch OD steel pipe with 8mm thickness, a 52mm granite filler and a 6mm steel wire. It is found that Ba-133 offers greater image-to-object fidelity in terms of shape and material discrimination compared to Cs-137, particularly for detailed inspections of insulated pipes. However, achieving this level of detail with Ba-133 requires longer scan times and produces a relatively noisier image. While both isotopes can produce cross-sectional images, Ba-133 excels in providing relatively faster scan and at a lower exposure risk.

## 4 Conclusions

Tomographic imaging allows non-invasive examination of material distribution, internal shapes and object structure. Effective shielding, minimising exposure time and maintaining safe distances are crucial for radiation safety in industrial CT. These measures help minimise operator exposure and ensure safe operations.

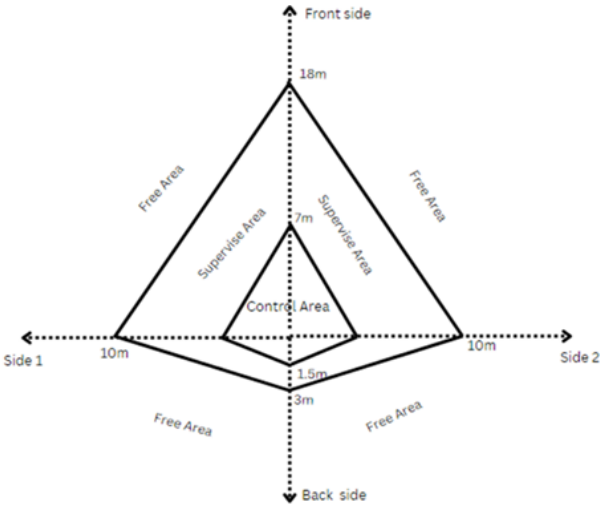



Figure 3: Safe zone is established by dose mapping the Cs-137 CT scanner work area. Source holders are fabricated from lead and tungsten shielding materials thus help reduce the radiation exposure to workers. CT operators located 3 meters facing away from the source opening and behind the CT computer are in the safe zone.

## References

ASTM E1441. Standard guide for computed tomography.

IAEA. 2011. Radiation safety in industrial radiography. *IAEA Safety Standards Series No. SSG-11*.

Individual Research Contribution Review, 2024: 430–431
*ISSN: 3083-922X*

# Comparative Analysis of Yxlon Imaging Systems with Different Focal to Film Distance (FFD): 700mm vs 1010mm

**Tengku Sarah Tengku Amran**
Industrial Technology Division, Malaysian Nuclear Agency
43000 Kajang, Selangor
sarah@nm.gov.my

## Abstract

This study examines the effects of different Focal to Film Distances (FFD) on radiographic image quality in non-destructive testing of welded samples. Specifically, it compares FFDs of 700mm and 1010mm to determine which distance provides better image clarity and defect detection capability. Radiographs were taken at both distances and analysed for sharpness, contrast, density, and the ability to reveal defects such as porosity and cracks. Contrary to the conventional preference for longer FFDs, the results show that the 700mm FFD yielded better overall image quality. Images taken at 700mm displayed higher contrast, clearer definition of defects, and achieved the optimal film density required for accurate defect detection. In contrast, the 1010mm FFD did not meet the necessary film density standards, resulting in lower-quality images that may obscure defects. These findings suggest that optimal FFDs enhance the detection and analysis of imperfections in welded structures, supporting the use of appropriate FFD for more accurate and reliable radiographic inspections in industrial applications.

**Keywords:** Radiographic image, Focal to Film Distances

## 1 Introduction

Radiographic testing (RT) is a vital non-destructive technique (NDT) employed to examine materials' internal structure and integrity, especially welded components (Cartz, 1996). The quality of the radiographic image is highly dependent on the Focal Film Distance (FFD), a key parameter that influences sharpness, contrast, and magnification. Traditionally, longer FFDs are believed to provide better image sharpness and less geometric distortion. However, this experiment challenges that assumption by comparing radiographic image quality and defect detection efficiency at two FFDs: 700mm and 1010mm. This study aims to demonstrate that an optimal FFD of 700mm can produce superior image quality, offering enhanced visibility of defects and improved diagnostic accuracy in welded samples. Additionally, it was found that the optimal film density required for accurate defect identification was only achieved at the 700mm FFD and not at 1010mm. This is caused by the voltage selection based on the exposure chart that refers to the 700 FFD. This observation highlights the importance of selecting the appropriate FFD to ensure high-quality radiographic images that meet the necessary standards for defect detection.

## 2 Methods

In the field of non-destructive testing, radiographic testing is a crucial technique used to examine the internal structure of welded samples without causing any damage. Proper preparation of these samples is essential to ensure accurate and reliable test results. The process begins by selecting welded samples that meet the specified thickness requirements, which in this case are 14 mm and 15 mm. It is vital to confirm that each sample conforms to these exact thickness specifications to maintain consistency and accuracy in testing. Once the correct thickness is verified, each sample must be identified using lead letters to mark it with a unique identifier as shown in Figure 1. This identification process, known as radiographic identification, is crucial for ensuring traceability and correct identification throughout the imaging and evaluation stages.

Following identification, an Image Quality Indicator (IQI) must be placed according to the standards specified for each thickness. The IQI, which varies based on the thickness of the sample, is strategically positioned on or above the welded structure to serve as a reference point for evaluating image quality. Made typically from the same material as the sample, the IQI helps in assessing the resolution and contrast of the radiographic images through its holes, thereby enabling a reliable evaluation of the internal features and potential defects in the welded samples. Then shim is kept below IQI to match the density of the IQI and the weld structure. This meticulous preparation process ensures that the imaging system and parameters used are capable of detecting specific sizes and types of flaws, thus guaranteeing the integrity and reliability of the radiographic testing results.

## 3 Results and Discussion

### 3.1 Density

Table 1 presents data on radiographic density measurements for welded sample Plate – A with thickness of 14 mm using a focal to film distance (FFD) of 1010 mm. This FFD was evaluated to determine if it could achieve adequate film density for clear and accurate radiographic images. The samples, identified as Plate A-3 and Plate A-4, were subjected to exposure conditions with a voltage of 180 kV and a current of 4.4 mA for 27 seconds.

The density values for the samples were measured at three points each as shown in Table 1. Plate A-3 showed densi-

Table 1: Density for FFD 1010 mm

| Sample | Voltage (kV) | Current (mA) | Time (sec) | Density | | | Thickness (mm) | Conclusion |
|---|---|---|---|---|---|---|---|---|
| Plate A - 3 | 180 | 4.4 | 27 | 1.21 | 1.41 | 1.41 | 14 | Film rejected |
| Plate A - 4 | | | | 1.31 | 1.38 | 1.41 | | Film rejected |

ties of 1.21, 1.41, and 1.41, while Plate A-4 had densities of 1.31, 1.38, and 1.41. These values are significantly below the acceptable range of 1.8 to 4.0 for radiographic evaluation, indicating that the film density achieved is insufficient. Low-density films result in poor image quality, making it challenging to detect such defects accurately. The samples had a thickness of 14 mm, which affects X-ray absorption and the resulting film density. Despite the consistent exposure conditions, the films were rejected due to their low density.

Next the experiment for FFD 700 mm was initiated. Table 2 presents data on radiographic density measurements for welded samples using a focal to film distance (FFD) of 700 mm. This FFD was selected to achieve higher film density, which is crucial for clear and accurate radiographic images. The sample, identified as Plate A-7, Plate A-8 was subjected to specific exposure conditions, all at a voltage of 180 kV. The current was kept constant at 4.4 mA, while the exposure times ranged from 27 seconds.

Table 2: Density for FFD 700 mm

| Sample | Voltage (kV) | Current (mA) | Time (sec) | Density | | | Thickness (mm) | Conclusion |
|---|---|---|---|---|---|---|---|---|
| Plate A - 7 | 180 | 4.4 | 27 | 2.10 | 2.21 | 2.28 | 14 | Film accepted |
| Plate A - 8 | | | | 2.05 | 2.14 | 2.14 | | Film accepted |

According to Table 2, Plate A-7 showed densities of 2.10, 2.21, and 2.28, while Plate A-8 had densities of 2.05, 2.14, and 2.14. These density values indicate that the film density achieved falls within the acceptable range for radiographic evaluation for x-ray, which is typically between 1.8 and 4.0. This range ensures that any potential defects such as porosity or cracks can be accurately identified. All films were accepted, suggesting that the 700 mm FFD reliably produces quality radiographic images. The results support the hypothesis that an optimal FFD can achieve higher film density, which is essential for better image clarity and defect visibility.

This outcome suggests that an FFD of 1010 mm is less effective in achieving the necessary film density compared to 700 mm, which has been shown to produce higher density and better image clarity. The results highlight the importance of selecting an appropriate FFD to ensure high-quality radiographic images that meet the required standards for defect detection.

### 3.2 Film Quality

The film in Figure 1 shows the different image quality for the sample with the same thickness but with different FFD of 700 mm and 1010 mm respectively. Here we can see the contrast of the image of the film that is in the acceptable and unacceptable range density. Distance (FFD) of 700 mm appear darker and clearer, allowing for easier identification of details and defects. In contrast, films taken at FFD 1010 mm appear more plain and less distinct, making it more challenging to discern finer details and defects. These observations emphasize the critical role of FFD in radiographic testing, as

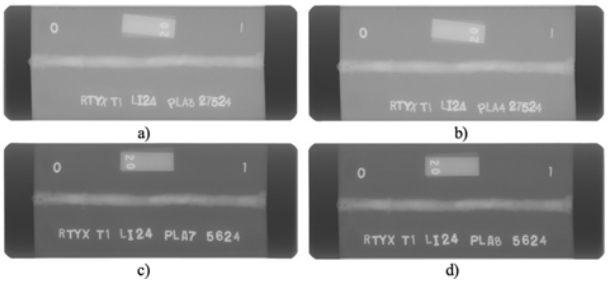



Figure 1: Film quality for, a) PLA - 3 and b) PLA - 4 for FFD 1010 mm and c) PLA - 7 and d) PLA - 8 for FFD 700 mm

it directly influences the visibility and resolution of inspection results. Adjusting FFD appropriately is essential for achieving optimal inspection outcomes and ensuring accurate defect detection.

## 4 Discussion

Based on the radargram, the images captured beneath the ground can be obtained directly using ground penetrating radar. This radargram shows a depth of approximately 2 meters. It also shows the distance of the data taking makes the user easier to identify the targeted area for marking and point reference. Therefore, based on data processing, it can be concluded that the application of GPR is a non-destructive, fast, and economical method for evaluating road structures. Through different data acquisition and processing techniques, results show that there is great success when using GPR for collecting information for verifying the state and condition of the materials. It breaks through the limitation of the insufficient number of cavity samples for 3D radar detection on the intelligent learning model training, reduces algorithm training costs, and improves identification accuracy.

## 5 Conclusion

In conclusion, optimizing the Focal-Film Distance (FFD) significantly impacts the clarity and resolution of Non-Destructive Testing (NDT) film results. Films captured at an FFD of 700 mm, specifically PLA - 7 and PLA - 8, demonstrated superior resolution with clearer visualization of the identification facilitating easier defect detection. Adherence to film density requirements further enhances reliability, ensuring consistent and precise radiographic testing evaluations. Conversely, films at FFD 1010 mm, like PLA - 3 and PLA - 4, which did not meet density standards, appeared less distinct and posed challenges in defect recognition. These findings underscore the critical role of both optimizing FFD and maintaining proper film density to achieve reliable defect detection and interpretation in radiographic industrial applications.

## References

Louis Cartz. 1996. Nondestructive testing: radiography, ultrasonics, liquid penetrant, magnetic particle, eddy current. *ASM International*.

Individual Research Contribution Review, 2024: 432–433
*ISSN: 3083-922X*

# Characterization of Cerium Phosphate from Malaysian Monazite

**Wilfred Paulus**
Industrial Technology Division, Malaysian Nuclear Agency
43000 Kajang, Selangor
wilfred@nm.gov.my

## Abstract

In this paper, cerium phosphate in Malaysian monazite mineral before and after grinding process has been

investigated. Energy-dispersive X- ray fluorescence (EDXRF) technique

was employed to determine chemical concentration of samples before and after the alkaline fusion process. Crystal structures and microanalysis of the sample were also determined using x-ray diffraction (XRD) and FESEM respectively. The results shows cerium phosphate structure crystal observed to be the major particles in the monazite samples. The introduction of grinding process has increased the XRD crystalline peaks in grounded samples.

**Keywords:** Monazite, cerium phosphate, grinding

## 1 Introduction

The Malaysian monazite is a rare earth phosphate mineral which contain significant amount of cerium (Ce) and other light rare earth elements (LREEs) such as lanthanum (La) and neodymium (Nd). These LREEs are valuable and have various industrial uses. In Malaysia, monazite is mainly found in 'amang', a by-product from tin mining processing (Hak, 2020). It also contains radioactive thorium and uranium (M.S., 2010).

## 2 Methods

Monazite used as the raw material in this study is originated from Perak, Malaysia. Figure 1 shows the typical grinding process of this raw material executed in this study. All samples before and after grinding were characterized using EDXRF, XRD, PSA and FESEM respectively.

## 3 Results & Discussion

Table 1: Chemical compositions in Malaysian Monazite.

| **Elements** | **Ce** | **La** | **Nd** | **Th** |
|---|---|---|---|---|
| **P** | | | | |
| **Concentration (wt.%)** | 29.11 | 6.70 | 8.74 | 6.85 |
| 6.33 | | | | |

Table 1 shows chemical composition in the Malaysian Monazite which was detrmined using EDXRF. The table shows Malaysian Monzite used in this study mainly contain of 29.11 wt.% of cerium (Ce). It also contain of other LREEs such as La and Nd.

Table 2: Median PSA particle size in samples.

| Grinding speed | Median particle size (µm) | | | | |
|---|---|---|---|---|---|
| | Control | 250 | 300 | 350 | 400 |
| (RPM) | 269.40 | 2.36 | 3.36 | 2.14 | 2.32 |

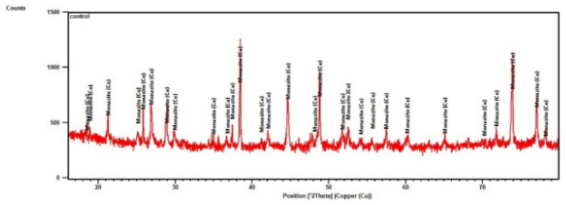


Figure 1: XRD pattern of Malaysian Monazite (control sample).

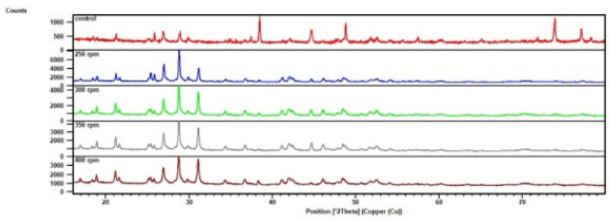


Figure 2: XRD pattern of Malaysian Monazite (control sample) after grounded at different speed (rpm).

Figure 1 and 2 shows XRD phase identification analysis of Malaysian monazite used in this study which has a dominant of a monoclinic cerium - Ce(PO4) crystal structure.

FESEM Figure 3 shows the microstructure of monazite samples before and after grinding at different speed (rpm).

## 4 Conclusion

Cerium phosphate is the dominant crystals structure in Malaysian Monazite mineral in terms of concentration, size and volume when compared to other impurity and REE elements.

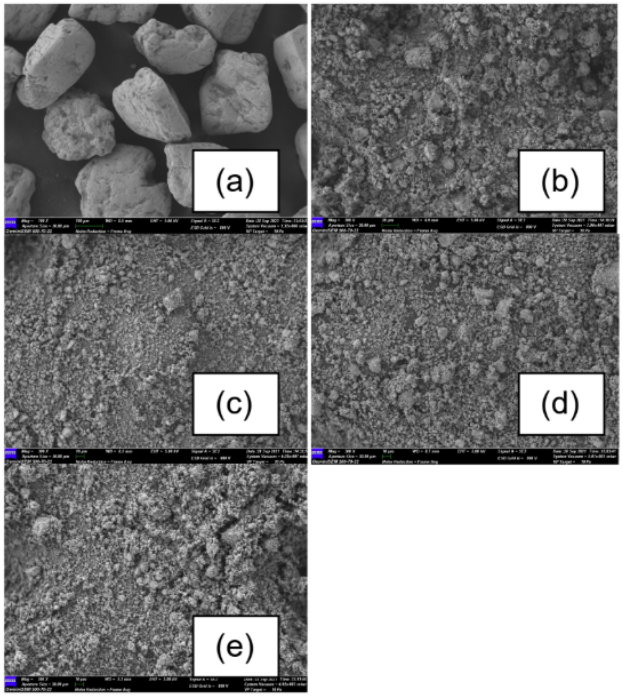



Figure 3: Monazite FESEM image after grounded at (a) control, (b) 250 rpm, (c) 300 rpm, (d) 350 rpm and (e) 400 rpm

## References

Che Rohaida Che Hak. 2020. Quantification of thorium and rare earth elemets in perak's ex-mining monazite. *Journal Sains Nuklear.*, 32(1).

Meor Yusof M.S. 2010. Recovery of uranium from malaysian non- conventional sources. *Journal of Nuclear and Related Technologies.*, 7(2).

Individual Research Contribution Review, 2024: 434–435
*ISSN: 3083-922X*

# Fabrication and Characterization of Aluminium Matrix Composite Reinforced with Micro Particle Boron Carbide using Stir Casting

**Zaifol Bin Samsu**
Industrial Technology Division, Malaysian Nuclear Agency
43000 Kajang, Selangor
zaifolsamsu@nm.gov.my

## Abstract

The development of aluminum matrix composites (AMCs) reinforced with boron carbide (B4C) micro-particles using the stir casting method has garnered considerable interest due to its ability to produce lightweight, high-strength materials for advanced engineering applications. This research focuses on the fabrication and analysis of AMCs incorporating varying weight percentages of B4C micro-particles. The stir casting technique was employed to achieve a uniform distribution of reinforcement particles within the aluminum matrix, enhancing the composite's mechanical and corrosion properties. Critical process parameters such as stirring speed, temperature, and stirring time were optimized to promote uniform microstructures and reduce defects. The fabricated composites underwent extensive evaluation, including microstructural examination, hardness, tensile strength, density, porosity and corrosion testing. The findings revealed notable improvements in mechanical performance with increasing B4C content, attributed to effective particle reinforcement and refined grain structures. This study underscores the potential of stir casting as a cost-effective and scalable approach for producing high-performance AMCs for applications in aerospace, automotive, and structural industries.

**Keywords:** Aluminium matrix composite, Boron Carbide, Stir Casting and mechanical properties

## 1 Introduction

The aerospace and automotive industries have encountered significant technological hurdles while striving to meet the demands and expectations of consumers. A predominant preference among manufacturers and designers is evident for materials that offer weight reduction advantages to meet their diverse needs. The materials used to build automobiles and aeroplanes should be lightweight, have a high specific strength, be able to withstand high temperatures, fatigue loads, corrosion, and cracking, and have a low wear rate. In the past, alloy steels were typically employed for parts of aeroplanes and automobiles. The advantages of ferrous metals are their widespread availability and low cost, but their disadvantages include their heavy weight, increased wear rate, and lower corrosion resistance. Aluminium, magnesium, titanium, and other nonferrous metals have garnered considerable interest for use in a variety of applications due to their lower densities than ferrous metals. Magnesium (Mg) is one of the nonferrous elements that is lightweight, but its usage in aircraft and automotive manufacture is limited because it seizes fire (Jojith et al., 2022; Kulekci, 2008). Aluminium (Al) costs 20 to 30 times less than titanium (Ti), which expends an amount of weight similar to magnesium (Mg). Since aluminium alloy (AA) is more durable than the majority of magnesium alloys, it is frequently utilized (Handbook, 1990). In comparison to monolithic materials, aluminium matrix composites (AMCs) offer a greater mix of mechanical, physical and thermal qualities. There are three type of common reinforcement that been used like alumina (Al2O3), silicon carbide (SiC) and boron carbide (B4C). Boron carbide have an advantage compare with SiC and Al2O3, specifically density (2.51 g.cm-3) (Mohanty et al., 2008) which is much less than Al2O3 and SiC, a very high degree of hardness (Hv = 30GPa) and wear resistance, a surprising lack of chemical activity and unique capability neutron absorption (Abenojar et al., 2007). These characteristics make B4C a great reinforcement for high performance of metal matrix composite.

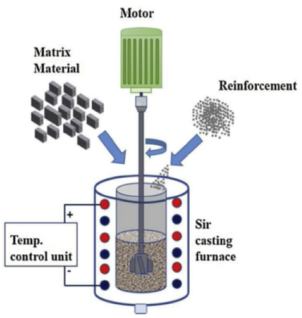



Figure 1: Stir Casting Process

## 2 Results

### 2.1 Microstructure Analysis

Refer Figure 2.

### 2.2 XRD Analysis

Refer Figure 3.

### 2.3 Density and Porosity

Refer Figure 4.

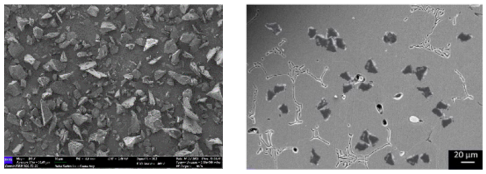



Figure 2: SEM Micrograph of (a) Micro particle B4C (b) Composite AAMC

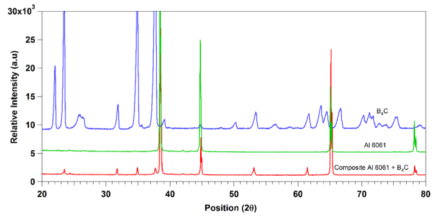



Figure 3: XRD analysis of B4C particle, Al6061 and Al-10%B4C composite

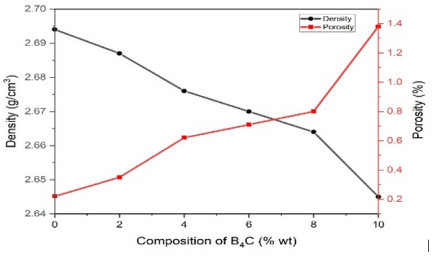



Figure 4: Density and porosity of AMC

### 2.4 Mechanical Properties

Refer Figure 5.

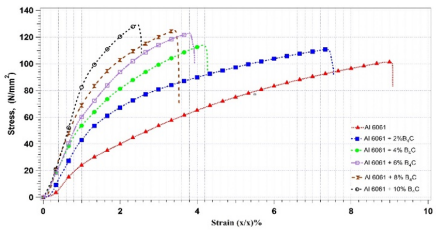



Figure 5: Stress strain curve of AMC with various of B4C composition

### 2.5 Corrosion Properties

Refer Figure 6.

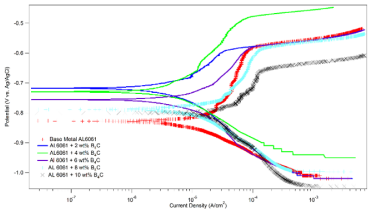


Figure 6: Tafel plot of AMC with various composition of B4C

## 3 Summary

This study explores the fabrication of aluminum matrix composites (AMCs) reinforced with boron carbide (B4C) microparticles using the stir casting technique. AMCs are known for their lightweight and high-strength properties, making them suitable for advanced engineering applications. By varying the weight fractions of B4C particles, the study examines the effects of reinforcement on the composite's mechanical and corrosion performance. The stir casting process was optimized for key parameters, including stirring speed, temperature, and holding time, to achieve uniform particle distribution and minimize defects. Comprehensive testing revealed that increasing the B4C content enhances hardness and tensile strength due to effective reinforcement and homogenous distribution. The results validate stir casting as an efficient and cost-effective method for producing AMCs, highlighting their potential for aerospace, automotive, and structural applications.

## References

J. Abenojar, F. Velasco, and M. A. Martínez. 2007. Optimization of processing parameters for the al+10 *Journal of Materials Processing Technology*, 1(184):441–446.

A. Handbook. 1990. Properties and selection: Irons, steels, and high-performance alloys. *ASM International*, 1.

R. Jojith, N. Radhika, and M. Govindaraju. 2022. Reciprocating wear behavioural analysis of heat-treated aluminium zro2/al7si0.3mg functionally graded composite through taguchi's optimization method. *Silicon*, 17(14):11337–11354.

M. K. Kulekci. 2008. Magnesium and its alloys applications in automotive industry. *The International Journal of Advanced Manufacturing Technology*, 39(9):851–865.

R. Mohanty, K. Balasubramanian, and S. K. Seshadri. 2008. Boron carbide-reinforced alumnium 1100 matrix composites: Fabrication and properties. *Materials Science and Engineering A-structural Materials Properties Microstructure and Processing - MATER SCI ENG A-STRUCT MATER*, (498):42–52.

Individual Research Contribution Review, 2024: 436–437
*ISSN: 3083-922X*

IRCR

# Intellectual Property Rights : Trend and Performance

**Abdul Quddoos Abu Bakar**
Planning and International Relation Division, Malaysian Nuclear Agency
43000 Kajang, Selangor
quddoos@nm.gov.my

## Abstract

This paper examines the current trends and performance of Intellectual Property Rights (IPR) in Nuclear Malaysia, exploring its impact on innovation, research, and development within the nuclear energy sector. It analyzes the strategic alignment between IPR frameworks and advancements in nuclear technology, as well as the challenges faced in protecting intellectual assets in this domain.

**Keywords:** Intellectual Property Rights (IPR),Innovation, Research

## 1 Introduction

Introduction Intellectual Property Rights (IPR) play a critical role in promoting innovation and safeguarding the intellectual assets of individuals and organizations. In Malaysia, particularly within the nuclear sector, the evolution of IPR is increasingly significant due to the growing emphasis on nuclear technology for sustainable energy. This paper discusses the trends and performance of IPR in the context of Nuclear Malaysia, highlighting its contributions and the associated challenges.

## 2 Methods

Overview of Intellectual Property Rights in Malaysia The Malaysian government has developed a comprehensive IPR framework to foster innovation and attract investment. Key elements include:

### 2.1 Patent and Utility Innovation (UI)

Protect inventions and technological advancements, crucial for the R&D in the nuclear sector. The Company is required to understand the content of the relevant flow chart and carry out the service according to the number of intellectual property specified, unless directed by the Agreement Administrator according to:

a. Patents (Amendment) Act 2022;

b. Patents (Amendment) Regulations 2022; and

c. Directives of the Patents Act 1983 and the Patents Regulations 1986 [P.U.(A)327/1986]

### 2.2 Trademarks

Help establish brand identity and consumer trust in nuclear technologies and services. The Company is required to understand the content of the relevant flow chart and carry out the service according to the number of intellectual property specified, unless directed by the Agreement Administrator according to :

a. The Trade Marks Act [Act 815] 2019, and relevant amended documents in force

b. Trademark Regulations 2022

### 2.3 Copyright

Protect the rights of creators in nuclear research and educational materials. The company is required to understand the content of the relevant flow chart and carry out the service according to the number of intellectual property specified, unless instructed by the Agreement Administrator according to:

a. Copyright Act 1987 (Act 332)

b. Copyright Act (Amendment 2022) (Act 1645) and documents relating to amendments in force

### 2.4 Industrial Design (ID)

The Company is required to understand the content of the relevant flow chart and carry out the service according to the number of intellectual property specified, unless directed by the Agreement Administrator according to:

1. Industrial Design Act [Act 552] 1996) and relevant amended documents in force

2. Industrial Design Regulations 1999

### 2.5 Plant Variety Protection

The Company is required to understand the content of the relevant flow chart and carry out the service according to the number of intellectual property specified, unless directed by the Agreement Administrator according to :

a. The Protection of New Varieties of Plants Act 2004 [Act 634] and related amended documents in force

b. Related regulations

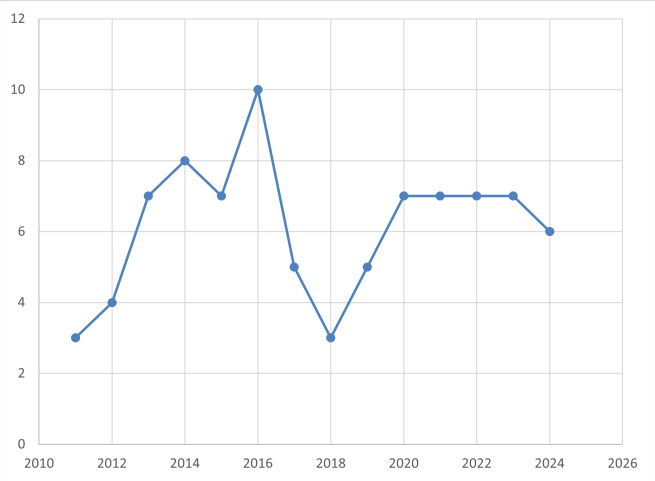



Figure 1: Chart Intelectual Property Rights: Trend and PerformanceTitle

## 3 Data/Results

Trends in Nuclear Malaysia's Intellectual Property Landscape is given in Figure 1. The nuclear sector in Malaysia is gaining momentum, primarily due to government initiatives aimed at promoting the use of nuclear energy as a reliable power source. Key trends observed include:

- Increased Patenting Activity: Research institutions and universities are enhancing their focus on patenting nuclear innovations, reflecting a shift towards formal recognition of intellectual contributions.
- Collaboration with International Entities: Partnerships with global nuclear organizations stimulate knowledge transfer and facilitate the protection of shared intellectual assets.
- Focus on Research and Development: Investment in R&D has surged, with universities and government agencies prioritizing nuclear technology research, which necessitates robust IPR management strategies.

## 4 Discussion

Performance Assessment of IPR in Nuclear Malaysia. The effectiveness of IPR in supporting advancements can be evaluated through several metrics:

- Growth in Patent Filings: The number of patents filed in the Nuklear Malaysia has shown a steady increase, indicating heightened innovation.
- Success in International Collaborations: Joint ventures and collaborations have led to successful technology transfers, demonstrating effective IPR management in cross-border contexts.
- Regulatory Framework Flexibility: The ability of the Malaysian IPR system to adapt to technological advancements ensures that the nuclear sector remains competitive and attractive to investors.

## 5 Challenges

Challenges in Intellectual Property Management Despite positive developments, several challenges persist:

- Lack of Awareness: There is a knowledge gap regarding the importance of IPR among local researchers and institutions, which can hinder innovation.
- Enforcement Issues: Effective enforcement of IPR regulations is critical, and shortcomings in this area can lead to intellectual property theft and reduced confidence in the system.
- Balancing Public Interest with Proprietorship: Ensuring that the public can access necessary technological advancements while also protecting inventors' rights remains a delicate balance.

## 6 Conclusion

The landscape of Intellectual Property Rights in Nuclear Malaysia is dynamic, reflecting both rising innovation and the complexities of managing intellectual assets in a high-stakes environment. To maximize the benefits of IPR in the nuclear sector, it is essential to enhance awareness, strengthen enforcement mechanisms, and foster a collaborative atmosphere between stakeholders. Through these initiatives, Nuclear Malaysia can secure its position as a leader in nuclear innovation, driving sustainable energy solutions for the future.

## Acknowledgements

The acknowledgments section of the paper on "Intellectual Property Rights: Trends and Performance" expresses gratitude to all contributors. The authors highlight the invaluable guidance from their academic advisors and mentors, as well as the enriching input from colleagues and peers. They appreciate the resources provided by various institutions and acknowledge the foundational work of previous researchers. Overall, the paper is recognized as a collaborative effort intended to advance the discourse on intellectual property rights and encourage further research.

Individual Research Contribution Review, 2024: 438–439
*ISSN: 3083-922X*

# Management of the Quality Program at the Malaysian Nuclear Agency (Nuklear Malaysia)

**Aisya Raihan bt Abdul Kadir**
Planning and International Relation Division, Malaysian Nuclear Agency
43000 Kajang, Selangor
aisya@nm.gov.my

## Abstract

Currently, nine facilities at the Malaysian Nuclear Agency (Nuklear Malaysia) have successfully maintained ten quality certifications and accreditations, including ISO 9001, ISO 13485, ISO/IEC 27001, ISO/IEC 17020, and ISO 17025. Each facility is required to conduct a series of audits to maintain these certifications and accreditations. The purpose of the audits is to ensure that the quality management system complies with the standards, achieves the facility's objectives, and provides management with insights to improve the efficiency of quality management. Since 2017, the Planning and International Relations Division (BPA) has been designated as the coordinator for internal audits at Nuklear Malaysia. BPA is also responsible for ensuring the effective implementation of these internal audits by updating and providing the Internal Audit Procedures as guidelines for managing audit activities at Nuklear Malaysia. The aim of this paper is to review the Opportunities for Improvement (OFI) and Non-Conformance (NC) reports issued by internal and external auditors and to update the internal audit procedure.

**Keywords:** Internal Audit, Internal Audit Procedure

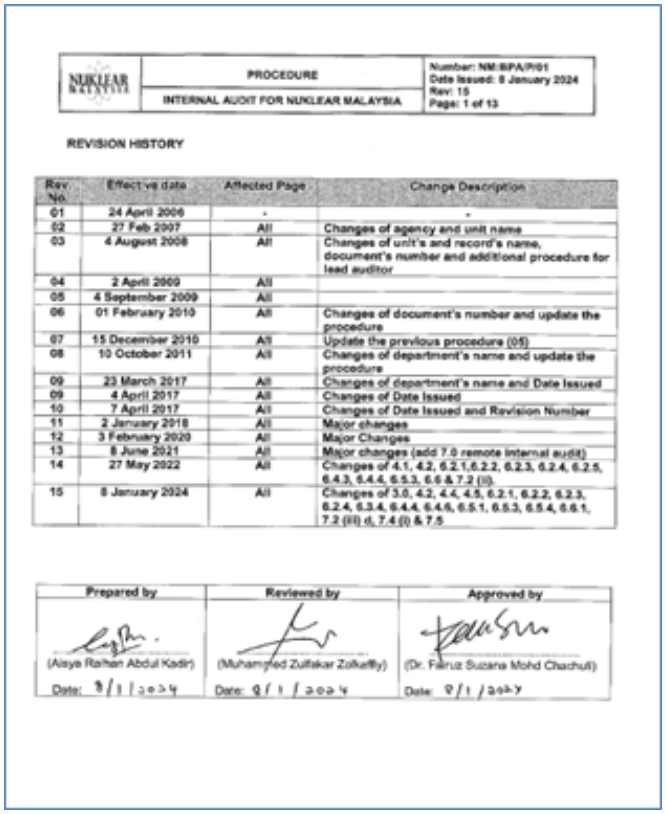
## 1 Introduction

The Malaysian Nuclear Agency (Nuklear Malaysia) has successfully maintained ten quality certifications and accreditations for nine facilities, including SINAGAMA, RAYMINTEX, Alurtron, the Centre of Nuclear Excellence (CoNE), the Waste Technology Development Centre (WasTeC), the Radiochemical and Environmental Laboratory (RAS), the Radiation Metrology Group (KMS), the Non-Ionizing Radiation Group (NIR), and the Information Technology & Application Centre (PTM).

The internal audit procedure serves as a guideline for internal auditors and facilities in managing internal audit activities for all certifications and accreditations at Nuklear Malaysia.

The current revision of the internal audit procedure is version 15, which has been effective since 8 January 2024 (BPA, 2024). BPA has updated the audit procedure based on the OFI/NCs reports issued by the internal auditors and the auditors from the Certification Body (External Audit).

The update of this procedure is also based on discussions and agreements made by the members during the Nuklear Malaysia Internal Audit Procedure Review Meeting. Figure 1 shows The updated Internal Audit Procedure (Revision 15). This procedure was prepared by Quality and Innovation Unit, BPA and approved by the Director of Planning & International Relations Division (BPA).



PROCEDURE
INTERNAL AUDIT FOR NUKLEAR MALAYSIA
Number: NM:BPA/PI/01
Date issued: 8 January 2024
Rev: 15
Page: 1 of 13

REVISION HISTORY

| Rev. No. | Effective date | Affected Page | Change Description |
|---|---|---|---|
| 01 | 24 April 2006 | - | - |
| 02 | 27 Feb 2007 | All | Changes of agency and unit name |
| 03 | 4 August 2008 | All | Changes of unit's and record's name, document's number and additional procedure for lead auditor |
| 04 | 2 April 2009 | All | |
| 05 | 4 September 2009 | All | |
| 06 | 01 February 2010 | All | Changes of document's number and update the procedure |
| 07 | 15 December 2010 | All | Update the previous procedure (05) |
| 08 | 10 October 2011 | All | Changes of department's name and update the procedure |
| 09 | 23 March 2017 | All | Changes of department's name and Date Issued |
| 09 | 4 April 2017 | All | Changes of Date Issued |
| 10 | 7 April 2017 | All | Changes of Date Issued and Revision Number |
| 11 | 2 January 2018 | All | Major changes |
| 12 | 3 February 2020 | All | Major Changes |
| 13 | 8 June 2021 | All | Major changes (add 7.0 remote internal audit) |
| 14 | 27 May 2022 | All | Changes of 4.1, 4.2, 6.2.1,6.2.2, 6.2.3, 6.2.4, 6.2.5, 6.4.3, 6.4.4, 6.5.3, 6.6 & 7.2 (ii). |
| 15 | 8 January 2024 | All | Changes of 3.0, 4.2, 4.4, 4.5, 6.2.1, 6.2.2, 6.2.3, 6.2.4, 6.3.4, 6.4.4, 6.4.6, 6.5.1, 6.5.3, 6.5.4, 6.6.1, 7.2 (iii) d, 7.4 (i) & 7.5 |

| Prepared by | Reviewed by | Approved by |
|---|---|---|
| (Aisya Raihan Abdul Kadir) | (Muhammad Zulfakar Zolkaffly) | (Dr. Faruz Suzana Mohd Chachuli) |
| Date: 9/1/2024 | Date: 9/1/2024 | Date: 9/1/2024 |

Figure 1: The updated Internal Audit Procedure (Revision 15)

## 2 Methods

Figure 2 shows the workflow for updating the internal audit procedure at Nuklear Malaysia. BPA organized the Nuklear Malaysia Internal Audit Procedure Review Meeting to discuss and obtain approval from the meeting members for updating this internal audit procedure.

## 3 Data/Results

Table 1 shows the OFI/NCs obtained by the facility during the internal and external audits in 2023. The facility has

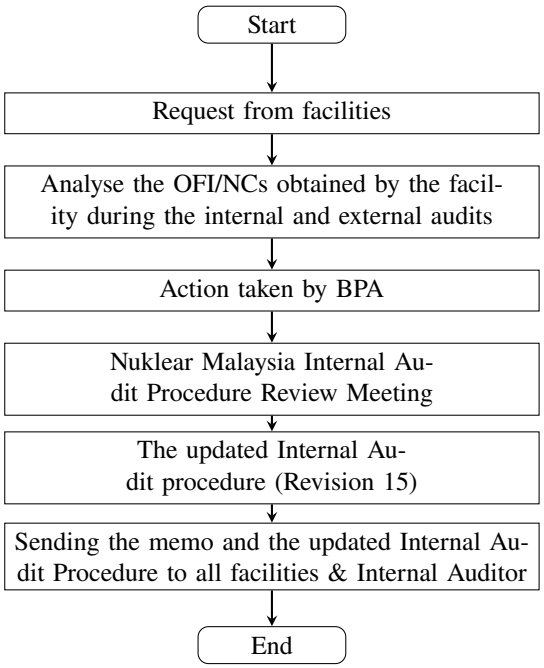



Figure 2: The workflow for updating the internal audit procedure at Nuklear Malaysia

| THE OFI/ NCS OBTAINED BY THE FACILITY DURING THE INTERNAL & EXTERNAL AUDIT IN 2023 | ACTION TAKEN BY BPA |
|---|---|
| OFI: How does an internal auditor differentiate between major and minor NC | Updating the internal audit procedure by include definitions that differentiate between major NC, minor NC, and OFI |
| NC : The lead auditor did not verify the corrective actions that implemented by auditee | An awareness course on the role of auditors in conducting audits was held during the Refresher Course on ISO 9001:2015, ISO/IEC 17020:2012, and PKP BCMS ISO 22301:2019 (Internal Auditing) on 21 May 2024 at Nuklear Malaysia. |

Table 1: The OFI/ NCS obtained by The Facility During The Internal & External Audit In 2023

requested BPA to take action regarding the OFI/NCs raised by either the internal or external auditors. These issues will be addressed in the Nuklear Malaysia Internal Audit Procedure Review Meeting for further discussion.

The meeting was attended by representatives from facilities with quality certifications and accreditations, as well as internal auditors from Nuklear Malaysia. Additionally, the update to the internal audit procedure included other suggestions and received approval from the meeting members. Other changes were made to the audit procedure, including items such as 4.2, 4.4, 4.5, 6.2.1, 6.2.2, 6.2.3, 6.2.4, 6.3.4, 6.4.4, 6.4.6, 6.5.1, 6.5.3, 6.5.4, 6.6.1, 7.2 (iii) d, 7.4 (i), and 7.5. After updating the procedure, BPA sent a copy of the memo and the updated procedure to all facilities and internal auditors via email for their reference and record.

## 4 Discussions/Conclusions

BPA plays a key role in assisting facilities in maintaining their quality certifications and accreditations. The audit procedure will be updated upon request from facilities with quality certifications and accreditations. This update to the internal audit procedure will enable both internal auditors and auditees to conduct audits more effectively. Furthermore, BPA also plays a role in ensuring that the competency of Internal Auditors consistently meets the requirements outlined in the updated Internal Audit Procedure (Revision 15).

## References

Nuklear Malaysia BPA. 2024. Prosedur audit dalaman nuklear malaysia.

Individual Research Contribution Review, 2024: 440–441
*ISSN: 3083-922X*

# Analysis of Potential Bilateral Cooperation in the Field of Nuclear Science and Technology Between Malaysian Nuclear Agency (Nuklear Malaysia) and Foreign Countries for the Year 2022-2024

**Azlinda Binti Aziz**
Planning and International Relation Division, Malaysian Nuclear Agency
43000 Kajang, Selangor
azlinda@nm.gov.my

## Abstract

The International Planning and Relations Division (BPA), Malaysian Nuclear Agency (Nuklear Malaysia) is responsible for coordinating and managing bilateral and multilateral cooperation activities in the field of nuclear science and technology with foreign countries. BPA coordinates and provides information to stakeholders, especially the International Division of Ministry of Science, Technology and Innovation (MOSTI) regarding international cooperation as well as coordinating and managing brief and speaking notes for bilateral and multilateral cooperation. In addition, BPA also manages visits and courtesy calls by foreign delegations to Nuklear Malaysia to explore cooperation opportunities in the field of nuclear science and technology. This initiative is important for both parties in strengthening cooperative relations, driving technology transfer as well as improving human resource development through training and education programs.

**Keywords:** bilateral, cooperation, nuclear

## 1 Introduction

The International Planning and Relations Division (BPA), Malaysian Nuclear Agency (Nuklear Malaysia) is responsible for coordinating and managing the Agency's bilateral and multilateral relations and cooperation activities to strengthen cooperation in the field of nuclear science and technology with foreign countries. BPA acts as a liaison to stakeholders, especially the International Division of Ministry of Science, Technology and Innovation (MOSTI) related to international cooperation through the coordination and management of brief and speaking notes of bilateral and multilateral cooperation in the field of nuclear science and technology between Nuklear Malaysia and foreign countries. BPA also coordinates and manages visits and courtesy calls of foreign delegations to Nuclear Malaysia to explore the potential of cooperation in the field of nuclear science and technology. This paper aims to analyze brief and speaking notes in the field of nuclear science and technology between the Malaysian Nuclear Agency and foreign countries to explore the potential of bilateral cooperation in the field of nuclear science and technology.

## 2 Methods

This brief and speaking notes are prepared based on the requirements of the International Division of MOSTI. This brief and speaking notes contain information on the latest status involving programs, projects, or activities of bilateral and multilateral cooperation within a period of five years, including Memorandum of Understanding or Memorandum of Agreement, issues that have arisen including the background, current status, and actions that have been taken as well as new proposals for potential programs or projects are negotiated through this collaboration. Brief and speaking notes will be provided if Malaysia will attend a high-level official meeting or visit abroad or Malaysia will receive a high-level official visit from a foreign country. The flowchart for the preparation of Brief and Speaking Notes are given in Figure 1.




Figure 1: Flowchart for Preparing Brief and Speaking Notes

## 3 Data/Results

Data is summarized in Table 1

| Frequency | Foreign Country | | |
|---|---|---|---|
| | 2022 | 2023 | 2024 |
| 1 | Bahrain, Belgium, Cambodia, Egypt, European Union, German, Iran, Italy, Jordan, Kazakhstan, Luxembourg, Mexico, Mozambique, Netherland, New Zealand, Norway, Palestine, Papua New Guinea, Qatar, Singapore, Spain, Sweden, Switzerland, United Arab Emirates, United Kingdom, United State, Uzbekistan, Vietnam. | Bangladesh, Brazil, Brunei Darussalam, Cambodia, Italy, Japan, Jordan, Maldives, Monaco, New Zealand, Norway, Pakistan, Palestine, Philippines, Portugal, People's Republic of China, Republic Indonesia, Republic of Uzbekistan, Singapore, Slovakia, Spain, Sri Lanka, Syria, Turkiye, Uganda, United Kingdom, United State. | Afghanistan, Argentina, Austria, Azerbaijan, Bahrain, Bangladesh, Bhutan, Cambodia, Denmark, India, Indonesia, Iraq, Italy, Jordan, Nepal, New Zealand, Pakistan, Philippines, Poland, Peru, Portugal, Qatar, Rwanda, Slovakia, Suriname, Switzerland, Thailand, United Arab Emirates, Uruguay, Venezuela. |
| 2 | Australia, Austria, Denmark, France, Kyrgyzstan, Laos, Myanmar, Tajikistan, Turkiye, Turmenistan. | Australia, Canada, Czech Republic, India, Netherland, Republic of Korea, Russia, Saudi Arabia, United Arab Emirates | Australia, Canada, China, Czech Republic, France, Hungary, Iran, Japan, Maldives, Republik of Uzbekistan, Singapore, Spain, Sri Lanka, United States. |
| 3 | Republic of China | Austria, France, Iran, German, Qatar, Thailand. | Saudi Arabia, Republic of Korea, Russia, United Kingdom. |
| 4 | Republic of Korea | | |
| 5 | Japan | | |
| **Total Countries** | **41** | **42** | **48** |
| **Total Brief Speaking Notes** | **60** | **64** | **70** |

Table 1: Frequency of brief and speaking notes for bilateral cooperation between Malaysia and foreign countries for a period of 3 years (2022 - 2024)

## 4 Discussions/Conclusions

The findings from the analysis of Table 1 show that the highest frequency of brief and speaking notes in the 3-year period from 2022 to 2024 are Japan, the Republic of Korea, Saudi Arabia, Austria, Iran, Germany, France, the People's Republic of China, Russia, Thailand, and the United Kingdom. Those countries have the potential to become cooperation partners with the Malaysian Nuclear Agency in the field of nuclear technology. However, only Saudi Arabia expressed interest in continuing bilateral cooperation through online discussions in March 2024.

In addition, Nuklear Malaysia also received visits and courtesy calls from the United States (Oct 2023), India (Oct 2023) and Argentina (June 2024) to explore potential cooperation in the field of nuclear technology even though these countries are not included in the list of potential countries as cooperation partner countries from the analysis carried out.

Until now Nuklear Malaysia still does not have an Agreement of Understanding with any foreign country related to science and nuclear technology in the medical and healthcare sectors, food and agriculture, device and equipment manufacturing, environmental and natural resource management, industrial applications and nuclear safety and security . However, these activities are carried out through multilateral cooperation, especially through the Technical Cooperation Program of the International Atomic Energy Agency (IAEA), the Association of Southeast Asian Nations (ASEAN).

However, Nuklear Malaysia has bilateral cooperation related to the Comprehensive Nuclear Test Ban Treaty (CTBT) where Nuklear Malaysia has signed a memorandum of understanding with the Australian Safeguards and Non-Proliferation Office (ASNO), Australia on April 4, 2024. CTBT activities are also carried out under the Preparatory Commission for the Comprehensive Nuclear Test Ban Treaty (CTBT Preparatory Commission).

Bilateral cooperation plays an important role in strengthening the cooperative relationship between the two parties in driving the transfer of technology and knowledge as well as the development of human resource capacity through training and education programs, at the same time providing great benefits to both countries.

Individual Research Contribution Review, 2024: 442–443
*ISSN: 3083-922X*

# Nuclear Energy to Support Net-Zero Transition in Malaysia by 2050: Strategies for Success

**Fairuz Suzana binti Mohd Chachuli**
Planning and International Relation Division, Malaysian Nuclear Agency
43000 Kajang, Selangor
fairuz@nm.gov.my

## Abstract

This project aims to evaluate the economic and environmental of potential six policy measures, including the introduction of nuclear energy in the national energy mix towards Malaysia's aims for Net Zero emissions by 2050 using the IAEA's MESSAGE model. The findings of this study will be utilized as a reference for policymakers and energy experts as they develop future sustainable energy plans for the country, to become carbon-neutral by 2050.

**Keywords:** MESSAGE, nuclear, optimization

## 1 Introduction

Malaysia is committed to low-carbon development aimed at restructuring the economic landscape to a more sustainable one. NETR has developed the Responsible Transition Pathway 2050 to shift Malaysia's energy systems from fossil fuel-based to greener and low-carbon systems. The TPES modelling indicated that our energy demand will increase marginally at 0.2% annually from 95 million tonnes of oil equivalent (Mtoe) in 2023 to 102 Mtoe in 2050. The Responsible Transition Pathway 2050 has also shown promising decarbonisation results as evidenced by the phasing out of coal and the reduction of fossil fuel reliance from 96% in 2023 to 77% in 2050. Natural gas is set to be not only a transitional fuel, but also the primary contributor of TPES at 57 Mtoe (56%) followed by renewables that include solar, hydro, and bioenergy, which collectively contribute 23% of TPES in 2050 from a mere 4% in 2023.

The Malaysian government has recently expressed a renewed willingness to incorporate nuclear power into the nation's future energy portfolio. The politically sensitive nature of nuclear power programs is a crucial element to consider. Consistent political support and a steadfast commitment from the government are essential for the success of a nuclear energy program. Policies must maintain stability and support the development of nuclear energy, ensuring that national energy objectives are achieved safely and sustainably.

## 2 Methods

Model for Energy Supply Strategy Alternatives and their General Environmental Impact (MESSAGE) combines technologies and fuels to construct so-called "energy chains", making it possible to map energy flows from supply (resource extraction) to demand (energy services). The model can help design long-term strategies by analyzing cost-optimal energy mixes, investment needs and other costs for new infrastructure, energy supply security, energy resource utilization, rate of introduction of new technologies (technology learning), and environmental constraints.

### 2.1 Development of reference energy system in the MESSAGE model

MESSAGE sets up models of energy supply and utilization and finds the best expansion path for the energy system based on certain fuel management in the medium and long-term period. The reference energy system has four stages shown in Figure 1. The stages are resources, primary, secondary and final.

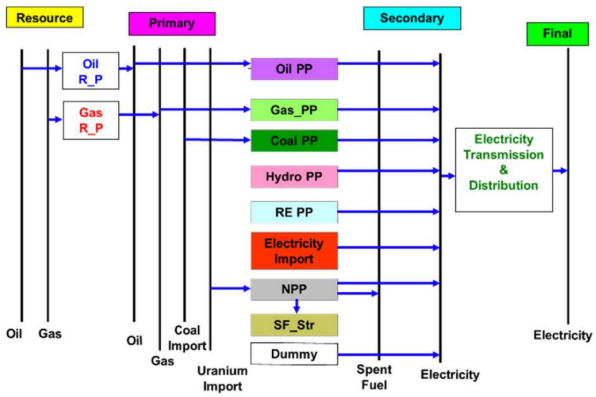



Figure 1: Reference Energy System in MESSAGE

### 2.2 Scope of the study

A national case study focused on Peninsular Malaysia is assessed through its techno-economic evaluation and optimization of the proposed reference energy system (RES) using IAEA MESSAGE model. The model developed in this case study evaluated different policy measures that support Malaysia's long-term energy transition policies and measures. The base year chosen in this case started in 2010 and the planning horizon covers up to 2050.

### 2.3 Policy measures to be analyzed

All scenarios to be evaluated under the Net Zero Carbon by 2050 are described as follows. The electricity demand of 13,999MW in the base year 2009 is recorded with a constant growth rate of 1.025%. However, from 2023 through 2027,

the growth rate is at 0.4%, whilst from 2028 to 2032 is 1.3% and between 2033 and 2042 the growth rate is 3.3%. The average constant growth rate during the whole study period from 2009 until 2050 is 1.025%. The peak electricity demand recorded in the year 2022 is 19,183 MW, the current year 2023 is 19,716 MW, whilst the year 2042 is 28,891 MW and the final year 2050 is 34,857 MW.

Policy measures evaluated using the IAEA MESSAGE model as follows:

a. New large nuclear power plant (NPP) 1400MW for 2 units with the start year 2040

b. New small-modular reactor (SMR) 300MW for 5 units with start year 2040

c. 2000 MW electricity import from Sarawak Hydro 100MW by 2030 and Laos-Thailand-Malaysia (LTM) 1000MW by 2027

d. Open capacity of renewable energy especially for solar

e. Retiring coal power plant and no new coal power plant addition

f. New gas power plant for combined-cycle power plant (CCGT) and no new open-cycle gas turbine (OCGT) power plant addition.

## 3 Data/Results

The results show that the green energy measures contribute an amount of 37,712 MW for six Net Zero Emissions strategies for Malaysia by 2050. The integration of nuclear energy, electricity import, renewable energy and new gas power plants compensates for the retirement and shut down of coal power plants with an amount of 27,806 MW, whilst the existing power plants are still operating. The electricity expansion for Peninsular Malaysia until the year 2050 is shown in Figure 2.

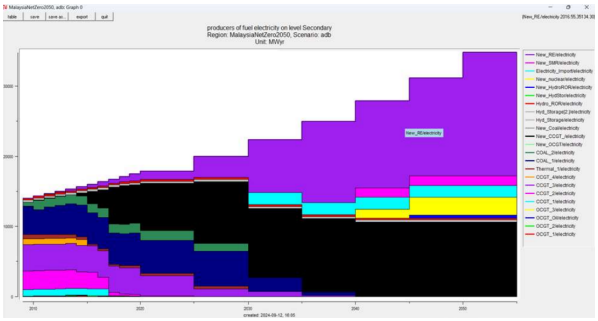


Figure 2: Reference Energy System in MESSAGE

### 3.1 Environmental Perspective

The result of the MESSAGE shows that the integration of six Net Zero Emissions strategies for Malaysia by 2050 has successfully reduced carbon emissions by 49.37% compared to the base year 2010. The carbon emissions for the year 2010 amounted to 76429 kton and reduced to 37736 kton by the year 2050. The total carbon emission reduction for Peninsular Malaysia until the year 2050 is shown in Figure 3.

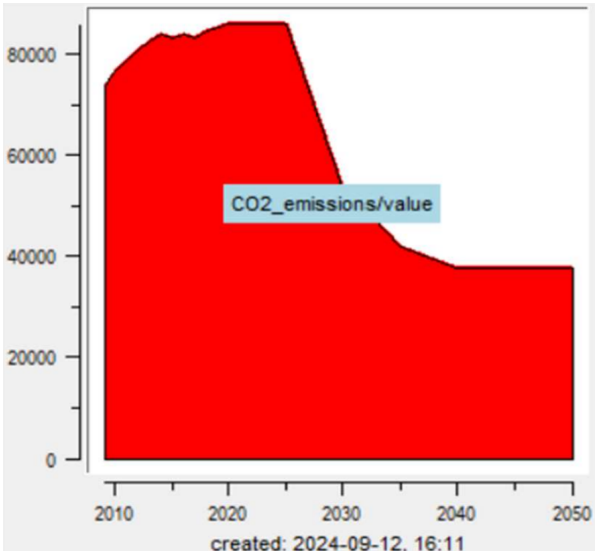



Figure 3: The reduction of carbon emissions based on Net Zero Emission by 2050 strategies.

## 4 Conclusions

The optimization of the MESSAGE model shows that the green policy measures including renewable energy, nuclear energy and electricity import exhibit a promising system in the study. Nuclear energy has the potential to assist Malaysia in achieving its clean energy objectives and transitioning from fossil fuels. Incorporating nuclear energy into the energy portfolio would support the government's objective of decreasing carbon emissions, given its status as a zero emission energy source. Although renewable sources such as solar and wind are advantageous, nuclear energy can offer dependable base load power to support intermittent renewables.

Individual Research Contribution Review, 2024: 444–445
*ISSN: 3083-922X*

# Potential and Optimization of Distributed Small Modular Nuclear Reactor-Solar Photovoltaics (DSMPV) Hybrid Energy Systems in Malaysia (IAEA CRP Project Code 25174)

**Fairuz Suzana binti Mohd Chachuli**
Planning and International Relation Division, Malaysian Nuclear Agency
43000 Kajang, Selangor
fairuz@nm.gov.my

## Abstract

This project aims to evaluate the economic and environment potential of distributed small modular nuclear reactor-solar photovoltaics (DSMPV) hybrid energy systems in Malaysia. The complementary operation design of the two technologies in a hybrid system will benefit in terms of greater energy and economic efficiency that can be achieved. The findings of this study will be utilised as a reference for policymakers and energy experts as they develop future sustainable energy plans for the country, with the goal of becoming carbon-neutral by 2050.

**Keywords:** hybrid, solar, nuclear, optimization

## 1 Introduction

Malaysia is at a tipping point in the fight against the climate and biodiversity crises, as it steps up efforts and commitments to transition to a low-carbon, climate-resilient economy. Malaysia's energy transition plans until 2040 will focuses on its power generation plan. The 12 Malaysia Plan has outlined Malaysia's path to net zero emissions. This includes achieving carbon neutrality by 2050 and phasing out coal-powered energy generation. Renewable energy generation is targeted to increase to 31 per cent of the total installed capacity in the country by 2025, as solar energy has the highest potential. However, solar energy, particularly photovoltaics, facing various challenges need to be tackled. Issues such as intermittency, vulnerability, battery storage, acquisition of land and materials as well as low efficiency of capacity factors will be need to properly manage if the country decides not to depend on fossil fuels.

## 2 Methods

A national case study is assessed through its technical evaluation and optimization of the proposed DSMPV-HES for different technical and operational environments that support Malaysia's long-term renewable energy transition policies. This objective includes various steps such as input data of the conceptual design of a DSMPV-HES in HOMER and a result analysis is obtained in terms of economic, technical and environmental perspectives. The research framework development are given by Figure 1.

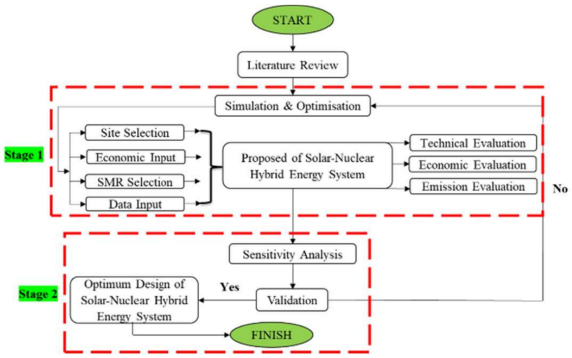



Figure 1: Development of Research Framework.

### 2.1 Development of research framework

A national case study is developed to optimize for long-term scenarios in Malaysia in Figure 2 with the potential of a nuclear-renewable hybrid energy system and high penetration of RE, battery energy storage system (BESS) to support more efficient utilization of solar and nuclear energy for electricity generation in Malaysia.




Figure 2: Development of case study.

### 2.2 Data Input

The SMR considered in this study is 50 MW power output capacity with an estimated capital cost is USD186 billion, whilst the replacement cost is USD0 and the O&M cost is USD1 million/year. It is assumed that the SMR will be operating for 60 years without replacement and the derating factor is 60%.

A 1 kWh generator set (GenSet) using diesel with a capital cost of USD500 is also considered in this case study. The replacement cost of GenSet is estimated at USD500 and the O&M cost is estimated at USD0.030/ operating hour whilst the diesel fuel price is at USD1/litre. The minimum load ratio for the GenSet is at 25% with a lifetime is 15,000 hours. The battery bank is integrated into the system to serve as an emergency or backup power source and might not needed when SMR can supply full time energy supply. The introduction of a converter becomes necessary with the presence of both AC and DC supply within the system.

## 3 Data/Results

A national case study is assessed through its technical evaluation and optimization of the proposed DSMPV-HES for different technical and operational environments that support Malaysia's long-term renewable energy transition policies. This objective includes various steps such as input data of the conceptual design of a DSMPV-HES in HOMER and a result analysis is obtained in terms of economic, technical and environmental perspectives. The results achieved in this study are explained further below.

### 3.1 Economic perspective

The optimization of DSMPV-HES shows that the hybrid energy system between SMR and solar farm exhibits a promising system in the study, as shown in Table 1.

| Hybrid Energy System | Net Present Cost (NPC) [USD million] | Cost of Electricity (COE) [USD] |
|---|---|---|
| SMR+solar farm+ converter | 224 | 1.10 |
| SMR+solar farm+ converter+battery | 224 | 1.10 |
| SMR + solar farm+ converter+GenSet | 227 | 1.11 |
| SMR + solar farm+ converter+battery+ Genset | 228 | 1.11 |

Table 1: The economic optimization of DSMPV-HES.

### 3.2 Technical Perspective

The total electricity generated from DSMPV-HES is at 264,663, 621 kWh/year, where the solar farm is estimated at 1,863,621 kWh/ year (0.704%), whilst the total electricity generated from the SMR is estimated at 262,800,000 (99.3%). The DSMPV-HES analysis shows that SMR provides electricity more than 99% than solar PV in the NRHES to provide electricity load for the community and industrial sector at Lumut, Perak.

### 3.3 Environmental Perspective

The result of the DSMPV-HES analysis shows that the hybrid system with diesel generator produces environmental burden as shown in Table 2. The carbon footprint associated with the site construction and equipment manufacturing is not encompassed within this analysis.

| Environmental burden | Emission (kg/year) |
|---|---|
| Carbon Dioxide | 9833 |
| Carbon Monoxide | 50.9 |
| Unburned Hydrocarbons | 2.70 |
| Particulate Matter | 0.435 |
| Sulfur Dioxide | 24.0 |
| Nitrogen Oxides | 9.75 |

Table 2: The environmental optimization of DSMPV-HES

## 4 Conclusions

The optimization of DSMPV-HES shows that the hybrid energy system between SMR and solar farm exhibits a promising system in the study.

Individual Research Contribution Review, 2024: 446–447
*ISSN: 3083-922X*

IRCR

# Malaysia: Advancing Research and Development on Nuclear Science and Technology through IAEA Technical Cooperation Program

**Hazmimi Kasim**
Planning and International Relation Division, Malaysian Nuclear Agency
43000 Kajang, Selangor
hazmimi@nm.gov.my

## Abstract

Malaysia has been an IAEA Member State since 1969, focusing on nuclear science and technology across areas such as radiation safety, industrial applications, human health, food and agriculture, and environmental management. As an important center for nuclear expertise in the region, the country actively participates in IAEA programs and initiatives, develops capabilities and continues to advance its nuclear infrastructure and researches through collaborations with international partners.

**Keywords:** technical cooperation, research and development, international relation

## 1 Introduction

Malaysia has made significant strides in nuclear technology since the late 19th century, and progressively developing through key milestones such as joining the International Atomic Energy Agency in 1969, establishing the Malaysian Nuclear Agency in 1972, and commissioning the Reactor TRIGA PUSPATI in 1982. The country has advanced nuclear science and technology across multiple sectors, including medicine, agriculture, and industrial applications (Hayati (1996), Daud and Kasim (2010), Kasim et al. (2011)). Supported by a comprehensive legal framework established by the Atomic Energy Licensing Act of 1984 and collaborative efforts with educational institutions, Malaysia has developed world-class nuclear facilities, becoming an IAEA International Collaborative Centre recognized in three different fields. This paper highlights Malaysia's progress in nuclear science and technology, aligning its development with national and international goals through strategic cooperation with global partners.

## 2 Methods

The study utilized a qualitative case study approach to identify and explore success stories in IAEA technical cooperation (TC) projects (IAEA (2021),IAEA (2022), IAEA (2023)), focusing on research and development (R&D) activities across two major thematic sectors. The case study method allowed for a nuanced understanding of the TC activities, providing insights into their achievements and thought patterns while offering a detailed and replicable exploration of the selected projects.

### 2.1 Case Study: Food and Agriculture

The application of nuclear science and technology in food and agriculture has expanded in tandem with national policies, focusing on increasing food production through plant breeding, and increasing the quality and safety of food through irradiation.

With support from the IAEA, a new facility using a 'chronic irradiation' technique to implement research and development activities to produce plant varieties, while minimizing radiation damage, was established.

#### 2.1.1 MAL 5033: Strengthening Analytical Capabilities for Food Safety and Food Security

Malaysia has developed advanced isotope techniques under the TC project MAL5033 to evaluate and mitigate greenhouse gases in agricultural systems, enabling precise quantification of emission pathways such as nitrification and denitrification. These methods help improve rice production, maintain soil health, and reduce greenhouse gas emissions, while innovative cosmic ray technology measuring soil moisture levels for efficient water management.

### 2.2 Case Study: Industrial applications and non-destructive testing

Malaysia established an accredited training and certification system for non-destructive testing (NDT) technologies, developing national expertise through training courses, fellowships, and equipment provision. In 2015-2027, Nuklear Malaysia was designated as an IAEA Collaborating Centre for NDT, reflecting its significant achievements including ISO 9712 and ISO 17024 accreditations. National NDT Certification Scheme highlighting Malaysia's leadership in NDT technology and cooperation with the IAEA for industrial application.

#### 2.2.1 MAL1017 – "Enhancing Capabilities in Nuclear and Related Technologies for Reliable and Sustainable Industries"

Under TC MAL 1017, Malaysia is focusing on the radiation processing techniques in industrial sector and developing R&D capacity in the utilization of irradiation technology to address plastic waste pollutions, in the recycling of PTFE through irradiation processes. The country is also pursuing its second application, involving a pyrolysis project that integrates radiation technology with conventional chemical recycling methods.

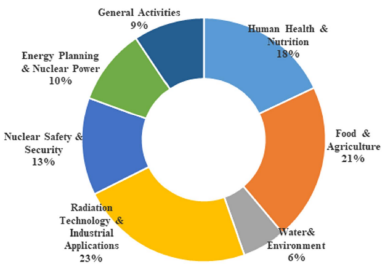



Figure 1: Thematic sectors of the IAEA National Technical Cooperation (TC) Projects 1976-2025

## 3 Data/Results

The IAEA assists member states in developing, strengthening, and maintaining human and institutional capacity for the safe, peaceful, and secure use of nuclear technology through its TC programme.

### 3.1 National TC project under IAEA TC Program in Malaysia 1976-2025

Since 1976, Malaysia has participated in 129 national projects, and 328 regional and interregional projects. Meanwhile, 10 active projects are now in progress, ranging from the 2022 to 2025 cycle. In realizing the future challenges and the potential of nuclear science and technology in the near future, Malaysia is committed to strengthening human capacity development by being actively involved in IAEA TC programme. Figure 1 shows how the national TC project under IAEA TC Program in Malaysia has been distributed its efforts across different areas from 1976 to 2025. Radiation technology and industrial applications represents the largest share, this indicating a significant focus on developing and applying radiation technologies in industrial settings. Food and agriculture as second major thematic sector shows substantial efforts in using nuclear techniques to improve agricultural practices and food security.

### 3.2 IAEA TC Achievement and Support in the 21st Century

The International Atomic Energy Agency (IAEA) has played a significant role in supporting Malaysia's development in nuclear science and technology since the country became a member state. TC projects that have been implemented, benefiting Malaysia through 632 fellowships and scientific visits, 1,357 training participants, 1,736 meeting participants, and 299 expert missions received in the 21st century. This extensive support has contributed to Malaysia's development of expertise in various areas such as non-destructive testing, mutation breeding, food irradiation, and addressing plastic pollution through nuclear techniques.

## 4 Discussion

### 4.1 International Cooperation Approach in Developing Nuclear Research Network

Malaysia has been an active member of the IAEA since 1969, and this partnership has been crucial in advancing nuclear science and technology within the country. The collaboration has expanded to include other United Nations organizations such as FAO, UNESCO, WHO, and UNIDO, creating a robust network for international cooperation. Additionally, Malaysia participates in regional and international network like the Forum for Nuclear Cooperation in Asia (FNCA), the Preparatory Commission for the Comprehensive Nuclear-Test-Ban Treaty Organisation (CTBTO), and ASEAN, to further strengthening its nuclear networking capabilities.

### 4.2 Leading the nuclear research and development

The Malaysian Nuclear Agency has established itself as a premier R&D institution, playing a crucial role in developing research activities and networks at national, regional, and international levels. Malaysia has been appointed as the Lead Country Coordinator for multiple technical cooperation projects under the Research Cooperative Agreement (RCA) in the Asia and Pacific region, including initiatives in radiation processing and non-destructive testing techniques. These achievements highlight the capabilities of Malaysian researchers and their ability to strengthen collaborative research networks while contributing to the country's socio-economic development.

### 4.3 Malaysia involvement in IAEA Initiatives

Malaysia has taken a proactive role in international initiatives led by the International Atomic Energy Agency (IAEA), emerging as a pilot country in the NUTEC Plastic Initiative to address plastic pollution through nuclear technology. By developing innovative research capacities in irradiation technology, the country has made significant progress in recycling poly-tetra fluoro-ethylene (PTFE) and contributing to microplastic monitoring methodologies. Additionally, Malaysia actively participates in the VETLAB and Zodiac network, with its Veterinary Research Institute designated as a Zodiac National Laboratory, demonstrating the nation's commitment to leveraging nuclear science and technology for addressing global challenges in environmental conservation and public health.

## References

Ainul Hayati Daud and Hazmimi Kasim. 2010. The impact of nuclear technology to the national socio-economy in malaysia. Technical report, Malaysian Nuclear Agency.

Ainul Hayati. 1996. Partners for development: Expert assistance in malaysia. *Iaea Bulletin*, page 39.

IAEA. 2021. Technical cooperation report for 2020. Technical Report GC(65)/INF/4, IAEA, July.

IAEA. 2022. Technical cooperation report for 2021. Technical Report GC(66)/INF/7, IAEA, September.

IAEA. 2023. Technical cooperation report for 2022. Technical Report GC(67)/INF/5, IAEA, August.

Hazmimi Kasim, Ainul Hayati Daud, Jamal Khaer Ibrahim, and Alawiah Musa. 2011. Impact of nuclear technology to the national socio-economy: Technical support by nuclear malaysia. In *Nuclear Technical Convention 2011*. Malaysian Nuclear Agency, Jul.

Individual Research Contribution Review, 2024: 448–449
*ISSN: 3083-922X*

# Outcome Based Analysis: Budget Process vs Performance

**Mohd Azmi**
Planning and International Relation Division, Malaysian Nuclear Agency
43000 Kajang, Selangor
m_azmi@nm.gov.my

## Abstract

This paper examines the current performance-based budgeting (PBB), a transformation of national budget process reform by the Government of Malaysia from existing Modified Budgeting System (MBS) that was rolled out in early of 1990s. Malaysian Nuclear Agency (Nuklear Malaysia) has experienced this reform for the past 10 years and monitored current trend and analysis for analyzing its impact on innovation, research, and development within the organization. This data can be use in the view of strategic alignment between performance indicator and financial budget in nuclear technology, as well as the challenges faced in securing a budget.

**Keywords:** Performance-based budgeting (PBB), Outcome, budget

## 1 Introduction

Outcome Based Budgeting is the step in the implementation of PBB. Introduced by Ministry of Finance to the MOSTI budgeting system beginning in 2015 which involve Nuklear Malaysia.

This paper discusses the trends and performance indicator in the context of Nuklear Malaysia, highlighting its contributions and the associated challenges.

## 2 Method

Malaysia has strategized its budgeting process as one of the central accounting mechanisms underpinning organizational control in the public sector. A key traditional focus of budgets in the public sector has been costs control. Conventionally, this aspect of budgeting has been structured on organizational segments or areas of responsibility and based on an input analysis of costs (Myers and Boothe, 2018).

As a result, traditional budgeting overlooks how organizations utilize available resources and the effectiveness with which they are deployed. This is a significant shortcoming, as it prevents a proper evaluation of resource efficiency and impact.

In reforming its budgeting process, newly introduce Malaysia's Outcome-Based Budgeting (OBB) demonstrates a clear and structured approach to linking national priorities with specific budget allocations. By utilizing a unified results framework, OBB ensures that resources are directed towards achieving measurable outcomes, enhancing accountability at every level of governance (MOSTI example Figure 1).

The integration of national strategies, ministerial outcomes, program goals, and activity results (MOSTI example in Figure 2) provides a comprehensive roadmap for translating high-level objectives into tangible actions and results.

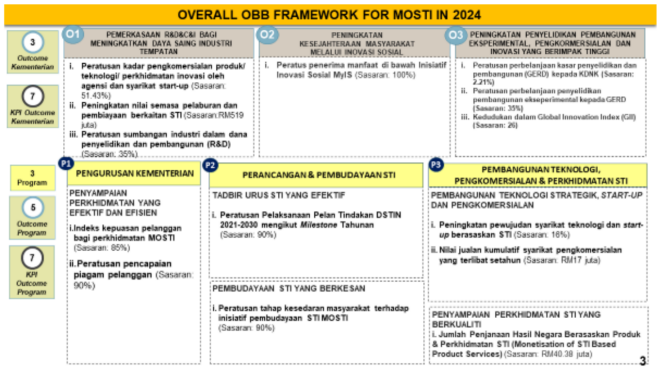



Figure 1: Ministerial outcome and program goals for MOSTI in 2024

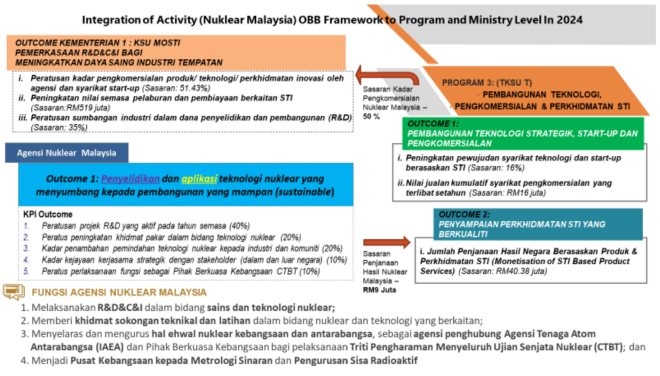



Figure 2: Integration of activity to the ministerial outcome and program goals for MOSTI in 2024

## 3 Data/Results

In line with the OBB process, Nuklear Malaysia has received a progressive budget for the period from 2011 to 2025. The operating and development budgets for this period are shown in Figure 3. It is noted that prior to 2015, the government used the MBS approach, while from 2015 onward, a reform was implemented using the PBB/OBB process.

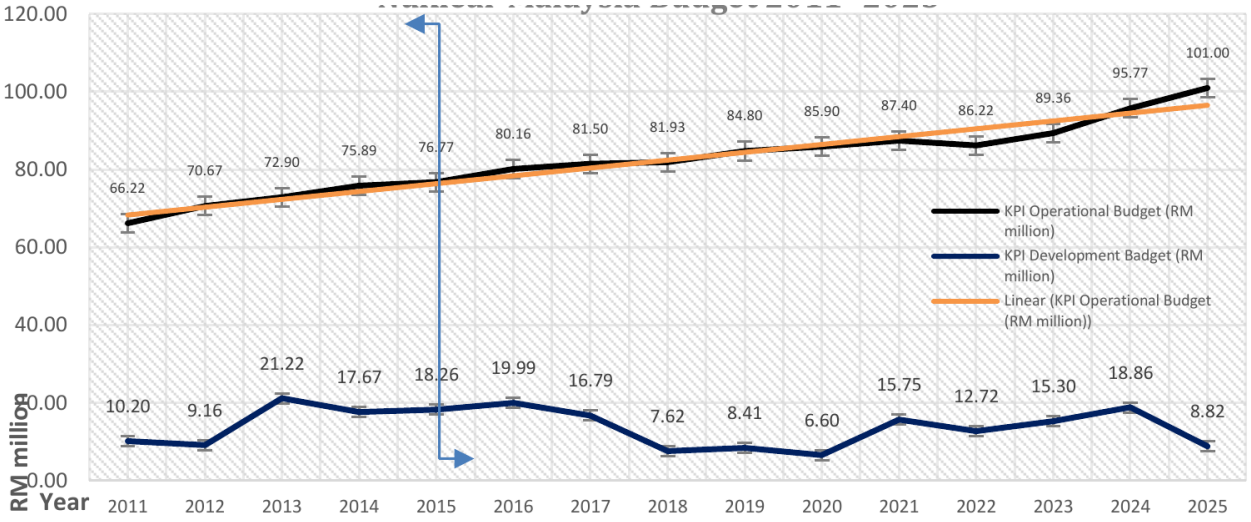



Figure 3: Nuklear Malaysia budget 2011 to 2025

To secure an annual budget, an organization has taken several steps, as outlined in the following PBB/OBB approach:

i Ministries, such as MOSTI, need to develop a Ministerial OBB Framework with Outcome and Output KPIs at both the ministry and program levels, while agencies within the activity-level OBB framework design and align their plans with the ministry, specifying KPIs based on their functions and contributions to national goals.

ii Performance reporting and evaluation of KPI outcomes and outputs are conducted quarterly at the ministry, program, and activity levels, while the Ministry of Finance (MOF) has introduced a procedure within the annual budget cycle to systematically assess performance across ministries and their agencies, providing crucial information for the Budget Review Officer to facilitate the screening of new budget requests.

iii The approved budget for all ministries will be documented in the National Budget Book, which will also include performance targets to be reviewed and commented on by the country's policymakers in Parliament.

iv During the budget review session, questions will be asked by the Honorable Members of Parliament and answered by the respective minister in charge which can include the performance target of each minister.

v The Supply Bill, also known as the budget for the new year, must be passed by a vote in both the Dewan Rakyat and Dewan

## 4 Discussion

Performance Assessment of Nuklear Malaysia presented to the BRO shown in Figure 4.

The lessons learned in securing a budget involving performance, include setting realistic objectives for achievable indicators, prioritizing programs with a genuine service delivery component at the national level, and considering analytical data and constraints.

Fig 3. Performance analysis (KPI Outcomes) during Budget Review by MOF in 2025

| NO | KPI OUTCOME (KP NUKLEAR MALAYSIA) | 2020 | 2021 | 2022 | 2023 | SASARAN 2024 | PENCAPAIAN Q1/ 2024 (SEHINGGA 31 MAC 2024) | SASARAN 2025 |
|---|---|---|---|---|---|---|---|---|
| 1 | Peratusan Projek R&D yang aktif pada tahun semasa | (P) : 187 - (S) : 150 | 263 - 160 | 209 - 170 | 201 - 200 | 190 | | 170 |
| 2 | Peratus Peningkatan khidmat pakar dalam bidang teknologi nuklear | (P) : 263 - (S) : 270 | 367 - 290 | 266 - 230 | 407 - 230 | 230 | | 460 |
| 3 | Kadar Penambahan pemindahan teknologi nuklear kepada industri dan komuniti | (P) : 17 - (S) : 23 | 29 - 25 | 23 - 20 | 28 - 20 | 21 | | 21 |
| 4 | Kadar kejayaan kerjasama strategik dengan stakeholder (dalam dan luar negara) | (P) : 93% - (S) : 100% | 76% - 95% | 92.71% - 95% | 52.86% - 95% | 95% | | 95% |
| 5 | Peratus perlaksanaan fungsi sebagai Pihak Berkuasa Kebangsaan CTBT | (P) : 100% - (S) : 100% | 93.33% - 100% | 112.5% - 100% | 100% - 100% | 100% (16 Aktiviti-laporan dirancang) | | 100% (9 Aktiviti-laporan dirancang) |

Figure 4: Performance analysis (KPI Outcome) during Budget Review by MOF in 2025

## 5 Challenges

The success of this initiative hinges on bridging the gap in personnel capacity, ensuring the necessary skills and knowledge in evaluating and interpreting the performance indicators reported through the MyResult MOF portal, ultimately enabling informed decision-making and improved outcomes.

## 6 Conclusion

The implementation of OBB has ensured a consistent method for documenting and validating the linkages between budget activities and ministerial strategies, enabled the MOF to identify potential duplication across agencies, improved internal governance and decision-making, leading to a more transparent and efficient system.

## References

C. Bernard Myers and Robert Boothe. 2018. Budgeting for performance in malaysia. Technical report, World Bank Group.

Individual Research Contribution Review, 2024: 450–451
*ISSN: 3083-922X*

# CTBT National Data Centre: Roles and Function

**Rozilawati Mohd Japar**
Planning and International Relation Division, Malaysian Nuclear Agency
43000 Kajang, Selangor
rozilawati@nm.gov.my

## Abstract

On July 23, 1998, the Malaysian Nuclear Agency (Nuclear Malaysia) became the National Authority for the Comprehensive Nuclear-Test-Ban Treaty (CTBT) in Malaysia. Malaysia ratified the Treaty on January 17, 2008. After approval, Nuclear Malaysia built the CTBT National Data Center (CTBT-NDC) or also known as My-NDC. This paper aims to clarify the roles and functions of CTBT-NDC, which provides technical support to the CTBT National Authority and promotes the use of IMS and IDC data for civil and scientific applications.

**Keywords:** National Data Centre, CTBT-NDC, Nuclear weapons

## 1 Introduction

Nuclear weapons endanger global security, with developments spurred by contentious testing that give data on efficacy while harming health and the environment. In response to worldwide pressure, the 1996 Comprehensive Nuclear-Test-Ban Treaty (CTBT) prohibits all nuclear explosions and gives Member States the authority to investigate any breaches, including on-site inspections. The International Data Centre (IDC) is at the heart of this, analyzing data from 337 global monitoring facilities. To meet the demand for independent analysis, National Data Centers were established, allowing Member States to undertake in-house reviews and give technical assistance to national authorities (Comprehensive Nuclear-Test-Ban Treaty Organization (CTBTO), 2024a). CTBT-NDCs were initially focused on verification, but they now advocate the use of monitoring data for civic and scientific reasons, expanding their significance in global security and other uses.

## 2 Methods

In terms of monitoring data, CTBT-NDC receives 4 types of monitoring data including seismic, hydroacoustic, infrasound and radionuclide data which are transmitted from IDC either via Virtual Private Network (VPN) or Very-Small-Aperture Terminal (VSAT) with the process flow given in Figure 1. Seismic, hydroacoustic, and infrasound data are classed as waveform. These monitoring data obtained at CTBT-NDC were further analyzed using the NDC-in-a-box software to determine the nature of any suspicious events that may be connected to nuclear weapon testing (Comprehensive Nuclear-Test-Ban Treaty Organization (CTBTO), 2024b).

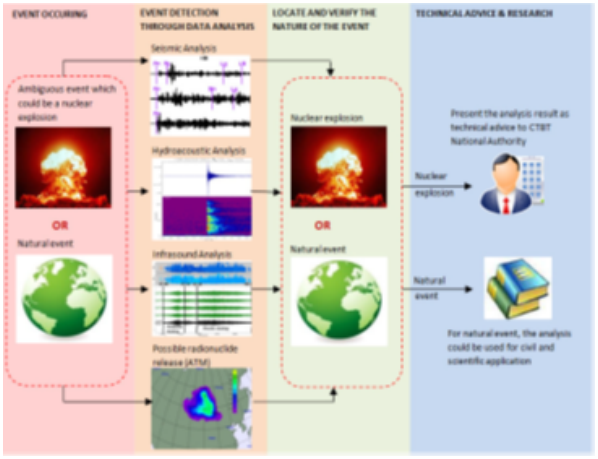



Figure 1: Process flow to analyze monitoring data for verification on the nature of an ambiguous event.

Any incident that transpired may be a nuclear weapon test or a natural disaster such as an earthquake. This event may result in seismic, hydroacoustic, and infrasound waves, as well as the discharge of radioactive particles. The emitted waves and radionuclides will be detected by IMS stations globally. The data from the IMS station will be transferred to CTBT-NDC via IDC. Next, CTBT-NDC will analyze the data to determine the event's type and location. If the occurrence is verified as a nuclear explosion, the CTBT-NDC will report the findings to the CTBT National Authority for further action (Comprehensive Nuclear-Test-Ban Treaty Organization (CTBTO), 2024c). If an event is categorized as a natural occurrence, the analysis will be recorded and can be used for civil and scientific application.

## 3 Results

The CTBT-NDC analysis process, which used the NDC-in-a-box software and monitoring data, was found to be reliable in giving essential information about any ambiguous nuclear explosive occurrence. Critical information could include the time and location of the suspicious occurrence, the magnitude of the seismic wave, and, in some cases, an estimate of the scale of the explosion. The waveform data (seismic, hydroacoustic, and infrasound) could promptly and precisely identify the incident while also determining the amplitude of

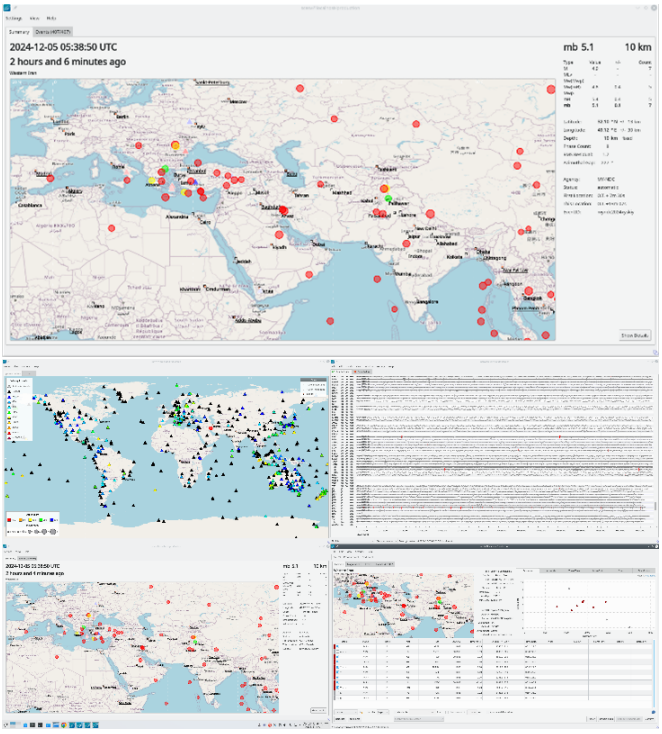



Figure 2: Example of seismic event monitoring map detected in Western Iran (2024-12-05, 05:38:50 UTC).

the wave caused by the nuclear explosion. The analysis result using seismic data alone might correctly locate the event with a small area of uncertainty as shown the example given by Figure 2.

## 4 Discussion/Conclusion

### 4.1 Discussion

The analytical results reported in the previous section clearly demonstrated the capabilities of CTBT-NDC's monitoring data to consistently identify nuclear weapon tests while also providing crucial information about the nuclear test. The information on the suspicious event proves to be extremely valuable to the CTBT National Authority in making an informed decision on the nature of the suspicious event, as well as considering exercising their right to request OSI when the Treaty is in force if the event is truly a nuclear weapons test.

### 4.2 Conclusion

The CTBT-NDC's major responsibility within the Treaty framework is to give close assistance to the CTBT National Authority in order to ensure compliance with Treaty stipulations. Close support might take the form of technical advice on a questionable occurrence, such as a nuclear bomb test. Thus, having the capacity to analyse monitoring data in-house is critical because it provides a check-and-balance to the IDC's analytical results.

## References

Comprehensive Nuclear-Test-Ban Treaty Organization (CTBTO). 2024a. History of the international data centre. http://www.ctbto.org/verification-regime/the-international-data-centre/history-of-the-international-data-centre.

Comprehensive Nuclear-Test-Ban Treaty Organization (CTBTO). 2024b. Ndc-in-a-box: A toolkit for national data centres. https://www.ctbto.org/verification-regime/ndc-in-a-box.

Comprehensive Nuclear-Test-Ban Treaty Organization (CTBTO). 2024c. The role of ndcs in verifying nuclear test bans. https://www.ctbto.org/national-data-centres.

Individual Research Contribution Review, 2024: 452–453
*ISSN: 3083-922X*

# Glabellan: Advancing from Process Development and IP Protection to Product Formulation and Validation

**Shaiful Azuar Mohamad**
Planning and International Relation Division, Malaysian Nuclear Agency
43000 Kajang, Selangor
azuar@nm.gov.my

## Abstract

The patent for the innovative process of producing polysaccharides from a mushroom strain is currently in the filing stage. This process utilizes submerged culture fermentation (SCF), a method that allows for the efficient cultivation of the fungal biomass under controlled conditions. After cultivation, the biomass undergoes an extraction process to isolate the polysaccharides, which are the core bioactive components of interest. These polysaccharides have been successfully trademarked under the name *Glabellan*.

**Keywords:** submerged culture fermentation, patent, trademark, product validation, *Glabellan*

## 1 Introduction

For intellectual property protection, several key mechanisms are available to safeguard innovations. These include patents, trademarks, copyrights, industrial designs, and trade secrets. Each of these tools serves a distinct purpose in protecting various aspects of a product or process.

The process of producing polysaccharides from submerged culture fermentation (SCF) was first documented in a publication by Mohamad et al. (2015) providing an early scientific basis for the innovation. Building on this work, the patent for the process was filed in 2018 to secure exclusive rights to the methodology and its applications. However, the time gap between the initial publication and the patent filing has raised some challenges as well as some issues during the Covid period.

The trademark for the product was successfully registered in 2022, marking a significant milestone. However, several attempts to secure grants for validation and pre-commercialization faced considerable challenges. In order to overcome these obstacles and advance the project, the researchers partnered with a company to develop a finalized product and conduct independent testing.

The current stage is often referred to as the "death valley" in product development—a critical phase where many promising innovations fail due to a lack of resources, technical hurdles, or market readiness. For *Glabellan*, overcoming the death valley will require a strategic approach that includes demonstrating the production feasibility, building industry partnerships, and securing funding. Successfully navigating this phase will enable *Glabellan* to transition from a promising laboratory discovery to commercial side of innovations.

## 2 Methods

*Pleurotus sp.* mycelium was initially cultured in petri dishes using the stock culture. The mycelium was subsequently transferred to a shake flask for further growth, followed by scaling up in a bioreactor to maximize biomass production. After harvesting, the biomass was dried and subjected to an extraction process to isolate the polysaccharides, which are trademarked as *Glabellan*.

The polysaccharide was initially produced in the laboratory at the Malaysian Nuclear Agency. The company then used the known and already tested concentration of polysaccharides to formulate the final product. Volunteers were subsequently selected to test and validate the finalized product for testimonial purposes.

## 3 Data/Results

In collaboration with the company working alongside the researchers, a product was developed for further testing and data collection. The sample of the final product are shown below in Figure 1.



Figure 1: Final product utilizing *Glabellan* as one of its ingredients

The data collected from the volunteers are currently still undergoing collection process. This stage involves organizing the various data points gathered during the testing, which includes feedback on product efficacy, safety, and any observed side effects or benefits.

These results will also help establish a strong case for regulatory approval and certification. Additionally, they will provide valuable insights into potential market acceptance, con-

sumer preferences, and identify areas that may require further improvement to optimize the product for its target audience.

## 4 Discussion/Conclusions

The trademark has been successfully registered, while the patent is still undergoing the examination process. Significant hurdles remain to be addressed before progressing to the next phase. The results from the volunteer testing will play a crucial role in advancing to the next stage of pre-commercialization.

## 5 Acknowledgments

Acknowledgement to the team members from BAB, BTP and the following students which are, Ilya Syakirah Abdul Rahim and Nur Adrianna Adam from UKM for assisting with the experimental works during their attachment at Nuclear Malaysia.

## References

Shaiful Azuar Mohamad, Mat Rasol Awang, Rusli Ibrahim, Choong Yew Keong, Mohd Yusof Hamzah, Rosnani Abdul Rashid, Sobri Hussein, Khairuddin Abdul Rahim, Fauzi Daud, Aidil Abdul Hamid, et al. 2015. Production of endopolysaccharides from malaysia's local mushrooms in air-lift bioreactor. *Advances in Bioscience and Biotechnology*, 6(07):456.

Individual Research Contribution Review, 2024: 454–455
*ISSN: 3083-922X*

# Research Distribution and Impact: A Strategic Assessment of Malaysian Nuclear Agency's R&D Portfolio (2024)

**Siti Najila Mohd Janib**
Research Management Centre, Malaysian Nuclear Agency
43000 Kajang, Selangor
najila@nm.gov.my

## Abstract

The Malaysian Nuclear Agency (Nuklear Malaysia) faces increasing challenges in optimizing its research portfolio amid evolving nuclear technology landscapes and resource constraints. This study presents a systematic analysis of research distribution and impact across Nuklear Malaysia's six technical divisions during 2024. Analysis of 148 research projects reveals an imbalanced portfolio with strong emphasis on industrial applications (23.6%) and nuclear applications in agriculture (21.6%), while critical areas of nuclear medicine and radiation safety show concerning underrepresentation (8.8% each). Technology Readiness Level assessment demonstrates significant disparities in technology maturation across focus areas, with industrial applications achieving implementation stages while safety-critical domains remain in early development. Publication analysis of 299 outputs reveals heavy reliance on technical documentation (58.5%) with critically low international visibility (2.3% in high-impact journals), indicating substantial gaps in research translation and global engagement.

**Keywords:** nuclear science and technology, technology readiness level, research output analysis

## 1 Introduction

Nuklear Malaysia's mandate in advancing nuclear science and technology faces unprecedented challenges in the current technological landscape. While the National Nuclear Technology Policy 2030 provides strategic direction, the institution grapples with fundamental questions of portfolio optimization and resource allocation. The critical need for balanced development across nuclear applications, particularly in safety and medical domains, demands systematic evaluation of current research distribution and impact.

This study addresses these challenges through comprehensive analysis of project distribution, research maturity, and scientific impact. The findings carry significant implications for strategic planning and research prioritization at the Agency.

## 2 Methods

This study employed a multi-dimensional analytical framework to evaluate Nuklear Malaysia's research portfolio across three critical domains: project distribution, technological maturity, and research impact. Data collection encompassed comprehensive institutional records from 2024, including research project documentation (N=148), publication outputs (N=299), and research and development deliverables (N=121).

The analytical framework integrated both quantitative and qualitative assessments. Projects were categorized using a hierarchical classification system aligned with the National Nuclear Technology Policy 2030 (DTNN 2030) focus areas. Technology Readiness Level (TRL) assessments employed standardized evaluation criteria, with particular attention to progression pathways in safety-critical domains. Publication impact analysis extended beyond simple metrics to examine patterns of research translation and international engagement.

## 3 Results

Analysis of Nuklear Malaysia's research portfolio revealed three key dimensions of performance: divisional research distribution, strategic focus areas, and research translation effectiveness. At the divisional level, research activities showed distinct operational patterns (Figure 1). The Radiation Processing Technology Division (BTS) led with 32 projects (21.6%) and demonstrated efficient conversion to 25 R&D outputs. The Agrotechnology and Biosciences Division (BAB) managed 28 projects (18.9%), while the Industrial Technology Division (BTI) executed 27 projects (18.2%). The Technical Support Division (BST) and Waste Technology and Environment Division (BAS) maintained balanced portfolios of 25 (16.9%) and 23 (15.5%) projects respectively. The Medical Technology Division (BTP) managed 13 projects (8.8%).

Strategic focus areas demonstrated varying levels of emphasis and maturity (Figure 2). Industrial applications represented the largest segment (23.6%), followed by food and agriculture (21.6%), both showing advanced technology readiness levels. Device and equipment manufacturing (18.9%) and environmental management (16.9%) exhibited balanced development stages, while medical applications (10.1%) and nuclear safety research (8.8%) remained predominantly in early development phases.

Research translation effectiveness varied across the organization (Figure 3). Publication analysis revealed BTI's strong performance (89 publications, 29.8%), followed by BAS (42, 14.0%) and BAB (38, 12.7%). Technical documentation dominated outputs (58.5%), with limited representation in high-impact international journals (2.3% in Q1/Q2). This pattern

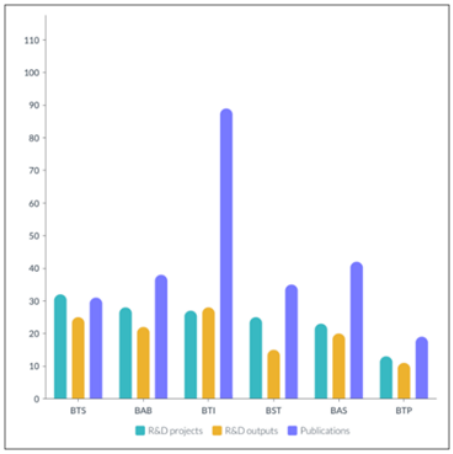



Figure 1: **Research output distribution across nuclear technology divisions (2024)**. Comparative analysis showing divisional patterns in research projects, publications, and R&D outputs, highlighting BTI's publication dominance (29.8%) and BTS's balanced performance across metrics.

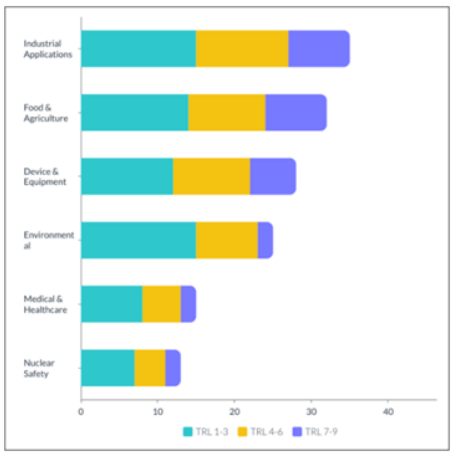



Figure 2: **Technology maturity assessment by research focus area (2024)**. Distribution of Technology Readiness Levels (TRL 1-9) across research domains, highlighting mature implementation in Industrial Applications and Food & Agriculture, while showing early-stage concentration in Environmental Management and Nuclear Safety.

suggests opportunities for enhancing research visibility while maintaining robust technical documentation.

## 4 Discussion

The analysis reveals important patterns in Nuklear Malaysia's research portfolio distribution, technology maturation, and research translation. Across technical divisions, the varying levels of R&D output conversion indicate different approaches to research execution and delivery. While some divisions demonstrate balanced output patterns, others show specialized

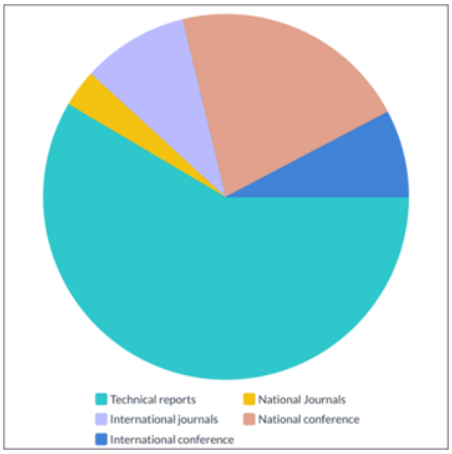



Figure 3: **Publication profile distribution in nuclear research (2024)**. Analysis of research outputs (N=299) showing distribution across publication types, highlighting predominance of technical reports (58.5%) and relative proportion of international publications (17.1%). Publication categories include technical reports, conference papers (national and international), and journal articles.

strengths in specific domains, suggesting opportunities for cross-divisional learning and resource optimization.

Focus area analysis highlights the institution's capacity to advance certain technological domains while maintaining development across others. The advanced maturity levels in industrial and agricultural applications demonstrate successful technology development pathways that could inform approaches in other domains. The early-stage concentration of environmental and safety projects presents opportunities for accelerated development through structured technology maturation approaches.

Publication patterns across divisions reflect broader institutional approaches to research documentation and communication. The strong technical documentation base provides a foundation for enhancing international research visibility through systematic translation of technical findings into scholarly outputs. BTI's publication profile offers insights for developing institutional approaches to research communication while preserving operational documentation strengths.

These findings suggest opportunities for strategic portfolio enhancement through integrated approaches to research management and technology development. Future initiatives should focus on leveraging existing institutional strengths while developing targeted approaches for accelerating technology maturation and enhancing research impact across all do.

Individual Research Contribution Review, 2024: 456–457
*ISSN: 3083-922X*

# Quarter Century of Progress: Malaysia's Nuclear Technology Journey Through FNCA Collaboration

**Siti Syarina Mat Salo**
Planning and International Relation Division, Malaysian Nuclear Agency
43000 Kajang, Selangor
sitisyarina@nm.gov.my

## Abstract

Over the past 25 years, Malaysia has actively participated in the Forum for Nuclear Cooperation in Asia (FNCA), contributing to collaborative efforts to advance nuclear science and technology for socio-economic development in Asia. Since joining as a founding member in 1999, Malaysia has engaged in 15 FNCA projects and attended 193 workshops and meetings. This paper explores Malaysia's participation over the past 25 years, focusing on its contributions to FNCA projects and their impact on national development.

**Keywords:** FNCA, nuclear science and technology

## 1 Introduction

The FNCA was established in 1999 as a collaborative effort to enhance the peaceful use of nuclear technology and foster closer cooperation among Asian countries in the field of nuclear technology (FNCA, 2024b). With 12 member countries (Australia, Bangladesh, China, Indonesia, Japan, Kazakhstan, South Korea, Malaysia, Mongolia, the Philippines, Thailand, and Vietnam), the FNCA provides a platform for sharing knowledge and expertise, as well as implementing collaborative projects (Machi, 2008). As a founding member, Malaysia has consistently participated in FNCA activities, aligning its national priorities with regional efforts to leverage nuclear science and technology for sustainable development (Machi, 2004). To facilitate this, the Malaysian Nuclear Agency (Nuklear Malaysia) has been assigned as the national coordinator for FNCA-related matters, demonstrating Malaysia's continued support for regional nuclear cooperation. This paper underscores FNCA's role in fostering regional collaboration and highlights Malaysia's potential for further contributions in sustainable nuclear technology development.

## 2 Methods

The study utilizes a mixed-method approach, combining quantitative analysis and qualitative assessment.

For the quantitative analysis, participation data was collected from records of FNCA projects, workshops, and meetings. The data spans from 1999 to 2024, covering metrics such as the number of projects participated and project areas of focus.

In the qualitative assessment, the outcomes of key FNCA projects were evaluated to determine their impact on Malaysia's overall growth and technological advancements. The assessment includes case studies on FNCA projects in mutation breeding, radiation processing and polymer modification, cyclotron and PET in medicine, radiation safety, and radioactive waste management

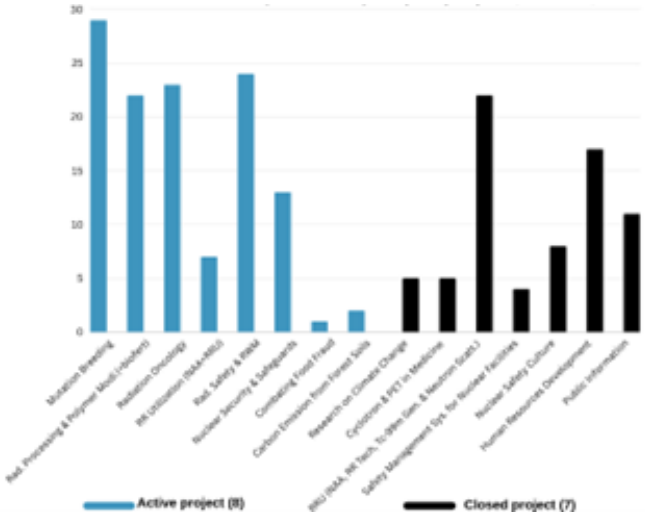



Figure 1: Number of workshops attended by Malaysia by projects (1999-2024

## 3 Data/Results

### 3.1 Overview of participation in FNCA activities

Since joining the FNCA in 1999, Malaysia has actively engaged in the FNCA collaborative initiatives aimed at advancing nuclear science and technology. To date, Malaysia has participated in 25 FNCA Ministerial Level Meetings (MLM), Senior Officials Meetings (SOM), and 24 Coordinator Meetings (CDM), demonstrating its continued leadership and commitment under the FNCA framework (FNCA, 2024a).

Over the past 25 years, Malaysia has also participated in 15 FNCA projects across four primary areas: radiation utilization development, research reactor utilization development, nuclear safety strengthening, and nuclear infrastructure strengthening as can be seen in Figure 1. Additionally, Malaysian representatives have attended a total of 193 FNCA project workshops, facilitating extensive knowledge exchange and capacity building.

### 3.2 Key Achievements from FNCA Projects

#### 3.2.1 Mutation Breeding for Sustainable Agriculture

Leveraging the knowledge shared through FNCA's platform for mutation breeding, Malaysia has made significant contributions to the development of advanced rice varieties with enhanced resistance to environmental stresses such as drought and salinity. These advancements have played a key part in enhancing food security and improving the livelihoods of farmers. Moreover, Malaysia has made notable progress in breeding disease-resistant bananas, insect-resistant orchids, and drought-tolerant soybeans, further advancing crop resilience. In recognition of these achievements, Malaysia was awarded the 2020 FNCA Excellent Research Team Award and the 2021 FNCA Excellent Researcher Breakthrough Prize, under this project.

#### 3.2.2 Radiation Processing and Polymer Modification for Agricultural Applications

Malaysia's involvement in radiation processing and polymer modification projects has contributed to the creation of high-quality, multifunctional biofertilizers. These biofertilizers, derived from natural polymers, provide an eco-friendly alternative to chemical fertilizers and have demonstrated the ability to improve agricultural productivity. Additionally, research has explored the synthesis of plant growth promoters (PGPs) through radiation degradation techniques, yielding positive effects on crop yields. Through workshops, shared projects, and information exchange, FNCA has contributed to enhancing Malaysia's capabilities in radiation processing, accelerating the development of sustainable agricultural solutions.

#### 3.2.3 Cyclotron and PET in Medicine

From 2006 to 2011, Malaysia took a leading role in the FNCA Cyclotron and PET in Medicine project, working alongside other FNCA member countries to improve the use of nuclear technology in healthcare. This collaboration led to the development of two important guidelines that have positively contributed both Malaysia and other FNCA member countries.

The first guideline, the "Guideline for Radiation Protection and Performance Evaluation of PET-CT Imaging," ensures the safe use of PET-CT systems while meeting performance standards for accurate diagnostics. The second guideline, the "Guideline for Quality Assurance and Quality Control of 18F-FDG Production," provides a framework to produce 18F-FDG, a key radiopharmaceutical used in PET scans. These guidelines have not only enhanced the quality and safety of PET-CT imaging in Malaysia but have also been shared with other FNCA member countries, contributing to the regional advancement of nuclear medicine.

#### 3.2.4 Radiation Safety and Radioactive Waste Management

Through collaboration within the FNCA, Malaysia has strengthened its radiation safety and radioactive waste management practices. This has been achieved through joint research, specialized workshop programs, and the use of consolidated reports that summarize key findings and progress. These reports have helped improve safety protocols to protect both people and the environment. By sharing knowledge, best practices, and insights from these consolidated reports, Malaysia has been able to adopt better methods for handling radiation and managing radioactive waste, ensuring a safer and more sustainable approach to these challenges.

## 4 Discussions/Conclusions

FNCA collaborations have a positive impact on Malaysia by enhancing its knowledge and capabilities in various non-power nuclear applications. Through collaborative projects, Malaysia has gained access to valuable expertise and resources in areas such as food and agriculture, medical and healthcare applications, environment, radiation safety and radioactive waste management. The collaborations foster regional cooperation, allowing Malaysia to share expertise and contribute to joint efforts in promoting safe and effective use of nuclear technology for peaceful purposes.

## References

FNCA. 2024a. Country report: Malaysia. presented at the fnca ministerial level meeting, tokyo, japan. https://www.fnca.mext.go.jp/.

FNCA. 2024b. Summary of fnca ministerial level meetings. https://www.fnca.mext.go.jp/.

Sueo Machi. 2004. Nuclear technology for sustainable development and fnca activities. In *Proceedings of the FNCA 2002 workshop on the utilization of research reactors*. Japan Atomic Energy Research Institute.

Sueo Machi. 2008. International cooperation of japan in asia for nuclear technology and application. In *The 16th pacific basin nuclear conference. Pacific partnership toward a sustainable nuclear future [2022]*. Atomic Energy Society of Japan.

Individual Research Contribution Review, 2024
*e-ISSN: 3083-922X*



eISSN 3083-922X

**The foto of fake fossilized spider where the 3D neutron tomographic image is at the frontpage.**

Back cover